U.S.NRC
United States Nuclear Regulatory Commission
Protecting People and the Environment

NUREG/CR-7287

Numerical Modeling of Local Intense Precipitation Processes

Office of Nuclear Regulatory Research

AVAILABILITY OF REFERENCE MATERIALS IN NRC PUBLICATIONS

NRC Reference Material

As of November 1999, you may electronically access NUREG-series publications and other NRC records at the NRC's Library at www.nrc.gov/reading-rm.html. Publicly released records include, to name a few, NUREG-series publications; *Federal Register* notices; applicant, licensee, and vendor documents and correspondence; NRC correspondence and internal memoranda; bulletins and information notices; inspection and investigative reports; licensee event reports; and Commission papers and their attachments.

NRC publications in the NUREG series, NRC regulations, and Title 10, "Energy," in the *Code of Federal Regulations* may also be purchased from one of these two sources:

1. **The Superintendent of Documents**
   U.S. Government Publishing Office
   Washington, DC 20402-0001
   Internet: https://bookstore.gpo.gov/
   Telephone: (202) 512-1800
   Fax: (202) 512-2104

2. **The National Technical Information Service**
   5301 Shawnee Road
   Alexandria, VA 22312-0002
   Internet: https://www.ntis.gov/
   1-800-553-6847 or, locally, (703) 605-6000

A single copy of each NRC draft report for comment is available free, to the extent of supply, upon written request as follows:

Address: **U.S. Nuclear Regulatory Commission**
Office of Administration
Digital Communications and Administrative Services Branch
Washington, DC 20555-0001
E-mail: Reproduction.Resource@nrc.gov
Facsimile: (301) 415-2289

Some publications in the NUREG series that are posted at the NRC's Web site address www.nrc.gov/reading-rm/doc-collections/nuregs are updated periodically and may differ from the last printed version. Although references to material found on a Web site bear the date the material was accessed, the material available on the date cited may subsequently be removed from the site.

Non-NRC Reference Material

Documents available from public and special technical libraries include all open literature items, such as books, journal articles, transactions, *Federal Register* notices, Federal and State legislation, and congressional reports. Such documents as theses, dissertations, foreign reports and translations, and non-NRC conference proceedings may be purchased from their sponsoring organization.

Copies of industry codes and standards used in a substantive manner in the NRC regulatory process are maintained at—

The NRC Technical Library
Two White Flint North
11545 Rockville Pike
Rockville, MD 20852-2738

These standards are available in the library for reference use by the public. Codes and standards are usually copyrighted and may be purchased from the originating organization or, if they are American National Standards, from—

American National Standards Institute
11 West 42nd Street
New York, NY 10036-8002
Internet: www.ansi.org
(212) 642-4900

Legally binding regulatory requirements are stated only in laws; NRC regulations; licenses, including technical specifications; or orders, not in NUREG-series publications. The views expressed in contractor prepared publications in this series are not necessarily those of the NRC.

The NUREG series comprises (1) technical and administrative reports and books prepared by the staff (NUREG–XXXX) or agency contractors (NUREG/CR–XXXX), (2) proceedings of conferences (NUREG/CP–XXXX), (3) reports resulting from international agreements (NUREG/IA–XXXX),(4) brochures (NUREG/BR–XXXX), and (5) compilations of legal decisions and orders of the Commission and the Atomic and Safety Licensing Boards and of Directors' decisions under Section 2.206 of the NRC's regulations (NUREG-0750), (6) Knowledge Management prepared by NRC staff or agency contractors (NUREG/KM-XXXX).

U.S.NRC
United States Nuclear Regulatory Commission
Protecting People and the Environment

NUREG/CR-7287

Numerical Modeling of Local Intense Precipitation Processes

Manuscript Completed: July 2023
Date Published: July 2023

Prepared by:
M. Levent Kavvas
M. Mure-ravaud
A. Dib
K. Ishida

Hydrologic Research Laboratory
Department of Civil & Environmental Engineering
University of California, Davis
1 Shields Avenue
Davis, CA 95616

Elena Yegorova, NRC Project Manager

Office of Nuclear Regulatory Research

ABSTRACT

Tropical Cyclones (TCs) and Mesoscale Convective Systems (MCSs) are recognized for their ability to generate intense precipitation that may in turn create disastrous floods. In this study, the suitability of the Weather Research and Forecasting (WRF) model to simulate local intense precipitation processes within severe MCSs and TCs was first assessed. Simulation results were compared with observations from the Stage IV precipitation dataset. Under an appropriate choice of the model's options, the model could reproduce the location, intensity, and structure of the intense precipitation fields. Second, physically-based storm transposition methods for the storm transpositions of MCSs and TCs were developed and applied to one MCS and four TCs. In each case, the objective was to find the amount of shift which maximizes the precipitation depth over a target area. Finally, future conditions from a General Circulation Model were downscaled over two regions (one for MCSs and one for TCs). The most intense future MCS and TC were then transposed to maximize the precipitation depth over the target area.

FOREWORD

The hurricane season in 2017 was a striking reminder of the destructive potential of storm systems affecting the United States. Hurricane Harvey is an emblematic example. It was the deadliest U.S. hurricane in terms of direct deaths since Hurricane Sandy (2012), the deadliest hurricane hitting Texas since 1919 and it tied Hurricane Katrina (2005) as the costliest U.S. Tropical Cyclone (TC) with $125 billion in damage. It produced exceptional rainfall over some of the most densely populated areas of the Gulf Coast including Houston, Texas with peak accumulation of 1539 mm (60.6 in.) near Nederland, Texas (Blake and Zelinsky, 2018). While the eastern U.S. often receives its most intense precipitation from TCs, other regions in the country may suffer from other types of storm systems with a wide range of spatial and temporal scales. Mesoscale Convective Systems (MCSs) are an example of storm events that can generate local extreme precipitation in several regions of the U.S. and in particular in the Midwest region. These systems are organized collections of several cumulonimbus clouds which interact at the regional-scale to form an extensive and nearly contiguous region of precipitation. Over the past decades, numerical modeling by means of regional atmospheric models (RAMs) has been put forward as a rigorous and increasingly efficient way to predict and reconstruct these storms, thus providing tremendous possibilities in better understanding their behaviors and structures. The Hydrologic Research Laboratory at the University of California Davis has extensive expertise in the numerical modeling of storm systems, especially atmospheric rivers in the Western U.S. (Ishida et al., 2014; Ohara et al., 2011a). This report summarizes the results from the project “Numerical Modeling of Local Intense Precipitation Processes” which aims at extending this numerical modeling effort to MCSs and TCs. Both storm systems differ in a considerable way from atmospheric rivers in terms of their spatial scales, temporal scales, and overall structures and behaviors. The Weather Research and Forecasting (WRF) model was first used to reconstruct several historical MCSs and TCs without nudging or data assimilation, thus proving the suitability of a RAM to simulate local intense precipitation processes within both storm systems. Storm transposition methodologies were then developed by accounting for the specificities of these storms and applied to one MCS and four hurricanes. Finally, future conditions were investigated by downscaling the Community Climate System Model version 4 (CCSM4) based on Representative Concentration Pathway (RCP) 4.5.

This work was supported by the U.S. Nuclear Regulatory Commission funded grant via the United States Geological Survey (USGS) Water Resources Research Act Program (Grand Award Number: SA14-2426-01).

TABLE OF CONTENTS

LIST OF FIGURES

LIST OF TABLES

EXECUTIVE SUMMARY

This report is the NUREG/CR Report for the project “Numerical Modeling of Local Intense Precipitation Processes”. It includes the major project accomplishments during the formal period from March 15, 2015 through March 15, 2018. The objective of this project is to assess the suitability of a regional numerical weather model to simulate local intense precipitation processes, and then investigate the physical mechanisms of storm systems that lead to extreme precipitation by means of a regional numerical weather model. As such, this project consists of six tasks. Task 1 is the literature review of local intense precipitation. Task 2 is the work plan development of this project. Task 3 involves the configuration and evaluation of the performance of a selected regional numerical weather model to simulate intense precipitation processes within several extreme Mesoscale Convective Systems (MCSs) and Tropical Cyclones (TCs) by comparing the model results to detailed time-space observations. Task 4 involves the investigation of the physical mechanisms of storm systems leading to local intense precipitation. Also during Task 4, the precipitation fields are maximized. Task 5 involves a knowledge transfer seminar for NRC staff. Finally, Task 6 involves the preparation of the final report for this project.

The Weather Research and Forecasting (WRF) model was used at 5-km resolution without nudging or data assimilation in order to reconstruct the intense precipitation fields associated with several historical MCSs and TCs which affected the United States. The storm events were selected within the time period from 2002 to the present, based on the NCEP Stage IV precipitation dataset, which is a mosaic of regional multi-sensor analysis generated by the NWS River Forecast Centers (RFCs) since 2002. These storms correspond to the most severe storms in the period studied, in terms of the generation of an intense precipitation field containing pockets of extreme rainfall. The model’s simulation nested domains were set up over a region in the Midwest so that the innermost domain covered the severe precipitation areas caused by 14 severe MCSs. However, several sets of simulation nested domains were prepared for the simulations of the TCs because of the diversity in the paths of these systems. While the outer domain was the same for all cases and was chosen so as to cover the paths of all the identified severe TCs, different inner domains were set up so as to include the severe precipitation areas caused by each individual TC. With these sets of simulation nested domains, the WRF model was configured to obtain the best results for the simulation of each of the selected severe MCSs and TCs with respect to the simulated and observed precipitation fields. The simulation results were compared with observations from the Stage IV precipitation dataset. More precisely, on the one hand, simulation results were evaluated by means of several metrics: the relative error for the simulation inner-domain total precipitation, the percentage of overlapping between the simulated and observed fields for several precipitation thresholds, and the precipitation field area ratio. On the other hand, the simulated and observed precipitation fields were plotted so as to visually appreciate the similarities and differences in the fields’ structure and intensity.

It was shown that under an appropriate choice of the model’s options and boundary conditions, the WRF model provided satisfactory results in reproducing the location, intensity, and structure of the intense precipitation fields of the historical MCSs and TCs. The model’s options that were investigated are the parameterization schemes including microphysics, cumulus parameterization, planetary boundary layer physics, long wave and short wave radiation physics, etc. Although certain combinations of the parameterization schemes provided in each case realistic results in terms of the precipitation field structure and intensity, placing these fields in the correct spatial locations required additional efforts, so that the best set of model options varied from one storm system to the other. Besides, the convergence of the vertically integrated vapor transport (IVT) was found to play a central role in the generation of intense precipitation in the simulated TCs.

In this study, the storm transposition of one MCS and four TCs was performed. The storm transposition methods were designed based on the specificities of MCSs and TCs. They are physically based as they use a RAM to numerically simulate the storms and their precipitation fields. As a result, these methods have the fundamental advantage of conserving the mass, momentum, and energy in the system since the RAM numerically solves the equations governing the conservation of these quantities. The objective is to find the amount of shift which maximizes the precipitation depth over a given target area, corresponding to the drainage basin of the city of Houston, MN for the MCS case and to the drainage basin of the city of Asheville, NC for the TC case.

Lastly, The Community Climate System Model version 4 (CCSM4) climate projection based on Representative Concentration Pathway (RCP) 4.5 was downscaled using the WRF model. In the MCS case, downscaling was performed for 2020-2100 using the same nested domains as for the reconstruction. Afterwards the most intense MCS during this time period was identified and transposed over the Houston, MN watershed. In the TC case, downscaling was performed for 2005-2100. 64 landfalling TCs were identified and the most intense TC was then transposed over the Asheville, NC watershed.

ABBREVIATIONS AND ACRONYMS

3D-VAR	Three-Dimensional Variational Data Assimilation
4D-VAR	Four-Dimensional Variational Data Assimilation
ABL	Atmospheric Boundary Layer
ARPS	Advanced Regional Prediction System
BB	Backbuilding/Quasi-Stationary
BC	Boundary Condition
BDA	Bogus Data Assimilation
BRAMS	Brazilian Regional Atmospheric Modeling System
CAPE	Convective Available Potential Energy
CCSM	Community Climate System Model
CCSM4	CCSM version 4
CFSR	Climate Forecast System Reanalysis
CMIP	Coupled Model Intercomparison Project
CMIP3	CMIP Phase 3
CMIP5	CMIP Phase 5
CMR	Central Mountain Range
CPS	Cumulus parameterization scheme
CV	Coefficient of variation
DA	Data assimilation
dBZ	Decibels of Z (Z represents the energy reflected back to the radar)
DD	Dynamical Downscaling
EnKF	Ensemble Kalman filter
ECMWF	European Centre for Medium-Range Weather Forecasts
ENSO	El Niño-Southern Oscillation
EPE	Extreme precipitation event
ERA40	ECMWF 40-year Re-Analysis
ESM	Earth System Model
ET	Extratropical transition
ETC	Extratropical cyclone
GCM	General Circulation Model
GFDL	Geophysical Fluid Dynamics Laboratory
GVAR	Global variable resolution
IBC	Initial and boundary condition
IC	Initial condition
IPCC	Intergovernmental Panel on Climate Change
IVT	Verticaly integrated vapor transport
JMA	Japanese Meteorological Agency
KF CPS	Kain-Fritsch cumulus parameterization scheme

LAM	Limited-area model
LLJ	Low-level jets
LS	Leading stratiform (precipitation mode)
LWR	Long wave radiation
MC2	Mesoscale Compressible Community model
MCC	Mesoscale convective complex
MCS	Mesoscale convective system
MCV	Mesoscale convective vortex
MDR	Main development region
MM5	Pennsylvania State University/National Center for Atmospheric Research mesoscale model
MP	Maximum precipitation
MPP	Maximum possible precipitation
MRI	Meteorological Research Institute
NAM	North American Model
NCAR	National Center for Atmospheric Research
NCEP	National Centers for Environmental Prediction
NCOMMAS	National Severe Storms Laboratory Collaborative Model for Mesoscale Atmospheric Simulation
NOAA	National Oceanic and Atmospheric Administration
NRC	Nuclear Regulatory Commission
NRCM	Nested Regional Climate Model
NSSL	National Severe Storms Laboratory
NWS	National Weather Service
PBL	Planetary boundary layer
PECS	Persistent elongated convective systems
PFAR	Precipitation Field Area Ratio
PGW-DD	Pseudo-global warming dynamical downscaling
PMP	Probable Maximum Precipitation
POM	Princeton Ocean Model
PRE	Predecessor rain event
PS	Parallel Stratiform (precipitation mode)
PW	(Total) precipitable water vapor
RAM	Regional Atmospheric Model
RAMS	Regional Atmospheric Modeling System
RCM	Regional Climate Model
RCP	Representative Concentration Pathway
RFC	River Forecast Center
RIJ	Rear-inflow jet
RMSE	Root-mean-square error
SAL	Saharian air layer
SD	Statistical Downscaling

SLP	Sea-level pressure
SRES	Special Report on Emissions Scenarios
SSHS	Saffir-Simpson Hurricane Scale
SST	Sea surface temperature
SWR	Short wave radiation
TC	Tropical Cyclone
TL/AS	Training Line/Adjoining Stratiform
TRMM	Tropical Rainfall Measuring Mission
TS	Trailing stratiform (precipitation mode) or Topical storm depending on context
TVA	Tennessee Valley Authority
UTC	Coordinated Universal Time
WMO	World Meteorological Organization
WRF	Weather Research and Forecasting
WRF-AWR	Advanced Weather Research WRF

1 LITERATURE REVIEW OF LOCAL INTENSE PRECIPITATION PROCESSES

1.1 Local Intense Precipitation Processes in the United States

According to De et al. (2004), “natural disasters […] wreak havoc and cause tremendous loss of property all over the world”. Easterling et al. (2000b) explained that more than 360 weather events occurred in the United States since 1987, and each of them produced more than $5 million losses. For example Hurricane Andrew (1992) in South Florida caused $30 billion damage while the Midwest flood of 1993 caused $19 billion damage. As population and infrastructure continue to increase, our society has become more vulnerable to extreme events (Easterling et al., 2000a; Kunkel et al., 1999). Flood is an example of a hydro-meteorological disaster that has a strong societal impact. In the United States, floods are the most chronic natural hazard and cause the greatest monetary losses (O'Connor and Costa, 2003). Flood damages increased steadily during the 20th century (Kunkel et al., 1999). While some relate these trends to development and flood policies that enhanced societal vulnerability, others point at the increase in heavy rainfall occurrences in certain regions of the United States (Karl and Knight, 1998; Kunkel et al., 2013; Peterson et al., 2013).

Heavy rainfalls are produced by weather systems spanning a wide range of characteristic lengths and time scales. Several studies have aimed at assigning a meteorological cause to extreme precipitation events. For instance, Maddox et al. (1979) analyzed 151 intense convective precipitation events that caused flash floods in the United States. A flash flood is “a flood caused by heavy or excessive rainfall in a short period of time, generally less than 6 hours ... they can occur within minutes or a few hours of excessive rainfall”[1]. Rainfall from Tropical Cyclones (TCs) was not considered. They classified the events into four categories: “mesohigh”, “frontal”, “western”, “synoptic”, and described the environment typically associated with each category. They observed that several features were common to most of the events. Among them, Maddox et al. (1979) noted that the “storms often occurred during nighttime hours”, and “convective storms and/or cells repeatedly formed and moved over the same area”. This characteristic is detailed in Section 1.2.

Kunkel et al. (2012) used a network of 935 National Weather Service (NWS) Cooperative Observer Program (COOP) stations in the coterminous U.S. for the period from 1908 to 2009 to identify extreme daily precipitation and assign a category of weather events to each of them. An extreme rainfall event was defined as an event exceeding a 5-year return period, which corresponds to a threshold ranging from less than 25 mm (1.0 in.) in some regions of the interior west to more than 200 mm (7.9 in.) along the Gulf Coast. One should note that this definition of an extreme rainfall event leads to select events that are not extreme compared to design levels for critical infrastructures such as large dams and nuclear power plants. They found out that 54% of extreme events were associated with extratropical cyclones (ETCs) near a front, 24% to ETCs near a low pressure center, 13% to TCs, 5% to mesoscale convective systems (MCSs), 3% to North American monsoon, 1% to air mass isolated convection, and 0.1 % to upslope flow. Kunkel at al. also described the regional and seasonal variability of the contribution of each category. While the annual contribution of ETCs near a front is by far the largest in almost all regions in the United States, ETCs near a low pressure center prevail in the Northwest and West, and TCs prevail in the Southeast. While the contribution of MCSs is large during the summer, their contribution is much smaller during the winter.

---

[1] https://www.weather.gov/mrx/flood_and_flash

However, the above results are very sensitive to the definition of an extreme rainfall event. Schumacher and Johnson (2005) performed a Weather Surveillance Radar-1988 Doppler (WSR-88D)-based analysis of a large sample of extreme rain events during 1999-2001 over the eastern two thirds of the United States. Their goal was to document the types of weather systems responsible for extreme precipitation and determine their convective organization. In order to select the events, they used rain gauge data from the NWS cooperative high-resolution 24-hr network (COOP) and the NCDC hourly precipitation dataset (HPD) DSI-3240. In this study, an event was considered as “extreme” if one or more gauges reported a 24-hr rainfall total greater than the 50-year recurrence interval amount for that location determined by Hershfield (1961). This corresponds to a threshold ranging from less than 102 mm (4.0 in.) in some regions of the interior west to more than 330 mm (13.0 in.) along the Gulf Coast. After having selected the events, they classified them either as tropical systems, synoptic systems, or MCSs. MCSs accounted for 65.5% of the events while synoptic systems accounted for 26.7% and tropical systems for 7.8%.

Both studies of Kunkel et al. (2012) and of Schumacher and Johnson (2005) recognize the ability of MCSs, TCs, and ETCs to generate localized extreme precipitation (exceedance of a given threshold amount observed at one station).

1.2 Mesoscale Convective Systems

1.2.1 Description, Classification and Climatology

A MCS is “an organized collection of two or more cumulonimbus clouds that interact to form an extensive region of precipitation” (Trapp, 2013). Contrary to a group of discrete cells, the precipitation in a MCS is nearly contiguous. A MCS has a length scale of 100 km and a time scale of a few hours (~1/*f*, where *f* is the Coriolis parameter), which is much longer than the typical duration of individual cumulonimbi in the mesoscale system (~ 1hour). MCSs are often conceptualized as squall lines, which are systems with a linear or quasi linear shape (Trapp, 2013). The prominent parts of a squall line consist of deep convective updrafts at the leading or downstream edge, an ascending front-to-rear flow, and a descending rear inflow (see Figure 1-1).

Two regions of precipitation are usually observed in a MCS: heavy convective showers in the region of convective updrafts, and stratiform rain whose location relative to the convective region depends significantly on the mid- and upper-tropospheric storm-relative winds (Houze, 2004; Trapp, 2013). The stratiform precipitation usually accounts for between one quarter and one half of the total MCS precipitation (Houze, 1993). Although radar data show that the trailing stratiform (TS) precipitation mode is more frequent in MCSs, leading stratiform (LS) and parallel stratiform (PS) precipitation modes are also frequent (Parker and Johnson, 2004; Trapp, 2013). Figure 1-2 presents idealized life cycles of these three precipitation modes.

The internal circulations of a MCS are influenced by the near-storm environment. In particular, the environmental vertical wind shear plays an important role. For instance, one can use the Rotunno-Klemp-Weisman (RKW) theory (Rotunno et al., 1988) to understand the role of environmental vertical wind shear in MCSs organization. This theory is expressed in terms of a horizontal vorticity balance between a buoyant updraft, a cold pool, and the environmental shear. According to the strength of the positive horizontal vorticity associated with the low-level environmental shear compared to the negative vorticity created by the cold pool, the updraft is either downshear- (see Figure 1-3.c) or upshear- (above the cold pool as it is the case in Figure 1-3.b) tilted.

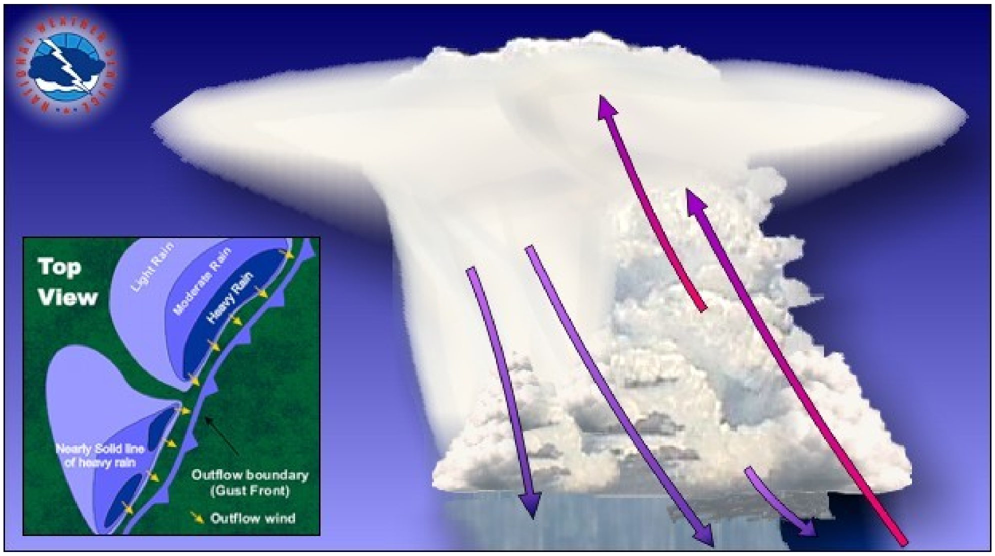

Figure 1-1 **Squall Line Thunderstorm Diagram. From http://www.crh.noaa.gov/images/oun/spotter/training/squallline_schematic.jpg**

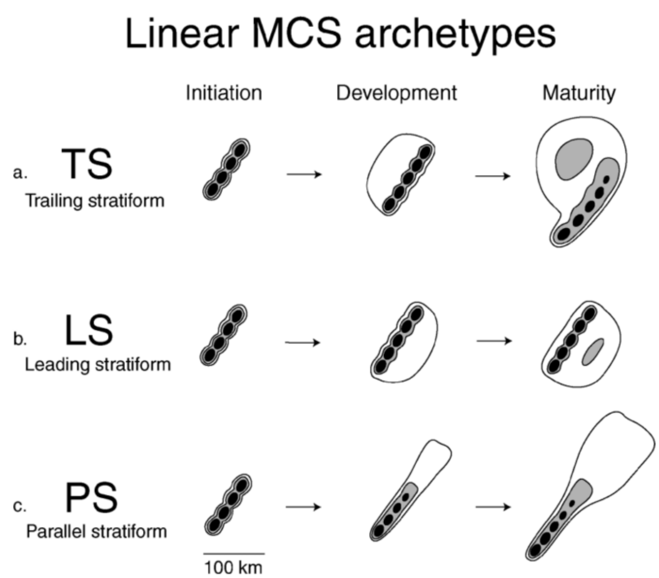

Figure 1-2 **Schematic Reflectivity Drawing of Idealized Life Cycles for Three Linear MCS Archetypes: (a) TS, (b) LS, and (c) PS**

Approximate intervals between phases: for TS 3-4 hr; for LS 2-3 hr; for PS 2-3h. Levels of shading (lighter to darker) roughly correspond to 20, 40 and 50 dBZ (unit for reflectivity; stands for decibels of Z, where Z represents the energy reflected back to the radar). From Parker and Johnson (2000).

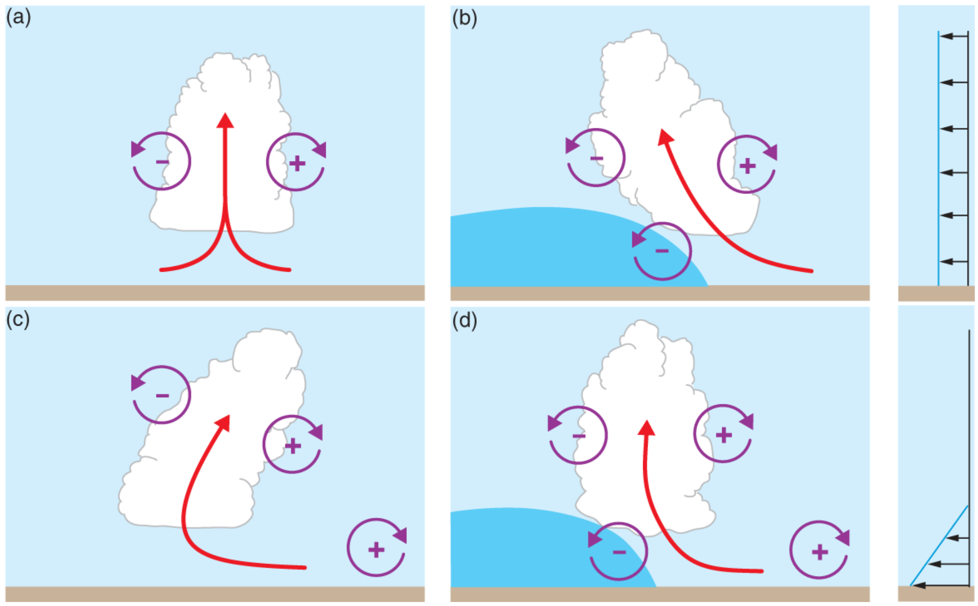

Figure 1-3 Schematic Diagram Showing how a Buoyant Updraft may be Influenced by Environmental Wind Shear and/or a Cold Pool

(a) With no environmental shear and no cold pool, the axis of the updraft produced by the thermally created, symmetric vorticity distribution is vertical. (b) With a cold pool, the distribution is biased by the negative vorticity of the underlying cold pool, causing the updraft to tilt over the cold pool. (c) With the environmental shear and no cold pool, the distribution is biased toward positive vorticity, causing the updraft to lean downshear. (d) With both a cold pool and shear, the two effects may negate each other and promote an erect updraft. Adapted from Rotunno et al. (1988).

Squall lines tend to be downshear-tilted in their early stages of development when the cold pool has not fully formed, and usually become upshear-tilted in late stages due to the strengthening of the cold pool over time. Horizontal vorticity of opposite signs in the rear part of the cold pool and in the upshear-tilted updraft results in the formation of a rear-inflow jet (RIJ). The RIJ in turn reinforces the vertical lifting at the gust front and helps the system maintenance. Depending on the strength of the low-level environmental shear, this rear-inflow can either remain elevated or spread laterally rearward of the gust front. This is observed in a special class of quasi linear convex shape MCSs called bow echoes which are associated with damaging surface winds. The most intense windstorm is called “derecho”. Ashley et al. (2005) showed that MCSs can produce derecho, and derecho-producing MCSs over the United States tend to group together and form derecho series.

MCSs frequently continue and even form well after local sunset (Trapp, 2013). With conditions associated with the stable nocturnal atmospheric boundary layer (ABL), the sustenance of a MCS depends mainly on the characteristics of the cold pool compared to those of the environment. Although air parcels in the ABL might be cooler than the air in the cold pool and flow under it, air parcels in higher levels can still be warmer and participate in the sustenance of the convective system. This elevated convection is facilitated by synoptic- and nonconvective mesoscale processes such as nocturnal low-level jets (LLJs) (Houze, 2004; Trapp, 2013). A LLJ is “a fast moving ribbon of air in the low levels of the atmosphere … it can rapidly transport Gulf moisture and warmer temperature to the North at speeds ranging from 25 to over 70 knots” (http://www.theweatherprediction.com/severe/llj/). Because they provide warm, moist air poleward and environmental vertical shear, LLJs often play a major role in the storm organization. Higgins et al. (1997) explained that “the LLJ has a considerable impact on the distribution and the intensity of nighttime precipitation over the central United States” and that “the impact of the LLJ on the overall moisture budget during summer is considerable with low-level inflow from the Gulf of Mexico increasing by more than 45%, on average, over nocturnal mean values”.

The movement of a MCS is the sum of the movement of the individual cells which is primarily due to advection, plus the system propagation which comprises the rate and location of new cell formation (Schumacher and Johnson, 2005; Trapp, 2013). MCSs often transition between different modes of convective organization over the course of their lifetimes because of the evolution of the intensity and orientation of the mean environmental wind (responsible for the advection of individual cells) relative to the system propagation.

As explained earlier, Schumacher and Johnson (2005) analyzed a large sample of extreme rain events during 1999-2001 over the eastern 2/3 of the United States in order to document the types of weather systems responsible for extreme precipitation. An event was considered as “extreme” if one or more gauges reported a 24-hr rainfall total greater than the 50-year recurrence interval amount. MCSs represented 65.5% of the events. Then Schumacher and Johnson used a classification for MCSs and determined the percentage of each MCS category. TS MCSs accounted for 17.1% of the observed MCSs, PS MCSs for 9.2%, LS MCSs for 2.6%, multiple MCSs (more than one MCS in a 24-hour period) for 3.9%, Training Line/Adjoining Stratiform (TL/AS) MCSs for 31.6%, and Backbuilding/Quasi-stationary (BB) MCSs for 19.7%. 15.8% of the MCSs could not be classified. TL/AS and BB MCSs correspond to specific configurations of the system propagation relative to individual cell movement suitable for tremendous precipitation over a given location. Schumacher and Johnson showed that during the period 1999-2001 these two categories of MCSs are predominant.

A TL/AS MCS is defined as “linear MCS with cell motion approximately parallel to the convective line ... as the cells move in a line parallel direction, there is very little motion in the line perpendicular direction, which distinguishes them from the TS and LS archetypes. This combination of motion characteristics leads to prolonged heavy convective rainfall at locations along the line of convective cells (i.e., a training line)” (Schumacher and Johnson, 2005). In contrast, BB MCSs “occur when convective cells repeatedly form upstream of their predecessors and pass over a particular area, leading to large local rainfall totals. Decaying cells move downstream and are replaced by cells reaching their mature stage” (Schumacher and Johnson, 2005). These authors mentioned that this type of MCS is difficult to predict since their initiation and maintenance occur on the mesoscale whereas TL/AS MCSs usually require a synoptic-scale front or preexisting outflow boundary. Figure 1-4 presents schematic diagrams of the radar-observed features of these two MCS types.

In another article, Schumacher and Johnson (2009) used a composite analysis to emphasize the similarities of 6 BB MCSs, which were all nocturnal midlatitude events that developed near a mesoscale convective vortex (MCV) or cutoff low and near the terminus of a LLJ. They remained quasi-stationary for 6-12 hours and caused tremendous precipitation (at least 200 mm [7.9 in.] which is actually far beyond the 50-year recurrence interval threshold) and flash flooding. MCVs usually outlive the MCS that spawned them and are often responsible for generating new convection. For this reason, the interaction of the MCV and the LLJ is important to initiation and maintenance of these systems. A key observation is that the systems studied exhibited low convective available potential energy (CAPE) and there was neither a front nor a preexisting strong surface boundary to help initiate the updrafts. It is actually suggested that low-level gravity waves may be an organizing mechanism instead of cold pools for BB MCSs (Schumacher, 2009; Schumacher and Johnson, 2008).

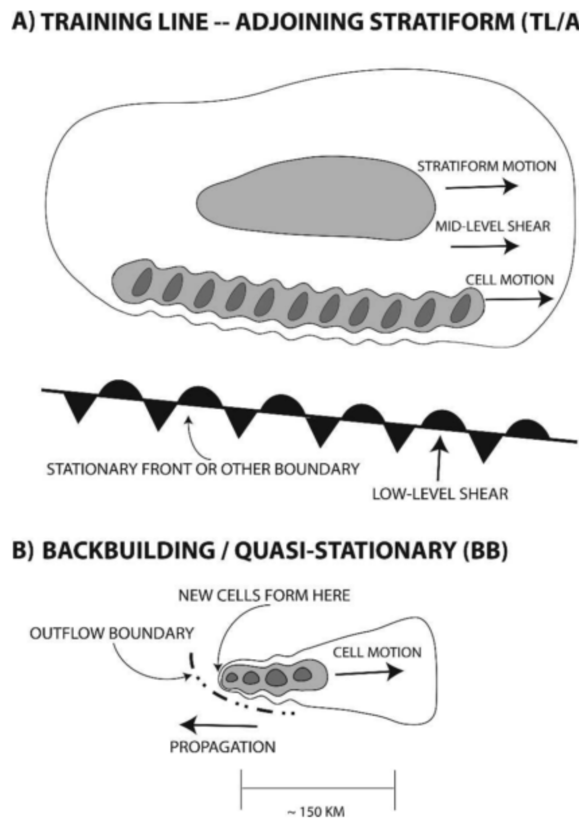

Figure 1-4 Schematic Diagram of the Radar-Observed Features of the (a) TL/AS and (b) BB Patterns of Extreme-Rain-Producing MCSs

Contours (and shading) represent approximate radar reflectivity values of 20, 40, and 50 dBZ. From Schumacher and Johnson (2005)

Numerous studies have reported on devastating floods caused by quasi-stationary convective storm events. For example, Petersen et al. (1999) presented the meteorological environment associated with the flash flood of 28 July 1997 in Fort Collins, Colorado. A quasi-stationary convective system produced heavy rainfall (more than 254 mm [10.0 in.] in 6 hours in the western part of the city). This event resulted in 5 fatalities and 200 million dollars in damage. Pontrelli et al. (1999) described the storm that resulted in heavy rainfall and flash flooding between 25 and 27 June 1995 in western Virginia. Two MCSs developed over Madison County. The first (the Piedmont storm) propagated slowly southward while the second (the Madison storm) remained quasi-stationary for approximately 8 hours and generated an accumulated rainfall of more than 600 mm (23.6 in.). Pontrelli et al. explained that “terrain-forcing coupled with cloud-scale and mesoscale processes permitted the genesis of new cells to remain quasi-stationary”. Another example, although less catastrophic in terms of human and material loss: on July 27th and 28th 2011, a back-building MCS caused extreme precipitation and flash-flooding in Dubuque (Iowa) and Jo Daviess Counties (Illinois) (see http://www.weather.gov/dvn/072711_dubuqueflashflood).

Numerous rainfall records were broken at the weather observation site at the Dubuque airport: most rainfall ever on July 27th (190 mm [7.5 in.]), most rainfall ever on July 28th (83 mm [3.3 in.]), most rainfall ever in a single day in July (190 mm [7.5 in.]), most rainfall ever in a 24-hr period (270 mm [10.6 in.]), most rainfall ever for the month of July (407 mm [16.0 in.]), and most rainfall ever for a single month (407 mm [16.0 in]).

As explained above, TL/AS and BB MCSs require special configuration of the environmental wind relative to system propagation to produce such extreme precipitation over the same point in space. Yet there exists a class of MCSs able to produce such precipitation over a given point just because of their large scales in time and space. These systems are called "mesoscale convective complexes" (MCC). Once satellite imagery became available in the 1970s, MCC studies became a popular topic in the literature (Milrad and Kelly, 2013). In 1980, Maddox (1980) proposed a definition for midlatitude MCCs. According to Maddox's definition, a MCC must have or are defined by the following physical characteristics:

- Size:
  A – Cloud shield with continuously low IR temperature ≤ -32°C must have an area ≥ 100,000 km^2

  B – Interior cold cloud region with temperature ≤ -52°C must have an area ≥ 50,000 km^2

- Initiation condition: Size definitions A and B are first satisfied
- Duration: Size definitions A and B must be met for a period ≥ 6h
- Maximum extent: Continuous cold cloud shield (IR temperature ≤ -32°C) reaches maximum size
- Shape: Eccentricity (minor axis/major axis) ≥ 0.7 at time of maximum extent
- Termination condition: Size definitions A and B are no longer satisfied

Certain authors amended this definition as they considered it to be too restrictive. For example, Augustine and Howard (1988; 1991) dropped the warmer threshold area measurement (≤ -32°C) as they considered it to be too subjective and unnecessary. Trapp (2013) explained that the previous satellite-based criteria do not take into account the way a MCC has been initiated. Weather radar observations allow distinguishing between "type-1" MCCs that are borne from cells initiating above a front, and "type-2" MCCs that are borne out of MCSs. Besides, the eccentricity requirement may lead to neglecting a large number of intense MCSs that meet Maddox's size requirement. Anderson and Arritt (1998) compared MCCs over the USA in 1992 and 1993 with another class of large and long-lived MCSs called "Persistent elongated convective systems" (PECSs). These events meet Maddox's definition except for the eccentricity (observed range 0.2 and 0.7). Anderson and Arritt showed that PECSs are, on average, more frequent and larger than MCCs.

Over 400 MCCs occur every year around the world and have been observed on all the continents except Antarctica (Laing and Fritsch, 1993a; Laing and Fritsch, 1993b; Laing and Fritsch, 2000; Laing and Michael Fritsch, 1997). For example, Velasco and Fritsch (1987) used IR satellite images from May 1981 to May 1983 to compare MCCs over midlatitude South America and midlatitude North America. They found out that South American MCCs are quite similar to North American MCCs but their size is about 60% larger, and that South American MCCs remain quasi-stationary during the warm season whereas MCCs in North America move poleward with the polar jet. In the United States MCCs occur mainly during the warm season between the Rocky Mountains and Appalachian Mountains (Ashley et al., 2003; Fritsch et al., 1986a; Fritsch and Maddox, 1981; Jirak et al., 2003; Maddox et al., 1982; Maddox, 1980; Maddox, 1983). Figure 1-5 shows the number of MCCs per year in the United States during a 15-year period (1978-1999).

Prevalence of MCCs during the warm season is depicted on Figure 1-6 where a boxplot of the number of MCCs per month derived from the same 15-year dataset is presented.

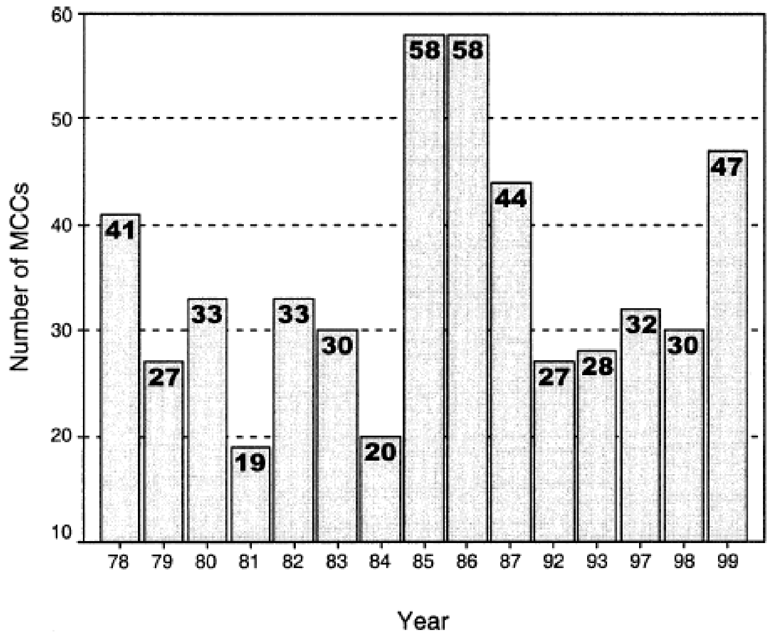

Figure 1-5 Number of MCCs Per Year for a 15-Year Period (1978-1999) in the United States. From Ashley et al. (2003)

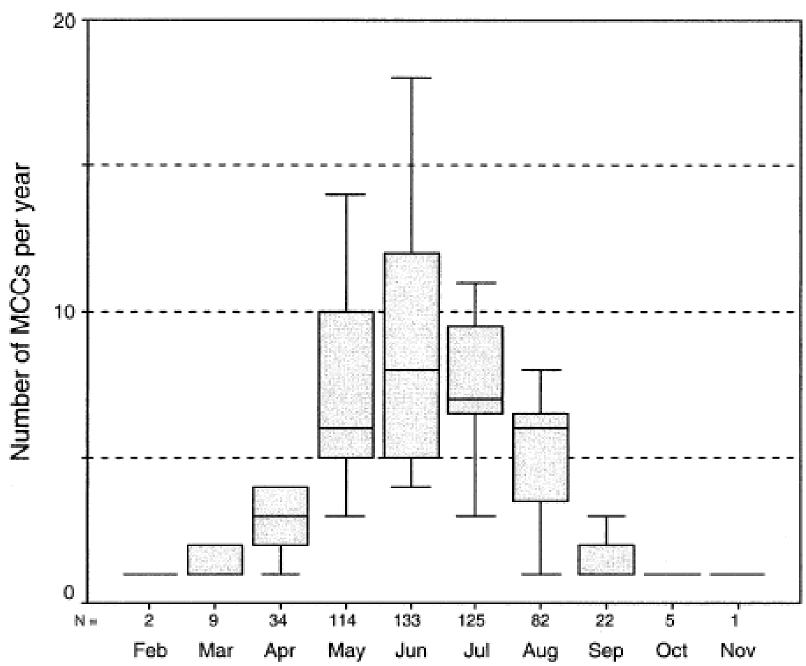

Figure 1-6 Box-and-Whisker Plot of the Number of MCCs Per Year in the United States as Derived from the 15-Year Dataset. From Ashley et al. (2003)

Jirak et al. (2007; 2003) explained that there are two reasons one should be willing to gain a deeper insight of MCSs and be able to predict them. First, MCSs bring essential rainfall for agriculture in central United States. Fritsch et al. (1986a) evaluated the contribution of precipitation from MCSs to the warm-season rainfall in the United States for 1982 (a "normal" year) and 1983 (a drought year). They found out that "mesoscale convective weather systems account for approximately 30% to 70% of the warm-season (April-September) precipitation over much of the region between the Rocky Mountains and the Mississippi River". Furthermore, they noticed that the MCSs' location, precipitation area and volumetric production changed noticeably from the normal year to the drought year although MCSs' frequency remained the same. Second, MCSs have the potential to "devastate property and possessions by producing severe weather" (Jirak and Cotton, 2007). Flash floods, damaging winds, hail and tornadoes are examples of severe weathers spawned by MCSs (Griffiths et al., 2009; Houze Jr et al., 1990; Jirak et al., 2003; Maddox, 1980; Trapp, 2013).

1.2.2 Numerical Modeling

Numerical models such as the Weather Research and Forecasting Model (WRF; Skamarock et al., 2008a) are used to get a better understanding of MCSs and to check their ability to simulate and forecast these systems. Until the 1970s, convective clouds were considered as subgrid-scale processes. Yet, a number of studies (e.g. Fritsch and Maddox, 1981) have shown that convective systems can organize at the mesoscale and impact the meso and synoptic scale environment. As a consequence, a numerical model should use fine enough grid resolution such as the one used in Section 3 (i.e. 5 km resolution) to reconstruct the MCSs' organization.

Table 1-1 Literature Review for Numerical Modeling of MCSs

References	Numerical Model	Description
Fritsch and Maddox (1981)		Used a 20-km grid mesh model to study the generation of convectively driven weather systems in the vicinity of the tropopause.
Zheng et al. (1995)	MM5	Investigated the effect of initialization on the ability of the model to simulate the 7 May 1985 MCS over Kansas and Oklahoma. They found out that static initialization techniques fail to simulate the observed evolution of the storm while improved dynamic initialization techniques using data assimilation (DA) are much more successful.
Gray (2000)	Model described in Shutts and Gray (1994)	Simulated a MCS during the Tropical Ocean Global Atmosphere Coupled Ocean Atmosphere Response Experiment (TOGA COARE) and explained that convective parameterizations tend to neglect mesoscale circulation if the grid spacing is too coarse.
Nachamkin and Cotton (2000) ; Nachamkin et al. (2000)	RAMS	Simulated the 19 July 1993 MCS into Kansas using 4 nested, moving grids.
Davis and Trier (2002)	MM5	Used numerical simulations under MM5 initialized by the analysis from the Rapid Update Cycle version 2 (RUC-2) to understand the interaction between the MCV and the MCS of the 27-28 May

Table 1-1 Literature Review for Numerical Modeling of MCSs (Continued)

		1998 over North-Central Texas and West Arkansas.
Zhang et al. (2003)	MM5	Used MM5 initialized by the National Centers for Environmental Prediction (NCEP) Aviation model to study the structure of a MCS which developed over the Taiwan Strait on 7 June 1998.
Parker and Johnson (2004)	ARPS	Described the evolution and dynamics of quasi-2D TS and LS MCS.
Nagarajan et al. (2001) ; Nagarajan et al. (2004)	MC2	Simulated a MCS which occurred during the 1991 Australian monsoon season. They showed that improving the initial moisture field in the European Centre for Medium-Range Weather Forecasts (ECMWF) analysis and some physical processes in the Kain-Fritsch cumulus parameterization scheme (KF CPS) noticeably enhanced the model-simulated life cycle of the storm.
Dawson and Xue (2006)	ARPS	Investigated the extent to which incorporating several different data sources, DA strategies, and a complex cloud-analysis procedure in the initial conditions (ICs) improves ARPS's forecasts of the 15-16 June 2002 MCS over the US central and southern plains. They showed that all the experiments succeeded in reproducing this strongly synoptically forced bow-echo-type MCS.
Correia Jr et al. (2008)	WRF	Used 10 km grid resolution to study the ability of two versions of the KF CPS to reproduce the development and propagation of MCSs.
Wandishin et al. (2008) ; Wandishin et al. (2010)	NCOMMAS	Performed 2D and 3D simulations to investigate the extent to which perturbations in the pre-convective environment of a MCS impact the development of the storm. They used ensemble member perturbations based on 24-hr forecast errors from the North American Model (NAM) and showed that a MCS develops within 100 km of the location of the control run in 70% of the runs.
Anabor et al. (2008) ; Anabor et al. (2009)	WRF	Studied serial MCSs over southeastern South America and explored the mechanisms of their upstream propagation. These serial events have a lifetime greater than individual MCSs and can last up to 70 hours.
Penide et al. (2010)	BRAMS	Simulated a MCS observed in the region of Niamey, Niger on 8 September 2006.
Zhang and Pu (2011)	WRF	Assimilated high temporal and vertical resolution wind observations from one single station obtained from Goddard Lidar Observatory for Winds (GLOW) using four-dimensional scheme (4DVAR) in order to simulate the 12-13 June 2002 MCS from Kansas and Oklahoma border to Texas. They showed that such DA improves significantly not only the wind field but also the temperature and

Table 1-1 Literature Review for Numerical Modeling of MCSs (Continued)

		moisture fields, providing a more realistic precipitation distribution.
Trier et al. (2011)	WRF	Studied the postsunrise reorganization of the MCS on 13 June 2002.
Schenkman et al. (2011) ; Schenkman et al. (2012)	ARPS	Simulated a MCS in central Oklahoma on 8-9 May 2007 using three-dimensional DA (3DVAR) of surface and upper-air observations. They studied the tornadogenesis processes associated with the mesovortices created by the MCS.
Snook et al. (2012)	ARPS	Simulated the 8-9 May 2007 MCS and used the ensemble Kalman Filter (EnKF) to assimilate radar data. The ensemble contained 40 members with different microphysics schemes in order to deal with the model physics uncertainty. The probabilistic 3-hr forecasts were good despite an observed bias in precipitation forecasts.
Cai and Yu (2012)	WRF	Simulated a MCS on April 17, 2011 in the Guangdong Province, China. They compared different shortwave and longwave parameterization schemes and showed that the results are much more sensitive to the longwave parameterization than to the shortwave parameterization.
Wheatley et al. (2014)	WRF	Investigated the ability of the WRF model with DA (EnKF) to simulate and forecast the 4-5 July 2003 bowing MCS over Indiana and Ohio with three different microphysical schemes of increasing order. They showed that the higher-order schemes give the best results although all three experiments produced a MCS similar to the observed one.

In Table 1-1, the abbreviations for the numerical models stand for:

- MM5: Pennsylvania State University/National Center for Atmospheric Research (PSU/NCAR) Mesoscale Model (Dudhia et al., 1999)
- RAMS: Regional Atmospheric Modeling System (Pielke et al., 1992)
- ARPS: Advanced Regional Prediction System (Xue et al., 1995)
- MC2: Mesoscale Community model (Benoit et al., 1997)
- NCOMMAS: National Severe Storms Laboratory (NSSL) Collaborative Model for Mesoscale Atmospheric Simulation (Wicker and Wilhelmson, 1995)
- WRF: Weather Research and Forecasting Model (Skamarock et al., 2008a)
- BRAMS: Brazilian Regional Atmospheric Modeling System (http://brams.cptec.inpe.br/)

Thus, based on the previous literature review, one can see that the WRF model has already been used to simulate MCSs, with and without DA. In this study, BB MCSs are of particular interest because of their ability to produce locally very severe precipitation over several hours. Several recent studies have shown the capability of the WRF model to simulate BB MCSs. For example, Schumacher and Johnson (2008) used the WRF model to simulate the 6-7 May 2000 BB MCS in Missouri. They noted that “convection-permitting simulations using the WRF model were successful in reproducing the quasi-stationary organization and evolution of this MCS". The storm produced more than 300 mm (12.0 in.) of rain in 9 hours to the southwest of the St. Louis metropolitan area. Zhao (2012) simulated the BB MCS in central China on 3 July 2008 using the WRF model. He described the interaction between the LLJ and the complex topography in the concerned region. He explained that the LLJ was blocked by the topographical barrier, which caused the MCS to remain quasi-stationary and produce the localized extreme precipitation. This example highlights the advantage of using a numerical model to estimate local rainfall depth in a complex environment.

1.3 <u>Tropical Cyclones</u>

1.3.1 Physical Structure

According to Chan and Kepert (2010), "TCs are intense atmospheric vortices that form over the warm tropical oceans". Approximately 80 TCs form worldwide every year (De et al., 2004). Their life duration is very variable as TCs can last from 1 day to several weeks. Even if TCs have usually horizontal extents of several hundreds of kilometers, the strongest winds, precipitation, and deep convection are located in a region of about 100 km in radius. As a consequence, TCs can be considered as mesoscale systems (Holton and Hakim, 2013). More precisely, a calm eye with a diameter between 20 and 100 km and pressure deficit up to 10% of the ambient atmosphere is surrounded by a slantwise ring of deep convective clouds that extends through the whole troposphere. This ring is called the "eyewall". The primary circulation of a TC consists of the cyclonic flow around the storm center while the weaker secondary circulation consists of "inflow concentrated in the boundary layer, upflow in the eyewall and spiral rainbands, and outflow in a thin layer beneath the tropopause" (Chan and Kepert, 2010; Holton and Hakim, 2013). The secondary circulation is the energy source of the TC, and its working may be idealized as a Carnot machine (Cram et al., 2007; Emanuel, 1991) as illustrated in Figure 1-7.

The gradient-wind form of the thermal wind equation shows that the temperature decreases when the radius increases (since azimuthal velocity decreases with height). As a result, TCs are warm-cored structures.

According to the maximum sustained (1-min mean) wind intensity, TCs are classified in the following categories: tropical depression if surface wind < 18 m s^{-1}, tropical storm (TS) if 18 m s^{-1} ≤ surface wind ≤ 32 m s^{-1}, and hurricane if surface wind ≥ 33 m s^{-1}. Hurricanes with surface wind speed larger than 50 m s^{-1} are named major hurricanes (Goldenberg and Shapiro, 1996; Shapiro and Goldenberg, 1998). Furthermore, the Saffir-Simpson Hurricane Scale (SSHS; Simpson and Saffir, 1974) is usually used to classify hurricanes in categories from 1 to 5 according to the maximum wind speed. For instance, major hurricanes correspond to categories 3, 4, and 5 on the SSHS.

Shapiro and Goldenberg (1998) explained that the Atlantic "systems that develop in the ["main development region" (MDR, the band from 10° to 20°N between the west coast of Africa and Central America)] are almost exclusively of easterly wave origin while many of the storms that develop to the north of 25°N […] are of baroclinic origin". Several studies (Goldenberg et al., 2001; Goldenberg and Shapiro, 1996; Landsea et al., 1998; Shapiro and Goldenberg, 1998) have shown that hurricane activity in the MDR are highly negatively correlated to the environmental vertical wind shear and to a less extent positively correlated to the sea surface temperatures (SSTs).

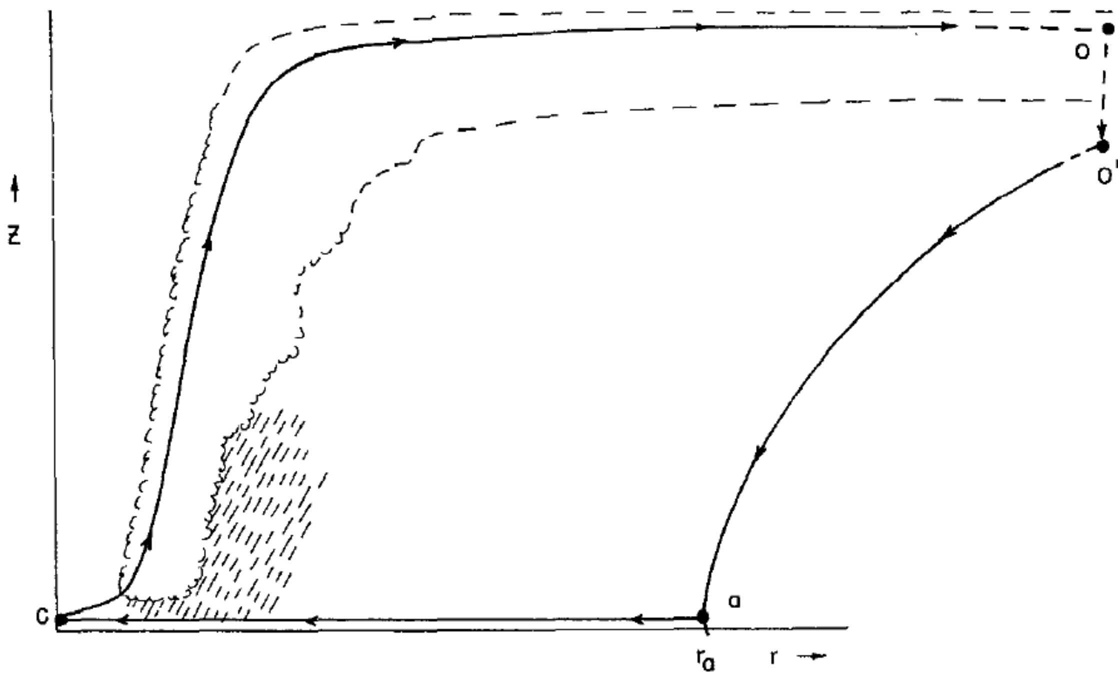

Figure 1-7 The Hurricane Carnot Cycle

Air begins spiraling in toward the storm center at point a acquiring entropy from the ocean surface at fixed temperature Ts. It then ascends adiabatically from point c, flowing out near the storm top to some large radius, denoted symbolically by point o. The excess entropy is lost by export or by electromagnetic radiation to space between o and o' at a much lower temperature To. The cycle is closed by integrating along an absolute vortex line between o' and a. The curves c-o and o'-a also represent surfaces of constant absolute angular momentum about the storm's axis (Emanuel, 1991).

In turn, the vertical wind shear in the MDR is positively correlated to El Niño-associated equatorial eastern Pacific SST anomalies, and negatively correlated to Sahelian rainfall anomalies. These mechanisms possess an inter-annual as well as inter-decadal variability and explain the fluctuations in hurricane activity over time (Goldenberg et al., 2001). For instance, the near-record hurricane activity in 1995 was associated with abnormally small wind shear and warm SST during the transition from El Niño to El Niña (Landsea et al., 1998).

When a decaying TC moves poleward into the midlatitudes, if the midlatitude environmental conditions are favorable and the TC interacts positively with this environment, it may re-intensify as an extra-tropical cyclone. This process is called "extratropical transition" (ET) (see for example Harr and Elsberry, 2000; Harr et al., 2000; Jones et al., 2003; Klein et al., 2000; Klein et al., 2002). ET is a serious forecast challenge. While satellite imagery would suggest the TC is weakening, it might be interacting with an extratropical system and might rapidly re-intensify. Its interaction with the midlatitude westerlies often increases its translation speed. As a result, large forecast errors in the system's track can occur and the time of warning is diminished. The decaying TC starts developing characteristic features such as high asymmetry, loss of warm core, fronts, tilt away from vertical, and so on. The wind field expands along with the area of heavy precipitation especially poleward and downstream of the storm. Consequently, the system does not need to make landfall to produce heavy rainfall on land. If it had to make landfall, since the grounds are already saturated because of precipitation away from the center of the storm, the precipitation around the remnant of the TC center might be extremely damaging (Chan and Kepert, 2010). Finally, in addition to the local impacts of an ETC, complex interactions taking place at the convective, storm, synoptic and even planetary scales affect the environment well downstream of the storm (Harr and Dea, 2009). Hurricane Floyd (1999) is an example of a hurricane which underwent ET. Atallah and Bosart (2003) explained that Floyd interacted with a midlatitude trough present in the Ohio valley while approaching the East Coast. This interaction created a baroclinic zone favorable for prolific precipitation. The forecasting systems were not able to anticipate this tremendous precipitation, which resulted in catastrophic flooding and several billion dollars in property damage.

1.3.2 Rainfall Distribution/Structure

Precipitation distribution in a TC is usually very spatially complex, variable in time and asymmetric. Lonfat et al. (2004) used Tropical Rainfall Measuring Mission (TRMM) observations associated with 260 TCs in order to analyze the relationship between rainfall distribution, storm intensity, and storm location. They found out the azimuthal mean rain rate increases with the storm intensity while the radius of maximum rainfall decreases. The highest rates were concentrated in a small fraction of the inner core area but accounted for half of the total rainfall amount. Precipitation asymmetry highly depends on both storm intensity and location, and tends to decrease with increasing intensity. Marks Jr (1985) studied the evolution of rainfall distribution and intensity in Hurricane Allen (1980) using reflectivity data from airborne radar systems for a six-day period. He explained that Hurricane Allen structure was characterized by a rapid contraction of the eyewall and the development of a secondary eyewall ("double eyewall structure"). The mean precipitation rates outside the eyewall were six times less than inside but accounted for 60% of the total rainfall. The distribution was asymmetric since "the maximum precipitation in the eyewall region was within 15-20° of the storm track".

Outer rainbands are another important feature of rainfall structure in TCs that may produce heavy local precipitation and urban flooding (Lin et al., 2010). Powell (1990a; 1990b) investigated the structure and dynamics of outer rainbands for several hurricanes. He showed that they have many similarities with squall lines. For instance, they are composed of a linear aggregate of convective cells and a region of stratiform rain. Hurricane rainbands either propagate spirally or remain storm-stationary.

Finally, as explained earlier in the paragraph on ETCs in Section 1.3.1, heavy precipitation can occur poleward and downstream of a TC or ETC. These rain events are called "predecessor rain events (PREs)". More precisely, a PRE is a "coherent region of heavy rainfall, with rainfall rates exceeding 100 mm (3.9 in.) in 24 hr that was positioned poleward and was separate from the main rain shield associated with the TC" (Cote, 2007; Galarneau et al., 2010). PREs occur approximately 1000 km ahead of their parent TC and 36 hours in advance. Their life duration is about 15 hours. They can occur with TCs of all intensities but are predominantly spawned by major hurricanes (Galarneau et al., 2010). PREs benefit from poleward transport of deep moisture from their parent TC. Galarneau et al. (2010) explained that 30% of all TCs that passed north of 20°N and west of 70°W produced at least 1 PRE and those PREs occurred predominantly in August and September. PREs can include MCSs. For instance, a nearly stationary MCS occurred in Hurricane Erin (2007) (Galarneau et al., 2010). Table 1-2 presents PREs that occurred in the United States during 1995-2008.

1.3.3 Numerical Modeling

In several countries such as the USA, TCs have a huge societal impact (Changnon et al., 2000; Pielke Jr and Landsea, 1998). As a result, it is very important to be able to simulate and forecast these storm events, hence the key role of numerical weather models. Because of computational power limitation, the first numerical models were relatively simple and made assumptions such as axisymmetry (Hack Jr, 1980; Ooyama, 1969; Rosenthal, 1970; Sundqvist, 1970a; Sundqvist, 1970b; Willoughby et al., 1984). Yet, they played an important role in getting a better understanding of TCs. Large improvements have been made over the past decades in simulating and forecasting TCs tracks. Elsberry (2005) reported in 2005 that "the first research goal of the U.S. Weather Research Program (USWRP) Hurricane Landfall (HL) focus has been achieved". This goal was to improve by 20% the accuracy of TC track forecast over 5 years. He explained that the program consequently shifted the focus on intensity change and rainfall prediction. Intensity prediction is a much more complicated task inasmuch as "track prediction depends more on large-scale processes and intensity depends on the inner-core dynamics and its relationship to the environment" (Davis et al., 2008; Marks and Shay, 1998). Precipitation and intensity prediction require taking explicitly into account processes occurring at the convection scale.

Below, several examples of relatively successful simulations of TC intensities and rain distributions with numerical models using an inner-grid resolution smaller than 5 kilometers are discussed. The discussion includes three examples of numerical weather models which have been used extensively to simulate TCs.

A first example of numerical models widely used to simulate and forecast hurricanes is the Geophysical Fluid Dynamics Laboratory (GFDL) Hurricane Prediction System (Bender et al., 2007; Kurihara et al., 1995; Kurihara et al., 1998). In 1995, the U.S. NWS adopted the GFDL model as an operational hurricane forecast system. Since 1998, the model benefited from several improvements such as the development of better initialization methods, the coupling to the Princeton Ocean Model (POM; Blumberg and Mellor, 1987), and refinement of the model resolution. Bender and Ginis (2000) investigated the sensitivity of simulated intensities to the aforementioned coupling to ocean circulation for TCs in the Gulf of Mexico and in the Western Atlantic. They found out that such a coupling is very important for a good prediction of the storms' intensities because "the cooling of the sea surface induced by the TC will have a significant impact on the intensity of observed storms, particularly for slow moving storms where the SST decrease is greater". Wu (2001) simulated the interaction between Typhoon Gladys (1994) and the Central Mountain Range (CMR) in Taiwan using the GFDL model. Sensitivity experiments highlighted the impact of model initialization on both the storm's track and intensity. Knutson and Tuleya (2004) used the GFDL model with four moist convection parameterizations and the outputs from nine Coupled Model Intercomparison Project (CMIP) climate models to investigate the sensitivity of idealized hurricane simulations to the choice of the model used to define the CO_2-warmed environment and the convective parameterization. Most of the combinations exhibited an increase in both the storms' intensities and precipitation rates while the frequency of TCs remained approximately the same over the coming century.

Table 1-2 Details of all Documented PREs over the United States East of the Rockies Associated with North Atlantic TCs during 1995-2008

The PRE parent TC, year, initiation date and time, and geographical location are listed (Galarneau et al., 2010)

TC (year)	Initiation (UTC)	Geographic location
Opal (1995)	0000 UTC 3 Oct	TX/LA/MS
Fran (1996)	0600 UTC 4 Sep	NC
Danny (1997)	0000 UTC 23 Jul	NC
Bonnie (1998)	0600 UTC 26 Aug	NY/PA
Bret (1999)	1800 UTC 23 Aug	TX
Floyd (1999)	1800 UTC 14 Sep	SC/NC/VA
Harvey (1999)	1800 UTC 20 Sep	GA/SC
Helene (2000)	1800 UTC 20 Sep	GA
Lili (2002)	1200 UTC 2 Oct	OK/KS/NE/IA
Grace (2003)	0000 UTC 31 Aug	OK/KS/MO
Isabel (2003)	1800 UTC 16 Aug	NY/MA/CT/RI/VT/NH
Alex (2004)	1800 UTC 2 Aug	NC/VA
Bonnie (2004)	1200 UTC 12 Aug	GA/SC/NC/VA/PA/NY
Charley (2004)	1200 UTC 13 Aug	FL/GA/SC
Frances (2004)	0600 UTC 8 Sep	NY
Gaston (2004)	1800 UTC 30 Aug	NY
Jeanne (2004)	0600 UTC 28 Sep	PA/NY/MA/CT/RI
Matthew (2004)	1800 UTC 7 Oct	AR/MO/LA
Dennis (2005)	1800 UTC 9 Jul	FL/GA/SC
Irene (2005)	0000 UTC 15 Aug	NY/CT/RI
Katrina (2005)	0600 UTC 29 Aug	KY
Ophelia (2005)	1200 UTC 15 Sep	NY/RI/MA
Rita (2005)	0000 UTC 25 Sep	NE/SD/IA/MN/WI
Wilma (2005)	0000 UTC 24 Oct	GA/SC
Alberto (2006)	1800 UTC 12 Jun	NC/SC
Ernesto (2006)	1800 UTC 30 Aug	NC
Erin (2007)	0000 UTC 19 Aug	MN/WI/IL
Ike (2008)	0600 UTC 13 Sep	MO/IL/IN/OH

MM5 has been used extensively to simulate TCs from 1997 to 2007. Liu, Zhang and Yau (1997; 1999; 2004; 2000; 2001; 2002) used MM5 to simulate Hurricane Andrew (1992) with a fine enough inner-grid resolution (6 km) to reproduce and study the inner-core axisymmetric as well as asymmetric storm structures. They suggested that "it may be possible to predict reasonably the track, intensity and inner-core structures of hurricanes from the tropical synoptic conditions if high resolution, realistic model physics, and initial vortices […] in relation to their larger-scale conditions […] are incorporated". Karyampudi et al. (1998) simulated Hurricane Florence (1988) with MM5. They investigated the sensitivity of the results to the ICs, to the formulation of cumulus parameterization, and to satellite-derived rain assimilation. They showed that the success of the assimilation scheme is highly dependent on the cumulus parameterization scheme. Zou and Xiao

(2000) made use of a bogus DA (BDA) scheme in MM5 to produce the initial structure of Hurricane Felix (1995). Zou and Xiao (2000) called “BDA” the fit of the model solution to an idealized vortex field (such as a surface low given by its central pressure and its maximum wind radius) through 4D-Var. This is important in order to obtain “a dynamically and thermodynamically consistent initial vortex that is compatible with the resolution and physics of the hurricane prediction model” (Zou and Xiao, 2000). In this case, the BDA improved noticeably the hurricane prediction. Braun and Tao (2000) used MM5 to simulate Hurricane Bob (1991) and study the extent to which the simulation depends on the choice of the planetary boundary layer (PBL) parameterization. They suggested that “the accurate forecasts of precipitation in hurricanes can be just as sensitive to the formulation of the PBL as they are to the cloud microphysical parameterization”. Frank and Ritchie (2001) performed simulations of TCs in idealized environments using MM5 in order to investigate the effect of vertical wind shear on the storms. They showed that the shear caused asymmetrization in the eyewall region structure and weakened the storm. Davis and Bosart (2001) simulated Hurricane Diana (1984) and described the different stages associated with the transformation of an initial baroclinic disturbance into Diana. Braun (2002) simulated Hurricane Bob, noting that the model produced “a realistic hurricane”. Braun et al. (2006) used MM5 to simulate Hurricane Bonnie (1998) at a horizontal resolution of 2-km. They studied the effects of vertical wind shear on the spatial distribution of vertical motion in the storm’s eyewall and found out that the shear caused a wavenumber-1 asymmetry in the time-averaged vertical motion and rainfall while instantaneous motion was concentrated in deep updraft towers on the downtilt side. In a companion article (Braun, 2006), Braun investigated water vapor, cloud condensate and precipitation budgets in Hurricane Bonnie. He explained that condensation in the eyewall occurs mainly in hot towers whereas outside of the eyewall precipitation is associated with stratiform precipitation processes. He also pointed out that the cumulative effect of numerical artificial source terms are non-negligible in the mass balance (13% of the total condensation and between 15% and 20% of the precipitation). Braun and Wu (2007; 2006) performed a similar study with Hurricane Erin (2001) as they showed that asymmetrization in the storm structure increases with the environmental vertical wind shear. Cram et al. (2007) used MM5 and adopted a Lagrangian approach to study transport and mixing processes between subdomains of Hurricane Bonnie. Wu et al. (2009) simulated the complex interaction between Typhoon Babs (1998), the East Asia winter monsoon, and the Taiwan terrain. Sensitivity experiments proved the importance of topography in rainfall distribution.

Since 2007, numerous studies reported successful simulations (according to the authors) of TCs with the WRF Model. For example, Davis et al. (2008) studied the ability of the WRF model to provide real-time forecasts of five landfalling hurricanes in 2005. Despite recurring errors, the authors explained that the model “revealed performance generally competitive with, and occasionally superior to, other operational forecasts for storm position and intensity”. Fierro et al. (2009) studied the sensitivity of the simulation of Hurricane Rita (2005) to the horizontal resolution using the WRF model. Grid spacing for the inner nest was taken from 1 km to 5 km with 1 km increments. Although structural differences were observed between simulations, compensation resulted in similar storm intensities. Xiao et al. (2009) performed three-dimensional DA (3DVAR) of Airborne Doppler radar data to initialize simulations of three hurricanes with the WRF model. DA improved markedly the forecasting performance of the model: storm intensities, vortex asymmetries, and rainbands were simulated better. Khain et al. (2010) used the WRF model to study how aerosols ingested into Hurricane Katrina (2005) impacted the storm’s intensity and structure. They explained that continental aerosols ingestion contributed to the enhancement of convection at the storm periphery and consequently weakened its intensity before landfall. Sippel et al. (2011) studied the interaction between TS Debby (2006) and the Saharan air layer (SAL) using ensemble forecasts with the WRF model. They showed the SAL slowed the storm intensification but is unlikely to be responsible for its dissipation. Trenberth et al. (2007) computed the moisture budgets for Hurricane Ivan (2004) and Hurricane Katrina (2005) using the WRF model. They found out that the main contribution to the moisture budget was not associated to the flux due to evaporation but was associated to low-level convergence.

One strength of numerical weather models such as the WRF model is their ability to account for the topography to compute precipitation. This is particularly important when one wants to reproduce or calculate precipitation maxima in a relatively mountainous region, whether it is for the simulation of TCs or MCSs. Below are examples illustrating the role of topography in generating local heavy rainfall in the case of hurricanes.

Wu et al. (2002) simulated successfully Typhoon Herb (1996) and its mesoscale rainfall distribution using MM5. Herb made landfall over Taiwan on 31 July 1996 and produced extremely heavy and damaging precipitation over the Central Mountain Range (CMR) with maximum precipitation of 1,736 mm (68.3 in.) in one day at Mount A-Li, and surface winds up to 65 meters per second. The authors explained that "the ability of the model to simulate successfully the observed rainfall is dependent on two factors: the model's horizontal grid spacing and its ability to describe the Taiwan terrain". They added that "the existence of the CMR has only a minor impact on the storm track, but it plays a key role in substantially increasing the total rainfall amounts over Taiwan". To support this assertion, they performed a sensitivity analysis and compared the results for different resolutions and in the cases where the terrain is taken/not taken into account. Ge et al. (2010) used the WRF model to simulate Typhoon Morakot (2009) and also noted the importance of the topography over Taiwan in producing heavy rainfall.

Lin et al. (2010) coupled the WRF model with the 2D, depth-averaged hydrodynamic Advanced Circulation Model (ADCIRC) in order to investigate storm surge in the Chesapeake Bay along with structure and evolution of extreme rainfall caused by Hurricane Isabel (2003). They explained that "interaction of the TC circulation with the complex terrain of the central Appalachians played an important role in flooding from Isabel and, more generally, in the flood hydrology of the central Appalachians".

1.4 Effect of Parameterization Schemes on Model Performance

Many researchers have performed comparative as well as sensitivity studies to investigate the importance of the choice of parameterization schemes in the performances of the WRF model. For example, Cai and Yu (2012) simulated a MCS with the WRF model using 5 longwave and 5 shortwave radiation parameterization schemes. They found that the simulated MCS was much more sensitive to the choice of the longwave radiation scheme than the choice of the shortwave radiation scheme. Crétat et al. (2012) used the WRF model to perform 27 experiments parameterized with 3 schemes for cumulus parameterization, 3 schemes for the PBL parameterization, and 3 schemes for the microphysics parameterization at a 35 km horizontal resolution in order to quantify uncertainties in the physical parameterizations as well as biases in simulated rainfall during a summer rainy season over Southern Africa. They showed that the amounts and location of seasonal rainfall were more sensitive to the cumulus parameterization than to PBL and microphysics parameterizations. They explained that for a given parameterization, different schemes can produce completely different biases. For instance, the Kain-Fritsch and the Grell schemes tended to overestimate rainfall amount and the number of rainy days, and underestimate the mean intensities. However, the Betts-Miller-Janjic scheme had the opposite effect. Crétat et al. (2012) also explained that "the influences of each type of schemes […] are approximately additive". This means that the bias produced by a given scheme for a given parameterization can be canceled or amplified by the bias created by a given scheme for another parameterization. In Crétat et al. (2012), the bias is measured as the difference between the simulated seasonal precipitation and the observed seasonal precipitation obtained from 5352 daily rain-gauge records extracted from the Water Research Commission database

(Lynch, 2003) on the one hand, and from the Global Precipitation Climatology Project (Xie et al., 2003) on the other hand.

Instead of investigating the sensitivity of the results to different parameterization schemes, Yang et al. (2012) focused on one parameterization scheme and studied the sensitivity of the results to the parameters used in this scheme. More precisely, they used high-resolution observational data over the Southern Great Plains to calibrate five input parameters in the new Kain-Fritsch convective parameterization scheme in the WRF model at a 25-km horizontal resolution and to validate the model's results. The simulation was from 1 May to 30 June 2007. Their goal was to investigate the extent to which this procedure can reduce model biases for precipitation and if the calibrated Kain-Fritsch scheme can be transferred successfully to other spatial scales and other regions exhibiting different physical processes and climatic regime. They found that the optimal parameters improved the simulation of the precipitation at a finer resolution (12-km), and in the case where the model was moved to the North America monsoon region. However, Yang et al. (2012) explained that their method has several limitations. For example, the optimized parameters might depend strongly on the microphysics parameterization scheme used for calibration. Furthermore, the climatic regimes of Southern Great Plains and North American Monsoon are dominated by convection. It is not certain that the optimized parameters will bring about better results for a very different climate regime compared to default parameters.

Finally, Jankov et al. (2005) studied the sensitivity and interactions of several parameterization schemes in the WRF model on the forecast of precipitation for eight MCSs. They ran a matrix of 18 WRF model parameterization configurations (3 cumulus parameterization schemes, 3 microphysical schemes, and 2 PBL schemes) at a 12-km horizontal resolution. Jankov et al. (2005) employed several methods (calculation of an equitable threat score and bias, calculation of correspondence ratios, calculation of squared correlation coefficients, and use of the "factor separation methodology") to quantify the effects of the variation of two different schemes and the extent to which schemes interacted (synergy between schemes). First, Jankov et al. (2005) observed that "no single model configuration was clearly better than the rest. The best configuration varied both in time and rainfall threshold". Second, the forecasts of average rain rate were found to be most sensitive to the choice of the cumulus parameterization scheme while forecasts of total rain volume were particularly sensitive to both the cumulus parameterization scheme and microphysics scheme. Third, the synergy between schemes was sometimes of comparable magnitude to the effects of changing only one scheme but was usually not statistically significant. Jankov et al. (2005) explained that this result may be due to the limited sample used to perform statistical analyzes and that synergy between schemes is a very important process that should be investigated further, more specifically when using ensembles to predict MCS rainfall.

Table 1-3 - Table 1-4 further illustrate parameterization uncertainties. Table 1-3 presents parameterization schemes suggested in the user's guide for the WRF model (Wang et al., 2011) for different applications. It is observed that even if there is no variation in the proposed parameterization schemes for longwave and shortwave radiation, the recommended scheme for microphysics varies with the target application. Table 1-4 presents parameterization schemes used to simulate MCSs with the WRF model in several studies mentioned in Section 1.2. These schemes usually differ from those suggested in the WRF user's guide (for example the Dudhia shortwave radiation parameterization and the Kain-Fritsch cumulus parameterization are used in place of the recommended schemes). Microphysics parameterizations are again the most varied. In addition, the number of vertical levels vary significantly from one study to the other. Finally, Table 1-5 presents parameterization schemes used to simulate TCs with the WRF model in several studies mentioned in Section 01.3 . It is noted that the schemes used in these studies are generally different from the hurricane application schemes suggested in the WRF user's guide. As in the case of MCSs, the Kain-Fritsch cumulus parameterization scheme is used predominantly, the number of vertical levels varies significantly from one study to another, and microphysics parameterization is the most varied. A list of the parameterization schemes, their code numbers, and their descriptions is provided in APPENDIX A .

Table 1-3 Parameterization Schemes Suggested in WRF User's Guide for Different Applications

Application	1-4 km grid distances, convection-permitting runs for 1-3 days run (as for the NCAR spring real-time convection forecast over the US in 2013)	10-20 km grid distances, 1-30 day runs (eg. NCAR daily real-time runs over the US)	Regional climate case at 10-30 km grid size (eg. Used in NCAR 's regional climate runs)	Hurricane application - 36,12, and 4 km nesting used by NCAR's real-time hurricane runs in 2012
Microphysics	New Thompson et al.	New Thompson et al.	WSM6	WSM6
Longwave radiation	RRTMG	RRTMG	RRTMG	RRTMG
Shortwave radiation	RRTMG	RRTMG	RRTMG	RRTMG
Radiation time step (minutes)	10	15	10	10
Surface layer	Eta similarity: based on Monin-Obukhov	Monin-Obukhov	Monin-Obukhov	Monin-Obukhov
Land surface	Noah Land Surface Model	Noah Land Surface Model	Noah Land Surface Model	Noah Land Surface Model
PBL	Mellor-Yamada-Janjic	Yonsei University	Yonsei University	Yonsei University
Cumulus param.	No parameterization	Grell-Freitas	Tiedtke scheme (only on 36 and 12 km grid)	Tiedtke scheme (only on 36 and 12 km grid)

Table 1-4 Illustration of Variation in Parameterization Schemes for MCSs Simulations Reviewed in Section 1.2 *

Study	Correia Jr et al. (2008)	Schumacher et al. (2008)	Anabor et al. (2009)	Zhang and Pu (2011)	Trier et al. (2011)	Zhao (2012)
MCS date	X	6-7 May 2000	X	12-13 June 2002	13 June 2002	3 July 2008
MCS location	X	Missouri	South America	Kansas, Oklahoma, Texas	Oklahoma	China
MCS type	idealized 2D MCS	Quasi stationary BB	Composite 10 serial MCSs	X	TL in the morning	Quasi stationary BB
Grid Size	10 km	9-3-1 km	10 km	9-3 km	3 km	15-5 km
Nb levels	51	48	32	38	42	41
Microphysics	WSM6	Lin (Purdue)	Lin (Purdue)	Lin (Purdue)	Thompson et al.	Eta (15 km), Lin (5 km)
Longwave radiation	X	RRTM	RRTM	RRTM	RRTM	RRTMG
Shortwave radiation	X	Dudhia	Dudhia	Dudhia	Dudhia	RRTMG
Land surface	X	Noah	5-layer from MM5	Noah	Noah	5-layer from MM5
PBL	Yonsei University	Yonsei University	Yonsei University	Yonsei University	Mellor-Yamada-Janjic	Yonsei University
cumulus param.	Kain-Fritsch	Kain-Fritsch (9 km)	Kain-Fritsch	Kain-Fritsch (9 km)	No param.	Grell-Devenyi (15 km)

*A “X” in a cell means either that the required information is not applicable for the associated study or that the information was not found in the article.

Table 1-5 Variation in Parameterization Schemes for TC Simulations Reviewed in Section 1.3 *

Study	Trenberth et al. (2007)	Davis et al. (2008)	Fierro et al. (2009)	Xiao et al. (2009)	Khain et al. (2010)	Sippel et al. (2011)
TC date and name	Ivan (2004) and Katrina (2005)	5 landfalling Atlantic hurricanes	Hurricane Rita (2005)	Jeanne (2004), Katrina (2005) and Rita (2005)	Katrina (2005)	TC Debby (2006)
Grid resolution	4 km	12 - 4 - 1.33 km	inner from 1 to 5 km (sensitivity study)	12 - 4 -1.33 km	9 - 3 km	27 - 9 - 3 km
Number levels	34	X	43	X	31	27
microphysics	X	WSM3	New Thompson et al.	WSM3	New Thompson et al.	WSM6
PBL	Yonsei University scheme	Yonsei University scheme	Mellor-Yamada-Janjic scheme	Yonsei University scheme	X	Yonsei University scheme
cumulus param.	No parameterization	Kain-Fritsch (only on 12 km)	Kain-Fritsch (outer domain only)	Kain-Fritsch (outer domain only)	X	Kain-Fritsch (on 27 and 9 km)

*A “X” in a cell means either that the required information is not applicable for the associated study or that the information was not found in the article.

1.5 Presentation of Other Classifications of Extreme Precipitation Events and Description of the NCEP Stage IV Product

The classifications of MCSs presented in Section 1.2 are subjective, predominantly based on the analysis of rainfall structural characteristics using, for example, radar imagery. Over the last years, several studies proposed other classifications. These classifications are more objective insomuch as they are the result of algorithms which identified and classified storms according to predefined criteria such as local return period and synoptic environmental conditions. One goal of such classifications is to enhance the ability of forecasters to detect regions where an extreme precipitation event is likely to occur depending on the region and the time of the year. It is difficult to say that one classification is better than another. The only way to do so is to put these classifications in such a perspective: for instance which classification if any offers the best tool set to forecasters? As explained in Section 1.2, a MCS evolves during its lifetime. For instance, it can be back-building for a few hours and then become trailing stratiform in response to changes in the synoptic and meso-scale environments.

Keene and Schumacher (2013) described a very particular type of MCS called “bow and arrow” that exhibits quasi-stationary convection in a specific region of the storm and can consequently cause local extreme precipitation. The “bow” refers to a bow echo. Bow echoes are mesoconvective structures characterized by a bow-shaped line of convective cells and the ability to create long swaths of damaging winds. In some cases, a trailing quasi-stationary convective region forms perpendicular to the bow. This is the “arrow”. The combination of the “bow” and “arrow” is particularly efficient in producing local extreme rainfall totals because “a combination of precipitation resulting from the bow echo and additional rainfall associated with the quasi-stationary (or back-building) convective arrow can result in a large amount of precipitation in a particular area” (Keene and Schumacher, 2013). Table 1-6 lists several bow and arrow events identified by Keene and Schumacher (2013):

Table 1-6 Dates of Bow and Arrow Events with their Location, Time of Day, Duration, Time Between Bow Echo and Formation of the Arrow. (Keene and Schumacher, 2013)*

Date	Location	Time (UTC)	Duration (h)	Time between bow echo and formation of arrow (h)
30 Aug 1999	South Dakota	0300, 0530	1.5, 3	1.5, 1.5
12 Jun 2003	Texas	0230	5	1
5 Jul 2003	Indiana–Illinois	0115, 0515	3, 2	4, 1.5
2 Jun 2004	Texas	0400	5	1.5
18 Jun 2006	Texas	0430	5	2
4 Jun 2008	Kansas	0315	3	1
26 Jun 2008	Iowa–Missouri	0645, 1100	3.5, 2	2, 1.5
3 May 2009	Texas–Louisiana	1225	2	2
8 May 2009	Missouri–Arkansas	1530	4	2
11 Jun 2009	Texas	0000	4	2.5
8 Jul 2009	Iowa–Nebraska	0600	3	2.5
18 Jun 2010	Iowa	1430	5	2.5
13 Jul 2010	Missouri–Arkansas	0830	2	5
15 Sep 2010	Nebraska–Kansas–Missouri	0300, 1130, 1600	6.5, 2, 4.5	1.5, 2.5, 1.5

* Times are in Coordinated Universal Time (UTC), and are determined based on the time that the first convective cells in the arrow are observed. Some of the cases were listed multiple times because there were multiple arrows on that day. The duration is the length of time (in hr) that the arrow was present in radar reflectivity (not the duration of the MCS as a whole)

Several recent studies which proposed methods to “objectively” (automatically) identify and/or classify extreme precipitation events are described below.

Konrad (2001) ranked the 47 heaviest precipitation events during the period 1950-1996 according to the heaviest precipitation observed over 10 different spatial scales (circular regions) ranging from 2500 km^2 (28-km radius) to 500,000 km^2 (399-km radius) for four regions of the United States given on Figure 1-8.

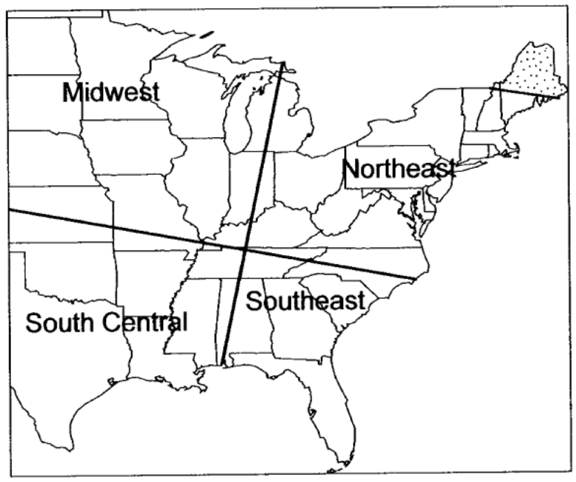

Figure 1-8 The Eastern United States as Defined in Konrad (2001)’s Study. The Dark Lines Indicate Boundaries Between each of the Four Subregions.

Konrad (2001) interpolated two-day precipitation amounts from all stations in the Cooperative Observer Network to a 10 km × 10 km spacing grid. Then, he used the following algorithm to determine regions containing the greatest mean precipitation totals for each scale. The circle associated with a given scale was moved pixel by pixel across the study domain. In order to construct an independent sample of precipitation regions, centers of circular domains need to be more than 1,000 km apart for a given two-day period. If this was not the case, regions with the lesser mean precipitation totals were not considered. Using this algorithm, most precipitation events were associated with one circle region for each scale, as illustrated in Figure 1-9.

Konrad (2001) explained that using a fixed shape for the moving window allows comparing precipitation totals of different events. However, a circular window underestimates areal precipitation of elongated or elliptical storms, as it is the case for the scale-1 circle for Hurricane Opal on Figure 1-9. Storm events were classified according to circulation features at the surface and at 500 hPa. A storm was classified as “cyclone” when a cyclone was present at 500-hPa in the vicinity of the event, as “wave” when a wave was present at 500-hPa in the vicinity of the event, as “tropical storm” when an organized tropical system (such as a hurricane) caused the precipitation event, or as “subtropical wave” if the event was “tied to a low-level trough rotating northward or northwestward around a large anticyclone” (Konrad, 2001).

Konrad (2001) observed that no storm is the most intense for all scales. For example, Hurricane Opal is the most intense for scales 1, 2, 3, 4, 5, 7 but not for scales 6, 8, 9, 10 (this might be related to some extent to the circular shape chosen for the moving window as explained earlier). According to the ranking obtained by Konrad (2001), the most intense storms at small scales are usually relatively less intense at larger scales. On the contrary, the most intense storms at large scales are generally not the most intense at small scales. This emphasizes the importance of the notion of scale to determine the maximum precipitation: a storm can produce extreme local precipitation totals without significant flooding at the watershed scale while another can generate tremendous precipitation amounts at the watershed scale without any local extreme precipitation.

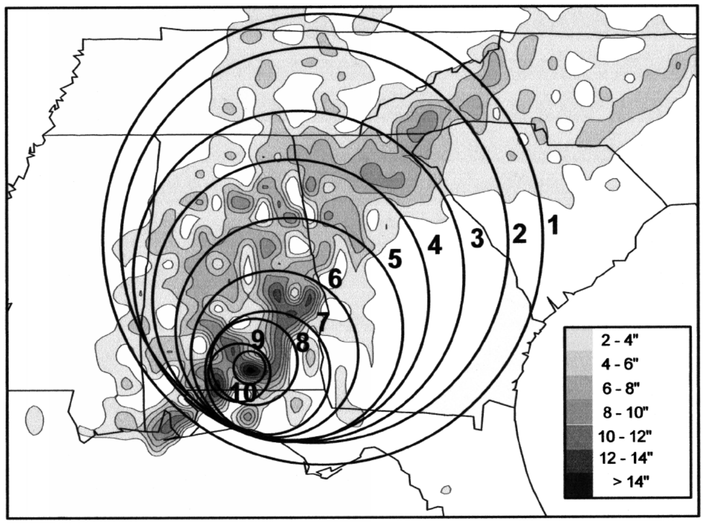

Figure 1-9 Two-Day Precipitation Totals Associated with Hurricane Opal

The circles circumscribe regions in which the heaviest mean precipitation totals were identified over each of the 10 scales. From Konrad (2001)

Hitchens et al. (2012) used an object-oriented identification algorithm in order to identify and provide a quantitative characterization of occurrences of hourly extreme precipitation in the Midwestern United States. The algorithm was applied to the NCEP stage II dataset between 1996 and 2010. "Objects" were defined as a set a pixels each exceeding a threshold of 6 mm hr^{-1} [0.2 in. hr^{-1}] and separated by no more than one pixel (the dimension of a pixel being 4 km × 4 km). It is noted that the idea of "object" was developed by Baldwin et al. (2005) who designed a completely automated rainfall classification procedure, rainfall systems being separated into convective (themselves divided into linear and cellular) and nonconvective.

Hitchens et al. (2012) identified 365,900 precipitation events in the Midwestern USA (that they defined as the area bounded by 36°- 47°N latitude and 80°- 97°W longitude). After performing quality control on the set of events, they identified events with a maximum precipitation rate in excess of the 99th percentile (equal to 55.4 mm hr^{-1} [2.2 in. hr^{-1}]). 3484 objects were selected, and they were considered as extreme precipitation events. Hitchens et al. (2012) found that the majority of the extreme objects occurred during the summer season, which is in agreement with other studies presented earlier. The objects ranged in size from 80 km^2 to 111,136 km^2. The smaller objects correspond to single-cell and small multicell systems. As illustrated on Figure 1-10, almost all these smaller objects occurred during the summer season and they represent a significant fraction of the total number of events (approximately one third). Hitchens et al. (2012) explained that even if non-extreme precipitation events are usually of smaller size compared to extreme events, one should not underestimate the contribution of summer small convective systems to extreme precipitation events: "although flash-flood events frequently are attributed to MCSs, individual convective storms such as supercell thunderstorms have been shown to generate extreme rainfall". Hitchens et al. (2012) also found that the characteristics of extreme precipitation vary with season and with time of day.

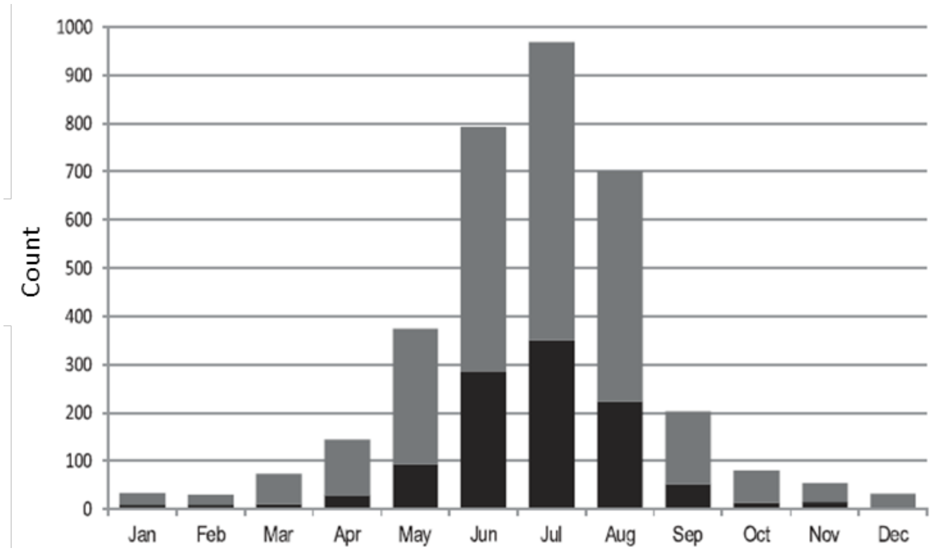

Figure 1-10 Frequency of Occurrences of Extreme Precipitation by Month

Objects with area sizes of 2000 km^2 or less are denoted in black, while the remaining objects are in gray. From Hitchens et al. (2012)

Moore et al. (2014) applied an object-based approach to 24-hr multisensor precipitation analyses from the NCEP Stage IV dataset so as to construct a 10-year (2002-2011) climatology of extreme precipitation events in the southeastern United States (defined as the region given in Figure 1-11). They identified extreme events using geographically varying upper quantiles (99th and 99.9th percentiles) of daily precipitation amounts. The resulting maps are presented in Figure 1-11.

Referring to Figure 1-11, the first step in the algorithm of Moore et al. (2014) is to determine each 24-hr period analysis comprising at least one grid point where the 99th percentile threshold is exceeded within the southeastern region (delineated in the figure by a heavy black line). When such a 24-hr period is found, the precipitation field is divided into sets of points below and above the 99th percentile threshold. An extreme precipitation event (EPE) object is defined as the union of areas of extreme precipitation (>99th percentile) separated by a distance no more than 100 km. Then, for each EPE object, the algorithm counts the number of grid points where the extreme precipitation thresholds are exceeded. The median number of such grid points is calculated for the whole population of objects, and the objects for which the number of extreme precipitation grid points is less than the median number are excluded in order to “eliminate spurious small-scale objects resulting from scattered convective or radar artifacts and to select only coherent events” (Moore et al., 2014). The final EPE object population was composed of 274 members. Moore et al. (2014) classified EPEs associated with a TC as “tropical” whereas other events were classified as “non-tropical”. For each non-tropical EPE, they calculated the 24-hr 1000-300-hPa vertically integrated water vapor transport (IVT) in order to classify further non-tropical extreme precipitation events as “strong IVT” events and “weak IVT” events. Moore et al. (2014) explained that “the objective of this stratification was to distinguish environments in which the synoptic-scale flow drives strong horizontal transports of thermodynamic ingredients for heavy precipitation, from more quiescent environments that involve weak transports yet very moist, conditionally unstable conditions supportive of deep moist convection”.

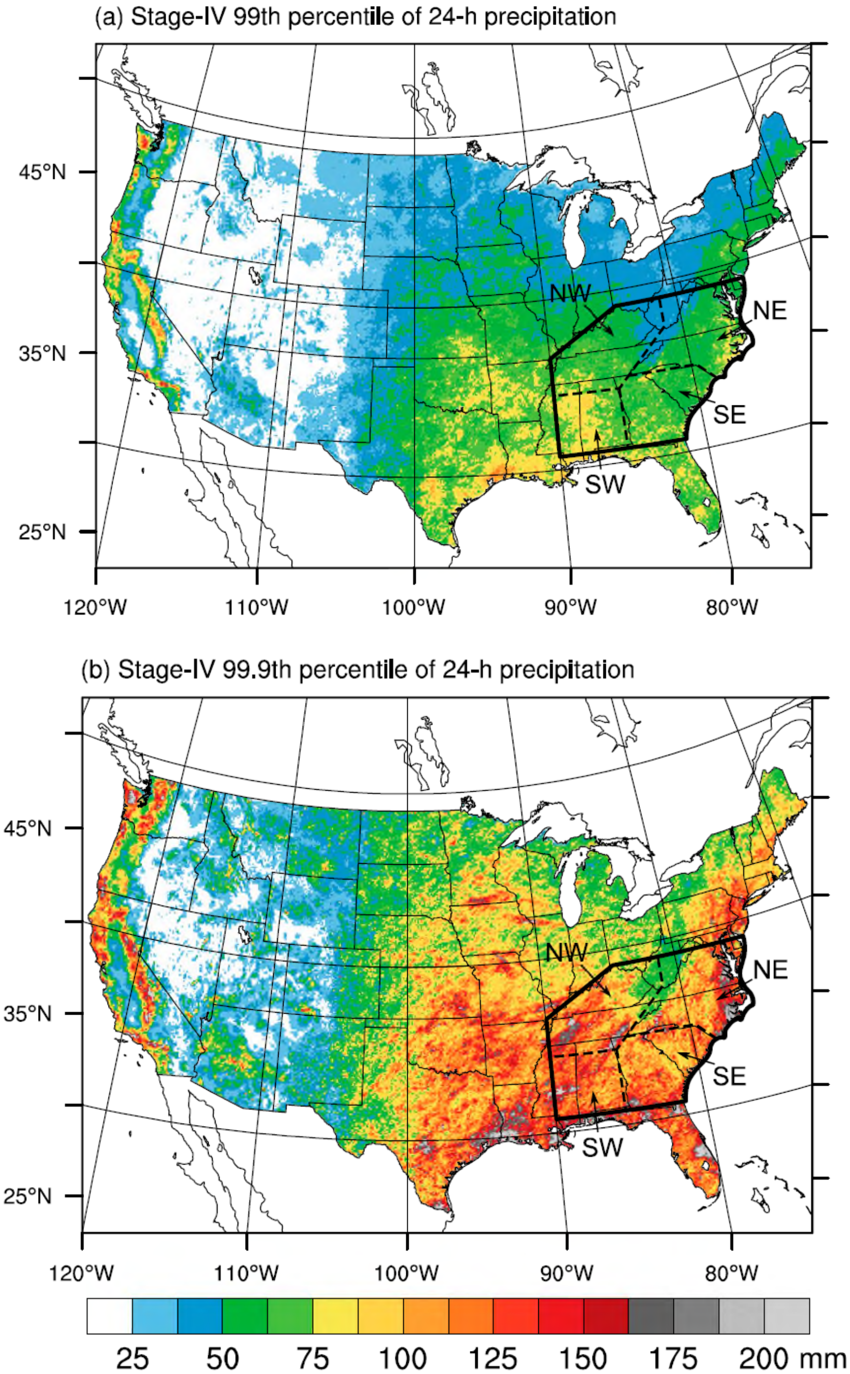

Figure 1-11 Maps of (a) the 99th Percentile and (b) the 99.9th Percentile of 24-hr Precipitation (mm) Calculated for all Days in the Stage IV Dataset During 2002-2011 with >0 mm of Precipitation

The thick black polygon denotes the boundaries of the southeastern domain. From Moore et al. (2014)

The results of Moore et al. (2014) complement and add another perspective on the results presented earlier. First, they found out tropical EPEs are less common, larger in size and rainfall amounts, and longer lived than non-tropical EPEs. The tropical EPEs occurred preferentially in summer and autumn and affected in particular the eastern portion of the southeastern US region, that is to say the eastern slopes of the Appalachian Mountains and the coast. In most of the studies presented earlier, it is shown that non-tropical extreme precipitation events (with a strong emphasis on MCSs) occur predominantly during the warm season. The method proposed by Moore et al. (2014) shows the situation is more complicated, at least in the southeastern US. Non-tropical EPEs affected most frequently the western portion of the southeastern region during the winter and spring, and the eastern portion of the region during summer. Their size is generally maximized in the winter and minimized in the summer. These points are illustrated in Figure 1-12 and Figure 1-13.

Figure 1-12 shows that there is a large inter-annual variation in the number of tropical as well as non-tropical extreme precipitation events. If the contribution from tropical and non-tropical events in Figure 1-12 (b) are summed it is seen that the number of extreme events is larger during the warm season, which is in agreement with the results reported previously (e.g. Hitchens et al., 2012). However, Figure 1-12 (b) also shows a substantial contribution of cool-season extreme events (in particular strong IVT events) in contrast to the results of Hitchens et al. (2012) for the Midwestern United States presented in Figure 1-10. This difference is certainly due to both the difference in location (southeastern vs. Midwestern) along with the differences in the algorithms used to define and identify extreme precipitation events.

IVT tended to be highest in winter and lowest in summer while precipitable water and CAPE were lowest in winter and highest in summer. Regional composites (Figure 1-14 below) clearly show the large differences in the environments characteristic of weak IVT extreme precipitation events and strong IVT extreme precipitation events. Strong IVT events have a strongly forced environment with prominent synoptic-scale features such as a corridor of IVT, an upper-level trough, and a surface cyclone. Weak IVT events possess a weakly-forced environment and rely consequently on high precipitable water conditions as well as high convective available potential energy to initiate and sustain smaller-scale deep convection. Moore et al. (2014) observed that storm durations and intensities were usually largest for spring and autumn, which reflects “the coincidence of relatively strong dynamical and thermodynamical influences during those seasons”.

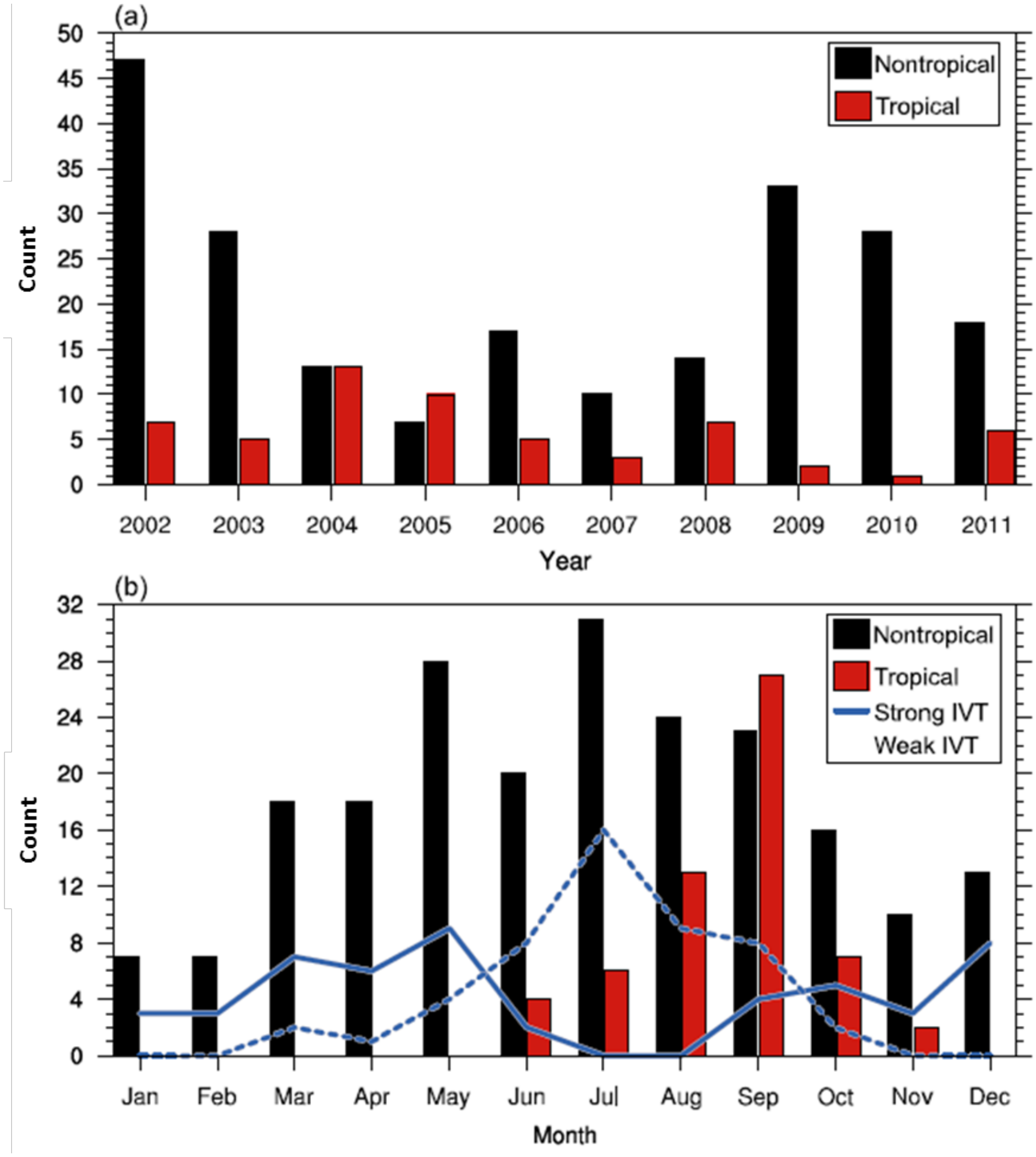

Figure 1-12 **The (a) Yearly and (b) Monthly Distributions of Non-Tropical (Black) and Tropical (Red) EPEs**

The monthly distributions of top 50 (strong IVT; solid blue line) and bottom 50 (weak IVT; dashed blue line) non-tropical EPEs with respect to IVT magnitude are shown in (b). From Moore et al. (2014).

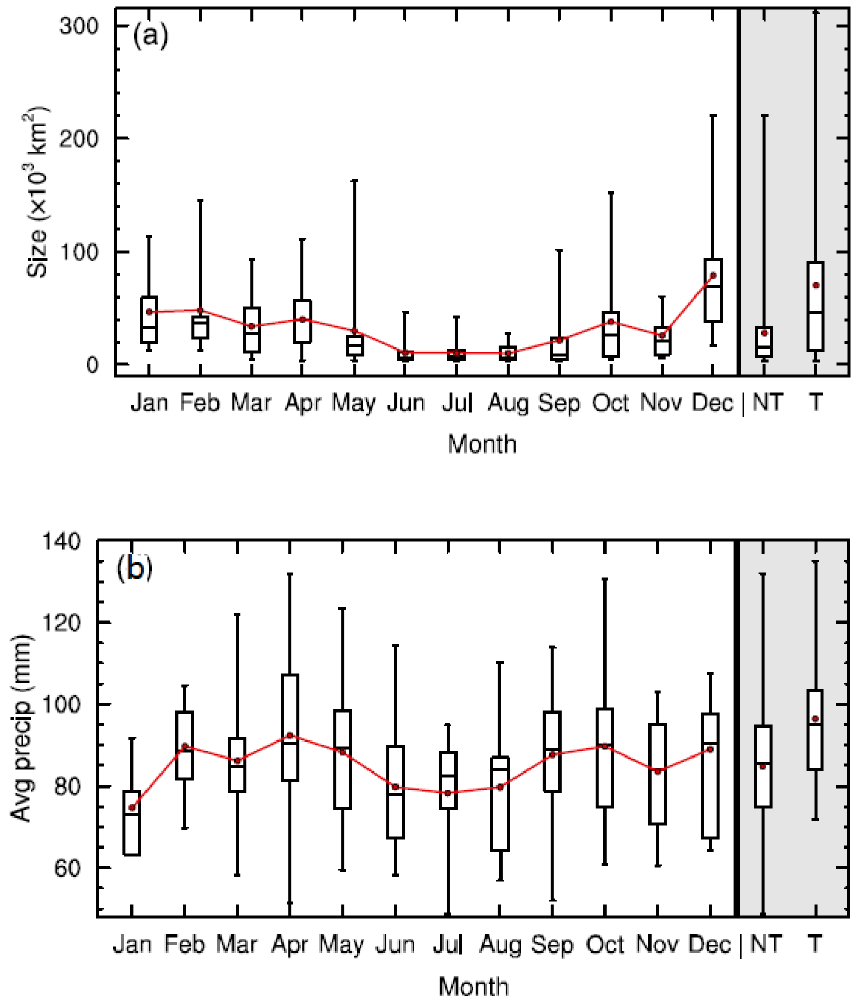

Figure 1-13 Box-and-Whisker Plots of (a) EPE Size (10^3 km^2), (b) Average Precipitation Over all Grid Points Associated with the EPE (mm), (c) Maximum 24-hr Precipitation (mm), and (d) Duration (hr)

Plots are shown for non-tropical EPEs separated by month as well as for all non-tropical and all tropical EPEs. From Moore et al. (2014). T: tropical; NT: non-tropical.

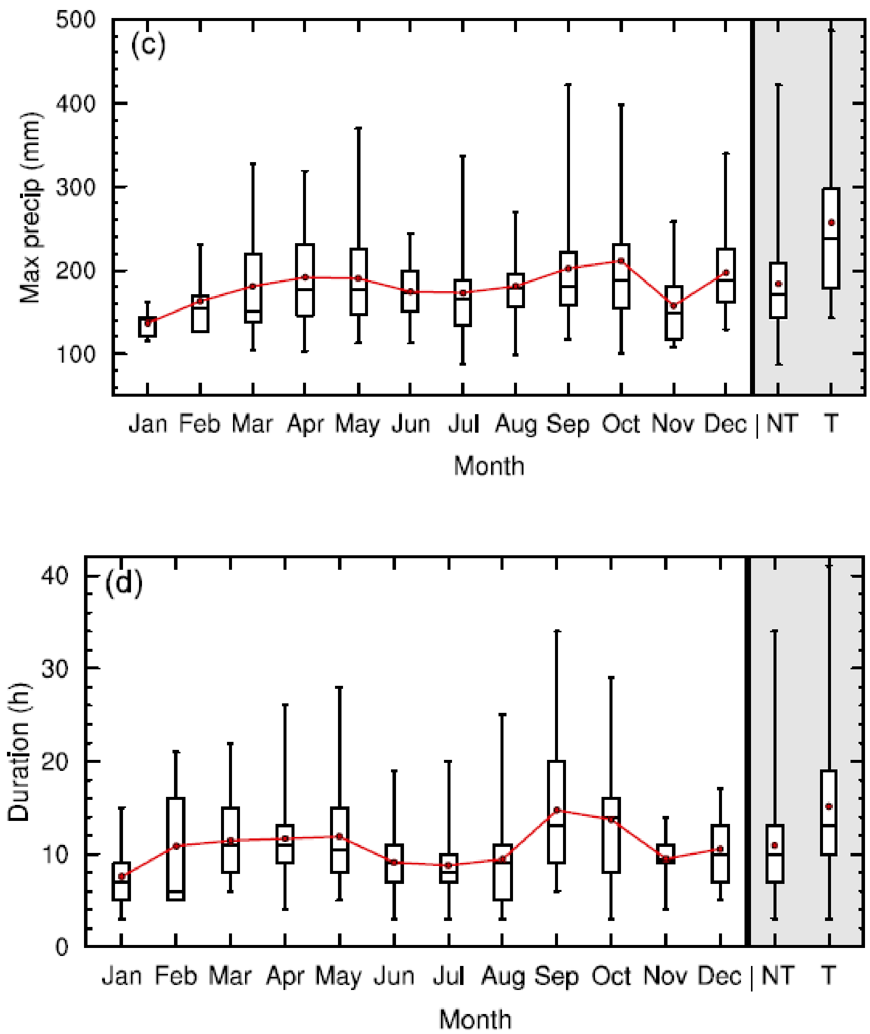

Figure 1-13 Box-and-Whisker Plots of (a) EPE Size (10^3 km^2), (b) Average Precipitation Over all Grid Points Associated with the EPE (mm), (c) Maximum 24-hr Precipitation (mm), and (d) Duration (hr)

Plots are shown for non-tropical EPEs separated by month as well as for all non-tropical and all tropical EPEs. From Moore et al. (2014). T: tropical; NT: non-tropical (Continued)

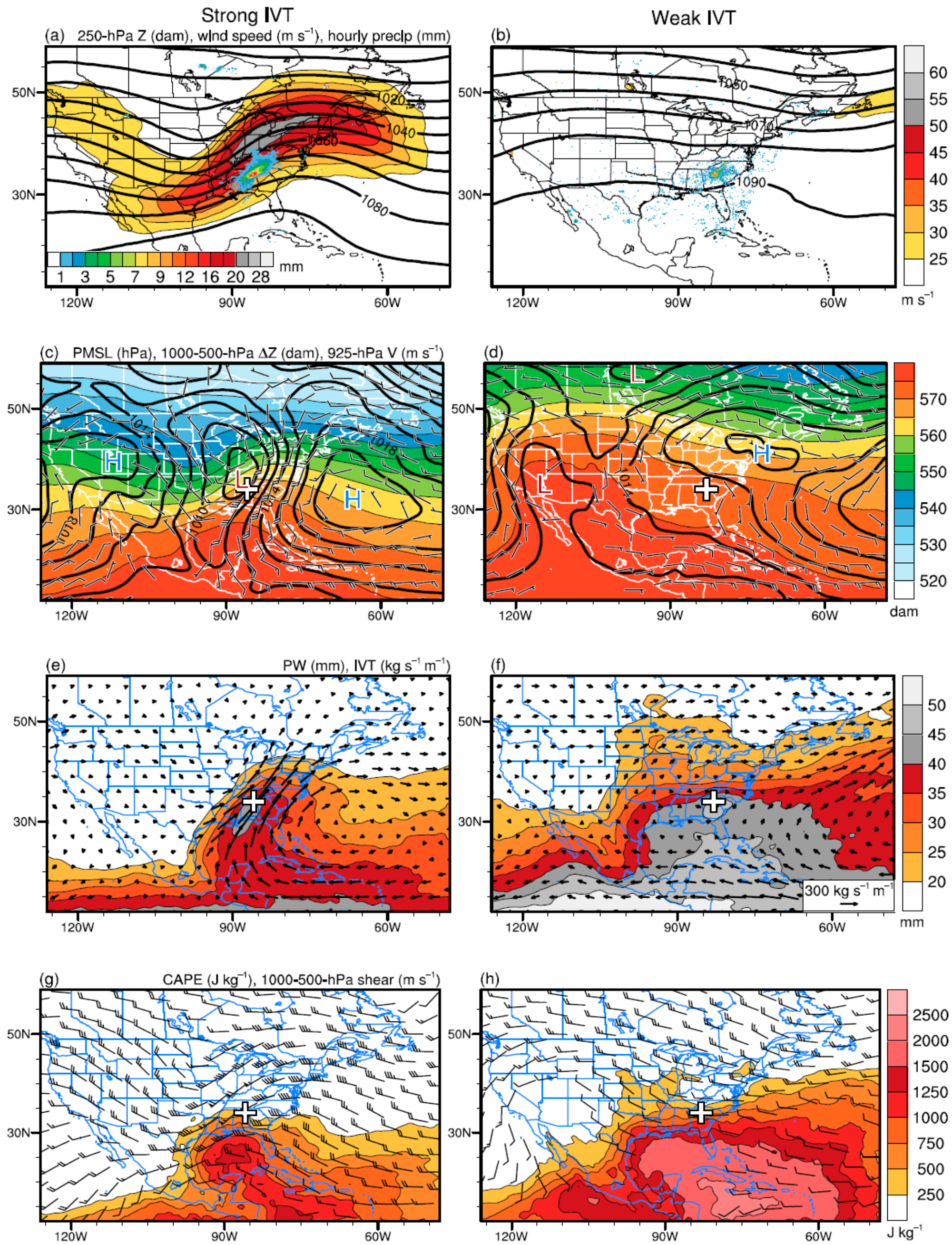

Figure 1-14 Composites for the (Left) Top 50 (Strong IVT) and (Right) Bottom 50 (Weak IVT) Non-Tropical EPEs with Respect to IVT Magnitude Showing: (a),(b) 250-hPa Geopotential Height (Contoured in Black Every 10 dam where 1 dam = 10 meters), Wind Speed (Shaded in m/s According to the Color Bar), and Stage IV Hourly Precipitation [Shaded in mm According to the Inset Color Bar in (a)]; (c),(d) SLP (Contoured in Black Every 2 hPa), 1000-500-hPa Thickness (Shaded in dam According to the Color Bar), and 925-hPa Wind; (e),(f) PW (Shaded in mm According to the Color Bar) and IVT Vectors [$kg\ m^{-1}\ s^{-1}$; Reference Vector in Bottom Right of (f)]; and (g),(h) Surface-Based CAPE (Shaded in $J\ kg^{-1}$ According to the Color Bar) and 1000-500-hPa Wind Shear. From Moore et al. (2014)

Peters and Schumacher (2014) applied a rotated principal component analysis to the atmospheric fields associated with a large set of TL/AS MCSs. This analysis led to two categories of events with specific meso-scale and synoptic characteristics. The first type of events was called “warm-season-type” because its upper-level characteristics are those of the North American summer. Warm-season-type events occurred within the right entrance region of upper-level jet streak. They were often preceded by a TS MCS. The second type of events was named “synoptic-type” because their upper-level characteristics are those of the spring and fall transition months during which synoptic systems prevail. Peters and Schumacher (2014) explained that synoptic-type systems “tended to exhibit greater horizontal extent than warm-season-type events, typically occurred downstream of a progressive upper-level trough, along a low-level potential temperature gradient with the warmest air to the southeast”. Low-level moisture in synoptic-type systems was smaller than low-level moisture in warm-season-type systems. Table 1-7 below presents the list of cases used by Peters and Schumacher (2014) to generate composite analyses.

Table 1-7 List of the Cases Used to Generate Composite Analyses, their Latitudes and Longitudes, and Synoptic Subtypes

Locations correspond to the grid point in the Stage IV precipitation analyses that experienced the maximum 1-hr precipitation accumulation from the TL/AS MCS. From Peters and Schumacher (2014)

Date	Subtype	Lat (°N)	Lon (°W)	Date	Subtype	Lat (°N)	Lon (°W)
3 Mar 2002	Synoptic	30.63	82.88	15 Sep 2004	Synoptic	43.88	94.63
19 Mar 2002	Synoptic	34.63	94.88	19 Oct 2004	Synoptic	35.05	87.81
8 Apr 2002	Synoptic	35.63	94.13	2 Nov 2004	Synoptic	28.63	96.38
11 Jun 2002	Synoptic	48.88	96.88	1 Apr 2005	Synoptic	30.63	87.63
23 Jun 2002	*Warm season*	*47.13*	*95.13*	4 Jun 2005	Synoptic	39.13	94.13
22 Aug 2002	*Warm season*	*42.38*	*90.38*	*10 Aug 2005*	*Warm season*	*31.38*	*96.88*
19 Oct 2002	Synoptic	33.13	95.63	*25 Aug 2005*	*Warm season*	*37.88*	*96.63*
21 Feb 2003	Synoptic	30.38	93.88	25 Sep 2005	Synoptic	44.00	89.63
7 Apr 2003	Synoptic	32.38	90.88	2 Jan 2006	Synoptic	27.38	82.63
8 Apr 2003	Synoptic	29.63	92.13	*22 Jun 2006*	*Warm season*	*41.38*	*82.63*
6 May 2003	Synoptic	35.38	84.63	*8 Sep 2006*	*Warm season*	*31.88*	*83.38*
8 May 2003	*Warm season*	*33.38*	*86.13*	23 Sep 2006	Synoptic	36.63	90.13
18 May 2003	*Warm season*	*30.88*	*87.88*	26 Oct 2006	Synoptic	31.38	95.13
12 Jun 2003	*Warm season*	*34.38*	*92.38*	*19 Aug 2007*	*Warm season*	*43.91*	*91.69*
25 Jun 2003	Synoptic	45.38	93.63	*21 Aug 2007*	*Warm season*	*40.83*	*82.86*
5 Jul 2003	*Warm season*	*40.63*	*86.38*	*7 Sep 2007*	*Warm season*	*39.91*	*96.19*
21 Jul 2003	*Warm season*	*28.38*	*96.88*	*7 Jun 2008*	*Warm season*	*39.93*	*86.78*
29 Aug 2003	*Warm season*	*37.38*	*95.88*	*25 Jun 2008*	*Warm season*	*40.00*	*93.94*
1 Sep 2003	*Warm season*	*39.63*	*88.88*	30 Apr 2009	Synoptic	33.91	97.19
28 Nov 2003	Synoptic	30.13	90.63	*8 Aug 2009*	*Warm season*	*44.91*	*94.69*
6 Feb 2004	Synoptic	33.13	88.13	*9 Aug 2009*	*Warm season*	*43.00*	*83.44*
26 Apr 2004	Synoptic	30.63	89.63	*13 Jun 2010*	*Warm season*	*36.58*	*101.11*
14 May 2004	*Warm season*	*28.63*	*95.88*	*23 Jul 2010*	*Warm season*	*42.66*	*91.61*
31 May 2004	Synoptic	37.88	83.88	*24 Jul 2010*	*Warm season*	*42.00*	*88.86*
29 Jul 2004	*Warm season*	*32.63*	*96.88*	*28 Jul 2011*	*Warm season*	*42.83*	*91.61*

2 FRAMEWORK FOR MODELING AND FOR ANALYSIS OF RESULTS

2.1 Regional Atmospheric Model for Simulating Severe Storm Events

Since the objective of this study is to assess the suitability of a regional atmospheric model (RAM) to simulate local intense precipitation processes within TCs and MCSs, some of the major tasks to be performed include using the selected RAM to reconstruct the intense precipitation fields associated with several historical TCs and MCSs, as well as to simulate TCs and MCSs for the future period of the 21st century. For the purpose of this study, the RAM employed to perform such simulations was the WRF model. Based on the literature review in Sections 1.2.2 and 1.3.3, the WRF model has been used extensively in recent studies for the simulation of MCSs and TCs. It is a relatively recent RAM benefitting from the joint efforts of several agencies as described below. In particular, the WRF model offers a wide range of parameterization schemes. It is available for free and it is easily downloadable and installable on a wide variety of Linux distributions and memory architectures (e.g., distributed memory).

The WRF model is a numerical weather prediction model used for research and operational applications to improve the understanding and prediction of mesoscale weather and to accelerate the transfer of research advances into operations. The model was developed as part of a multi-agency effort coordinated by the NCAR Mesoscale and Microscale Meteorology (MMM) Division, the National Oceanic and Atmospheric Administration's (NOAA) NCEP and Earth System Research Laboratory (ESRL), the Department of Defense's Air Force Weather Agency (AFWA) and Naval Research Laboratory (NRL), the Center for Analysis and Prediction of Storms (CAPS) at the University of Oklahoma, and the Federal Aviation Administration (FAA), with the participation of university scientists (Skamarock et al., 2008b). The WRF model can be used for a variety of applications including, real-time numerical weather prediction, DA development, parameterization, regional climate modeling, air quality modeling, atmosphere-ocean coupling, and idealized simulations (Skamarock et al., 2008b).

Note that the WRF Model is a fully compressible and nonhydrostatic model. It uses a terrain-following mass vertical coordinate in its vertical coordinate formulations and is conservative for scalar variables. The model uses the Runge-Kutta 2nd and 3rd order time integration schemes, and 2nd and 6th order advection schemes in both the horizontal and vertical directions (Skamarock et al., 2008b). The grid staggering scheme used by the model is the Arakawa C-grid. It is important to note that the WRF model has multiple options for physical parameterization, which include: microphysics, convective parameterization, cumulus parameterization, PBL, land surface models, and longwave and shortwave radiation. Such options are a crucial part of the WRF model configuration. Details on these options and their parameterization schemes can be obtained from WRF User Guide (Wang et al., 2016).

For the purpose of this study, the modeling system used included the Advanced Research WRF (ARW) dynamics solver, physics options, initialization capabilities, boundary conditions (BCs), and grid-nesting techniques. It is important to note, however, that the WRF model was run for this study in the simulation (offline) mode, which means that it was only subject to the influence of its initial and boundary conditions (IBCs), and no observation was used to improve the simulations through nudging or other DA techniques.

Nudging is a data assimilation method that constrains the evolution of the simulated phenomena so that it stays close to the evolution of a predefined reference (Hoke & Anthes, 1976). Nudging is implemented in the model by adding artificial forcing terms to the governing equations that reflect the difference between the best estimate of the observed state and the model state at a given location and time.

Numerous studies have shown that regional numerical weather models perform relatively well in reconstructing such storms in the forecasting mode where such techniques are used to improve the model's performances (Schenkman et al., 2012; Wheatley et al., 2014). However, in the context of climate change where one may be interested in simulating the storms of the future, it is important to evaluate the performances of regional numerical weather models in the simulation mode, since no observation is available for the future that allows using nudging or DA.

Therefore, in this study, the WRF model was run in the simulation mode at a 5-km resolution in order to reconstruct the intense precipitation fields associated with several historical TCs and MCSs which affected the United States, as well as to simulate the intense precipitation fields of TCs and MCSs in future projections. The process through which this was done is called Dynamical Downscaling (DD). According to the GFDL website[2], DD refers to the use of high-resolution regional simulations to dynamically extrapolate the effects of large-scale climate processes to regional or local scales of interest. For the simulations of the MCSs, the model's simulation nested domains were set up over a region in the Midwest so that the innermost domain covered the severe precipitation areas caused by these storm systems (more details provided in Chapter 3). However, several sets of simulation nested domains were prepared for the simulations of the TCs because of the diversity in the paths of these systems. More precisely, while the outer domain was the same for all cases and was chosen so as to cover the paths of all the identified severe TCs, different inner domains were set up so as to include the severe precipitation areas caused by each individual TC (more details provided in Chapter 4). With these sets of simulation nested domains, the WRF model was later configured to obtain the best results for the simulation of each of the selected severe MCSs and TCs storm events with respect to the simulated and observed precipitation fields.

2.2 Atmospheric Data Used for WRF Model Simulations

2.2.1 Data for Initial and Boundary Conditions

In order to run the WRF model, IBCs are needed. The datasets used to provide IBCs for historical and future conditions are now described. Note that the WRF model requires the following state variables in its IBCs:

1) Surface variables: skin temperature, temperature at 2 meters, relative humidity at 2 meters, wind speed at 10 meters, surface pressure, pressure at mean sea level;

2) Pressure level variables: temperature, wind speed, relative humidity, geopotential height.

2.2.1.1 Historical Atmospheric Reanalysis Data for Historical WRF Model Runs

In order to reconstruct historical storm events in the Midwestern and Eastern United States for the purpose of this study, the IBCs of the numerical model runs of the WRF model were obtained from the Climate Forecast System Reanalysis (CFSR; Saha *et al.*, 2010). CFSR is produced by NCEP in the United States, and is a so-called second generation reanalysis. A second generation reanalysis is provided at a finer spatial resolution and utilizes a newer DA system than a first

[2] https://www.gfdl.noaa.gov/climate-model-downscaling/

generation reanalysis such as NCEP/NCAR Reanalysis (Kalnay et al., 1996) and NCEP/DOE Reanalysis AMIP-II (Kanamitsu et al., 2002), and so on.

The provided spatial and temporal resolutions of CFSR are respectively 0.5 x 0.5 degrees (56 km x 56 km) and 6 hours. The spatial resolution of CFSR is the finest among the second generation reanalysis datasets including ERA-Interim (Berrisford et al., 2009) and JRA-55 (Ebita et al., 2011). Thus, CFSR could be considered as the most suitable reanalysis dataset for use as input for a regional atmospheric simulation within the United States.

2.2.1.2 General Circulation Model (GCM) Atmospheric Data for Future Projection WRF Model Runs

In order to simulate future storm events in the Midwestern and Eastern United states for the future years of the 21st century, one GCM was selected for this study. The selection of the GCM for this study involved looking at the best performance of different GCMs with respect to precipitation, which is the variable of most interest for this study.

Figure 2-1, copied from Figure 9.7 (Flato et al., 2014), assesses the performance of different GCMs in simulating a set of global measures using a root-mean-square error (RMSE) approach based on the global climatology (1980-2005) by normalizing the error by the median error of all CMIP phase 5 (CMIP5) model results. These global measures include precipitation (represented as *PR* in Figure 2-1) among other variables such as longwave and shortwave radiation, winds, and temperature. In this figure, the rows and columns represent individual variables and models, respectively, where the normalized RMSE is shown in colors; a white color indicates unavailable model results. A diagonal split of a grid square shows the relative error with respect to both the default reference data set (upper left triangle) and the alternate (lower right triangle). As an example, a value of 0.30 indicates that a model’s RMSE is 30% larger than the median CMIP5 error for that variable.

An examination of Figure 2-1 shows that among the 11 top-performing models for simulating global precipitation climatology there are four American GCMs/ESMs. They are CCSM4, CESM1 (CAM5), CESM1 (FASTCHEM) and CESM1 (WACCM). Upon further analysis of these four GCMs/ESMs (Flato et al., 2014), one can see that CESM1 (WACCM) has a grid resolution of 1.9 x 2.5 degrees (211 km x 278 km) while the other three models have grid resolutions of 0.9 x 1.25 degrees (100 km x 139 km). Among the three finer grid resolution models, only CCSM4 and CESM1 (FASTCHEM) have fully interactive aerosol modules, and only CESM1(FASTCHEM) has atmospheric chemistry module. All of the four models have the same ocean and sea ice components. As such, the best model to use for the purpose of this study for 21st century climate projections appears to be CESM1(FASTCHEM), with CCSM4 being the second best model. However, the climate projections from CESM1(FASTCHEM) could not be retrieved from CMIP5 by the project team. Since the project team was successful in retrieving the 21st century climate projections of CCSM4, this model was selected for use in this study.

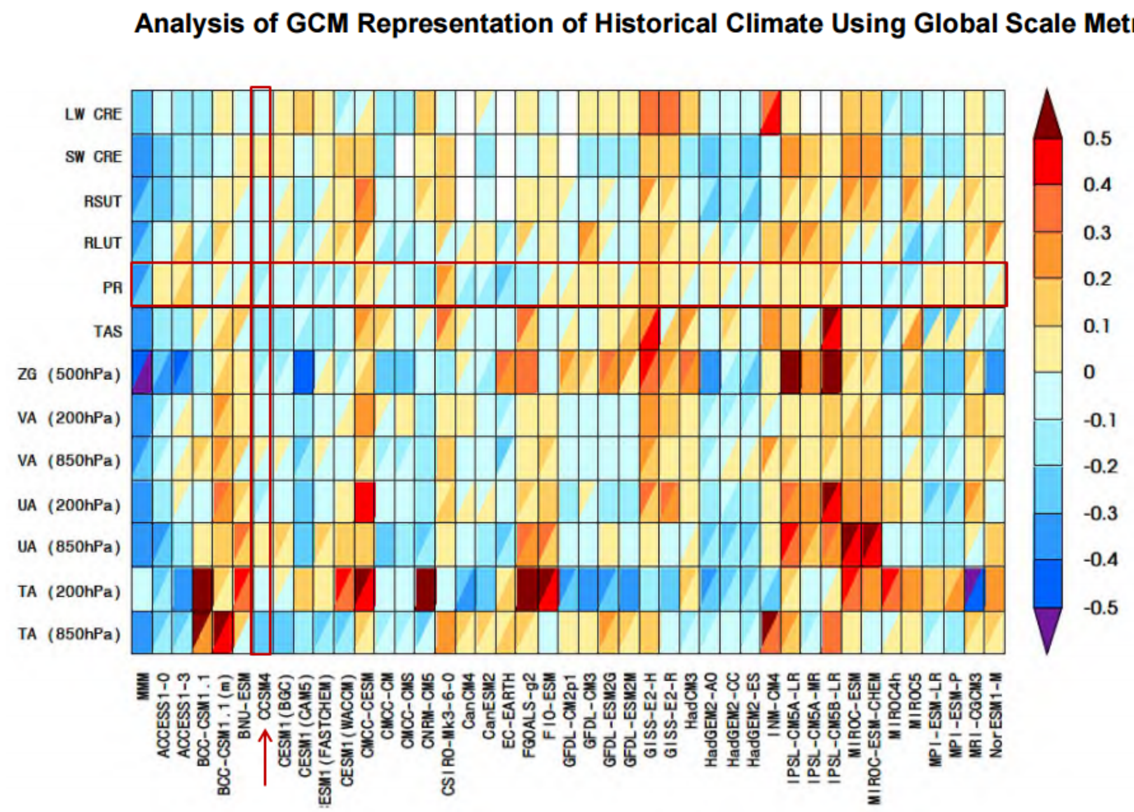

Figure 2-1 **Analysis of GCM Representation of Historical Climate Using Global Scale Metrics; from Flato et al. (2014)**

The full name of CCSM4 is the Community Climate System Model (CCSM) version 4 (CCSM4; Gent et al., 2011). CCSM4 is a coupled climate model developed by NCAR to simulate the global climate system (Bitz et al., 2012). The model is composed of four separate components which simulate the earth's atmosphere, ocean, land surface, and sea-ice simultaneously. CCSM4 has a horizontal grid resolution of 0.9° longitude by 1.25° latitude (100 km x 139 km).

GCMs like CCSM4 are usually driven by Representative Concentration Pathways (RCPs), which are in turn greenhouse gas concentration trajectories for the future (Moss et al., 2010; van Vuuren et al., 2011). These RCPs describe a total of four possible climate futures: one mitigation scenario (RCP2.6), two intermediate stabilization scenarios (RCP4.5 and RCP6.0), and one very high baseline emission scenario (RCP8.5). The numerical values of the RCP scenarios represent the radiative forcing values of the year 2100 relative to pre-industrial levels, measured in Watts per m^2 ($W\ m^{-2}$) (Clarke et al., 2007; van Vuuren et al., 2011). Thus, RCP2.6 represents an increase of 2.6 $W\ m^{-2}$ for radiative forcing levels by the end of 2100, whereas and RCP8.5 means an increase of 8.5 $W\ m^{-2}$.

For the purpose of this study, future climate change projection data simulated by CCSM4 based on RCP4.5 was used for the simulation of future severe TCs and MCSs. For this specific RCP (RCP4.5), radiative forcing relative to pre-industrial levels is projected to increase to approximately 4.5 $W\ m^{-2}$ by 2100 and is stabilized after 2100 (Clarke et al., 2007).

2.2.2 Observation Data for WRF Model Configuration and Validation

For the performance evaluation of numerical model runs of the WRF model and for the analysis of precipitation processes, the NCEP Stage IV precipitation analyses were used in this study. Several researchers have recently used the NCEP Stage IV precipitation analyses to investigate extreme precipitation events in the United States (e.g. Davis et al., 2006; Kursinski and Mullen, 2008; Moore et al., 2014; Peters and Schumacher, 2014; Stevenson and Schumacher, 2014). Stage IV is a mosaic of regional multi-sensor analysis generated by the NWS River Forecast Centers (RFCs) since December 2001 (Lin and Mitchell, 2005). It combines rain gauge data and radar-estimated rainfall. The Stage IV precipitation analysis gridded data files are available on the NCAR Earth Observing Laboratory (EOL) website (http://data.eol.ucar.edu/codiac/dss/id=21.093) from 01/01/2002 to present. Three time-resolutions are available: 1-hr, 6-hr, and 24-hr time intervals. The horizontal resolution is 4 km.

The 6- and 24-hourly analyses are constantly quality controlled manually by the 12 RFCs. The 1-hr analyses undergo less consistent quality control. Stevenson and Schumacher (2014) used the Stage IV precipitation analyses in order to identify extreme precipitation events in the Central and Eastern United States during 2002 – 2011. Extreme precipitation events were defined based on the exceedance of the 50- and 100-year recurrence interval thresholds constructed by Hershfield (1961) for the three time intervals (1, 6, and 24 hours). Grid points exceeding the thresholds were subject to an extensive additional quality control performed by comparing the Next Generation Weather Radar National Mosaic Reflectivity animations to the Stage IV analyses. The results of this additional quality control are summarized in Table 2-1.

Table 2-1 The Percentage of Points Discarded in Stevenson and Schumacher (2014) for the Two Different Recurrence Intervals (50- and 100-year) and Three Different Time Intervals (1,6, and 24 hr)

	1 hr	6 hr	24 hr
50-year	84.0%	11.3%	6.0%
100-year	89.0%	17.5%	9.5%

As can be seen in Table 2-1, more than 80% of the points were discarded for the 1-hr time interval against respectively less than 20% and less than 10% for the 6-hr time interval and 24-hr time interval. These results clearly illustrate the benefit of the manual quality control performed by the RFCs on the 6-hr and 24-hr time-interval precipitation analyses.

Since Stage IV is a processed multi-sensor dataset, it does not require additional data processing unlike original radar data and original satellite data. Stage IV data are provided in the GRIB format, which is one of the most popular file formats for atmospheric data. There are many applications and programming libraries available in public.

2.3 Metrics for Performance Assessment of the WRF Model

For the purpose of this project, the performance of the WRF model was evaluated in two ways. The first way involved visually comparing the simulated and observed (Stage IV) precipitation fields to visually appreciate their similarities and differences with respect to the position, texture, and intensity of the fields. The second way involved using three quantitative metrics to determine whether WRF could adequately and correctly model the precipitation amount, the storm location, and the storm size.

The first quantitative metric was the relative error in the inner-domain-averaged total precipitation. The relative error is a percentage value equal to

$$\left(\frac{P_{T_{sim}} - P_{T_{obs}}}{P_{T_{obs}}}\right) \times 100$$

where $P_{T_{sim}}$ was computed by accumulating simulated precipitation for a given time period at each cell which was then averaged over the inner domain, and $P_{T_{obs}}$ was defined similarly for the observed precipitation. The relative error in the inner-domain-averaged total precipitation indicated if the model adequately simulated the total precipitation amount over the period of interest. However, it did not indicate if the model correctly distributed this amount in space and time. It also did not indicate if the model could reproduce the range of precipitation depths.

The second quantitative metric utilized for model assessment was the overlap percentage, which was computed for several precipitation thresholds. The overlap percentage is equal to the ratio calculated as the number of grid points where both the observation and the simulation are above a certain threshold, divided by the number of grid points where the observation is above said threshold, multiplied by 100. For example, an overlap percentage of 25% for a given threshold meant that the intense part of the simulated field overlapped with 25% of the area of the intense part of the observed field for that threshold. The overlap percentage indicated whether the model could place the storm system in the appropriate location.

The overlap percentage, however, did not give any information about the relative sizes of the observed and simulated fields. In fact, the larger the size of the simulated field, the more likely it is to include the observed field, and the more likely it is to produce a high overlap percentage; but this may come at the expense of a simulated field size that is much larger than the observed field size. For example, suppose that the size of the observed precipitation field above a certain percentile threshold was 500 square kilometers, while it was 2,000 square kilometers for the simulated field. In this case, since the model overestimated the size of the precipitation field above the given threshold, it is likely to give good results in terms of the overlap percentage for this threshold. In order to address this issue, a third quantitative metric was calculated for the model performance in this study, and this was the area ratio between the simulated and observed precipitation fields (i.e., precipitation field area ratio; PFAR) for each threshold. If this ratio was less than one, it meant that the model underestimated the size of the precipitation field above the threshold. If the ratio was larger than one, it meant that the model overestimated the size of the precipitation field above the threshold. In this manner, while the overlap percentage provided indication of the proper placement of the simulated storm, the PFAR complimented the overlap percentage by providing an indication of the proper sizing of the simulated precipitation fields.

Note that in this study, both the overlap percentage and PFAR were computed at six difference precipitation thresholds. These six precipitation thresholds corresponded to the percentiles for the observed precipitation depth, and they included the: 50th percentile, 75th percentile, 90th percentile, 95th percentile, 97.5th percentile, and 99th percentile thresholds. For example, the 90th percentile is equal to the accumulated precipitation depth such that 10% of the grid points received an accumulated precipitation larger than this value, and 90% of the grid points received an accumulated precipitation smaller than this value. As a result, the larger the percentile, the more intense the associated accumulated precipitation is.

To further clarify the computation of the overlap percentage and the PFAR, their calculation is illustrated using a sample storm, the September 25, 2005 MCS, plotted on Figure 2-2. This figure shows the regions of “Hit-Hit”, “Hit-Miss”, and “Miss-Hit” for the 50th, 75th, 90th, 95th, 97.5th, and 99th percentiles for this MCS. “Hit-Hit” means that both the simulation and the observation are above the threshold at a given location (red color). “Hit-Miss” means that the simulated precipitation was below the threshold whereas the observed precipitation was above the threshold at a given location (green color). Finally, “Miss-Hit” means that the model-simulated precipitation was over the threshold whereas the observed precipitation was actually below the threshold (blue color); in a forecasting framework, this would correspond to a false alert. Within the framework of Figure 2-2, the two statistics can be computed as follows:

$$Overlap\ percentage\ = \frac{red}{red + green} = \frac{"Hit - Hit"}{"Hit - Hit" + "Hit - Miss"}$$

and

$$Precipitation\ Field\ Area\ Ratio\ (PFAR) = \frac{red + blue}{red + green} = \frac{"Hit - Hit"\ +\ "Miss - Hit"}{"Hit - Hit" + "Hit - Miss"}$$

For this specific example shown in Figure 2-2, the overlap percentage for the 50th, 75th, 90th, 95th, 97.5th, and 99th percentiles were 52%, 51%, 43%, 48%, 57%, and 50%, respectively, and the PFAR were 0.56, 0.73, 0.93, 1.27, 1.53, and 1.96, respectively. As a consequence, in terms of the metrics computed for assessing the performance of the WRF model in reconstructing historical intense storm events in this study, the best model performance would be obtained when the relative error is small, when the overlap percentage is close to 100%, and when the PFAR is close to 1.

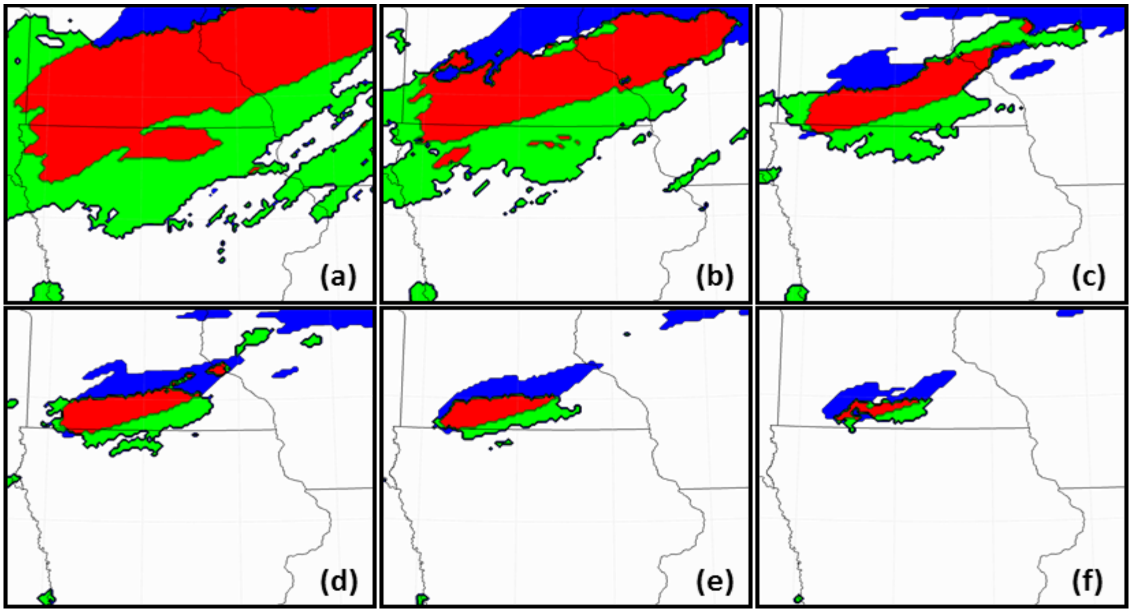

Figure 2-2 **Regions of "Hit-Hit" (red), "Hit-Miss" (green), and "Miss-Hit" (blue) for (a) the 50th Percentile, (b) the 75th Percentile, (c) the 90th Percentile, (d) the 95th Percentile, (e) the 97.5th Percentile, and (f) the 99th Percentile for the September 25, 2005 MCS**

2.4 WRF Model Configuration by Choosing the "Best" Model Parameterization Scheme for Storm Reconstruction

For the reconstruction of the historical TCs and MCSs, the WRF model was configured by trying different combinations of the parameterization and configuration options. These options included the parameterization schemes such as microphysics, cumulus parameterization, PBL physics, longwave and shortwave radiation physics, and surface layer options, as well as the vertical resolution (number of layers), the time step, and other options related to the physics and dynamics. These options were changed until the best results were obtained for the simulation of each of the selected severe historical storm events with respect to the simulated and observed precipitation fields.

In this report, what is called the "best" simulation corresponded to the best compromise between a qualitative examination of the accumulated precipitation plots and the quantitative results in terms of performance statistics. The former check involved a visual comparison of the simulated results against the observations, and the latter check involved the computation of the three metrics for model performance, as presented in the previous section. Indeed, certain configurations of the WRF model's options produced satisfactory results in terms of the statistics, but an unrealistic precipitation field. Such configurations were rejected. On the other hand, certain configurations produced a realistic precipitation field, but unsatisfactory performances relative to the statistics. Such configurations were also rejected.

It should be noted that it was not possible to investigate all the possible combinations of the WRF model's options since the WRF model offers several million possible combinations of the parameterization schemes alone. However, a large number of combinations were investigated for each of the storm events (TC or MCS), but the number of combinations that were tested varied from one storm event to another. In general, it was observed that, in each case, several combinations systematically produced a realistic storm event in terms of the precipitation field's texture and intensity. However, as DA was not used in this study, placing the storm in the correct location required additional efforts, which were not the same for all storm events.

Moreover, it should also be noted that placing the storm in the correct location was considered of great importance during the selection of the best simulated storm. This is because the correct positioning of the storm's location and orientation, as compared to the observation, allows one to resolve the climate dynamics and to replicate the hydroclimatic conditions of the observed storm event as it actually occurred over the appropriate geographical area. With this validated replication of the observed storm event in hand, there was greater confidence in transposing this storm to an area of interest by a physically based method with the use of the WRF model, which crucially conserves the mass, momentum, and energy over the modeling domain. Furthermore, the transposition of the storm event can be optimized based on its location in order to maximize its contribution to the precipitation over the area of interest, thus maximizing its effect over that area. Such a physically based method for storm transposition and precipitation maximization overcomes many of the issues of the traditional methods, which may be highly dependent on observation records and unable to deal with nonstationarity, and it can also be applied for the future projection data obtained from GCMs. As such, it is clear that the correct positioning of the simulated storm event is of great importance for the subsequent tasks of this project involving storm transposition and storm location optimization for the greatest precipitation depth effect.

2.5 Additional Analysis of WRF Results

After selecting the best simulation result for a specific storm event, and in order to investigate the moisture transport responsible for generating intense precipitation, the precipitable water field as well as the integrated water vapor transport field had to be reconstructed. These two variables were not directly included in the WRF model's outputs. They required additional post-processing of the water vapor mixing ratio field, the wind field, the potential temperature field, the geopotential height field, and the pressure field.

The total precipitable water vapor (*PW*) is a scalar field. It is equal to the total depth of water in an atmospheric column, if all this water precipitated as rainfall. It is usually given in millimeters. In mathematical terms, *PW* can be written as the following mathematical relationship:

$$PW = \int_{z=0}^{z_{top}} \rho_v \, dz = \int_{z=0}^{z_{top}} q_v \, \rho \, dz = \frac{1}{g} \int_{p=0}^{p_{surf}} q_v \, dp$$

In this equation, z is the vertical coordinate (height), z_{top} is the height of the top of the atmosphere, $z = 0$ is the local ground elevation, ρ_v is density of the water vapor, q_v is the water vapor mixing ratio, ρ is the density of dry air, p is pressure, p_{surf} is the surface pressure, and g is the gravitational acceleration.

As for the *IVT* or moisture advection, it is a 2-dimensional vector field which gives the horizontal transport of water vapor by the wind. *IVT* is given by the following mathematical relationship:

$$IVT = \int_{z=0}^{z_{top}} \rho_v \, \boldsymbol{U} \, dz = \int_{z=0}^{z_{top}} q_v \, \rho \, \boldsymbol{U} \, dz = \frac{1}{g} \int_{p=0}^{p_{surf}} q_v \, \boldsymbol{U} \, dp$$

where $\boldsymbol{U}$ is the wind field, and where the other variables are as described above.

3 NUMERICAL SIMULATION OF MESOSCALE CONVECTIVE SYSTEMS

This chapter presents the results of the numerical simulations of fourteen intense historical MCSs selected for this project. The intense MCSs simulated for this project were selected within the time period from 2002 to the present, based on the NCEP Stage IV precipitation dataset, described in detail in Chapter 2. These selected storm events correspond to the most severe storms, in terms of the generation of an intense precipitation field containing pockets of extreme rainfall.

The website *http://schumacher.atmos.colostate.edu/precip_monitor/* shows a list of events per year determined from Stage IV data which are deemed to be extreme events by having exceeded a certain threshold which is based on a certain time interval (e.g., 6-hr or 24-hr) and based on a certain recurrence interval (e.g., 50-year or 100-year). The intense MCSs for this project were selected from that list on the basis of being MCSs with precipitation amounts passing the threshold of the 24-hour accumulated precipitation for a 100-year recurrence period. As such, the fourteen selected MCSs that are presented in this report are the events with the following dates:

- June 22, 2002
- August 22, 2002
- September 15, 2004
- June 25, 2005
- August 17, 2005
- September 25, 2005
- July 18, 2007
- August 19, 2007
- June 5, 2008
- August 8, 2009
- July 23, 2010
- September 23, 2010
- July 28, 2011
- June 22, 2013

For the simulations of these historical MCSs, two nested domains were set up for the WRF model so that the inner domain covers an area where intense precipitation is frequently caused by MCSs and inside which the fourteen selected MCSs have occurred. The two domains are shown on Figure 3-1, where the outer domain has a resolution of 15 km (76 x 58) and the inner domain has a resolution of 5 km (166 x 188). The IBCs for the simulation domains were obtained from CFSR, which is provided by NCEP at 0.5 x 0.5 degrees spatial resolution and 6-hour temporal resolution (more details provided in Chapter 2). The WRF simulations were run with a total of 40 vertical levels.

Figure 3-1 The Two Nested Domains for the WRF Model Simulations of MCSs

The outer domain (in brown) has a resolution of 15 km, and the inner domain (in orange) has a resolution of 5 km.

For all the selected historical MCSs, the WRF model was configured by trying different combinations of the parameterization and configuration options until the best results were obtained for the simulation of each of the selected severe historical MCSs with respect to the simulated and observed precipitation fields. The best simulated result was determined based on a combination of a visual check comparing the simulated and observed fields, as well as based on a statistical check of the results of the three computed metrics for model performance assessment. A detailed explanation of these checks is provided in Chapter 2. The WRF model performance and parameterization schemes are summarized at the end of the chapter.

3.1 Numerical Simulation of the June 22, 2002 MCS

The June 22, 2002 MCS was one of the extreme storm events that were identified within the simulation region of the WRF model of this study. Among all the parameterization scheme combinations that were attempted during the calibration process of the WRF model for this storm event, Table 3-1 shows the parameterization scheme combination that provided the best reconstruction results. The results of this reconstruction are shown in Figure 3-2, Figure 3-3, and Table 3-2.

Figure 3-2 shows the plots of the 24-hr accumulated precipitation fields for this storm event. The left figure shows the observed precipitation field, and the right figure shows the simulated precipitation field that was obtained from the WRF model simulation that was done by using the best parameterization scheme combination. Visually comparing both of these figures showed that the simulated MCS was quite similar in shape, texture, and location to the observed MCS. Moreover, the relative error in the inner-domain-averaged total precipitation was computed to be only around 8.4%, which in turn shows that the model was capable of simulating the total precipitation depth relatively well.

In addition to the visual representation of the reconstructed MCS and its comparison to the observation, the results for the statistical metrics were also analyzed (Table 3-2 and Figure 3-3). For the 90th percentile threshold, for example, the overlap percentage was found to be around 74% and the PFAR was equal to 1.08. Hence, at that threshold value, the simulated precipitation field above the threshold overlapped 74% of the observed precipitation field above the threshold, thus showing a good placement of the storm. Moreover, with a PFAR of 1.08, the size of the simulated precipitation field was relatively close to the size of the observed precipitation field.

From Table 3-2, it is clear, however, that the overlap percentage tends to decrease at higher percentile threshold values. Nonetheless, even at the percentile thresholds corresponding to the regions of intense precipitation (e.g., the 95th, 97.5th, and 99th percentiles), it is clear that there was still relatively good overlap between the simulations and the observations, with the minimum overlap percentage being around 45% at the 99th percentile threshold. This shows the capability of the WRF model in placing the MCS in the appropriate location, even at the regions of intense precipitation.

As for the PFAR values shown in Table 3-2, the values ranged between 0.48 and 1.68, revealing that the size of the precipitation field by the WRF model sometimes either underestimated or overestimated the observed fields. However, the WRF model was still capable of producing a very good match between the simulated and observed field sizes, even at the regions of most intense precipitation. As such, this shows the ability of the WRF model in simulating the regions of precipitation quite well with respect to their sizes at the different percentile thresholds.

Figure B-1 of APPENDIX B shows the hourly precipitation field, water vapor flux fields, and the precipitable water plotted for the dates ranging from 06/21/2002 at 14h to 06/22/2002 at 19h. The hourly precipitable water and vapor flux fields are shown on the left plots, while the hourly precipitation fields are shown on the right plots. From this sequence of plots, one can see the evolution of the storm event with regards to the plotted fields. The plots show that relatively high-moisture atmospheric flow came into the domain causing intense precipitation on June 22 mainly in the northeastern part of the domain over the state of Wisconsin, from June 22 at 00h to June 22 at 08h. Consequently, this continuous precipitation formed heavy 24-hour precipitation during this storm event.

Table 3-1 Best Parameterization Schemes Combination for the Numerical Simulation of the June 22, 2002 MCS Event

Option	Option name/value
Microphysics	WRF Double Moment 5-class (WDM5)
Cumulus Parameterization (domain 1 only)	Tiedtke
PBL	Mellor-Yamada-Nakanishi-Niino (MYNN) 3rd Level TKE
Longwave Radiation	Goddard
Shortwave Radiation	Community Atmospheric Model (CAM)
Surface Layer	Mellor-Yamada-Nakanishi-Niino (MYNN)
Number of vertical layers	40
Time step	1.5 minutes

Table 3-2 Statistics of the Simulated Results for the June 22, 2002 MCS

The values in parentheses show the corresponding percentile value of the observed precipitation. PFAR: precipitation field area ratio.

	50th Percentile Threshold (0.1 mm)	**75th Percentile Threshold** (3.6 mm)	**90th Percentile Threshold** (16.9 mm)	**95th Percentile Threshold** (29.6 mm)	**97.5th Percentile Threshold** (47.0 mm)	**99th Percentile Threshold** (82.9 mm)
Overlap Percentage	48%	50%	74%	73%	57%	45%
PFAR	0.48	0.55	1.08	1.36	1.56	1.68

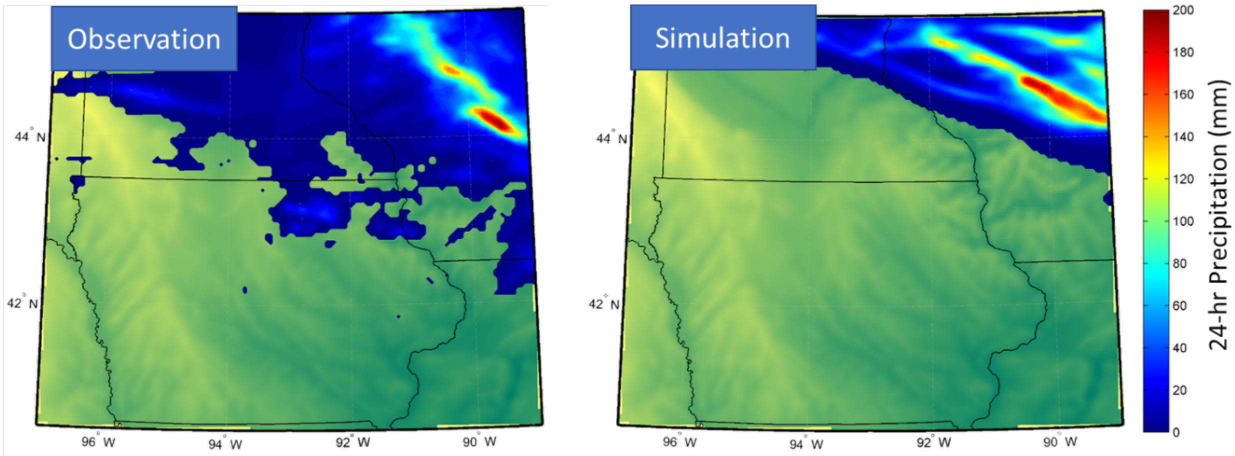

Figure 3-2 Observed (Left) and Simulated (Right) 24-hr Accumulated Precipitation Fields During the June 22, 2002 MCS

Total accumulated precipitation from 06/21/2002 at 19h to 06/22/2002 at 19h.

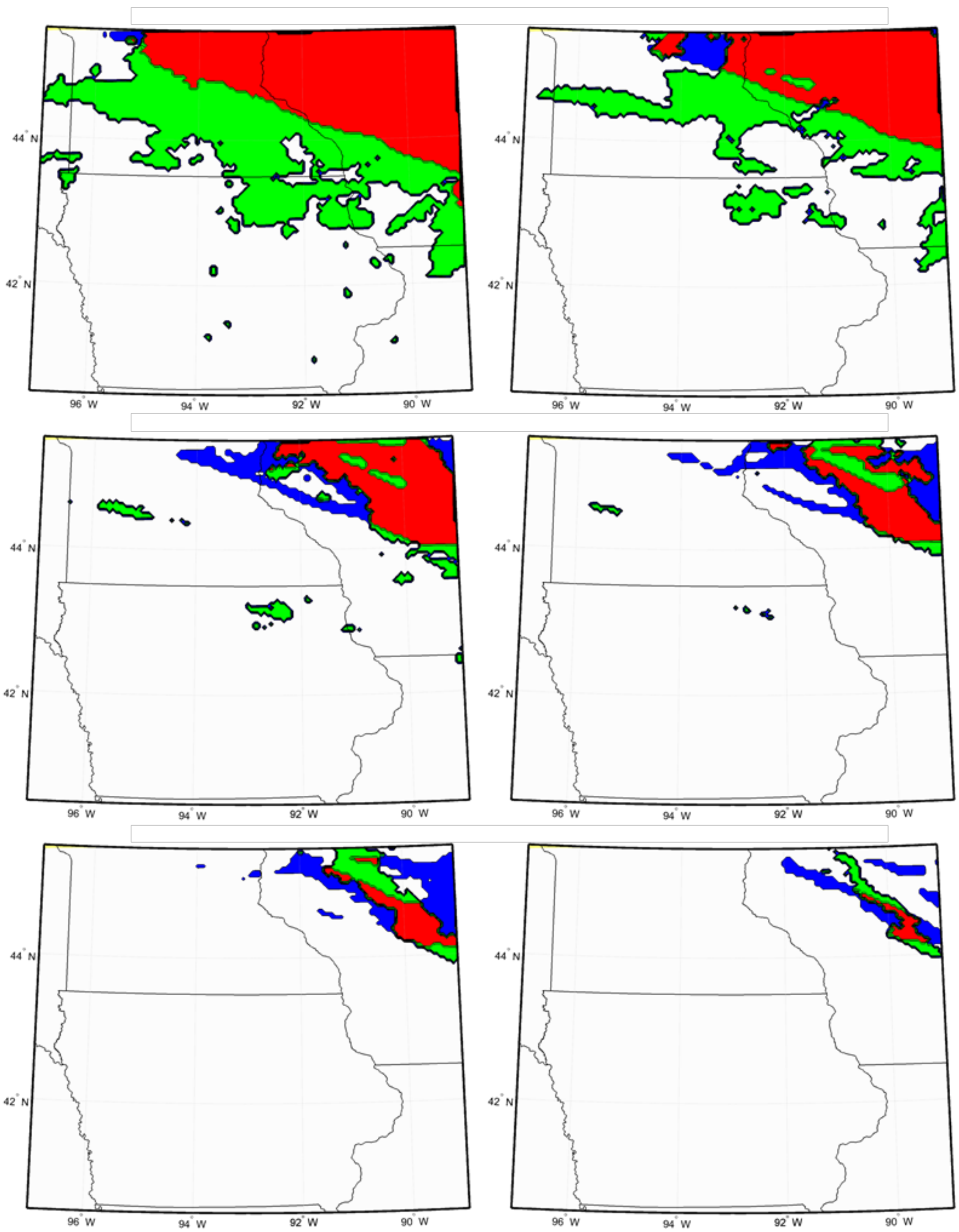

Figure 3-3 Overlapped Field of 24-hour Accumulated Precipitation Above the 50th, 75th, 90th, 95th, 97.5th, and 99th Percentile Values (from Left to Right and from the Top to the Bottom) During the June 22, 2002 MCS

Blue area: only simulation; green area: only observation; red area: both.

3.2 Numerical Simulation of the August 22, 2002 MCS

The August 22, 2002 MCS was another of the extreme storm events that were identified within the simulation region of the WRF model of this study. Among all the parameterization scheme combinations that were attempted during the calibration process of the WRF model for this storm event, Table 3-3 shows the parameterization scheme combination that provided the best reconstruction results. The results of this reconstruction are shown in Figure 3-4, Figure 3-5, and Table 3-4.

Figure 3-4 shows the plots of the 24-hr accumulated precipitation fields for this storm event. The left figure shows the observed precipitation field, and the right figure shows the simulated precipitation field that was obtained from the WRF model simulation that was done by using the best parameterization scheme combination. Visually comparing both of these figures showed that the simulated MCS was quite similar in shape, texture, and location to the observed MCS. Moreover, the relative error in the inner-domain-averaged total precipitation was computed to be only around 5.8%, which in turn shows that the model was capable of simulating the total precipitation depth relatively well.

In addition to the visual representation of the reconstructed MCS and its comparison to the observation, the results for the statistical metrics were also analyzed (Table 3-4 and Figure 3-5). For the 50th percentile threshold, for example, the overlap percentage was found to be around 58% and the PFAR was equal to 0.92. Hence, at that threshold value, the simulated precipitation field above the threshold overlapped 58% of the observed precipitation field above the threshold, thus showing a good placement of the storm. Moreover, with a PFAR of 0.92, the size of the simulated precipitation field was relatively close to the size of the observed precipitation field.

From Table 3-4, it is clear, however, that the overlap percentage tends to decrease at higher percentile threshold values. Nonetheless, even at the percentile thresholds corresponding to the regions of intense precipitation (e.g., the 95th, 97.5th, and 99th percentiles), it is clear that there was still relatively good overlap between the simulations and the observations, with the minimum overlap percentage being around 18% at the 99th percentile threshold. This shows the capability of the WRF model in placing the MCS in the appropriate location, even at the regions of intense precipitation.

As for the PFAR values shown in Table 3-4, the values ranged between 0.78 and 1.20 according to the threshold value, revealing that the size of the precipitation field simulated by the WRF model was sometimes either slightly underestimated or slightly overestimated. However, the WRF model was still capable of producing a very good match between the simulated and observed field sizes, even at the regions of most intense precipitation. As such, this shows the ability of the WRF model in simulating the regions of precipitation quite well with respect to their sizes at the different percentile thresholds.

Figure B-2 of APPENDIX B shows the hourly precipitation field, water vapor flux fields, and the precipitable water plotted for the dates ranging from 08/20/2002 at 20h to 08/22/2002 at 16h. The hourly precipitable water and vapor flux fields are shown on the left plots, while the hourly precipitation fields are shown on the right plots. From this sequence of plots, one can see the evolution of the storm event with regards to the plotted fields. The plots show that relatively high-moisture atmospheric flow came into the domain causing intense precipitation on August 21-22 mainly in the eastern part of the domain over the boundary between the states of Wisconsin, Iowa, and Illinois, from August 21 at 22h to August 22 at 04h. Consequently, this continuous precipitation formed heavy 24-hour precipitation during this storm event.

Table 3-3 Best Parameterization Schemes Combination for the Numerical Simulation of the August 22, 2002 MCS Event

Option	Option name/value
Microphysics	Stony-Brook University (SBU-YLin)
Cumulus Parameterization (domain 1 only)	Tiedtke
PBL	Total Energy-Mass Flux (TEMF)
Longwave Radiation	Rapid Radiative Transfer Model (RRTM)
Shortwave Radiation	Rapid Radiative Transfer Model for General Circulation Models (RRTMG)
Surface Layer	Total Energy-Mass Flux (TEMF)
Number of vertical layers	40
Time step	1.5 minutes

Table 3-4 Statistics of the Simulated Results for the August 22, 2002 MCS

The values in parentheses show the corresponding percentile value of the observed precipitation. PFAR: precipitation field area ratio.

	50^{th} Percentile Threshold (13.1 mm)	75^{th} Percentile Threshold (27.9 mm)	90^{th} Percentile Threshold (44.6 mm)	95^{th} Percentile Threshold (60.3 mm)	97.5^{th} Percentile Threshold (80.6 mm)	99^{th} Percentile Threshold (123.0 mm)
Overlap Percentage	58%	38%	31%	34%	39%	18%
PFAR	0.92	0.97	0.98	1.14	1.20	0.78

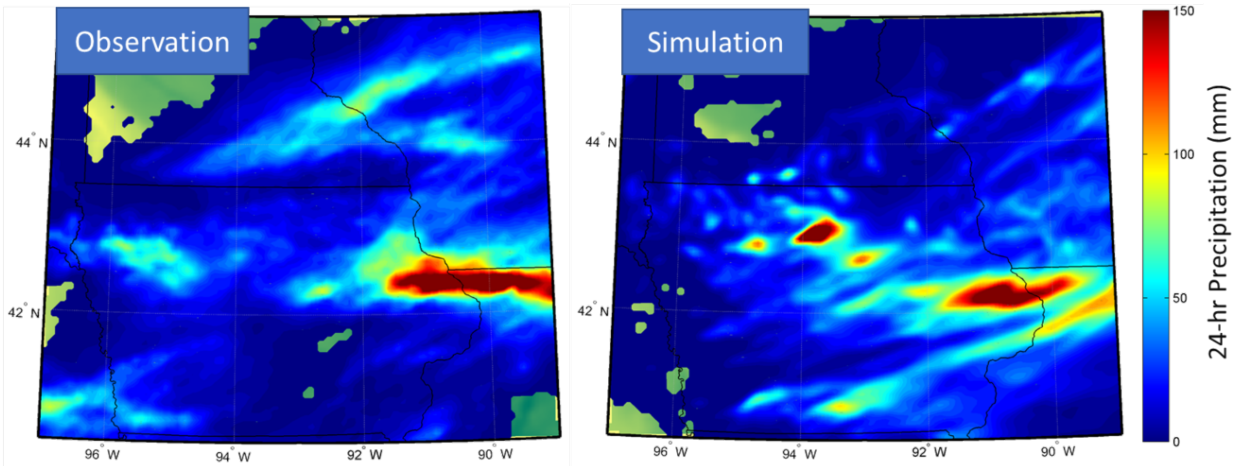

Figure 3-4 Observed (Left) and Simulated (Right) 24-hr Accumulated Precipitation Fields During the August 22, 2002 MCS

Total accumulated precipitation from 08/21/2002 at 16h to 08/22/2002 at 16h.

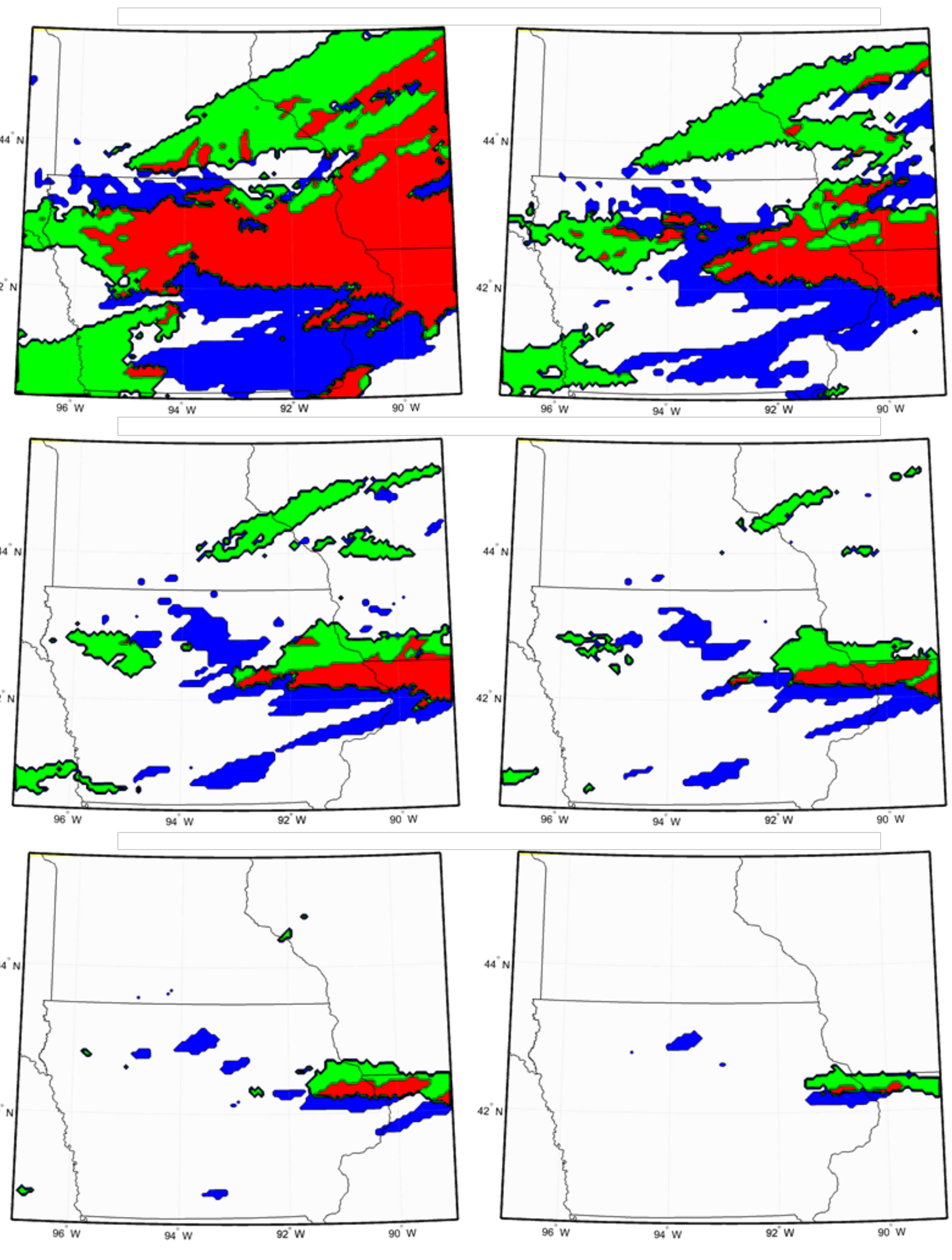

Figure 3-5 Overlapped Field of 24-hour Accumulated Precipitation Above the 50th, 75th, 90th, 95th, 97.5th, and 99th Percentile Values (from Left to Right and from the Top to the Bottom) During the August 22, 2002 MCS

Blue area: only simulation; green area: only observation; red area: both.

3.3 Numerical Simulation of the September 15, 2004 MCS

The September 15, 2004 MCS was another of the extreme storm events that were identified within the simulation region of the WRF model of this study. Among all the parameterization scheme combinations that were attempted during the calibration process of the WRF model for this storm event, Table 3-5 shows the parameterization scheme combination that provided the best reconstruction results. The results of this reconstruction are shown in Figure 3-6, Figure 3-7, and Table 3-6.

Figure 3-6 shows the plots of the 24-hr accumulated precipitation fields for this storm event. The left figure shows the observed precipitation field, and the right figure shows the simulated precipitation field that was obtained from the WRF model simulation performed with the best parameterization scheme combination. Visually comparing both of these figures showed that the simulated MCS was quite similar in shape, texture, and location to the observed MCS. Moreover, the relative error in the inner-domain-averaged total precipitation was computed to be around -10.6%, which in turn shows that the model was capable of simulating the total precipitation depth relatively well.

In addition to the visual representation of the reconstructed MCS and its comparison to the observation, the results for the statistical metrics were also analyzed (Table 3-6 and Figure 3-7). For the 90th percentile threshold, for example, the overlap percentage was found to be around 47% and the PFAR was equal to 1.14. Hence, at that threshold value, the simulated precipitation field above the threshold overlapped 47% of the observed precipitation field above the threshold, thus showing a good placement of the storm. Moreover, with a PFAR of 1.14, the size of the simulated precipitation field was relatively close to the size of the observed precipitation field.

From Table 3-6, it is clear, however, that the overlap percentage tends to decrease at higher percentile threshold values. Nonetheless, even at the percentile thresholds corresponding to the regions of intense precipitation (e.g., the 95th, 97.5th, and 99th percentiles), it is clear that there was still relatively good overlap between the simulations and the observations, with the minimum overlap percentage being around 19% at the 99th percentile threshold. This shows the capability of the WRF model in placing the MCS in the appropriate location, even at the regions of intense precipitation.

As for the PFAR values shown in Table 3-6, the values ranged between 0.66 and 2.22, revealing that the WRF model sometimes either underestimated or overestimated the size of the precipitation field. However, the WRF model was still capable of producing a very good match between the simulated and observed field sizes, even at the regions of most intense precipitation. As such, this shows the ability of the WRF model in simulating the regions of precipitation quite well with respect to their sizes at the different percentile thresholds.

Figure B-3 of APPENDIX B shows the hourly precipitation field, water vapor flux fields, and the precipitable water plotted for the dates ranging from 09/13/2004 at 20h to 09/15/2004 at 16h. The hourly precipitable water and vapor flux fields are shown on the left plots, while the hourly precipitation fields are shown on the right plots. From this sequence of plots, one can see the evolution of the storm event with regards to the plotted fields. The plots show that relatively high-moisture atmospheric flow came into the domain causing intense precipitation on September 15 mainly over the states of Iowa and Minnesota, from September 15 at 01h to September 15 at 07h. Consequently, this continuous precipitation formed heavy 24-hour precipitation during this storm event.

Table 3-5 **Best Parameterization Scheme Combination for the Numerical Simulation of the September 15, 2004 MCS Event**

Option	Option name/value
Microphysics	Goddard GCE
Cumulus Parameterization (domain 1 only)	Kain-Fritsch (old)
Planetary Boundary Layer	NCEP Global Forecast System (NCEP GFS)
Longwave Radiation	Goddard
Shortwave Radiation	Community Atmospheric Model (CAM)
Surface Layer	NCEP Global Forecast System (NCEP GFS)
Number of vertical layers	40
Time step	1.5 minutes

Table 3-6 **Statistics of the Simulated Results for the September 15, 2004 MCS**

The values in parentheses show the corresponding percentile value of the observed precipitation. PFAR: precipitation field area ratio.

	50^{th} Percentile Threshold (3.6 mm)	75^{th} Percentile Threshold (27.8 mm)	90^{th} Percentile Threshold (67.8 mm)	95^{th} Percentile Threshold (100.8 mm)	97.5^{th} Percentile Threshold (132.7 mm)	99^{th} Percentile Threshold (158.4 mm)
Overlap Percentage	65%	56%	47%	36%	27%	19%
PFAR	0.66	0.79	1.14	1.61	2.01	2.22

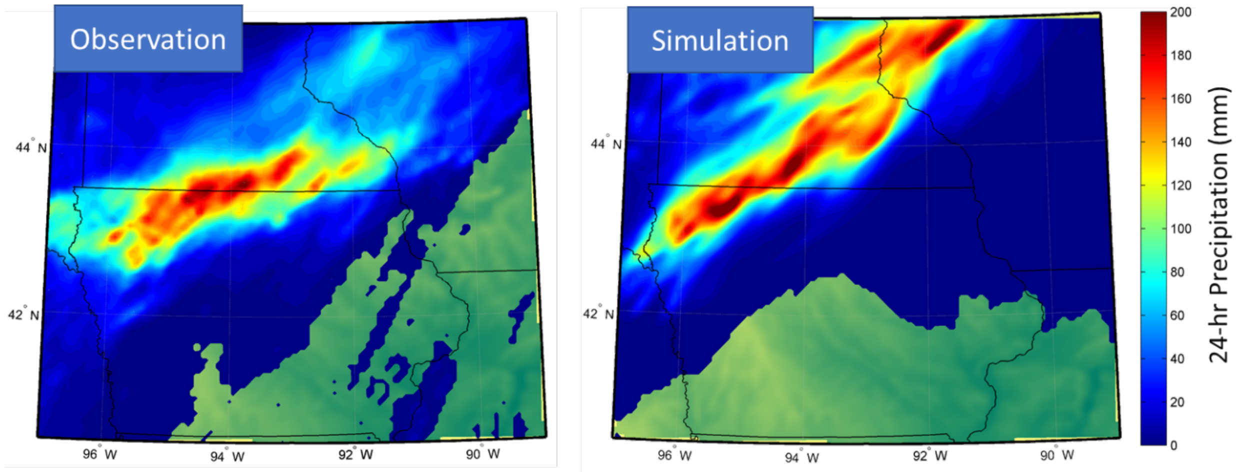

Figure 3-6 Observed (Left) and Simulated (Right) 24-hr Accumulated Precipitation Fields During the September 15, 2004 MCS

Total accumulated precipitation from 09/14/2004 at 12h to 09/15/2004 at 12h.

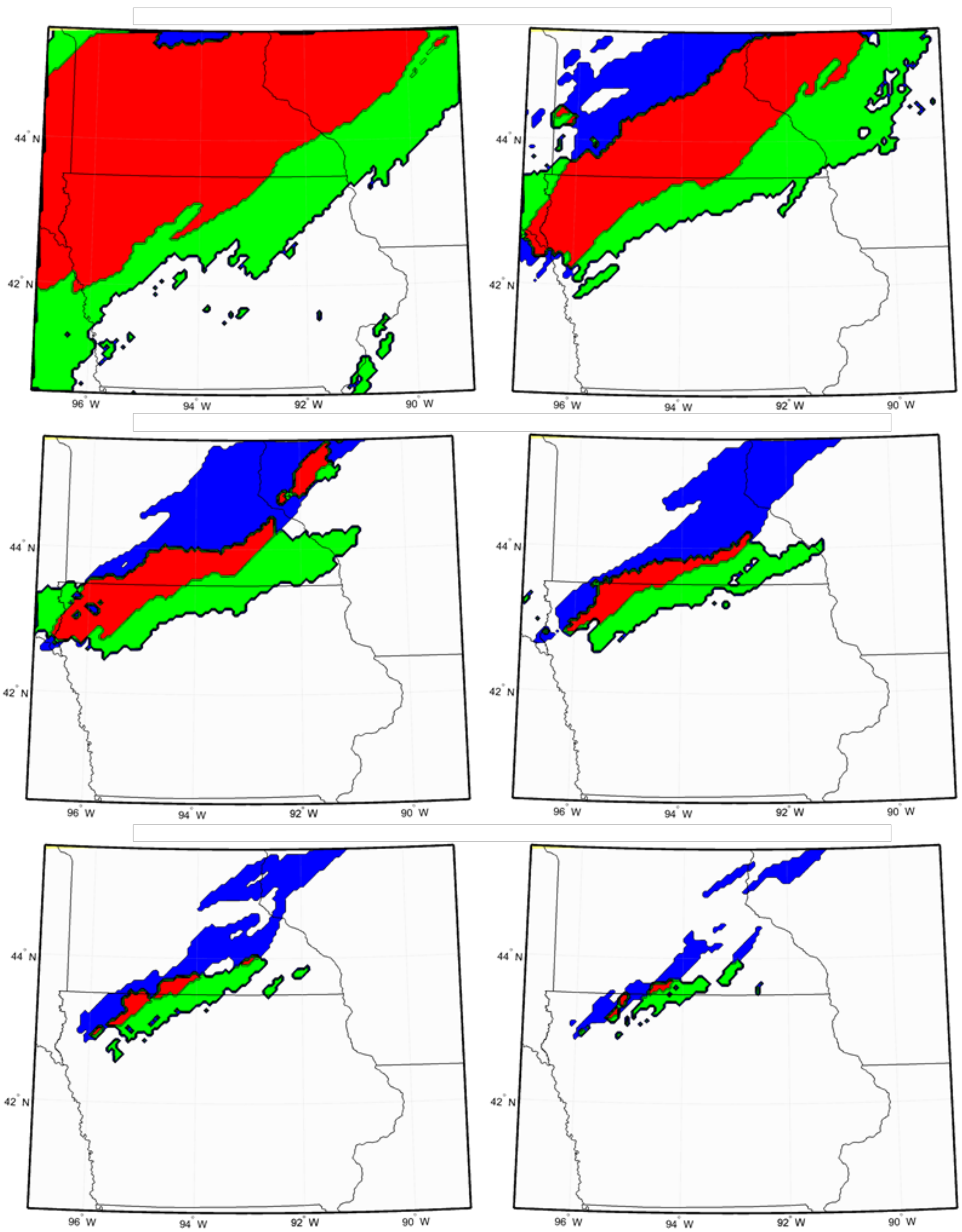

Figure 3-7 Overlapped Field of 24-hour Accumulated Precipitation Above the 50th, 75th, 90th, 95th, 97.5th, and 99th Percentile Values (from Left to Right and from the Top to the Bottom) During the September 15, 2004 MCS

Blue area: only simulation; green area: only observation; red area: both.

3.4 Numerical Simulation of the June 25, 2005 MCS

The June 25, 2005 MCS was another of the extreme storm events that were identified within the simulation region of the WRF model of this study. Among all the parameterization scheme combinations that were attempted during the calibration process of the WRF model for this storm event, Table 3-7 shows the parameterization scheme combination that provided the best reconstruction results. The results of this reconstruction are shown in Figure 3-8, Figure 3-9, and Table 3-8.

Figure 3-8 shows the plots of the 24-hr accumulated precipitation fields for this storm event. The left figure shows the observed precipitation field, and the right figure shows the simulated precipitation field that was obtained from the WRF model simulation performed with the best parameterization scheme combination. Visually comparing both of these figures showed that the simulated MCS was quite similar in shape, texture, and location to the observed MCS. While the relative error in the inner-domain-averaged total precipitation was computed to be around -20.7%, the model can still be considered to be capable of adequately simulating the total precipitation depth.

In addition to the visual representation of the reconstructed MCS and its comparison to the observation, the results for the statistical metrics were also analyzed (Table 3-8 and Figure 3-9). For the 95th percentile threshold, for example, the overlap percentage was found to be around 44% and the PFAR was equal to 0.84. Hence, at that threshold value, the simulated precipitation field above the threshold overlapped 44% of the observed precipitation field above the threshold, thus showing a good placement of the storm. Moreover, with a PFAR of 0.84, the size of the simulated precipitation field was relatively close to the size of the observed precipitation field.

From Table 3-8, it is clear, however, that the overlap percentage tends to decrease at higher percentile threshold values. Nonetheless, even at the percentile thresholds corresponding to the regions of intense precipitation (e.g., the 95th, 97.5th, and 99th percentiles), it is clear that there was still relatively good overlap between the simulations and the observations, with the minimum overlap percentage being around 21% at the 99th percentile threshold. This shows the capability of the WRF model in placing the MCS in the appropriate location, even at the regions of intense precipitation.

As for the PFAR values shown in Table 3-8, the values ranged between 0.52 and 1.21, revealing that the size of the precipitation field from the WRF model was sometimes either slightly underestimated or slightly overestimated. However, the WRF model was still capable of producing a very good match between the simulated and observed field sizes, even at the regions of most intense precipitation. As such, this shows the ability of the WRF model in simulating the regions of precipitation quite well with respect to their sizes at the different percentile thresholds.

Figure B-4 of APPENDIX B shows the hourly precipitation field, water vapor flux fields, and the precipitable water plotted for the dates ranging from 06/24/2005 at 13h to 06/25/2005 at 18h. The hourly precipitable water and vapor flux fields are shown on the left plots, while the hourly precipitation fields are shown on the right plots. From this sequence of plots, one can see the evolution of the storm event with regards to the plotted fields. The plots show that relatively high-moisture atmospheric flow came into the domain causing intense precipitation on June 25 mainly in the middle of the simulation domain over the state of Iowa, from June 25 at 05h to June 25 at 11h. Consequently, this continuous precipitation formed heavy 24-hour precipitation during this storm event.

Table 3-7 Best Parameterization Scheme Combination for the Numerical Simulation of the June 25, 2005 MCS event

Option	Option name/value
Microphysics	Lin et al.
Cumulus Parameterization (domain 1 only)	Tiedtke
PBL	NCEP Global Forecast System (NCEP GFS)
Longwave Radiation	Community Atmospheric Model (CAM)
Shortwave Radiation	Rapid Radiative Transfer Model for General Circulation Models (RRTMG)
Surface Layer	NCEP Global Forecast System (NCEP GFS)
Number of vertical layers	40
Time step	1.5 minutes

Table 3-8 Statistics of the Simulated Results for the June 25, 2005 MCS

The values in parentheses show the corresponding percentile value of the observed precipitation. PFAR: precipitation field area ratio.

	50^{th} Percentile Threshold (0.4 mm)	75^{th} Percentile Threshold (8.3 mm)	90^{th} Percentile Threshold (33.5 mm)	95^{th} Percentile Threshold (49.1 mm)	97.5^{th} Percentile Threshold (61.3 mm)	99^{th} Percentile Threshold (93.5 mm)
Overlap Percentage	57%	47%	46%	44%	39%	21%
PFAR	0.66	0.52	0.63	0.84	1.21	1.11

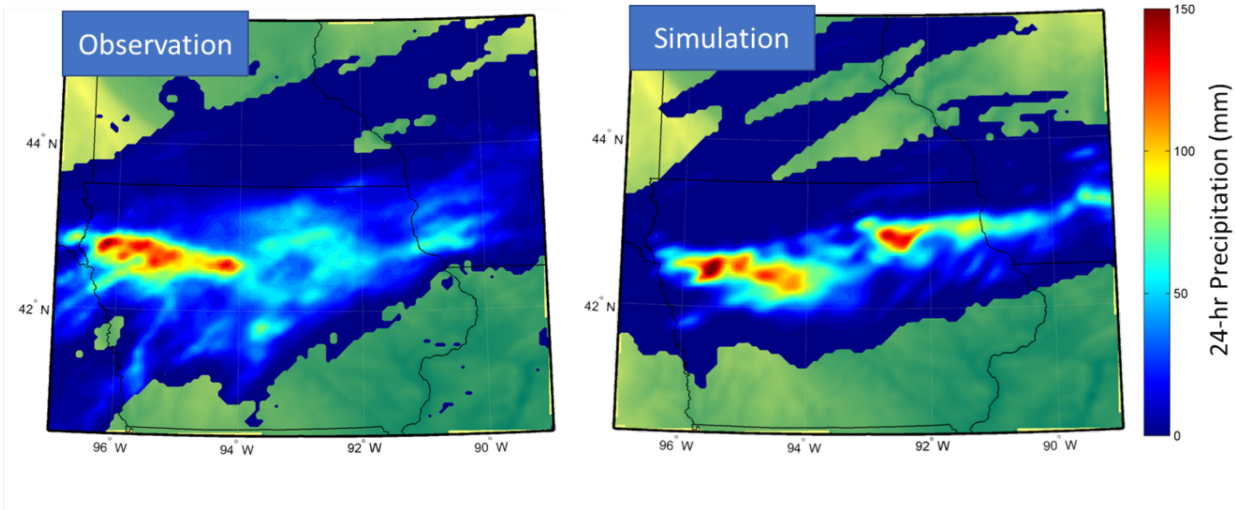

Figure 3-8 Observed (Left) and Simulated (Right) 24-hr Accumulated Precipitation Fields During the June 25, 2005 MCS

Total accumulated precipitation from 06/24/2005 at 18h to 06/25/2005 at 18h.

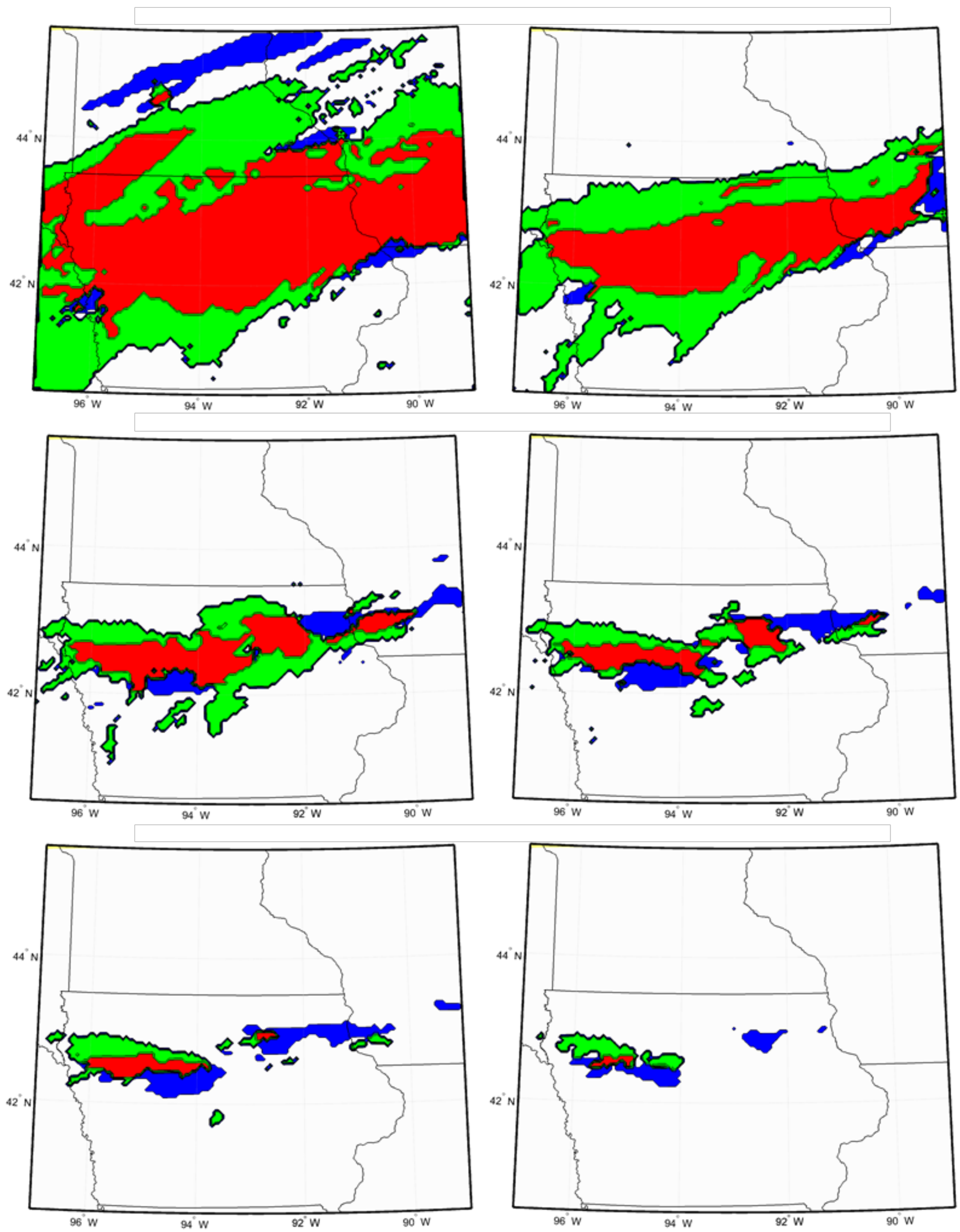

Figure 3-9 Overlapped Field of 24-hour Accumulated Precipitation Above the 50th, 75th, 90th, 95th, 97.5th, and 99th Percentile Values (from Left to Right and from the Top to the Bottom) During the June 25, 2005 MCS

Blue area: only simulation; green area: only observation; red area: both.

3.5 Numerical Simulation of the August 17, 2005 MCS

The August 17, 2005 MCS was another of the extreme storm events that were identified within the simulation region of the WRF model of this study. Among all the parameterization scheme combinations that were attempted during the calibration process of the WRF model for this storm event, Table 3-9 shows the parameterization scheme combination that provided the best reconstruction results. The results of this reconstruction are shown in Figure 3-10, Figure 3-11, and Table 3-10.

Figure 3-10 shows the plots of the 24-hr accumulated precipitation fields for this storm event. The left figure shows the observed precipitation field, and the right figure shows the simulated precipitation field that was obtained from the WRF model simulation that was done by using the best parameterization scheme combination. Visually comparing both of these figures showed that the simulated MCS was quite similar in shape, texture, and location to the observed MCS. Moreover, the relative error in the inner-domain-averaged total precipitation was computed to be only around 7.4%, which in turn shows that the model was capable of simulating the total precipitation depth relatively well.

In addition to the visual representation of the reconstructed MCS and its comparison to the observation, the results for the statistical metrics were also analyzed (Table 3-10 and Figure 3-11). For the 50th percentile threshold, for example, the overlap percentage was found to be around 64% and the PFAR was equal to 0.95. Hence, at that threshold value, the simulated precipitation field above the threshold overlapped 64% of the observed precipitation field above the threshold, thus showing a good placement of the storm. Moreover, with a PFAR of 0.95, the size of the simulated precipitation field was relatively close to the size of the observed precipitation field.

From Table 3-10, it is clear, however, that the overlap percentage tends to decrease at higher percentile threshold values. Nonetheless, even at the percentile thresholds corresponding to the regions of intense precipitation (e.g., the 95th, 97.5th, and 99th percentiles), it is clear that there was still relatively good overlap between the simulations and the observations, with the minimum overlap percentage being around 42% at the 97.5th percentile threshold. This shows the capability of the WRF model in placing the MCS in the appropriate location, even at the regions of intense precipitation.

As for the PFAR values shown in Table 3-10, the values ranged between 0.95 and 1.86, revealing that the WRF model rarely underestimated but mostly overestimated the size of the precipitation field. However, the WRF model was still capable of producing a very good match between the simulated and observed field sizes, even at the regions of most intense precipitation. As such, this shows the ability of the WRF model in simulating the regions of precipitation quite well with respect to their sizes at the different percentile thresholds.

Figure B-5 of APPENDIX B shows the hourly precipitation field, water vapor flux fields, and the precipitable water plotted for the dates ranging from 08/17/2005 at 16h to 08/19/2005 at 06h. The hourly precipitable water and vapor flux fields are shown on the left plots, while the hourly precipitation fields are shown on the right plots. From this sequence of plots, one can see the evolution of the storm event with regards to the plotted fields. The plots show that relatively high-moisture atmospheric flow came into the domain causing intense precipitation on August 18 mainly in the part of the domain over the boundary between the states of Minnesota and Iowa, from August 18 at 01h to August 18 at 11h. Consequently, this continuous precipitation formed heavy 24-hour precipitation during this storm event.

Table 3-9 Best Parameterization Scheme Combination for the Numerical Simulation of the August 17, 2005 MCS Event

Option	Option name/value
Microphysics	WRF Single-moment 6-class (WSM6)
Cumulus Parameterization (domain 1 only)	Old GFS Simplified Arakawa-Schubert (SAS)
PBL	Mellor-Yamada-Janjic (MYJ) TKE
Longwave Radiation	Rapid Radiative Transfer Model (RRTM)
Shortwave Radiation	Dudhia
Surface Layer	Monin-Obukhov
Number of vertical layers	40
Time step	1.5 minutes

Table 3-10 Statistics of the Simulated Results for the August 17, 2005 MCS

The values in parentheses show the corresponding percentile value of the observed precipitation. PFAR: precipitation field area ratio.

	50th Percentile Threshold (4.0 mm)	**75th Percentile Threshold** (15.7 mm)	**90th Percentile Threshold** (32.5 mm)	**95th Percentile Threshold** (46.4 mm)	**97.5th Percentile Threshold** (59.4 mm)	**99th Percentile Threshold** (75.9 mm)
Overlap Percentage	64%	56%	57.7%	51%	42%	43%
PFAR	0.95	0.99	1.23	1.34	1.41	1.86

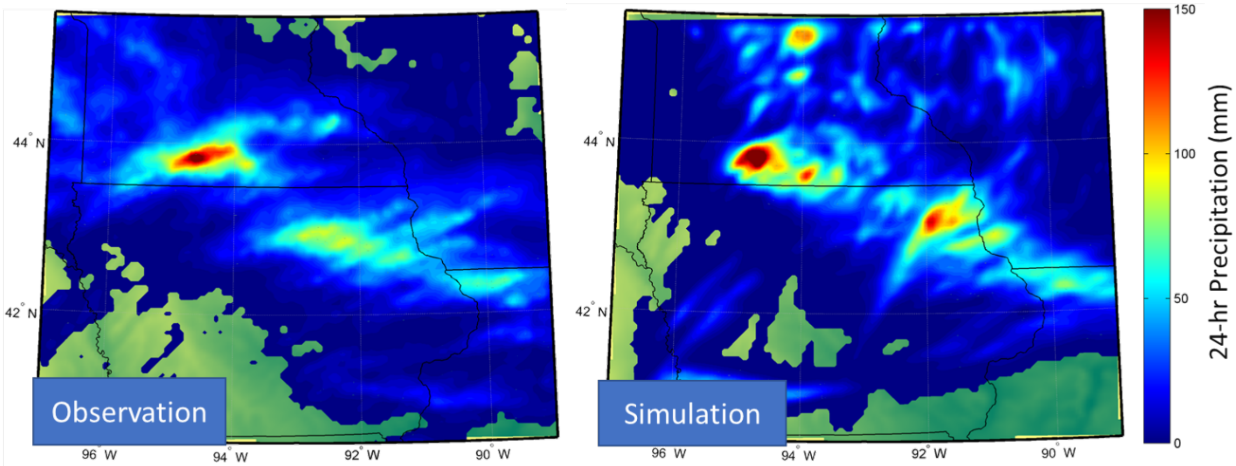

Figure 3-10 Observed (Left) and Simulated (Right) 24-hr Accumulated Precipitation Fields During the August 17, 2005 MCS

Total accumulated precipitation from 08/17/2005 at 20h to 08/18/2005 at 20h.

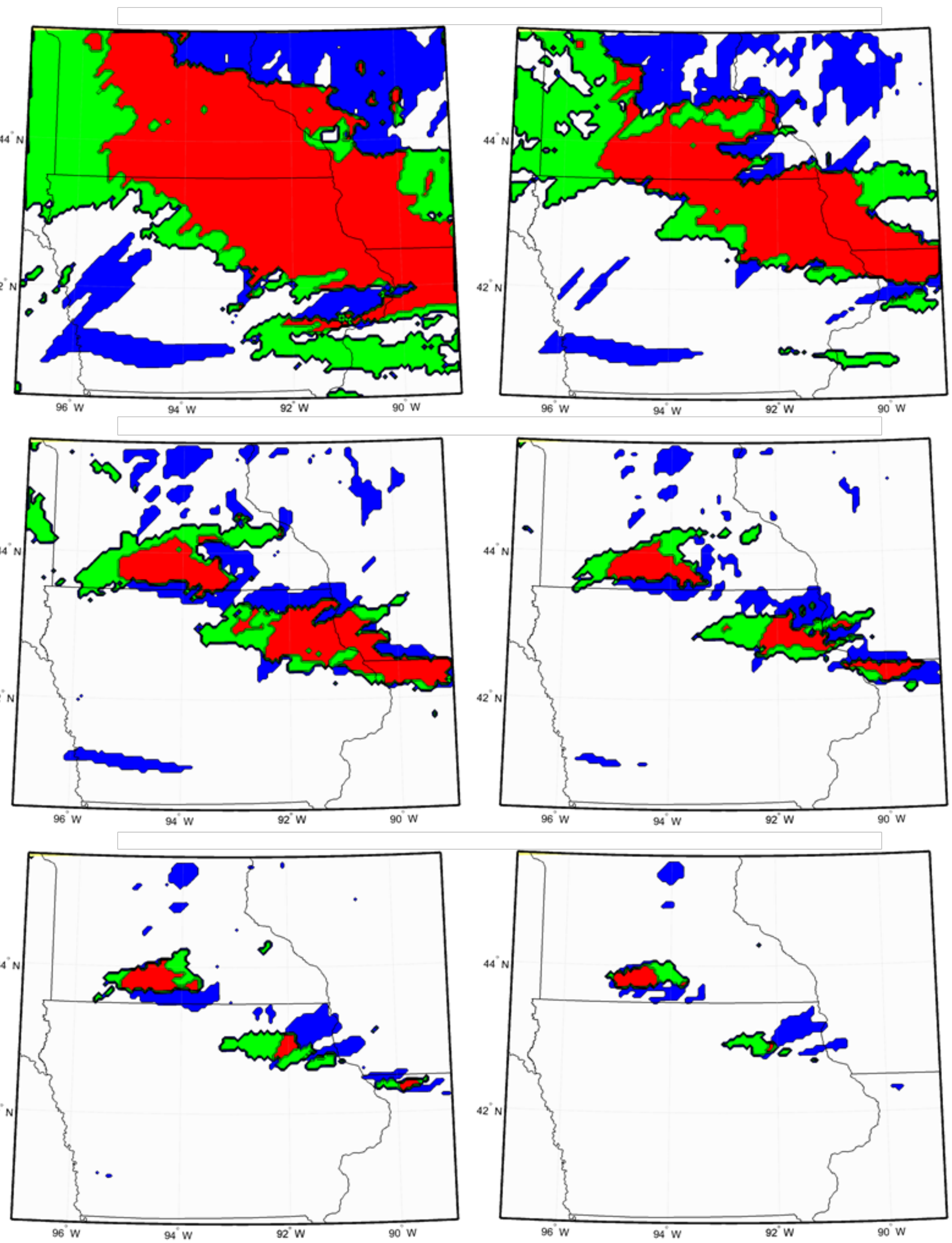

Figure 3-11 Overlapped Field of 24-hour Accumulated Precipitation Above the 50th, 75th, 90th, 95th, 97.5th, and 99th Percentile Values (from Left to Right and from the Top to the Bottom) During the August 17, 2005 MCS

Blue area: only simulation; green area: only observation; red area: both.

3.6 Numerical Simulation of the September 25, 2005 MCS

The September 25, 2005 MCS was another of the extreme storm events that were identified within the simulation region of the WRF model of this study. Among all the parameterization scheme combinations that were attempted during the calibration process of the WRF model for this storm event, Table 3-11 shows the parameterization scheme combination that provided the best reconstruction results. The results of this reconstruction are shown in Figure 3-12, Figure 3-13, and Table 3-12.

Figure 3-12 shows the plots of the 24-hr accumulated precipitation fields for this storm event. The left figure shows the observed precipitation field, and the right figure shows the simulated precipitation field that was obtained from the WRF model simulation that was done by using the best parameterization scheme combination. Visually comparing both of these figures showed that the simulated MCS was quite similar in shape, texture, and location to the observed MCS. While the relative error in the inner-domain-averaged total precipitation was computed to be around -17.3%, the model can still be considered to be capable of adequately simulating the total precipitation depth.

In addition to the visual representation of the reconstructed MCS and its comparison to the observation, the results for the statistical metrics were also analyzed (Table 3-12 and Figure 3-13). For the 75th percentile threshold, for example, the overlap percentage was found to be around 51% and the PFAR was equal to 0.73. Hence, at that threshold value, the simulated precipitation field above the threshold overlapped 51% of the observed precipitation field above the threshold, thus showing a good placement of the storm. Moreover, with a PFAR of 0.73, the size of the simulated precipitation field was relatively close to the size of the observed precipitation field.

From Table 3-12, it is clear that even at the percentile thresholds corresponding to the regions of intense precipitation (e.g., the 95th, 97.5th, and 99th percentiles), there was still relatively good overlap between the simulations and the observations. In fact, the overlap percentage was around 50% at the 99th percentile threshold, with a PFAR of around 1.96. The minimum overlap percentage was around 43%, and it was obtained at the 90th percentile threshold. This shows the capability of the WRF model in placing the MCS in the appropriate location, even at the regions of intense precipitation.

As for the PFAR values shown in Table 3-12, the values ranged between 0.56 and 1.96, revealing that the size of the precipitation field simulated by the WRF model was sometimes either underestimated or overestimated. However, the WRF model was still capable of producing a very good match between the simulated and observed field sizes, even at the regions of most intense precipitation. As such, this shows the ability of the WRF model in simulating the regions of precipitation quite well with respect to their sizes at the different percentile thresholds.

Figure B-6 of APPENDIX B shows the hourly precipitation field, water vapor flux fields, and the precipitable water plotted for the dates ranging from 09/24/2005 at 17h to 09/26/2005 at 07h. The hourly precipitable water and vapor flux fields are shown on the left plots, while the hourly precipitation fields are shown on the right plots. From this sequence of plots, one can see the evolution of the storm event with regards to the plotted fields. The plots show that relatively high-moisture atmospheric flow came into the domain causing intense precipitation on September 25 mainly in the part of the domain over the boundary between the states of Iowa and Minnesota, from September 25 at 02h to September 25 at 07h. Consequently, this continuous precipitation formed heavy 24-hour precipitation during this storm event.

Table 3-11 Best Parameterization Scheme Combination for the Numerical Simulation of the September 25, 2005 MCS Event

Option	Option name/value
Microphysics	Goddard GCE
Cumulus Parameterization (domain 1 only)	Kain-Fritsch
PBL	Bougeault-Lacarrere (BouLac)
Longwave Radiation	Rapid Radiative Transfer Model (RRTM)
Shortwave Radiation	Dudhia
Surface Layer	Revised MM5 Monin-Obukhov
Number of vertical layers	40
Time step	1.5 minutes

Table 3-12 Statistics of the Simulated Results for the September 25, 2005 MCS

The values in parentheses show the corresponding percentile value of the observed precipitation. PFAR: precipitation field area ratio.

	50th Percentile Threshold (10.7 mm)	**75th Percentile Threshold** (29.1 mm)	**90th Percentile Threshold** (58.2 mm)	**95th Percentile Threshold** (76.4 mm)	**97.5th Percentile Threshold** (98.0 mm)	**99th Percentile Threshold** (135.0 mm)
Overlap Percentage	52%	51%	43%	48%	57%	50%
PFAR	0.56	0.73	0.93	1.27	1.53	1.96

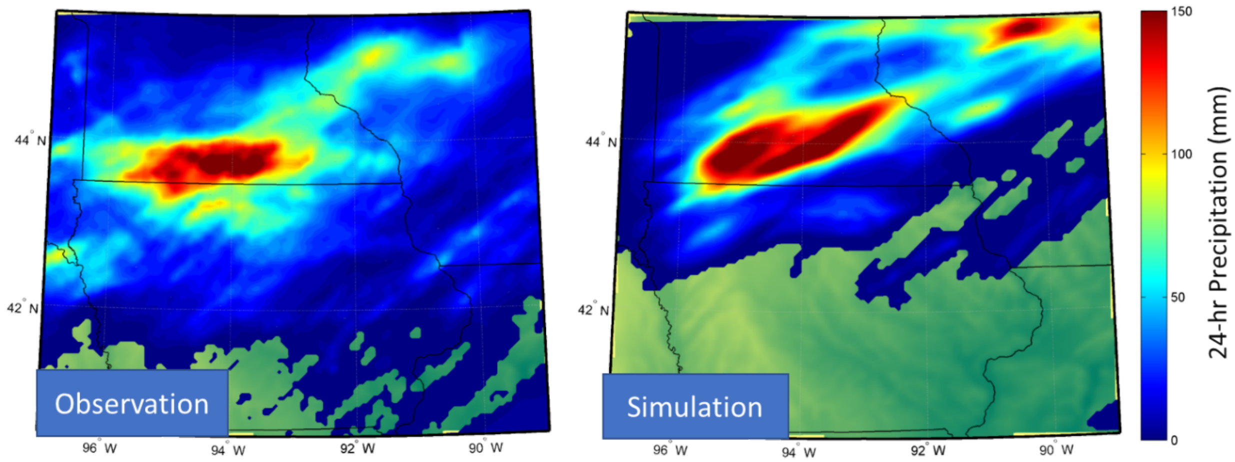

Figure 3-12 Observed (Left) and Simulated (Right) 24-hr Accumulated Precipitation Fields During the September 25, 2005 MCS

Total accumulated precipitation from 09/24/2005 at 21h to 09/25/2005 at 21h.

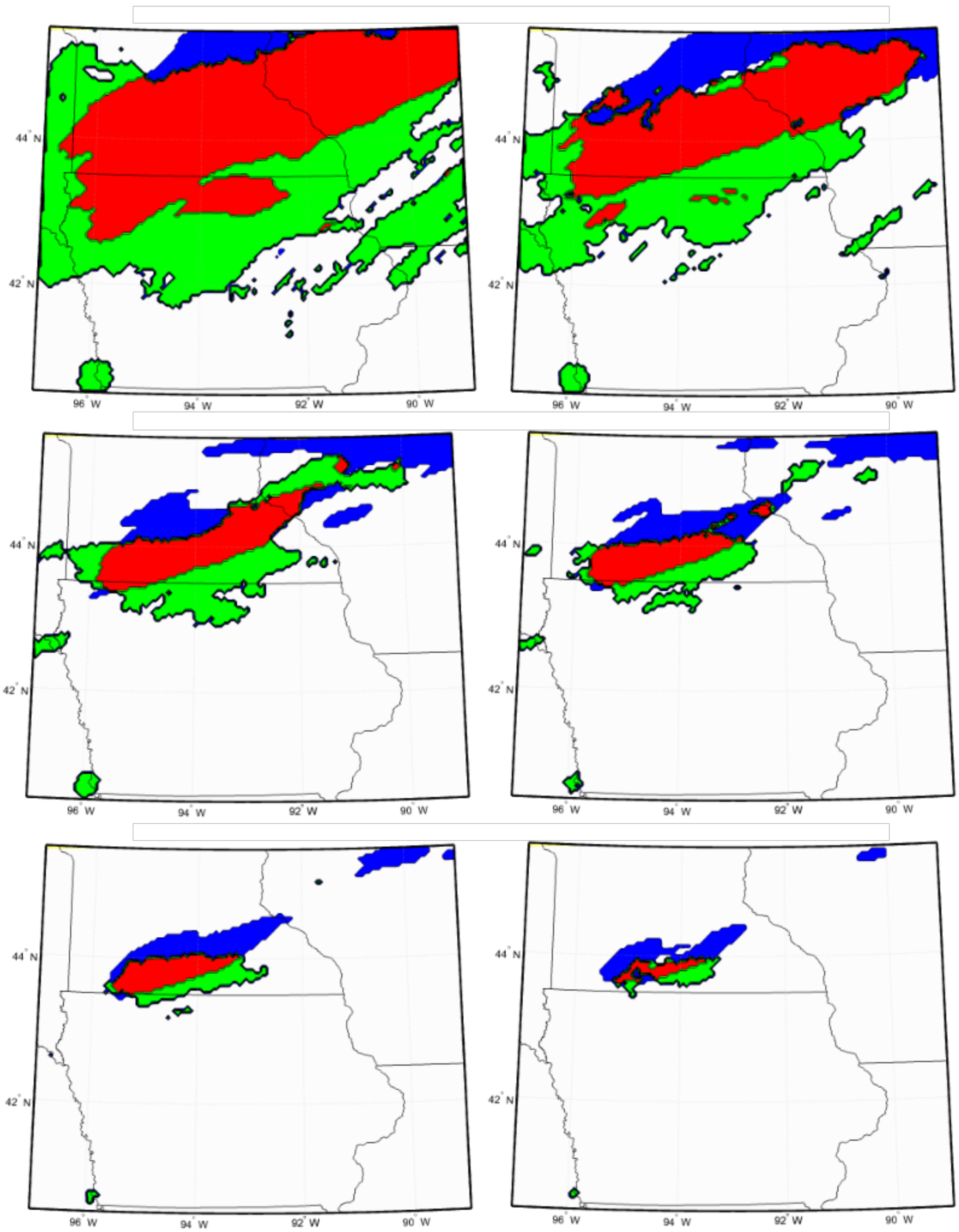

Figure 3-13 Overlapped Field of 24-hour Accumulated Precipitation Above the 50th, 75th, 90th, 95th, 97.5th, and 99th Percentile Values (from Left to Right and from the Top to the Bottom) During the September 25, 2005 MCS

Blue area: only simulation; green area: only observation; red area: both.

3.7 Numerical Simulation of the July 18, 2007 MCS

The July 18, 2007 MCS was another of the extreme storm events that were identified within the simulation region of the WRF model of this study. Among all the parameterization scheme combinations that were attempted during the calibration process of the WRF model for this storm event, Table 3-13 shows the parameterization scheme combination that provided the best reconstruction results. The results of this reconstruction are shown in Figure 3-14, Figure 3-15, and Table 3-14.

Figure 3-14 shows the plots of the 24-hr accumulated precipitation fields for this storm event. The left figure shows the observed precipitation field, and the right figure shows the simulated precipitation field that was obtained from the WRF model simulation that was done by using the best parameterization scheme combination. Visually comparing both of these figures showed that the simulated MCS was quite similar in shape, texture, and location to the observed MCS. Moreover, the relative error in the inner-domain-averaged total precipitation was computed to be only around -4.5%, which in turn shows that the model was capable of simulating the total precipitation depth relatively well.

In addition to the visual representation of the reconstructed MCS and its comparison to the observation, the results for the statistical metrics were also analyzed (Table 3-14 and Figure 3-15). For the 75th percentile threshold, for example, the overlap percentage was found to be around 57% and the PFAR was equal to 1.08. Hence, at that threshold value, the simulated precipitation field above the threshold overlapped 57% of the observed precipitation field above the threshold, thus showing a good placement of the storm. Moreover, with a PFAR of 1.08, the size of the simulated precipitation field was relatively close to the size of the observed precipitation field.

From Table 3-14, it is clear that even at the percentile thresholds corresponding to the regions of intense precipitation (e.g., the 95th, 97.5th, and 99th percentiles), there was still relatively good overlap between the simulations and the observations. In fact, the overlap percentage was around 55% at the 99th percentile threshold, with a PFAR of around 1.67. The minimum overlap percentage was around 41%, and it was obtained at the 90th percentile threshold. This shows the capability of the WRF model in placing the MCS in the appropriate location, even at the regions of intense precipitation.

As for the PFAR values shown in Table 3-14, the values ranged between 1.06 and 2.01, revealing that the size of the precipitation field simulated by the WRF model was mostly overestimated. However, the WRF model was still capable of producing a very good match between the simulated and observed field sizes, even at the regions of most intense precipitation. As such, this shows the ability of the WRF model in simulating the regions of precipitation quite well with respect to their sizes at the different percentile thresholds.

Figure B-7 of APPENDIX B shows the hourly precipitation field, water vapor flux fields, and the precipitable water plotted for the dates ranging from 07/17/2007 at 01h to 07/18/2007 at 12h. The hourly precipitable water and vapor flux fields are shown on the left plots, while the hourly precipitation fields are shown on the right plots. From this sequence of plots, one can see the evolution of the storm event with regards to the plotted fields. The plots show that relatively high-moisture atmospheric flow came into the domain causing intense precipitation on July 18 mainly in the part of the domain over the boundary between the states of Iowa, Wisconsin, and Minnesota, from July 18 at 02h to July 18 at 10h. Consequently, this continuous precipitation formed heavy 24-hour precipitation during this storm event.

Table 3-13 Best Parameterization Scheme Combination for the Numerical Simulation of the July 18, 2007 MCS Event

Option	Option name/value
Microphysics	WRF Double Moment 6-class (WDM6)
Cumulus Parameterization (domain 1 only)	Grell 3D ensemble (new)
PBL	NCEP Global Forecast System (NCEP GFS)
Longwave Radiation	GFDL
Shortwave Radiation	Rapid Radiative Transfer Model for General Circulation Models (RRTMG)
Surface Layer	NCEP Global Forecast System (NCEP GFS)
Number of vertical layers	40
Time step	1.5 minutes

Table 3-14 Statistics of the Simulated Results for the July 18, 2007 MCS

The values in parentheses show the corresponding percentile value of the observed precipitation. PFAR: precipitation field area ratio.

	50^{th} Percentile Threshold (0.1 mm)	75^{th} Percentile Threshold (5.2 mm)	90^{th} Percentile Threshold (28.7 mm)	95^{th} Percentile Threshold (39.6 mm)	97.5^{th} Percentile Threshold (53.6 mm)	99^{th} Percentile Threshold (74.2 mm)
Overlap Percentage	92%	57%	41%	47%	51%	55%
PFAR	2.01	1.08	1.06	1.52	1.87	1.67

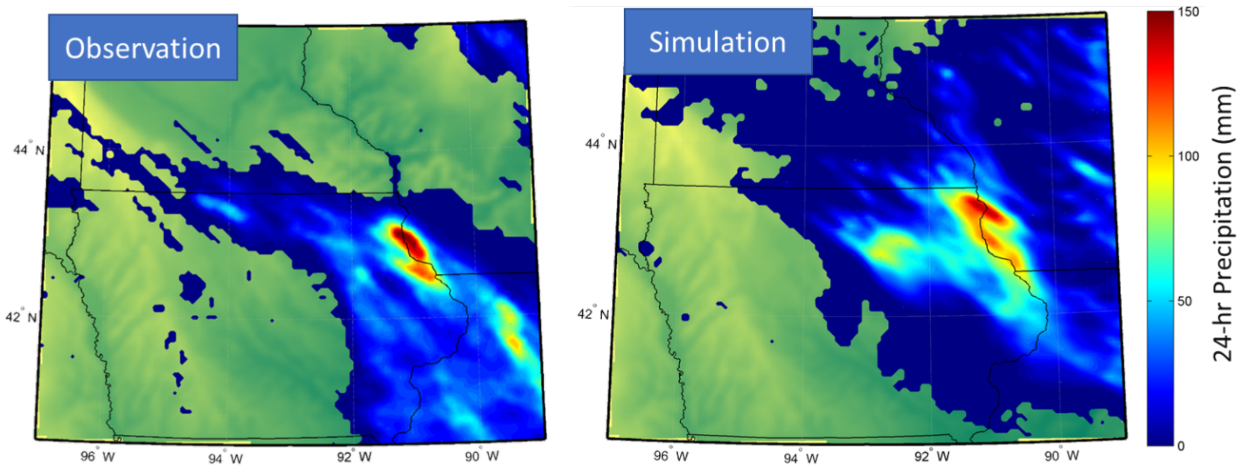

Figure 3-14 Observed (Left) and Simulated (Right) 24-hr Accumulated Precipitation Fields During the July 18, 2007 MCS

Total accumulated precipitation from 07/17/2007 at 11h to 07/18/2007 at 11h.

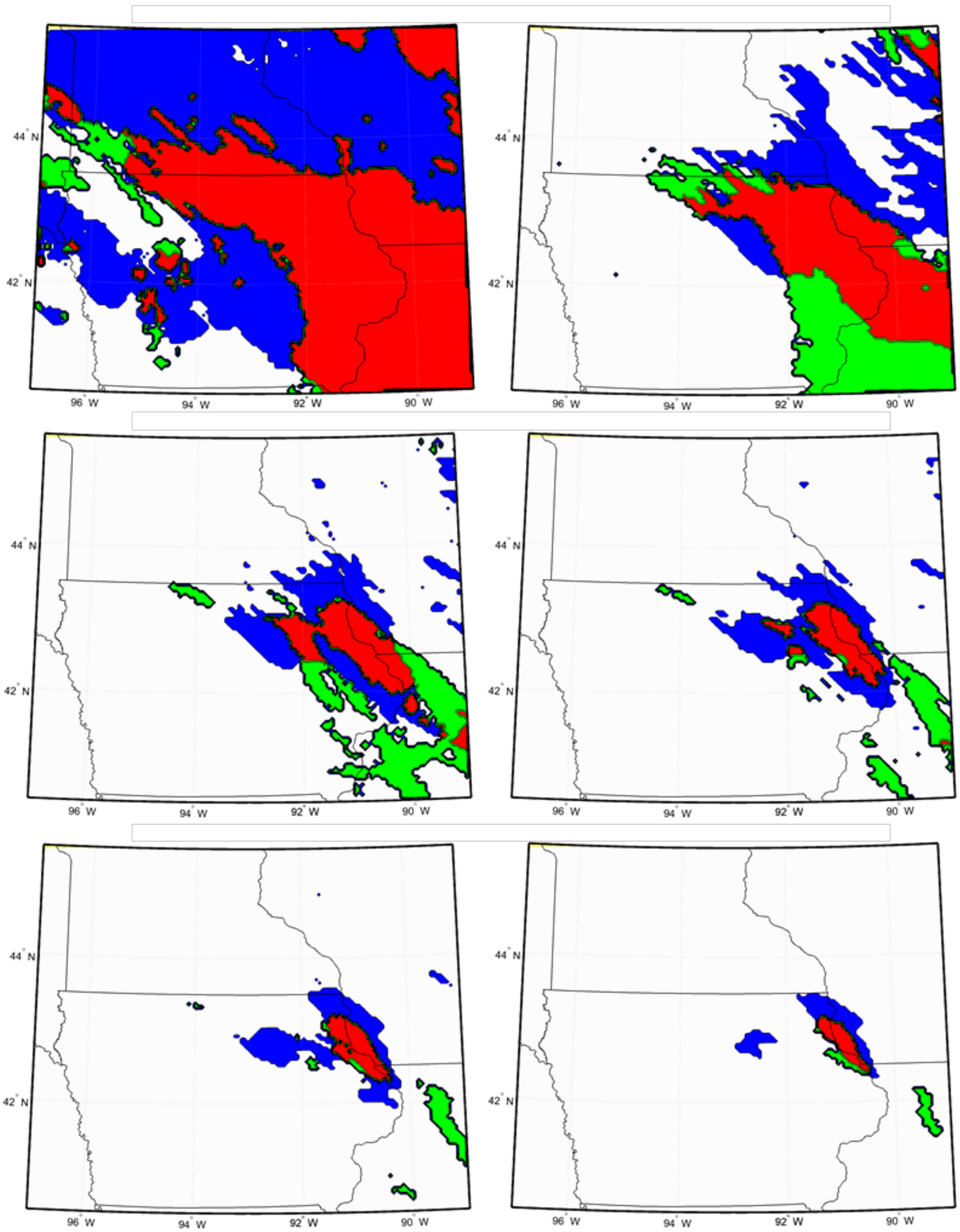

Figure 3-15 Overlapped Field of 24-hour Accumulated Precipitation Above the 50th, 75th, 90th, 95th, 97.5th, and 99th Percentile Values (from Left to Right and from the Top to the Bottom) During the July 18, 2007 MCS

Blue area: only simulation; green area: only observation; red area: both.

3.8 Numerical Simulation of the August 19, 2007 MCS

The August 19, 2007 MCS was another of the extreme storm events that were identified within the simulation region of the WRF model of this study. Among all the parameterization scheme combinations that were attempted during the calibration process of the WRF model for this storm event, Table 3-15 shows the parameterization scheme combination that provided the best reconstruction results. The results of this reconstruction are shown in Figure 3-16, Figure 3-17, and Table 3-16.

Figure 3-16 shows the plots of the 24-hr accumulated precipitation fields for this storm event. The left figure shows the observed precipitation field, and the right figure shows the simulated precipitation field that was obtained from the WRF model simulation that was done by using the best parameterization scheme combination. Visually comparing both of these figures showed that the simulated MCS was quite similar in shape, texture, and location to the observed MCS. Moreover, the relative error in the inner-domain-averaged total precipitation was computed to be around 15.9%, which in turn shows that the model was capable of simulating the total precipitation depth adequately well.

In addition to the visual representation of the reconstructed MCS and its comparison to the observation, the results for the statistical metrics were also analyzed (Table 3-16 and Figure 3-17). For the 50th percentile threshold, for example, the overlap percentage was found to be around 78% and the PFAR was equal to 0.95. Hence, at that threshold value, the simulated precipitation field above the threshold overlapped 78% of the observed precipitation field above the threshold, thus showing a good placement of the storm. Moreover, with a PFAR of 0.95, the size of the simulated precipitation field was relatively close to the size of the observed precipitation field.

From Table 3-16, it is clear that even at the percentile thresholds corresponding to the regions of intense precipitation (e.g., the 95th, 97.5th, and 99th percentiles), there was still relatively good overlap between the simulations and the observations. In fact, the overlap percentage was around 61% at the 99th percentile threshold, with a PFAR of around 1.21; this overlap percentage was also the minimum overlap percentage among all percentile thresholds. This shows the capability of the WRF model in placing the MCS in the appropriate location, even at the regions of intense precipitation.

As for the PFAR values shown in Table 3-16, the values ranged between 0.95 and 1.80, revealing that the WRF model rarely underestimated but mostly overestimated the size of the precipitation field. However, the WRF model was still capable of producing a very good match between the simulated and observed field sizes, even at the regions of most intense precipitation. As such, this shows the ability of the WRF model in simulating the regions of precipitation quite well with respect to their sizes at the different percentile thresholds.

Figure B-8 of APPENDIX B shows the hourly precipitation field, water vapor flux fields, and the precipitable water plotted for the dates ranging from 08/18/2007 at 16h to 08/20/2007 at 12h. The hourly precipitable water and vapor flux fields are shown on the left plots, while the hourly precipitation fields are shown on the right plots. From this sequence of plots, one can see the evolution of the storm event with regards to the plotted fields. The plots show that relatively high-moisture atmospheric flow came into the domain causing intense precipitation on August 19 mainly in the part of the domain over the boundary between the states of Iowa, Wisconsin, and Minnesota, from August 19 at 00h to August 19 at 14h. Consequently, this continuous precipitation formed heavy 24-hour precipitation during this storm event.

Table 3-15 Best Parameterization Schemes Combination for the Numerical Simulation of the August 19, 2007 MCS Event

Option	Option name/value
Microphysics	Stony-Brook University Scheme (SBU-YLin)
Cumulus Parameterization (domain 1 only)	Kain-Fritsch
PBL	Total Energy-Mass Flux (TEMF)
Longwave Radiation	Rapid Radiative Transfer Model (RRTM)
Shortwave Radiation	Dudhia
Surface Layer	Total Energy-Mass Flux (TEMF)
Number of vertical layers	40
Time step	1.5 minutes

Table 3-16 Statistics of the Simulated Results for the August 19, 2007 MCS

The values in parentheses show the corresponding percentile value of the observed precipitation. PFAR: precipitation field area ratio.

	50^{th} Percentile Threshold (6.8 mm)	75^{th} Percentile Threshold (32.8 mm)	90^{th} Percentile Threshold (78.7 mm)	95^{th} Percentile Threshold (105.4 mm)	97.5^{th} Percentile Threshold (133.8 mm)	99^{th} Percentile Threshold (175.2 mm)
Overlap Percentage	78%	68%	71%	68%	71%	61%
PFAR	0.95	1.11	1.34	1.64	1.80	1.21

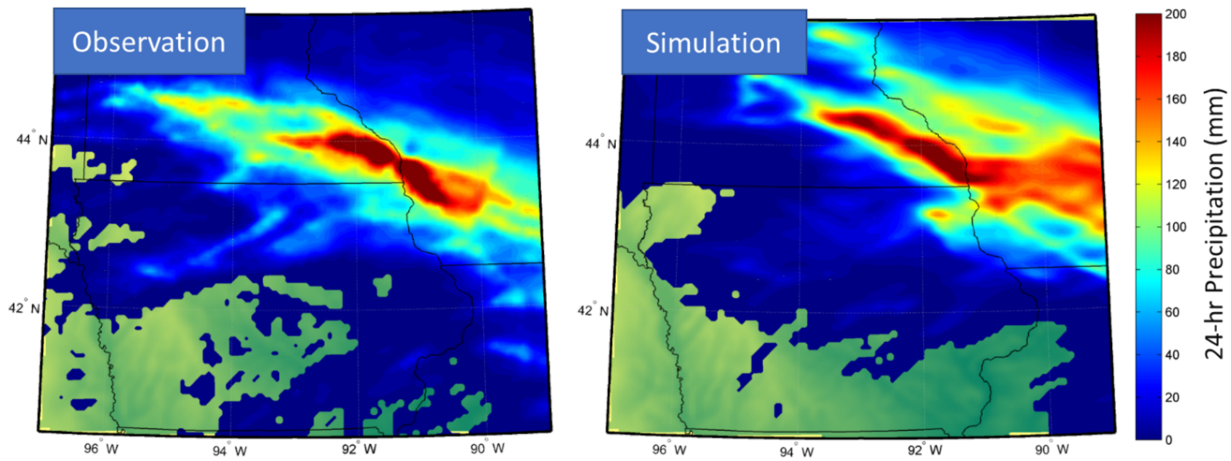

Figure 3-16 Observed (Left) and Simulated (Right) 24-hr Accumulated Precipitation Fields During the August 19, 2007 MCS

Total accumulated precipitation from 08/18/2007 at 18h to 08/19/2007 at 18h.

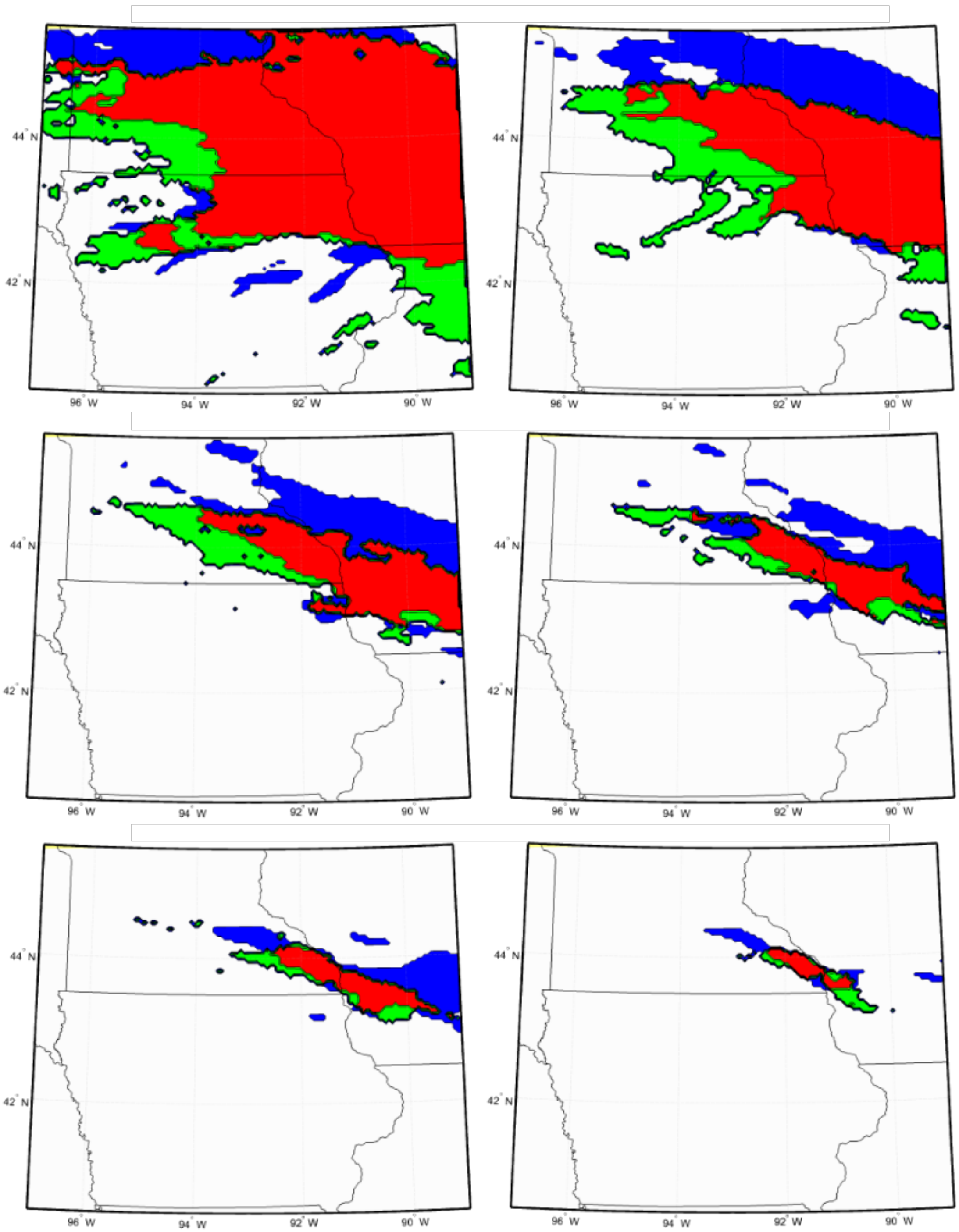

Figure 3-17 Overlapped Field of 24-hour Accumulated Precipitation Above the 50th, 75th, 90th, 95th, 97.5th, and 99th Percentile Values (from Left to Right and from the Top to the Bottom) During the August 19, 2007 MCS

Blue area: only simulation; green area: only observation; red area: both.

3.9 Numerical Simulation of the June 5, 2008 MCS

The June 5, 2008 MCS was another of the extreme storm events that were identified within the simulation region of the WRF model of this study. Among all the parameterization scheme combinations that were attempted during the calibration process of the WRF model for this storm event, Table 3-17 shows the parameterization scheme combination that provided the best reconstruction results. The results of this reconstruction are shown in Figure 3-18, Figure 3-19, and Table 3-18.

Figure 3-18 shows the plots of the 24-hr accumulated precipitation fields for this storm event. The left figure shows the observed precipitation field, and the right figure shows the simulated precipitation field that was obtained from the WRF model simulation that was done by using the best parameterization scheme combination. Visually comparing both of these figures showed that the simulated MCS was quite similar in shape, texture, and location to the observed MCS. While the relative error in the inner-domain-averaged total precipitation was computed to be around -26%, the model can still be considered of being capable of adequately simulating the total precipitation depth.

In addition to the visual representation of the reconstructed MCS and its comparison to the observation, the results for the statistical metrics were also analyzed (Table 3-18 and Figure 3-19). For the 50th percentile threshold, for example, the overlap percentage was found to be around 41% and the PFAR was equal to 0.58. Hence, at that threshold value, the simulated precipitation field above the threshold overlapped 41% of the observed precipitation field above the threshold, thus showing a good placement of the storm. Moreover, with a PFAR of 0.58, the size of the simulated precipitation field was adequately close to the size of the observed precipitation field.

From Table 3-18, it is clear that the overlap percentage tends to decrease at higher percentile threshold values. Nonetheless, even at the percentile thresholds corresponding to the regions of intense precipitation (e.g., the 95th, 97.5th, and 99th percentiles), it is clear that there was still relatively good overlap between the simulations and the observations, with the minimum overlap percentage being around 23% at the 99th percentile threshold. This shows the capability of the WRF model in placing the MCS in the appropriate location, even at the regions of intense precipitation.

As for the PFAR values shown in Table 3-18, the values ranged between 0.51 and 1.54, revealing that the size of the precipitation field simulated by the WRF model was sometimes either underestimated or overestimated. However, the WRF model was still capable of producing a very good match between the simulated and observed field sizes, even at the regions of most intense precipitation. As such, this shows the ability of the WRF model in simulating the regions of precipitation quite well with respect to their sizes at the different percentile thresholds.

Figure B-9 of APPENDIX B shows the hourly precipitation field, water vapor flux fields, and the precipitable water plotted for the dates ranging from 06/04/2008 at 18h to 06/06/2008 at 14h. The hourly precipitable water and vapor flux fields are shown on the left plots, while the hourly precipitation fields are shown on the right plots. From this sequence of plots, one can see the evolution of the storm event with regards to the plotted fields. The plots show that relatively high-moisture atmospheric flow came into the domain causing intense precipitation on June 5 mainly in the southern part of the simulation domain, close to the southern border of the state of Iowa, from June 5 at 02h to June 5 at 16h. Consequently, this continuous precipitation formed heavy 24-hour precipitation during this storm event.

Table 3-17 Best Parameterization Schemes Combination for the Numerical Simulation of the June 5, 2008 MCS Event

Option	Option name/value
Microphysics	WRF Single-moment 5-class (WSM5)
Cumulus Parameterization (domain 1 only)	Grell-Devenyi ensemble
PBL	Mellor-Yamada-Janjic (MYJ) TKE
Longwave Radiation	Rapid Radiative Transfer Model for General Circulation Models (RRTMG)
Shortwave Radiation	Goddard
Surface Layer	Monin-Obukhov
Number of vertical layers	40
Time step	1.5 minutes

Table 3-18 Statistics of the Simulated Results for the June 5, 2008 MCS

The values in parentheses show the corresponding percentile value of the observed precipitation. PFAR: precipitation field area ratio.

	50th Percentile Threshold (9.3 mm)	**75th Percentile Threshold** (24.2 mm)	**90th Percentile Threshold** (39.4 mm)	**95th Percentile Threshold** (49.2 mm)	**97.5th Percentile Threshold** (62.1 mm)	**99th Percentile Threshold** (87.8 mm)
Overlap Percentage	41%	27%	23%	24%	28%	23%
PFAR	0.58	0.51	0.73	1.06	1.33	1.54

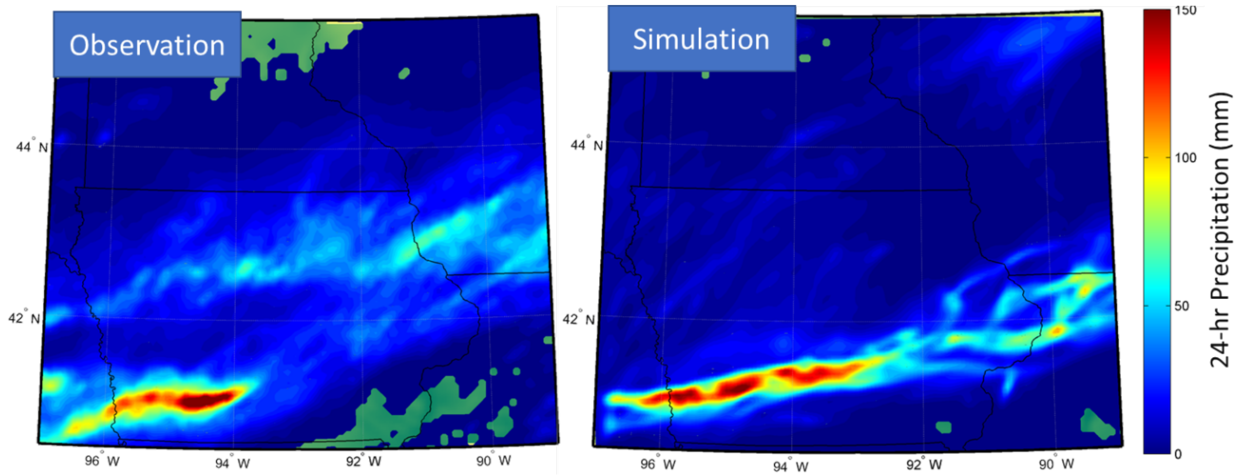

Figure 3-18 Observed (Left) and Simulated (Right) 24-hr Accumulated Precipitation Fields During the June 5, 2008 MCS

Total accumulated precipitation from 06/04/2008 at 18h to 06/05/2008 at 18h.

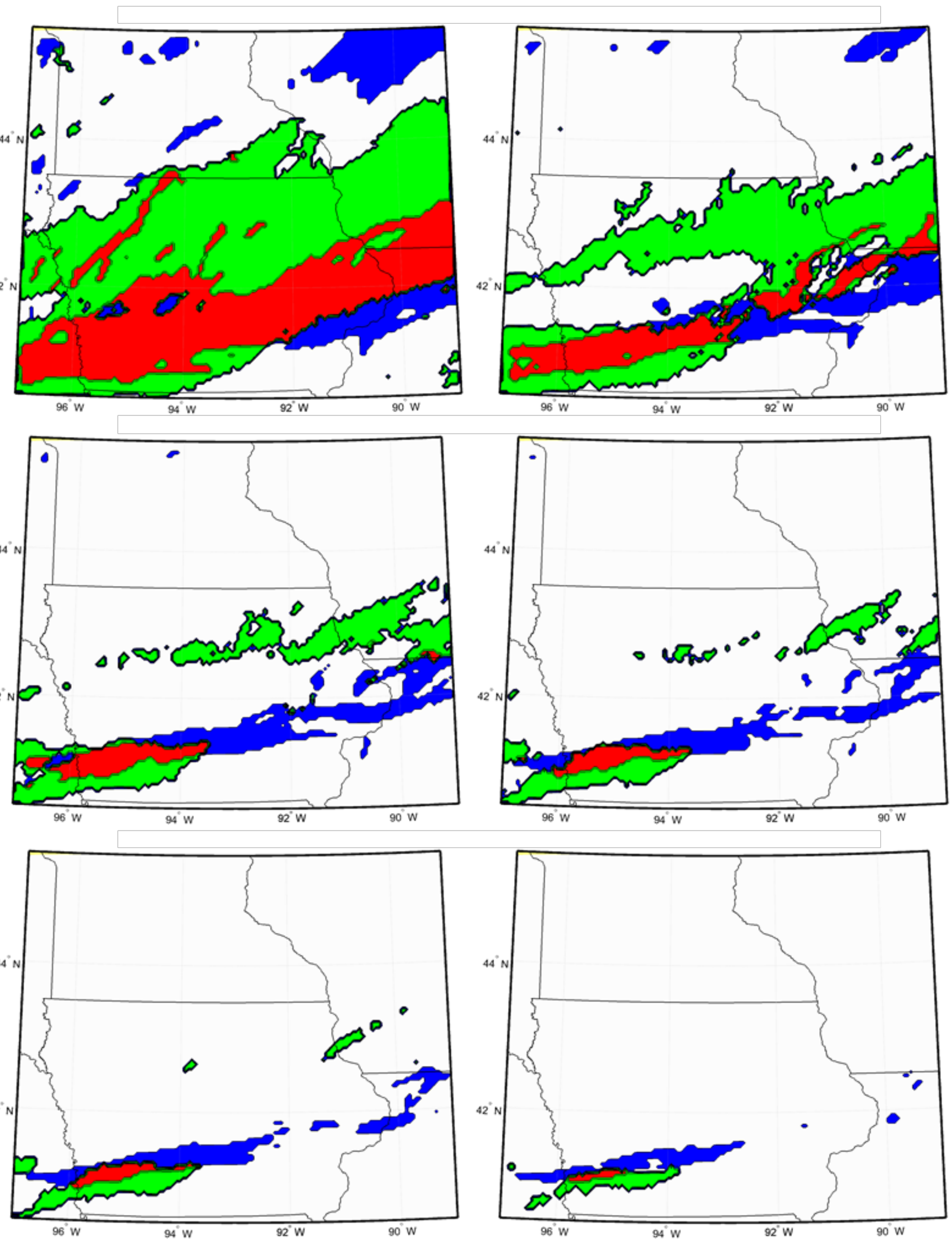

Figure 3-19 Overlapped Field of 24-hour Accumulated Precipitation Above the 50th, 75th, 90th, 95th, 97.5th, and 99th Percentile Values (from Left to Right and from the Top to the Bottom) During the June 5, 2008 MCS

Blue area: only simulation; green area: only observation; red area: both.

3.10 <u>Numerical Simulation of the August 8, 2009 MCS</u>

The August 8, 2009 MCS was another of the extreme storm events that were identified within the simulation region of the WRF model of this study. Among all the parameterization scheme combinations that were attempted during the calibration process of the WRF model for this storm event, Table 3-19 shows the parameterization scheme combination that provided the best reconstruction results. The results of this reconstruction are shown in Figure 3-20, Figure 3-21, and Table 3-20.

Figure 3-20 shows the plots of the 24-hr accumulated precipitation fields for this storm event. The left figure shows the observed precipitation field, and the right figure shows the simulated precipitation field that was obtained from the WRF model simulation that was done by using the best parameterization scheme combination. Visually comparing both of these figures showed that the simulated MCS was quite similar in shape, texture, and location to the observed MCS. While the relative error in the inner-domain-averaged total precipitation was computed to be around -23.7%, the model can still be considered of being capable of adequately simulating the total precipitation depth.

In addition to the visual representation of the reconstructed MCS and its comparison to the observation, the results for the statistical metrics were also analyzed (Table 3-20 and Figure 3-21). For the 50th percentile threshold, for example, the overlap percentage was found to be around 55% and the PFAR was equal to 0.59. Hence, at that threshold value, the simulated precipitation field above the threshold overlapped 55% of the observed precipitation field above the threshold, thus showing a good placement of the storm. Moreover, with a PFAR of 0.59, the size of the simulated precipitation field was adequately close to the size of the observed precipitation field.

From Table 3-20, it is clear that even at the percentile thresholds corresponding to the regions of intense precipitation (e.g., the 95th, 97.5th, and 99th percentiles), there was still relatively good overlap between the simulations and the observations. In fact, the overlap percentage was around 68% at the 99th percentile threshold, with a PFAR of around 2.35. The minimum overlap percentage was around 33%, and it was obtained at the 75th percentile threshold. This shows the capability of the WRF model in placing the MCS in the appropriate location, even at the regions of intense precipitation.

As for the PFAR values shown in Table 3-20, the values ranged between 0.59 and 2.35, revealing that the size of the precipitation field simulated by the WRF model was sometimes either underestimated or overestimated. However, the WRF model was still capable of producing a very good match between the simulated and observed field sizes, even at the regions of most intense precipitation. As such, this shows the ability of the WRF model in simulating the regions of precipitation quite well with respect to their sizes at the different percentile thresholds.

Figure B-10 of APPENDIX B shows the hourly precipitation field, water vapor flux fields, and the precipitable water plotted for the dates ranging from 08/07/2009 at 08h to 08/08/2009 at 19h. The hourly precipitable water and vapor flux fields are shown on the left plots, while the hourly precipitation fields are shown on the right plots. From this sequence of plots, one can see the evolution of the storm event with regards to the plotted fields. The plots show that relatively high-moisture atmospheric flow came into the domain causing intense precipitation on August 8 mainly in the northeastern part of the simulation domain, close to the boundary between the states of Minnesota and Wisconsin, from August 8 at 03h to August 8 at 08h. Consequently, this continuous precipitation formed heavy 24-hour precipitation during this storm event.

Table 3-19 Best Parameterization Schemes Combination for the Numerical Simulation of the August 8, 2009 MCS Event

Option	Option name/value
Microphysics	WRF Double Moment 6-class (WDM6)
Cumulus Parameterization (domain 1 only)	Grell-Devenyi
PBL	Mellor-Yamada-Janvic (MYJ)
Longwave Radiation	Community Atmospheric Model (CAM)
Shortwave Radiation	Dudhia
Surface Layer	Monin-Obukhov
Number of vertical layers	40
Time step	1.5 minutes

Table 3-20 Statistics of the Simulated Results for the August 8, 2009 MCS

The values in parentheses show the corresponding percentile value of the observed precipitation. PFAR: precipitation field area ratio.

	50th Percentile Threshold (8.7 mm)	**75th Percentile Threshold** (25.6 mm)	**90th Percentile Threshold** (41.4 mm)	**95th Percentile Threshold** (55.0 mm)	**97.5th Percentile Threshold** (69.4 mm)	**99th Percentile Threshold** (96.0 mm)
Overlap Percentage	55%	33%	38%	46%	54%	68%
PFAR	0.59	0.50	0.78	1.18	1.80	2.35

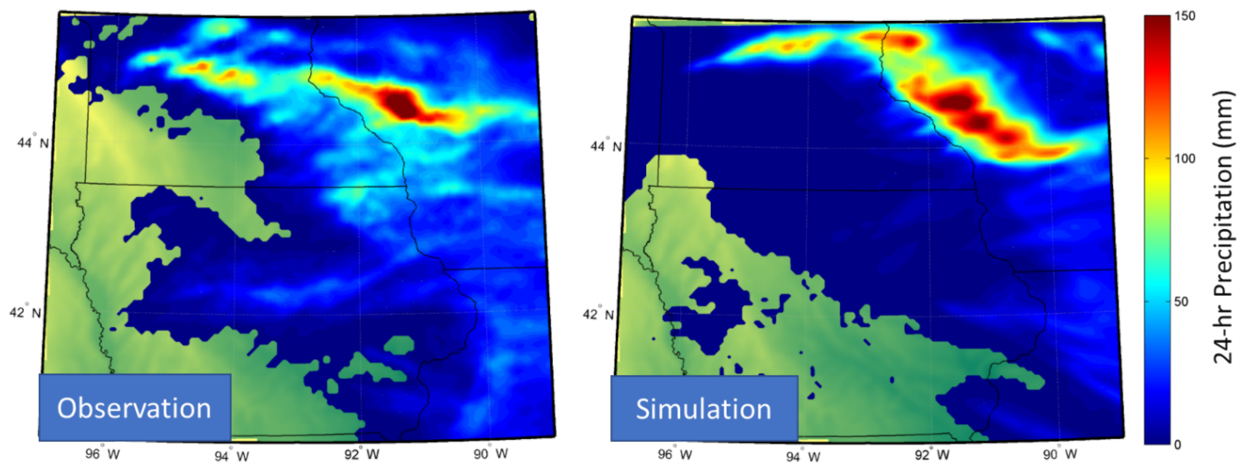

Figure 3-20 Observed (Left) and Simulated (Right) 24-hr Accumulated Precipitation Fields During the August 8, 2009 MCS

Total accumulated precipitation from 08/07/2009 at 18h to 08/08/2009 at 18h.

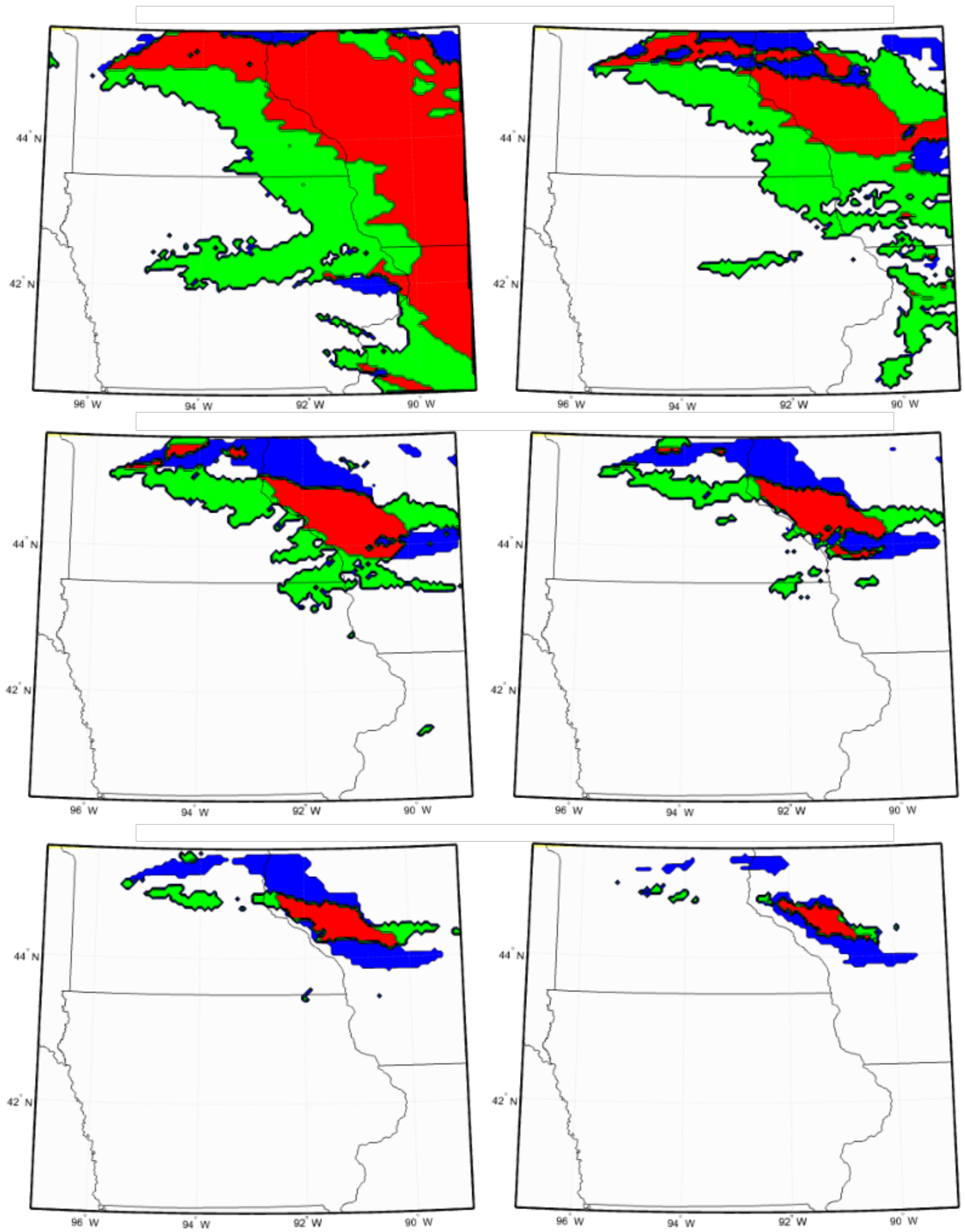

Figure 3-21 Overlapped Field of 24-hour Accumulated Precipitation Above the 50th, 75th, 90th, 95th, 97.5th, and 99th Percentile Values (from Left to Right and from the Top to the Bottom) During the August 8, 2009 MCS

Blue area: only simulation; green area: only observation; red area: both.

3.11 Numerical Simulation of the July 23, 2010 MCS

The July 23, 2010 MCS was another of the extreme storm events that were identified within the simulation region of the WRF model of this study. Among all the parameterization scheme combinations that were attempted during the calibration process of the WRF model for this storm event, Table 3-21 shows the parameterization scheme combination that provided the best reconstruction results. The results of this reconstruction are shown in Figure 3-22, Figure 3-23, and Table 3-22.

Figure 3-22 shows the plots of the 24-hr accumulated precipitation fields for this storm event. The left figure shows the observed precipitation field, and the right figure shows the simulated precipitation field that was obtained from the WRF model simulation that was done by using the best parameterization scheme combination. Visually comparing both of these figures showed that the simulated MCS was quite similar in shape, texture, and location to the observed MCS. Moreover, the relative error in the inner-domain-averaged total precipitation was computed to be only around 2.51%, which in turn shows that the model was capable of simulating the total precipitation depth relatively well.

In addition to the visual representation of the reconstructed MCS and its comparison to the observation, the results for the statistical metrics were also analyzed (Table 3-22 and Figure 3-23). For the 50th percentile threshold, for example, the overlap percentage was found to be around 72% and the PFAR was equal to 1.11. Hence, at that threshold value, the simulated precipitation field above the threshold overlapped 72% of the observed precipitation field above the threshold, thus showing a good placement of the storm. Moreover, with a PFAR of 1.11, the size of the simulated precipitation field was relatively close to the size of the observed precipitation field.

From Table 3-22, it is clear, however, that the overlap percentage tends to decrease at higher percentile threshold values. Nonetheless, even at the percentile thresholds corresponding to the regions of intense precipitation (e.g., the 95th, 97.5th, and 99th percentiles), it is clear that there was still relatively good overlap between the simulations and the observations, with the minimum overlap percentage being around 32% at the 99th percentile threshold. This shows the capability of the WRF model in placing the MCS in the appropriate location, even at the regions of intense precipitation.

As for the PFAR values shown in Table 3-22, the values ranged between 0.93 and 1.89, revealing that the WRF model rarely underestimated but mostly overestimated the size of the precipitation field. However, the WRF model was still capable of producing a very good match between the simulated and observed field sizes, even at the regions of most intense precipitation. As such, this shows the ability of the WRF model in simulating the regions of precipitation quite well with respect to their sizes at the different percentile thresholds.

Figure B-11 of APPENDIX B shows the hourly precipitation field, water vapor flux fields, and the precipitable water plotted for the dates ranging from 07/22/2010 at 18h to 07/23/2010 at 17h. The hourly precipitable water and vapor flux fields are shown on the left plots, while the hourly precipitation fields are shown on the right plots. From this sequence of plots, one can see the evolution of the storm event with regards to the plotted fields. The plots show that relatively high-moisture atmospheric flow came into the domain causing intense precipitation on July 23 mainly in the eastern part of the domain around the area surrounding the boundary between states of Wisconsin, Iowa and Illinois, from July 23 at 00h to July 23 at 10h. Consequently, this continuous precipitation formed heavy 24-hour precipitation during this storm event.

Table 3-21 Best Parameterization Schemes Combination for the Numerical Simulation of the July 23, 2010 MCS Event

Option	Option name/value
Microphysics	WRF double moment 5-class (WDM5)
Cumulus Parameterization (domain 1 only)	Kain-Fritsch (old)
PBL	Total Energy-Mass Flux (TEMF)
Longwave Radiation	Rapid Radiative Transfer Model (RRTM)
Shortwave Radiation	GFDL
Surface Layer	Total Energy-Mass Flux (TEMF)
Number of vertical layers	40
Time step	1.5 minutes

Table 3-22 Statistics of the Simulated Results for the July 23, 2010 MCS

The values in parentheses show the corresponding percentile value of the observed precipitation. PFAR: precipitation field area ratio.

	50th Percentile Threshold (2.0 mm)	75th Percentile Threshold (13.6 mm)	90th Percentile Threshold (40.6 mm)	95th Percentile Threshold (64.4 mm)	97.5th Percentile Threshold (91.8 mm)	99th Percentile Threshold (134.8 mm)
Overlap Percentage	72%	78%	55%	47%	55%	32%
PFAR	1.11	1.59	1.89	1.53	1.25	0.93

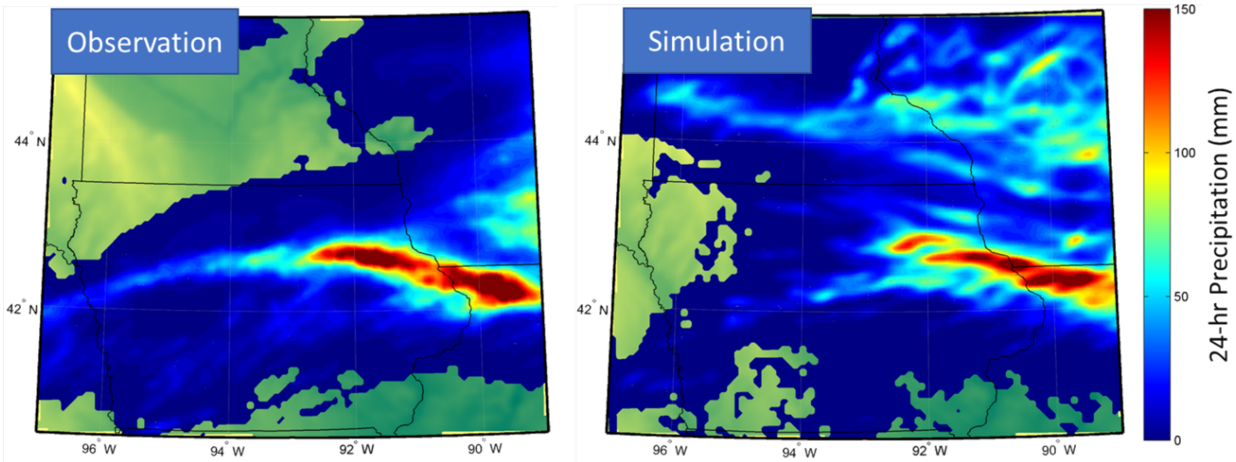

Figure 3-22 Observed (Left) and Simulated (Right) 24-hr Accumulated Precipitation Fields During the July 23, 2010 MCS

Total accumulated precipitation from 07/22/2010 at 18h to 07/23/2010 at 18h.

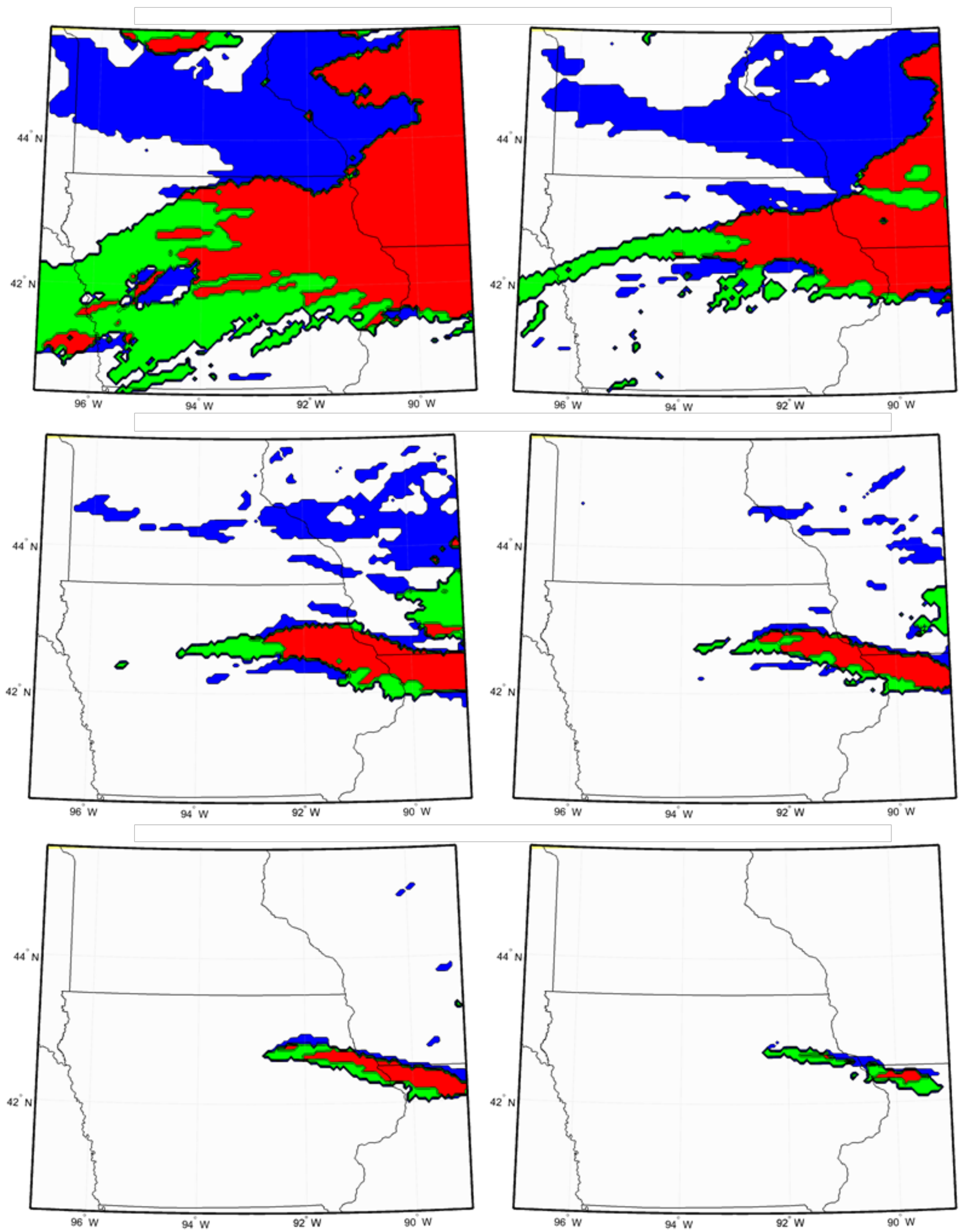

Figure 3-23 Overlapped Field of 24-hour Accumulated Precipitation Above the 50th, 75th, 90th, 95th, 97.5th, and 99th Percentile Values (from Left to Right and from the Top to the Bottom) During the July 23, 2010 MCS

Blue area: only simulation; green area: only observation; red area: both.

3.12 Numerical Simulation of the September 23, 2010 MCS

The September 23, 2010 MCS was another of the extreme storm events that were identified within the simulation region of the WRF model of this study. Among all the parameterization scheme combinations that were attempted during the calibration process of the WRF model for this storm event, Table 3-23 shows the parameterization scheme combination that provided the best reconstruction results. The results of this reconstruction are shown in Figure 3-24, Figure 3-25, and Table 3-24.

Figure 3-24 shows the plots of the 24-hr accumulated precipitation fields for this storm event. The left figure shows the observed precipitation field, and the right figure shows the simulated precipitation field that was obtained from the WRF model simulation that was done by using the best parameterization scheme combination. Visually comparing both of these figures showed that the simulated MCS was quite similar to the observed MCS. Moreover, the relative error in the inner-domain-averaged total precipitation was computed to be only around -4.4%, which in turn shows that the model was capable of simulating the total precipitation depth relatively well.

In addition to the visual representation of the reconstructed MCS and its comparison to the observation, the results for the statistical metrics were also analyzed (Table 3-24 and Figure 3-25). For the 75th percentile threshold, for example, the overlap percentage was found to be around 74% and the PFAR was equal to 0.96. Hence, at that threshold value, the simulated precipitation field above the threshold overlapped 74% of the observed precipitation field above the threshold, thus showing a good placement of the storm. Moreover, with a PFAR of 0.96, the size of the simulated precipitation field was relatively close to the size of the observed precipitation field.

From Table 3-24, it is clear, however, that the overlap percentage tends to decrease at higher percentile threshold values. Nonetheless, even at the percentile thresholds corresponding to the regions of intense precipitation (e.g., the 95th, 97.5th, and 99th percentiles), it is clear that there was still relatively good overlap between the simulations and the observations, with the minimum overlap percentage being around 31% at the 99th percentile threshold. This shows the capability of the WRF model in placing the MCS in the appropriate location, even at the regions of intense precipitation.

As for the PFAR values shown in Table 3-24, the values ranged between 0.92 and 1.04, revealing that the size of the precipitation field simulated by the WRF model was very close to the size of the observed precipitation field for most of the percentile threshold values. As such, the WRF model was capable of producing a very good match between the simulated and observed field sizes, even at the regions of most intense precipitation. As such, this shows the ability of the WRF model in simulating the regions of precipitation quite well with respect to their sizes at the different percentile thresholds.

Figure B-12 of APPENDIX B shows the hourly precipitation field, water vapor flux fields, and the precipitable water plotted for the dates ranging from 09/22/2010 at 17h to 09/24/2010 at 10h. The hourly precipitable water and vapor flux fields are shown on the left plots, while the hourly precipitation fields are shown on the right plots. From this sequence of plots, one can see the evolution of the storm event with regards to the plotted fields. The plots show that relatively high-moisture atmospheric flow came into the domain causing intense precipitation on September 22-23 mainly in the northern part of the simulation domain along the southern border of the state of Minnesota, from September 22 at 21h to September 23 at 09h. Consequently, this continuous precipitation formed heavy 24-hour precipitation during this storm event.

Table 3-23 Best Parameterization Schemes Combination for the Numerical Simulation of the September 23, 2010 MCS Event

Option	Option name/value
Microphysics	Morrison 2-moment
Cumulus Parameterization (domain 1 only)	Old GFS Simplified Arakawa-Schubert (SAS)
PBL	Yonsei University Scheme (YSU)
Longwave Radiation	Rapid Radiative Transfer Model (RRTM)
Shortwave Radiation	Dudhia
Surface Layer	Revised MM5 Monin-Obukhov
Number of vertical layers	40
Time step	1.5 minutes

Table 3-24 Statistics of the Simulated Results for the September 23, 2010 MCS

The values in parentheses show the corresponding percentile value of the observed precipitation. PFAR: precipitation field area ratio.

	50^{th} Percentile Threshold (4.8 mm)	**75^{th} Percentile Threshold** (46.8 mm)	**90^{th} Percentile Threshold** (94.0 mm)	**95^{th} Percentile Threshold** (116.0 mm)	**97.5^{th} Percentile Threshold** (136.1 mm)	**99^{th} Percentile Threshold** (156.1 mm)
Overlap Percentage	84%	74%	55%	38%	38%	31%
PFAR	0.92	0.96	1.04	1.02	0.92	0.81

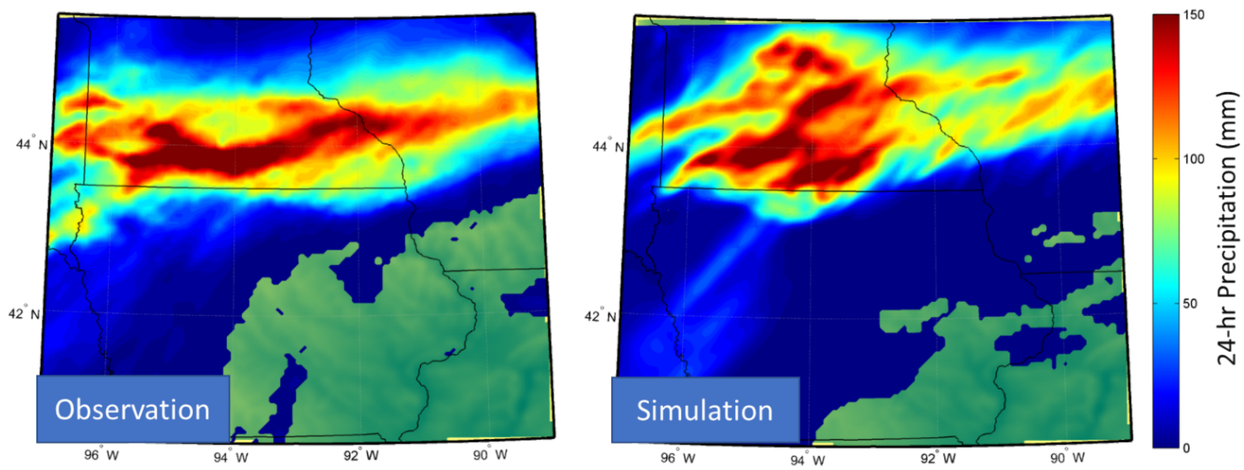

Figure 3-24 Observed (Left) and Simulated (right) 24-hr Accumulated Precipitation Fields During the September 23, 2010 MCS

Total accumulated precipitation from 09/22/2010 at 18h to 09/23/2010 at 18h.

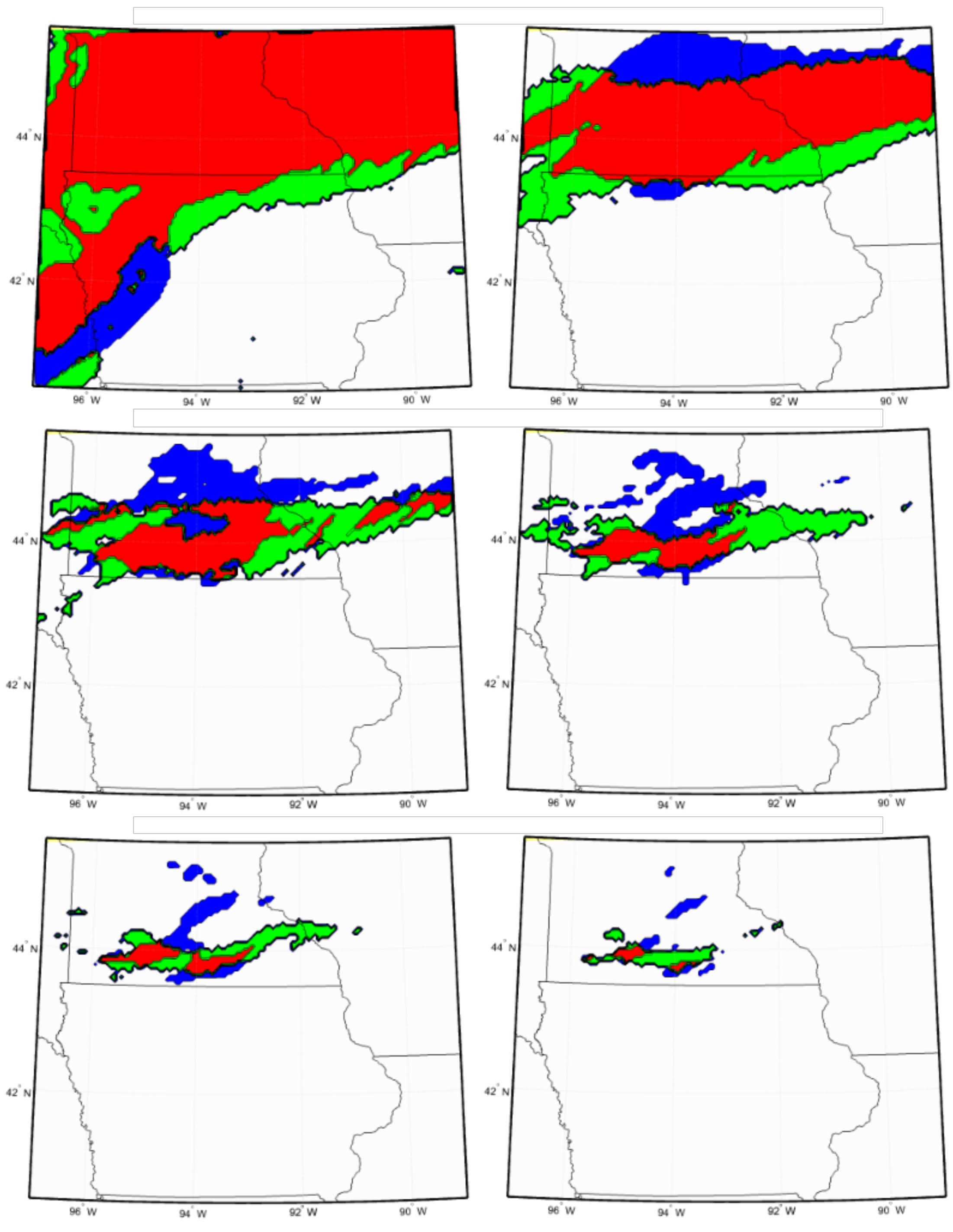

Figure 3-25 Overlapped Field of 24-hour Accumulated Precipitation Above the 50th, 75th, 90th, 95th, 97.5th, and 99th Percentile Values (from Left to Right and from the Top to the Bottom) During the September 23, 2010 MCS

Blue area: only simulation; green area: only observation; red area: both.

3.13 Numerical Simulation of the July 28, 2011 MCS

The July 28, 2011 MCS was another of the extreme storm events that were identified within the simulation region of the WRF model of this study. Among all the parameterization scheme combinations that were attempted during the calibration process of the WRF model for this storm event, Table 3-25 shows the parameterization scheme combination that provided the best reconstruction results. The results of this reconstruction are shown in Figure 3-26, Figure 3-27, and Table 3-26.

Figure 3-26 shows the plots of the 24-hr accumulated precipitation fields for this storm event. The left figure shows the observed precipitation field, and the right figure shows the simulated precipitation field that was obtained from the WRF model simulation that was done by using the best parameterization scheme combination. Visually comparing both of these figures showed that the simulated MCS was very similar in shape, texture, and location to the observed MCS. Moreover, the relative error in the inner-domain-averaged total precipitation was computed to be only around 7.0%, which in turn shows that the model was capable of simulating the total precipitation depth relatively well.

In addition to the visual representation of the reconstructed MCS and its comparison to the observation, the results for the statistical metrics were also analyzed (Table 3-26 and Figure 3-27). For the 90th percentile threshold, for example, the overlap percentage was found to be around 71% and the PFAR was equal to 1.29. Hence, at that threshold value, the simulated precipitation field above the threshold overlapped 71% of the observed precipitation field above the threshold, thus showing a good placement of the storm. Moreover, with a PFAR of 1.29, the size of the simulated precipitation field was relatively close to the size of the observed precipitation field.

From Table 3-26, it is clear that even at the percentile thresholds corresponding to the regions of intense precipitation (e.g., the 95th, 97.5th, and 99th percentiles), there was still relatively good overlap between the simulations and the observations. In fact, the overlap percentage was around 62% at the 99th percentile threshold, with a PFAR of around 1.14. The minimum overlap percentage was around 43%, and it was obtained at the 75th percentile threshold. This shows the capability of the WRF model in placing the MCS in the appropriate location, even at the regions of intense precipitation.

As for the PFAR values shown in Table 3-26, the values ranged between 0.49 and 1.54, revealing that the size of the precipitation field simulated by the WRF model was sometimes either underestimated or overestimated. However, the WRF model was still capable of producing a very good match between the simulated and observed field sizes, even at the regions of most intense precipitation. As such, this shows the ability of the WRF model in simulating the regions of precipitation quite well with respect to their sizes at the different percentile thresholds.

Figure B-13 of APPENDIX B shows the hourly precipitation field, water vapor flux fields, and the precipitable water plotted for the dates ranging from 07/27/2011 at 10h to 07/28/2011 at 16h. The hourly precipitable water and vapor flux fields are shown on the left plots, while the hourly precipitation fields are shown on the right plots. From this sequence of plots, one can see the evolution of the storm event with regards to the plotted fields. The plots show that relatively high-moisture atmospheric flow came into the domain causing intense precipitation on July 27-28 mainly in the eastern part of the domain over the boundary between the states of Iowa, Wisconsin, and Illinois, from July 27 at 23h to July 28 at 09h. Consequently, this continuous precipitation formed heavy 24-hour precipitation during this storm event.

Table 3-25 Best Parameterization Schemes Combination for the Numerical Simulation of the July 28, 2011 MCS Event

Option	Option name/value
Microphysics	WRF Double Moment 6-class (WDM6)
Cumulus Parameterization (domain 1 only)	New Simplified Arakawa-Schubert (SAS)
PBL	Mellor-Yamada-Nakanishi-Niino (MYNN) 3rd Level TKE
Longwave Radiation	Rapid Radiative Transfer Model (RRTM)
Shortwave Radiation	Dudhia
Surface Layer	Mellor-Yamada-Nakanishi-Niino (MYNN)
Number of vertical layers	40
Time step	1.5 minutes

Table 3-26 Statistics of the Simulated Results for the July 28, 2011 MCS

The values in parentheses show the corresponding percentile value of the observed precipitation. PFAR: precipitation field area ratio.

	50^{th} Percentile Threshold (1.3 mm)	75^{th} Percentile Threshold (9.1 mm)	90^{th} Percentile Threshold (20.3 mm)	95^{th} Percentile Threshold (32.8 mm)	97.5^{th} Percentile Threshold (55.8 mm)	99^{th} Percentile Threshold (132.6 mm)
Overlap Percentage	44%	43%	71%	77%	77%	62%
PFAR	0.49	0.66	1.29	1.54	1.48	1.14

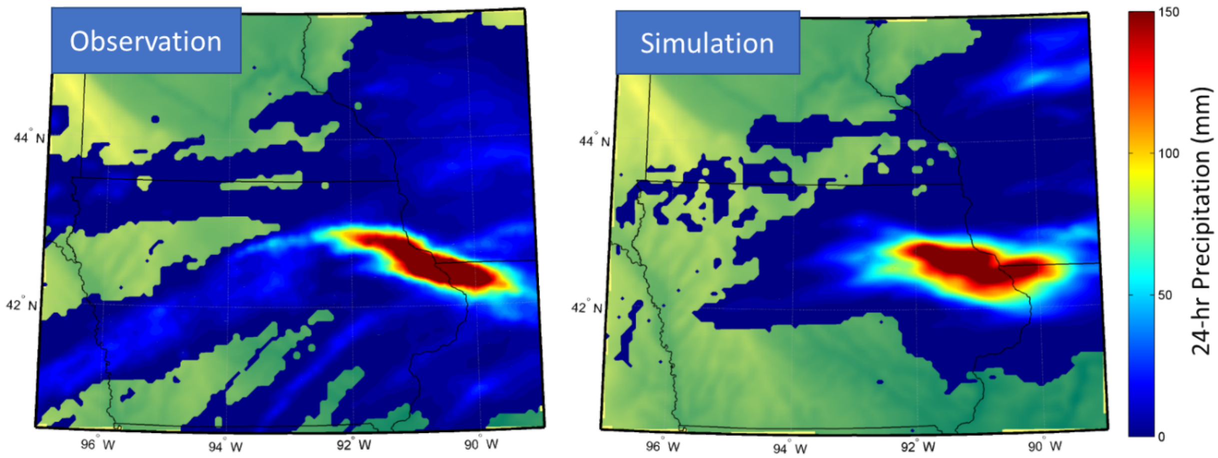

Figure 3-26 Observed (Left) and Simulated (Right) 24-hr Accumulated Precipitation Fields During the July 28, 2011 MCS

Total accumulated precipitation from 07/27/2011 at 15h to 07/28/2011 at 15h

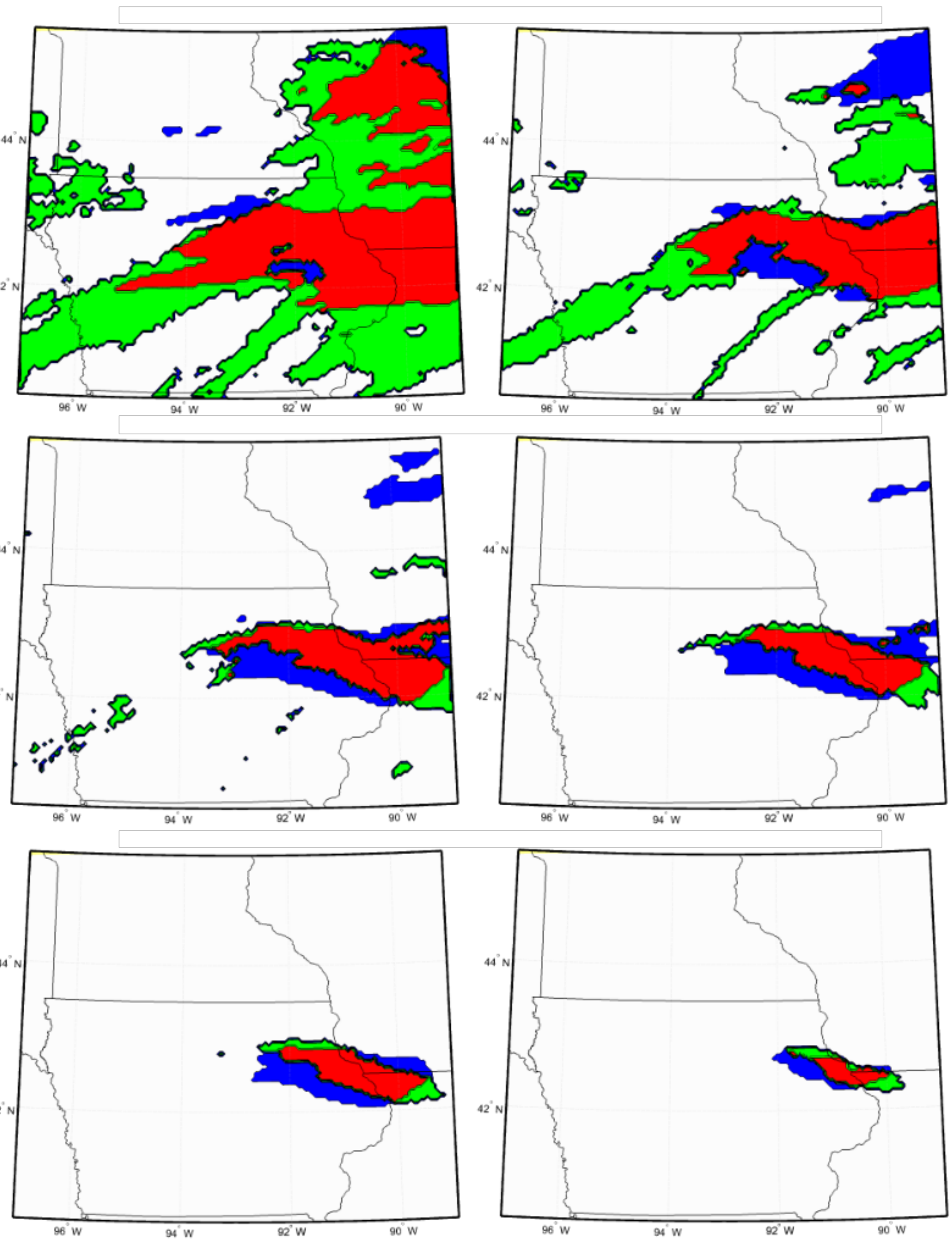

Figure 3-27 Overlapped Field of 24-hour Accumulated Precipitation Above the 50th, 75th, 90th, 95th, 97.5th, and 99th Percentile Values (from Left to Right and from the Top to the Bottom) During the July 28, 2011 MCS

Blue area: only simulation; green area: only observation; red area: both.

3.14 Numerical Simulation of the June 22, 2013 MCS

The June 22, 2013 MCS was the last of the extreme storm events that were identified within the simulation region of the WRF model of this study. Among all the parameterization scheme combinations that were attempted during the calibration process of the WRF model for this storm event, Table 3-27 shows the parameterization scheme combination that provided the best reconstruction results. The results of this reconstruction are shown in Figure 3-28, Figure 3-29, and Table 3-28.

Figure 3-28 shows the plots of the 24-hr accumulated precipitation fields for this storm event. The left figure shows the observed precipitation field, and the right figure shows the simulated precipitation field that was obtained from the WRF model simulation that was done by using the best parameterization scheme combination. Visually comparing both of these figures showed that the simulated MCS was somewhat similar to the observed MCS. Moreover, the relative error in the inner-domain-averaged total precipitation was computed to be only around 6.0%, which in turn shows that the model was capable of simulating the total precipitation depth relatively well.

In addition to the visual representation of the reconstructed MCS and its comparison to the observation, the results for the statistical metrics were also analyzed (Table 3-28 and Figure 3-29). For the 50th percentile threshold, for example, the overlap percentage was found to be around 71% and the PFAR was equal to 0.8. Hence, at that threshold value, the simulated precipitation field above the threshold overlapped 71% of the observed precipitation field above the threshold, thus showing a good placement of the storm. Moreover, with a PFAR of 0.8, the size of the simulated precipitation field was relatively close to the size of the observed precipitation field.

From Table 3-28, it is clear, however, that the overlap percentage tends to decrease at higher percentile threshold values. Nonetheless, even at the percentile thresholds corresponding to the regions of intense precipitation (e.g., the 95th, 97.5th, and 99th percentiles), it is clear that there was still relatively good overlap between the simulations and the observations, with the minimum overlap percentage being around 35% at the 99th percentile threshold. This shows the capability of the WRF model in placing the MCS in the appropriate location, even at the regions of intense precipitation.

As for the PFAR values shown in Table 3-28, the values ranged between 0.93 and 2.73, revealing that the WRF model rarely underestimated but mostly overestimated the size of the precipitation field. The high PFAR at the 99th threshold mostly comes because of the intense pockets of precipitation simulated to be occurring at the eastern-most region of the simulation figure. However, among all simulations that were run for this storm event, this result provided the best combination regarding the location of the storm and the computed statistics. Therefore, one may still consider that the WRF model was still capable of producing a good match between the simulated and observed field sizes for most of the percentile thresholds.

Figure B-14 of APPENDIX B shows the hourly precipitation field, water vapor flux fields, and the precipitable water plotted for the dates ranging from 06/21/2013 at 17h to 06/22/2013 at 19h. The hourly precipitable water and vapor flux fields are shown on the left plots, while the hourly precipitation fields are shown on the right plots. From this sequence of plots, one can see the evolution of the storm event with regards to the plotted fields. The plots show that relatively high-moisture atmospheric flow came into the domain causing intense precipitation on June 22 mainly in the northeastern part of the domain along a diagonal pathway moving in a southeastern direction and starting from the state of Minnesota towards Wisconsin and Illinois; this intense precipitation occurred from June 22 at 01h to June 22 at 09h. Consequently, this continuous precipitation formed heavy 24-hour precipitation during this storm event.

Table 3-27 Best Parameterization Schemes Combination for the Numerical Simulation of the June 22, 2013 MCS Event

Option	Option name/value
Microphysics	WRF Single-moment 6-class (WSM6)
Cumulus Parameterization (domain 1 only)	Kain-Fritsch (new)
PBL	Mellor-Yamada-Janjic (MYJ) TKE
Longwave Radiation	Goddard
Shortwave Radiation	Goddard (old)
Surface Layer	Monin-Obukhov
Number of vertical layers	40
Time step	1.5 minutes

Table 3-28 Statistics of the Simulated Results for the June 22, 2013 MCS

The values in parentheses show the corresponding percentile value of the observed precipitation. PFAR: precipitation field area ratio.

	50th Percentile Threshold (7.8 mm)	**75th Percentile Threshold** (24.6 mm)	**90th Percentile Threshold** (43.1 mm)	**95th Percentile Threshold** (54.4 mm)	**97.5th Percentile Threshold** (65.5 mm)	**99th Percentile Threshold** (78.7 mm)
Overlap Percentage	71%	64%	56%	49%	40%	35%
PFAR	0.80	1.05	1.40	1.74	2.08	2.73

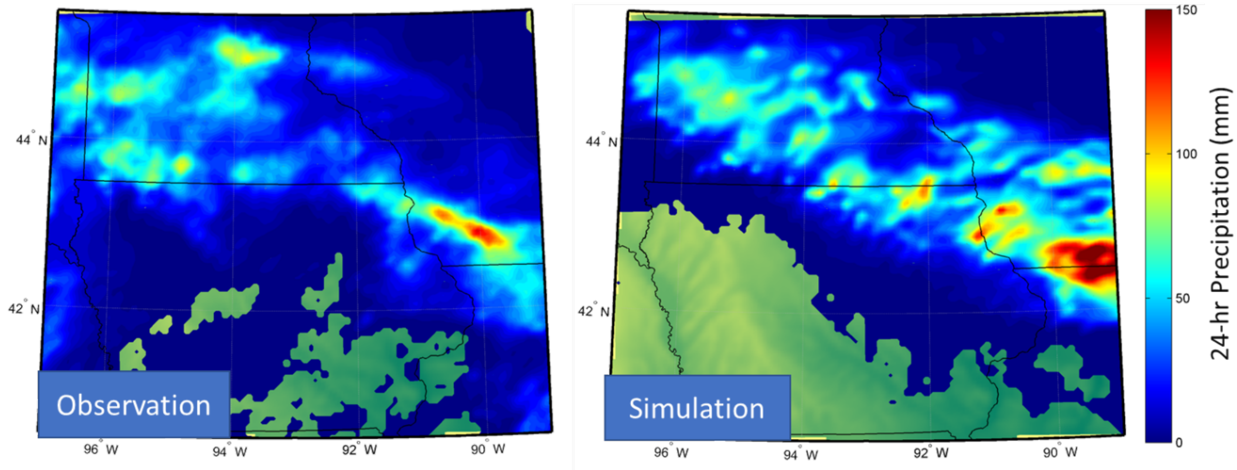

Figure 3-28 Observed (Left) and Simulated (Right) 24-hr Accumulated Precipitation Fields During the June 22, 2013 MCS

Total accumulated precipitation from 06/21/2013 at 19h to 06/22/2013 at 19h.

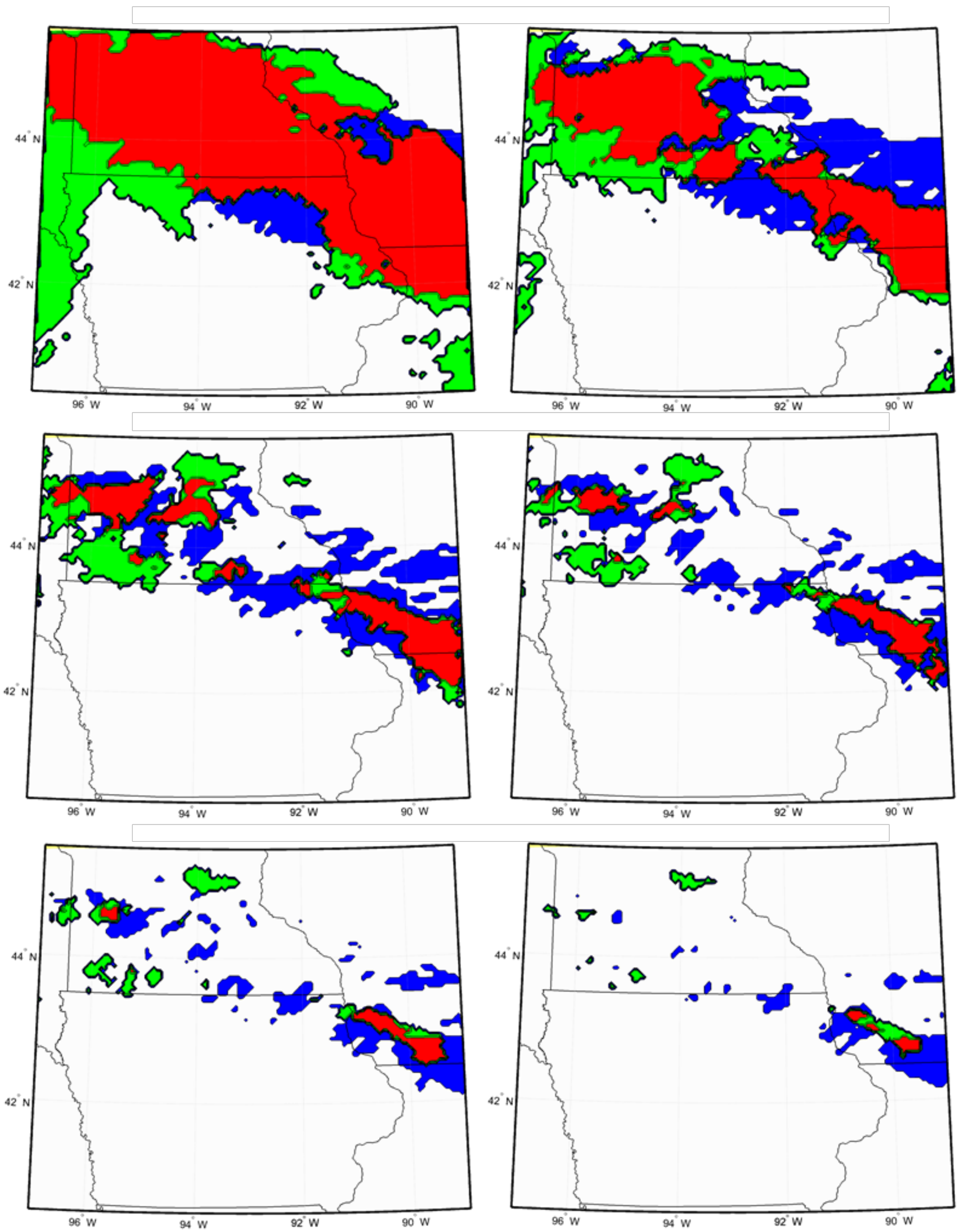

Figure 3-29 Overlapped Field of 24-hour Accumulated Precipitation Above the 50th, 75th, 90th, 95th, 97.5th, and 99th Percentile Values (from Left to Right and from the Top to the Bottom) During the June 22, 2013 MCS

Blue area: only simulation; green area: only observation; red area: both.

3.15 Summary of the WRF Model Performance and WRF Model Parameterization Schemes

In this section, the WRF model parameterization schemes used for the simulations presented in the previous sections are summarized (Table 3-29). Note that 40 vertical model layers and a time step of 1.5 minutes were used in all cases. The WRF model performance in terms of the quantitative metrics are also summarized in Table 3-30 and Table 3-31.

Table 3-29 Summary of WRF Model Options Used for the Simulation of the 14 Historical MCSs

The code numbers for each parameterization are the same as the code numbers used in WRF (version 3.7) and are detailed in APPENDIX A . Additional information and references may be found in the user manual (NCAR, 2016).

MCS Event	Microphysics	Cumulus	PBL	LWR	SWR	Surface Layer
June 22, 2002	14	6	6	5	3	5
August 22, 2002	13	6	10	1	4	10
September 15, 2004	7	99	3	5	3	3
June 25, 2005	2	6	3	3	4	3
August 17, 2005	6	4	2	1	1	2
September 25, 2005	7	1	8	1	1	1
July 18, 2007	16	5	3	99	4	3
August 19, 2007	13	1	10	1	1	10
June 5, 2008	4	93	2	4	5	2
August 8, 2009	16	93	2	3	1	2
July 23, 2010	14	99	10	1	99	10
September 23, 2010	10	4	1	1	1	1
July 28, 2011	16	14	6	1	1	5
June 22, 2013	6	1	2	5	2	2

Table 3-30 Summary of the WRF Model Performance in Terms of the Relative Error for the Reconstructed MCSs

MCS event	Relative error
June 22, 2002	8.4%
August 22, 2002	5.8%
September 15, 2004	-10.6%
June 25, 2005	-20.7%
August 17, 2005	7.4%
September 25, 2005	-17.3%
July 18, 2007	-4.5%
August 19, 2007	15.9%
June 5, 2008	-26%
August 8, 2009	-23.7%
July 23, 2010	2.51%
September 23, 2010	-4.4%
July 28, 2011	-7.0%
June 22, 2013	6.0%

Table 3-31 Summary of the WRF Model Performance in Terms of the Overlap Percentage and PFAR for the Reconstructed MCSs

MCS event	Metric	50th Percentile Threshold	75th Percentile Threshold	90th Percentile Threshold	95th Percentile Threshold	97.5th Percentile Threshold	99th Percentile Threshold
June 22, 2002	% overlap	48%	50%	74%	73%	57%	45%
	PFAR	0.48	0.55	1.08	1.36	1.56	1.68
August 22, 2002	% overlap	58%	38%	31%	34%	39%	18%
	PFAR	0.92	0.97	0.98	1.14	1.20	0.78
September 15, 2004	% overlap	65%	56%	47%	36%	27%	19%
	PFAR	0.66	0.79	1.14	1.61	2.01	2.22
June 25, 2005	% overlap	57%	47%	46%	44%	39%	21%
	PFAR	0.66	0.52	0.63	0.84	1.21	1.11
August 17, 2005	% overlap	64%	56%	57.7%	51%	42%	43%
	PFAR	0.95	0.99	1.23	1.34	1.41	1.86
September 25, 2005	% overlap	52%	51%	43%	48%	57%	50%
	PFAR	0.56	0.73	0.93	1.27	1.53	1.96
July 18, 2007	% overlap	92%	57%	41%	47%	51%	55%
	PFAR	2.01	1.08	1.06	1.52	1.87	1.67
August 19, 2007	% overlap	78%	68%	71%	68%	71%	61%
	PFAR	0.95	1.11	1.34	1.64	1.80	1.21
June 5, 2008	% overlap	41%	27%	23%	24%	28%	23%
	PFAR	0.58	0.51	0.73	1.06	1.33	1.54
August 8, 2009	% overlap	55%	33%	38%	46%	54%	68%
	PFAR	0.59	0.50	0.78	1.18	1.80	2.35

Table 3-31 Summary of the WRF Model Performance in Terms of the Overlap Percentage and PFAR for the Reconstructed MCSs (Continued)

July 23, 2010	% overlap	72%	78%	55%	47%	55%	32%
	PFAR	1.11	1.59	1.89	1.53	1.25	0.93
September 23, 2010	% overlap	84%	74%	55%	38%	38%	31%
	PFAR	0.92	0.96	1.04	1.02	0.92	0.81
July 28, 2011	% overlap	44%	43%	71%	77%	77%	62%
	PFAR	0.49	0.66	1.29	1.54	1.48	1.14
June 22, 2013	% overlap	71%	64%	56%	49%	40%	35%
	PFAR	0.80	1.05	1.40	1.74	2.08	2.73

4 NUMERICAL RECONSTRUCTION OF THE PRECIPITATION FIELDS AND MOISTURE TRANSPORT FIELDS ASSOCIATED WITH INTENSE TROPICAL CYCLONES

4.1 Introduction

TCs are widely recognized for their ability to generate intense precipitation that may in turn create disastrous floods. According to Chan and Kepert (2010), "TCs are intense atmospheric vortices that form over the warm tropical oceans". Precipitation distribution in a TC is usually very spatially complex, and time dependent (Lonfat et al., 2004; Marks Jr, 1985). Asymmetric outer rainbands are an important feature of the rainfall structure in TCs that may produce heavy local precipitation and urban flooding (Lin et al., 2010). Powell (1990a; 1990b) investigated the structure and dynamics of outer rainbands for several hurricanes based on in situ and remote observations (e.g., airborne radar, dropsondes). He showed that they have many similarities with squall lines with, for instance, a linear aggregate of convective cells and a region of stratiform rain.

Due to the hydrodynamic and thermodynamic complexity of TCs, numerical weather models are generally used for their reconstruction and forecasting. These models solve numerically the governing equations for the conservation of mass, momentum, and energy.

A first example of numerical models widely used to simulate and forecast TCs is the GFDL Hurricane Prediction System (Bender et al., 2007; Kurihara et al., 1995; Kurihara et al., 1998), used as an operational hurricane forecast system by the U.S. NWS starting in 1995. Since its adoption, the model has undergone continued improvements such as the development of better initialization methods, coupling to the POM, and refinement of model resolution. Wu (2001) used the GFDL model to simulate the interaction between Typhoon Gladys (1994) and the Central Mountain Range (CMR) in Taiwan. Sensitivity experiments highlighted the impact of model initialization on both the storm's track and intensity.

MM5 has been used extensively to simulate TCs from 1997 to 2007. Liu, Zhang and Yau (1997; 1999; 2004; 2000; 2001; 2002) used MM5 to simulate Hurricane Andrew (1992) with a 6 km inner-grid resolution, sufficient to reproduce and study the inner-core axisymmetric as well as asymmetric storm structures. They suggested that "it may be possible to predict reasonably the track, intensity and inner-core structures of hurricanes from the tropical synoptic conditions if high resolution, realistic model physics, and initial vortices […] in relation to their larger-scale conditions […] are incorporated". Karyampudi et al. (1998) simulated Hurricane Florence (1988) with MM5, investigating the sensitivity of the results to ICs, cumulus parameterization formulation, and satellite-derived rainfall assimilation. They showed that assimilation scheme success is highly dependent on the cumulus parameterization scheme. Zou and Xiao (2000) used a BDA scheme in MM5 to produce the initial structure of Hurricane Felix (1995). The BDA scheme employed an idealized vortex field (a surface low consistent with storm central pressure and its maximum wind radius) ingested into the model via 4-dimensional variational DA (4D-Var). The 4D-Var framework was used to obtain a dynamically and thermodynamically consistent initial vortex that is compatible with the resolution and physics of the hurricane prediction model. In this case, the BDA noticeably improved the hurricane prediction in terms of track and vortex structure. Braun and Tao (2000) used MM5 to study the sensitivity of high-resolution simulations of Hurricane Bob (1991) to the choice of the PBL parameterization. They suggested that the accurate forecasts of precipitation in hurricanes can be just as sensitive to the PBL formulation as they are to cloud microphysics parameterization. Frank and Ritchie (2001) performed TC simulations in idealized environments using MM5 to investigate the effect of vertical wind shear on the storms. They showed that the shear caused asymmetrization in the eyewall region structure and weakened the storm. Davis and Bosart (2001) simulated Hurricane Diana (1984) and described the different stages associated with the transformation of an initial baroclinic disturbance into a TC. Wu et al. (2002) simulated Typhoon Herb (1996) and its mesoscale rainfall distribution using MM5. Herb produced extremely heavy and damaging precipitation over the Central Mountain Range (CMR) of Taiwan with maximum precipitation of 1,736 mm (68.3 in.) in one day at Mount A-Li, and surface winds up to 65 meters per second. The authors explained that "the ability of the model to simulate successfully the observed rainfall is dependent on two factors: the model's horizontal grid spacing and its ability to describe the Taiwan terrain". They added that "the existence of the CMR has only a minor impact on the storm track, but it plays a key role in substantially increasing the total rainfall amounts over Taiwan". Braun et al. (2006) used MM5 to simulate Hurricane Bonnie (1998) at a horizontal resolution of 2-km. They studied the effects of vertical wind shear on the spatial distribution of the vertical motion in the storm's eyewall and found that the shear caused asymmetry in the time-averaged vertical motion and rainfall, while instantaneous motion was concentrated in deep updraft towers on the downtilt side.

Since 2007, numerous studies reported successful simulations of TCs with the WRF model. Davis et al. (2008) studied the ability of the Advanced Weather Research WRF (WRF-AWR) model to provide real-time forecasts of five landfalling hurricanes in 2005. Despite recurring errors with respect to intensification and inner-core dynamics, the authors explained that the model "revealed performance generally competitive with, and occasionally superior to, other operational forecasts for storm position and intensity". Fierro et al. (2009) studied horizontal resolution impacts on the microphysical and kinematic structure of a numerically simulated TC using WRF-AWR. Simulations of Hurricane Rita (2005) were performed with inner nest grid spacing from 1 km to 5 km with 1 km increments. Although structural differences were observed between simulations, compensation resulted in similar storm intensities, indicating that resolution increases (in this range) may not be as important as other model features such as physical parameterization and initial condition specification. Xiao et al. (2009) performed three-dimensional variational DA (3DVAR) of Airborne Doppler radar data to initialize simulations of three hurricanes with the Advanced Research Hurricane WRF model. 3DVAR with airborne radar data improved markedly the forecasting performance of the model: storm intensities, vortex asymmetries, and rainbands were simulated better compared to a simulation initialized with an NCEP Global Forecast System analysis, and conventional DA, without airborne radar, respectively. Khain et al. (2010) used the WRF model to study how aerosols, ingested into Hurricane Katrina (2005), impacted the storm's intensity and structure. They explained that the ingestion of continental aerosols contributed to the enhancement of convection at the storm periphery and consequently weakened its intensity before landfall. Trenberth et al. (2007) computed the moisture budgets for Hurricane Ivan (2004) and Hurricane Katrina (2005) using the WRF model. They found that the main contribution to the moisture budget was not associated to the flux due to evaporation but was associated to low-level convergence. Lin et al. (2010) coupled the WRF-AWR model with the 2D, depth-averaged hydrodynamic Advanced Circulation Model (ADCIRC) in order to investigate storm surge in the Chesapeake Bay along with structure and evolution of extreme rainfall caused by Hurricane Isabel (2003). They explained that "interaction of the TC circulation with the complex terrain of the central Appalachians played an important role in flooding from Isabel and, more generally, in the flood hydrology of the central Appalachians".

In this chapter, the suitability of a regional atmospheric model (RAM) to simulate local intense precipitation processes within TCs is assessed and the moisture transport fields responsible for the generation of local intense precipitation is investigated. The WRF model was run at 5-km inner-domain grid resolution to simulate 13 TCs which affected the United States between 1999 and 2016. It was run in the offline mode in order to evaluate its performance in simulating the precipitation fields of intense TCs when it is only subject to the influence of its IBCs, without nudging or DA.

Section 4.2 presents the modeling and validation frameworks. More specifically, it describes the nested simulation domains and the IBCs, and the metrics used to assess the model's performance. Section 4.3 presents the simulation results. Section 4.4 investigates the sensitivity of the precipitation field in Hurricane Gustav (2008) to the choice of the parameterization schemes. Finally, Section 4.5 gives a conclusion.

4.2 Modeling and Validation Frameworks

Apart from Hurricane Floyd (1999), the TCs were selected within the time period from 2002 to 2016, based on the NCEP Stage IV precipitation dataset. The most intense TCs with regards to precipitation were identified using the website *http://schumacher.atmos.colostate.edu/precip_monitor/atlas14* from the Precipitation Systems Research Group in Colorado State University Department of Atmospheric Science. This website lists every event for which a given threshold (e.g. 100-year return period, 24 hour) was exceeded at least one grid cell in Stage IV. The selected storms are among the most severe TCs during 2002-2016 in terms of the generation of an intense precipitation field.

The TCs were simulated with the WRF model Version 3.7 (Skamarock and Klemp, 2008) at 5-km inner-domain resolution, with 38 vertical layers and a time step of 3 min. CFSR was used for IBCs. Several sets of 3-level nested domains were prepared for the simulations of the 13 TCs because of the diversity in the tracks. While the outermost domain was the same for all cases and was chosen to cover the paths of all the identified TCs, different inner domains were set up in order to include the intense precipitation regions of each individual TC (Figure 4-1). For each TC, the simulation inner domains (domains 2 and 3) were selected in order to cover as large a fraction of the observed precipitation field as possible, while limiting their sizes to reduce the computational effort. In most cases, the simulation inner domain covers more or less the entirety of the observed precipitation field in the United States. However, in some cases (e.g. TS Lee), the TC generated a very large precipitation field, containing widely separated intense precipitation regions. In such cases, only the portion of the intense precipitation field around the location of landfall was reconstructed.

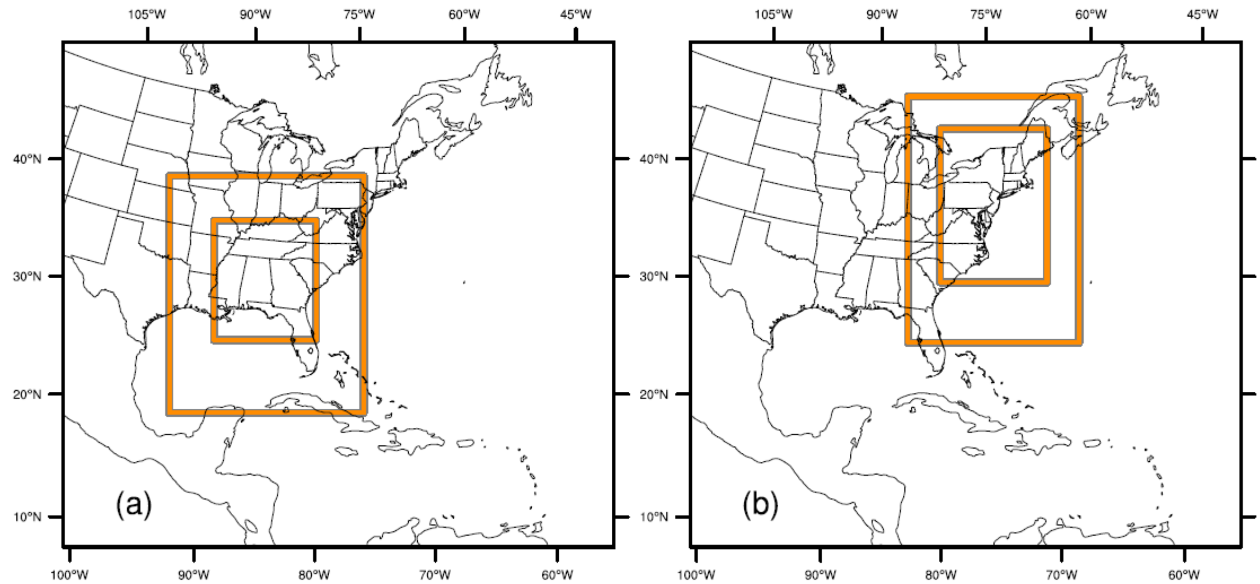

Figure 4-1 Examples of Simulation Nested Domains for (a) Hurricane Ivan (2004), and (b) Hurricane Irene (2011)

The outermost domain (i.e. Domain 1) is the same for all TCs and has a spatial resolution of 45 km. Domains 2 and 3 have resolutions of 15 km and 5 km, respectively.

The WRF model's parameterization schemes were chosen for each of the selected TCs in order to obtain the best simulation results with respect to the simulated and observed precipitation fields. The WRF model (Version 3.7) offers 24 microphysics options (i.e. schemes), 12 PBL options, 13 cumulus options, 8 shortwave radiation physics options, 8 longwave radiation physics options, 7 surface layer options, and 7 land-surface options (NCAR, 2016). Although certain combinations are invalid because some options are not compatible, there still remain several million possible combinations of the parameterization schemes alone. Establishing what is the best combination would require investigating all possible combinations for all storm events, which is not tractable. The goal of this chapter is not to determine the "best" options for the simulation of TCs, but rather to show that it is possible to simulate realistically the intense precipitation field in a TC, in terms of its location, structure and intensity, by choosing an appropriate combination of the parameterization schemes. Such a combination was searched starting from a list of combinations based on the literature and on the authors' experience in the numerical modeling of storm events. The search was terminated as soon as satisfactory results were obtained. As a result, no conclusion should be drawn from the results in Section 4.3 regarding whether a given scheme is better than another. Section 4.4 offers some insight into this issue by investigating the sensitivity of the results to the choice of the parameterization schemes for Hurricane Gustav (2008).

The model's performance was evaluated in two ways. First, the most realistic results were determined by plotting and comparing visually the simulated and observed precipitation fields. Then the best results were selected based on the performance in terms of the three metrics presented in Section 2.3.

4.3 Simulation Results

Table 4-1 shows the list of the TCs simulated in this study. All these TCs were responsible for generating intense precipitation in the United States. Except for Hurricane Floyd, they all happened within the time period of the Stage IV precipitation analyses. Table 4-2 gives the options used for the simulations.

Table 4-1 List of the TCs Simulated in this Study

The information regarding the date, maximum wind speed, minimum central pressure and category are from the website http://weather.unisys.com/hurricanes.

Name	Date	Wind (kn)	Pressure (mbar)	Category[a]
Hurricane Floyd	7-19 Sep 1999	135	921	4
Hurricane Isidore	14-27 Sep 2002	110	934	3
Hurricane Frances	25 Aug - 10 Sep 2004	125	935	4
Hurricane Ivan	2-24 Sep 2004	145	910	5
Hurricane Jeanne	13-29 Sep 2004	105	950	3
Hurricane Ernesto	24 Aug - 4 Sep 2006	65	985	1
TS Fay	15-28 Aug 2008	60	986	-
Hurricane Gustav	25 Aug - 5 Sep 2008	135	941	4
Hurricane Irene	21-30 Aug 2011	105	942	3
TS Lee	2-6 Sep 2011	50	986	-
Hurricane Isaac	20 Aug - 1 Sep 2012	70	965	1
Hurricane Sandy	21-31 Oct 2012	100	940	3
Hurricane Matthew	28 Sep - 9 Oct 2016	140	934	5

[a] category is based on the SSHS

Table 4-2 Parameterization Schemes Used for the Simulation of the TCs

The code numbers for each parameterization are the same as the code numbers used in WRF (version 3.7) and are detailed in APPENDIX A . Additional information and references may be found in the user manual (NCAR, 2016).

	Floyd	Isidore	Frances	Ivan	Jeanne	Ernesto	Fay	Gustav	Irene	Lee	Isaac	Sandy	Matthew
Microphysics	16	2	13	16	13	5	16	7	6	21	2	16	7
Cumulus parameterization[a]	14	93	2	14	3	2	2	14	93	14	93	14	14
PBL	8	2	8	2	7	8		8	1	8	1	8	8
Longwave Radiation	99	5	4	1	5	5	3	5	3	31	1	5	5
Shortwave Radiation	99	5	4	1	5	99	2	5	3	5	1	5	5
Land Surface	3	2	3	2	3	3	3	3	2	3	2	3	3
Surface Layer	1	2	1	2	1	1	1	1	1	1	91	1	1

[a] Cumulus parameterization was used only in the outer and intermediate domains.

In the following the plots of the observed and simulated accumulated precipitation fields in the inner domain and the results in terms of the performance metrics are presented for every TC (and summarized in subsection 4.3.14). The figures also show the plots of the IVT fields and their divergence.

In each case, the graph of the divergence of the time-averaged IVT field as a function of the precipitation depth is provided in order to illustrate the importance of moisture convergence in the generation of intense precipitation in TCs. Since the simulation inner domains contain a large number of grid points (~10^4-10^5 according to the case), the IVT divergence field and the precipitation field were averaged towards a coarser grid containing 400 grid points (corresponding to a 20x20 mesh in the case of a square inner domain) in order to facilitate the analysis of the dependence of the precipitation depth on IVT divergence.

4.3.1 Hurricane Floyd (1999)

According to the NWS website[3], "Floyd was a large and intense Cape Verde hurricane that pounded the Bahama Islands, seriously threatened Florida, struck the coast of North Carolina and moved up the East Coast into New England. It neared category five intensity on the SSHS as it approached the Bahamas, and produced a flooding catastrophe in the eastern United States, particularly in North Carolina". A Cape Verde-type hurricane is an Atlantic basin TC that develops into a TS fairly close (<1000 km) of the Cape Verde Islands and becomes a hurricane before reaching the Caribbean (http://www.aoml.noaa.gov/hrd/tcfaq/A2.html).

Hurricane Floyd produced a storm surge of about 10 feet, and made landfall with sustained winds of 110 mph (Pasch et al., 1999). It spawned many tornadoes in North Carolina, and heavy rainfall in portions of North Carolina, Virginia, Maryland, Delaware, New Jersey, and other portions of New England.

Figure 4-2 shows the simulation nested domains used for the reconstruction of Hurricane Floyd.

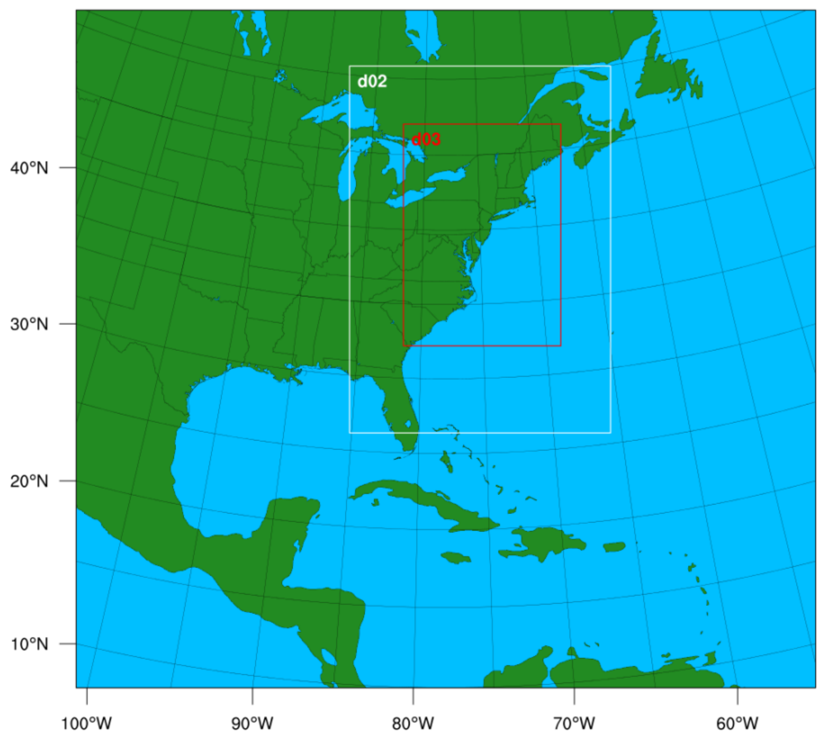

Figure 4-2 Simulation Nested Domains for Hurricane Floyd

The spatial resolutions from Domain 1 (outer domain) to Domain 3 (inner domain) are 45 km, 15 km, and 5 km. The number of grid points is 120 x 110 (zonal x meridional) for Domain 1, 127 x 178 for Domain 2, and 229 x 322 for Domain 3.

[3] http://www.weather.gov/

Figure 4-3 shows the observed 72-hr accumulated precipitation field in Hurricane Floyd whereas Figure 4-4a shows the simulated field. There is an excellent agreement between the observed and the simulated precipitation fields, both in terms of the field's location and intensity. Figure 4-4b presents the IVT field and its divergence averaged over the duration of the simulation. The link between precipitation depth and moisture convergence appears clearly in Figure 4-4, and is quantitatively expressed in Figure 4-5 which shows the IVT divergence as a function of the precipitation depth. The coefficient of determination is close to 1 (R^2=0.89) and the slope of the regression line close to -1. This shows that, in Hurricane Floyd, 2-dimensional moisture convergence was a major factor in the generation of intense precipitation. The grid points above the 80th percentile of the ground surface elevation (represented by blue crosses in Figure 4-5) exhibit the same behavior as the points below this threshold (red dots) in terms of their spread around the regression line. However it is observed that the most intense precipitation occurred in locations below the 80th percentile of the ground surface elevation, which is in agreement with Figure 4-4. The dotted line in Figure 4-5 has a slope of -1 and an intercept of 0. It shows the limit case for which all the converged moisture is transformed into precipitation. This line will be called the bisector line. It is observed that the regression line is above the bisector line, and its intercept is positive. A possible explanation is that the IVT divergence has been averaged over the duration of the simulation: at a given point, moisture divergence (negative convergence) can occur during the simulation which reduces the average value of the moisture convergence. Another possible explanation is that some processes not captured by the 2-dimensional moisture advection (e.g. convection) transformed the moisture already present in an atmospheric column into precipitation, so that more moisture precipitates than the moisture brought into the atmospheric column by convergence of the IVT.

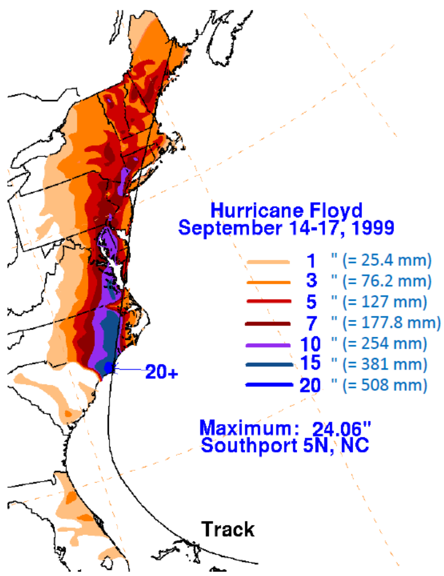

Figure 4-3 Observed 72-hr (from 09/14/1999 00:00 UTC until 09/17/1999 00:00 UTC) Accumulated Precipitation Field in Hurricane Floyd (Adapted from NOAA; http://www.wpc.ncep.noaa.gov/tropical/rain/floyd1999.html)

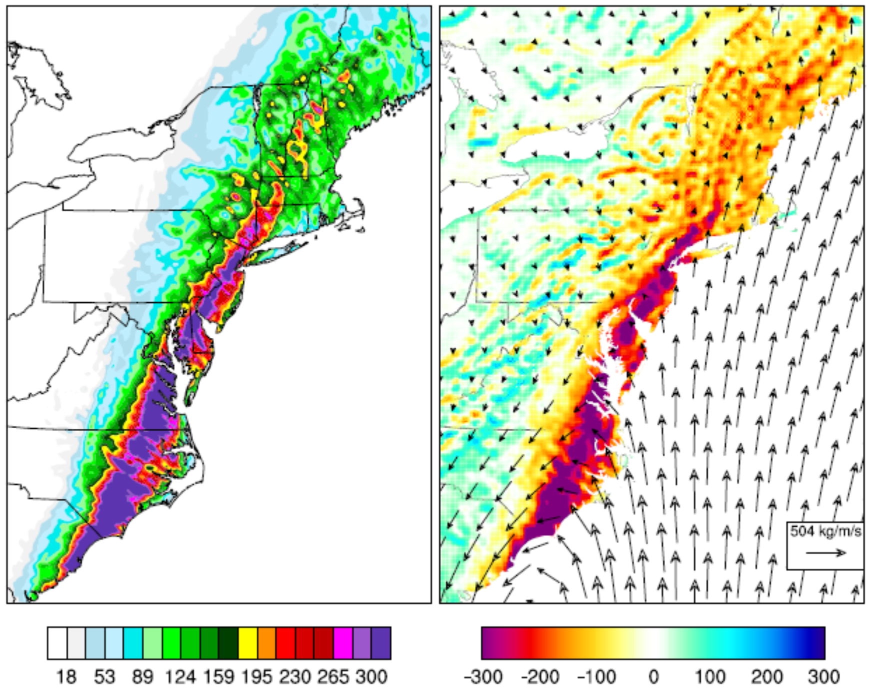

Figure 4-4 **(a) Hurricane Floyd Inner-Domain Simulated Accumulated Precipitation Field (from 09/15 06:00 UTC to 09/18 06:00 UTC)**

(b) Arrow field: time-averaged (from 09/15 06:00 UTC to 09/18 06:00 UTC) integrated vapor transport (kg m^{-1} s^{-1}). Color plot: divergence of the time-averaged integrated vapor transport field (mm).

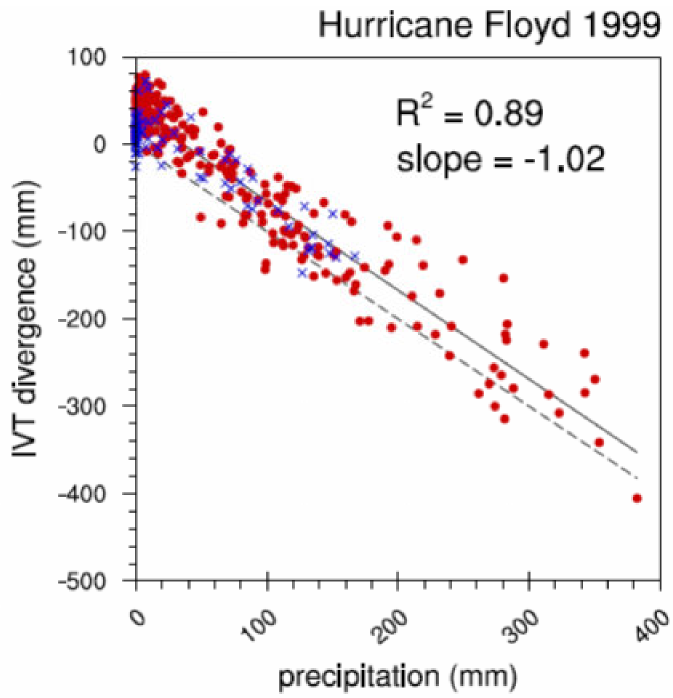

Figure 4-5 Divergence of the Time-Averaged Integrated Vapor Transport Field (mm) as a Function of the Precipitation Depth (mm) in Hurricane Floyd

Red dots correspond to the locations where the ground surface elevation is below the 80th percentile of the ground surface elevation in the simulation inner domain; whereas blue crosses correspond to the locations where the ground surface elevation is above this threshold. The solid line is the regression line. Its associated coefficient of determination (R^2) and slope are given on the figure. The dotted line has a slope of -1 and an intercept of 0.

The 6-hourly evolution of the reconstructed PW field and IVT field in Hurricane Floyd is given in Appendix B.2.1.

4.3.2 Hurricane Isidore (2002)

Hurricane Isidore originated from a tropical wave off the coast of Africa on September 9th (Avila, 2002). It was a slow-moving TC which hit the northern Yucatan Peninsula as a category 3 hurricane on the SSHS, and made landfall on the Louisiana coast as a strong TS. Its primary impact was the heavy rainfall which fell from the central United States Gulf coast into the Ohio Valley, with a maximum of 406.4 mm (16.0 in.) at Metairie, Louisiana.

Figure 4-6 shows the simulation nested domains used for the reconstruction of Hurricane Isidore.

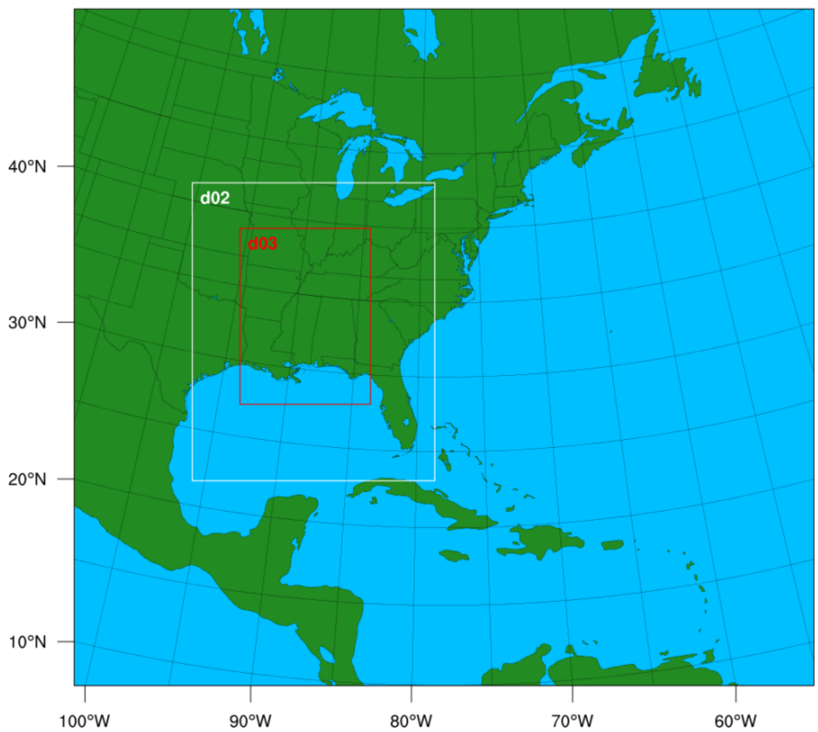

Figure 4-6 Simulation Nested Domains for Hurricane Isidore

The spatial resolutions from Domain 1 (outer domain) to Domain 3 (inner domain) are 45 km, 15 km, and 5 km. The number of grid points is 120 x 110 (zonal x meridional) for Domain 1, 118 x 145 for Domain 2, and 190 x 256 for Domain 3.

The WRF model gave excellent results for the reconstruction of this TC's precipitation field. The relative error for the total accumulated precipitation is less than 5%. Furthermore, the overlap percentage remains relatively large as the threshold increases, and is still larger than 10% for the 99th percentile. The PFAR is close to 1 for all precipitation thresholds, except for the 99th percentile for which the model overestimated the size of the precipitation field. This can be seen in Figure 4-8 as the size of the purple region is slightly larger in the case of the simulated field.

Table 4-3 Hurricane Isidore WRF Simulation Performance Summary

Relative error		+3.0%
50^{th} percentile threshold	% overlap	73%
	PFAR	0.92
75^{th} percentile threshold	% overlap	70%
	PFAR	1.00
90^{th} percentile threshold	% overlap	54%
	PFAR	1.11
95^{th} percentile threshold	% overlap	41%
	PFAR	1.28
97.5^{th} percentile threshold	% overlap	34%
	PFAR	1.38
99^{th} percentile threshold	% overlap	20%
	PFAR	1.85

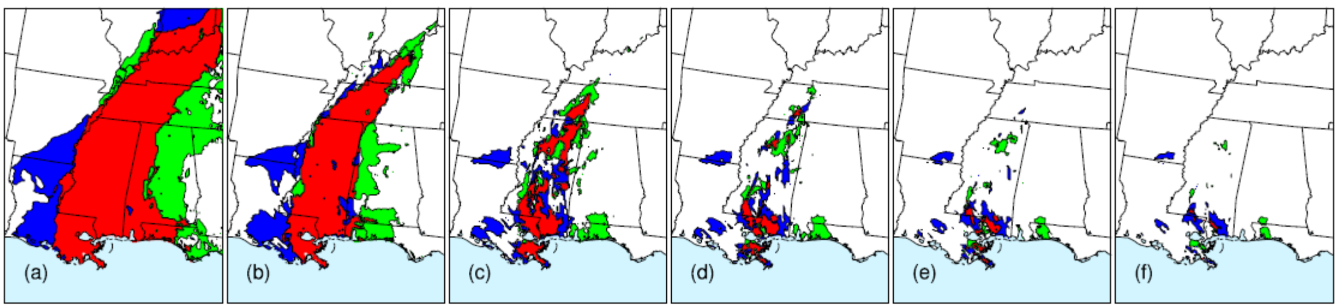

Figure 4-7 Overlapped Field Above the (a) 50^{th}, (b) 75^{th}, (c) 90^{th}, (d) 95^{th}, (e) 97.5^{th}, and (f) 99^{th} Percentile Values During Hurricane Isidore

Blue area: only simulation; green area: only observation; red area: both.

Figure 4-8c shows the IVT field and its divergence averaged over the duration of the simulation. It is observed that the regions of intense moisture convergence closely coincide with the regions of intense precipitation shown in Figure 4-8b. In fact, Figure 4-9 shows that the regression line for the IVT divergence as a function of the precipitation depth is almost superimposed with the bisector line, indicating that, once again, moisture convergence played a central role in the formation of intense precipitation in this TC. However the spread around the regression line is non-negligible, especially for the lowest values of the precipitation depth. For the lowest precipitation depths (< 30mm), the grid points above the 80^{th} percentile of the ground surface elevation (blue crosses) exhibit the same behavior as the grid points below this threshold (red dots): divergence is mainly positive. However for larger precipitation depths (> 30 mm), it is observed that most of the grid points above the 80^{th} percentile of the ground surface elevation fall below the bisector line which shows that, at these locations, moisture convergence only partially fed the precipitation process.

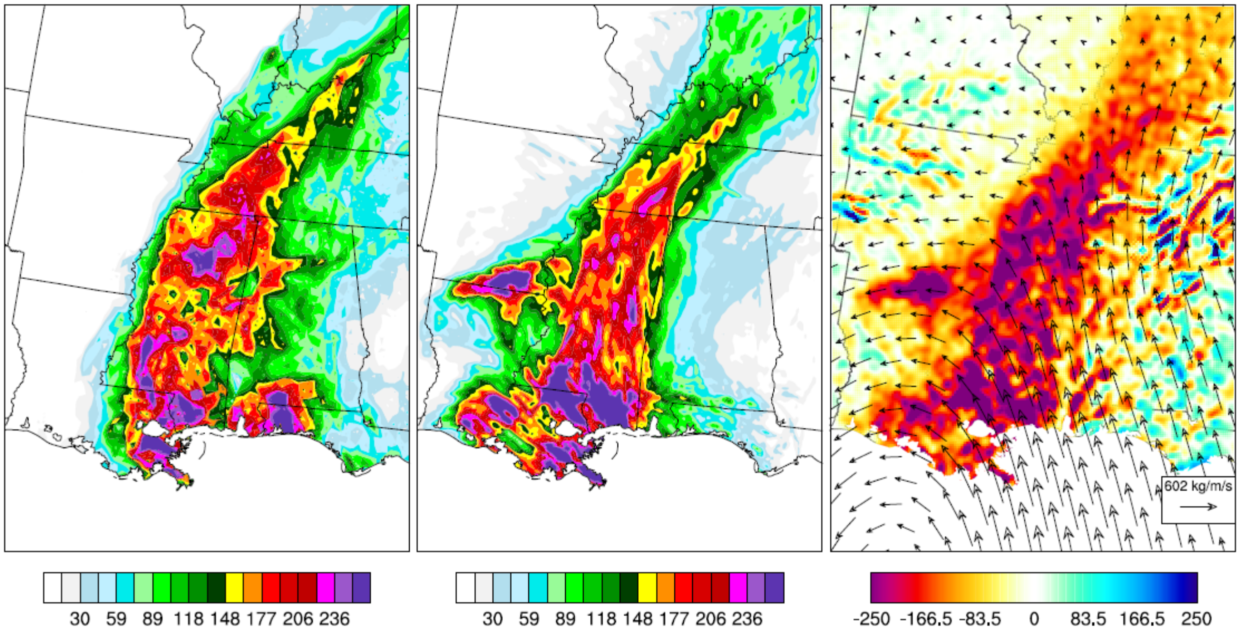

Figure 4-8 **(a) Hurricane Isidore Inner-Domain Observed Accumulated Precipitation Field (from 09/24 00:00 UTC to 09/28 00:00 UTC)**

(b) Inner-domain simulated accumulated precipitation field (from 09/24 00:00 UTC to 09/28 00:00 UTC). (c) Arrow field: time-averaged (from 09/24 00:00 UTC to 09/28 00:00 UTC) integrated vapor transport (kg m^{-1} s^{-1}). Color plot: divergence of the time-averaged integrated vapor transport field (mm).

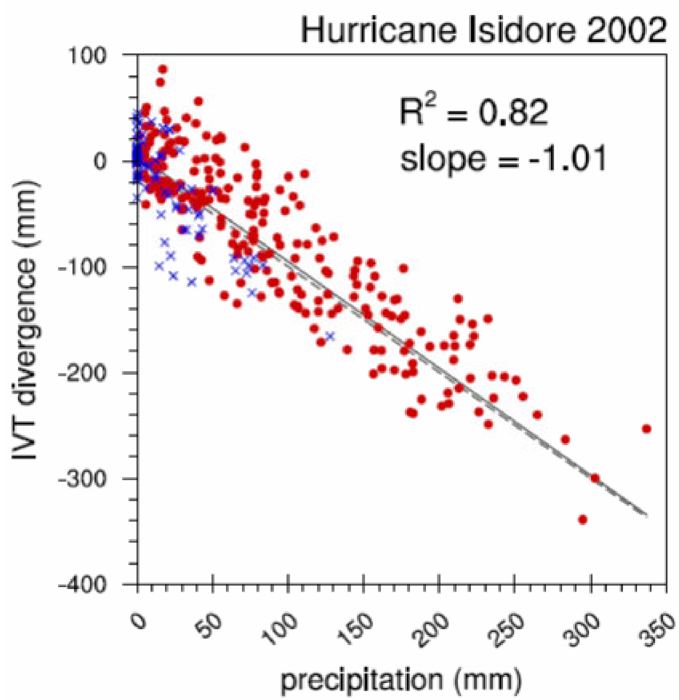

Figure 4-9 Divergence of the Time-Averaged Integrated Vapor Transport Field (mm) as a Function of the Precipitation Depth (mm) in Hurricane Isidore

Red dots correspond to the locations where the ground surface elevation is below the 80th percentile of the ground surface elevation in the simulation inner domain; whereas blue crosses correspond to the locations where the ground surface elevation is above this threshold. The solid line is the regression line. Its associated coefficient of determination (R^2) and slope are given on the figure. The dotted line has a slope of -1 and an intercept of 0.

The 6-hourly evolution of the reconstructed PW field and IVT field in Hurricane Isidore is given in Appendix B.2.2.

4.3.3 Hurricane Frances (2004)

Hurricane Frances peaked as a category 4 hurricane on the SSHS. It was a Cape Verde-type hurricane (Beven, 2005). It made landfall on September 5th in South-East Florida as a Category 2 hurricane. It gradually weakened as it moved slowly across the Florida Peninsula, and emerged into the northeastern Gulf of Mexico as a TS on September 6th. After making a final landfall in the Florida Big Bend, Frances re-curved northeastward into the westerlies over eastern Alabama and western Georgia. It became extratropical over West Virginia on September 9th and moved across New York, New England, and southeastern Canada (Beven, 2005).

Hurricane Frances produced significant storm surges along both the Atlantic and Gulf coasts of Florida, with a maximum of 5.89 ft above mean sea level. It caused widespread heavy rainfall and associated flooding over much of the eastern United States, and spawned about 100 tornadoes, mainly in South Carolina. Frances caused $4.43 billion in damages to insured property in the United States according to the American Insurances Service Group, with $4.11 billion occurring in Florida. The total U.S. damage was estimated at $9.507 billion (Beven, 2005).

Figure 4-10 shows the simulation nested domains used for the reconstruction of Hurricane Frances.

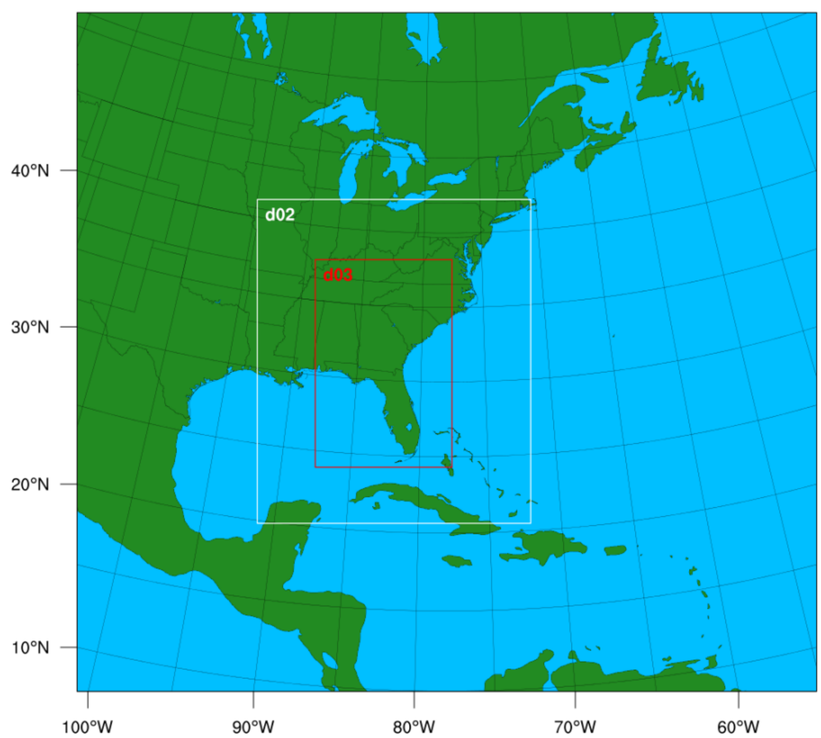

Figure 4-10 Simulation Nested Domains for Hurricane Frances

The spatial resolutions from Domain 1 (outer domain) to Domain 3 (inner domain) are 45 km, 15 km, and 5 km. The number of grid points is 120 x 110 (zonal x meridional) for Domain 1, 133 x 157 for Domain 2, and 199 x 301 for Domain 3.

Figure 4-12 shows that the model managed to place the precipitation field in the observed location, including heavy rainfall that fell in western North Carolina. Furthermore it gave good results in terms of the overlap percentage, while the PFAR remains close to 1 up to the 90th percentile threshold. However, the model slightly overestimated the total precipitation amount (relative error = 12%), as well as the size of the most intense part of the precipitation field corresponding to the 95th, 97.5th and 99th percentile thresholds.

Table 4-4 Hurricane Frances WRF Simulation Performance Summary

Relative error		+12%
50th percentile threshold	% overlap	85%
	PFAR	1.12
75th percentile threshold	% overlap	75%
	PFAR	1.20
90th percentile threshold	% overlap	62%
	PFAR	1.34
95th percentile threshold	% overlap	49%
	PFAR	1.58
97.5th percentile threshold	% overlap	44%
	PFAR	1.82
99th percentile threshold	% overlap	20%
	PFAR	1.81

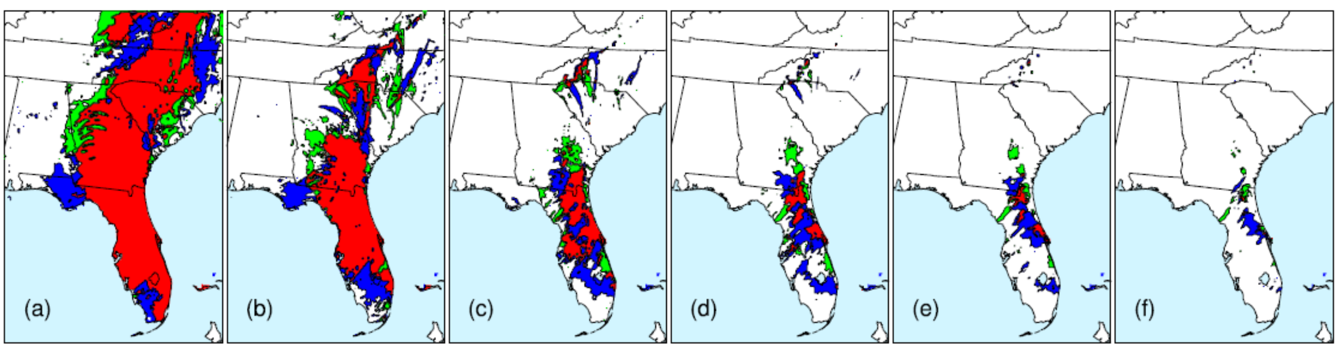

Figure 4-11 Overlapped Field Above the (a) 50th, (b) 75th, (c) 90th, (d) 95th, (e) 97.5th, and (f) 99th Percentile Values During Hurricane Frances

Blue area: only simulation; green area: only observation; red area: both.

Figure 4-12c shows the IVT field in Hurricane Frances and its divergence. The regions of most intense moisture convergence clearly correspond to the regions of most intense precipitation shown in Figure 4-12b. In particular, two regions of intense moisture convergence are observed. The first is in Florida and the second along the central section of the Appalachian Mountains. Figure 4-13 shows the divergence of the IVT as a function of the precipitation depth. As for the previous TCs, moisture convergence in Hurricane Frances played a central role in the formation of intense precipitation. However, the coefficient of determination is smaller (**R^2=0.79**) than in the previous cases and the slope of the regression line (equal to -0.93) further from -1. In particular it is observed that for the precipitation depths larger than 100 mm (3.9 in.), the grid points above the 80th percentile of the ground surface elevation (blue crosses) exhibit a behavior noticeably different from the grid points below the threshold: they are significantly below the regression line, and even below the bisector line. These results are in agreement with Figure 4-12c which shows that a large IVT convergence occurred along the Appalachian Mountains but did not cause a large precipitation depth except in a small region in western North Carolina. This behavior significantly increases the spread around the regression line thus decreasing the coefficient of determination.

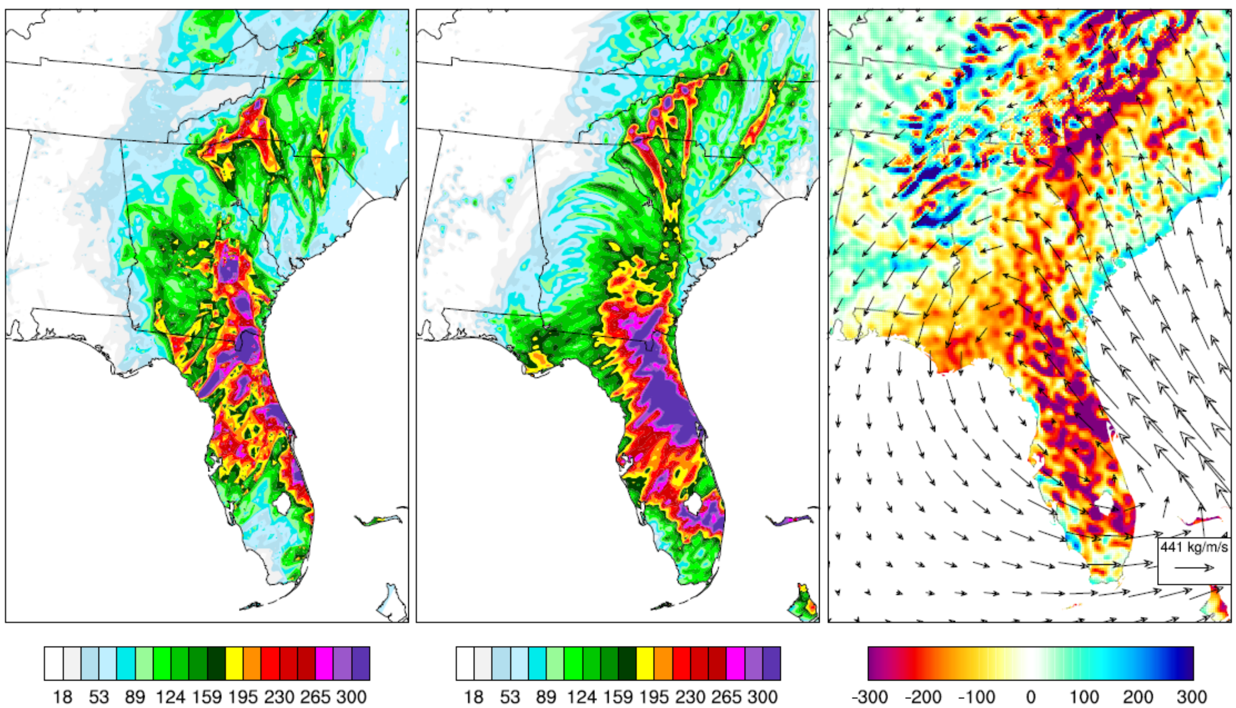

Figure 4-12 (a) Hurricane Frances Inner-Domain Observed Accumulated Precipitation Field (from 09/03 00:00 UTC to 09/10 00:00 UTC)

(b) Inner-domain simulated accumulated precipitation field (from 09/03 00:00 UTC to 09/10 00:00 UTC). (c) Arrow field: time-averaged (from 09/03 00:00 UTC to 09/10 00:00 UTC) integrated vapor transport (kg m^{-1} s^{-1}). Color plot: divergence of the time-averaged integrated vapor transport field (mm).

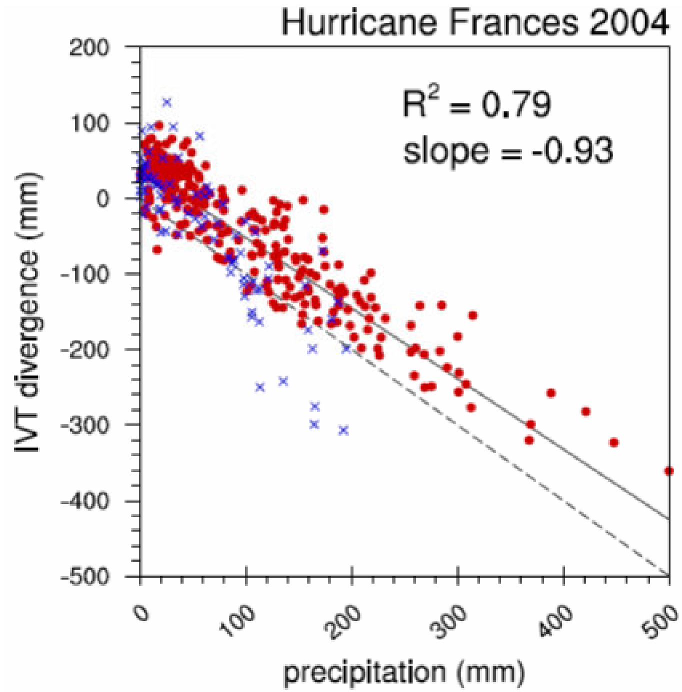

Figure 4-13 Divergence of the Time-Averaged Integrated Vapor Transport Field (mm) as a Function of the Precipitation Depth (mm) in Hurricane Frances

Red dots correspond to the locations where the ground surface elevation is below the 80^{th} percentile of the ground surface elevation in the simulation inner domain; whereas blue crosses correspond to the locations where the ground surface elevation is above this threshold. The solid line is the regression line. Its associated coefficient of determination (R^2) and slope are given on the figure. The dotted line has a slope of -1 and an intercept of 0.

The 6-hourly evolution of the reconstructed PW field and IVT field in Hurricane Frances is given in Appendix B.2.3.

4.3.4 Hurricane Ivan (2004)

According to Stewart (2004), “Ivan was a classical, long-lived Cape Verde hurricane that reached Category 5 strength three times on the SSHS. It was also the strongest hurricane on record that far southeast of the Lesser Antilles. Ivan caused considerable damage and loss of life as it passed through the Caribbean Sea.” Hurricane Ivan was the third of four hurricanes to impact Florida within a six-week period during the highly active 2004 hurricane season. It made landfall as a Category 3 hurricane just west of Gulf Shores, Alabama on September 16th. It was directly responsible for 25 deaths in the United States, mainly due to tornado, storm surge, and fresh water floods. It destroyed millions of acres of woodlands and forests. Total damage from the storm was estimated to equal $18.82 billion (Stewart, 2004).

Figure 4-14 shows the simulation nested domains used for the reconstruction of Hurricane Ivan.

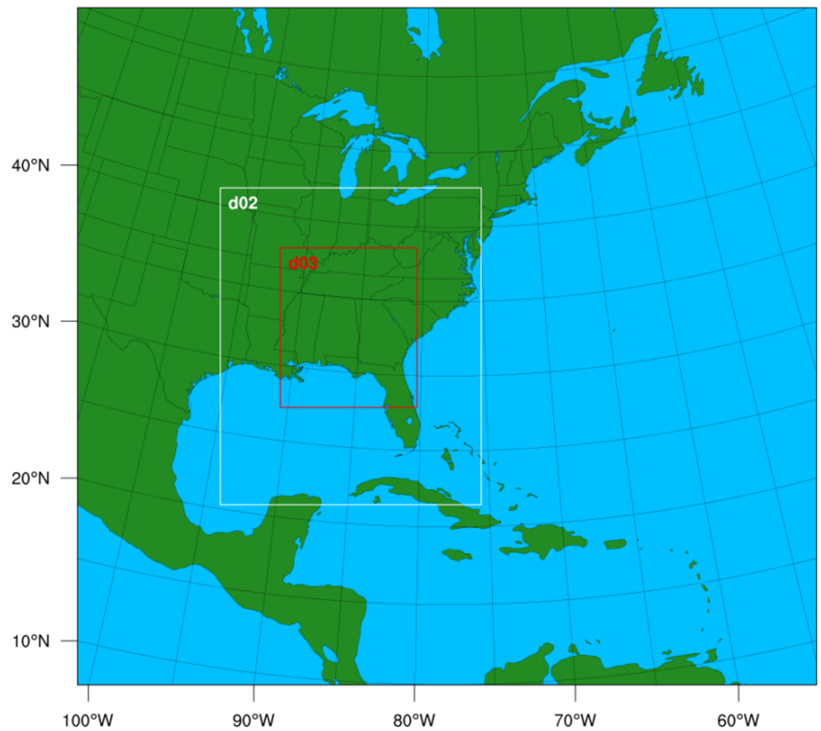

Figure 4-14 Simulation Nested Domains for Hurricane Ivan

The spatial resolutions from Domain 1 (outer domain) to Domain 3 (inner domain) are 45 km, 15 km, and 5 km. The number of grid points is 120 x 110 (zonal x meridional) for Domain 1, 127 x 154 for Domain 2, and 199 x 232 for Domain 3.

The model provided overall good results for the reconstruction of the precipitation field in Hurricane Ivan. It overestimated the total precipitation amount, but the relative error remains small, less than 10%. The results in terms of the overlap percentage are good, but this needs to be put in perspective of the results in terms of the PFAR. For example, the model clearly overestimated the size of the precipitation field over the 99th percentile threshold (PFAR = 2.79). This can be observed in Figure 4-16 where the size of the purple region near the location of landfall is significantly larger in the case of the simulation.

Table 4-5 Hurricane Ivan WRF Simulation Performance Summary

Relative error		+6.3%
50th percentile threshold	% overlap	85%
	PFAR	1.01
75th percentile threshold	% overlap	65%
	PFAR	1.02
90th percentile threshold	% overlap	59%
	PFAR	1.36
95th percentile threshold	% overlap	59%
	PFAR	1.66
97.5th percentile threshold	% overlap	59%
	PFAR	2.04
99th percentile threshold	% overlap	62%
	PFAR	2.79

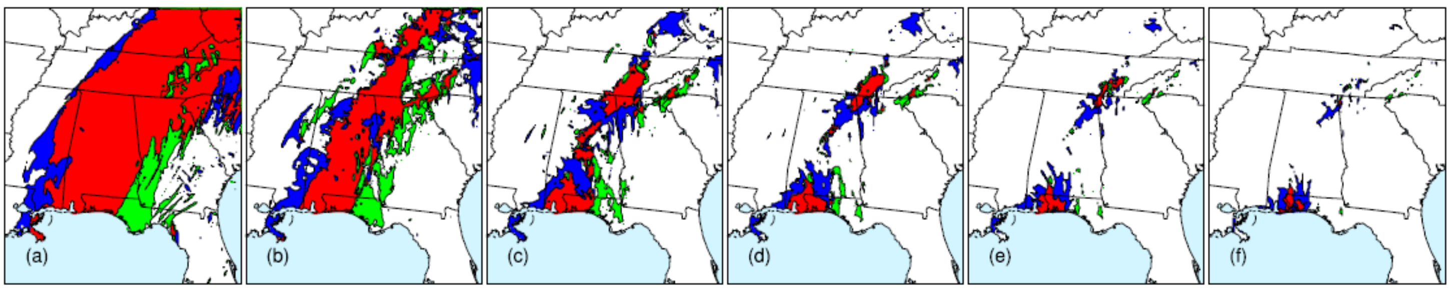

Figure 4-15 Overlapped Field Above the (a) 50th, (b) 75th, (c) 90th, (d) 95th, (e) 97.5th, and (f) 99th Percentile Values During Hurricane Ivan

Blue area: only simulation; green area: only observation; red area: both.

Figure 4-16c shows the IVT field and its divergence in Hurricane Ivan. It is observed that the regions of intense precipitation appearing in Figure 4-16b are associated with regions of intense moisture convergence. However, Figure 4-16c also exhibits regions of intense moisture convergence along the Appalachian Mountains that are not associated with intense precipitation. This appears clearly in Figure 4-17 as a large fraction of the blue crosses representing grid points above the 80th percentile of the ground surface elevation lies below both the regression line and the bisector line. These points also strongly participate in decreasing the coefficient of determination which is smaller than in the previous cases (R^2 = 0.76) as well as in decreasing the slope of the regression line which is smaller than -1.

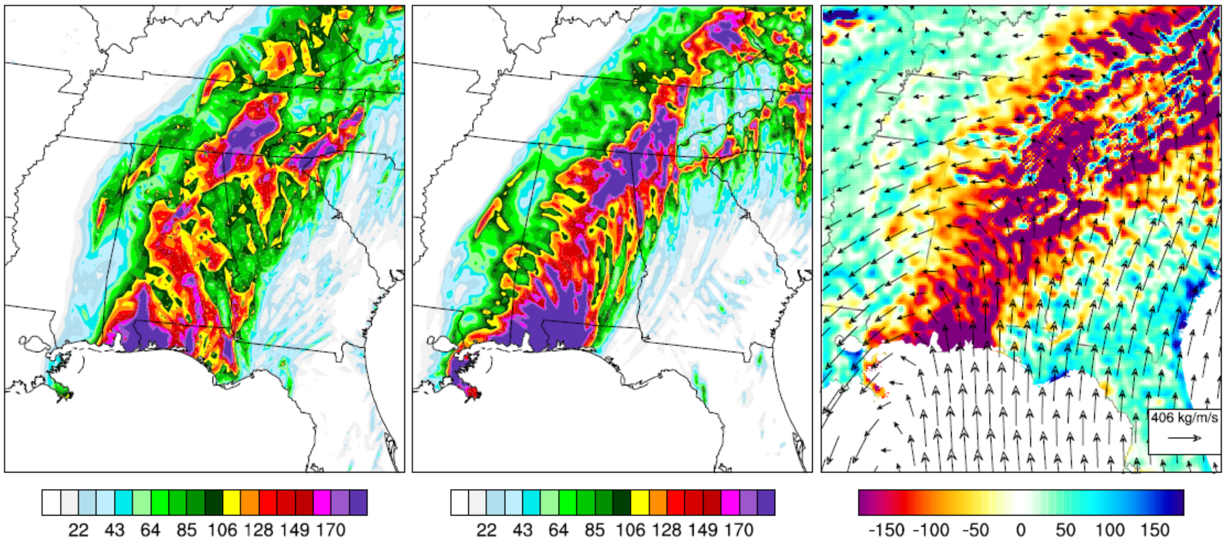

Figure 4-16 **(a) Hurricane Ivan Inner-Domain Observed Accumulated Precipitation Field (from 09/14 00:00 UTC to 09/19 00:00 UTC)**

(b) Inner-domain simulated accumulated precipitation field (from 09/14 00:00 UTC to 09/19 00:00 UTC). (c) Arrow field: time-averaged (from 09/14 00:00 UTC to 09/19 00:00 UTC) integrated vapor transport (kg m^{-1} s^{-1}). Color plot: divergence of the time-averaged integrated vapor transport field (mm).

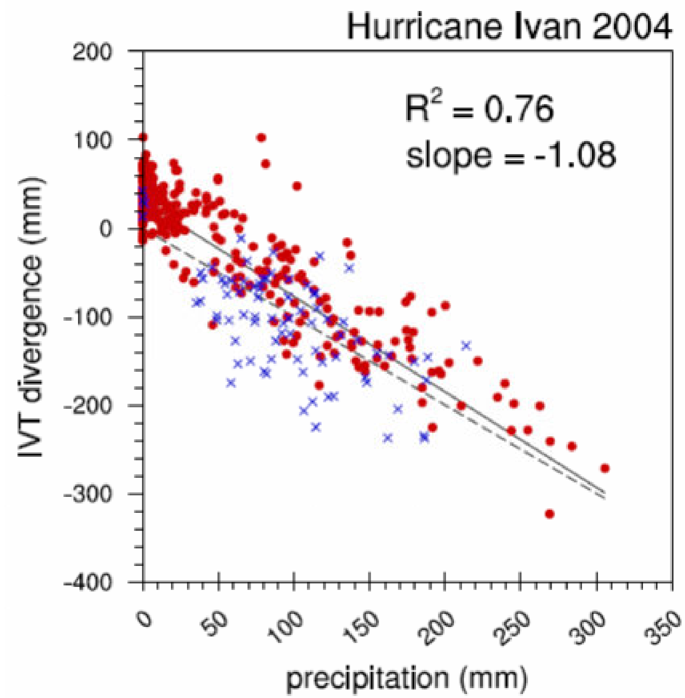

Figure 4-17 Divergence of the Time-Averaged Integrated Vapor Transport Field (mm) as a Function of the Precipitation Depth (mm) in Hurricane Ivan

Red dots correspond to the locations where the ground surface elevation is below the 80th percentile of the ground surface elevation in the simulation inner domain; whereas blue crosses correspond to the locations where the ground surface elevation is above this threshold. The solid line is the regression line. Its associated coefficient of determination (R^2) and slope are given on the figure. The dotted line has a slope of -1 and an intercept of 0.

The 6-hourly evolution of the reconstructed PW field and IVT field in Hurricane Ivan is given in Appendix B.2.4.

4.3.5 Hurricane Jeanne (2004)

Jeanne formed from a tropical wave that moved from Africa to the eastern tropical Atlantic Ocean on September 7th (Lawrence and Cobb, 2005). It peaked as a Category 3 Hurricane, and was the deadliest hurricane of the 2004 Atlantic hurricane season. It caused at least 3,000 deaths in Haiti, from torrential rainfall flooding. Jeanne made landfall on the east coast of Florida early on September 26th. Jeanne weakened as it moved across central Florida to a TS on September 26th, and further to a tropical depression about 24 hours later while moving across central Georgia accompanied by intense precipitation. The total U.S damage from Hurricane Jeanne was estimated at $7.66 billion (Lawrence and Cobb, 2005).

Figure 4-18 shows the simulation nested domains used for the reconstruction of Hurricane Jeanne. Hurricane Jeanne was difficult to reconstruct. After investigating the parameterization schemes, the model time step was also tuned to further improve the results. A time step of 2 min was used in this case.

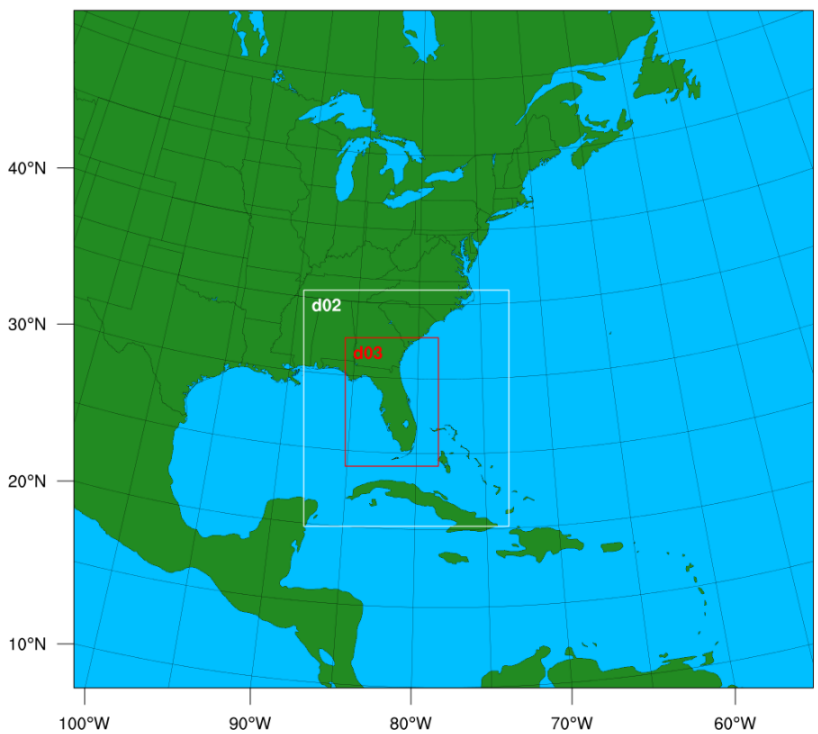

Figure 4-18 Simulation Nested Domains for Hurricane Jeanne

The spatial resolutions from Domain 1 (outer domain) to Domain 3 (inner domain) are 45 km, 15 km, and 5 km. The number of grid points is 120 x 110 (zonal x meridional) for Domain 1, 100 x 115 for Domain 2, and 136 x 187 for Domain 3.

The model provided overall satisfactory results for this TC. The total precipitation amount was slightly overestimated but the relative error remains less than 20%. The percentage of overlapping and the PFAR are satisfactory for the 50th and 75th percentiles. The PFAR is also satisfactory for the 99th percentile. However, the model significantly overestimated the size of the field over the 90th, 95th, and 97.5th percentiles. This can be observed on Figure 4-20 as the size of the red region is significantly larger for the simulated field than for the observed field.

Table 4-6 Hurricane Jeanne WRF Simulation Performance Summary

Relative error		+14.7%
50th percentile threshold	% overlap	78%
	PFAR	1.08
75th percentile threshold	% overlap	73%
	PFAR	1.40
90th percentile threshold	% overlap	69%
	PFAR	2.23
95th percentile threshold	% overlap	67%
	PFAR	2.35
97.5th percentile threshold	% overlap	56%
	PFAR	2.35
99th percentile threshold	% overlap	25%
	PFAR	1.38

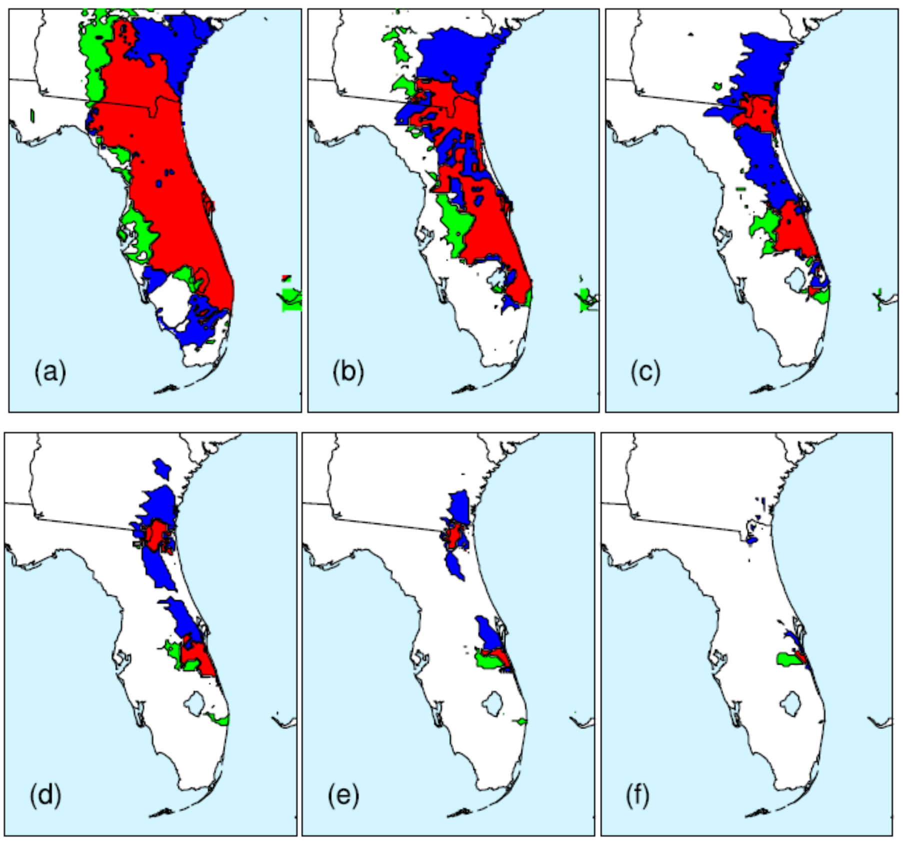

Figure 4-19 Overlapped Field Above the (a) 50th, (b) 75th, (c) 90th, (d) 95th, (e) 97.5th, and (f) 99th Percentile Values During Hurricane Jeanne

Blue area: only simulation; green area: only observation; red area: both.

Figure 4-20c presents the IVT and its divergence in Hurricane Jeanne. Comparing Figure 4-20b and Figure 4-20c it appears that the regions of most intense precipitation correspond to the regions where the moisture convergence was the largest. Figure 4-21 quantifies this relationship between IVT divergence and precipitation depth. It shows a relatively large coefficient of determination (R^2 = 0.84) and also shows that the slope of the regression line is close to -1 so that, in average over the duration of the simulation, about all the moisture that converges at a location is transformed into precipitation.

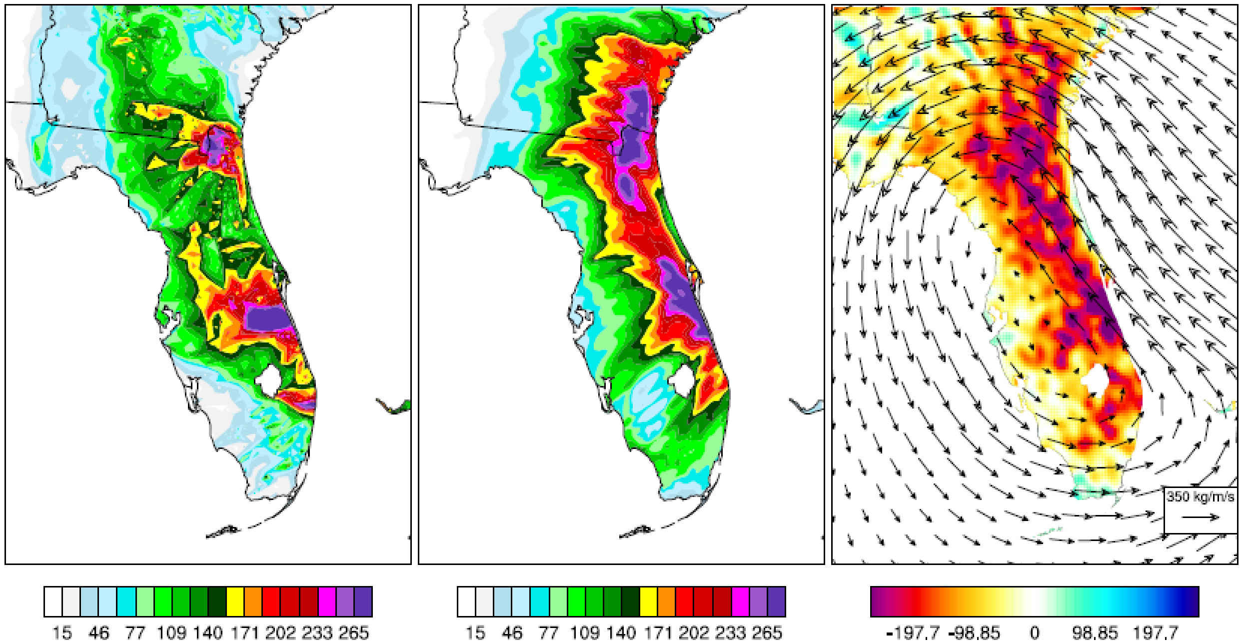

Figure 4-20 (a) Hurricane Jeanne Inner-Domain Observed Accumulated Precipitation Field (from 09/24 00:00 UTC to 09/30 18:00 UTC)

(b) Inner-domain simulated accumulated precipitation field (from 09/24 00:00 UTC to 09/30 18:00 UTC). (c) Arrow field: time-averaged (from 09/24 00:00 UTC to 09/30 18:00 UTC) integrated vapor transport (kg m^{-1} s^{-1}). Color plot: divergence of the time-averaged integrated vapor transport field (mm).

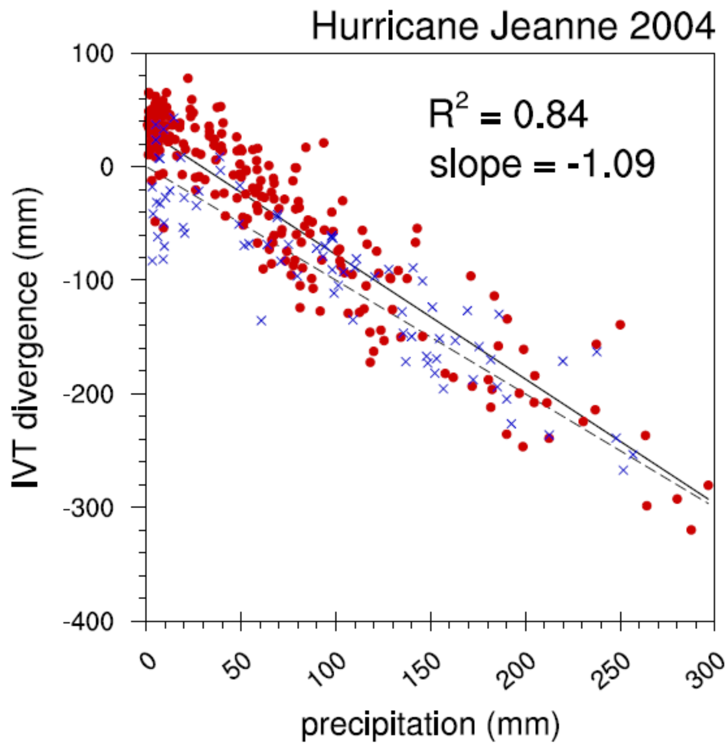

Figure 4-21 Divergence of the Time-Averaged Integrated Vapor Transport Field (mm) as a Function of the Precipitation Depth (mm) in Hurricane Jeanne

Red dots correspond to the locations where the ground surface elevation is below the 80th percentile of the ground surface elevation in the simulation inner domain; whereas blue crosses correspond to the locations where the ground surface elevation is above this threshold. The solid line is the regression line. Its associated coefficient of determination (R^2) and slope are given on the figure. The dotted line has a slope of -1 and an intercept of 0.

The 6-hourly evolution of the reconstructed PW field and IVT field in Hurricane Jeanne is given in Appendix B.2.5.

4.3.6 Hurricane Ernesto (2006)

Hurricane Ernesto peaked as a weak Category 1 hurricane on the SSHS over the central Caribbean Sea. It originated from a tropical wave which emerged from the west coast of Africa on August 18th and moved over the tropical Atlantic during the following days (Knabb and Mainelli, 2006). In the United States, it first made landfall in the upper Florida Keys on August 30th. A second landfall occurred in Florida mainland a short time later. Ernesto moved northward across the center of the Florida Peninsula as a TS and emerged over the Atlantic Ocean early on August 31st. Its impacts in Florida were limited. While moving over the Atlantic, Ernesto intensified as a strong TS and continued moving north-northeastward. It made a final landfall in eastern North Carolina on September 1st, where it spawned torrential rainfall and floods. Strong winds and heavy rains also impacted portions of Virginia, Maryland, Delaware, and New Jersey (Knabb and Mainelli, 2006).

Figure 4-22 shows the simulation nested domains used for the reconstruction of Hurricane Ernesto.

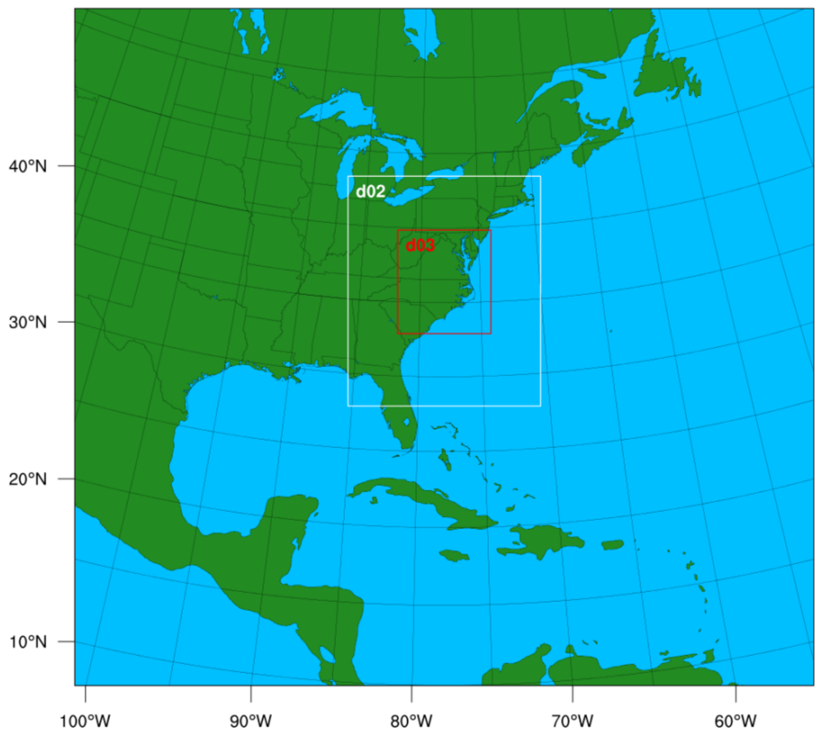

Figure 4-22 Simulation Nested Domains for Hurricane Ernesto

The spatial resolutions from Domain 1 (outer domain) to Domain 3 (inner domain) are 45 km, 15 km, and 5 km. The number of grid points is 120 x 110 (zonal x meridional) for Domain 1, 94 x 112 for Domain 2, and 136 x 151 for Domain 3.

The WRF model provided satisfactory results for the simulation of the precipitation field in Hurricane Ernesto. The total precipitation amount was overestimated but the relative error remains reasonable (relative error = +15%). The size of the precipitation field above the 50th percentile and 99th percentile threshold was well reproduced as the PFAR is close to1. However, the model noticeably overestimated the size of the field above the other thresholds. The overlap percentage remains large ($\geq 30\%$) until the 97.5th percentile threshold but drops to 5.4% for the 99th percentile threshold.

Table 4-7 Hurricane Ernesto WRF Simulation Performance Summary

Relative error		+15%
50th percentile threshold	% overlap	79%
	PFAR	1.10
75th percentile threshold	% overlap	83%
	PFAR	1.48
90th percentile threshold	% overlap	75%
	PFAR	1.77
95th percentile threshold	% overlap	51%
	PFAR	1.87
97.5th percentile threshold	% overlap	30%
	PFAR	1.74
99th percentile threshold	% overlap	5.4%
	PFAR	0.97

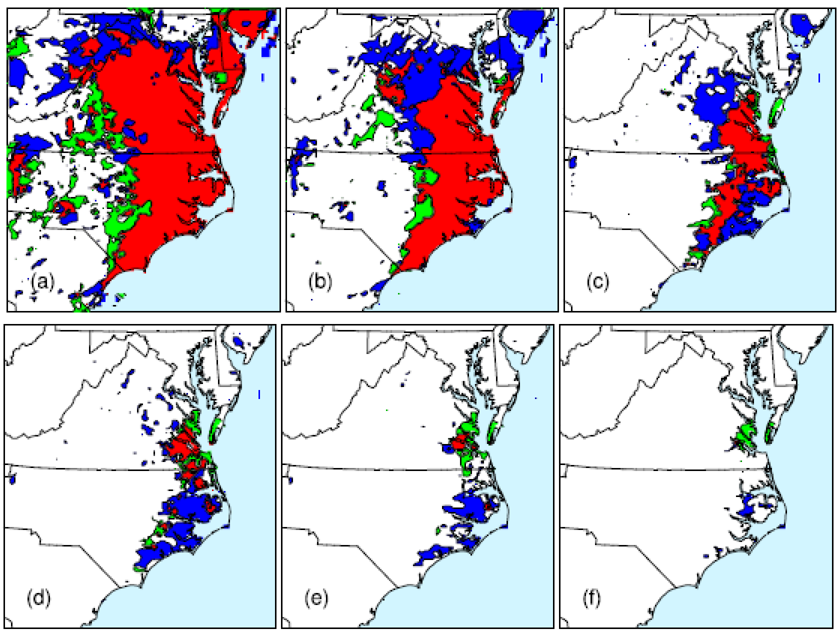

Figure 4-23 Overlapped Field Above the (a) 50th, (b) 75th, (c) 90th, (d) 95th, (e) 97.5th, and (f) 99th Percentile Values During Hurricane Ernesto

Blue area: only simulation; green area: only observation; red area: both.

Figure 4-24c gives the IVT field and its divergence in Hurricane Ernesto. The regions of intense precipitation shown in Figure 4-24b are clearly associated with regions of intense moisture convergence. However the reverse is not true as there are in the Appalachian Mountains regions with large moisture convergence but low precipitation depth. These grid points correspond to the blue crosses in Figure 4-25. It is observed that they participate in increasing the spread of the cloud of points around the regression line and thus decrease the coefficient of determination. Compared to the previous storms, the slope of the regression line is small in absolute value (-0.89), although the grid points associated with the largest precipitation depth are close to the bisector line.

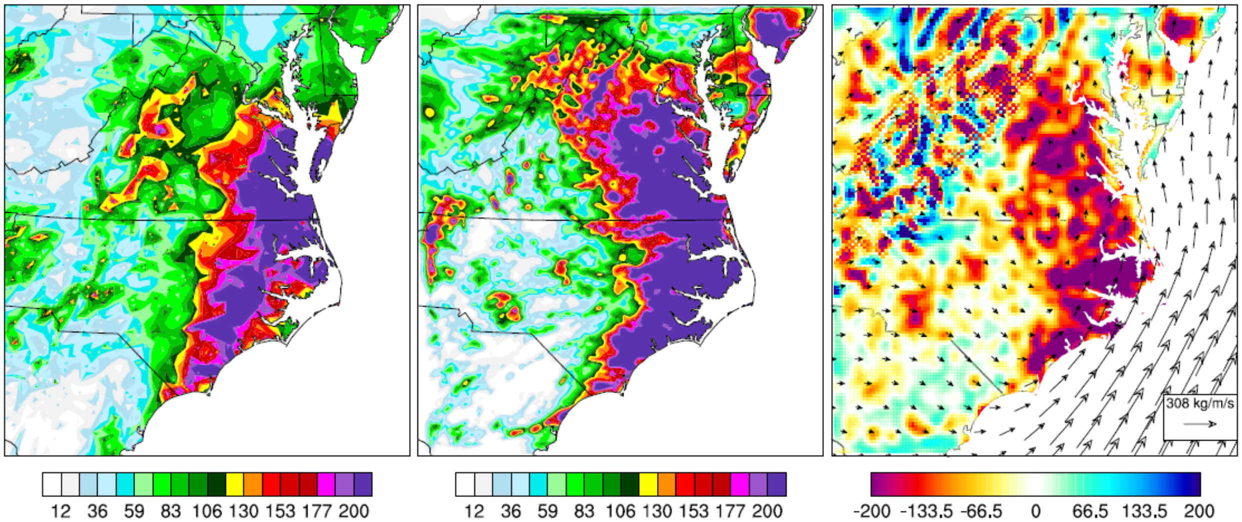

Figure 4-24 **(a) Hurricane Ernesto Inner-Domain Observed Accumulated Precipitation Field (from 08/28 12:00 UTC to 09/05 00:00 UTC)**

(b) Inner-domain simulated accumulated precipitation field (from 08/28 12:00 UTC to 09/05 00:00 UTC). (c) Arrow field: time-averaged (from 08/28 12:00 UTC to 09/05 00:00 UTC) integrated vapor transport (kg m^{-1} s^{-1}). Color plot: divergence of the time-averaged integrated vapor transport field (mm).

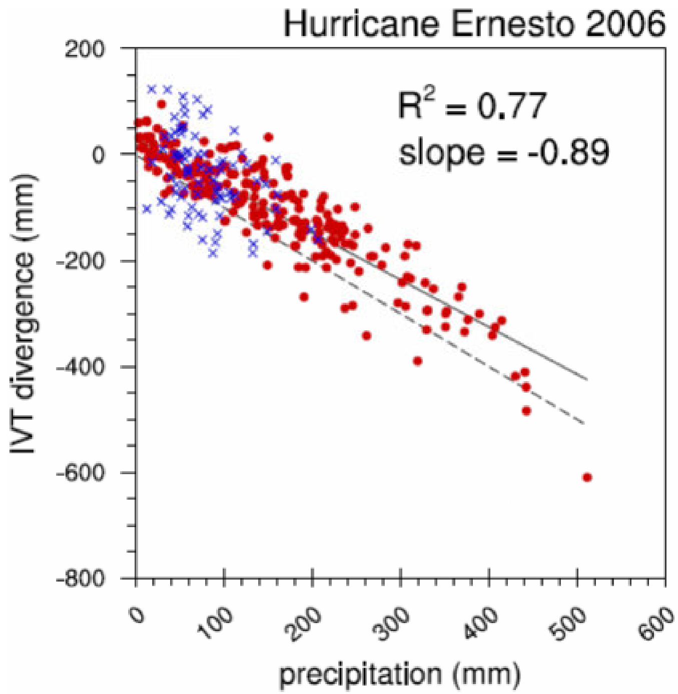

Figure 4-25 Divergence of the Time-Averaged Integrated Vapor Transport Field (mm) as a Function of the Precipitation depth (mm) in Hurricane Ernesto

Red dots correspond to the locations where the ground surface elevation is below the 80th percentile of the ground surface elevation in the simulation inner domain; whereas blue crosses correspond to the locations where the ground surface elevation is above this threshold. The solid line is the regression line. Its associated coefficient of determination (R^2) and slope are given on the figure. The dotted line has a slope of -1 and an intercept of 0.

The 6-hourly evolution of the reconstructed PW field and IVT field in Hurricane Ernesto is given in Appendix B.2.6.

4.3.7 TS Fay (2008)

According to Stewart and Beven (2008), ''Fay was a long-lived TS that made eight landfalls – including a record four landfalls in Florida – and produced torrential rainfall that caused extensive floods across the Dominican Republic, Haiti, Cuba, and Florida''. It originated from a tropical wave that emerged off the coast of Africa on August 6th and moved rapidly west-northwestward. Storm surge and its associated effects were relatively minimal. However, TS Fay produced 81 tornadoes across five states, and generated intense precipitation in Florida and southern Georgia. Rainfall maxima of 703.6 mm (27.7 in.) were measured near Melbourne, Florida. Significant floods occurred in east-central Florida. Total damage from Fay in the United States were about $560 million, mainly from rainfall-induced floods (Stewart and Beven, 2008).

Figure 4-26 shows the simulation nested domains used for the reconstruction of TS Fay. TS Fay was difficult to reconstruct. After investigating the parameterization schemes, the number of model vertical levels was also tuned to further improve the results. 30 vertical levels were used in this case.

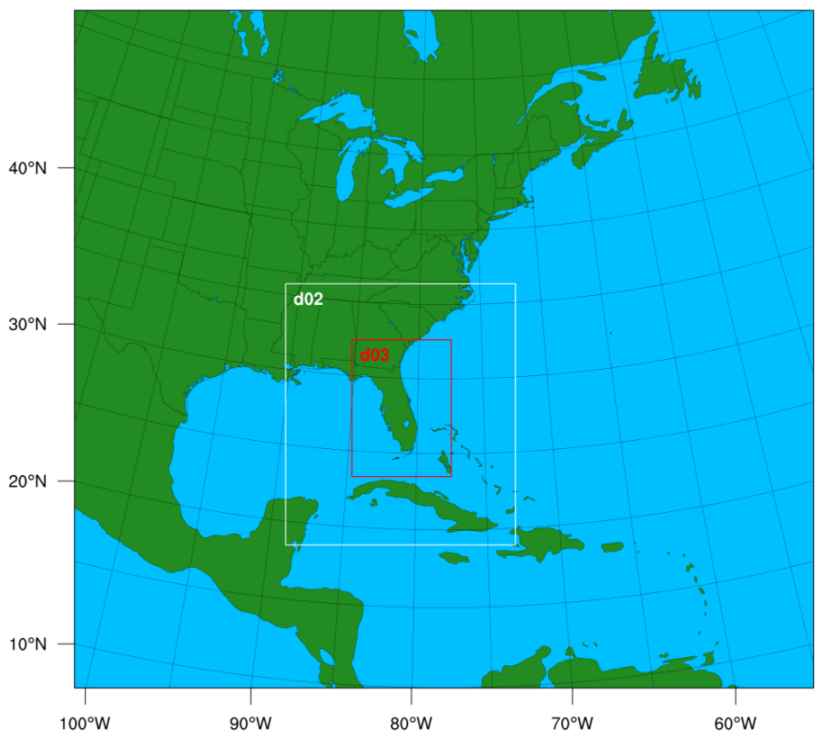

Figure 4-26 Simulation Nested Domains for TS Fay

The spatial resolutions from Domain 1 (outer domain) to Domain 3 (inner domain) are 45 km, 15 km, and 5 km. The number of grid points is 120 x 110 (zonal x meridional) for Domain 1, 112 x 127 for Domain 2, and 145 x 199 for Domain 3.

The model provided satisfactory results for the reconstruction of the precipitation field of TS Fay. It underestimated the total precipitation amount, but the relative error remains reasonable. The percentage of overlapping for the median is relatively small (only 57%) compared to most of the other simulated TCs, but it decreases slowly as the depth threshold increases. It is still larger than 20% for the most intense thresholds, although the model overestimated the size of the precipitation field for these thresholds. These results can be inferred from Figure 4-28. Indeed, on this figure it is observed that the model placed the storm slightly to the south of the observation. In particular, almost no rainfall fell on the eastern portion of the boundary between Florida and Georgia in the case of the simulation, which differs from the observation. This explains why the percentage of overlapping is relatively small for the 50th and 75th percentiles. However, the model successfully reproduced the intense rainfall that fell on the western portion of the boundary between Florida and Georgia, which allows the percentages of overlapping to remain large even for the most intense thresholds.

Table 4-8 TS Fay WRF Simulation Performance Summary

Relative error		-11.0%
50th percentile threshold	% overlap	57%
	PFAR	0.81
75th percentile threshold	% overlap	42%
	PFAR	0.98
90th percentile threshold	% overlap	32%
	PFAR	1.18
95th percentile threshold	% overlap	30%
	PFAR	1.38
97.5th percentile threshold	% overlap	22%
	PFAR	1.56
99th percentile threshold	% overlap	22%
	PFAR	1.98

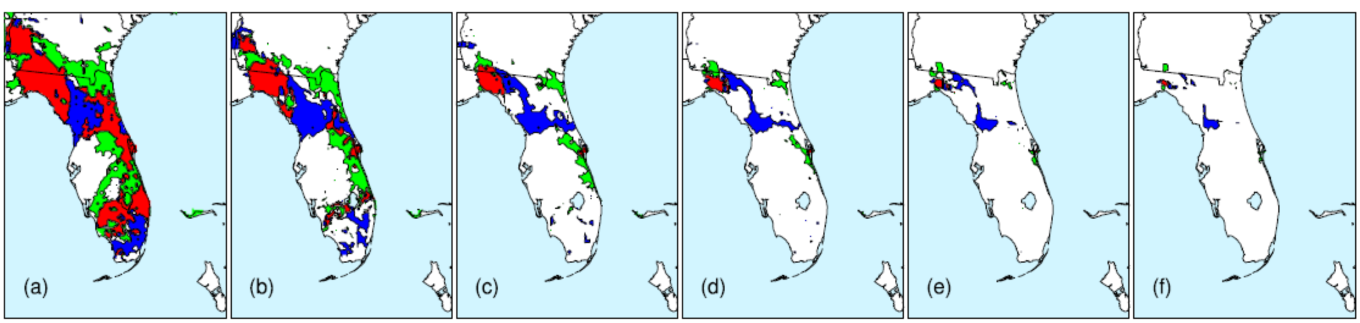

Figure 4-27 Overlapped Field Above the (a) 50th, (b) 75th, (c) 90th, (d) 95th, (e) 97.5th, and (f) 99th Percentile Values During TS Fay

Blue area: only simulation; green area: only observation; red area: both.

Figure 4-28c presents the time-averaged IVT in TS Fay and its divergence. Comparing Figure 4-28b and Figure 4-28c it clearly appears that the regions of intense precipitation closely coincide with the region of most intense IVT convergence. Figure 4-29 supports this finding as it shows that there is a strong quantitative relationship between precipitation depth and moisture convergence. Indeed, the coefficient of determination for the linear regression of the IVT divergence as a function of precipitation depth is relatively close to 1 ($R^2 = 0.82$). Besides, the slope of the regression line is close to -1 showing that, in average over the duration of the simulation, about all the moisture that converges above a given location falls upon this location as rainfall.

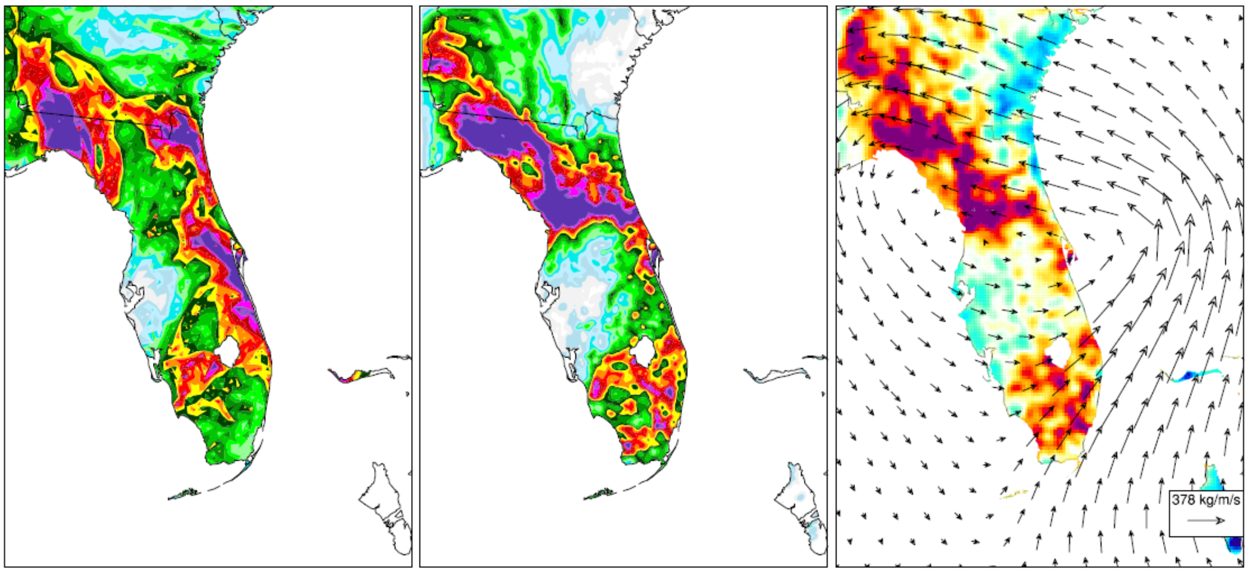

Figure 4-28 (a) TS Fay Inner-Domain Observed Accumulated Precipitation Field (from 08/17 12:00 UTC to 08/28 00:00 UTC)

(b) Inner-domain simulated accumulated precipitation field (from 08/17 12:00 UTC to 08/28 00:00 UTC). (c) Arrow field: time-averaged (from 08/17 12:00 UTC to 08/28 00:00 UTC) integrated vapor transport (kg m^{-1} s^{-1}). Color plot: divergence of the time-averaged integrated vapor transport field (mm).

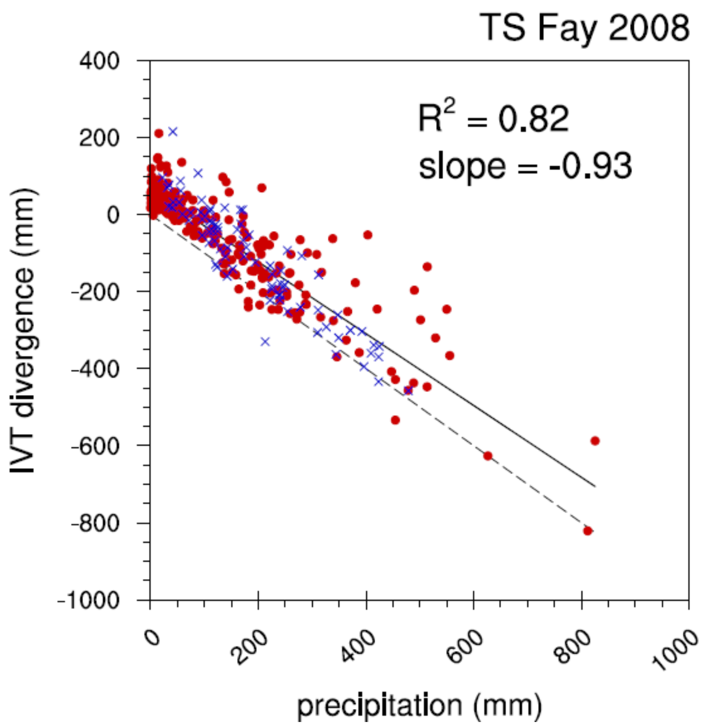

Figure 4-29 Divergence of the Time-Averaged Integrated Vapor Transport Field (mm) as a Function of the Precipitation Depth (mm) in TS Fay

Red dots correspond to the locations where the ground surface elevation is below the 80th percentile of the ground surface elevation in the simulation inner domain; whereas blue crosses correspond to the locations where the ground surface elevation is above this threshold. The solid line is the regression line. Its associated coefficient of determination (R^2) and slope are given on the figure. The dotted line has a slope of -1 and an intercept of 0.

The 6-hourly evolution of the reconstructed PW field and IVT field in TS Fay is given in Appendix B.2.7**.**

4.3.8 Hurricane Gustav (2008)

Hurricane Gustav formed from a tropical wave which move off the African coast on August 13th (Beven and Kimberlain, 2009). Gustav peaked as a Category 4 hurricane before making landfall on the coast of the Isle of Youth, Cuba on August 30th. In the United States, Hurricane Gustav made landfall as a category 2 hurricane near Cocodrie, Louisiana on September 1st. On September 2nd, it became a tropical depression over northwestern Louisiana, and then moved over southwestern Arkansas, northeastern Texas, and southeastern Oklahoma. On September 4th, it interacted with a mid- to upper-level trough and became extratropical.
Gustav caused widespread storm surge along the northern Gulf coast, with surges of 12-13 feet occurring along the Louisiana coast southeast of New Orleans. It is also responsible for heavy rains and widespread freshwater flooding. A storm total of 533.4 mm (21.0 in.) was measured at Larto Lake, Louisiana. Finally, Hurricane Gustav produced 41 tornadoes, including 21 tornadoes in Mississippi and 11 tornadoes in Louisiana. Total damage in the United States was estimated to equal $4.618 billion (Beven and Kimberlain, 2009).

Figure 4-30 shows the simulation nested domains used for the reconstruction of Hurricane Gustav.

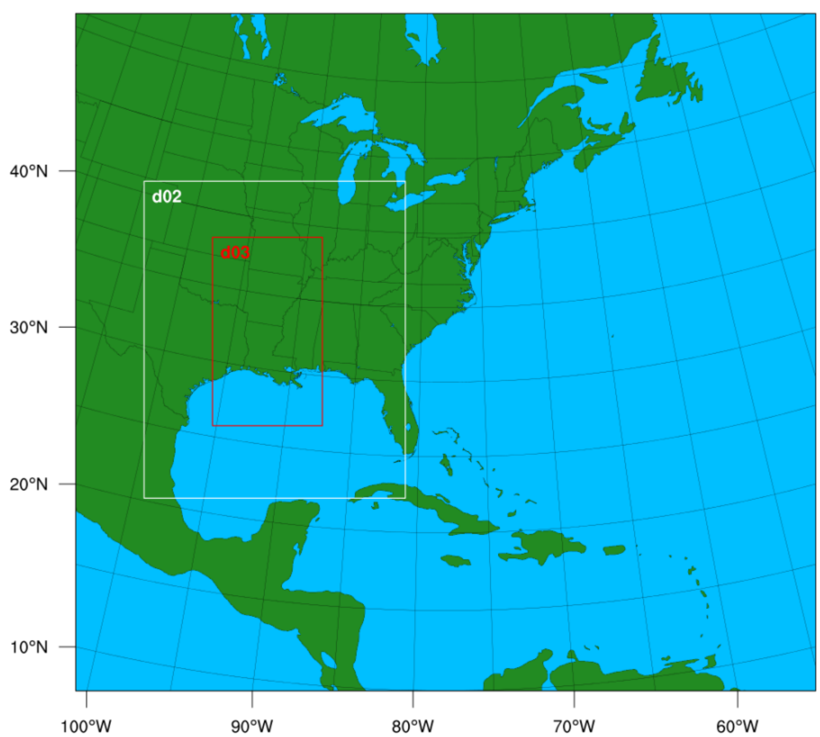

Figure 4-30 Simulation Nested Domains for Hurricane Gustav

The spatial resolutions from Domain 1 (outer domain) to Domain 3 (inner domain) are 45 km, 15 km, and 5 km. The number of grid points is 120 x 110 (zonal x meridional) for Domain 1, 127 x 154 for Domain 2, and 160 x 274 for Domain 3.

The results for Hurricane Gustav are overall very satisfactory. The overlap percentage is large for all precipitation thresholds while the PFAR remains close to 1. The model underestimated the size of the precipitation field for the less intense thresholds, which can be seen in Figure 4-32 as the green portion of the field is smaller for the simulated field than for the observed field. This explains the underestimation of the total precipitation amount (relative error = -16%).

Table 4-9 Hurricane Gustav WRF Simulation Performance Summary

Relative error		-16%
50th percentile threshold	% overlap	66%
	PFAR	0.76
75th percentile threshold	% overlap	59%
	PFAR	0.72
90th percentile threshold	% overlap	53%
	PFAR	0.90
95th percentile threshold	% overlap	53%
	PFAR	1.19
97.5th percentile threshold	% overlap	41%
	PFAR	1.41
99th percentile threshold	% overlap	32%
	PFAR	1.34

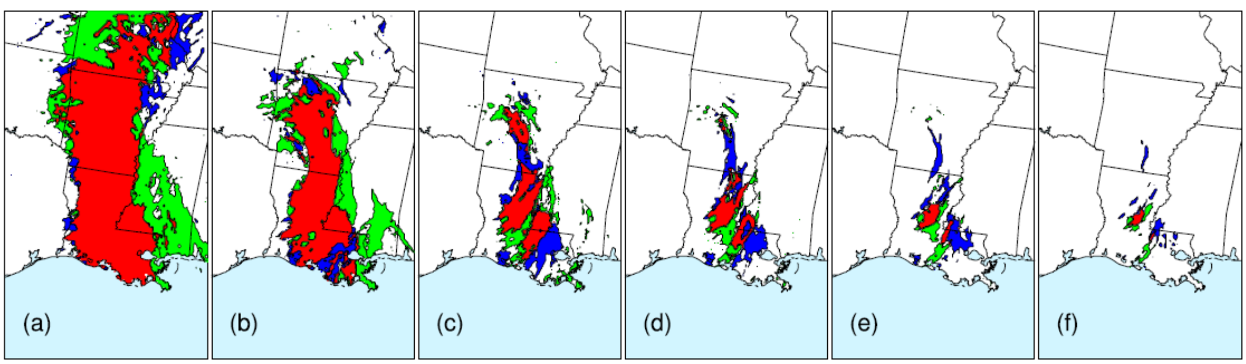

Figure 4-31 Overlapped Field Above the (a) 50th, (b) 75th, (c) 90th, (d) 95th, (e) 97.5th, and (f) 99th Percentile Values During Hurricane Gustav

Blue area: only simulation; green area: only observation; red area: both.

Figure 4-32c shows the IVT field and its divergence in Hurricane Gustav. As for the previous TCs, the match between precipitation depth (see Figure 4-32b) and magnitude of the moisture convergence is obvious. However, Figure 4-33 shows a relatively small coefficient of determination (R^2=0.72) for the IVT divergence as a function of the precipitation depth even if the slope of the regression line is close to -1. It is observed that several of the grid points above the 80th percentile of the ground surface elevation (blue crosses in Figure 4-33) lie far from the regression line which participate in decreasing the coefficient of determination. These grid points correspond to the mountainous regions in western and northern Arkansas, southern Missouri, eastern Oklahoma, and southeastern Kansas where large magnitudes of the IVT divergence are observed without significant precipitation (see Figure 4-32).

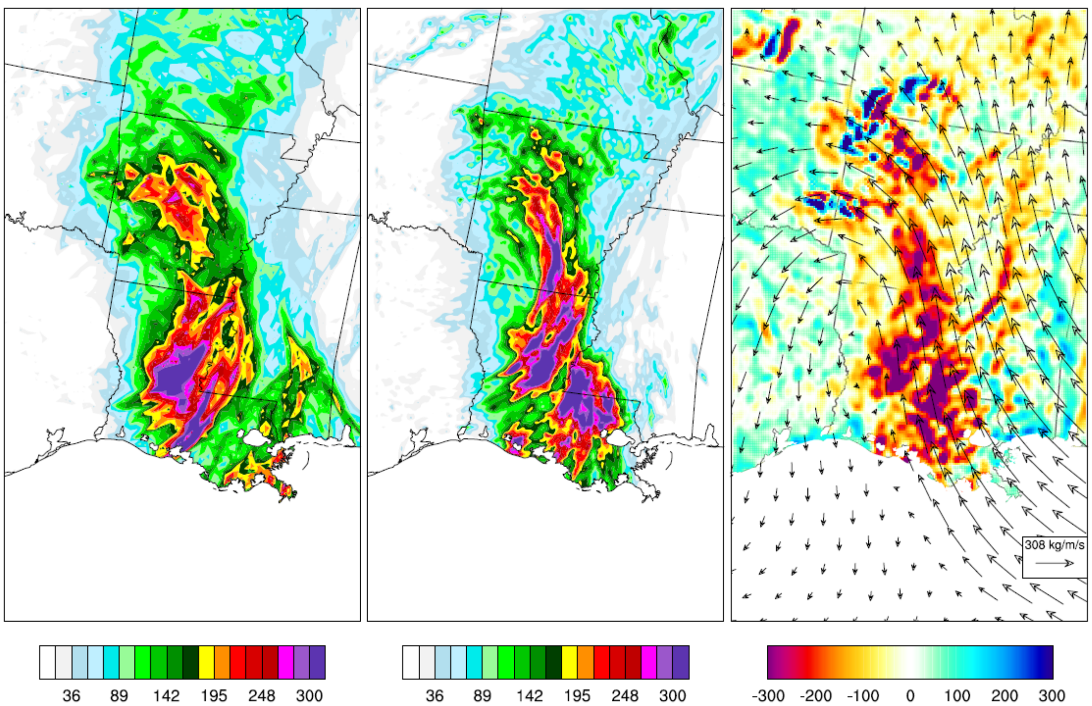

Figure 4-32 (a) Hurricane Gustav Inner-Domain Observed Accumulated Precipitation Field (from 08/29 18:00 UTC to 09/05 12:00 UTC)

(b) Inner-domain simulated accumulated precipitation field (from 08/29 18:00 UTC to 09/05 12:00 UTC). (c) Arrow field: time-averaged (from 08/29 18:00 UTC to 09/05 12:00 UTC) integrated vapor transport (kg m^{-1} s^{-1}). Color plot: divergence of the time-averaged integrated vapor transport field (mm).

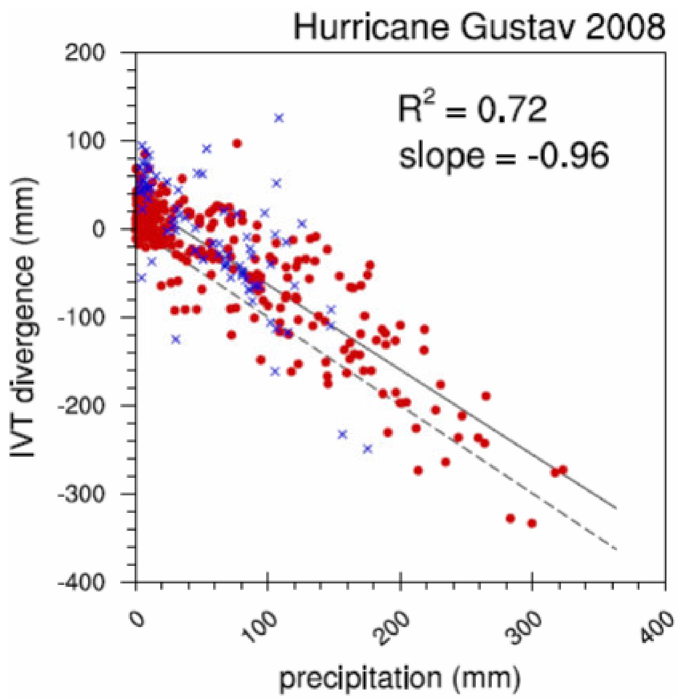

Figure 4-33 Divergence of the Time-Averaged Integrated Vapor Transport Field (mm) as a Function of the Precipitation Depth (mm) in Hurricane Gustav

Red dots correspond to the locations where the ground surface elevation is below the 80th percentile of the ground surface elevation in the simulation inner domain; whereas blue crosses correspond to the locations where the ground surface elevation is above this threshold. The solid line is the regression line. Its associated coefficient of determination (R^2) and slope are given on the figure. The dotted line has a slope of -1 and an intercept of 0.

The 6-hourly evolution of the reconstructed PW field and IVT field in Hurricane Gustav is given in Appendix B.2.8.

4.3.9 Hurricane Irene (2011)

Irene formed from a vigorous tropical wave that moved off the coast of Africa on August 15th (Avila and Cangialosi, 2011). It peaked as a Category 3 hurricane on the SSHS. However, it was a Category 1 hurricane when it made landfall in North Carolina on August 27th. It made another landfall in New Jersey on August 28th, and moved over Brooklyn, New York and Manhattan, New York City. It then continued north-northeastward over the northeastern United States.

Hurricane Irene produced a large swath of heavy rains along the East Coast from North Carolina northward (Avila and Cangialosi, 2011). The maximum observed precipitation depth was 398.8 mm (15.7 in.) in Bayboro, North Carolina. As Irene was a large hurricane, it produced high waves and storm surge over a large portion of the western Atlantic basin. It also spawned several tornadoes along its path over the eastern United States. Total damage estimate is $15.8 billion.

Figure 4-34 shows the simulation nested domains used for the reconstruction of Hurricane Irene.

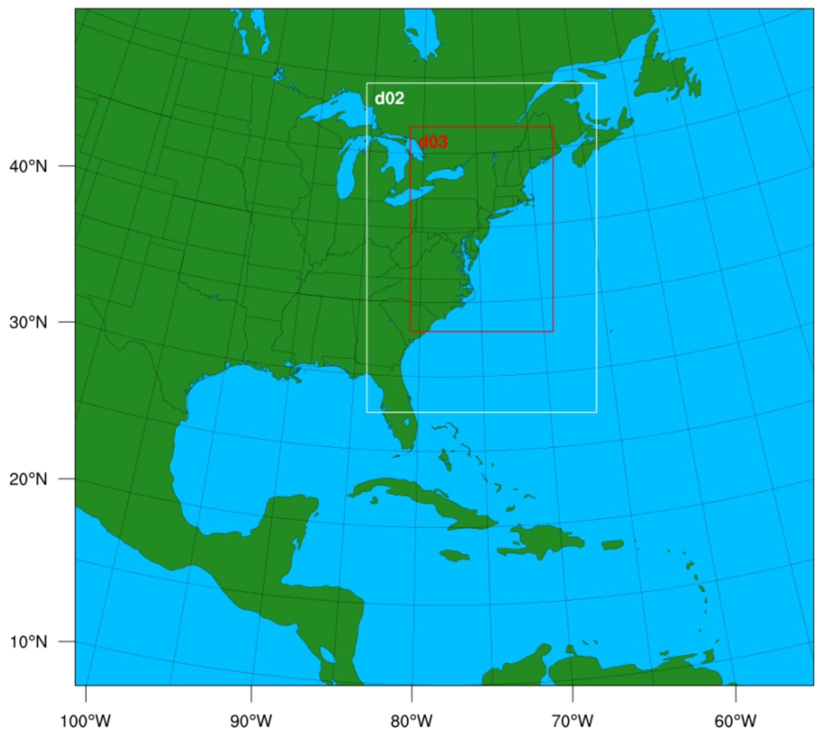

Figure 4-34 Simulation Nested Domains for Hurricane Irene

The spatial resolutions from Domain 1 (outer domain) to Domain 3 (inner domain) are 45 km, 15 km, and 5 km. The number of grid points is 120 x 110 (zonal x meridional) for Domain 1, 112 x 160 for Domain 2, and 208 x 298 for Domain 3.

According to Table 4-10, the WRF model gave very satisfactory results for the simulation of the precipitation field in Hurricane Irene. The overlap percentage is larger than 45% for all thresholds until the 97.5th percentile threshold. On the other hand, the PFAR is close to 1 for all thresholds. In particular it is exactly 1 for the 95th percentile. The model underestimated the total precipitation amount, but the relative error remains small in magnitude.

Table 4-10 Hurricane Irene WRF Simulation Performance Summary

Relative error		-9.6%
50th percentile threshold	% overlap	78%
	PFAR	0.87
75th percentile threshold	% overlap	67%
	PFAR	0.84
90th percentile threshold	% overlap	64%
	PFAR	0.90
95th percentile threshold	% overlap	60%
	PFAR	1.00
97.5th percentile threshold	% overlap	46%
	PFAR	1.08
99th percentile threshold	% overlap	19%
	PFAR	1.22

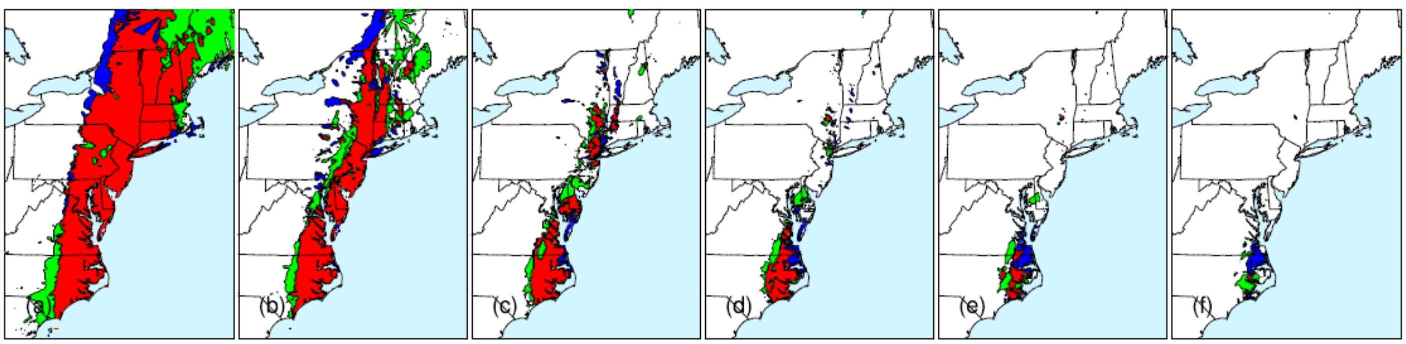

Figure 4-35 Overlapped Field Above the (a) 50th, (b) 75th, (c) 90th, (d) 95th, (e) 97.5th, and (f) 99th Percentile Values During Hurricane Irene

Blue area: only simulation; green area: only observation; red area: both.

Figure 4-36c presents the IVT field in Hurricane Irene and its divergence. As for the previous TCs, it appears clearly that moisture convergence played a predominant role in the generation of intense precipitation in this hurricane. Actually, the regression line in **Figure** 4-37 has a slope of -0.99. However the spread around the regression line is noticeable and the coefficient of determination is equal to 0.82. The grid points above the 80th percentile of the ground surface elevation (blue crosses) do not exhibit a behavior that is different from the other grid points (red dots). As for the other cases the regression line is above the bisector line showing that, in average over the duration of the simulation, precipitation tends to be larger than net moisture convergence in the atmospheric columns.

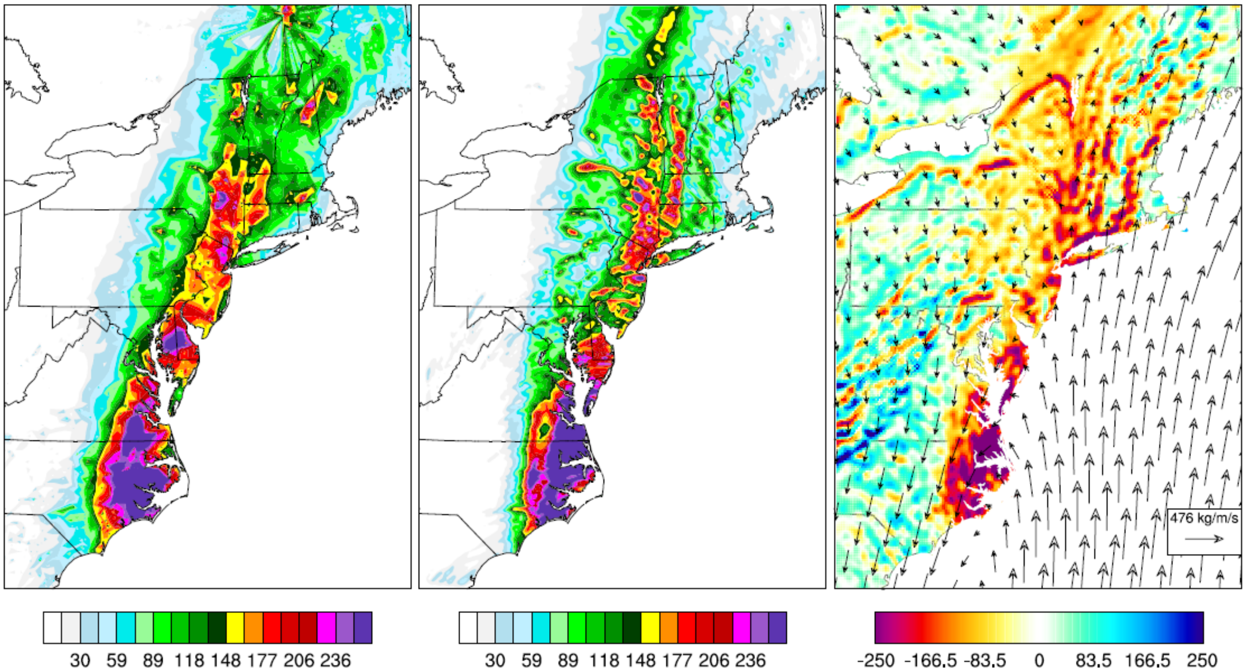

Figure 4-36 **(a) Hurricane Irene Inner-Domain Observed Accumulated Precipitation Field (from 08/26 00:00 UTC to 08/30 12:00 UTC)**

(b) Inner-domain simulated accumulated precipitation field (from 08/26 00:00 UTC to 08/30 12:00 UTC). (c) Arrow field: time-averaged (from 08/26 00:00 UTC to 08/30 12:00 UTC) integrated vapor transport (kg m^{-1} s^{-1}). Color plot: divergence of the time-averaged integrated vapor transport field (mm).

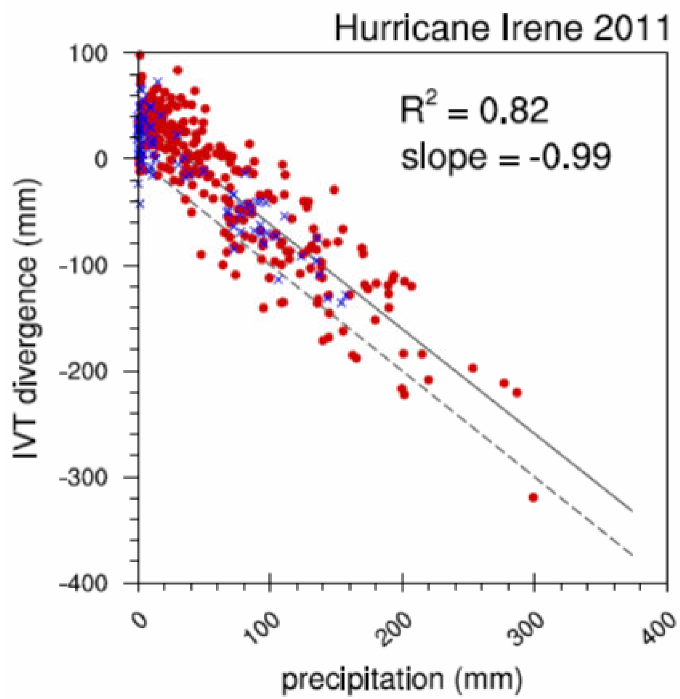

Figure 4-37 Divergence of the Time-Averaged Integrated Vapor Transport Field (mm) as a Function of the Precipitation Depth (mm) in Hurricane Irene

Red dots correspond to the locations where the ground surface elevation is below the 80th percentile of the ground surface elevation in the simulation inner domain; whereas blue crosses correspond to the locations where the ground surface elevation is above this threshold. The solid line is the regression line. Its associated coefficient of determination (R^2) and slope are given on the figure. The dotted line has a slope of -1 and an intercept of 0.

The 6-hourly evolution of the reconstructed PW field and IVT field in Hurricane Irene is given in Appendix B.2.9.

4.3.10 TS Lee (2011)

TS Lee originated from a tropical wave which moved off the west coast of Africa on August 18th. It made landfall along the cost of Louisiana early on September 4th. Afterwards it moved north-northeastward and became nearly stationary over south-central Louisiana later on September 4th (Brown, 2011). The next day it became extratropical as it interacted with a strong southward-moving cold front and became stronger. It then moved across southern Mississippi and southern Alabama, and dissipated over northwestern Georgia.

TS Lee produced elevated water levels along the northern Gulf Coast from Louisiana eastward into the Florida Panhandle. It also produced heavy rainfall over a large region from southeastern Louisiana eastward across southern Mississippi and southern Alabama, with a maximum of 393.7 mm (15.5 in.) at Holden, Louisiana. Besides, intense precipitation with about 178-254-mm rains fell along a large swath north of the cyclone's center path across south-central Mississippi, northern Alabama, northwestern Georgia, and eastern Tennessee. These are the regions that were focused on for the simulations. However, Brown (2011) explained that a second area was affected by extreme precipitation: ''as moisture from Lee and its remnants spread northeastward along a frontal boundary that became stationary across the Mid-Atlantic States and southern New York [it] produced a second area of extremely heavy rainfall from eastern Virginia northward across Maryland, eastern Pennsylvania, New Jersey, southern New York, and portions of southern New England from 5 through 10 September''. Major flooding occurred along Susquehanna River.

Figure 4-38 shows the simulation nested domains used for the reconstruction of TS Lee.

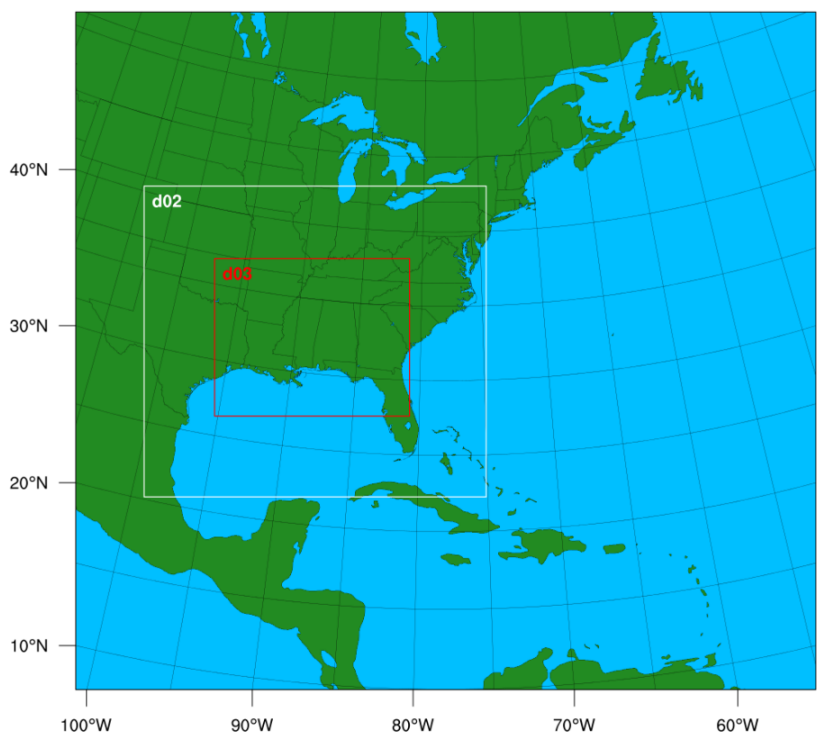

Figure 4-38 Simulation Nested Domains for TS Lee

The spatial resolutions from Domain 1 (outer domain) to Domain 3 (inner domain) are 45 km, 15 km, and 5 km. The number of grid points is 120 x 110

(zonal x meridional) for Domain 1, 166 x 151 for Domain 2, and 283 x 229 for Domain 3.

The WRF model provided overall satisfactory results for the simulation of TS Lee. Table 4-11 shows that the total precipitation amount was significantly underestimated since the relative error is equal to -26%. Looking at the other metrics, it is understood that this is due to the underestimation of the size of the precipitation field above the 50th percentile and 75th percentile thresholds (PFAR = 0.63 and PFAR = 0.65), or in other words to the underestimation of the least intense precipitation. Indeed, it is observed in Figure 4-40 that the sizes of the blue and green regions are smaller in the simulated precipitation field (Figure 4-40a) than in the observed precipitation field (Figure 4-40a). Besides the model overestimated the size of the precipitation field above the 99th percentile threshold (PFAR = 2.33) mainly due to too intense precipitation around the location of landfall (see the purple region in Figure 4-40f). However the model satisfactorily reproduced the size of the precipitation field above the other thresholds, and the overlap percentage is large for all the thresholds.

Table 4-11 TS Lee WRF Simulation Performance Summary

Relative error		-26%
50th percentile threshold	% overlap	61%
	PFAR	0.63
75th percentile threshold	% overlap	53%
	PFAR	0.65
90th percentile threshold	% overlap	56%
	PFAR	0.93
95th percentile threshold	% overlap	46%
	PFAR	0.95
97.5th percentile threshold	% overlap	43%
	PFAR	1.25
99th percentile threshold	% overlap	46%
	PFAR	2.33

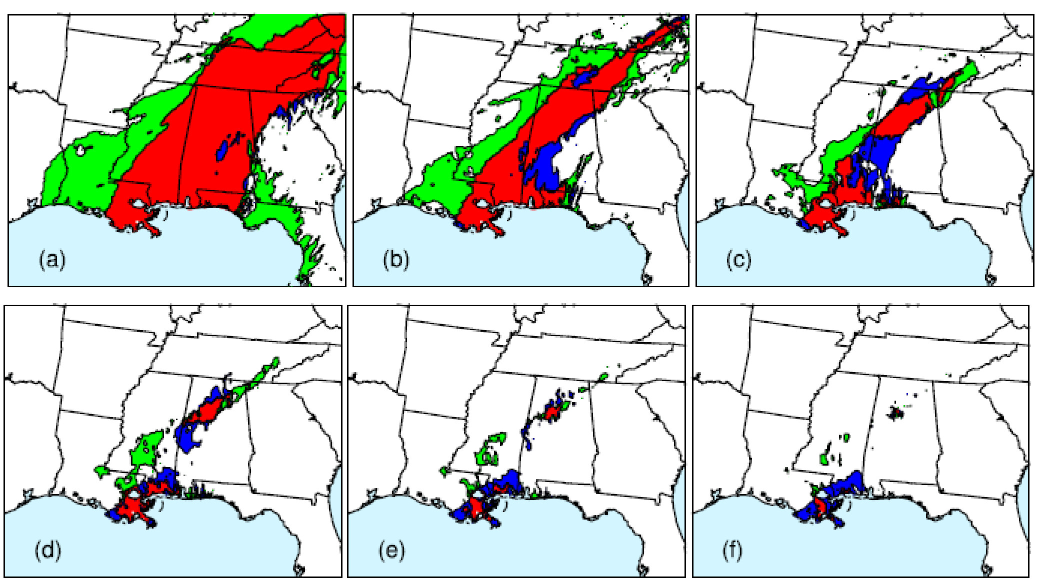

Figure 4-39 Overlapped Field Above the (a) 50th, (b) 75th, (c) 90th, (d) 95th, (e) 97.5th, and (f) 99th Percentile Values During TS Lee

Blue area: only simulation; green area: only observation; red area: both.

Figure 4-40c shows the IVT field and its divergence. It clearly appears that the swathe of intense precipitation in Figure 4-40b coincide with the swathe of intense moisture convergence in Figure 4-40c. Figure 4-41 shows the graph of the IVT divergence as a function of the precipitation depth. It is seen that the coefficient of determination is relatively large (R^2 = 0.84). The slope of the regression line, equal to -0.89, is close to -1, but less so than in most of the cases presented previously.

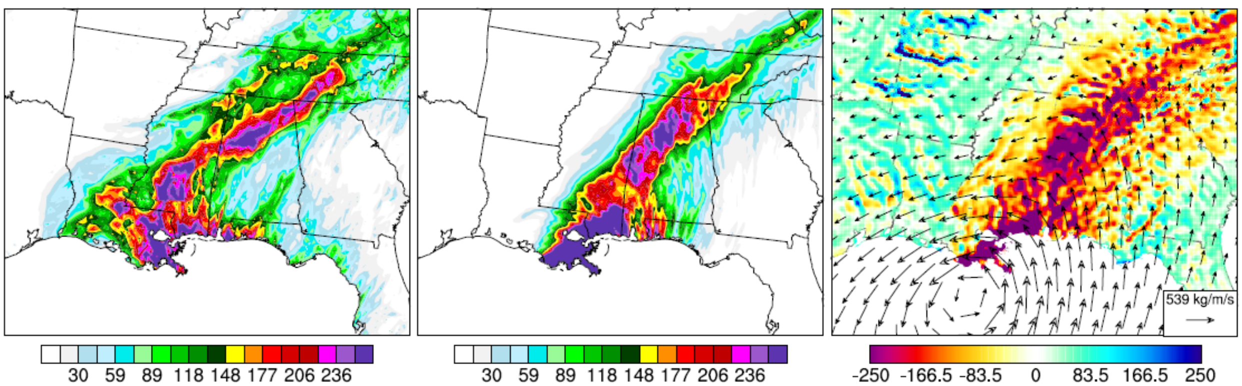

Figure 4-40 (a) TS Lee Inner-Domain Observed Accumulated Precipitation Field (from 09/01 00:00 UTC to 09/07 00:00 UTC)

(b) Inner-domain simulated accumulated precipitation field (from 09/01 00:00 UTC to 09/07 00:00 UTC). (c) Arrow field: time-averaged (from 09/01 00:00 UTC to 09/07 00:00 UTC) integrated vapor transport (kg m^{-1} s^{-1}). Color plot: divergence of the time-averaged integrated vapor transport field (mm).

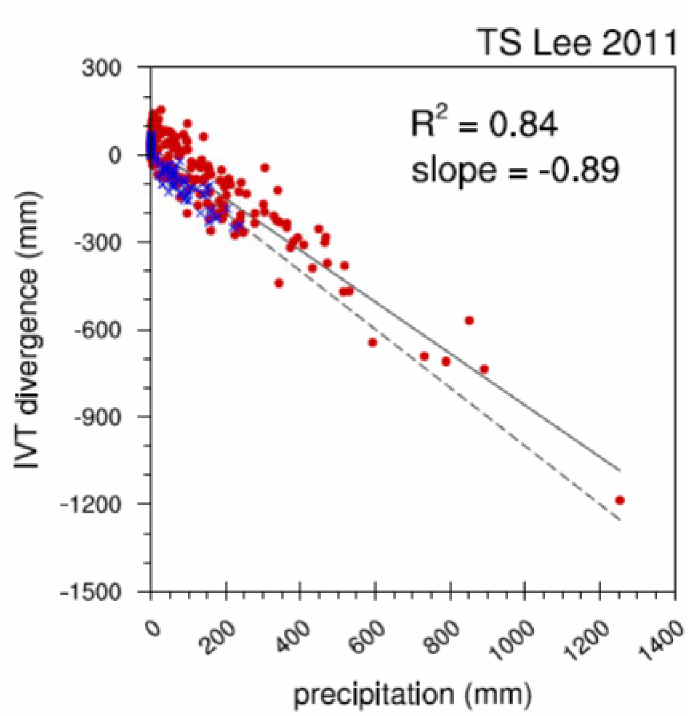

Figure 4-41 Divergence of the Time-Averaged Integrated Vapor Transport Field (mm) as a Function of the Precipitation Depth (mm) in TS Lee

Red dots correspond to the locations where the ground surface elevation is below the 80th percentile of the ground surface elevation in the simulation inner domain; whereas blue crosses correspond to the locations where the ground surface elevation is above this threshold. The solid line is the regression line. Its associated coefficient of determination (R^2) and slope are given on the figure. The dotted line has a slope of -1 and an intercept of 0.

The 6-hourly evolution of the reconstructed PW field and IVT field in TS Lee is given in Appendix B.2.10.

4.3.11 Hurricane Isaac (2012)

Isaac formed from a tropical wave which moved off the West African coast on August 16th. It spent most of its life as a TS, and became a category 1 hurricane only a few hours before making landfall in southeastern Louisiana on August 29th (Berg, 2013). As it moved inland, Isaac weakened to a TC and further to a tropical depression on August 31st after crossing into southern Arkansas. The cyclone then moved into Missouri where it dissipated. However, its remnants moved northeastward and eastward across Missouri and Illinois spawning several tornadoes across the Mississippi Valley (Berg, 2013).

Hurricane Isaac created an extensive storm surge along the northern Gulf of Mexico, especially in Louisiana, Mississippi and Alabama, with a measured maximum of 11.03 feet above normal tide levels at Shell Beach, Louisiana. This storm surge in turn caused significant inundations. Isaac was also responsible for generating intense precipitation and associated flooding. Before reaching Louisiana, on its path, it first produced around a hundred or more millimeters of rainfall in Florida, causing severe flooding over parts of South Florida and East-Central Florida. Furthermore, "most of extreme southwestern Alabama, southern Mississippi and southeastern Louisiana received greater than 254 mm (10.0 in.) of rain, which produced both flash flooding and river flooding. The highest totals measured in each state were 355.6 mm (14.0 in.) in Grand Bay, Alabama, 563.9 mm (22.2 in.) in Pascagoula, Mississippi, and 525.8 mm (20.7 in.) in New Orleans, Louisiana. The heavy rains caused moderate to record flooding on several rivers in southern Mississippi and southeastern Louisiana" (Berg, 2013). The total United States damage estimate due to this storm is about $2.35 billion.

Figure 4-42 shows the simulation nested domains used for the reconstruction of Hurricane Isaac. Hurricane Isaac was difficult to reconstruct. After investigating the parameterization schemes, the number of model vertical levels and the time step were also tuned to further improve the results. 53 vertical levels and a time step of 1 min were used in this case.

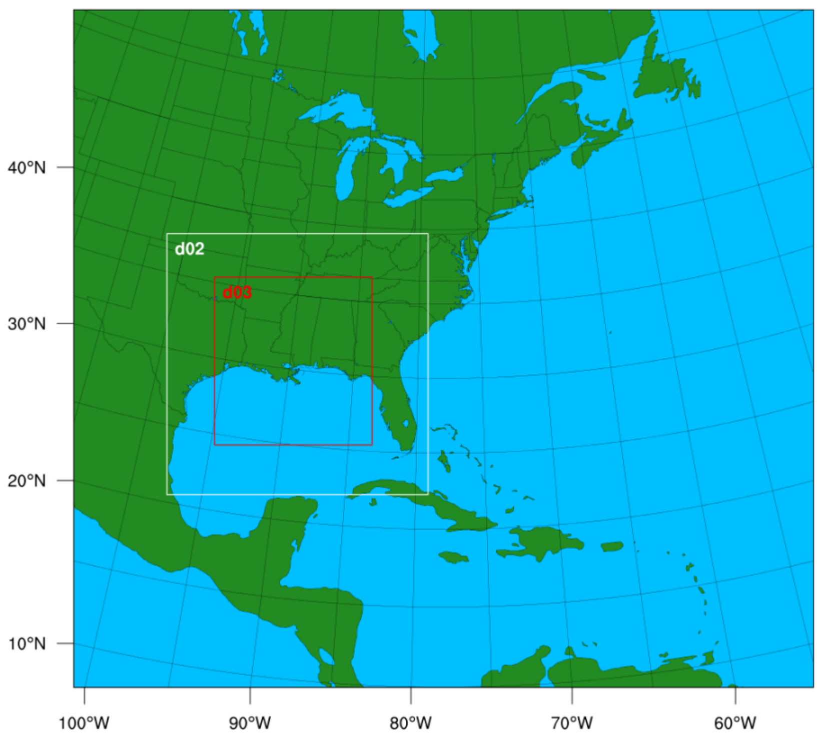

Figure 4-42 Simulation Nested Domains for Hurricane Isaac

The spatial resolutions from Domain 1 (outer domain) to Domain 3 (inner domain) are 45 km, 15 km, and 5 km. The number of grid points is 120 x 110 (zonal x meridional) for Domain 1, 127 x 127 for Domain 2, and 229 x 244 for Domain 3.

Compared to other TCs, the size of the precipitation field produced by Hurricane Isaac is relatively small, and there is a sharp transition from small to large precipitation depths (Figure 4-44). The results are overall satisfactory for this TC. The model slightly underestimated the total precipitation amount (relative error = -13%). However it managed to place the precipitation field in the observed location, despite its small size, and the fact that the PFAR is less than 1 for all thresholds except the 99th percentile threshold.

Table 4-12 Hurricane Isaac WRF Simulation Performance Summary

Relative error		-13%
50th percentile threshold	% overlap	56%
	PFAR	0.87
75th percentile threshold	% overlap	49%
	PFAR	0.94
90th percentile threshold	% overlap	53%
	PFAR	0.84
95th percentile	% overlap	56%
	PFAR	0.72
97.5th percentile threshold	% overlap	40%
	PFAR	0.79
99th percentile threshold	% overlap	26%
	PFAR	1.27

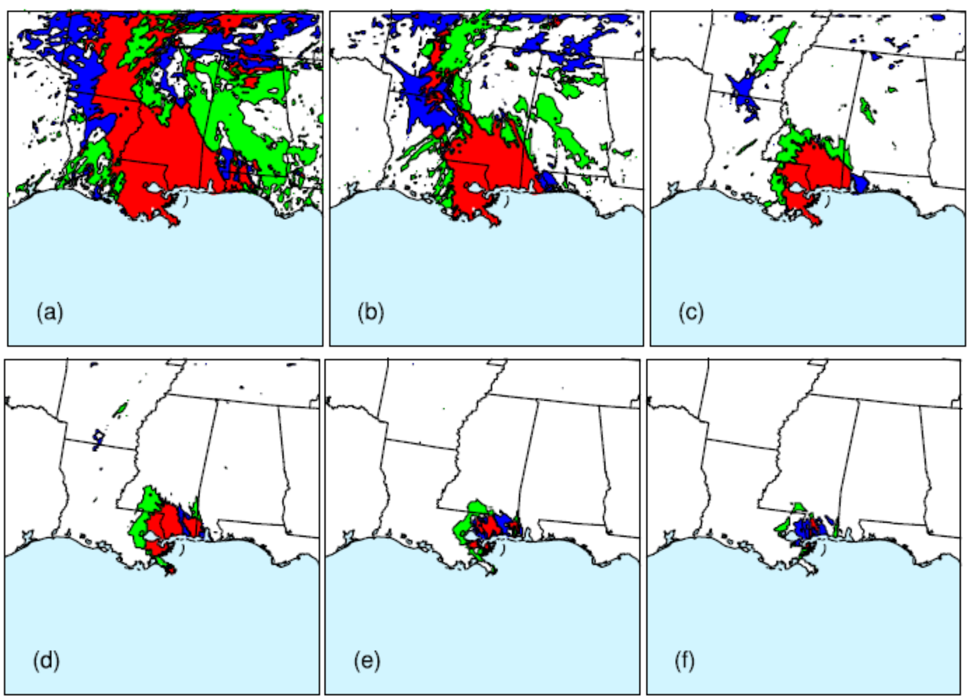

Figure 4-43 Overlapped Field Above the (a) 50th, (b) 75th, (c) 90th, (d) 95th, (e) 97.5th, and (f) 99th Percentile Values During Hurricane Isaac

Blue area: only simulation; green area: only observation; red area: both.

Figure 4-44c shows the IVT field and its divergence in Hurricane Isaac. It appears that the regions of intense precipitation in Figure 4-44b correspond to regions of large IVT convergence in Figure 4-44c. However there are regions of large IVT convergence but small precipitation depth, such as in eastern Tennessee, which is a mountainous region. This is why many of the blue crosses in Figure 4-45 (representing grid points above the 80th percentile of the ground surface elevation) are below the regression line, and even below the bisector line, increasing the spread of the cloud of points around the regression line. Yet the coefficient of determination remains relatively large (**R^2 = 0.81**) while the slope of the regression line is very close to -1.

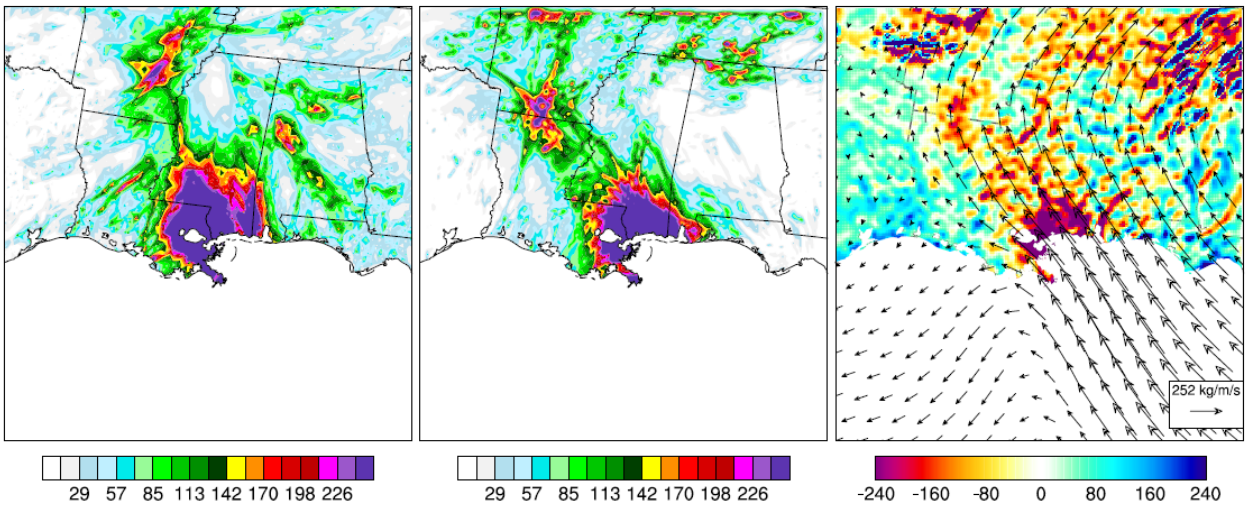

Figure 4-44 (a) Hurricane Isaac Inner-Domain Observed Accumulated Precipitation Field (from 08/25 00:00 UTC to 09/04 12:00 UTC)

(b) Inner-domain simulated accumulated precipitation field (from 08/25 00:00 UTC to 09/04 12:00 UTC). (c) Arrow field: time-averaged (from 08/25 00:00 UTC to 09/04 12:00 UTC) integrated vapor transport (kg m^{-1} s^{-1}). Color plot: divergence of the time-averaged integrated vapor transport field (mm).

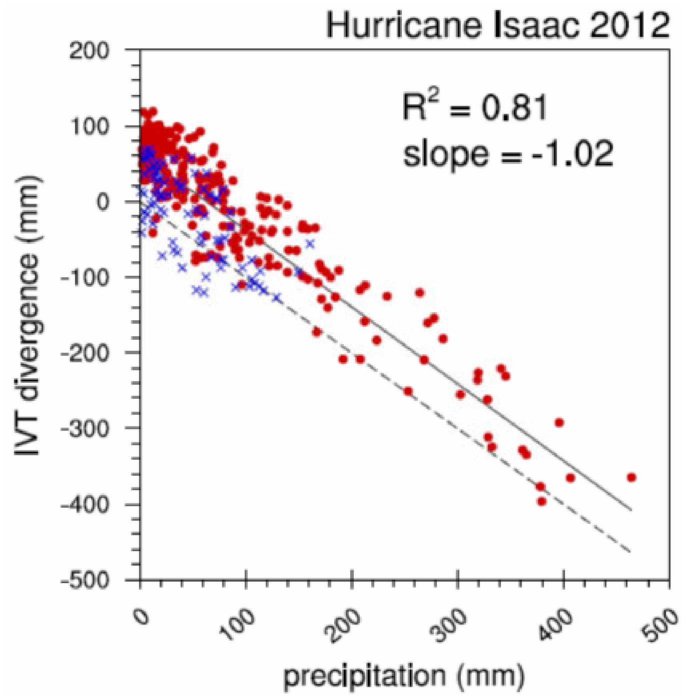

Figure 4-45 Divergence of the Time-Averaged Integrated Vapor Transport Field (mm) as a Function of the Precipitation Depth (mm) in Hurricane Isaac

Red dots correspond to the locations where the ground surface elevation is below the 80th percentile of the ground surface elevation in the simulation inner domain; whereas blue crosses correspond to the locations where the ground surface elevation is above this threshold. The solid line is the regression line. Its associated coefficient of determination (R^2) and slope are given on the figure. The dotted line has a slope of -1 and an intercept of 0.

The 6-hourly evolution of the reconstructed PW field and IVT field in Hurricane Isaac is given in Appendix B.2.11.

4.3.12 Hurricane Sandy (2012)

According to Blake et al. (2013), "Sandy was a classic late-season hurricane in the southwestern Caribbean Sea". Its origin was primarily associated with a tropical wave which moved off the west coast of Africa on October 11th. Sandy was a Category 3 hurricane on the SSHS at its peak intensity when it made landfall in Cuba. It made landfall near Brigantine in New Jersey on October 29th as an ETC. Because of its very large size, it caused water levels to rise along the entire East Coast. In particular, it caused catastrophic storm surge into the New Jersey and New York coastlines. The storm produced widespread heavy snow in the Appalachian Mountains from western North Carolina northeastward through southwestern Pennsylvania, which is exceptionally rare for a TS or one which just lost tropical characteristics (Blake et al., 2013). It also produced heavy rains in eastern Maryland and Virginia, southern Delaware, and southern New Jersey, with a peak amount of 325.1 mm (12.8 in.) in Bellevue, Maryland. Flooding from this intense precipitation in the Mid-Atlantic region only caused minor damage. However, "rainfall did contribute, along with storm surge, to the flooding in New York and New Jersey, adjacent to the Hudson River" (Blake et al., 2013). Sandy was responsible for at least 147 direct deaths across the Atlantic basin, 72 of which occurred in the mid-Atlantic and northeastern United States. At least 3,650,000 houses were either damaged or destroyed, mainly because of storm surge and/or waves. Total damage from the storm was estimated to equal $50 billion, making Hurricane Sandy the second-costliest cyclone to hit the United States since 1900 (Blake et al., 2013).

Figure 4-46 shows the simulation nested domains used for the reconstruction of Hurricane Sandy.

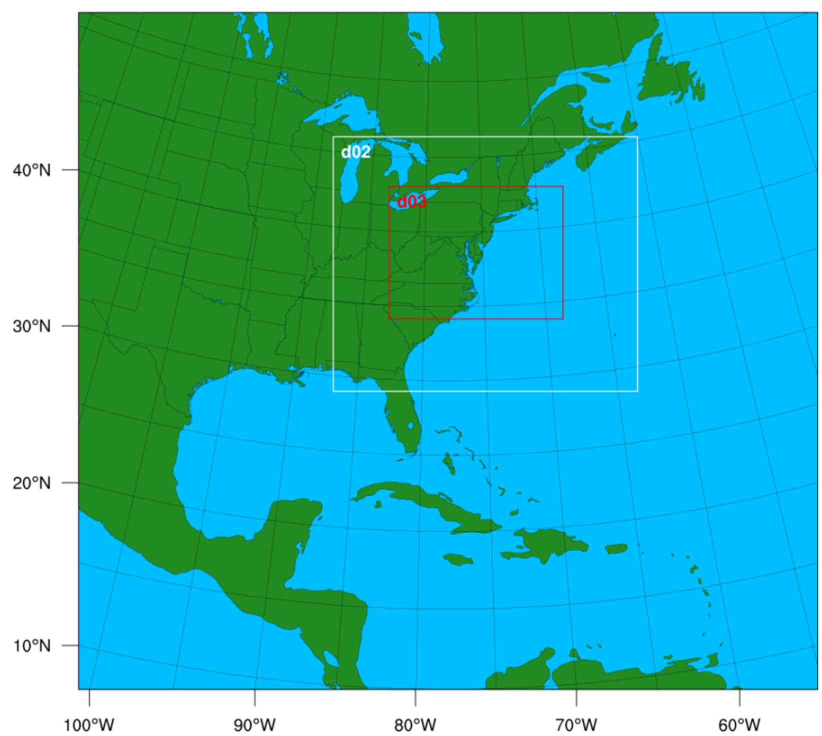

Figure 4-46 Simulation Nested Domains for Hurricane Sandy

The spatial resolutions from Domain 1 (outer domain) to Domain 3 (inner domain) are 45 km, 15 km, and 5 km. The number of grid points is 120 x 110 (zonal x meridional) for Domain 1, 148 x 124 for Domain 2, and 253 x 193 for Domain 3.

In the case of Hurricane Sandy, the model slightly overestimated the total precipitation amount (relative error = 12%). The overlap percentage is very good for the 50th, 75th, and 90th percentile, but then decreases significantly starting at the 95th percentile. However, the PFAR is less than 1 for the 95th and 97.5th percentiles, which shows the overlap is entirely due to a good placement of the storm for these thresholds, and not to an overestimation of the field's size.

Table 4-13 Hurricane Sandy WRF Simulation Performance Summary

Relative error		+12%
50th percentile threshold	% overlap	92%
	PFAR	1.16
75th percentile threshold	% overlap	69%
	PFAR	1.20
90th percentile threshold	% overlap	68%
	PFAR	1.17
95th percentile threshold	% overlap	23%
	PFAR	0.78
97.5th percentile threshold	% overlap	7.6%
	PFAR	0.89
99th percentile threshold	% overlap	1.1%
	PFAR	1.36

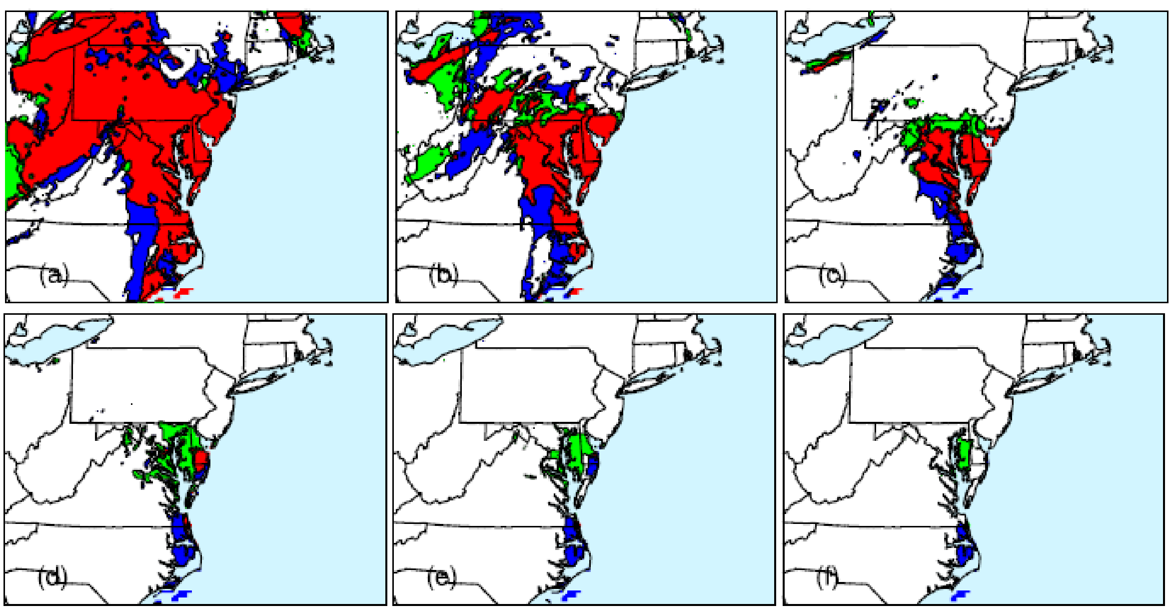

Figure 4-47 Overlapped Field Above the (a) 50th, (b) 75th, (c) 90th, (d) 95th, (e) 97.5th, and (f) 99th Percentile Values During Hurricane Sandy

Blue area: only simulation; green area: only observation; red area: both.

Figure 4-48c presents the IVT field and its divergence in Hurricane Sandy. It appears that the regions of intense precipitation (see Figure 4-48b) correspond to the regions of intense IVT convergence. However the relationship between these two quantities seems to be weaker than in the previous cases. Indeed there are regions of intense precipitation for which the IVT convergence was only moderate. This is for example the case in eastern Virginia and southern New Jersey. These results are in agreement with the graph of the IVT divergence as a function of the precipitation depth presented in Figure 4-49 since the coefficient of determination is relatively small ($R^2 = 0.77$) and the slope of the regression line is also relatively small (in absolute value) compared to the previous cases. This shows that, in the case of Hurricane Sandy, the time-averaged IVT convergence is a good qualitative indicator to explain the presence of precipitation but is not sufficient to adequately account for precipitation depth quantitatively.

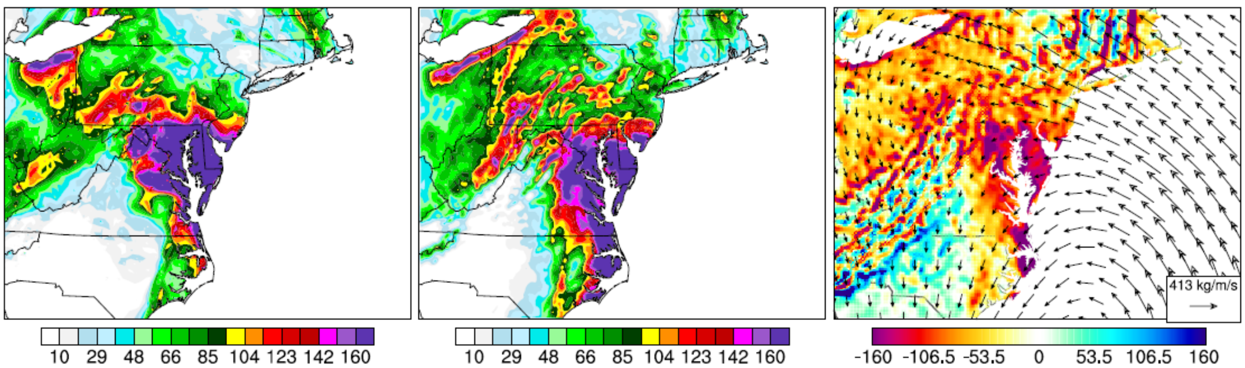

Figure 4-48 (a) Hurricane Sandy Inner-Domain Observed Accumulated Precipitation Field (from 10/27 00:00 UTC to 10/31 12:00 UTC)

(b) Inner-domain simulated accumulated precipitation field (from 10/27 00:00 UTC to 10/31 12:00 UTC). (c) Arrow field: time-averaged (from 10/27 00:00 UTC to 10/31 12:00 UTC) integrated vapor transport (kg m^{-1} s^{-1}). Color plot: divergence of the time-averaged integrated vapor transport field (mm).

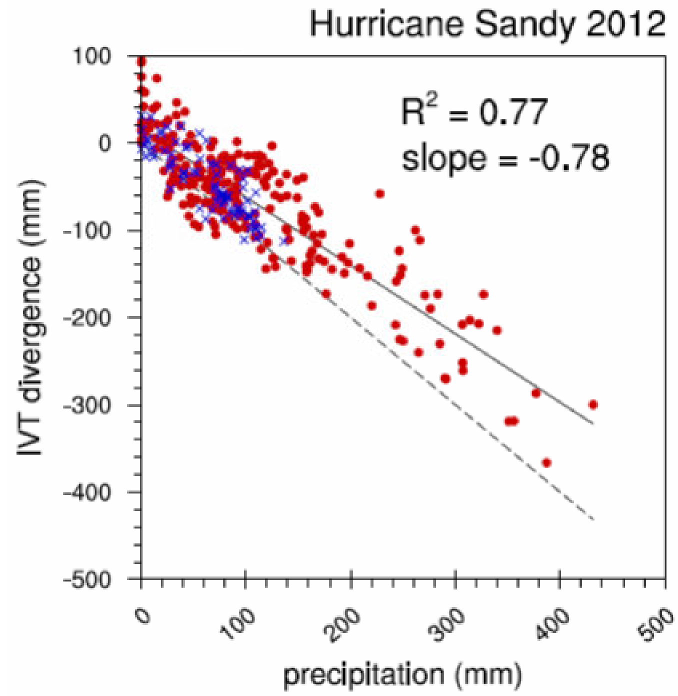

Figure 4-49 Divergence of the Time-Averaged Integrated Vapor Transport Field (mm) as a Function of the Precipitation Depth (mm) in Hurricane Sandy

Red dots correspond to the locations where the ground surface elevation is below the 80th percentile of the ground surface elevation in the simulation inner domain; whereas blue crosses correspond to the locations where the ground surface elevation is above this threshold. The solid line is the regression line. Its associated coefficient of determination (R^2) and slope are given on the figure. The dotted line has a slope of -1 and an intercept of 0.

The 6-hourly evolution of the reconstructed PW field and IVT field in Hurricane Sandy is given in Appendix B.2.12.

4.3.13 Hurricane Matthew (2016)

Hurricane Matthew peaked as a category 5 hurricane, and was the first hurricane to reach this intensity since 2007. It originated from a tropical wave which emerged from the west coast of Africa on September 22nd. In the United States, it made landfall as a category 1 hurricane in South Carolina on October 8th, and re-emerged shortly afterward into the Atlantic where it completed its transition into an ETC. Hurricane Matthew caused significant storm surge and associated flooding in Florida, Georgia, South Carolina, and North Carolina. In Florida, a peak surge of 9.88 feet was measured at Fernandina Beach. Heavy precipitation from Matthew produced widespread record river flooding and flash flooding to eastern North Carolina where hourly rainfall estimates were as large as 177.8 mm (7.0 in.) per hour. Florida, Georgia, South Carolina and Virginia were also strongly impacted by heavy rains, with 444.5 mm (17.5 in.) measured at Savannah, Georgia, 355.6 mm (14.0 in.) at Beaufort, South Carolina, 309.9 mm (12.2 in.) at Virginia Beach, Virginia, and 228.6 mm (9.0 in.) at Orlando, Florida. Hurricane Matthew was responsible for over 1,600 deaths including 49 in the United States. Total damage is estimated at $15 billion, making Hurricane Matthew the costliest hurricane since Hurricane Sandy (2012) and the 9th costliest hurricane in U.S. history. References for this paragraph are: https://en.wikipedia.org/wiki/Hurricane_Matthew and https://weather.com/storms/hurricane/news/hurricane-matthew-bahamas-florida-georgia-carolinas-forecast.

Figure 4-50 shows the simulation nested domains used for the reconstruction of Hurricane Matthew.

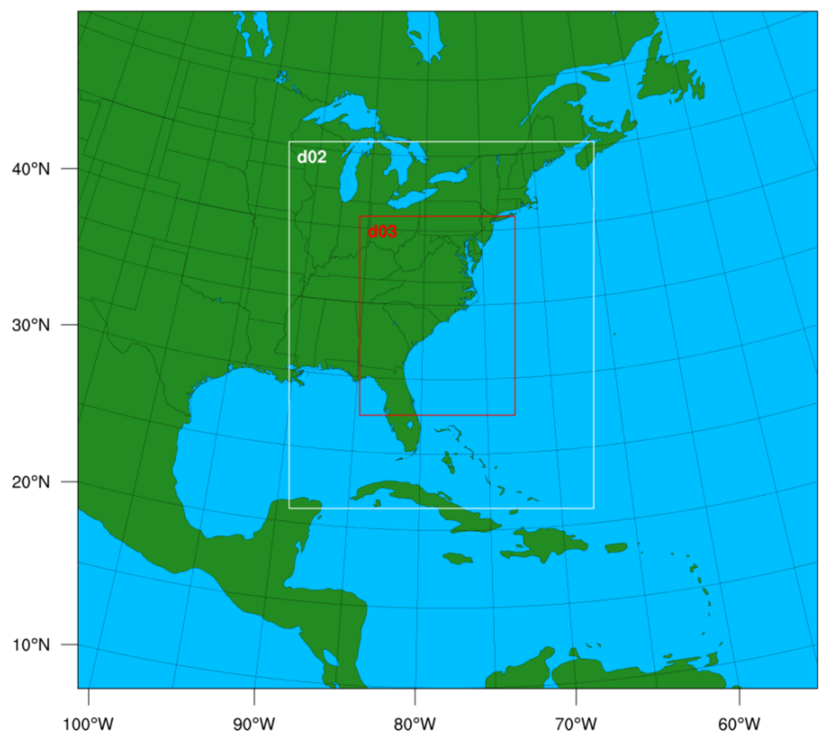

Figure 4-50 Simulation Nested Domains for Hurricane Matthew

The spatial resolutions from Domain 1 (outer domain) to Domain 3 (inner domain) are 45 km, 15 km, and 5 km. The number of grid points is 120 x 110 (zonal x meridional) for Domain 1, 148 x 178 for Domain 2, and 226 x 289 for Domain 3.

The WRF model provided excellent results for the simulation of the precipitation field in Hurricane Matthew. The magnitude of the relative error is small (relative error = -6.4% indicating a slight underestimation of the total precipitation amount). The overlap percentage is good for all thresholds even if the PFAR is less than 1 for 3 thresholds, which shows that the precipitation field was placed in the observed location including the most intense part of the field.

Table 4-14 Hurricane Matthew WRF Simulation Performance Summary

Relative error		-6.4%
50^{th} percentile threshold	% overlap	77%
	PFAR	0.83
75^{th} percentile threshold	% overlap	77%
	PFAR	0.89
90^{th} percentile threshold	% overlap	64%
	PFAR	1.11
95^{th} percentile threshold	% overlap	46%
	PFAR	1.07
97.5^{th} percentile threshold	% overlap	40%
	PFAR	1.06
99^{th} percentile threshold	% overlap	20%
	PFAR	0.79

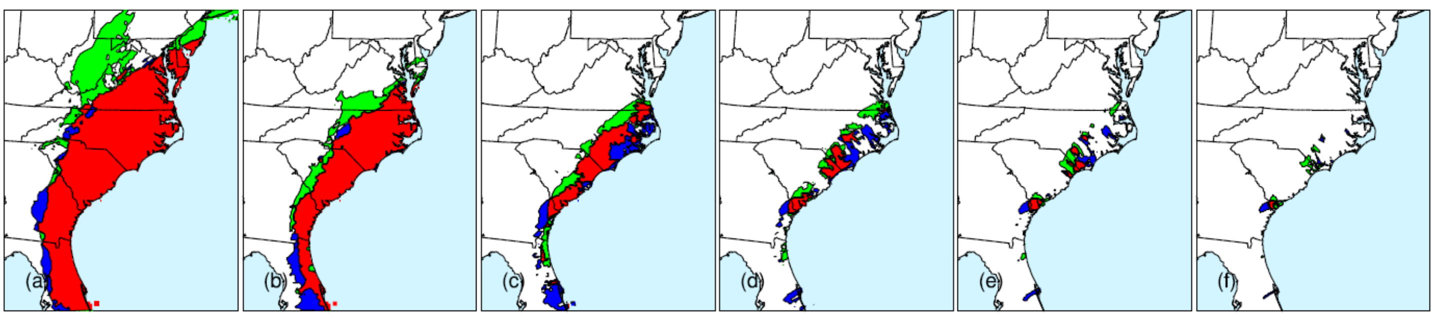

Figure 4-51 Overlapped Field Above the (a) 50^{th}, (b) 75^{th}, (c) 90^{th}, (d) 95^{th}, (e) 97.5^{th}, and (f) 99^{th} Percentile Values During Hurricane Matthew

Blue area: only simulation; green area: only observation; red area: both.

Figure 4-52c presents the IVT field in Hurricane Matthew and its divergence. It is clear that the regions of intense precipitation (see Figure 4-52b) closely coincide with the regions of large IVT convergence. Figure 4-53 confirms that the IVT convergence is an excellent quantitative indicator to explain intense precipitation. Indeed, the coefficient of determination is good (**R^2 = 0.88**). The slope of the regression line is close to -1 but less so than in several of the cases treated previously. However the red dots representing the grid points with the largest precipitation depths are located below the regression line which shows that, in Hurricane Matthew, the most intense precipitation were likely to be entirely triggered by moisture convergence.

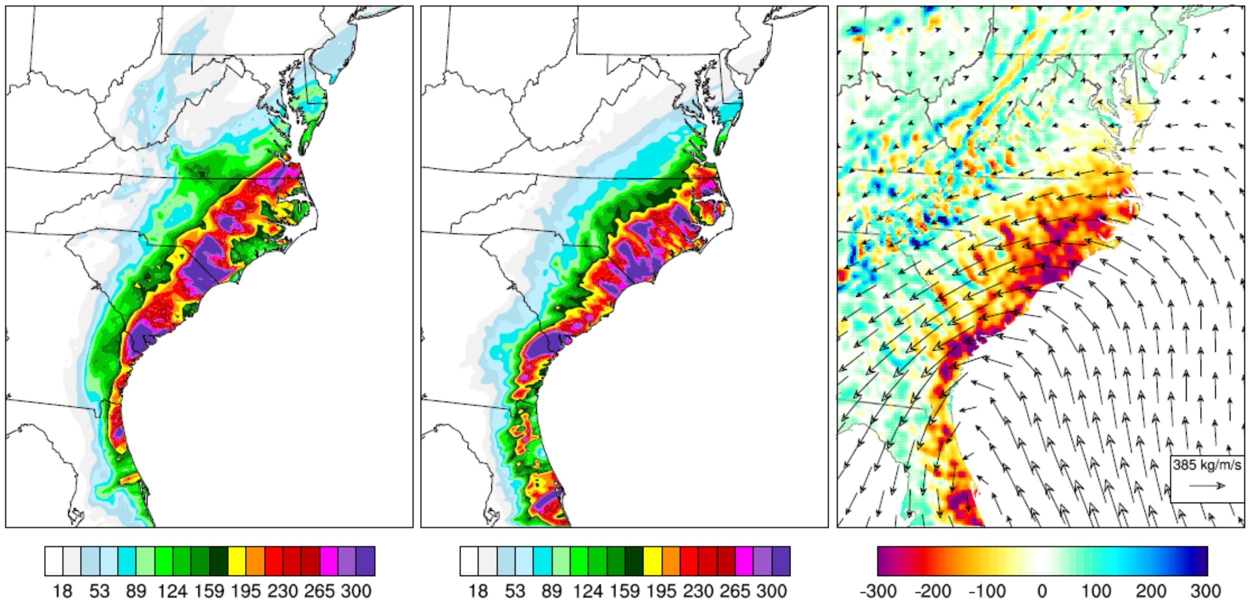

Figure 4-52 (a) Hurricane Matthew Inner-Domain Observed Accumulated Precipitation Field (from 10/05 00:00 UTC to 10/10 00:00 UTC)

(b) Inner-domain simulated accumulated precipitation field (from 10/05 00:00 UTC to 10/10 00:00 UTC). (c) Arrow field: time-averaged (from 10/05 00:00 UTC to 10/10 00:00 UTC) integrated vapor transport (kg m^{-1} s^{-1}). Color plot: divergence of the time-averaged integrated vapor transport field (mm).

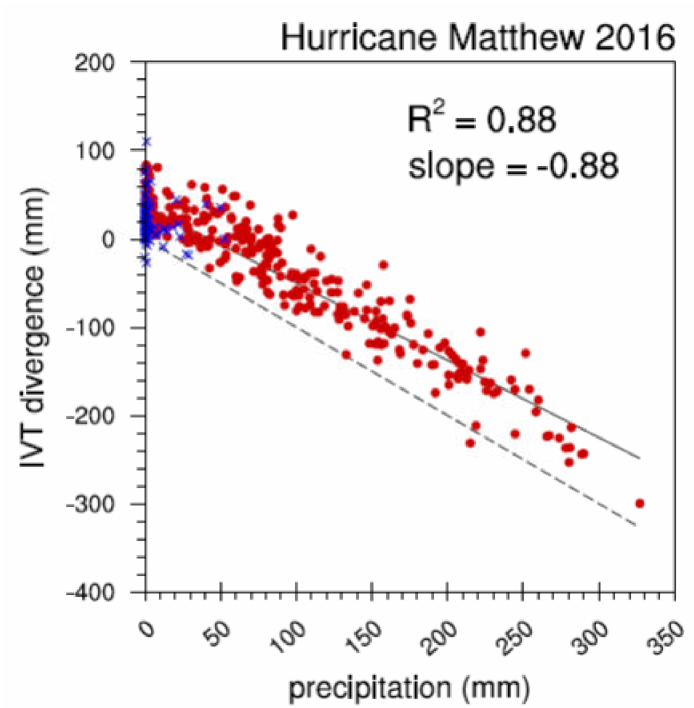

Figure 4-53 Divergence of the Time-Averaged Integrated Vapor Transport Field (mm) as a Function of the Precipitation Depth (mm) in Hurricane Matthew

Red dots correspond to the locations where the ground surface elevation is below the 80th percentile of the ground surface elevation in the simulation inner domain; whereas blue crosses correspond to the locations where the ground surface elevation is above this threshold. The solid line is the regression line. Its associated coefficient of determination (R^2) and slope are given on the figure. The dotted line has a slope of -1 and an intercept of 0.

The 6-hourly evolution of the reconstructed PW field and IVT field in Hurricane Matthew is given in Appendix B.2.13.

4.3.14 Summary of the WRF Model Performance

In this subsection, the performance of the WRF model in terms of the relative error on the one hand (Table 4-15), and in terms of the overlap percentage and PFAR on the other hand (Table 4-16) are summarized.

Table 4-15 Summary of the WRF Model Performance in Terms of the Relative Error for the Simulation of the Historical TCs

TC name	Relative error
Hurricane Isidore	+3.0%
Hurricane Frances	+12%
Hurricane Ivan	+6.3%
Hurricane Jeanne	+14.7%
Hurricane Ernesto	+15%
TS Fay	-11%
Hurricane Gustav	-16%
Hurricane Irene	-9.6%
TS Lee	-26%
Hurricane Isaac	-13%
Hurricane Sandy	+12%
Hurricane Matthew	-6.4%

Table 4-16 Summary of the WRF Model Performance in Terms of the Overlap Percentage and PFAR for the Simulation of the Historical TCs

TC name	Metric	50th Percentile Threshold	75th Percentile Threshold	90th Percentile Threshold	95th Percentile Threshold	97.5th Percentile Threshold	99th Percentile Threshold
Hurricane Isidore	% overlap	73%	70%	54%	41%	34%	20%
	PFAR	0.92	1.00	1.11	1.28	1.38	1.85
Hurricane Frances	% overlap	85%	75%	62%	49%	44%	20%
	PFAR	1.12	1.20	1.34	1.58	1.82	1.81
Hurricane Ivan	% overlap	85%	65%	59%	59%	59%	62%
	PFAR	1.01	1.02	1.36	1.66	2.04	2.79
Hurricane Jeanne	% overlap	78%	73%	69%	67%	56%	25%
	PFAR	1.08	1.40	2.23	2.35	2.35	1.38
Hurricane Ernesto	% overlap	79%	83%	75%	51%	30%	5.4%
	PFAR	1.10	1.48	1.77	1.87	1.74	0.97

Table 4-16 Summary of the WRF Model Performance in Terms of the Overlap Percentage and PFAR for the Simulation of the Historical TCs (Continued)

TS Fay	% overlap	57%	42%	32%	30%	22%	22%
	PFAR	0.81	0.98	1.18	1.38	1.56	1.98
Hurricane Gustav	% overlap	66%	59%	53%	53%	41%	32%
	PFAR	0.76	0.72	0.90	1.19	1.41	1.34
Hurricane Irene	% overlap	78%	67%	64%	60%	46%	19%
	PFAR	0.87	0.84	0.90	1.00	1.08	1.22
TS Lee	% overlap	61%	53%	56%	46%	43%	46%
	PFAR	0.63	0.65	0.93	0.95	1.25	2.33
Hurricane Isaac	% overlap	56%	49%	53%	56%	40%	26%
	PFAR	0.87	0.94	0.84	0.72	0.79	1.27
Hurricane Sandy	% overlap	92%	69%	68%	23%	7.6%	1.1%
	PFAR	1.16	1.20	1.17	0.78	0.89	1.36
Hurricane Matthew	% overlap	77%	77%	64%	46%	40%	20%
	PFAR	0.83	0.89	1.11	1.07	1.06	0.79

4.4 Sensitivity Analysis

In this section, the sensitivity of the precipitation field in Hurricane Gustav to the choice of the parameterization schemes is investigated. Starting from the combination of the schemes given in Table 4-2, the microphysics option, cumulus option, PBL option, LWR option, and SWR option are changed one at a time while fixing all the other options. 16 microphysics options, 10 cumulus options, 8 PBL options, 5 LWR options, and 7 SWR options were tested.

4.4.1 Microphysics Parameterization

Figure 4-54 shows how the precipitation field in Hurricane Gustav changes in the inner domain as the microphysics option is changed while fixing the other options. It is observed that changing the microphysics option brings changes in the structure, intensity, and location of the simulated precipitation field. However, compared to other parameterizations investigated in the following, this sensitivity is small. Indeed, except for option No. 1, the precipitation fields are close to the precipitation field in the control run corresponding to option No. 7 (highlighted in red in Figure 4-54). In the case of option No. 1, there is almost no precipitation in the simulation inner domain. Yet it should not be concluded that this scheme fails to generate intense precipitation. In fact, the reason for the absence of intense precipitation in the inner domain is that the trajectory of the TC was substantially modified so that the storm only marginally affected the inner domain. Besides, Table 4-18 shows that several microphysics options provided quantitative results in terms of the three metrics competitive with those of the control run.

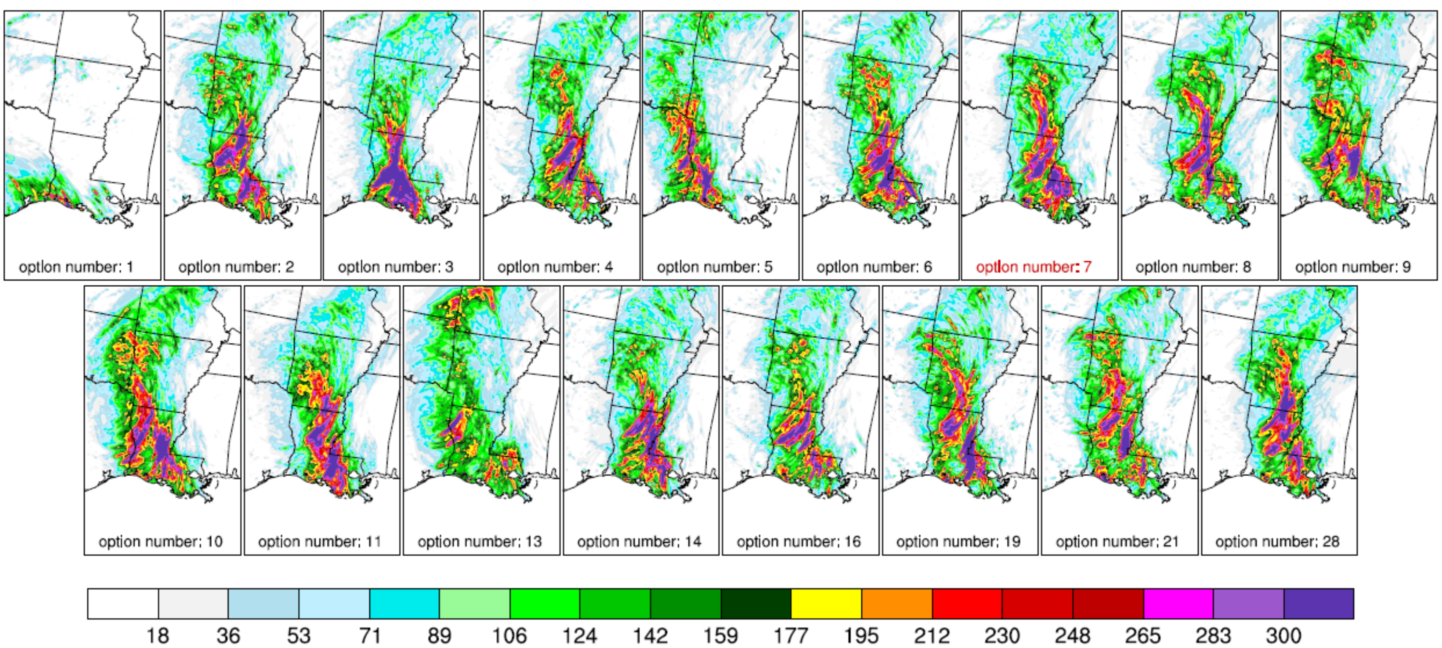

Figure 4-54 Hurricane Gustav Inner-Domain Simulated Accumulated Precipitation Fields (from 08/29 18:00 UTC to 09/05 12:00 UTC) when the Microphysics Option is Changed while Fixing the Other Options

The option numbers provided at the bottom of each plot are those used in WRF (version 3.7); they are detailed in APPENDIX A. The option number of the control run is shown in red.

Table 4-17 Hurricane Gustav WRF Simulation Performance Summary when the Microphysics Option is Changed while Fixing the Other Options

The performance of the control run is specified in the column in red.

Option number		7	1	2	3	4	5	6	8	9
Relative error		-0.16	-0.77	-0.16	-0.21	-0.17	-0.24	-0.16	-0.16	-0.08
50th percentile	% overlap	66%	7%	64%	59%	74%	33%	69%	71%	61%
	PFAR	0.76	0.20	0.79	0.70	0.81	0.73	0.77	0.78	0.88
75th percentile	% overlap	59%	3%	50%	36%	60%	13%	58%	63%	37%
	PFAR	0.72	0.16	0.80	0.53	0.75	0.65	0.76	0.78	0.98
90th percentile	% overlap	53%	1%	31%	32%	43%	9%	48%	47%	19%
	PFAR	0.90	0.10	0.76	0.70	0.74	0.65	0.88	0.77	0.78
95th percentile	% overlap	53%	0%	34%	43%	33%	6%	49%	43%	19%
	PFAR	1.19	0.09	0.97	1.06	0.87	0.64	1.06	0.91	0.76
97.5th percentile	% overlap	41%	0%	28%	55%	17%	3%	35%	28%	19%
	PFAR	1.41	0.08	1.22	1.63	0.98	0.60	1.17	0.99	0.74
99th percentile	% overlap	32%	0%	10%	55%	1%	3%	14%	8%	15%
	PFAR	1.34	0.07	1.44	2.86	1.19	0.67	1.47	1.08	0.90

Option number		7	10	11	13	14	16	19	21	28
Relative error		-0.16	-0.03	-0.16	-0.10	-0.21	-0.23	-0.15	-0.14	-0.16
50th percentile	% overlap	66%	63%	68%	64%	66%	66%	66%	66%	71%
	PFAR	0.76	0.92	0.74	0.94	0.72	0.74	0.77	0.81	0.78
75th percentile	% overlap	59%	43%	56%	36%	55%	52%	54%	55%	64%
	PFAR	0.72	1.06	0.71	0.93	0.67	0.69	0.80	0.85	0.76
90th percentile	% overlap	53%	31%	51%	7%	45%	31%	43%	29%	48%
	PFAR	0.90	1.07	0.94	0.48	0.73	0.65	0.88	0.86	0.84
95th percentile	% overlap	53%	38%	52%	2%	37%	29%	35%	22%	40%
	PFAR	1.19	1.21	1.23	0.34	0.97	0.72	1.11	0.91	1.01
97.5th percentile	% overlap	41%	45%	40%	0%	24%	21%	27%	19%	29%
	PFAR	1.41	1.25	1.38	0.24	1.19	0.79	1.26	0.92	1.12
99th percentile	% overlap	32%	42%	20%	0%	6%	12%	23%	20%	20%
	PFAR	1.34	1.39	1.37	0.23	1.43	0.80	1.64	1.01	1.33

4.4.2 Cumulus Parameterization

Figure 4-55 shows how the precipitation field in the simulation inner domain in Hurricane Gustav changes as the cumulus option is changed while fixing the other options[4]. It is observed that the sensitivity to the choice of the cumulus option is larger than that for the microphysics parameterization, especially as far as the location of the precipitation field is concerned. Indeed, in four simulations corresponding to options No. 3, 4, 5 and 93, the TC's track was modified to such an extent that the storm did not affect the simulation inner domain, versus only one simulation in the case of the microphysics parameterization presented in the previous subsection. In fact, only for options No. 6 and 84 the precipitation field was somehow placed in the same location as the control run corresponding to option No. 14 (highlighted in red in Figure 4-55). Besides, as far as the precipitation depth is concerned, all the simulations for which Hurricane Gustav affected the inner domain exhibit a precipitation field that is too intense, except for option No. 84 for which the precipitation depth is about the same as in the control run. This is in agreement with the results in terms of the metrics presented in Table 4-19. Indeed by looking at the PFAR for the most intense thresholds it is observed that the size of the precipitation field above these thresholds was significantly overestimated except for option No. 84.

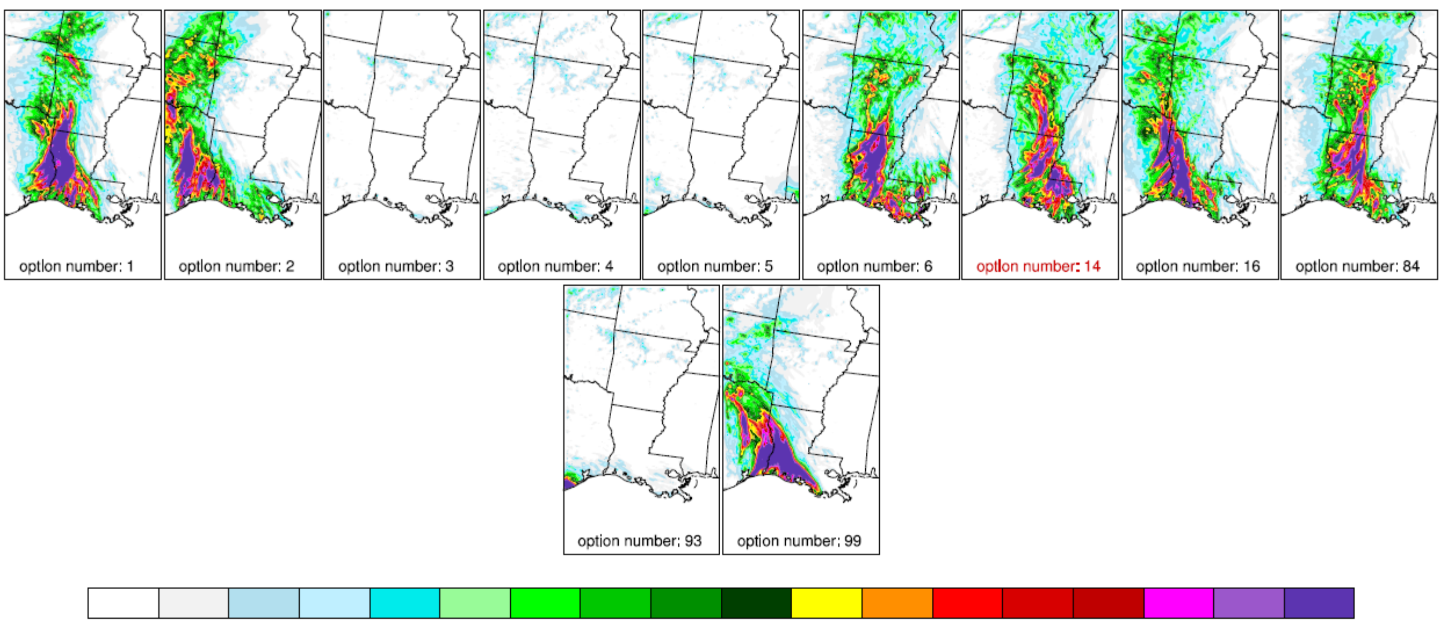

Figure 4-55 Hurricane Gustav Inner-Domain Simulated Accumulated Precipitation Fields (from 08/29 18:00 UTC to 09/05 12:00 UTC) when the Cumulus Option is Changed while Fixing the Other Options

The option numbers provided at the bottom of each plot are those used in WRF (version 3.7); they are detailed in APPENDIX A. The option number of the control run is shown in red.

[4] It is noted that cumulus parameterization was used only in the outer and intermediate domains.

Table 4-18 Hurricane Gustav WRF Simulation Performance Summary when the Cumulus Option is Changed while Fixing the Other Options

The performance of the control run is specified in the column in red.

Option number		14	1	2	3	4	5
Relative error		-0.16	-0.11	-0.15	-0.96	-0.88	-0.89
50th percentile	% overlap	66%	46%	29%	0%	1%	1%
	PFAR	0.76	0.73	0.79	0.01	0.03	0.04
75th percentile	% overlap	59%	25%	9%	0%	0%	0%
	PFAR	0.72	0.83	0.94	0.00	0.01	0.00
90th percentile	% overlap	53%	18%	0%	0%	0%	0%
	PFAR	0.90	0.99	0.92	0.00	0.00	0.00
95th percentile	% overlap	53%	16%	0%	0%	0%	0%
	PFAR	1.19	1.41	1.14	0.00	0.00	0.00
97.5th percentile	% overlap	41%	13%	0%	0%	0%	0%
	PFAR	1.41	2.15	1.43	0.00	0.00	0.00
99th percentile	% overlap	32%	2%	0%	0%	0%	0%
	PFAR	1.34	3.73	2.01	0.00	0.00	0.00

Option number		14	6	16	84	93	99
Relative error		-0.16	-0.05	-0.06	-0.17	-0.88	-0.28
50th percentile	% overlap	66%	72%	47%	61%	1%	15%
	PFAR	0.76	0.86	0.89	0.73	0.04	0.52
75th percentile	% overlap	59%	50%	20%	51%	0%	10%
	PFAR	0.72	0.79	0.80	0.79	0.03	0.57
90th percentile	% overlap	53%	37%	14%	39%	0%	11%
	PFAR	0.90	0.93	0.86	0.83	0.04	0.89
95th percentile	% overlap	53%	36%	11%	38%	0%	12%
	PFAR	1.19	1.29	1.23	1.10	0.07	1.42
97.5th percentile	% overlap	41%	34%	5%	33%	0%	12%
	PFAR	1.41	1.75	1.79	1.28	0.12	2.21
99th percentile	% overlap	32%	23%	1%	28%	0%	10%
	PFAR	1.34	2.69	3.00	1.18	0.25	3.64

4.4.3 PBL Parameterization

Figure 4-56 presents the precipitation field in the simulation inner domain in Hurricane Gustav when the PBL option is changed while fixing the other options. It is observed that, although the location of the precipitation field changes in the inner domain as the scheme is changed, all the simulations produced a TC that affected the inner domain, so that the TC's track seems to be less sensitive to the choice of the PBL option than it is to the choice of the microphysics and cumulus options discussed previously. However it is observed that the structure and intensity of the precipitation field change significantly as the PBL scheme is changed. Looking at Table 4-20, it is seen that all the simulations provided good results in terms of the relative error, meaning that changing the PBL option does not affect noticeably the total precipitation amount. However, the PFAR significantly changes when the scheme is modified, especially for the largest thresholds. Thus in the case of Hurricane Gustav changing the PBL option mainly affected the precipitation depth distribution and the spatial structure of the precipitation field.

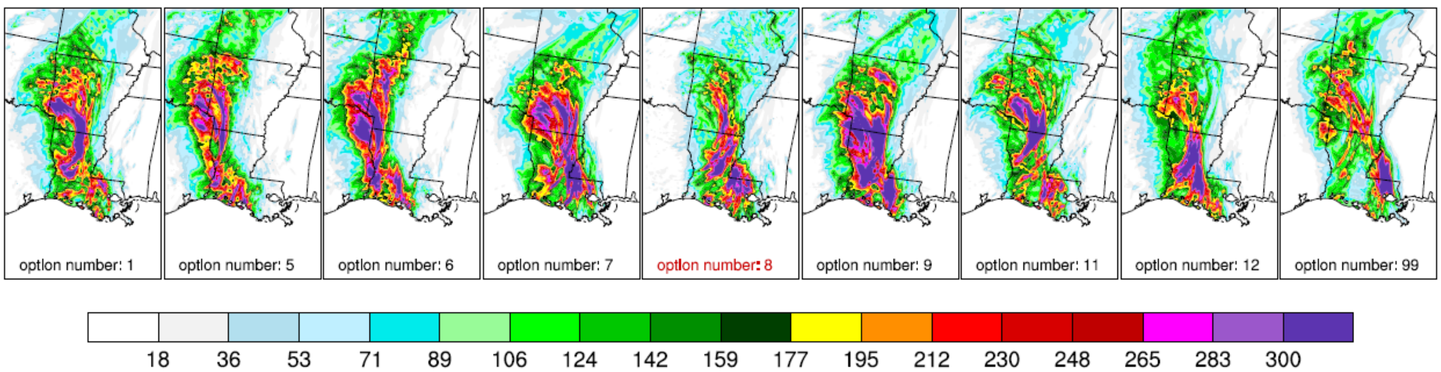

Figure 4-56 Hurricane Gustav Inner-Domain Simulated Accumulated Precipitation Fields (from 08/29 18:00 UTC to 09/05 12:00 UTC) when the PBL Option Is Changed while Fixing the Other Options

The option numbers provided at the bottom of each plot are those used in WRF (version 3.7); they are detailed in APPENDIX A. The option number of the control run is shown in red.

Table 4-19 Hurricane Gustav WRF Simulation Performance Summary when the PBL Option is Changed while Fixing the Other Options

The Performance of the Control Run is Specified in the Column in Red.

Option number		8	1	5	6	7
Relative error		-0.16	-0.04	-0.04	0.00	0.02
50th percentile	% overlap	66%	67%	49%	49%	72%
	PFAR	0.76	0.86	0.87	0.84	0.92
75th percentile	% overlap	59%	58%	29%	30%	68%
	PFAR	0.72	1.04	1.06	1.06	1.04
90th percentile	% overlap	53%	43%	16%	20%	60%
	PFAR	0.90	1.15	1.30	1.46	1.44
95th percentile	% overlap	53%	27%	8%	17%	55%
	PFAR	1.19	1.28	1.47	2.01	1.99
97.5th percentile	% overlap	41%	11%	4%	12%	36%
	PFAR	1.41	1.38	1.39	2.32	2.36
99th percentile	% overlap	32%	4%	3%	2%	13%
	PFAR	1.34	1.73	0.93	2.43	2.36

Option number		8	9	11	12	99
Relative error		-0.16	0.08	-0.05	-0.09	-0.15
50th percentile	% overlap	66%	65%	66%	59%	68%
	PFAR	0.76	0.90	0.87	0.85	0.83
75th percentile	% overlap	59%	57%	55%	47%	50%
	PFAR	0.72	1.04	0.97	0.97	0.87
90th percentile	% overlap	53%	47%	29%	35%	26%
	PFAR	0.90	1.54	0.95	0.87	0.84
95th percentile	% overlap	53%	49%	23%	41%	11%
	PFAR	1.19	2.38	1.09	0.94	0.79
97.5th percentile	% overlap	41%	52%	13%	40%	3%
	PFAR	1.41	3.42	1.36	1.17	0.69
99th percentile	% overlap	32%	32%	5%	21%	0%
	PFAR	1.34	4.36	1.89	1.51	0.96

4.4.4 LWR Parameterization

Figure 4-57 presents the precipitation field in the simulation inner domain in Hurricane Gustav when the LWR option is changed while fixing the other options. It is observed that, although changing the LWR scheme affects the precipitation field, this sensitivity is much less than for the other parameterizations discussed previously. In fact, Table 4-21 shows that the metrics do not change noticeably when the LWR scheme is changed, except for the 99th percentile threshold for which significant changes in the overlap percentage and moderate changes in the PFAR are observed.

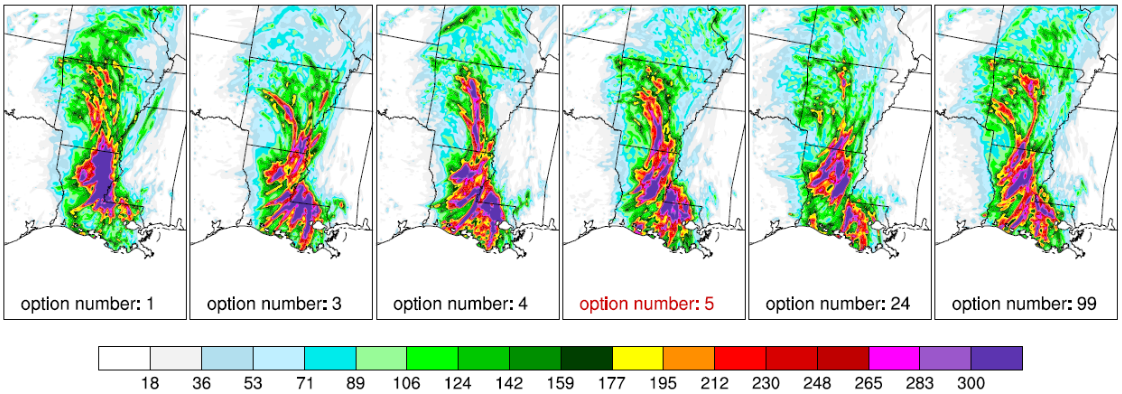

Figure 4-57 Hurricane Gustav Inner-Domain Simulated Accumulated Precipitation Fields (from 08/29 18:00 UTC to 09/05 12:00 UTC) when the LWR Option is Changed while Fixing the Other Options

The option numbers provided at the bottom of each plot are those used in WRF (version 3.7); they are detailed in APPENDIX A. The option number of the control run is shown in red.

Table 4-20 Hurricane Gustav WRF Simulation Performance Summary when the LWR Option is Changed while Fixing the Other Options

The Performance of the Control Run is Specified in the Column in Red.

Option number		5	1	3	4	24	99
Relative error		-0.16	-0.12	-0.23	-0.19	-0.20	-0.13
50th percentile	% overlap	66%	71%	59%	68%	66%	71%
	PFAR	0.76	0.82	0.67	0.72	0.78	0.85
75th percentile	% overlap	59%	58%	54%	56%	45%	52%
	PFAR	0.72	0.83	0.67	0.69	0.69	0.69
90th percentile	% overlap	53%	46%	45%	54%	29%	38%
	PFAR	0.90	0.75	0.80	0.93	0.67	0.82
95th percentile	% overlap	53%	46%	40%	49%	33%	36%
	PFAR	1.19	0.92	1.05	1.27	0.85	0.97
97.5th percentile	% overlap	41%	42%	25%	27%	33%	24%
	PFAR	1.41	1.23	1.23	1.57	0.95	0.95
99th percentile	% overlap	32%	34%	5%	8%	33%	2%
	PFAR	1.34	2.00	1.28	1.74	0.99	0.79

4.4.5 SWR parameterization

Figure 4-58 shows the precipitation field in the simulation inner domain in Hurricane Gustav when the SWR option is changed while fixing the other options. As for the LWR option, it is observed that the sensitivity of the precipitation field to the choice of the SWR option is significantly less than for the choice of the microphysics, cumulus, and PBL options. All the SWR schemes produced a precipitation field that is similar to the precipitation field of the control run (corresponding to option No. 5), except for option No. 7 for which the size of the field was underestimated. More precisely, Table 4-22 shows that option No. 7 underestimated the total precipitation amount as well as the size of the field above all thresholds, except the 99th percentile threshold for which the PFAR is larger than 1.

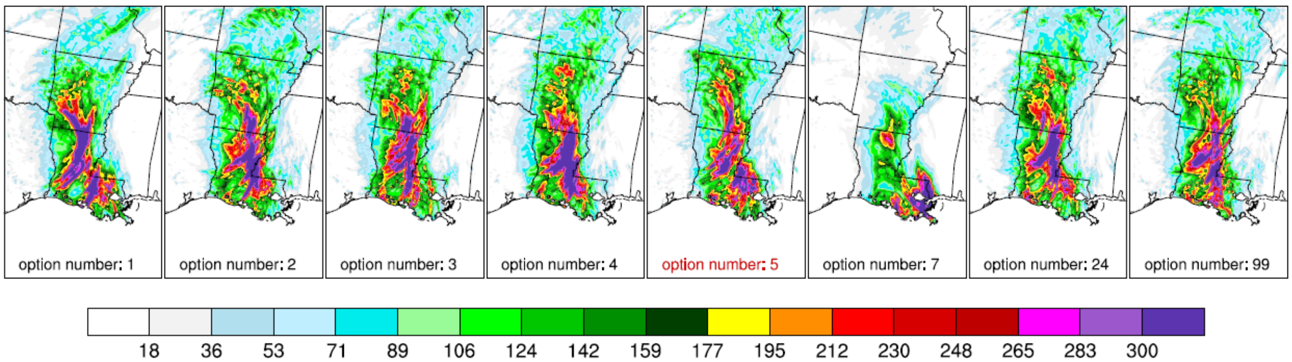

Figure 4-58 Hurricane Gustav Inner-Domain Simulated Accumulated Precipitation Fields (from 08/29 18:00 UTC to 09/05 12:00 UTC) when the SWR Option is Changed while Fixing the Other Options

The option numbers provided at the bottom of each plot are those used in WRF (version 3.7); they are detailed in APPENDIX A. The option number of the control run is shown in red.

Table 4-21 Hurricane Gustav WRF Simulation Performance Summary when the SWR Option is Changed while Fixing the Other Options

The performance of the control run is specified in the shaded line.

Option number		5	1	2	3	4	7	24	99
Relative error		-0.16	-0.16	-0.11	-0.15	-0.12	-0.48	-0.15	-0.18
50th percentile	% overlap	66%	65%	72%	67%	66%	35%	68%	66%
	PFAR	0.76	0.75	0.84	0.75	0.79	0.37	0.79	0.75
75th percentile	% overlap	59%	54%	64%	60%	54%	34%	57%	58%
	PFAR	0.72	0.75	0.83	0.78	0.76	0.41	0.78	0.75
90th percentile	% overlap	53%	40%	52%	44%	48%	11%	44%	46%
	PFAR	0.90	0.87	0.86	0.90	0.87	0.42	0.86	0.79
95th percentile	% overlap	53%	46%	51%	50%	57%	5%	47%	49%
	PFAR	1.19	1.14	1.08	1.17	1.18	0.58	1.05	0.97
97.5th percentile	% overlap	41%	50%	44%	42%	65%	1%	37%	39%
	PFAR	1.41	1.54	1.32	1.35	1.54	0.82	1.20	1.11
99th percentile	% overlap	32%	40%	28%	21%	48%	0%	13%	9%
	PFAR	1.34	2.47	1.94	1.45	2.47	1.32	1.64	1.21

4.4.6 Mean and Standard Deviation

In the previous subsections the sensitivity of the precipitation field in Hurricane Gustav to the choice of the model's parameterization schemes was examined by investigating how the plots of the field and how the quantitative metrics change when one option is changed while fixing the other options. The most sensitive parameterizations were identified qualitatively by comparing the magnitude of the changes in the metrics and in the location, structure and intensity of the precipitation field between one parameterization and another (e.g. microphysics parameterization vs. cumulus parameterization). In this subsection, the mean, standard deviation, and coefficient of variation (CV) of the metrics for each parameterization are calculated in order to supplement the discussion with a more quantitative approach. The coefficient of variation is equal to the ratio of the standard deviation to the absolute value of the mean. It expresses the extent of variability in relation to the mean of the population. Results are given in Table 4-23, Table 4-24, and Figure 4-59.

From Table 4-23 it is observed that, in average, the WRF model tends to underestimate the total precipitation amount in the simulation inner domain since the relative error is negative for all parameterizations. However, the reason why the relative error is so large in magnitude in the case of the cumulus parameterization is that 4 simulations out of the 11 simulations produced a TC that did not affect the inner domain (see Figure 4-55). This is in agreement with the fact that the PFAR is smaller than 1 for the lowest thresholds (50th, 75th, and 90th percentiles) for all parameterizations (except for the PBL and 90th percentile threshold). Besides, it is observed that the PFAR increases as the threshold increases. In particular, at the 99th percentile threshold, the PFAR is significantly larger than 1 showing that the WRF model tended to overestimate the most intense precipitation in Hurricane Gustav, especially for the cumulus, PBL, and SWR parameterizations.

The performance in terms of the overlap percentage is moderate due to the fact that the location and structure of the precipitation field change significantly as the scheme is modified. However, despite this sensitivity, the mean overlap percentage is positive for all parameterizations and all thresholds, even the most intense threshold.

Table 4-22 Mean Value of the Quantitative Metrics for Each Parameterization, Obtained by Averaging over the Different Option Numbers

Option		Microphysics	Cumulus	PBL	LWR	SWR
Relative error		-0.19	-0.42	-0.05	-0.17	-0.19
50th percentile	% overlap	61%	31%	62%	67%	63%
	PFAR	0.75	0.49	0.86	0.77	0.72
75th percentile	% overlap	47%	20%	50%	54%	55%
	PFAR	0.74	0.50	0.97	0.71	0.72
90th percentile	% overlap	33%	16%	37%	44%	42%
	PFAR	0.75	0.58	1.16	0.81	0.81
95th percentile	% overlap	31%	15%	31%	43%	45%
	PFAR	0.88	0.81	1.46	1.04	1.04
97.5th percentile	% overlap	25%	12%	23%	32%	40%
	PFAR	1.00	1.10	1.72	1.22	1.29
99th percentile	% overlap	17%	9%	13%	19%	24%
	PFAR	1.19	1.62	1.95	1.36	1.73

Table 4-23 is valuable insomuch as it shows which parameterization to focus the calibration effort on when optimizing a given quantitative metric. For example it shows that one should pay particular attention to the cumulus parameterization when minimizing the relative error, whereas particular attention should be given to the PBL parameterization when investigating the most intense part of the precipitation field. It is noted that this analysis was performed for only one TC, and the results will not necessarily apply in general.

As far as the sensitivity of a given metric to the choice of the scheme is concerned, the standard deviation and the CV are better suited than the mean to address this issue. Results are given in Table 4-24 and Figure 4-59. As far as the relative error is concerned, the most sensitive parameterization based on the CV is the PBL parameterization, followed by the cumulus parameterization, microphysics parameterization, SWR parameterization and LWR parameterization. The CV is large in the case of the PBL parameterization although the standard deviation is relatively small because the standard deviation is larger than the mean in this case. For the other metrics, the most sensitive parameterization is the cumulus parameterization, which is not surprising since several of the simulations placed the precipitation field outside the inner domain. For the 50th percentile threshold, it is observed that the overlap percentage and the PFAR are much less sensitive to the choice of the scheme for the other parameterizations. As the threshold increases, the sensitivity to the other parameterizations increases both in magnitude (larger CVs) as well as in proportion to the CV for the cumulus parameterization. Overall, the sensitivity to the LWR parameterization seems to be the smallest, in agreement with the qualitative comparison performed in the previous subsections.

Table 4-23 Standard Deviation of the Quantitative Metrics for Each Parameterization

Option		Microphysics	Cumulus	PBL	LWR	SWR
Relative error		0.16	0.39	0.08	0.04	0.12
50th percentile	% overlap	16%	29%	8%	5%	11%
	PFAR	0.16	0.38	0.05	0.06	0.15
75th percentile	% overlap	17%	23%	13%	5%	9%
	PFAR	0.20	0.40	0.11	0.06	0.13
90th percentile	% overlap	16%	19%	15%	9%	13%
	PFAR	0.22	0.45	0.28	0.09	0.16
95th percentile	% overlap	16%	19%	18%	8%	17%
	PFAR	0.31	0.63	0.54	0.16	0.20
97.5th percentile	% overlap	15%	16%	18%	8%	18%
	PFAR	0.41	0.90	0.83	0.24	0.24
99th percentile	% overlap	15%	13%	13%	15%	16%
	PFAR	0.61	1.47	1.05	0.45	0.51

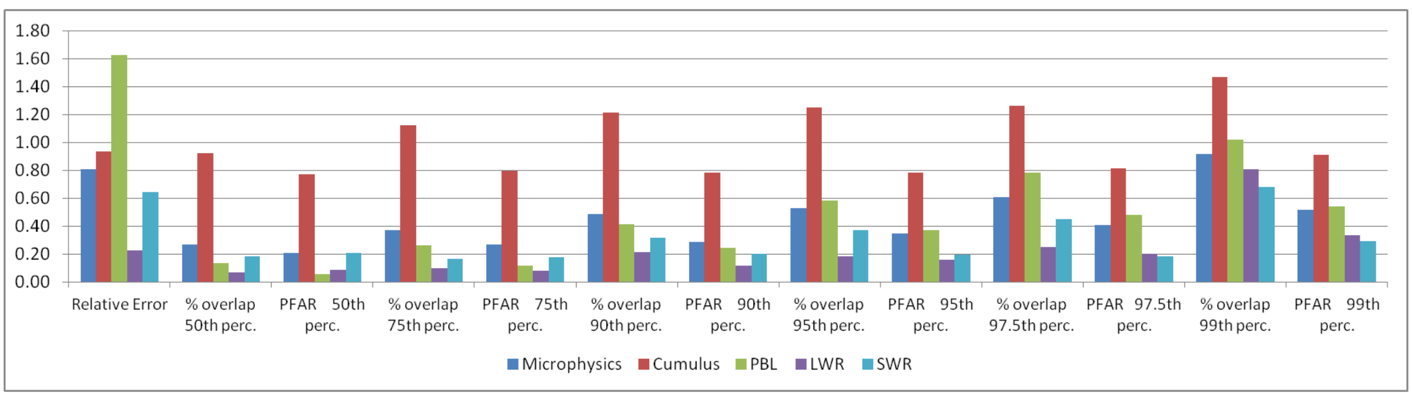

Figure 4-59 Coefficient of Variation for Each of the Model's Parameterizations and for Each Quantitative Metric

4.5 Conclusion of Chapter 4

This chapter presented the results for the numerical simulation of 13 historical TCs. More specifically, the precipitation fields of these storms and their underlying moisture transport fields were reconstructed with the WRF model at 5-km resolution, without any nudging or DA. It is shown that under an appropriate choice of the model's parameterization schemes and BCs, the WRF model provided satisfactory results in simulating the location, intensity, and structure of the intense precipitation fields in the TCs. Although certain combinations of the parameterization schemes provided in each case realistic results in terms of the precipitation fields' structures and intensities, placing these fields in the observed spatial locations required additional efforts, so that the "best" set of options varies from one case to the other. The investigation of the IVT and its divergence showed that moisture convergence is generally a key factor for the generation of intense precipitation in TCs. This chapter also presents a sensitivity analysis of the precipitation field in Hurricane Gustav on the choice of the parameterization schemes. In this analysis, each option was changed one at a time while fixing the other options. It was observed that modifying one option can bring significant changes to the precipitation field's location, structure, and intensity, as well as to the quantitative metrics used for the model's validation. The cumulus parameterization was observed to be the most sensitive because changing the cumulus parameterization scheme can change the track of the TC to such an extent that the storm does not affect the simulation inner domain anymore.

5 PHYSICALLY BASED STORM TRANSPOSITION OF A HISTORICAL MESOSCALE CONVECTIVE SYSTEM

This chapter presents the results of the transposition of a MCS over a specified target region through a physically based approach by using a RAM. With such a transposition, one can estimate the largest precipitation amount that could have been physically caused by the storm over the target region had the storm occurred in a different location relative to the watershed, especially if it had occurred closer to or directly over the watershed. The storm transposition method used in this exercise was based on the maximum precipitation estimation methods developed and discussed in the studies by Ohara et al. (2011b) and Ishida et al. (2015). In these studies, storm transposition was achieved through the shifting of the IBCs of the RAM and through running the atmospheric model with the new IBCs. Because an atmospheric model solves the governing conservation equations, this transposition method has the advantage of conserving of the mass, momentum, and energy in all the simulation domains. It also has the advantage of account the effects of topography and other important physical features which may have a major effect on the precipitation.

For the transposition exercise of this project, the WRF model was used. The target watershed that was selected for the transposition of a MCS was the basin located in the southeastern part of the state of Minnesota, close to the borders of the states of Wisconsin and Iowa. This watershed has an outlet at Houston, as shown in Figure 5-1, and it is called the Root River basin above Houston.

Figure 5-1 Location of the Target Watershed Selected for the Transposition Exercise

The target watershed is called the Root River above Houston.

The MCS selected for the transposition exercise was the July 18, 2007 MCS. The reconstruction of this MCS was presented in Chapter 3 of this report, which showed that this storm was simulated with very good visual and statistical results. The comparison between the observed and simulated precipitation fields of this MCS were provided in Figure 3-14.

Plotting the target watershed along with the MCS (Figure 5-2), one can see that the target watershed is located to the northwest of the intense precipitation region of the selected MCS. As a result of the location of the watershed with respect to the MCS, the main directions of shifting for this attempted transposition exercise were decided to be the North, the West, and the Northwest directions. While shifting was attempted mainly in these three directions, it was still carried out in the remaining directions, but in a smaller amount. It is important to note that the shifting of the BCs was performed in two directions (North-South and East-West), with regular increments chosen in each of the directions.

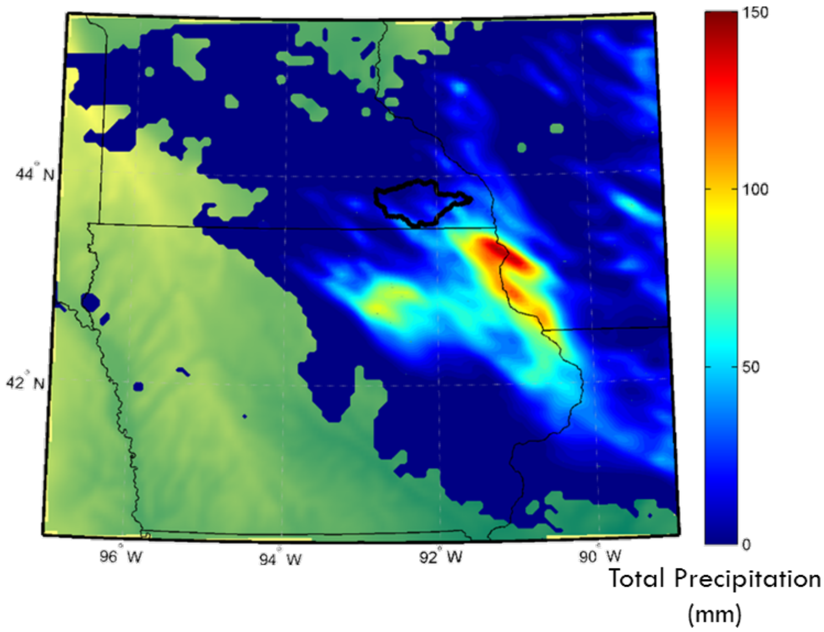

Figure 5-2 Location of the Target Watershed (Root River Above Houston) with Respect to the July 18, 2007 MCS

Therefore, for this transposition exercise, first, 0.3-degree increments were used for shifting in the North-South direction, and 0.3-degree increments for shifting in the East-West direction. Then, for each shifting position, the WRF model was run to simulate the MCS corresponding to these shifting positions. Then, the 24-hr basin average precipitation over the target watershed was computed for each of the shifting positions. Finally, the results of the 24-hr basin average precipitation were plotted on a figure as shown on Figure 5-3.

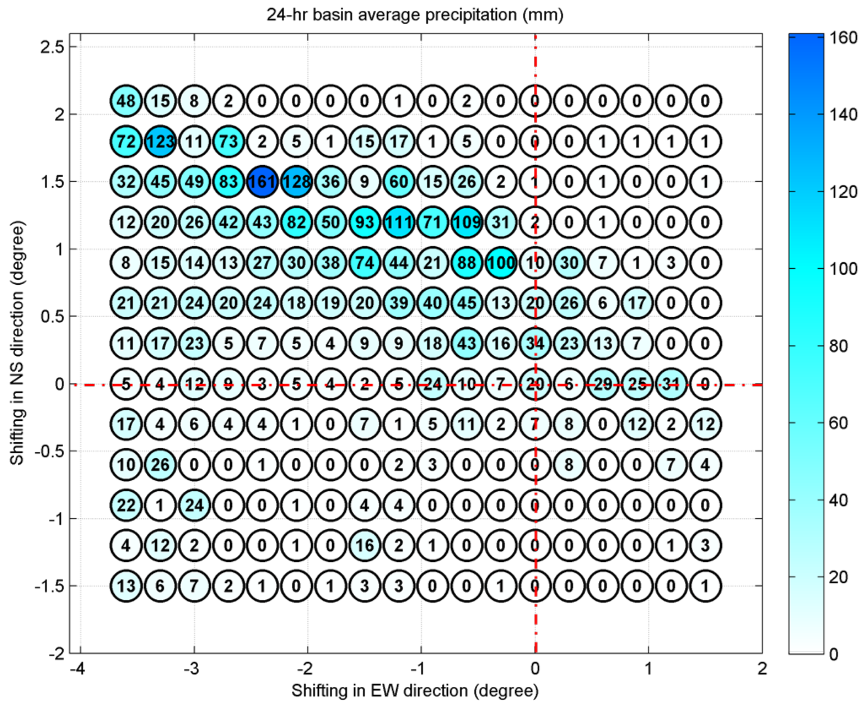

Figure 5-3 Plot of the 24-hr Basin Average Precipitation Over the Root River Above Houston (Target Watershed) as a Function of the Degree of Shifting of the Domain BCs Corresponding to the July 18, 2007 MCS

The numbers and the colors represent the values of the 24-hr basin average precipitation for each of the shifting positions.

In Figure 5-3, the x-axis represents the degrees of shifting in the East-West (EW) direction, the y-axis represents the degrees of shifting in the North-South (NS) direction, and the intersection of the dashed red lines represents the location of the origin, which corresponds to the no-shifting position. The numbers inside the circles and the color intensity of the circles both represent the values of the 24-hr basin average precipitation for each of the specific shifting positions. From this figure, one can see that the 24-hr basin average precipitation over the target watershed increases mainly when shifting occurs along the northwest (NW) direction, relative to the original, no-shifting position. Along this direction, the maximum precipitation was found to be around 161 mm (6.3 in.) at a shifting position of [+1.5° N, +2.4° W]. This is in contrast to the value of the 24-hr basin average precipitation computed at the no-shifting position, which was equal to only 20 mm (0.8 in.). Moreover, note that the shifting direction causing the greatest increase in precipitation (i.e., NW) was the same as the direction of the location of the target watershed relative to the original, unshifted MCS (Figure 5-2), thus showing some consistency in the results.

In order to visualize why such a difference in precipitation occurred between the unshifted and shifted conditions, the plots of a few of the shifted results of Figure 5-3 are provided on Figure 5-4. These include the plots of three shifting positions, as well as the plot for the no-shifting position. From these figures, one can see that the shifting of the BCs in the NW direction allowed the MCS to occur either closer to ([+0.9° N, +0.6° W]), or directly over ([+1.5° N, +2.1° W] and [+1.5° N,

+2.4° W]), the target watershed. Moreover, it is clear from those plots that the shifting also affected the shape and the intensity of the precipitation for the shifted MCSs.

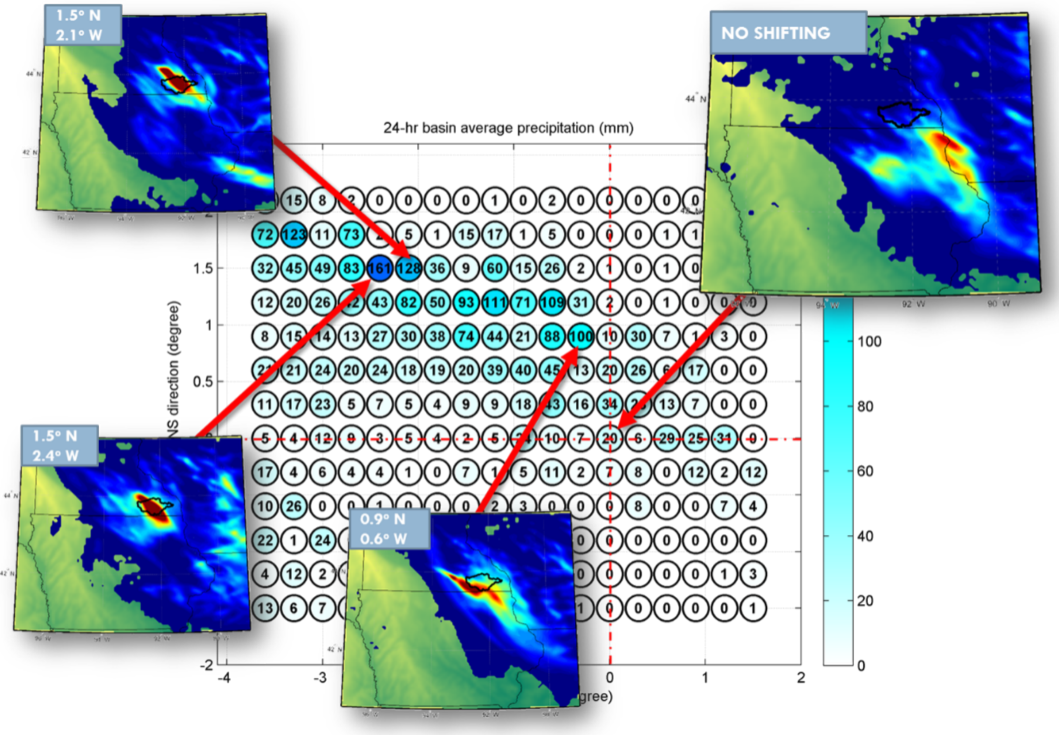

Figure 5-4 **A Few Plots of the MCSs Corresponding to Some of the Shifting Positions, Including the No-Shifting Position**

Recall that the largest 24-hr basin average precipitation from the shifted MCSs had a value of 161 mm (6.3 in.) and occurred for a shifting position of [+1.5° N, +2.4° W]. This shifting position was the area of highest precipitation attained from the transposition exercise. As a result, the first grid-refinement exercise was performed around this area of the highest precipitation. This refinement involved using 0.1-degree increments, as opposed to the original 0.3-degree increments used to produce Figure 5-3. The area of this refinement is represented by the red box shown on the top left corner of Figure 5-5, and it encompasses the two largest precipitation depths, which are 161 mm (6.3 in.) and 128 mm (5.0 in.).

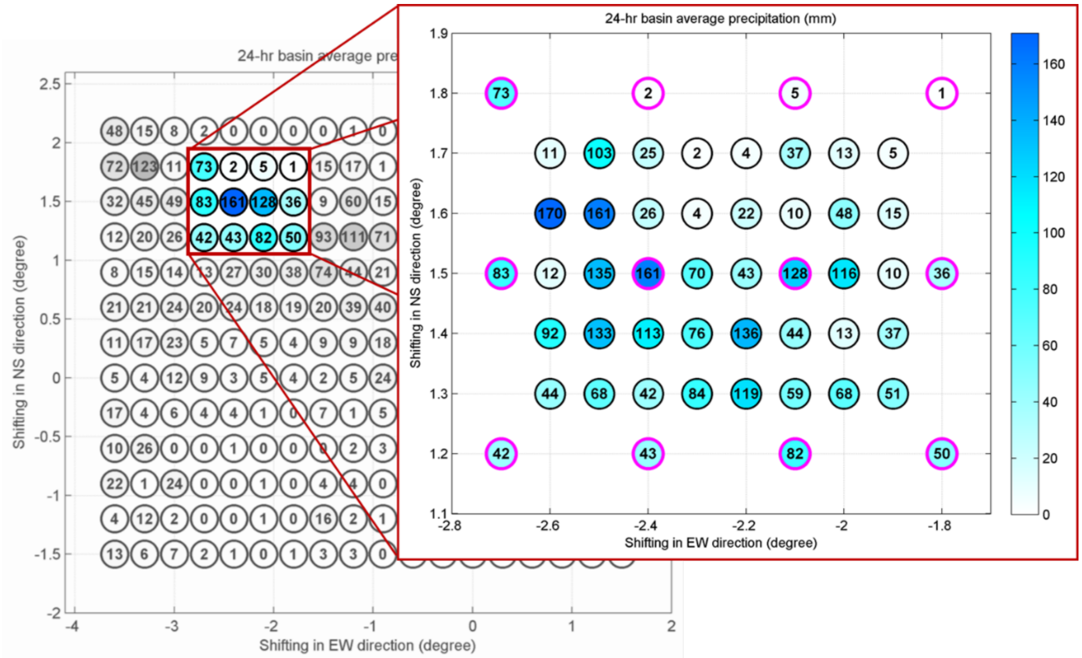

Figure 5-5 Area Selected for the First Grid-Refinement Exercise

Zoomed-in figure shows the results of the original transposition exercise (circles with pink boundaries) and the new results of the first grid-refinement exercise (circles with black boundaries).

The results of the first grid-refinement are shown on the zoomed-in plot of Figure 5-5. In this plot, the circles with the pink boundaries represent the original precipitation values that were obtained from the first transposition exercise using the 0.3-degree increments. The circles with the black boundaries represent the newly computed precipitation values obtained for the refinement exercise, with a 0.1-degree increment. From the refinement results, one can find a new maximum 24-hr basin average precipitation value, which is equal to 170 mm (6.7 in.). This corresponds to a shifting position of [+1.6º N, +2.6º W].

Figure 5-6 provides plots of the MCS corresponding to the original maximum basin average precipitation of 161 mm (6.3 in.), and the two MCSs causing the largest basin average precipitations for the first refinement exercise. These latter two MCSs correspond to shifting positions of [+1.6º N, +2.5º W] and [+1.6º N, +2.6º W]. Therefore, since the location of these two MCSs was the area of highest precipitation attained from the first refinement exercise, the second grid-refinement exercise was performed around this area. This refinement involved using 0.05-degree increments, as opposed to the 0.1-degree increments used for the first refinement exercise that produced the results of Figure 5-5. The area of this second refinement is represented by the red box shown on the left of Figure 5-7, and it encompasses the three largest precipitation depths obtained from the original and first-refinement transposition exercises: 161 mm, 161 mm, and 170 mm (6.3 in., 6.3 in., 6.7 in.).

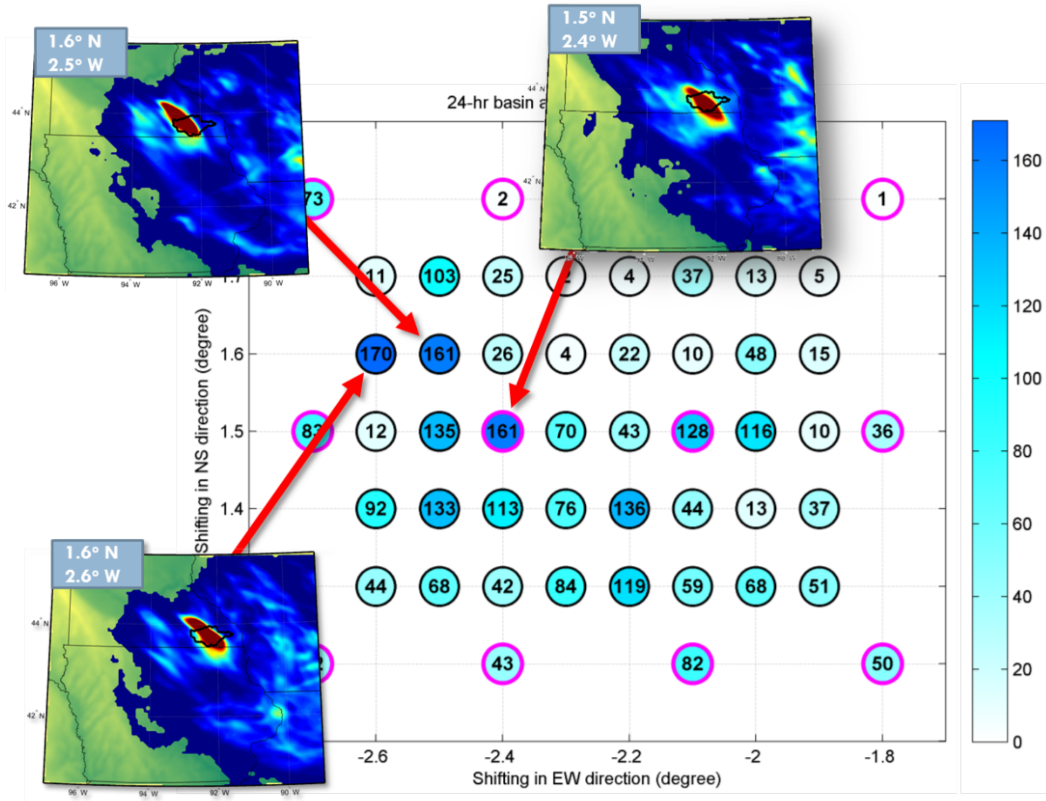

Figure 5-6 **Plots of the MCSs Corresponding to the Largest Basin Average Precipitation of the Original Transposition Exercise (161 mm; 6.3 in.) and the Two Largest Basin Average Precipitations of the Refinement Exercise (161 mm and 170 mm [6.3 in. and 6.7 in.]).**

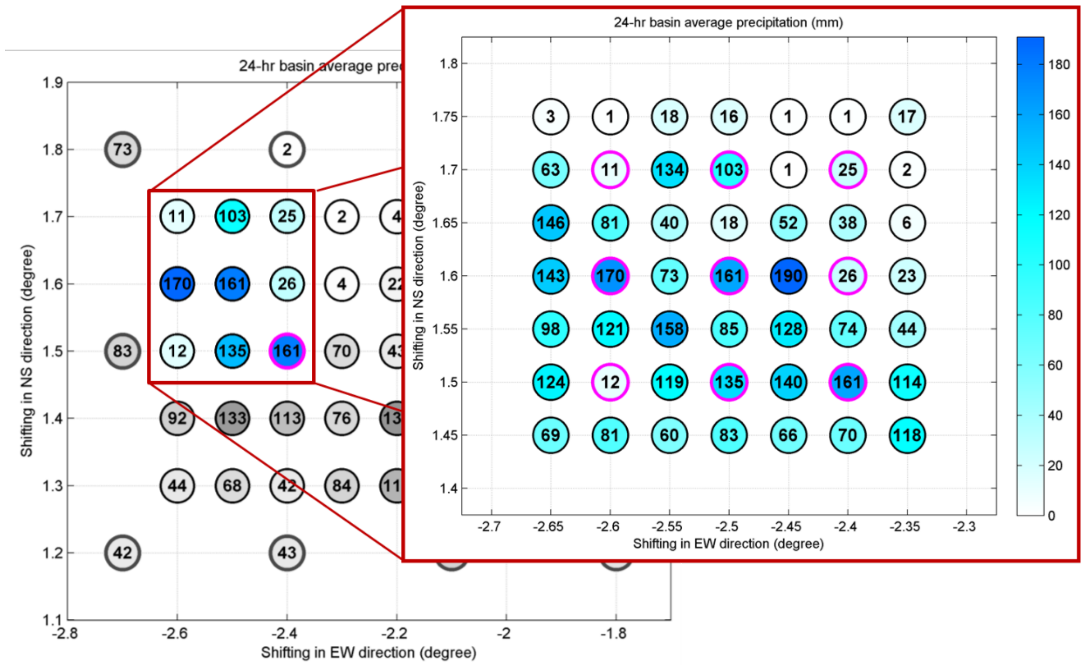

Figure 5-7 Area Selected for the Second Grid-Refinement Exercise

Zoomed-in figure shows the results of the original first-refinement exercise (circles with pink boundaries) and the new results of the second grid-refinement exercise (circles with black boundaries).

The results of the second grid-refinement are shown on the zoomed-in plot of Figure 5-7. In this plot, the circles with the pink boundaries represent the precipitation values that were obtained from the first refinement exercise using the 0.1-degree increments. The circles with the black boundaries represent the newly computed precipitation values obtained for the second refinement exercise, with a 0.05-degree increment. Once again, from the second refinement results, a new maximum 24-hr basin average precipitation value can be found. This maximum is equal to 190 mm (7.5 in.), and it corresponds to a shifting position of [+1.6° N, +2.45° W], whose plot is shown on Figure 5-8. Determining that a refinement of the level of 0.05 degrees was enough for this purpose, no further refinement under 0.05 degrees was performed.

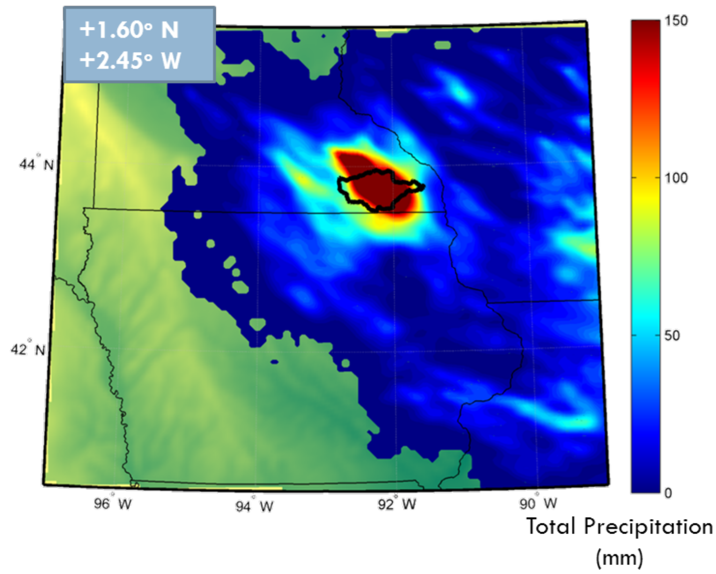

Figure 5-8 **Simulated 24-hr Accumulated Precipitation Fields During the July 18, 2007 MCS Resulting from a Transposition by [+1.60° N, +2.45° W]**

Total accumulated precipitation computed from 07/17/2007 at 11h to 07/18/2007 at 11h.

Therefore, with this transposition exercise, it was possible to transpose the July 18, 2007 MCS to a location that produces a 24-hr basin average precipitation (190 mm [7.5 in.], Figure 5-8) that is almost 10 times greater than that of the original, no-shifting condition (20 mm [0.8 in.], Figure 5-2). This was achieved by shifting the BCs by [+1.6° N, +2.45° W]. Comparing the figures for the unshifted (Figure 5-2) and the transposed (Figure 5-8) MCSs, it is clear that the transposition allowed the MCS to occur directly over the target watershed, thus increasing its effect on the basin average precipitation value. Moreover, the transposed MCS clearly has a higher intensity as well as a different shape when compared to the unshifted MCS. This comes as a result of using a physically based method that conserves mass, momentum, and energy, and that incorporates all other major physical factors into the simulation. Therefore, as a result of this transposition exercise, it was possible to find that the 24-hr basin average precipitation of the July 18, 2007 MCS could have physically been as high as 190 mm (7.5 in.) if this specific MCS had occurred slightly northwest of its original location.

However, it should be noted that the maximum 24-hr basin average precipitation obtained from this exercise for the July 18, 2007 MCS does not represent the largest possible basin average precipitation that could have been obtained over the Root River basin above Houston. In order to determine such a value, it would be necessary to perform the transposition for all the historical intense MCSs over the target watershed. Such an exercise would allow one to find the maximum 24-hr basin average precipitation for that target region.

6 PHYSICALLY BASED STORM TRANSPOSITION OF FOUR TROPICAL CYCLONES

6.1 Introduction

The design of a large structure, such as a dam or a nuclear plant located near a stream, requires estimating how large a flood can be at its specific location. Several methods have been proposed for such an estimation. In most cases flood frequency analysis (FFA) is the preferred approach. FFA analysis uses historical measured data, sometimes combined with paleoflood data[5], in order to reconstruct the flood frequency curve at a specific location along a stream. The frequency of extreme floods is then estimated by extrapolating the flood frequency curve for a return period beyond the available data by the use of some statistical distribution. Another approach for the design of large structures is to determine the Probable Maximum Flood (PMF), which represents the potential maximum runoff resulting from the most severe combination of hydrological and meteorological conditions that are considered reasonably possible for a particular drainage basin (Shalaby, 1994). As extreme floods are usually triggered by extreme precipitation, it is legitimate to start the investigation of extreme floods by looking for the most extreme precipitation events that can occur over the basin containing the structure. As a result, hydrologists and meteorologists developed the concept of Probable Maximum Precipitation (PMP), which is the greatest depth of precipitation for a given duration meteorologically possible for a design watershed or a given storm area at a particular location at a particular time of year, with no allowance made for long-term climatic trends (World Meteorological Organization (WMO), 2009). The most widely used methods of PMP estimation are (WMO, 2009):

a) The local method (local storm maximization or local model);

b) The transposition method (storm transposition or transposition model);

c) The combination method (temporal and spatial maximization of storm or storm combination or combination model);

d) The inferential method (theoretical model or ratiocination model);

e) The generalized method (generalized estimation);

f) The statistical method (statistical estimation).

These methods have been used for several decades in order to provide PMP estimates in several countries including the United Stated (Hershfield, 1961; Hershfield, 1965; Corrigan et al., 1999), China (Zhan and Zhou, 1984), India (Rakhecha and Soman, 1994; Kulkarni et al., 2010), Thailand (Tingsanchali and Tanmanee, 2012), and Spain (Casas et al., 2008; Casas et al., 2011). The main advantage of these methods is that they are in general relatively simple to apply and do not require significant computational resources. However, there are several drawbacks to using these methods. Some of these methods, such as Hershfield (1961)'s statistical method, strongly depend on observation data. According to Nobilis et al. (1991), Hershfield's method misestimates PMP values if the observation data include outliers. Furthermore, according to Koutsoyiannis (1999), there is no plausible reason to consider the estimates from Hershfield's statistical method as PMP values as these estimates show no

[5] Paleoflood hydrology is the reconstruction of the magnitude and frequency of recent, past, or ancient floods using geological evidence (Kochel and Baker, 1982). This includes erosional landforms, sediments, damage to vegetation and high-water marks.

evidence of the upper limit of precipitation. Other methods are more physically based but tend to make unjustified simplifications. For example, the transposition method assumes that it is possible to identify a “meteorologically homogeneous region” around the target area which sets the transposition limits, so that, if a given storm occurred in this region, its precipitation field may be transposed to the target area for the purpose of PMP estimation. The application of the storm transposition method can be flawed to the extent that the transposed precipitation field is usually significantly different from the original precipitation field in terms of its structure and intensity, as is shown in this study for the case of TCs. Another example is the generalized estimation, which involves a moisture maximization step. The moisture maximization model is a linearized meteorological model that maximizes severe precipitation by the ratio of the maximum to the actual precipitable water. Precipitable water is calculated using persisting 12-hr or 24-hr dew points at the surface based on the assumption of a saturated pseudo-adiabatic atmosphere (WMO, 2009). The application of this moisture maximization method can be flawed to the extent that the relationship between precipitable water and dew point temperature at the surface is nonlinear (Abbs, 1999).

Recently, new methods for the estimation of the PMP have been developed. Ohara et al. (2011), Ishida et al. (2014) and Ishida et al. (2015) proposed a physically based approach for the estimation of the PMP, which they called “maximum precipitation” (MP) to distinguish it from the traditional PMP. In this approach, they used a RAM to reconstruct, through DD, the precipitation fields associated with intense atmospheric rivers[6] in California. Contrary to the traditional PMP approaches mentioned previously, their method has the advantage of conserving the mass, momentum and energy in the simulation domains, since the atmospheric model solves numerically the governing equations for the conservation of these quantities. Using a RAM also allows taking into account explicitly the effects of certain features that may generate extreme precipitation over a given area. For instance, RAMs explicitly account for the topography, which has been shown to play a major role in the generation of heavy rainfall in certain geographical regions (Wu et al., 2002; Ge et al., 2010; Lin et al., 2010).

The maximization of the precipitation from atmospheric rivers over a target basin (Ohara et al., 2011; Ishida et al., 2014; Ishida et al., 2015) consists of 1) shifting the atmospheric state variables at the boundaries of the simulation outer domain, and 2) setting the relative humidity at the boundaries of the simulation outer domain to 100%. The first step (shifting) brings the storm over the target area, while the second step (moisture maximization) further maximizes the precipitation over this target area. Ishida et al. (2014) (2015) successfully applied this method to three watersheds in Northern California, subject to intense precipitation from atmospheric rivers. This physically based precipitation maximization method through the shifting of the BCs is well suited for the maximization of precipitation from atmospheric rivers because the simulation of atmospheric rivers is essentially a boundary value problem: the severe conditions responsible for intense precipitation such as large moisture transport penetrate the simulation outer domain through the boundaries. On the other hand, several studies (e.g. Zou and Xiao, 2000; Wu, 2001) have emphasized the importance of using a realistic initial vortex for the numerical simulation of a TC. To this extent, the simulation of a TC is more of an initial value problem than it is a boundary value problem. As such, this chapter presents a new method for the storm transposition of TCs.

To the authors’ knowledge, this is the first study investigating a physically based method to maximize the precipitation from a TC over a given target area in the eastern United States. Lee et al. (2017) investigated the effects of increasing the sea temperature and maximizing the moisture at the domain’s boundaries on the precipitation caused by Hurricane Rusa (2002) in

[6] An atmospheric river is a narrow corridor of concentrated moisture in the atmosphere.

Korea. They showed that the storm simulated within the aforementioned framework (i.e. increased sea temperature and increased moisture at the boundaries) produced significantly more rainfall over Korea than the historical storm. However, an increase in the precipitation depth over the target area due to an increase in temperature and boundary moisture may occur only if the original TC already spawned significant precipitation over this target area, as it is the case for Hurricane Rusa over Korea. In the case where the original TC did not affect the target area, increasing sea temperature and boundary moisture is unlikely to move the storm to the target area. As a result, in the general case, modifying sea temperature and moisture at the model's boundaries cannot answer the question: what would have happened if a given TC passed over a specified target area?

Therefore, in this study, precipitation from a TC over a target watershed is maximized by shifting the initial vortex of the TC. Emphasis is put on precipitation because of its importance in the design of large structures such as dams and nuclear plants, and because it is the subject of this project. However, the transposition method proposed in this report can also be used to investigate what would have been the wind field or any other atmospheric field if the TC happened to pass over the target area. It is shown that, due to the nonlinearity in the dynamics of a TC, a very small shift of the initial vortex can result in a significant change in the track of the storm, sometimes by several hundreds of kilometers, allowing the intense precipitation field from an originally distant TC to move over the target area.

Section 6.2 provides the technical details regarding the transposition (i.e. shifting) of the initial vortex. Section 6.3 applies the transposition method to Hurricane Ivan (2004). Section 6.4 presents the results for the transposition of three other TCs, namely Hurricane Floyd (1999), Hurricane Frances (2004), and Hurricane Isaac (2012). Section 6.5 proposes a procedure for the physically based estimation of the PMP for a target area for which intense precipitation is caused by TCs, as it is usually the case in the Eastern United States for a sufficiently large area[7]. Finally, Section 6.6 offers conclusions and perspectives.

6.2 Description of the TC Transposition Method

IBCs used for DD with a RAM are usually obtained from the output of coarse-resolution reanalysis atmospheric data or of a GCM. This section presents a method to shift the location of a TC in the ICs. The objective of this transposition is to modify the track of the storm so that its precipitation field moves over a specified target area.

The transposition of the TC in the ICs is performed by executing the following procedure:

1. Identify the location (x_c, y_c) of the center of low pressure;
2. Identify the radius R of the cyclone;
3. Remove the TC from the background atmospheric fields (geopotential height, wind velocity, relative humidity, surface pressure, etc.) by cutting off the inside of the circle of center (x_c, y_c) and of radius R from the original atmospheric fields;
4. Interpolate the background fields to the inside of the circle;

[7] According to Zurndorfer et al. (1986), the type of storm which will produce the rains of PMP magnitude over small basins (< 100 mi^2) in and near the Tennessee River Watershed is of the thunderstorm variety, whereas for larger basins (> 100 mi^2) the primary rain producing storms are more likely to be TCs or decadent TCs potentially interacting and combining with other systems.

5. Compute the perturbation fields by subtracting the background fields obtained in step 4 from the original fields. The perturbation fields are zero everywhere except inside the circle;
6. Shift the perturbation fields;
7. Add the shifted perturbation fields to the corresponding background fields obtained in step 4.

This procedure is illustrated in Figure 6-4 for the surface zonal wind velocity (i.e. for the x-component of the surface wind field) in Hurricane Ivan (2004). In practice, the storm will not be perfectly axisymmetric so that the radius *R* in step 2 may be defined as the radius of the circle that contains the region of influence of the TC. The size of this region of influence can vary from one atmospheric field to another (e.g. wind velocity field vs. temperature field) as well as with height (e.g. surface wind field vs. wind field on the 500 mbar surface).

The transposition method assumes that it is possible to separate the contribution of the TC from its background environment. Ideally, the shifting exercise should be performed while the TC is still over the ocean, far from land and especially from its location of landfall. Furthermore, the shifting exercise should be performed before the TC starts its ET, in which case the system starts developing characteristic features such as high asymmetry, loss of warm core, fronts, tilt away from vertical, expansion of the wind field, and strong interaction with the midlatitude westerlies and possibly with extratropical systems (Chan and Kepert, 2010). After a TC starts its ET, it may be difficult to assess what part of the field is due to the TC and what part of the field is due to other systems.

On the other hand, if the shifting exercise is performed too early during the life cycle of the TC, the initial vortex may be too weak, which will impact the quality of the simulations and the intensity of the storm in its mature stage. As a consequence, one needs to be particularly careful in choosing the simulation start date so that the best compromise is found between the aforementioned restrictions regarding the initial TC.

The interpolation method used in step 4 is now described. Let us consider a given atmospheric field (e.g. the surface pressure field). The original field is denoted by F_1 and the field after transposition by F_2. The interpolation is performed by executing the following procedure:

1. Consider a square of side *2a* with *a* > *R* (Figure 6-1);
2. For every point (x_i,y_i) lying within the circle of center (x_c,y_c) and of radius *R*, that is to say the points for which $d_{ic} \equiv \sqrt{(x_i - x_c)^2 + (y_i - y_c)^2} \leq R$, go to step 3;
3. Assign to every point (x_o,y_o) lying within the square but outside the circle a weight inversely proportional to the distance between (x_o,y_o) and (x_i,y_i) . This weight can be computed as $w_o = \mathcal{N}\ [(x_o - x_i)^2 + (y_o - y_i)^2]^{-\frac{n}{2}}$ where $\mathcal{N}$ is a normalizing factor ensuring that the sum of the w_o is equal to 1 and n is an arbitrary positive constant;
4. Define $F_{tmp}(x_i, y_i) \equiv \sum_o\ w_o\, F_1(x_o, y_o)$ where the summation is over all points (x_o,y_o) identified in step 3, that is to say the points lying within the square but outside the circle;
5. Compute $F_2(x_i, y_i) =\ \alpha\, F_{tmp}(x_i, y_i) +\ (1 - \alpha)\, F_1(x_i, y_i)$.

The last step is a smoothing step ensuring that the interpolated field inside the circle matches smoothly with the original field outside the circle. In this study, $a = 1.1\ \times R$ and n =6 were used. Besides α was chosen such that α = 1 if $d_{ic} \leq 0.75\,R$ and $\alpha = \exp\left(-\frac{d_{ic} - 0.75\,R}{R}\right)$ if $d_{ic} > 0.75\,R$.

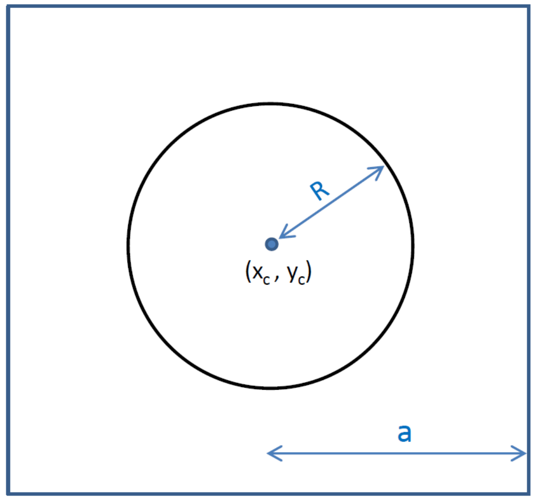

Figure 6-1 Configuration Used for the Interpolation of the Background Atmospheric Fields

The black circle of center (x_c,y_c) and of radius *R* is the region of influence of the TC. The blue square of side 2*a* is the region used to reconstruct the background fields inside the circle through interpolation.

6.3 Transposition of Hurricane Ivan (2004)

According to Stewart (2004), Ivan was a classical, long-lived Cape Verde hurricane. It reached Category 5 strength three times on the SSHS, and was the strongest hurricane on record that far south east of the Lesser Antilles. It caused considerable damage and loss of life as it passed through the Caribbean Sea. Ivan made landfall as a Category 3 hurricane just west of Gulf Shores, Alabama on September 16th, 2004. It spawned heavy precipitation ranging from 76-178 mm (3-7 in.) in depth along a large swath from Alabama and the Florida panhandle northeastward across the eastern Tennessee Valley and into the New England area (Figure 6-8c).

In this study, Hurricane Ivan was simulated with the WRF model (Skamarock and Klemp, 2008) (Version 3.7). No observation was used for nudging or DA (since the location of the storm is modified in the ICs), so that the model was only subject to the influence of the IBCs. The IBCs were obtained from CFSR. CFSR is produced by the U.S. NWS/NCEP at 0.5° x 0.5° (56 km x 56 km) spatial resolution and 6-hr temporal resolution. Three nested domains were used for the simulations (Figure 6-2). The spatial resolution of the outer (i.e. parent) domain, intermediate domain, and inner domain are 45 km, 15 km, and 5 km, respectively. The outer domain is composed of 160 x 120 nodes (zonal direction x meridional direction) while the intermediate domain is composed of 154 x 151 nodes and the inner domain is composed of 256 x 238 nodes.

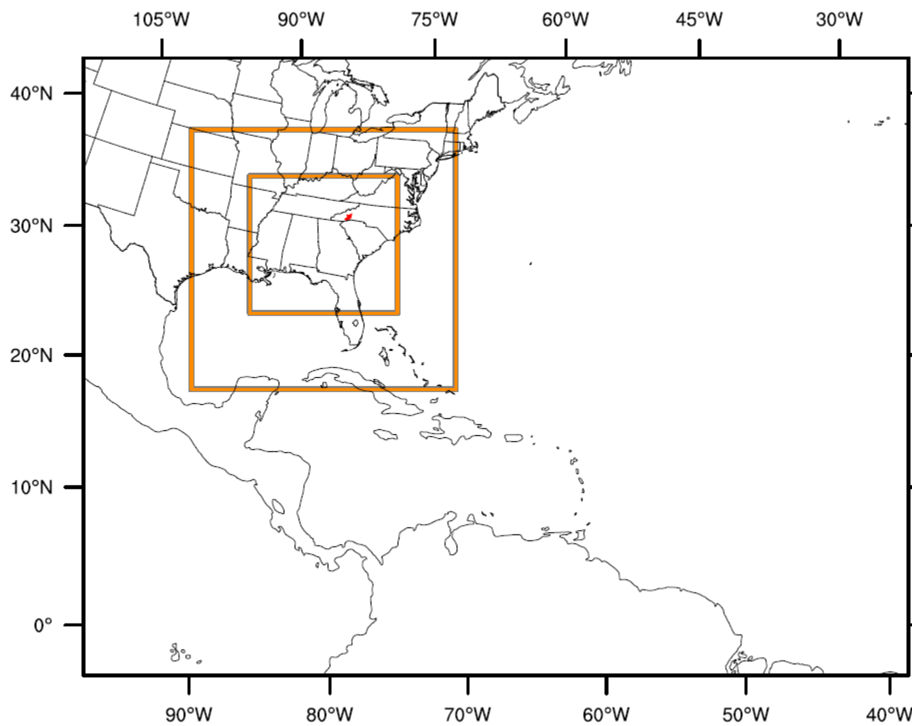

Figure 6-2 Nested Domains Used for the Simulations of Hurricane Ivan

The small red area in western North Carolina is the target watershed, presented in Figure 6-3.

Two-way nesting was used for the simulations, meaning that the different domains (outer, intermediate and inner) are run simultaneously and communicate with each other. The top of the model in the vertical extent was taken at 50 mbar, with a total of 38 vertical layers, and a time step of 3 minutes was used. A simple 1-dimensional ocean mixed layer model was used following that of Pollard et al. (1972). The parameterization schemes used for the simulations of Hurricane Ivan are given in Table 6-1. This combination of the parameterization schemes comes from the calibration of the WRF model for the reconstruction of Hurricane Ivan, which is discussed in Section 4.3.4 . Cumulus parameterization was used only in the outer and intermediate domains. The simulation start date is 09/06/2004 00:00 UTC. At that time, Hurricane Ivan was located off the coasts of French Guiana and Suriname (see Figure 6-4 and Figure 6-5).

Table 6-1 Parameterization Schemes Used for the Simulation of Hurricane Ivan

Parameterization	Scheme Name
Microphysics	WRF Double Moment 6-class (WDM6)
Cumulus Parameterization (domains 1 and 2 only)	New Simplified Arakawa-Schubert (SAS)
PBL	Mellor-Yamada-Janjic (MYJ)
Longwave Radiation	Rapid Radiative Transfer Model (RRTM)
Shortwave Radiation	Dudhia
Land Surface	Unified Noah Land Surface Model
Surface Layer	Eta Similarity Scheme

The target area selected for this study is the drainage basin of the city of Asheville in North Carolina (Figure 6-3). This watershed has a surface area of approximately 2,400 km^2 (930 mi^2) and contains 88 nodes of the model's inner domain. It lies within the region of influence of TCs (Zurndorfer et al., 1986). In fact, both TCs making landfall along the Gulf Coast and TCs making landfall along the Atlantic Coast can affect this watershed.

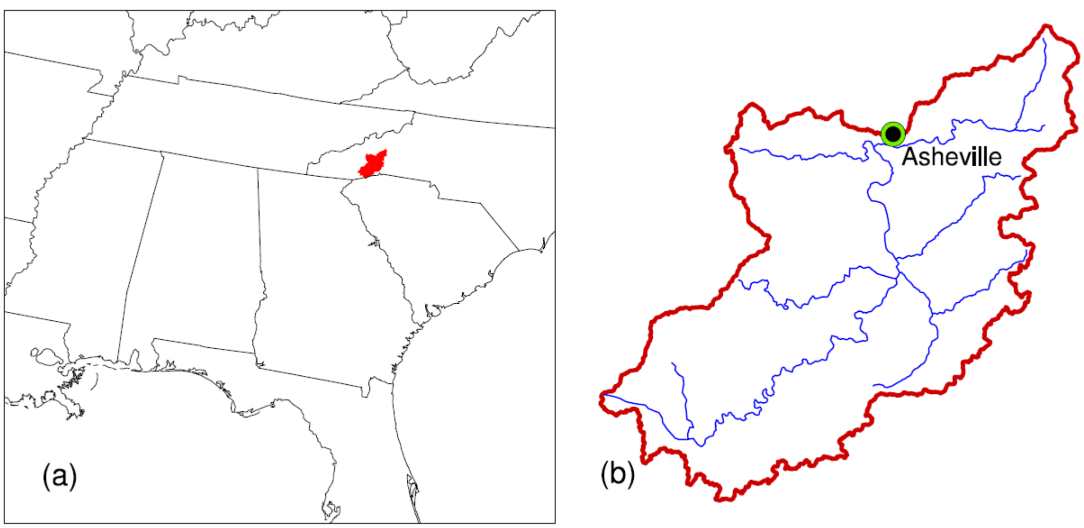

Figure 6-3 Target Area Used for the Transposition

(a) The target area is shown in red within the model's inner domain. (b) The target area corresponds to the drainage basin of the city of Asheville, N.C.

As an illustration of the transposition method, Figure 6-4 shows the transposition of the surface zonal wind velocity in Hurricane Ivan for an amount of shift of 0.95° E and 4.10° N. The predominance of the red and green colors in the top most plot shows that the storm is initially embedded within the trade winds[8]. As expected for a TC, the perturbation zonal wind field clearly exhibits a dipolar nature as can be seen in the right and bottom-right plots in Figure 6-4.

8 The trade winds are prevailing easterly winds that circle the Earth near the equator.

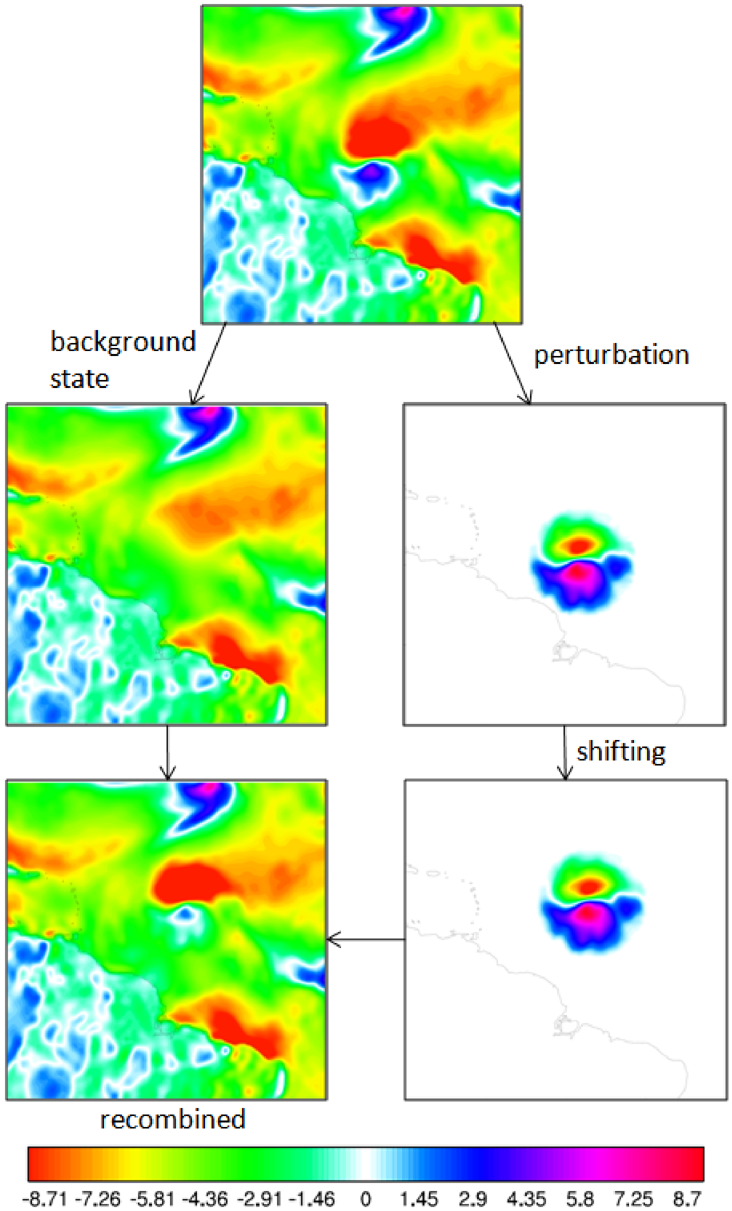

Figure 6-4 Application of the Transposition Procedure to the Initial Surface Zonal Wind Velocity (m s^{-1}) in Hurricane Ivan (2004)

Hurricane Ivan was transposed in a direction orthogonal to its direction of propagation at the simulation start date (Figure 6-5). The transposition exercise was first performed for 29 increments of shift (including zero shift), from 1.67° W and 7.18° S to 1.67° E and 7.18° N, which corresponds to the black dots in Figure 42. The WRF model was run for each of these amounts of shift, and the maximum 72-hour (3-day) accumulated precipitation over the target watershed, which corresponds to the 72-hr time window that contains the largest basin average precipitation depth, was calculated for every simulation. Results for this first step are presented in Figure 6-6. Note that the shifting results are represented by plotting them only against the West-East component of the shift that occurs along the line of black dots shown in Figure 6-5. As such, the *x*-axis of Figure 6-6a ranges from 1.67° W to 1.67° E. From this figure, it is observed that as the amount of shift increases from 1.67° W and 7.18° S, the 72-hr basin average precipitation depth suddenly increases from about 2 mm (0.1 in.) for an amount of shift of 1.19° W and 5.13° S to 310 mm (12.2 in.) for an amount of shift of 1.07° W and 4.61° S. The 72-hr basin average precipitation depth remains larger than 100 mm (3.9 in.) until the amount of shift is increased over 0.71° E and 3.08° N for which the 72-hr basin average precipitation depth drops to about 11 mm (0.4 in.).

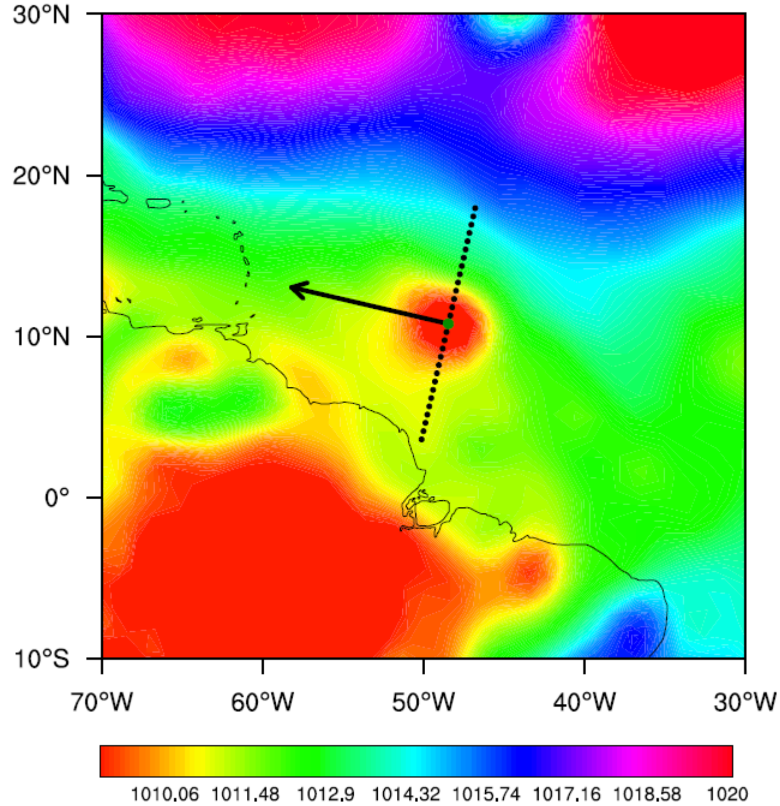

Figure 6-5 The Color Plot Shows the Mean Sea-Level Pressure (SLP) Field (mbar) on 09/06/2014 00:00 UTC (from CFSR) for Zero Shift

The green point shows the location of the center of low pressure in the original TC (zero shift). The black points show the location of the center of low pressure after shifting. The black arrow indicates the direction of propagation of Hurricane Ivan.

Figure 6-6a shows that the shifting window from 1.07° W and 4.61° S to 0.60° E and 2.56° N corresponds to the amounts of shift for which the target watershed is affected by the intense part of the precipitation field spawned by Hurricane Ivan. The two largest 72-hr basin average precipitation depths occurred for an amount of shift of 1.07° W and 4.61° S, for which it is 310 mm (12.2 in.), and for an amount of shift of 0.24° W and 1.02° S, for which it is 234 mm (9.2 in.).

The second step of the maximization procedure (through storm transposition) is to refine around the local maxima obtained in the previous step. This refinement was performed by considering the increments of shift halfway between the local maxima and the neighboring increments of shift. The results for the two aforementioned maxima of the 72-hr basin average precipitation depth are presented in Figure 6-6b. The first refinement confirms that the first peak of the 72-hr basin average precipitation occurring for an amount of shift of 1.07° W and 4.61° S is larger than the peak associated with an amount of shift of 0.24° W and 1.02° S. As a result, the last refinement presented in Figure 6-6c is performed only around the first peak. As many refinement steps as necessary can be carried out. In the case of the transposition of Hurricane Ivan, Figure 6-6 shows that the maximum 72-hr basin average precipitation depth does not change appreciably from the second refinement step to the third refinement step. As a result, an estimation of the maximum 72-hr basin average precipitation depth that Hurricane Ivan could have caused over the Asheville watershed (if it had passed over this area) is given by the red diamond in Figure 6-6c and it is equal to approximately 348 mm (13.7 in.).

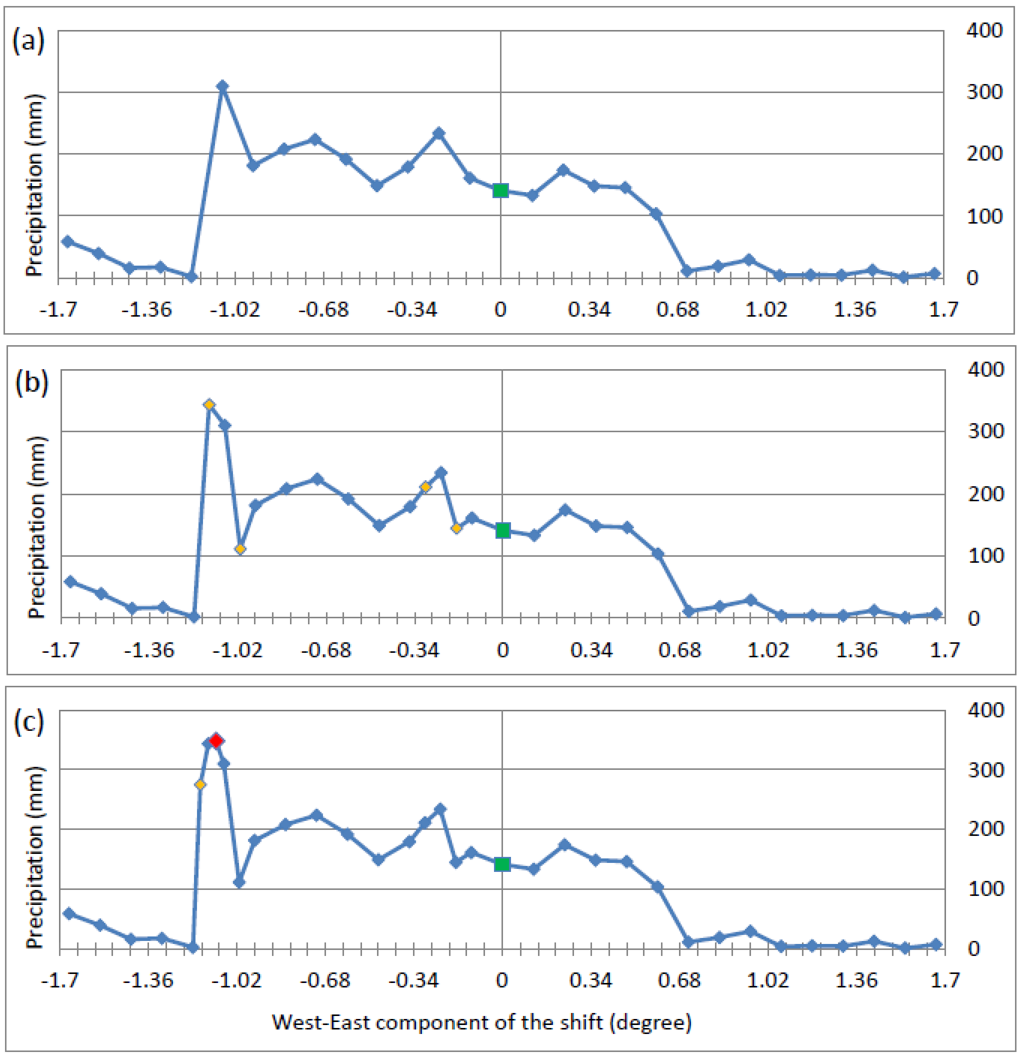

Figure 6-6 **72-hr Basin Average Precipitation Depth as a Function of the West-East Component of the Shift Along the Transect Shown in Figure 6-5**

(a) Results for the 29 increments of shift first considered (Figure 6-5). (b) Results after the first refinement. (c) Results after the second refinement. The green square gives the 72-hr basin average precipitation depth in the case of no shift. The yellow diamonds show the refinement performed around the local maxima. The red diamond in (c) indicates the maximum 72-hr basin average precipitation depth.

Figure 6-7 shows that Hurricane Ivan responds nonlinearly to the transposition of its ICs. Indeed the location of the precipitation field does not change homogeneously as the amount of shift is increased from 1.67° W and 7.18° S to 1.67° E and 7.18° N. For example, the 72-hr accumulated precipitation field corresponding to an amount of shift of 1.07° W and 4.61° S (third plot on Row 2 in Figure 6-7) is located east of the 72-hr accumulated precipitation field corresponding to an amount of shift of 1.01° W and 4.36° S (fourth plot on Row 2 in Figure 6-7). This behavior explains the presence of multiple peaks in the graphs of the 72-hr basin average precipitation depth as a function of the zonal component of the shift presented in Figure 6-6. This nonlinear response of the TC's track to a change in location of the initial vortex is even more striking in the case of Hurricane Frances presented in Section 6.4.

Figure 6-7 also shows that the simulated precipitation field in the case of zero shift (third plot on Row 4) is located east of the observed precipitation field (Figure 6-8c). Given 1) the strong nonlinearity involved in the dynamics of a TC, 2) the fact that no nudging and DA were used, and 3) the early simulation start date (about ten days before the time of landfall), it is not expected that the numerical model manages to reproduce accurately the track of the TC, including the time and location of landfall. Therefore, in order to place the simulated precipitation field in the right location, it is necessary to use a later simulation start date, as was done for the calibration of the WRF model discussed in Section 4 for which the simulation start date was only two days before the time of landfall.

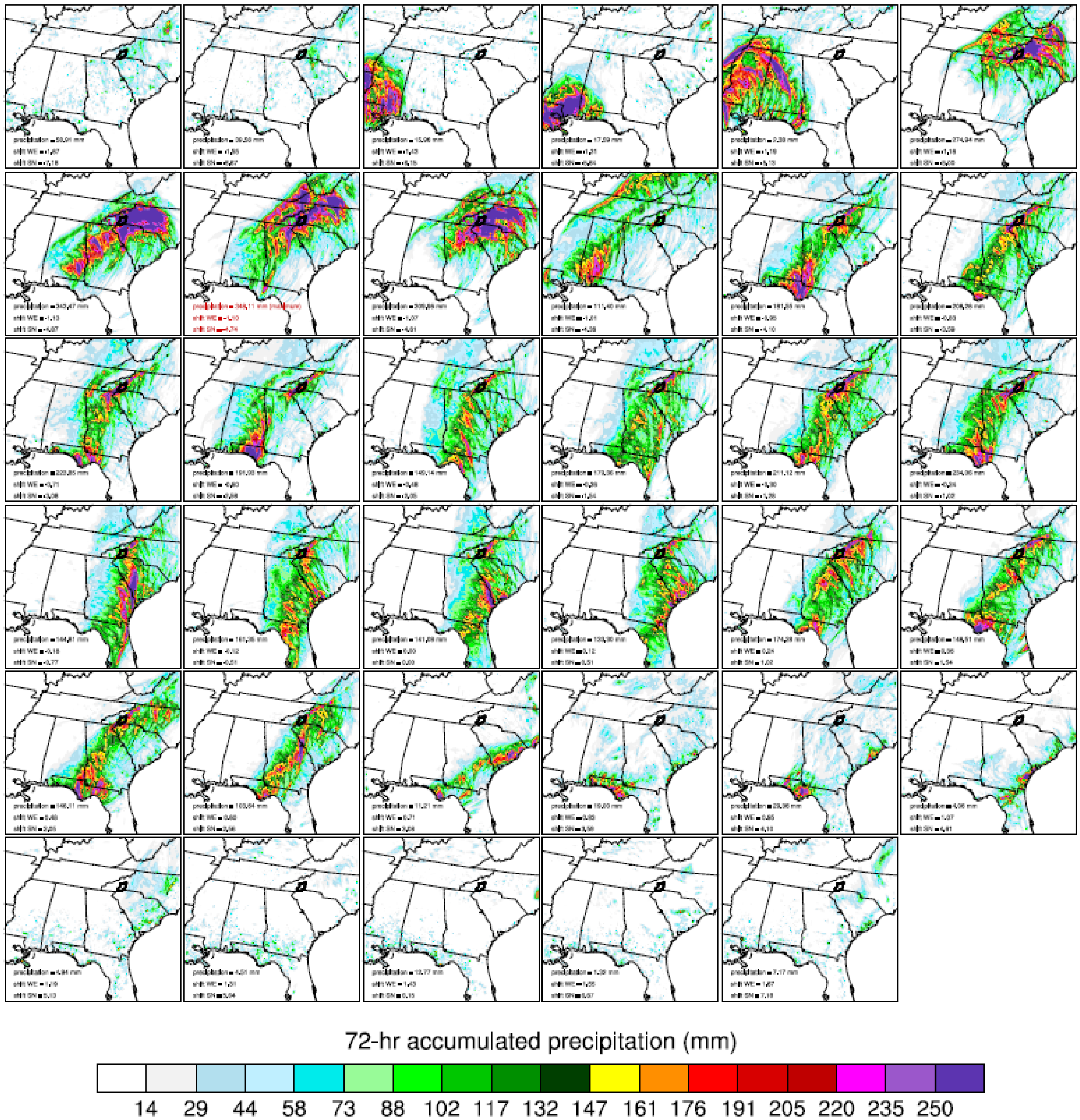

Figure 6-7 72-hr Accumulated Precipitation Depth Field as a Function of the Amount of Shift

The first plot (top-left) corresponds to the most westerly and southerly shift (1.67° W and 7.18° S) while the last plot (bottom-right) corresponds to the most easterly and northerly shift (1.67° E and 7.18° N). The maximum 72-hr basin average precipitation depth is obtained for the 8th plot (second plot on Row 2).

Figure 6-8 compares the 7-day accumulated precipitation field (from 09/14 00:00 UTC until 09/21 00:00 UTC) for the simulation which maximized the 72-hr basin average precipitation depth to the observed 7-day accumulated precipitation field obtained from the NCEP Stage IV precipitation dataset (Lin and Mitchell, 2005)[9]. It is observed that the maximized precipitation field is overall significantly more intense than the observed field, which shows that the physically based transposition method does not result in a simple transposition of the storm's precipitation field, as it is often assumed in the traditional PMP approaches.

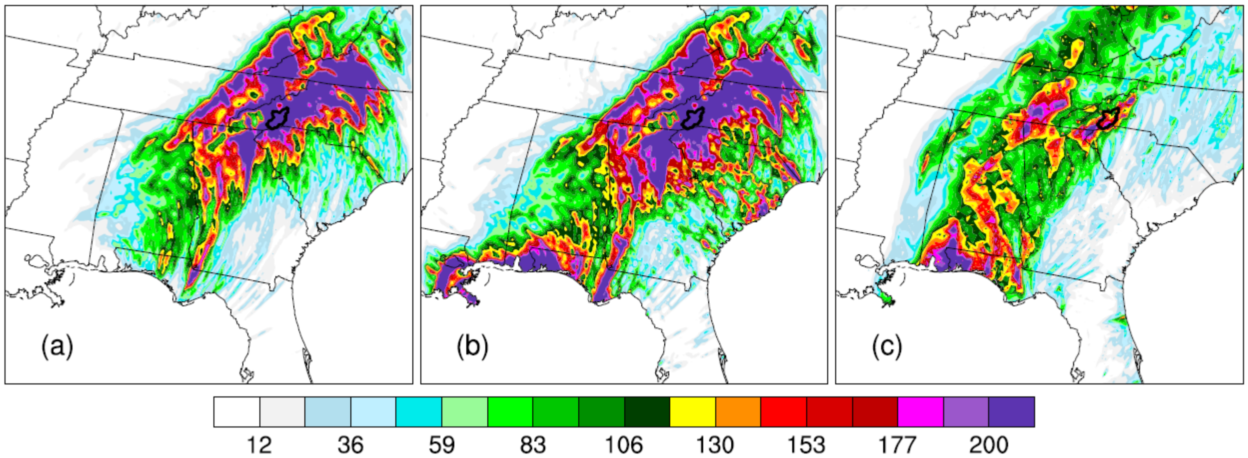

Figure 6-8 (a) 72-hr Accumulated Precipitation Depth (mm) Field (from 09/16 08:00 UTC until 09/19 08:00 UTC) for the Simulation Which Maximized the 72-hr Basin Average Precipitation Depth

(b) 7-day accumulated precipitation field (from 09/14 00:00 UTC until 09/21 00:00 UTC) for the simulation which maximized the 72-hr basin average precipitation depth. (c) Observed 7-day accumulated precipitation field (from 09/14 00:00 UTC until 09/21 00:00 UTC).

In order to explain the difference in intensity between the maximized precipitation field and the observed precipitation field, the time-averaged IVT field and its divergence were calculated for 1) the storm resulting from the maximization of the 72-hr basin average precipitation depth (corresponding to Figure 6-8b) and 2) the storm resulting from the calibration of the WRF model (corresponding to **Figure 4-16**b). Given the good agreement between the observed precipitation field (Figure 6-8c) and the precipitation field of the storm resulting from the calibration (**Figure 4-16**b), the simulated moisture transport field (in calibration) is expected to be close to the moisture transport field of the original (i.e. observed) storm.

Results are presented in Figure 6-9. The vector field shows the IVT averaged over the period from 09/14 00:00 UTC until 09/21 00:00 UTC. The associated color plot gives the divergence of the time-averaged IVT field. Positive values indicate a decrease of the mass of water vapor contained in an atmospheric column whereas negative values indicate an increase in the mass of water vapor contained in an atmospheric column. Comparing Figure 6-9a with Figure 6-8b on the one hand, and Figure 6-9b with **Figure 4-16**b on the other hand, it is obvious that the regions of intense precipitation coincide with the regions where the convergence (the negative of the divergence) of the IVT is maximized. As a result, the local increase of water vapor in the atmosphere through convergence of the IVT is likely to have played a major role in the generation of intense precipitation in Hurricane Ivan. Interestingly, the magnitude of the IVT in the storm resulting from the maximization is only slightly larger than the magnitude of the IVT in

[9] Stage IV is a NCEP-generated mosaic of regional multi-sensor precipitation analysis produced by National Weather Service River Forecast Centers (RFCs) since 2002

the storm resulting from the calibration. In particular, around the target area and downstream from the target area, both magnitudes are approximately the same. As a consequence, the significant increase in the intensity of the precipitation field in Hurricane Ivan between the maximized case and the calibrated case seems to be due to an increase of the convergence of the IVT rather than to an increase of the magnitude of the IVT.

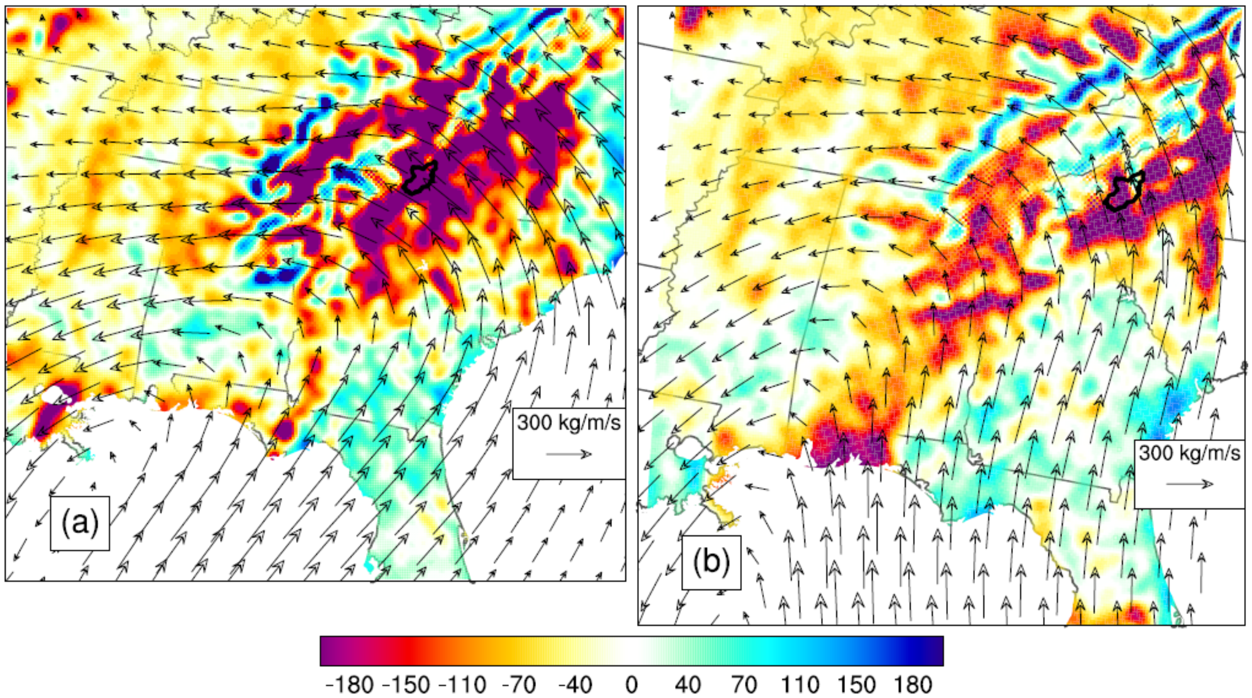

Figure 6-9 Arrow Field: Time-Averaged (from 09/14 00:00 UTC to 09/21 00:00 UTC) Integrated Vapor Transport (kg m^{-1} s^{-1})

Color plot: Divergence of the time-averaged integrated vapor transport field (mm) for (a) the simulation which maximized the 72-hr basin average precipitation depth from Hurricane Ivan and (b) the simulation resulting from the calibration of the WRF model.

6.4 Transposition of Hurricanes Floyd (1999), Frances (2004) and Isaac (2012)

In this section, the transposition method is applied to three other TCs that generated torrential precipitation in the United States: Hurricane Floyd (1999), Hurricane Frances (2004), and Hurricane Isaac (2012). The WRF model's options and the simulation start dates used for the simulations of these TCs are given in Table 6-2. They were selected based on the calibration of the model discussed in Section 4. Other modeling choices (time step, number of vertical layers, etc.) are the same as for Hurricane Ivan as discussed at the beginning of Section 6.3. IBCs are from CFSR. The nested domains used for the simulation of Hurricane Isaac are the same as for Hurricane Ivan. In the case of Hurricanes Floyd and Frances, the intermediate and inner domains were taken slightly more east in order to account for the location of the precipitation fields in the original storms.

Table 6-2 WRF Options and Simulation Start Dates Used for the Simulations of Hurricanes Floyd, Frances and Isaac

	Floyd	Frances	Isaac
Microphysics	WRF Double Moment 6-class (WDM6)	Stony-Brook University Scheme (SBU-YLin)	Lin (Purdue)
Cumulus Parameterization (domains 1 and 2 only)	New Simplified Arakawa-Schubert (SAS)	Betts-Miller-Janjic	Grell-Devenyi
PBL	Bougeault-Lacarrere (BouLac)	Bougeault-Lacarrere (BouLac)	Yonsei University Scheme (YSU)
Longwave Radiation	GFDL	Rapid Radiative Transfer Model for General Circulation Models (RRTMG)	Rapid Radiative Transfer Model (RRTM)
Shortwave Radiation	GFDL	Rapid Radiative Transfer Model for General Circulation Models (RRTMG)	Dudhia
Land Surface	Rapid Update Cycle (RUC) Land Surface Model	Rapid Update Cycle (RUC) Land Surface Model	Unified Noah Land Surface Model
Surface Layer	Revised MM5 Similarity Scheme	Revised MM5 Similarity Scheme	MM5 Similarity Scheme
Simulation start date	09/11 00:00 UTC	08/30 00:00 UTC	08/25 06:00 UTC

Figure 6-10 shows the location of the center of low mean SLP before transposition (corresponding to the green points) and after transposition (corresponding to the black points). In the case of Hurricane Ivan, Figure 6-7 shows that the precipitation field for zero shift (third plot on Row 4) already goes through the target watershed. This is the reason why the amounts of shift were considered symmetrically around zero for Hurricane Ivan (Figure 6-5). In the case of Hurricane Floyd, the precipitation field for zero shift is located significantly east of the target watershed (not shown), which explains why only negative amounts of shift (westerly and southerly) were considered for Hurricane Floyd (Figure 6-10a). In the case of Hurricane Frances, the precipitation field corresponding to zero shift is located slightly west of the target watershed (not shown), which explains why more positive (easterly and northerly) than negative (westerly and southerly) amounts of shift were considered (Figure 6-10b). Finally, in the case of Hurricane Isaac, the precipitation field corresponding to zero shift is located significantly west of the target watershed (not shown), which explains why positive amounts of shift (easterly and northerly) were predominantly considered (Figure 6-10c).

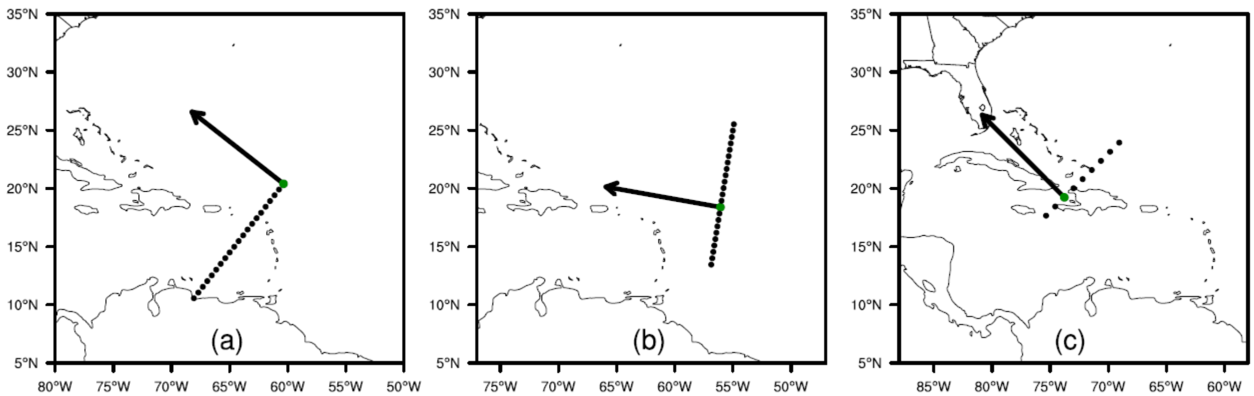

Figure 6-10 Location of the Center of Low Mean SLP in the ICs Before Shifting (Green Point) and After Shifting (Black Points) for (a) Hurricane Floyd, (b) Hurricane Frances and (c) Hurricane Isaac

The black arrows show the direction of storm propagation.

The results for the transposition of these three hurricanes are presented in Figure 6-11. Figure 6-11 shows the 72-hr basin average precipitation depth as a function of the zonal component of the shift. The y-axis represents the precipitation depth of the 72-hr time window for which the precipitation over the target is the largest for each simulation.

It is observed that the results for the transposition of Hurricanes Floyd and Isaac (Figure 6-11a and c) are similar to the results for the transposition of Hurricane Ivan to the extent that the graphs of the 72-hr basin average precipitation depth as a function of the zonal component of the shift contain well defined peaks, and the maximum 72-hr precipitation depths (given by the red diamonds) were obtained through the refinement steps described in Section 6.3. However, the results are significantly different in the case of Hurricane Frances (Figure 6-11b). Indeed the graph of the 72-hr basin average precipitation depth as a function of the zonal component of the shift is very oscillatory. Actually, the refinement procedure failed in the case of Hurricane Frances. As refinement steps were performed, new peaks kept appearing in the graph and the existing peaks got narrower. As a result, it was necessary to use a much finer shifting increment for the whole shifting window from 0.077° W and 0.48° S to 0.65° E and 4.0° N in order to obtain Figure 6-11b.

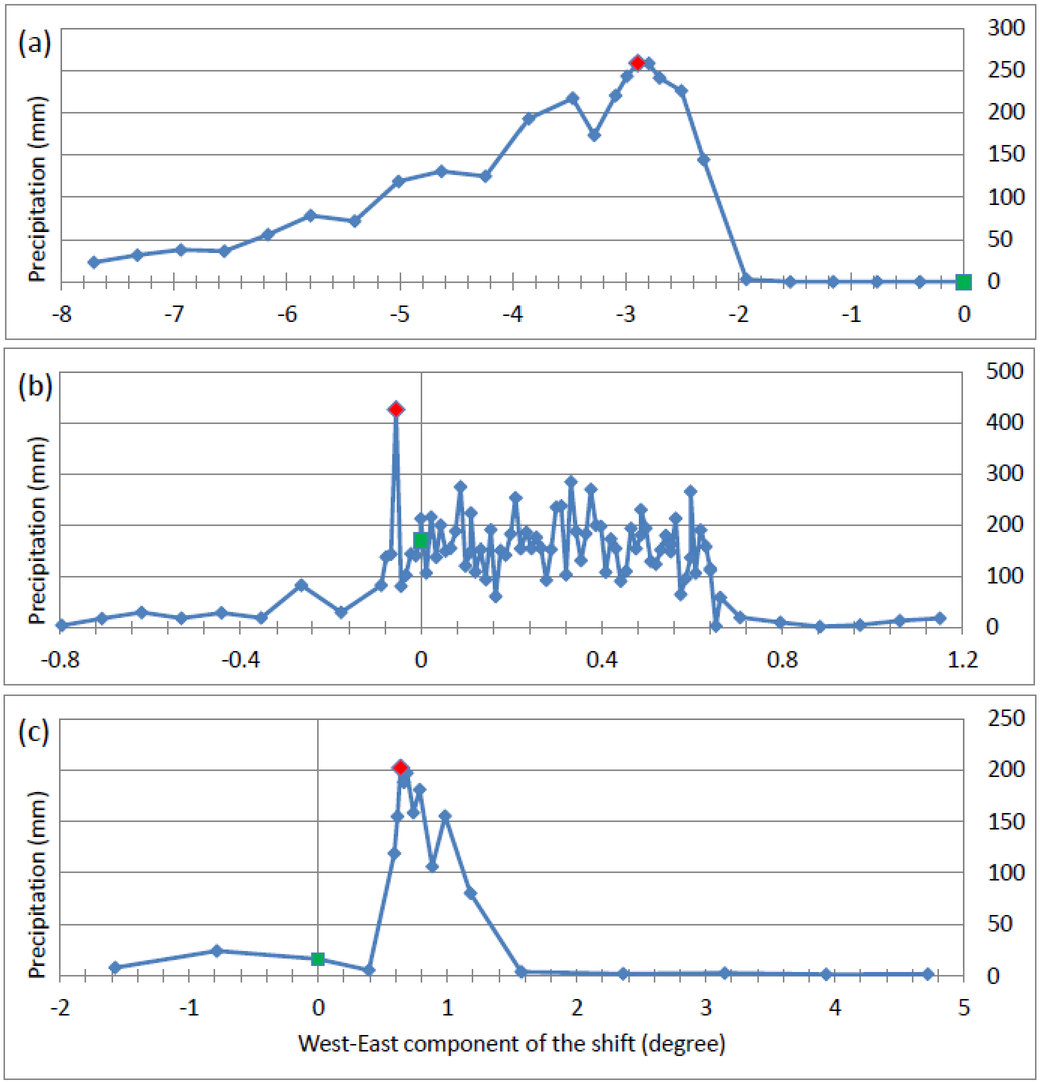

Figure 6-11 72-hr Basin Average Precipitation Depth as a Function of the Amount of Shift Along the Transects Shown in Figure 6-10 for (a) Hurricane Floyd, (b) Hurricane Frances, and (c) Hurricane Isaac

The green squares give the 72-hr basin average precipitation depth for zero shift. The red diamonds give the maximum 72-hr basin average precipitation depth.

The simulated track of Hurricane Frances was observed to be extremely sensitive to the location of the initial vortex. For example, Figure 6-12 shows the 7-day accumulated precipitation field (from 09/04/2004 00:00 UTC until 09/11/2004 00:00 UTC) and the track of the storm (given by the black dots) for the simulation which maximized the 72-hr basin average precipitation depth (Figure 6-12b), and for the simulations associated with a shifting amount slightly more south-west (Figure 6-12a), and slightly more north-east (Figure 6-12c) than for the maximized case. More precisely, the shifting amount for Figure 6-12a is 0.066° W and 0.41° S, whereas it is 0.055° W and 0.34° S for Figure 6-12b, and 0.044° W and 0.27° S for Figure 6-12c. As a result, only about 0.07° (~ 8 km) separates the initial vortex in the simulations corresponding to Figure 6-12a and Figure 6-12c from the initial vortex in the simulation corresponding to Figure 6-12b. Yet, it is striking to see how different the tracks are. The locations of landfall differ by more than 100 km between one case and another, causing the intense precipitation from Hurricane Frances to affect different regions. Furthermore, the track does not respond homogenously to the amount of shift of the initial vortex. Indeed, it would be expected for the track in Figure 6-12c to be located east of the track in Figure 6-12b since the initial vortex for the simulation corresponding to Figure 6-12b is located more west and south than the initial vortex for the simulation corresponding to Figure 6-12c. Not only the track of Hurricane Frances in Figure 6-12c is located west of the track in Figure 6-12b, but also it is located west of the track in Figure 6-12a, for which the initial vortex is even more west and south. Actually, the three tracks remain close to each other until Hurricane Frances approaches southeastern Florida (not shown). As Frances gets closer to southeastern Florida, and especially after landfall, a dramatic change is observed in the behavior of the track of the storm, leading to the results of Figure 6-12.

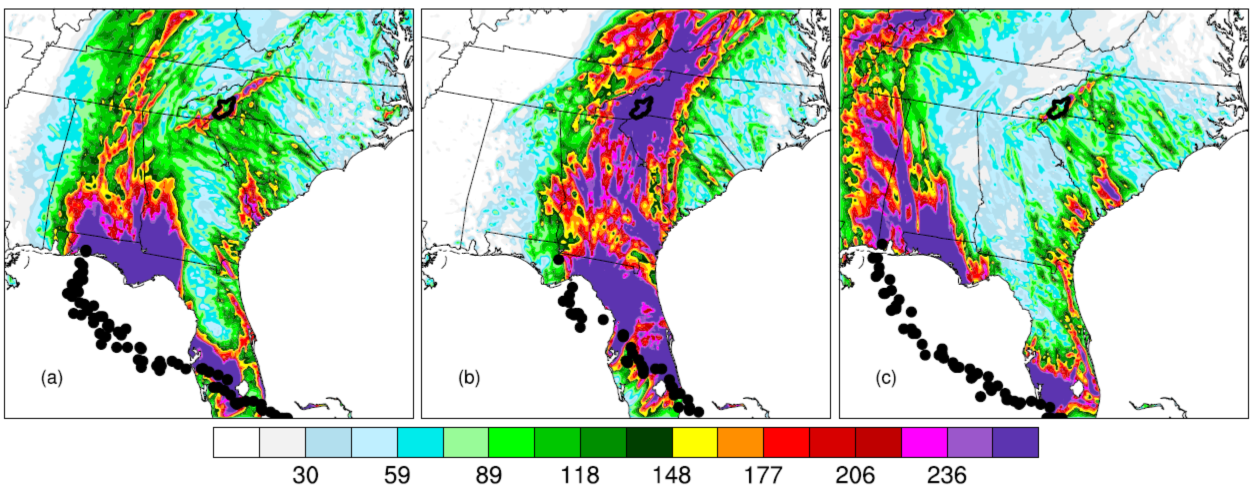

Figure 6-12 Illustration of the Sensitivity of the Track of Hurricane Frances to the Location of the Storm at the Simulation Start Date

The color plot gives the 7-day (from 09/04/2004 00:00 UTC until 09/11/2004 00:00 UTC) accumulated precipitation (mm) field in Hurricane Frances for (a) the simulation associated with an amount of shift of 0.066° W and 0.41° S; (b) the simulation which maximized the 72-hr basin average precipitation depth, corresponding to an amount of shift of 0.055° W and 0.34° S; and (c) the simulation associated with an amount of shift of 0.044° W and 0.27° S. The black dots show the location of the center of low surface pressure with an hourly time increment from 09/04/2004 00:00 UTC until the time of second landfall.

Figure 6-13, Figure 6-14 and Figure 6-15 present the precipitation fields (in the inner domain) for the simulations which maximized the 72-hr basin average precipitation depth (corresponding to the red diamonds in Figure 6-11) along with the observed precipitation fields for Hurricanes Floyd, Frances, and Isaac, respectively. In the case of Hurricanes Frances and Isaac, the observed precipitation fields were obtained from the NCEP Stage IV dataset, whereas the observed precipitation field for Hurricane Floyd (which occurred before the period of availability of Stage IV starting in 2002) was obtained from the National Oceanic and Atmospheric Administration (NOAA)[10].

Figure 6-14 shows that, for Hurricane Frances, the maximized precipitation field is overall significantly more intense than the observed precipitation field, as was the case for Hurricane Ivan. However, in the case of Hurricane Isaac (Figure 6-15), the maximized precipitation field is overall as intense as the observed precipitation field, whereas in the case of Hurricane Floyd (Figure 6-13) the maximized precipitation field is overall slightly less intense than the observed precipitation field. These results confirm that the transposition method does not lead to a simple transposition of the observed precipitation field over the target area. The intensity and structure of the transposed precipitation field depend on the new track of the TC, and on how the transposed TC interacts with its environment including the local topography and the presence of other synoptic and mesoscale systems. These interactions are explicitly accounted for by the RAM which crucially conserves the mass, momentum, and energy.

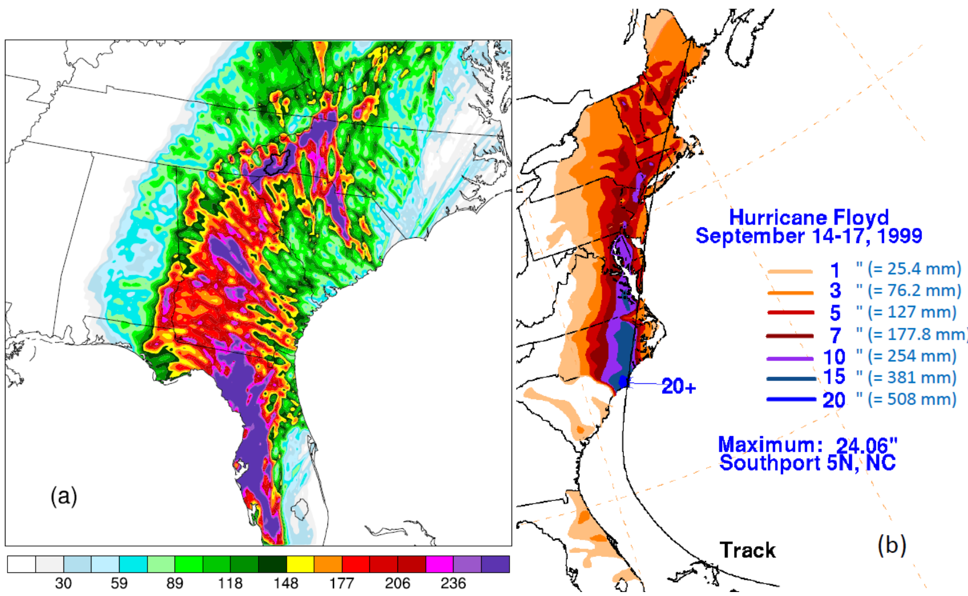

Figure 6-13 (a) 72-hr (from 09/15/1999 06:00 UTC until 09/18/1999 06:00 UTC) Accumulated Precipitation (mm) Field in Hurricane Floyd for the Simulation which Maximized the 72-hr Basin Average Precipitation Depth

(b) Observed 72-hr (from 09/14/1999 00:00 UTC until 09/17/1999 00:00 UTC) accumulated precipitation field in Hurricane Floyd (adapted from NOAA http://www.wpc.ncep.noaa.gov/tropical/rain/floyd1999.html)

10 http://www.wpc.ncep.noaa.gov/tropical/rain/floyd1999.html

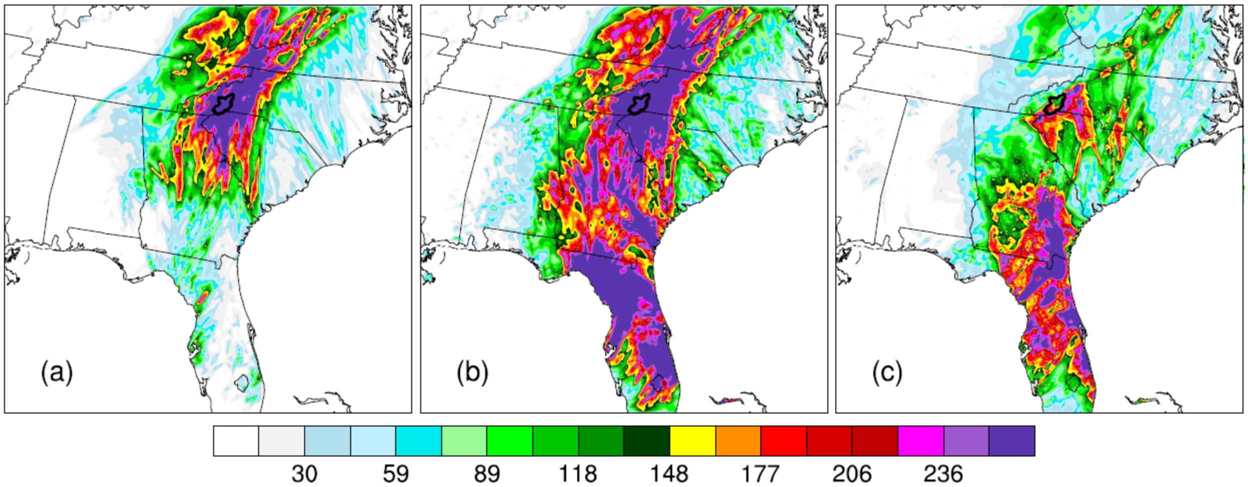

Figure 6-14 **(a) 72-hr (from 09/06/2004 23:00 UTC until 09/09/2004 23:00 UTC) Accumulated Precipitation (mm) Field in Hurricane Frances for the Simulation which Maximized the 72-hr Basin Average Precipitation Depth**

(b) 7-day (from 09/04/2004 00:00 UTC until 09/11/2004 00:00 UTC) accumulated precipitation field in Hurricane Frances for the simulation which maximized the 72-hr basin average precipitation depth. (c) Observed 7-day (from 09/04/2004 00:00 UTC until 09/11/2004 00:00 UTC) accumulated precipitation field in Hurricane Frances.

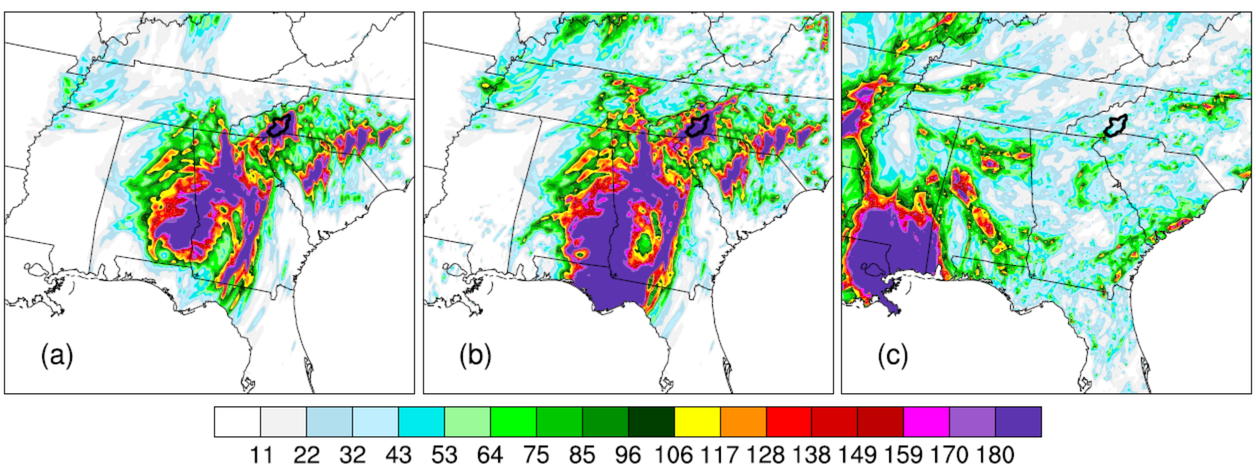

Figure 6-15 **(a) 72-hr (from 08/29/2012 12:00 UTC until 09/01/2012 12:00 UTC) Accumulated Precipitation (mm) field in Hurricane Isaac for the Simulation which Maximized the 72-hr Basin Average Precipitation Depth**

(b) 7-day (from 08/28/2012 12:00 UTC until 09/04/2012 12:00 UTC) accumulated precipitation field in Hurricane Isaac for the simulation which maximized the 72-hr basin average precipitation depth. (c) Observed 7-day (from 08/28/2012 12:00 UTC until 09/04/2012 12:00 UTC) accumulated precipitation field in Hurricane Isaac.

The maximum 72-hr basin average precipitation depth over the Asheville watershed obtained in this study from the maximization (through transposition) of the precipitation from four hurricanes is equal to 427 mm (16.8 in.). It resulted from the transposition of Hurricane Frances. Interestingly, this amount compares favorably with estimates obtained using the traditional approach. Zurndorfer et al. (1986) provided estimates of 1- to 72-hr PMP and Tennessee Valley Authority (TVA) precipitation for basins ranging between 5 and 3,000 mi^2 in the Tennessee Valley watershed. The TVA precipitation was defined as "the level of precipitation resulting from transposition and adjustment (without maximization) of outstanding storms". In this case, "maximization" refers to the moisture maximization step as discussed in the introduction. Their estimate of the 72-hr TVA precipitation for the drainage basin of the city of Asheville was 503 mm (19.8 in.), which is relatively close to the maximum 72-hr precipitation depth obtained from the numerical atmospheric model-based transposition of Hurricane Frances. However, their estimate for the 72-hr PMP was 869 mm (34.2 in.), which is about twice as large as the maximum 72-hr precipitation depth obtained from the physically based transposition of Hurricane Frances.

6.5 Procedure for the Physically Based Estimation of the PMP Through Numerical Transposition of TCs

In the previous sections, a new method to maximize the precipitation from a TC over a specified target area was presented and applied to four hurricanes that spawned torrential precipitation in the United States. The drainage basin of the city of Asheville was used as the target area. In this section, a procedure to estimate the PMP for a target area whose intense precipitation is caused by TCs is proposed, as it is usually the case for a sufficiently large[11] watershed in the eastern United States.

The first step is to identify the TCs that can potentially generate intense precipitation over the target area. It was shown previously that the track of a TC may be very sensitive to small changes in the location of the storm at the simulation start date, and that the response of the track to such changes may be highly nonlinear. As a result, a TC that affected a region far from the target may still be able to produce significant precipitation over the target after transposition. Similarly, a TC that did not originally make landfall may be brought over land and pass over the target after transposition. Thus most historical TCs should be considered, except for those for which it is obvious that a small shift of the initial vortex will not bring the TC over the target area. Let us write N_{TC} as the number of TCs selected in the first step.

Second, for each of these N_{TC} TCs, it is necessary to calibrate the WRF model in order to identify an appropriate set of the model's physics parameterization options. In this study, one set of options for each storm (Table 6-1 and Table 6-2) was considered. However, several sets of options may provide satisfactory calibration results. If this is the case, one should consider all the sets of the model's options that give satisfactory calibration results for a given TC in order to account for the model uncertainties. Let us write $N_{so}(i)$ the number of sets of options retained for the ith TC.

Ideally, the choice of the simulation start date should respect the restrictions emphasized in Section 6.2 including the facts that the TC in the ICs should be far enough from land, it should be intense enough, and it should not have started its ET. In this study, one simulation start date

[11] > 100 mi^2 according to Zurndorfer et al. (1986)

was considered for each event. For example, in the case of Hurricane Ivan, the simulation start date was 09/06/2004 00:00 UTC. However, in order to account for the uncertainties related to the ICs in the estimation of the PMP, one should consider as many simulation start dates as possible, making sure that they (ideally) satisfy the aforementioned restrictions. For example, in the case of Hurricane Ivan, since the CFSR data used for IBCs is provided with a temporal resolution of 6 hours, one may also consider the following simulation start dates: 09/05/2004 18:00 UTC, 09/06/2004 06:00 UTC, 09/06/2004 12:00 UTC, 09/06/2004 18:00 UTC, etc. Let us write $N_{ic}(i)$ as the number of simulation start dates retained for the i^{th} TC. Different reanalysis atmospheric datasets may also be used to account for uncertainties related to the IBCs.

An estimate of the PMP over the target area is obtained by applying the transposition method presented in this report to all the identified TCs and for all the corresponding sets of options and simulation start dates. This amounts to performing the transposition exercise N times where $N = \sum_{i=1}^{N_{TC}} N_{so}(i) \times N_{ic}(i)$. This corresponds to a significant computational effort. However, with today's technology, such a computational effort is feasible. Several recent studies reported on the application of the DD technique to the PMP estimation problem and other hydrological problems. For example, Ishida et al. (2014) maximized the 72-hr basin-average precipitation depth for 61 atmospheric rivers over three watersheds in California using the atmospheric BC shifting method discussed in the introduction. This amounted to thousands of simulations performed with MM5 with 4-level nested domains and spatial resolution from 81 km in the outer domain to 3 km in the inner domain. Trinh et al. (2016) simulated future flow conditions in the Cache Creek watershed in California over the 21st century. To achieve this objective, they dynamically downscaled to 3-km resolution thirteen climate projections from two GCMs under four emission scenarios and several ICs, and used these atmospheric state variables as input to the WEHY model, a physically based watershed hydrology model based on upscaled conservation equations (Chen et al., 2004a; Chen et al., 2004b; Kavvas et al., 2004).

Moreover, in this study, the shifting increment used in the transposition of the four hurricanes was relatively small. For example, 29 increments of shift were first considered for Hurricane Ivan. In practice, many TCs can be ruled out by performing the transposition exercise with a larger shifting increment. For example, one may first consider five increments of shift and check if the TC gets closer from the target. If this is not the case, this TC can be disregarded for the purpose of PMP estimation.

In the end, one obtains N realizations of a TC spawning intense precipitation over the target area. The PMP may be chosen as the largest 72-hr (or other duration) basin average precipitation depth among these N realizations. Besides, the proposed procedure offers a way to quantify the uncertainties associated with the PMP estimate due the uncertainties in the model and in the ICs. Suppose that the maximum precipitation depth over the target is obtained for the j^{th} TC. In this case, one may investigate the $N_{so}(j) \times N_{ic}(j)$ realizations of this storm in order to analyze how sensitive the maximized precipitation depth is to the model's options and to the initial environment.

Finally, it is noted that the proposed procedure for the estimation of the PMP can handle non-stationarity in the hydroclimate, which is not the case for the traditional approaches. Indeed, since it is physically based, the transposition method can be applied to future TCs, through DD of projections from GCMs, which would allow investigating how the PMP evolves as the climate changes.

6.6 Conclusion of Chapter 6

In this chapter, a storm transposition method designed for the transposition of TCs was presented. This method is physically based, as it uses a RAM to numerically simulate a TC and its precipitation field. As a result, it has the fundamental advantage of conserving the mass, momentum, and energy in the system since the RAM numerically solves the equations governing the conservation of these quantities. The storm transposition method is based on the shifting of the initial vortex of the TC at the simulation start date. More precisely, the TC in the ICs is first separated from its background environment, then shifted, and finally recombined with the background environment. The objective of this method is to find the amount of shift which maximizes the precipitation depth over a given target area. In this study, the transposition method was applied to four hurricanes that had spawned torrential precipitation in the United States, namely Hurricanes Floyd (1999), Frances (2004), Ivan (2004), and Isaac (2012). The drainage basin of the city of Asheville was selected as the target. It was found that the tracks of these TCs are generally very sensitive to changes in the location of the initial vortex, and that the response of the tracks to such changes is nonlinear. In particular, a small shift of the initial vortex can result in a significant change in the location, structure, and intensity of the precipitation field, thus putting into question both the legitimacy of the conventional transposition of the precipitation field from the TC (as is often the case in the traditional PMP approaches) and the existence of a meteorologically homogeneous region that sets the transposition limits. The precipitation fields resulting from the numerical atmospheric model-based maximization (through transposition) of Hurricanes Frances and Ivan are overall significantly more intense than the observed precipitation fields. The investigation of the IVT and its convergence in the case of Hurricane Ivan revealed that the increased intensity in the maximized precipitation field is due to an increase in the convergence of the IVT rather than to an increase in the magnitude of the IVT. In the case of Hurricane Floyd, the numerical atmospheric model maximized precipitation field was overall slightly less intense than the observed precipitation field, whereas for Hurricane Isaac, the maximized precipitation field was overall as intense as the observed precipitation field. The maximum 72-hr basin average precipitation depth resulting from the transposition of the four hurricanes was equal to 427 mm (16.8 in.). It compares favorably to the 72-hr TVA precipitation obtained by the generalized method (Zurndorfer et al., 1986) which is equal to 503 mm (19.8 in.), but remains about half of the 72-hr PMP obtained with the generalized method which is equal to 869 mm (34.2 in.). Finally, a procedure is proposed for the physically based estimation of the PMP over a given target area based on the transposition method. Preferably, the transposition exercise should be performed using different sets of the RAM's options, and different simulation start dates, in order to quantify the uncertainties in the PMP estimate due to the model uncertainties and uncertainties in the ICs.

7 SIMULATIONS OF FUTURE INTENSE MESOSCALE CONVECTIVE SYSTEMS FOR THE 21ST CENTURY

To explore the 21st century extreme precipitation conditions, as compared to the historical extreme conditions, one GCM climate projection for the 21st century was selected for this study to be analyzed for its extreme precipitation events after dynamically downscaling this projection over the model regions of the selected severe MCSs by means of the WRF model. The GCM selected for this study was CCSM4 and the corresponding RCP chosen was RCP4.5 (as discussed in more details in Chapter 2).

To determine the most intense future MCS for the 21st century over a target watershed in the Midwestern United States, the CCSM4 RCP4.5 climate projection was first downscaled to a finer resolution of 5 km x 5 km using the WRF model. Since this chapter deals with simulating MCSs, the future simulations presented in this chapter were performed by the WRF being parameterized using the parameterization scheme that was chosen for the August 19, 2007 MCS (see Figure 3-16), which was the most intense MCS within the 2002-2011 period (Stevenson and Schumacher, 2014). The methods and results for these future simulations of the severe MCSs are presented below.

7.1 Identifying Extreme Rain Events and MCSs in the Future Projections

After downscaling the climate projection for CCSM4 RCP4.5 using the WRF model, the results of the future simulations were analyzed to find the extreme future MCSs. For this purpose, it was crucial to first identify the extreme rain events in these future simulations, and afterwards, to identify if an extreme rain even is a MCS or not.

(Schumacher and Johnson (2005); Schumacher and Johnson (2006)) defined an “event” as being a weather system that produces one or more rainfall observations above a given threshold. In other words, if the accumulated rainfall for at least one gauge (when dealing with ground observation data) or one grid cell (when dealing with gridded data) exceeded the specified threshold, then the corresponding weather system would be considered an event. Following this definition, the same authors then defined an event to be “extreme” when the accumulated rainfall at one or more gauges or grid cells exceeded a historical recurrence interval threshold for a certain time interval. (Schumacher and Johnson (2005); Schumacher and Johnson (2006)) defined extreme events as those with 24-hr precipitation amounts exceeding the 50-year recurrence interval amount for a specific location, while Stevenson and Schumacher (2014) defined them based on the 24-hr precipitation exceeding either the 50-year or 100-year recurrence interval amount for a specific location. These historical recurrence interval threshold values that were used to identify extreme storm events were previously developed for the United States by Hershfield (1961) for different time durations (30 minutes to 24 hours) and different recurrence intervals (1 year to 100 years). A plot showing the precipitation threshold values for the 50-year recurrence interval over 24-hr is given in Figure 7-1.

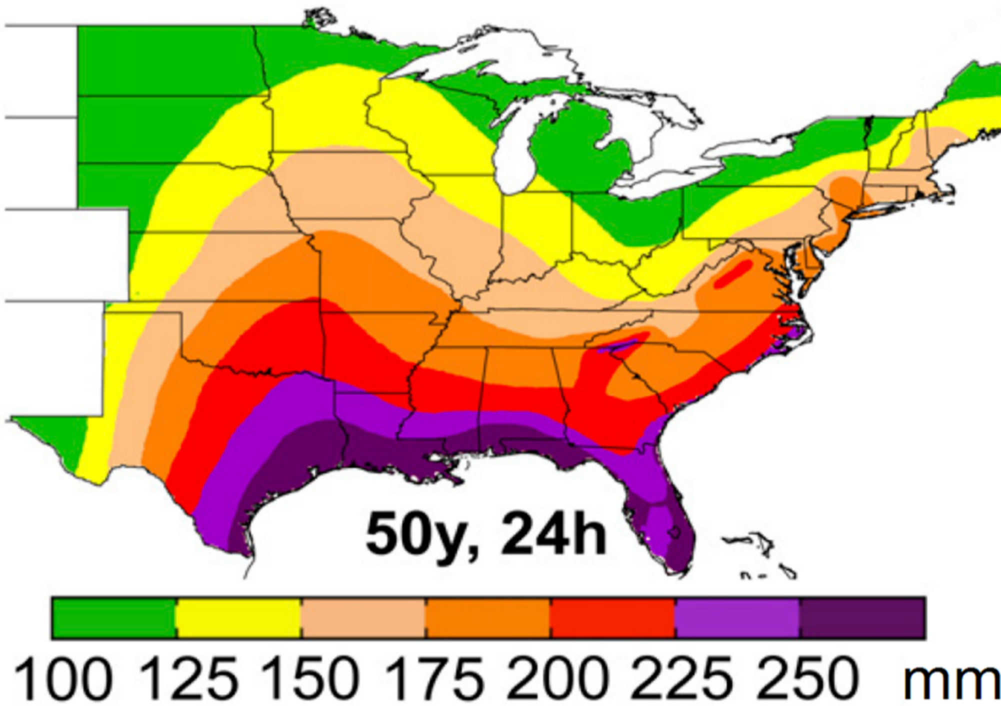

Figure 7-1 Precipitation Threshold Values (mm) for the 50-Year Recurrence Interval Over 24-hr Time Intervals (from Hershfield (1961) and Stevenson and Schumacher (2014))

Following the identification of an extreme event by using information provided in figures such as Figure 7-1, (Schumacher and Johnson (2005); Schumacher and Johnson (2006)) as well as Stevenson and Schumacher (2014) further classified extreme events into MCSs, synoptic systems, or tropical systems. The authors classified an event as a MCS if it was a convective system having areal extents greater than 100 km in at least one direction, and with durations between 3 and 24 hours, which is consistent with the criteria of Orlanski (1975) and Parker and Johnson (2000). However, the authors specified that any convective system that persisted longer than 24 hours or that was elongated to lengths greater than 1000 km would no longer be considered a MCS but would be classified as a synoptic system instead.

Therefore, for the purpose of this study, similar criteria to those of (Schumacher and Johnson (2005); Schumacher and Johnson (2006)) as well as Stevenson and Schumacher (2014) were followed to identify extreme storm events from the results of the future simulations (CCSM4 RCP4.5), and to select the events that would be classified as MCSs from these extreme storm events. The list of criteria used in this study to identify a storm event as an intense MCS is as shown below; this list of criteria states that the storm event must:

- Be identified as an extreme event based on the 50-year recurrence interval threshold for 24-hr accumulated precipitation (Figure 7-1),
- Have a duration between 3 and 24 hours,
- Have an areal extent larger than 100 km (but not larger than 1,000 km),
- Occur within the warm-season months of April to September, which is the time when MCSs usually occur (Fritsch et al., 1986b), and
- Appear as a solid line, broken line, or a cluster of cells with pockets of deep convective precipitation, which is the usual appearance of MCSs (NSSL, 2012).

7.2 Determining the Most Intense MCS Over Target Region for the Future

The criteria defined in the previous section were used to identify and select all intense MCSs projected to occur for the future years of the 21st century as simulated by the WRF model using CCSM4 RCP4.5. These intense MCSs were identified for the future years of 2020 through 2099, with several intense MCSs usually being identified for each year. The intensity of the identified MCSs was measured based on their corresponding 24-hr basin average precipitation over a target region. The selected target region was the same watershed used for the transposition exercise of Chapter 5, which was the Root River basin above Houston shown in Figure 5-1.

Hence, once the intense MCSs were identified for the future projections, the 24-hr basin average precipitation was computed for each of the identified MCSs over the Root River basin above Houston. Then, for each year, the MCS that produced the highest 24-hr basin average precipitation was selected as the most intense MCS over the target region for that specific year. By doing this, a list was created of the most intense MCSs over the target region, in which case this list was being composed of one MCS per year (the most intense one). Once the list was complete, it was possible to use it to select the most intense MCS over the target region among all future years of the 21st century.

The most intense MCS rainfall per year for the whole future 80 years of the 21st century, from 2020 through 2099 (i.e. annual maximum series), is given in Figure 7-2. This figure provides a summary of the MCSs that are projected to produce the highest 24-hr basin average precipitation during each of these future years (i.e., the yearly maximum 24-hr basin average precipitation), where the results are divided into two 40-year periods: from 2020 through 2059 shown in Figure 7-2a, and from 2060 through 2099 shown in Figure 7-2b. The x-axes in these plots represent the dates of the most intense MCSs, written as YYYYMMDD. The y-axes represent the yearly maximum 24-hr basin average precipitation that was computed for each of the selected MCSs over the Root River basin above Houston. General statistics for the yearly maximum 24-hr basin average precipitation produced by these intense MCSs are provided in Table 7-1, showing the mean and standard deviation of the 24-hr basin average precipitation for the whole 80-year future period, as well as for the first 40 and the last 40 years separately. Finally, the plots of the 24-hr accumulated precipitation fields for each of the intense MCSs that were summarized in Figure 7-2 are shown in Figure 7-3, where the dates of the MCSs are presented on the top of the plots as YYYY.MM.DD.

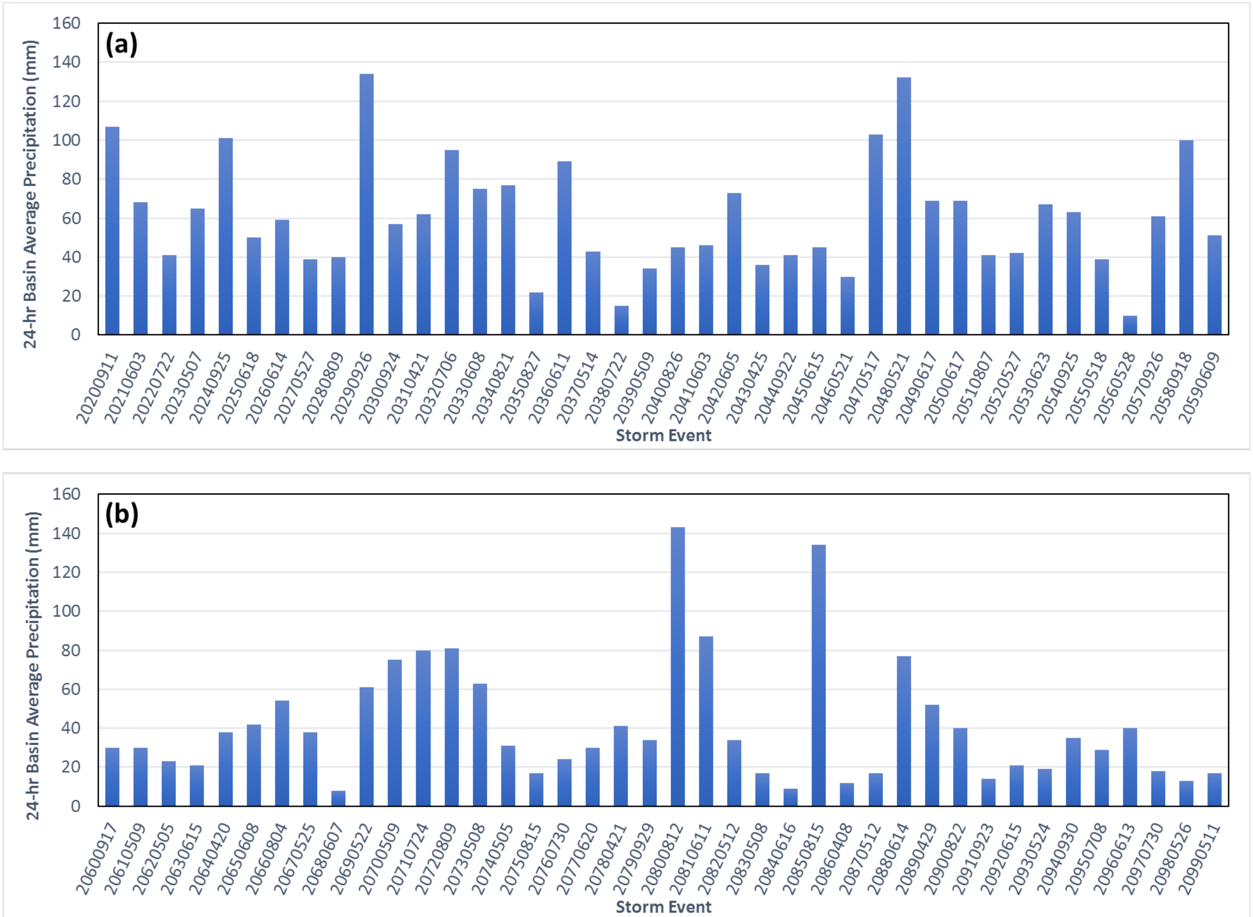

Figure 7-2 **Date and 24-hr Basin Average Precipitation of the Most Intense MCS Identified for each of the Future Years of the 21st Century: (a) for the First 40 Years from 2020 to 2059, and (b) for the Last 40 Years from 2060 to 2099**

Table 7-1 **Statistics for the Yearly Maximum 24-hr Basin Average Precipitation Over the Target Watershed Computed Using the Selected Most Intense MCS for Each Future Year**

Statistics were determined for the first 40 future years, the last 40 future years, and the whole 80 future years of the 21st century.

	2020 – 2059	2060 – 2099	2020 – 2099
Mean (mm)	64	41	53
Std. Dev. (mm)	31.21	31.16	33.08

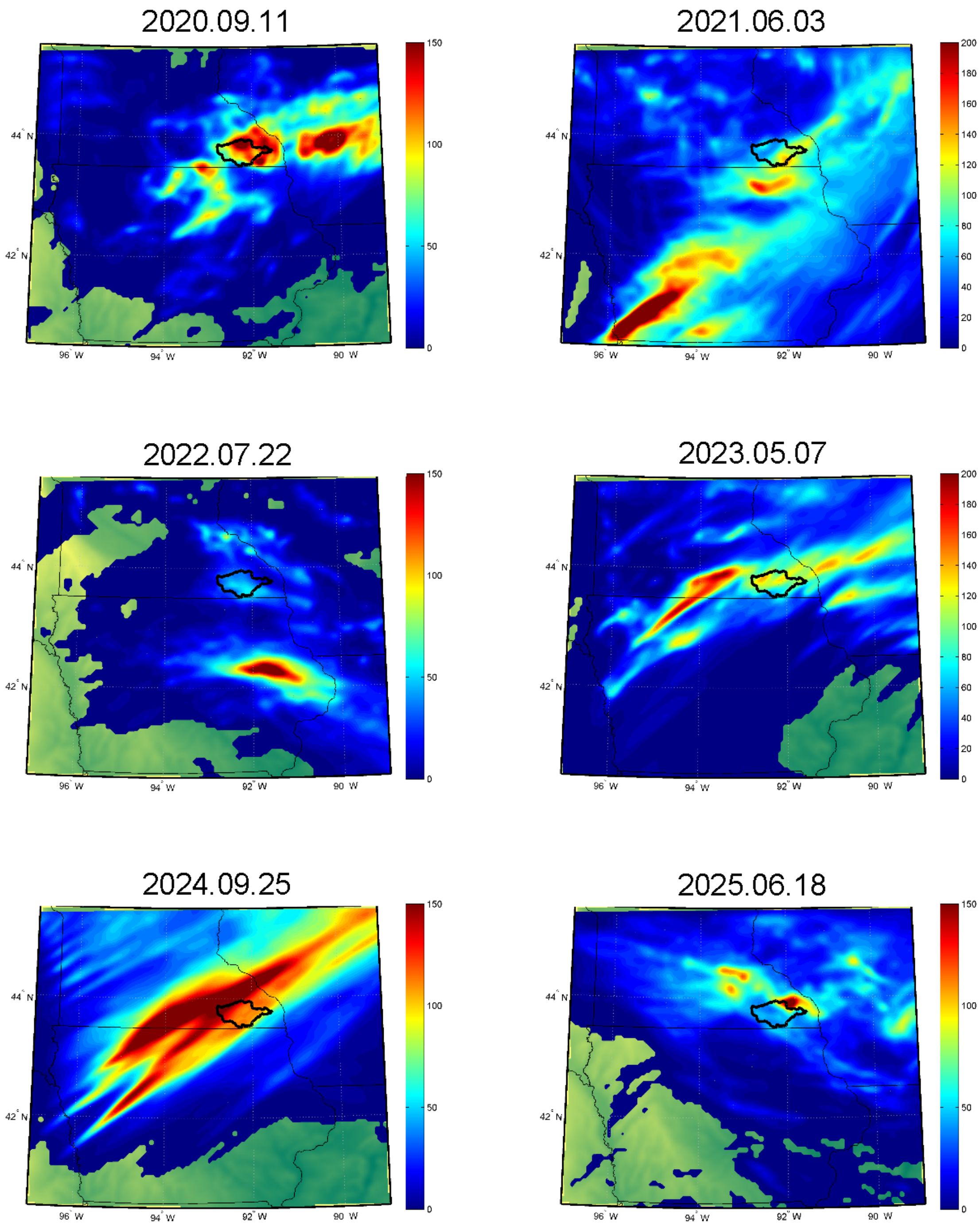

Figure 7-3 **Plots of the Most Intense MCSs for the Each of the Future Years of the 21st Century (2020 – 2099) Selected Based on the 24-hr Basin Average Precipitation Computed Over the Root River Above Houston Basin (Black Contour)**

Event date shown as YYYY.MM.DD. Colormap shows the 24-hr accumulated precipitation fields in mm.

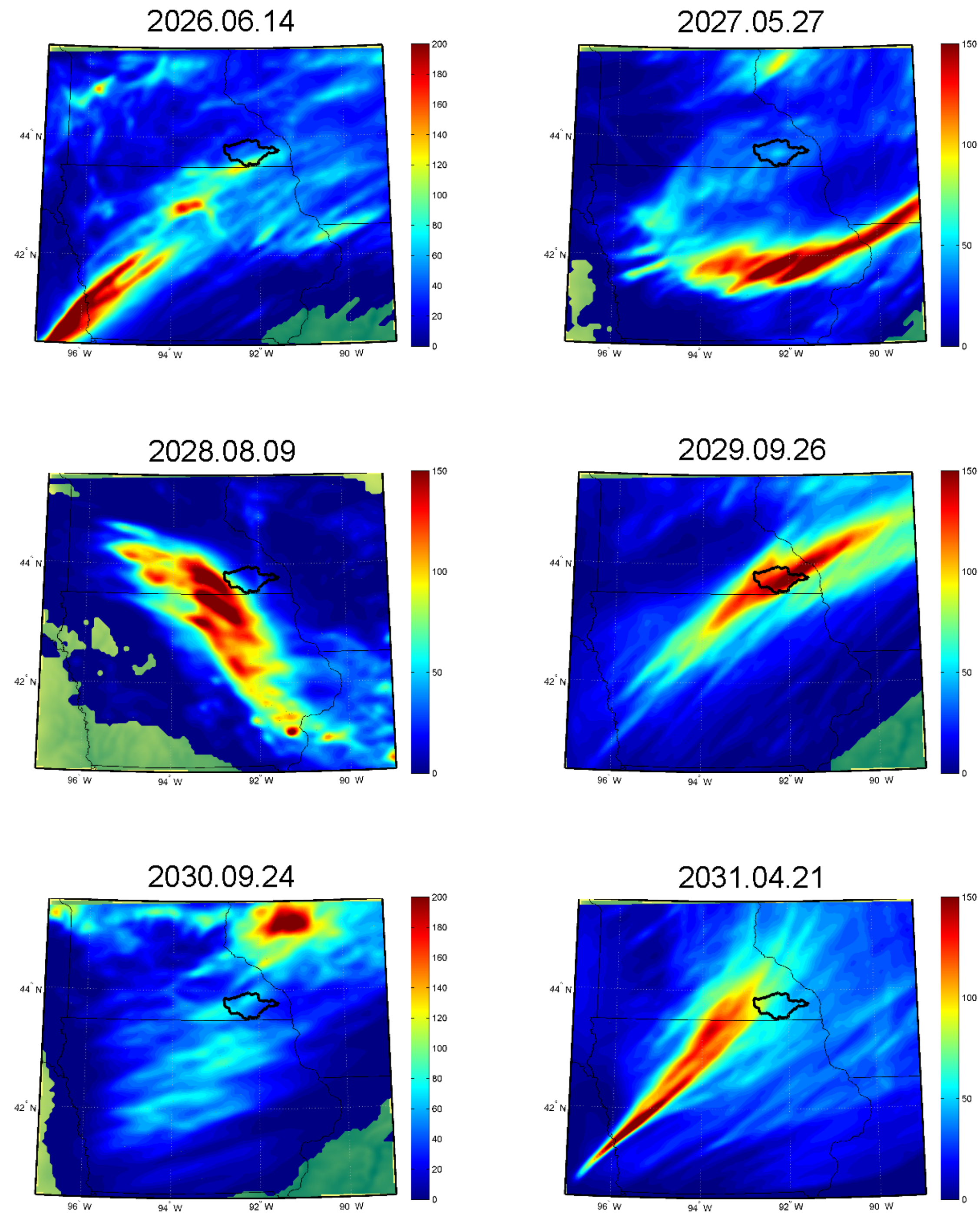

Figure 7-3 **Plots of the Most Intense MCSs for the Each of the Future Years of the 21st Century (2020 – 2099) Selected Based on the 24-hr Basin Average Precipitation Computed Over the Root River Above Houston Basin (Black Contour)**

Event date shown as YYYY.MM.DD. Colormap shows the 24-hr accumulated precipitation fields in mm (Continued).

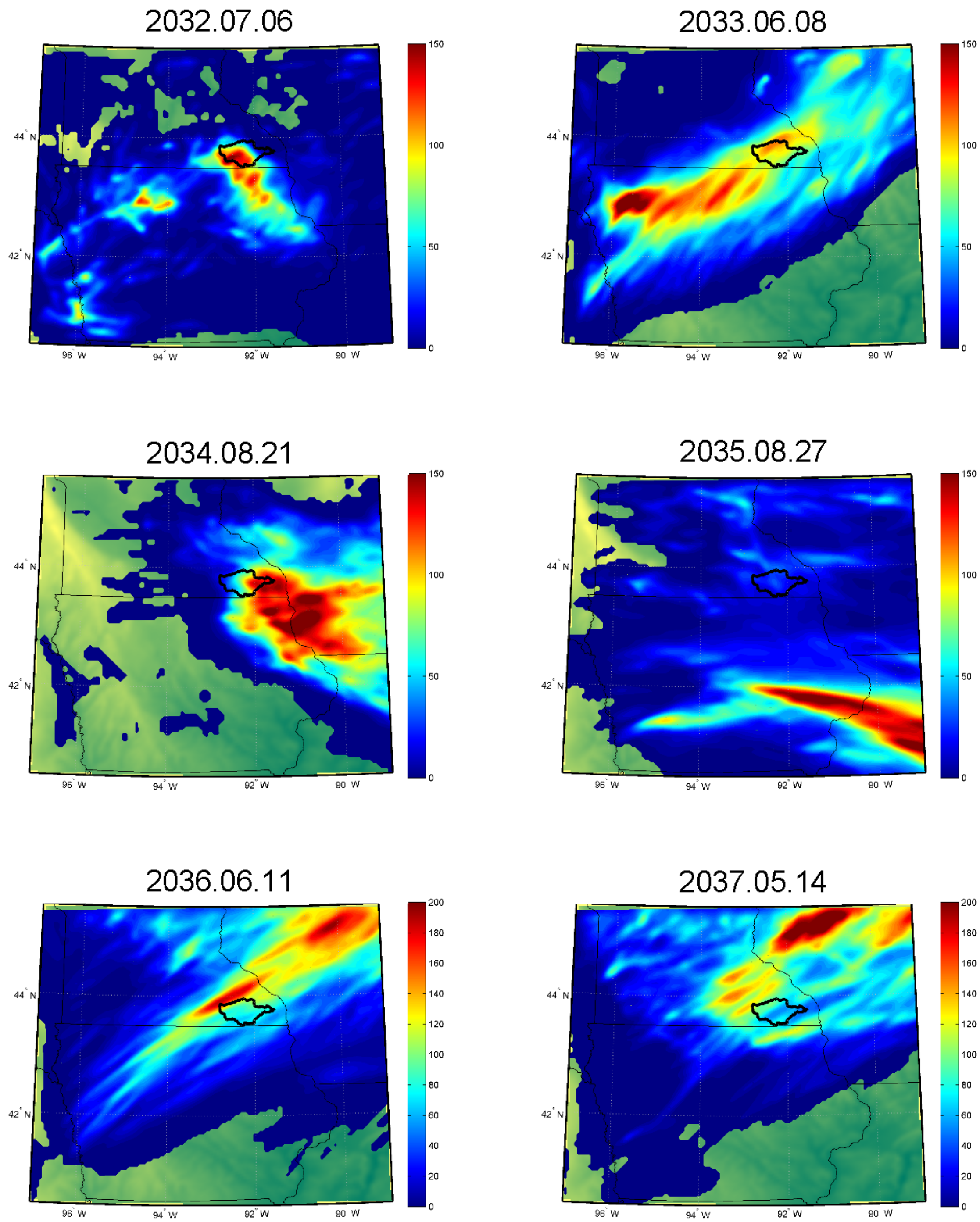

Figure 7-3 **Plots of the Most Intense MCSs for the Each of the Future Years of the 21st Century (2020 – 2099) Selected Based on the 24-hr Basin Average Precipitation Computed Over the Root River Above Houston Basin (Black Contour)**

Event date shown as YYYY.MM.DD. Colormap shows the 24-hr accumulated precipitation fields in mm (Continued).

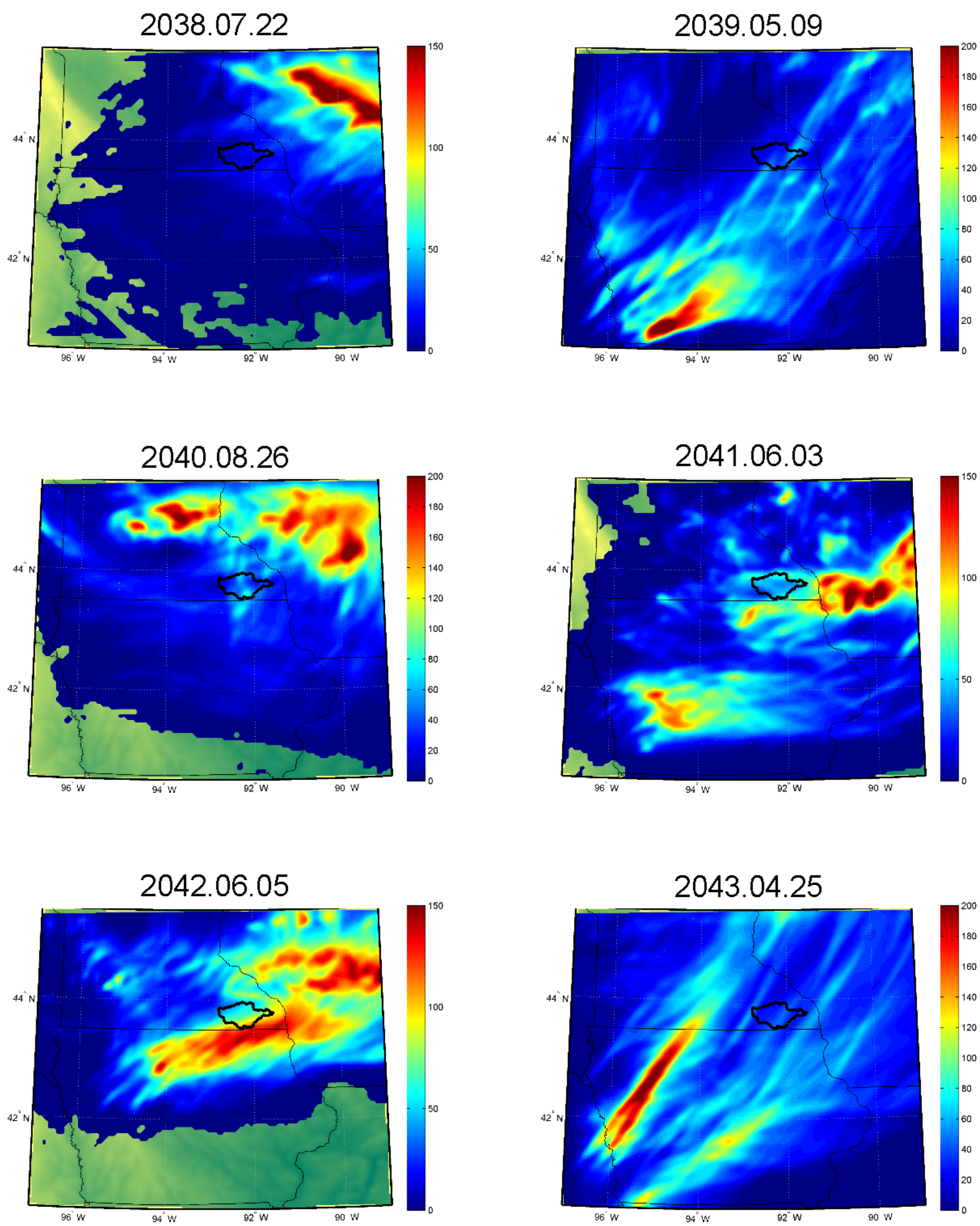

Figure 7-3 **Plots of the Most Intense MCSs for the Each of the Future Years of the 21st Century (2020 – 2099) Selected Based on the 24-hr Basin Average Precipitation Computed Over the Root River Above Houston Basin (Black Contour)**

Event date shown as YYYY.MM.DD. Colormap shows the 24-hr accumulated precipitation fields in mm (Continued).

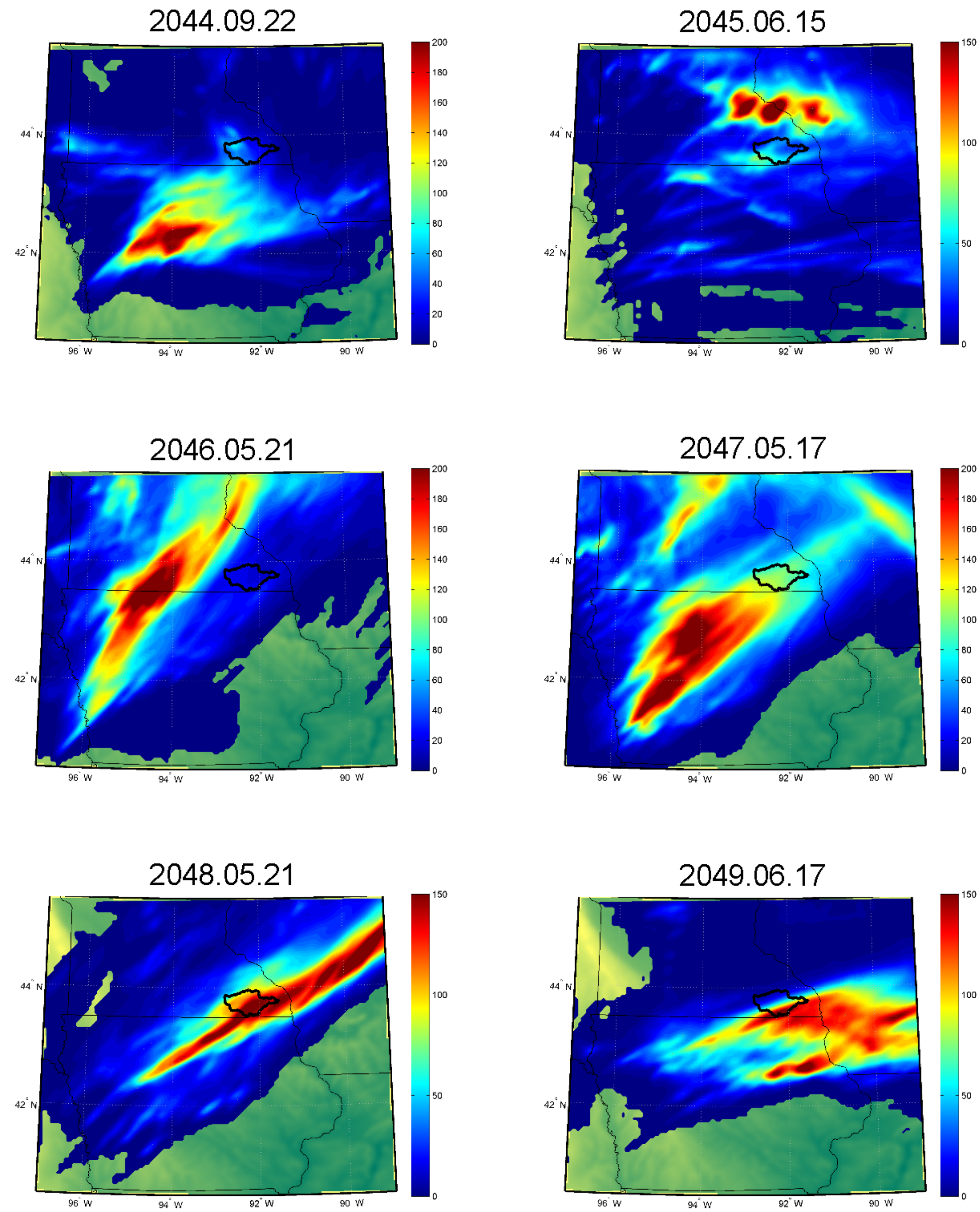

Figure 7-3 Plots of the Most Intense MCSs for the Each of the Future Years of the 21st Century (2020 – 2099) Selected Based on the 24-hr Basin Average Precipitation Computed Over the Root River Above Houston Basin (Black Contour)

Event date shown as YYYY.MM.DD. Colormap shows the 24-hr accumulated precipitation fields in mm (Continued).

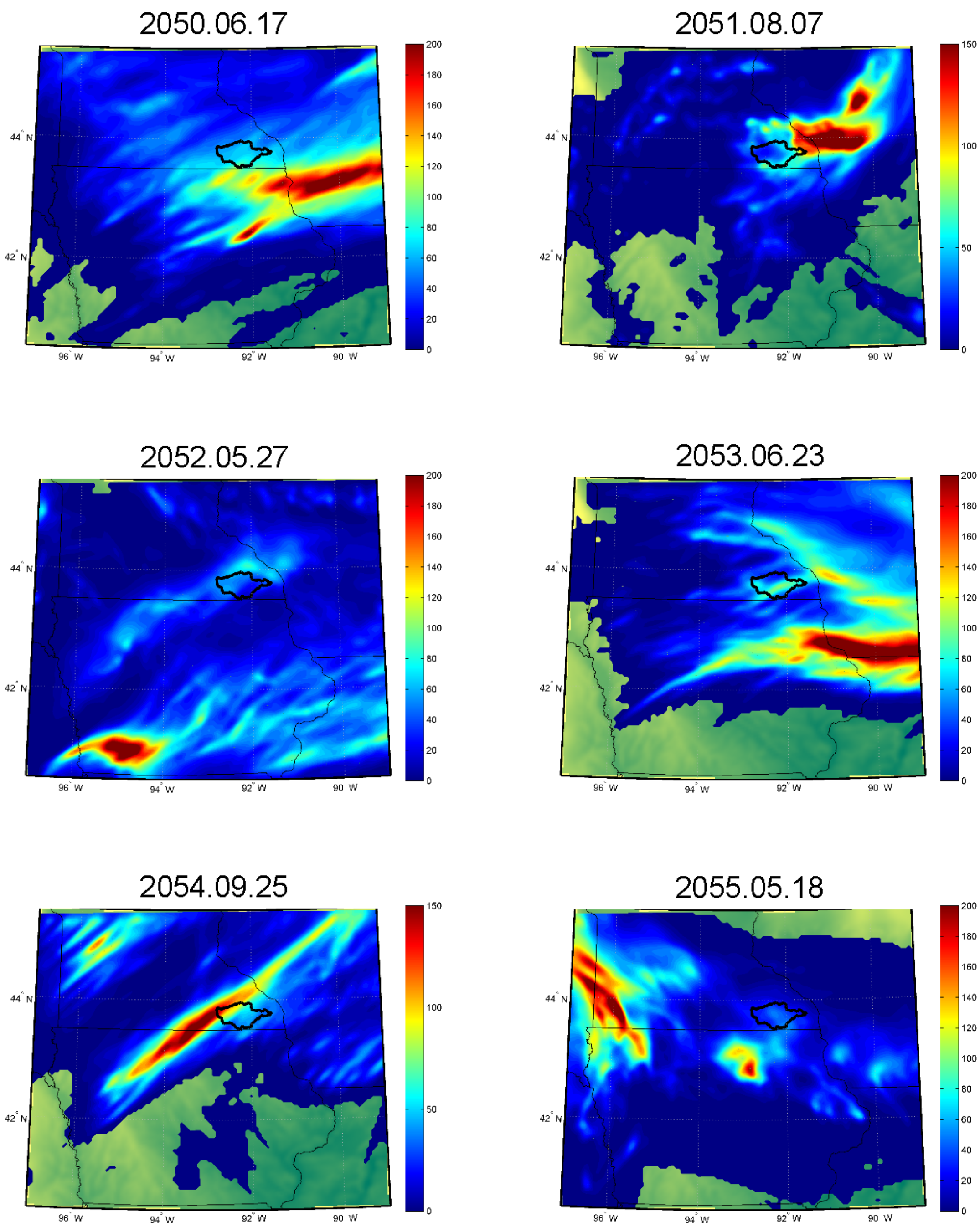

Figure 7-3 Plots of the Most Intense MCSs for the Each of the Future Years of the 21st Century (2020 – 2099) Selected Based on the 24-hr Basin Average Precipitation Computed Over the Root River Above Houston Basin (Black Contour)

Event date shown as YYYY.MM.DD. Colormap shows the 24-hr accumulated precipitation fields in mm (Continued).

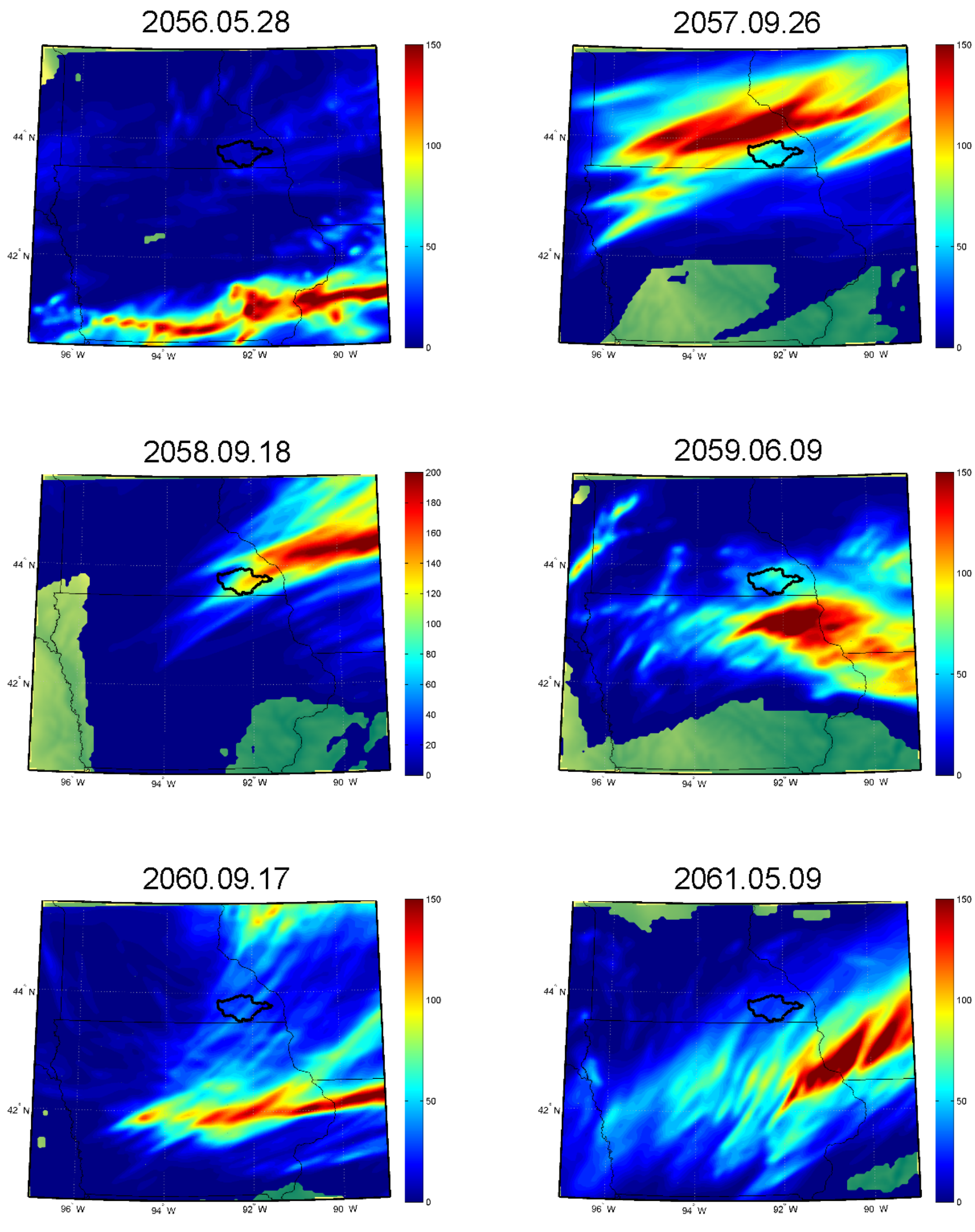

Figure 7-3 Plots of the Most Intense MCSs for the Each of the Future Years of the 21st Century (2020 – 2099) Selected Based on the 24-hr Basin Average Precipitation Computed Over the Root River Above Houston Basin (Black Contour)

Event date shown as YYYY.MM.DD. Colormap shows the 24-hr accumulated precipitation fields in mm (Continued).

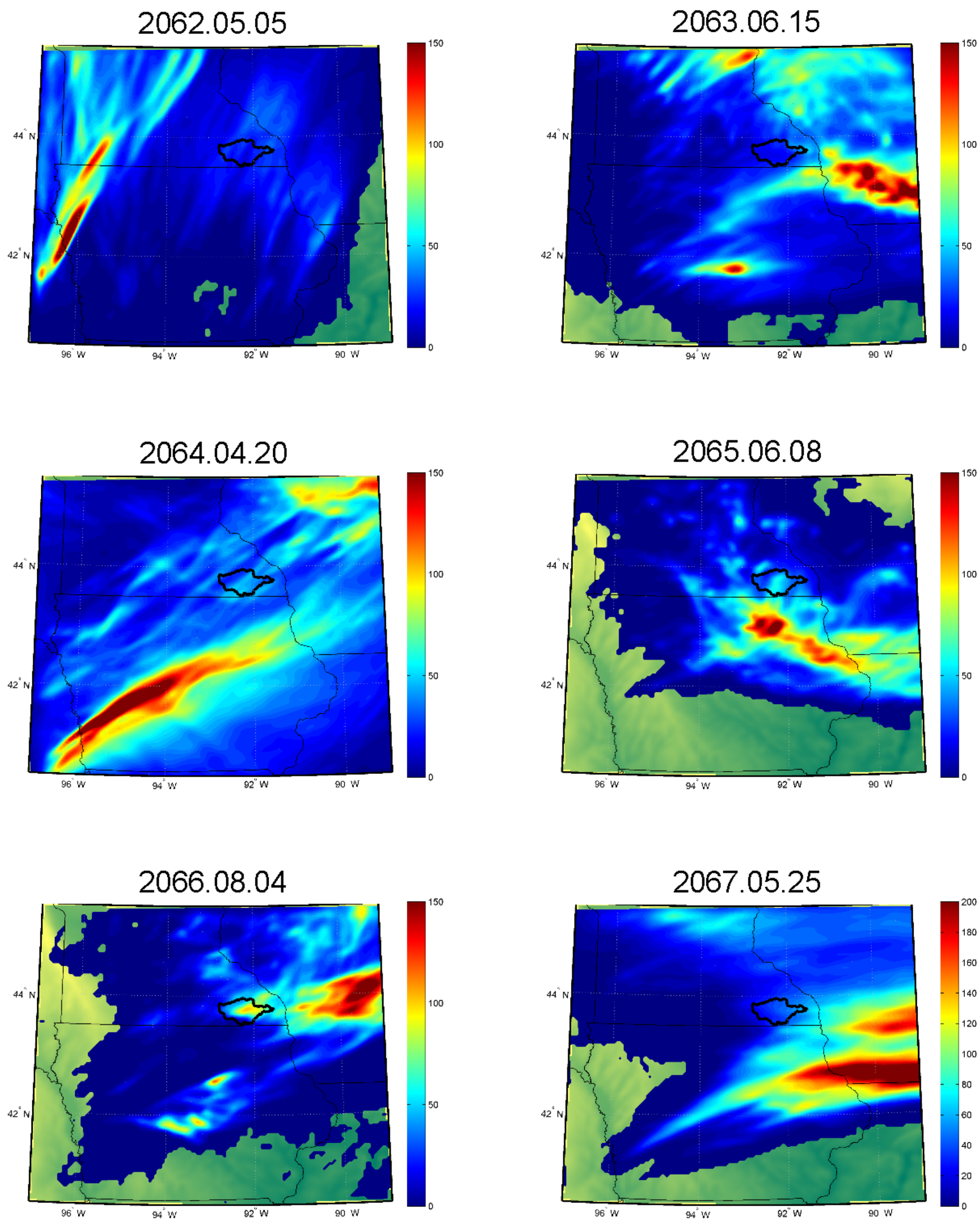

Figure 7-3 Plots of the Most Intense MCSs for the Each of the Future Years of the 21st Century (2020 – 2099) Selected Based on the 24-hr Basin Average Precipitation Computed Over the Root River Above Houston Basin (Black Contour)

Event date shown as YYYY.MM.DD. Colormap shows the 24-hr accumulated precipitation fields in mm (Continued).

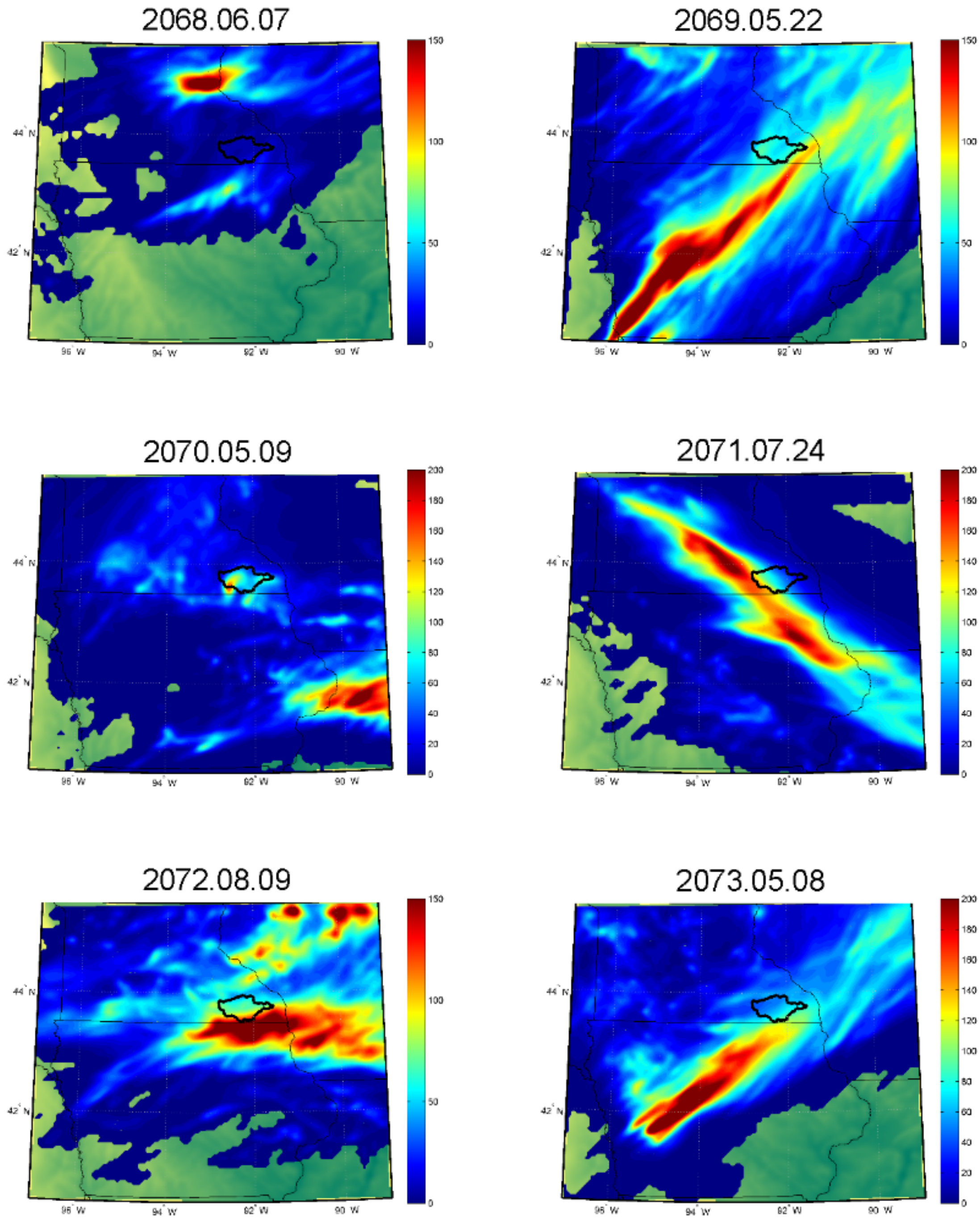

Figure 7-3 **Plots of the Most Intense MCSs for the Each of the Future Years of the 21st Century (2020 – 2099) Selected Based on the 24-hr Basin Average Precipitation Computed Over the Root River Above Houston Basin (Black Contour)**

Event date shown as YYYY.MM.DD. Colormap shows the 24-hr accumulated precipitation fields in mm (Continued).

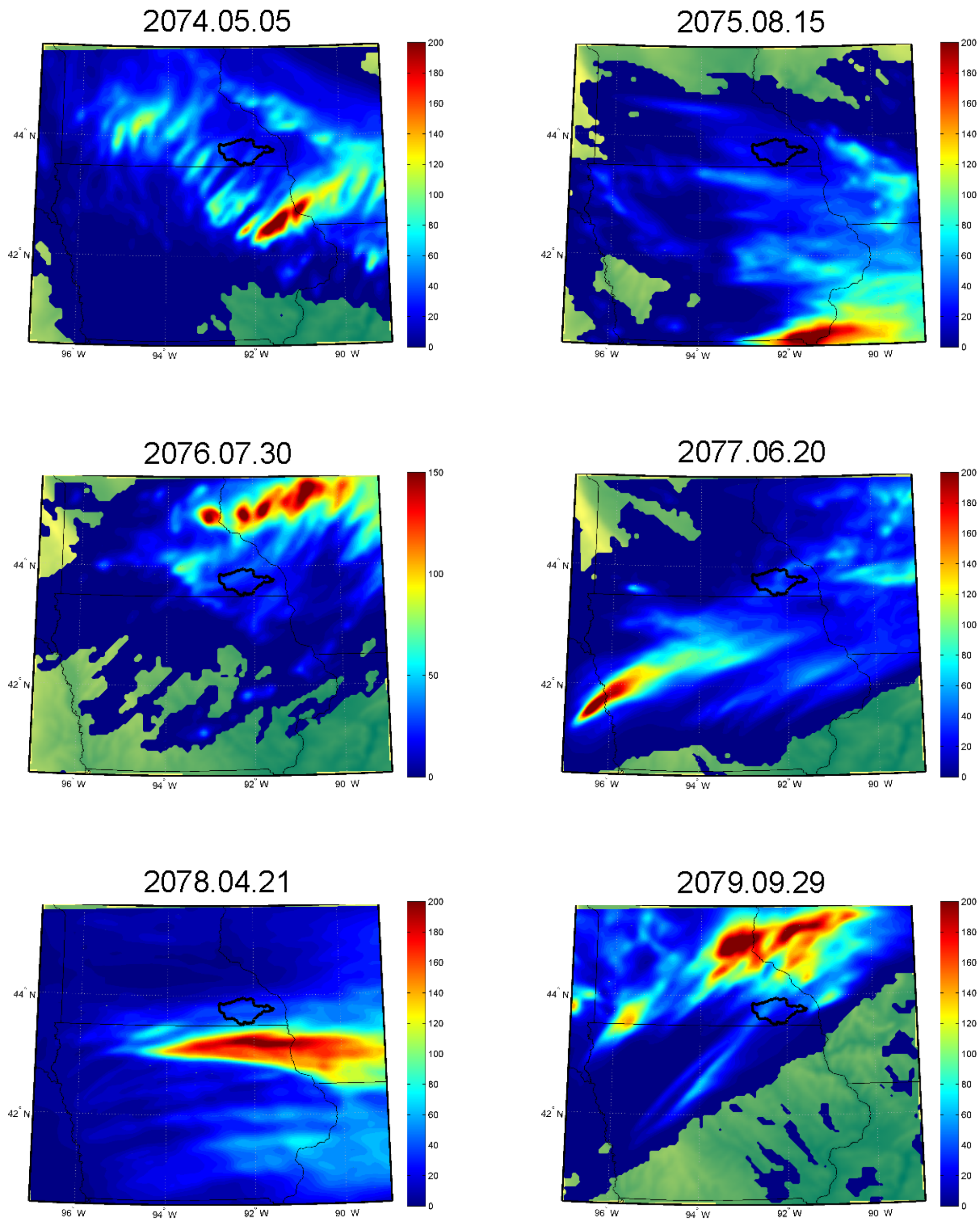

Figure 7-3 **Plots of the Most Intense MCSs for the Each of the Future Years of the 21st Century (2020 – 2099) Selected Based on the 24-hr Basin Average Precipitation Computed Over the Root River Above Houston Basin (Black Contour)**

Event date shown as YYYY.MM.DD. Colormap shows the 24-hr accumulated precipitation fields in mm (Continued).

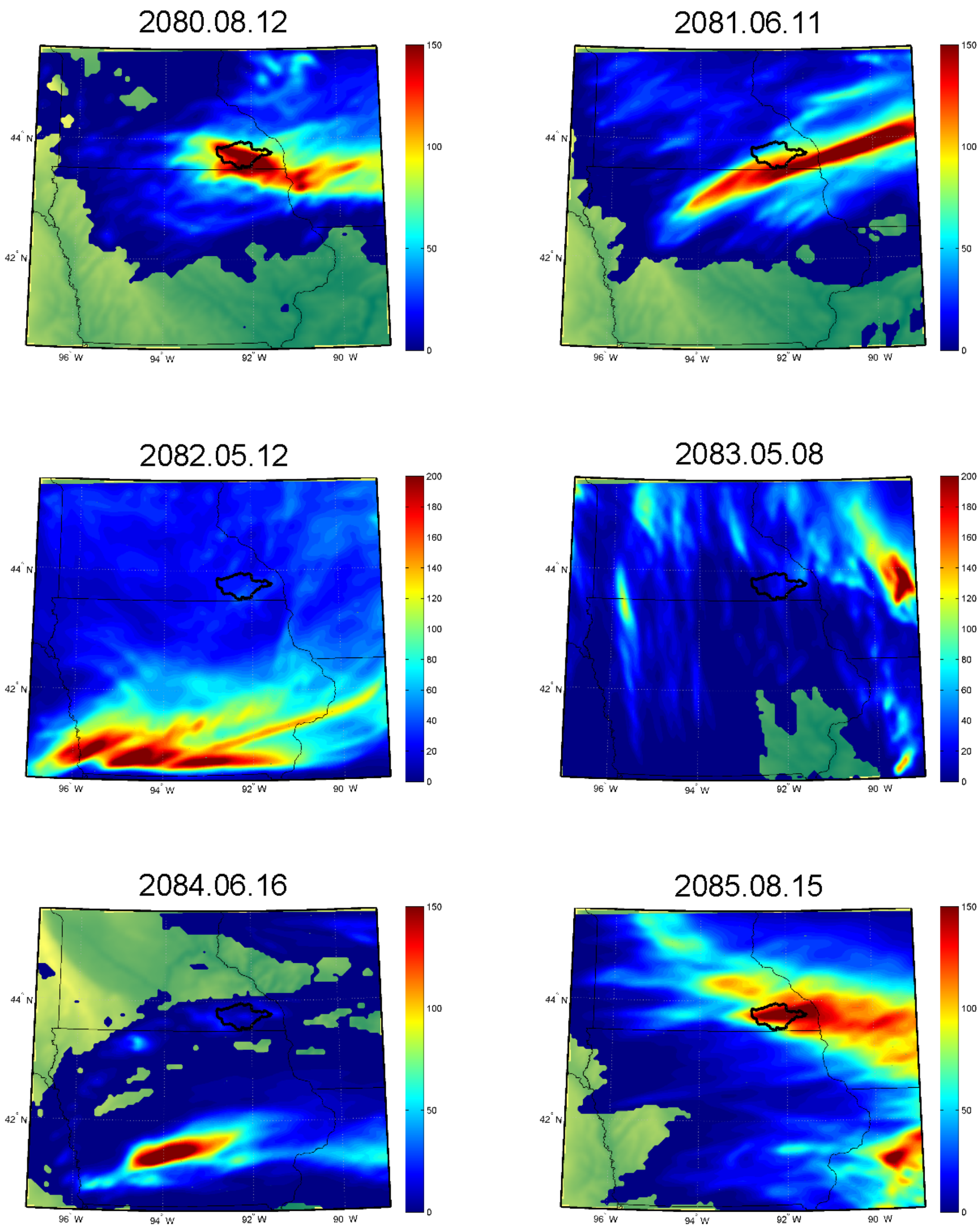

Figure 7-3 **Plots of the Most Intense MCSs for the Each of the Future Years of the 21st Century (2020 – 2099) Selected Based on the 24-hr Basin Average Precipitation Computed Over the Root River Above Houston Basin (Black Contour)**

Event date shown as YYYY.MM.DD. Colormap shows the 24-hr accumulated precipitation fields in mm (Continued).

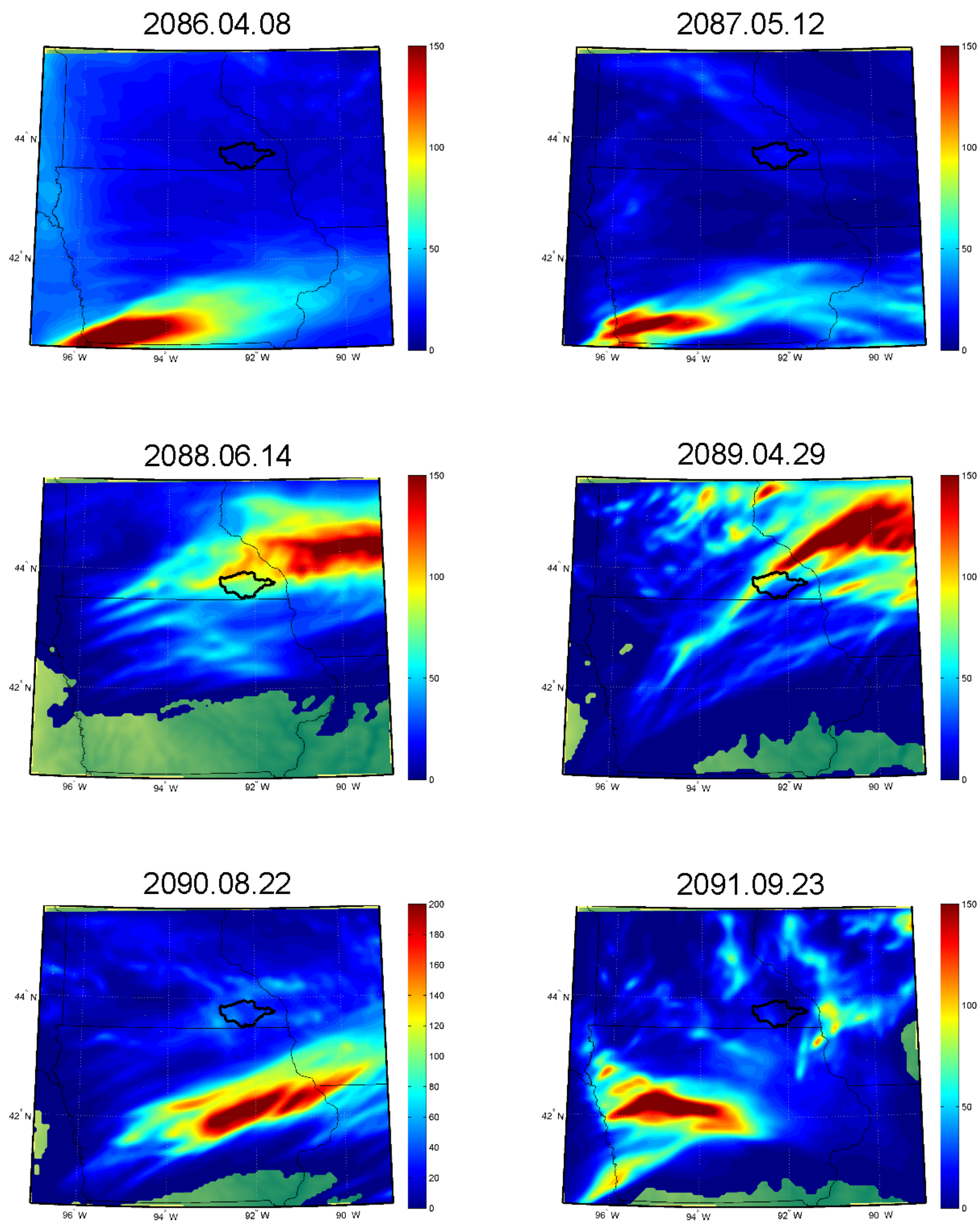

Figure 7-3 Plots of the Most Intense MCSs for the Each of the Future Years of the 21st Century (2020 – 2099) Selected Based on the 24-hr Basin Average Precipitation Computed Over the Root River Above Houston Basin (Black Contour)

Event date shown as YYYY.MM.DD. Colormap shows the 24-hr accumulated precipitation fields in mm (Continued).

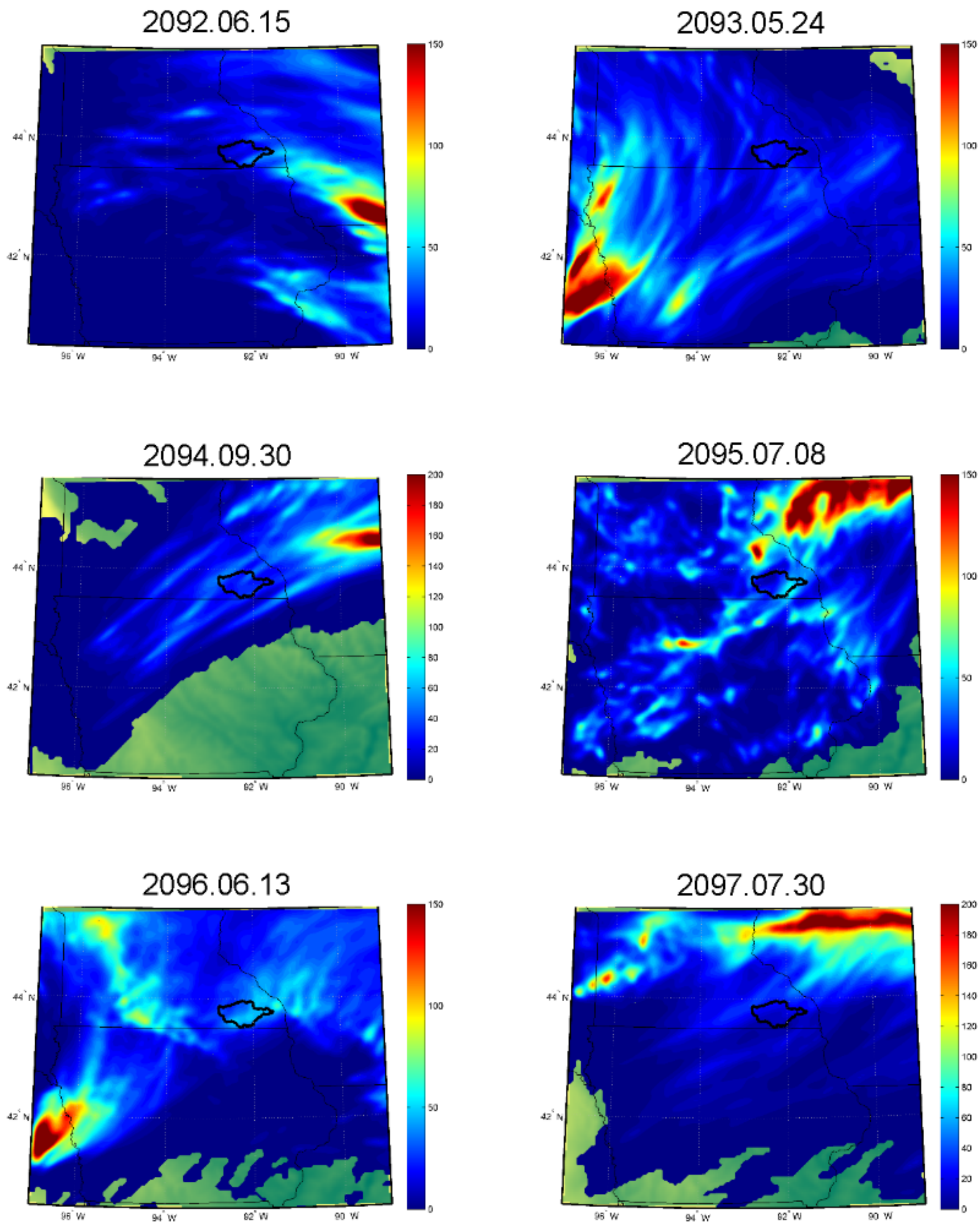

Figure 7-3 **Plots of the Most Intense MCSs for the Each of the Future Years of the 21st Century (2020 – 2099) Selected Based on the 24-hr Basin Average Precipitation Computed Over the Root River Above Houston Basin (Black Contour)**

Event date shown as YYYY.MM.DD. Colormap shows the 24-hr accumulated precipitation fields in mm (Continued).

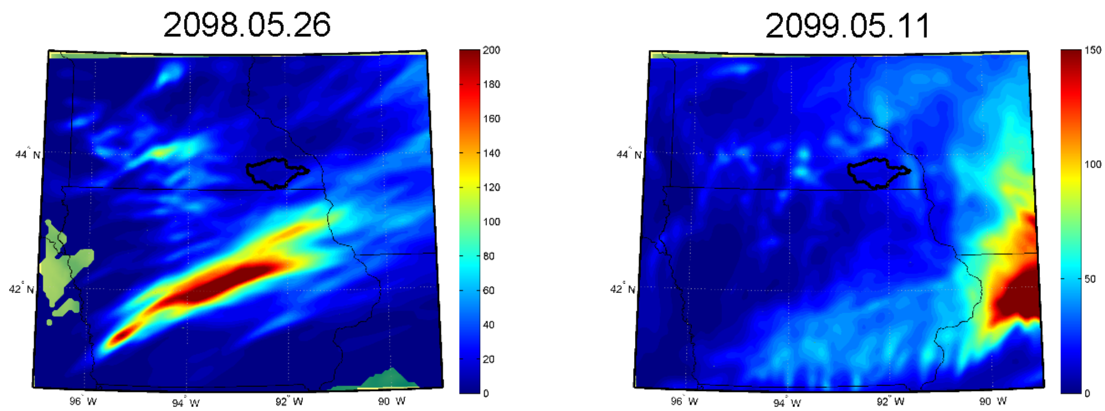

Figure 7-3 Plots of the Most Intense MCSs for the Each of the Future Years of the 21st Century (2020 – 2099) Selected Based on the 24-hr Basin Average Precipitation Computed Over the Root River Above Houston Basin (Black Contour)

Event date shown as YYYY.MM.DD. Colormap shows the 24-hr accumulated precipitation fields in mm (Continued).

Observing Figure 7-2, one can see that the yearly maximum 24-hr basin average precipitation over the target watershed shows quite a bit of variation among the future years. However, the amount of variation was found to be somewhat similar between the first and last 40-year periods, as well as for the whole future 21st century as shown in Table 7-1. Moreover, from the graphs of Figure 7-2, one can see that for the future years from 2020 to 2099, the yearly maximum 24-hr basin average precipitation over the target watershed is expected to range from a minimum of 8 mm (0.3 in.) in 2068 to a maximum of 143 mm (5.6 in.) in 2080. This is indeed comparable to the range that would be obtained if a similar analysis was performed for the years corresponding to the fourteen historical MCSs that were reconstructed in a previous chapter of this report. For those historical years, the values of the yearly maximum 24-hr basin average precipitation over the target watershed ranged from a minimum of 10 mm (0.4 in.) in 2002 to a maximum of 128 mm (5.0 in.) in 2007.

While the variation in the 24-hr basin average precipitation is expected to be somewhat steady throughout the two 40-year halves of the future period as discussed above, its value is expected to be around 35% lower on average for the last 40-year period (with a mean of 41 mm [1.6 in.]) when compared to the first 40-year period (with a mean of 64 mm [2.5 in.]) (Table 7-1). This may also be clear from the bar graphs shown in Figure 7-2, where Figure 7-2b shows bars with generally lower values than those on Figure 7-2a. Furthermore, there is an expected decreasing trend in the value of the yearly maximum 24-hr basing average precipitation over all three periods of Table 7-1, only one of which is significant at the 95% level (using the Mann-Kendall non-parametric test), which is the trend corresponding to the whole future period of 80 years.

However, it is crucial to note that the smaller mean of the yearly maximum 24-hr basin average precipitation expected for the second 40-year period of the 21st century, as well as the expected decreasing trends of this basin average precipitation do not necessarily project a reduction in the intensity of precipitation in the Midwestern United States or in the area encompassed by the simulation domain of this study. Indeed, the value of the basin average precipitation computed over the target watershed is highly dependent on the location of the MCS and of its intense precipitation with respect to the target watershed. As such, the reduction in the 24-hr basin average precipitation, on average, in the second half of the 21st century and throughout the whole future period may simply be a result of a lesser number of MCSs occurring close to or over the target watershed rather than being a projected reduction in precipitation amounts.

In fact, this can be clearly seen when comparing several of the figures shown in Figure 7-3. For example, one of the simulated MCSs expected to produce a relatively high yearly maximum 24-hr basin average precipitation over the target watershed is the September 26, 2029 MCS (134 mm [5.3 in.]). On the other hand, one of the simulated MCSs expected to produce some of the lowest yearly maximum 24-hr basin average precipitation is the July 22, 2038 MCS (15 mm [0.6 in.]). When looking at the precipitation fields of these two MCSs (Figure 7-3), one may notice that both are quite similar with respect to the intensity of the storm systems occurring within the simulation domain. However, what causes the 2029 MCS to produce much larger basin average precipitation amounts is the fact that it directly hits the target watershed, causing intense precipitation to fall directly within the watershed. This is in contrast to the 2038 MCS, in which case the storm system occurs far enough from the target watershed that the effect of its intense precipitation on the basin average value is minimal.

Note that, looking through all the plots of Figure 7-3, one can see that for the MCSs of the second 40-year future period (2060 to 2099), the storm events generally show a lower tendency to occur close to or directly over the target watershed as compared to the first 40-year future period (2020 to 2059). As such, that would be a significant reason for the smaller amounts of the yearly maximum 24-hr basin average precipitation over the target watershed (on average) in the later years of the 21st century. Therefore, it may be concluded that while all plotted MCSs for the future period appear as intense storms with regions of intense local precipitation (Figure 7-3), the location of the intense MCS seems to play an extremely important role in the value of the basin average precipitation computed over the target watershed (compare Figure 7-2 with Figure 7-3).

Another confirmation that shows that the results of the future simulations do not necessarily reveal a reduction in the intensity of the MCSs involves the fact that the highest yearly maximum 24-hr basin average precipitation is expected to be produced by the August 12, 2080 MCS, with a value of around 143 mm (5.6 in.). Note that this storm event occurs in the second 40-year half of the 21st century, where the yearly maximum 24-hr basin average value was found to be generally lower on average (Table 7-1). Again, it is clear from Figure 7-3 that the reason for this high basin average precipitation is the occurrence of the storm event and its intense precipitation over the target watershed. In any case, from what has been previously discussed, it may be stated that the most intense MCS over the Root River basin above Houston was projected to be the August 12, 2080 MCS, which was simulated to produce around 143 mm (5.6 in.) of 24-hr basin average precipitation over the target watershed.

It should be stressed that this work is exploratory, it only considered one future climate realization from one model. If one's objective were to conduct a detailed study for a watershed, then multiple future climate realizations would be downscaled and examined.

7.3 Physically Based Storm Transposition of the August 12, 2080 MCS

With the most intense MCS over the future period of the 21st century for the target region of interest being determined, another task of this study involved performing the transposition of this storm event in order to estimate the largest 24-hr basin average precipitation that could have been physically caused by the storm over the target region had the storm occurred in a slightly different location. The transposition method used in this section was the same physically based method that was explained and performed on a historical MCS in Chapter 5, which was based on the shifting of the IBCs of the WRF model. The target watershed used for this transposition exercise is again the same Root River basin above Houston shown in Figure 5-1.

The plot of the target watershed along with the future MCS to be transposed can be seen in Figure 7-4, reproduced here from Figure 7-3 for convenience. From this figure, one can see that the target watershed falls directly under the storm event, where a large portion of the region of intense precipitation of the MCS directly falls over the target watershed. As a result of the location of the watershed with respect to the MCS, there was no clear main shifting directions for this attempted transposition exercise, unlike the case for the transposition of the historical MCS (Chapter 5). As a result, the extent of the transposition was decided to be carried equally in all directions. However, similarly to the previous transposition exercise, the shifting of the BCs was performed along two directions (North-South and East-West), with regular increments chosen in each of the directions.

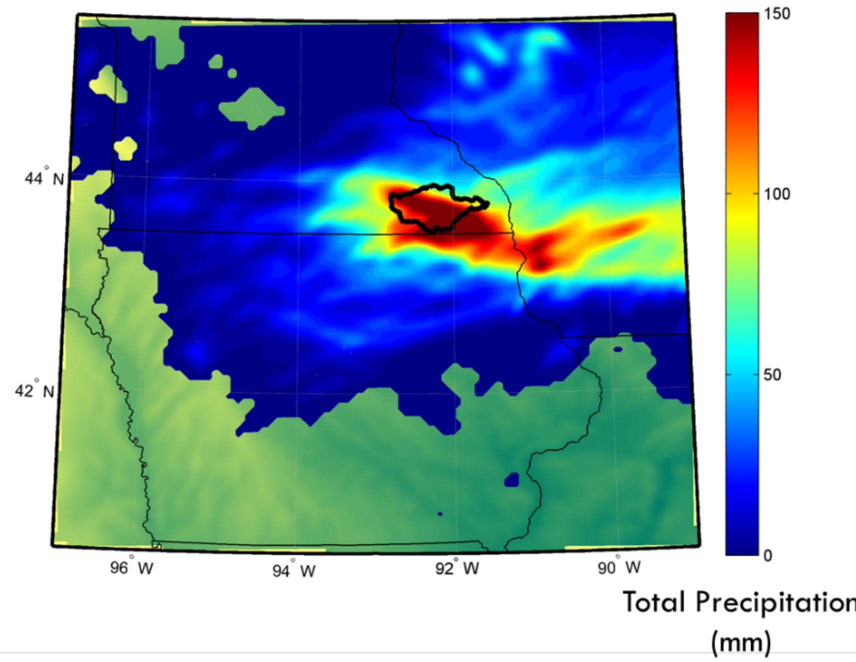

Figure 7-4 Location of the Target Watershed (Root River Above Houston) with Respect to the August 12, 2080 MCS

Therefore, for this transposition exercise, first, 0.2-degree increments were used for shifting in the North-South direction up to 1 degree in each direction, and 0.2-degree increments were used for shifting in the East-West direction up to 1 degree in each direction. Then, for each shifting position, the WRF model was run to simulate the MCS corresponding to these shifting positions. After this, the 24-hr basin average precipitation over the target watershed was computed for each of the shifting positions. Finally, the results of the 24-hr basin average precipitation were plotted on a figure, as shown on Figure 7-5.

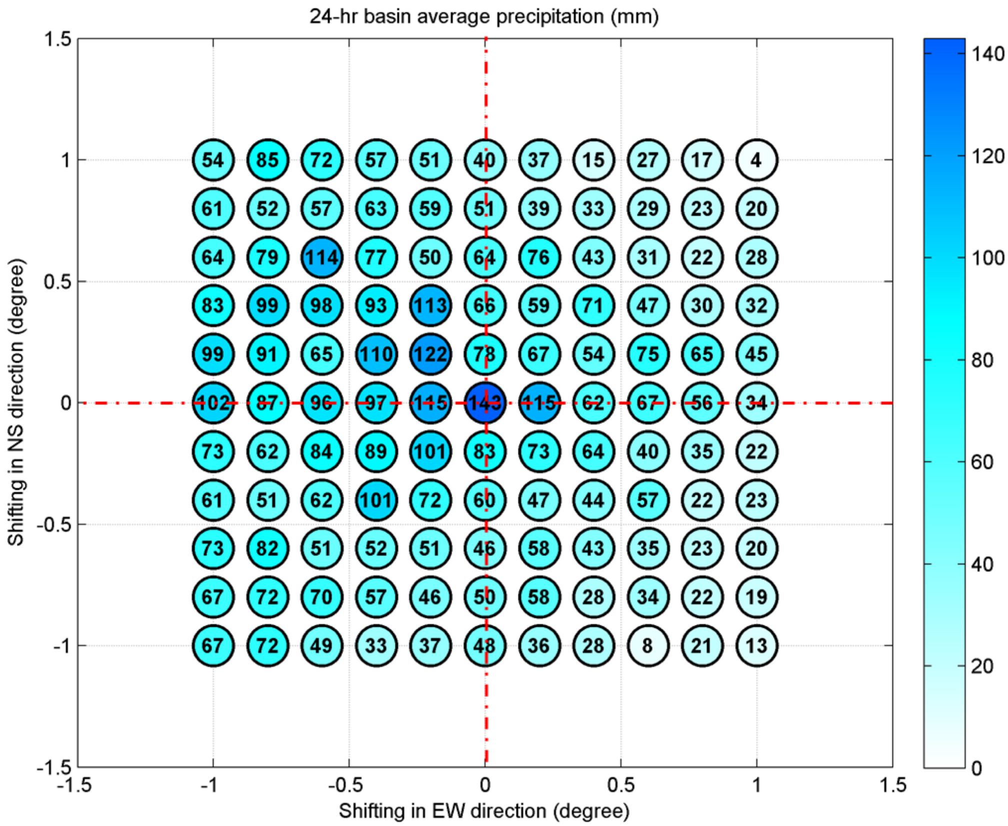

Figure 7-5 Plot of the 24-hr Basin Average Precipitation Over the Root River Above Houston (Target Watershed) as a Function of the Degree of Shifting of the Domain BCs Corresponding to the August 12, 2080 MCS

The numbers and the colors represent the values of the 24-hr basin average precipitation for each of the shifting positions.

In Figure 7-5, the x-axis represents the degrees of shifting in the East-West (EW) direction, the y-axis represents the degrees of shifting in the North-South (NS) direction, and the intersection of the dashed red lines represents the location of the origin, which corresponds to the no-shifting position. The numbers inside the circles and the color intensity of the circles both represent the values of the 24-hr basin average precipitation for each of the specific shifting positions.

From this figure, one can see that the 24-hr basin average precipitation over the target watershed decreased, relative to the no-shifting position, when shifting occurred along any of the directions. While a few shifting positions close to the no-shifting position had provided 24-hr basin average precipitation values that were still relatively high (e.g., 122 mm [4.8 in.], 115 mm [4.5 in.], and 113 mm [4.4 in.]), none had exceeded that of the no-shifting position (143 mm [5.6 in.]). Moreover, one can see that the 24-hr basin average precipitation values decreased much faster when shifting towards the east as opposed to shifting towards the west, as is clear from the faster-fading colors on the right half of the Figure 7-5. This may be due to the location of MCS with respect to the target watershed, where most of the MCS falls either directly over the watershed or generally to the east of the watershed (Figure 7-4). In any case, the second highest 24-hr basin average precipitation obtained, following the no-shifting position, was found to be 122 mm (4.8 in.) at a shifting position of [+0.2° N, +0.2° W].

In order to visualize how and why different shifting positions cause a difference in the basin average precipitation, the plots of a few of the shifted results of Figure 7-5 are provided on Figure 7-6. These include the plots of three shifting positions, as well as the plot for the no-shifting position for comparison. From these figures, one can see for example, that the shifting of the BCs in the SW direction (e.g., [+0.2° S, +0.8° W]) caused the MCS to occur slightly south of the target watershed and to move slightly west, thus greatly reducing the basin average precipitation value over the target watershed. Moreover, it is clear from these plots that the shifting also affected the shape and the intensity of the precipitation for the shifted MCSs.

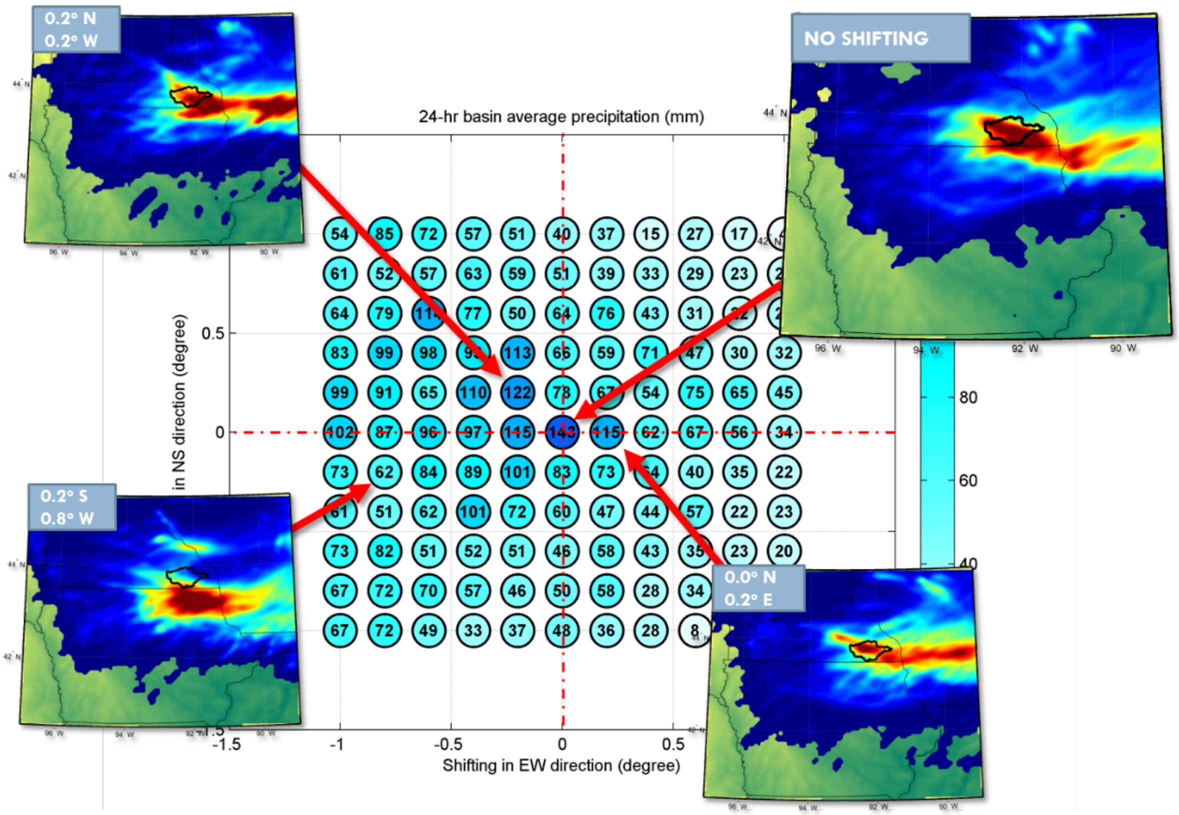

Figure 7-6 A Few Plots of the MCSs Corresponding to Some of the Shifting Positions, Including the No-Shifting Position

Even with the transposition exercise just performed, it is important to note that the unshifted MCS still had the largest 24-hr basin average precipitation, while a few shifted locations around it had lower values which can still be considered high. As such, the area surrounding the no-shifting location was considered to be the area of highest precipitation, and this area of highest precipitation was chosen for the first grid-refinement exercise. This refinement involved using 0.1-degree increments, as opposed to the original 0.2-degree increments used to produce Figure 7-5. The area of this refinement is represented by the red box shown on the left of Figure 7-7, and it encompasses the three largest precipitations, which are 143 mm (5.6 in.), 122 mm (4.8 in.), and 115 mm (4.5 in.).

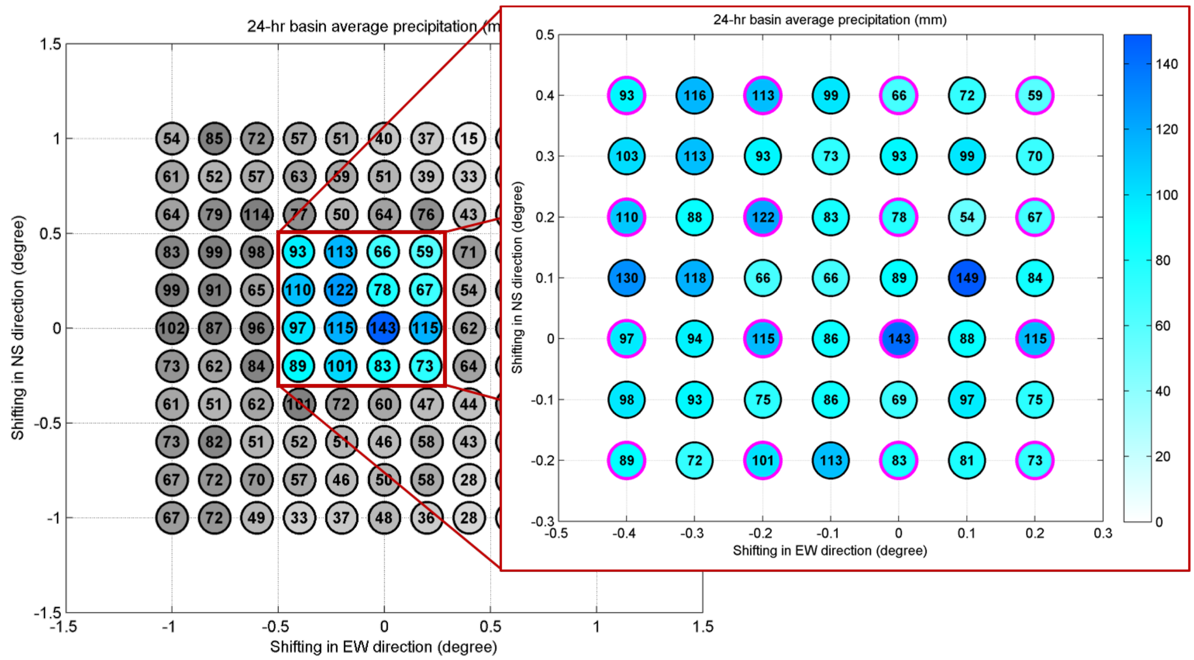

Figure 7-7 Area Selected for the First Grid-Refinement Exercise

Zoomed-in figure shows the results of the original transposition exercise (circles with pink boundaries) and the new results of the first grid-refinement exercise (circles with black boundaries).

The results of the first grid-refinement are shown on the zoomed-in plot of Figure 7-7. In this plot, the circles with the pink boundaries represent the original precipitation values that were obtained from the first transposition exercise using the 0.2-degree increments. The circles with the black boundaries represent the newly computed precipitation values obtained for the refinement exercise, with a 0.1-degree increment. From the refinement results, this time it was possible to find a new maximum 24-hr basin average precipitation value, which was equal to 149 mm (5.9 in.). This corresponded to a shifting position of [+0.1° N, +0.1° E].

Figure 7-8 provides plots of the MCS corresponding to the original maximum basin average precipitation of 143 mm (5.6 in.) for the unshifted position, as well as for the MCS of the newly found maximum obtained from the refinement (149 mm [5.9 in.]), and also for the MCS for the third highest basin average precipitation (130 mm [5.1 in.]). These latter two MCSs corresponded to shifting positions of [+0.1° N, +0.1° E] and [+0.1° N, +0.4° W]. Since a new maximum emerged from this first refinement exercise, a second grid-refinement exercise was performed. This time, the refinement was performed around the highest two basin average precipitation values, a region which was considered to be the area of highest precipitation. This second refinement involved using 0.02-degree increments, as opposed to the 0.1-degree increments used for the first refinement exercise that produced the results of Figure 7-7. The area of this second refinement is represented by the red box shown on the left of Figure 7-9, and it encompasses the two largest precipitations obtained from the original and first-refinement transposition exercises (143 mm [5.6 in.] and 149 mm [5.9 in.]).

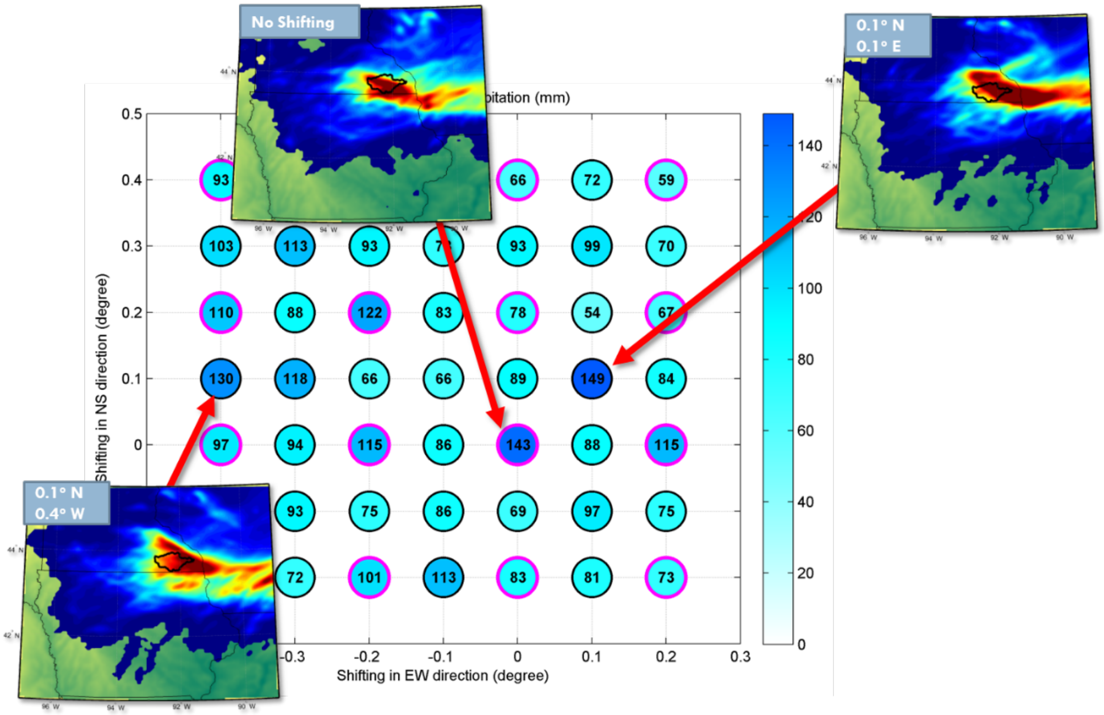

Figure 7-8 Plots of the MCS Corresponding to the Largest Basin Average Precipitation of the First Refinement Exercise (149 mm [5.9 in.]) as well as the Two MCSs Corresponding to the Second Two Highest Basin Average Precipitation Values (143 mm [5.6 in.] and 130 mm [5.1 in.])

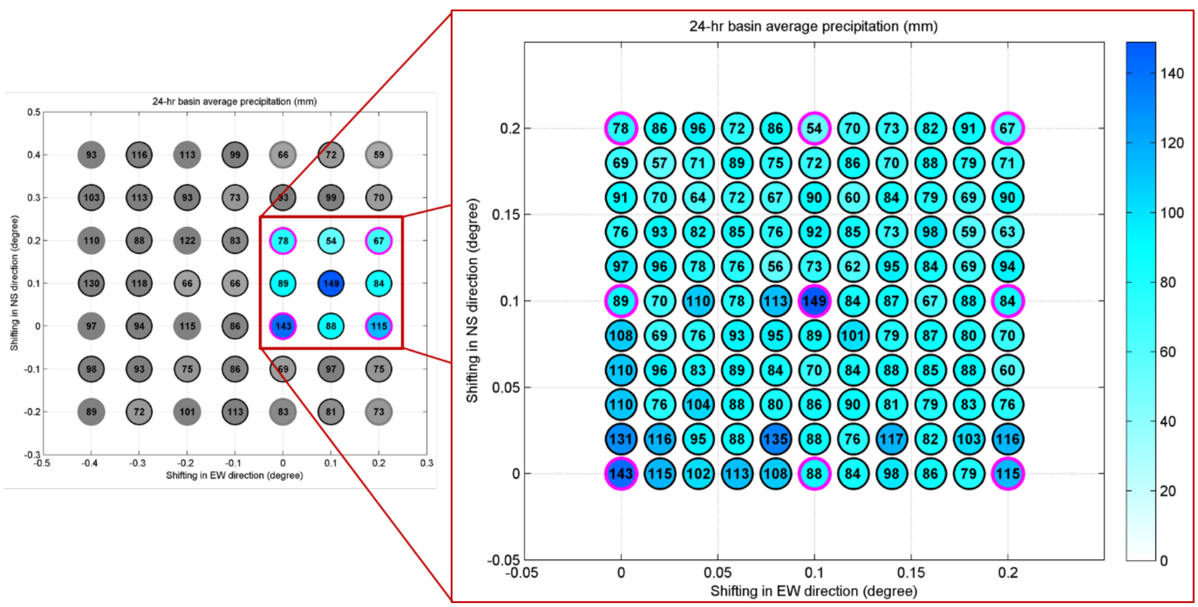

Figure 7-9 Area Selected for the Second Grid-Refinement Exercise

Zoomed-in figure shows the results of the first grid-refinement exercise (circles with pink boundaries) and the new results of the second grid-refinement exercise (circles with black boundaries).

The results of the second grid-refinement are shown on the zoomed-in plot of Figure 7-9. In this plot, the circles with the pink boundaries represent the precipitation values that were obtained from the first refinement exercise using the 0.1-degree increments. The circles with the black boundaries represent the newly computed basin average precipitation values obtained for the second refinement exercise, with a 0.02-degree increment. This time, from the second refinement results, no new maximum 24-hr basin average precipitation value was found. From the newly found values of the second grid-refinement, a high value of 135 mm (5.3 in.) was produced with a shift of [+0.02° N, +0.08° E]; however, none of the newly computed precipitations exceeded the maximum of 149 mm (5.9 in.). Seeing that with this second fine grid-refinement there was no increase in the basin average precipitation, it was determined that a refinement of the level of 0.02 degrees was enough for this purpose; thus, no further refinement under 0.02 degrees was performed.

Therefore, with this transposition exercise, it was possible to transpose the August 12, 2080 MCS to a location that produced a 24-hr basin average precipitation (149 mm [5.9 in.], Figure 7-10) that is only slightly greater than that of the original, no-shifting condition (143 mm [5.6 in.], Figure 7-4). This was achieved by shifting the BCs by [+0.1° N, +0.1° E]. Comparing the figures for the unshifted (Figure 7-4) and the transposed (Figure 7-10) MCSs, it is clear that the transposition caused the MCS to occur slightly to the north and east of its original location. This is clear because in the former case (Figure 7-4), the MCS covers most of the watershed except part of the northeastern side, whereas for the latter case (Figure 7-10), the MCS covers most of the watershed except part of the southwestern side. Moreover, the transposed MCS clearly has a larger area of intense precipitation as well as a different shape when compared to the unshifted MCS. This comes as a result of using a physically based method that conserves mass, momentum, and energy, and that incorporates all other major physical factors into the simulation.

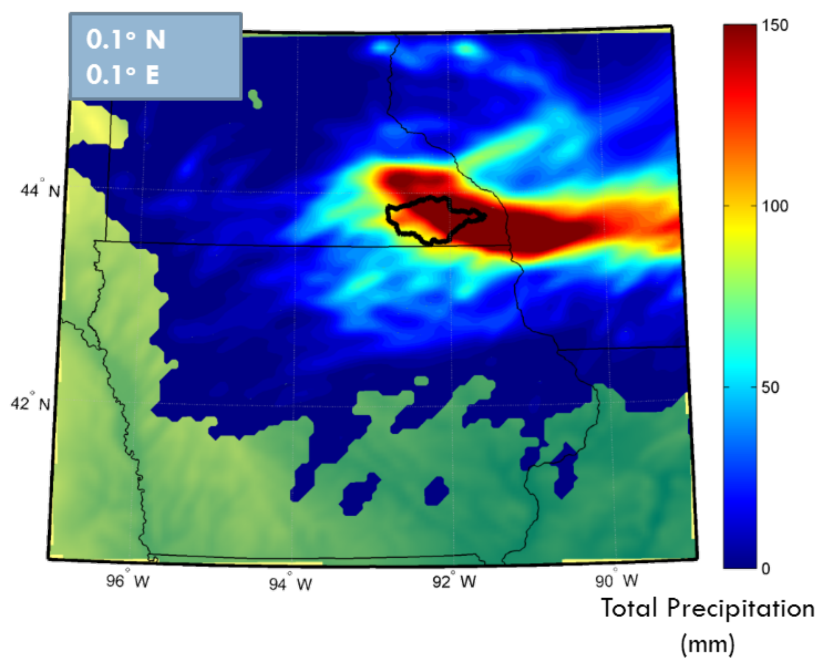

Figure 7-10 Simulated 24-hr Accumulated Precipitation Fields During the August 12, 2080 MCS Resulting from a Transposition by [+0.1° N, +0.1° E]

Total accumulated precipitation computed from 08/11/2080 at 20h to 08/12/2080 at 20h.

As a result of this transposition exercise, it was possible to find that the 24-hr basin average precipitation of the August 12, 2080 MCS would not be expected to produce a much larger basin average precipitation even if it occurred in a slightly different location than its original location. The major reason for this conclusion is that the intense MCS was already located in a position where it covered most of the target watershed. In this case, the original, unshifted MCS had the potential to produce very high 24-hr basin average precipitation. This is unlike the case for the transposition exercise performed for the historical MCS (Chapter 5), in which case the unshifted MCS was quite far from the target watershed, and the transposition allowed the storm to occur directly over the watershed, thus significantly increasing its basin average precipitation. As such, in the case of the August 12, 2080 MCS, there was very little that could be done with transposing the MCS to increase the basin average precipitation, and this was revealed very clearly in the previous discussion and the results of the transposition and the grid refinements.

However, it should be noted that the maximum 24-hr basin average precipitation obtained from this exercise for the August 12, 2080 MCS does not represent the largest basin average precipitation that may be obtained over the Root River basin above Houston in the future years. In order to determine such a value, it would be necessary to perform the transposition for all future intense MCSs over the target watershed. Such an exercise would allow one to find the maximum 24-hr basin average precipitation projected for that target region. This is because some other future intense MCSs may be even more intense than the August 12, 2080 MCS, but may have occurred far enough from the target watershed that their corresponding basin average precipitation was low. Transposing these intense MCSs over the target watershed may indeed lead to much higher 24-hr basin average precipitation values that would be able to exceed the 149 mm (5.9 in.), which was determined in this section for the August 12, 2080 MCS. From such an exercise of transposing all the future MCSs of the 21st century, one can then get a more realistic idea of the maximum 24-hr basin average precipitation that could be physically expected to occur over the target watershed during the future years of the 21st century due to intense MCSs occurring in the Midwestern United States.

8 SIMULATION OF FUTURE TCS IN THE ATLANTIC OCEAN WITH THE WRF MODEL

In order to explore the 21st century extreme precipitation conditions, as compared to the historical extreme conditions, one GCM climate projection for the 21st century was selected and analyzed for its extreme precipitation events after dynamically downscaling this projection by means of the WRF model. As discussed in Chapter 2, this projection is CCSM4 based on RCP 4.5.

This chapter provides results for the DD of TCs from CCSM4.

8.1 Literature Review

Three different approaches are available to investigate changes in TCs due to climate change using GCMs (Bengtsson et al., 2007; Emanuel, 2013). The first approach is to use predictors for the development of TSs, which relates the observed frequencies of tropical cyclogenesis to large-scale environmental factors. This approach has the advantage to be applicable at low resolution, to have a strong empirical foundation and to be easy to apply to reanalysis or model datasets. However, several problems exist with current predictors such as the overestimation of the importance given to SST in some studies. Moreover, it only accounts for the locations and frequencies of TCs, and does not predict changes in the intensity or in the track of TCs. Finally, such predictors are generally developed and calibrated to reproduce regional variability, and they might not be able to accurately respond to global changes. The second approach consists of the direct use of GCM outputs to identify TCs. In order to be applicable, this approach requires sufficient horizontal resolution. However, due to the computational cost associated with the run of GCMs, coarse resolutions are usually used so that TCs are poorly resolved, especially the most powerful storms, resulting in a significant truncation of the intensity spectrum. In fact, in early studies, TCs are instead referred to as “hurricane-type vortices” (e.g., Bengtsson et al., 1996) to emphasize the limitations of the models to reproduce actual TCs. Algorithms have been developed in order to detect TCs in GCM outputs. The criteria used for such identification are usually the presence of a warm core, the maximum wind speed at the surface, and the central surface pressure. Nevertheless, a universally agreed-on algorithm still does not exist. A third technique is DD which is the approach used in this project. DD allows better spatial resolution of the TCs since regional or local models have a finer resolution than GCMs. Yet DD also has shortcomings. For example, there is a lack of feedback between the simulated TCs to the global climate system. Moreover, problems can arise due to the mismatch between the regional model physics and the global model physics.

Several studies attempted to investigate the changes in TC activity in the future by direct use a GCM, corresponding to the second approach emphasized in the previous paragraph. One of the first attempt was done by Broccoli and Manabe (1990). They assessed the possibility of using a climate model to investigate the effects of greenhouse warming on the climatology of TCs. Numerical experiments were performed with the GFDL global climate model with two different horizontal resolutions: 1) 4.5° x 7.5° (500 km x 833 km) (latitude x longitude) and 2) 2.25° x 3.75° (250 km x 417 km). The model used 9 vertical layers. They also consider two treatments of cloud cover. First, they used a prescribed cloud distribution based on climatological data. Second, they used a simple cloud model with overcast cloud if the relative humidity exceeds a certain threshold and clear sky otherwise, while no explicit treatment of cloud microphysics processes was incorporated. They found that the runs using higher resolution managed to capture several structural characteristics of TCs such as the presence of a warm core, near saturation at the cyclone center, strong upward motion, and the presence of a large comma-shaped area of precipitation around the center. However, this resolution remained too coarse to resolve such structural features as eyewalls and spiral bands. The model produced a realistic global distribution of TCs. Differences in the number of storms were observed between the two treatments of cloud covers, with more frequent storms for the variable cloud cover. Results regarding the response of TC climatology to a doubling in C02 concentration were inconclusive. Indeed, with the prescribed cloudiness, they obtained a significant increase in the number of storm-days, which measures the combination of the number of TCs and their duration. However, with cloud feedback, the model gave a significant decrease in the number of storm-days. These results are not affected by the change in horizontal resolution.

Bengtsson et al. (1996) used the ECHAM3[12] atmospheric model at T106 resolution (i.e. a mesh with lat x lon = 160 x 320 nodes) in order to investigate the influence of greenhouse warming on the climatology of TCs. The anomalies in SSTs were obtained from a previous climate change experiment with a low resolution ocean-atmosphere coupled model that was integrated for 100 years from 1985 to 2085 with the assumption of an approximate 1% annual increase in C02, corresponding to Scenario A of the Intergovernmental Panel on Climate Change (IPCC). They forced the model on the lower boundary with SST data at the time when the atmospheric concentration of C02 has doubled. More precisely, the difference in SST between the future climate and the present climate were calculated, and this anomaly was added to the actual monthly SSTs. The model was integrated for a 5-year period, for which 54 TCs per year were produced in average. They found that the global distribution and seasonal variability of TCs when the atmospheric C02 has doubled is in agreement with the geographical distribution and seasonal variability of the present climate. However, the number of storms was reduced. They suggested that such a decrease in the counts of TCs was due to a change in the large scale circulation, such as a strengthening of the upper air westerlies, and a weakening of the Hadley circulation. Furthermore, they showed that the low level vorticity is generally reduced compared to present climate, whereas the vertical tropospheric wind shear is somehow increased. Moreover, they claimed that the characteristic structure of hurricanes can be reproduced very realistically with a T106 horizontal resolution. According to the authors, experiments with a coarser resolution produce in general fewer storms. They insisted that, in order to produce a realistic number of storms, coast lines and orographical details need to be well described. Although a significant reduction in the number of TCs was observed, there was no reduction in the strength of TCs. They noted that the most powerful storm under the doubled CO_2 conditions had higher maximum wind speed than the most powerful storm under the current conditions.

Oouchi et al. (2006) investigated the changes in the frequency and intensity of TCs in a greenhouse-warmed climate using a high-resolution (20 km grid resolution) global atmospheric model from the Meteorological Research Institute (MRI)/Japan Meteorological Agency (JMA). They performed two experiments for a 10-year simulation period. The first experiment is for the present climate whereas the second experiment corresponds to a future greenhouse-warmed climate for which the greenhouse-gas concentration and SSTs are increased. The high-resolution GCM was run on the Earth Simulator (Sato, 2004). 60 vertical levels were used with the model top at 0.1 hPa. The 10-year period for the simulation of the present climate was from 1982 to 1993. For the simulation of the future climate, they calculated the change in SST due to global warming based on the IPCC A1B emission scenario, for which the CO_2 concentration approximately doubles around the 2080-99 period. More precisely, they subtracted the average SSTs over 1979-98 from the average SSTs over 2080-2099 obtained from the MRI-CGCM2.3 (Yukimoto et al.,

[12] ECHAM is an atmospheric GCM, developed at the Max Planck Institute for Meteorology (http://www.mpimet.mpg.de/en/science/models/echam.html)

2006) having a significantly coarser resolution (about 2.8 x 2.8 degrees grid spacing or 311 km x 311 km), and then added this perturbation onto the observed SSTs. Furthermore, for the warmer climate experiment, they took the concentrations of the greenhouse gas and the aerosols from the values of the year 2090 in A1B scenario. Due to the higher resolution compared to previous climate models, the authors showed that this GCM managed to capture the typical inner structure of TCs, including varying rainfall intensity substructures in the TC rainbands. They found that the TC frequency in the warm-climate decreases by 30 % globally, but increases in the North Atlantic compared to present. Moreover, they observed an increase in the number of the intense TCs. In particular, the most intense storm in the warmer climate had a MSW larger than for the present climate by 7.3 m s^{-1} in the Northern Hemisphere, and by 3.3 m s^{-1} in the Southern Hemisphere. According to the authors, the decrease of the total number of TCs is likely to be due to the stabilization of the atmosphere in the warmer climate. Besides, although previous experiments have found a certain homogeneity in the changes in TC intensity and frequency from basin to basin, the authors found that changes are basin-dependent. For example, Knutson and Tuleya (1999) found an increase in the intensity of TCs in all basins under the future conditions, whereas in this study changes in intensity are basin- dependent. The authors emphasized that the increase in resolution to a 20-km grid does not solve all the problems identified in previous studies. In particular, there are still deficiencies in reproducing the frequency, intensity, and geographical distribution of TCs, as well as to properly account for intense hurricanes with wind speed larger than 60 m s^{-1}. They claimed that a major advancement in their work was that their GCM is able to represent directly TCs, including their inner structures and spontaneous development, instead of relying on some artificial forcing or seeding.

Bengtsson et al. (2007) used the Max Planck Institute (MPI) coupled (ECHAM5/MPI-OM) and atmosphere (ECHAM5) climate models to study the effects of changing climate conditions on the frequency and intensity of TCs in the Northern Hemisphere. Three horizontal grid resolutions were used: T63 resolution, T313 resolution, and T319 resolution. Four criteria were used to identify TCs, namely an intensity threshold for the vorticity at 850 hPa, a minimum reduction of vorticity between 850 hPa and 250 hPa, the existence of a positive vorticity center at all levels between 850 and 250 hPA, and the minimum number of consecutive time step for which the previous three criteria are attained. First, the model was run for the coarser resolution for three 30-year periods at the end of the 19th, 20th, and 21st centuries using the IPCC Special Report on Emissions Scenarios (SRES) scenario A1B. The number of TCs between the 19th and 20st century were approximately the same whereas the number of TCs significantly decreases by the end of the 21st century, by about 20%. Besides, with the T63 resolution, the number of the intense storms remained the same. Second, the model was run for the intermediate grid resolution using SSTs from the T63 resolution runs. In this case, the authors noted a 10% decrease in the number of TCs in the 21st century, and a substantial increase in the number of the most intense storms. For example there was 1/3 times more TCs with a maximum wind speed of 50 m s^{-1} in the 21st century. The largest intensification was observed in the Eastern Pacific and in the Atlantic where there was no significant change in the total number of TCs. With the finer resolution grid, the model was run only for the last 20 years of the 20th and 21st century. The results in terms of the number of TCs were similar to the results obtained with the T213 grid, except that the TCs were in general more intense. It was also observed that the size of the TCs decreased as the resolution was increased from T63 to T319, by a factor of about 2.3. Besides, as the resolution was increased from T63 to T213, the number of TCs was multiplied by about 3, whereas the number of TCs in the T319 experiment was similar to the T213 experiment. The authors indentified two competitive processes affecting TCs in future warmer conditions. On the one hand, the reduction in vertical circulation and the increase in static stability seemed to be responsible for a reduction in the number of TCs. On the other hand, the increase in water vapor and in temperature provides more energy to the storms, so that higher specific humidity and increased SSTs will result in stronger TCs whenever favorable conditions occur.

Murakami et al. (2012) investigated the changes in TC activity in the future using a new version of the high-resolution 20- and 60-km-mesh MRI atmospheric GCM (MRI-AGCM version 3.2). They showed that the new version of the model produced a more realistic simulation of the distribution of TCs in the present (1979-2003) than the previous version (version 3.1). They suggested that these improvements may be due to the improvements in the simulation of the vertical velocity and large-scale vorticity fields, consistent with improvements in the simulation of precipitation. Furthermore, the 20-km resolution version 3.2 was able to simulate the very intense TCs (categories 4 and 5) reasonably well compared with observations, and the authors emphasized that it was the first time that a GCM had been able to capture such intense TCs through a multidecadal simulation. They explained that such improvements in simulating very intense TCs was due to a new cumulus convection scheme in version 3.2. They used both versions of the model to simulate the future climate for the period 2075-99 under the IPCC A1B scenario. They found a consistent decrease in the number of TCs globally and in both hemispheres in the warmer climate by 13%-25%, with some differences in basin-scale TC numbers between the two versions. Both versions also projected an increase in the frequency of intense TCs, with a smaller increase for the version 3.2 due to a substantial decrease in TC intensity over the South Pacific Ocean compared to version 3.1. They examined several dynamical and thermodynamic backgrounds fields to assess the contributions in the changes in the frequency of TC genesis. The most highly correlated factor was the projected changes in the variance of tropical synoptic-scale disturbances, followed by the changes in the relative vorticity at 850 hPA and the changes in the vertical velocity at 500 hPa; the changes in vorticity and vertical velocities being associated with the projected weakening of the Walker circulation.

Due to the large computational costs associated with the direct simulation of TCs with GCMs, and their usual inability to capture the most intense hurricanes, several studies used DD to investigate the change in TC activity in the future climate. A first example is given by a series of articles by Thomas R. Knutson and coworkers.

Knutson and Tuleya (1999) used the GFDL regional high-resolution hurricane prediction system in order to study the consequences of a C02-induced global warming on the intensity of strong hurricanes. The outputs from the GFDL R30-resolution global coupled climate model were used as ICs and BCs for the regional model. In Knutson and Manabe (1998), this global model was run for a 120-year period twice: 1) for a control run with CO2 kept constant at present day levels, and 2) for an idealized transient increase in C02 concentration by 1% per year. Knutson and Tuleya (1999) downscaled to ~18 km grid resolution 51 TCs in the northwest Pacific for both the present-day conditions, and the future conditions. These storms were taken from years 70 to 120 in the aforementioned experiments. For each storm, the regional model was run for a 5-day period without ocean coupling. In the future climate, SSTs are warmer by approximately 2.2°C on average, the lower troposphere is warmer by about 2.5°C, the upper troposphere is warmer by more than 5°C, and there is an increase in the environmental convective available energy (CAPE). Knutson and Tuleya (1999) also performed idealized experiments with an initial disturbance embedded in simplified flow fields for all basins. Idealized experiments were used in order to reduce the noise due to the synoptic variability of transient flow features. The simplified flow fields were characterized by an approximately uniform SST, by the absence of other initial disturbances, and by the absence of land. The large-scale environment was obtained by averaging in time and space SSTs, temperature, and water vapor fields. Besides, the wind field was taken as a uniform easterly flow at all levels. Knutson and Tuleya (1999) found that TCs in the future climate are more intense than in the present climate. More precisely, their surface wind speed was about 3-7 m/s (5%-11%) larger, and the central surface pressure was decreased by 7-24 hPa. Besides, near-storm precipitation was increased by about 28% in the warmer climate. They also observed that future TCs are slightly larger than present TCs: the radius of hurricane force winds was 2-3 % larger in the future and the storm penetrated slightly higher into the troposphere. The storm tracks in the future climate were very similar to those in the present climate. The results for the idealized experiments were in agreement with the downscaling of the 51 TCs. According to the authors, it shows that the results obtained for the NW Pacific are also qualitatively applicable to other basins. Besides, they explained that the effects of the stabilization of the troposphere due to enhanced warming in the upper troposphere which would tend to reduce the strength of TCs is counterbalanced by the large increase of water vapor content in the lower troposphere, so that stronger TCs are actually produced in the warmer climate. Finally, the authors pointed out that the absence of ocean-coupling in their simulations is an important limitation.

Knutson et al. (2007) used a 18-km-grid regional nested model in order to simulate 27 Atlantic hurricane seasons, and more specifically the period from August-October starting in 1980 until 2006. The atmospheric dynamical core was the GFDL RAM. The modeling domain covered the tropical Atlantic, subtropical Atlantic, the Gulf of Mexico, and parts of western Africa. The model used 690x300 nodes and 45 vertical levels. No cumulus parameterization was used. NCEP-1 reanalysis was used to force the model on the boundaries and to nudge the interior through a spectral nudging approach. In particular, observed atmospheric state was used to force the model on its lateral boundaries and observed SST was used to force the model at the lower boundary. Small-scale transients including TCs up to category 4 hurricanes were generated by the model constrained on the large scales by the nudging. This modeling approach relies on the quality of large-scale atmospheric conditions. An algorithm was used to detect and track TCs. They used several statistics in order to evaluate the model's performance: hurricane counts, accumulated cyclone energy (ACE), and the power dissipation index (PDI, a measure of the destructive potential of storms). Results were satisfactory as the model succeeded in reproducing the trend toward increasing activity over the period 1980-2005, and other interannual variations. It also accounted for observed statistical relations between El Niño-Southern Oscillation (ENSO) and TC frequency. However, the model had some limitations. In particular, spurious storm developments were observed particularly in subtropical latitudes, and the frequency of TS was too high. Besides, category 5 hurricanes could not be simulated. They observed that the storminess of the model was sensitive to the strength of the nudging: the weaker the nudging the larger the number of simulated storms. They hypothesized that this behavior is due to the fact that, when the model is run without nudging, the vertical mean thermodynamic profile is too unstable, causing excessive storm development. Using cumulus parameterization tended to correct this issue, but in this case too little contrast was observed between the very active season in 1995 and the very inactive season in 1982. They concluded that the strength of the interior nudging in the model is an important optimization parameter. They also used precipitation in order to assess the model's performance, because precipitation is only indirectly affected by the nudging. The model produced a realistic Atlantic Intertropical Convergence Zone (ITCZ) and a realistic precipitation storm track along the U.S. East Coast. However, it produced substantially more precipitation than observed in the extreme eastern Pacific. A sample hurricane was examined to show that the model succeeded in reproducing features such as rainbands and a clearly discernible eye. In addition, they suggested that the forcing of interior circulation features is less important than the forcing of the mean thermodynamics state. In fact, experiments showed that nudging of the wind alone caused excessive storm activity and too little contrast between the seasons in 1995 and in 1982. They pointed out that not only the model is sensitive to what variables are nudged but also what time scale is used for the nudging.

Knutson et al. (2008) used the modeling framework of Knutson et al. (2007) described in the previous paragraph to investigate the effects of the changes in large-scale climate which are projected to take place by the end of the 21st century on Atlantic TC activity with an ensemble of GCMs. They run each of the hurricane seasons (August-October) for the period from 1980 to 2006 by keeping the daily to multidecadal variations unchanged, and by altering the mean atmospheric state (which are used by the interior nudging) and SSTs according to late 21st century changes predicted by an ensemble of models from the World Climate Research Program CMIP phase 3 (CMIP3) under IPCC emissions scenario A1B. The future climate state is characterized by warmer Atlantic SSTs (by 1.72 °C), increased vertical wind shear, increased upper-tropospheric warming relative to the surface, and reduced low- to mid-tropospheric relative humidity in the Caribbean. More precisely, in the climate change experiment, the original observed conditions were altered by a time-invariant three-dimensional climate change perturbation, so that the large-scale interannual to multidecadal variations in the interior, and the high-frequency weather variability imposed at the boundaries were kept unchanged. This approach is often referred to as the *pseudo-global warning dynamical downscaling* (PGW-DD) method. Knutson et al. (2008) explained that one advantage of this approach is to avoid the direct use of climate model simulations: GCMs' outputs have known biases that can distort the simulations of TCs. The PGW-DD method reduces the model bias contained in the GCMs. On the other hand, the PGW-DD method makes strong assumptions. Since the governing equations are nonlinear, adding perturbations fields due to climate change to the present-day atmospheric fields may result in imbalances between nonlinear terms, such as the advection terms (Kawase et al., 2009). Knutson et al. (2008) pointed out that some indices such as the PDI which are strongly influenced by the intense hurricanes should be approached with caution because the model could not simulate hurricane as intense as observed during the period 1980-2006. In particular, the most intense simulated central pressures were approximately equal to 937 hPa, compared to 882 hPa for the observation, whereas the most intense simulated surface winds were approximately equal to 47 m s^{-1}, compared to 85 m s^{-1} for the observation. They found that the model produced significantly less TS (-27%), hurricanes (-18%), and major hurricanes (-8%) under the future conditions. However the frequency and intensity of the strongest hurricanes increased, both with respect to surface wind speed, and with respect to central pressure. In particular, 12 hurricanes with wind speed above 45 m s^{-1} occurred in the warm-climate runs, against 5 in the control runs. Furthermore, they noted a significant increase in the near-hurricane rainfall rates by 34%, 23% and 10% when averaged within 50km, 100 km and 400 km of the storm center, respectively. Nevertheless, they explained that such results should be taken with caution because the composite hurricane precipitation rates in the control model were higher than observed. The authors noted that results obtained with individual GCM can differ substantially from the results obtained with the ensemble mean (as discussed in the next paragraph). As a result, this study relied on the assumption that the average downscaled TCs response to climate change can be approximated by downscaling the 18-model ensemble mean. In other words, the assumption was made that taking the average of the downscaling results from individual GCMs gives similar results than the downscaling of the ensemble mean of these GCMs.

Bender et al. (2010) used two operational versions of the GFDL hurricane model to further downscale the results from Knutson et al. (2008) in order to be able to reproduce major hurricanes (categories 3 to 5). This includes the downscaling with the ZETAC model[13] of the ensemble mean of 18 GCM projections, as well as four individual GCM projections. The GCMs were from CMIP3 and they used the IPCC A1B emissions scenario, as detailed in the previous paragraph. They found that the frequency of category 4 and 5 hurricanes will nearly double by the end of the 21st century while the overall frequency of TCs will decrease. Furthermore, the largest increase in the

[13] https://www.gfdl.noaa.gov/hurricane-regional-modeling/

frequency of cat. 4 and 5 hurricanes were observed in the Western Atlantic, north of 20°N. They found substantial difference in the results between the four GCMs. For instance, the experiment using the Hadley Centre UK Meteorological Office UKMO-HadCM3 predicted a decrease in all TC categories. They also found an increase in hurricane damage potential in the United States, by 30% for the CMIP3 18-model ensemble. This increase is due to the fact that major hurricanes account for most of normalized hurricane damage in the U.S. although they represent only a small fraction of U.S. landfall. For example, very intense hurricanes (cat. 4 and 5) account for 6% of U.S. landfall, but for 48% of all hurricane damage.

Knutson et al. (2013) used DD to investigate the robustness of potential changes in hurricane activity to 21st century projections of climate change in the Atlantic region. They examined multimodel ensembles from both CMIP3 with SRES A1B scenario for the late 21st century, and CMIP5 with RCP 4.5 scenario for the early and late 21st century. They also downscaled 10 of the CMIP3 models to study the spread of the results. Three different DD models were used to obtain the TC projections. First, the ZETAC model, a regional 18-km grid atmospheric model, was used. In order to explore the effects of climate changes with this model, the authors used the PGW-DD method as in Knutson et al. (2008): they perturbed the reanalysis input with GCM-projected changes in SSTs, temperature, moisture, and large-scale circulation. This implies that the climate change runs had the same interannual variability as the control run (present conditions) since an August-October mean climate change perturbation which remains constant from year to year is added to the NCEP reanalysis. More precisely, for the CMIP3 18-model ensemble, the time-invariant three-dimensional perturbation fields were obtained by subtracting the August-October time-average fields for the period 2001-2020 from the August-October time-average fields for the period 2081-2100. The authors reminded that this perturbation approach allows avoiding the direct use of climate model simulations, as explained in Knutson et al. (2008). According to the authors, climate model simulations have known biases, and in particular, they usually fail in producing intense hurricanes or realistic eyewall structures because of their coarse resolution, which can distort the simulation through downscaling of TCs. For the CMIP5 18-model ensemble experiment, anomalies were obtained by subtracting the average fields for the period 1986-2005 from those for the period 2016-35 (early 21st century) and 2081-2100 (late 21st century). Second, they repeated the experiment for a significantly coarser atmospheric model, the High-resolution Atmospheric Model (HiRAM, Zhao et al., 2009) which has a horizontal resolution of 50 km. Third, they used two versions of the GFDL hurricane model at 9-km resolution in order to downscale all the TCs from the 18-km runs to be able to account for the intensity of hurricanes up to cat. 4 and 5. The GFDL hurricane model used 3-level nested moveable domains and was couple to the three-dimensional POM. The authors claimed that this modeling framework allows investigating the sensitivity of the results to different sources of uncertainties. Indeed, uncertainties in the large-scale projected climate changes are accounted for by the two different ensembles (CMIP3 vs. CMIP5) and the individual CMIP3 models, whereas the model uncertainties and uncertainties related to the resolution are accounted for by using the three aforementioned models. Spectral nudging was used with the ZETAC model in order to make sure that the model's large-scale solution remains close to either the NCEP reanalysis for the simulation of the present climate, or the GCMs for the simulation of the future climate. The model was run without subgrid-scale moist convection parameterization. Knutson et al. (2013) explained that the objective of these modeling choices (spectral nudging + absence of CP) is to maintain a realistic large-scale thermodynamic state while allowing the model to resolve condensation and convection on smaller scale to produce storm genesis. They found a substantial decrease in the frequency of TCs. In particular, they obtained a 27% decrease for the CMIP3 ensemble, a 20% decrease for CMPI5-early ensemble, and a 23% decrease for CMIP5-late ensemble. Besides, a statistically significant decrease in TC frequency was obtained for 5 of the 10 individual CMIP3 models. As far as the frequency of very intense hurricanes (cat. 4 and 5) is concerned, a large increase of 87 % is found using CMIP3 ensemble, whereas a substantially smaller increase is obtained using CMIP5 ensemble, equal to 45% for the CMIP5-early scenario, and 39% for the CMIP5-late scenario. On the other hand, the authors found a substantial increase in the lifetime maximum hurricane intensity, by 4% for CMIP3 and by 5% for CMIP5. Finally, a robust increase in hurricane rainfall rates was observed. For example, rainfall rates in the inner core increased by 20% to 30% for the late 21st century. However, precipitation results obtained in this study mainly represented hurricane-related precipitation over the ocean (as opposed to landfalling or inland precipitation), because each storm downscaled with the GDFL hurricane model was simulated for a maximum duration of 5 days (in order to limit the computational effort), and TCs generally spent most of these 5 days over the ocean.

Wright et al. (2015) used the model outputs from Knutson et al. (2008) and Knutson et al. (2013) in order to investigate the frequency of landfalling TCs over the eastern U.S. and their rainfall properties in a future warmer climate. While the frequency of TCs substantially decreased over the Atlantic Ocean, there was no significant decrease of the landfalling TCs in the CMIP5 simulations. However, they observed a 27% decrease in frequency of landfalling TCs in the CMIP3 simulations. Before performing the climate change experiments, the downscaling of 27 August-October seasons from 1980 to 2006 was compared to observations, in order to assess the performance of the RCM in reproducing the tracks and rainfall of landfalling TCs. Despite overall satisfactory results, a spatial bias was found in the results towards heavier precipitation over southeast states, and lighter precipitation over the Mid-Atlantic States. Besides, Wright et al. (2015) found a significant increase over the 21st century in the TC rainfall intensities outside of the eyewall region by 15% for CMIP3 simulations and 10% for CMIP5 simulations for tracks over the eastern U.S., whereas over the ocean the largest percentage increases were observed closer to the storm center with similar magnitudes of increase.

Finally, Knutson et al. (2015) used a two-step DD framework to derive global projections of intense TC activity. The first step consisted in a global simulation with the GFDL High Resolution Atmospheric Model C180 (HiRAM C180) with a horizontal resolution of 50 km. The second step used the GFDL hurricane model with 3-level nested domains down to 6-km resolution to perform the DD of each individual TC. The GDFL was coupled with the POM, allowing the simulation of "cold wakes" which create a negative feedback on TC intensity. The outer domain for the DD was kept stationary while the two innermost domains moved along with each storm. While HiRAM produced a realistic distribution of TC genesis, it could not capture hurricanes with winds of category 4 and 5 intensity. Using the GFDL hurricane model enabled to simulate these very intense hurricanes, although the model underestimated the number of cat. 5 hurricanes. The DD approach was first evaluated by simulating the global TC activity for the period 1980-2008 using interannually varying SST and sea ice distributions. 3081 TCs were simulated, compared to 2518 storms in observations. Besides, present-day and late 21st century climate conditions were compared using two sets of 20-year simulations based on a repeating seasonal cycle design. More precisely, 20 repeating cycles of SST and external forcings were used instead of the interannually varying SST and external forcings so as to reduce the misleading influence of interannual variability ("noise") on the climate sensitivity runs. For the present-day experiment, they used observed SSTs (from the HadISST SST dataset) and sea ice distributions whereas for the late 21st century experiment they used altered SSTs, sea ice concentration, and greenhouse concentration obtained from a 13-member multimodel ensemble from CMIP5 with RCP4.5. They found a global decrease in the frequency of TCs in the warmer climate of the late 21st century, and an increase in TC intensity, in the number of days with a very intense (cat. 4 and 5) hurricane, and in precipitation rates. More precisely, the frequency of TCs decreased by 16% globally whereas the frequency of cat. 4 and 5 hurricanes increased by 24% and the frequency of hurricanes with maximum wind speeds larger than 65 m s^{-1} by 59%. Their results suggested a link between the change in TC intensity and the change in average TC precipitation rate. In particular, they explained that the troposphere in the future warmer climate will contain more water vapor. As a result, moisture convergence is expected to increase, causing in turn larger precipitation rates. However, if the intensity of TCs decreases in a given basin, the increase in water vapor may be offset by the decrease in the wind velocities, resulting in smaller moisture convergence, and smaller precipitation rates. Knutson et al. (2015) emphasized that they obtained substantial variations from one basin to another so that the global changes do not necessarily reflect changes in a given basin. For instance, TC frequency increased in central and eastern North Pacific, and the frequency of cat. 4-5 hurricanes decreased in the southwest Pacific, eastern Indian Ocean basins, and parts of the southwest Pacific. They claimed that this interbasin spread is due mainly to the variation in the magnitude of SST change between one basin and another. More generally, they noted a strong correlation between most of the metrics used in the paper and the basinwide SST changes. Only the precipitation rates in cat. 3-5 hurricanes seemed to be uncorrelated to the magnitude in SST changes. Their modeling approach also succeeded in producing a realistic distribution of outer storm size, and they found that the projected median storm size will remain constant globally, with increases in all basins but a decrease in the northwest Pacific.

Several recent studies used the WRF model to downscale global climate projections from GCMs. Hill and Lackmann (2011) used the WRF model with high-resolution (6-km and 2-km grid spacing) in order to analyze the change of maximum TC intensity and structure in a warming climate under idealized conditions. More precisely, the impact of thermodynamic changes in the tropical environment, including changes in SST, atmospheric temperature, and moisture were investigated, as well as the sensitivity of the result to the choice of the scheme used for the parameterization of the model surface and of the PBL. Furthermore, sensitivity to environmental changes was examined by using an ensemble of GCM projections from three emissions scenarios. Current climate conditions were obtained by averaging the NCEP-NCAR reanalysis data for the period 1990-99 over the region extending from 8.5°-15°N and 40°-60°W in the western portion of the tropical Atlantic TC main development region (MDR), resulting in horizontally uniform fields. Besides, SST was obtained from Advanced Very High Resolution Radiometer (AVHRR) infrared satellite SST data (Reynolds et al., 2007) and was also horizontally and temporally averaged. Future climate conditions were obtained from 13 GCM simulations from CMIP3 corresponding to three emission scenarios. The projected changes in temperature, moisture and SST was computed by subtracting the 1990-99 mean from the 2090-99 mean, averaged spatially over the aforementioned region. These projected changes were added to the reanalysis-derived current climate conditions in order to obtain the future climate conditions. The ideal TC inserted in the each of the horizontally uniform environments was an axisymmetric warm-core vortex, with maximum winds of about 30 m s^{-1} and a minimum SLP of about 981 hPa. The authors performed a total of 78 simulations at 6-km resolution with the WRF model corresponding to the 13 GCMs, with three emission scenarios and two combinations of the model physics. Additional experiments were also conducted with a finer resolution (2-km resolution) within the 6-km grid for the ensemble-mean projected changes for every emission scenario. The authors explained that, although the choice of the combination of the model's options substantially affect the simulated TC, the simulated changes in TC intensity and structure between the TC corresponding to the present conditions and the TC corresponding to the future conditions are less significant. Although 75 of 78 simulations indicated an increase in TC, Hill and Lackmann (2011) observed a large spread between these simulations. According to them, based on the simulation with 6-km grid resolution, the most likely increase in TC intensity due to climate change is 9-12%, although the largest increase was 22%. Moreover, the results in terms of the increase in CPD were similar between the B1 emission scenarios for which SST increases by 1.4°C and the A2 emission scenarios for which the SST increases by 2.7°C. The authors explained that these results are due to the lapse rate stabilization in the troposphere, referring to the stabilization effects caused by the maximized warming in the upper troposphere. It was also observed from the simulations at 6-km resolution that the ensemble-mean projected changes are similar to the projected changes obtained by running the model using the ensemble-mean environmental conditions, which justify comparing the results at 6-km resolution with the results at 2-km resolution obtained with the ensemble-mean environmental conditions only (to limit the computational effort). At 2-km resolution, the authors noted larger changes in the CPD. Larger rainfall rates in the region with 500 km from the center were observed for the future conditions. The authors suggested that this increase is due to an increase in water vapor and in moisture convergence. There was also a substantial increase in the 5-day average rainfall, by up to 19% within 100 km from the center and up to 23% within 200 km. They explained that this increase in the total precipitation was mainly due to the increase in atmospheric water vapor. It was found that the increase in TC intensity due to climate changes was caused by the increase in latent heat release due to the large tropospheric water vapor, and to the intensification of the precipitation mass sink effect due to the larger precipitation rates, rather than being caused by an increase of the thermodynamic efficiency related to the temperature difference between the low-level inflow and high-level outflow, which was actually found to decrease in the future conditions.

Done et al. (2015) used the atmospheric component of the Nested Regional Climate Model (NRCM), a DD tool based on the WRF model, to dynamically downscale large-scale climate data with a focus on the simulation of TCs. More precisely, they simulated current and future TC activity in the North Atlantic to show the sensitivity and limitations of the DD approach by examining the effects of climate biases, resolution, and domain size. They explained that TCs are high-impact events which are challenging to investigate due to their regional variability, rarity, and due to the large uncertainties related to future regional changes. Global climate data were obtained from CCSM version 3 with the A2 scenario. The outputs from CCSM were used as ICs and BCs for the NRCM. Two nested domains were used for the downscaling (see Figure 8-1). The parent domain had a horizontal resolution of 36 km whereas the inner domain had a horizontal resolution of 12 km. The simulations were performed with one-way nesting.

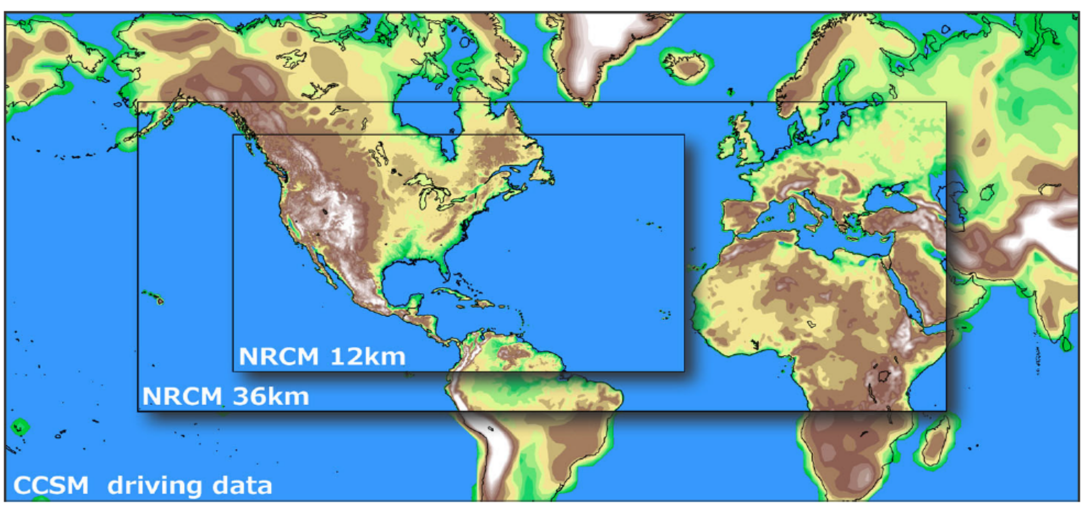

Figure 8-1 NRCM Model Domains at 36 km Grid Spacing (Large Black Box) and 12 km Grid Spacing (Small Black Box)

Model terrain height (shaded) is shown at the different model resolutions and extends beyond the 36 km domain to indicate the resolution of the driving CCSM. From Done et al. (2015).

The model was run for three time periods. First, they covered the period from 1995 to 2005, which corresponds to the base climate. Additionally, two future decades were considered: from 2020 to 2030, and from 2045 to 2055. They showed the importance of the domain location, size, and resolution in order to include important regional climate processes. The authors emphasized the importance of using a sufficient resolution for the simulation of TCs. They showed that, at 36 km resolution, the simulated storms had a simple circular structure, whereas at 12 km resolution, the model could reproduce substructures such as spiral rain bands, and the asymmetries of the eye-wall. The domain needs to be large enough not only to reproduce the individual TCs, but also to capture the associated climate response (upscale interactions). They explained that if the domain is too small, it will be too closely coupled with the driving GCM and the effects would be similar to performing nudging. Besides, they claimed that African easterly waves are not well reproduced by CCSM so that the region of formation of these waves should be included in the simulation domain. Done et al. (2011) illustrated the need to account for bias in the driving GCM. They explained that the simulations driven directly by CCSM produce too strong large-scale flow at upper-levels over the tropical North Atlantic which is responsible for generating anomalously strong wind shear, therefore preventing the genesis of TCs. Through sensitivity analysis, they found that this anomalously strong wind shear was caused by the dynamical propagation of the information on the western and eastern boundaries on the one hand, and by a warm SST bias in the eastern Pacific Ocean on the other hand, creating a permanent El Nino condition characterized by a modified Walker Circulation responsible for the strong wind shear. They had to perform the bias correction before the simulations (i.e. by correcting the CCSM data directly) because no TC was simulated with the biased ICs and BCs. The bias correction was performed by writing the 6-hourly CCSM4 data and the 6-hourly NCEP/NCAR Reanalysis Project (NNRP) data as the sum of a background state plus a perturbation. In both cases, the background state was obtained by averaging over the 20-year period from 1975 to 1994. Afterwards, the bias was removed by replacing the background state of CCSM by the background state of NNRP. They found that the wind shear over the tropical Atlantic was significantly improved when the NRCM was run with the bias-corrected BCs, which allowed the genesis of TCs, with an average of 7.6 North Atlantic TCs annually for current conditions (1995-2005), 8.5 events per year for the period 2020-2030, and 10.4 events per year for the period 2045-2055. Finally, they showed the benefits of combining the DD approach and the statistical downscaling (SD) approach to obtain useful and credible information. They explained that the DD approach is limited by the computational cost associated to it, so that usually only a short period and a small number of events can be simulated. Using statistical methods is a way to complement the DD approach, as it enables increasing the sample size with no significant computational effort required. In particular, they discussed two SD approaches: first a method using empirical relationships with large-scale data from global model or reanalysis, and second a method using extreme values statistics to study changes in the most intense TCs (which would require a much finer resolution to be accounted for).

The DD approach presented so far is the most common. First the large scale fields are obtained by using a GCM with coarse resolution. These fields are then used as input data to a RCM with a finer resolution over a region of interest, within a one-way nesting framework. This approach is sometimes referred to as the limited-area model (LAM). The LAM is not the only DD technique. A few studies evaluated other DD techniques in comparison to LAM. Caron et al. (2011) used the global environmental multiscale (GEM) model in order to study how a change in the model resolution impacts the Atlantic TC activity. The horizontal resolution was increased for 2° (222 km) to 0.3° (33 km). They found that, as the resolution is increased, the simulated Atlantic TCs became more realistic, and they suggested that this improvement was due to a better representation of the African Easterly Waves. Finer resolutions also improve the spatial distribution of the Genesis Potential Index (GPI), which is constructed based on the large-scale fields known to affect cyclone formation. On the one hand, the GEM was run with a uniform grid, with two horizontal grid resolutions: 2° and 1° (111 km). On the other hand, they investigated two methods in order to obtain high resolution (0.3°) over a region extending from the Eastern Pacific to the Arabian Sea, and from about 5° south to about 45° north, while the remaining part of the globe was covered with a 2° resolution grid. The first method was DD with a LAM using one way-nesting, and the second method consisted in using the GEM model with a global variable resolution (GVAR), which allows feedbacks between the high-resolution and low-resolution regions. The high-resolution part of the GVAR coincided with the nested domain, so that it was possible to compare the two DD approaches. No spectral nudging was used for the LAM. In all cases, they simulated 28 Atlantic hurricane seasons from 1979 to 2006. The results were also compared to the dynamical DD with LAM of the ECMWF Reanalysis data. They found that the DD of the reanalysis provided the more realistic results in terms of the variability of Atlantic TCs. Besides, the simulations using the GVAR were found to be more accurate than the simulations corresponding to LAM-GEM. Finally, by using a smaller domain for the LAM, they demonstrated that an accurate representation of African Easterly Waves is very important to simulate the variability of Atlantic TCs. This is because African Easterly waves often serve as precursor systems for downstream cyclogenesis. As the resolution was increased from 2° (uniform global simulation), to 0.3° (GVAR), the number of simulated TCs went from 63 to 282, while 314 TCs were present in the observations (HURDAT database). Furthermore, the cyclogenesis locations and the tracks of the TCs were more realistic with the GVAR compared to the global simulations. They observed that the global simulations at 2° resolution performed well in reproducing the ENSO interannual variability, so that the large-scale forcing of the tropical Atlantic from the Pacific is realistic even for the coarser simulations. However, they found that the LAM-GEM simulations failed in reproducing satisfactorily teleconnections from the Pacific into the Atlantic compared to the GVAR or to the LAM-ECMWF, resulting in significantly worse results in terms of several metrics used to evaluate the performance in reproducing the TC variability. Moreover, the LAM-GEM simulations overall failed in reproducing the relationship between the vertical wind shear in the MDR and the Sahel rainfall, due to an inability to reproduce the strength of African Easterly Waves, which in turn degraded the performance in reproducing the relationship between Sahel rainfall and TC activity. The simulations using GVAR performed significantly better in this regard.

DD to a fine enough resolution using a LAM or GVAR requires large computational resources, which limits the number of numerical experiments that can be performed, as well as the duration of the simulated period. This represents a significant drawback in the context of climate change because it would be very beneficial to evaluate the sensitivity of the simulation results to the modeling choices, including the choice of the GCM used for ICs and BCs, the choice of the emission scenario, the choice of the RCM used for DD, the choice of the RCM's options such as parameterization schemes, the choice of the horizontal and vertical resolutions, of the domain size and location, etc. Although some national and international programs started to move in this direction such as the *Prediction of Regional scenarios and Uncertainties for Defining EuropeaN Climate change risks and Effects* (PRUDENCE) in Europe (Christensen et al., 2007) and the *North American Regional Climate Change Assessment Program* (NARCCAP) in North America (Mearns et al., 2009), such involved sensitivity analyses are not tractable currently for usual DD approaches such as LAM or GVAR. Alternatives have been proposed for the evaluation of the response of TC activity to climate change.

For example, Emanuel et al. (2008) described a DD/SD approach to downscale TC climatologies from global analyses and models. This approach uses both thermodynamic and kinematic statistics derived from global model or reanalysis to generate a large number ($\sim10^3$-10^4) of synthetic TCs. More precisely, the technique uses monthly mean sea surface temperature and atmospheric temperature, and daily horizontal winds at 850 hPa and at 250 hPa. It starts with the random seeding in space and time of all ocean basins with weak, warm-core vortices. The motion of these vortices was determined by a beta-and-advection model whereas their intensity was computed using a coupled ocean-atmosphere numerical model. The track model uses the winds from the global model or reanalysis, whereas the intensity model uses winds, sea surface temperatures, and atmospheric temperature. Additionally, the beta-and-advection model uses synthetic wind time series at two levels (850 hPa and 250 hPa) represented as Fourier series of random phase constrained to have the monthly means, variances, and covariances from reanalysis or global models, and to have a geostrophic turbulence power-law distribution of kinetic energy. The intensity model is called the “Coupled Hurricane Intensity Prediction System” (CHIPS). It has the advantage to be formulated in angular momentum coordinate, which allows having a high radial resolution of the inner core region. They observed that, because of low midtropospheric humidity, low potential intensity, and/or too much wind shear, most of the initial seeds die without achieving TS strength. They showed that the climatology of the surviving TCs agrees reasonably with the spatial, seasonal, and interannual variability of observed storms. The technique was applied to the outputs from 7 GCMs. In order to assess the change in TC activity due to global warming, they simulated 2,000 TCs in each of 5 basins for the last 20 years of the 20th century and for the last 20 years of the 22nd century. IPCC scenario A1b was used, for which atmospheric C02 concentration increases to 720 ppm by 2100 and is then held constant at this value. The simulations showed potentially significant changes in TC activity. However, the sign and magnitude of these changes significantly depended on the basin under investigation, as well as on the GCM. In the end, they concluded that global warming should decrease the frequency of hurricanes and increase their intensity in some locations. Besides, Emanuel (2013) applied the downscaling technique to six CMIP5 global models under the RCP8.5 emissions. The author found an increase in global TC activity. Both the frequency and intensity of TCs were projected to increase in the North Pacific region, North Atlantic Ocean, and South Indian Oceans, which contrasts with the results obtained by applying the same downscaling technique to CMIP3-generation models as well as with the results from other investigations detailed in this literature review.

This literature review showed that several approaches are available to study TCs in the future. DD which is the approach used in this project is one of them. Several guidelines and precautions may be identified from this literature review to perform DD of future Atlantic TCs:

- The resolution in the simulation inner domain should be fine enough to simulate important features of TCs. In this project, a spatial resolution of 5 km in the inner domain was selected which, according to the results of Chapter 4, is fine enough to simulate the precipitation fields caused by TCs.

- The simulation outer domain should be large enough for the following reasons. First, the region of formation of African easterly waves should be included in the outer domain because these waves play an important role in the formation of TCs. Second, if the outer domain is too small, it will be too closely coupled with the driving GCM and consequently unable to capture upscale interactions. This can be all the more problematic if the GCM used for IBCs is biased. This is the reason why a large outer domain was used in this chapter (Figure 8-2).

- The presence of bias in the driving GCM may prevent the WRF model from generating its own TCs. In this case, it is necessary to correct the bias in the IBCs. Fortunately, in this study, the WRF model was able to create its own TCs with the original CCSM4 RCP4.5 projection used for IBCs without having to perform bias correction.

8.2 Simulation Results

Based on the literature review of Section 8.1, DD of CCSM4 was performed over a large outer domain shown in Figure 8-2 at 45-km spatial resolution. A large intermediate domain (15-km resolution) encompassing the Eastern U.S. was also used in order to account for the diversity in TC's tracks and landfall locations.

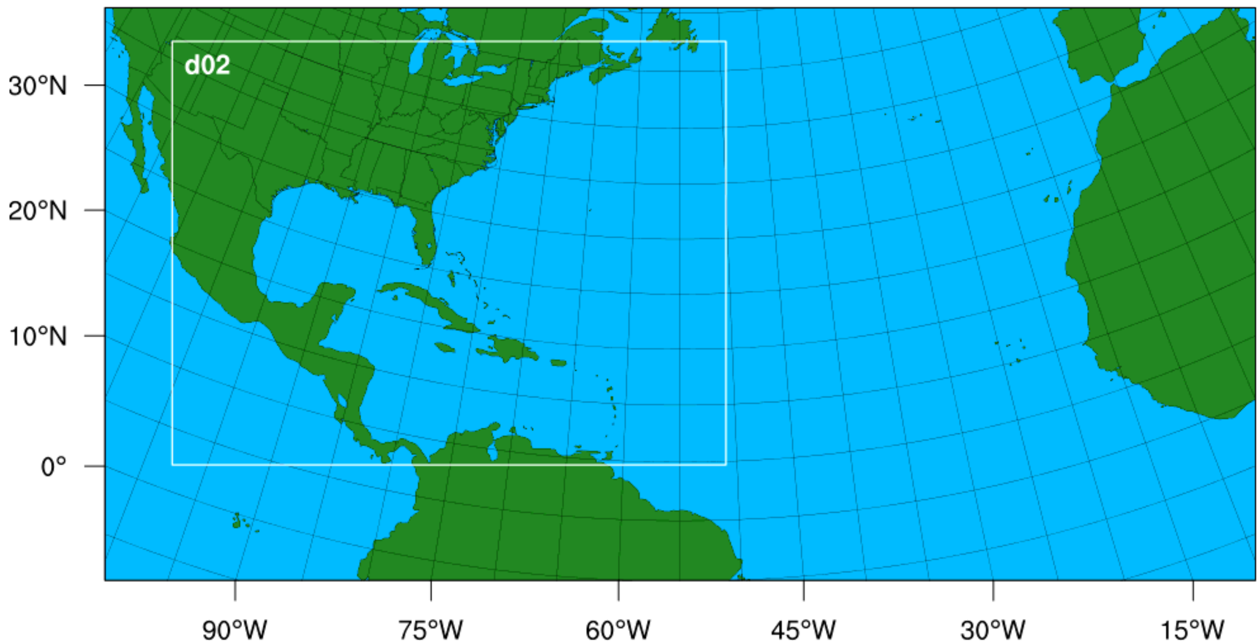

Figure 8-2 Outer Domain and Intermediate Domain Used for DD of CCSM4

On the other hand, using a fixed inner domain (5-km resolution) resulted in an overwhelming computational load so that the inner domain was created manually case by case according to the location of the precipitation field in the intermediate domain in order to make the exercise tractable.

In order to detect TCs in the WRF outputs at 45-km and 15-km resolutions, the SLP and surface meridional wind speed fields were examined visually. A TC has a clear signature in these fields. As illustrated in Figure 8-3, a TC is associated with a local minimum of SLP (Figure 8-3(a)) whereas it is associated with a dipole of surface meridional wind speed (Figure 8-3 (b)). The dipolar structure is less obvious if looking at the surface zonal wind speed field because of the common presence of a strong background zonal wind corresponding for example to the trade winds in the tropics, hence the benefits of working with the meridional component of the surface wind for the purpose of identifying TCs.

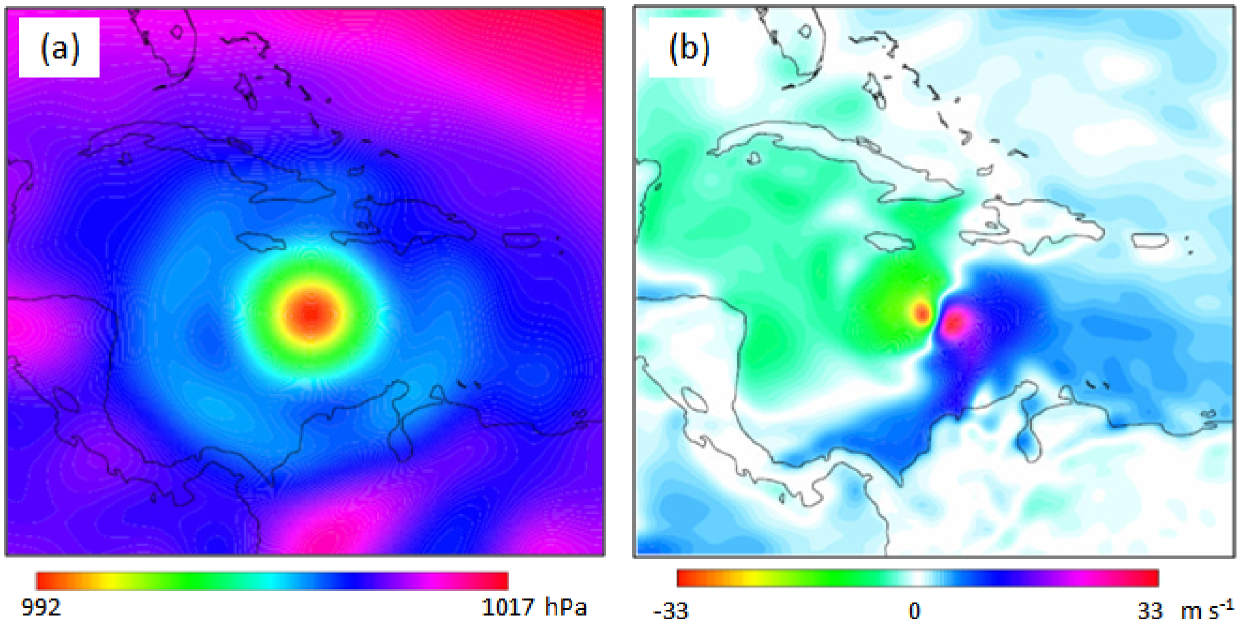

Figure 8-3 Example of (a) the SLP Field and (b) the Surface Meridional Wind Speed Field in Hurricane Matthew on 10/03/2016 06:00 UT

DD of CCSM4 was then performed for each hurricane season (defined as the time interval between the beginning of July and the end of November) during the period 2005-2100. Given the time constraint in this project, the set of options used for the simulations was chosen arbitrarily and it corresponds to the set used for the reconstruction and transposition of Hurricane Ivan since the focus was put on this storm in Chapter 6. Preferably, such a DD exercise should be performed with several sets of model options to investigate the sensitivity of the DD results to these options.

Within the period 2005-2100, 64 landfalling TCs were detected. The precipitation fields of these landfalling TCs in the simulation inner domains are shown in Figure 8-4. Table 8-1 provides information on the simulation start and end dates.

Table 8-1 Simulation Start Dates, Simulation End Dates, and Number Of Inner-Domain Grid Points Above the Precipitation Depth Threshold (Figure 8-4) for the TCs Shown in Figure 8-5

The TC with the largest number of grid points above the precipitation threshold is highlighted in red.

Event #	Simulation start date in intermediate domain	Simulation end date in intermediate domain	Simulation start date in inner domain	Simulation end date in inner domain	Number of grid points above threshold
1	2005-08-10_18:00:00	2005-08-24_18:00:00	2005-08-14_18:00:00	2005-08-17_18:00:00	217
2	2005-08-27_12:00:00	2005-09-10_12:00:00	2005-08-29_18:00:00	2005-09-02_18:00:00	935
3	2006-08-14_12:00:00	2006-08-28_12:00:00	2006-08-17_06:00:00	2006-08-21_06:00:00	256
4	2009-08-12_06:00:00	2009-08-26_06:00:00	2009-08-14_06:00:00	2009-08-19_12:00:00	33
5	2010-09-10_12:00:00	2010-09-24_12:00:00	2010-09-13_12:00:00	2010-09-16_12:00:00	15
6	2011-08-02_18:00:00	2011-08-16_18:00:00	2011-08-04_18:00:00	2011-08-07_18:00:00	19
7	2012-08-23_06:00:00	2012-09-06_06:00:00	2012-08-25_00:00:00	2012-08-28_00:00:00	36
8	2012-08-26_18:00:00	2012-09-09_18:00:00	2012-08-30_00:00:00	2012-09-02_00:00:00	97
9	2013-08-14_12:00:00	2013-08-28_12:00:00	2013-08-18_00:00:00	2013-08-21_00:00:00	38
10	2015-08-28_12:00:00	2015-09-11_12:00:00	2015-08-30_00:00:00	2015-09-02_18:00:00	221
11	2017-08-28_00:00:00	2017-09-11_00:00:00	2017-08-31_00:00:00	2017-09-03_18:00:00	0
12	2020-07-30_12:00:00	2020-08-13_12:00:00	2020-08-05_18:00:00	2020-08-09_12:00:00	0
13	2020-09-15_06:00:00	2020-09-29_06:00:00	2020-09-20_18:00:00	2020-09-23_18:00:00	0
14	2021-08-07_18:00:00	2021-08-21_18:00:00	2021-08-10_18:00:00	2021-08-13_18:00:00	20
15	2021-08-15_18:00:00	2021-08-29_18:00:00	2021-08-20_00:00:00	2021-08-23_18:00:00	509
16	2021-08-27_06:00:00	2021-09-10_06:00:00	2021-08-28_06:00:00	2021-08-31_06:00:00	4
17	2021-10-11_00:00:00	2021-10-25_00:00:00	2021-10-15_06:00:00	2021-10-18_06:00:00	453
18	2024-09-03_00:00:00	2024-09-17_00:00:00	2024-09-04_18:00:00	2024-09-08_00:00:00	96
19	2024-09-10_06:00:00	2024-09-24_06:00:00	2024-09-15_00:00:00	2024-09-18_00:00:00	62

Table 8-1 Simulation Start Dates, Simulation End Dates, and Number Of Inner-Domain Grid Points Above the Precipitation Depth Threshold (Figure 8-4) for the TCs Shown in Figure 8-5

The TC with the largest number of grid points above the precipitation threshold is highlighted in red (Continued).

Event #	Simulation start date in intermediate domain	Simulation end date in intermediate domain	Simulation start date in inner domain	Simulation end date in inner domain	Number of grid points above threshold
20	2025-08-22_06:00:00	2025-09-05_06:00:00	2025-08-25_00:00:00	2025-08-28_06:00:00	43
21	2027-09-03_18:00:00	2027-09-17_18:00:00	2027-09-07_00:00:00	2027-09-10_18:00:00	346
22	2030-08-19_00:00:00	2030-09-02_00:00:00	2030-08-21_12:00:00	2030-08-25_18:00:00	10
23	2031-08-29_00:00:00	2031-09-12_00:00:00	2031-09-02_00:00:00	2031-09-05_12:00:00	822
24	2032-09-23_00:00:00	2032-10-07_00:00:00	2032-09-27_18:00:00	2032-09-30_18:00:00	49
25	2033-08-26_12:00:00	2033-09-09_12:00:00	2033-08-28_12:00:00	2033-09-01_00:00:00	51
26	2033-09-03_00:00:00	2033-09-17_00:00:00	2033-09-04_06:00:00	2033-09-08_00:00:00	211
27	2033-09-21_18:00:00	2033-10-05_18:00:00	2033-09-23_18:00:00	2033-09-26_18:00:00	482
28	2034-09-04_06:00:00	2034-09-18_06:00:00	2034-09-07_18:00:00	2034-09-10_18:00:00	0
29	2037-07-17_18:00:00	2037-07-31_18:00:00	2037-07-19_06:00:00	2037-07-23_00:00:00	16
30	2037-09-23_06:00:00	2037-10-07_06:00:00	2037-09-26_12:00:00	2037-09-29_12:00:00	30
31	2038-08-30_18:00:00	2038-09-13_18:00:00	2038-09-02_12:00:00	2038-09-05_12:00:00	562
32	2038-09-03_00:00:00	2038-09-17_00:00:00	2038-09-08_00:00:00	2038-09-11_00:00:00	4
33	2040-07-12_00:00:00	2040-07-26_00:00:00	2040-07-19_12:00:00	2040-07-22_12:00:00	17
34	2043-08-21_06:00:00	2043-09-04_06:00:00	2043-08-24_06:00:00	2043-08-27_06:00:00	6
35	2043-08-26_06:00:00	2043-09-09_06:00:00	2043-09-02_12:00:00	2043-09-05_12:00:00	853
36	2047-08-20_18:00:00	2047-09-03_18:00:00	2047-08-25_00:00:00	2047-08-28_00:00:00	113
37	2047-08-24_12:00:00	2047-09-07_12:00:00	2047-09-04_06:00:00	2047-09-07_12:00:00	205
38	2048-09-23_00:00:00	2048-10-07_00:00:00	2048-09-29_00:00:00	2048-10-02_00:00:00	389

Table 8-1 Simulation Start Dates, Simulation End Dates, and Number Of Inner-Domain Grid Points Above the Precipitation Depth Threshold (Figure 8-4) for the TCs Shown in Figure 8-5

The TC with the largest number of grid points above the precipitation threshold is highlighted in red (Continued).

Event #	Simulation start date in intermediate domain	Simulation end date in intermediate domain	Simulation start date in inner domain	Simulation end date in inner domain	Number of grid points above threshold
39	2049-08-31_12:00:00	2049-09-14_12:00:00	2049-09-03_18:00:00	2049-09-09_06:00:00	632
40	2050-09-26_00:00:00	2050-10-10_00:00:00	2050-09-27_18:00:00	2050-09-30_18:00:00	723
41	2052-08-28_00:00:00	2052-09-11_00:00:00	2052-08-31_00:00:00	2052-09-03_12:00:00	245
42	2057-08-30_00:00:00	2057-09-13_00:00:00	2057-09-01_06:00:00	2057-09-04_12:00:00	48
43	2057-09-27_18:00:00	2057-10-11_18:00:00	2057-10-01_00:00:00	2057-10-04_00:00:00	27
44	2062-09-09_06:00:00	2062-09-23_06:00:00	2062-09-12_06:00:00	2062-09-15_06:00:00	165
45	2064-09-13_18:00:00	2064-09-27_18:00:00	2064-09-17_18:00:00	2064-09-21_12:00:00	1445
46	2066-08-16_18:00:00	2066-08-30_18:00:00	2066-08-19_18:00:00	2066-08-22_18:00:00	0
47	2066-08-22_06:00:00	2066-09-05_06:00:00	2066-08-24_12:00:00	2066-08-27_12:00:00	28
48	2067-08-26_12:00:00	2067-09-09_12:00:00	2067-08-30_00:00:00	2067-09-02_06:00:00	759
49	2068-08-12_18:00:00	2068-08-26_18:00:00	2068-08-16_06:00:00	2068-08-19_18:00:00	29
50	2068-08-24_00:00:00	2068-09-07_00:00:00	2068-08-29_00:00:00	2068-09-01_00:00:00	302
51	2071-08-29_12:00:00	2071-09-12_12:00:00	2071-09-01_00:00:00	2071-09-04_00:00:00	415
52	2073-09-17_18:00:00	2073-10-01_18:00:00	2073-09-23_00:00:00	2073-09-27_00:00:00	448
53	2078-07-28_06:00:00	2078-08-11_06:00:00	2078-07-30_00:00:00	2078-08-02_00:00:00	0
54	2078-08-04_00:00:00	2078-08-18_00:00:00	2078-08-06_06:00:00	2078-08-09_06:00:00	564
55	2080-09-07_00:00:00	2080-09-21_00:00:00	2080-09-11_12:00:00	2080-09-14_18:00:00	433
56	2080-09-18_12:00:00	2080-10-02_12:00:00	2080-09-22_00:00:00	2080-09-25_00:00:00	286
57	2081-09-24_00:00:00	2081-10-08_00:00:00	2081-10-02_12:00:00	2081-10-05_12:00:00	530

Table 8-1 Simulation Start Dates, Simulation End Dates, and Number Of Inner-Domain Grid Points Above the Precipitation Depth Threshold (Figure 8-4) for the TCs Shown in Figure 8-5

The TC with the largest number of grid points above the precipitation threshold is highlighted in red (Continued).

58	2085-09-14_12:00:00	2085-09-28_12:00:00	2085-09-20_06:00:00	2085-09-26_00:00:00	283
59	2088-08-18_00:00:00	2088-09-01_00:00:00	2088-08-22_12:00:00	2088-08-26_12:00:00	192
60	2088-08-30_06:00:00	2088-09-13_06:00:00	2088-09-02_12:00:00	2088-09-07_06:00:00	40
61	2089-09-13_00:00:00	2089-09-27_00:00:00	2089-09-16_00:00:00	2089-09-19_00:00:00	10
62	2089-09-17_06:00:00	2089-10-01_06:00:00	2089-09-22_00:00:00	2089-09-25_06:00:00	1189
63	2092-08-16_12:00:00	2092-08-30_12:00:00	2092-08-18_00:00:00	2092-08-23_12:00:00	525
64	2098-08-18_18:00:00	2098-09-01_18:00:00	2098-08-25_00:00:00	2098-08-28_00:00:00	271

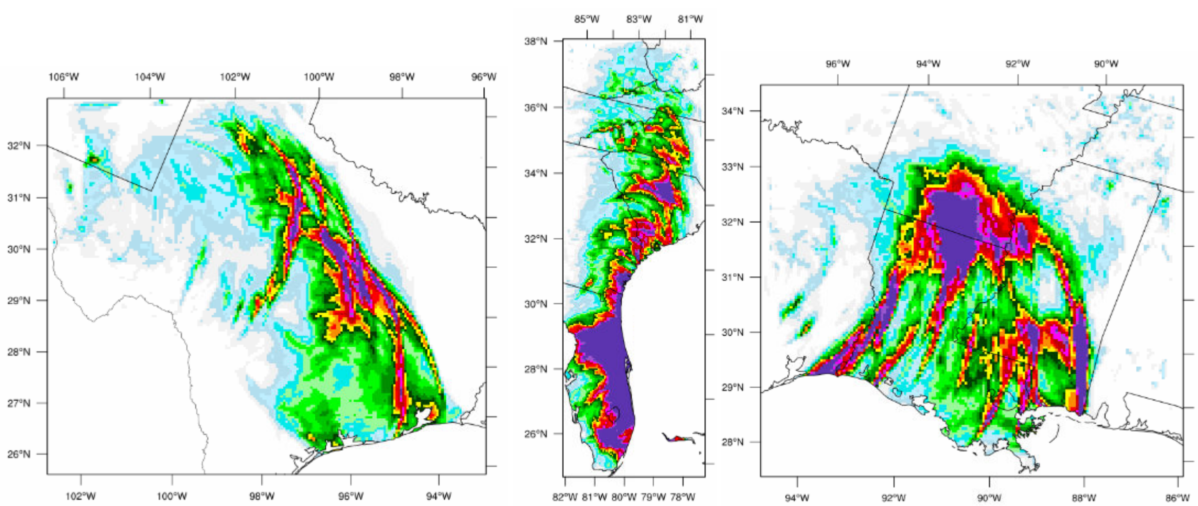

Figure 8-4 Downscaling Results in Simulation Inner Domains

TCs are given in the same order as in Table 8-1, from left to right and from top to bottom.

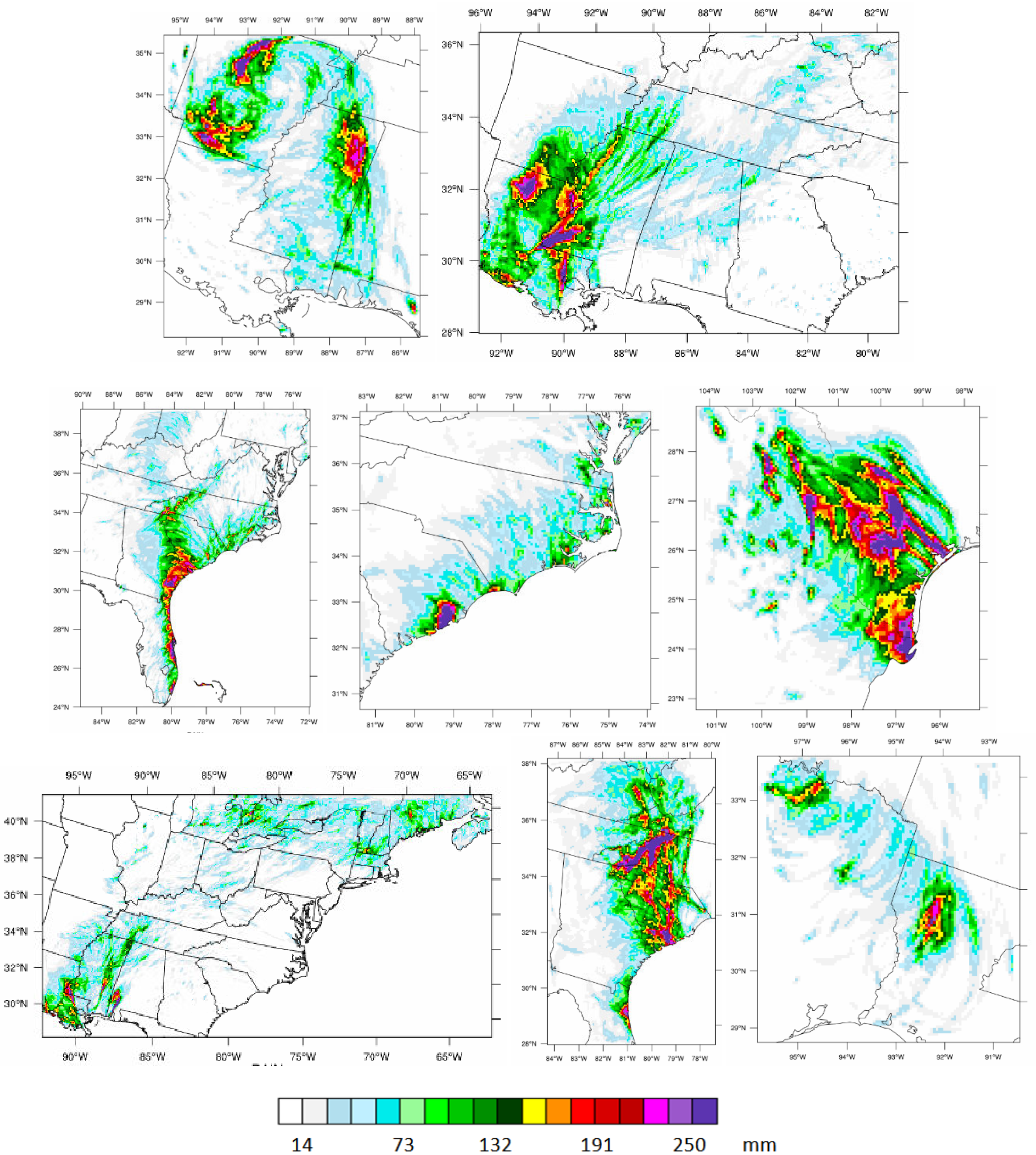

Figure 8-4 Downscaling Results in Simulation Inner Domains

TCs are given in the same order as in Table 8-1, from left to right and from top to bottom (Continued).

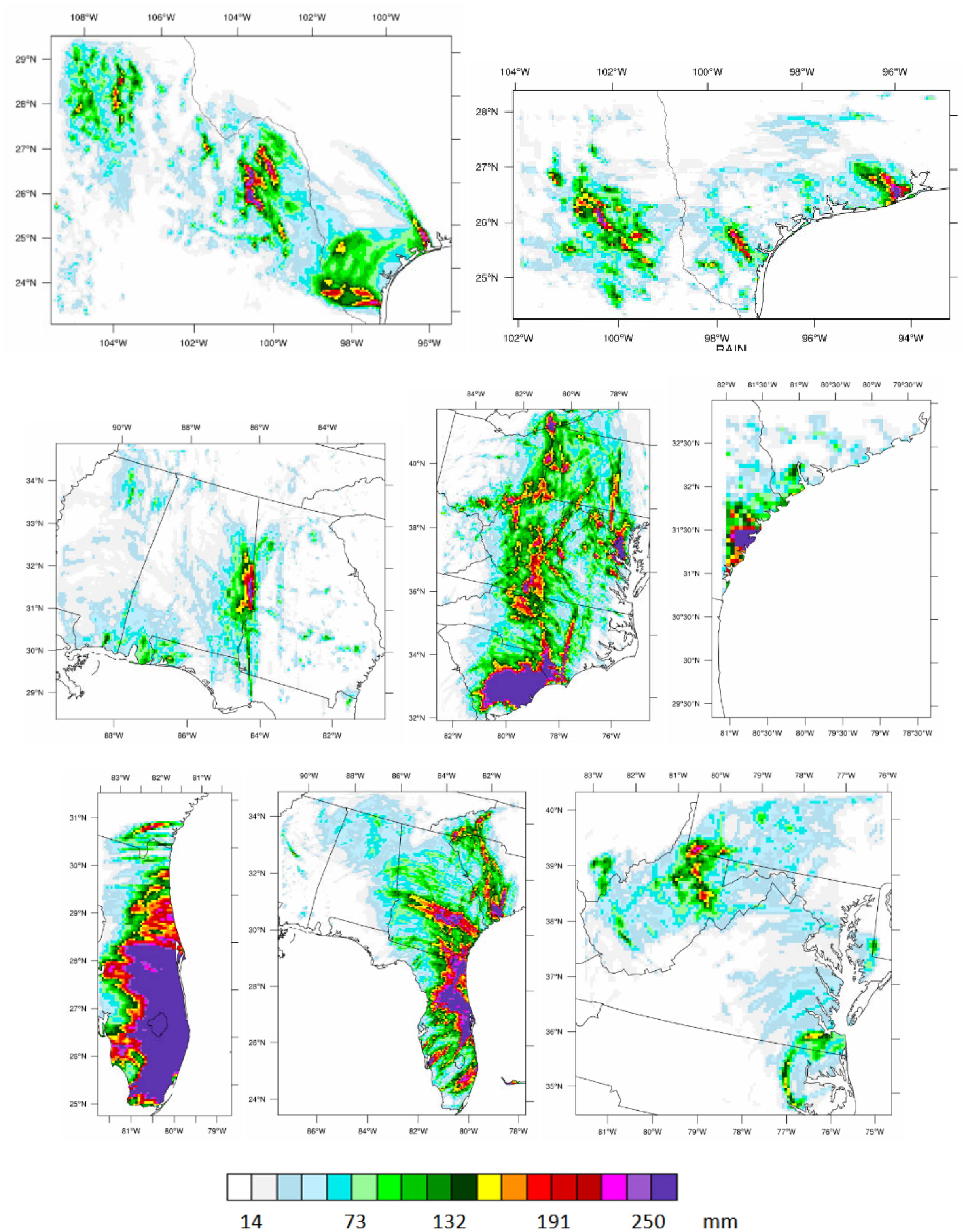

Figure 8-4 Downscaling Results in Simulation Inner Domains

TCs are given in the same order as in Table 8-1, from left to right and from top to bottom (Continued).

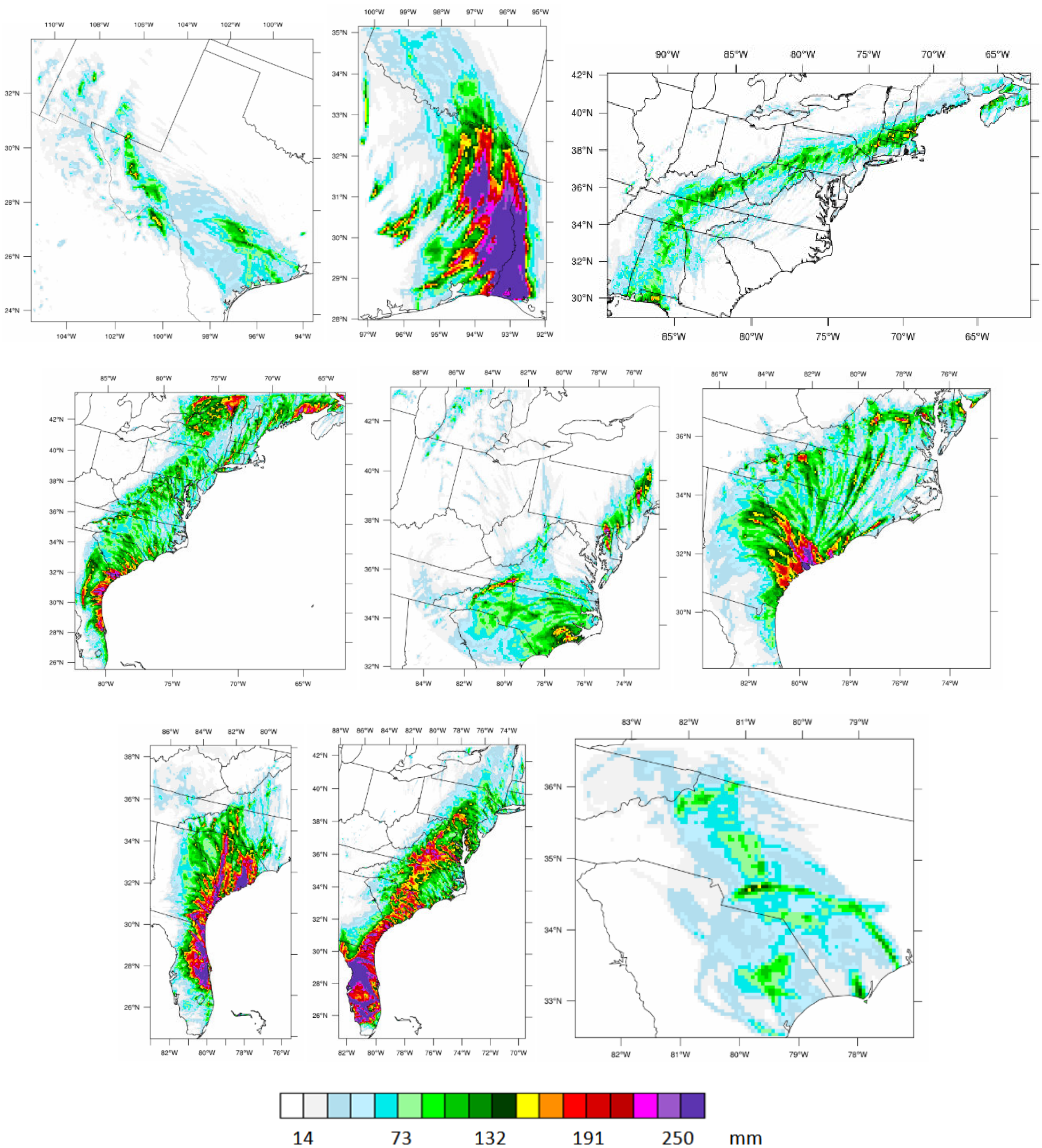

Figure 8-4 Downscaling Results in Simulation Inner Domains

TCs are given in the same order as in Table 8-1, from left to right and from top to bottom (Continued).

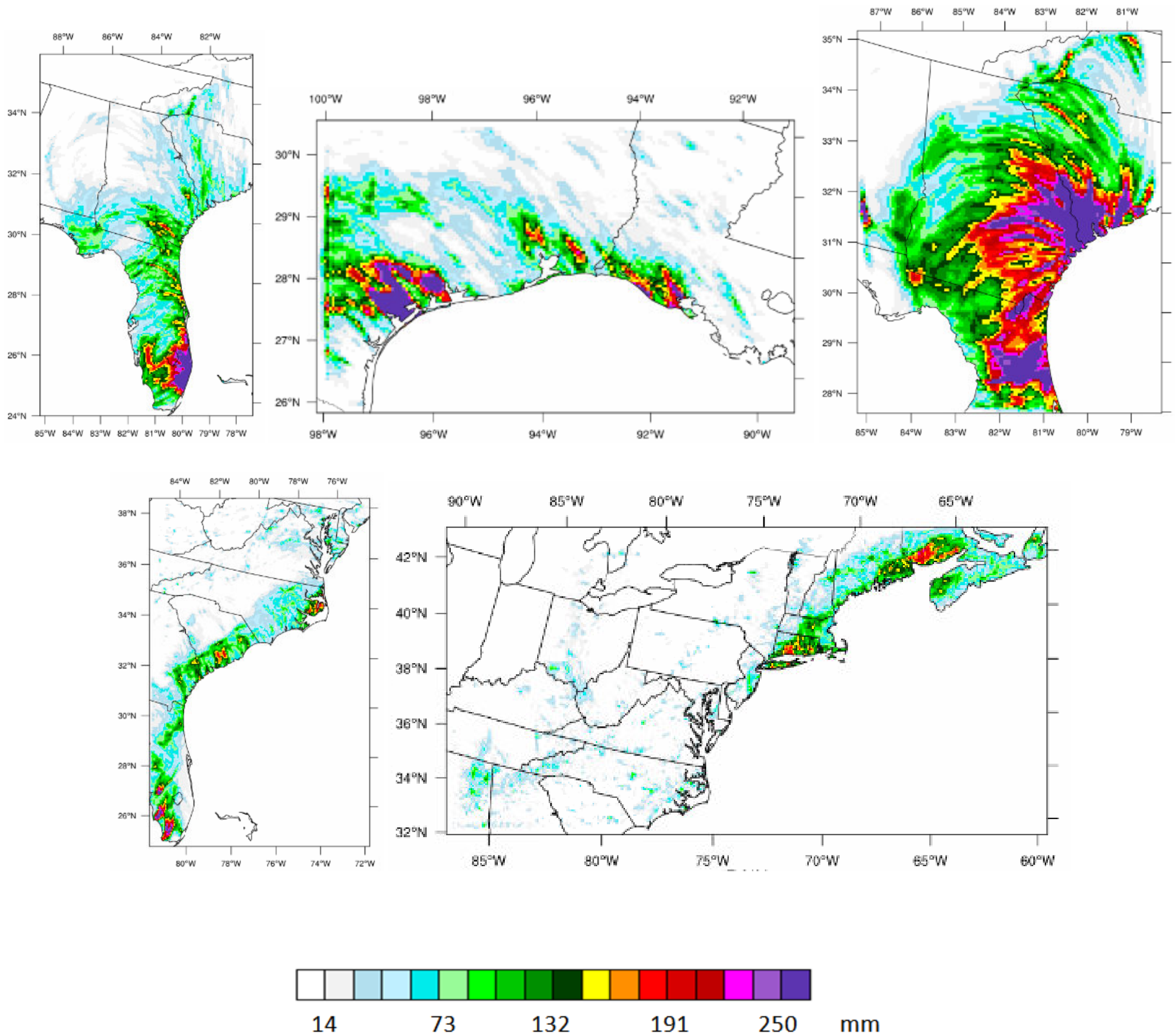

Figure 8-4 Downscaling Results in Simulation Inner Domains

TCs are given in the same order as in Table 8-1, from left to right and from top to bottom (Continued).

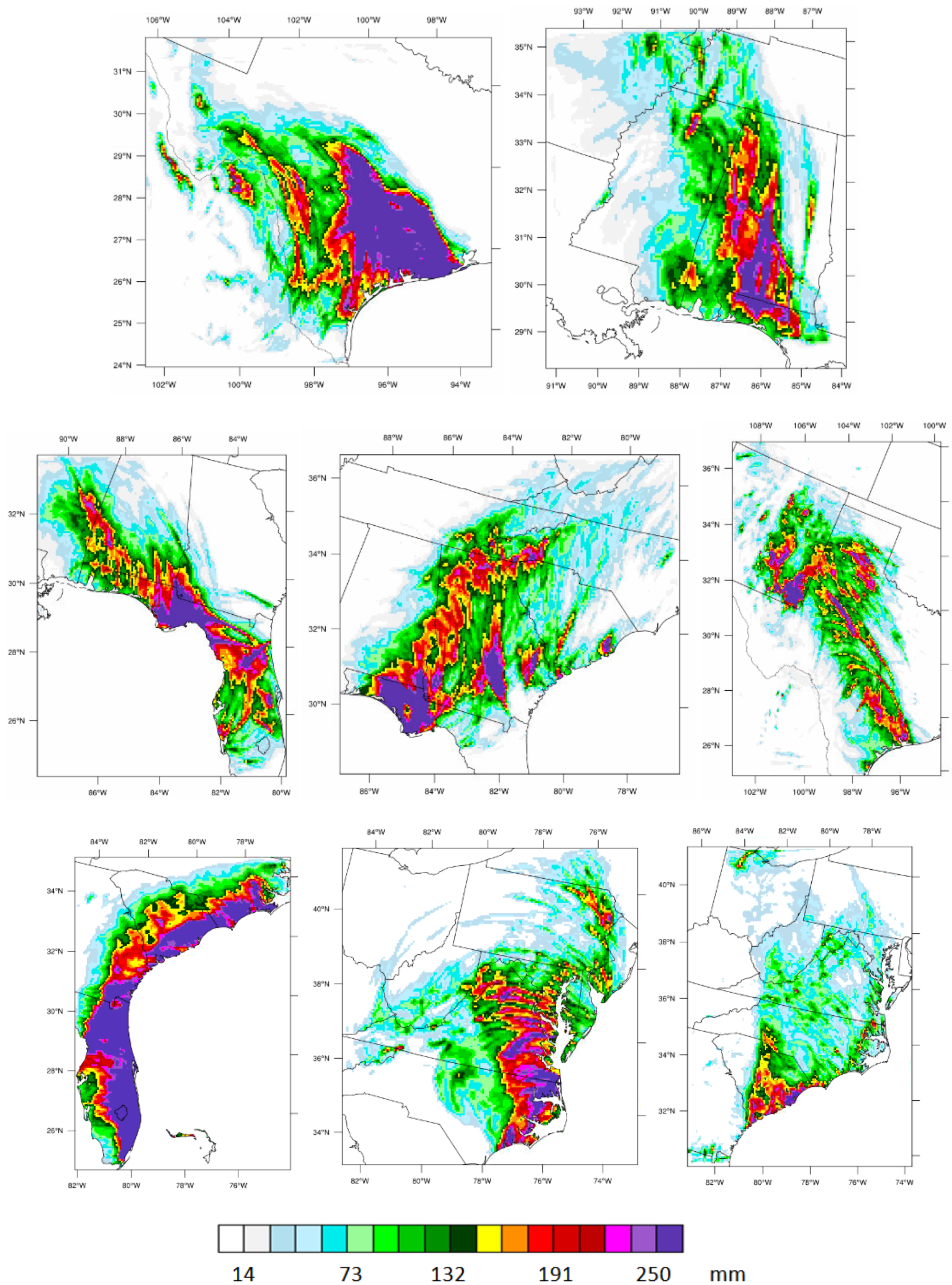

Figure 8-4 Downscaling Results in Simulation Inner Domains

TCs are given in the same order as in Table 8-1, from left to right and from top to bottom (Continued).

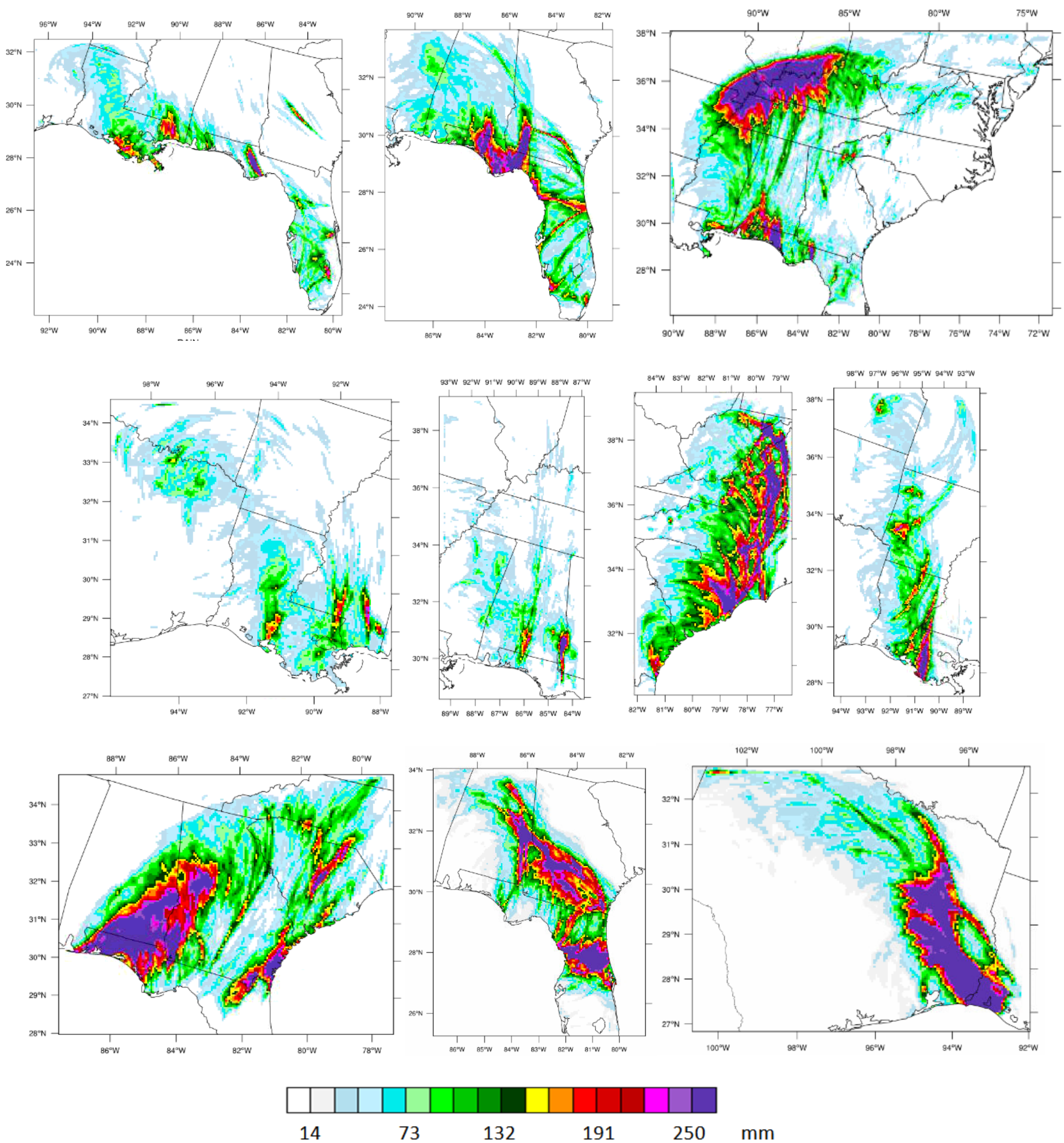

Figure 8-4 Downscaling Results in Simulation Inner Domains

TCs are given in the same order as in Table 8-1, from left to right and from top to bottom (Continued).

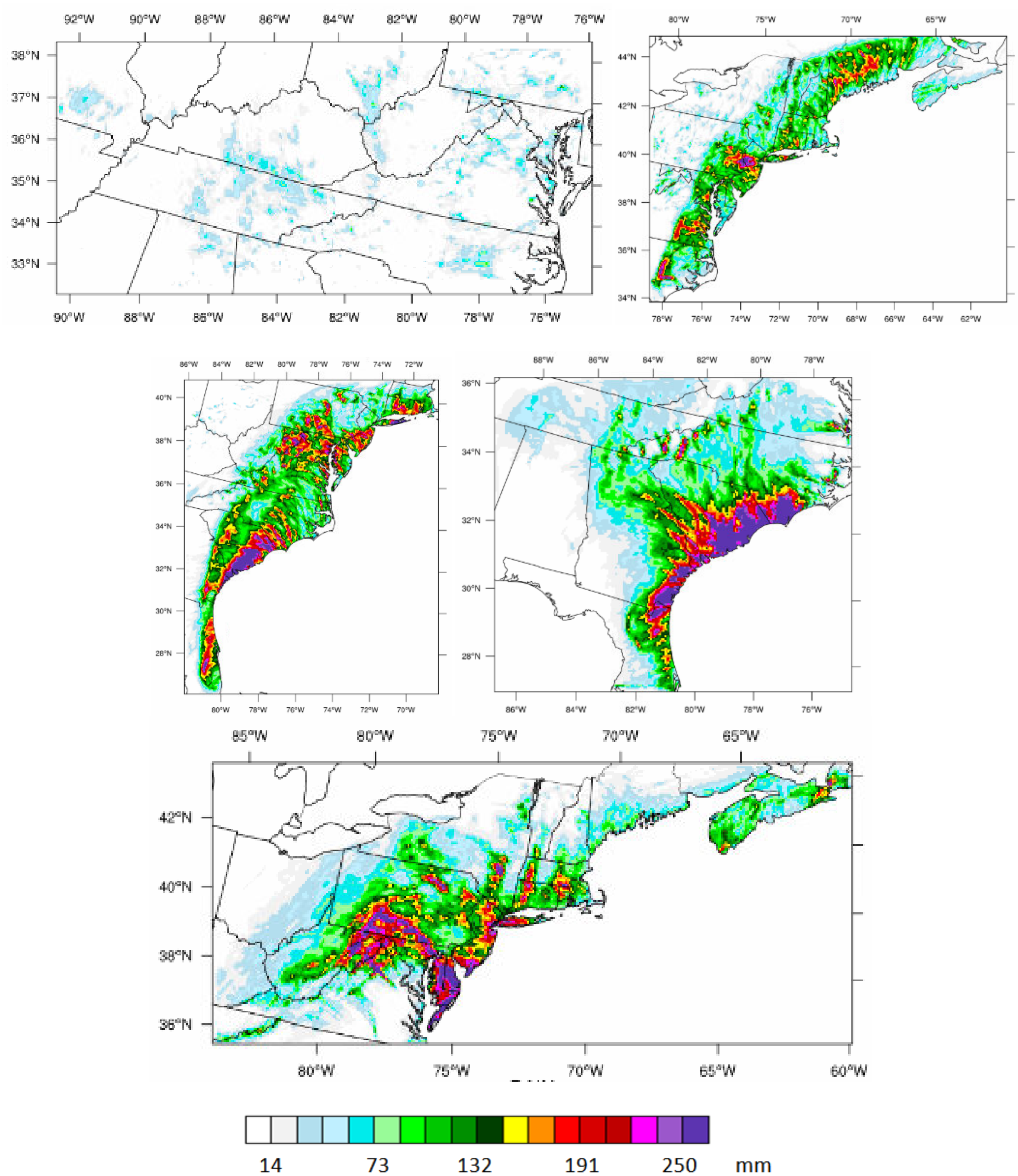

Figure 8-4 Downscaling Results in Simulation Inner Domains

TCs are given in the same order as in Table 8-1, from left to right and from top to bottom (Continued).

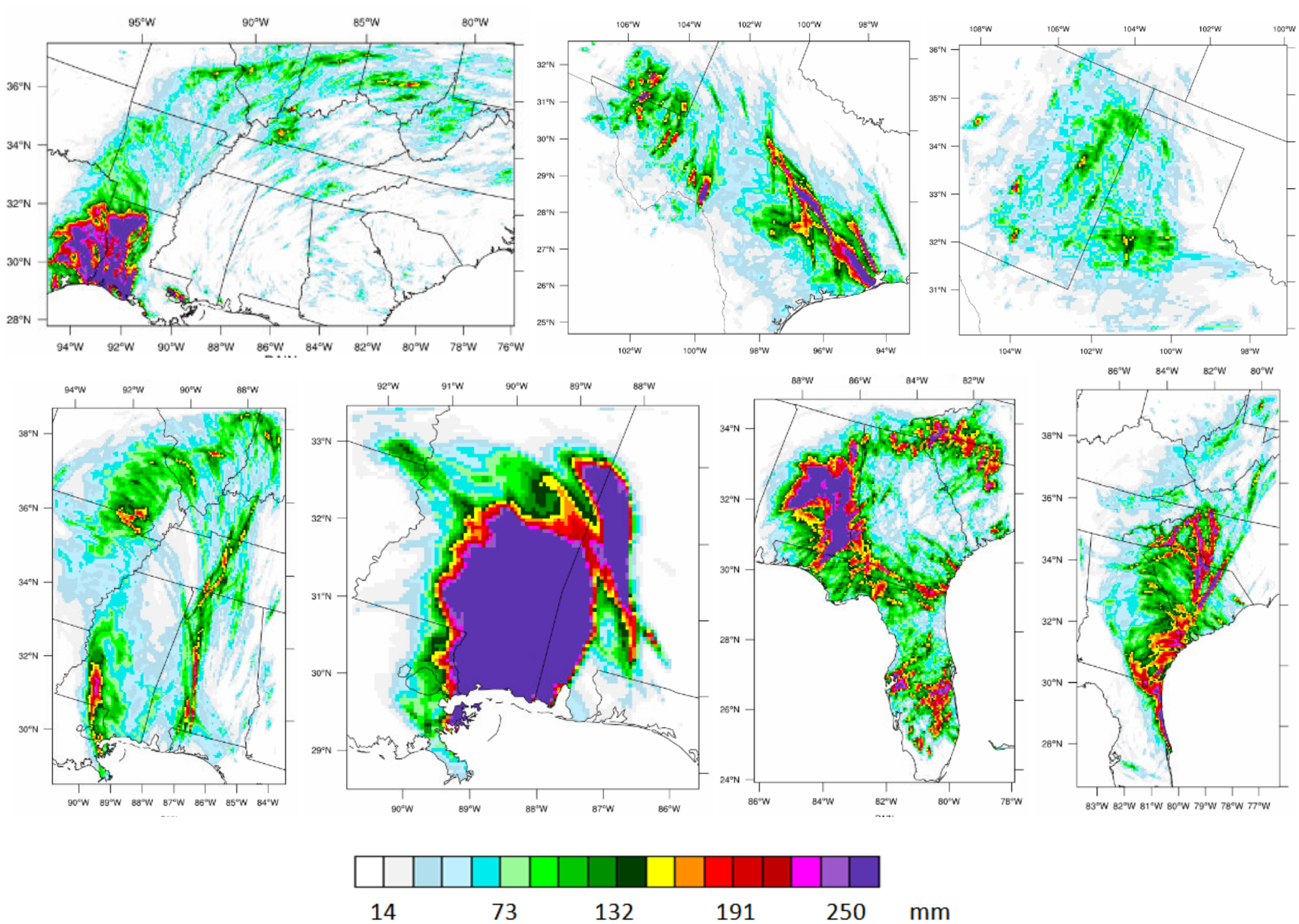

Figure 8-4 Downscaling Results in Simulation Inner Domains

TCs are given in the same order as in Table 8-1, from left to right and from top to bottom (Continued).

8.3 Storm Transposition of the Most Intense Future TC

Similar to Stevenson and Schumacher (2014), the most intense future TC was determined based on the number of grid points above the 100-yr, 24-hr precipitation depth threshold. The TC with the largest number of points above the threshold was taken as the most intense future TC. The 100-yr, 24-hr precipitation depth field was obtained from the NOAA Hydrometeorological Design Studies Center[14] except for the state of Texas for which it was obtained from the Automated Geospatial Watershed Assessment Tool[15].

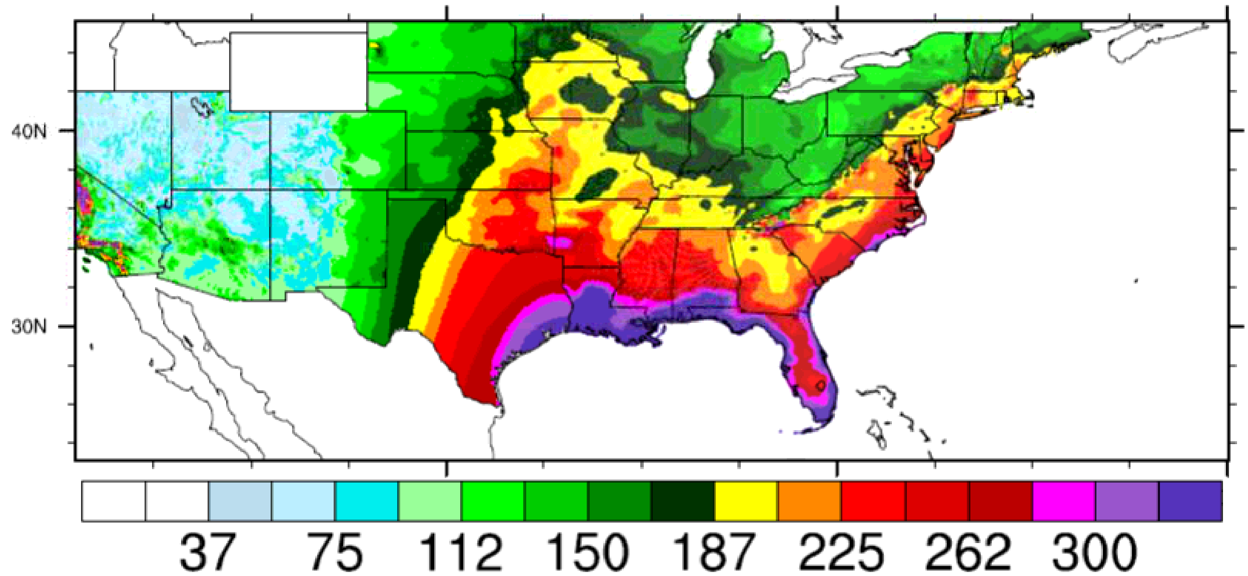

Figure 8-5 100-yr, 24-hr Precipitation Depth Threshold Field Used to Determine the Most Intense Future TC

The number of grid points above the 100-yr, 24-hr threshold (Figure 8-5) for each of the future TC is given in the right column of Table 8-1. It is observed that the most intense TC based on this criterion is the TC occurring in September 2064. Its precipitation field is shown in Figure 8-4 and in more details in Figure 8-6 below.

[14] http://www.nws.noaa.gov/oh/hdsc/
[15] https://www.tucson.ars.ag.gov/agwa/

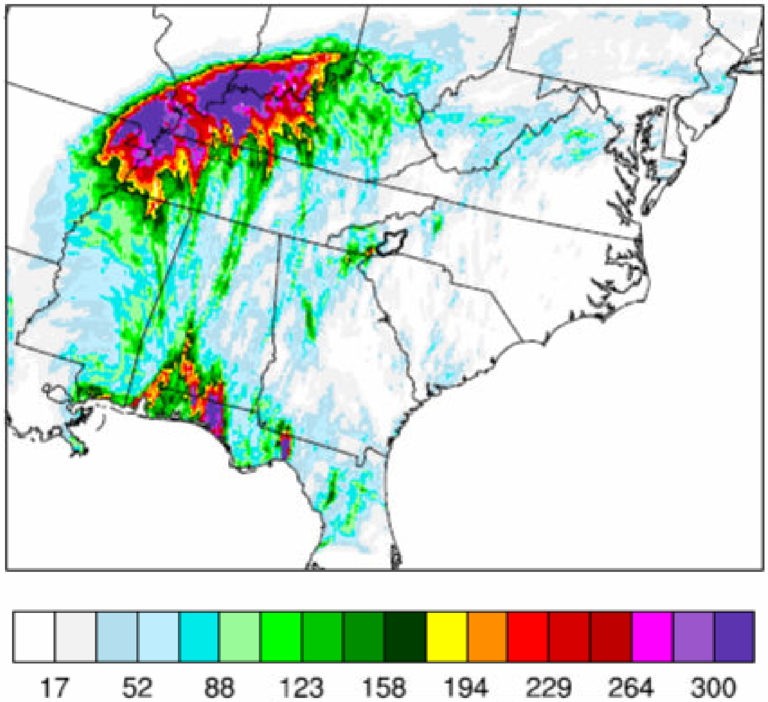

Figure 8-5 Precipitation Depth Field (mm) in the September 2064 TC Accumulated from 09/17/2064 18:00 UTC to 09/21/2064 12:00 UTC

For the storm transposition of this TC, the WRF model was run using two-way nesting with the set of nested domains shown in Figure 8-7. In this case, the domains were fixed from the onset because the objective is to determine the precipitation depth over the target area. This target area is the same as in Chapter 6: it is the drainage basin of the city of Asheville, NC (see Figure 6-3).

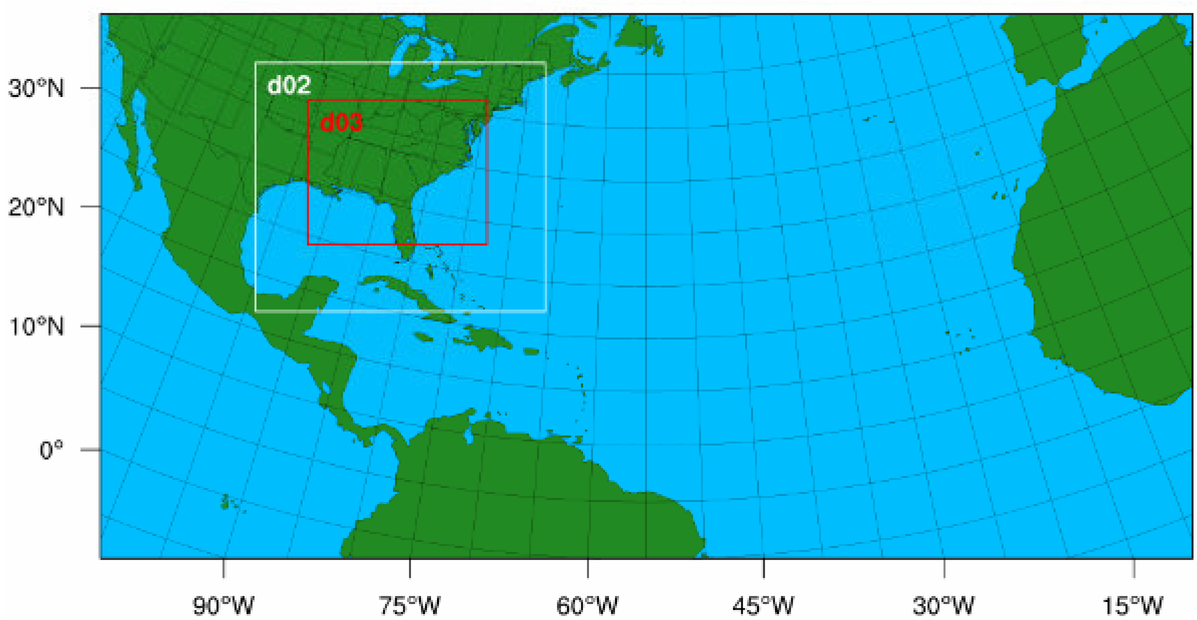

Figure 8-6 Nested Domains Used for the Storm Transposition of the September 2064 TC

Figure 8-8 shows the location of the center of low pressure in the IC on 09/13 18:00 UTC for no shift (green dot) and after shifting of the vortex (black dots). The storm transposition was performed using the method presented in Chapter 6. The TC was shifted to the right of its trajectory only because the simulated precipitation field for no shift occurs significantly west of the target area.

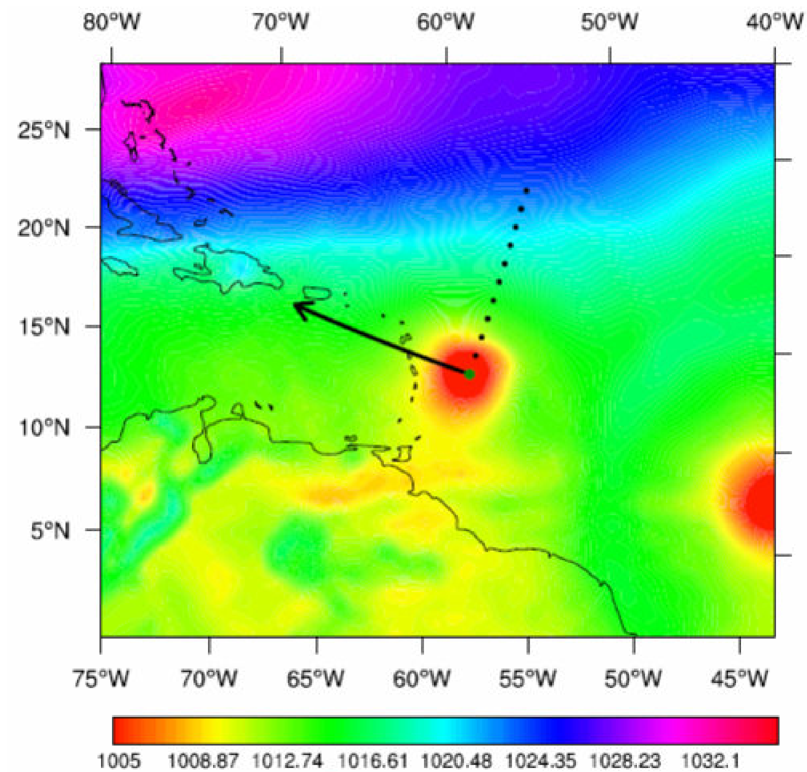

Figure 8-7 The Color Plot Gives the SLP Field (hPa) at the Simulation Start Date 09/13/2064 18:00 UTC for the Case of No Shift

The green dot gives the location of the center of low pressure for no shift whereas the black dots give the location of the center of low pressure after shifting. The black arrow gives the direction of propagation of the TC.

Figure 8-9 presents the storm transposition results. The September 2064 TC was first transposed using the amounts of shift shown in Figure 8-8, which corresponds to Figure 8-9(a). Afterwards, two refinement steps were performed corresponding to Figure 8-9(b) and Figure 8-9(c). The maximum 72-hr basin average precipitation depth obtained after two refinement steps was equal to 319 mm (12.6 in). It was obtained for an amount of shift of 0.22°E and 0.72°N. The precipitation depth field and moisture transport field associated with this maximum 72-hrbasin average precipitation depth are given in Figure 8-10.

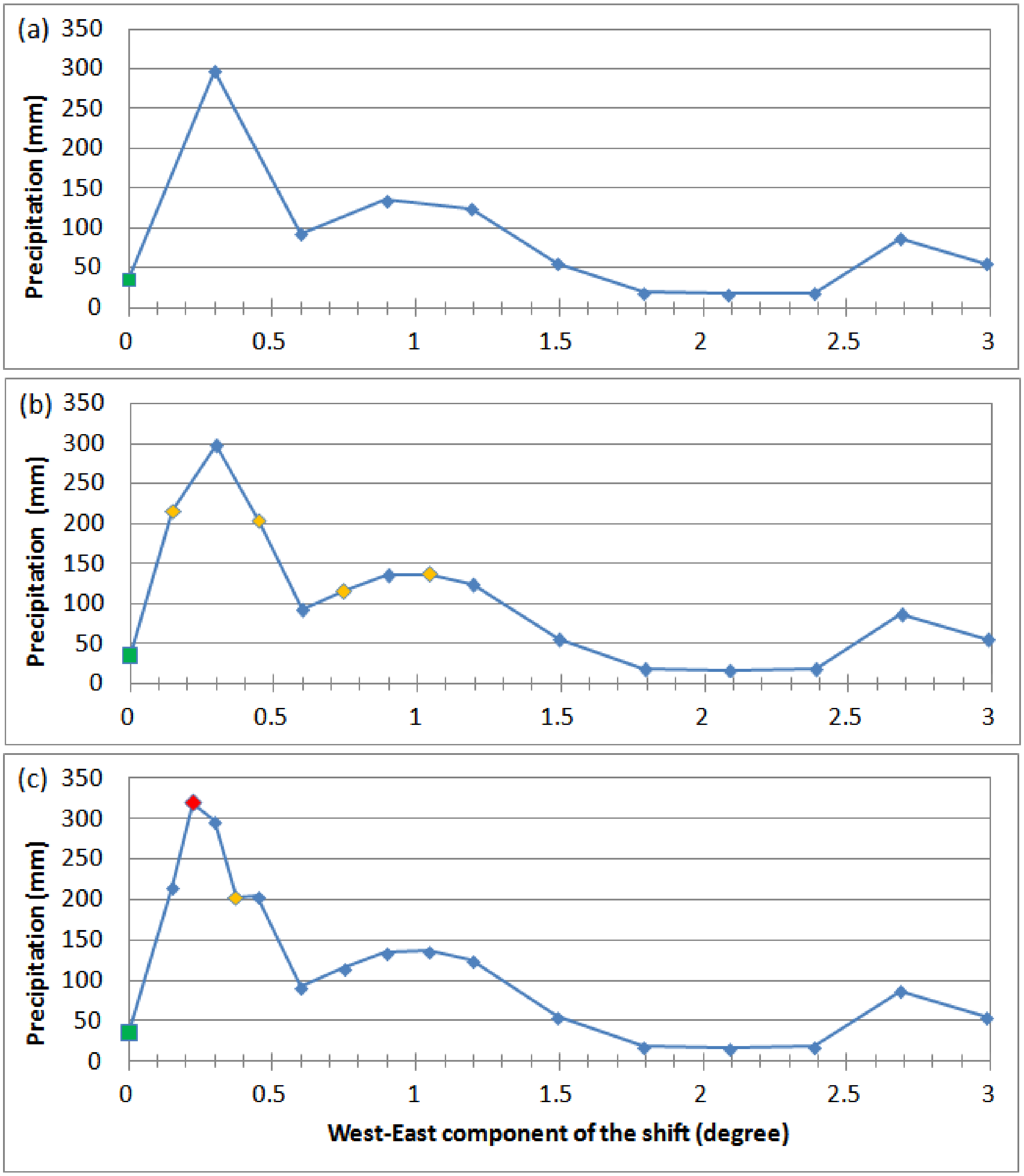

Figure 8-8 Storm Transposition Results for the September 2064 TC

The 72-hr basin average precipitation depth is given as a function of the zonal component of the shift (a) provides the results for the amounts of shift presented in Figure 8-8 whereas (b) and (c) show the refinement around the local maxima given by the yellow and red diamonds. The green square indicates the 72-hr basin average precipitation depth for no shift. The red diamond indicate the maximum 72-hr basin average precipitation depth obtained after two refinement steps.

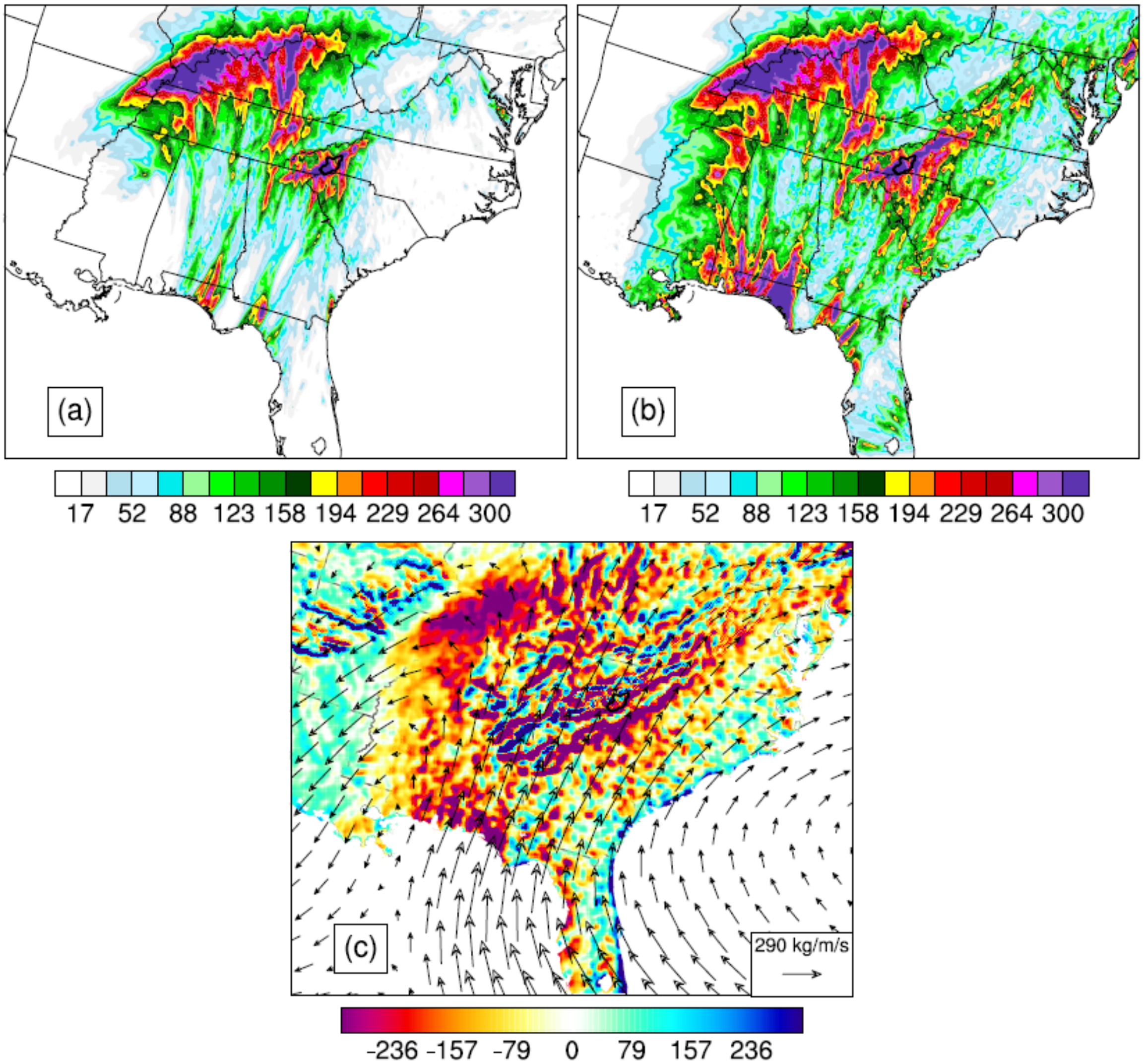

Figure 8-9 **(a) 72-hr Accumulated Precipitation Depth (mm) Field (from 09/19/2064 14:00 UTC until 09/22/2064 14:00 UTC) for the Simulation Which Maximized The 72-hr Basin Average Precipitation Depth for the September 2064 TC**

(b) 14-day accumulated precipitation field (from 09/13/2064 18:00 UTC until 09/27/2064 18:00 UTC) for the simulation which maximized the 72-hr basin average precipitation depth (c) the arrow field gives the time-averaged (from 09/13/2064 18:00 UTC until 09/27/2064 18:00 UTC) IVT field (kg m^{-1} s^{-1}) and the color plot gives its divergence (mm).

Upon examining Figure 8-10(c), it is observed that the regions of intense precipitation coincide with the regions where the convergence of the IVT is the largest. Besides, the TC produced a large precipitation field with a complex structure. Indeed, intense precipitation fell in three separate regions. First, the TC causes intense precipitation around the location of landfall in northwestern Florida, southern Mississippi and southern Alabama (see Figure 8-10(b)). Looking at Figure 8-10(c), it is clear that this intense precipitation was due to a decrease of the magnitude of the IVT over land, causing moisture to accumulate in this region.

Second, intense precipitation fell far inland, mostly in Kentucky and to a lesser extent in the surrounding states. This region of intense precipitation is similar to the one shown in Figure 8-6 but slightly to the east. In this case, Figure 8-10(c) shows that IVT convergence was large because of a sudden change of direction of the IVT field. As a result, intense precipitation fell in this region because of the complexity of the temporal and spatial structures of the IVT field after the TC landfall.

The third region of intense precipitation occurred over the Appalachian Mountains, and was caused by the complicated interaction between the wind field and the topography. As observed in the Chapter for the reconstructed historical TCs, the IVT divergence field is characterized by rapid spatial changes between regions of large divergence (in blue in Figure 8-10(c)) and regions of large convergence (in purple in Figure 8-10(c)).

The intense precipitation that fell over the target area belongs to the third region (Appalachian Mountains). This explains why the 72-hr basin average accumulated precipitation depth is not as large as one would expect after performing the storm transposition of such an intense storm. The maximized basin average accumulated precipitation depth was 319 mm, which is for example less than the maximized 72-hr basin average accumulated precipitation depth obtained from the storm transposition of Hurricane Ivan (348 mm; see Section 6.3) and of Hurricane Frances (427 mm, see Section 6.4). In fact, when the region of very intense precipitation of the original storm (Figure 8-6) was moved over the target area, its precipitation structure changed substantially due to the complex interaction of the topography with the storm dynamics and thermodynamics. This is in agreement with the findings of Chapter 6: the precipitation field caused by the shifted TC may be significantly different in structure and intensity from the precipitation field of the unshifted TC because the mechanisms responsible for generating this intense precipitation may be different.

This has important implications. First, whatever criterion is used to identify the most intense storms (in our case the 100-yr, 24-hr threshold), these storms may not be the most intense storms when brought over the target area. As a result, the methodology used in some of the traditional PMP approaches consisting in identifying the most intense surrounding storms and bringing them over the target area (modulo some adjustments) is flawed. Second, in order to estimate the PMP over the target region, all the TCs should be transposed, not only the most intense, because the interaction of the IVT field caused by the TC with the new environment may generate intense precipitation even if it was not the case for the original unshifted TC.

9 CONCLUSIONS

This report assessed the suitability of the WRF model to simulate local intense precipitation processes occurring from MCSs in the Midwestern United States and from TCs in the Eastern United States. It also investigated physical mechanisms of such storm systems that lead to extreme precipitation by means of the WRF model, which was selected as the regional numerical weather model for this project based on the literature review presented in this report. IBCs for the numerical model simulations were selected for a historical period and a future period. CFSR reanalysis dataset was used for the historical period, and CCSM4 RCP4.5 future climate projection was used for a future period. The NCEP Stage-IV precipitation dataset provided spatially and temporally fine-scale precipitation observation data which was used for model configuration and validation Furthermore, 14 severe MCSs and 13 severe TCs were selected within the time period from 2002 to the present to assess the suitability of the WRF model in modeling local intense precipitation processes.

The results for the numerical simulation of these historical intense TCs and MCSs were presented. The NCEP Stage IV precipitation dataset was used for model validation. More specifically, the intense precipitation fields of these storms and their underlying moisture transport fields were reconstructed with the WRF model at a 5-km resolution, without any nudging or DA. It was shown that under an appropriate choice of the model's options and BCs, the WRF model provided satisfactory results in reproducing the location, intensity, and structure of the intense precipitation fields of the historical TCs and MCSs. The model's options that were investigated included the parameterization schemes such as microphysics, cumulus parameterization, PBL physics, long wave and short wave radiation physics, among a few others. Although certain combinations of the parameterization schemes provided, in each case, realistic results in terms of the precipitation fields' intensities and structures, placing these fields in the correct spatial locations required additional efforts, so that the best set of model's options varied from one storm system to the other.

In addition to assessing the suitability of the WRF model to simulate local intense precipitation processes within intense MCSs, this report presented the results for the physically based storm transposition (i.e. spatial shifting) of the July 18, 2007 MCS precipitation field. The storm transposition method was based on the shifting of the IBCs of the WRF model domains, after which the WRF model was run to simulate the new conditions. Using such a method to perform a transposition exercise and to perform two grid refinement exercises, it was possible to transpose the July 18, 2007 MCS precipitation field directly over the target watershed (Root River at Houston, MN), leading to a change in its 24-hr basin average precipitation from 20 mm (0.8 in.; for the original, unshifted case) to 190 mm (7.5 in.; for the shifted case). In addition to the increase in the basin average precipitation, the shape and intensity of the shifted MCS precipitation field were also found to have changed. As such, this transposition method did not simply transpose the observed precipitation field over the target area. In fact, due to it being physically based, this method took into consideration all physical factors affecting the storm, and thus the new and shifted MCS precipitation resulted from its interaction with the topography and other major factors; thus, the shifted rainfall field was not a result of a simple spatial shifting of the original storm rainfall. This is one of the major advantages of such a physically based method. Besides, using a RAM for the storm transposition exercise allows overcoming the issue of nonstationarity whereas traditional methods are often highly dependent on observation records and are unable to deal with nonstationarity.

Besides the transposition of a MCS precipitation, in this report, a storm transposition method designed for the transposition of TC precipitation was also presented. This method was physically based, as it used a RAM to numerically simulate a TC and its precipitation field. As a result, it had the fundamental advantage of conserving the mass, momentum, and energy in the system since the RAM numerically solves the equations governing the conservation of these quantities. The storm transposition method was based on the shifting of the initial vortex of the TC at the simulation start date. More precisely, the TC in the ICs was first separated from its background environment, then shifted, and finally recombined with the background environment. The objective of this method was to find the amount of shift which maximizes the precipitation depth over a given target area. In this study, the transposition method was applied to four hurricanes that had spawned heavy precipitation in the United States, namely Hurricanes Floyd (1999), Frances (2004), Ivan (2004), and Isaac (2012). The drainage basin of the city of Asheville, NC was selected as the target. It was found that the tracks of these TCs were generally very sensitive to changes in the location of the initial vortex, and that the response of the tracks to such changes was nonlinear. In particular, a small shift of the initial vortex could result in a significant change in the location, structure, and intensity of the precipitation field, thus putting into question both the legitimacy of the conventional transposition of the precipitation field from the TC (as is often the case in the traditional PMP approaches) and the existence of a meteorologically homogeneous region that sets the transposition limits. The precipitation fields resulting from the numerical atmospheric model-based maximization (through transposition) of Hurricanes Frances and Ivan were overall significantly more intense than the observed precipitation fields. The investigation of the IVT and its convergence in the case of Hurricane Ivan revealed that the increased intensity in the maximized precipitation field was due to an increase in the convergence of the IVT rather than to an increase in the magnitude of the IVT. In the case of Hurricane Floyd, the numerical atmospheric model maximized precipitation field was overall slightly less intense than the observed precipitation field, whereas for Hurricane Isaac, the maximized precipitation field was overall as intense as the observed precipitation field. The maximum 72-hr basin average precipitation depth resulting from the transposition of the four hurricanes was equal to 427 mm (16.8 in.). It compares favorably to the 72-hr TVA precipitation obtained by the generalized method (Zurndorfer et al., 1986) which is equal to 503 mm (19.8 in.), but remains about half of the 72-hr PMP obtained with the generalized method which is equal to 869 mm (34.2 in.). Finally, a procedure was proposed for the physically based estimation of the PMP over a given target area based on the transposition method. Preferably, the transposition exercise should be performed using different sets of the RAM's options, and different simulation start dates, in order to quantify the uncertainties in the PMP estimate due to the model uncertainties and uncertainties in the ICs.

Finally, this report simulated and explored the intense future MCSs and TCs of the 21st century in an attempt to determine the most severe of each of these storm events that would affect a specific target watershed. For this reason, the CCSM4 RCP4.5 climate projection was downscaled to 5 km over the Midwestern and Eastern United States using the WRF model.

For the case of MCSs, the downscaling was performed for 2020-2100, from which the most intense MCSs over the River Root basin above Houston were identified, for each year. From these results, it is clear that the location of the intense MCS seemed to play an extremely important role in the value of the basin average precipitation depth computed over the target watershed. While some events seemed more intense than others, their location further away from the target watershed of interest deemed them less intense with regards to the computed basin average precipitation depth over the target watershed. From these results, however, it was possible to note that the maximum 24-hr basin average precipitation depth simulated to occur over the 80 future years of the 21st century, over the Root River basin above Houston, was around 143 mm (5.6 in.), produced by the August 12, 2080 MCS. Following this result, the same physically based transposition exercise that was attempted for the July 18, 2007 MCS was then attempted for this future MCS of August 12, 2080 to find if the precipitation depth may be further maximized over the target watershed. This transposition exercise revealed that, unlike the case of the July 18, 2007 MCS, the 24-hr basin average precipitation produced by the August 12, 2080 MCS would not be expected to produce a much larger basin average precipitation depth even if it occurred in a slightly different location than its original location. The major reason for this conclusion was that the intense MCS was already located in a position where it covered most of the target watershed. As such, there was very little that could be done with transposing the MCS to increase the basin average precipitation, and this was revealed very clearly in the results of the transposition and the grid refinements performed. However, it should be noted that the maximum 24-hr basin average precipitation obtained from this exercise for the August 12, 2080 MCS does not represent the largest basin average precipitation that may be obtained over the Root River basin above Houston in the future years. In order to determine such a value, it would be necessary to perform the transposition for all future intense MCSs over the target watershed. From such an exercise, one can then get a more realistic idea of the maximum 24-hr basin average precipitation depth that could be physically expected to occur over the target watershed during the future years of the 21st century due to intense MCSs occurring in the Midwestern United States.

For the case of TCs, DD was performed for 2005-2100. First the WRF model was run at 45 km resolution over a large simulation outer domain encompassing the eastern Atlantic Ocean and western coast of Africa in order to include the region of formation of TCs. TCs in the WRF outputs at 45 km resolution were then identified by visual examination of the SLP field and meridional surface wind speed field. 64 landfalling TCs were found and further downscaled to 15 km resolution using a fixed intermediate domain and to 5 km resolution. The location and size of the inner domain used for the last downscaling step at 5 km resolution were chosen case by case based on the location of the precipitation field produced in the intermediate domain. The number of grid points in the inner domain where the precipitation depth produced by the TC exceeded the 100-year, 24-hr precipitation depth was used as a criterion to identify the most intense future TC. The September 2064 TC was found to be the most intense with the largest number of grid points above the 100-year, 24-hr precipitation depth. In this case, intense precipitation fell far inland, in western Kentucky and in the surrounding states. This TC was then transposed in order to maximize the 72-hr precipitation depth over the drainage basin of the city of Asheville, NC. Investigating the moisture transport field led to the conclusion that the intense precipitation that fell over the target area in the maximized case was caused by the interaction of the incoming moisture with the complicated terrain of the Appalachian Mountains. On the contrary, the region of intense precipitation observed in the original unshifted TC and which was also present in the maximized case was associated with a large moisture convergence due to the complex spatiotemporal structure of the IVT field. As a result, not only the most intense TC but all TCs should be transposed in order to estimate the PMP over the target area since the precipitation field over the new location may be fundamentally different in its structure and intensity if different underlying mechanisms are responsible for the generation of intense precipitation.

This study showed that a regional numerical weather model is suitable to simulate local intense precipitation processes in MCSs and TCs. This indicates that numerical simulations of intense precipitation processes can be used for both deterministic and probabilistic flood hazard applications. In the deterministic approach, simulations can provide physically-based alternatives to current heuristic moisture maximization and storm transposition techniques used to derive probable maximum precipitation (PMP). In the probabilistic approach, numerical simulations can be used within a Monte Carlo framework to provide precipitation magnitude estimates with associated uncertainty.

10 REFERENCES

Anabor, V., Stensrud, D.J. and de Moraes, O.L., 2008. Serial upstream-propagating mesoscale convective system events over southeastern South America. Monthly Weather Review, 136(8): 3087-3105.

Anabor, V., Stensrud, D.J. and de Moraes, O.L.L., 2009. Simulation of a Serial Upstream-Propagating Mesoscale Convective System Event over Southeastern South America Using Composite Initial Conditions. Monthly Weather Review, 137(7): 2144-2163.

Anderson, C.J. and Arritt, R.W., 1998. Mesoscale convective complexes and persistent elongated convective systems over the United States during 1992 and 1993. Monthly weather review, 126(3): 578-599.

Ashley, W.S., Mote, T.L. and Bentley, M.L., 2005. On the episodic nature of derecho-producing convective systems in the United States. International journal of climatology, 25(14): 1915-1932.

Ashley, W.S. et al., 2003. Distribution of mesoscale convective complex rainfall in the United States. Monthly weather review, 131(12): 3003-3017.

Atallah, E.H. and Bosart, L.F., 2003. The extratropical transition and precipitation distribution of Hurricane Floyd (1999). Monthly Weather Review, 131(6): 1063-1081.

Augustine, J.A. and Howard, K.W., 1988. Mesoscale convective complexes over the United States during 1985. Monthly weather review, 116(3): 685-701.

Augustine, J.A. and Howard, K.W., 1991. Mesoscale convective complexes over the United States during 1986 and 1987. Monthly weather review, 119(7): 1575-1589.

Avila, L.A., 2002. Tropical Cyclone Report Hurricane Isidore 14-27 September 2002. National Hurricane Center.

Avila, L.A. and Cangialosi, J., 2011. Tropical Cyclone Report Hurricane Irene (AL092011) 21-28 August 2011. National Hurricane Center.

Baldwin, M.E., Kain, J.S. and Lakshmivarahan, S., 2005. Development of an automated classification procedure for rainfall systems. Monthly weather review, 133(4): 844-862.

Bender, M.A. and Ginis, I., 2000. Real-case simulations of hurricane-ocean interaction using a high-resolution coupled model: Effects on hurricane intensity. Monthly Weather Review, 128(4): 917-946.

Bender, M.A., Ginis, I., Tuleya, R., Thomas, B. and Marchok, T., 2007. The operational GFDL coupled hurricane-ocean prediction system and a summary of its performance. Monthly Weather Review, 135(12): 3965-3989.

Bender, M.A. et al., 2010. Modeled impact of anthropogenic warming on the frequency of intense Atlantic hurricanes. Science, 327(5964): 454-458.

Bengtsson, L., Botzet, M. and Esch, M., 1996. Will greenhouse gas-induced warming over the next 50 years lead to higher frequency and greater intensity of hurricanes? Tellus A, 48(1): 57-73.

Bengtsson, L. et al., 2007. How may tropical cyclones change in a warmer climate? Tellus a, 59(4): 539-561.

Benoit, R. et al., 1997. The Canadian MC2: A semi-Lagrangian, semi-implicit wideband atmospheric model suited for finescale process studies and simulation. Monthly Weather Review, 125(10): 2382-2415.

Berg, R., 2013. Tropical Cyclone Report Hurricane Isaac (AL092012) 21 August - 1 September 2012. National Hurricane Center.

Berrisford, P. et al., 2009. ERA report series - The ERA-Interim archive Version 1.0, Weather, pp. 16.

Beven, J.L., 2005. Tropical Cyclone Report Hurricane Frances 25 August - 8 September 2004. National Hurricane Center.

Beven, J.L. and Kimberlain, T.B., 2009. Tropical Cyclone Report Hurricane Gustav (AL072008) 25 August - 4 September 2008. National Hurricane Center.

Bitz, C.M. et al., 2012. Climate Sensitivity of the Community Climate System Model, Version 4. Journal of Climate, 25: 3053-3070.

Blake, E.S., Kimberlain, T.B., Berg, R.J., Cangialosi, J.P. and Beven, J.L., 2013. Tropical Cyclone Report Hurricane Sandy (AL182012) 22-29 October 2012. National Hurricane Center.

Blake, E.S. and Zelinsky, D.A., 2018. National Hurricane Center. Tropical Cyclone Report. Hurricane Harvey. . NOAA AL092017.

Blumberg, A.F. and Mellor, G.L., 1987. A description of a three-dimensional coastal ocean circulation model. Three-dimensional coastal ocean models: 1-16.

Braun, S.A., 2002. A cloud-resolving simulation of Hurricane Bob (1991): Storm structure and eyewall buoyancy. Monthly weather review, 130(6): 1573-1592.

Braun, S.A., 2006. High-resolution simulation of Hurricane Bonnie (1998). Part II: water budget. Journal of the atmospheric sciences, 63(1): 43-64.

Braun, S.A., Montgomery, M.T. and Pu, Z., 2006. High-resolution simulation of Hurricane Bonnie (1998). Part I: The organization of eyewall vertical motion. Journal of the atmospheric sciences, 63(1): 19-42.

Braun, S.A. and Tao, W.-K., 2000. Sensitivity of high-resolution simulations of Hurricane Bob (1991) to planetary boundary layer parameterizations. Monthly Weather Review, 128(12): 3941-3961.

Braun, S.A. and Wu, L., 2007. A numerical study of Hurricane Erin (2001). Part II: Shear and the organization of eyewall vertical motion. Monthly weather review, 135(4): 1179-1194.

Broccoli, A. and Manabe, S., 1990. Can existing climate models be used to study anthropogenic changes in tropical cyclone climate? Geophysical Research Letters, 17(11): 1917-1920.

Brown, D.P., 2011. Tropical Cyclone Report Tropical Storm Lee (AL132011) 2-5 September 2011. National Hurricane Center.

Cai, S. and Yu, H., 2012. Analysis of different weather research and forecasting radiation schemes' impact on the numerical simulation of a typical mesoscale convective weather in China. Journal of Atmospheric and Solar-Terrestrial Physics, 80: 68-72.

Caron, L.-P., Jones, C.G. and Winger, K., 2011. Impact of resolution and downscaling technique in simulating recent Atlantic tropical cylone activity. Climate dynamics, 37(5-6): 869-892.

Chan, J.C. and Kepert, J.D., 2010. Global perspectives on Tropical cyclones: From science to mitigation, 4. World Scientific.

Changnon, S.A., Pielke Jr, R.A., Changnon, D., Sylves, R.T. and Pulwarty, R., 2000. Human Factors Explain the Increased Losses from Weather and Climate Extremes*. Bulletin of the American Meteorological Society, 81(3): 437-442.

Christensen, J.H., Carter, T.R., Rummukainen, M. and Amanatidis, G., 2007. Evaluating the performance and utility of regional climate models: the PRUDENCE project. Climatic Change, 81: 1-6.

Clarke, L. et al., 2007. Scenarios of Greenhouse Gas Emissions and Atmospheric Concentrations. Sub-report 2.1A of Synthesis and Assessment Product 2.1 by the U.S. Climate Change Science Program and the Subcommittee on Global Change Research, Washington, DC, USA, pp. 154.

Correia Jr, J., Arritt, R.W. and Anderson, C.J., 2008. Idealized mesoscale convective system structure and propagation using convective parameterization. Monthly Weather Review, 136(7): 2422-2442.

Cote, M.R., 2007. Predecessor rain events in advance of tropical cyclones, Faculty of the University at Albany, State University of New York.

Cram, T.A., Persing, J., Montgomery, M.T. and Braun, S.A., 2007. A Lagrangian trajectory view on transport and mixing processes between the eye, eyewall, and environment using a

high-resolution simulation of Hurricane Bonnie (1998). Journal of the atmospheric sciences, 64(6): 1835-1856.
Crétat, J., Pohl, B., Richard, Y. and Drobinski, P., 2012. Uncertainties in simulating regional climate of Southern Africa: sensitivity to physical parameterizations using WRF. Climate dynamics, 38(3-4): 613-634.
Davis, C., Brown, B. and Bullock, R., 2006. Object-based verification of precipitation forecasts. Part I: Methodology and application to mesoscale rain areas. Monthly Weather Review, 134(7): 1772-1784.
Davis, C. et al., 2008. Prediction of landfalling hurricanes with the Advanced Hurricane WRF model. Monthly weather review, 136(6): 1990-2005.
Davis, C.A. and Bosart, L.F., 2001. Numerical simulations of the genesis of Hurricane Diana (1984). Part I: Control simulation. Monthly weather review, 129(8): 1859-1881.
Davis, C.A. and Trier, S.B., 2002. Cloud-resolving simulations of mesoscale vortex intensification and its effect on a serial mesoscale convective system. Monthly weather review, 130(12): 2839-2858.
Dawson, D.T. and Xue, M., 2006. Numerical forecasts of the 15-16 June 2002 southern plains mesoscale convective system: impact of mesoscale data and cloud analysis. Monthly weather review, 134(6): 1607-1629.
De, U., Khole, M. and Dandekar, M., 2004. Natural hazards associated with meteorological extreme events. Natural Hazards, 31(2): 487-497.
Done, J., Holland, G., Bruyere, C. and Suzuki-Parker, A., 2011. Effects of climate variability and change on Gulf of Mexico tropical cyclone activity, Offshore Technology Conference. Offshore Technology Conference.
Done, J.M., Holland, G.J., Bruyère, C.L., Leung, L.R. and Suzuki-Parker, A., 2015. Modeling high-impact weather and climate: lessons from a tropical cyclone perspective. Climatic Change, 129(3-4): 381-395.
Dudhia, J., Gill, D., Manning, K., Wang, W. and Bruyere, C., 1999. PSU NCAR Mesoscale Modeling System Tutorial Class Notes and User's Guide: MM5 Modeling System Version 3.
Easterling, D.R. et al., 2000a. Observed Variability and Trends in Extreme Climate Events: A Brief Review*. Bulletin of the American Meteorological Society, 81(3): 417-425.
Easterling, D.R. et al., 2000b. Climate extremes: observations, modeling, and impacts. science, 289(5487): 2068-2074.
Ebita, A. et al., 2011. The Japanese 55-year Reanalysis "JRA-55": An Interim Report, Scientific Online Letters on the Atmosphere, pp. 149-152.
Elsberry, R.L., 2005. Achievement of USWRP hurricane landfall research goal. Bulletin of the American Meteorological Society, 86(5): 643-645.
Emanuel, K., Sundararajan, R. and Williams, J., 2008. Hurricanes and global warming: Results from downscaling IPCC AR4 simulations. Bulletin of the American Meteorological Society, 89(3): 347-367.
Emanuel, K.A., 1991. The theory of hurricanes. Annual Review of Fluid Mechanics, 23(1): 179-196.
Emanuel, K.A., 2013. Downscaling CMIP5 climate models shows increased tropical cyclone activity over the 21st century. Proceedings of the National Academy of Sciences, 110(30): 12219-12224.
Fierro, A.O., Rogers, R.F., Marks, F.D. and Nolan, D.S., 2009. The impact of horizontal grid spacing on the microphysical and kinematic structures of strong tropical cyclones simulated with the WRF-ARW model. Monthly Weather Review, 137(11): 3717-3743.
Flato, G. et al., 2014. Evaluation of Climate Models. Climate Change 2013: The Physical Science Basis: 741-866.

Frank, W.M. and Ritchie, E.A., 2001. Effects of vertical wind shear on the intensity and structure of numerically simulated hurricanes. Monthly weather review, 129(9): 2249-2269.

Fritsch, J., Kane, R. and Chelius, C., 1986a. The contribution of mesoscale convective weather systems to the warm-season precipitation in the United States. Journal of climate and applied meteorology, 25(10): 1333-1345.

Fritsch, J. and Maddox, R., 1981. Convectively driven mesoscale weather systems aloft. Part II: Numerical simulations. Journal of Applied Meteorology, 20(1): 20-26.

Fritsch, J.M., Kane, R.J. and Chelius, C.R., 1986b. The Contribution of Mesoscale Convective Weather Systems to the Warm-Season Precipitation in the United-States. Journal of Climate and Applied Meteorology, 25(10): 1333-1345.

Galarneau, T.J., Bosart, L.F. and Schumacher, R.S., 2010. Predecessor Rain Events ahead of Tropical Cyclones. Monthly Weather Review, 138(8): 3272-3297.

Ge, X., Li, T., Zhang, S. and Peng, M., 2010. What causes the extremely heavy rainfall in Taiwan during Typhoon Morakot (2009)? Atmospheric science letters, 11(1): 46-50.

Gent, P.R. et al., 2011. The Community Climate System Model Version 4. Journal of Climate, 24(19): 4973-4991.

Goldenberg, S.B., Landsea, C.W., Mestas-Nuñez, A.M. and Gray, W.M., 2001. The recent increase in Atlantic hurricane activity: Causes and implications. Science, 293(5529): 474-479.

Goldenberg, S.B. and Shapiro, L.J., 1996. Physical mechanisms for the association of El Nino and West African rainfall with Atlantic major hurricane activity. Journal of Climate, 9(6): 1169-1187.

Gray, M., 2000. Characteristics of numerically simulated mesoscale convective systems and their application to parameterization. Journal of the atmospheric sciences, 57(24): 3953-3970.

Griffiths, P.G. et al., 2009. Spatial distribution and frequency of precipitation during an extreme event: July 2006 mesoscale convective complexes and floods in southeastern Arizona. Water resources research, 45(7).

Hack Jr, J.J., 1980. The Role of Convective-Scale Processes in Tropical Cyclone Development.

Harr, P.A. and Dea, J.M., 2009. Downstream development associated with the extratropical transition of tropical cyclones over the western North Pacific. Monthly Weather Review, 137(4): 1295-1319.

Harr, P.A. and Elsberry, R.L., 2000. Extratropical transition of tropical cyclones over the western North Pacific. Part I: Evolution of structural characteristics during the transition process. Monthly weather review, 128(8): 2613-2633.

Harr, P.A., Elsberry, R.L. and Hogan, T.F., 2000. Extratropical transition of tropical cyclones over the western North Pacific. Part II: The impact of midlatitude circulation characteristics. Monthly weather review, 128(8): 2634-2653.

Hershfield, D.M., 1961. Rainfall frequency atlas of the United States: For durations from 30 minutes to 24 hours and return periods from 1 to 100 years. Department of Commerce, Weather Bureau.

Higgins, R., Yao, Y., Yarosh, E., Janowiak, J.E. and Mo, K., 1997. Influence of the Great Plains low-level jet on summertime precipitation and moisture transport over the central United States. Journal of Climate, 10(3): 481-507.

Hill, K.A. and Lackmann, G.M., 2011. The impact of future climate change on TC intensity and structure: A downscaling approach. Journal of Climate, 24(17): 4644-4661.

Hitchens, N.M., Baldwin, M.E. and Trapp, R.J., 2012. An object-oriented characterization of extreme precipitation-producing convective systems in the midwestern United States. Monthly Weather Review, 140(4): 1356-1366.

Hoke, J. E., & Anthes, R. A., 1976. The initialization of numerical models by a dynamic-initialization technique. Monthly Weather Review, 104(12), 1551–1556.

Holton, J.R. and Hakim, G.J., 2013. An introduction to dynamic meteorology. Academic press.

Houze Jr, R.A., Smull, B.F. and Dodge, P., 1990. Mesoscale organization of springtime rainstorms in Oklahoma. Monthly Weather Review, 118(3): 613-654.
Houze, R.A., 1993. Cloud Dynamics, vol. 53 of the International Geophysics Series. Academic Press, San Diego.
Houze, R.A., 2004. Mesoscale convective systems. Reviews of Geophysics, 42(4).
Ishida, K. et al., 2014. Physically Based Estimation of Maximum Precipitation over Three Watersheds in Northern California: Atmospheric Boundary Condition Shifting. Journal of Hydrologic Engineering.
Ishida, K. et al., 2015. Physically Based Estimation of Maximum Precipitation over Three Watersheds in Northern California: Atmospheric Boundary Condition Shifting. Journal of Hydrologic Engineering, 20(4).
Jankov, I., Gallus Jr, W.A., Segal, M., Shaw, B. and Koch, S.E., 2005. The impact of different WRF model physical parameterizations and their interactions on warm season MCS rainfall. Weather and forecasting, 20(6): 1048-1060.
Jirak, I.L. and Cotton, W.R., 2007. Observational analysis of the predictability of mesoscale convective systems. Weather and Forecasting, 22(4): 813-838.
Jirak, I.L., Cotton, W.R. and McAnelly, R.L., 2003. Satellite and radar survey of mesoscale convective system development. Monthly weather review, 131(10): 2428-2449.
Jones, S.C. et al., 2003. The extratropical transition of tropical cyclones: Forecast challenges, current understanding, and future directions. Weather and Forecasting, 18(6): 1052-1092.
Kalnay, E. et al., 1996. The NCEP/NCAR 40-Year Reanalysis Project. Bulletin of the American Meteorological Society, 77: 437-471.
Kanamitsu, M. et al., 2002. NCEP-DOE AMIP-II reanalysis (R-2). Bulletin of the American Meteorological Society, 83: 1631-1643+1559.
Karl, T.R. and Knight, R.W., 1998. Secular trends of precipitation amount, frequency, and intensity in the United States. Bulletin of the American Meteorological society, 79(2): 231-241.
Karyampudi, V.M., Lai, G.S. and Manobianco, J., 1998. Impact of initial conditions, rainfall assimilation, and cumulus parameterization on simulations of Hurricane Florence (1988). Monthly weather review, 126(12): 3077-3101.
Kawase, H. et al., 2009. Intermodel variability of future changes in the Baiu rainband estimated by the pseudo global warming downscaling method. Journal of Geophysical Research: Atmospheres, 114(D24).
Keene, K.M. and Schumacher, R.S., 2013. The bow and arrow mesoscale convective structure. Monthly Weather Review, 141(5): 1648-1672.
Khain, A., Lynn, B. and Dudhia, J., 2010. Aerosol effects on intensity of landfalling hurricanes as seen from simulations with the WRF model with spectral bin microphysics. Journal of the Atmospheric Sciences, 67(2): 365-384.
Klein, P.M., Harr, P.A. and Elsberry, R.L., 2000. Extratropical transition of western North Pacific tropical cyclones: An overview and conceptual model of the transformation stage. Weather and forecasting, 15(4): 373-395.
Klein, P.M., Harr, P.A. and Elsberry, R.L., 2002. Extratropical transition of western North Pacific tropical cyclones: Midlatitude and tropical cyclone contributions to reintensification. Monthly weather review, 130(9): 2240-2259.
Knabb, R.D. and Mainelli, M., 2006. Tropical Cyclone Report Hurricane Ernesto 24 August - 1 September 2006. National Hurricane Center.
Knutson, T. and Tuleya, R., 1999. Increased hurricane intensities with CO2-induced warming as simulated using the GFDL hurricane prediction system. Climate Dynamics, 15(7): 503-519.
Knutson, T.R. and Manabe, S., 1998. Model assessment of decadal variability and trends in the tropical Pacific Ocean. Journal of Climate, 11(9): 2273-2296.

Knutson, T.R., Sirutis, J.J., Garner, S.T., Held, I.M. and Tuleya, R.E., 2007. Simulation of the recent multidecadal increase of Atlantic hurricane activity using an 18-km-grid regional model. Bulletin of the American Meteorological Society, 88(10): 1549-1565.
Knutson, T.R., Sirutis, J.J., Garner, S.T., Vecchi, G.A. and Held, I.M., 2008. Simulated reduction in Atlantic hurricane frequency under twenty-first-century warming conditions. Nature geoscience, 1(6): 359.
Knutson, T.R. et al., 2013. Dynamical downscaling projections of twenty-first-century Atlantic hurricane activity: CMIP3 and CMIP5 model-based scenarios. Journal of Climate, 26(17): 6591-6617.
Knutson, T.R. et al., 2015. Global projections of intense tropical cyclone activity for the late twenty-first century from dynamical downscaling of CMIP5/RCP4. 5 scenarios. Journal of Climate, 28(18): 7203-7224.
Knutson, T.R. and Tuleya, R.E., 2004. Impact of CO2-induced warming on simulated hurricane intensity and precipitation: Sensitivity to the choice of climate model and convective parameterization. Journal of Climate, 17(18): 3477-3495.
Konrad, C.E., 2001. The Most Extreme Precipitation Events over the Eastern United States from 1950 to 1996: Considerations of Scale. Journal of Hydrometeorology, 2(3): 309-325.
Kunkel, K.E. et al., 2012. Meteorological causes of the secular variations in observed extreme precipitation events for the conterminous United States. Journal of Hydrometeorology, 13(3): 1131-1141.
Kunkel, K.E. et al., 2013. Monitoring and understanding trends in extreme storms: State of knowledge. Bulletin of the American Meteorological Society, 94(4): 499-514.
Kunkel, K.E., Pielke Jr, R.A. and Changnon, S.A., 1999. Temporal fluctuations in weather and climate extremes that cause economic and human health impacts: A review. Bulletin of the American Meteorological Society, 80(6): 1077-1098.
Kurihara, Y., Bender, M.A., Tuleya, R.E. and Ross, R.J., 1995. Improvements in the GFDL hurricane prediction system. Monthly Weather Review, 123(9): 2791-2801.
Kurihara, Y., Tuleya, R.E. and Bender, M.A., 1998. The GFDL hurricane prediction system and its performance in the 1995 hurricane season. Monthly weather review, 126(5): 1306-1322.
Kursinski, A.L. and Mullen, S.L., 2008. Spatiotemporal variability of hourly precipitation over the eastern contiguous United States from Stage IV multisensor analyses. Journal of Hydrometeorology, 9(1): 3-21.
Laing, A.G. and Fritsch, J.M., 1993a. Mesoscale convective complexes in Africa. Monthly weather review, 121(8): 2254-2263.
Laing, A.G. and Fritsch, J.M., 1993b. Mesoscale convective complexes over the Indian monsoon region. Journal of climate, 6(5): 911-919.
Laing, A.G. and Fritsch, J.M., 2000. The large-scale environments of the global populations of mesoscale convective complexes. Monthly Weather Review, 128(8): 2756-2776.
Laing, A.G. and Michael Fritsch, J., 1997. The global population of mesoscale convective complexes. Quarterly Journal of the Royal Meteorological Society, 123(538): 389-405.
Landsea, C.W., Bell, G.D., Gray, W.M. and Goldenberg, S.B., 1998. The extremely active 1995 Atlantic hurricane season: Environmental conditions and verification of seasonal forecasts. Monthly Weather Review, 126(5): 1174-1193.
Lawrence, M.B. and Cobb, H.D., 2005. Tropical Cyclone Report Hurricane Jeanne 13-28 September 2004. National Hurricane Center.
Lin, N., Smith, J.A., Villarini, G., Marchok, T.P. and Baeck, M.L., 2010. Modeling extreme rainfall, winds, and surge from Hurricane Isabel (2003). Weather and Forecasting, 25(5): 1342-1361.
Lin, Y. and Mitchell, K.E., 2005. The NCEP Stage II/IV hourly precipitation analyses: Development and applications.

Liu, Y., Zhang, D.-L. and Yau, M., 1997. A multiscale numerical study of Hurricane Andrew (1992). Part I: Explicit simulation and verification. Monthly weather review, 125(12): 3073-3093.
Liu, Y., Zhang, D.-L. and Yau, M., 1999. A multiscale numerical study of Hurricane Andrew (1992). Part II: Kinematics and inner-core structures. Monthly weather review, 127(11): 2597-2616.
Lonfat, M., Marks Jr, F.D. and Chen, S.S., 2004. Precipitation distribution in tropical cyclones using the Tropical Rainfall Measuring Mission (TRMM) microwave imager: A global perspective. Monthly Weather Review, 132(7): 1645-1660.
Lynch, S., 2003. Development of a raster database of annual, monthly and daily rainfall for Southern Africa. . WRC Rep. N 1156/1/03, 78 pp.
Maddox, R., Rodgers, D. and Howard, K., 1982. Mesoscale convective complexes over the United States during 1981-Annual summary. Monthly Weather Review, 110(10): 1501-1514.
Maddox, R.A., 1980. Meoscale convective complexes. Bulletin of the American Meteorological Society, 61(11): 1374-1387.
Maddox, R.A., 1983. Large-scale meteorological conditions associated with midlatitude, mesoscale convective complexes. Monthly Weather Review, 111(7): 1475-1493.
Maddox, R.A., Chappell, C.F. and Hoxit, L.R., 1979. Synoptic and Meso-α Scale Aspects of Flash Flood Events 1. Bulletin of the American Meteorological Society, 60(2): 115-123.
Marks, F.D. and Shay, L.K., 1998. Landfalling tropical cyclones: Forecast problems and associated research opportunities. Bulletin of the American Meteorological Society, 79(2): 305-323.
Marks Jr, F.D., 1985. Evolution of the structure of precipitation in Hurricane Allen (1980). Monthly weather review, 113(6): 909-930.
Mearns, L.O. et al., 2009. A regional climate change assessment program for North America. Eos, Transactions American Geophysical Union, 90(36): 311-311.
Milrad, S.M. and Kelly, C.M., 2013. Synoptic-Scale Precursors, Characteristics and Typing of Nocturnal Mesoscale Convective Complexes in the Great Plains. 2013.
Moore, B.J., Mahoney, K.M., Sukovich, E.M., Cifelli, R. and Hamill, T.M., 2014. Climatology and Environmental Characteristics of Extreme Precipitation Events in the Southeastern United States. Mon Weather Rev, 143(3): 718-741.
Moss, R.H. et al., 2010. The next generation of scenarios for climate change research and assessment. Nature, 463: 747-56.
Murakami, H. et al., 2012. Future changes in tropical cyclone activity projected by the new high-resolution MRI-AGCM. Journal of Climate, 25(9): 3237-3260.
Nachamkin, J.E. and Cotton, W.R., 2000. Interactions between a developing mesoscale convective system and its environment. Part II: Numerical simulation. Monthly Weather Review, 128(5): 1225-1244.
Nachamkin, J.E., McAnelly, R.L. and Cotton, W.R., 2000. Interactions between a developing mesoscale convective system and its environment. Part I: Observational analysis. Monthly Weather Review, 128(5): 1205-1224.
Nagarajan, B., Yau, M. and Zhang, D.-L., 2001. A numerical study of a mesoscale convective system during TOGA COARE. Part I: Model description and verification. Monthly weather review, 129(10): 2501-2520.
Nagarajan, B., Yau, M. and Zhang, D.-L., 2004. A numerical study of a mesoscale convective system during TOGA COARE. Part II: Organization. Monthly weather review, 132(4): 1000-1017.
NCAR, M.M.M.D.-. 2016. ARW Version 3 Modeling System User's Guide.
NSSL, 2012. Severe Weather: Thunderstorm Types.

O'Connor, J.E. and Costa, J.E., 2003. Large floods in the United States: Where they happen and why, Circular 1245. US Geological Survey.
Ohara, N. et al., 2011a. Physically based estimation of maximum precipitation over American River watershed, California. Journal of Hydrologic Engineering, 16(4): 351-361.
Ohara, N. et al., 2011b. Physically Based Estimation of Maximum Precipitation over American River Watershed, California. J. Hydrol. Eng., 16(4): 351-361.
Oouchi, K. et al., 2006. Tropical cyclone climatology in a global-warming climate as simulated in a 20 km-mesh global atmospheric model: Frequency and wind intensity analyses. Journal of the Meteorological Society of Japan. Ser. II, 84(2): 259-276.
Ooyama, K., 1969. Numerical simulation of the life cycle of tropical cyclones. Journal of the Atmospheric Sciences, 26(1): 3-40.
Orlanski, I., 1975. Rational Subdivision of Scales for Atmospheric Processes. Bulletin of the American Meteorological Society, 56(5): 527-530.
Parker, M.D. and Johnson, R.H., 2000. Organizational modes of midlatitude mesoscale convective systems. Mon Weather Rev, 128(10): 3413-3436.
Parker, M.D. and Johnson, R.H., 2004. Structures and dynamics of quasi-2D mesoscale convective systems. Journal of the atmospheric sciences, 61(5): 545-567.
Pasch, R.J., Kimberlain, T.B. and Stewart, S.R., 1999. Preliminary Report Hurricane Floyd. National Hurricane Center.
Penide, G. et al., 2010. Numerical simulation of the 7 to 9 September 2006 AMMA mesoscale convective system: Evaluation of the dynamics and cloud microphysics using synthetic observations. Quarterly Journal of the Royal Meteorological Society, 136(S1): 304-322.
Peters, J.M. and Schumacher, R.S., 2014. Objective Categorization of Heavy-Rain-Producing MCS Synoptic Types by Rotated Principal Component Analysis. Monthly Weather Review, 142(5): 1716-1737.
Petersen, W.A. et al., 1999. Mesoscale and radar observations of the Fort Collins flash flood of 28 July 1997. Bulletin of the American Meteorological Society, 80(2): 191-216.
Peterson, T.C. et al., 2013. Monitoring and understanding changes in heat waves, cold waves, floods, and droughts in the United States: State of knowledge. Bulletin of the American Meteorological Society, 94(6): 821-834.
Pielke Jr, R.A. and Landsea, C.W., 1998. Normalized hurricane damages in the United States: 1925-95. Weather and Forecasting, 13(3): 621-631.
Pielke, R. et al., 1992. A comprehensive meteorological modeling system—RAMS. Meteorology and Atmospheric Physics, 49(1-4): 69-91.
Pontrelli, M.D., Bryan, G. and Fritsch, J., 1999. The Madison County, Virginia, flash flood of 27 June 1995. Weather and forecasting, 14(3): 384-404.
Powell, M.D., 1990a. Boundary layer structure and dynamics in outer hurricane rainbands. Part I: Mesoscale rainfall and kinematic structure. Monthly Weather Review, 118(4): 891-917.
Powell, M.D., 1990b. Boundary layer structure and dynamics in outer hurricane rainbands. Part II: Downdraft modification and mixed layer recovery. Monthly Weather Review, 118(4): 918-938.
Reynolds, R.W. et al., 2007. Daily high-resolution-blended analyses for sea surface temperature. Journal of Climate, 20(22): 5473-5496.
Rosenthal, S.L., 1970. Experiments with a numerical model of tropical cyclone development: Some effects of radial resolution. Monthly Weather Review, 98(2): 106-120.
Rotunno, R., Klemp, J.B. and Weisman, M.L., 1988. A theory for strong, long-lived squall lines. Journal of the Atmospheric Sciences, 45(3): 463-485.
Saha, S. et al., 2010. The NCEP climate forecast system reanalysis. Bulletin of the American Meteorological Society, 91: 1015-1057.
Sato, T., 2004. The earth simulator: roles and impacts. Nuclear Physics B-Proceedings Supplements, 129: 102-108.

Schenkman, A.D., Xue, M. and Shapiro, A., 2012. Tornadogenesis in a Simulated Mesovortex within a Mesoscale Convective System. J Atmos Sci, 69(11): 3372-3390.
Schenkman, A.D., Xue, M., Shapiro, A., Brewster, K. and Gao, J., 2011. The analysis and prediction of the 8-9 May 2007 Oklahoma tornadic mesoscale convective system by assimilating WSR-88D and CASA radar data using 3DVAR. Monthly Weather Review, 139(1): 224-246.
Schumacher, R.S., 2009. Mechanisms for quasi-stationary behavior in simulated heavy-rain-producing convective systems. Journal of the Atmospheric Sciences, 66(6): 1543-1568.
Schumacher, R.S. and Johnson, R.H., 2005. Organization and environmental properties of extreme-rain-producing mesoscale convective systems. Monthly weather review, 133(4): 961-976.
Schumacher, R.S. and Johnson, R.H., 2006. Characteristics of US extreme rain events during 1999-2003. Weather and Forecasting, 21(1): 69-85.
Schumacher, R.S. and Johnson, R.H., 2008. Mesoscale Processes Contributing to Extreme Rainfall in a Midlatitude Warm-Season Flash Flood*. Monthly Weather Review, 136(10): 3964-3986.
Schumacher, R.S. and Johnson, R.H., 2009. Quasi-stationary, extreme-rain-producing convective systems associated with midlevel cyclonic circulations. Weather and Forecasting, 24(2): 555-574.
Shapiro, L.J. and Goldenberg, S.B., 1998. Atlantic sea surface temperatures and tropical cyclone formation. Journal of Climate, 11(4): 578-590.
Shutts, G. and Gray, M., 1994. A numerical modelling study of the geostrophic adjustment process following deep convection. Quarterly Journal of the Royal Meteorological Society, 120(519): 1145-1178.
Simpson, R.H. and Saffir, H., 1974. The hurricane disaster potential scale. Weatherwise, 27(8): 169.
Sippel, J.A., Braun, S.A. and Shie, C.-L., 2011. Environmental influences on the strength of Tropical Storm Debby (2006). Journal of the Atmospheric Sciences, 68(11): 2557-2581.
Skamarock, W. et al., 2008a. A description of the advanced research WRF version 3, NCAR, Tech. Note, Mesoscale and Microscale Meteorology Division. National Center for Atmospheric Research, Boulder, Colorado, USA.
Skamarock, W.C. and Klemp, J.B., 2008. A time-split nonhydrostatic atmospheric model for weather research and forecasting applications. Journal of Computational Physics, 227(7): 3465-3485.
Skamarock, W.C. et al., 2008b. A description of the Advanced Research WRF Version 3, NCAR Tehnical Note NCAR/TN-475+STR, 1-113 pp.
Snook, N., Xue, M. and Jung, Y., 2012. Ensemble probabilistic forecasts of a tornadic mesoscale convective system from ensemble Kalman filter analyses using WSR-88D and CASA radar data. Monthly Weather Review, 140(7): 2126-2146.
Stevenson, S.N. and Schumacher, R.S., 2014. A 10-year Survey of Extreme Rainfall Events in the Central and Eastern US using Gridded Multi-Sensor Precipitation Analyses. Monthly Weather Review(2014).
Stewart, S.R., 2004. Tropical Cyclone Report Hurricane Ivan 2-24 September 2004. National Hurricane Center.
Stewart, S.R. and Beven, J.L., 2008. Tropical Storm Report Tropical Storm Fay (AL062008) 15-26 August 2008. National Hurricane Center.
Sundqvist, H., 1970a. Numerical simulation of the development of tropical cyclones with a ten-level model. Part I. Tellus, 22(4): 359-390.
Sundqvist, H., 1970b. Numerical simulation of the development of tropical cyclones with a ten-level model. Part II. Tellus, 22(5): 504-510.

Trapp, R.J., 2013. Mesoscale-Convective Processes in the Atmosphere. Cambridge University Press.
Trenberth, K.E., Davis, C.A. and Fasullo, J., 2007. Water and energy budgets of hurricanes: Case studies of Ivan and Katrina. Journal of Geophysical Research: Atmospheres (1984–2012), 112(D23).
Trier, S.B., Marsham, J.H., Davis, C.A. and Ahijevych, D.A., 2011. Numerical simulations of the postsunrise reorganization of a nocturnal mesoscale convective system during 13 June IHOP_2002. Journal of the Atmospheric Sciences, 68(12): 2988-3011.
van Vuuren, D.P. et al., 2011. The representative concentration pathways: an overview. Climatic Change, 109(1-2): 5-31.
Velasco, I. and Fritsch, J.M., 1987. Mesoscale convective complexes in the Americas. Journal of Geophysical Research: Atmospheres (1984–2012), 92(D8): 9591-9613.
Wandishin, M.S., Stensrud, D.J., Mullen, S.L. and Wicker, L.J., 2008. On the predictability of mesoscale convective systems: Two-dimensional simulations. Weather and Forecasting, 23(5): 773-785.
Wandishin, M.S., Stensrud, D.J., Mullen, S.L. and Wicker, L.J., 2010. On the predictability of mesoscale convective systems: Three-dimensional simulations. Monthly Weather Review, 138(3): 863-885.
Wang, W., Bruyere, C. and Duda, M., 2011. WRF-ARW V3: User's Guide. URL: http://www.mmm.ucar.edu/wrf/users (accessed: 11.01. 2013).
Wang, W. et al., 2016. ARW Version 3 Modeling System User's Guide, MMM; NCAR.
Wheatley, D.M., Yussouf, N. and Stensrud, D.J., 2014. Ensemble Kalman Filter Analyses and Forecasts of a Severe Mesoscale Convective System Using Different Choices of Microphysics Schemes. Monthly Weather Review, 142(9): 3243-3263.
Wicker, L.J. and Wilhelmson, R.B., 1995. Simulation and analysis of tornado development and decay within a three-dimensional supercell thunderstorm. Journal of the Atmospheric Sciences, 52(15): 2675-2703.
Willoughby, H.E., Jin, H.-L., Lord, S.J. and Piotrowicz, J.M., 1984. Hurricane structure and evolution as simulated by an axisymmetric, nonhydrostatic numerical model. Journal of the atmospheric sciences, 41(7): 1169-1186.
Wright, D.B., Knutson, T.R. and Smith, J.A., 2015. Regional climate model projections of rainfall from US landfalling tropical cyclones. Climate dynamics, 45(11-12): 3365-3379.
Wu, C.-C., 2001. Numerical simulation of Typhoon Gladys (1994) and its interaction with Taiwan terrain using the GFDL hurricane model. Monthly weather review, 129(6): 1533-1549.
Wu, C.-C., Cheung, K.K. and Lo, Y.-Y., 2009. Numerical study of the rainfall event due to the interaction of Typhoon Babs (1998) and the northeasterly monsoon. Monthly Weather Review, 137(7): 2049-2064.
Wu, C.-C., Yen, T.-H., Kuo, Y.-H. and Wang, W., 2002. Rainfall simulation associated with Typhoon Herb (1996) near Taiwan. Part I: The topographic effect. Weather and forecasting, 17(5): 1001-1015.
Wu, L., Braun, S.A., Halverson, J. and Heymsfield, G., 2006. A numerical study of Hurricane Erin (2001). Part I: Model verification and storm evolution. Journal of the atmospheric sciences, 63(1): 65-86.
Xiao, Q. et al., 2009. Experiments of hurricane initialization with airborne Doppler radar data for the Advanced Research Hurricane WRF (AHW) model. Monthly Weather Review, 137(9): 2758-2777.
Xie, P. et al., 2003. GPCP pentad precipitation analyses: An experimental dataset based on gauge observations and satellite estimates. Journal of Climate, 16(13): 2197-2214.
Xue, M., Droegemeier, K.K., Wong, V., Shapiro, A. and Brewster, K., 1995. ARPS version 4.0 user's guide. Center for Analysis and Prediction of Storms, University of Oklahoma, 100.

Yang, B., Qian, Y., Lin, G., Leung, R. and Zhang, Y., 2012. Some issues in uncertainty quantification and parameter tuning: a case study of convective parameterization scheme in the WRF regional climate model. Atmospheric Chemistry and Physics, 12(5): 2409-2427.

Yau, M., Liu, Y., Zhang, D.-L. and Chen, Y., 2004. A multiscale numerical study of Hurricane Andrew (1992). Part VI: Small-scale inner-core structures and wind streaks. Monthly weather review, 132(6): 1410-1433.

Yukimoto, S. et al., 2006. Present-day climate and climate sensitivity in the Meteorological Research Institute coupled GCM version 2.3 (MRI-CGCM2. 3). Journal of the Meteorological Society of Japan. Ser. II, 84(2): 333-363.

Zhang, D.-L., Liu, Y. and Yau, M., 2000. A multiscale numerical study of Hurricane Andrew (1992). Part III: Dynamically induced vertical motion. Monthly weather review, 128(11): 3772-3788.

Zhang, D.-L., Liu, Y. and Yau, M., 2001. A multiscale numerical study of Hurricane Andrew (1992). Part IV: Unbalanced flows. Monthly weather review, 129(1): 92-107.

Zhang, D.-L., Liu, Y. and Yau, M., 2002. A multiscale numerical study of Hurricane Andrew (1992). Part V: Inner-core thermodynamics. Monthly weather review, 130(11): 2745-2763.

Zhang, L. and Pu, Z., 2011. Four-Dimensional Assimilation of Multitime Wind Profiles over a Single Station and Numerical Simulation of a Mesoscale Convective System Observed during IHOP_2002. Monthly Weather Review, 139(11): 3369-3388.

Zhang, Q.-H., Lau, K.-H., Kuo, Y.-H. and Chen, S.-J., 2003. A numerical study of a mesoscale convective system over the Taiwan Strait. Monthly weather review, 131(6): 1150-1170.

Zhao, M., Held, I.M., Lin, S.-J. and Vecchi, G.A., 2009. Simulations of global hurricane climatology, interannual variability, and response to global warming using a 50-km resolution GCM. Journal of Climate, 22(24): 6653-6678.

Zhao, Y., 2012. Numerical investigation of a localized extremely heavy rainfall event in complex topographic area during midsummer. Atmospheric Research, 113: 22-39.

Zheng, Y., Xu, Q. and Stensrud, D.J., 1995. A numerical simulation of the 7 May 1985 mesoscale convective system. Monthly weather review, 123(6): 1781-1799.

Zou, X. and Xiao, Q., 2000. Studies on the initialization and simulation of a mature hurricane using a variational bogus data assimilation scheme. Journal of the atmospheric sciences, 57(6): 836-860.

Zurndorfer, E., Schwarz, F., Hansen, E., Fenn, D. and Miller, J., 1986. Probable Maximum and TVA Precipitation Estimates with Areal Distribution for Tennessee River Drainages less than 3,000 Mi2 in Area, Hydrometeorological Report.

APPENDIX A PARAMETERIZATION SCHEMES IN THE WRF MODEL

This appendix provides the names, code numbers, and brief explanations of the WRF model's options used in Chapter 4 for the reconstruction of several historical TCs. This information is from the ARW Version 3 Modeling System User's Guide.

- Microphysics options:
    1. **Kessler scheme:** A warm-rain (i.e. no ice) scheme used commonly in idealized cloud modeling studies.
    2. **Lin et al. (Purdue) scheme:** A sophisticated scheme that has ice, snow and graupel processes, suitable for real-data high-resolution simulations.
    3. **WRF Single-moment 3-class simple ice (WSM3) scheme:** A simple, efficient scheme with ice and snow processes suitable for mesoscale grid sizes.
    4. **WRF Single-moment 5-class (WSM5) scheme:** A slightly more sophisticated version of option 3 that allows for mixed-phase processes and super-cooled water.
    5. **Ferrier (new Eta) scheme:** The operational microphysics in NCEP models. A simple efficient scheme with diagnostic mixed-phase processes (for fine resolutions < 5 km).
    6. **WRF Single-moment 6-class graupel (WSM6) scheme:** A scheme with ice, snow and graupel processes suitable for high-resolution simulations.
    7. **Goddard GCE scheme:** A scheme with ice, snow and graupel processes suitable for high-resolution simulations.
    8. **Thompson graupel scheme (New Thompson et al.):** A new scheme with ice, snow and graupel processes suitable for high-resolution simulations.
    9. **Milbrandt-Yau 2-moment scheme:** This scheme includes separate categories for hail and graupel with double-moment cloud, rain, ice, snow, graupel and hail.
    10. **Morrison 2-moment scheme:** Double-moment ice, snow, rain and graupel for cloud-resolving simulations.
    11. **Community Atmospheric Model (CAM) 5.1 5-class scheme**
    13. **Stony-Brook University (SBU-YLin) 5-class scheme:** This is a 5-class scheme with riming intensity predicted to account for mixed-phase processes.
    14. **WRF double moment 5-class (WDM5) scheme:** This scheme has double-moment rain. Cloud and CCN for warm processes, but is otherwise like WSM5.
    16. **WRF double moment 6-class (WDM6) scheme:** This scheme has double-moment rain. Cloud and CCN for warm processes, but is otherwise like WSM6.
    17. **National Severe Storm Laboratory (NSSL) 2-moment 4-ice scheme with steady background cloud condensation nuclei (CCN) scheme:** A two-moment scheme for cloud droplets, rain drops, ice crystals, snow, graupel, and hail. It also predicts average graupel particle density, which allows graupel to span the range from frozen drops to low-density graupel.
    18. **NSSL 2-moment 4-ice with predicted CCN scheme:** An additional option of NSSL to predict cloud condensation nuclei (CCN) concentration (intended for idealized simulations). The scheme is intended for cloud-resolving simulations (dx <= 2km) in research applications.
    19. **NSSL 1-moment 6-class scheme:** A single-moment version of the NSSL scheme.
    21. **NSSL-LFO 1-moment 6-class scheme:** Similar to Gilmore et al. (2004).
    22. **NSSL 2-moment 3-ice scheme without hail:** A two-moment version of the NSSL scheme without hail.
    28. **aerosol-aware Thompson scheme:** This scheme considers water- and ice-friendly
    29. aerosols. A climatology dataset may be used to specify initial and boundary conditions for the aerosol variables.

30. **Hebrew University of Jerusalem, Israel (HUJI) spectral bin scheme, fast version**
32. **HUJI spectral bin scheme, full version**
95. **Ferrier (old Eta), operational North American Mesoscale Model (WRF NMM) scheme**
98. **Thompson scheme in V3.0**

- Longwave radiation options:
  1. **Rapid Radiative Transfer Model (RRTM) scheme:** An accurate scheme using look-up tables for efficiency. Accounts for multiple bands, and microphysics species.
  3. **CAM scheme:** From the CAM 3 climate model used in CCSM. Allows for aerosols and trace gases.
  4. **RRTM for General Circulation Models (RRTMG) scheme:** It includes the MCICA method of random cloud overlap.
  5. **Goddard scheme:** Efficient, multiple bands, ozone from climatology.
  7. **Fu-Liou-Gu (FLG) scheme:** Multiple bands, cloud and cloud fraction effects, ozone
  8. profile from climatology and tracer gases.
  24. **Fast RRTMG scheme for GPU and MIC:** Fast version of option 4.
  31. **Earth Held-Suarez forcing scheme**
  99. **GFDL (Eta) scheme:** Eta operational radiation scheme. An older multi-band scheme with carbon dioxide, ozone and microphysics effects.

- Shortwave radiation options:
  1. **Dudhia scheme:** Simple downward integration allowing efficiently for clouds and clear-sky absorption and scattering.
  2. **Old Goddard scheme:** Two-stream multi-band scheme with ozone from climatology and cloud effects.
  3. **CAM scheme:** From the CAM 3 climate model used in CCSM. Allows for aerosols and trace gases.
  4. **RRTMG scheme:** A new shortwave scheme with the MCICA method of random cloud overlap.
  5. **New Goddard scheme:** Efficient, multiple bands, ozone from climatology.
  7. **FLG scheme:** Multiple bands, cloud and cloud fraction effects, ozone profile from climatology, can allow for aerosols.
  24. **Fast RRTMG scheme for GPU and MIC:** Fast version of option 4.
  99. **GFDL (Eta) scheme:** Eta operational scheme. Two-stream multi-band scheme with ozone from climatology and cloud effects.

- Surface layer options:
  1. **Revised MM5 Monin-Obukhov scheme:** Based on Monin-Obukhov with Carslon-Boland viscous sub-layer and standard similarity functions from look-up tables.
  2. **Monin-Obukhov (Janjic Eta) scheme:** Used in Eta model. Based on Monin-Obukhov with Zilitinkevich thermal roughness length and standard similarity functions from look-up tables.
  3. **NCEP Global Forecast System (GFS) scheme**
  4. **Quasi-Normal Scale Elimination (QNSE) scheme:** Quasi-Normal Scale Elimination PBL scheme's surface layer option.
  5. **Mellor-Yamada-Nakanishi-Niino (MYNN) scheme:** Nakanishi and Niino PBL's surface layer scheme.
  7. **Pleim-Xiu scheme**
  10. **Total Energy-Mass Flux (TEMF) scheme**
  91. **Old MM5 scheme**

- Land surface options:
    1. **5-layer thermal diffusion scheme:** Soil temperature only scheme, using five layers.
    2. **Unified Noah land-surface model:** Unified NCEP/NCAR/AFWA scheme with soil temperature and moisture in four layers, fractional snow cover and frozen soil physics.
    3. **Rapid Update Cycle (RUC) land surface model:** RUC operational scheme with soil temperature and moisture in six layers, multi-layer snow and frozen soil physics.
    4. **Noah-MP scheme:** Uses multiple options for key land-atmosphere interaction processes. Noah-MP contains a separate vegetation canopy and a multi-layer snow pack.
    5. **Community Land Model Version 4 (CLM4):** It contains sophisticated treatment of biogeophysics, hydrology, biogeochemistry, and dynamic vegetation.
    7. **Pleim-Xiu scheme:** Two-layer scheme with vegetation and sub-grid tiling.
    8. **Simplified Simple Biosphere (SSiB) scheme:** SSiB-3 includes three snow layers to realistically simulate snow processes, including destructive metamorphism, densification process due to snow load, and snow melting, which substantially enhances the model's ability for the cold season study.

- PBL options:
    1. **Yonsei University (YSU) scheme:** Non-local-K scheme with explicit entrainment layer and parabolic K profile in unstable mixed layer.
    2. **Mellor-Yamada-Janjic (Eta) TKE scheme:** Eta operational scheme. One-dimensional prognostic turbulent kinetic energy scheme with local vertical mixing.
    3. **NCEP GFS scheme**
    4. **QNSE-EDMF scheme:** A TKE-prediction option that uses a new theory for stably stratified regions.
    5. **Mellor-Yamada-Nakanishi-Niino (MYNN) 2.5 level TKE scheme:** Predicts sub-grid TKE terms.
    6. **MYNN 3rd level TKE scheme:** Predicts TKE and other second-moment terms.
    7. **Asymmetric Convection Model 2 (ACM2) scheme:** Asymmetric Convective Model with non-local upward mixing and local downward mixing.
    8. **Bougeault-Lacarrere (BouLac) TKE scheme:** A TKE-prediction option. Designed for use with BEP urban model.
    9. **University of Washington (UW) TKE scheme:** TKE scheme from CESM climate model.
    10. **TEMF scheme:** Sub-grid total energy prognostic variable, plus mass-flux type shallow convection.
    11. **Shin-Hong 'scale-aware' scheme:** Includes scale dependency for vertical transport in convective PBL. Vertical mixing in the stable PBL and free atmosphere follows YSU. This scheme also has diagnosed TKE and mixing length output.
    12. **Grenier-Bretherton-McCaa (GBM) TKE-type scheme:** This is a TKE scheme. Tested in cloudtopped PBL cases.
    99. **Medium Range Forecast (MRF) scheme:** Older version of option 1 with implicit treatment of entrainment layer as part of non-local-K mixed layer.

- Cumulus options:
    1. **Kain-Fritsch (new Eta) scheme:** Deep and shallow convection sub-grid scheme using a mass flux approach with downdrafts and CAPE removal time scale.
    2. **Betts-Miller-Janjic scheme:** Operational Eta scheme. Column moist adjustment scheme relaxing towards a well-mixed profile.
    3. **Grell-Freitas ensemble scheme:** An improved Grell-Devenyi scheme that tries to smooth the transition to cloud-resolving scales, as proposed by Arakawa et al. (2004).

4. **Old GFS Simplified Arakawa-Schubert (SAS) scheme:** Simple mass-flux scheme with quasi-equilibrium closure with shallow mixing scheme (and momentum transport in NMM only).
5. **New Grell scheme (G3):** An improved version of the Grell-Devenyi scheme that may also be used on high resolution (in addition to coarser resolutions) if subsidence spreading option is turned on.
6. **Tiedtke scheme:** Mass-flux type scheme with CAPE-removal time scale, shallow component and momentum transport.
7. **Zhang-McFarlane scheme:** Mass-flux CAPE-removal type deep convection from CESM climate model with momentum transport.
11. **Multi-scale Kain-Fritsch scheme**
14. **New SAS scheme:** New mass-flux scheme with deep and shallow components and momentum transport.
16. **New Tiedtke scheme:** Similar to the Tiedtke scheme used in REGCM4 and ECMWF.
84. **New SAS HWRF scheme:** New mass-flux scheme with deep and shallow components and momentum transport.
93. **Grell-Devenyi ensemble scheme:** Multi-closure, multi-parameter, ensemble method with typically 144 sub-grid members.
99. **Previous Kain-Fritsch scheme:** Deep convection scheme using a mass flux approach with downdrafts and CAPE removal time scale.

APPENDIX B PRECIPITABLE WATER FIELDS AND INTEGRATED WATER VAPOR TRANSPORT FIELDS IN THE RECONSTRUCTED MESOSCALE CONVECTIVE SYSTEMS AND TROPICAL CYCLONES

This section provides the plots of the PW and IVT fields within the reconstructed MCSs (Chapter 3) and TCs (Chapter 4).

B.1 Mesoscale Convective Systems

B.1.1 June 22, 2002 MCS

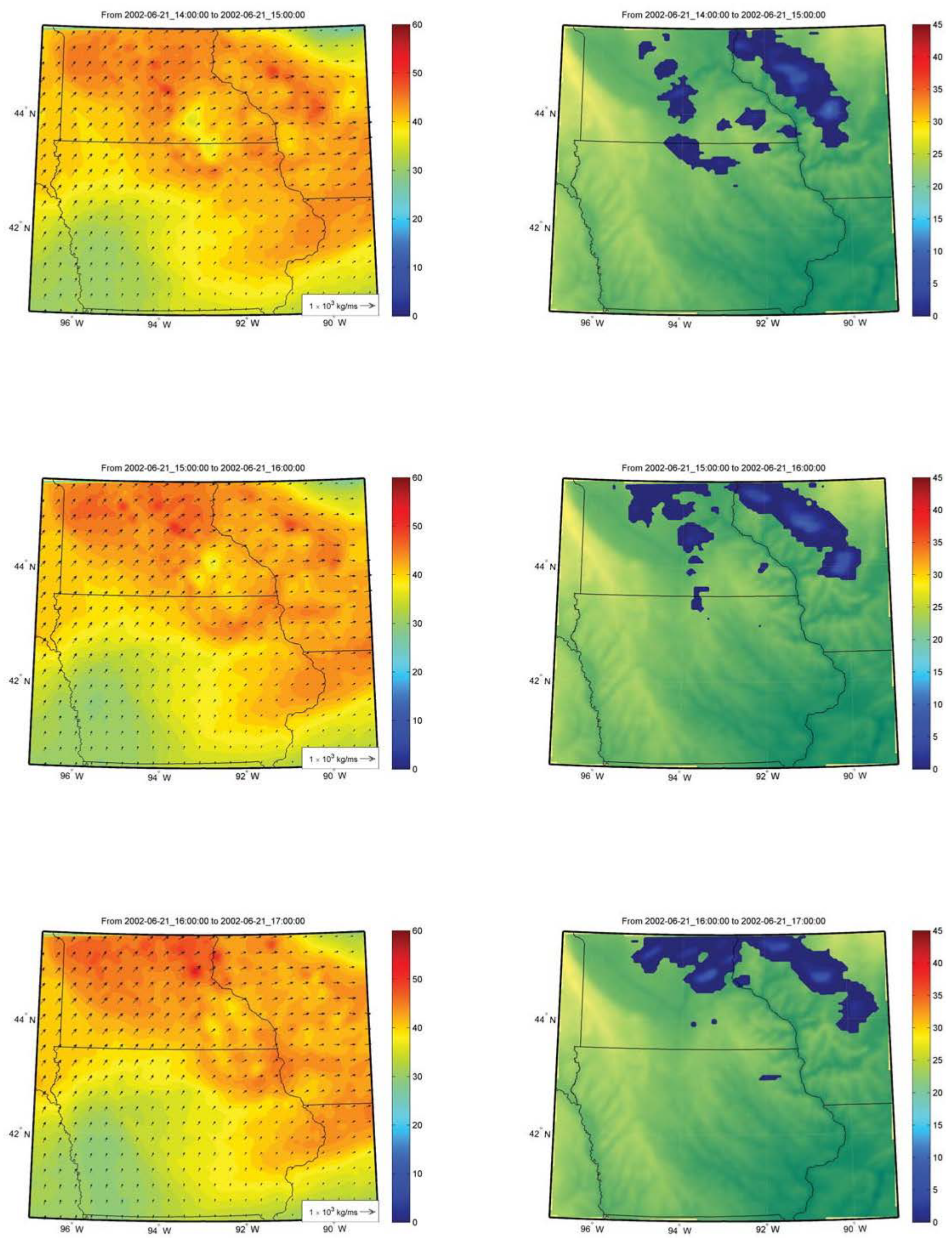

Figure B-1 Hourly Simulated Precipitable Water (Left, Colormap [mm]) and Water Vapor Flux Fields (Left, Arrows [kg m^{-1} s^{-1}]) and Precipitation Fields (Right, Colormap [mm]) for the June 22, 2002 MCS

Plots shown from 06/21/2002 at 14hr to 06/22/2002 at 19hr.

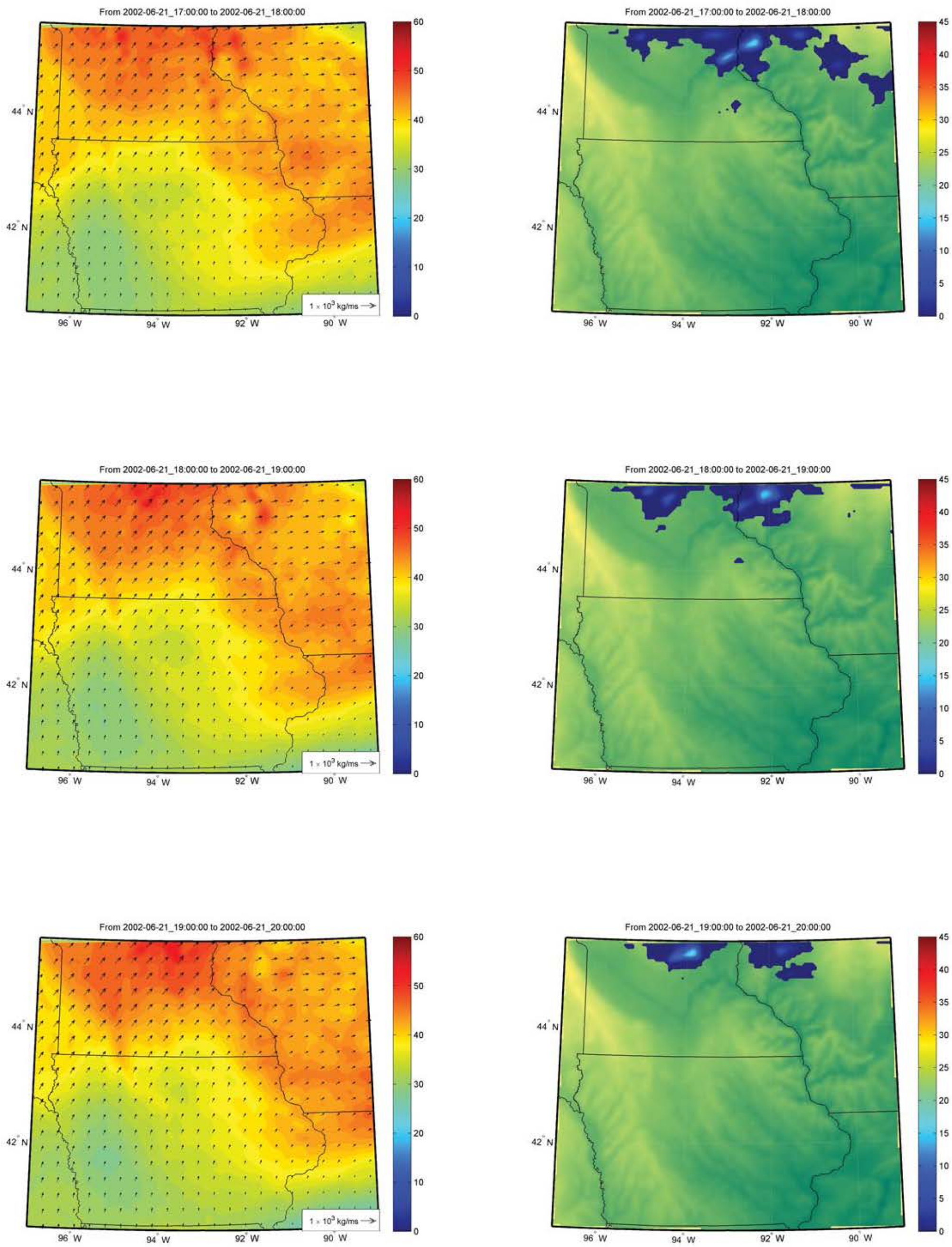

Figure B-1 Hourly Simulated Precipitable Water (Left, Colormap [mm]) and Water Vapor Flux Fields (Left, Arrows [kg m^{-1} s^{-1}]) and Precipitation Fields (Right, Colormap [mm]) for the June 22, 2002 MCS

Plots shown from 06/21/2002 at 14hr to 06/22/2002 at 19hr (Continued).

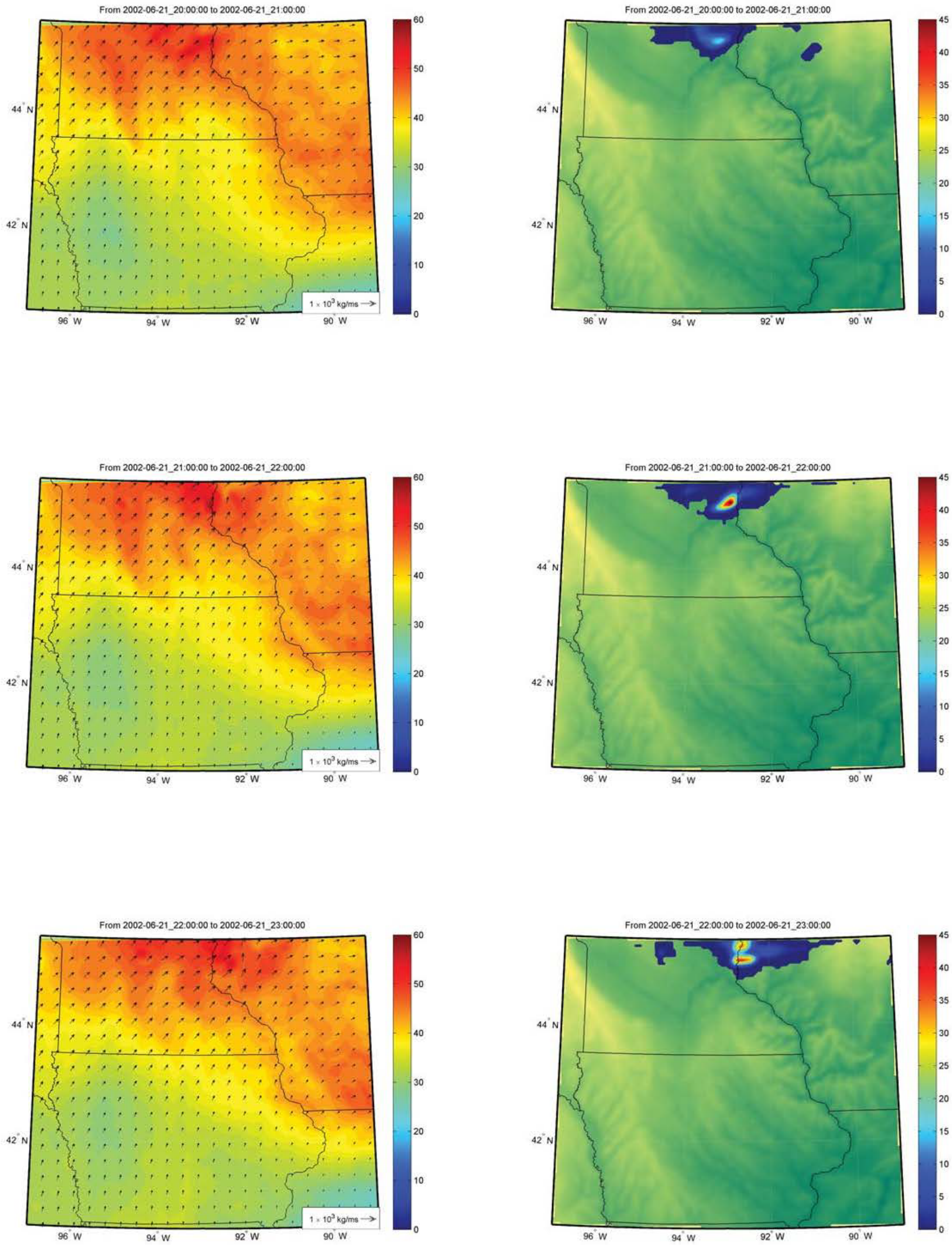

Figure B-1 **Hourly Simulated Precipitable Water (Left, Colormap [mm]) and Water Vapor Flux Fields (Left, Arrows [kg m^{-1} s^{-1}]) and Precipitation Fields (Right, Colormap [mm]) for the June 22, 2002 MCS**

Plots shown from 06/21/2002 at 14hr to 06/22/2002 at 19hr (Continued).

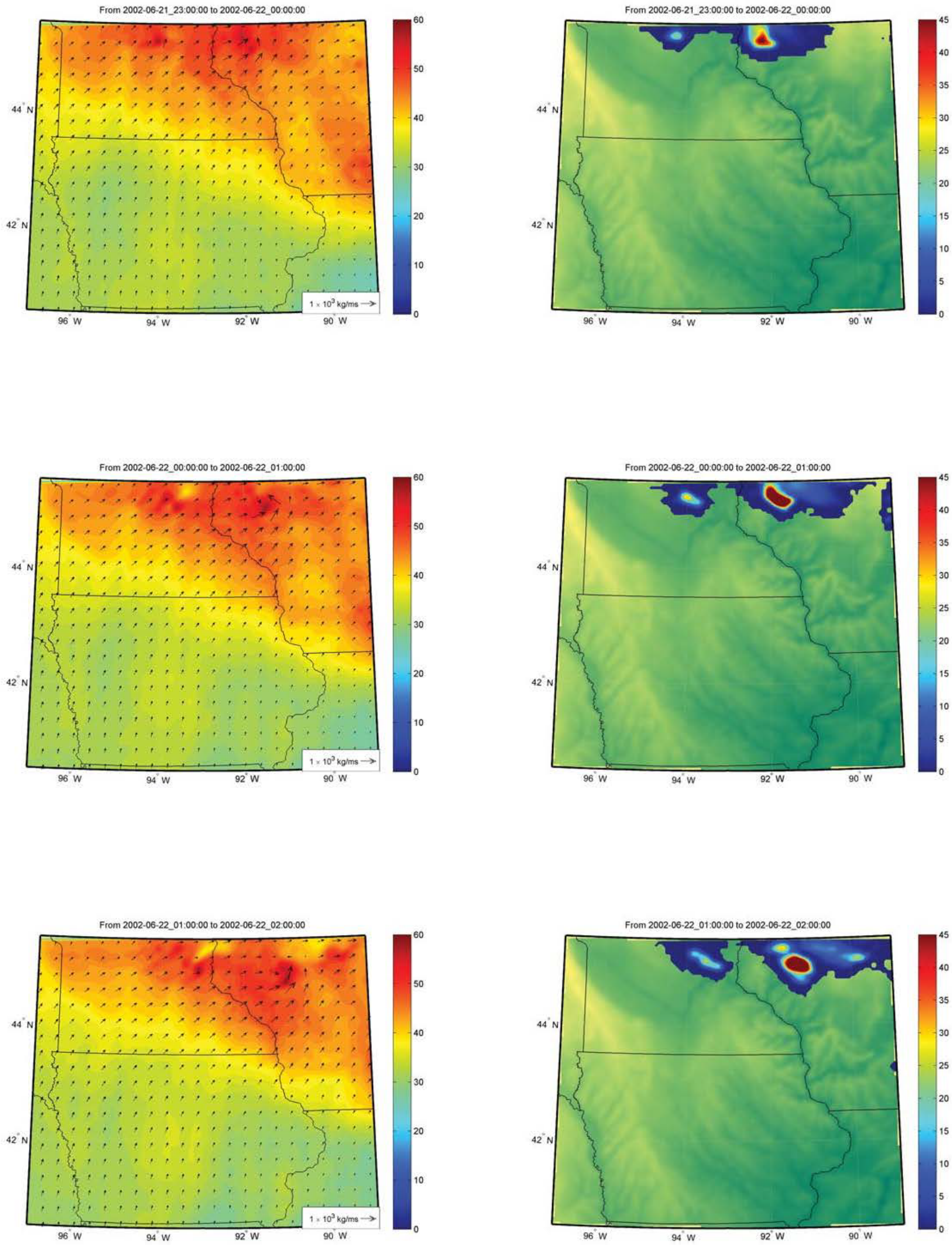

Figure B-1 **Hourly Simulated Precipitable Water (Left, Colormap [mm]) and Water Vapor Flux Fields (Left, Arrows [kg m^{-1} s^{-1}]) and Precipitation Fields (Right, Colormap [mm]) for the June 22, 2002 MCS**

Plots shown from 06/21/2002 at 14hr to 06/22/2002 at 19hr (Continued).

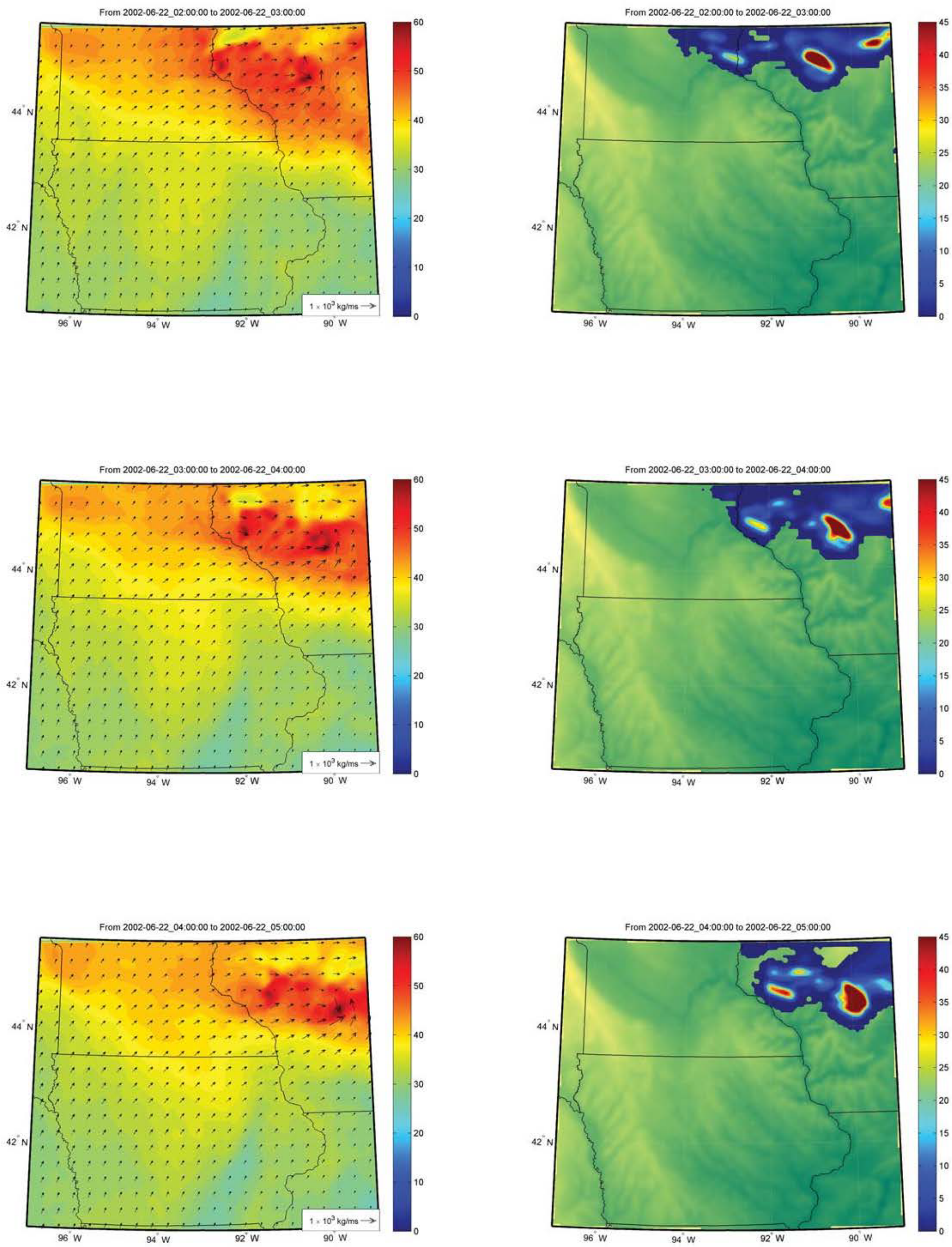

Figure B-1 Hourly Simulated Precipitable Water (Left, Colormap [mm]) and Water Vapor Flux Fields (Left, Arrows [kg m^{-1} s^{-1}]) and Precipitation Fields (Right, Colormap [mm]) for the June 22, 2002 MCS

Plots shown from 06/21/2002 at 14hr to 06/22/2002 at 19hr (Continued).

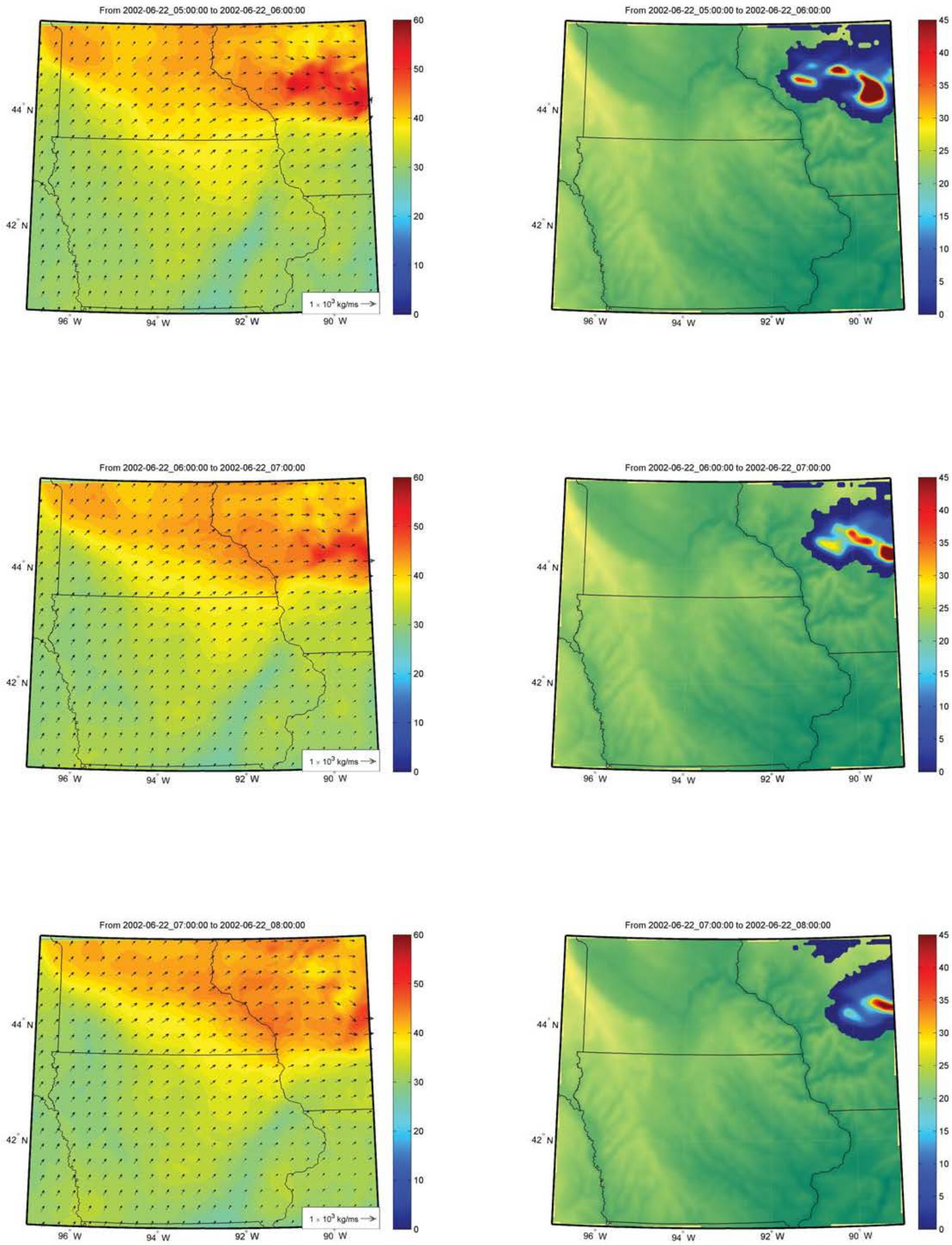

Figure B-1 Hourly Simulated Precipitable Water (Left, Colormap [mm]) and Water Vapor Flux Fields (Left, Arrows [kg m^{-1} s^{-1}]) and Precipitation Fields (Right, Colormap [mm]) for the June 22, 2002 MCS

Plots shown from 06/21/2002 at 14hr to 06/22/2002 at 19hr (Continued).

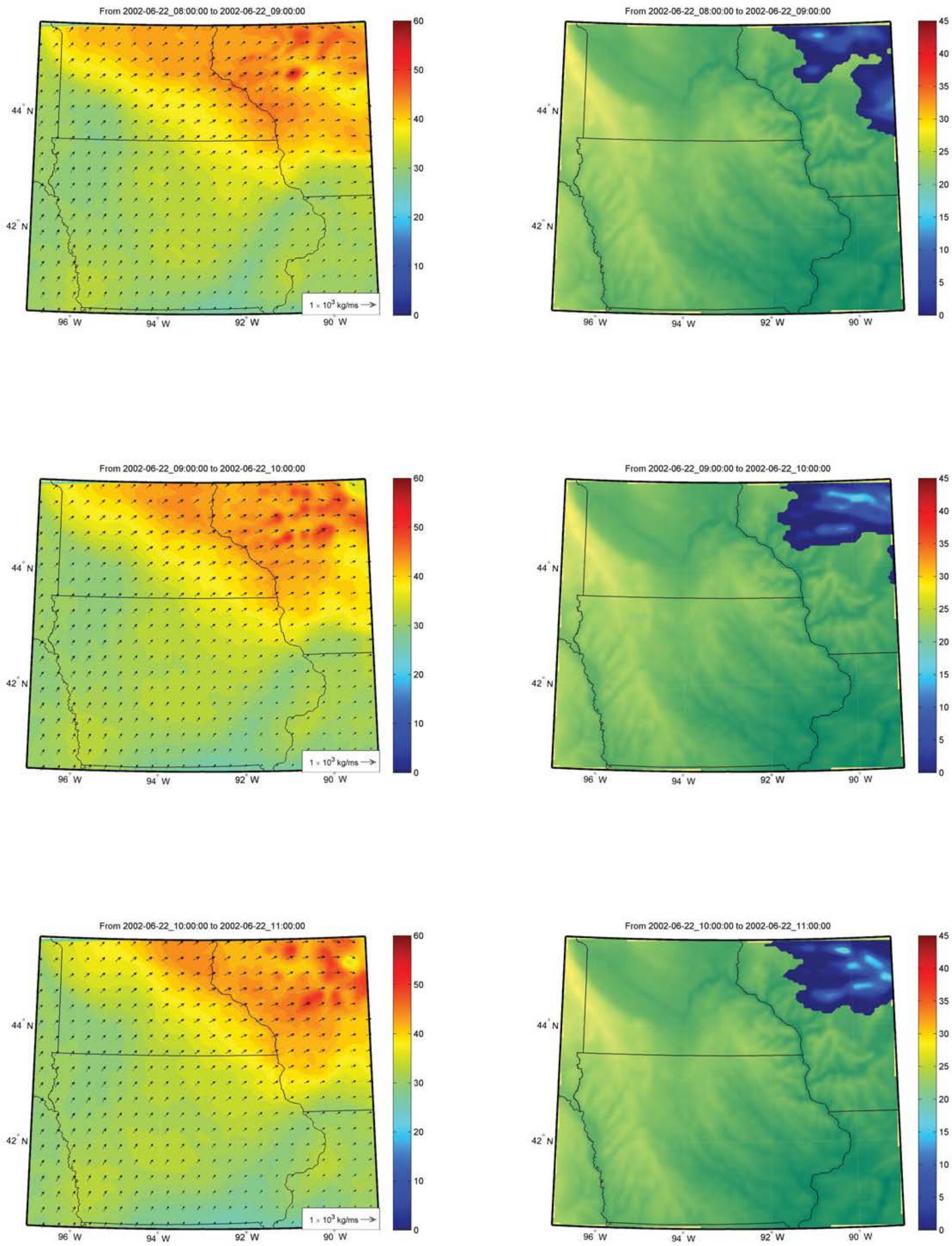

Figure B-1 Hourly Simulated Precipitable Water (Left, Colormap [mm]) and Water Vapor Flux Fields (Left, Arrows [kg m^{-1} s^{-1}]) and Precipitation Fields (Right, Colormap [mm]) for the June 22, 2002 MCS

Plots shown from 06/21/2002 at 14hr to 06/22/2002 at 19hr (Continued).

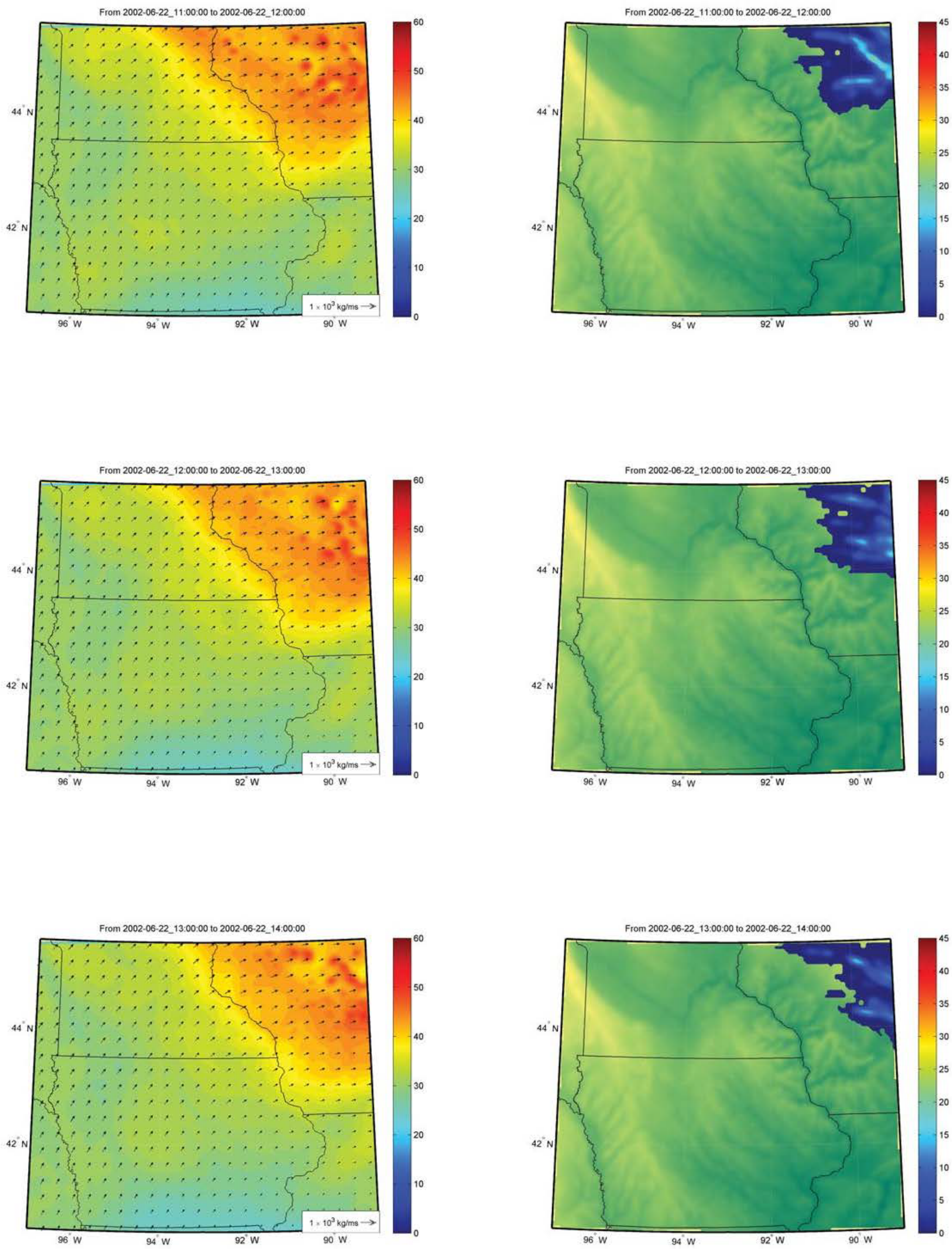

Figure B-1 **Hourly Simulated Precipitable Water (Left, Colormap [mm]) and Water Vapor Flux Fields (Left, Arrows [kg m^{-1} s^{-1}]) and Precipitation Fields (Right, Colormap [mm]) for the June 22, 2002 MCS**

Plots shown from 06/21/2002 at 14hr to 06/22/2002 at 19hr (Continued).

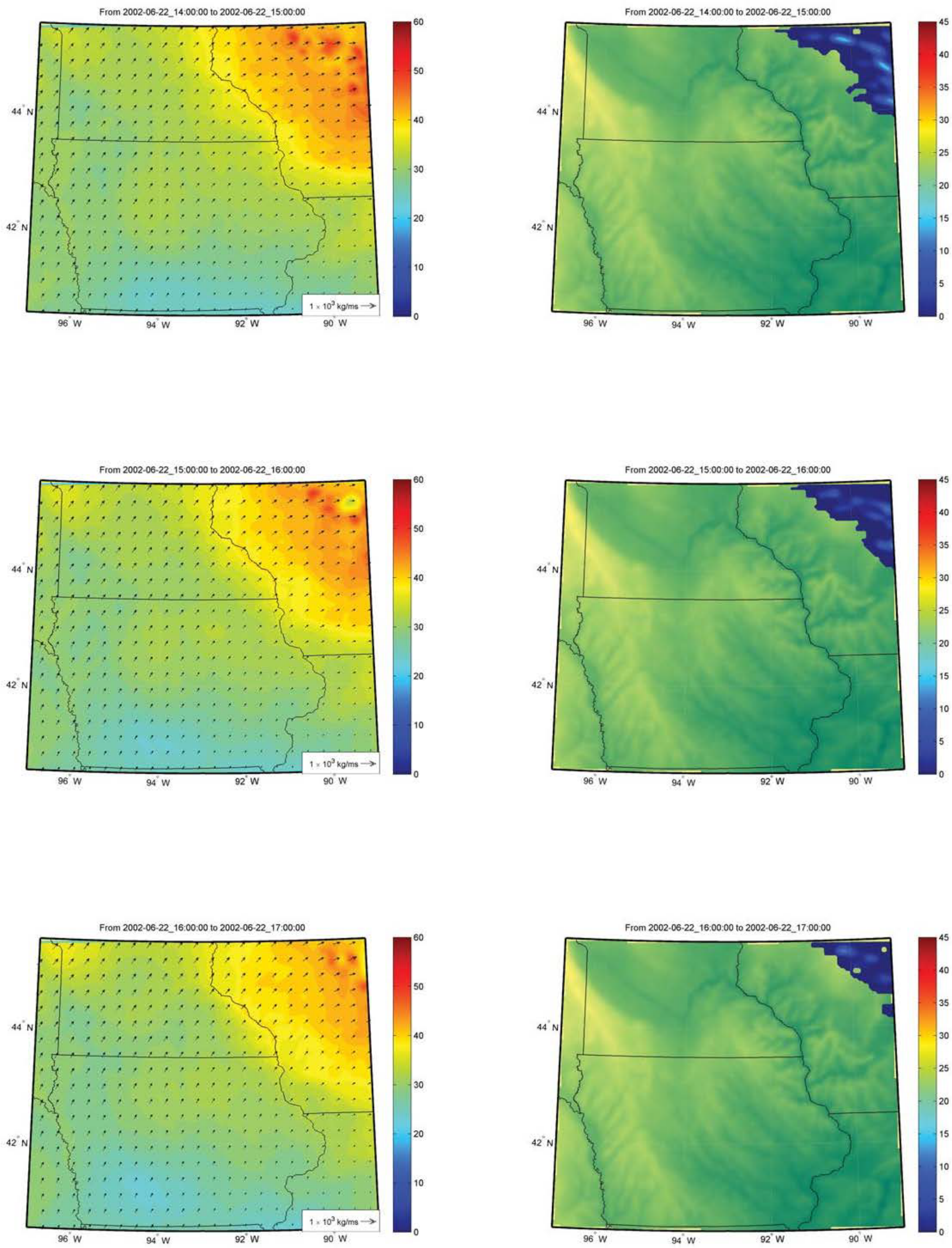

Figure B-1 Hourly Simulated Precipitable Water (Left, Colormap [mm]) and Water Vapor Flux Fields (Left, Arrows [kg m^{-1} s^{-1}]) and Precipitation Fields (Right, Colormap [mm]) for the June 22, 2002 MCS

Plots shown from 06/21/2002 at 14hr to 06/22/2002 at 19hr (Continued).

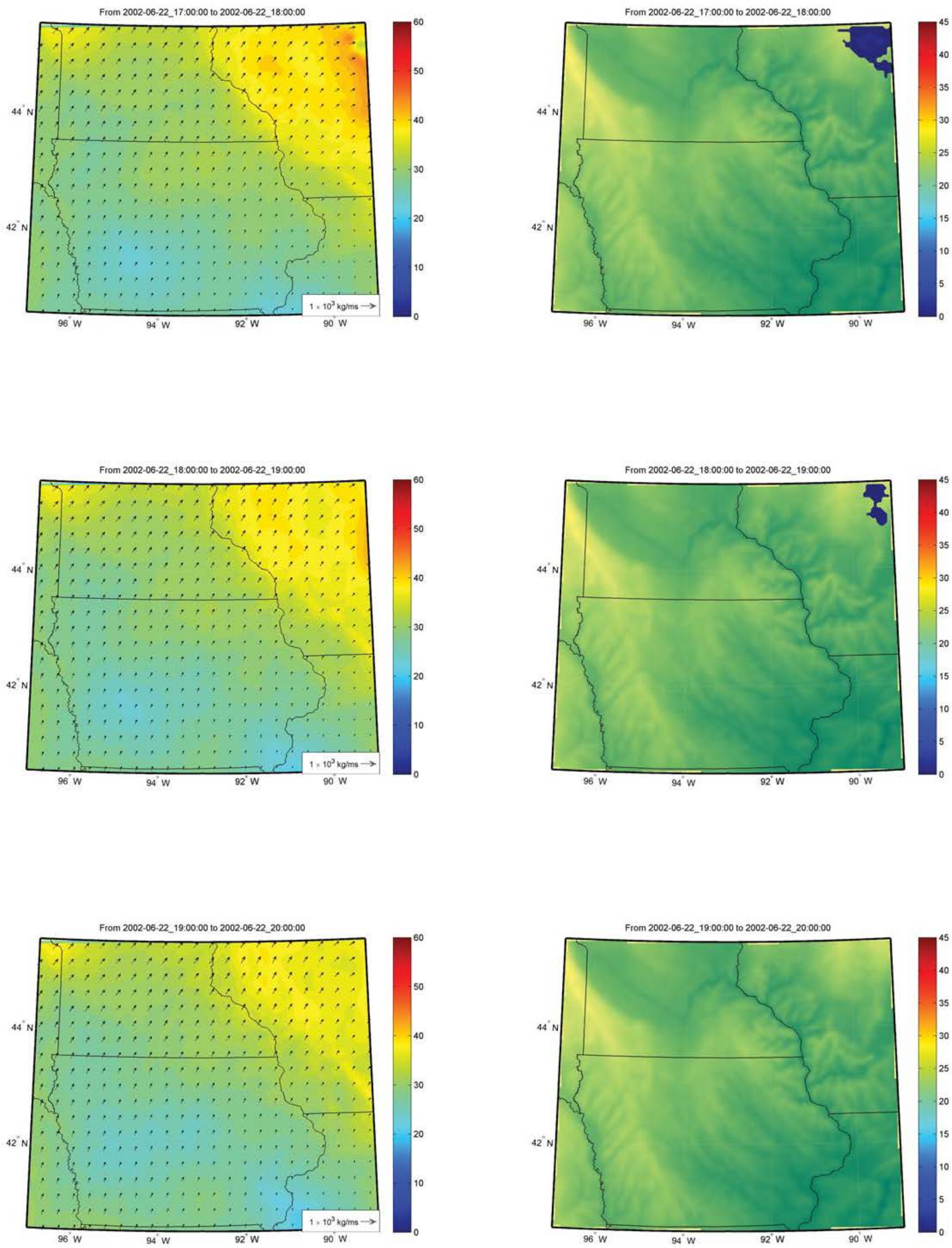

Figure B-1 Hourly Simulated Precipitable Water (Left, Colormap [mm]) and Water Vapor Flux Fields (Left, Arrows [kg m^{-1} s^{-1}]) and Precipitation Fields (Right, Colormap [mm]) for the June 22, 2002 MCS

Plots shown from 06/21/2002 at 14hr to 06/22/2002 at 19hr (Continued).

B.1.2 August 22, 2002 MCS

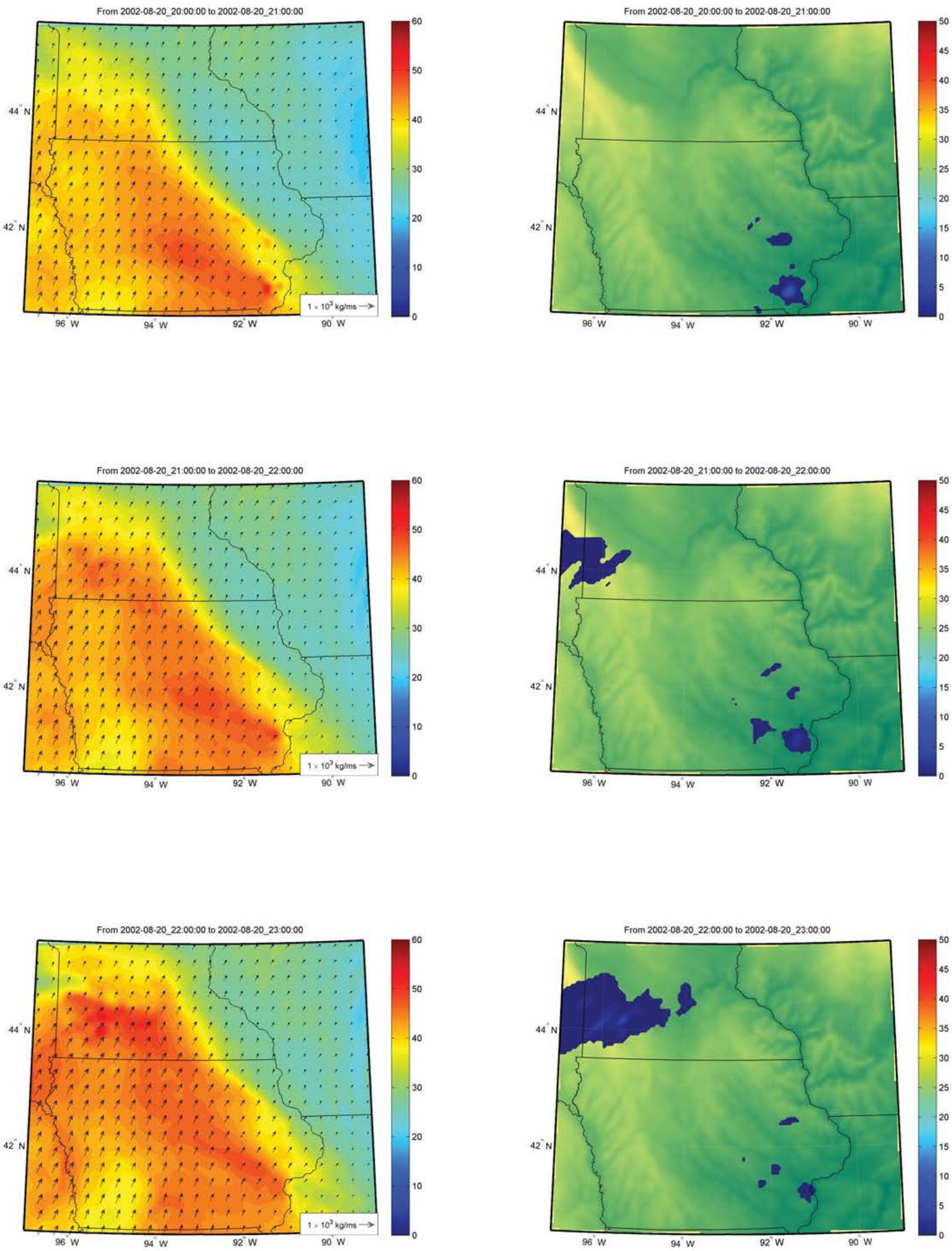

Figure B-2 **Hourly simulated Precipitable Water (Left, Colormap [mm]) and Water Vapor Flux Fields (Left, Arrows [kg m^{-1} s^{-1}]) and Precipitation Fields (Right, Colormap [mm]) for the August 22, 2002 MCS**

Plots shown from 08/20/2002 at 20hr to 08/22/2002 at 16hr.

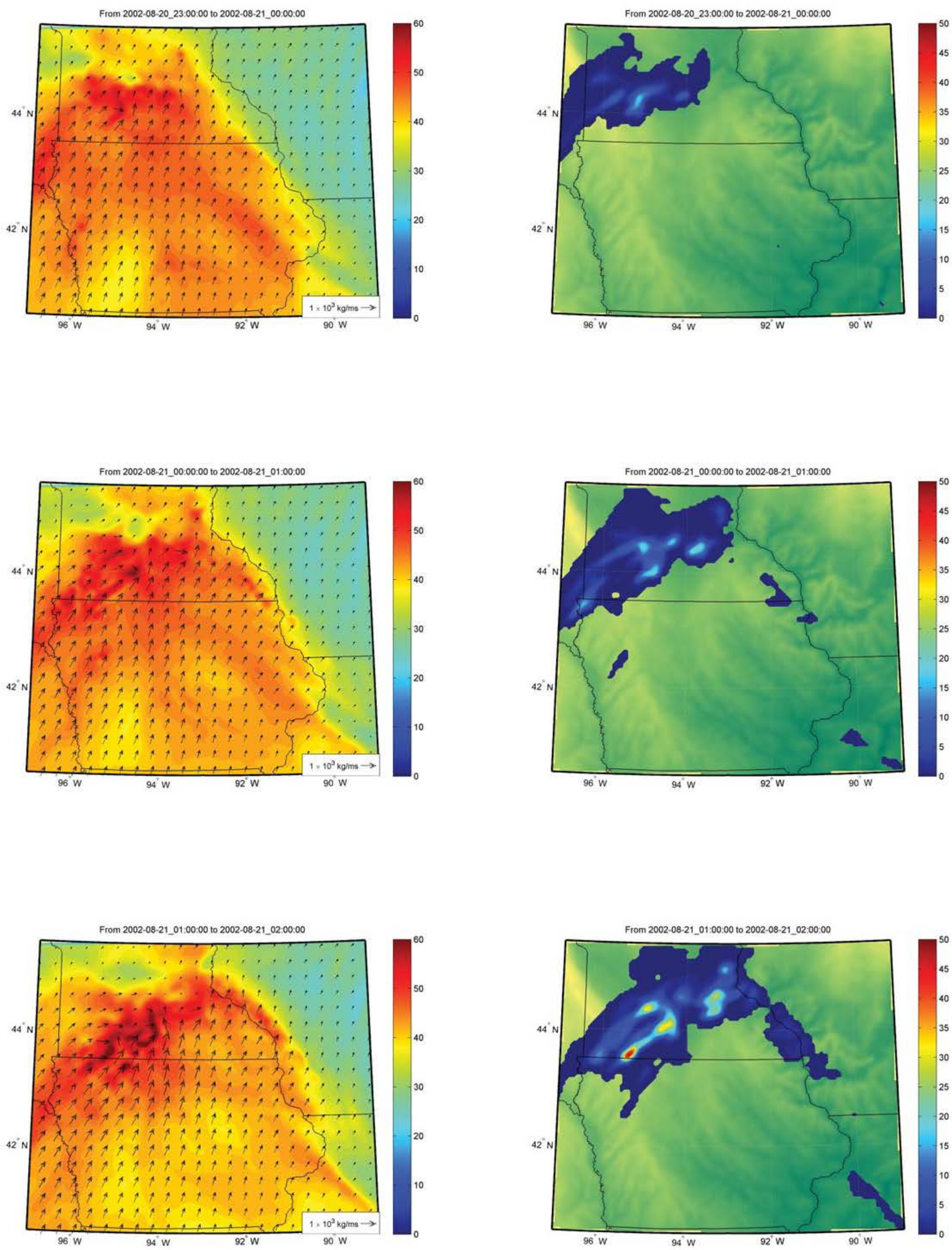

Figure B-2 **Hourly simulated Precipitable Water (Left, Colormap [mm]) and Water Vapor Flux Fields (Left, Arrows [kg m^{-1} s^{-1}]) and Precipitation Fields (Right, Colormap [mm]) for the August 22, 2002 MCS**

Plots shown from 08/20/2002 at 20hr to 08/22/2002 at 16hr (Continued).

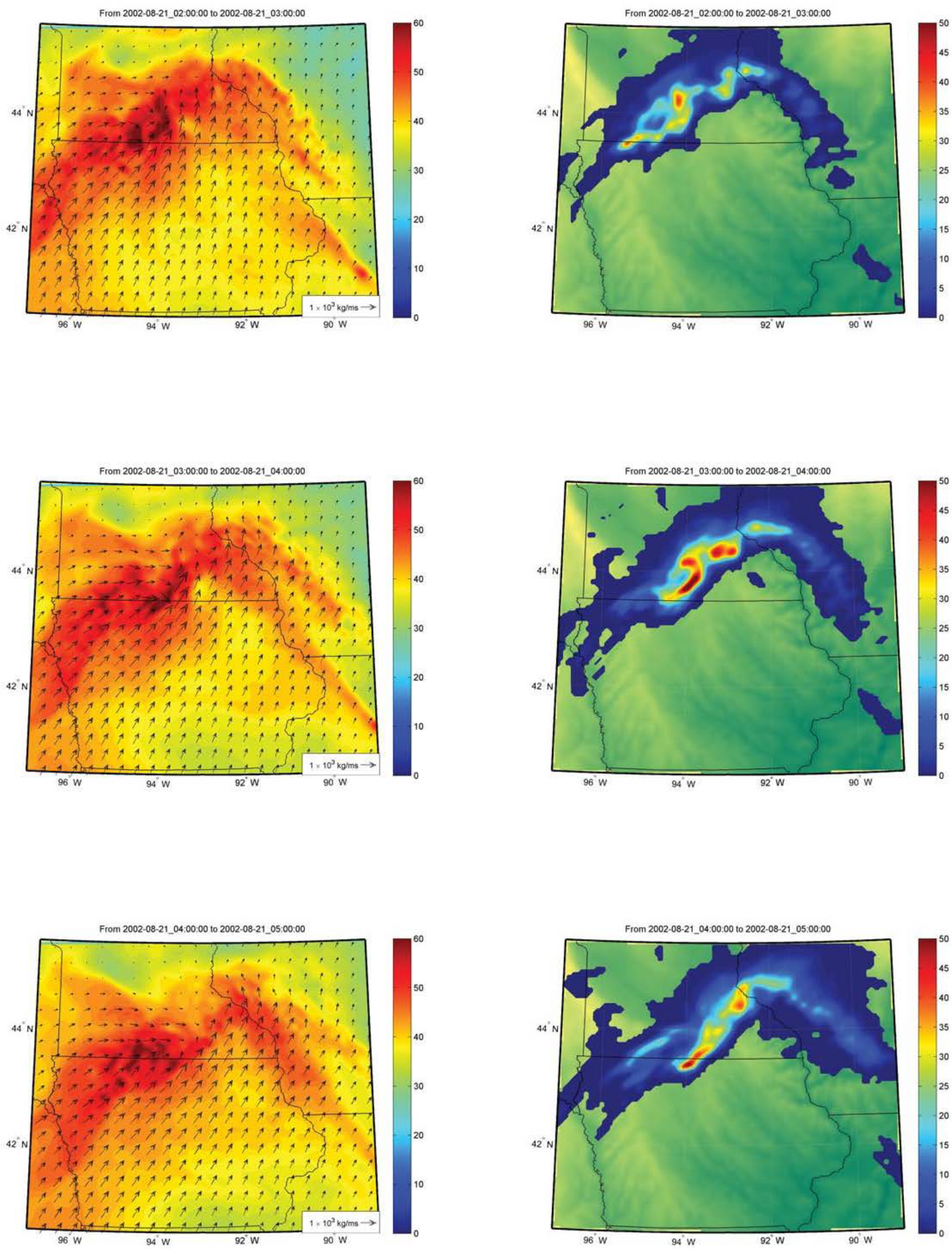

Figure B-2 **Hourly simulated Precipitable Water (Left, Colormap [mm]) and Water Vapor Flux Fields (Left, Arrows [kg m^{-1} s^{-1}]) and Precipitation Fields (Right, Colormap [mm]) for the August 22, 2002 MCS**

Plots shown from 08/20/2002 at 20hr to 08/22/2002 at 16hr (Continued).

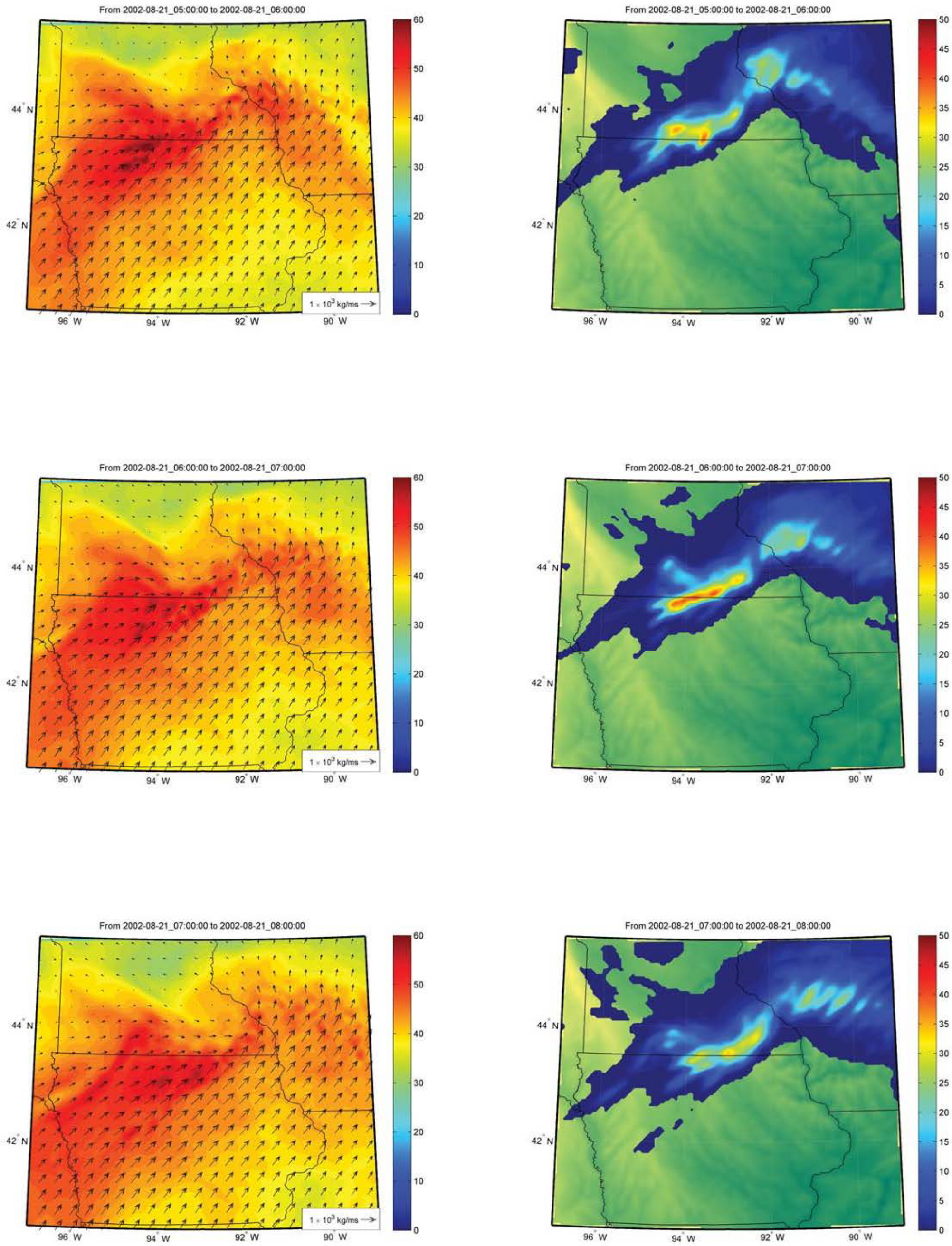

Figure B-2 Hourly simulated Precipitable Water (Left, Colormap [mm]) and Water Vapor Flux Fields (Left, Arrows [kg m^{-1} s^{-1}]) and Precipitation Fields (Right, Colormap [mm]) for the August 22, 2002 MCS

Plots shown from 08/20/2002 at 20hr to 08/22/2002 at 16hr (Continued).

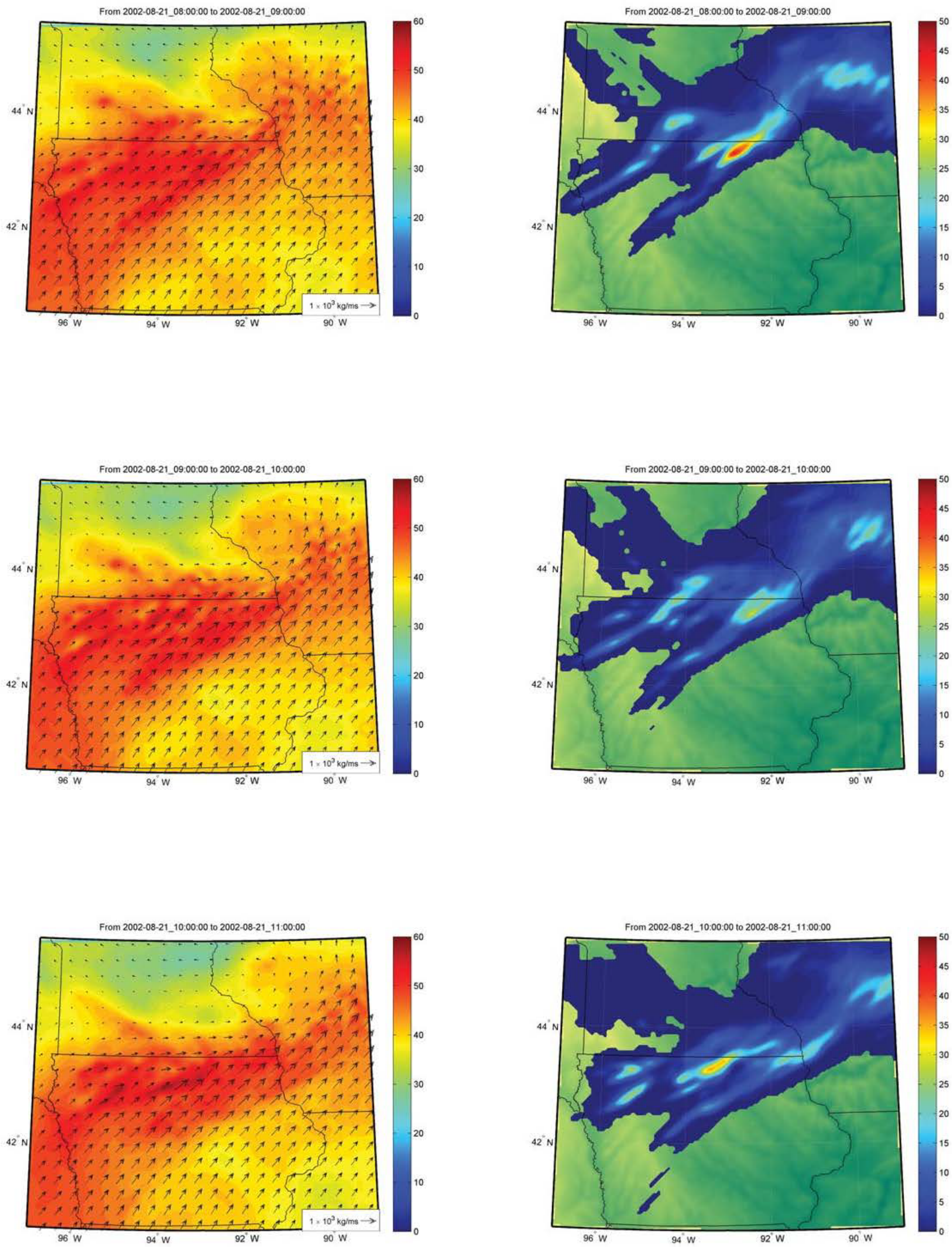

Figure B-2 **Hourly simulated Precipitable Water (Left, Colormap [mm]) and Water Vapor Flux Fields (Left, Arrows [kg m^{-1} s^{-1}]) and Precipitation Fields (Right, Colormap [mm]) for the August 22, 2002 MCS**

Plots shown from 08/20/2002 at 20hr to 08/22/2002 at 16hr (Continued).

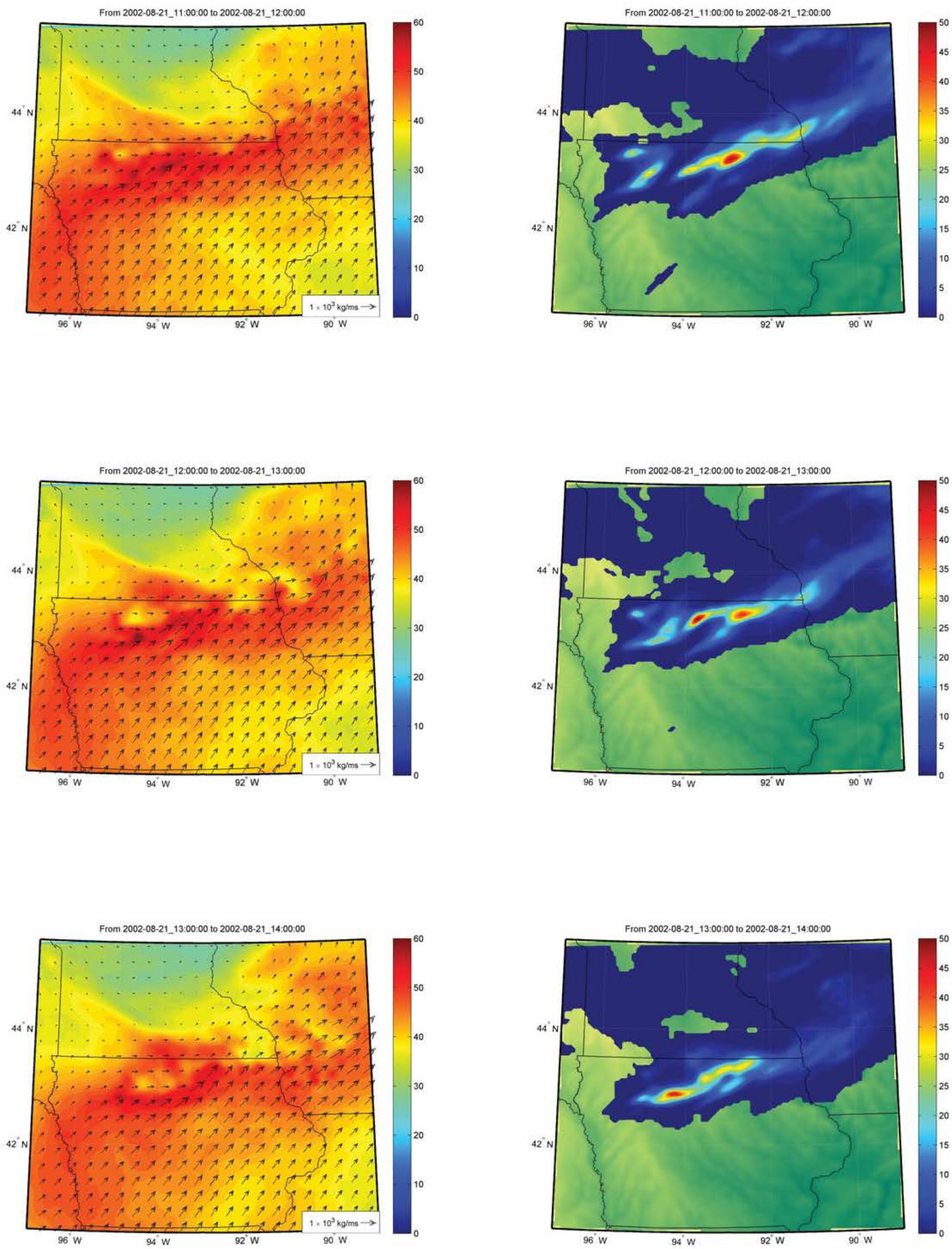

Figure B-2 **Hourly simulated Precipitable Water (Left, Colormap [mm]) and Water Vapor Flux Fields (Left, Arrows [kg m^{-1} s^{-1}]) and Precipitation Fields (Right, Colormap [mm]) for the August 22, 2002 MCS**

Plots shown from 08/20/2002 at 20hr to 08/22/2002 at 16hr (Continued).

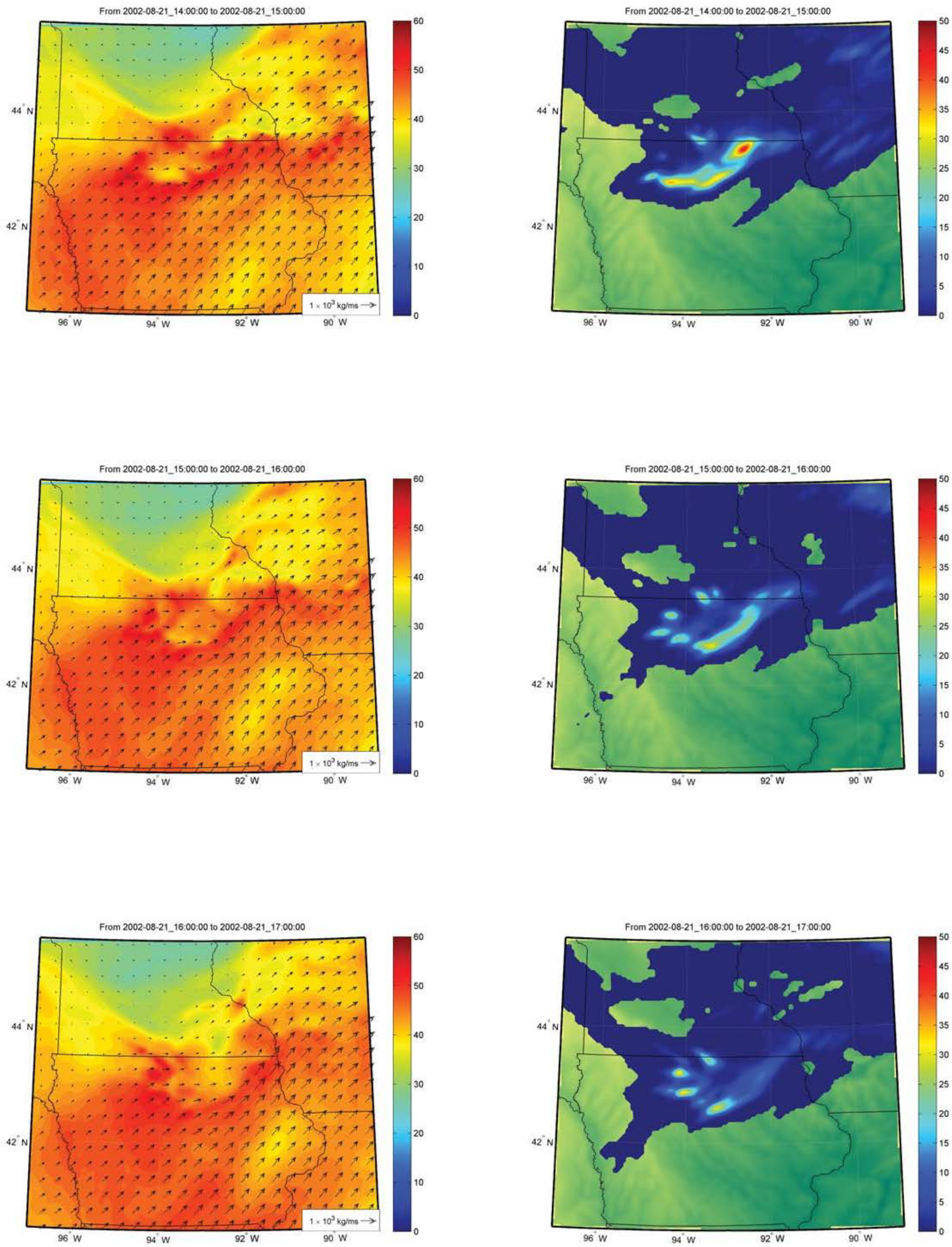

Figure B-2 **Hourly simulated Precipitable Water (Left, Colormap [mm]) and Water Vapor Flux Fields (Left, Arrows [kg m^{-1} s^{-1}]) and Precipitation Fields (Right, Colormap [mm]) for the August 22, 2002 MCS**

Plots shown from 08/20/2002 at 20hr to 08/22/2002 at 16hr (Continued).

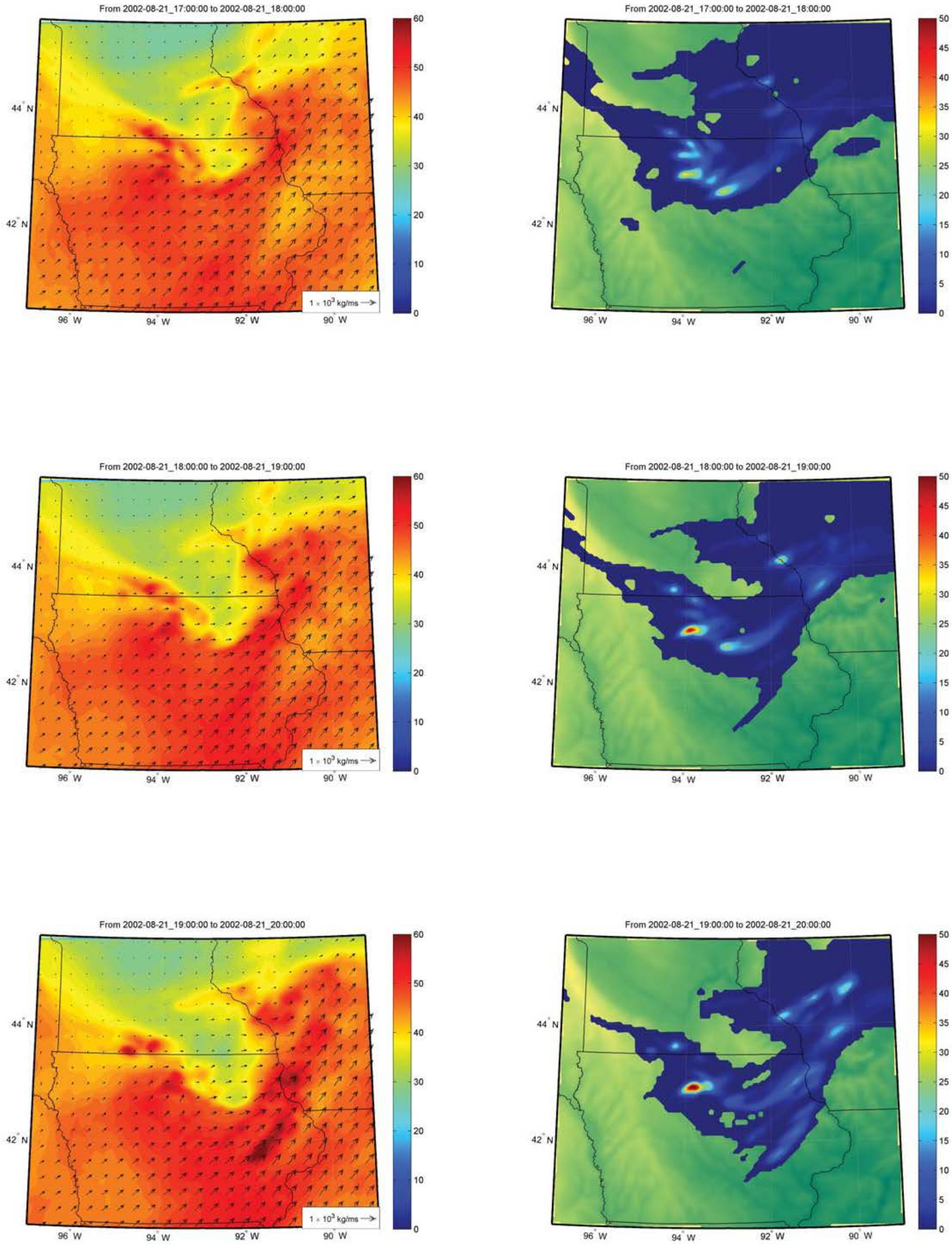

Figure B-2 Hourly simulated Precipitable Water (Left, Colormap [mm]) and Water Vapor Flux Fields (Left, Arrows [kg m^{-1} s^{-1}]) and Precipitation Fields (Right, Colormap [mm]) for the August 22, 2002 MCS

Plots shown from 08/20/2002 at 20hr to 08/22/2002 at 16hr (Continued).

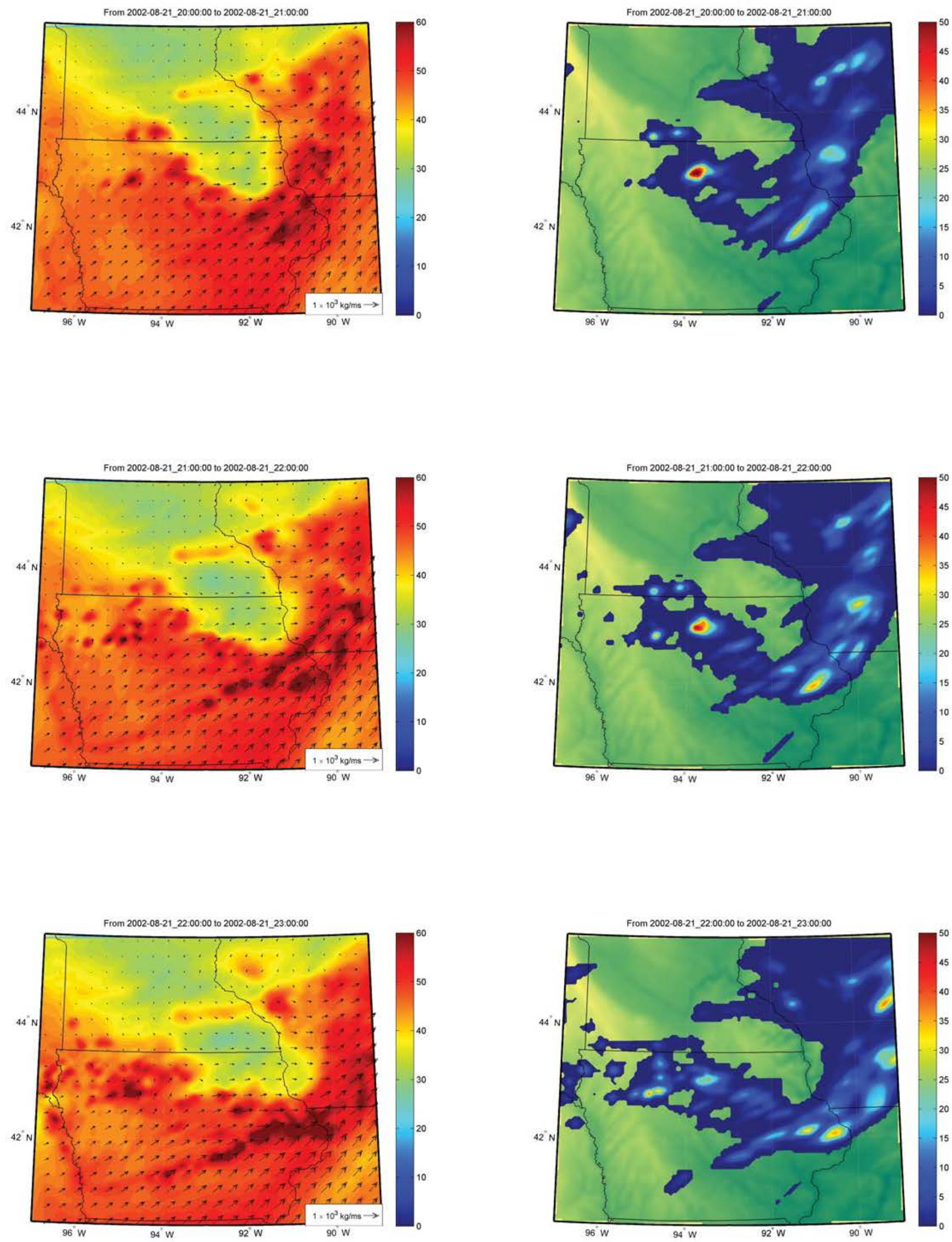

Figure B-2 Hourly simulated Precipitable Water (Left, Colormap [mm]) and Water Vapor Flux Fields (Left, Arrows [kg m^{-1} s^{-1}]) and Precipitation Fields (Right, Colormap [mm]) for the August 22, 2002 MCS

Plots shown from 08/20/2002 at 20hr to 08/22/2002 at 16hr (Continued).

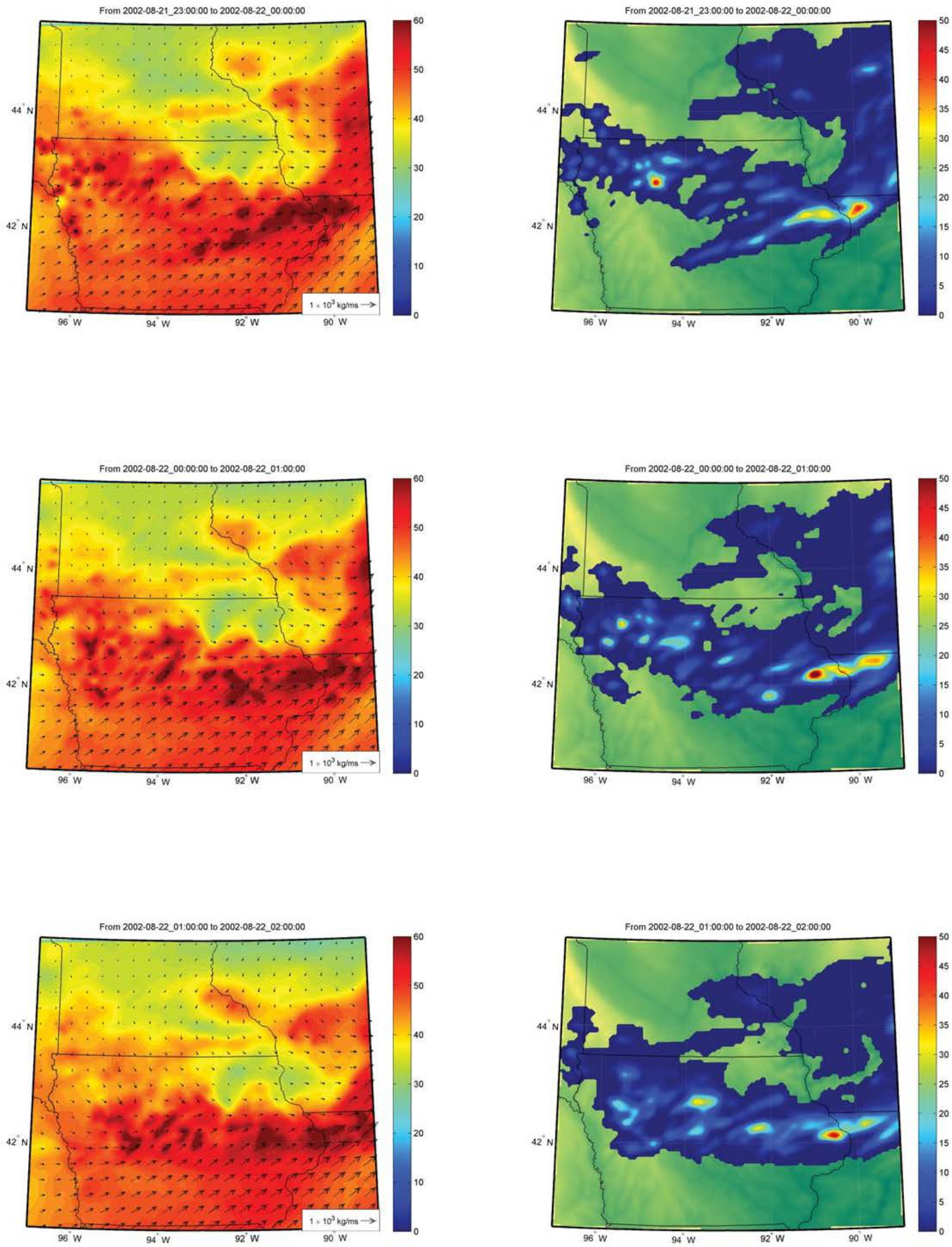

Figure B-2 Hourly simulated Precipitable Water (Left, Colormap [mm]) and Water Vapor Flux Fields (Left, Arrows [kg m^{-1} s^{-1}]) and Precipitation Fields (Right, Colormap [mm]) for the August 22, 2002 MCS

Plots shown from 08/20/2002 at 20hr to 08/22/2002 at 16hr (Continued).

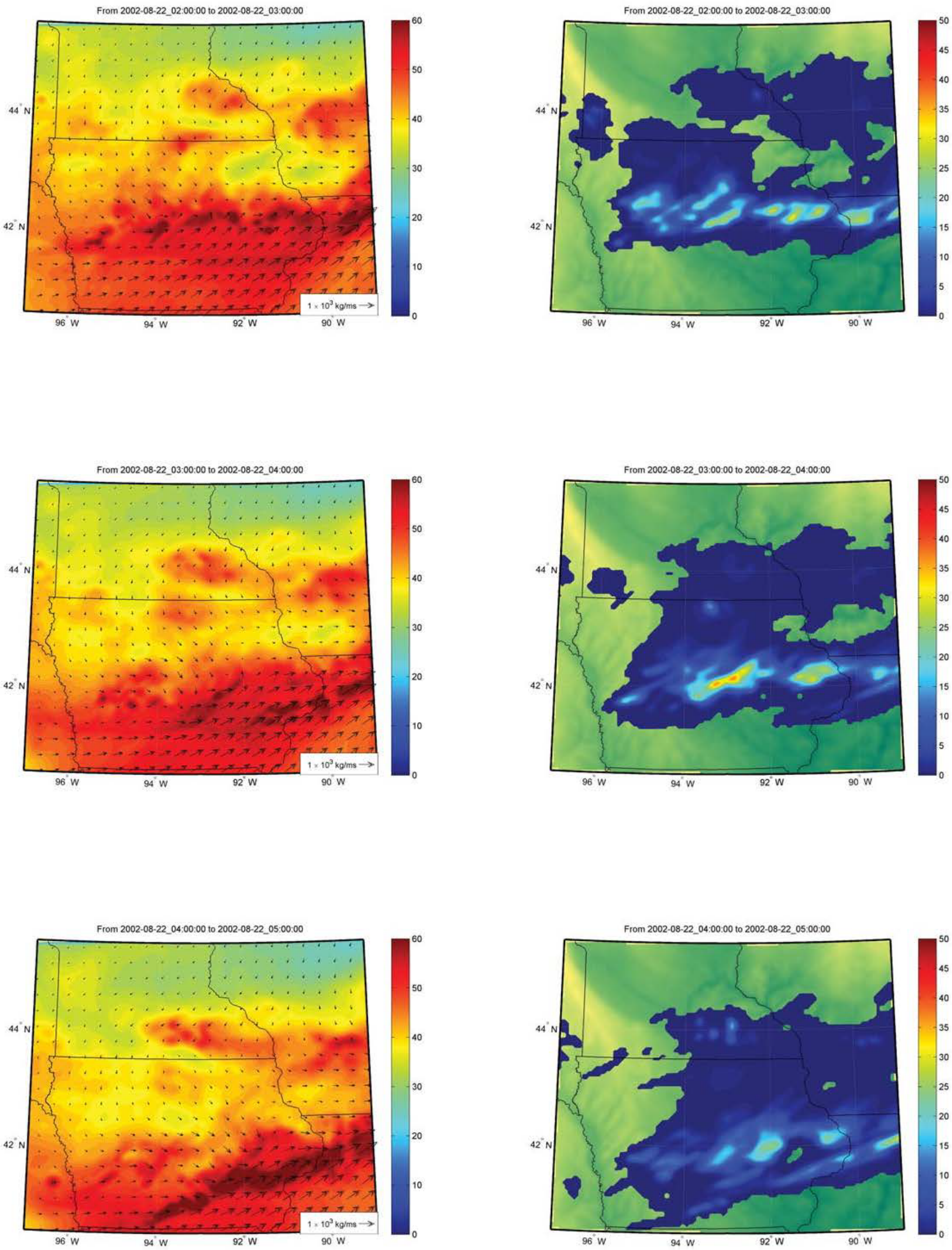

Figure B-2 **Hourly simulated Precipitable Water (Left, Colormap [mm]) and Water Vapor Flux Fields (Left, Arrows [kg m^{-1} s^{-1}]) and Precipitation Fields (Right, Colormap [mm]) for the August 22, 2002 MCS**

Plots shown from 08/20/2002 at 20hr to 08/22/2002 at 16hr (Continued).

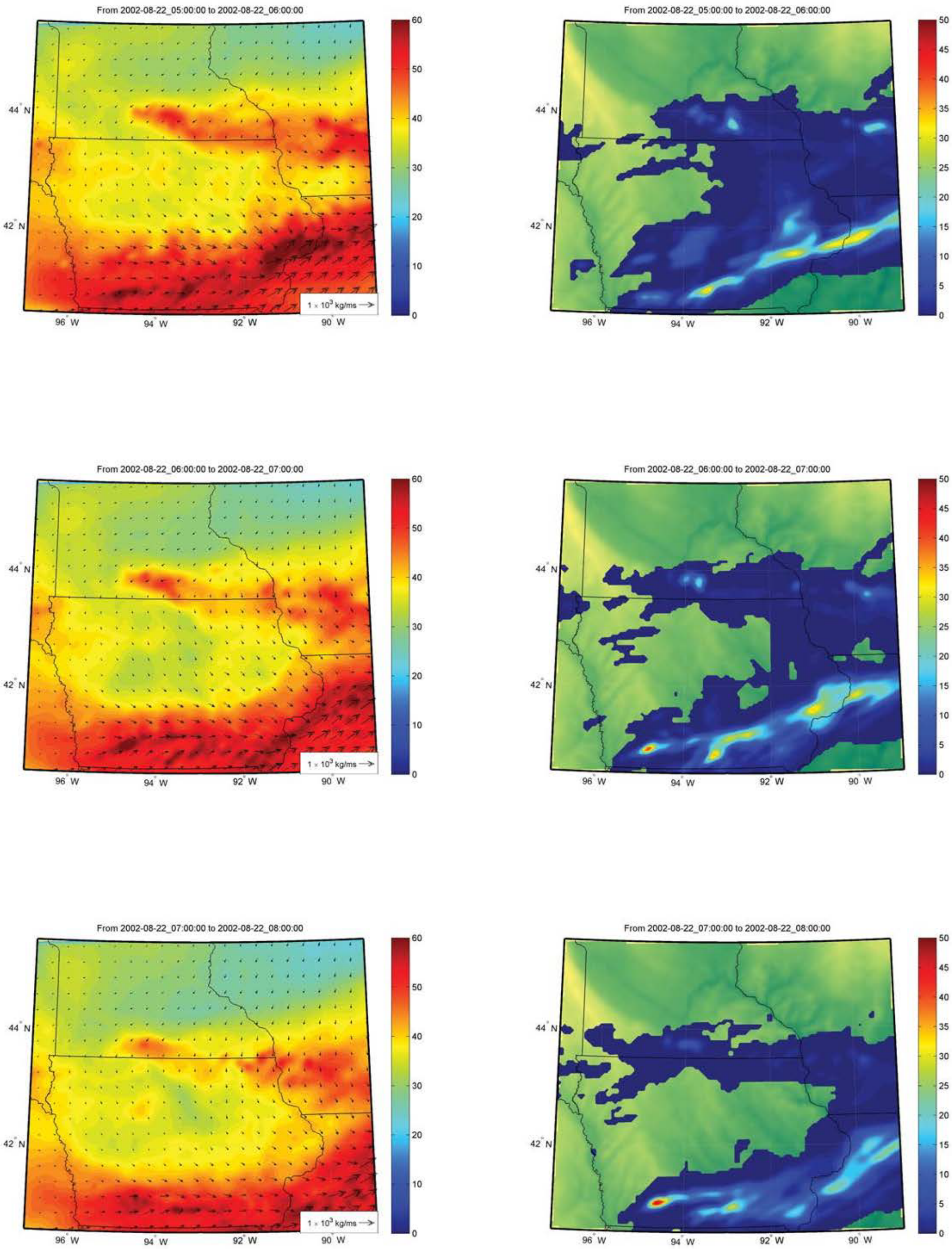

Figure B-2 **Hourly simulated Precipitable Water (Left, Colormap [mm]) and Water Vapor Flux Fields (Left, Arrows [kg m^{-1} s^{-1}]) and Precipitation Fields (Right, Colormap [mm]) for the August 22, 2002 MCS**

Plots shown from 08/20/2002 at 20hr to 08/22/2002 at 16hr (Continued).

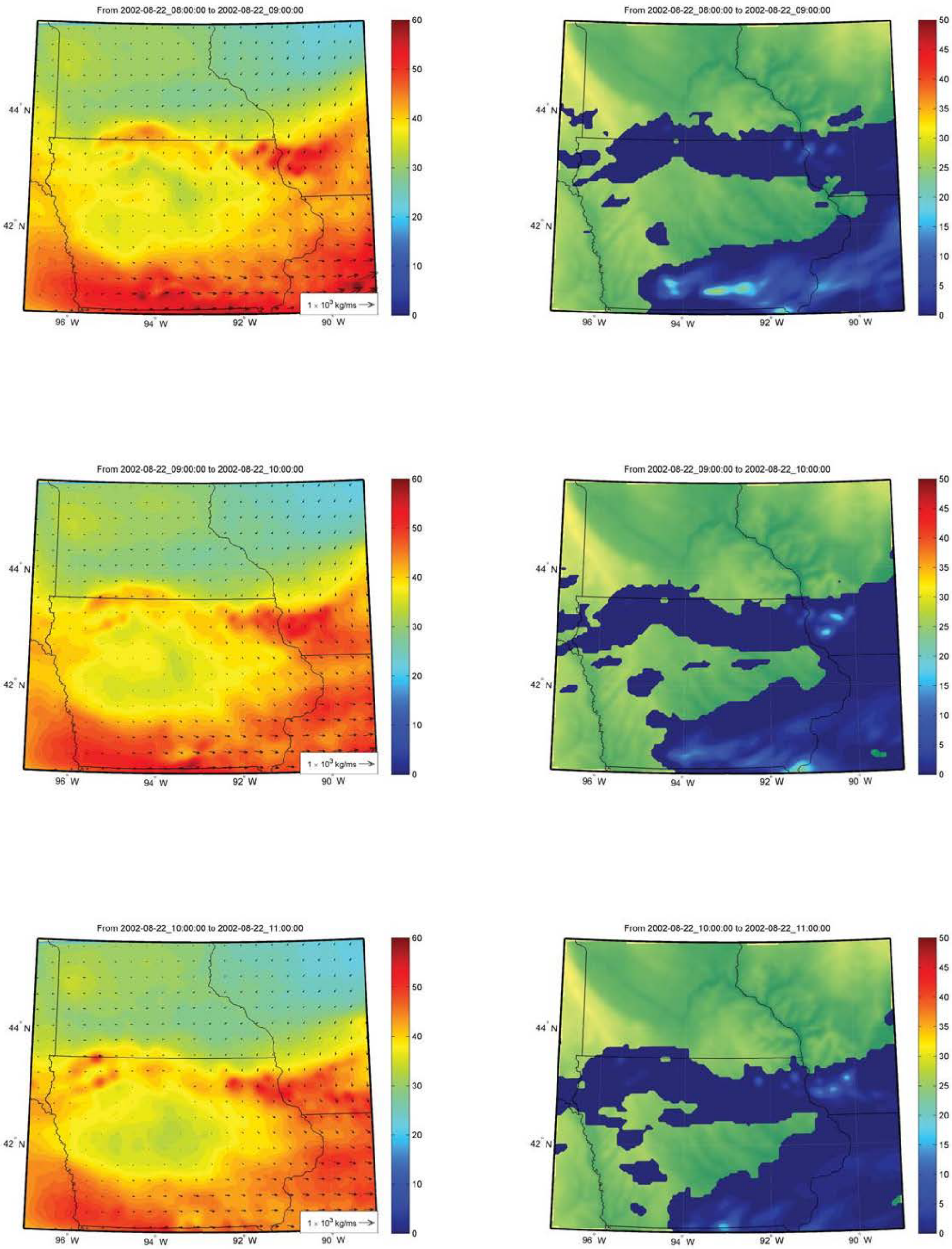

Figure B-2 Hourly simulated Precipitable Water (Left, Colormap [mm]) and Water Vapor Flux Fields (Left, Arrows [kg m^{-1} s^{-1}]) and Precipitation Fields (Right, Colormap [mm]) for the August 22, 2002 MCS

Plots shown from 08/20/2002 at 20hr to 08/22/2002 at 16hr (Continued).

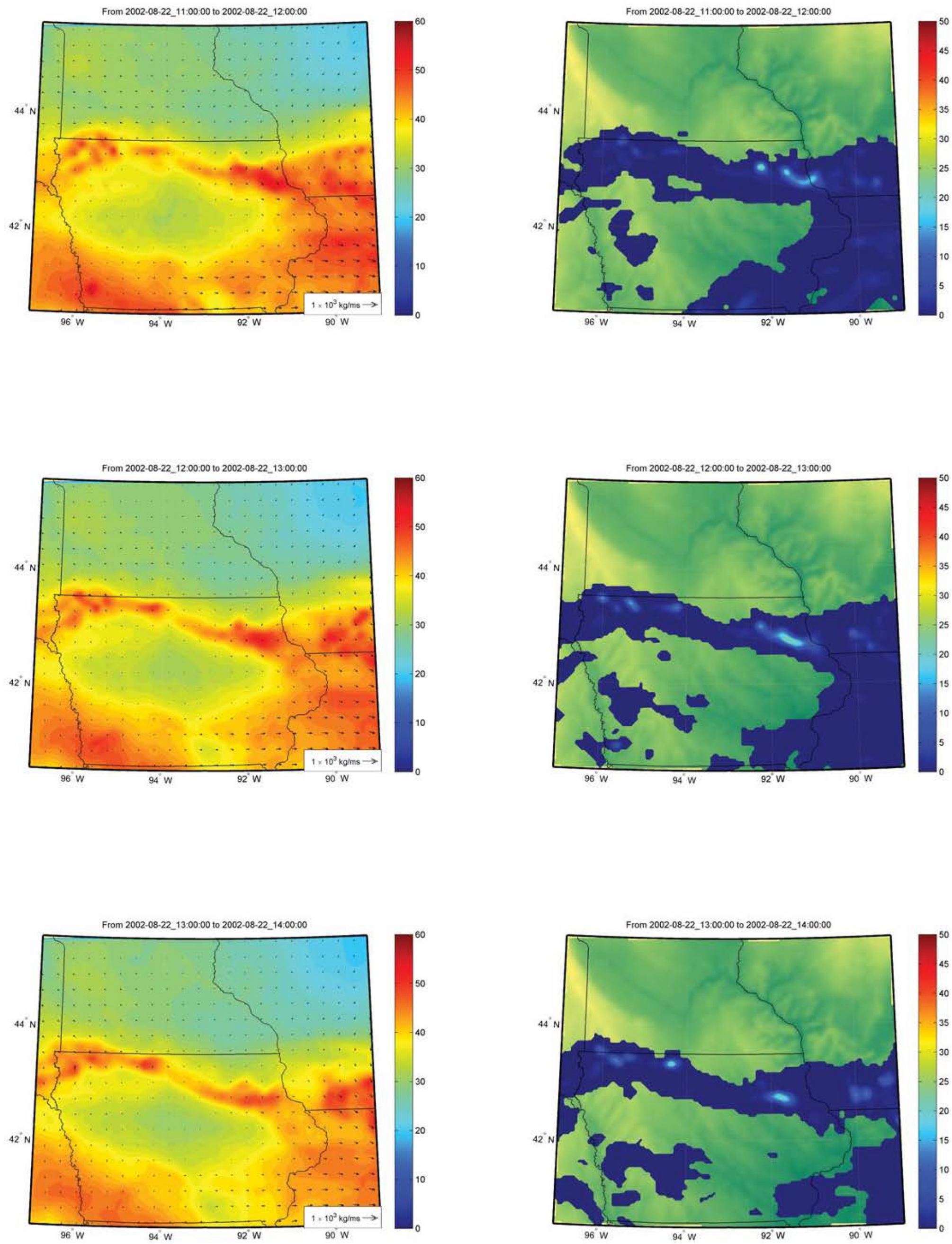

Figure B-2 Hourly simulated Precipitable Water (Left, Colormap [mm]) and Water Vapor Flux Fields (Left, Arrows [kg m^{-1} s^{-1}]) and Precipitation Fields (Right, Colormap [mm]) for the August 22, 2002 MCS

Plots shown from 08/20/2002 at 20hr to 08/22/2002 at 16hr (Continued).

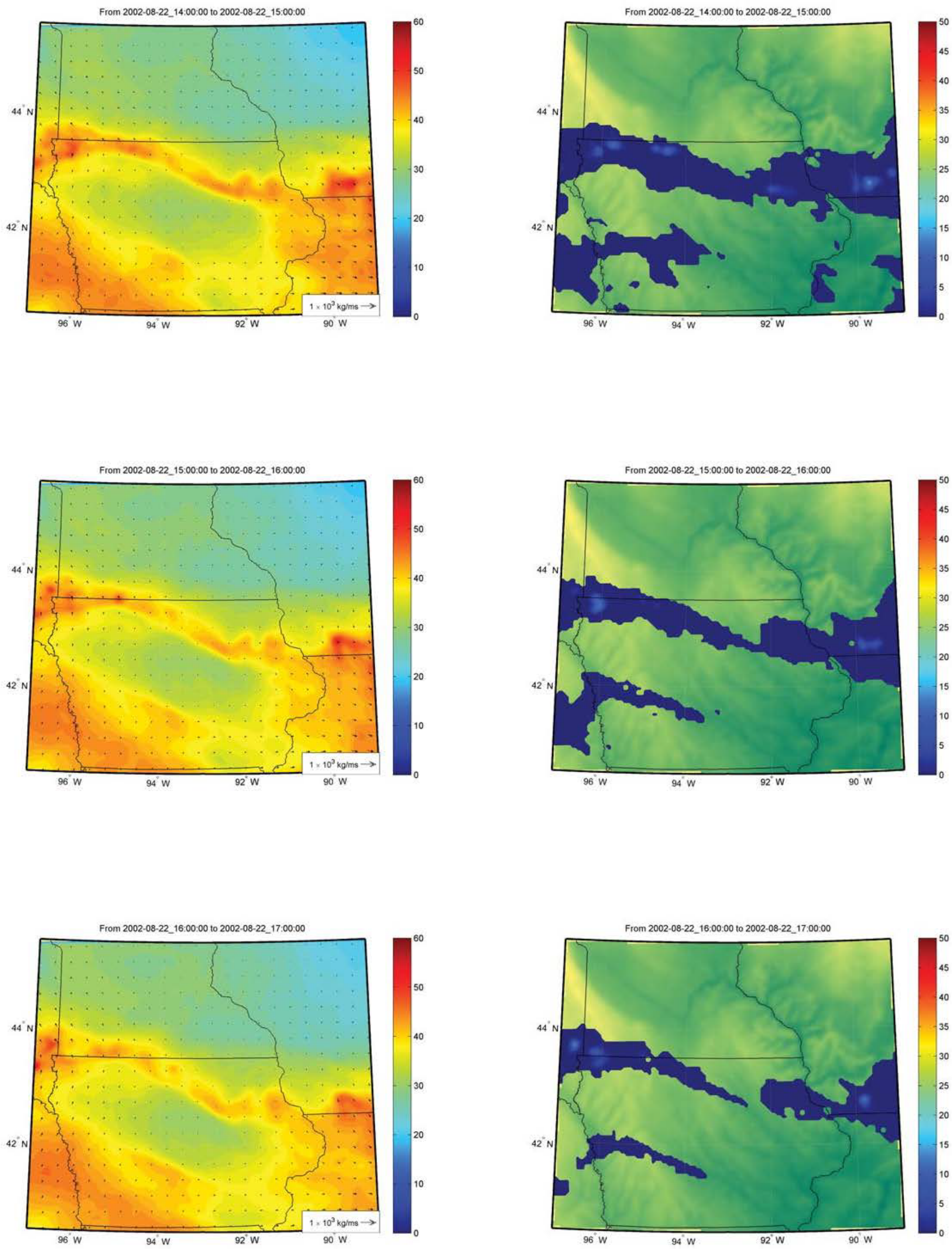

Figure B-2 **Hourly simulated Precipitable Water (Left, Colormap [mm]) and Water Vapor Flux Fields (Left, Arrows [kg m^{-1} s^{-1}]) and Precipitation Fields (Right, Colormap [mm]) for the August 22, 2002 MCS**

Plots shown from 08/20/2002 at 20hr to 08/22/2002 at 16hr (Continued).

B.1.3 September 15, 2004 MCS

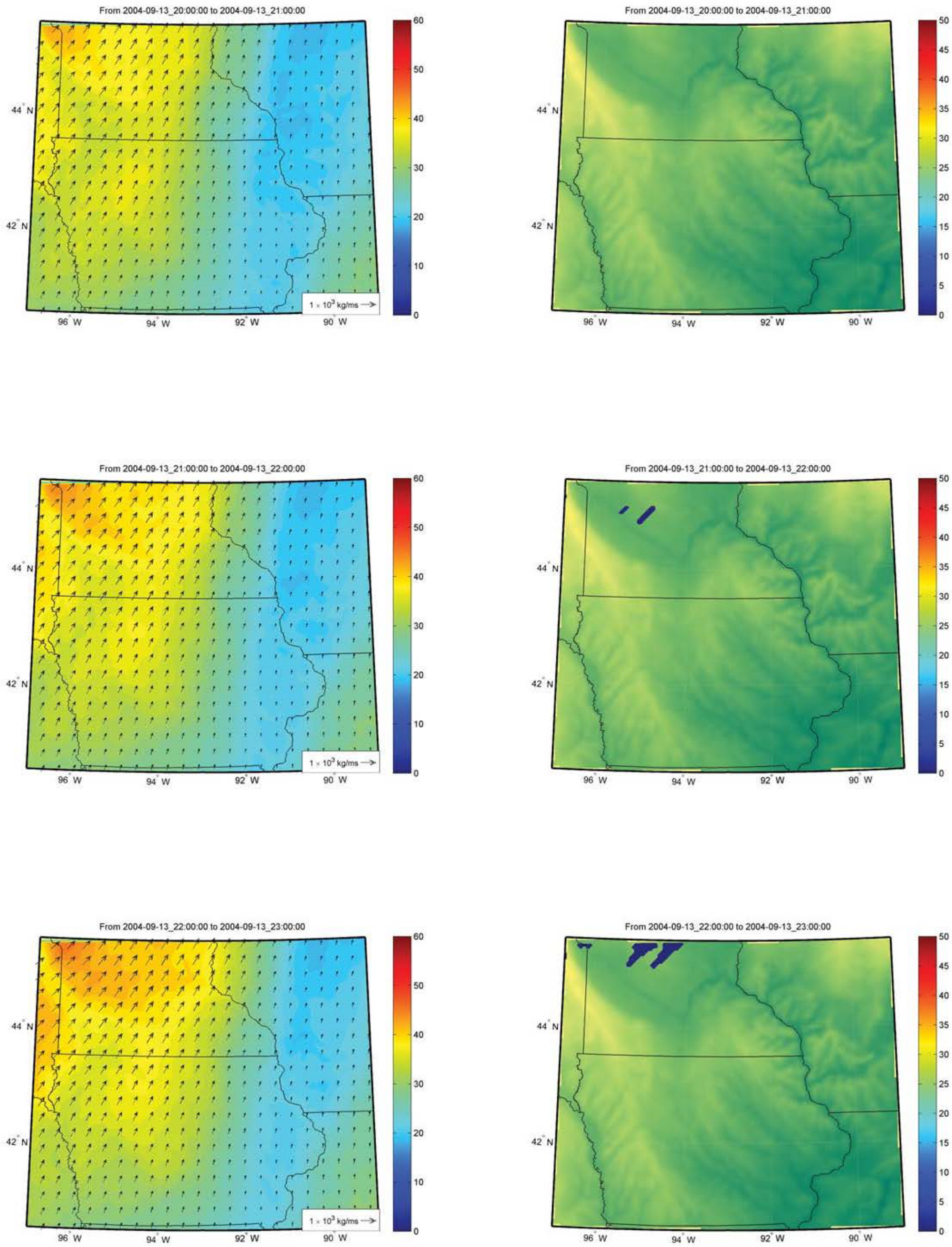

Figure B-3 **Hourly Simulated Precipitable Water (Left, Colormap [mm]) and Water Vapor Flux Fields (Left, Arrows [kg m^{-1} s^{-1}]) and Precipitation Fields (Right, Colormap [mm]) for the September 15, 2004 MCS**

Plots shown from 09/13/2004 at 20hr to 09/15/2004 at 16hr.

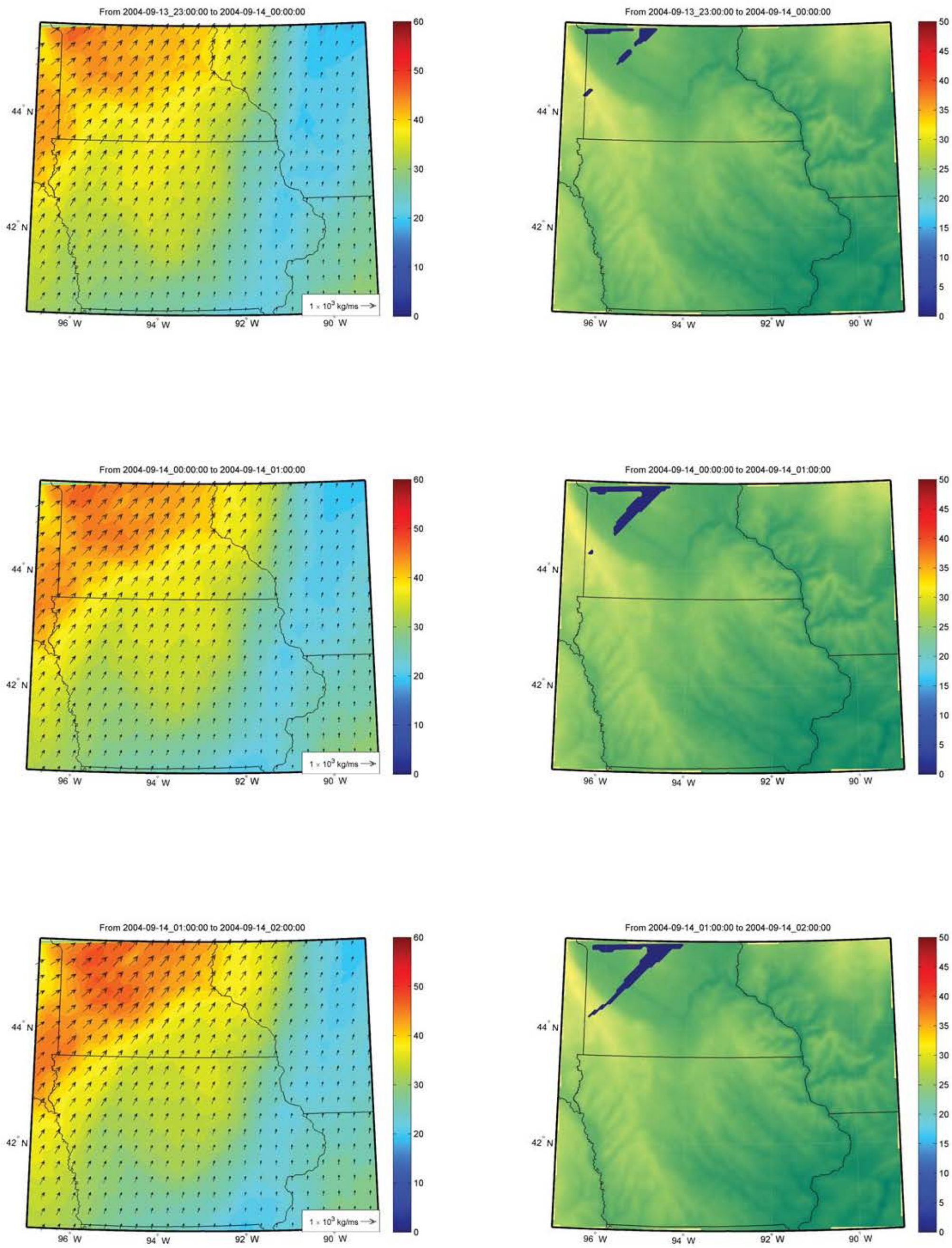

Figure B-3 Hourly Simulated Precipitable Water (Left, Colormap [mm]) and Water Vapor Flux Fields (Left, Arrows [kg m^{-1} s^{-1}]) and Precipitation Fields (Right, Colormap [mm]) for the September 15, 2004 MCS

Plots shown from 09/13/2004 at 20hr to 09/15/2004 at 16hr (Continued).

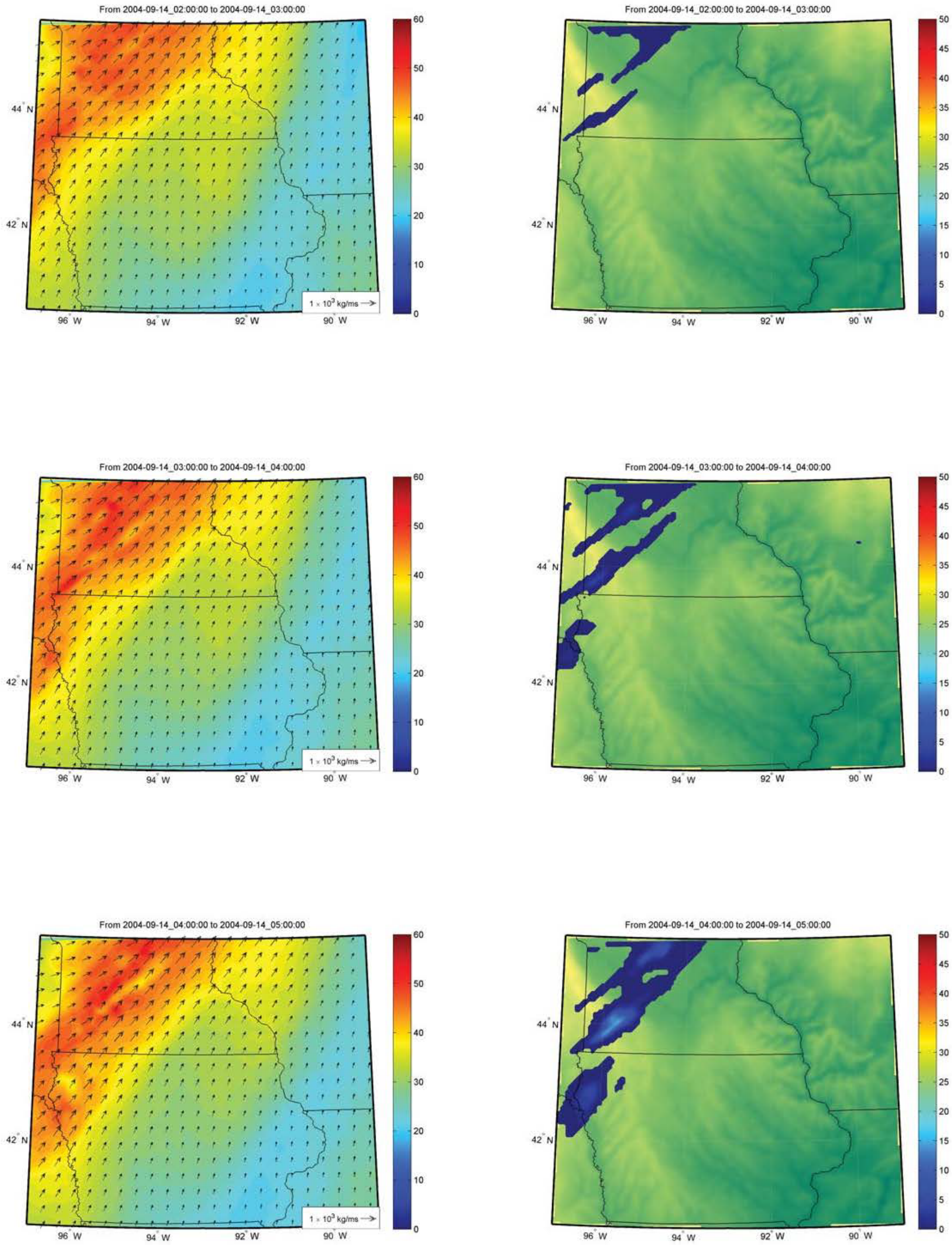

Figure B-3 Hourly Simulated Precipitable Water (Left, Colormap [mm]) and Water Vapor Flux Fields (Left, Arrows [kg m^{-1} s^{-1}]) and Precipitation Fields (Right, Colormap [mm]) for the September 15, 2004 MCS

Plots shown from 09/13/2004 at 20hr to 09/15/2004 at 16hr (Continued).

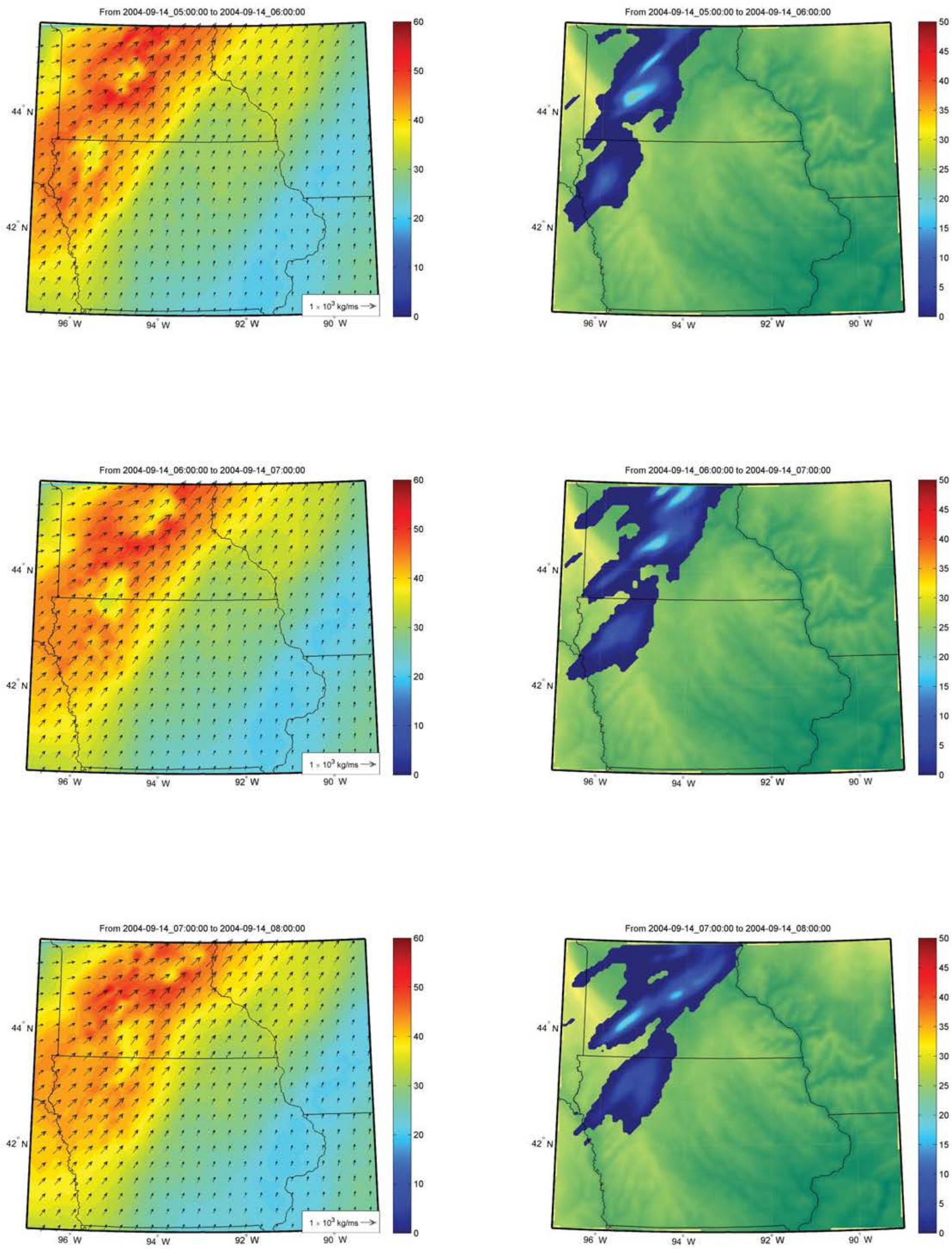

Figure B-3 Hourly Simulated Precipitable Water (Left, Colormap [mm]) and Water Vapor Flux Fields (Left, Arrows [kg m^{-1} s^{-1}]) and Precipitation Fields (Right, Colormap [mm]) for the September 15, 2004 MCS

Plots shown from 09/13/2004 at 20hr to 09/15/2004 at 16hr (Continued).

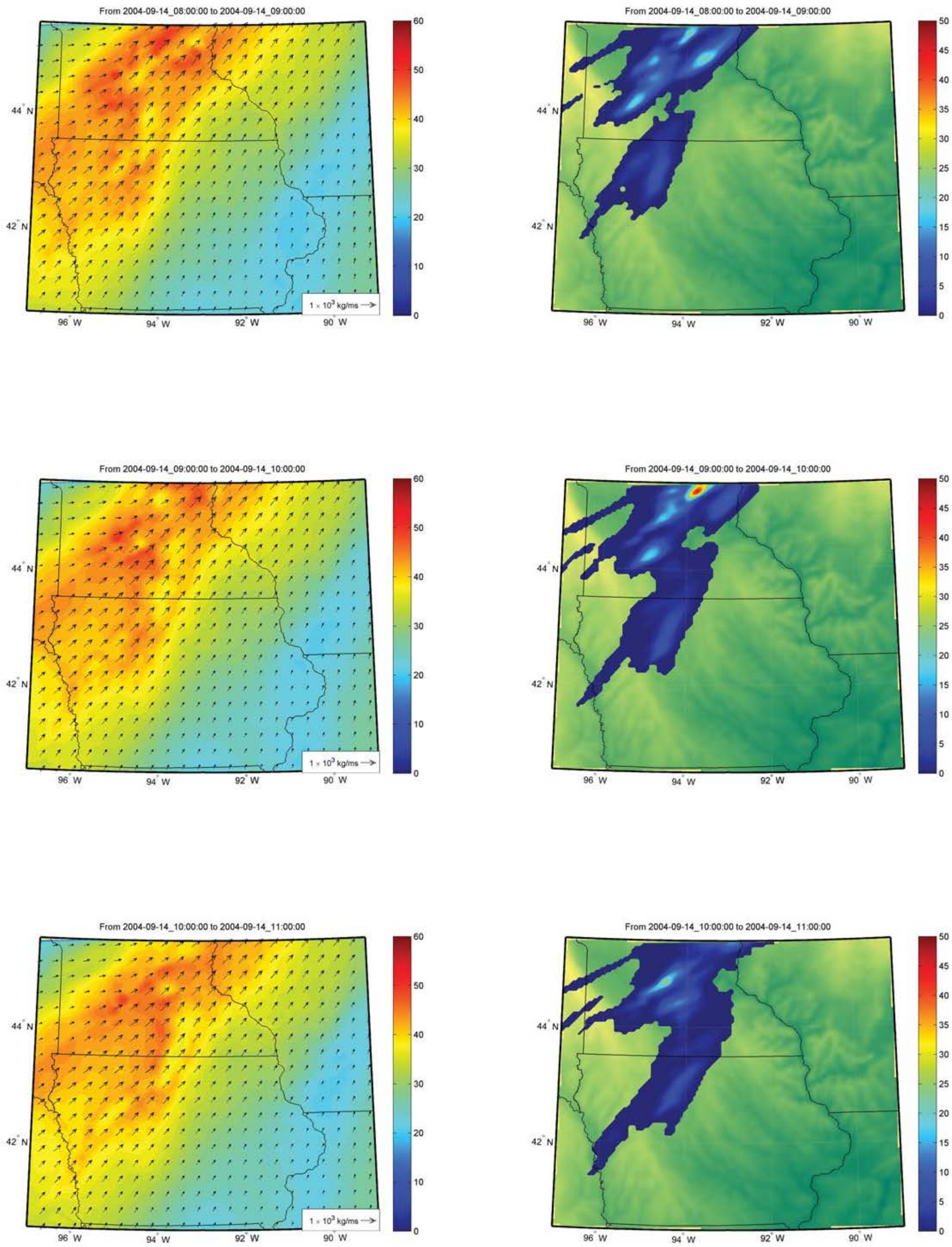

Figure B-3 Hourly Simulated Precipitable Water (Left, Colormap [mm]) and Water Vapor Flux Fields (Left, Arrows [kg m^{-1} s^{-1}]) and Precipitation Fields (Right, Colormap [mm]) for the September 15, 2004 MCS

Plots shown from 09/13/2004 at 20hr to 09/15/2004 at 16hr (Continued).

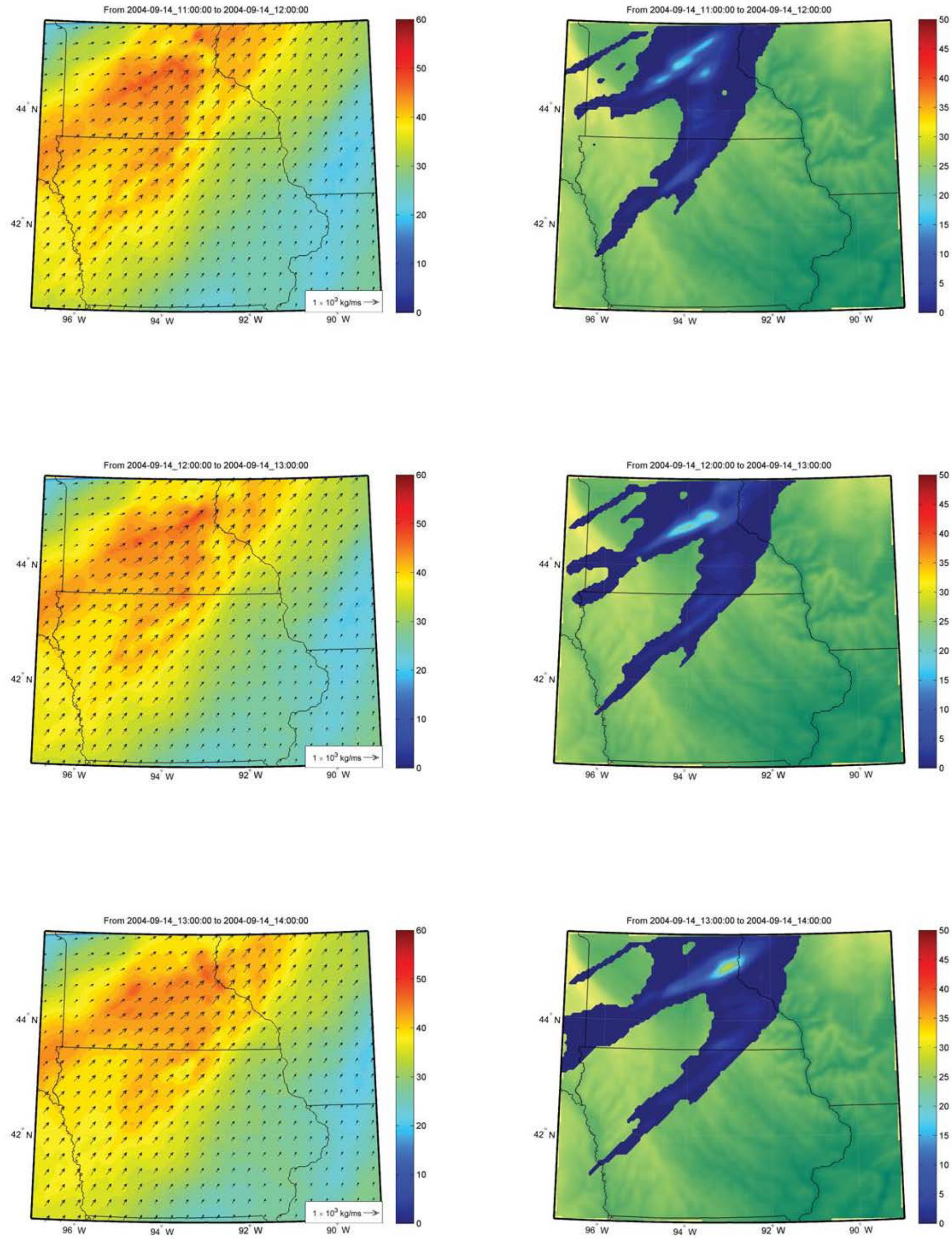

Figure B-3 **Hourly Simulated Precipitable Water (Left, Colormap [mm]) and Water Vapor Flux Fields (Left, Arrows [kg m^{-1} s^{-1}]) and Precipitation Fields (Right, Colormap [mm]) for the September 15, 2004 MCS**

Plots shown from 09/13/2004 at 20hr to 09/15/2004 at 16hr (Continued).

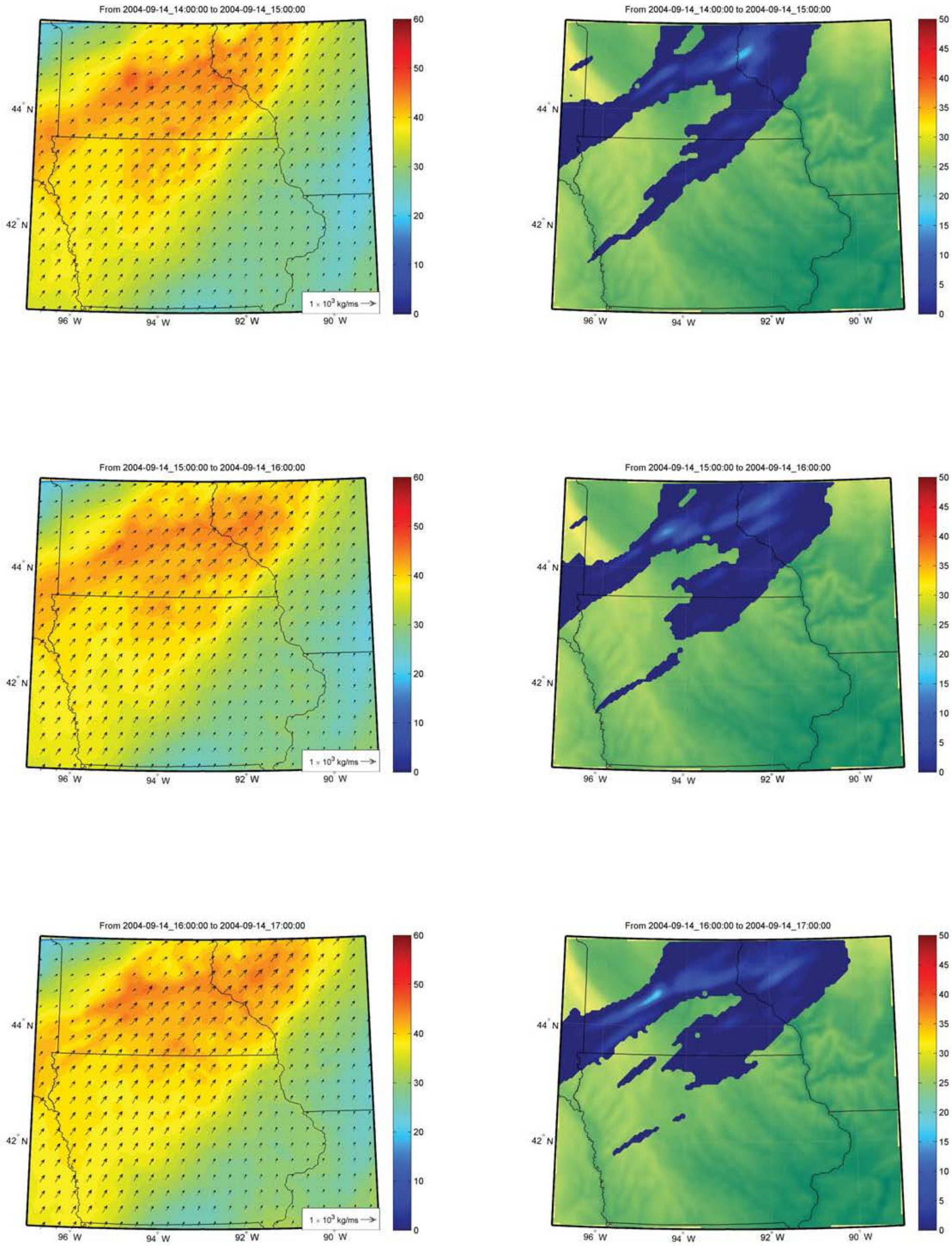

Figure B-3 Hourly Simulated Precipitable Water (Left, Colormap [mm]) and Water Vapor Flux Fields (Left, Arrows [kg m^{-1} s^{-1}]) and Precipitation Fields (Right, Colormap [mm]) for the September 15, 2004 MCS

Plots shown from 09/13/2004 at 20hr to 09/15/2004 at 16hr (Continued).

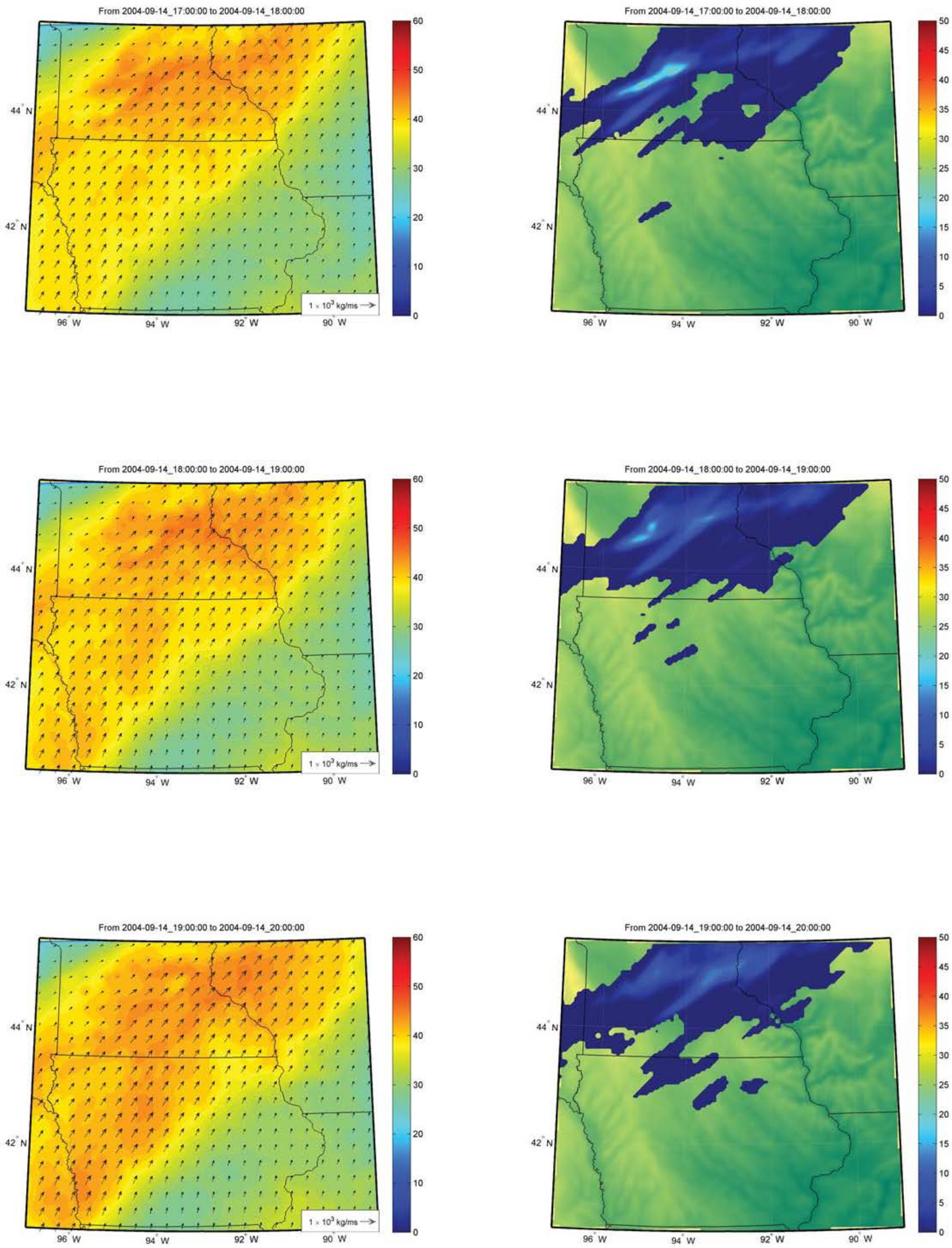

Figure B-3 Hourly Simulated Precipitable Water (Left, Colormap [mm]) and Water Vapor Flux Fields (Left, Arrows [kg m^{-1} s^{-1}]) and Precipitation Fields (Right, Colormap [mm]) for the September 15, 2004 MCS

Plots shown from 09/13/2004 at 20hr to 09/15/2004 at 16hr (Continued).

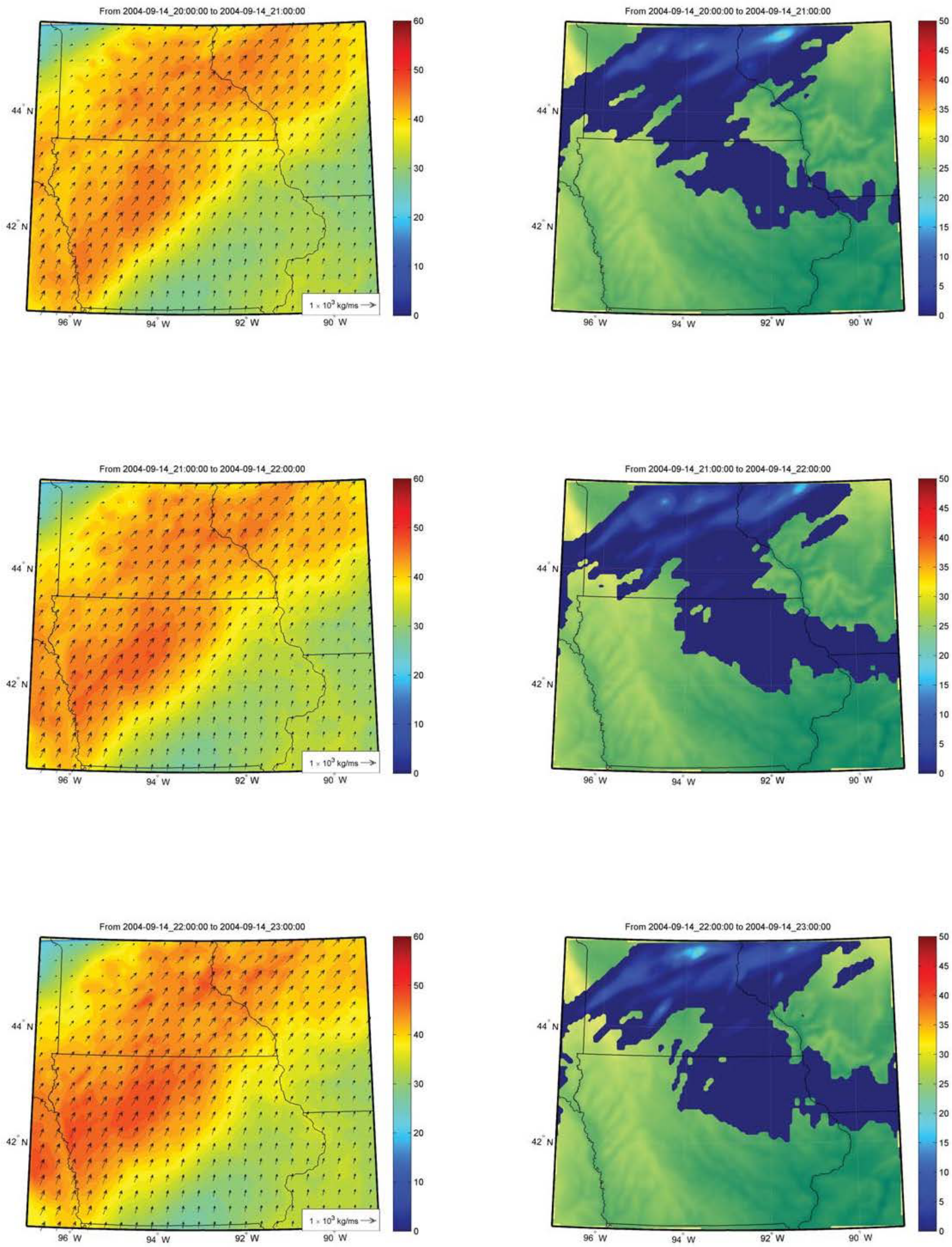

Figure B-3 Hourly Simulated Precipitable Water (Left, Colormap [mm]) and Water Vapor Flux Fields (Left, Arrows [kg m^{-1} s^{-1}]) and Precipitation Fields (Right, Colormap [mm]) for the September 15, 2004 MCS

Plots shown from 09/13/2004 at 20hr to 09/15/2004 at 16hr (Continued).

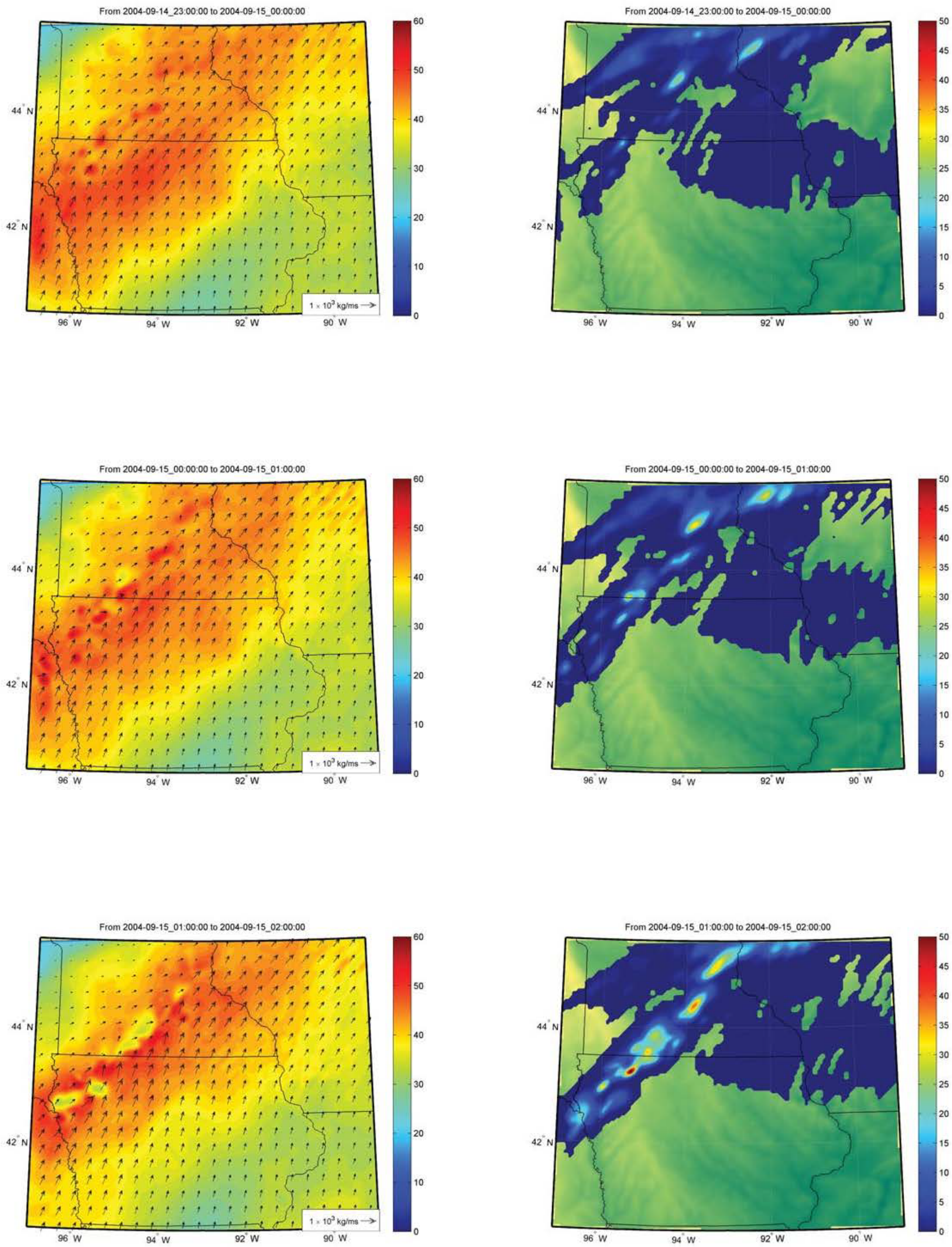

Figure B-3 Hourly Simulated Precipitable Water (Left, Colormap [mm]) and Water Vapor Flux Fields (Left, Arrows [kg m^{-1} s^{-1}]) and Precipitation Fields (Right, Colormap [mm]) for the September 15, 2004 MCS

Plots shown from 09/13/2004 at 20hr to 09/15/2004 at 16hr (Continued).

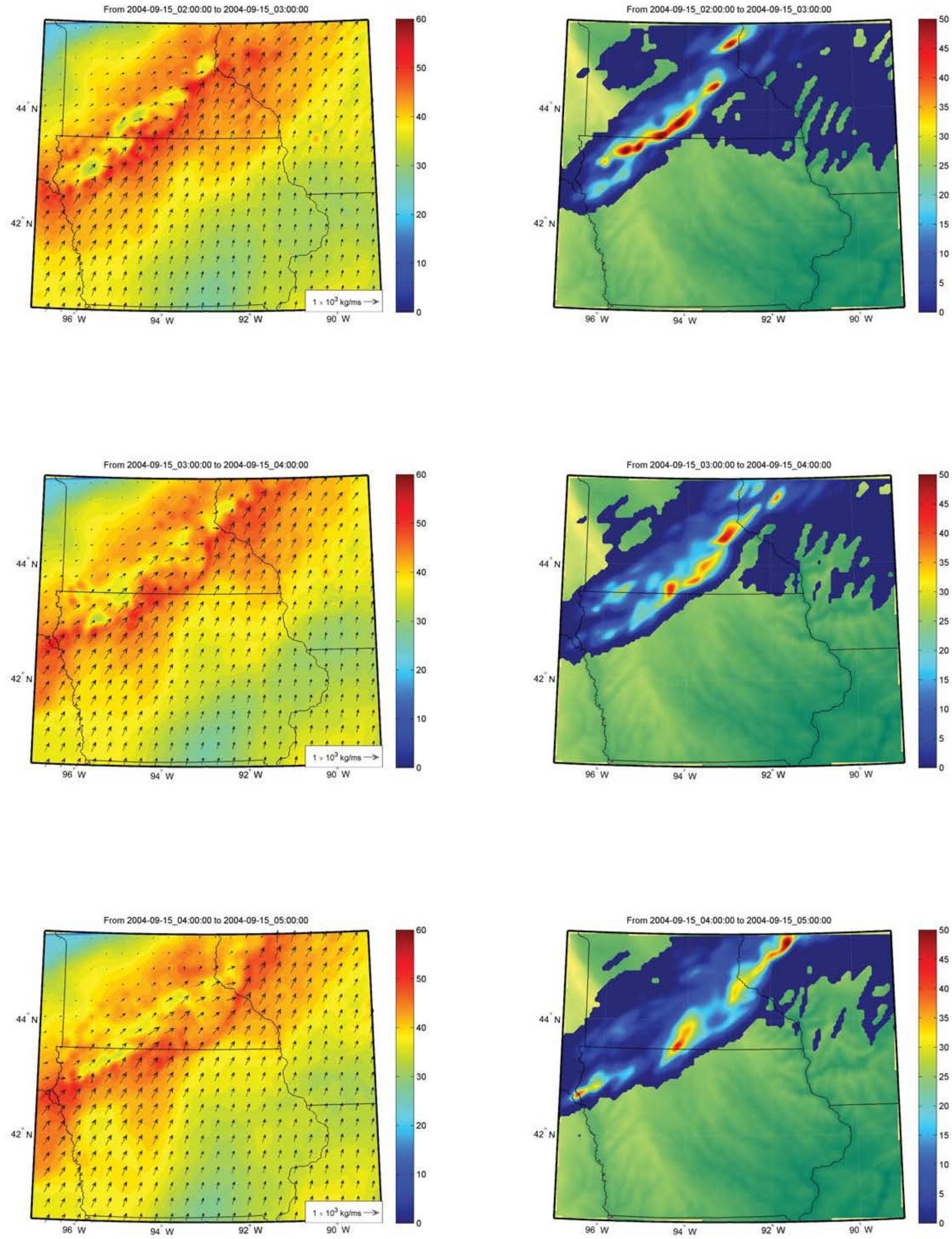

Figure B-3 Hourly Simulated Precipitable Water (Left, Colormap [mm]) and Water Vapor Flux Fields (Left, Arrows [kg m^{-1} s^{-1}]) and Precipitation Fields (Right, Colormap [mm]) for the September 15, 2004 MCS

Plots shown from 09/13/2004 at 20hr to 09/15/2004 at 16hr (Continued).

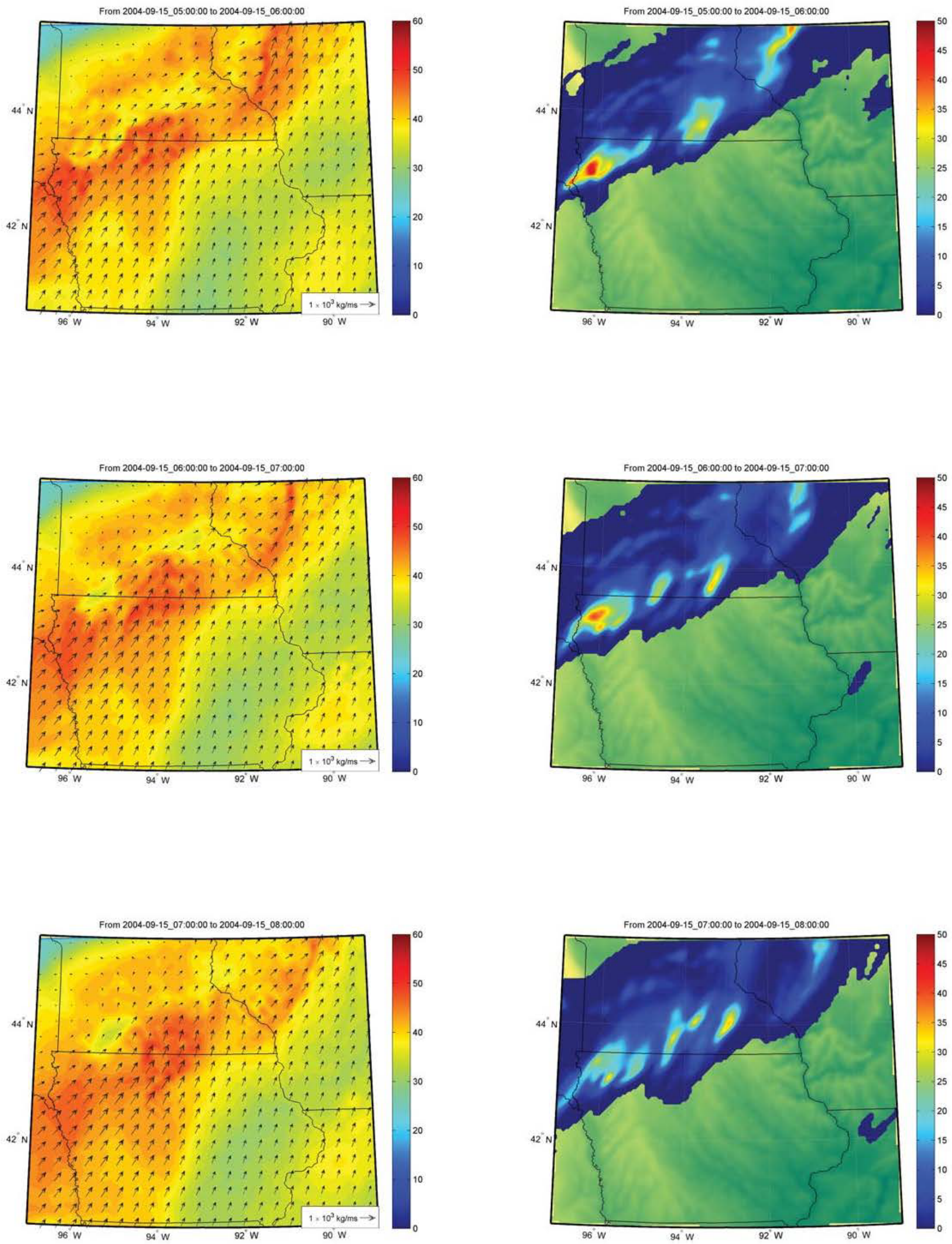

Figure B-3 Hourly Simulated Precipitable Water (Left, Colormap [mm]) and Water Vapor Flux Fields (Left, Arrows [kg m^{-1} s^{-1}]) and Precipitation Fields (Right, Colormap [mm]) for the September 15, 2004 MCS

Plots shown from 09/13/2004 at 20hr to 09/15/2004 at 16hr (Continued).

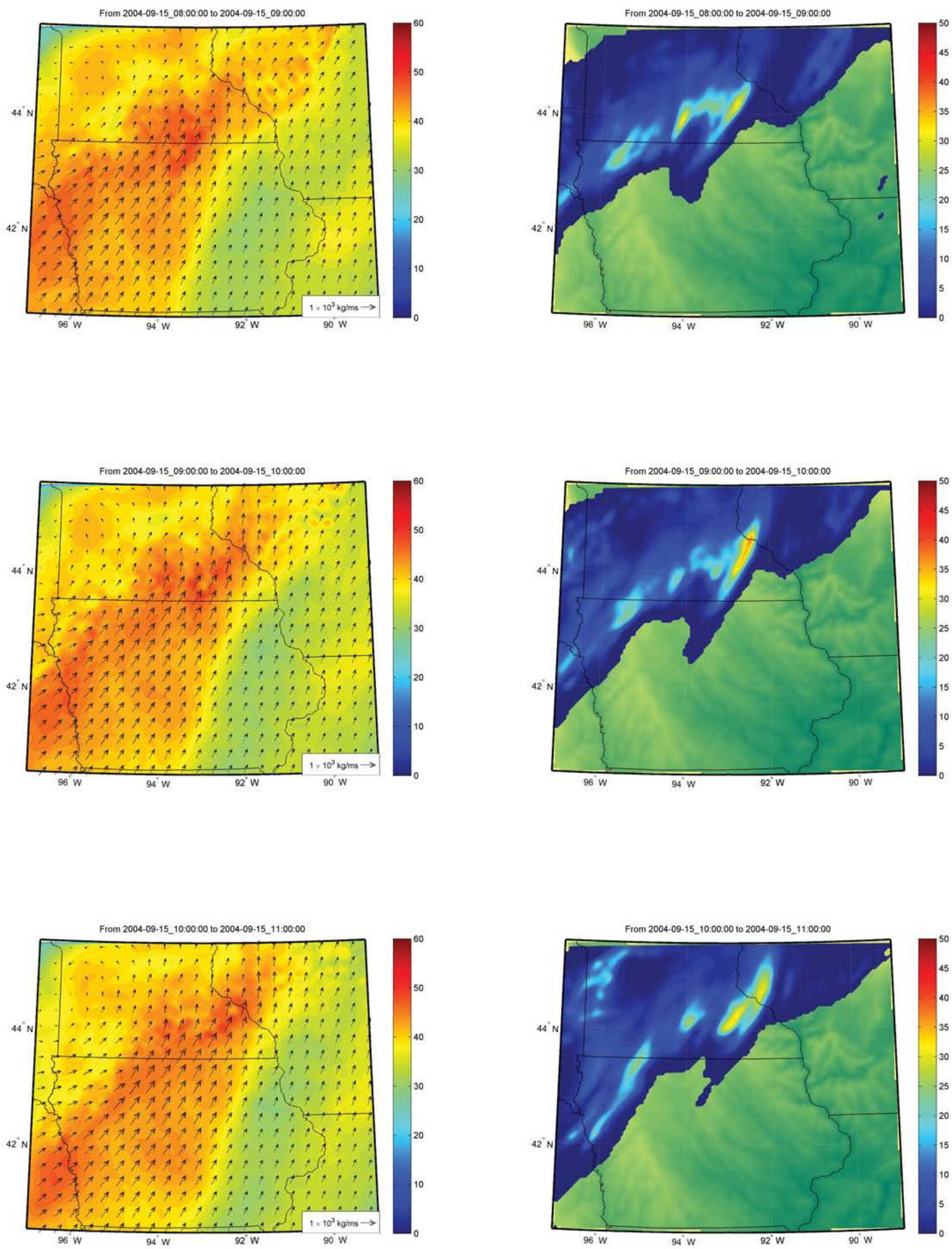

Figure B-3 **Hourly Simulated Precipitable Water (Left, Colormap [mm]) and Water Vapor Flux Fields (Left, Arrows [kg m^{-1} s^{-1}]) and Precipitation Fields (Right, Colormap [mm]) for the September 15, 2004 MCS**

Plots shown from 09/13/2004 at 20hr to 09/15/2004 at 16hr (Continued).

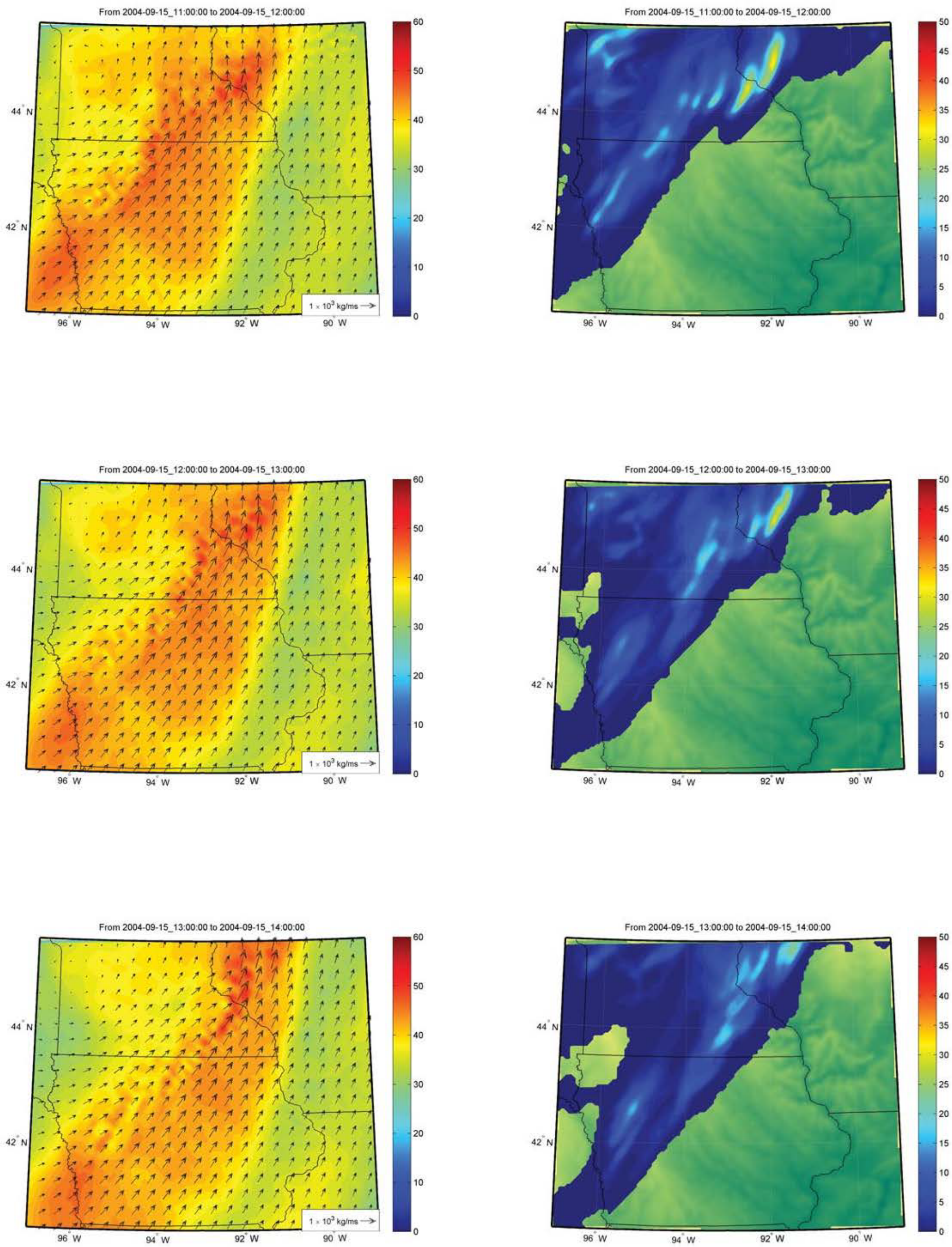

Figure B-3　Hourly Simulated Precipitable Water (Left, Colormap [mm]) and Water Vapor Flux Fields (Left, Arrows [kg m^{-1} s^{-1}]) and Precipitation Fields (Right, Colormap [mm]) for the September 15, 2004 MCS

Plots shown from 09/13/2004 at 20hr to 09/15/2004 at 16hr (Continued).

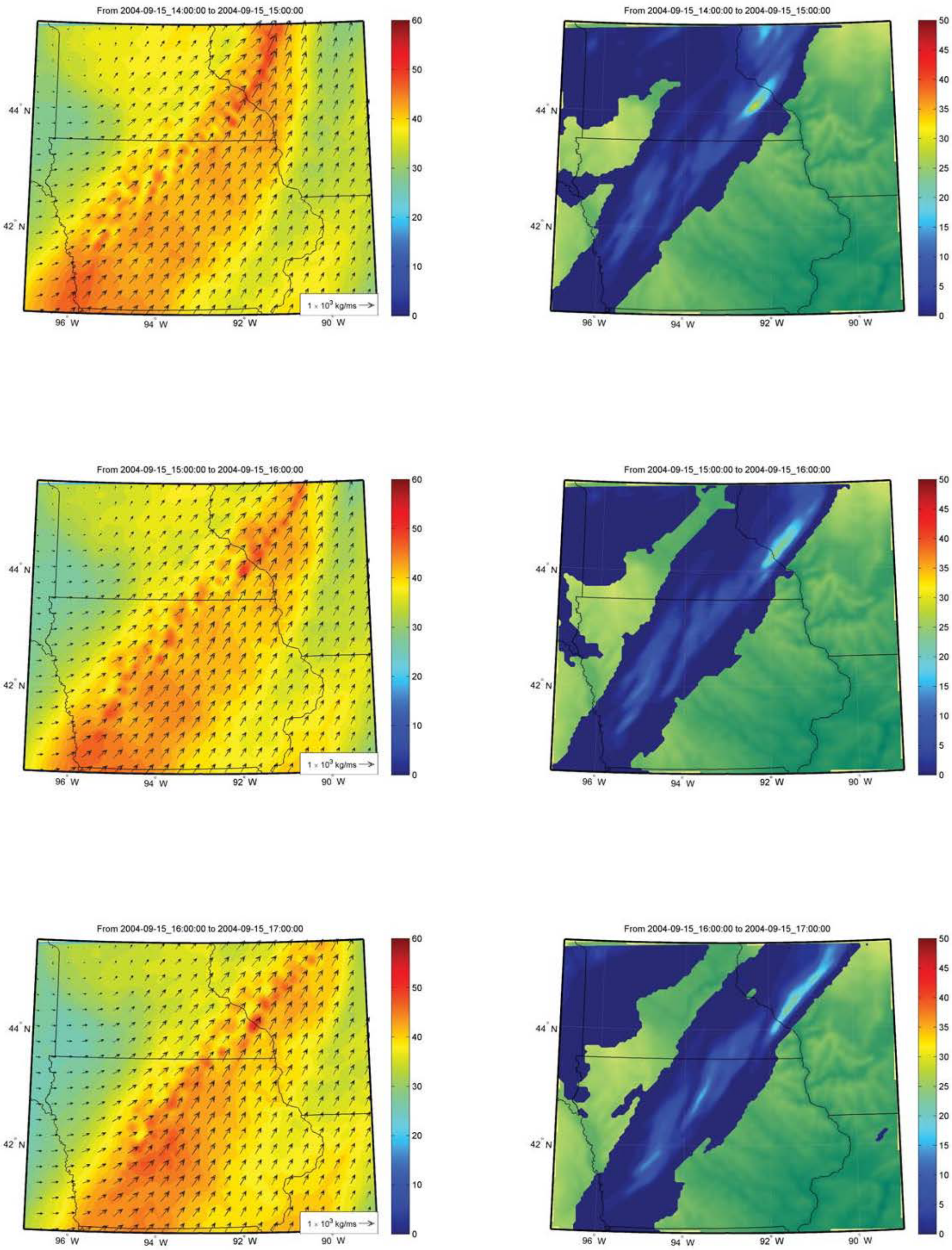

Figure B-3 Hourly Simulated Precipitable Water (Left, Colormap [mm]) and Water Vapor Flux Fields (Left, Arrows [kg m^{-1} s^{-1}]) and Precipitation Fields (Right, Colormap [mm]) for the September 15, 2004 MCS

Plots shown from 09/13/2004 at 20hr to 09/15/2004 at 16hr (Continued).

B.1.4 June 25, 2005 MCS

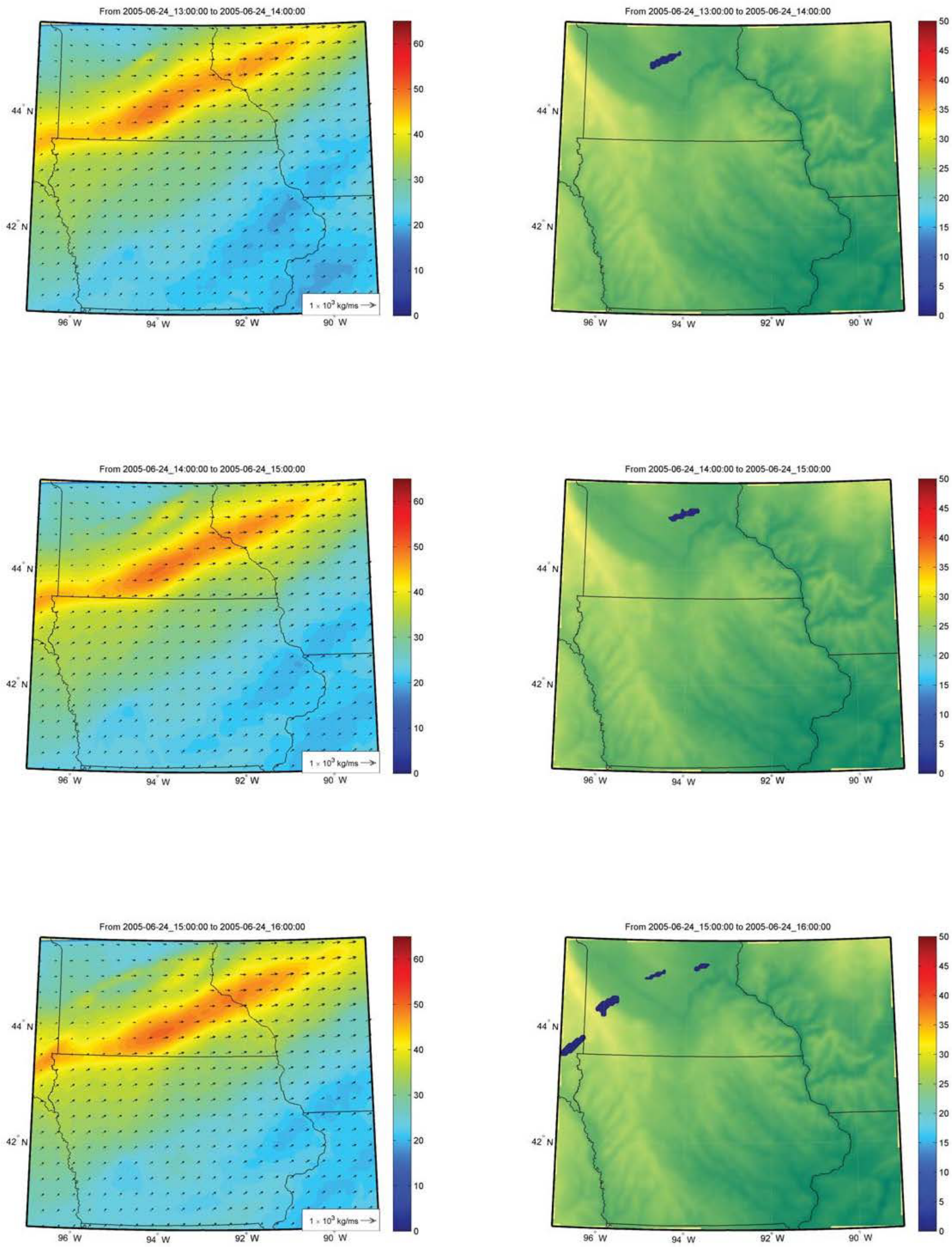

Figure B-4 Hourly Simulated Precipitable Water (Left, Colormap [mm]) and Water Vapor Flux Fields (Left, Arrows [kg m^{-1} s^{-1}]) and Precipitation Fields (Right, Colormap [mm]) for the June 25, 2005 MCS

Plots shown from 06/24/2005 at 13hr to 06/25/2005 at 18hr.

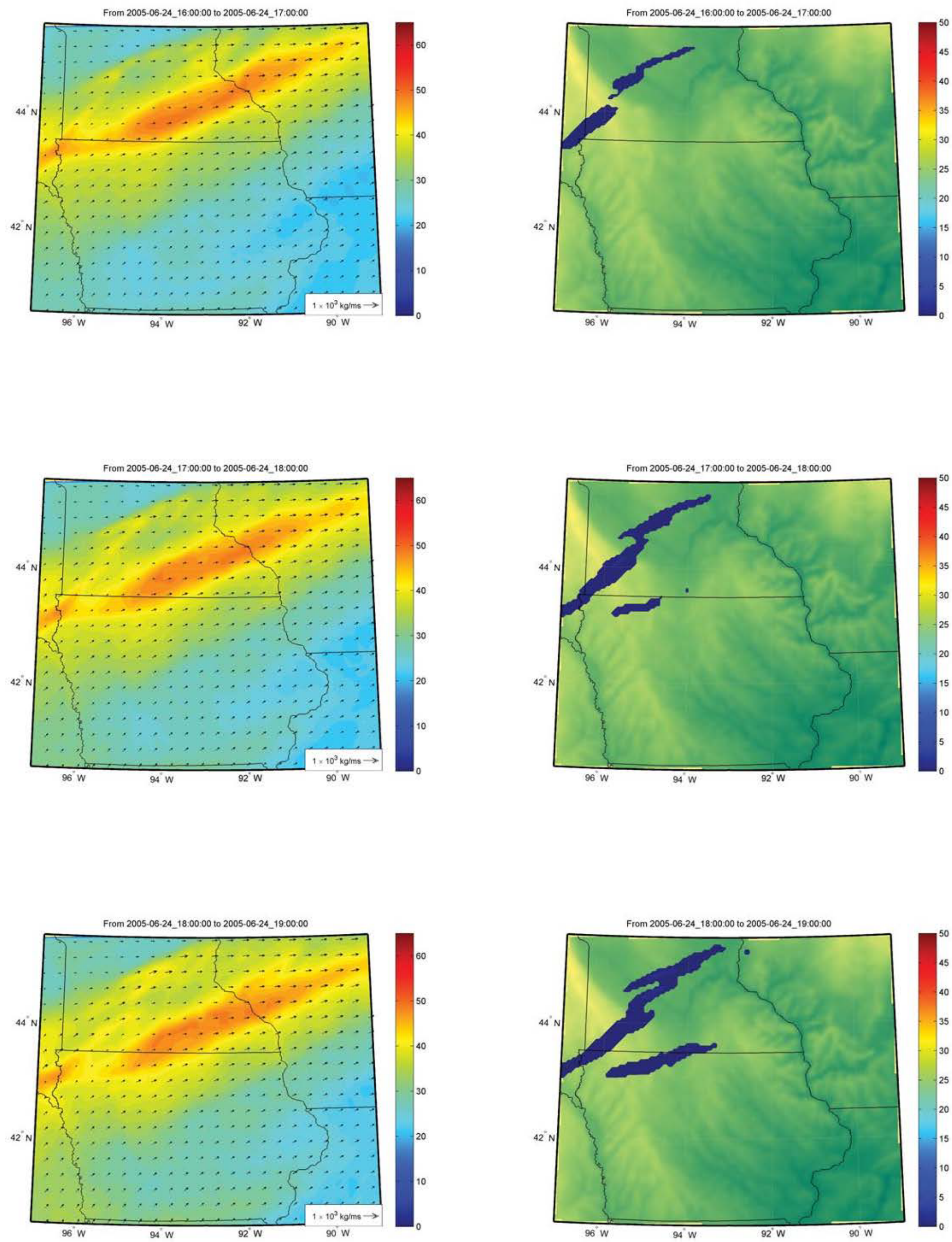

Figure B-4 Hourly Simulated Precipitable Water (Left, Colormap [mm]) and Water Vapor Flux Fields (Left, Arrows [kg m^{-1} s^{-1}]) and Precipitation Fields (Right, Colormap [mm]) for the June 25, 2005 MCS

Plots shown from 06/24/2005 at 13hr to 06/25/2005 at 18hr (Continued).

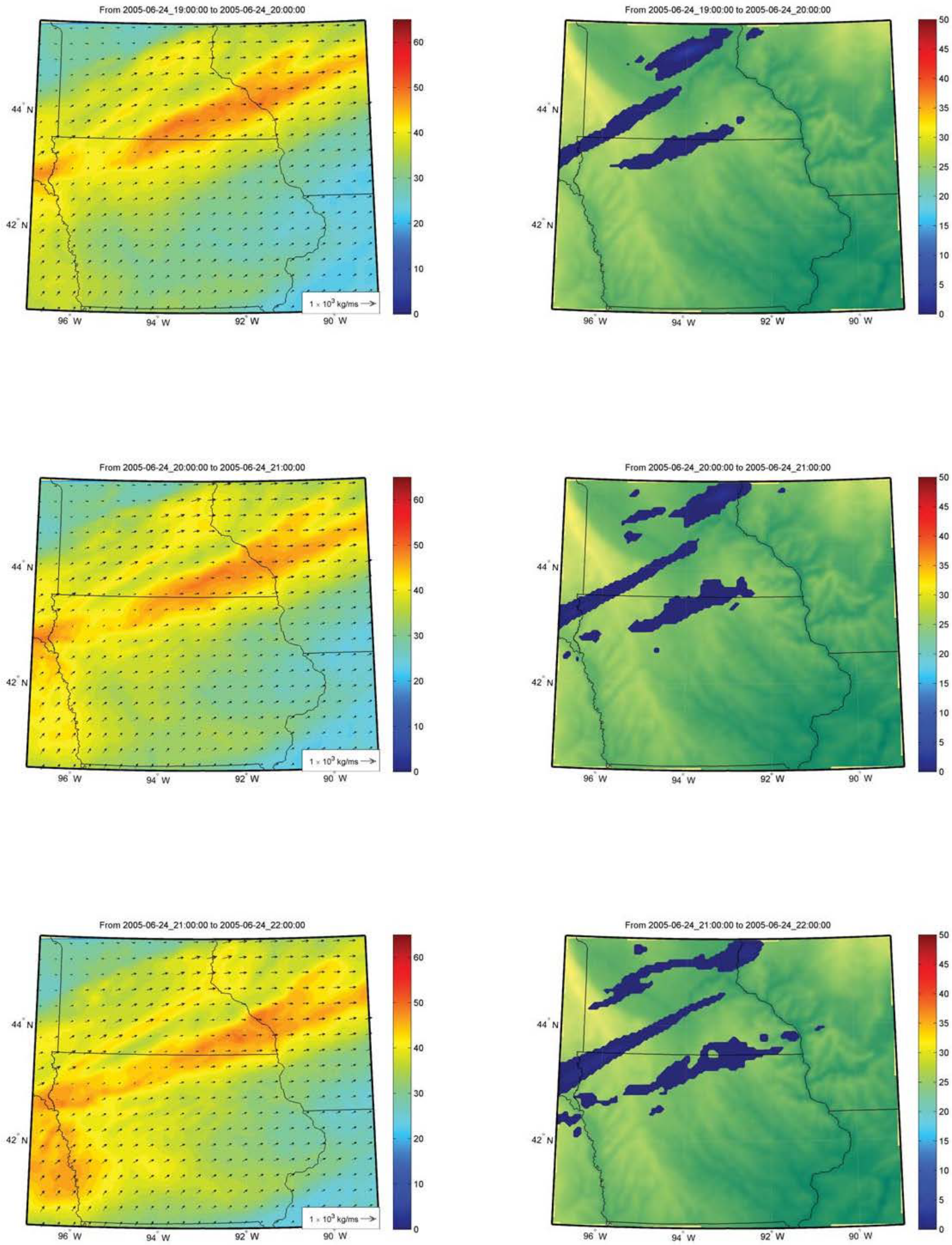

Figure B-4 Hourly Simulated Precipitable Water (Left, Colormap [mm]) and Water Vapor Flux Fields (Left, Arrows [kg m^{-1} s^{-1}]) and Precipitation Fields (Right, Colormap [mm]) for the June 25, 2005 MCS

Plots shown from 06/24/2005 at 13hr to 06/25/2005 at 18hr (Continued).

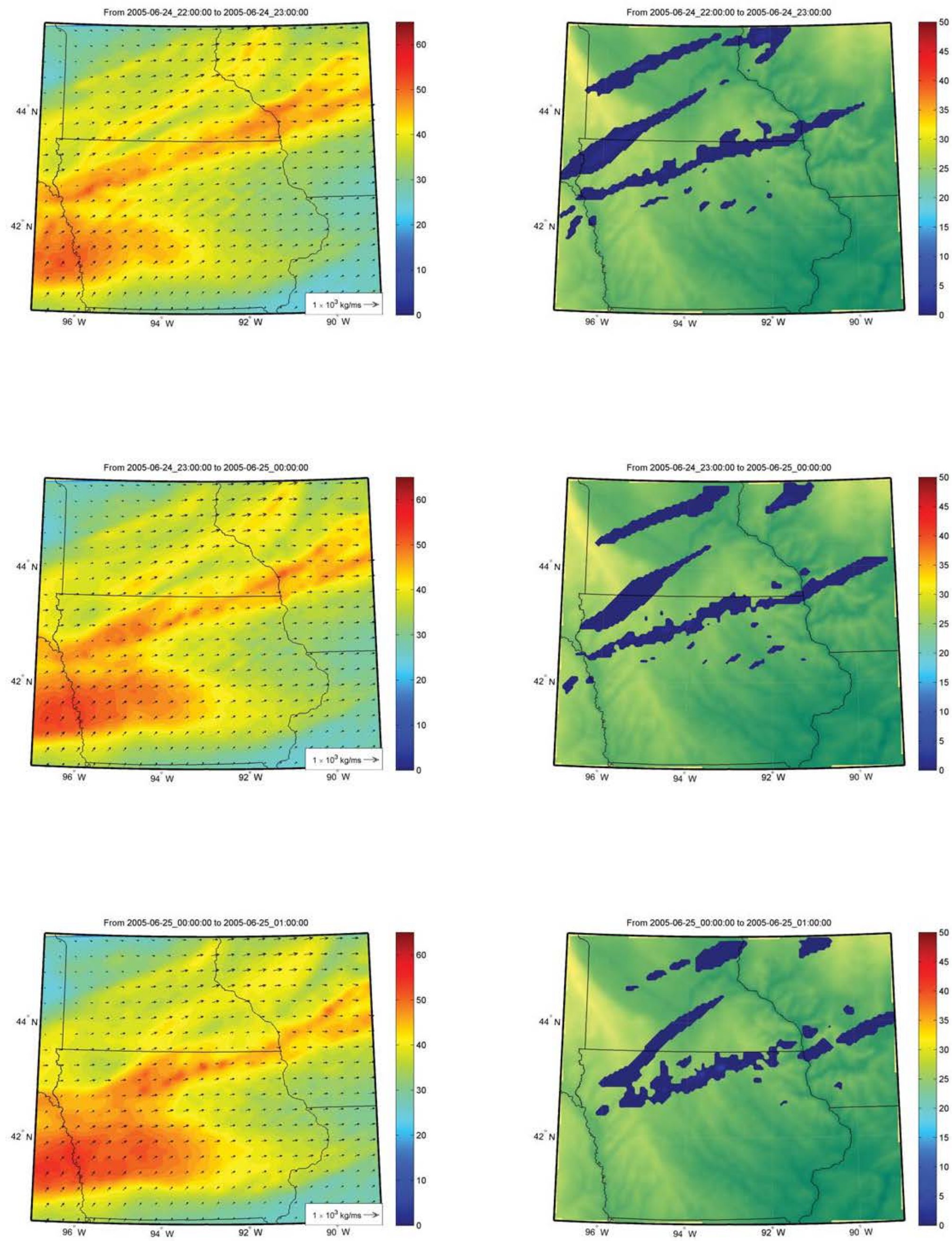

Figure B-4 **Hourly Simulated Precipitable Water (Left, Colormap [mm]) and Water Vapor Flux Fields (Left, Arrows [kg m^{-1} s^{-1}]) and Precipitation Fields (Right, Colormap [mm]) for the June 25, 2005 MCS**

Plots shown from 06/24/2005 at 13hr to 06/25/2005 at 18hr (Continued).

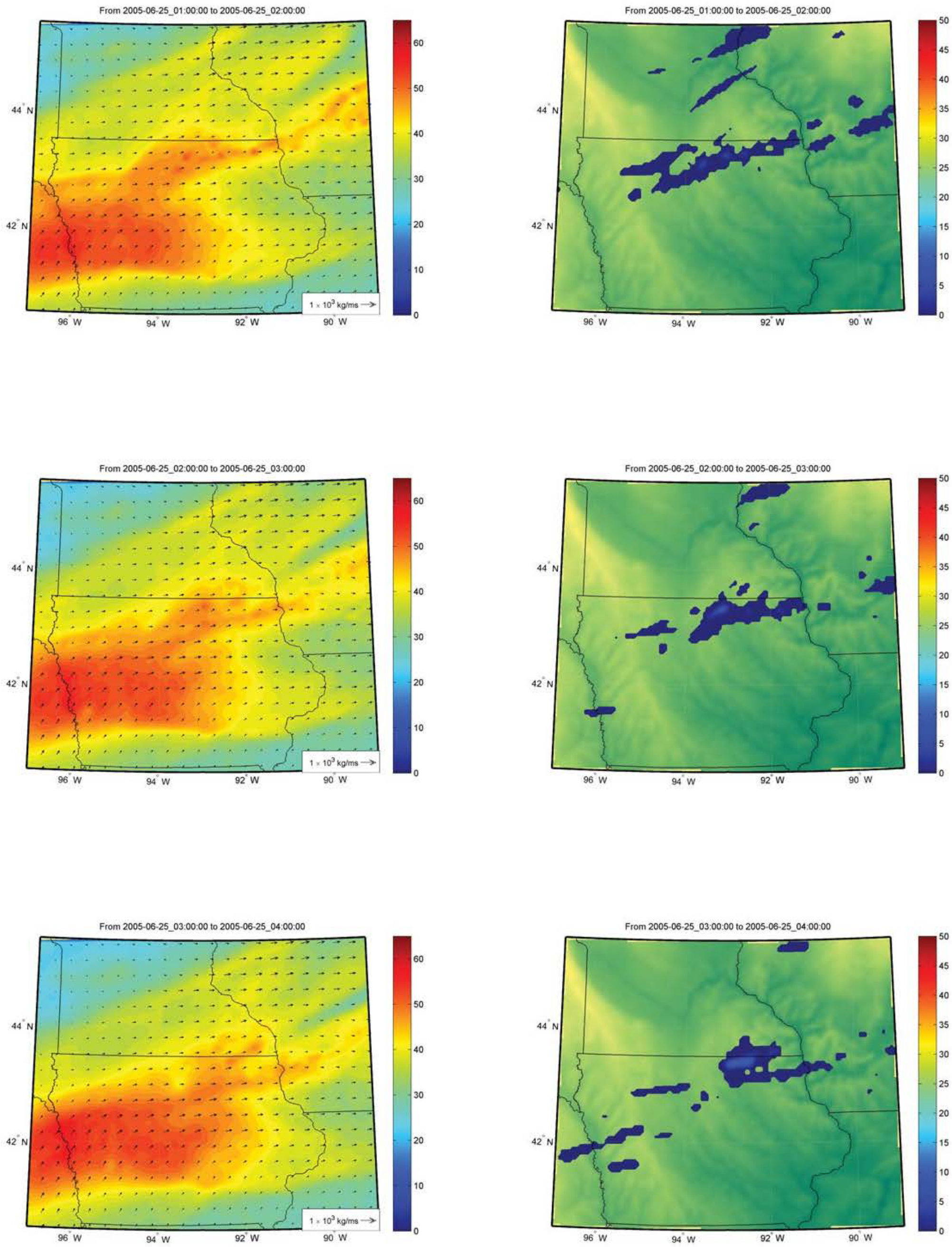

Figure B-4 Hourly Simulated Precipitable Water (Left, Colormap [mm]) and Water Vapor Flux Fields (Left, Arrows [kg m^{-1} s^{-1}]) and Precipitation Fields (Right, Colormap [mm]) for the June 25, 2005 MCS

Plots shown from 06/24/2005 at 13hr to 06/25/2005 at 18hr (Continued).

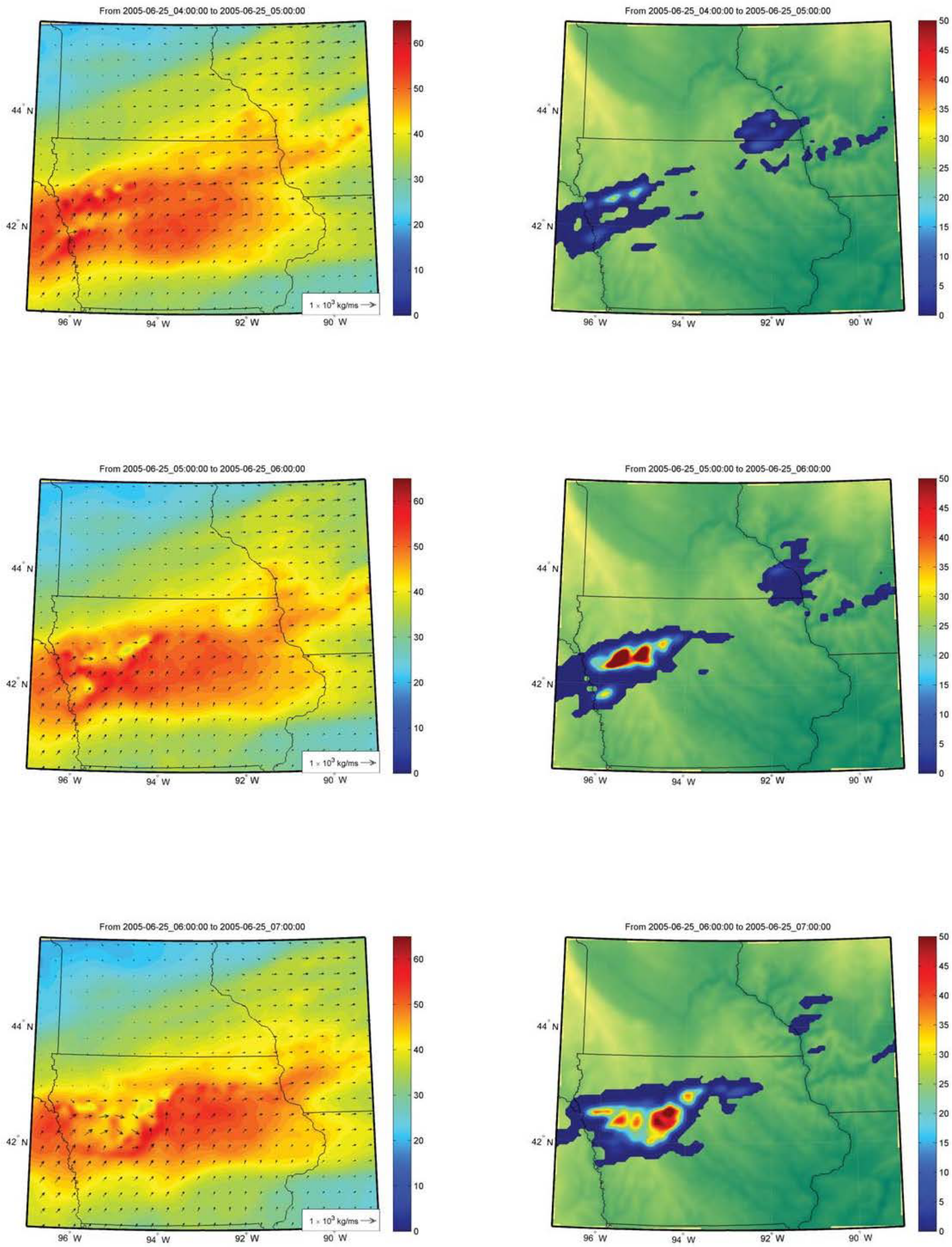

Figure B-4 Hourly Simulated Precipitable Water (Left, Colormap [mm]) and Water Vapor Flux Fields (Left, Arrows [kg m^{-1} s^{-1}]) and Precipitation Fields (Right, Colormap [mm]) for the June 25, 2005 MCS

Plots shown from 06/24/2005 at 13hr to 06/25/2005 at 18hr (Continued).

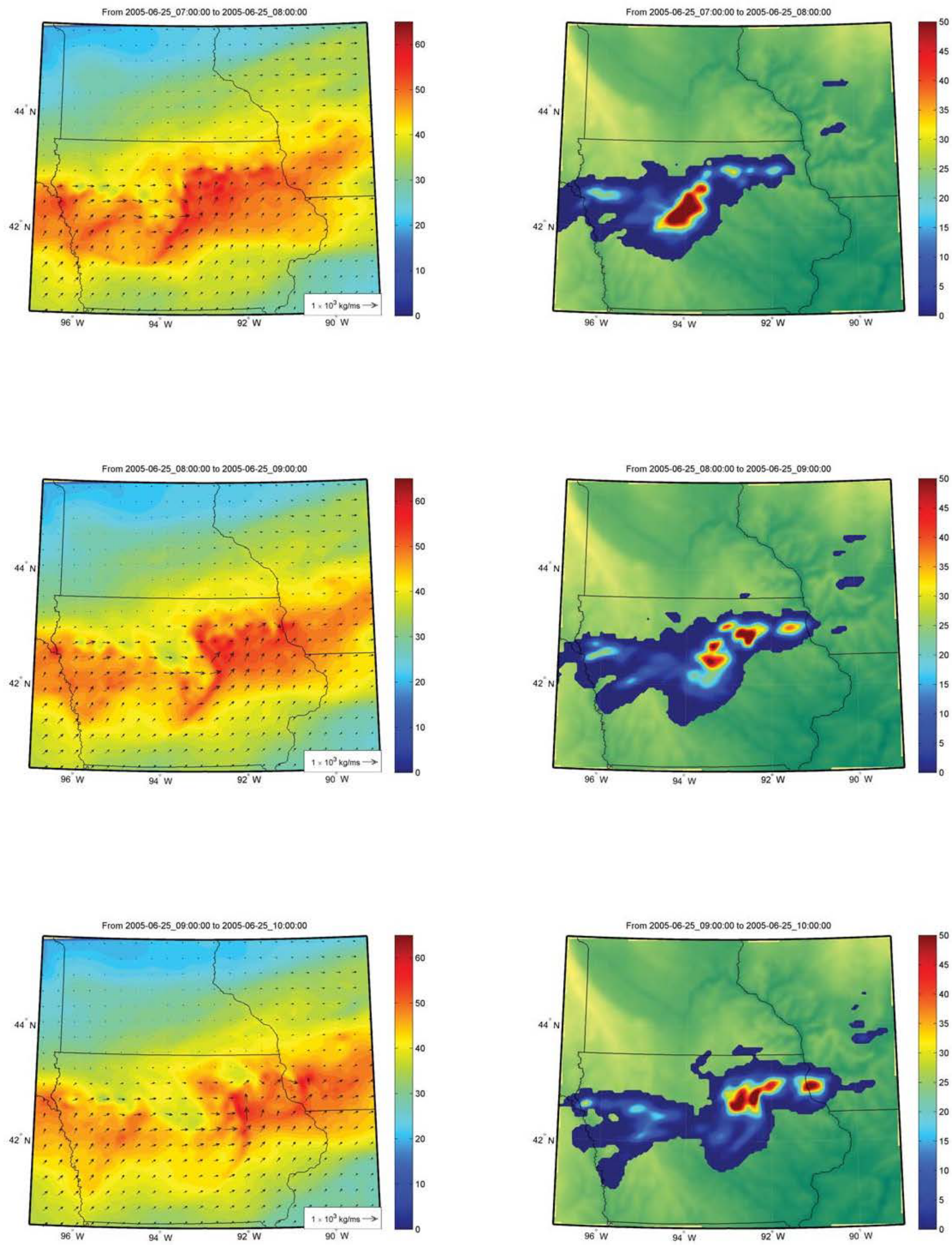

Figure B-4 **Hourly Simulated Precipitable Water (Left, Colormap [mm]) and Water Vapor Flux Fields (Left, Arrows [kg m^{-1} s^{-1}]) and Precipitation Fields (Right, Colormap [mm]) for the June 25, 2005 MCS**

Plots shown from 06/24/2005 at 13hr to 06/25/2005 at 18hr (Continued).

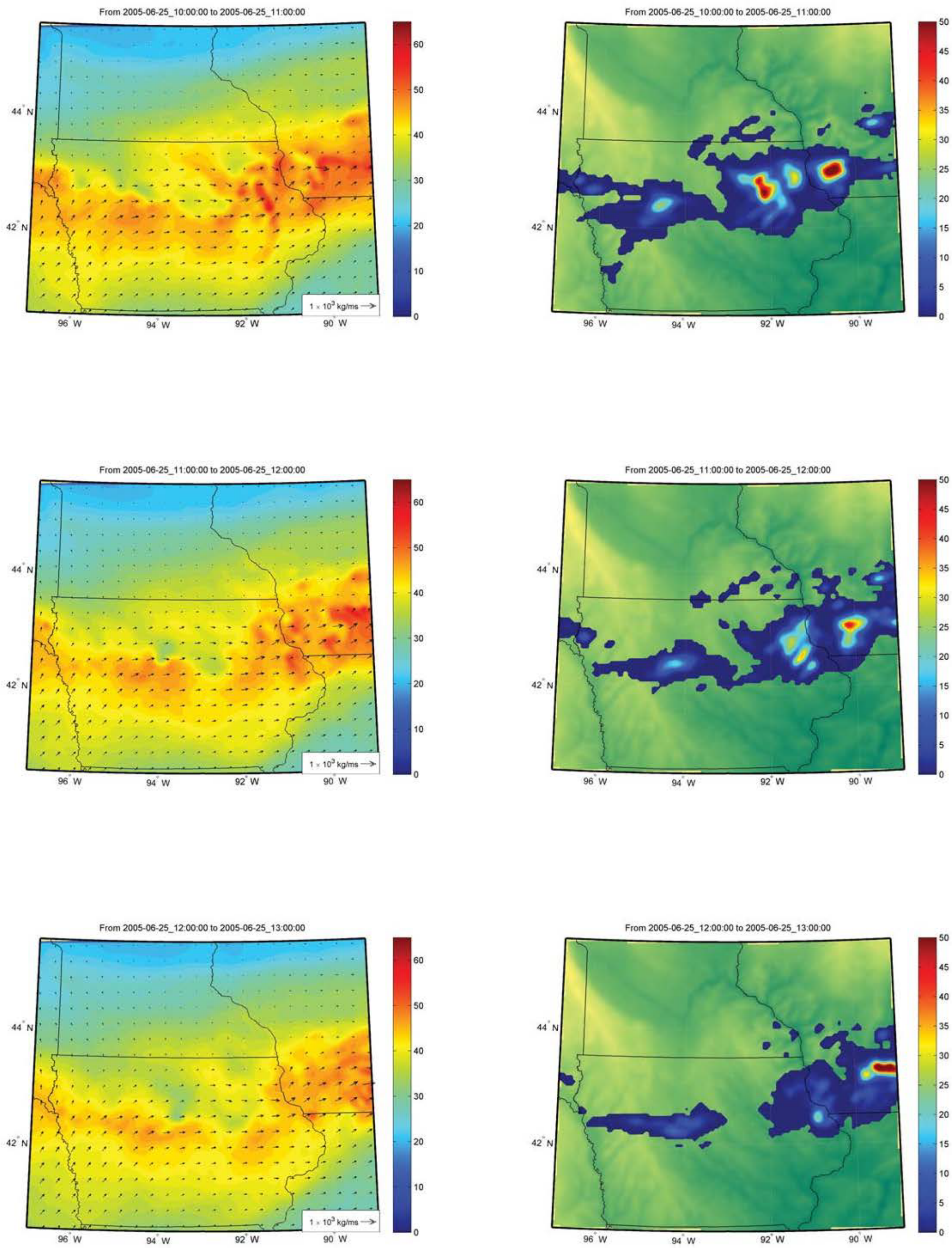

Figure B-4 **Hourly Simulated Precipitable Water (Left, Colormap [mm]) and Water Vapor Flux Fields (Left, Arrows [kg m^{-1} s^{-1}]) and Precipitation Fields (Right, Colormap [mm]) for the June 25, 2005 MCS**

Plots shown from 06/24/2005 at 13hr to 06/25/2005 at 18hr (Continued).

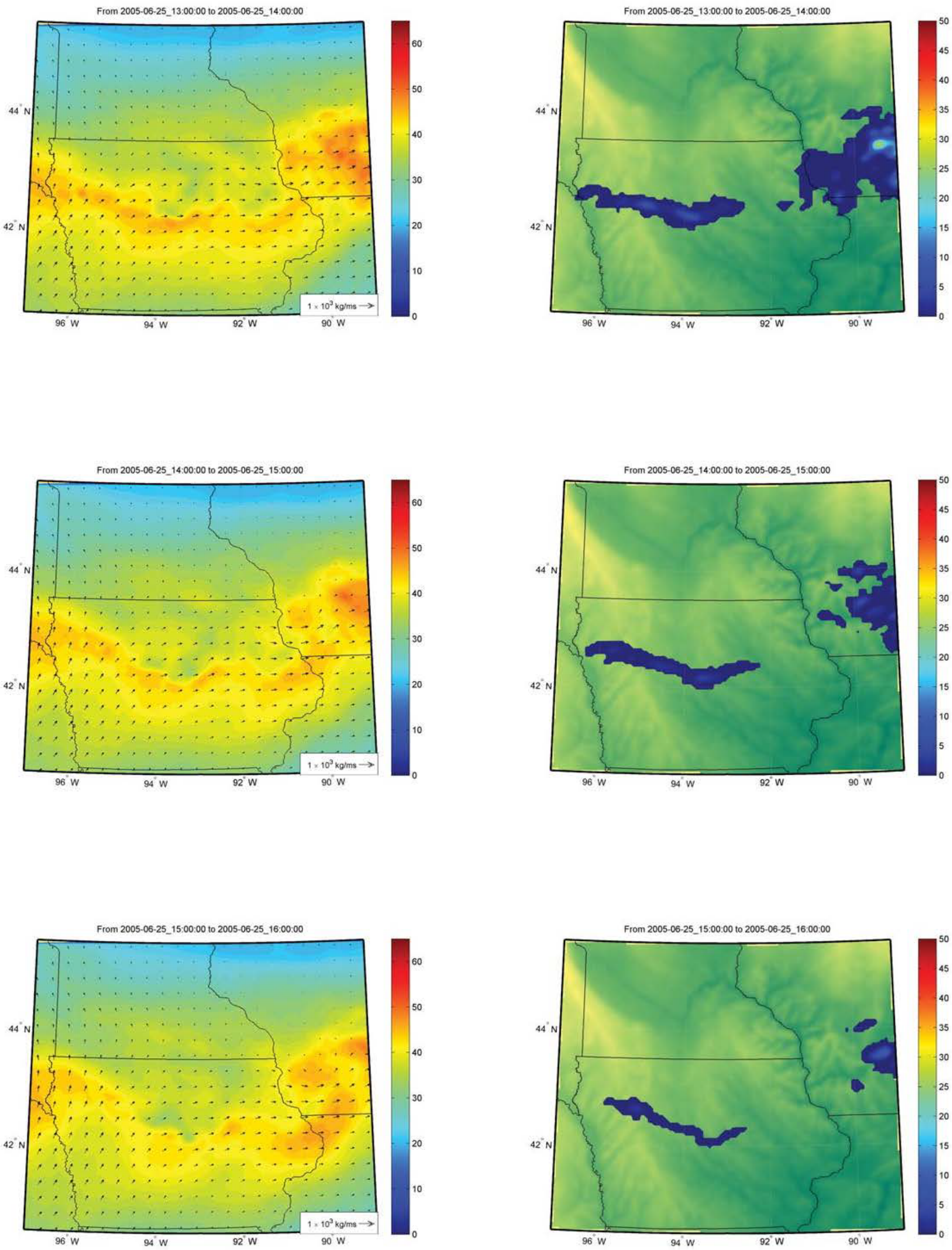

Figure B-4 **Hourly Simulated Precipitable Water (Left, Colormap [mm]) and Water Vapor Flux Fields (Left, Arrows [kg m^{-1} s^{-1}]) and Precipitation Fields (Right, Colormap [mm]) for the June 25, 2005 MCS**

Plots shown from 06/24/2005 at 13hr to 06/25/2005 at 18hr (Continued).

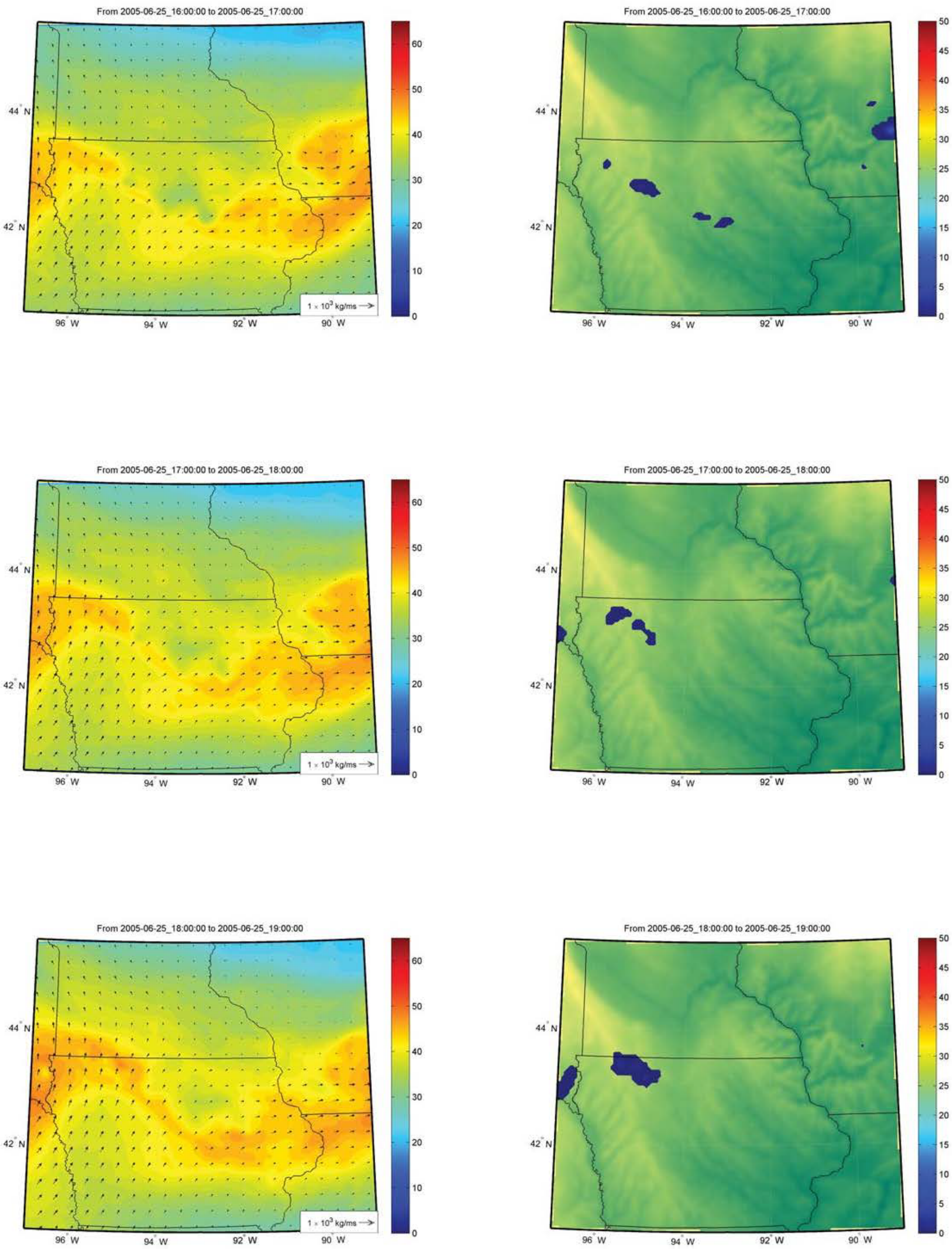

Figure B-4 Hourly Simulated Precipitable Water (Left, Colormap [mm]) and Water Vapor Flux Fields (Left, Arrows [kg m^{-1} s^{-1}]) and Precipitation Fields (Right, Colormap [mm]) for the June 25, 2005 MCS

Plots shown from 06/24/2005 at 13hr to 06/25/2005 at 18hr (Continued).

B.1.5 August 17, 2005 MCS

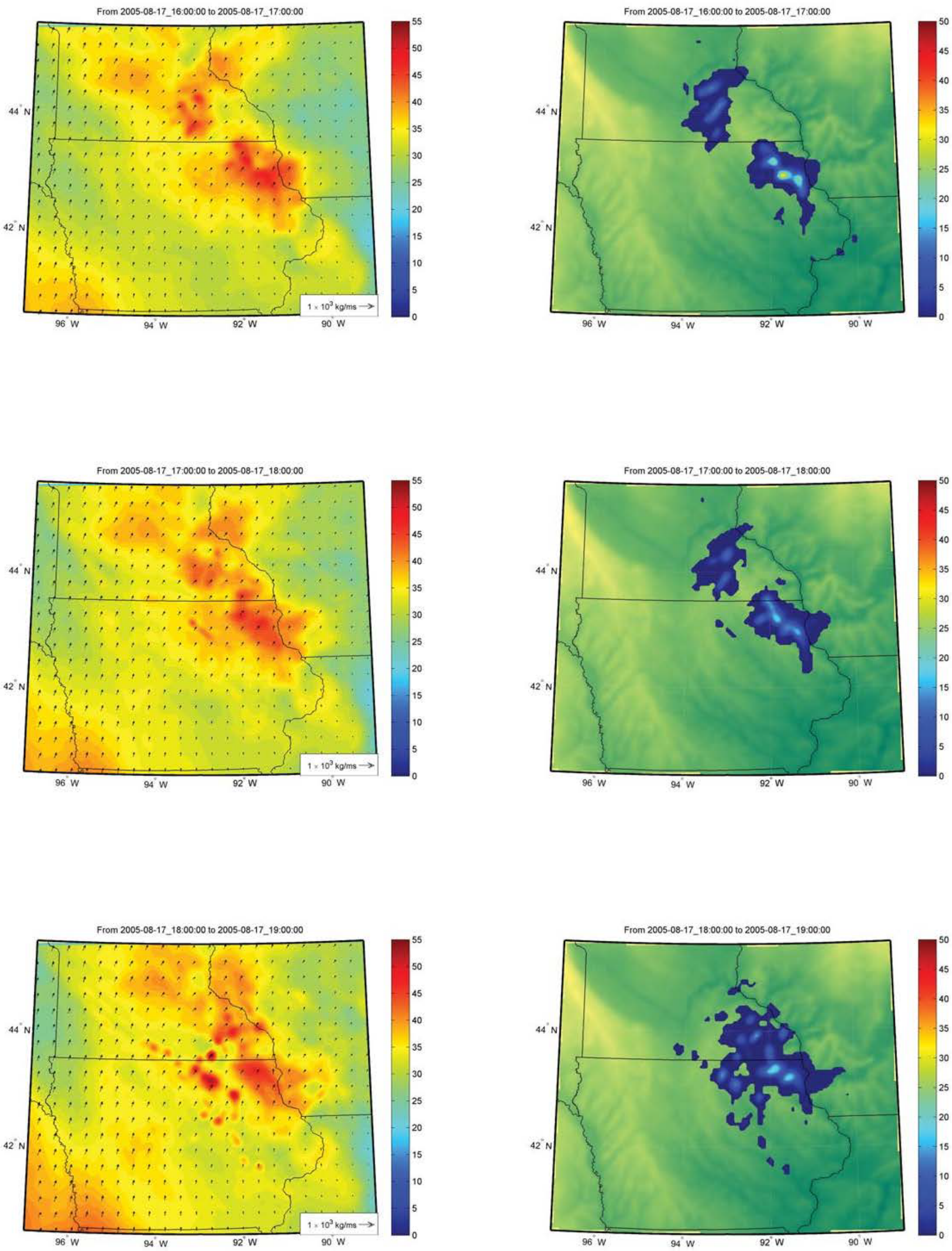

Figure B-5 Hourly Simulated Precipitable Water (Left, Colormap [mm]) and Water Vapor Flux Fields (Left, Arrows [kg m^{-1} s^{-1}]) and Precipitation Fields (Right, Colormap [mm]) for the August 17, 2005 MCS

Plots shown from 08/17/2005 at 16hr to 08/19/2005 at 06hr.

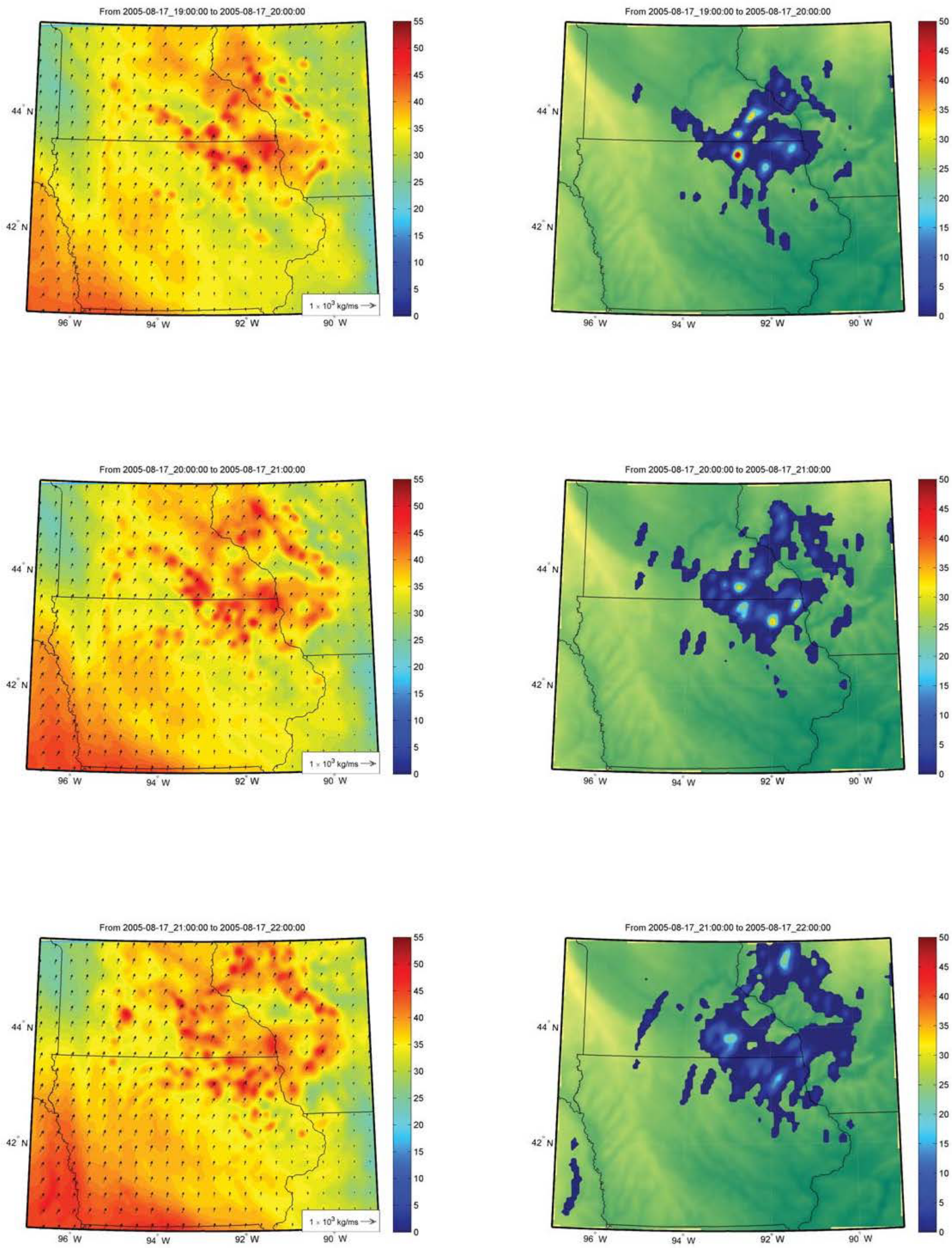

Figure B-5 Hourly Simulated Precipitable Water (Left, Colormap [mm]) and Water Vapor Flux Fields (Left, Arrows [kg m^{-1} s^{-1}]) and Precipitation Fields (Right, Colormap [mm]) for the August 17, 2005 MCS

Plots shown from 08/17/2005 at 16hr to 08/19/2005 at 06hr (Continued).

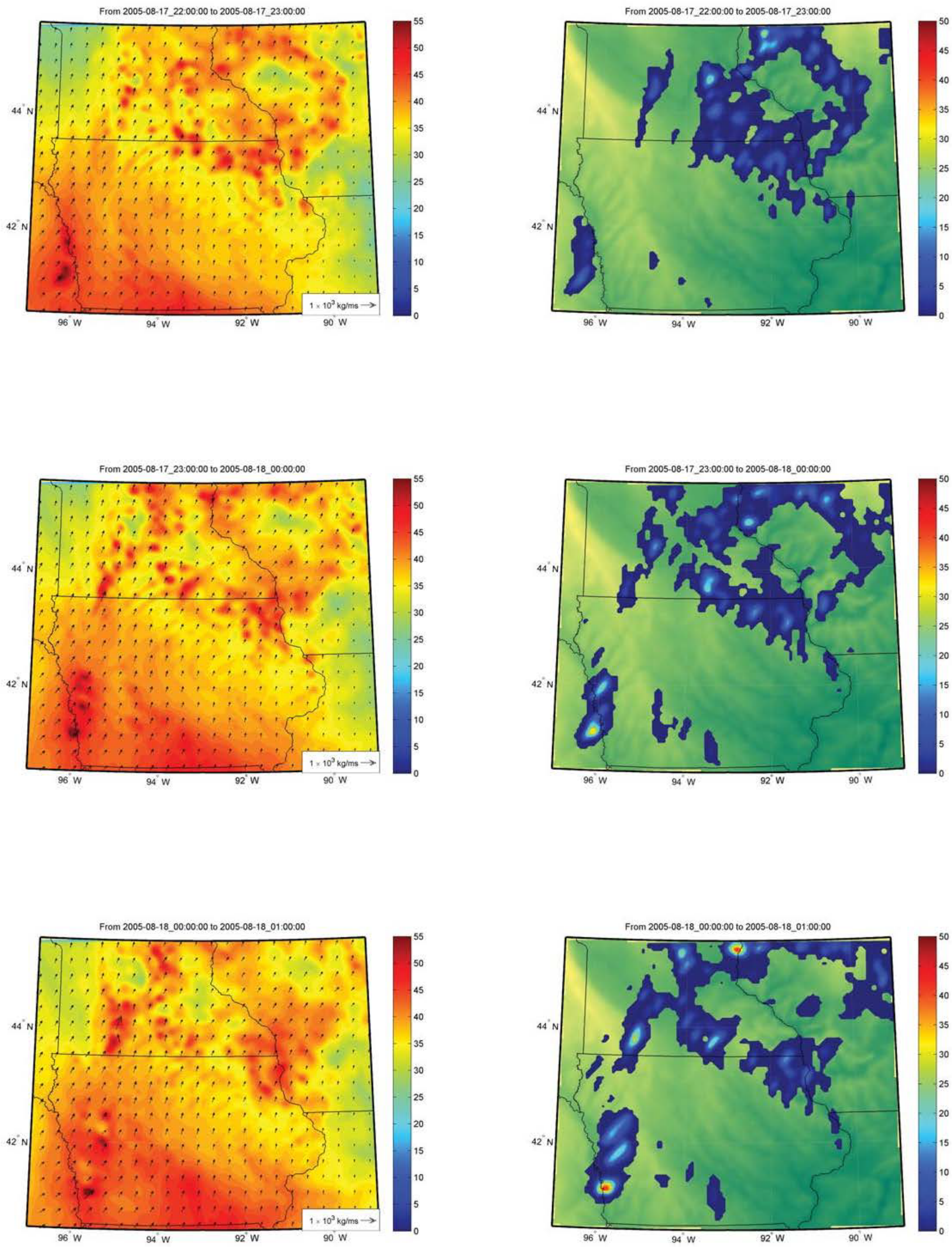

Figure B-5 Hourly Simulated Precipitable Water (Left, Colormap [mm]) and Water Vapor Flux Fields (Left, Arrows [kg m^{-1} s^{-1}]) and Precipitation Fields (Right, Colormap [mm]) for the August 17, 2005 MCS

Plots shown from 08/17/2005 at 16hr to 08/19/2005 at 06hr (Continued).

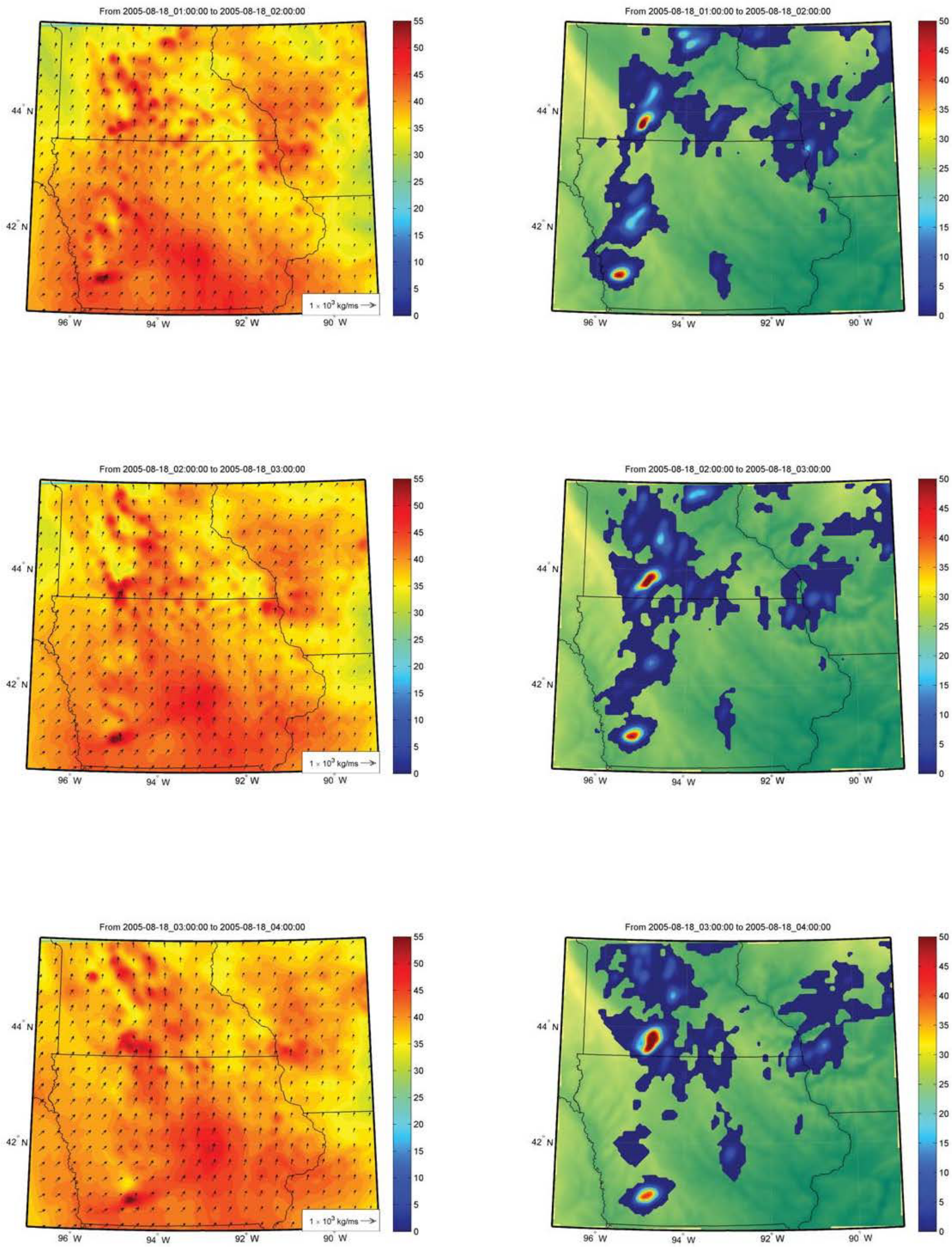

Figure B-5 Hourly Simulated Precipitable Water (Left, Colormap [mm]) and Water Vapor Flux Fields (Left, Arrows [kg m^{-1} s^{-1}]) and Precipitation Fields (Right, Colormap [mm]) for the August 17, 2005 MCS

Plots shown from 08/17/2005 at 16hr to 08/19/2005 at 06hr (Continued).

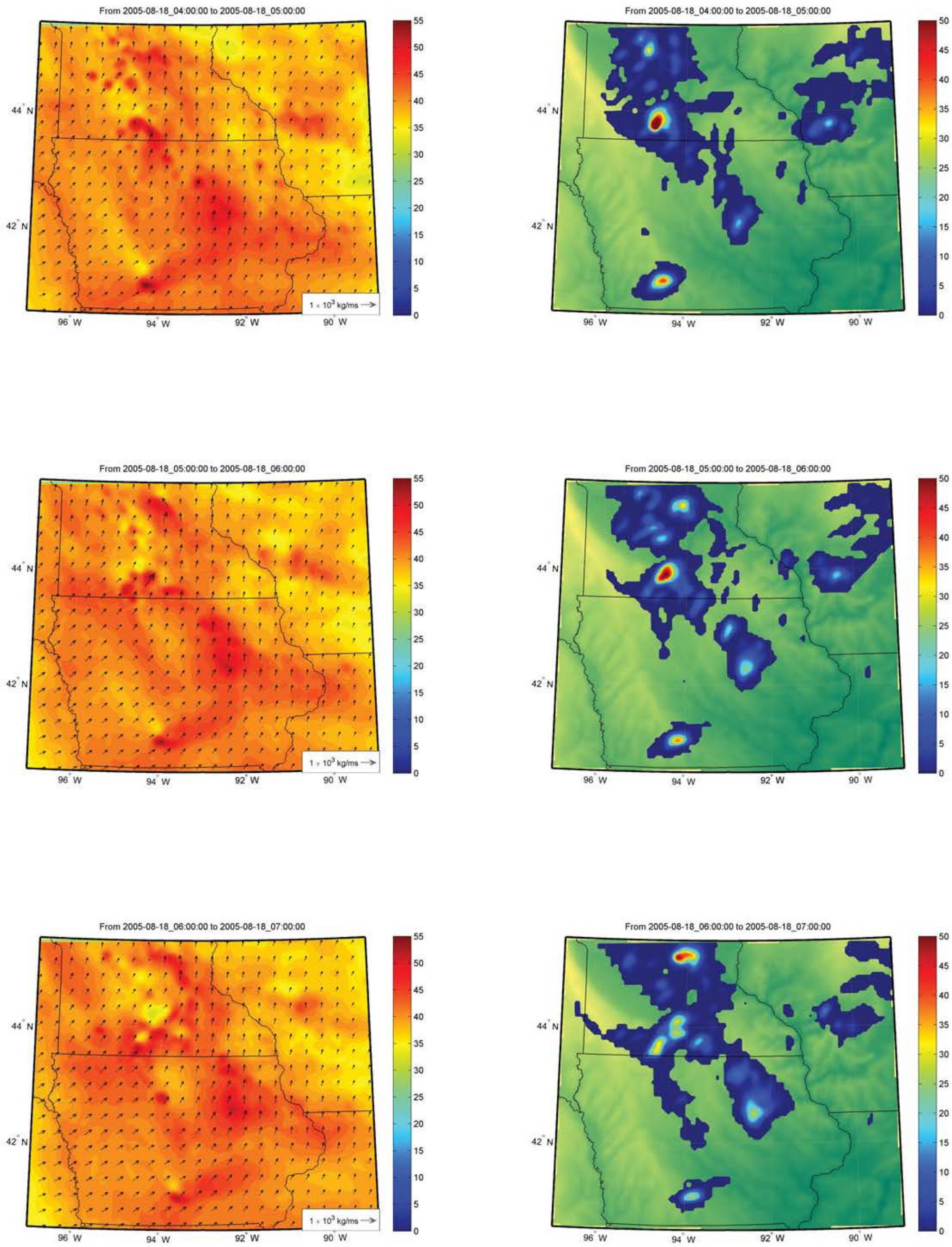

Figure B-5 Hourly Simulated Precipitable Water (Left, Colormap [mm]) and Water Vapor Flux Fields (Left, Arrows [kg m^{-1} s^{-1}]) and Precipitation Fields (Right, Colormap [mm]) for the August 17, 2005 MCS

Plots shown from 08/17/2005 at 16hr to 08/19/2005 at 06hr (Continued).

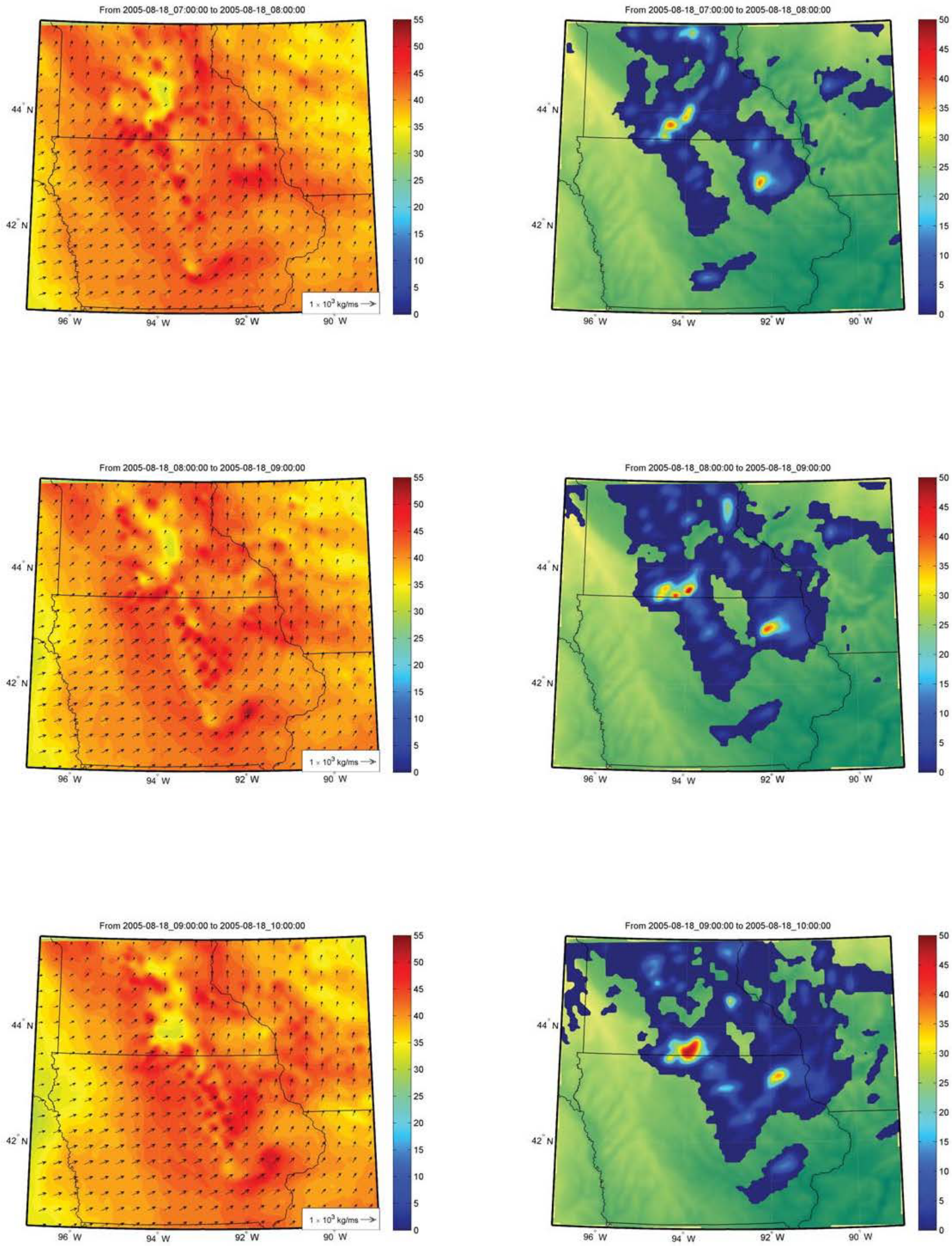

Figure B-5 **Hourly Simulated Precipitable Water (Left, Colormap [mm]) and Water Vapor Flux Fields (Left, Arrows [kg m^{-1} s^{-1}]) and Precipitation Fields (Right, Colormap [mm]) for the August 17, 2005 MCS**

Plots shown from 08/17/2005 at 16hr to 08/19/2005 at 06hr (Continued).

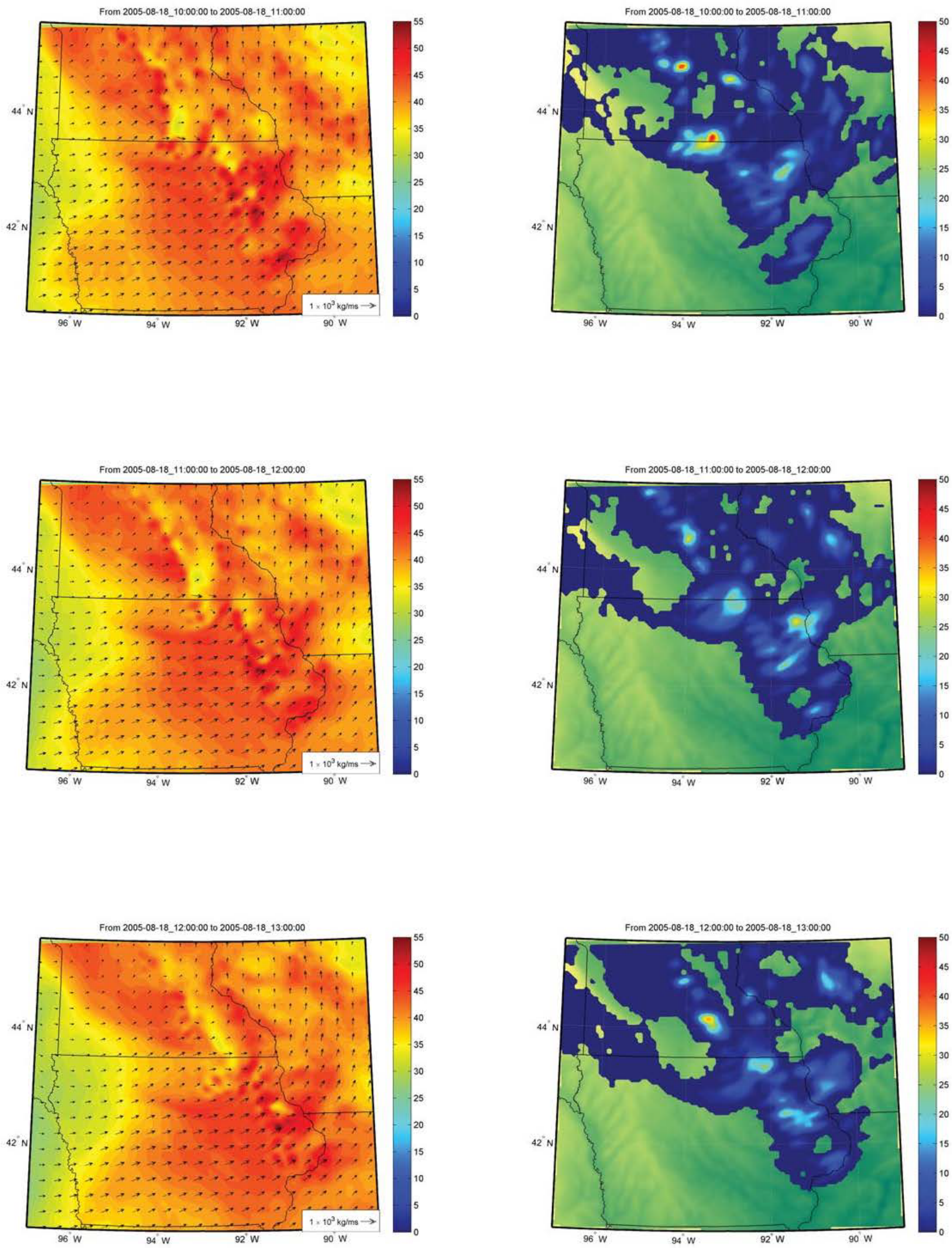

Figure B-5 Hourly Simulated Precipitable Water (Left, Colormap [mm]) and Water Vapor Flux Fields (Left, Arrows [kg m^{-1} s^{-1}]) and Precipitation Fields (Right, Colormap [mm]) for the August 17, 2005 MCS

Plots shown from 08/17/2005 at 16hr to 08/19/2005 at 06hr (Continued).

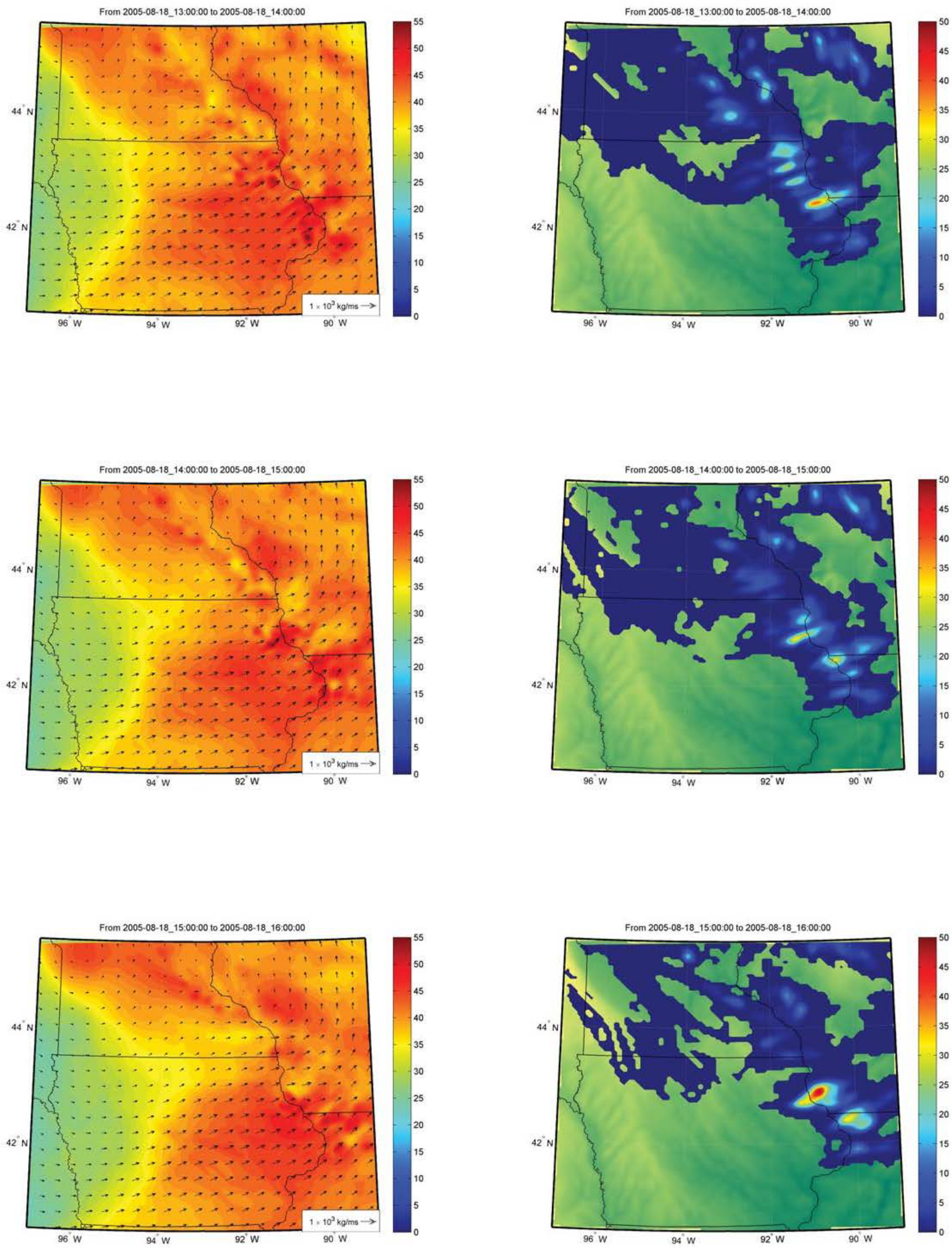

Figure B-5 Hourly Simulated Precipitable Water (Left, Colormap [mm]) and Water Vapor Flux Fields (Left, Arrows [kg m^{-1} s^{-1}]) and Precipitation Fields (Right, Colormap [mm]) for the August 17, 2005 MCS

Plots shown from 08/17/2005 at 16hr to 08/19/2005 at 06hr (Continued).

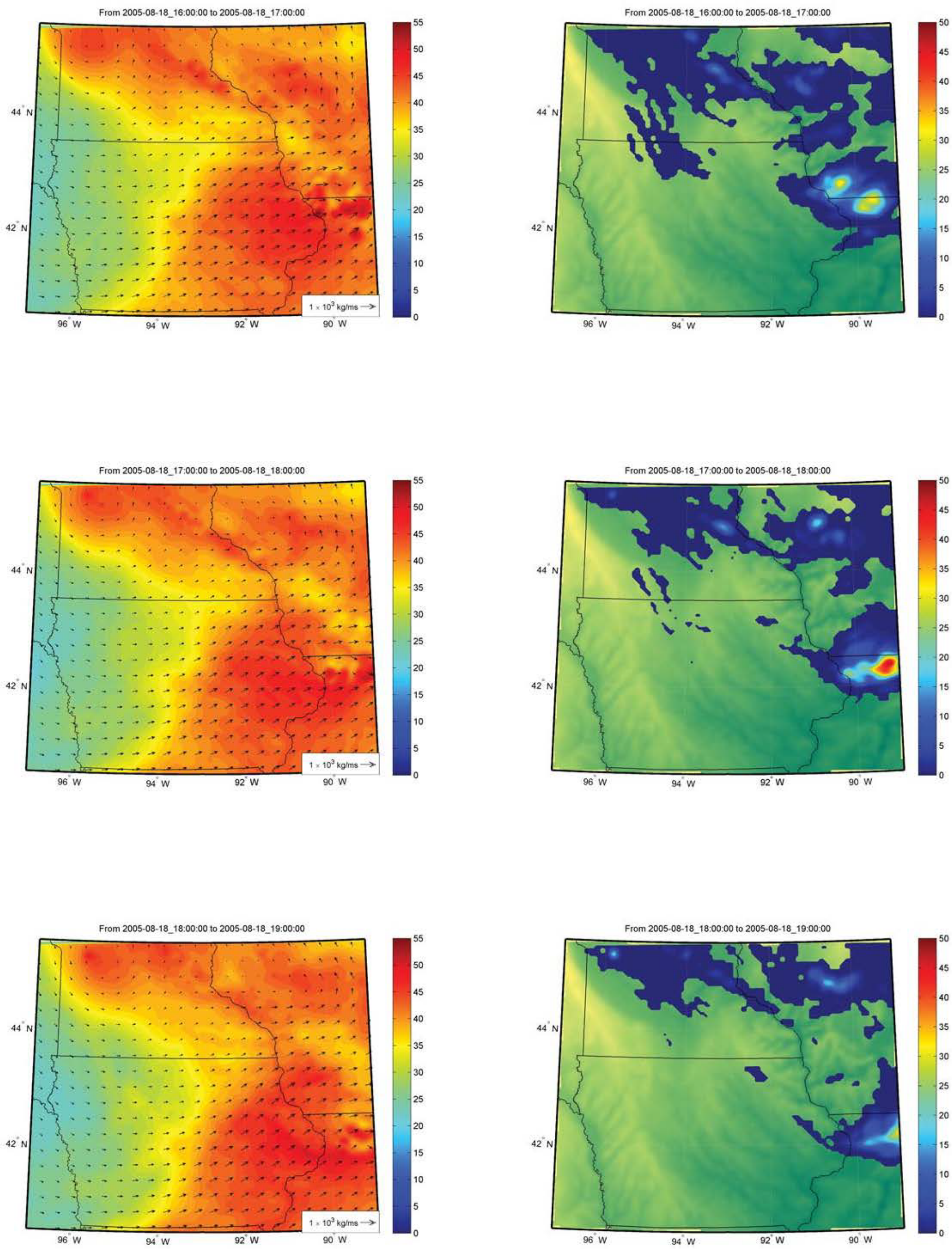

Figure B-5 Hourly Simulated Precipitable Water (Left, Colormap [mm]) and Water Vapor Flux Fields (Left, Arrows [kg m^{-1} s^{-1}]) and Precipitation Fields (Right, Colormap [mm]) for the August 17, 2005 MCS

Plots shown from 08/17/2005 at 16hr to 08/19/2005 at 06hr (Continued).

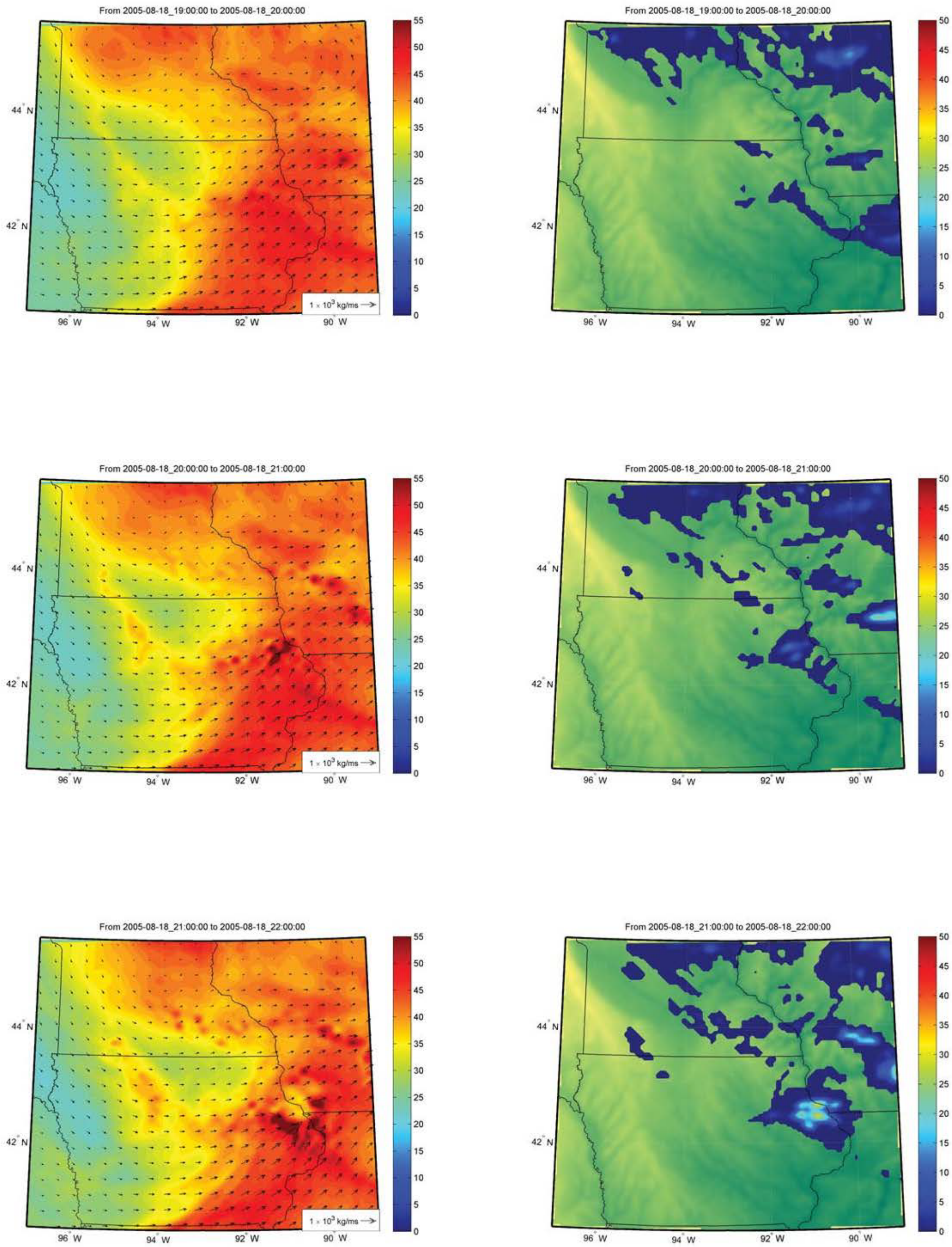

Figure B-5 Hourly Simulated Precipitable Water (Left, Colormap [mm]) and Water Vapor Flux Fields (Left, Arrows [kg m^{-1} s^{-1}]) and Precipitation Fields (Right, Colormap [mm]) for the August 17, 2005 MCS

Plots shown from 08/17/2005 at 16hr to 08/19/2005 at 06hr (Continued).

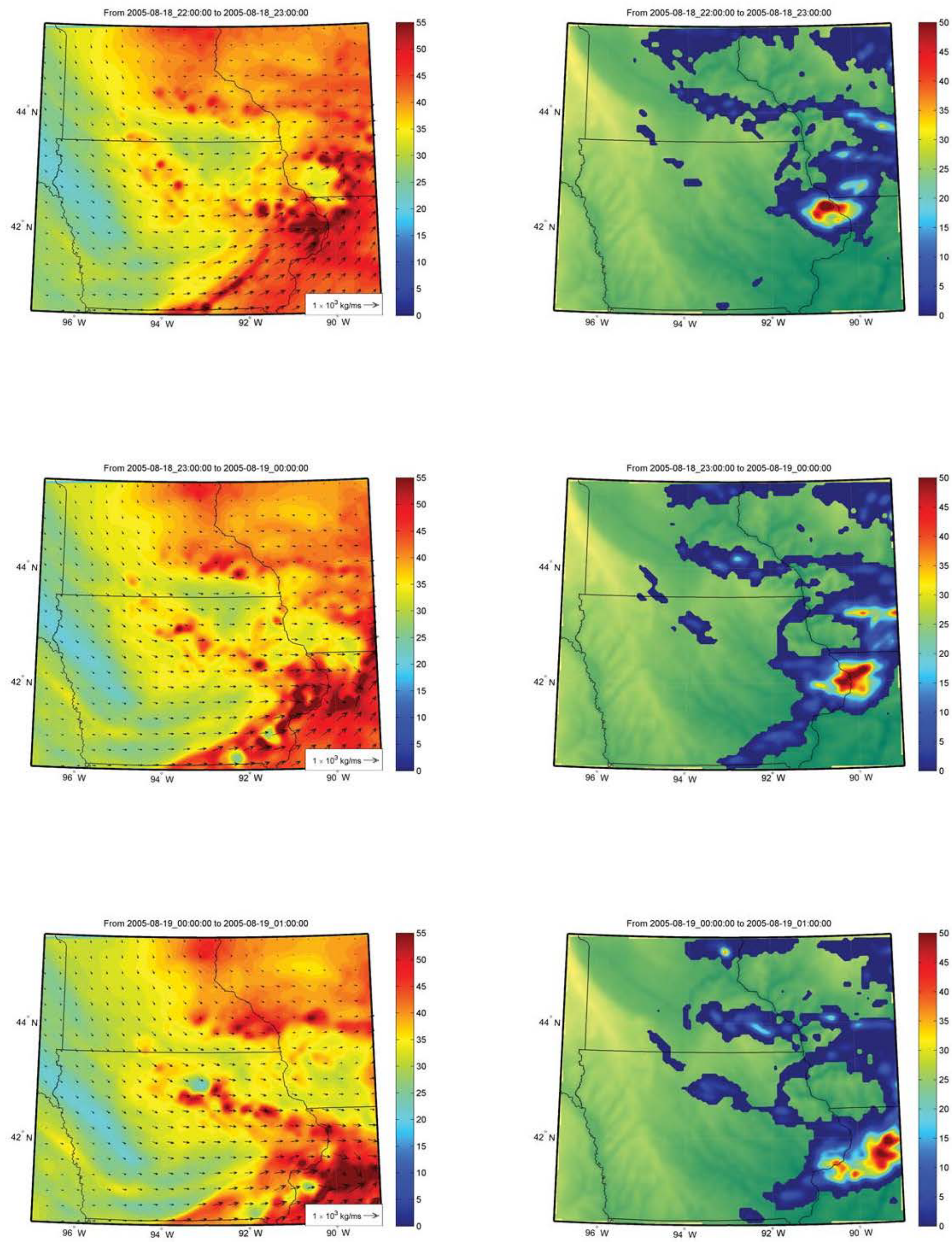

Figure B-5 **Hourly Simulated Precipitable Water (Left, Colormap [mm]) and Water Vapor Flux Fields (Left, Arrows [kg m^{-1} s^{-1}]) and Precipitation Fields (Right, Colormap [mm]) for the August 17, 2005 MCS**

Plots shown from 08/17/2005 at 16hr to 08/19/2005 at 06hr (Continued).

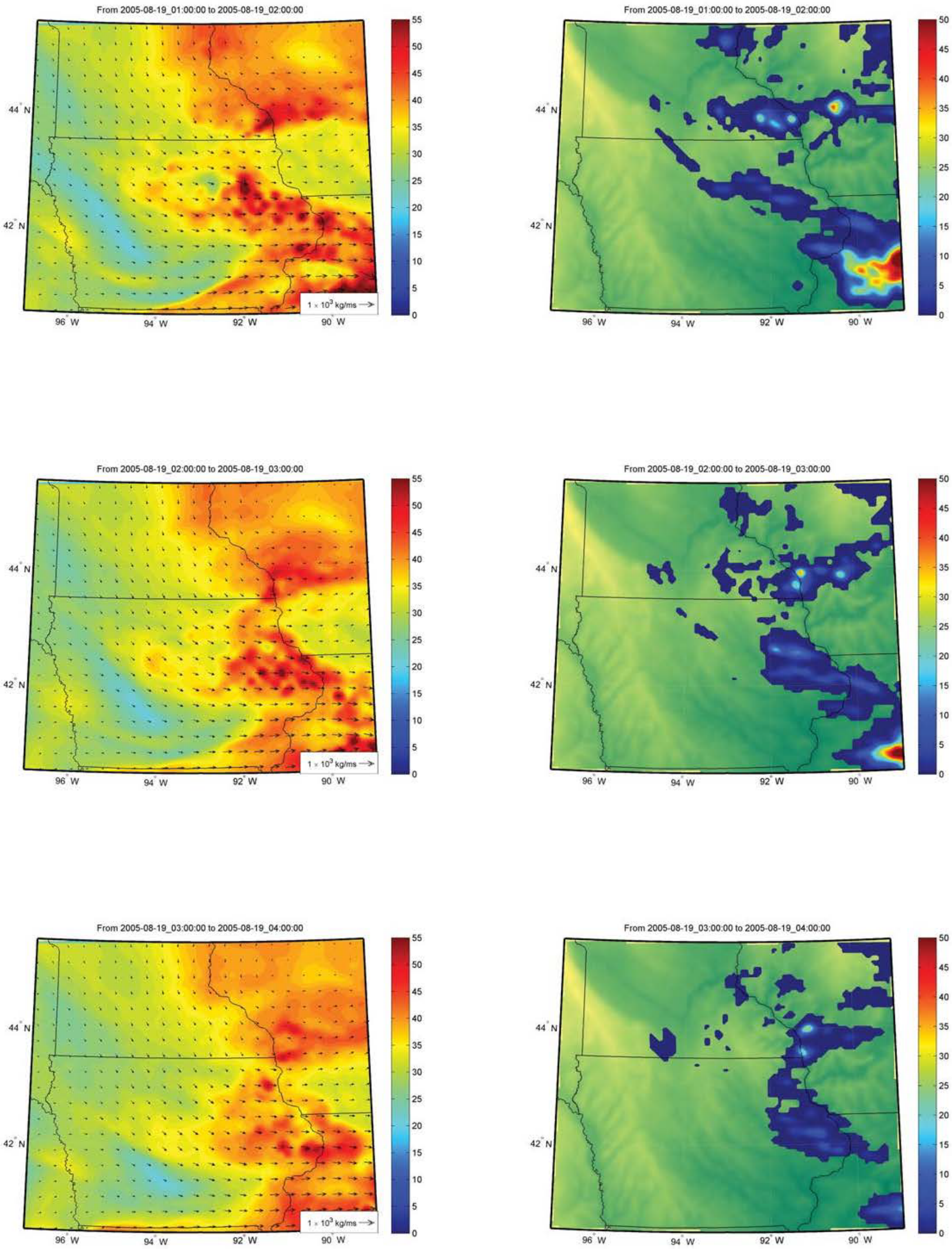

Figure B-5 Hourly Simulated Precipitable Water (Left, Colormap [mm]) and Water Vapor Flux Fields (Left, Arrows [kg m^{-1} s^{-1}]) and Precipitation Fields (Right, Colormap [mm]) for the August 17, 2005 MCS

Plots shown from 08/17/2005 at 16hr to 08/19/2005 at 06hr (Continued).

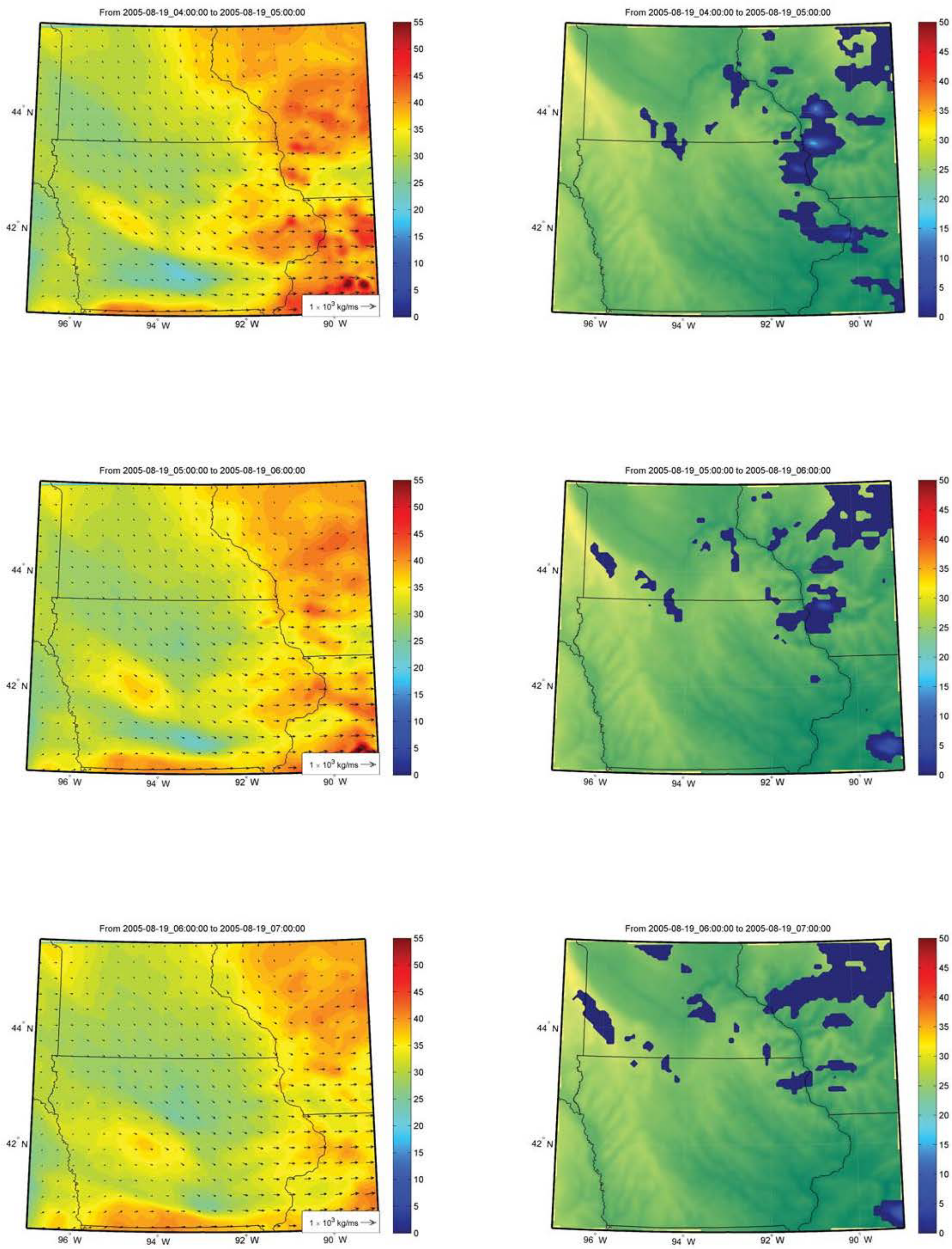

Figure B-5 Hourly Simulated Precipitable Water (Left, Colormap [mm]) and Water Vapor Flux Fields (Left, Arrows [kg m^{-1} s^{-1}]) and Precipitation Fields (Right, Colormap [mm]) for the August 17, 2005 MCS

Plots shown from 08/17/2005 at 16hr to 08/19/2005 at 06hr (Continued).

B.1.6 September 25, 2005 MCS

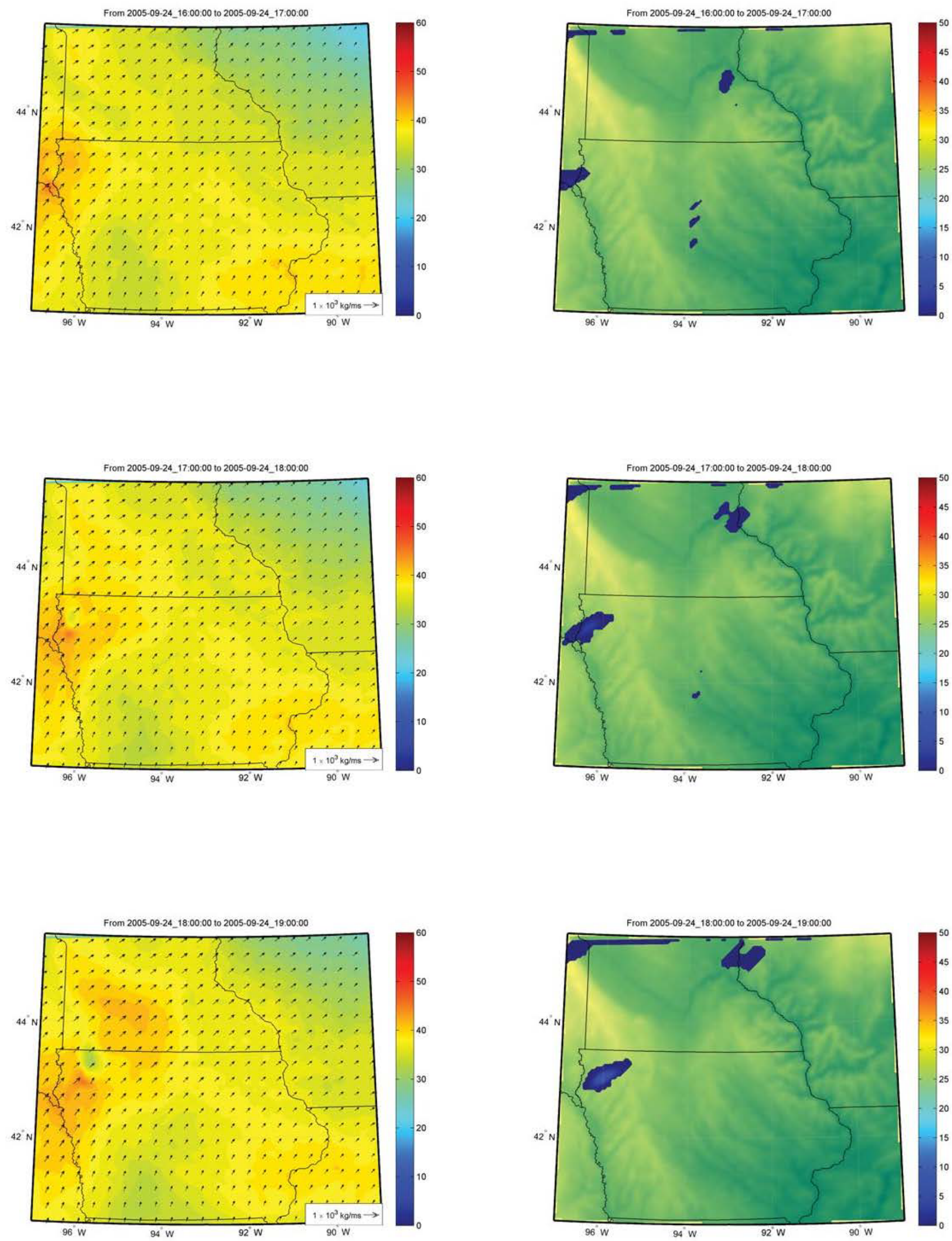

Figure B-6 Hourly Simulated Precipitable Water (Left, Colormap [mm]) and Water Vapor Flux Fields (Left, Arrows [kg m^{-1} s^{-1}]) and Precipitation Fields (Right, Colormap [mm]) for the September 25, 2005 MCS

Plots shown from 09/24/2005 at 17hr to 09/26/2005 at 07hr.

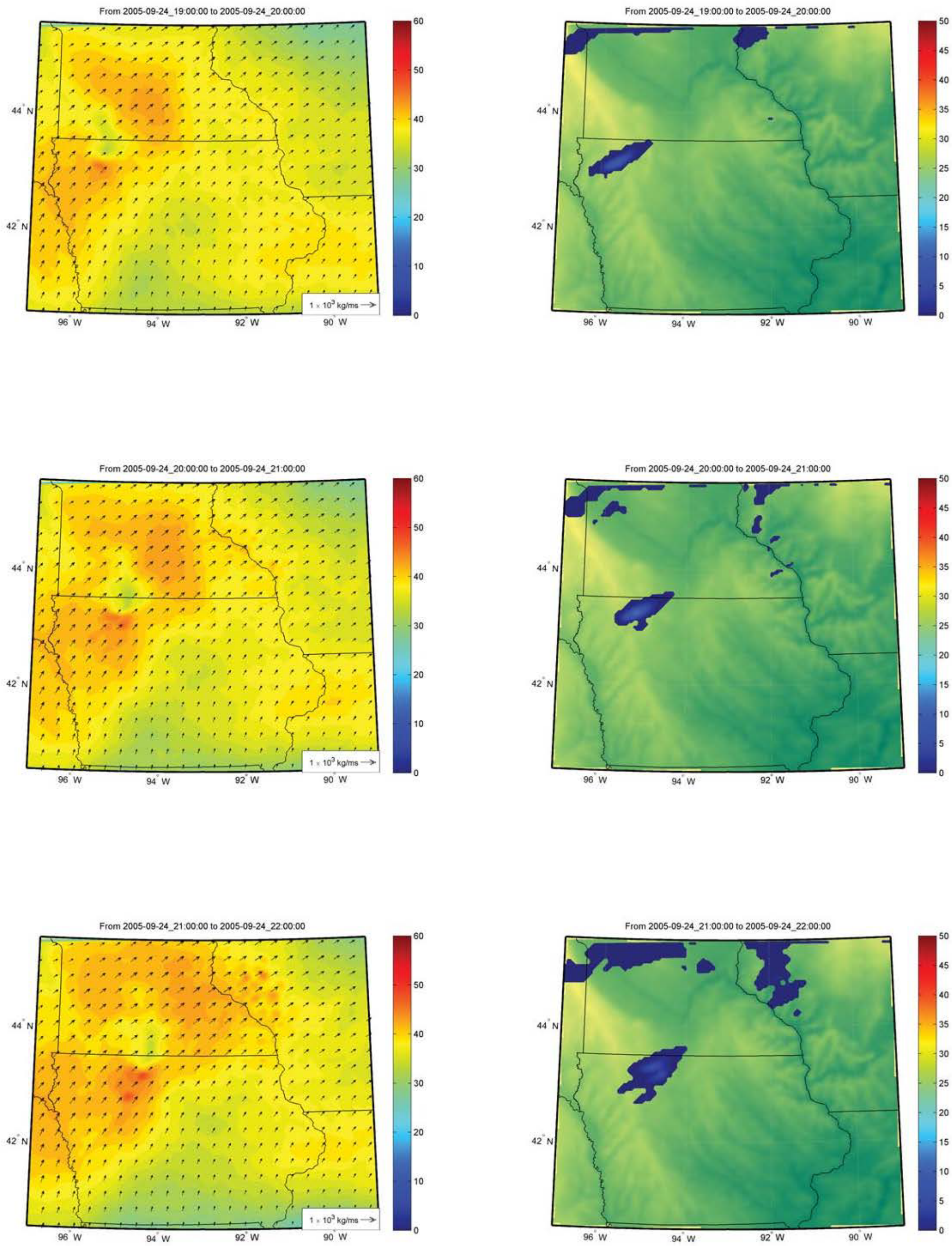

Figure B-6 Hourly Simulated Precipitable Water (Left, Colormap [mm]) and Water Vapor Flux Fields (Left, Arrows [kg m^{-1} s^{-1}]) and Precipitation Fields (Right, Colormap [mm]) for the September 25, 2005 MCS

Plots shown from 09/24/2005 at 17hr to 09/26/2005 at 07hr (Continued).

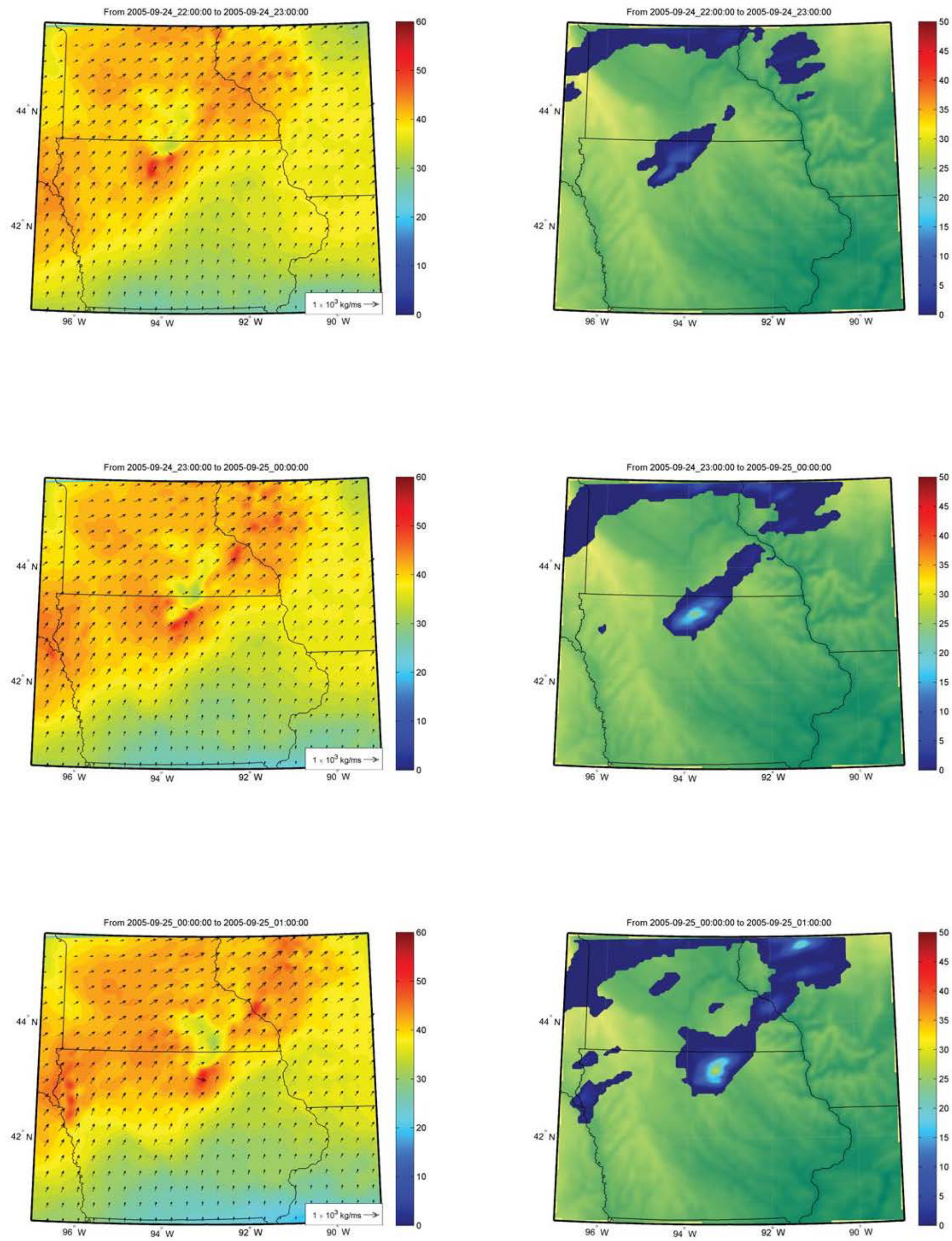

Figure B-6 Hourly Simulated Precipitable Water (Left, Colormap [mm]) and Water Vapor Flux Fields (Left, Arrows [kg m^{-1} s^{-1}]) and Precipitation Fields (Right, Colormap [mm]) for the September 25, 2005 MCS

Plots shown from 09/24/2005 at 17hr to 09/26/2005 at 07hr (Continued).

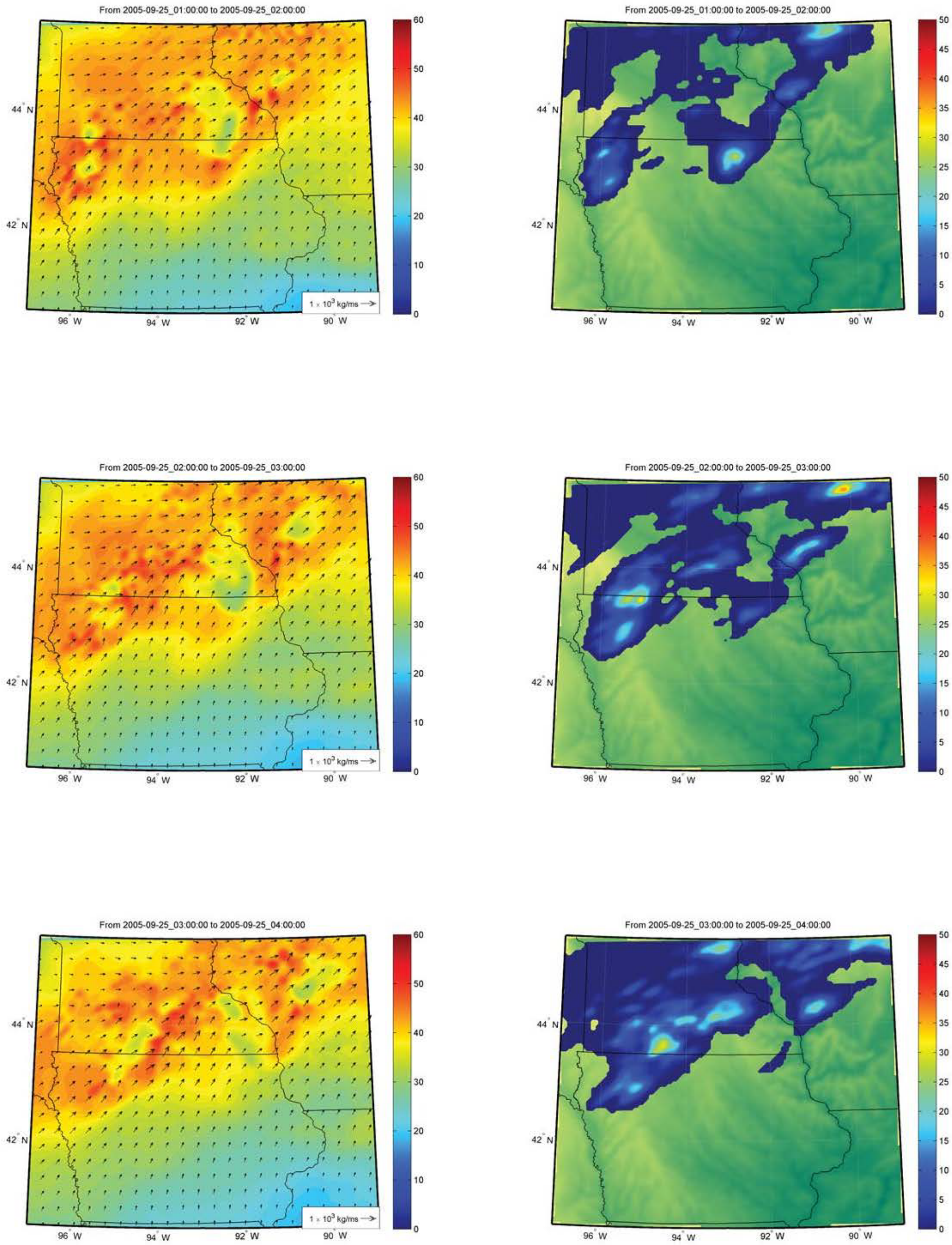

Figure B-6 Hourly Simulated Precipitable Water (Left, Colormap [mm]) and Water Vapor Flux Fields (Left, Arrows [kg m^{-1} s^{-1}]) and Precipitation Fields (Right, Colormap [mm]) for the September 25, 2005 MCS

Plots shown from 09/24/2005 at 17hr to 09/26/2005 at 07hr (Continued).

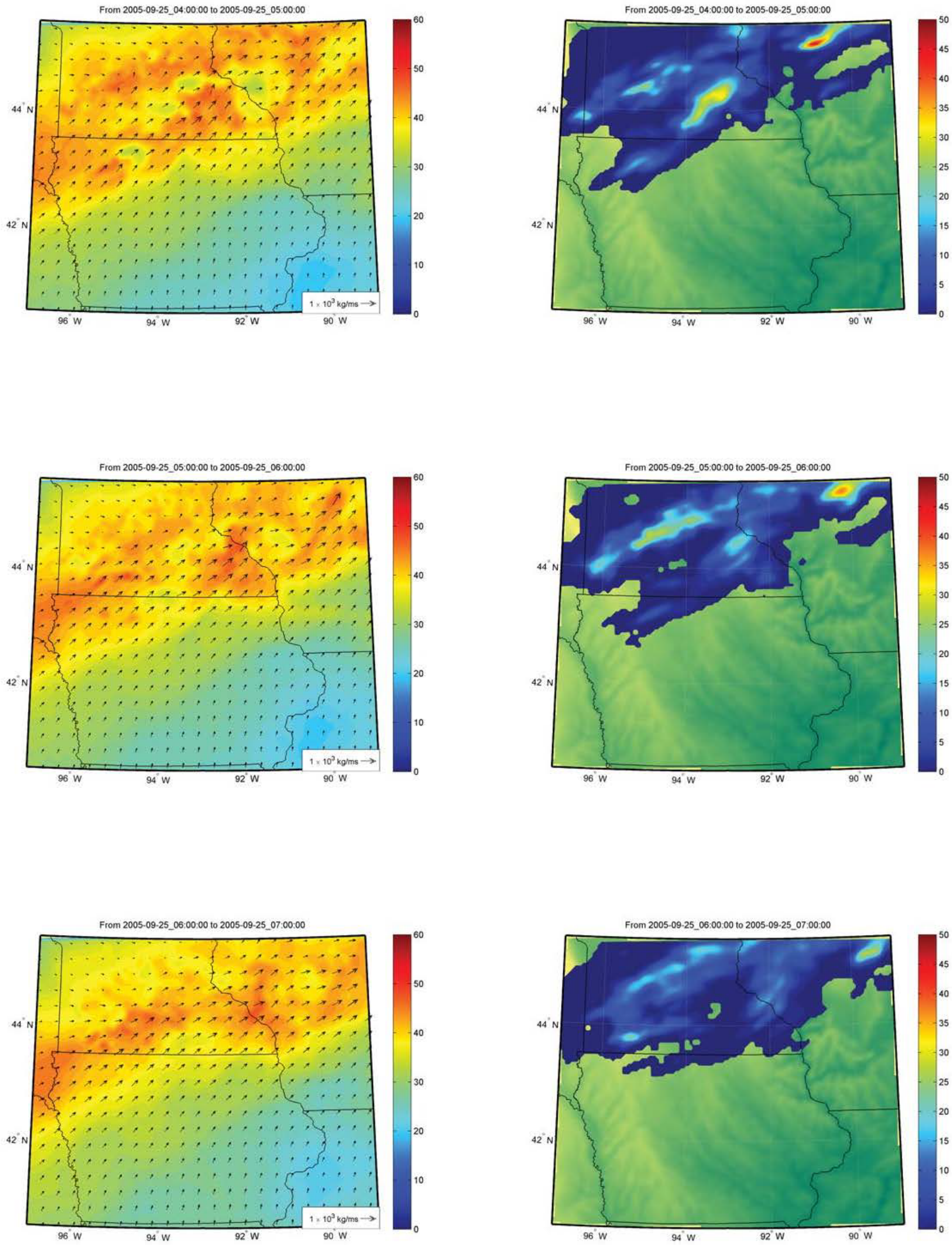

Figure B-6 Hourly Simulated Precipitable Water (Left, Colormap [mm]) and Water Vapor Flux Fields (Left, Arrows [kg m^{-1} s^{-1}]) and Precipitation Fields (Right, Colormap [mm]) for the September 25, 2005 MCS

Plots shown from 09/24/2005 at 17hr to 09/26/2005 at 07hr (Continued).

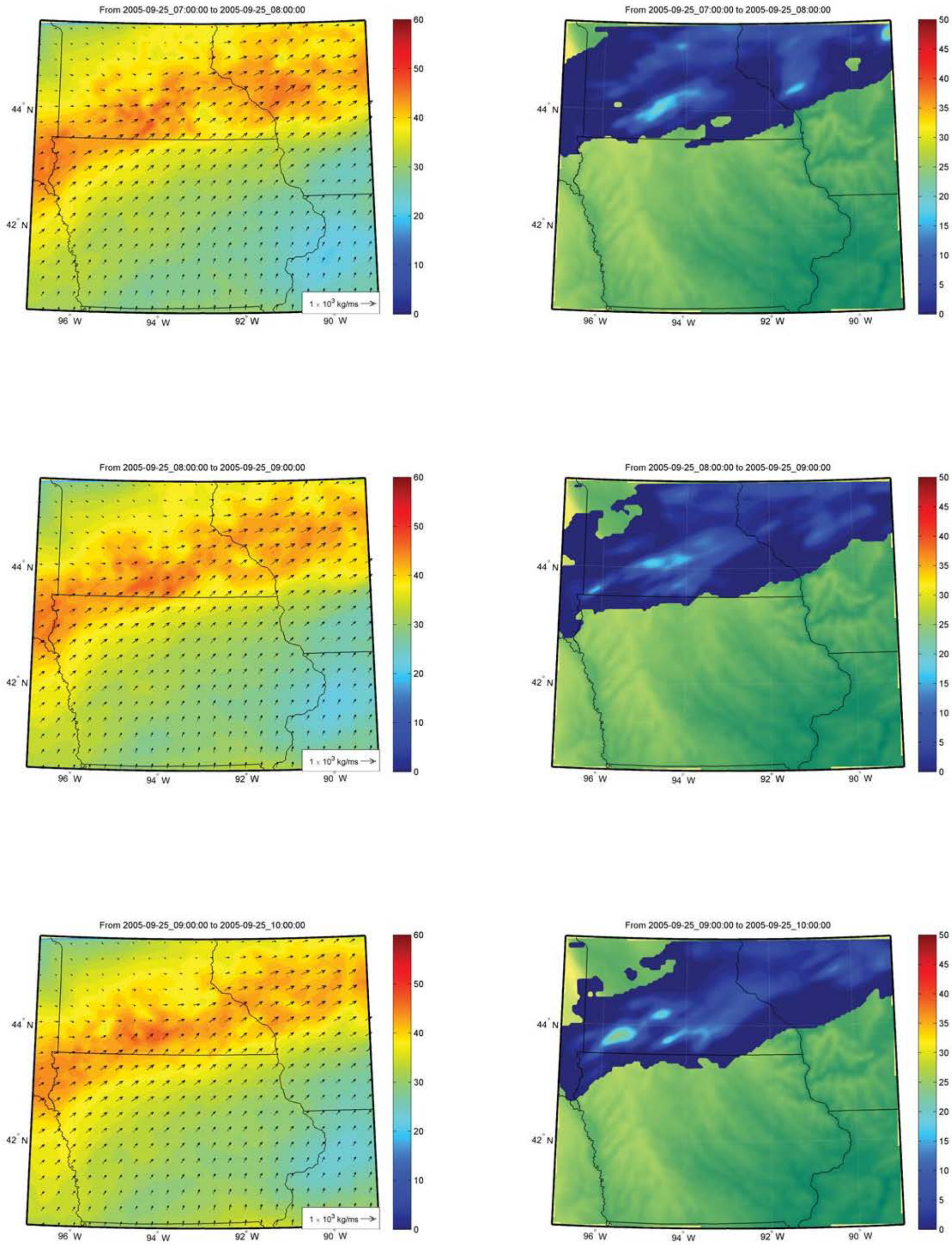

Figure B-6 Hourly Simulated Precipitable Water (Left, Colormap [mm]) and Water Vapor Flux Fields (Left, Arrows [kg m^{-1} s^{-1}]) and Precipitation Fields (Right, Colormap [mm]) for the September 25, 2005 MCS

Plots shown from 09/24/2005 at 17hr to 09/26/2005 at 07hr (Continued).

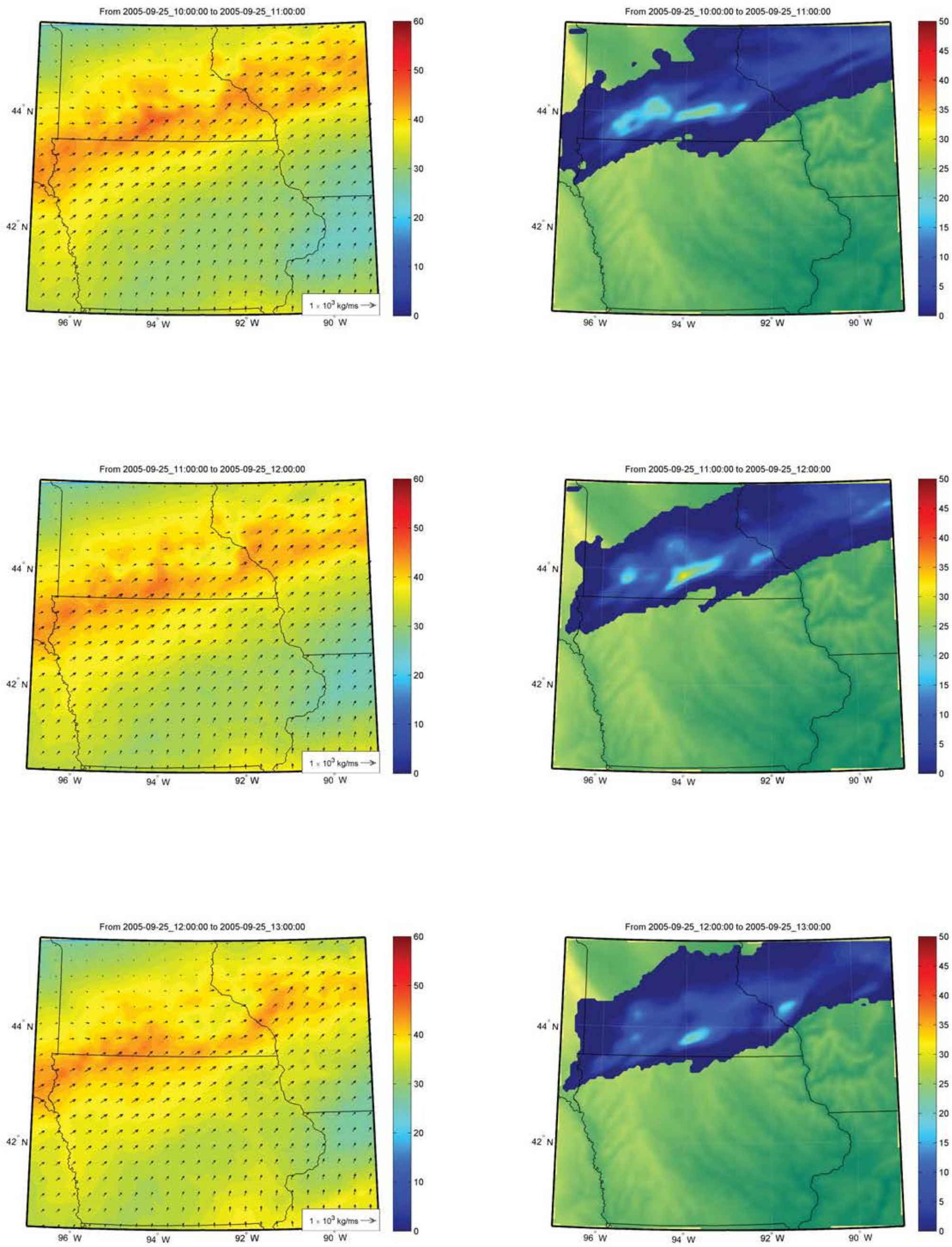

Figure B-6 Hourly Simulated Precipitable Water (Left, Colormap [mm]) and Water Vapor Flux Fields (Left, Arrows [kg m^{-1} s^{-1}]) and Precipitation Fields (Right, Colormap [mm]) for the September 25, 2005 MCS

Plots shown from 09/24/2005 at 17hr to 09/26/2005 at 07hr (Continued).

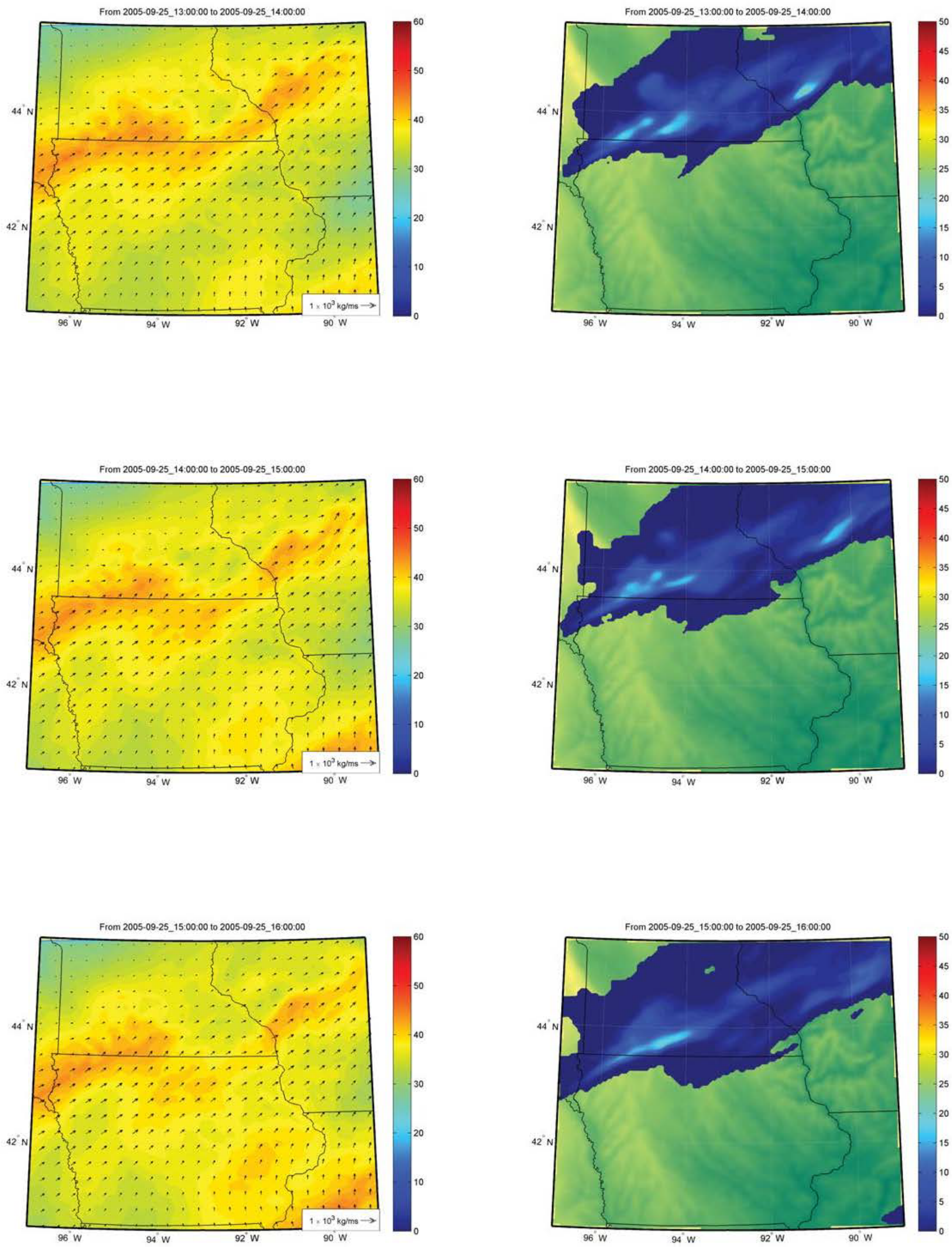

Figure B-6 **Hourly Simulated Precipitable Water (Left, Colormap [mm]) and Water Vapor Flux Fields (Left, Arrows [kg m^{-1} s^{-1}]) and Precipitation Fields (Right, Colormap [mm]) for the September 25, 2005 MCS**

Plots shown from 09/24/2005 at 17hr to 09/26/2005 at 07hr (Continued).

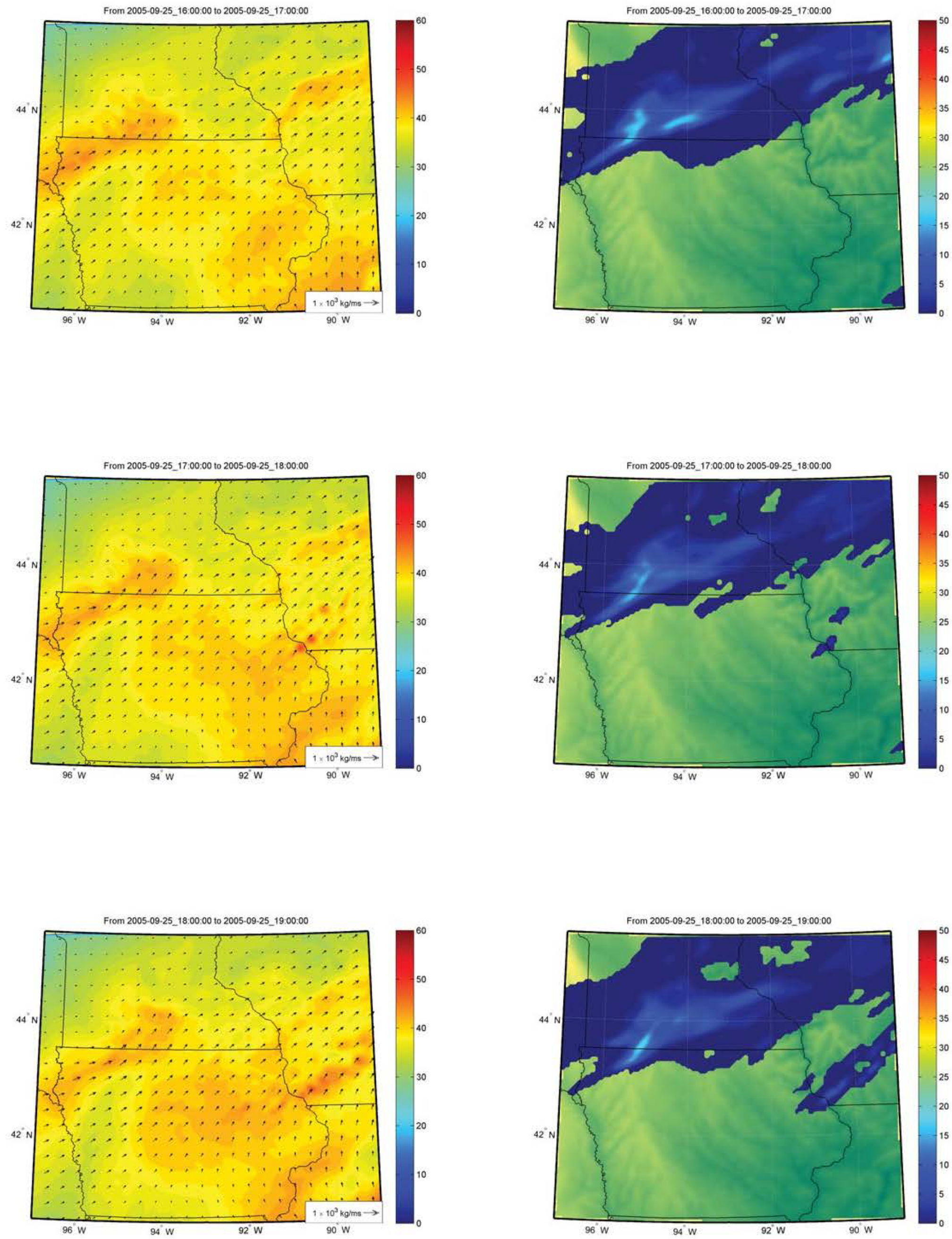

Figure B-6 **Hourly Simulated Precipitable Water (Left, Colormap [mm]) and Water Vapor Flux Fields (Left, Arrows [kg m^{-1} s^{-1}]) and Precipitation Fields (Right, Colormap [mm]) for the September 25, 2005 MCS**

Plots shown from 09/24/2005 at 17hr to 09/26/2005 at 07hr (Continued).

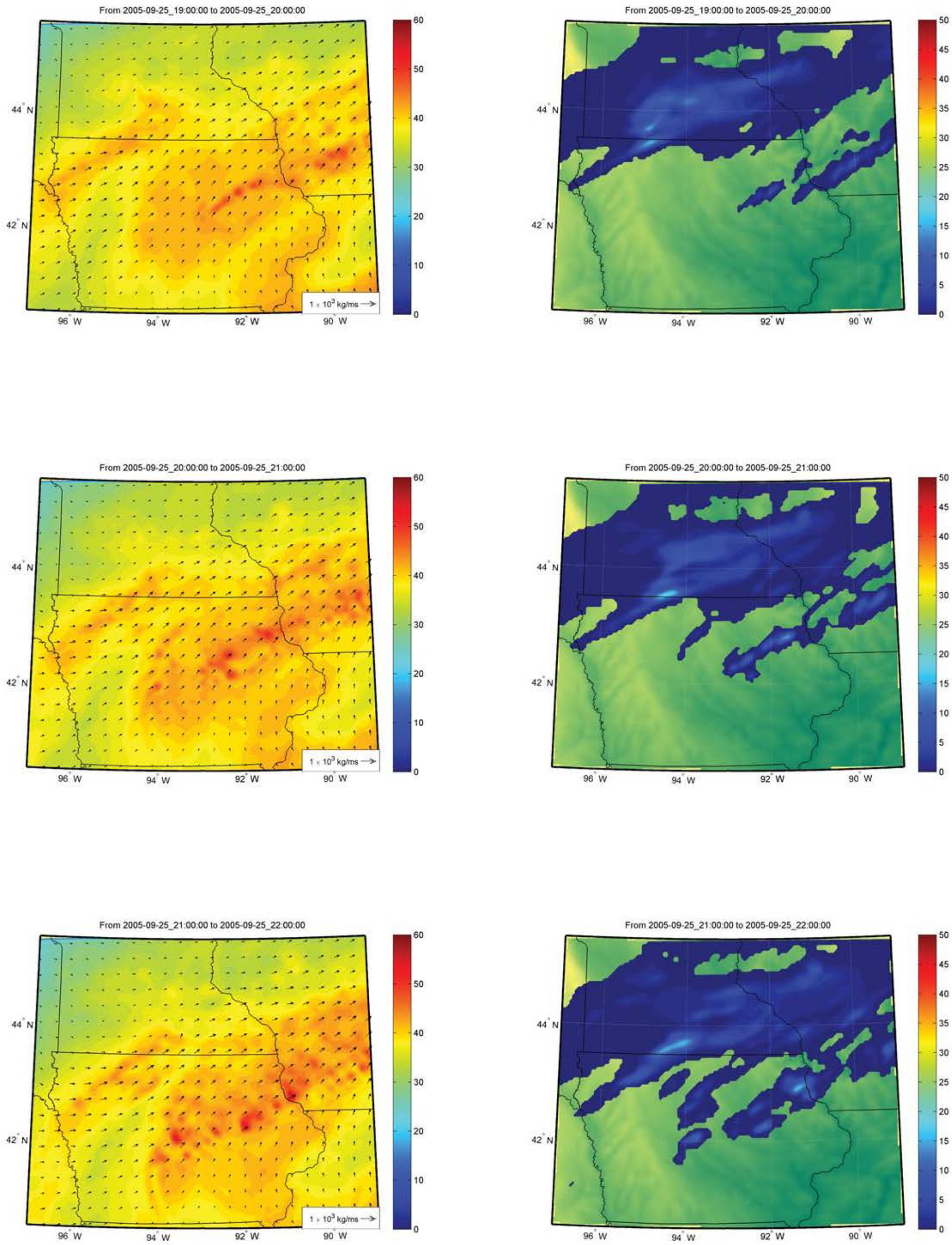

Figure B-6 **Hourly Simulated Precipitable Water (Left, Colormap [mm]) and Water Vapor Flux Fields (Left, Arrows [kg m^{-1} s^{-1}]) and Precipitation Fields (Right, Colormap [mm]) for the September 25, 2005 MCS**

Plots shown from 09/24/2005 at 17hr to 09/26/2005 at 07hr (Continued).

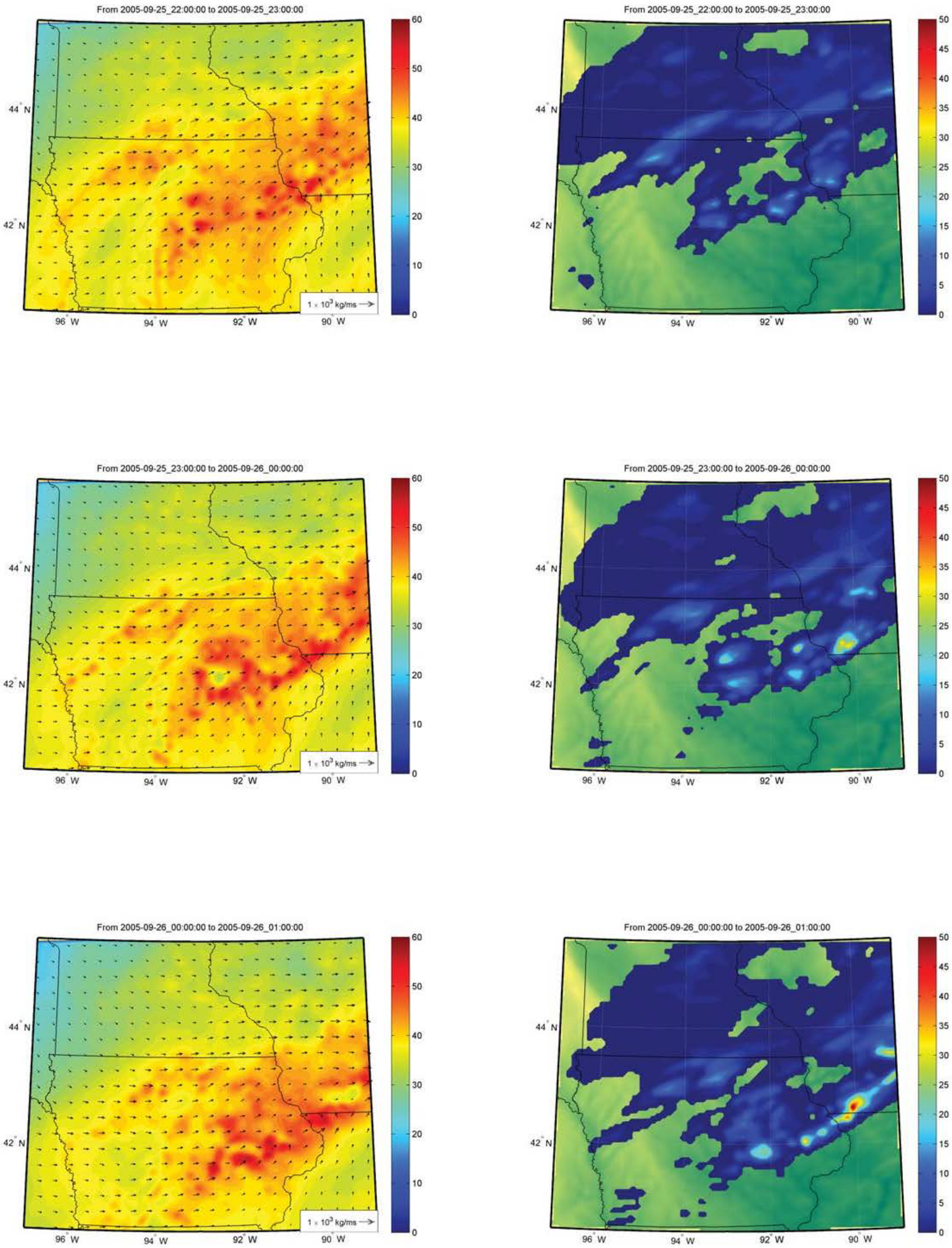

Figure B-6 Hourly Simulated Precipitable Water (Left, Colormap [mm]) and Water Vapor Flux Fields (Left, Arrows [kg m^{-1} s^{-1}]) and Precipitation Fields (Right, Colormap [mm]) for the September 25, 2005 MCS

Plots shown from 09/24/2005 at 17hr to 09/26/2005 at 07hr (Continued).

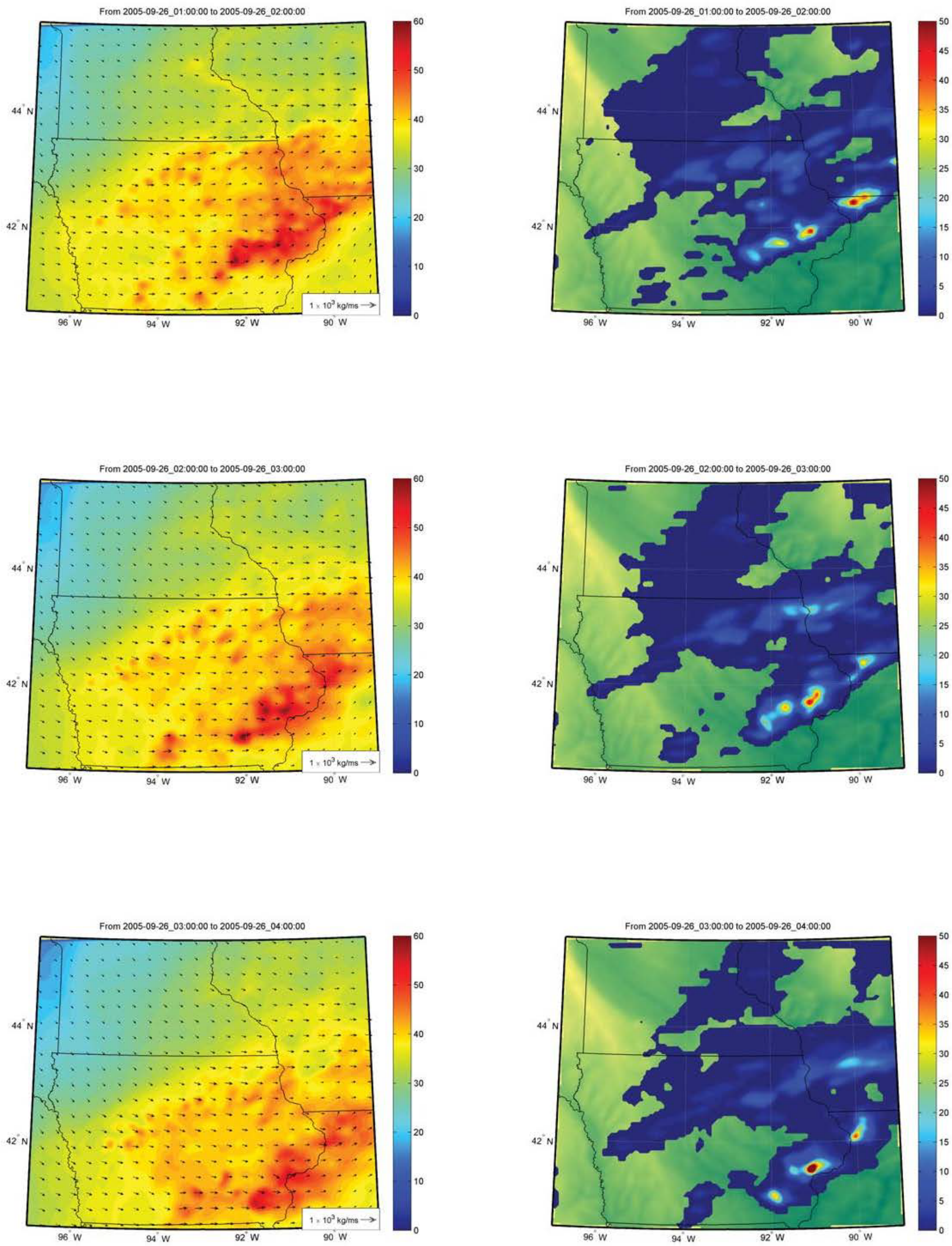

Figure B-6 Hourly Simulated Precipitable Water (Left, Colormap [mm]) and Water Vapor Flux Fields (Left, Arrows [kg m^{-1} s^{-1}]) and Precipitation Fields (Right, Colormap [mm]) for the September 25, 2005 MCS

Plots shown from 09/24/2005 at 17hr to 09/26/2005 at 07hr (Continued).

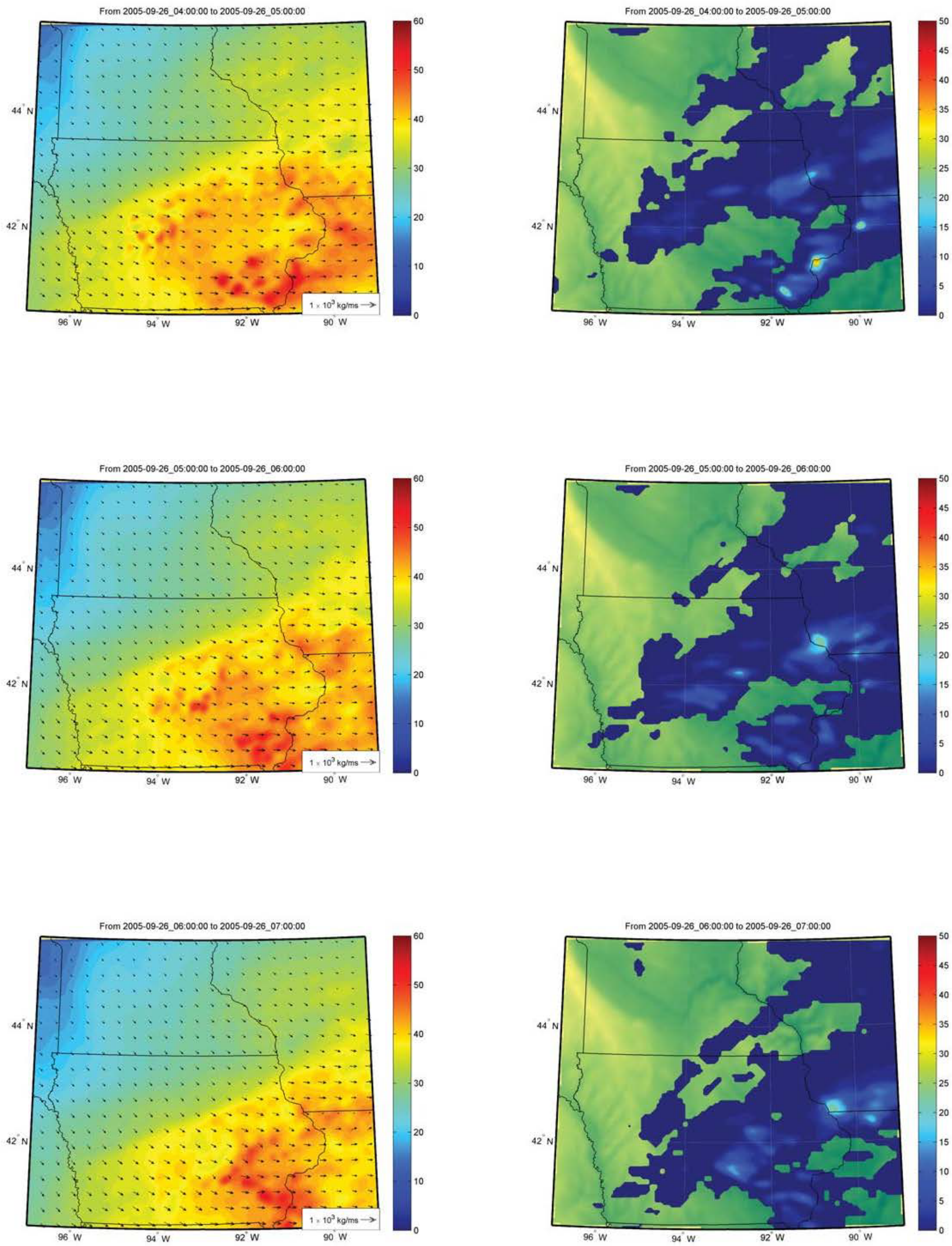

Figure B-6 Hourly Simulated Precipitable Water (Left, Colormap [mm]) and Water Vapor Flux Fields (Left, Arrows [kg m^{-1} s^{-1}]) and Precipitation Fields (Right, Colormap [mm]) for the September 25, 2005 MCS

Plots shown from 09/24/2005 at 17hr to 09/26/2005 at 07hr (Continued).

B.1.7 July 18, 2007 MCS

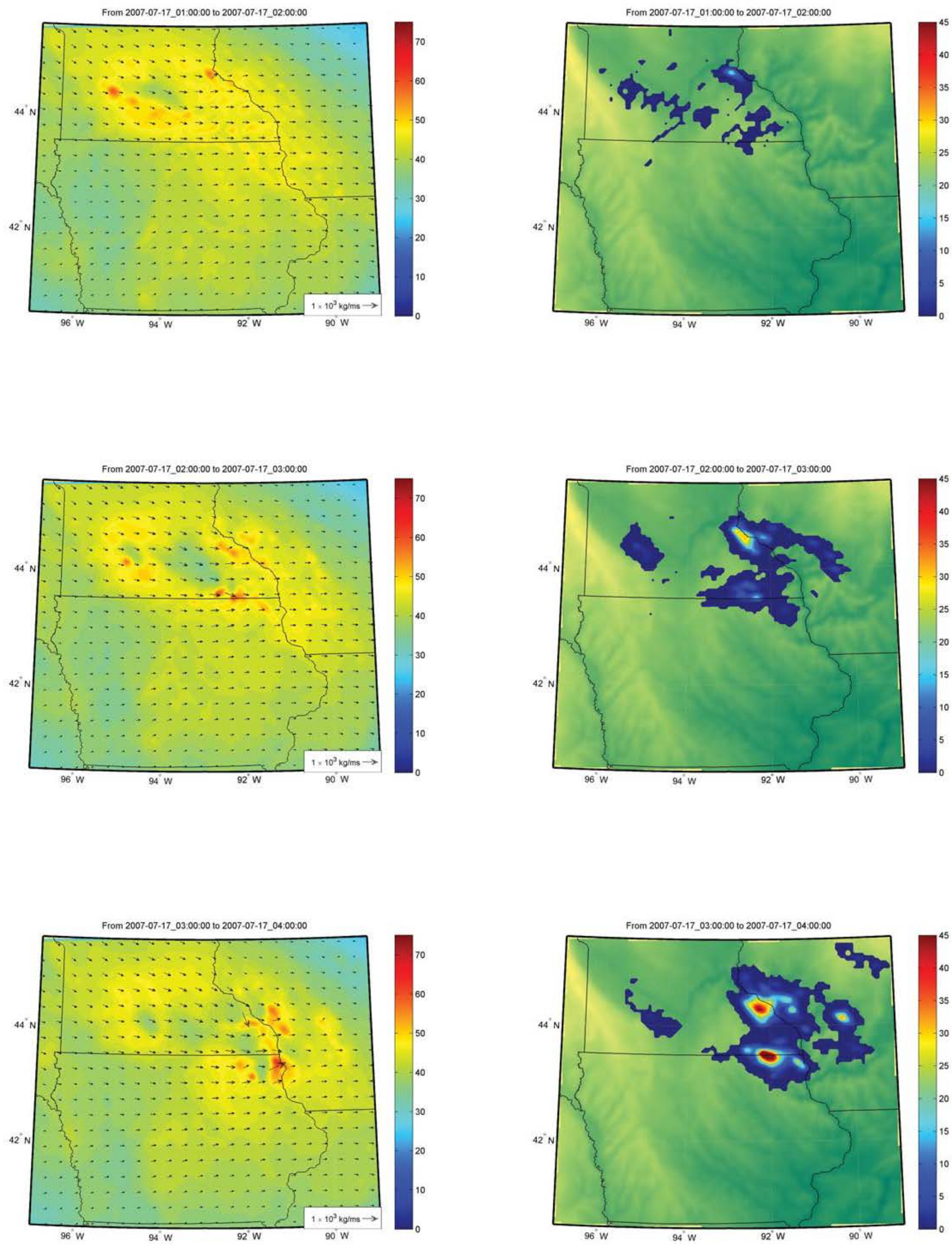

Figure B-7 Hourly Simulated Precipitable Water (Left, Colormap [mm]) and Water Vapor Flux Fields (Left, Arrows [kg m^{-1} s^{-1}]) and Precipitation Fields (Right, Colormap [mm]) for the July 18, 2007 MCS

Plots shown from 07/17/2007 at 01hr to 07/18/2007 at 12hr.

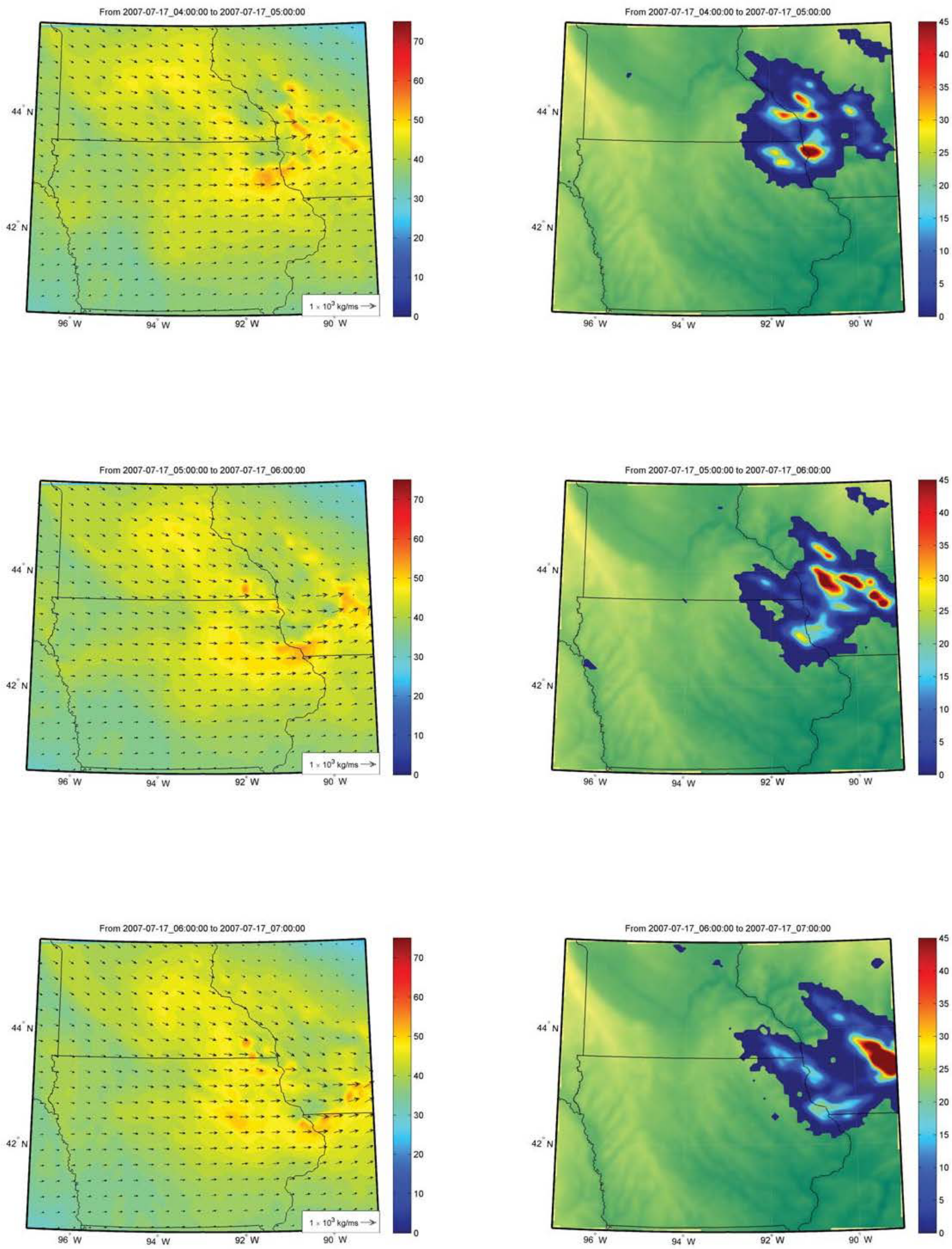

Figure B-7 Hourly Simulated Precipitable Water (Left, Colormap [mm]) and Water Vapor Flux Fields (Left, Arrows [kg m^{-1} s^{-1}]) and Precipitation Fields (Right, Colormap [mm]) for the July 18, 2007 MCS

Plots shown from 07/17/2007 at 01hr to 07/18/2007 at 12hr (Continued).

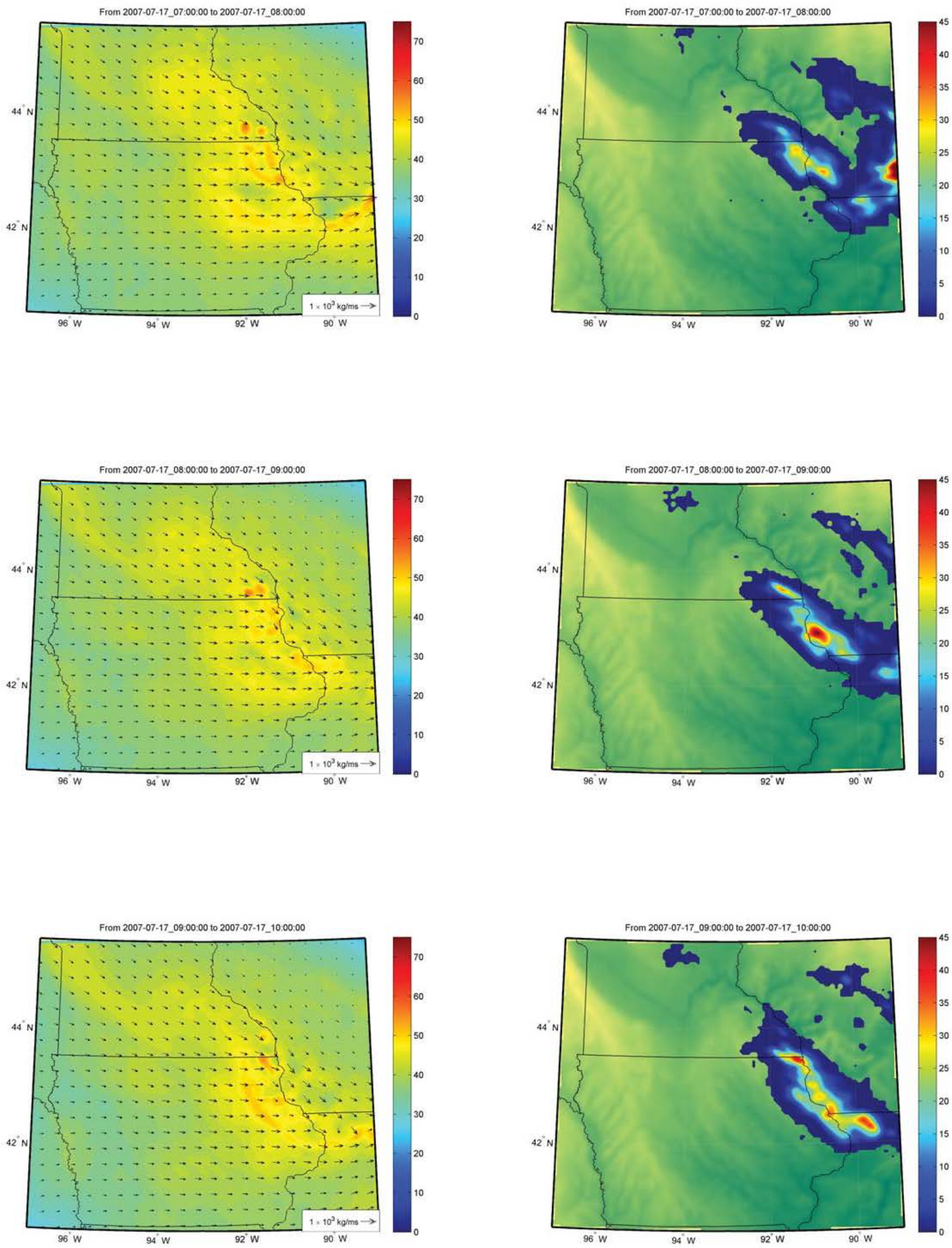

Figure B-7 **Hourly Simulated Precipitable Water (Left, Colormap [mm]) and Water Vapor Flux Fields (Left, Arrows [kg m^{-1} s^{-1}]) and Precipitation Fields (Right, Colormap [mm]) for the July 18, 2007 MCS**

Plots shown from 07/17/2007 at 01hr to 07/18/2007 at 12hr (Continued).

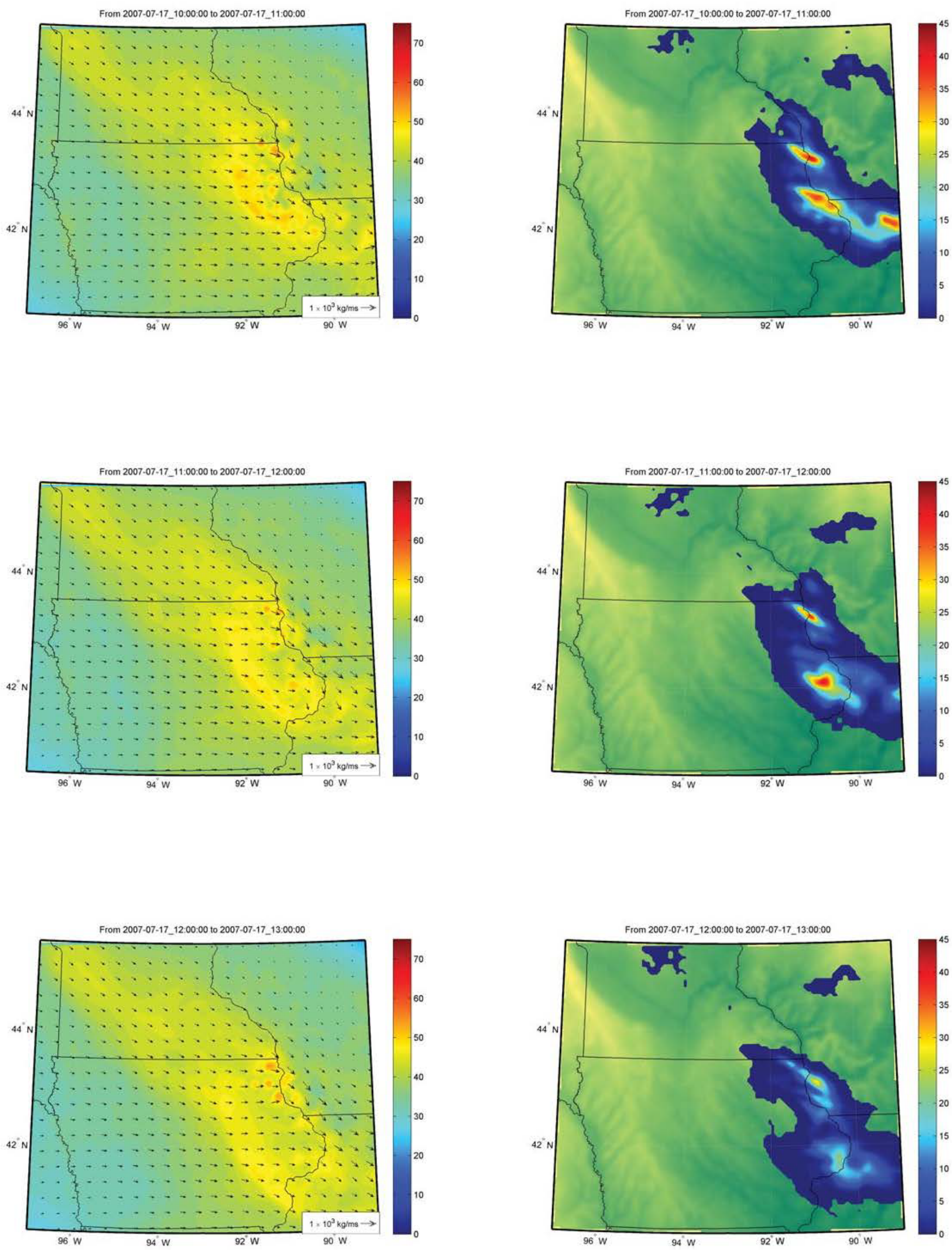

Figure B-7 **Hourly Simulated Precipitable Water (Left, Colormap [mm]) and Water Vapor Flux Fields (Left, Arrows [kg m^{-1} s^{-1}]) and Precipitation Fields (Right, Colormap [mm]) for the July 18, 2007 MCS**

Plots shown from 07/17/2007 at 01hr to 07/18/2007 at 12hr (Continued).

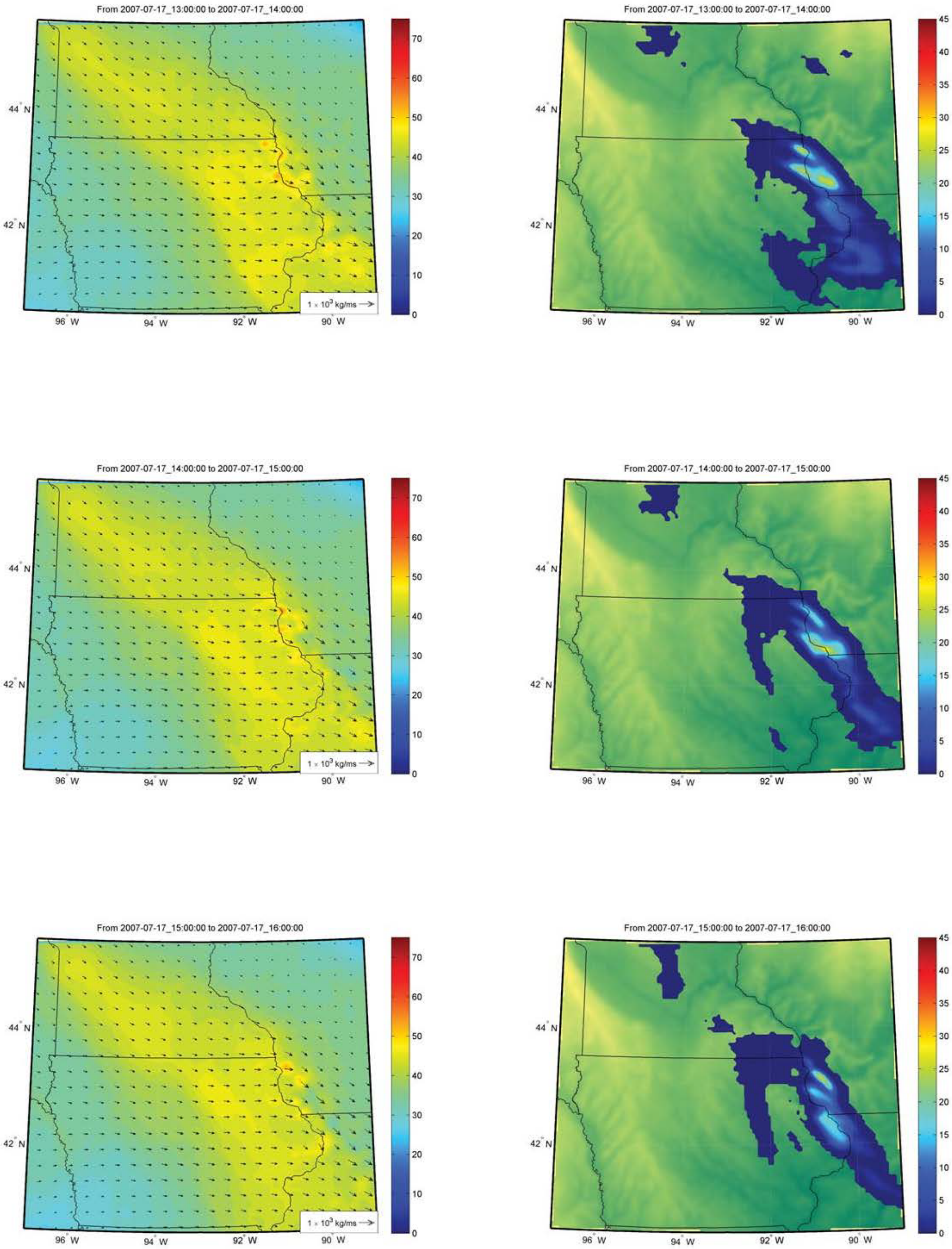

Figure B-7 Hourly Simulated Precipitable Water (Left, Colormap [mm]) and Water Vapor Flux Fields (Left, Arrows [kg m^{-1} s^{-1}]) and Precipitation Fields (Right, Colormap [mm]) for the July 18, 2007 MCS

Plots shown from 07/17/2007 at 01hr to 07/18/2007 at 12hr (Continued).

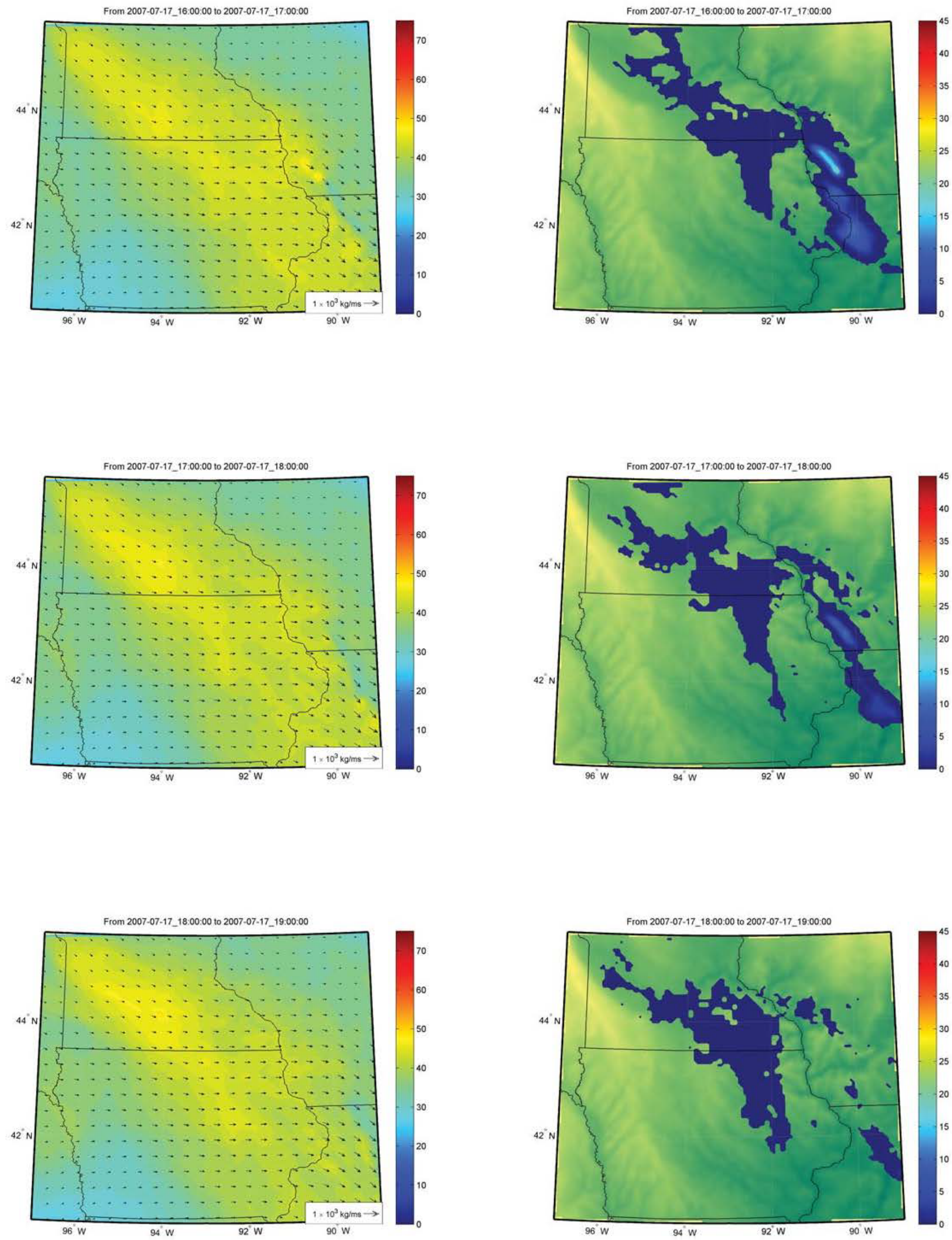

Figure B-7 **Hourly Simulated Precipitable Water (Left, Colormap [mm]) and Water Vapor Flux Fields (Left, Arrows [kg m^{-1} s^{-1}]) and Precipitation Fields (Right, Colormap [mm]) for the July 18, 2007 MCS**

Plots shown from 07/17/2007 at 01hr to 07/18/2007 at 12hr (Continued).

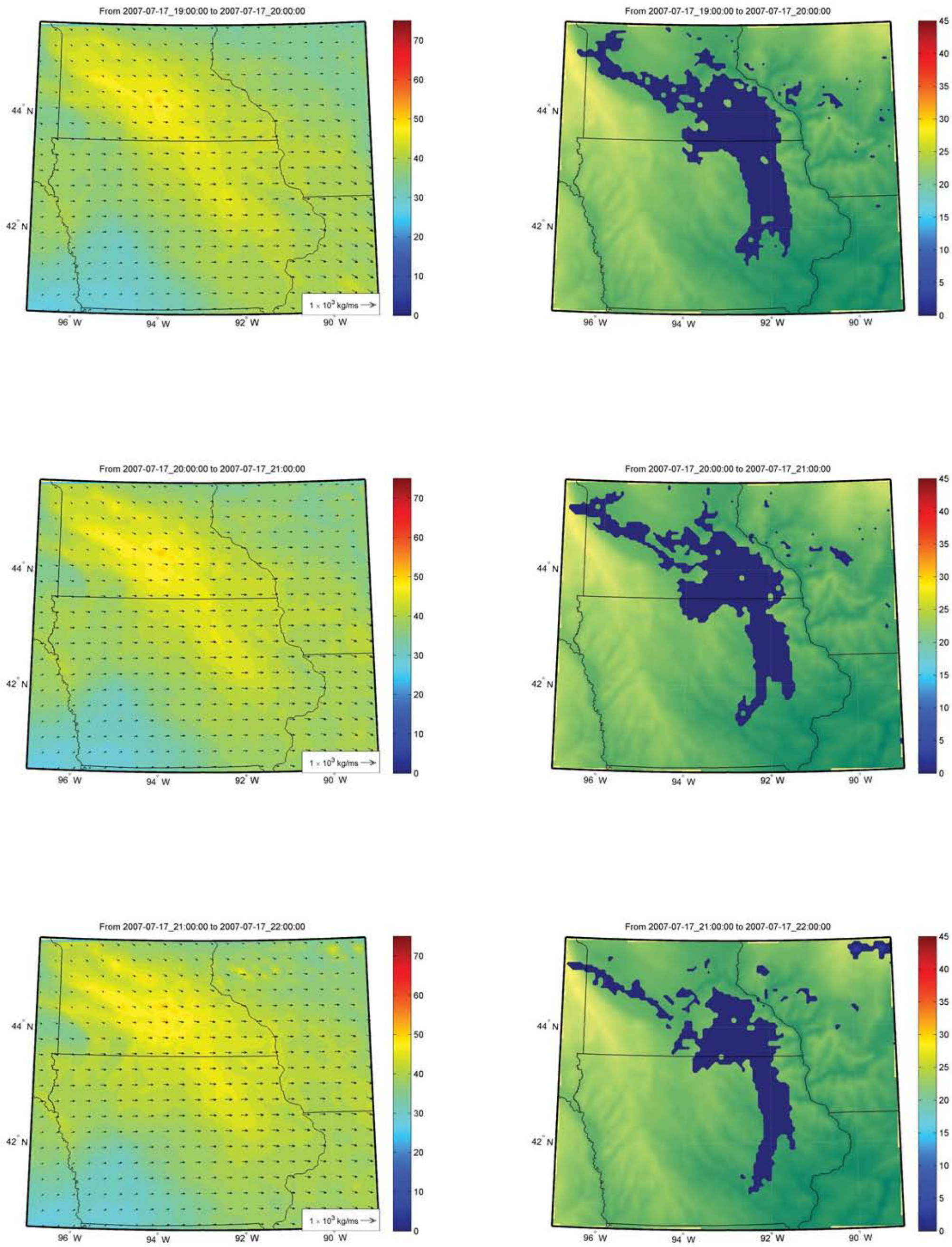

Figure B-7 Hourly Simulated Precipitable Water (Left, Colormap [mm]) and Water Vapor Flux Fields (Left, Arrows [kg m^{-1} s^{-1}]) and Precipitation Fields (Right, Colormap [mm]) for the July 18, 2007 MCS

Plots shown from 07/17/2007 at 01hr to 07/18/2007 at 12hr (Continued).

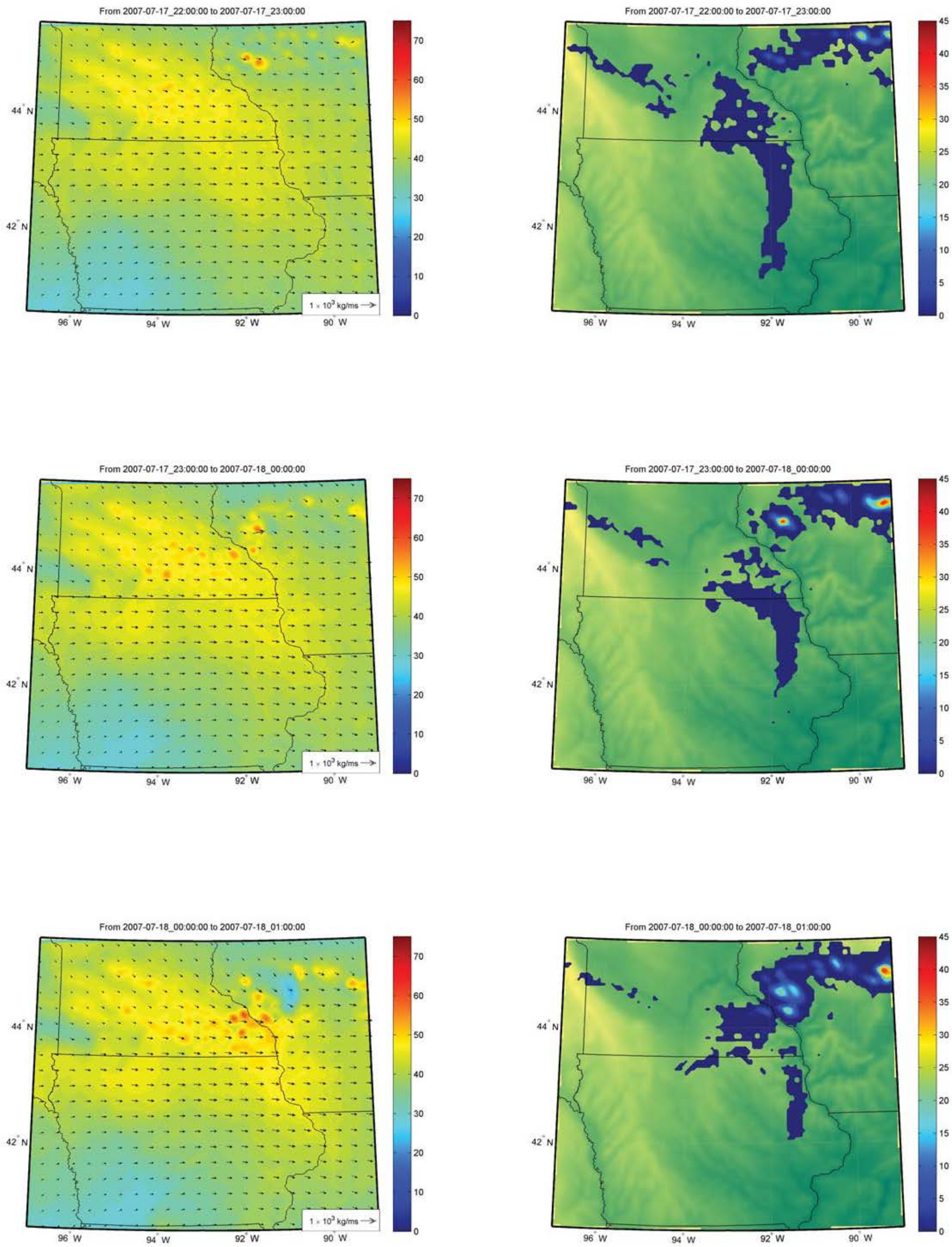

Figure B-7 Hourly Simulated Precipitable Water (Left, Colormap [mm]) and Water Vapor Flux Fields (Left, Arrows [kg m^{-1} s^{-1}]) and Precipitation Fields (Right, Colormap [mm]) for the July 18, 2007 MCS

Plots shown from 07/17/2007 at 01hr to 07/18/2007 at 12hr (Continued).

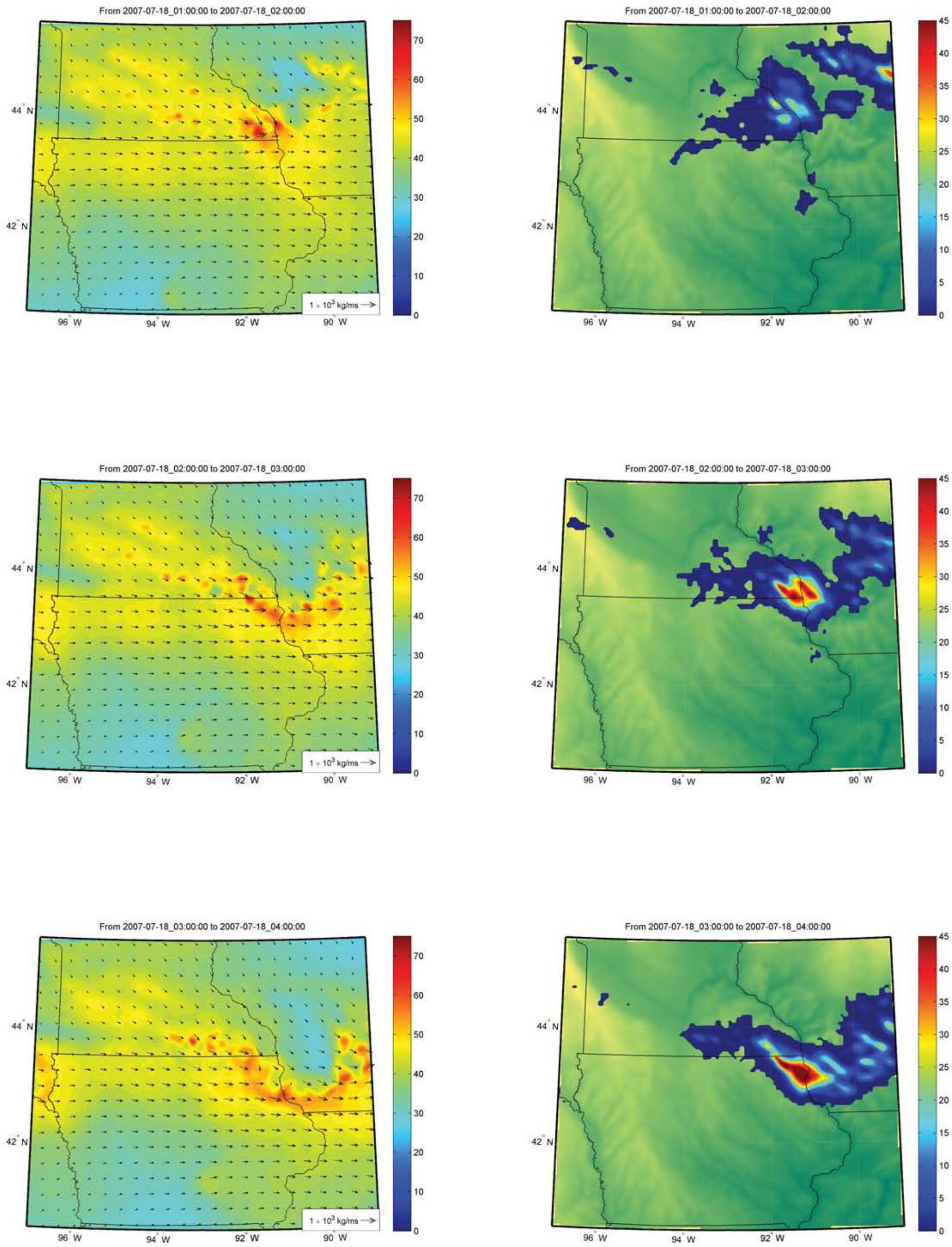

Figure B-7 **Hourly Simulated Precipitable Water (Left, Colormap [mm]) and Water Vapor Flux Fields (Left, Arrows [kg m^{-1} s^{-1}]) and Precipitation Fields (Right, Colormap [mm]) for the July 18, 2007 MCS**

Plots shown from 07/17/2007 at 01hr to 07/18/2007 at 12hr (Continued).

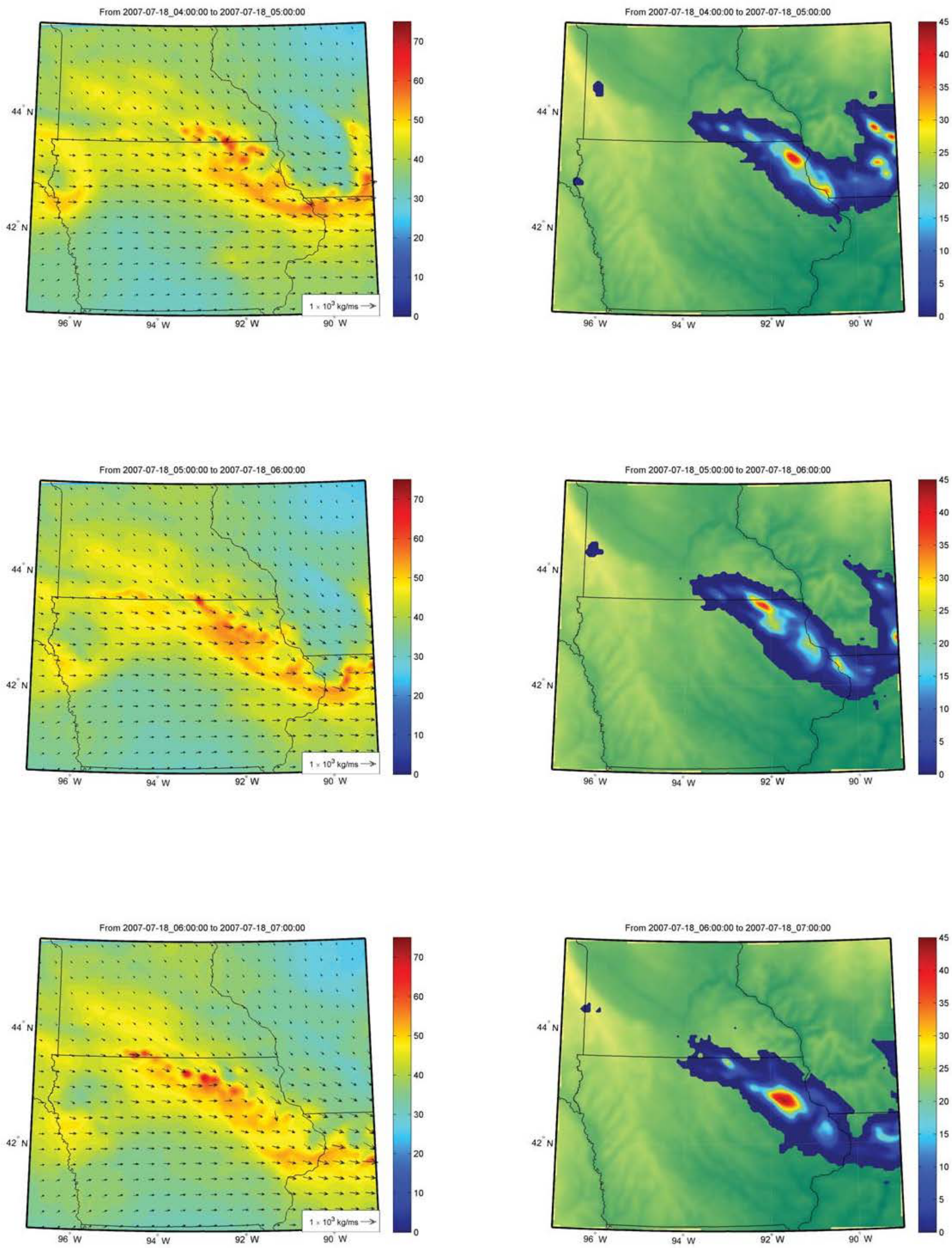

Figure B-7 Hourly Simulated Precipitable Water (Left, Colormap [mm]) and Water Vapor Flux Fields (Left, Arrows [kg m^{-1} s^{-1}]) and Precipitation Fields (Right, Colormap [mm]) for the July 18, 2007 MCS

Plots shown from 07/17/2007 at 01hr to 07/18/2007 at 12hr (Continued).

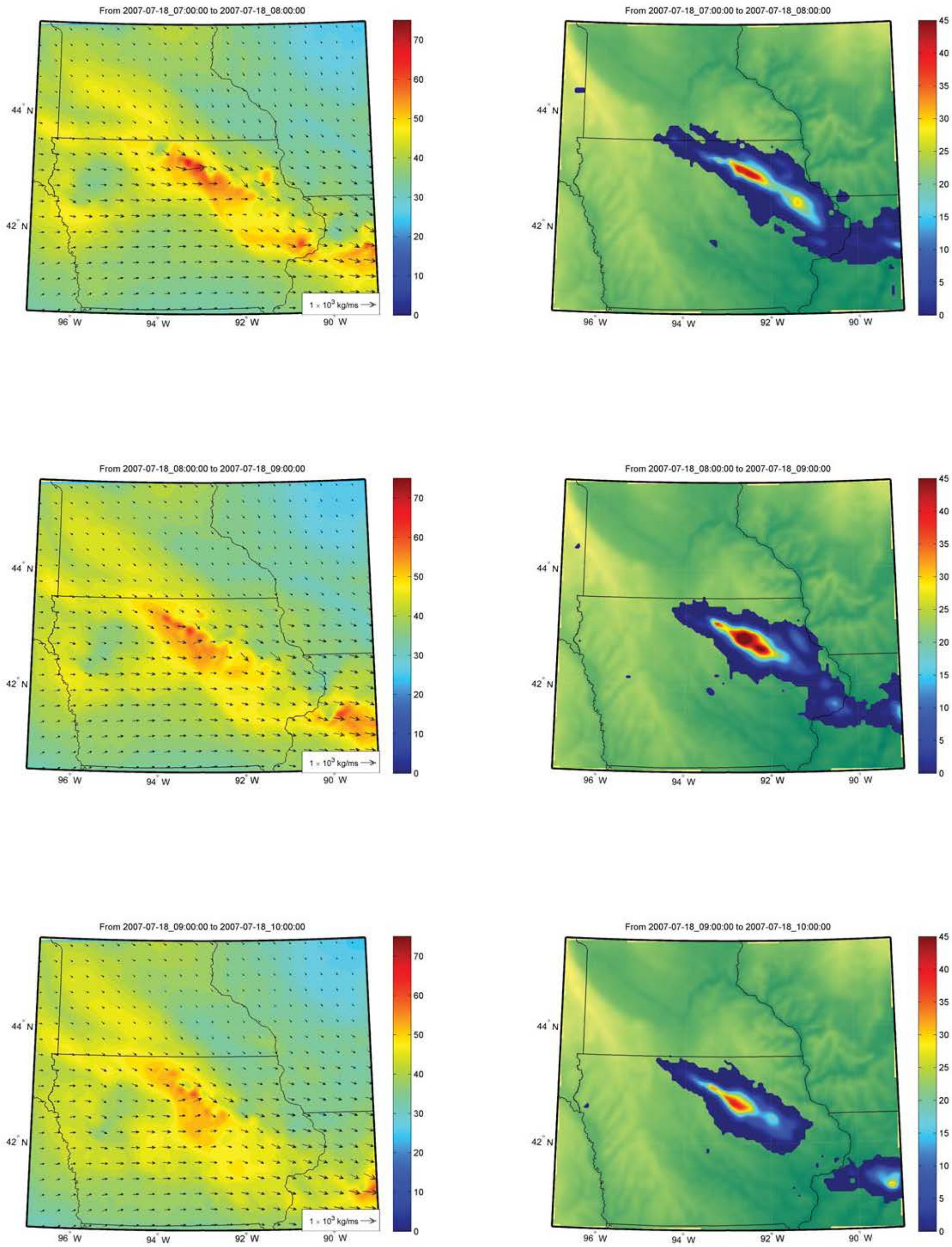

Figure B-7 Hourly Simulated Precipitable Water (Left, Colormap [mm]) and Water Vapor Flux Fields (Left, Arrows [kg m^{-1} s^{-1}]) and Precipitation Fields (Right, Colormap [mm]) for the July 18, 2007 MCS

Plots shown from 07/17/2007 at 01hr to 07/18/2007 at 12hr (Continued).

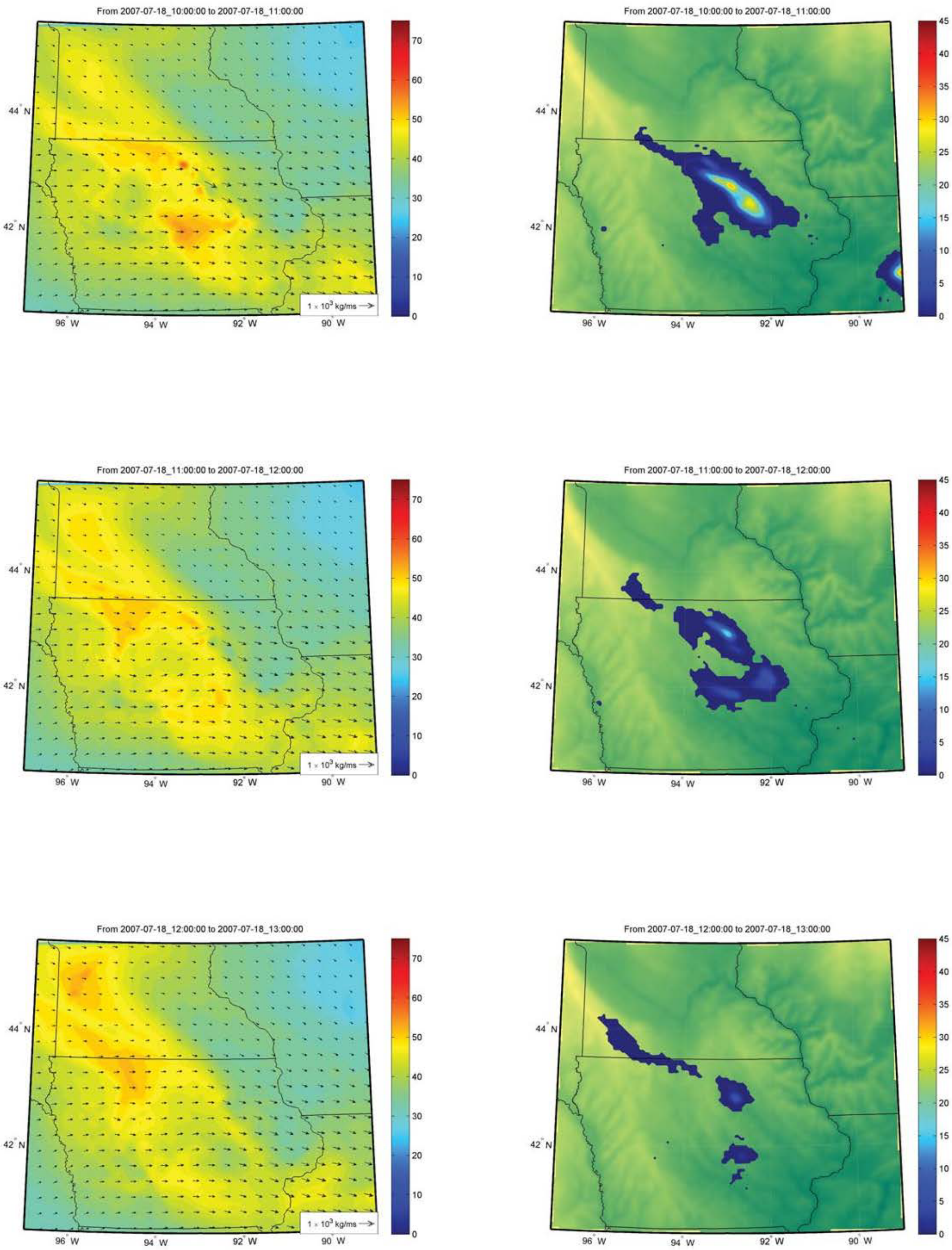

Figure B-7 Hourly Simulated Precipitable Water (Left, Colormap [mm]) and Water Vapor Flux Fields (Left, Arrows [kg m^{-1} s^{-1}]) and Precipitation Fields (Right, Colormap [mm]) for the July 18, 2007 MCS

Plots shown from 07/17/2007 at 01hr to 07/18/2007 at 12hr (Continued).

B.1.8 August 19, 2007 MCS

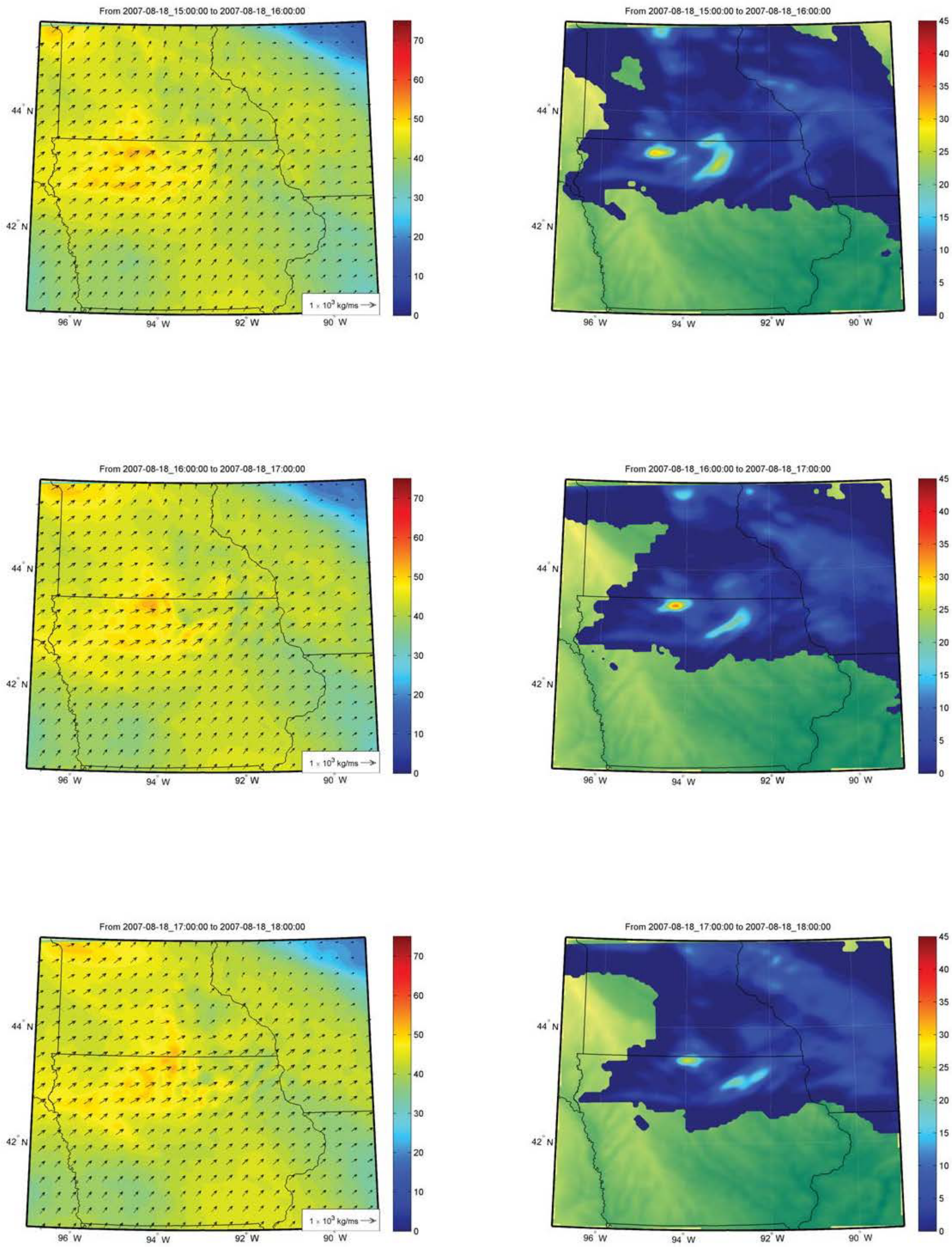

Figure B-8 Hourly Simulated Precipitable Water (Left, Colormap [mm]) and Water Vapor Flux Fields (Left, Arrows [kg m^{-1} s^{-1}]) and Precipitation Fields (Right, Colormap [mm]) for the August 19, 2007 MCS

Plots shown from 08/18/2007 at 16hr to 08/20/2007 at 12hr.

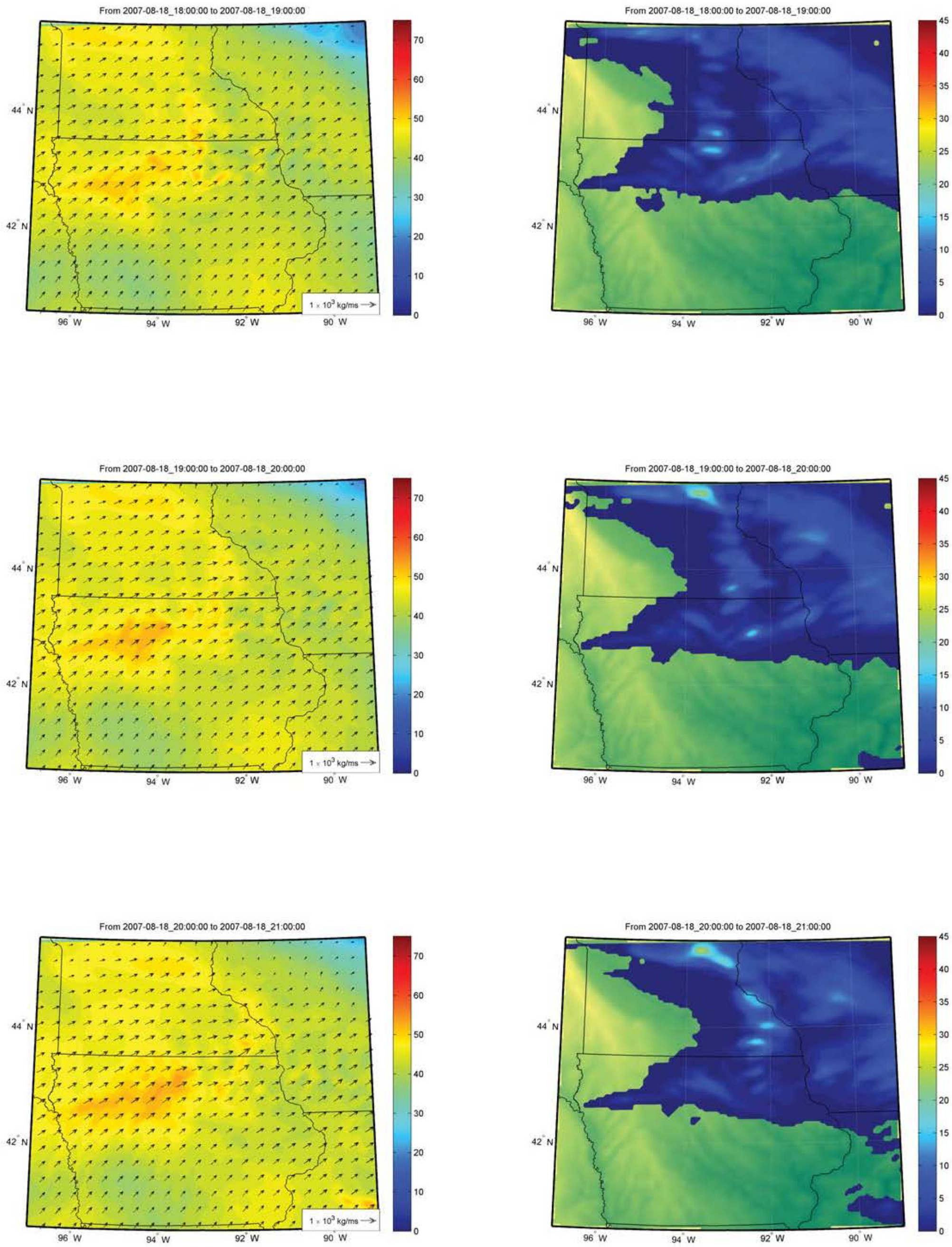

Figure B-8 Hourly Simulated Precipitable Water (Left, Colormap [mm]) and Water Vapor Flux Fields (Left, Arrows [kg m^{-1} s^{-1}]) and Precipitation Fields (Right, Colormap [mm]) for the August 19, 2007 MCS

Plots shown from 08/18/2007 at 16hr to 08/20/2007 at 12hr (Continued).

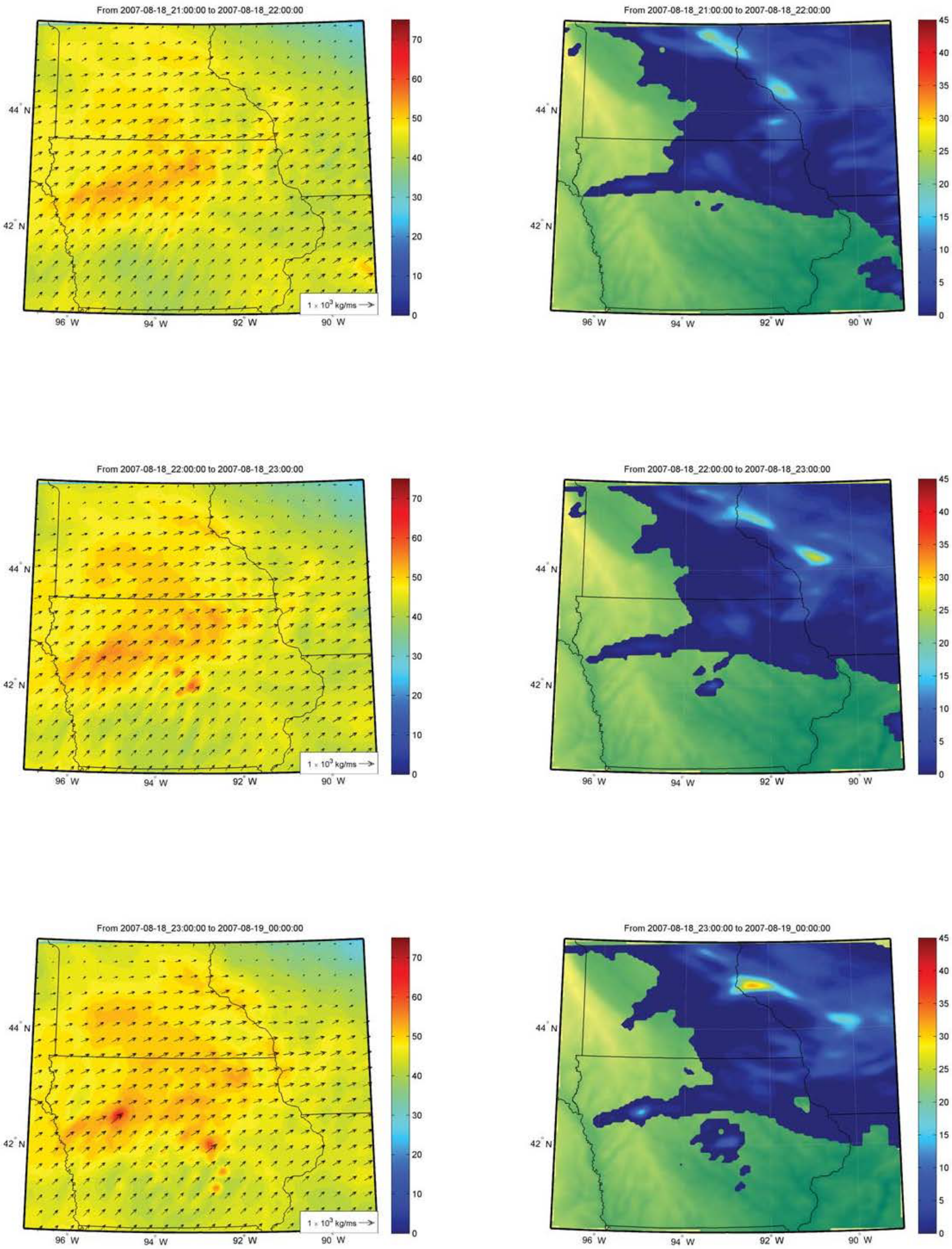

Figure B-8 **Hourly Simulated Precipitable Water (Left, Colormap [mm]) and Water Vapor Flux Fields (Left, Arrows [kg m^{-1} s^{-1}]) and Precipitation Fields (Right, Colormap [mm]) for the August 19, 2007 MCS**

Plots shown from 08/18/2007 at 16hr to 08/20/2007 at 12hr (Continued).

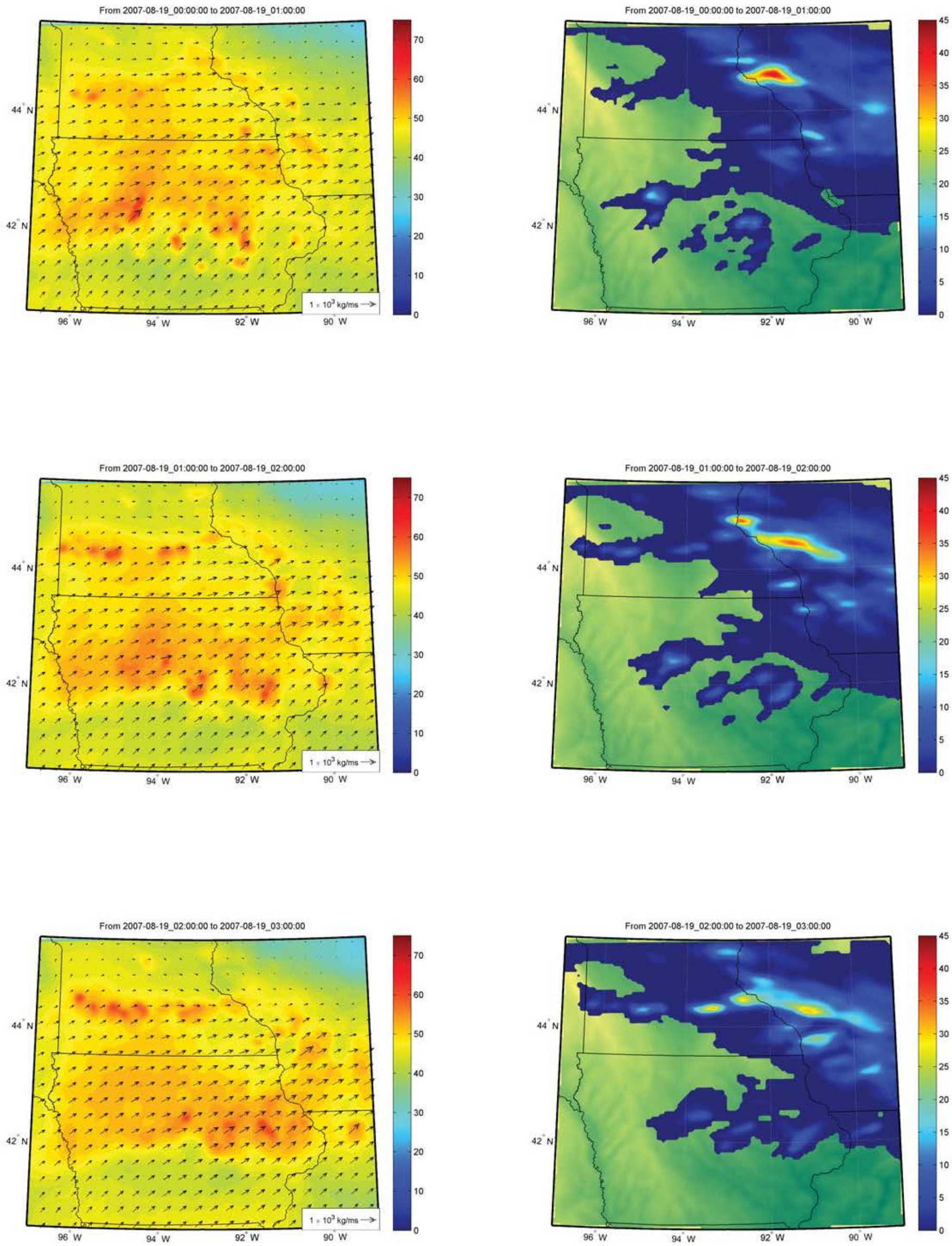

Figure B-8 Hourly Simulated Precipitable Water (Left, Colormap [mm]) and Water Vapor Flux Fields (Left, Arrows [kg m^{-1} s^{-1}]) and Precipitation Fields (Right, Colormap [mm]) for the August 19, 2007 MCS

Plots shown from 08/18/2007 at 16hr to 08/20/2007 at 12hr (Continued).

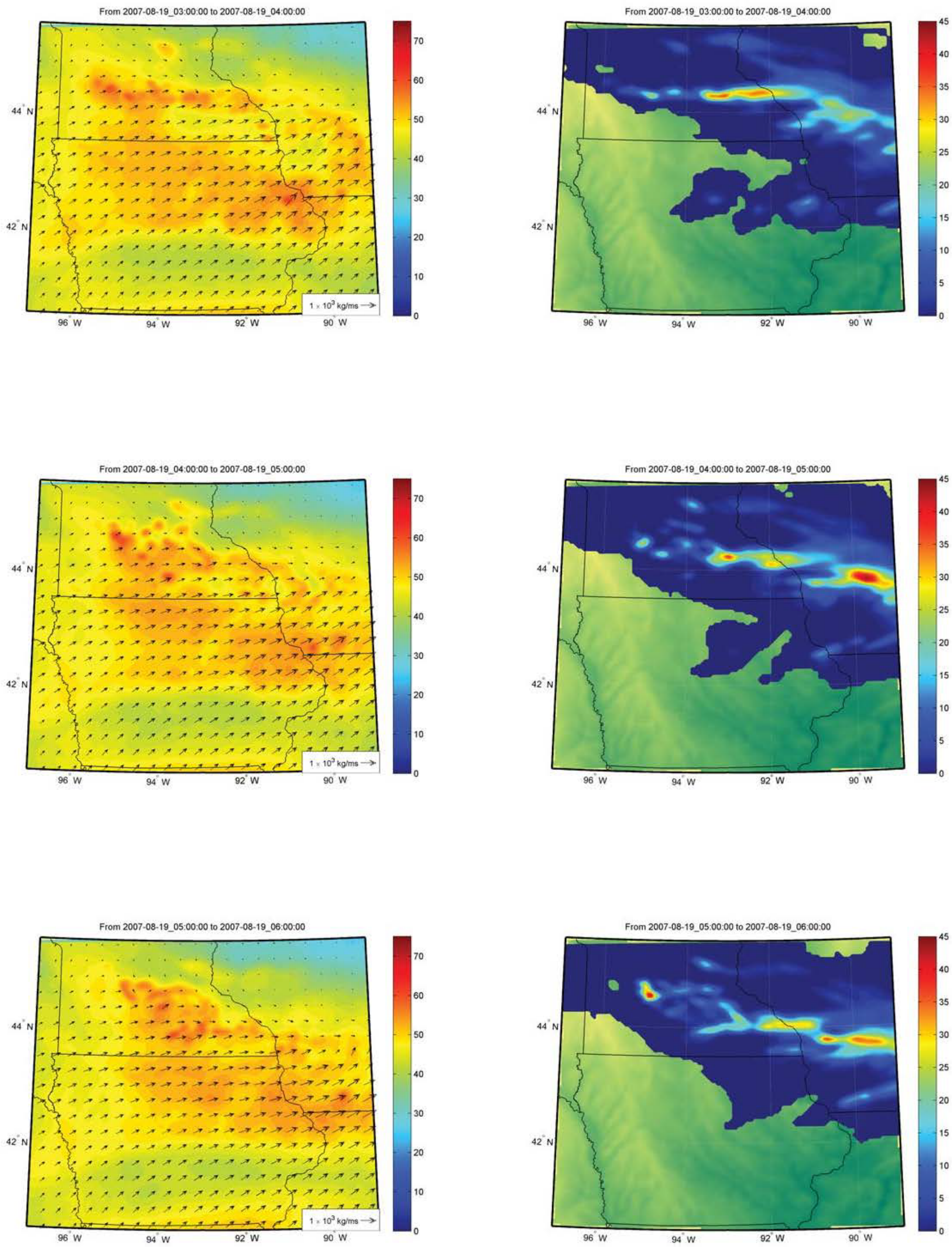

Figure B-8 Hourly Simulated Precipitable Water (Left, Colormap [mm]) and Water Vapor Flux Fields (Left, Arrows [kg m^{-1} s^{-1}]) and Precipitation Fields (Right, Colormap [mm]) for the August 19, 2007 MCS

Plots shown from 08/18/2007 at 16hr to 08/20/2007 at 12hr (Continued).

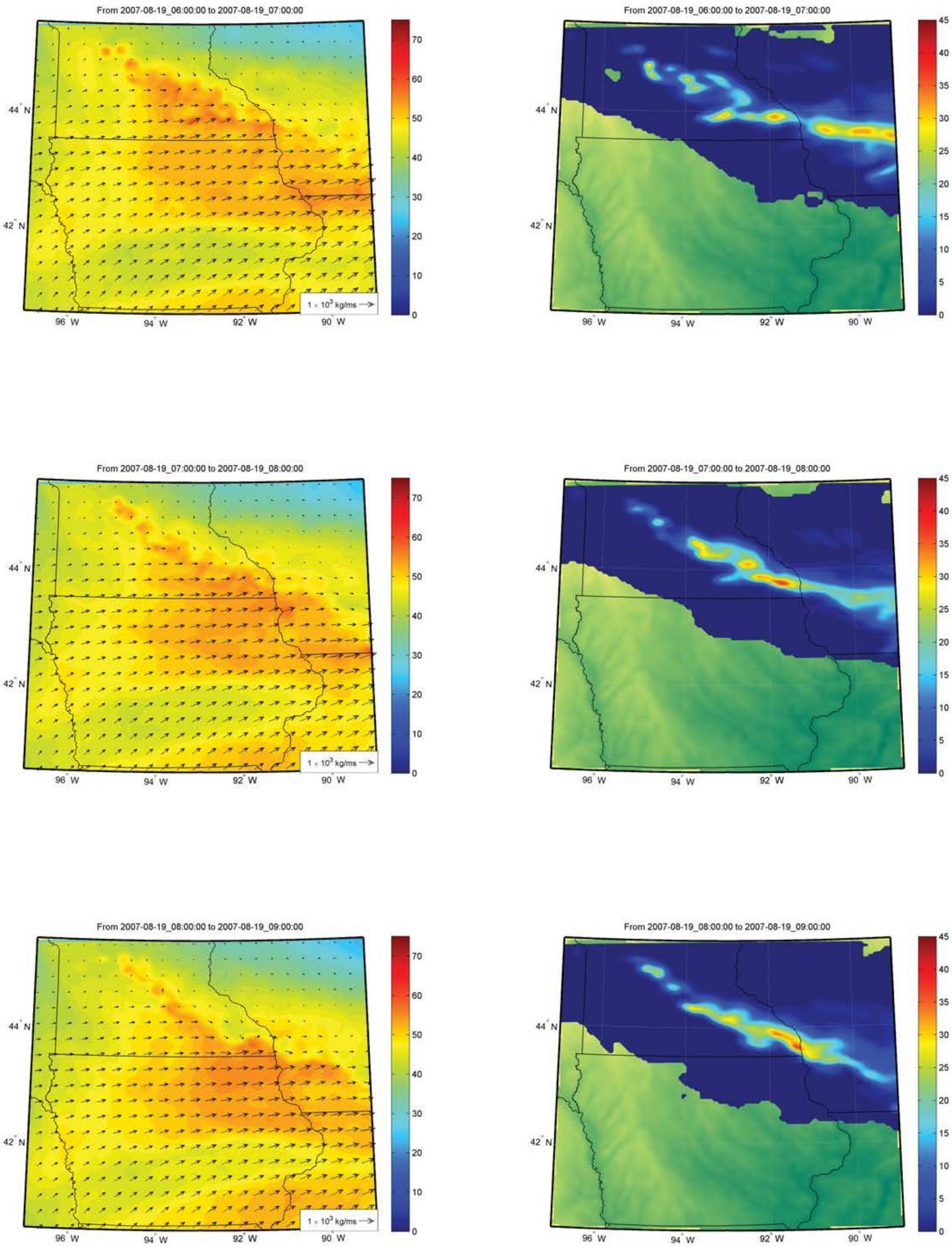

Figure B-8 **Hourly Simulated Precipitable Water (Left, Colormap [mm]) and Water Vapor Flux Fields (Left, Arrows [kg m^{-1} s^{-1}]) and Precipitation Fields (Right, Colormap [mm]) for the August 19, 2007 MCS**

Plots shown from 08/18/2007 at 16hr to 08/20/2007 at 12hr (Continued).

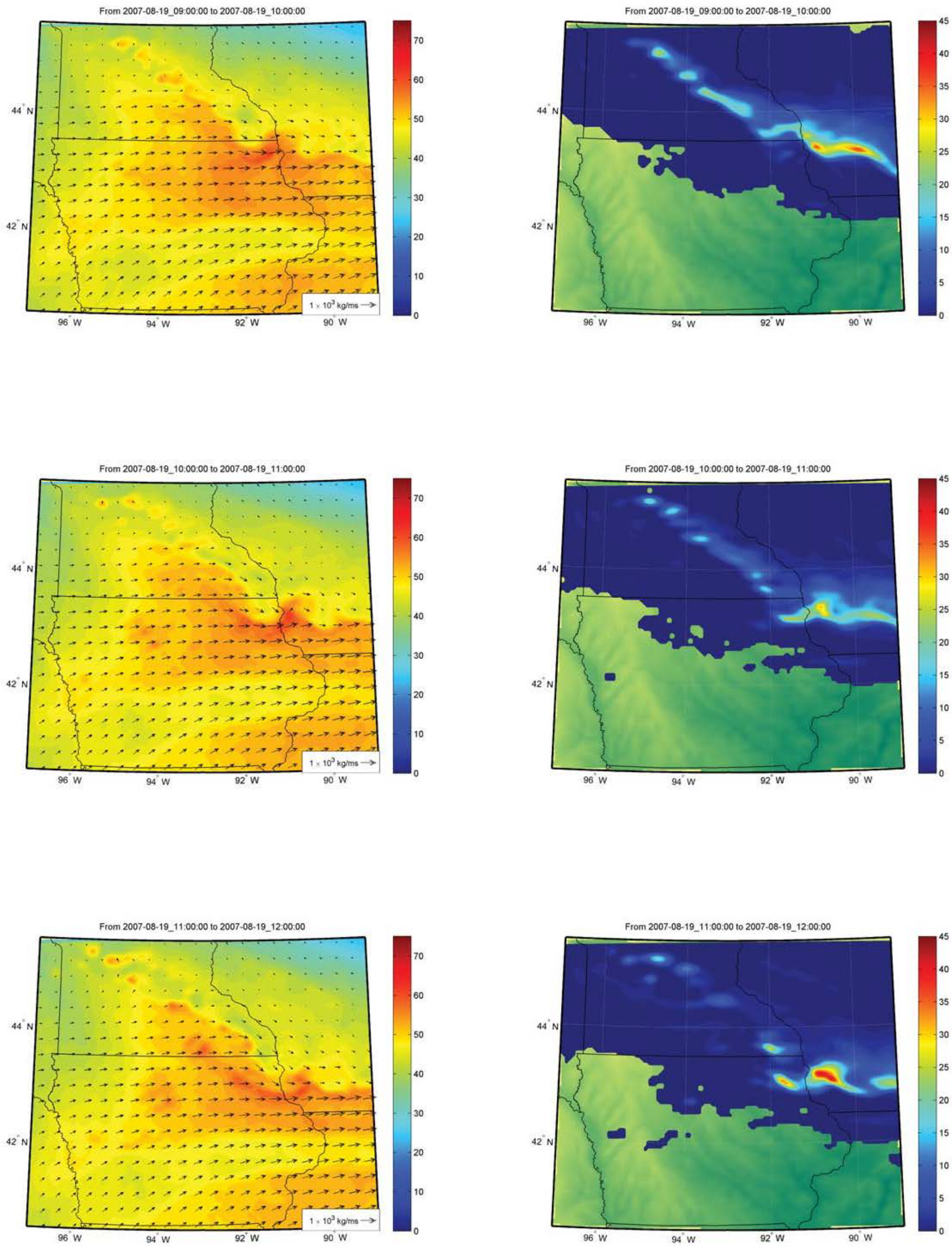

Figure B-8 Hourly Simulated Precipitable Water (Left, Colormap [mm]) and Water Vapor Flux Fields (Left, Arrows [kg m^{-1} s^{-1}]) and Precipitation Fields (Right, Colormap [mm]) for the August 19, 2007 MCS

Plots shown from 08/18/2007 at 16hr to 08/20/2007 at 12hr (Continued).

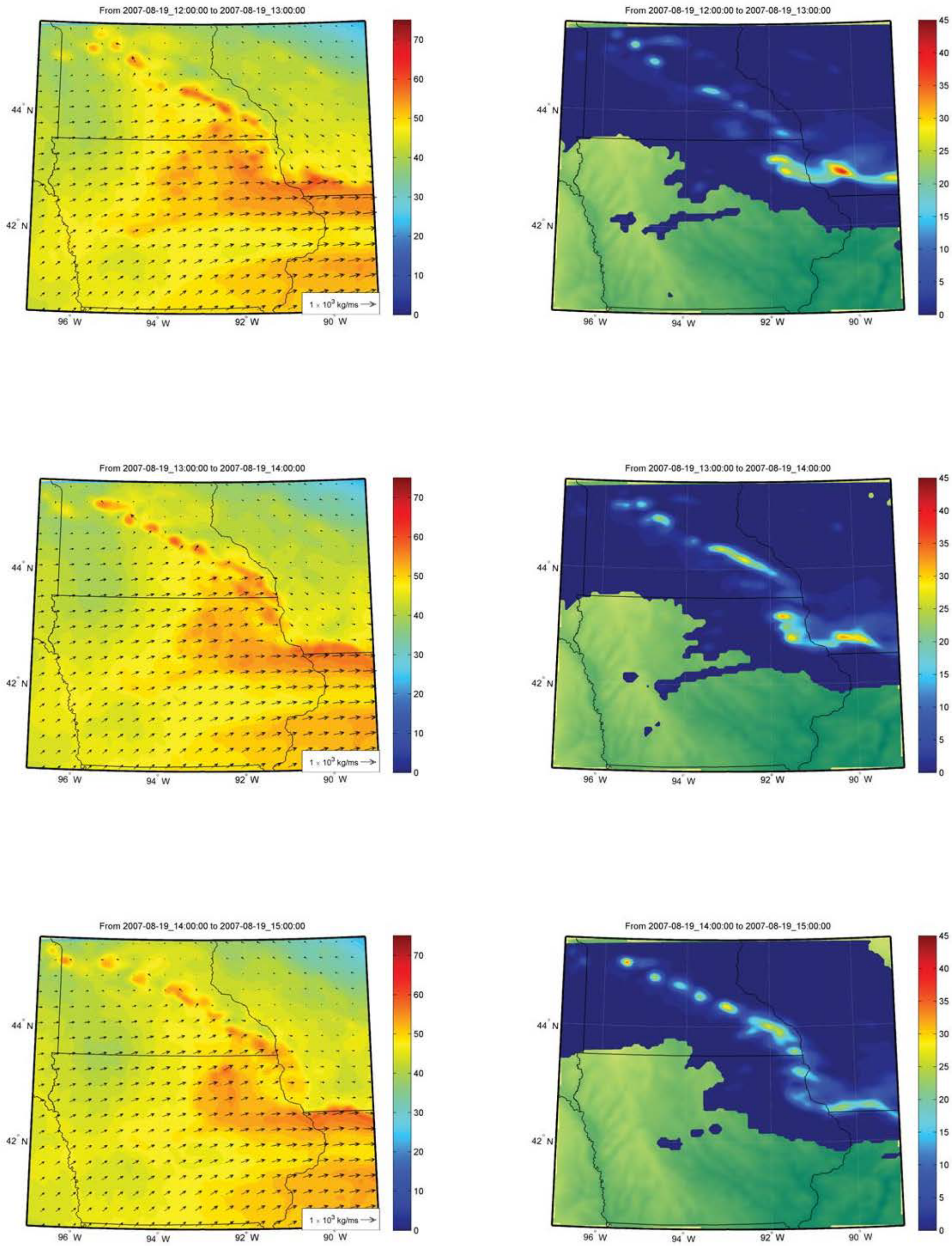

Figure B-8 Hourly Simulated Precipitable Water (Left, Colormap [mm]) and Water Vapor Flux Fields (Left, Arrows [kg m^{-1} s^{-1}]) and Precipitation Fields (Right, Colormap [mm]) for the August 19, 2007 MCS

Plots shown from 08/18/2007 at 16hr to 08/20/2007 at 12hr (Continued).

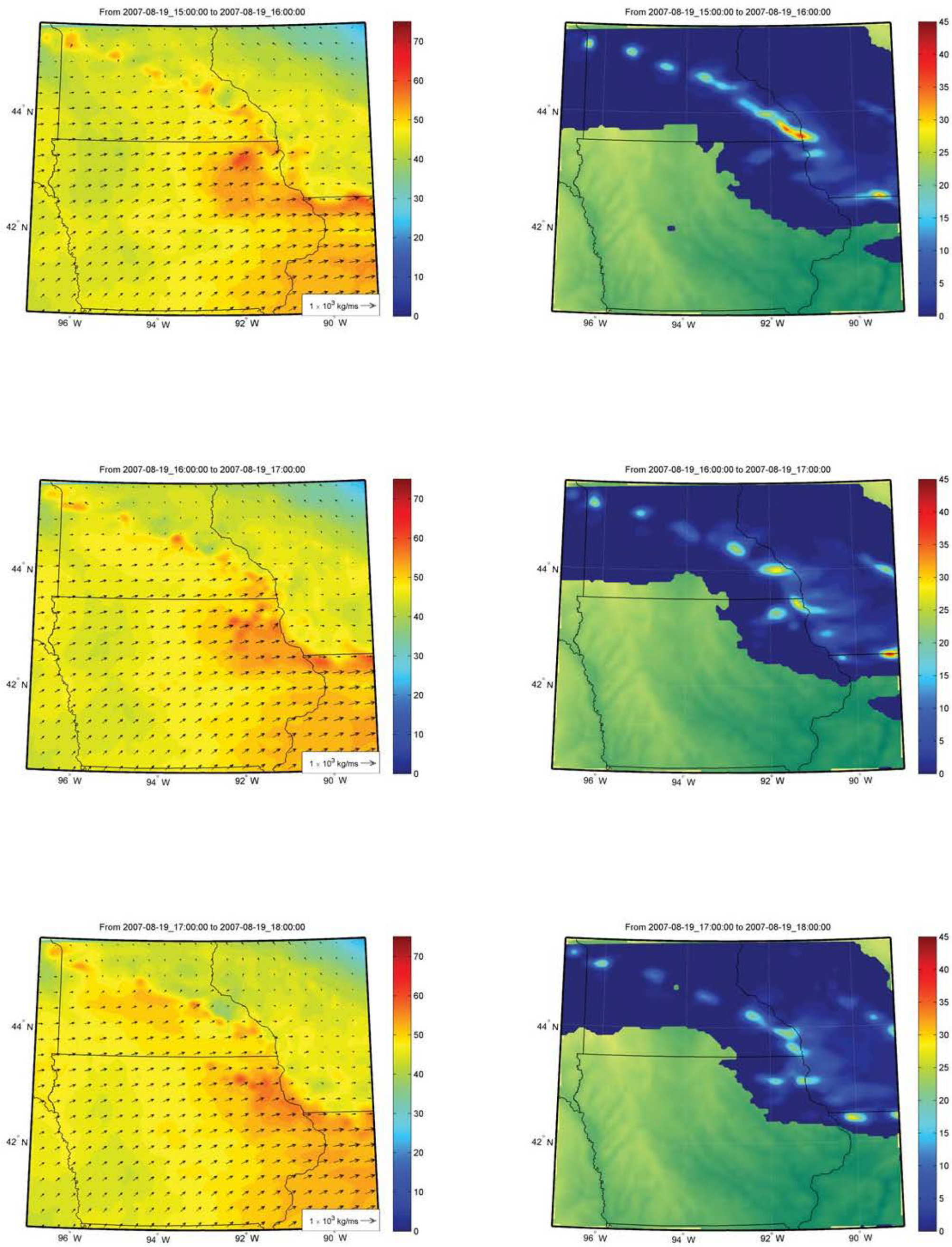

Figure B-8 Hourly Simulated Precipitable Water (Left, Colormap [mm]) and Water Vapor Flux Fields (Left, Arrows [kg m^{-1} s^{-1}]) and Precipitation Fields (Right, Colormap [mm]) for the August 19, 2007 MCS

Plots shown from 08/18/2007 at 16hr to 08/20/2007 at 12hr (Continued).

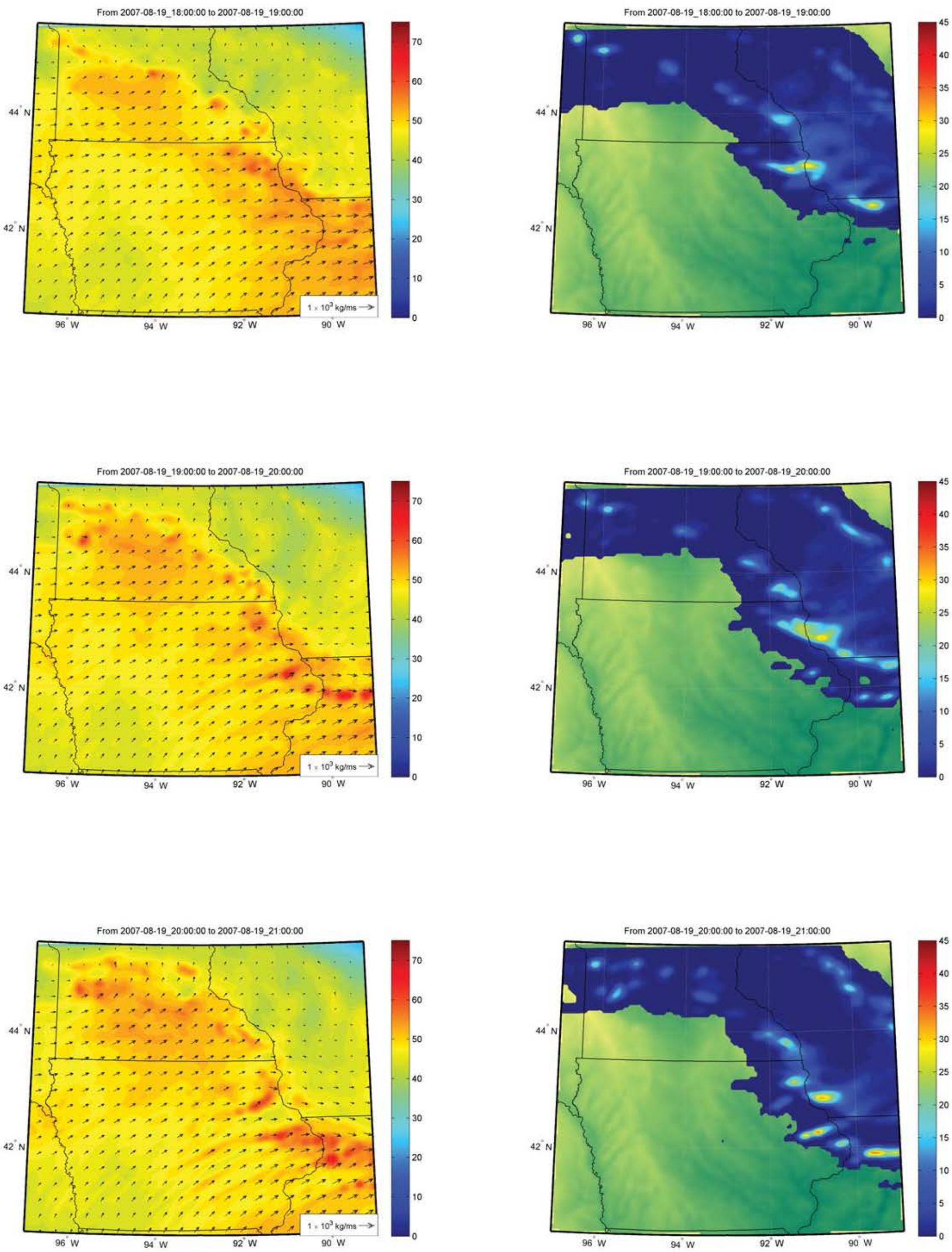

Figure B-8 Hourly Simulated Precipitable Water (Left, Colormap [mm]) and Water Vapor Flux Fields (Left, Arrows [kg m^{-1} s^{-1}]) and Precipitation Fields (Right, Colormap [mm]) for the August 19, 2007 MCS

Plots shown from 08/18/2007 at 16hr to 08/20/2007 at 12hr (Continued).

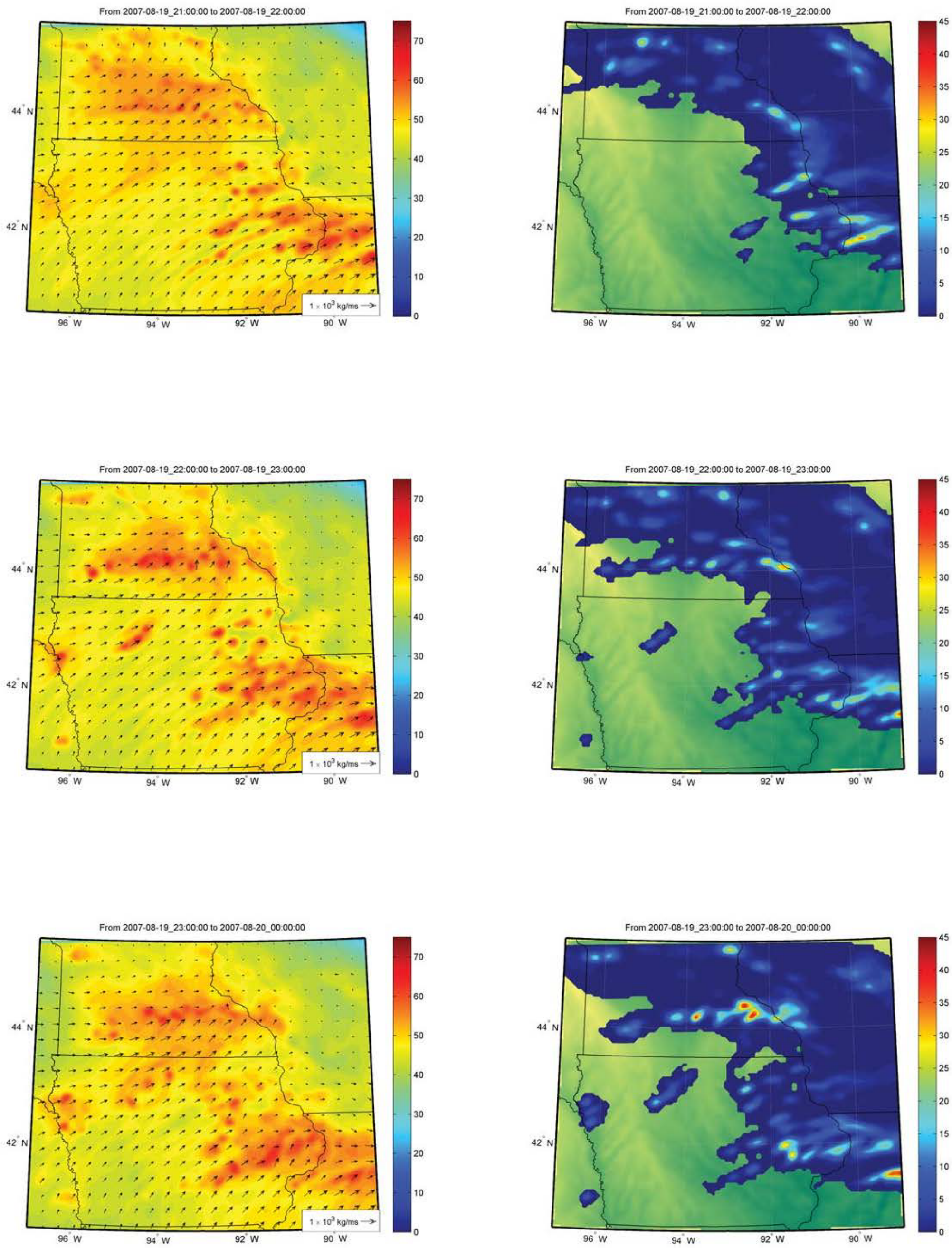

Figure B-8 **Hourly Simulated Precipitable Water (Left, Colormap [mm]) and Water Vapor Flux Fields (Left, Arrows [kg m^{-1} s^{-1}]) and Precipitation Fields (Right, Colormap [mm]) for the August 19, 2007 MCS**

Plots shown from 08/18/2007 at 16hr to 08/20/2007 at 12hr (Continued).

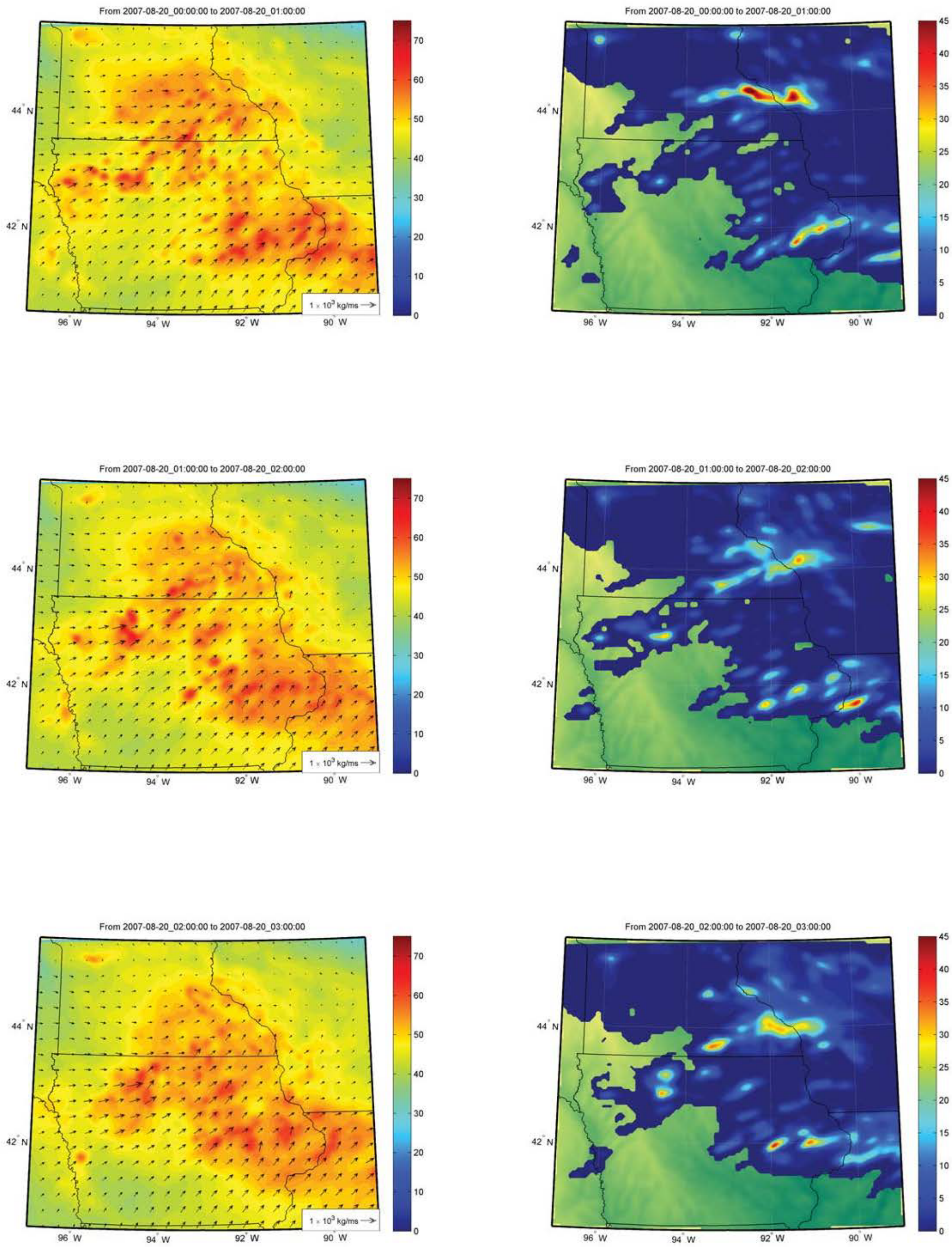

Figure B-8 Hourly Simulated Precipitable Water (Left, Colormap [mm]) and Water Vapor Flux Fields (Left, Arrows [kg m^{-1} s^{-1}]) and Precipitation Fields (Right, Colormap [mm]) for the August 19, 2007 MCS

Plots shown from 08/18/2007 at 16hr to 08/20/2007 at 12hr (Continued).

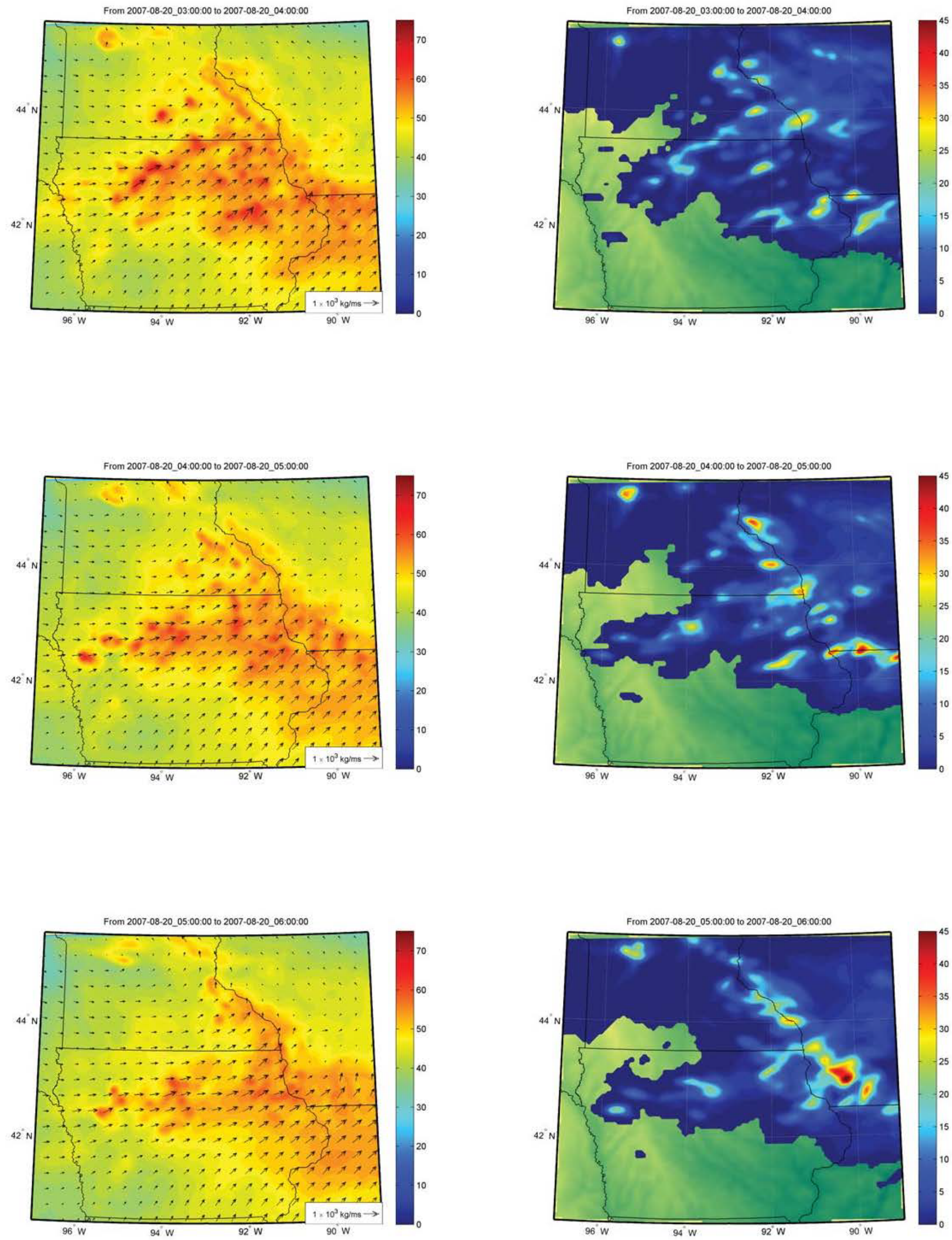

Figure B-8 Hourly Simulated Precipitable Water (Left, Colormap [mm]) and Water Vapor Flux Fields (Left, Arrows [kg m^{-1} s^{-1}]) and Precipitation Fields (Right, Colormap [mm]) for the August 19, 2007 MCS

Plots shown from 08/18/2007 at 16hr to 08/20/2007 at 12hr (Continued).

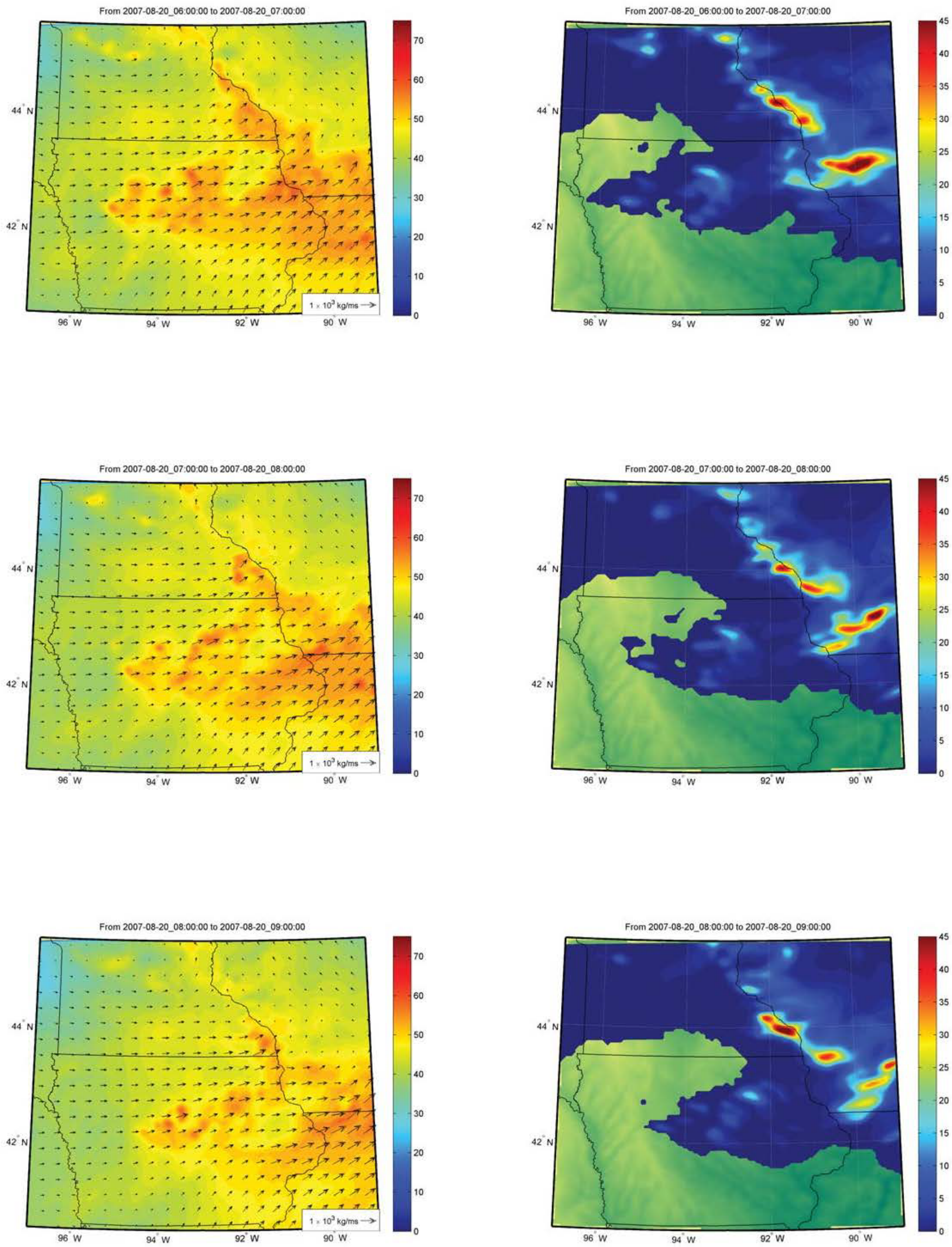

Figure B-8 Hourly Simulated Precipitable Water (Left, Colormap [mm]) and Water Vapor Flux Fields (Left, Arrows [kg m^{-1} s^{-1}]) and Precipitation Fields (Right, Colormap [mm]) for the August 19, 2007 MCS

Plots shown from 08/18/2007 at 16hr to 08/20/2007 at 12hr (Continued).

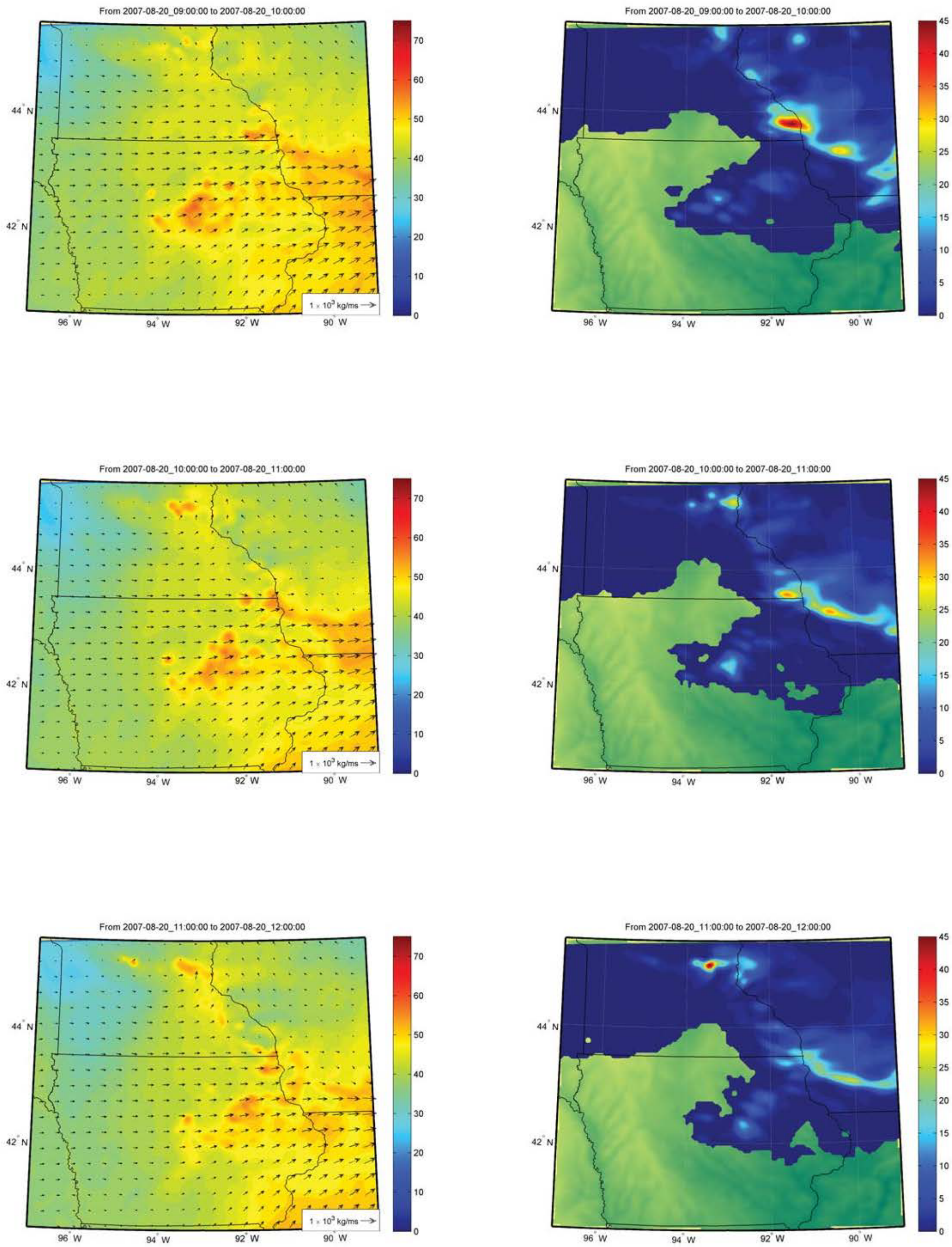

Figure B-8 Hourly Simulated Precipitable Water (Left, Colormap [mm]) and Water Vapor Flux Fields (Left, Arrows [kg m^{-1} s^{-1}]) and Precipitation Fields (Right, Colormap [mm]) for the August 19, 2007 MCS

Plots shown from 08/18/2007 at 16hr to 08/20/2007 at 12hr (Continued).

B.1.9 June 5, 2008 MCS

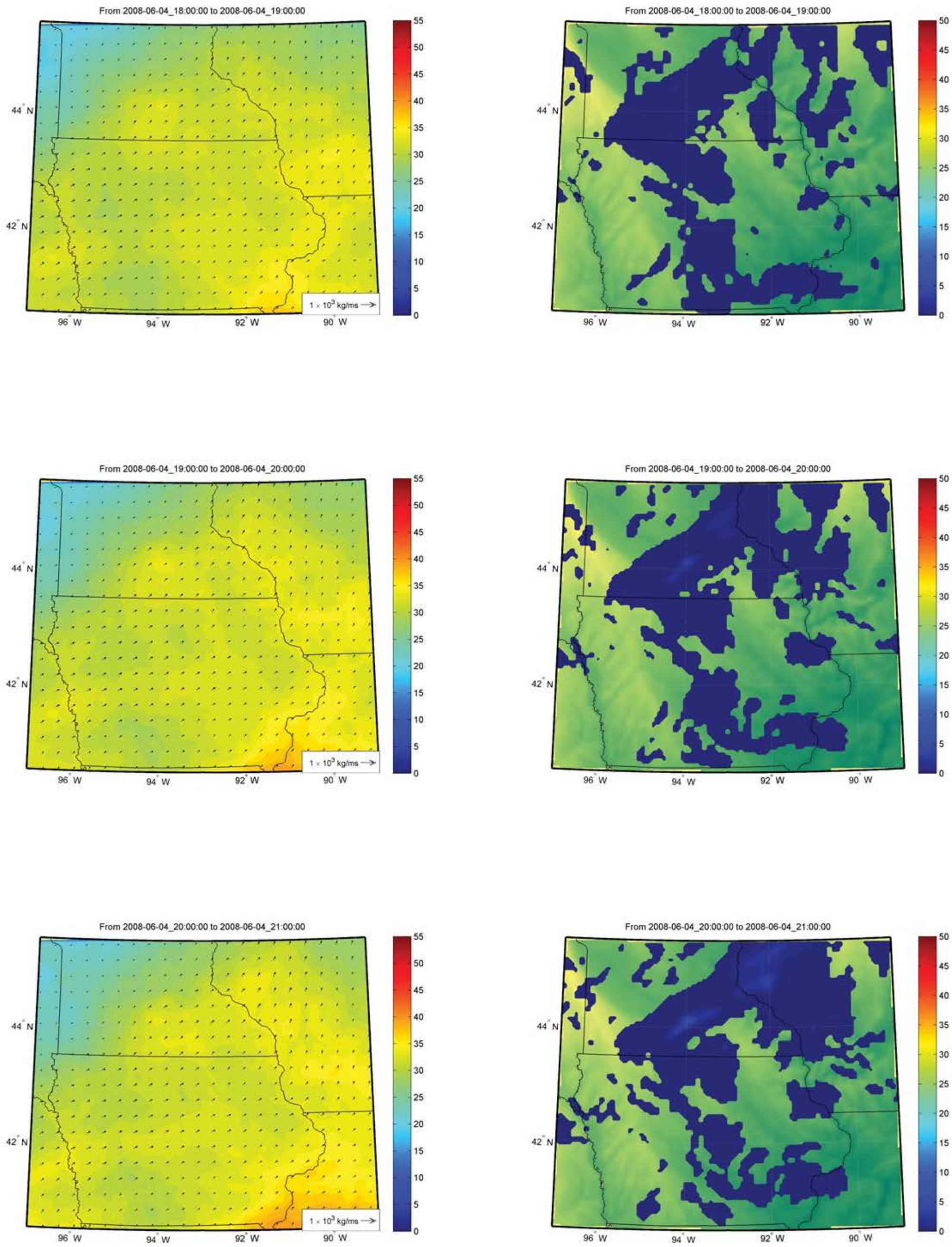

Figure B-9 **Hourly Simulated Precipitable Water (Left, Colormap [mm]) and Water Vapor Flux Fields (Left, Arrows [kg m^{-1} s^{-1}]) and Precipitation Fields (Right, Colormap [mm]) for the June 5, 2008 MCS**

Plots shown from 06/04/2008 at 18hr to 06/06/2008 at 14hr.

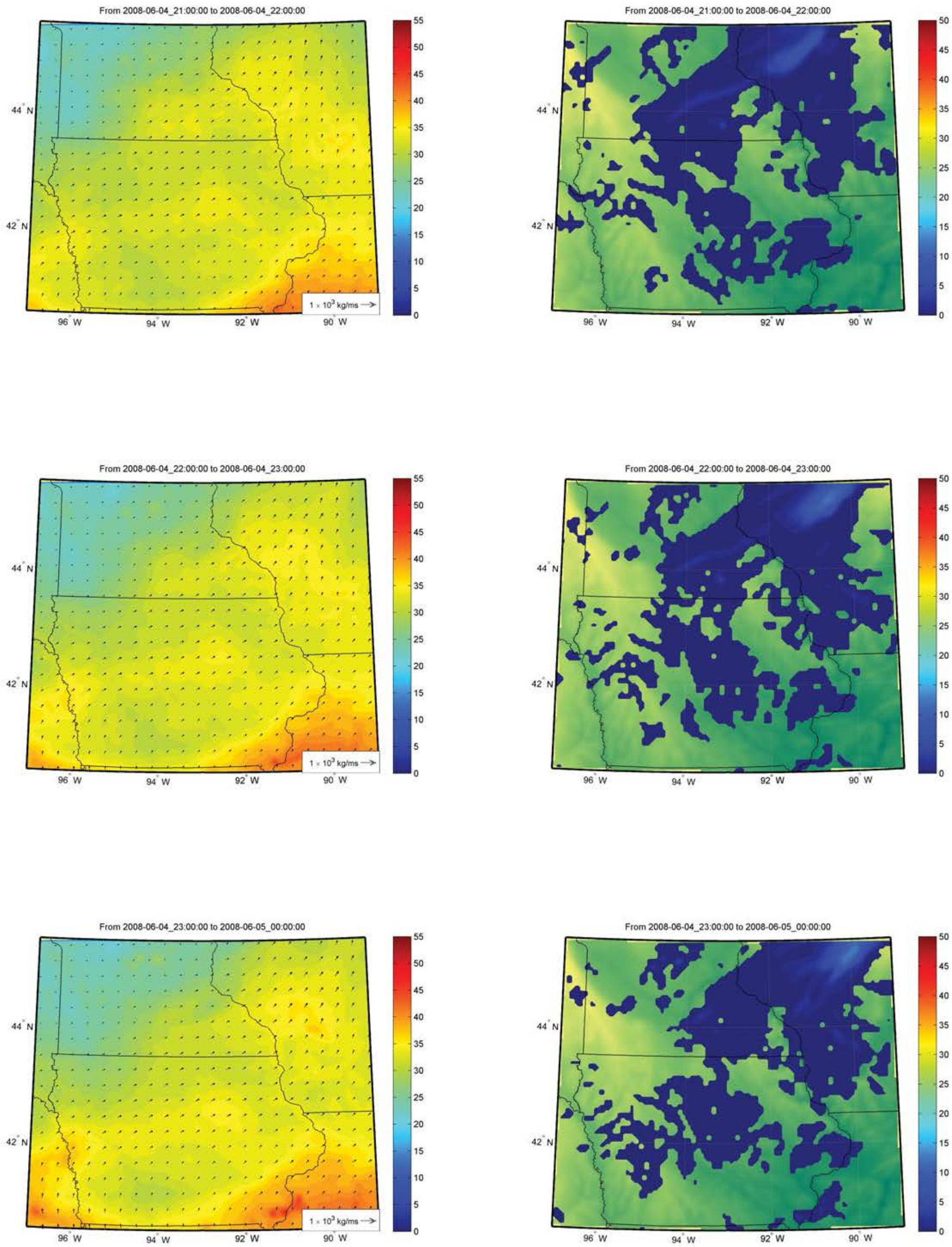

Figure B-9 **Hourly Simulated Precipitable Water (Left, Colormap [mm]) and Water Vapor Flux Fields (Left, Arrows [kg m^{-1} s^{-1}]) and Precipitation Fields (Right, Colormap [mm]) for the June 5, 2008 MCS**

Plots shown from 06/04/2008 at 18hr to 06/06/2008 at 14hr (Continued).

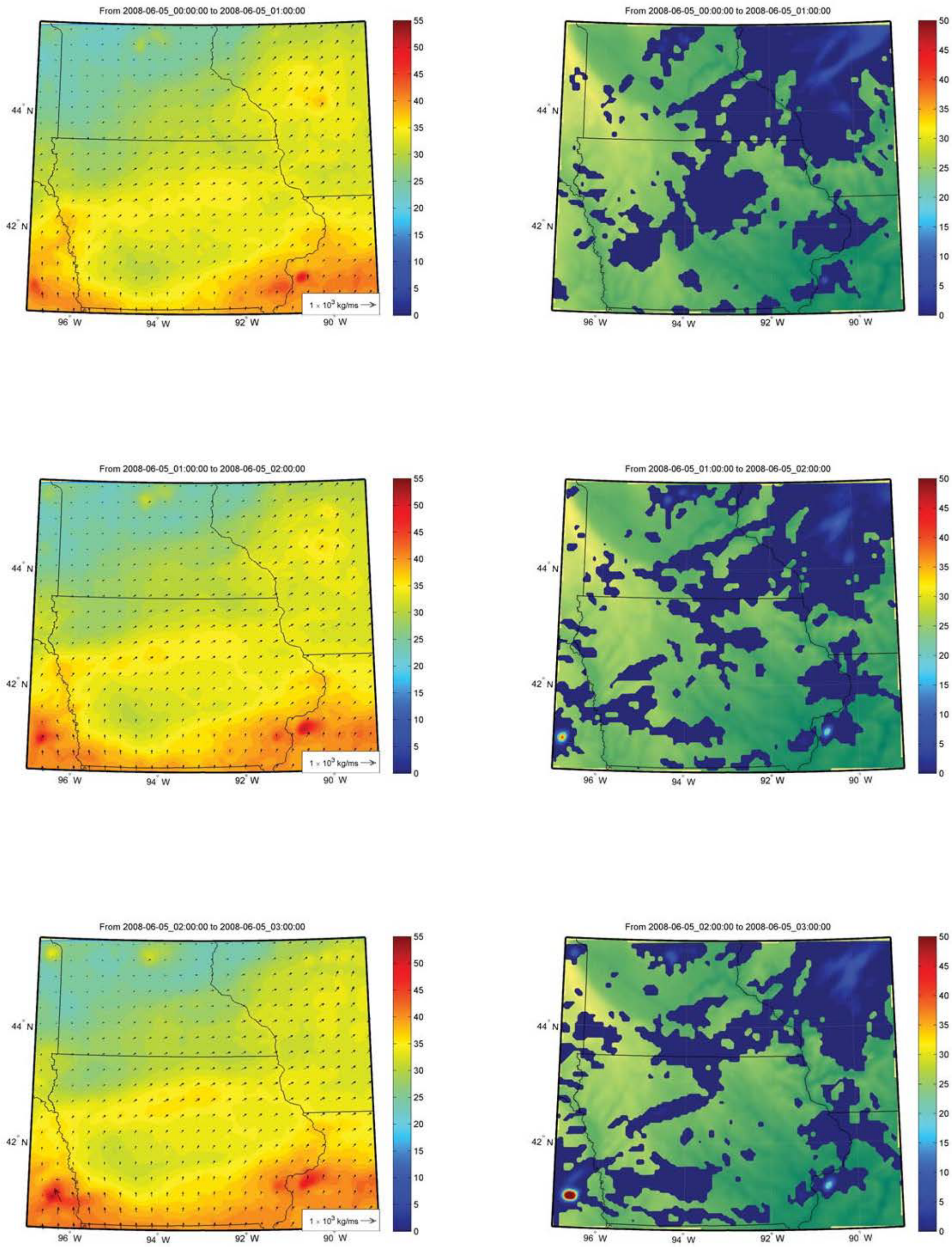

Figure B-9 Hourly Simulated Precipitable Water (Left, Colormap [mm]) and Water Vapor Flux Fields (Left, Arrows [kg m^{-1} s^{-1}]) and Precipitation Fields (Right, Colormap [mm]) for the June 5, 2008 MCS

Plots shown from 06/04/2008 at 18hr to 06/06/2008 at 14hr (Continued).

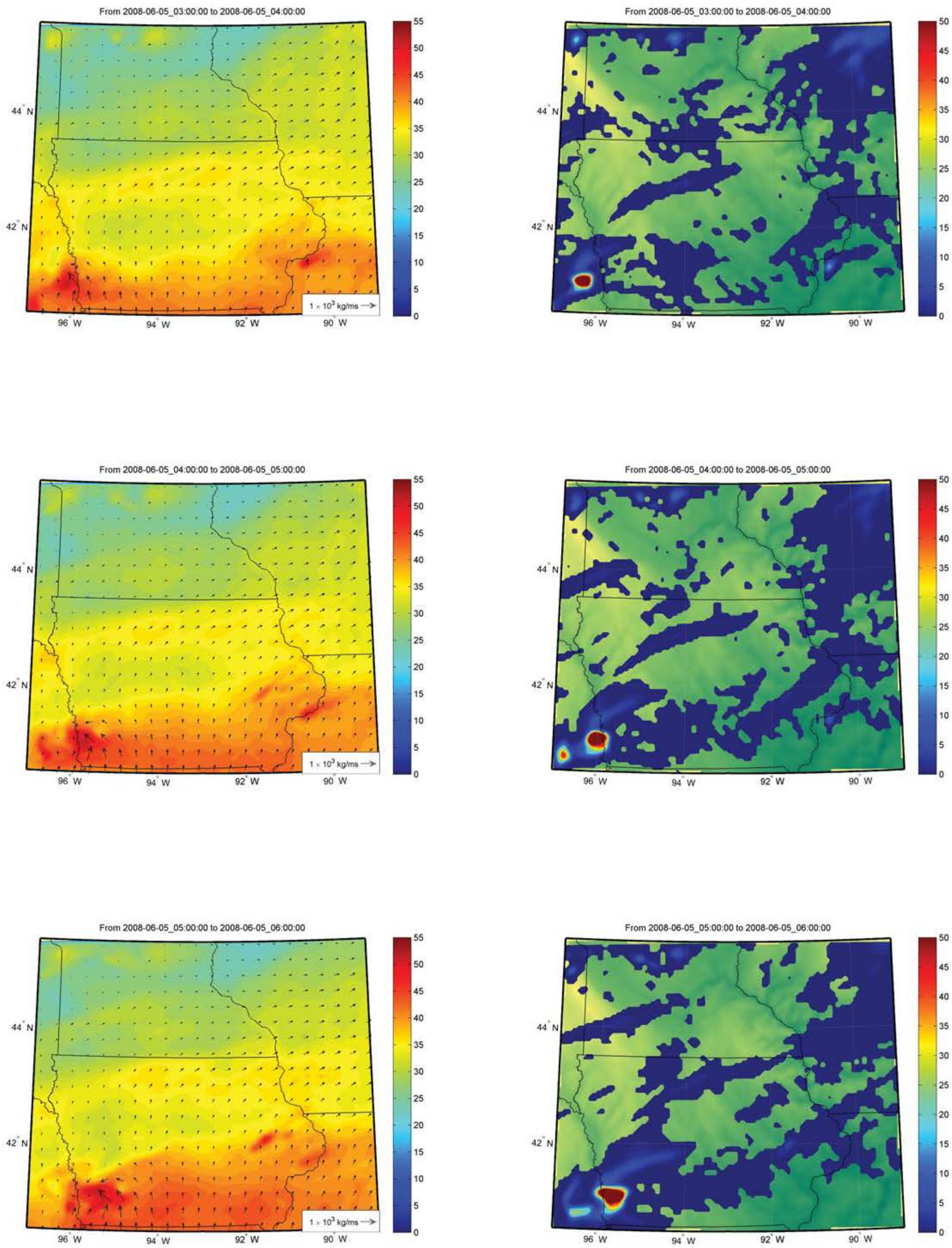

Figure B-9 Hourly Simulated Precipitable Water (Left, Colormap [mm]) and Water Vapor Flux Fields (Left, Arrows [kg m^{-1} s^{-1}]) and Precipitation Fields (Right, Colormap [mm]) for the June 5, 2008 MCS

Plots shown from 06/04/2008 at 18hr to 06/06/2008 at 14hr (Continued).

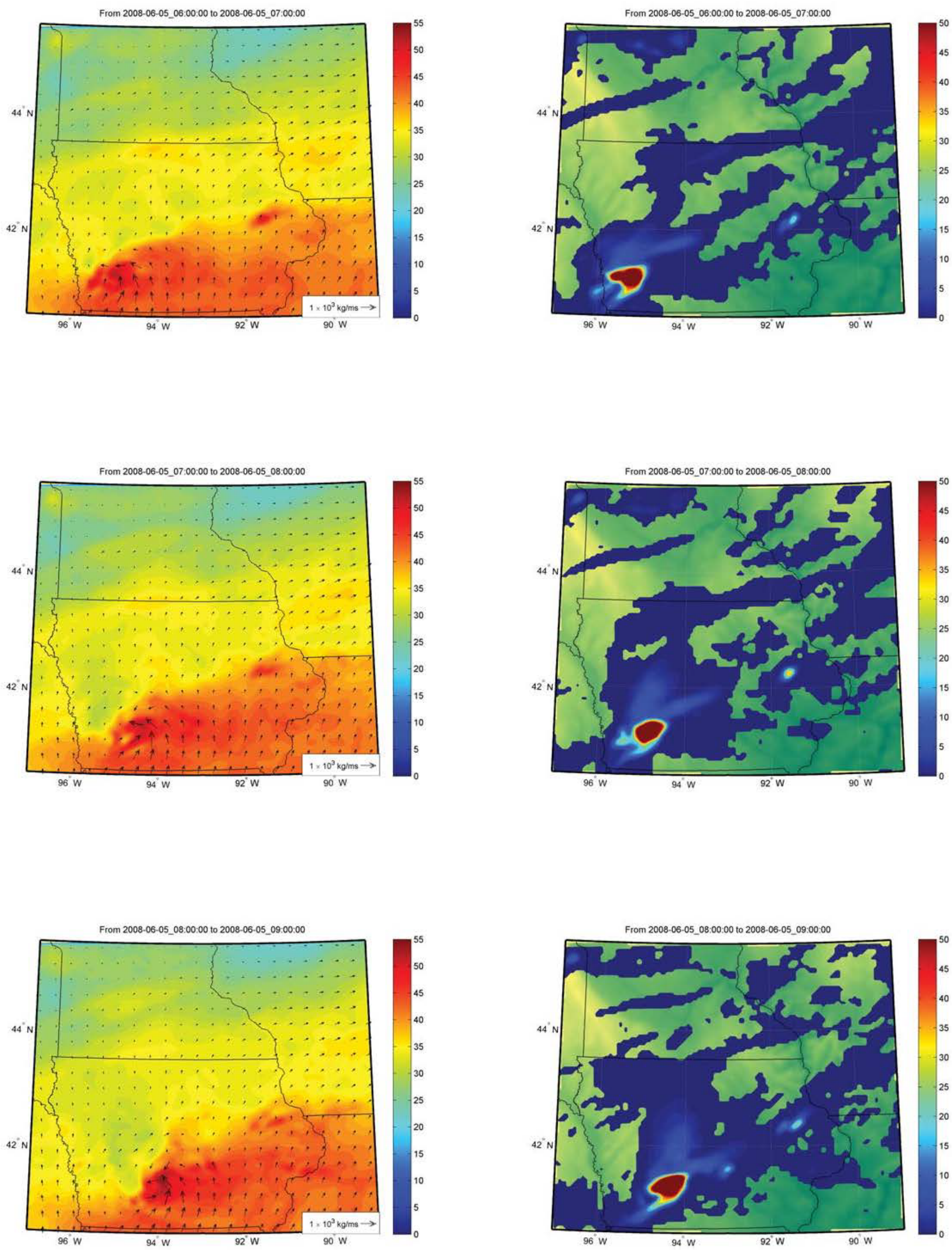

Figure B-9 **Hourly Simulated Precipitable Water (Left, Colormap [mm]) and Water Vapor Flux Fields (Left, Arrows [kg m^{-1} s^{-1}]) and Precipitation Fields (Right, Colormap [mm]) for the June 5, 2008 MCS**

Plots shown from 06/04/2008 at 18hr to 06/06/2008 at 14hr (Continued).

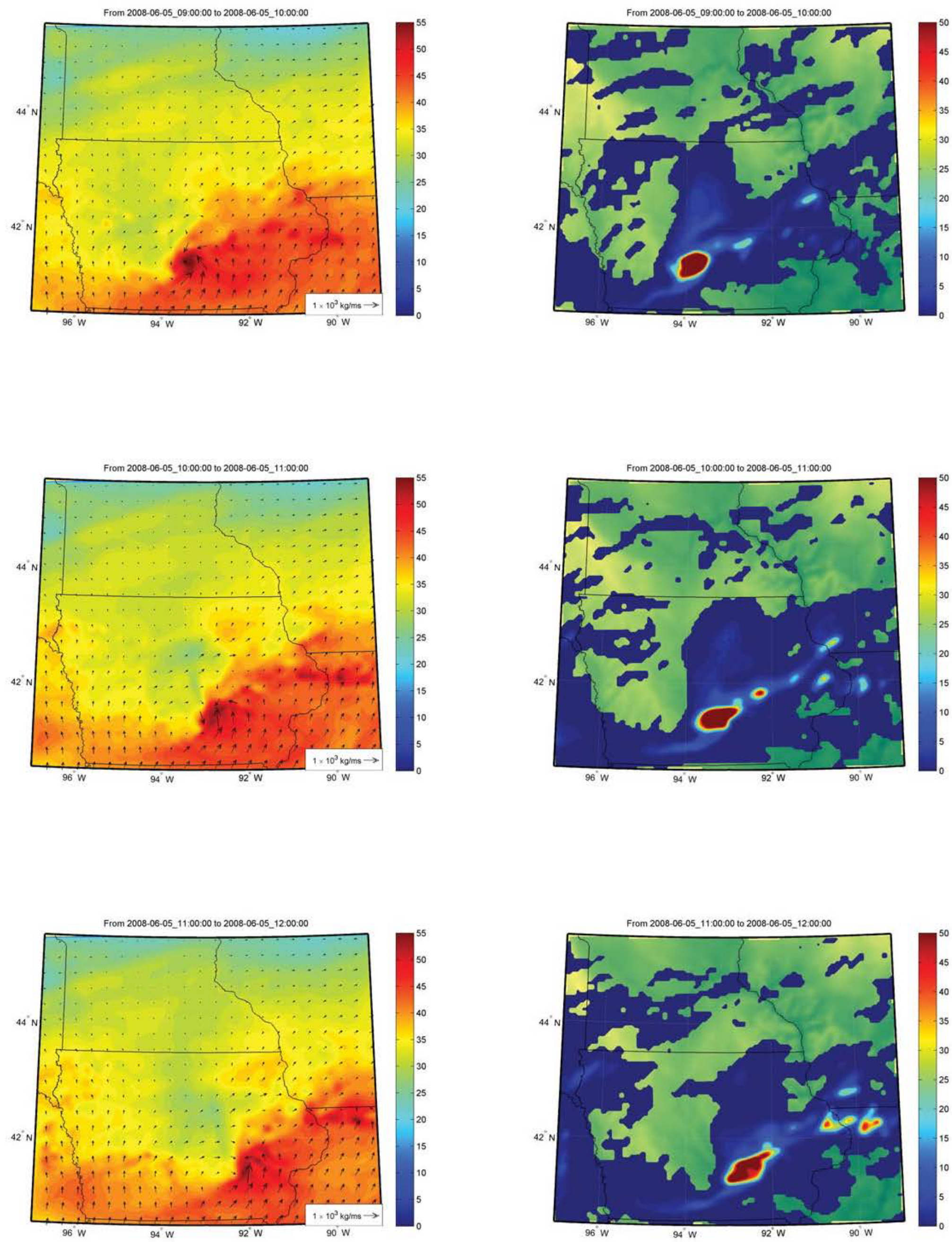

Figure B-9 **Hourly Simulated Precipitable Water (Left, Colormap [mm]) and Water Vapor Flux Fields (Left, Arrows [kg m^{-1} s^{-1}]) and Precipitation Fields (Right, Colormap [mm]) for the June 5, 2008 MCS**

Plots shown from 06/04/2008 at 18hr to 06/06/2008 at 14hr (Continued).

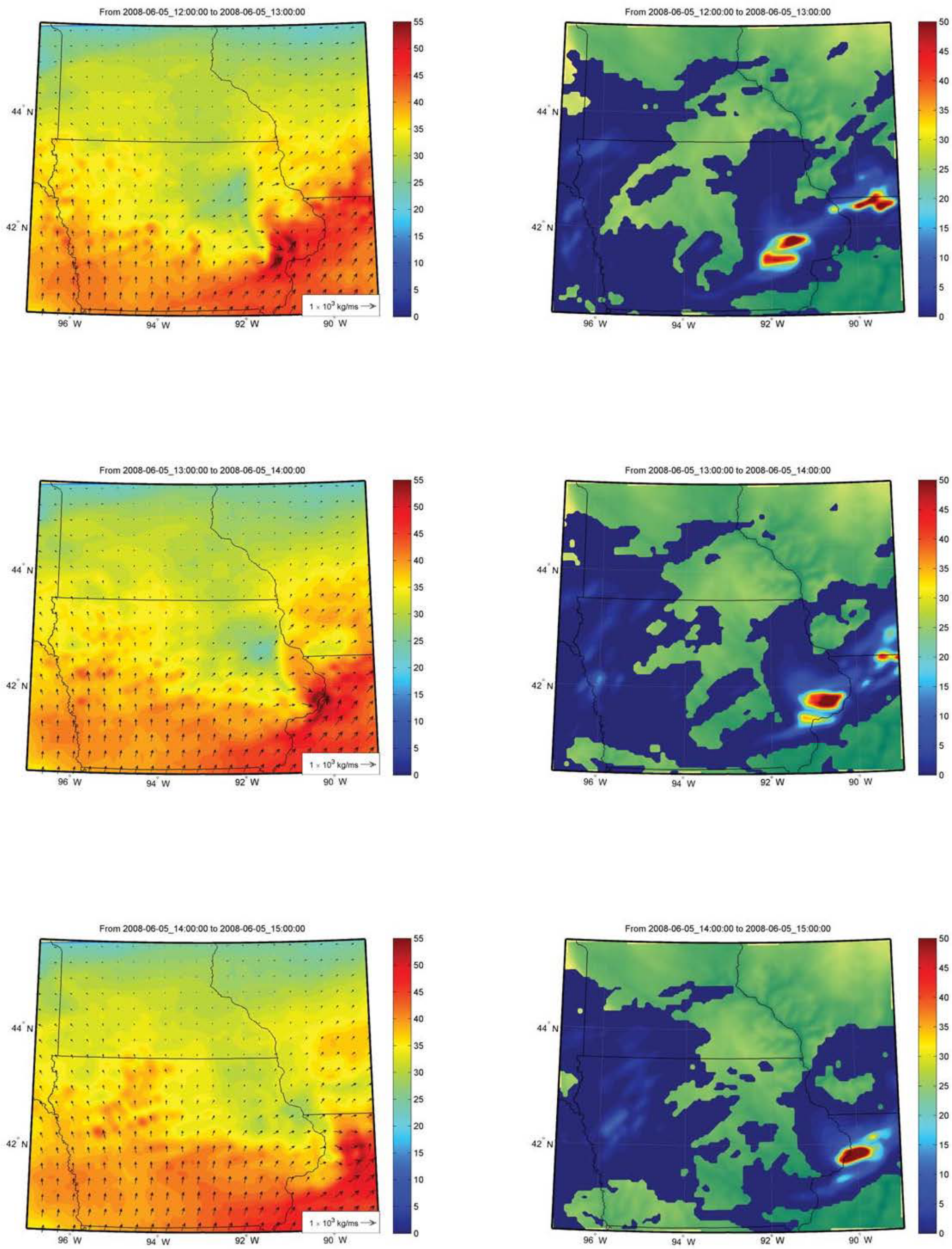

Figure B-9 Hourly Simulated Precipitable Water (Left, Colormap [mm]) and Water Vapor Flux Fields (Left, Arrows [kg m^{-1} s^{-1}]) and Precipitation Fields (Right, Colormap [mm]) for the June 5, 2008 MCS

Plots shown from 06/04/2008 at 18hr to 06/06/2008 at 14hr (Continued).

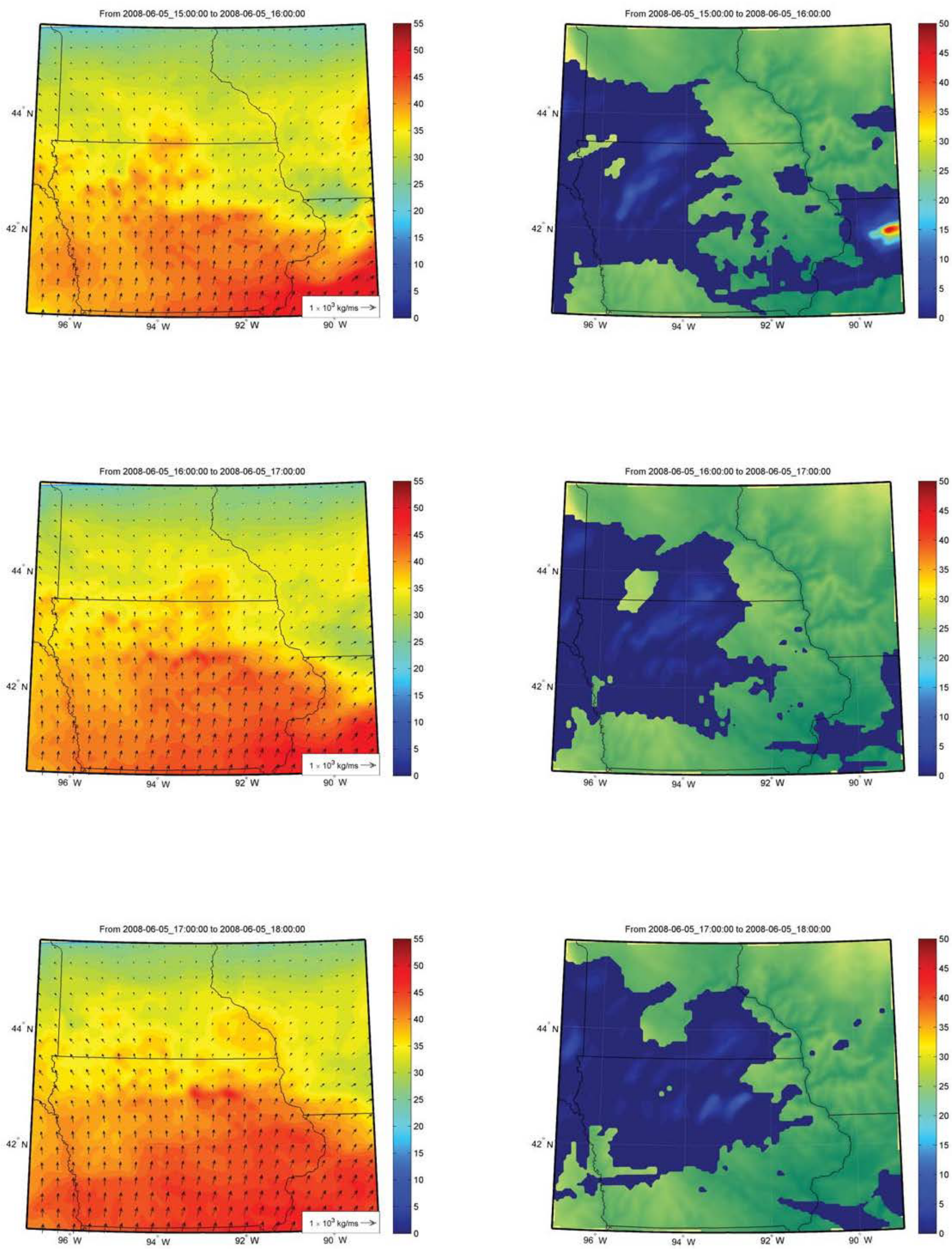

Figure B-9 **Hourly Simulated Precipitable Water (Left, Colormap [mm]) and Water Vapor Flux Fields (Left, Arrows [kg m^{-1} s^{-1}]) and Precipitation Fields (Right, Colormap [mm]) for the June 5, 2008 MCS**

Plots shown from 06/04/2008 at 18hr to 06/06/2008 at 14hr (Continued).

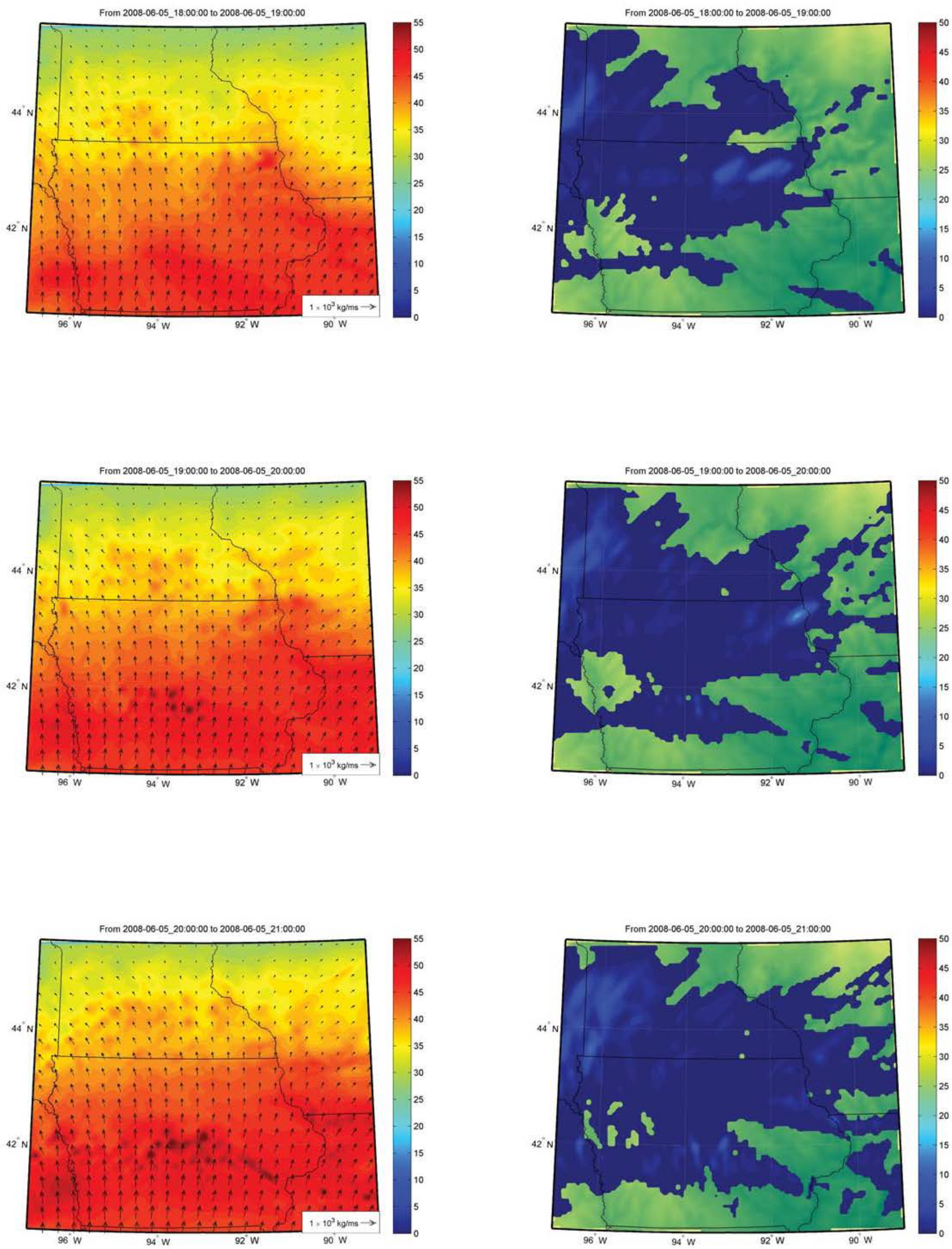

Figure B-9 Hourly Simulated Precipitable Water (Left, Colormap [mm]) and Water Vapor Flux Fields (Left, Arrows [kg m^{-1} s^{-1}]) and Precipitation Fields (Right, Colormap [mm]) for the June 5, 2008 MCS

Plots shown from 06/04/2008 at 18hr to 06/06/2008 at 14hr (Continued).

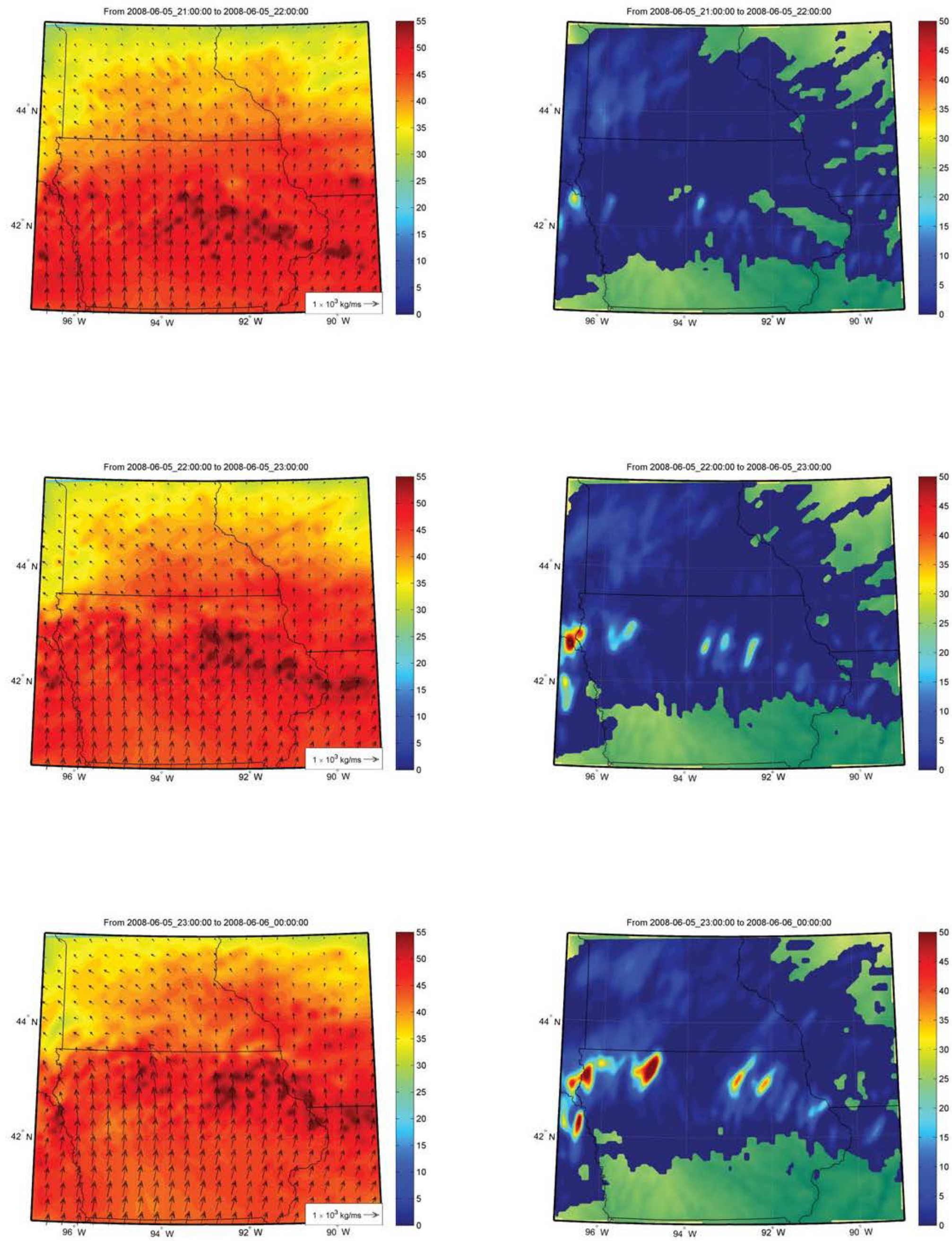

Figure B-9 Hourly Simulated Precipitable Water (Left, Colormap [mm]) and Water Vapor Flux Fields (Left, Arrows [kg m^{-1} s^{-1}]) and Precipitation Fields (Right, Colormap [mm]) for the June 5, 2008 MCS

Plots shown from 06/04/2008 at 18hr to 06/06/2008 at 14hr (Continued).

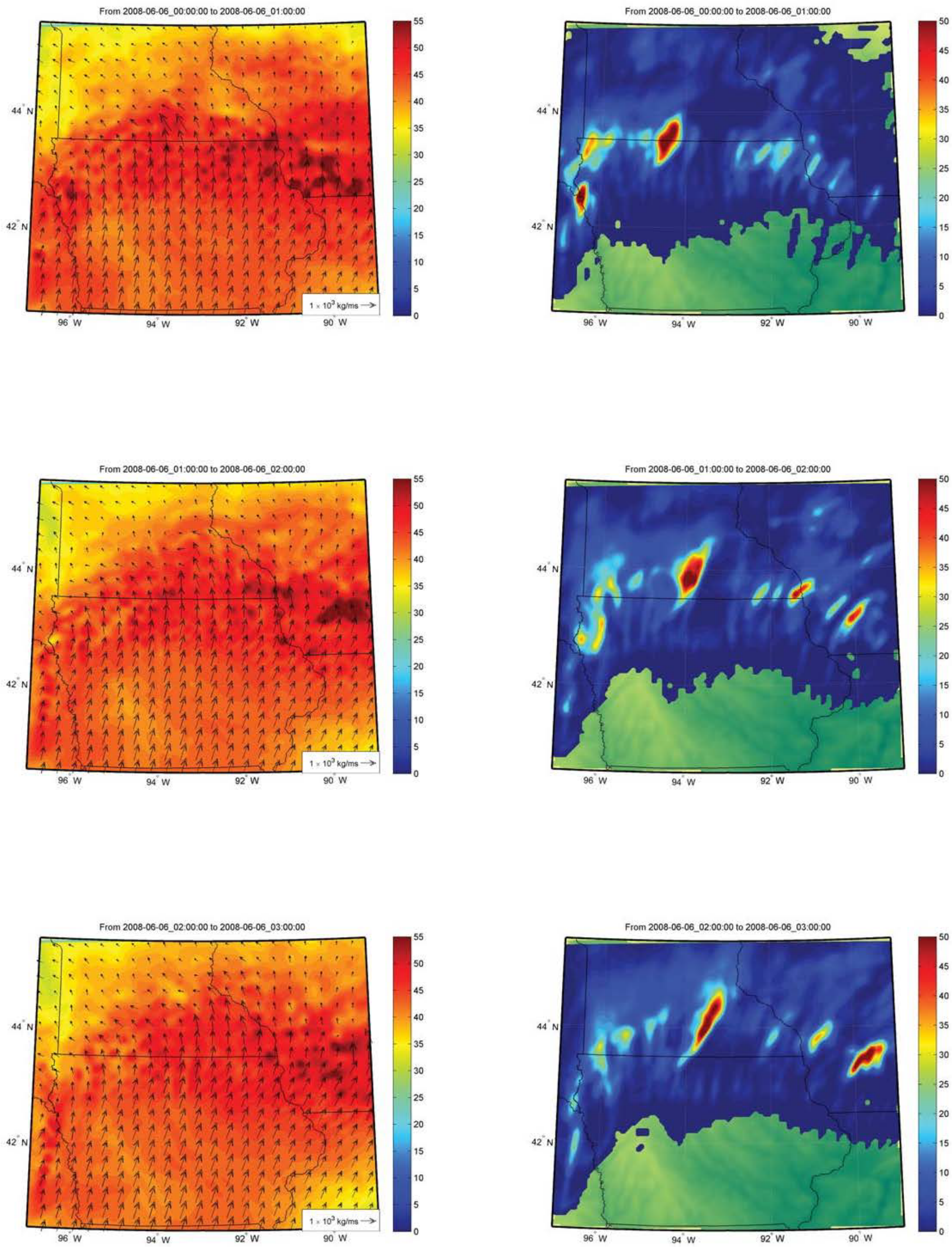

Figure B-9 Hourly Simulated Precipitable Water (Left, Colormap [mm]) and Water Vapor Flux Fields (Left, Arrows [kg m^{-1} s^{-1}]) and Precipitation Fields (Right, Colormap [mm]) for the June 5, 2008 MCS

Plots shown from 06/04/2008 at 18hr to 06/06/2008 at 14hr (Continued).

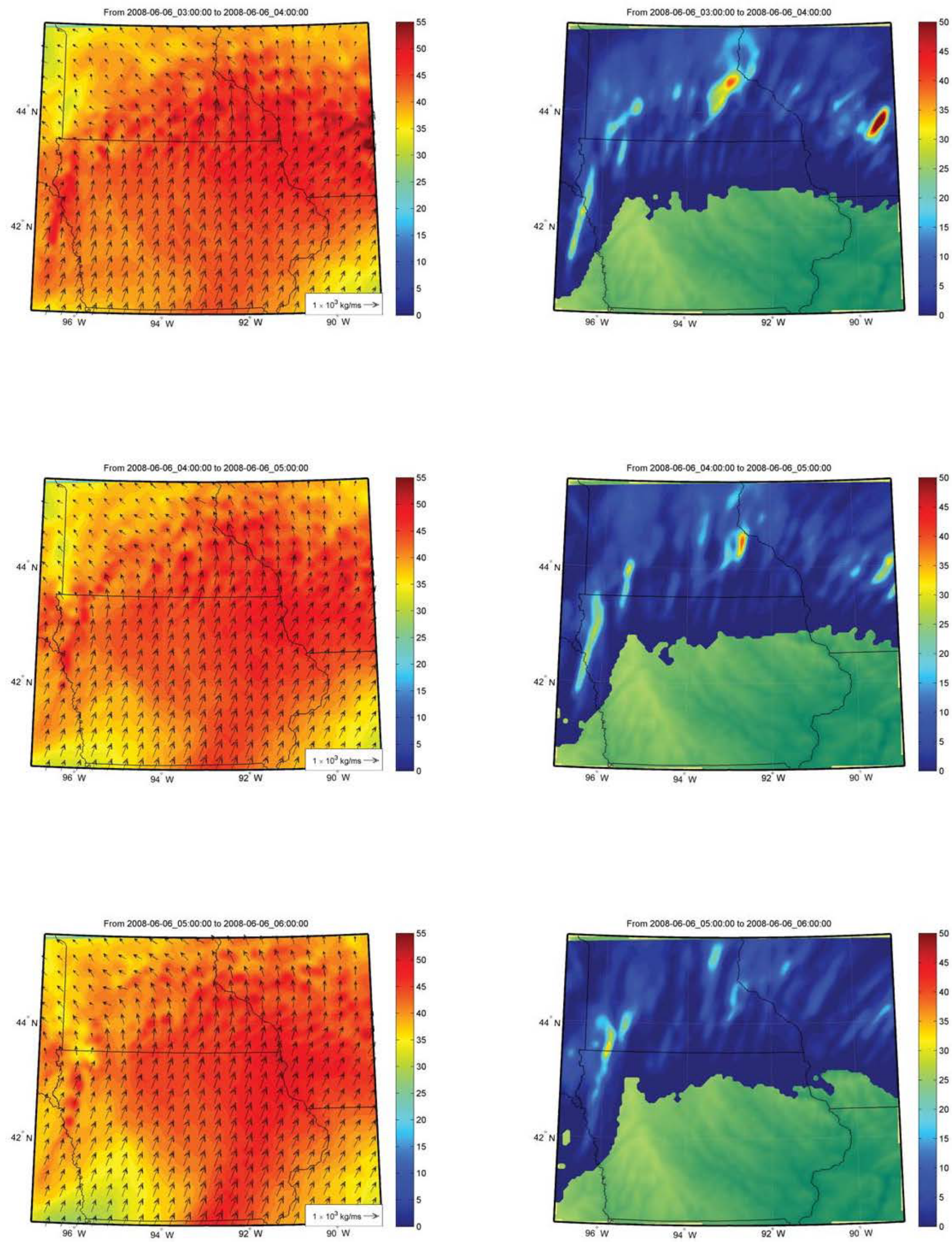

Figure B-9 **Hourly Simulated Precipitable Water (Left, Colormap [mm]) and Water Vapor Flux Fields (Left, Arrows [kg m^{-1} s^{-1}]) and Precipitation Fields (Right, Colormap [mm]) for the June 5, 2008 MCS**

Plots shown from 06/04/2008 at 18hr to 06/06/2008 at 14hr (Continued).

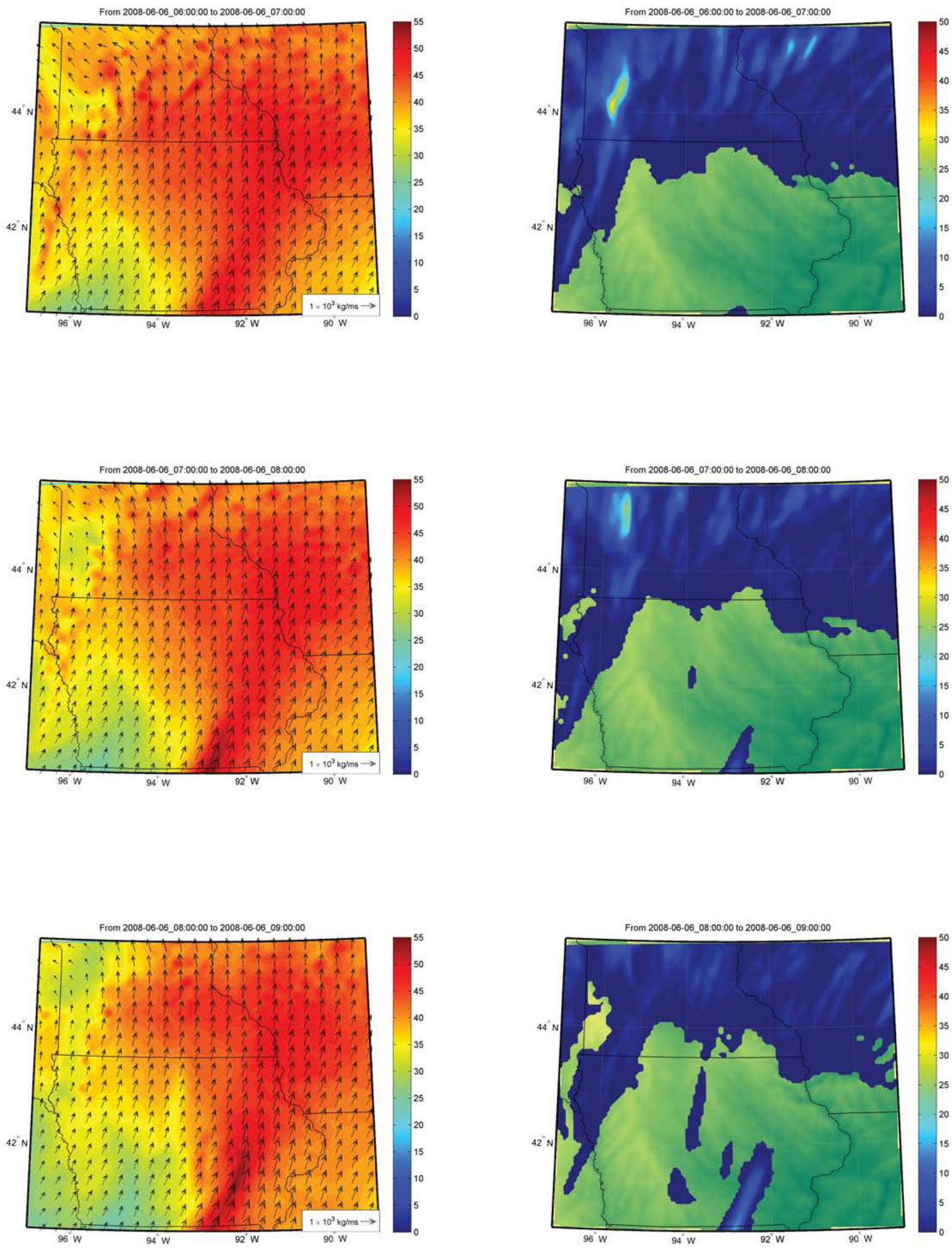

Figure B-9 Hourly Simulated Precipitable Water (Left, Colormap [mm]) and Water Vapor Flux Fields (Left, Arrows [kg m^{-1} s^{-1}]) and Precipitation Fields (Right, Colormap [mm]) for the June 5, 2008 MCS

Plots shown from 06/04/2008 at 18hr to 06/06/2008 at 14hr (Continued).

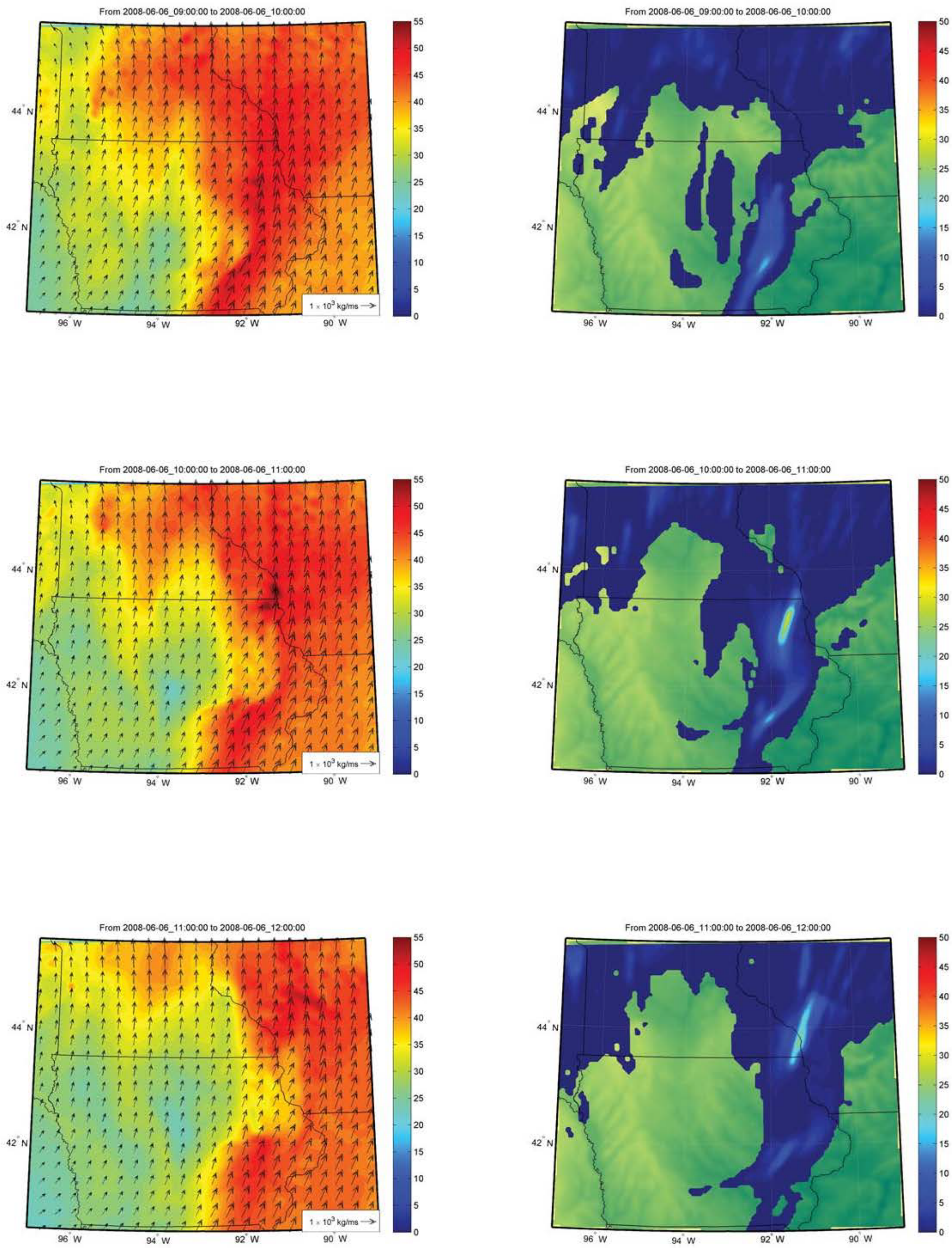

Figure B-9 **Hourly Simulated Precipitable Water (Left, Colormap [mm]) and Water Vapor Flux Fields (Left, Arrows [kg m^{-1} s^{-1}]) and Precipitation Fields (Right, Colormap [mm]) for the June 5, 2008 MCS**

Plots shown from 06/04/2008 at 18hr to 06/06/2008 at 14hr (Continued).

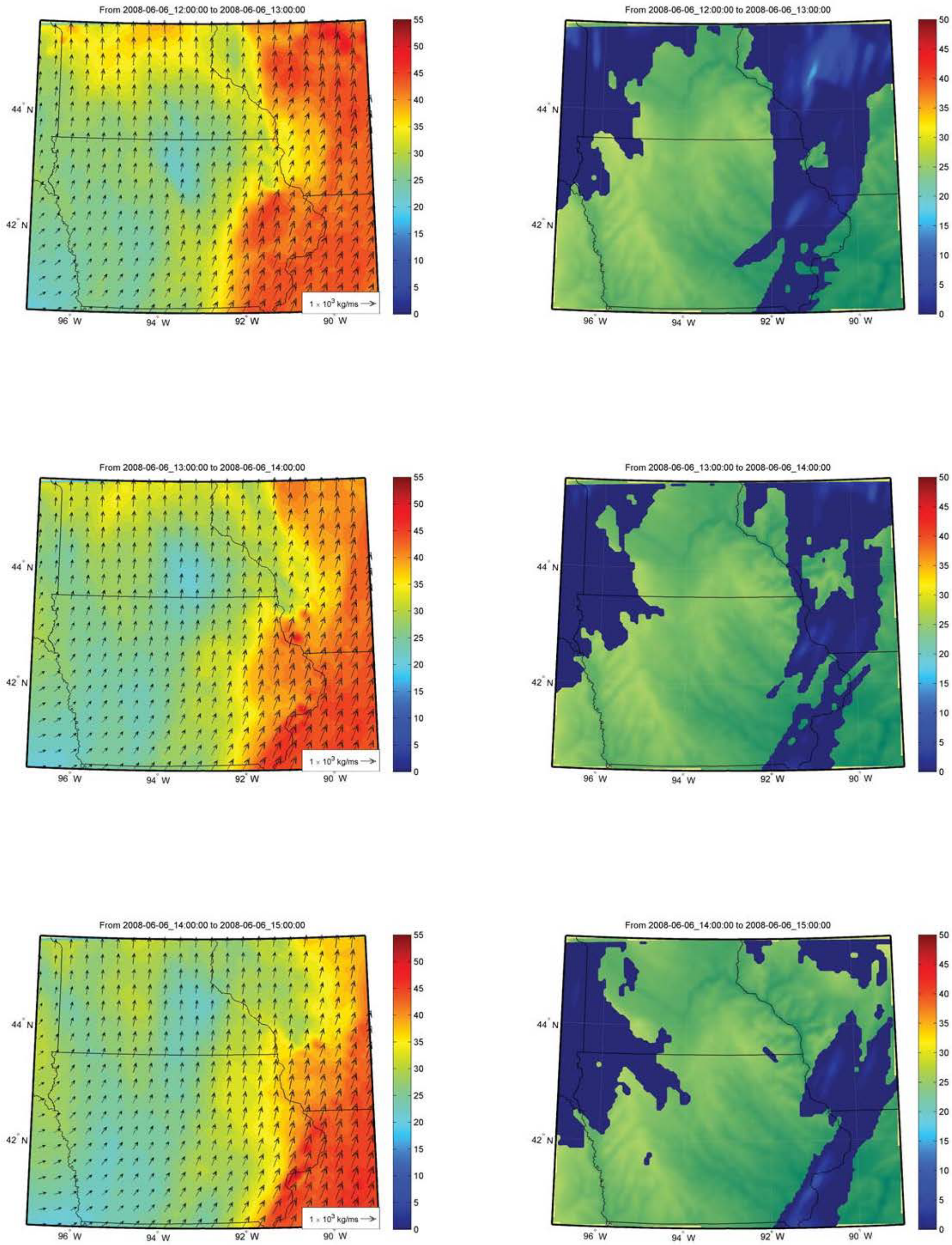

Figure B-9 Hourly Simulated Precipitable Water (Left, Colormap [mm]) and Water Vapor Flux Fields (Left, Arrows [kg m^{-1} s^{-1}]) and Precipitation Fields (Right, Colormap [mm]) for the June 5, 2008 MCS

Plots shown from 06/04/2008 at 18hr to 06/06/2008 at 14hr (Continued).

B.1.10 August 8, 2009 MCS

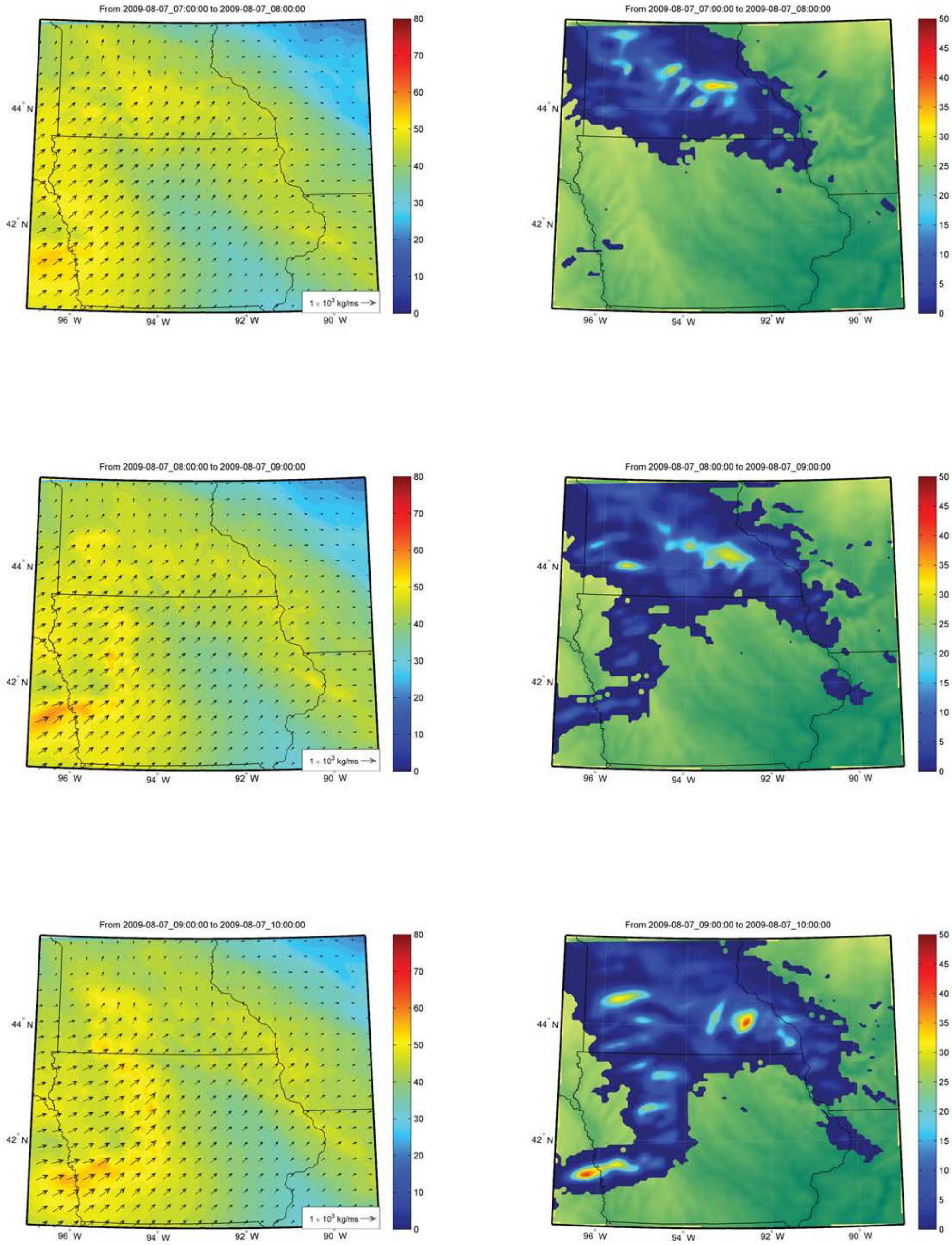

Figure B-10 Hourly Simulated Precipitable Water (Left, Colormap [mm]) and Water Vapor Flux Fields (Left, Arrows [kg m^{-1} s^{-1}]) and Precipitation Fields (Right, Colormap [mm]) for the August 8, 2009 MCS

Plots shown from 08/07/2009 at 08hr to 08/08/2009 at 19hr.

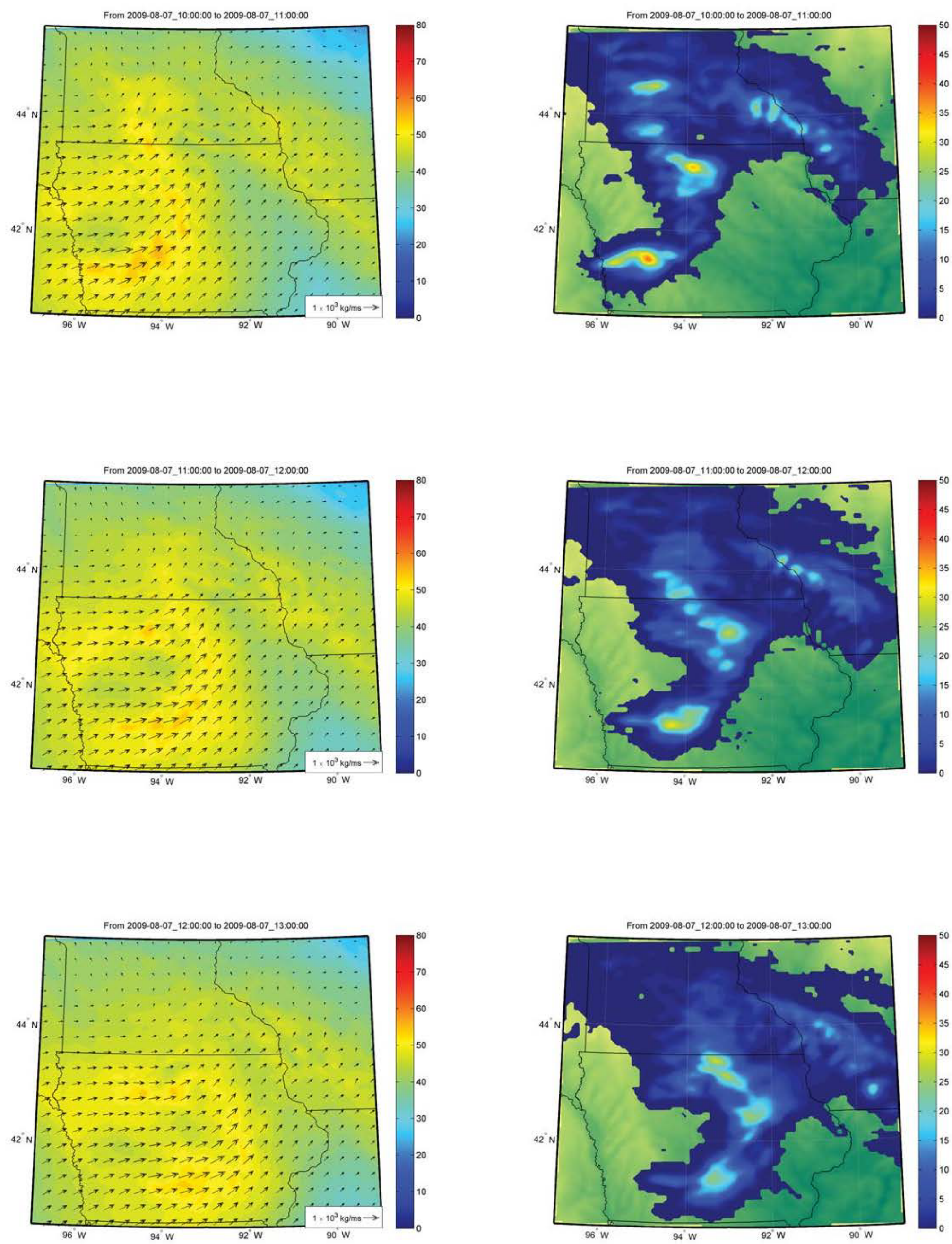

Figure B-10 Hourly Simulated Precipitable Water (Left, Colormap [mm]) and Water Vapor Flux Fields (Left, Arrows [kg m^{-1} s^{-1}]) and Precipitation Fields (Right, Colormap [mm]) for the August 8, 2009 MCS

Plots shown from 08/07/2009 at 08hr to 08/08/2009 at 19hr (Continued).

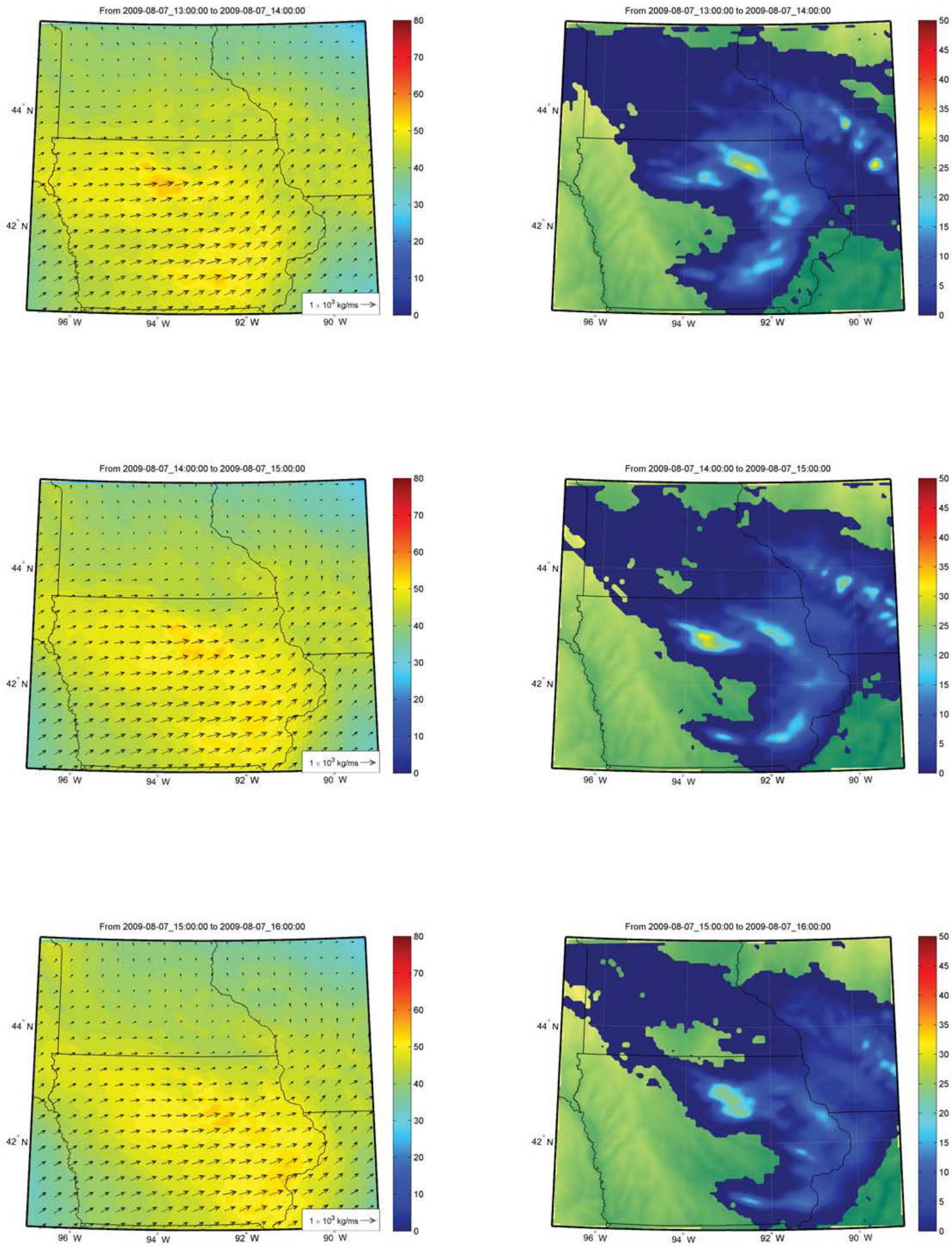

Figure B-10 **Hourly Simulated Precipitable Water (Left, Colormap [mm]) and Water Vapor Flux Fields (Left, Arrows [kg m^{-1} s^{-1}]) and Precipitation Fields (Right, Colormap [mm]) for the August 8, 2009 MCS**

Plots shown from 08/07/2009 at 08hr to 08/08/2009 at 19hr (Continued).

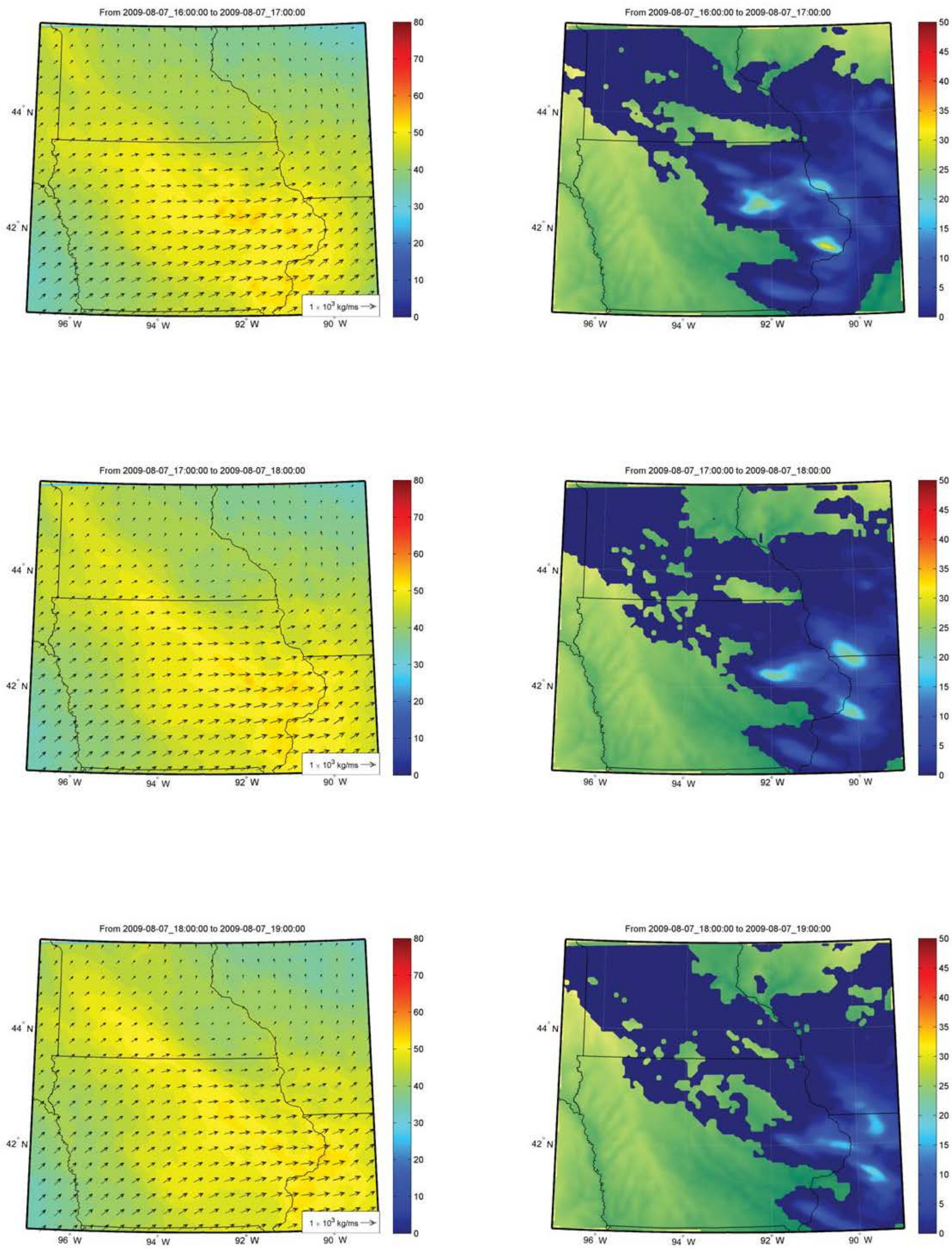

Figure B-10 Hourly Simulated Precipitable Water (Left, Colormap [mm]) and Water Vapor Flux Fields (Left, Arrows [kg m^{-1} s^{-1}]) and Precipitation Fields (Right, Colormap [mm]) for the August 8, 2009 MCS

Plots shown from 08/07/2009 at 08hr to 08/08/2009 at 19hr (Continued).

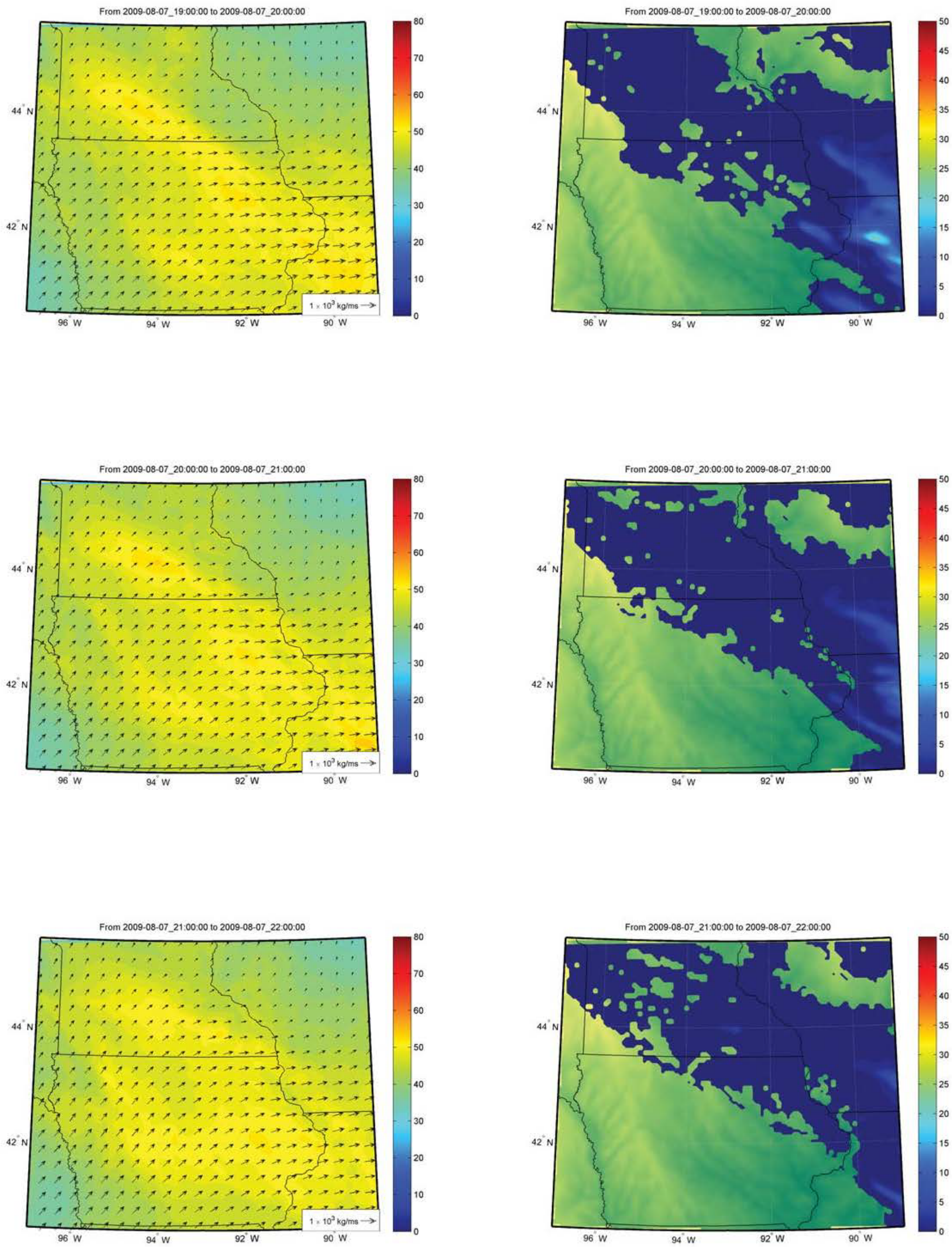

Figure B-10 Hourly Simulated Precipitable Water (Left, Colormap [mm]) and Water Vapor Flux Fields (Left, Arrows [kg m^{-1} s^{-1}]) and Precipitation Fields (Right, Colormap [mm]) for the August 8, 2009 MCS

Plots shown from 08/07/2009 at 08hr to 08/08/2009 at 19hr (Continued).

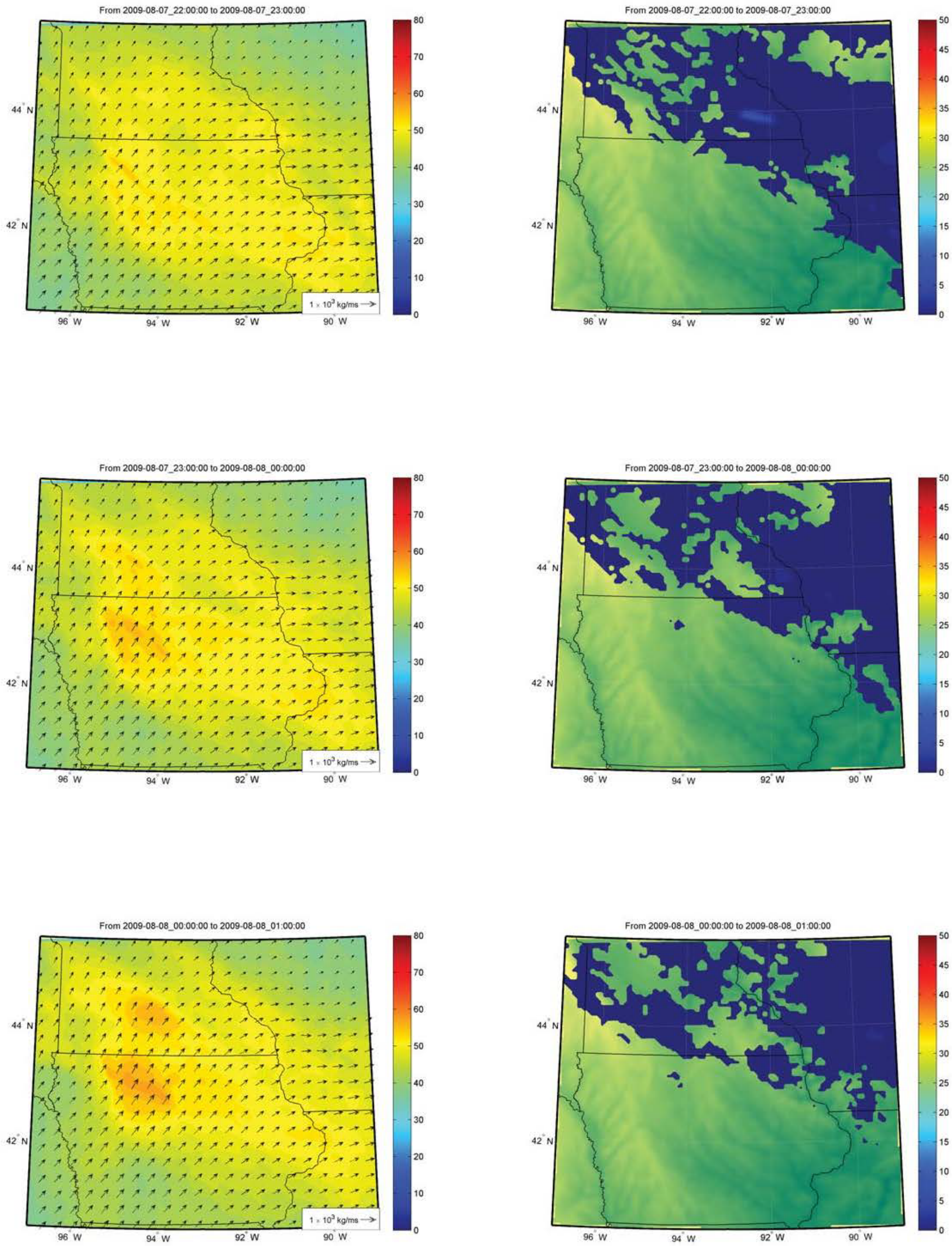

Figure B-10 Hourly Simulated Precipitable Water (Left, Colormap [mm]) and Water Vapor Flux Fields (Left, Arrows [kg m^{-1} s^{-1}]) and Precipitation Fields (Right, Colormap [mm]) for the August 8, 2009 MCS

Plots shown from 08/07/2009 at 08hr to 08/08/2009 at 19hr (Continued).

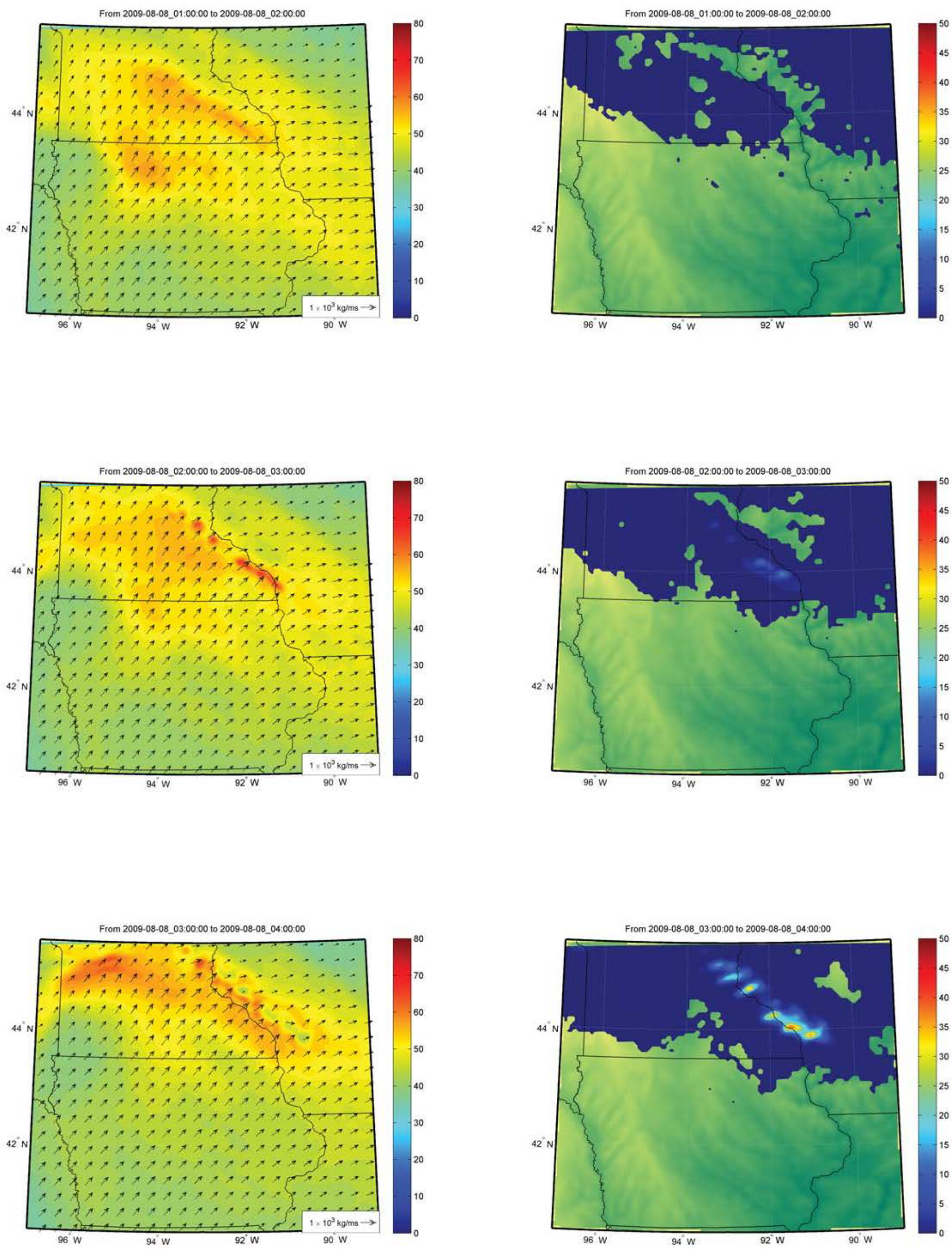

Figure B-10 Hourly Simulated Precipitable Water (Left, Colormap [mm]) and Water Vapor Flux Fields (Left, Arrows [kg m^{-1} s^{-1}]) and Precipitation Fields (Right, Colormap [mm]) for the August 8, 2009 MCS

Plots shown from 08/07/2009 at 08hr to 08/08/2009 at 19hr (Continued).

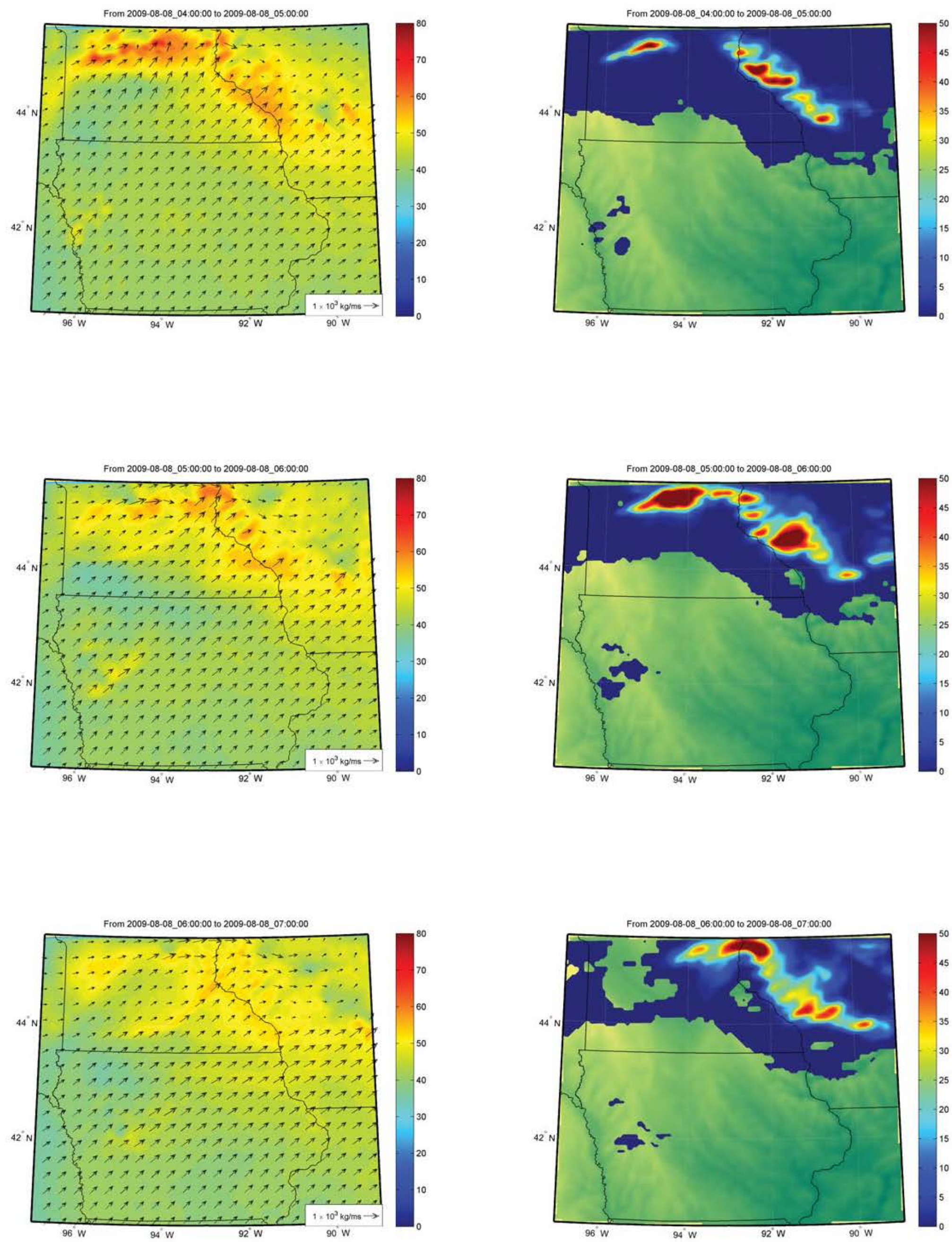

Figure B-10 **Hourly Simulated Precipitable Water (Left, Colormap [mm]) and Water Vapor Flux Fields (Left, Arrows [kg m^{-1} s^{-1}]) and Precipitation Fields (Right, Colormap [mm]) for the August 8, 2009 MCS**

Plots shown from 08/07/2009 at 08hr to 08/08/2009 at 19hr (Continued).

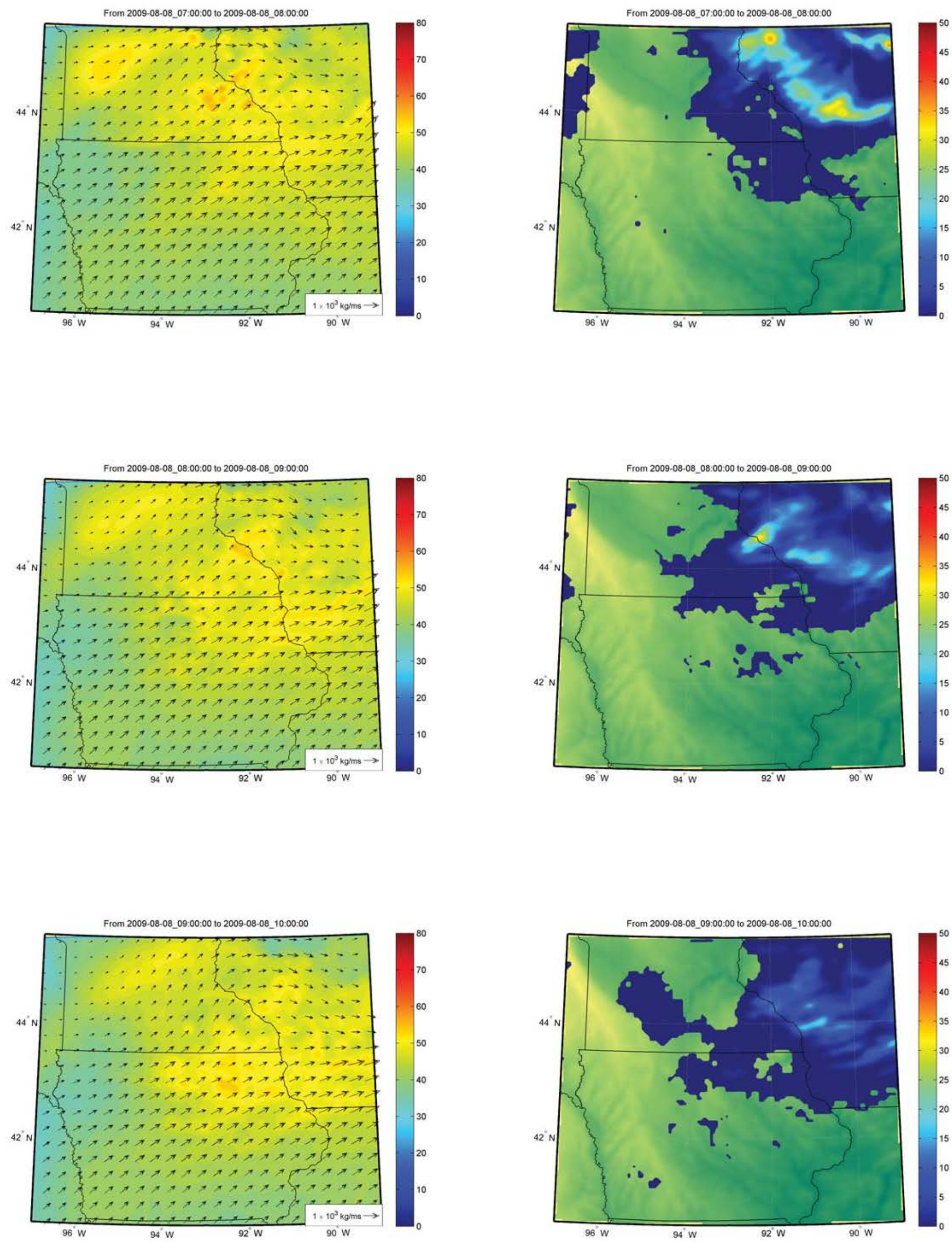

Figure B-10 Hourly Simulated Precipitable Water (Left, Colormap [mm]) and Water Vapor Flux Fields (Left, Arrows [kg m^{-1} s^{-1}]) and Precipitation Fields (Right, Colormap [mm]) for the August 8, 2009 MCS

Plots shown from 08/07/2009 at 08hr to 08/08/2009 at 19hr (Continued).

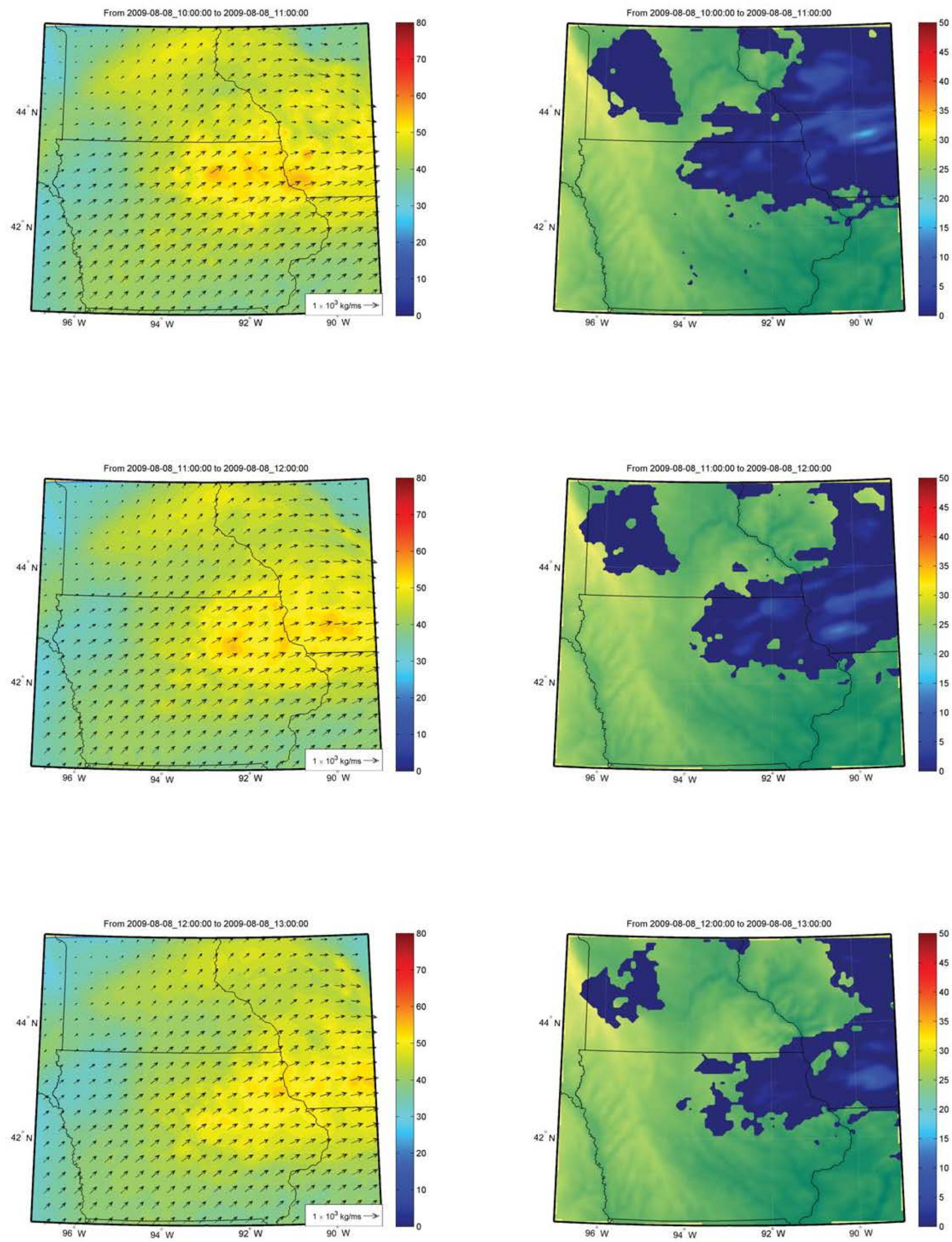

Figure B-10 Hourly Simulated Precipitable Water (Left, Colormap [mm]) and Water Vapor Flux Fields (Left, Arrows [kg m^{-1} s^{-1}]) and Precipitation Fields (Right, Colormap [mm]) for the August 8, 2009 MCS

Plots shown from 08/07/2009 at 08hr to 08/08/2009 at 19hr (Continued).

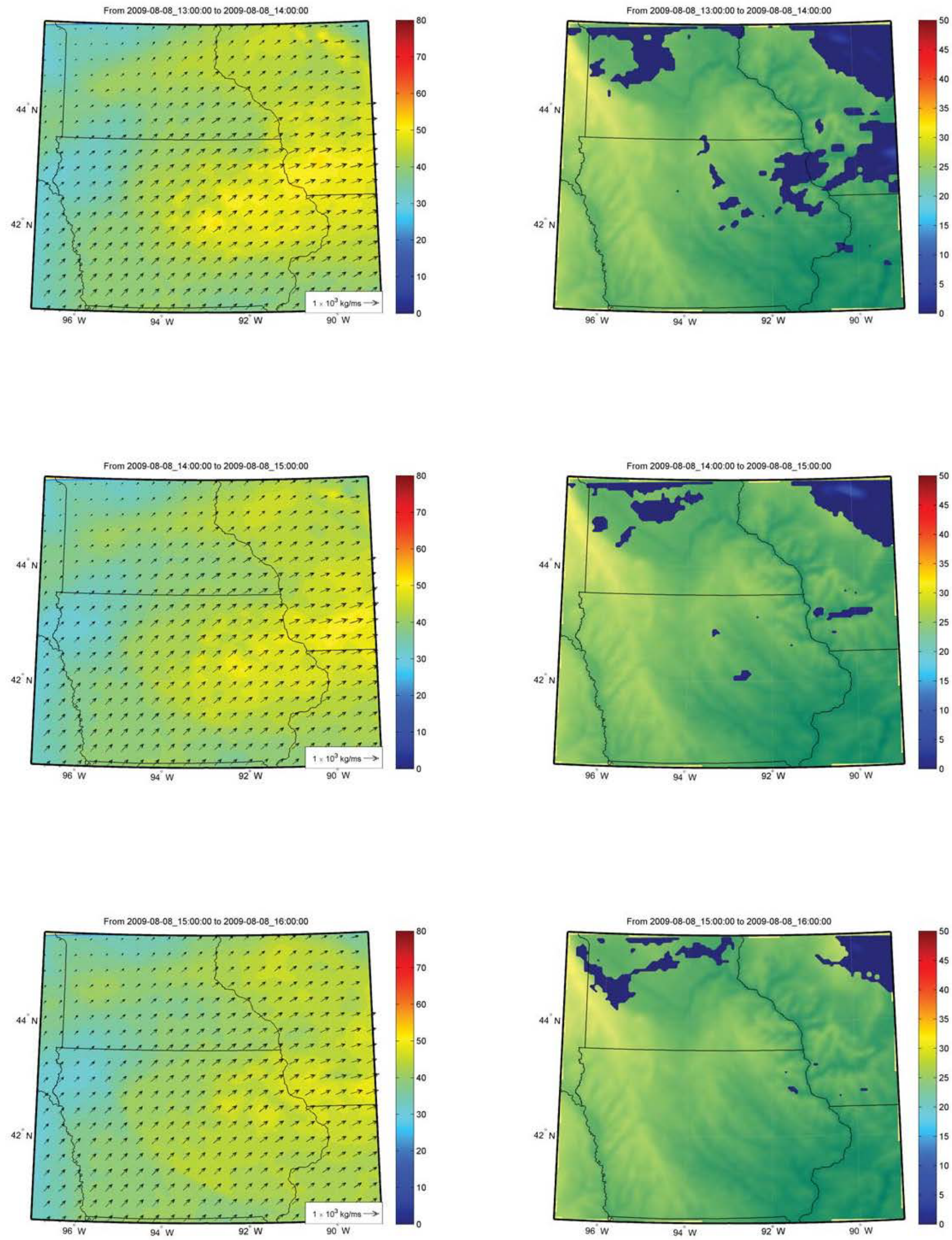

Figure B-10 Hourly Simulated Precipitable Water (Left, Colormap [mm]) and Water Vapor Flux Fields (Left, Arrows [kg m^{-1} s^{-1}]) and Precipitation Fields (Right, Colormap [mm]) for the August 8, 2009 MCS

Plots shown from 08/07/2009 at 08hr to 08/08/2009 at 19hr (Continued).

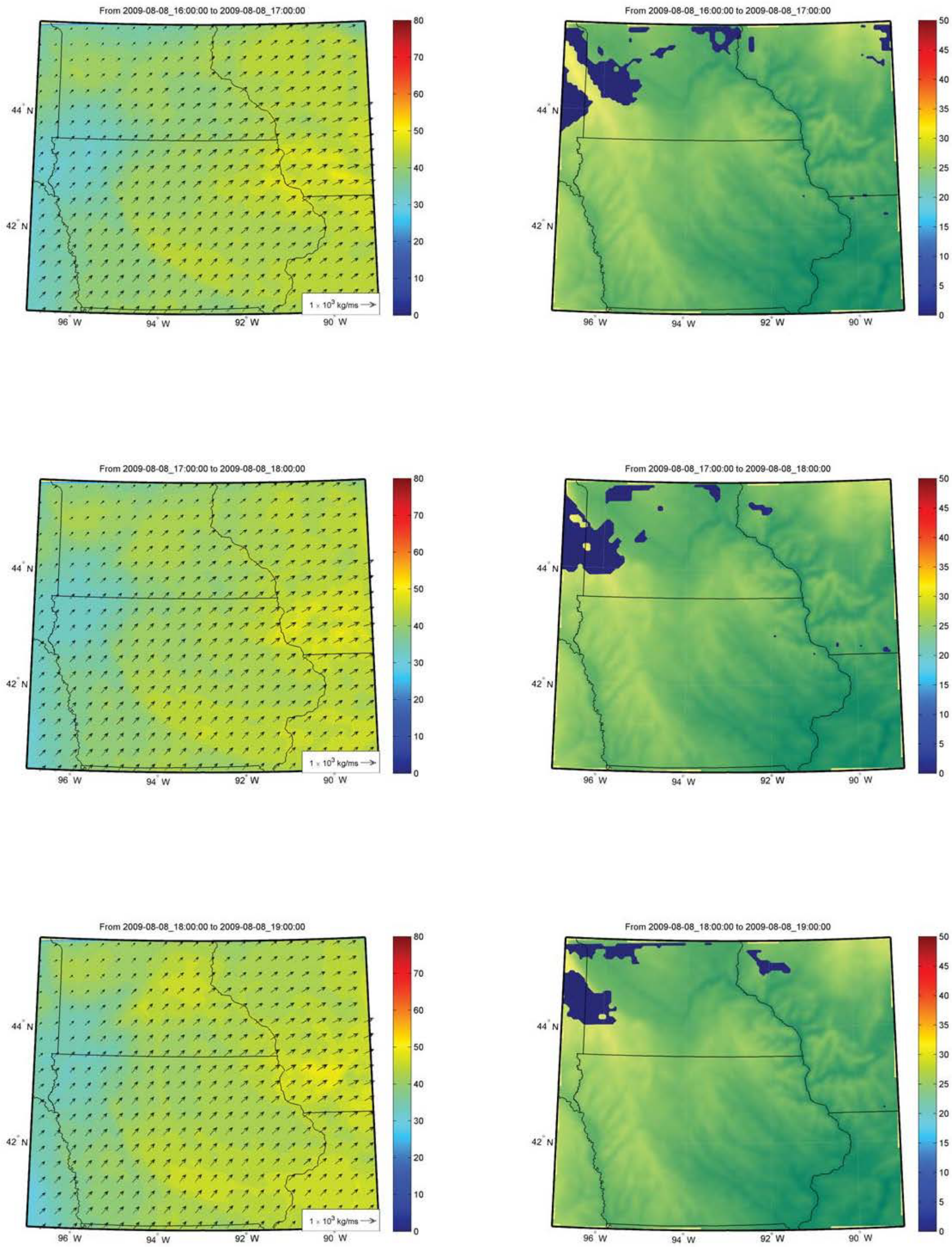

Figure B-10 Hourly Simulated Precipitable Water (Left, Colormap [mm]) and Water Vapor Flux Fields (Left, Arrows [kg m^{-1} s^{-1}]) and Precipitation Fields (Right, Colormap [mm]) for the August 8, 2009 MCS

Plots shown from 08/07/2009 at 08hr to 08/08/2009 at 19hr (Continued).

B.1.11 July 23, 2010 MCS

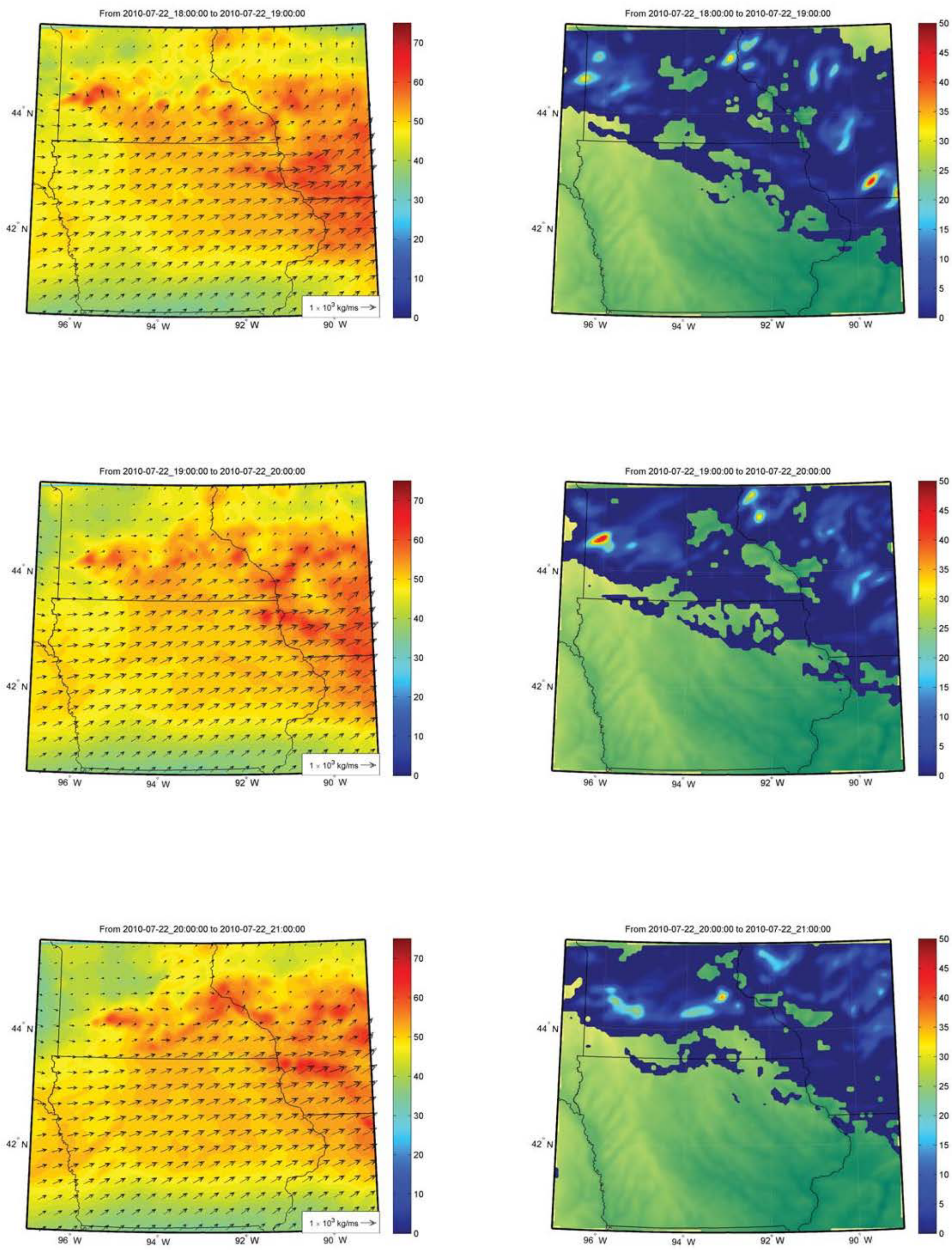

Figure B-11 Hourly Simulated Precipitable Water (Left, Colormap [mm]) and Water Vapor Flux Fields (Left, Arrows [kg m^{-1} s^{-1}]) and Precipitation Fields (Right, Colormap [mm]) for the July 23, 2010 MCS

Plots shown from 07/22/2010 at 18hr to 07/23/2010 at 17hr.

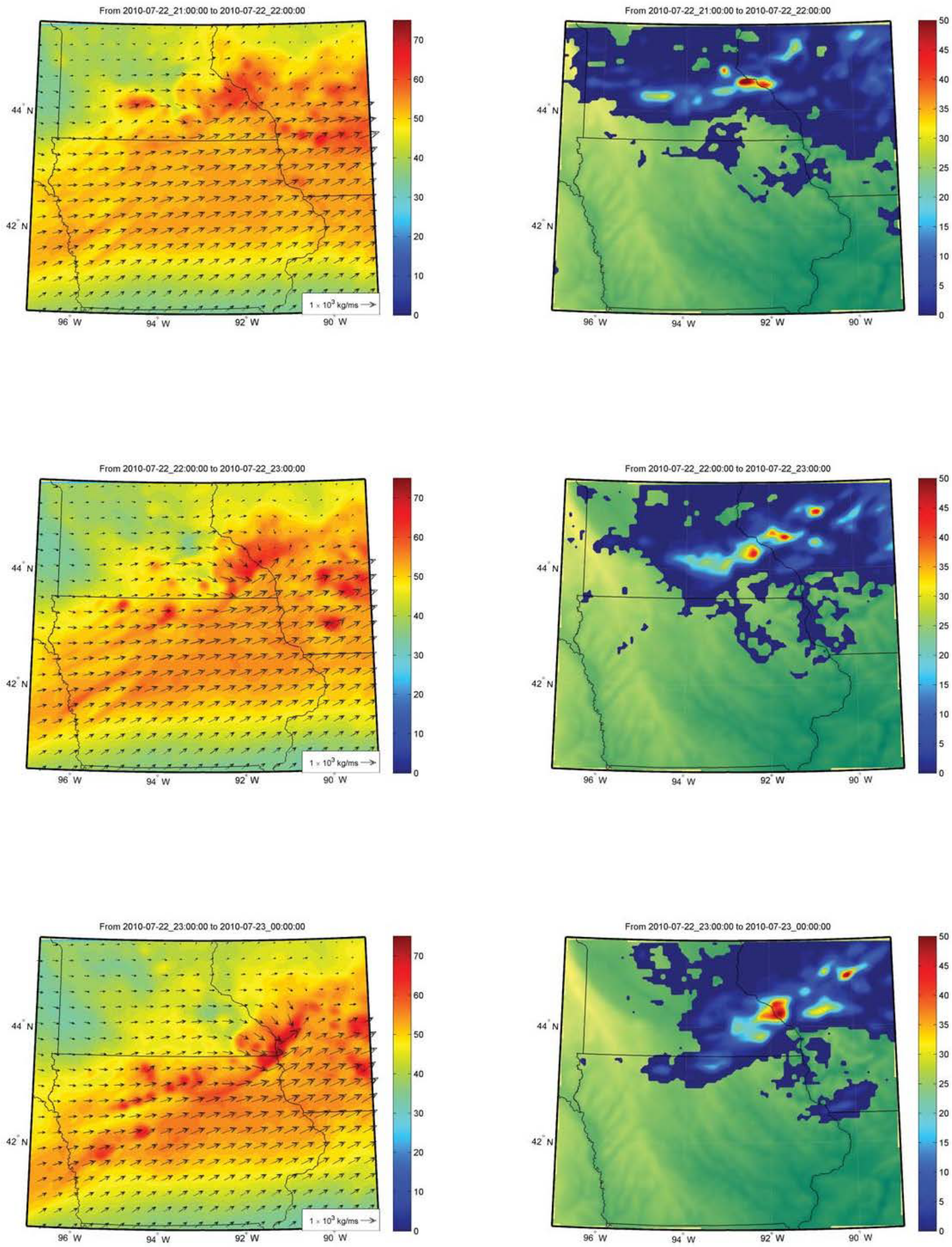

Figure B-11 **Hourly Simulated Precipitable Water (Left, Colormap [mm]) and Water Vapor Flux Fields (Left, Arrows [kg m^{-1} s^{-1}]) and Precipitation Fields (Right, Colormap [mm]) for the July 23, 2010 MCS**

Plots shown from 07/22/2010 at 18hr to 07/23/2010 at 17hr (Continued).

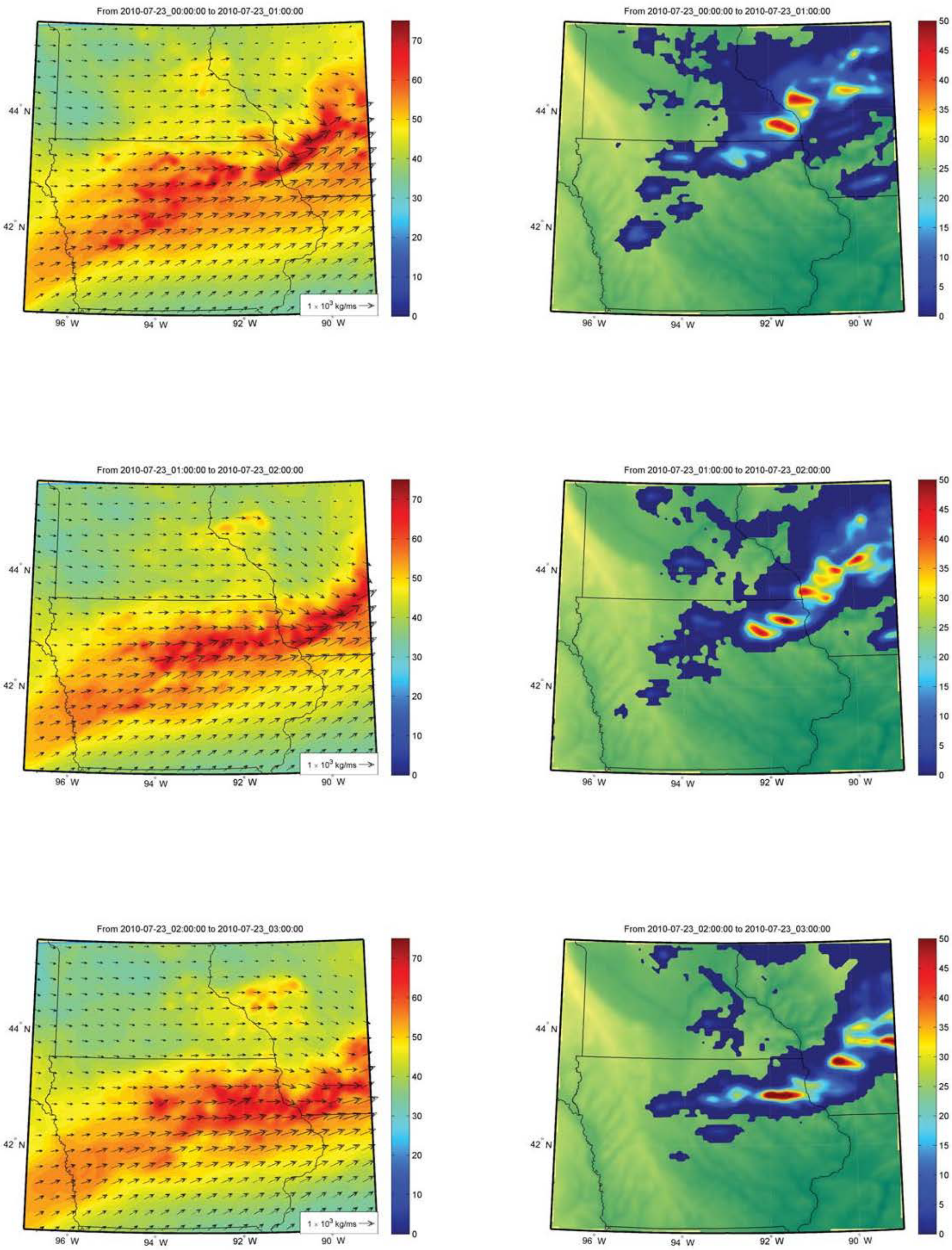

Figure B-11 Hourly Simulated Precipitable Water (Left, Colormap [mm]) and Water Vapor Flux Fields (Left, Arrows [kg m^{-1} s^{-1}]) and Precipitation Fields (Right, Colormap [mm]) for the July 23, 2010 MCS

Plots shown from 07/22/2010 at 18hr to 07/23/2010 at 17hr (Continued).

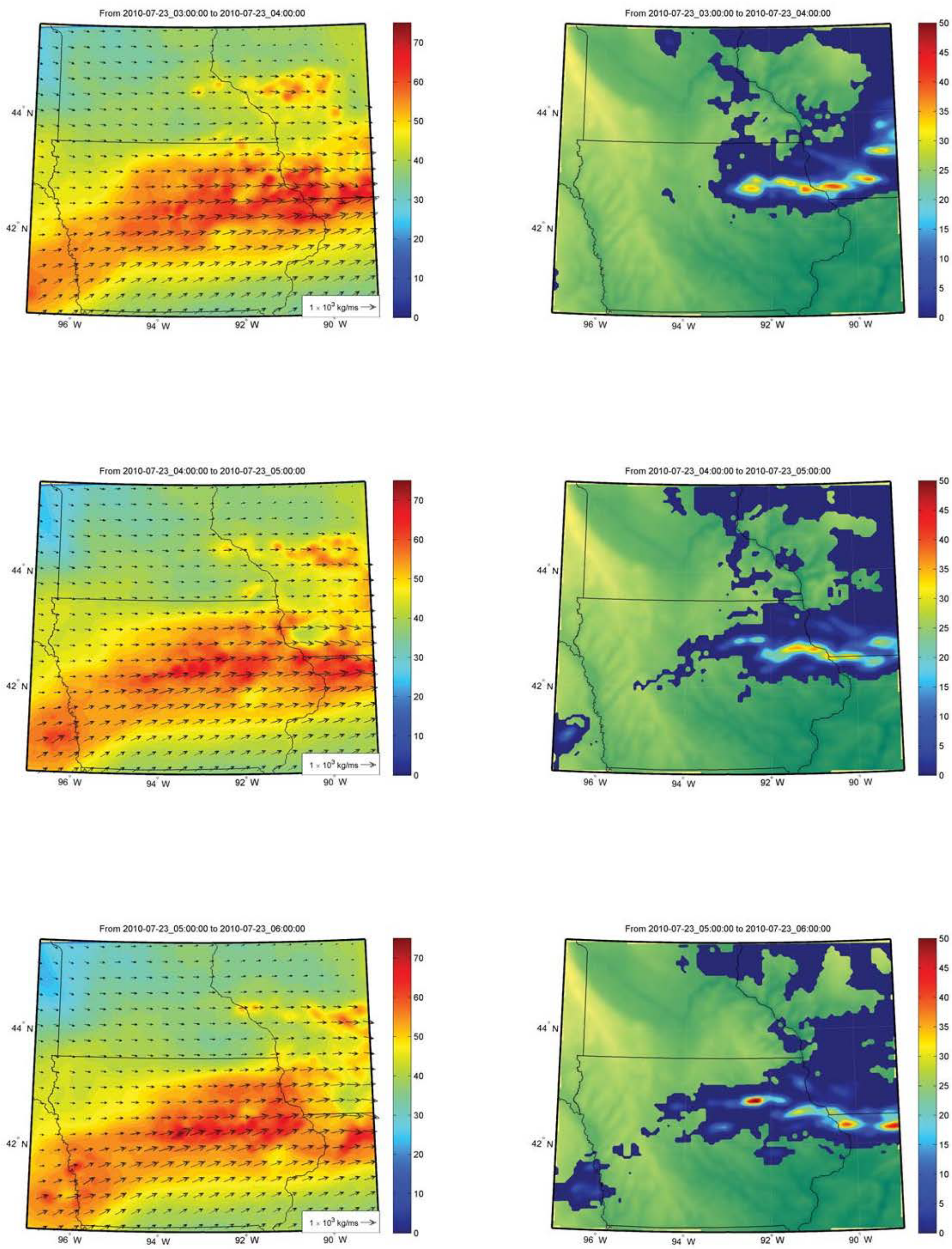

Figure B-11 Hourly Simulated Precipitable Water (Left, Colormap [mm]) and Water Vapor Flux Fields (Left, Arrows [kg m^{-1} s^{-1}]) and Precipitation Fields (Right, Colormap [mm]) for the July 23, 2010 MCS

Plots shown from 07/22/2010 at 18hr to 07/23/2010 at 17hr (Continued).

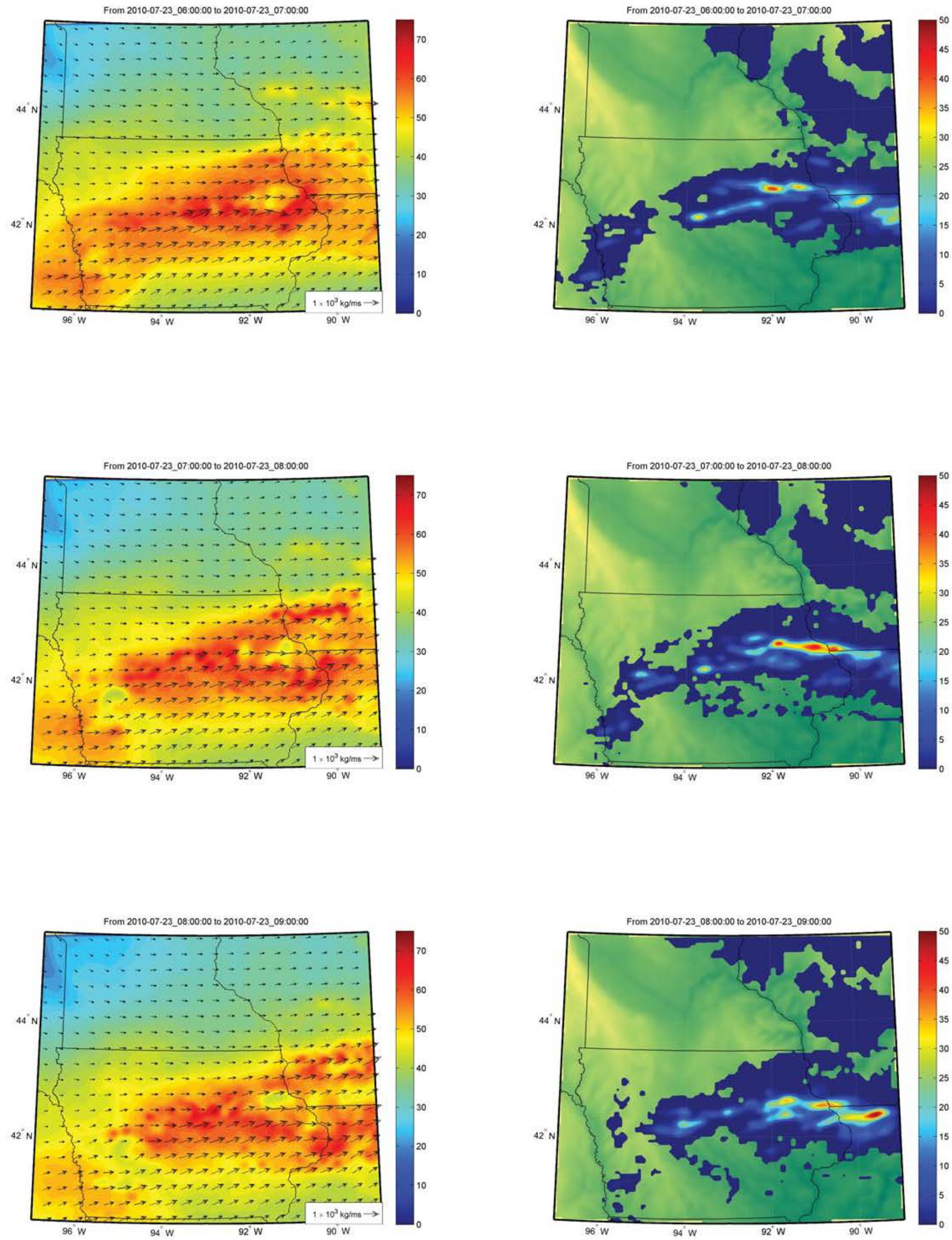

Figure B-11 Hourly Simulated Precipitable Water (Left, Colormap [mm]) and Water Vapor Flux Fields (Left, Arrows [kg m^{-1} s^{-1}]) and Precipitation Fields (Right, Colormap [mm]) for the July 23, 2010 MCS

Plots shown from 07/22/2010 at 18hr to 07/23/2010 at 17hr (Continued).

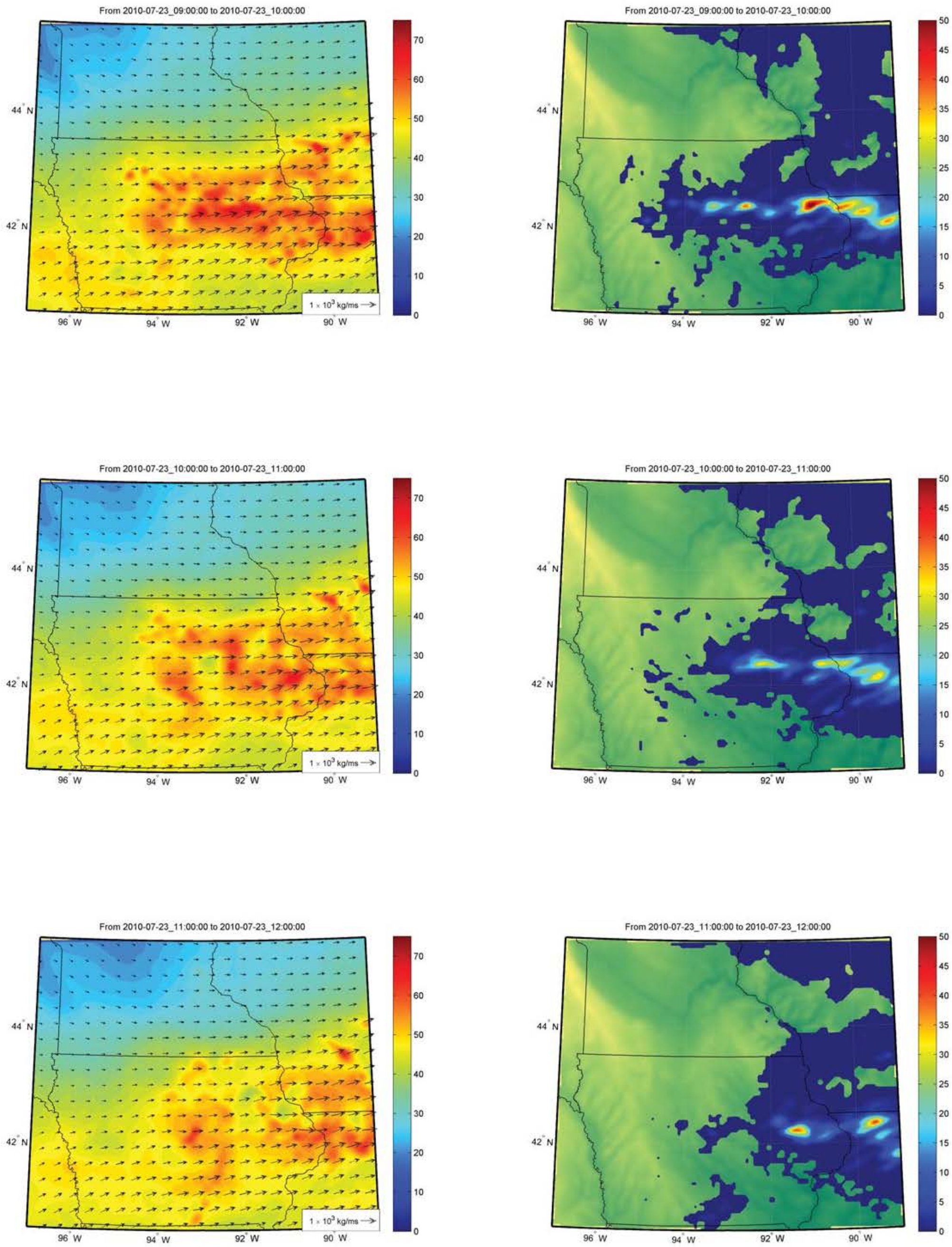

Figure B-11 Hourly Simulated Precipitable Water (Left, Colormap [mm]) and Water Vapor Flux Fields (Left, Arrows [kg m^{-1} s^{-1}]) and Precipitation Fields (Right, Colormap [mm]) for the July 23, 2010 MCS

Plots shown from 07/22/2010 at 18hr to 07/23/2010 at 17hr (Continued).

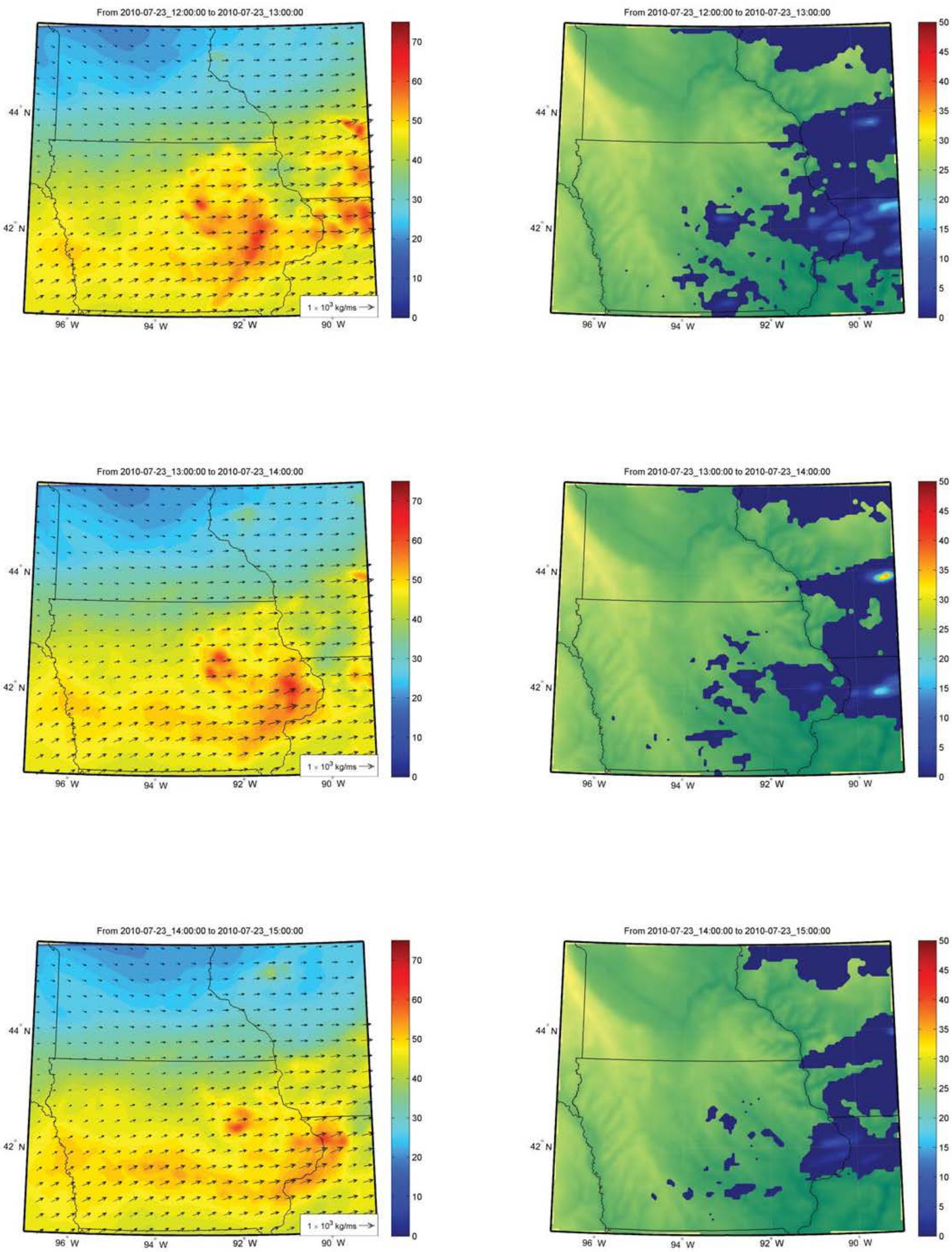

Figure B-11 **Hourly Simulated Precipitable Water (Left, Colormap [mm]) and Water Vapor Flux Fields (Left, Arrows [kg m^{-1} s^{-1}]) and Precipitation Fields (Right, Colormap [mm]) for the July 23, 2010 MCS**

Plots shown from 07/22/2010 at 18hr to 07/23/2010 at 17hr (Continued).

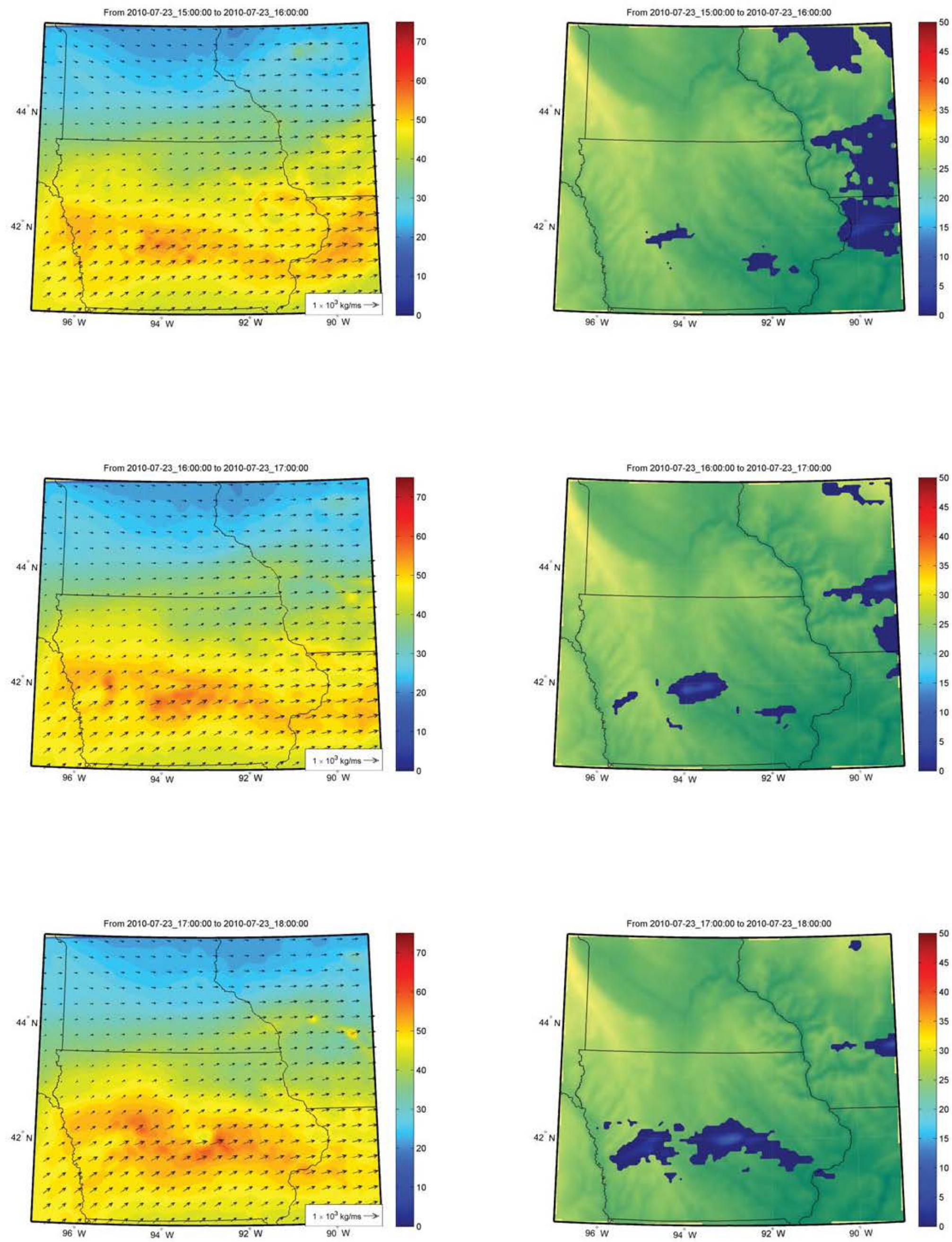

Figure B-11 **Hourly Simulated Precipitable Water (Left, Colormap [mm]) and Water Vapor Flux Fields (Left, Arrows [kg m^{-1} s^{-1}]) and Precipitation Fields (Right, Colormap [mm]) for the July 23, 2010 MCS**

Plots shown from 07/22/2010 at 18hr to 07/23/2010 at 17hr (Continued).

B.1.12 September 23, 2010 MCS

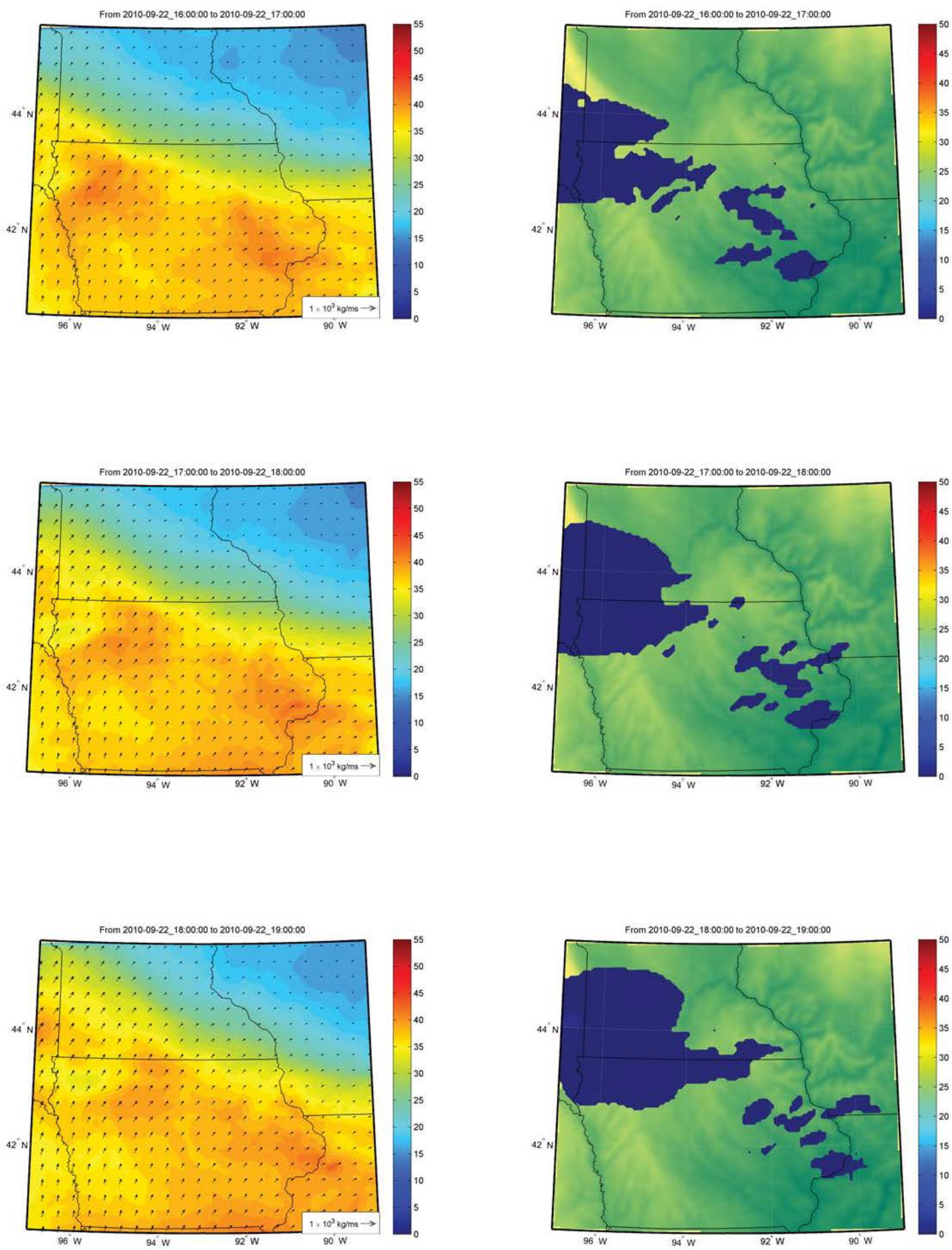

Figure B-12 Hourly Simulated Precipitable Water (Left, Colormap [mm]) and Water Vapor Flux Fields (Left, Arrows [kg m^{-1} s^{-1}]) and Precipitation Fields (Right, Colormap [mm]) for the September 23, 2010 MCS

Plots shown from 09/22/2010 at 17hr to 09/24/2010 at 10hr.

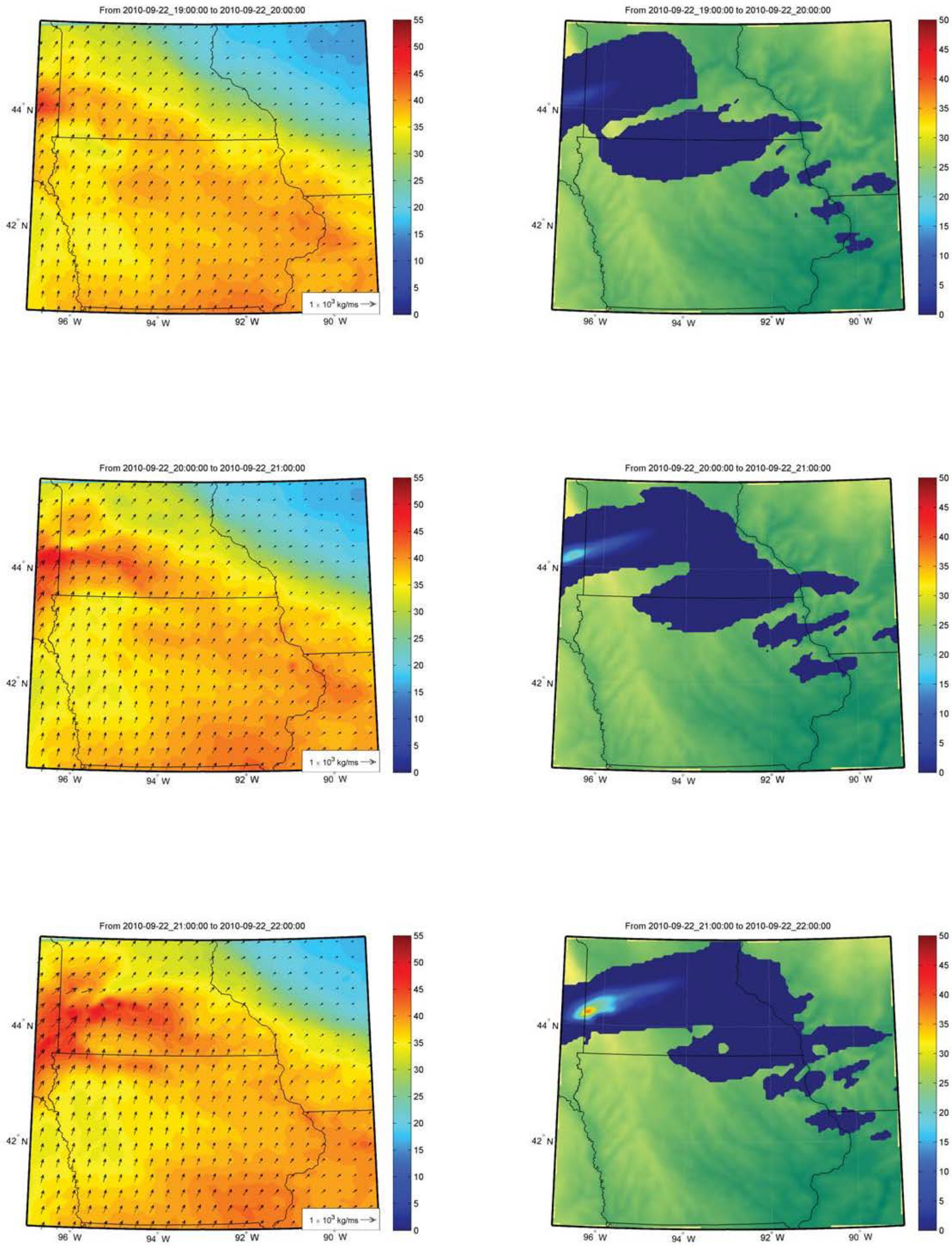

Figure B-12 **Hourly Simulated Precipitable Water (Left, Colormap [mm]) and Water Vapor Flux Fields (Left, Arrows [kg m^{-1} s^{-1}]) and Precipitation Fields (Right, Colormap [mm]) for the September 23, 2010 MCS**

Plots shown from 09/22/2010 at 17hr to 09/24/2010 at 10hr (Continued).

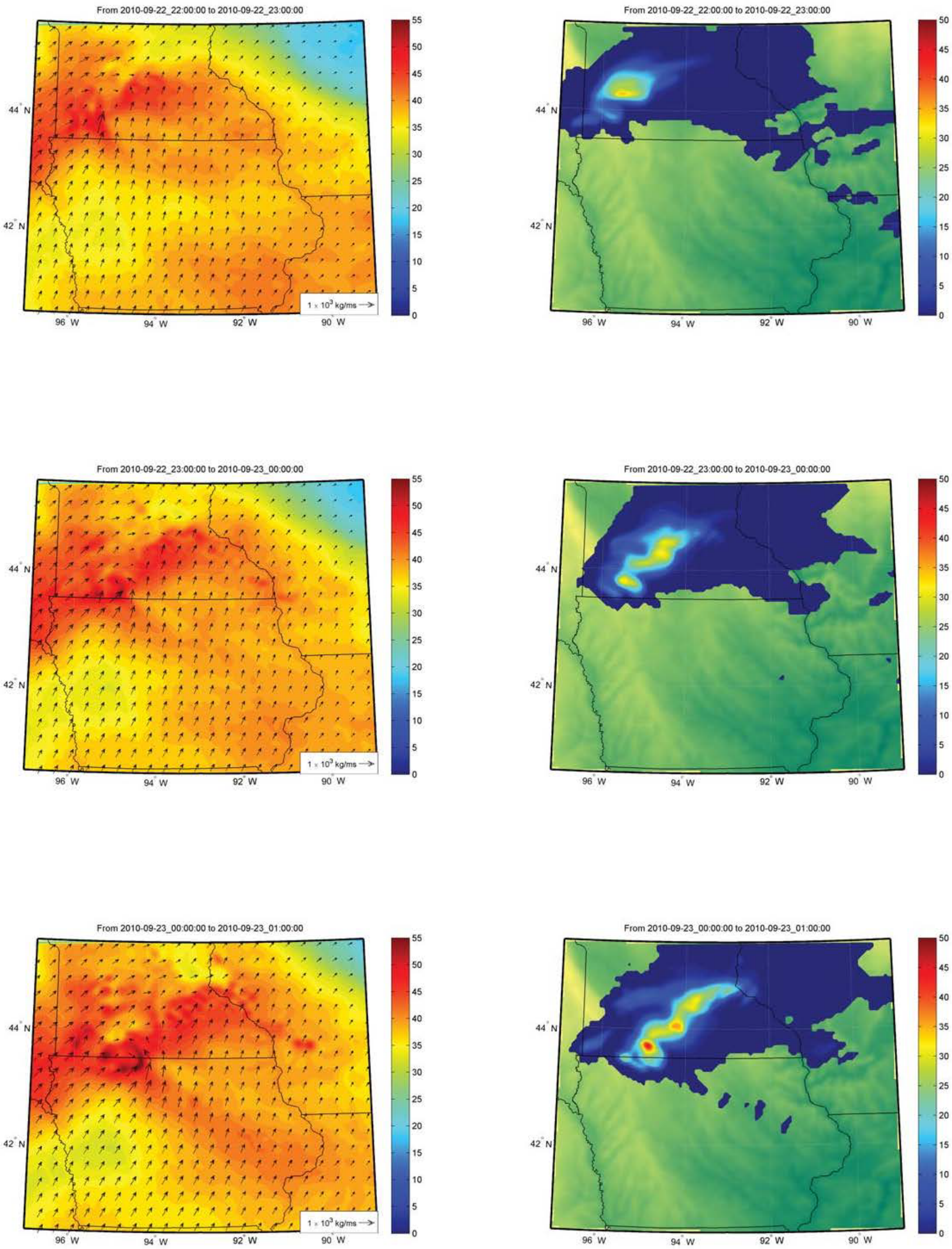

Figure B-12 Hourly Simulated Precipitable Water (Left, Colormap [mm]) and Water Vapor Flux Fields (Left, Arrows [kg m^{-1} s^{-1}]) and Precipitation Fields (Right, Colormap [mm]) for the September 23, 2010 MCS

Plots shown from 09/22/2010 at 17hr to 09/24/2010 at 10hr (Continued).

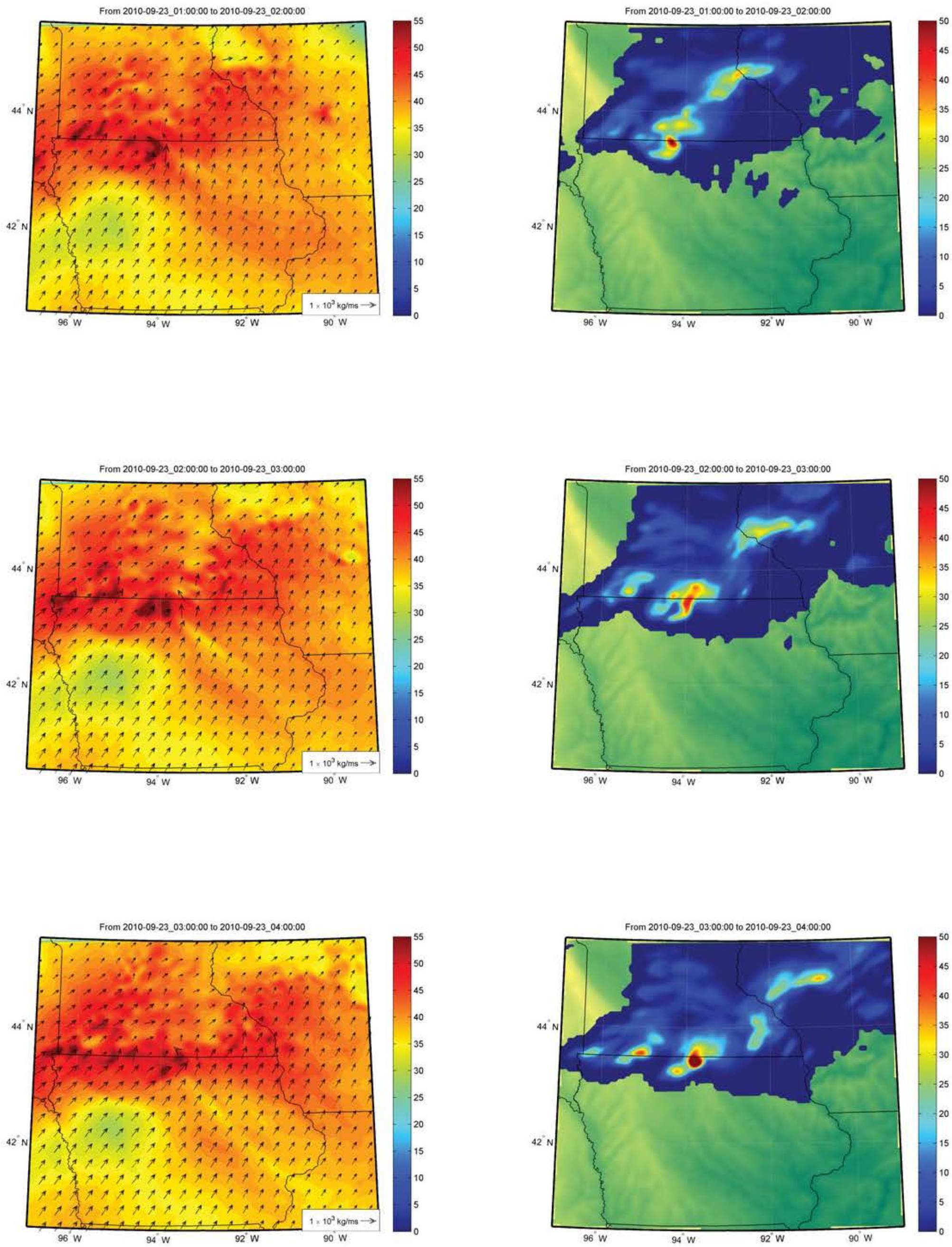

Figure B-12 Hourly Simulated Precipitable Water (Left, Colormap [mm]) and Water Vapor Flux Fields (Left, Arrows [kg m^{-1} s^{-1}]) and Precipitation Fields (Right, Colormap [mm]) for the September 23, 2010 MCS

Plots shown from 09/22/2010 at 17hr to 09/24/2010 at 10hr (Continued).

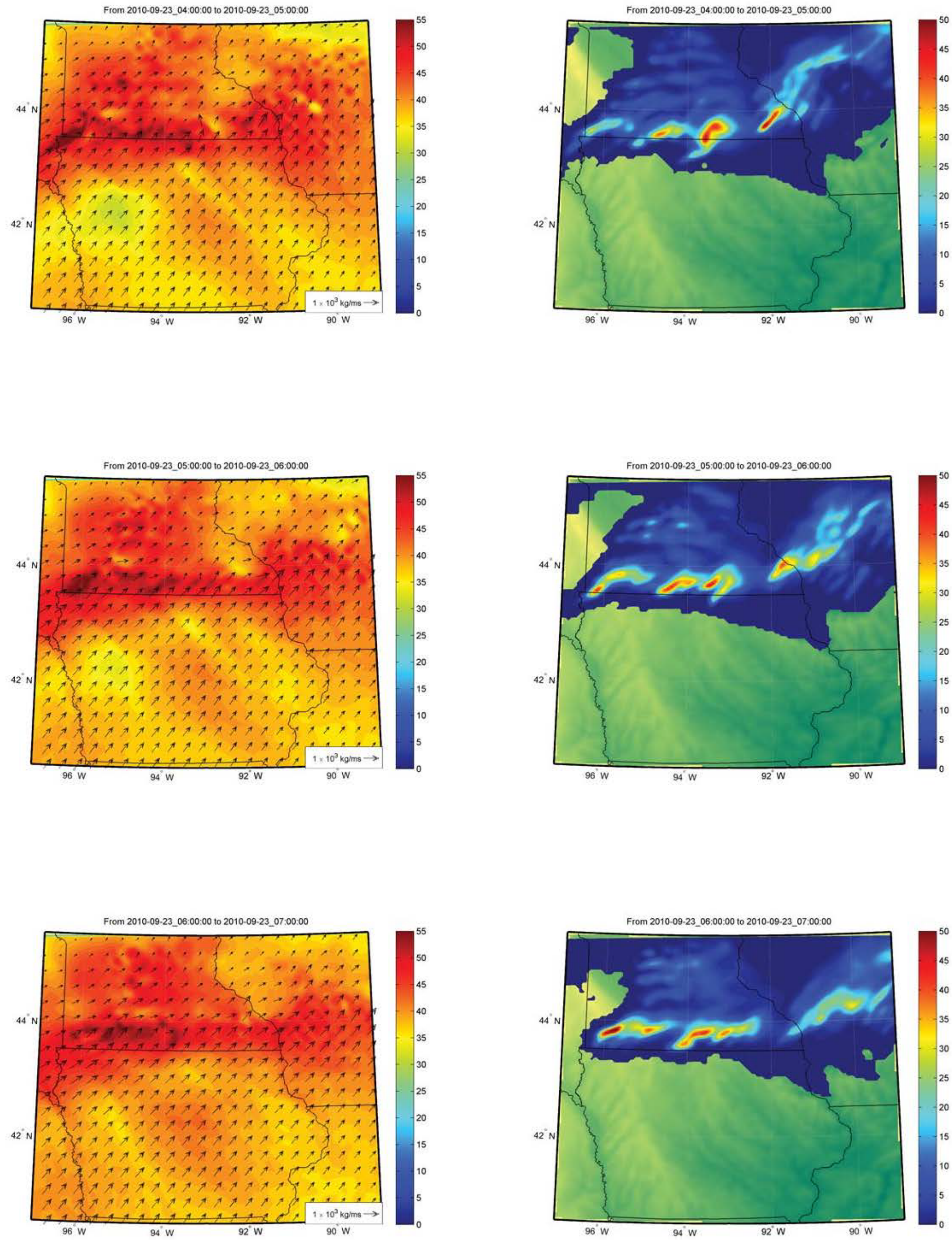

Figure B-12 Hourly Simulated Precipitable Water (Left, Colormap [mm]) and Water Vapor Flux Fields (Left, Arrows [kg m^{-1} s^{-1}]) and Precipitation Fields (Right, Colormap [mm]) for the September 23, 2010 MCS

Plots shown from 09/22/2010 at 17hr to 09/24/2010 at 10hr (Continued).

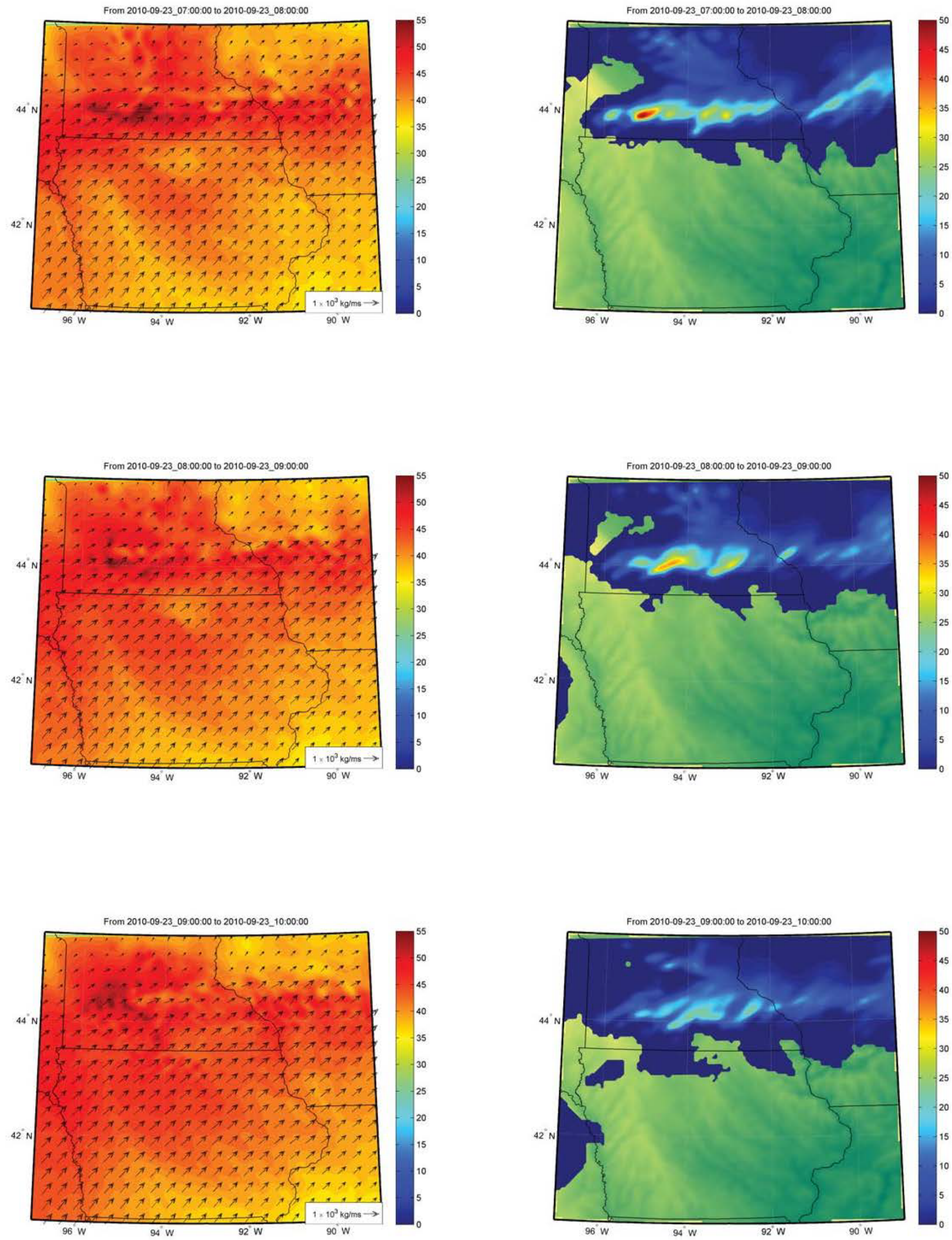

Figure B-12 Hourly Simulated Precipitable Water (Left, Colormap [mm]) and Water Vapor Flux Fields (Left, Arrows [kg m^{-1} s^{-1}]) and Precipitation Fields (Right, Colormap [mm]) for the September 23, 2010 MCS

Plots shown from 09/22/2010 at 17hr to 09/24/2010 at 10hr (Continued).

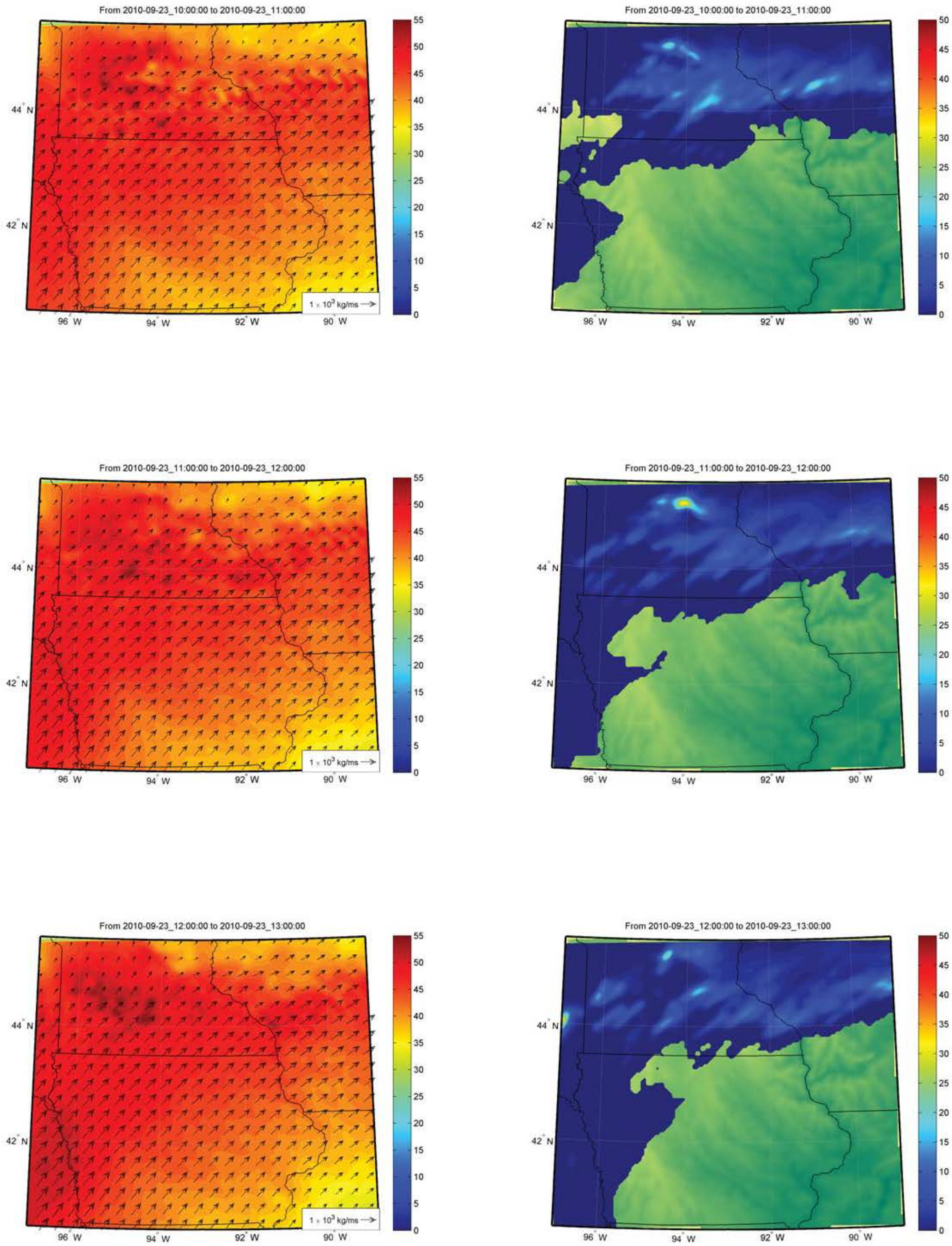

Figure B-12 **Hourly Simulated Precipitable Water (Left, Colormap [mm]) and Water Vapor Flux Fields (Left, Arrows [kg m^{-1} s^{-1}]) and Precipitation Fields (Right, Colormap [mm]) for the September 23, 2010 MCS**

Plots shown from 09/22/2010 at 17hr to 09/24/2010 at 10hr (Continued).

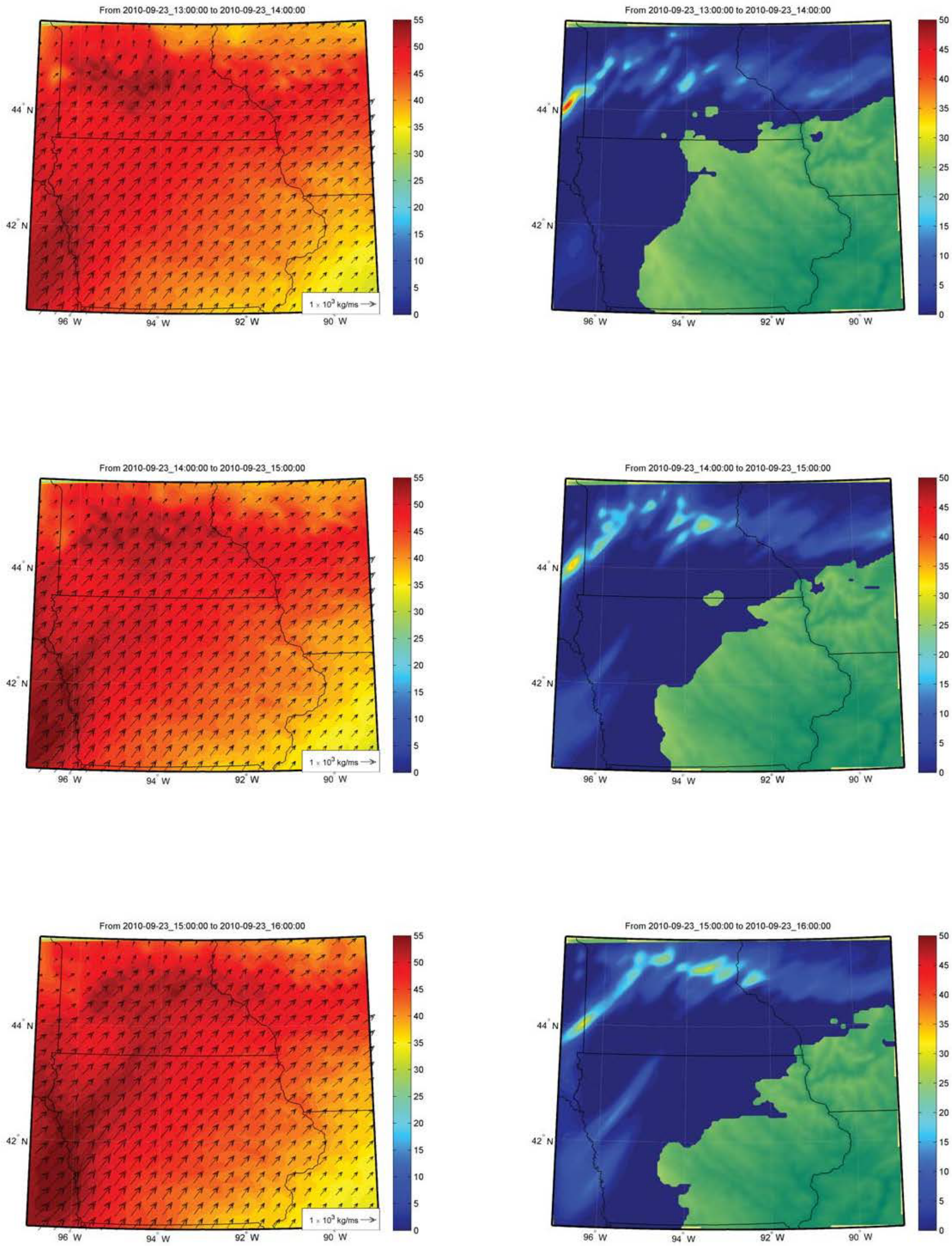

Figure B-12 **Hourly Simulated Precipitable Water (Left, Colormap [mm]) and Water Vapor Flux Fields (Left, Arrows [kg m^{-1} s^{-1}]) and Precipitation Fields (Right, Colormap [mm]) for the September 23, 2010 MCS**

Plots shown from 09/22/2010 at 17hr to 09/24/2010 at 10hr (Continued).

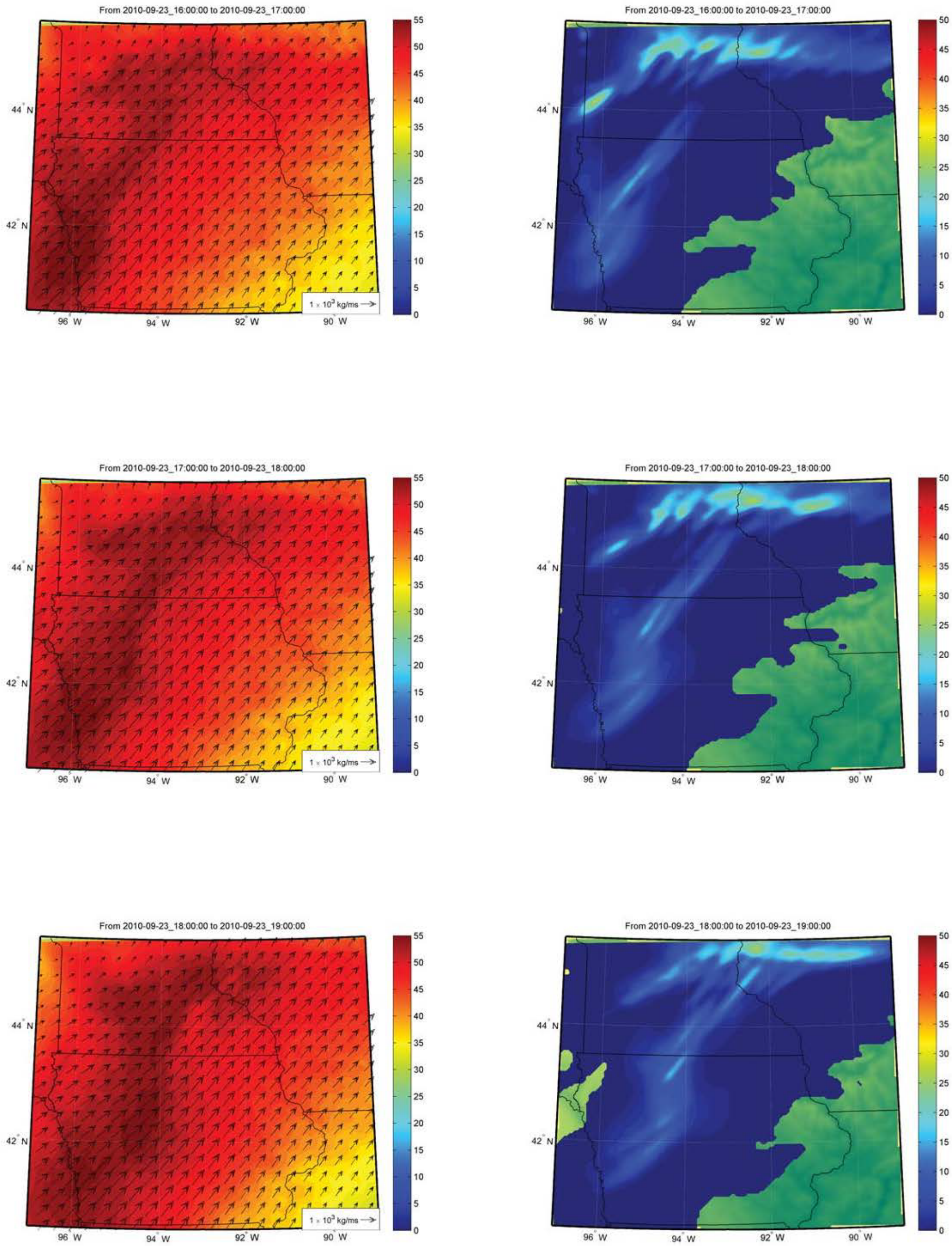

Figure B-12 Hourly Simulated Precipitable Water (Left, Colormap [mm]) and Water Vapor Flux Fields (Left, Arrows [kg m^{-1} s^{-1}]) and Precipitation Fields (Right, Colormap [mm]) for the September 23, 2010 MCS

Plots shown from 09/22/2010 at 17hr to 09/24/2010 at 10hr (Continued).

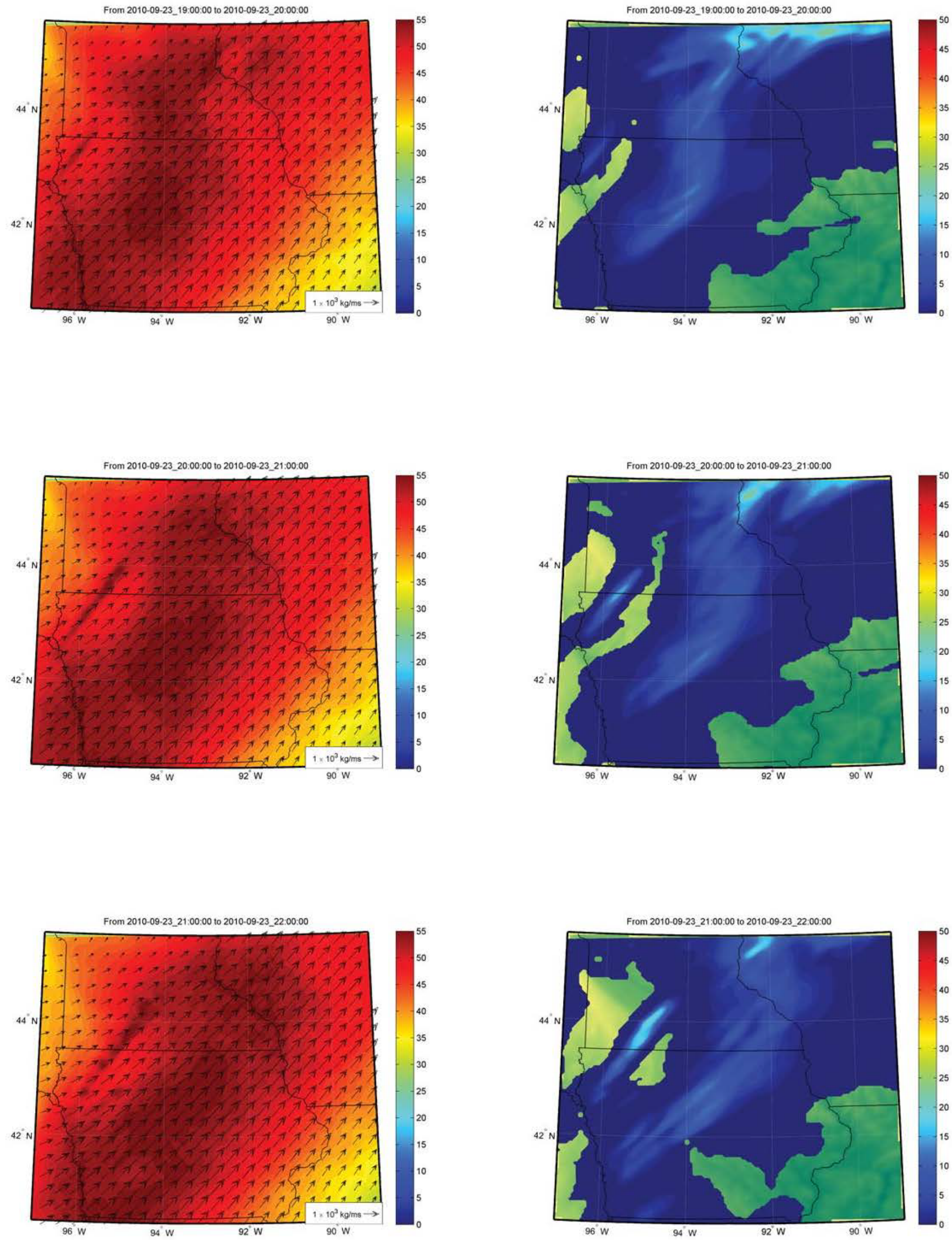

Figure B-12 Hourly Simulated Precipitable Water (Left, Colormap [mm]) and Water Vapor Flux Fields (Left, Arrows [kg m^{-1} s^{-1}]) and Precipitation Fields (Right, Colormap [mm]) for the September 23, 2010 MCS

Plots shown from 09/22/2010 at 17hr to 09/24/2010 at 10hr (Continued).

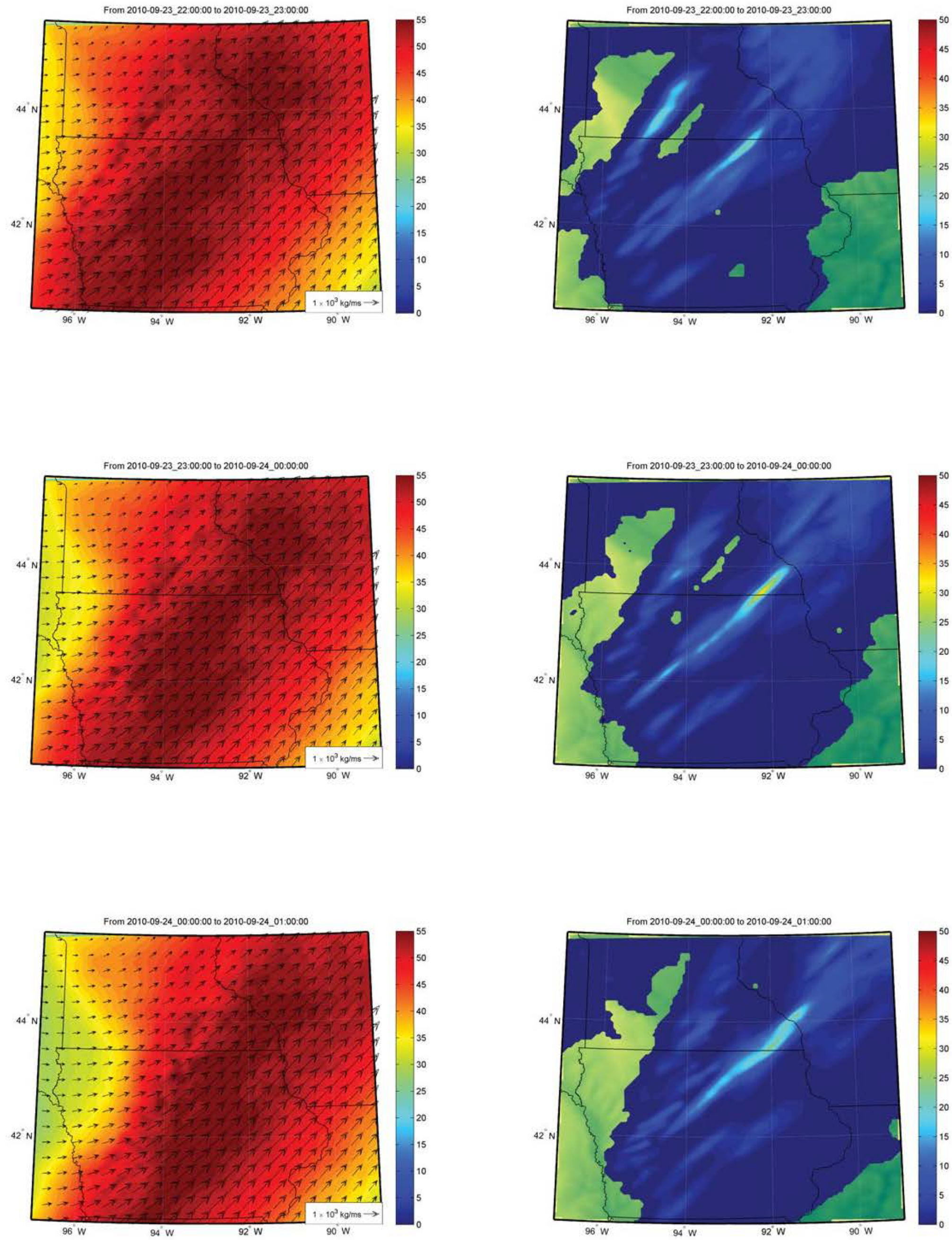

Figure B-12 Hourly Simulated Precipitable Water (Left, Colormap [mm]) and Water Vapor Flux Fields (Left, Arrows [kg m^{-1} s^{-1}]) and Precipitation Fields (Right, Colormap [mm]) for the September 23, 2010 MCS

Plots shown from 09/22/2010 at 17hr to 09/24/2010 at 10hr (Continued).

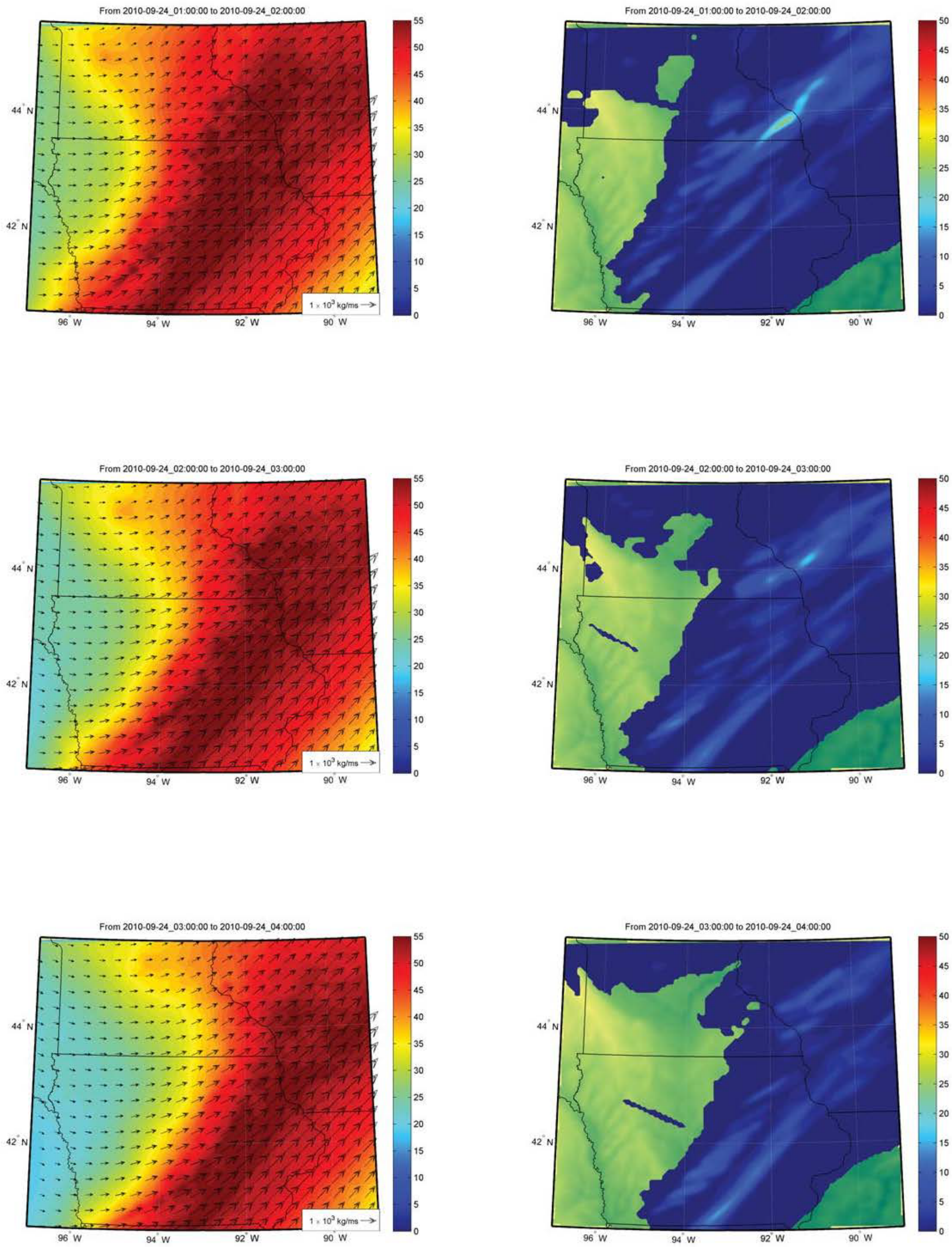

Figure B-12 Hourly Simulated Precipitable Water (Left, Colormap [mm]) and Water Vapor Flux Fields (Left, Arrows [kg m^{-1} s^{-1}]) and Precipitation Fields (Right, Colormap [mm]) for the September 23, 2010 MCS

Plots shown from 09/22/2010 at 17hr to 09/24/2010 at 10hr (Continued).

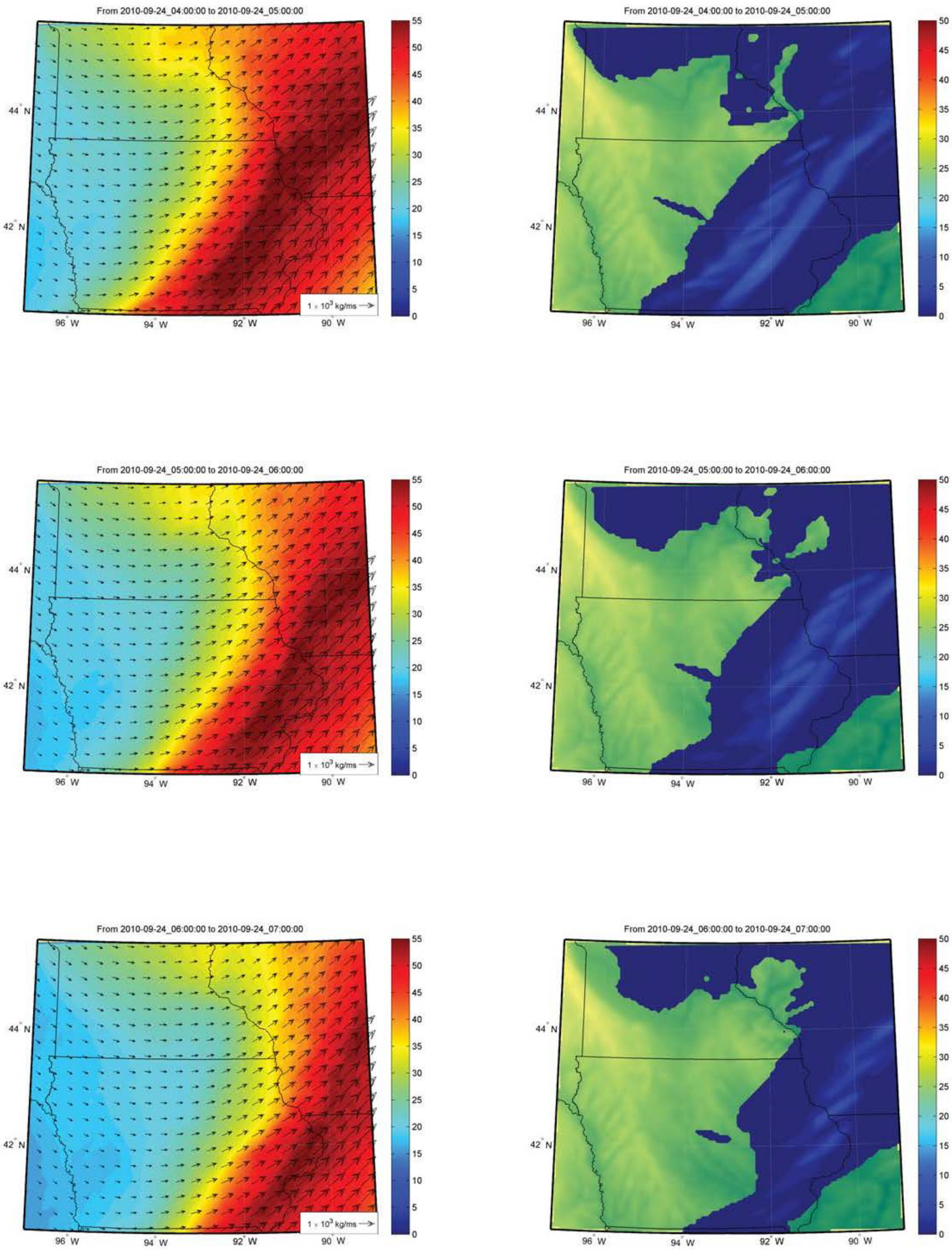

Figure B-12 Hourly Simulated Precipitable Water (Left, Colormap [mm]) and Water Vapor Flux Fields (Left, Arrows [kg m^{-1} s^{-1}]) and Precipitation Fields (Right, Colormap [mm]) for the September 23, 2010 MCS

Plots shown from 09/22/2010 at 17hr to 09/24/2010 at 10hr (Continued).

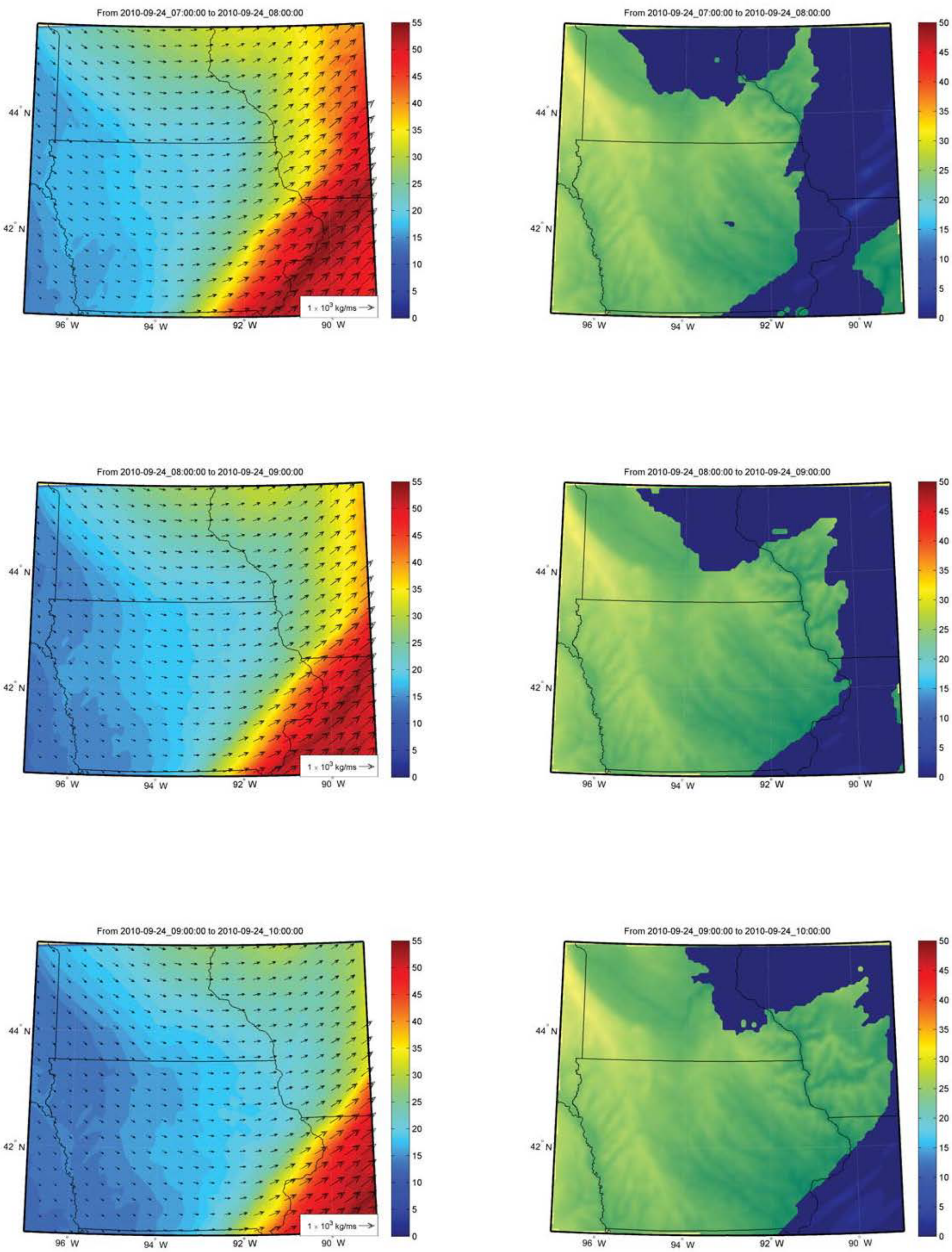

Figure B-12 Hourly Simulated Precipitable Water (Left, Colormap [mm]) and Water Vapor Flux Fields (Left, Arrows [kg m^{-1} s^{-1}]) and Precipitation Fields (Right, Colormap [mm]) for the September 23, 2010 MCS

Plots shown from 09/22/2010 at 17hr to 09/24/2010 at 10hr (Continued).

B.1.13 July 28, 2011 MCS

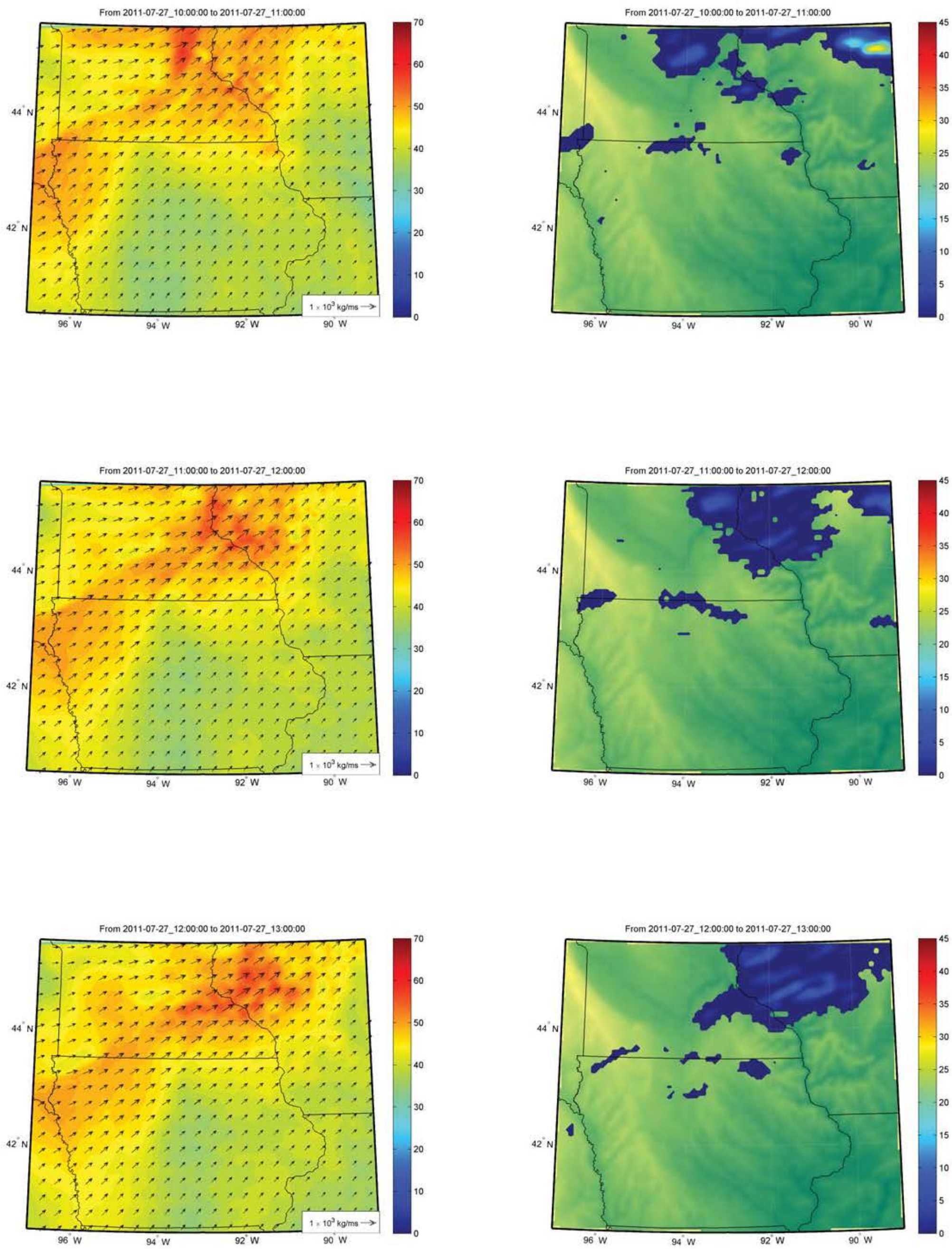

Figure B-13 Hourly Simulated Precipitable Water (Left, Colormap [mm]) and Water Vapor Flux Fields (Left, Arrows [kg m^{-1} s^{-1}]) and Precipitation Fields (Right, Colormap [mm]) for the July 28, 2011 MCS

Plots shown from 07/27/2011 at 10hr to 07/28/2011 at 16hr.

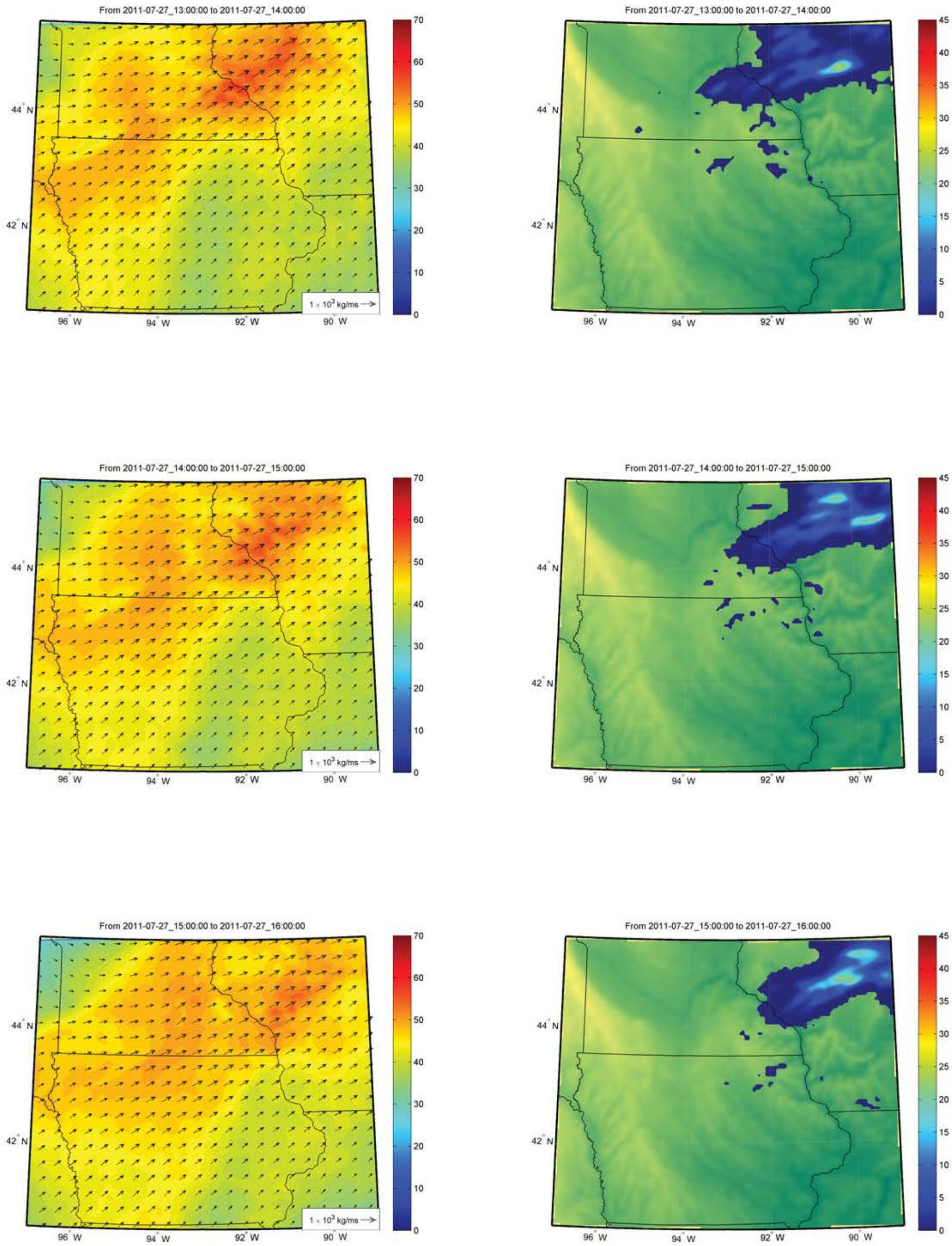

Figure B-13 Hourly Simulated Precipitable Water (Left, Colormap [mm]) and Water Vapor Flux Fields (Left, Arrows [kg m^{-1} s^{-1}]) and Precipitation Fields (Right, Colormap [mm]) for the July 28, 2011 MCS

Plots shown from 07/27/2011 at 10hr to 07/28/2011 at 16hr (Continued).

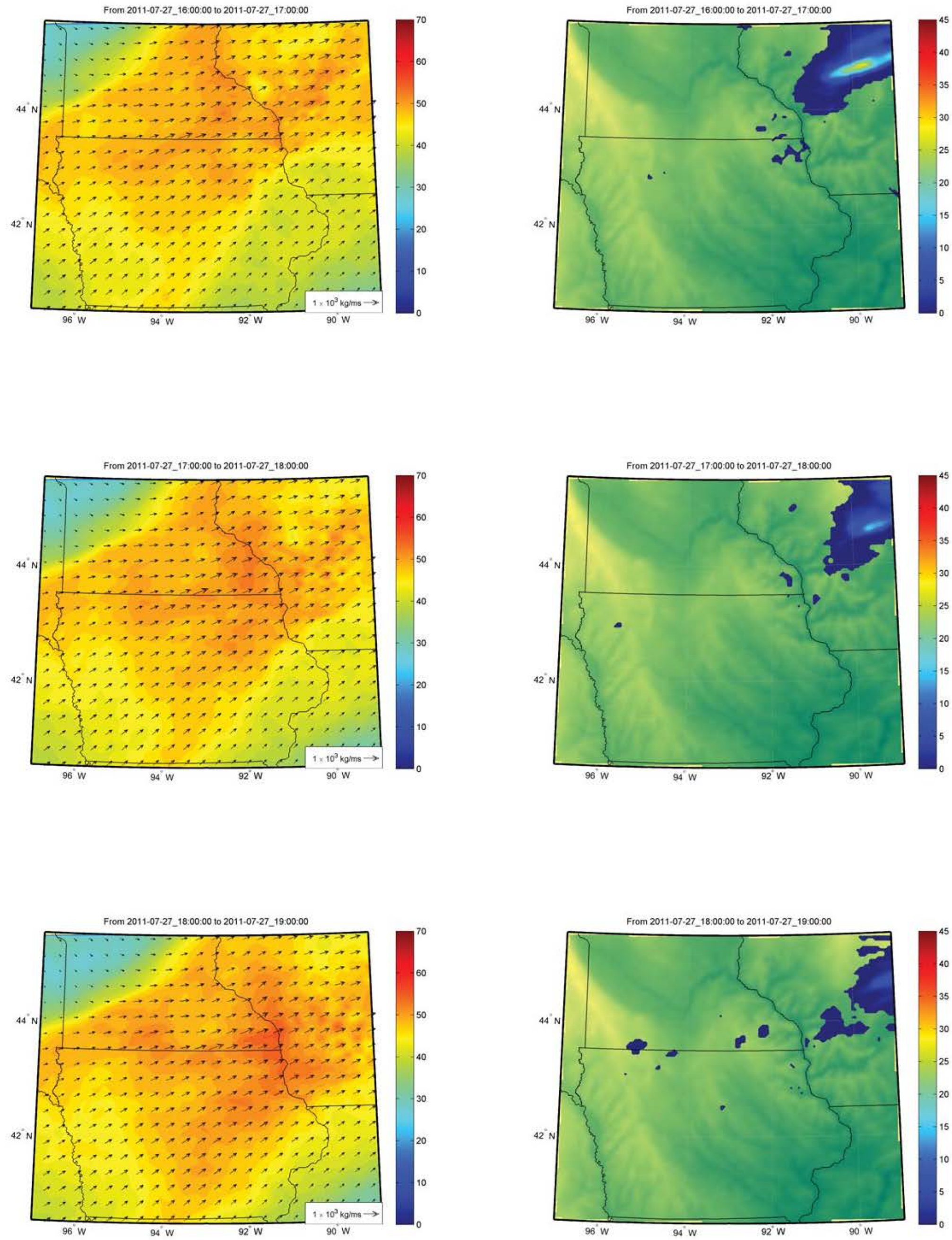

Figure B-13 Hourly Simulated Precipitable Water (Left, Colormap [mm]) and Water Vapor Flux Fields (Left, Arrows [kg m^{-1} s^{-1}]) and Precipitation Fields (Right, Colormap [mm]) for the July 28, 2011 MCS

Plots shown from 07/27/2011 at 10hr to 07/28/2011 at 16hr (Continued).

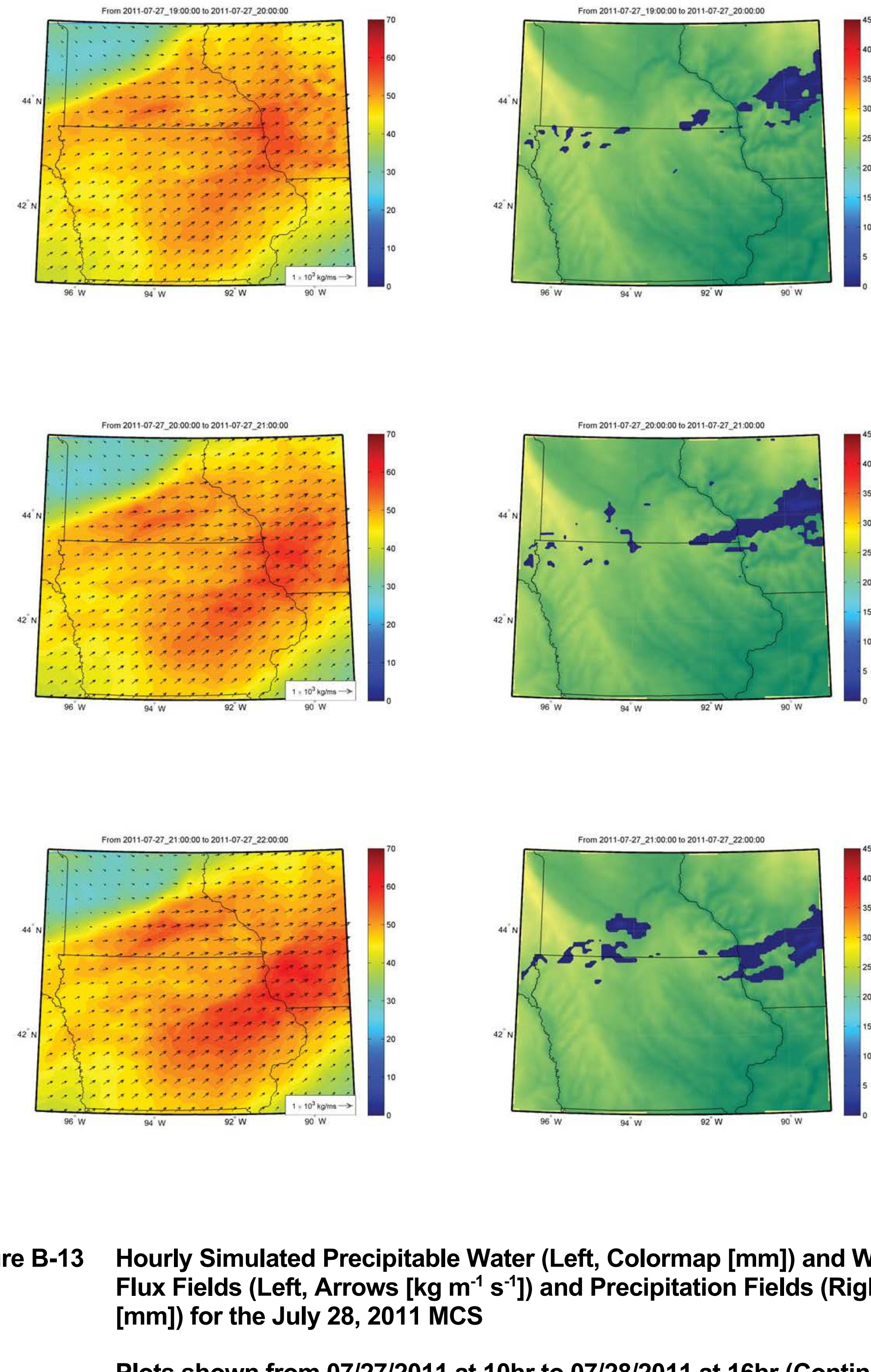

Figure B-13 **Hourly Simulated Precipitable Water (Left, Colormap [mm]) and Water Vapor Flux Fields (Left, Arrows [kg m^{-1} s^{-1}]) and Precipitation Fields (Right, Colormap [mm]) for the July 28, 2011 MCS**

Plots shown from 07/27/2011 at 10hr to 07/28/2011 at 16hr (Continued).

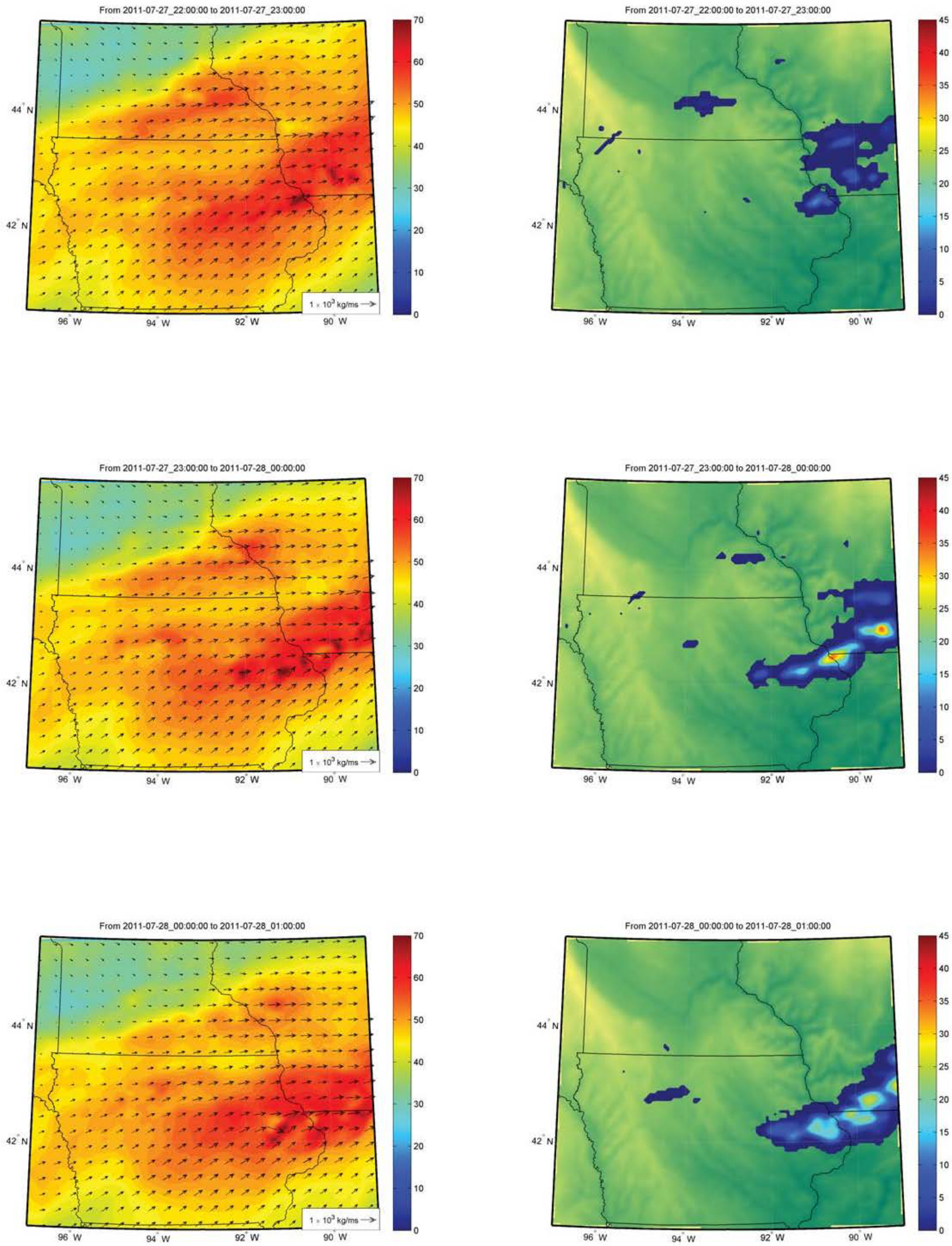

Figure B-13 **Hourly Simulated Precipitable Water (Left, Colormap [mm]) and Water Vapor Flux Fields (Left, Arrows [kg m^{-1} s^{-1}]) and Precipitation Fields (Right, Colormap [mm]) for the July 28, 2011 MCS**

Plots shown from 07/27/2011 at 10hr to 07/28/2011 at 16hr (Continued).

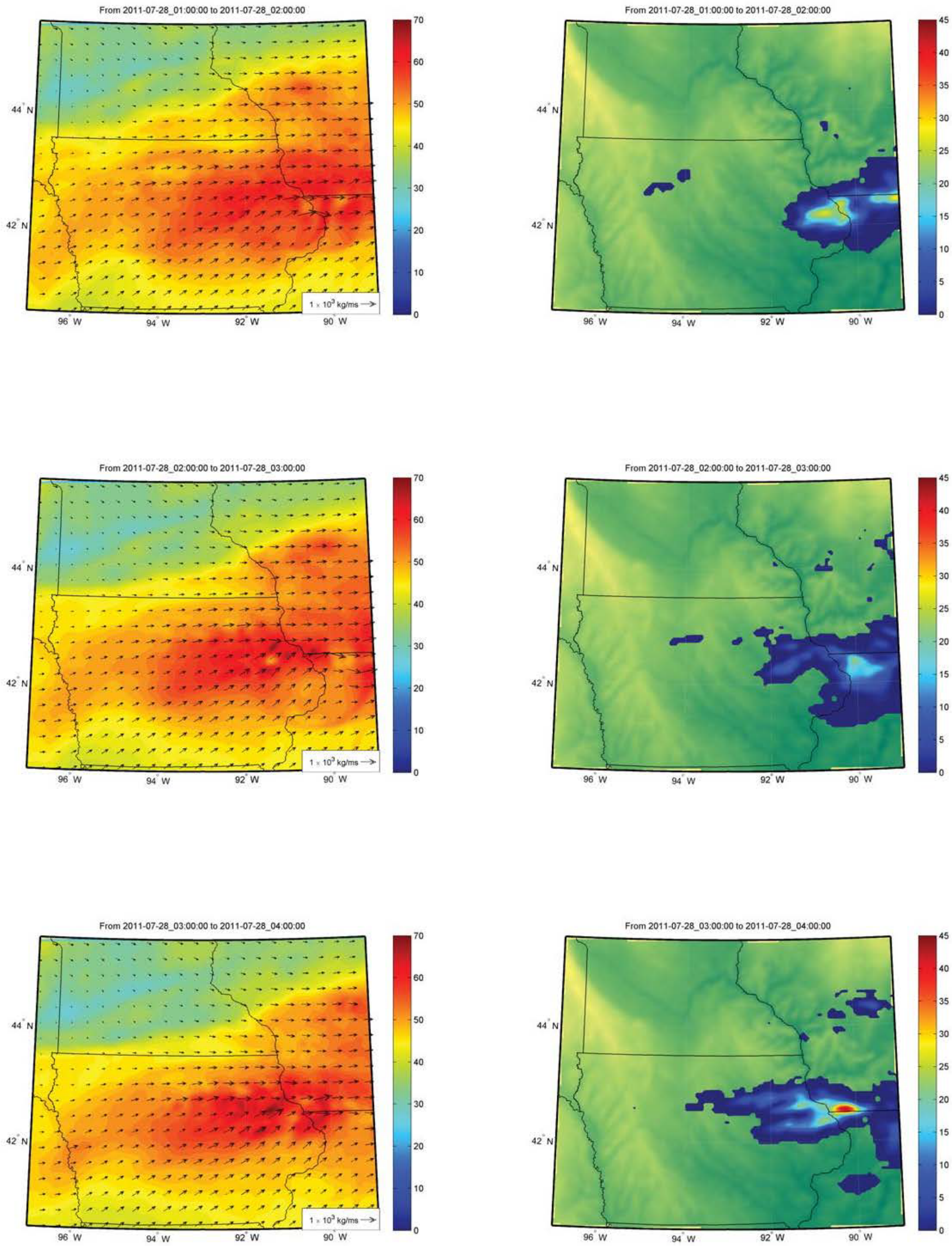

Figure B-13 **Hourly Simulated Precipitable Water (Left, Colormap [mm]) and Water Vapor Flux Fields (Left, Arrows [kg m^{-1} s^{-1}]) and Precipitation Fields (Right, Colormap [mm]) for the July 28, 2011 MCS**

Plots shown from 07/27/2011 at 10hr to 07/28/2011 at 16hr (Continued).

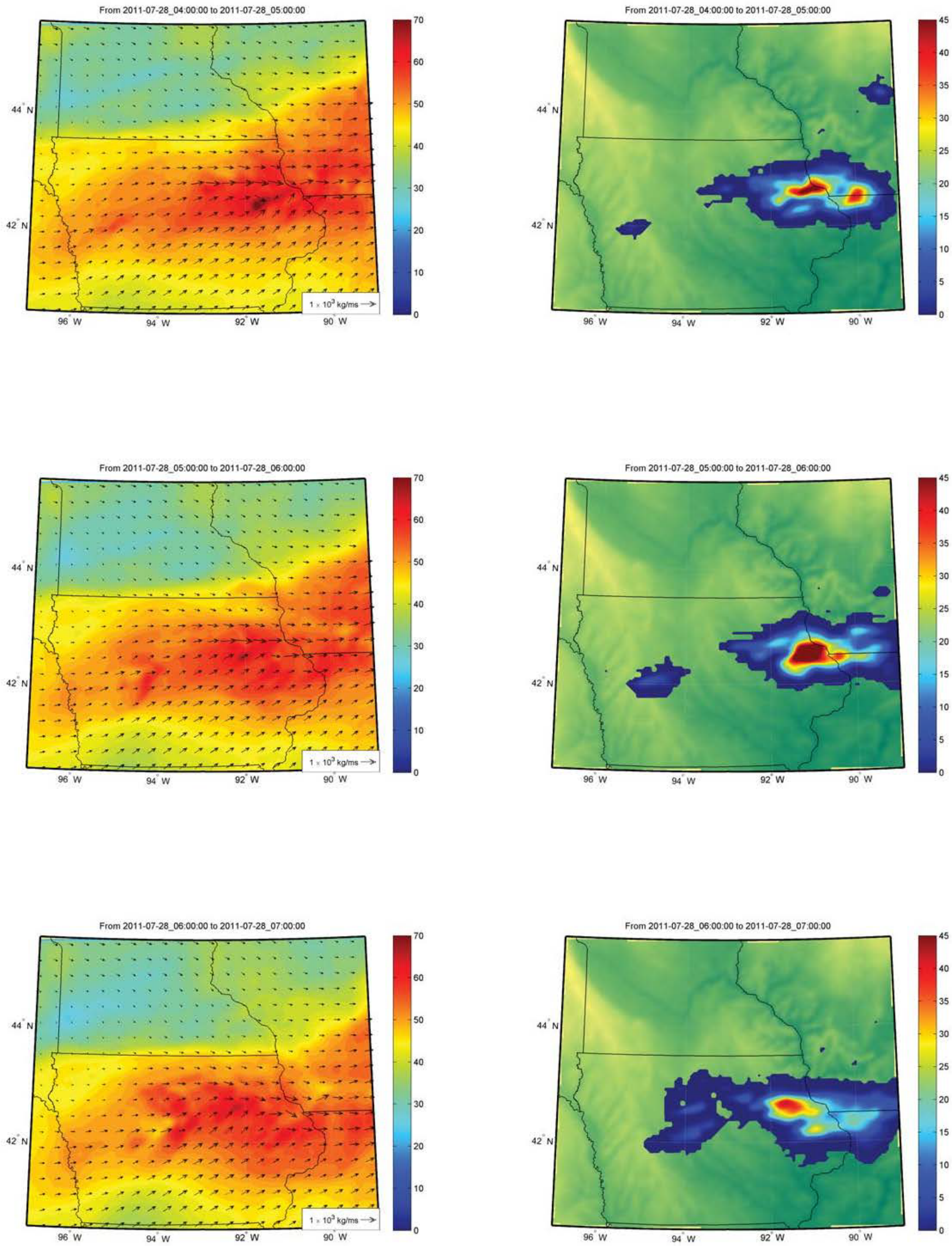

Figure B-13 Hourly Simulated Precipitable Water (Left, Colormap [mm]) and Water Vapor Flux Fields (Left, Arrows [kg m^{-1} s^{-1}]) and Precipitation Fields (Right, Colormap [mm]) for the July 28, 2011 MCS

Plots shown from 07/27/2011 at 10hr to 07/28/2011 at 16hr (Continued).

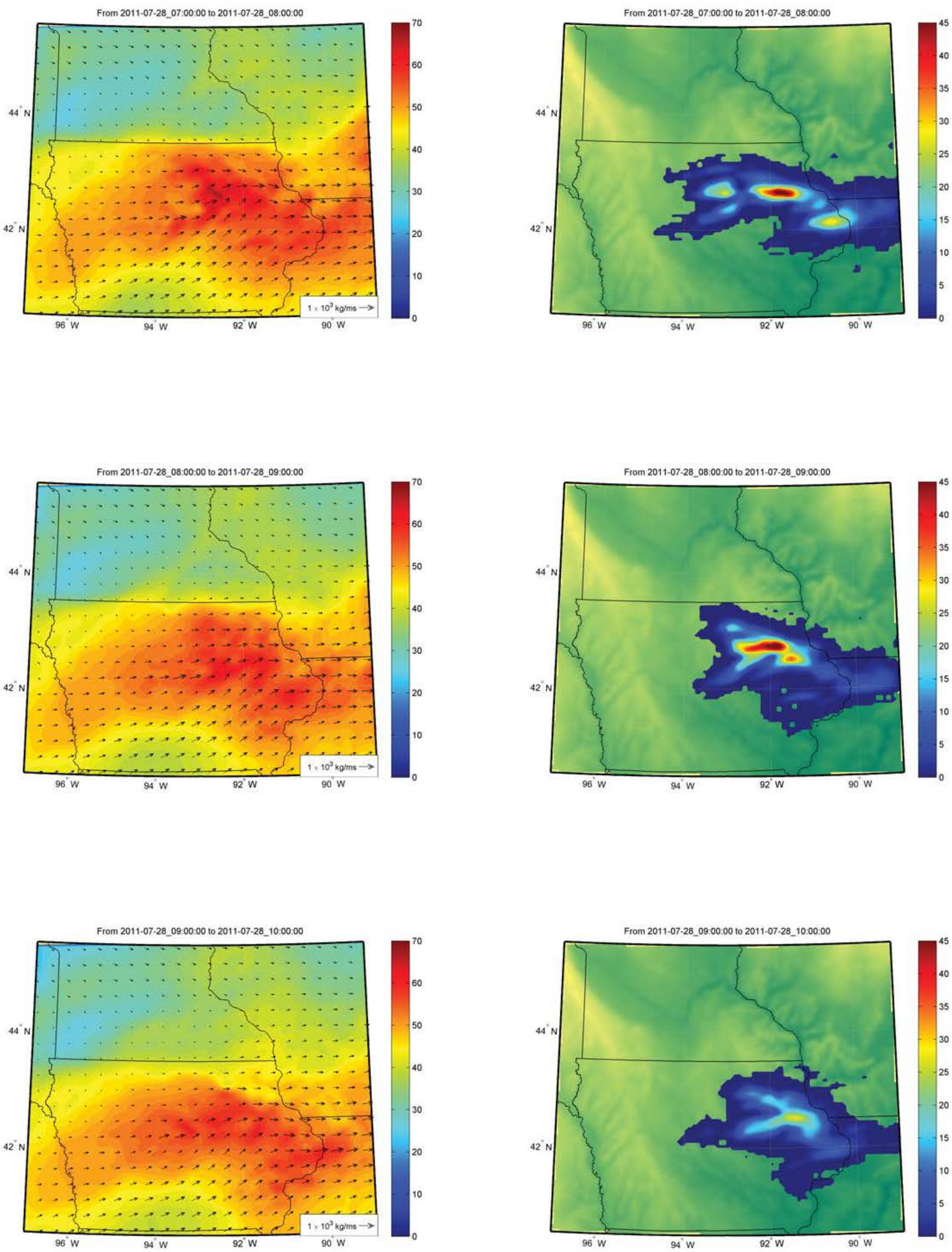

Figure B-13 Hourly Simulated Precipitable Water (Left, Colormap [mm]) and Water Vapor Flux Fields (Left, Arrows [kg m^{-1} s^{-1}]) and Precipitation Fields (Right, Colormap [mm]) for the July 28, 2011 MCS

Plots shown from 07/27/2011 at 10hr to 07/28/2011 at 16hr (Continued).

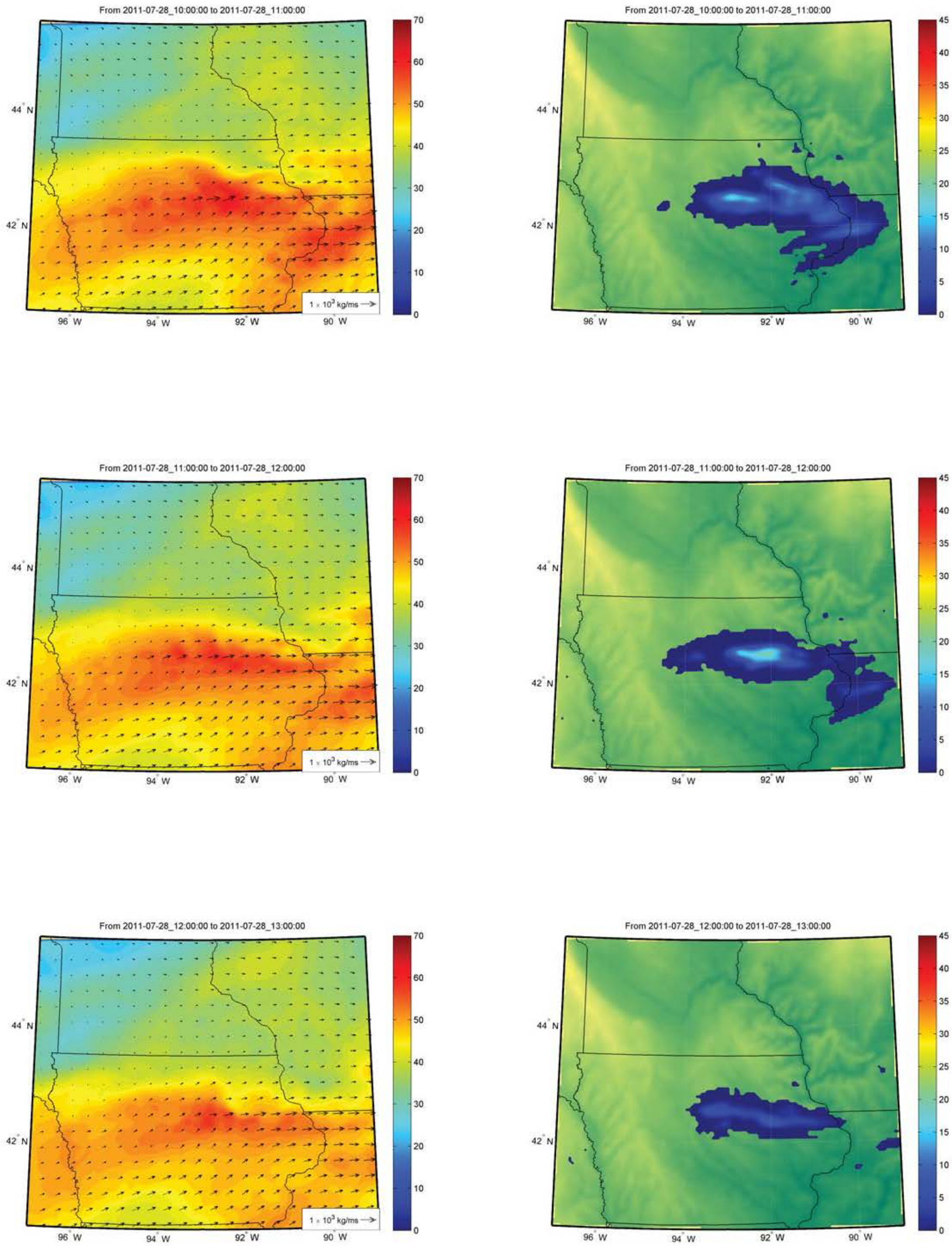

Figure B-13 Hourly Simulated Precipitable Water (Left, Colormap [mm]) and Water Vapor Flux Fields (Left, Arrows [kg m^{-1} s^{-1}]) and Precipitation Fields (Right, Colormap [mm]) for the July 28, 2011 MCS

Plots shown from 07/27/2011 at 10hr to 07/28/2011 at 16hr (Continued).

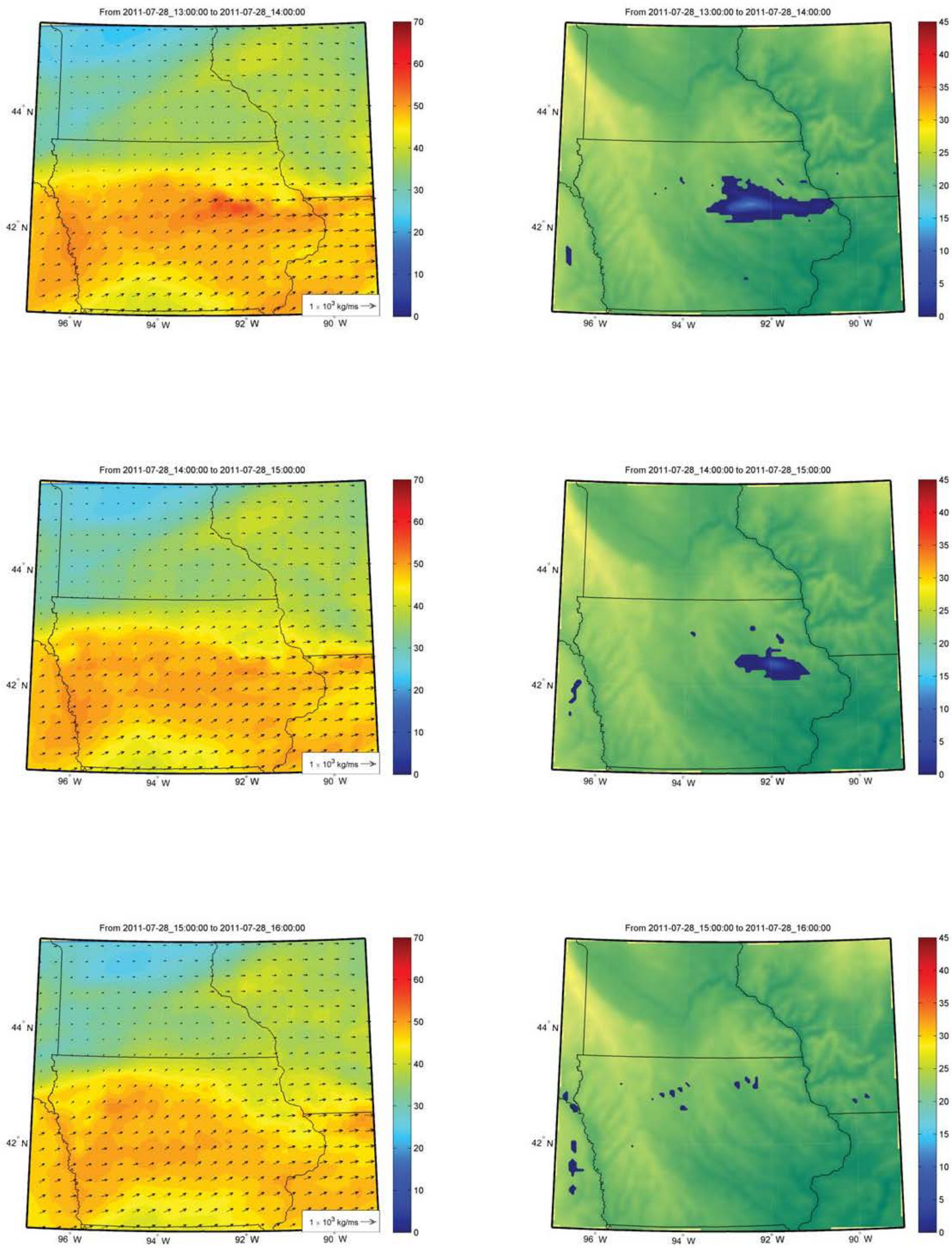

Figure B-13 Hourly Simulated Precipitable Water (Left, Colormap [mm]) and Water Vapor Flux Fields (Left, Arrows [kg m^{-1} s^{-1}]) and Precipitation Fields (Right, Colormap [mm]) for the July 28, 2011 MCS

Plots shown from 07/27/2011 at 10hr to 07/28/2011 at 16hr (Continued).

B.1.14 June 22, 2013 MCS

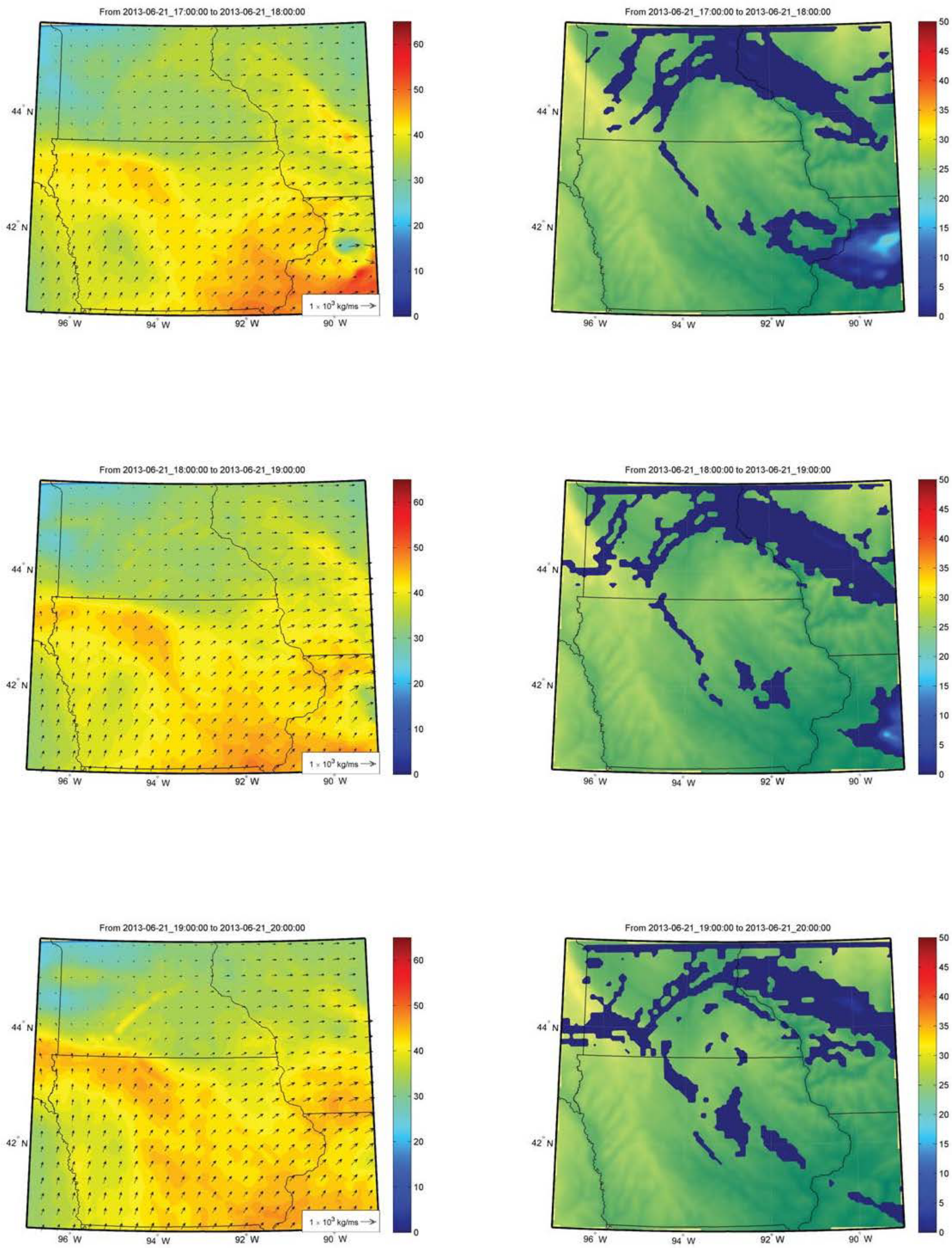

Figure B-14 Hourly Simulated Precipitable Water (Left, Colormap [mm]) and Water Vapor Flux Fields (Left, Arrows [kg m^{-1} s^{-1}]) and Precipitation Fields (Right, Colormap [mm]) for the June 22, 2013 MCS

Plots shown from 06/21/2013 at 17hr to 06/22/2013 at 19hr.

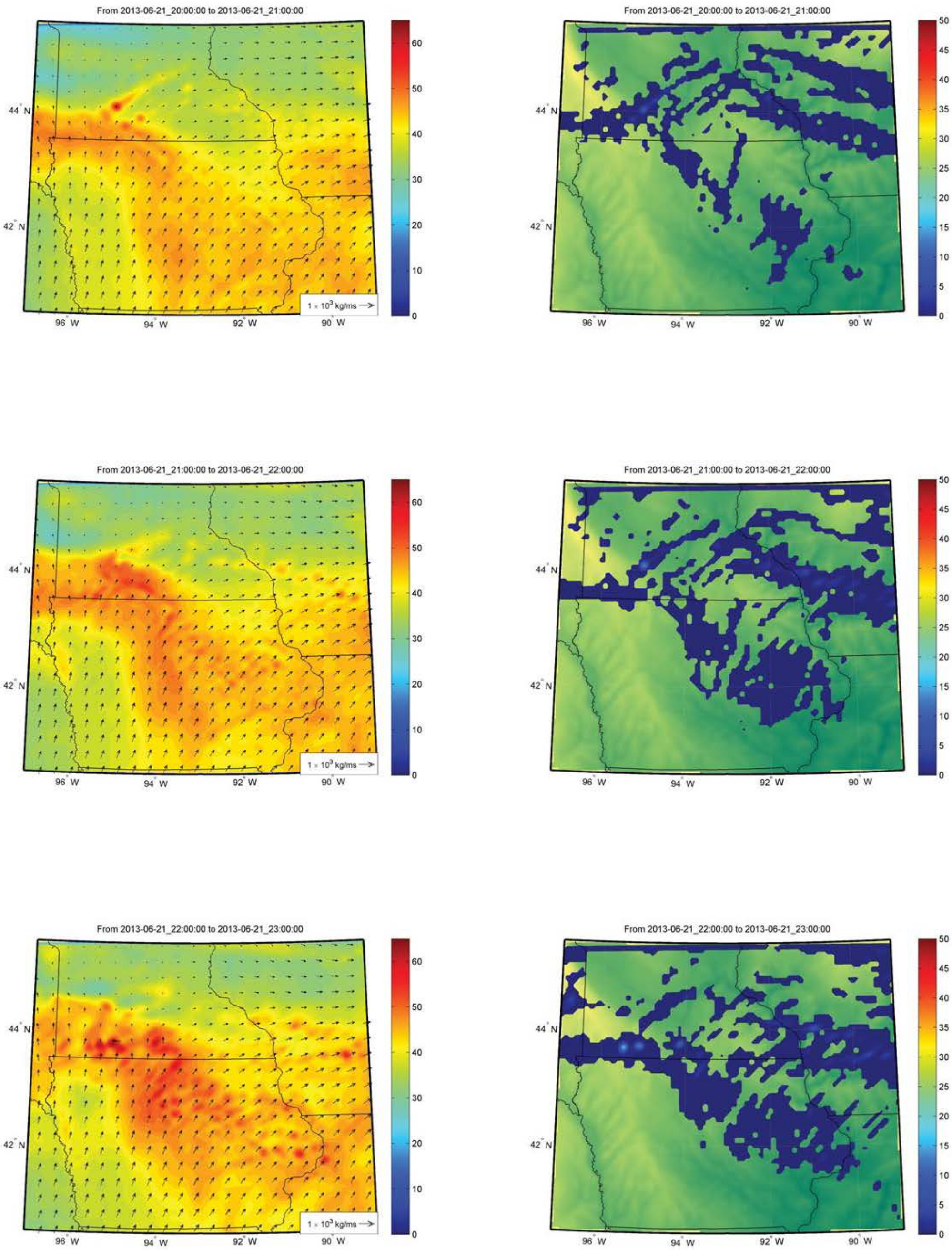

Figure B-14 Hourly Simulated Precipitable Water (Left, Colormap [mm]) and Water Vapor Flux Fields (Left, Arrows [kg m^{-1} s^{-1}]) and Precipitation Fields (Right, Colormap [mm]) for the June 22, 2013 MCS

Plots shown from 06/21/2013 at 17hr to 06/22/2013 at 19hr (Continued).

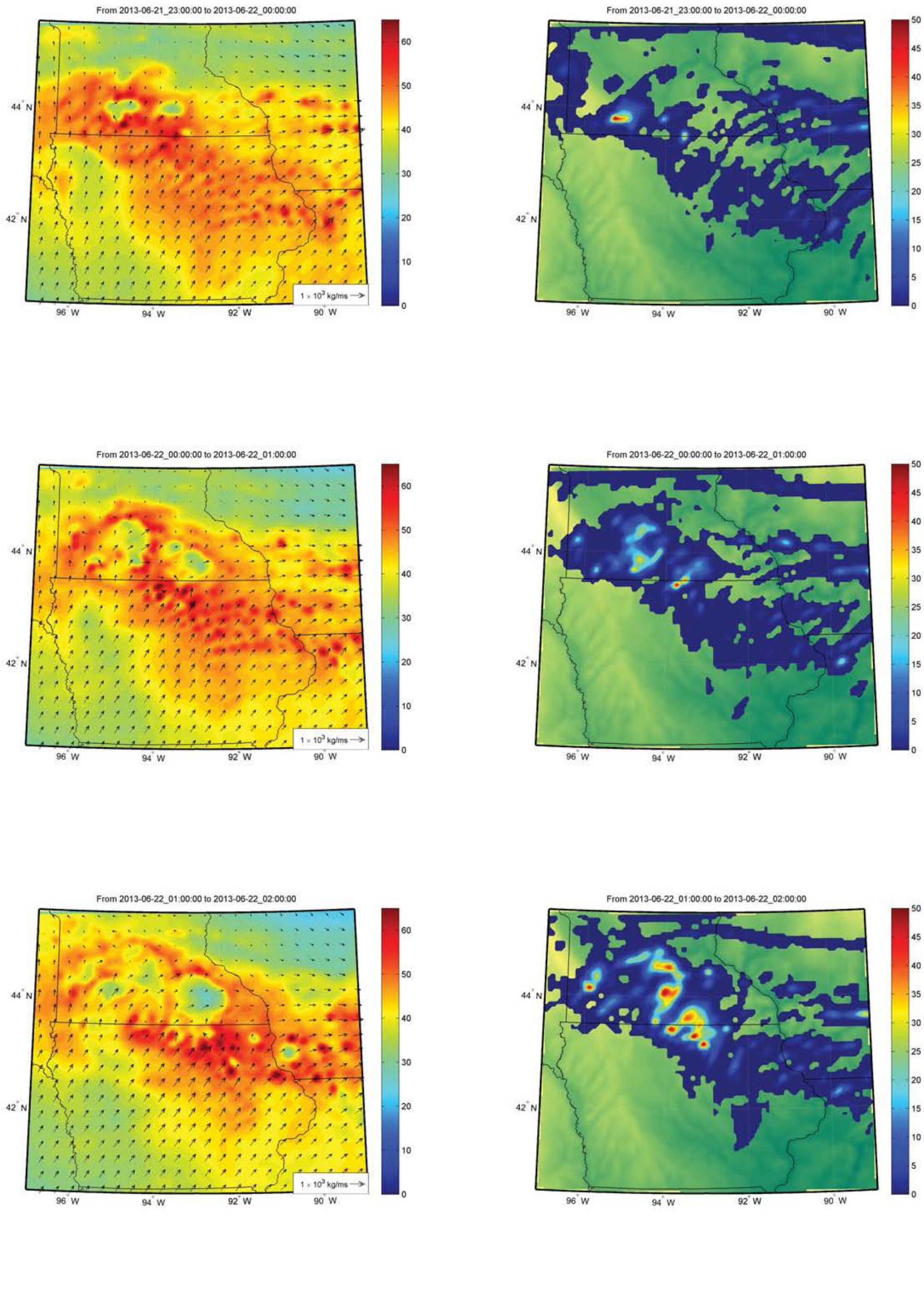

Figure B-14 Hourly Simulated Precipitable Water (Left, Colormap [mm]) and Water Vapor Flux Fields (Left, Arrows [kg m^{-1} s^{-1}]) and Precipitation Fields (Right, Colormap [mm]) for the June 22, 2013 MCS

Plots shown from 06/21/2013 at 17hr to 06/22/2013 at 19hr (Continued).

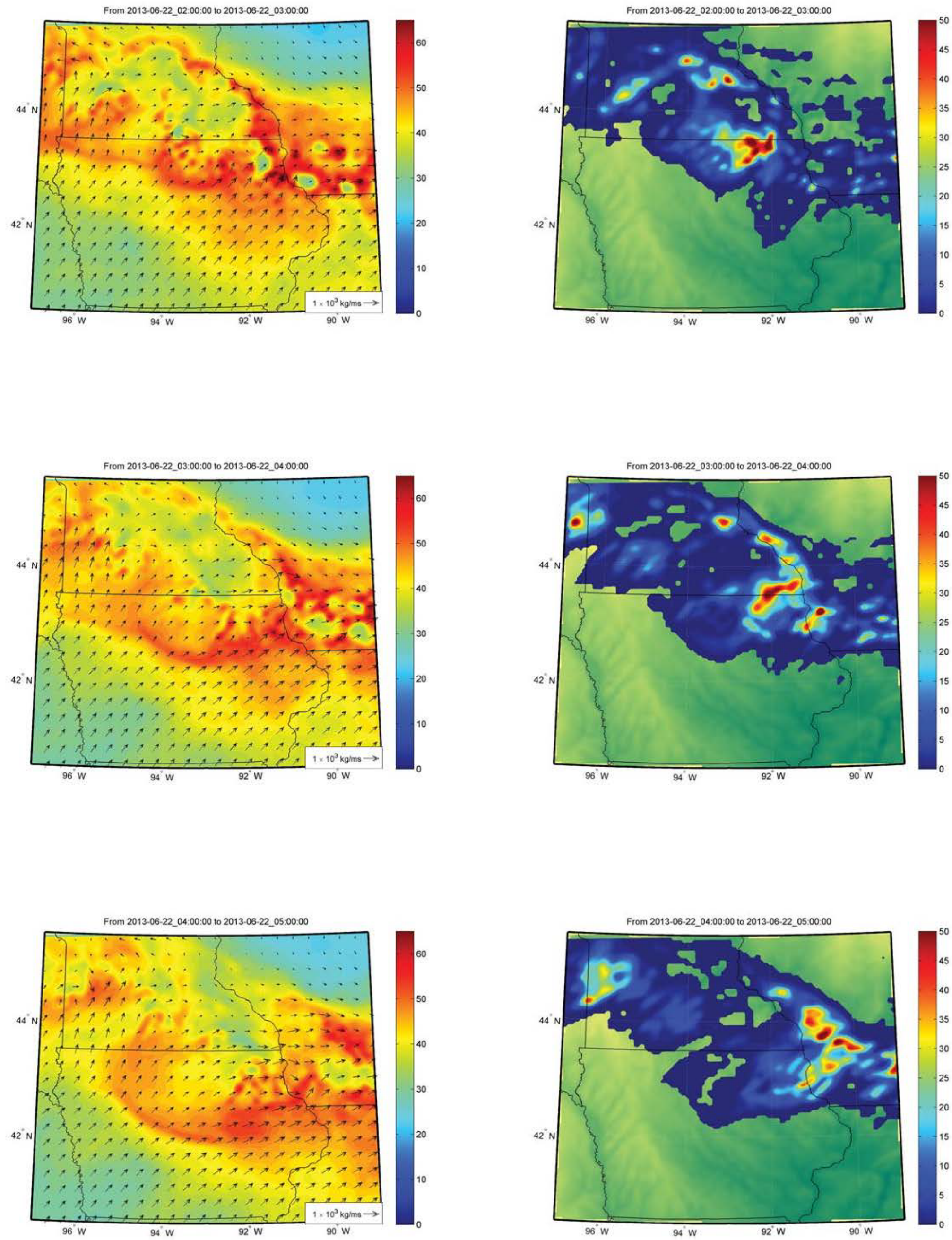

Figure B-14 Hourly Simulated Precipitable Water (Left, Colormap [mm]) and Water Vapor Flux Fields (Left, Arrows [kg m^{-1} s^{-1}]) and Precipitation Fields (Right, Colormap [mm]) for the June 22, 2013 MCS

Plots shown from 06/21/2013 at 17hr to 06/22/2013 at 19hr (Continued).

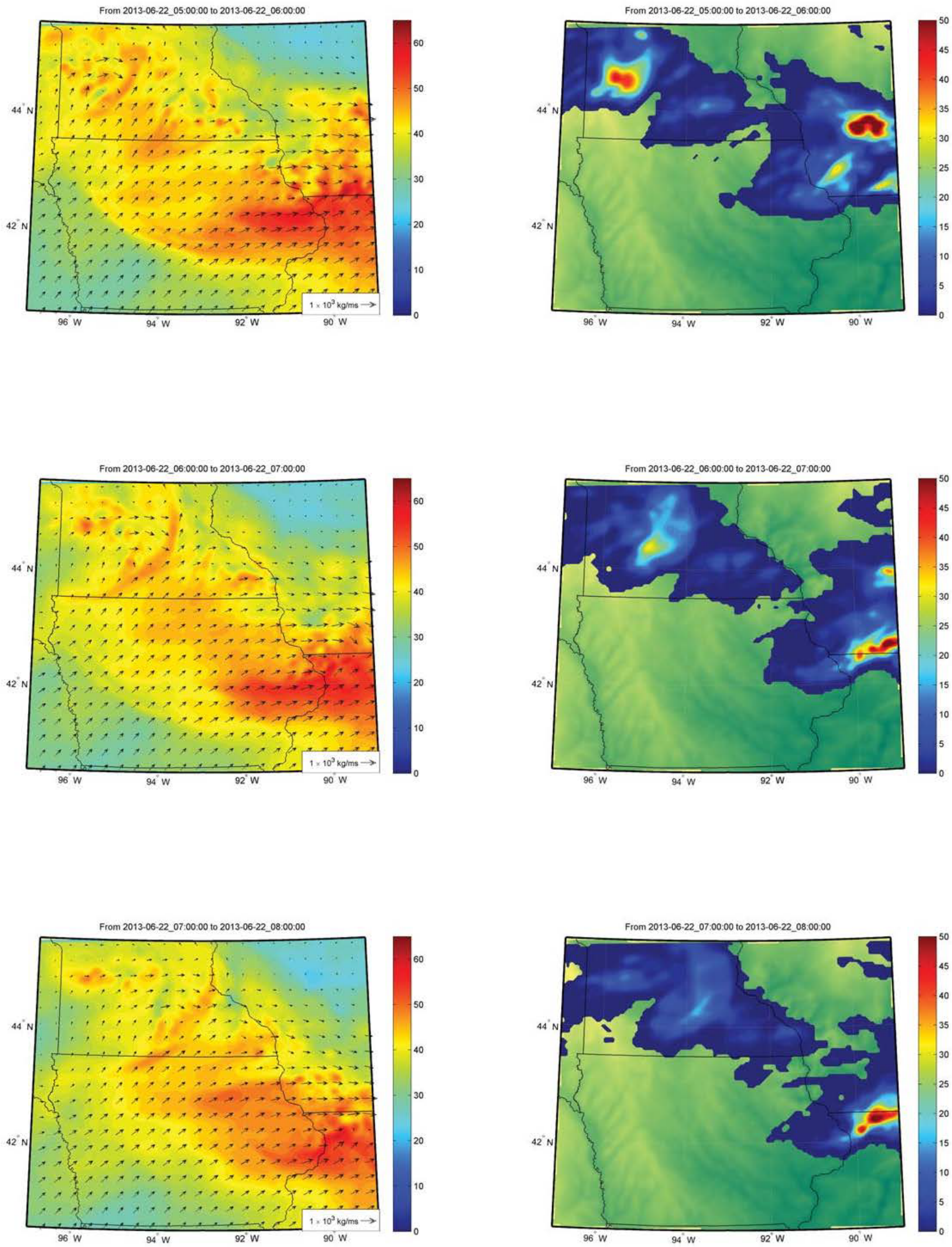

Figure B-14 Hourly Simulated Precipitable Water (Left, Colormap [mm]) and Water Vapor Flux Fields (Left, Arrows [kg m^{-1} s^{-1}]) and Precipitation Fields (Right, Colormap [mm]) for the June 22, 2013 MCS

Plots shown from 06/21/2013 at 17hr to 06/22/2013 at 19hr (Continued).

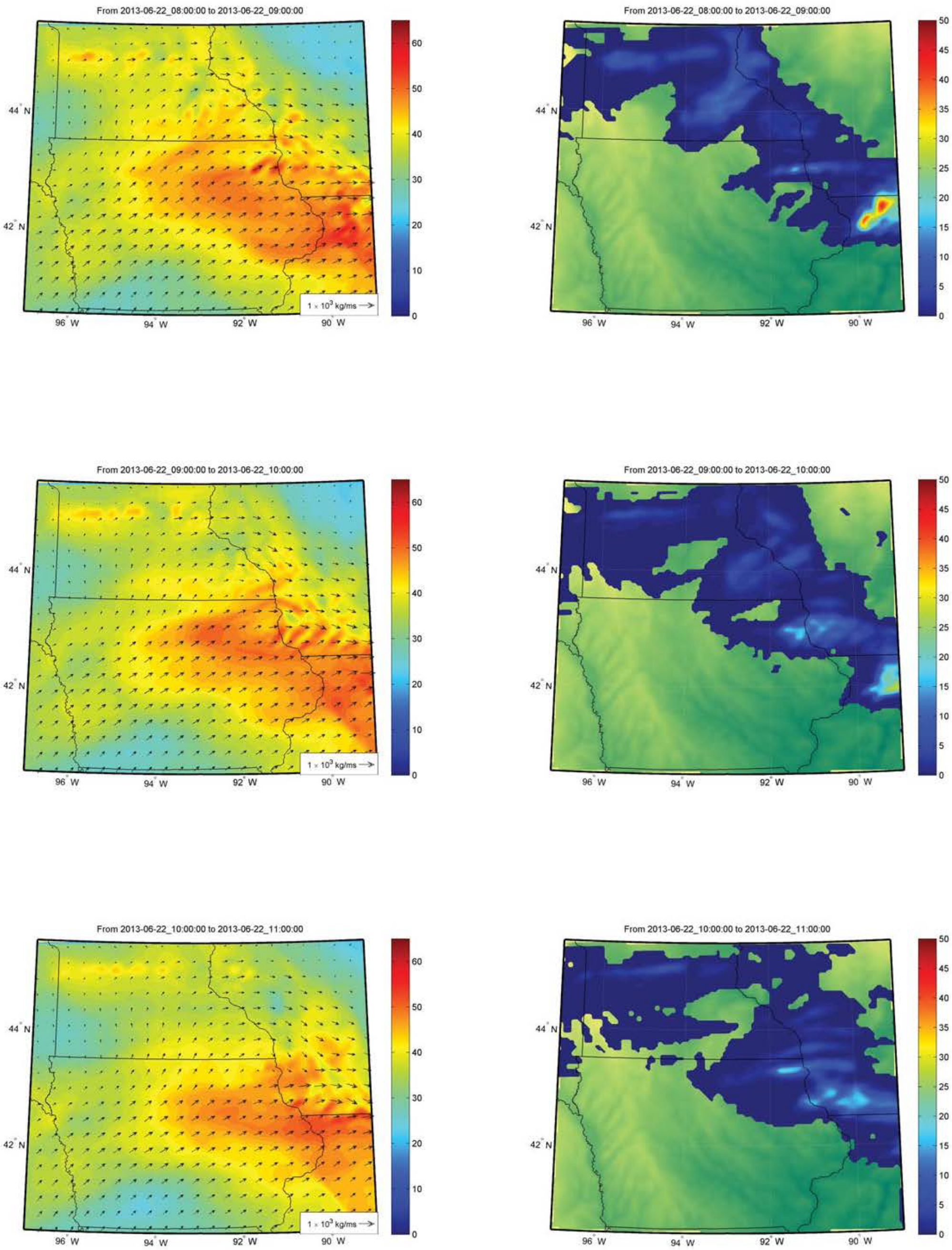

Figure B-14 Hourly Simulated Precipitable Water (Left, Colormap [mm]) and Water Vapor Flux Fields (Left, Arrows [kg m^{-1} s^{-1}]) and Precipitation Fields (Right, Colormap [mm]) for the June 22, 2013 MCS

Plots shown from 06/21/2013 at 17hr to 06/22/2013 at 19hr (Continued).

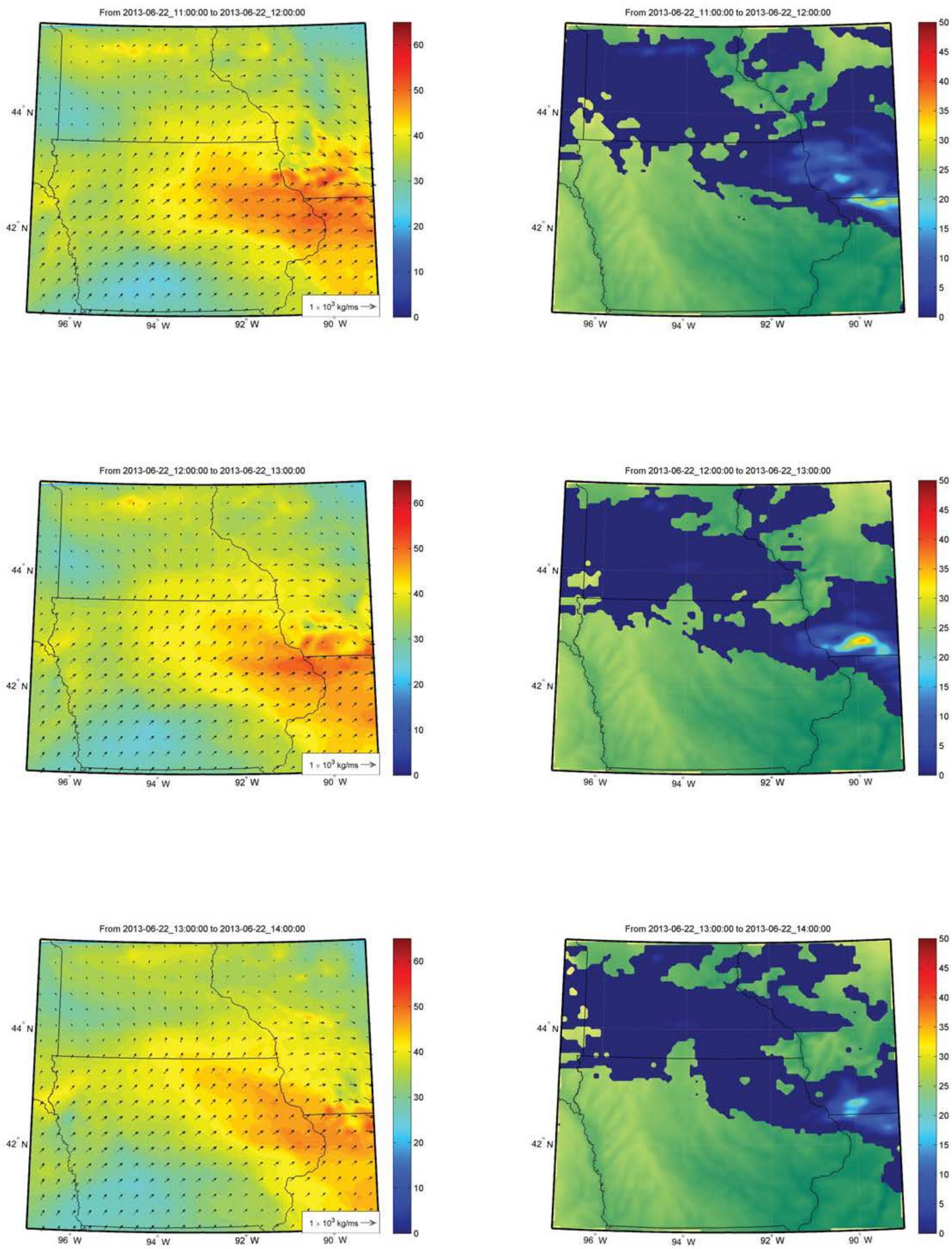

Figure B-14 Hourly Simulated Precipitable Water (Left, Colormap [mm]) and Water Vapor Flux Fields (Left, Arrows [kg m^{-1} s^{-1}]) and Precipitation Fields (Right, Colormap [mm]) for the June 22, 2013 MCS

Plots shown from 06/21/2013 at 17hr to 06/22/2013 at 19hr (Continued).

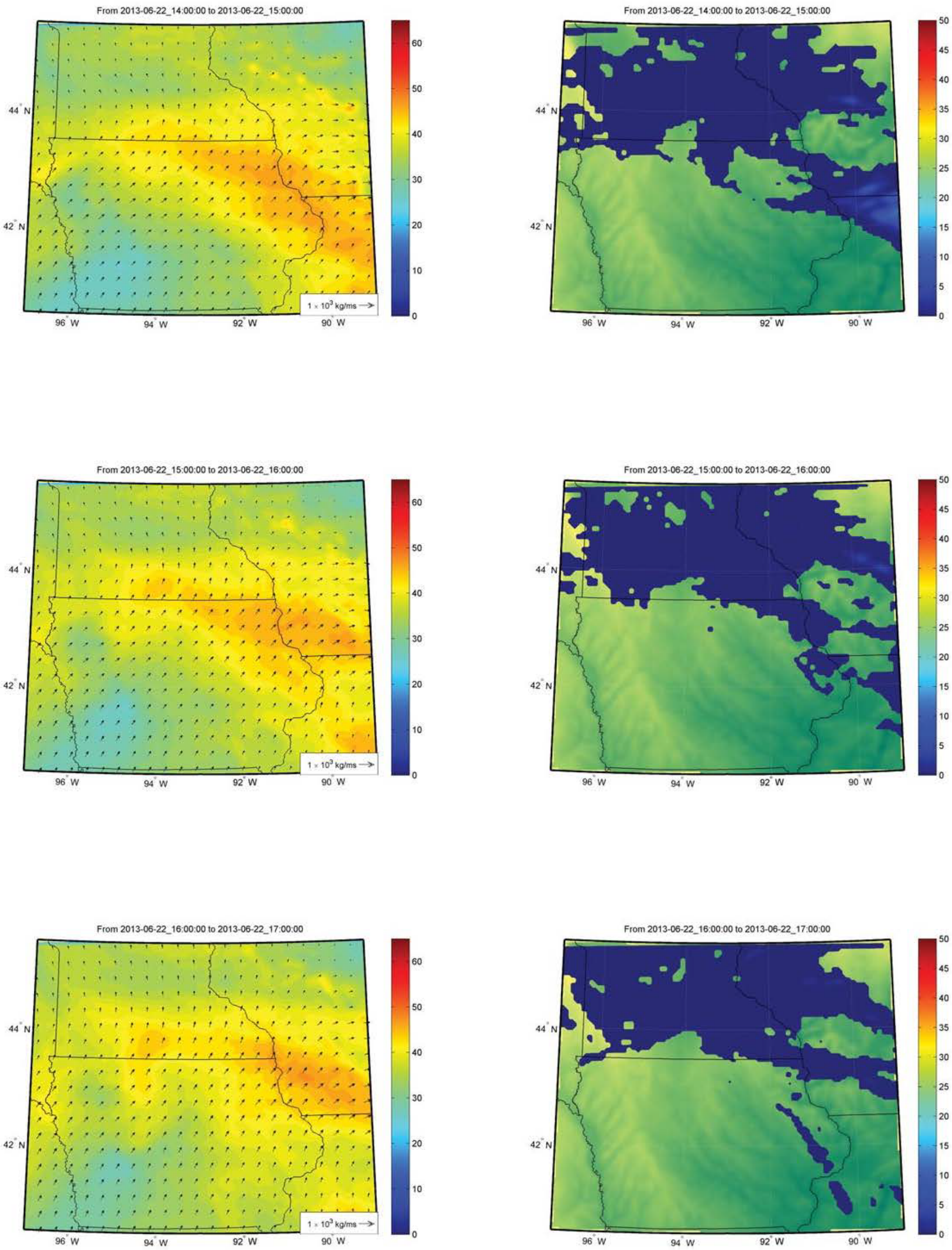

Figure B-14 Hourly Simulated Precipitable Water (Left, Colormap [mm]) and Water Vapor Flux Fields (Left, Arrows [kg m^{-1} s^{-1}]) and Precipitation Fields (Right, Colormap [mm]) for the June 22, 2013 MCS

Plots shown from 06/21/2013 at 17hr to 06/22/2013 at 19hr (Continued).

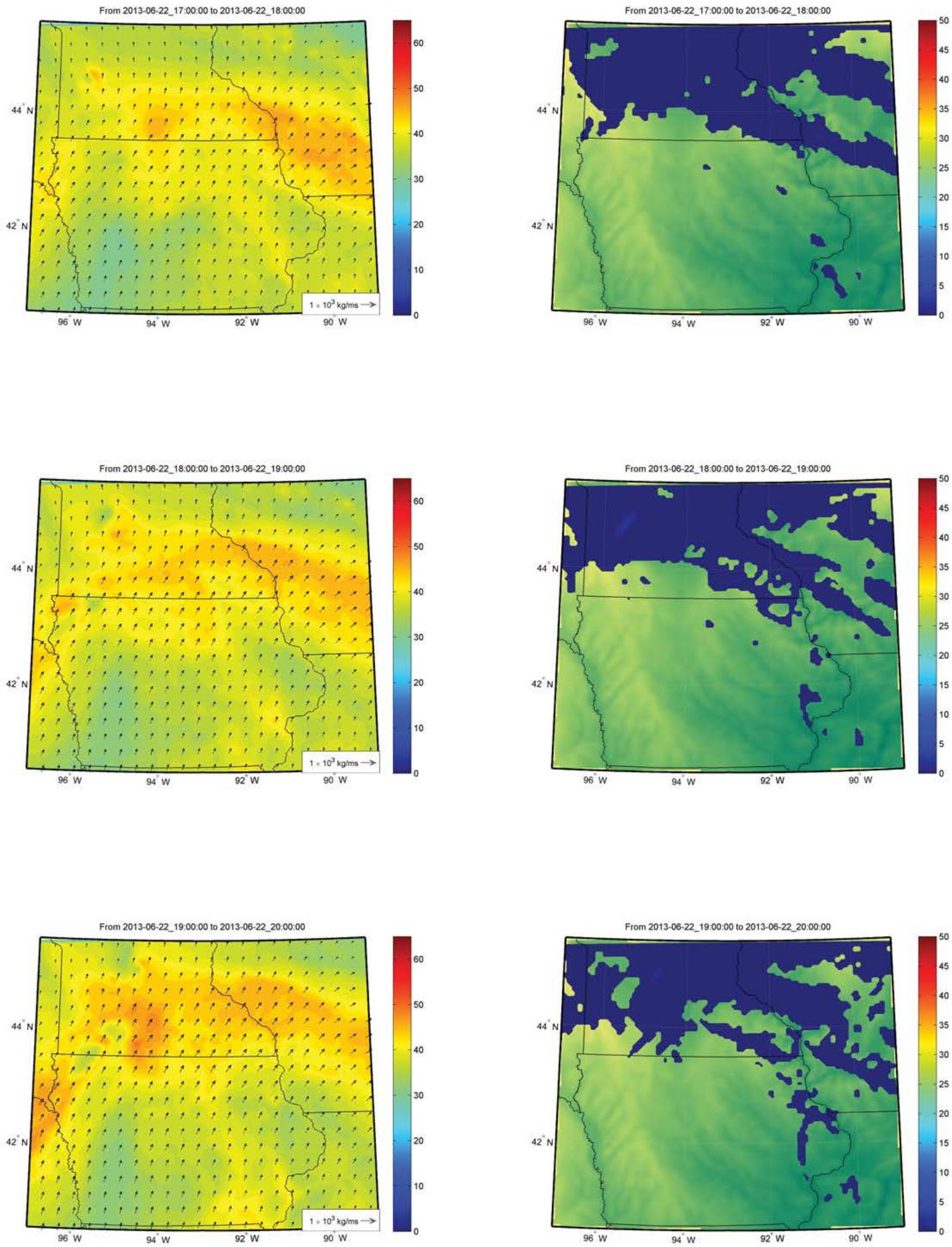

Figure B-14 **Hourly Simulated Precipitable Water (Left, Colormap [mm]) and Water Vapor Flux Fields (Left, Arrows [kg m^{-1} s^{-1}]) and Precipitation Fields (Right, Colormap [mm]) for the June 22, 2013 MCS**

Plots shown from 06/21/2013 at 17hr to 06/22/2013 at 19hr (Continued).

B.2 Tropical Cyclones

B.2.1 Hurricane Floyd (1999)

Figure B-15 shows the 6-hourly evolution of the reconstructed PW field and IVT field in Hurricane Floyd. It also shows the 6-hourly accumulated precipitation field associated with the PW and IVT.

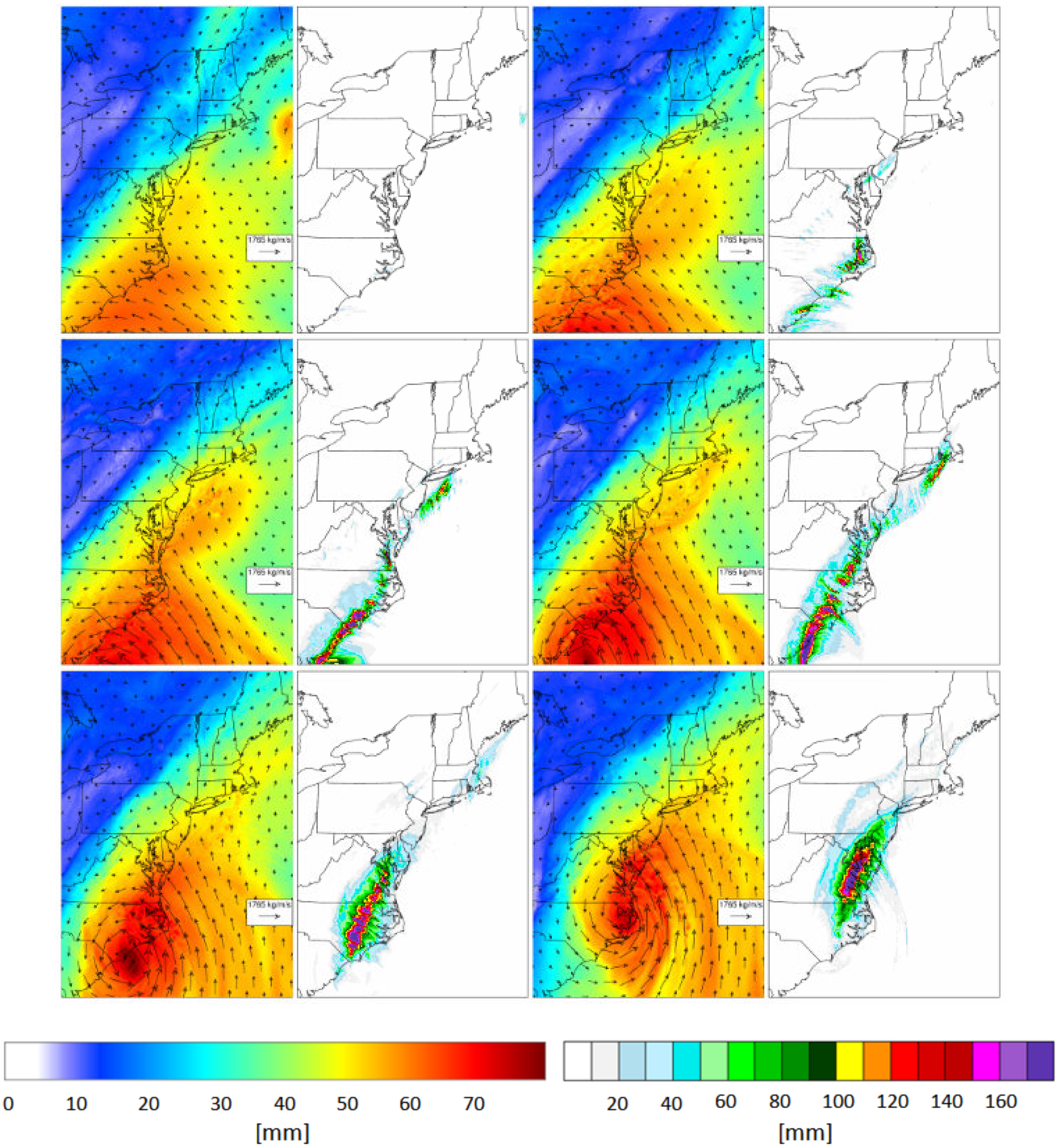

Figure B-15 6-Hourly Simulated Precipitable Water and Integrated Water Vapor Transport (Left) and its Corresponding 6-Hourly Accumulated Simulated Precipitation (Right) for Hurricane Floyd

The sequence goes from 09/15 06h until 09/18 06h. The reference arrow in the white box (⟶) shows an IVT vector with a magnitude of 1765 kg m^{-1} s^{-1}.

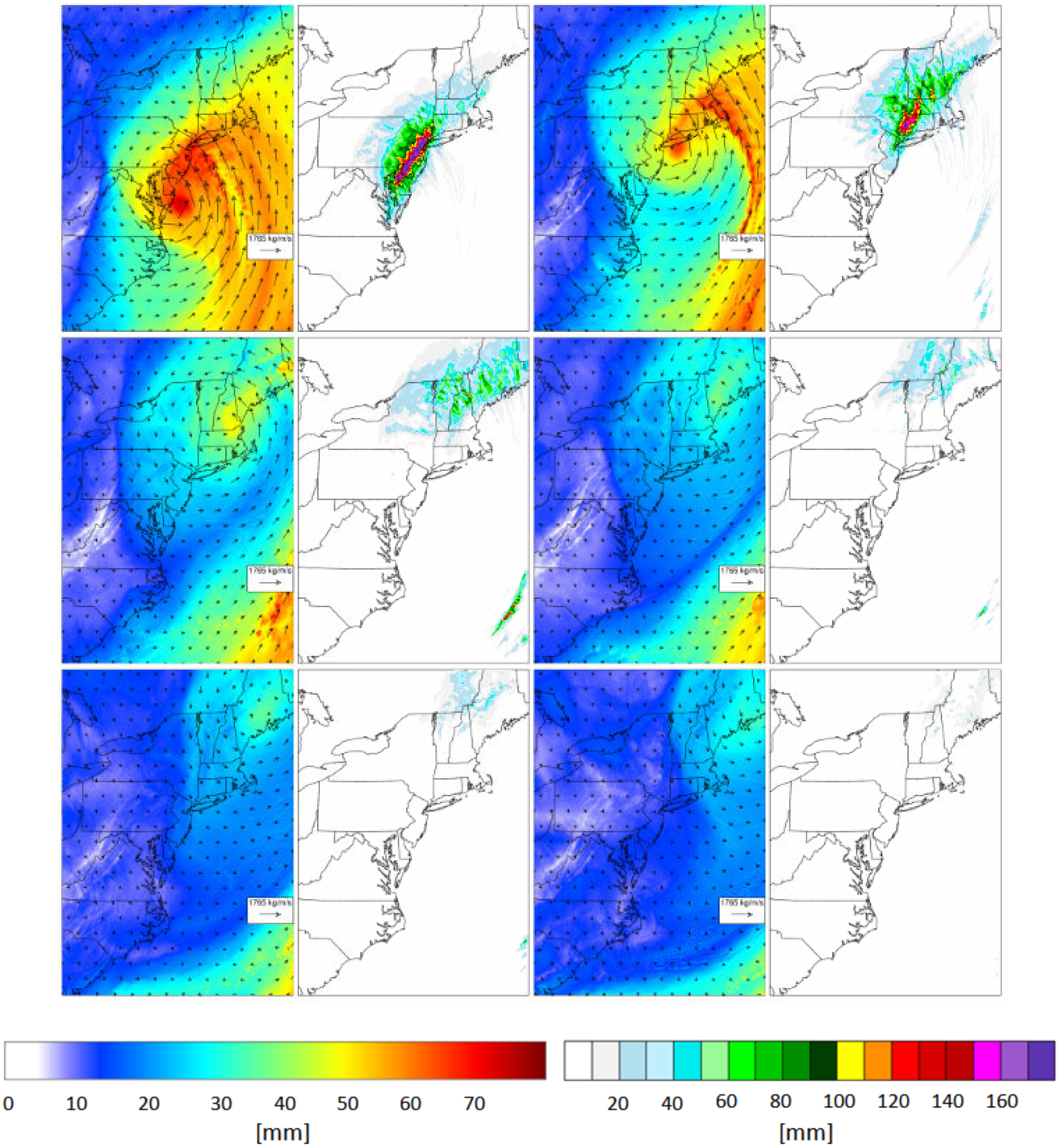

Figure B-15 6-Hourly Simulated Precipitable Water and Integrated Water Vapor Transport (Left) and its Corresponding 6-Hourly Accumulated Simulated Precipitation (Right) for Hurricane Floyd

The sequence goes from 09/15 06h until 09/18 06h. The reference arrow in the white box (⟶) shows an IVT vector with a magnitude of 1765 kg m^{-1} s^{-1} (Continued).

B.2.2 Hurricane Isidore (2002)

Figure B-16 shows the 6-hourly evolution of the reconstructed PW field and IVT field in Hurricane Isidore. It also shows the 6-hourly accumulated precipitation field associated with the PW and IVT.

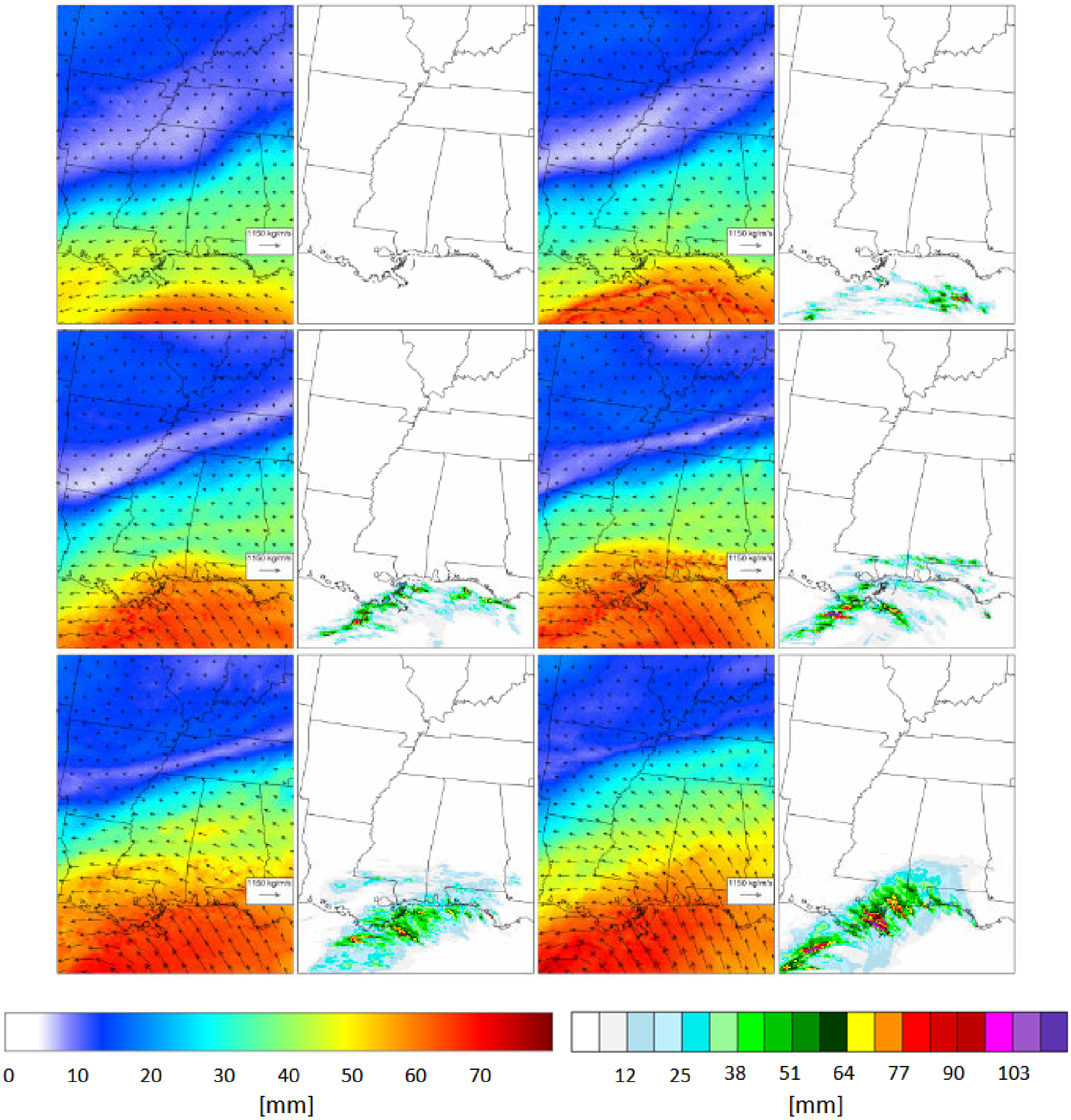

Figure B-16 6-Hourly Simulated Precipitable Water and Integrated Water Vapor Transport (Left) and its Corresponding 6-Hourly Accumulated Simulated Precipitation (Right) for Hurricane Isidore

The sequence goes from 09/24 00h until 09/28 00h. The reference arrow in the white box (⟶) shows an IVT vector with a magnitude of 1150 kg m^{-1} s^{-1}.

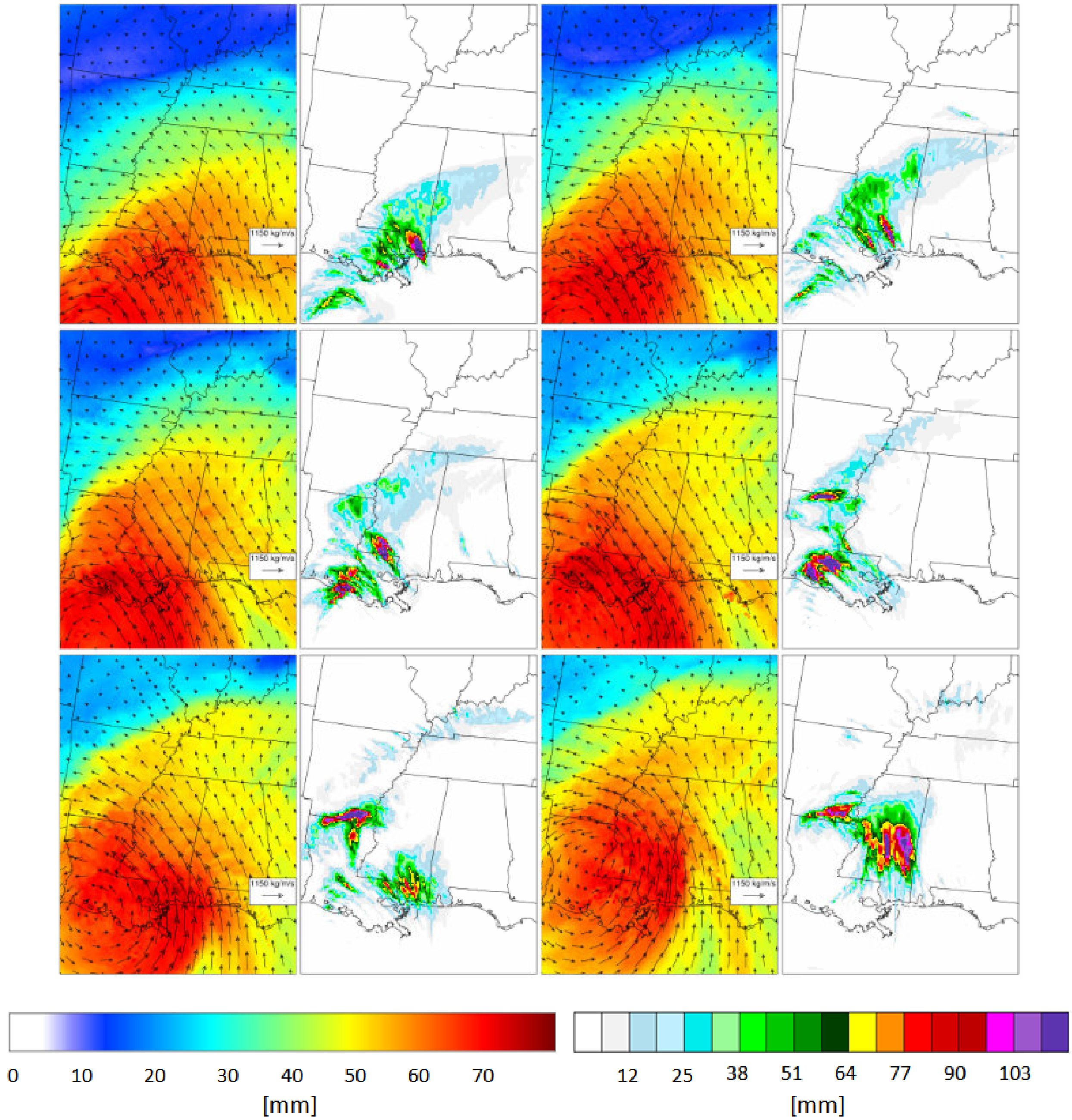

Figure B-16 6-Hourly Simulated Precipitable Water and Integrated Water Vapor Transport (Left) and its Corresponding 6-Hourly Accumulated Simulated Precipitation (Right) for Hurricane Isidore

The sequence goes from 09/24 00h until 09/28 00h. The reference arrow in the white box (⟶) shows an IVT vector with a magnitude of 1150 kg m^{-1} s^{-1} (Continued).

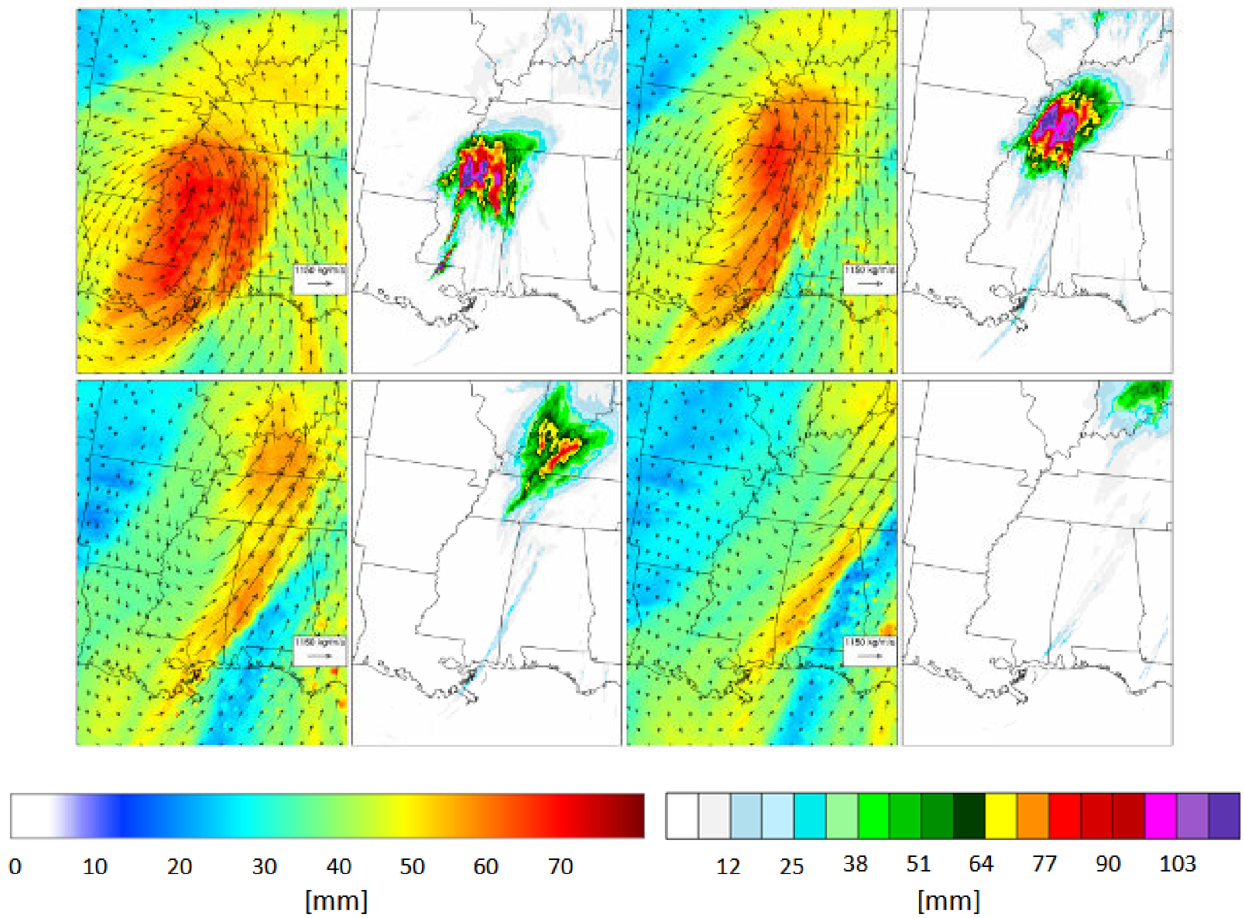

Figure B-16 6-Hourly Simulated Precipitable Water and Integrated Water Vapor Transport (Left) and its Corresponding 6-Hourly Accumulated Simulated Precipitation (Right) for Hurricane Isidore

The sequence goes from 09/24 00h until 09/28 00h. The reference arrow in the white box (⟶) shows an IVT vector with a magnitude of 1150 kg m^{-1} s^{-1} (Continued).

B.2.3 Hurricane Frances (2004)

Figure B-17 shows the 6-hourly evolution of the reconstructed PW field and IVT field in Hurricane Frances. It also shows the 6-hourly accumulated precipitation field associated with the PW and IVT.

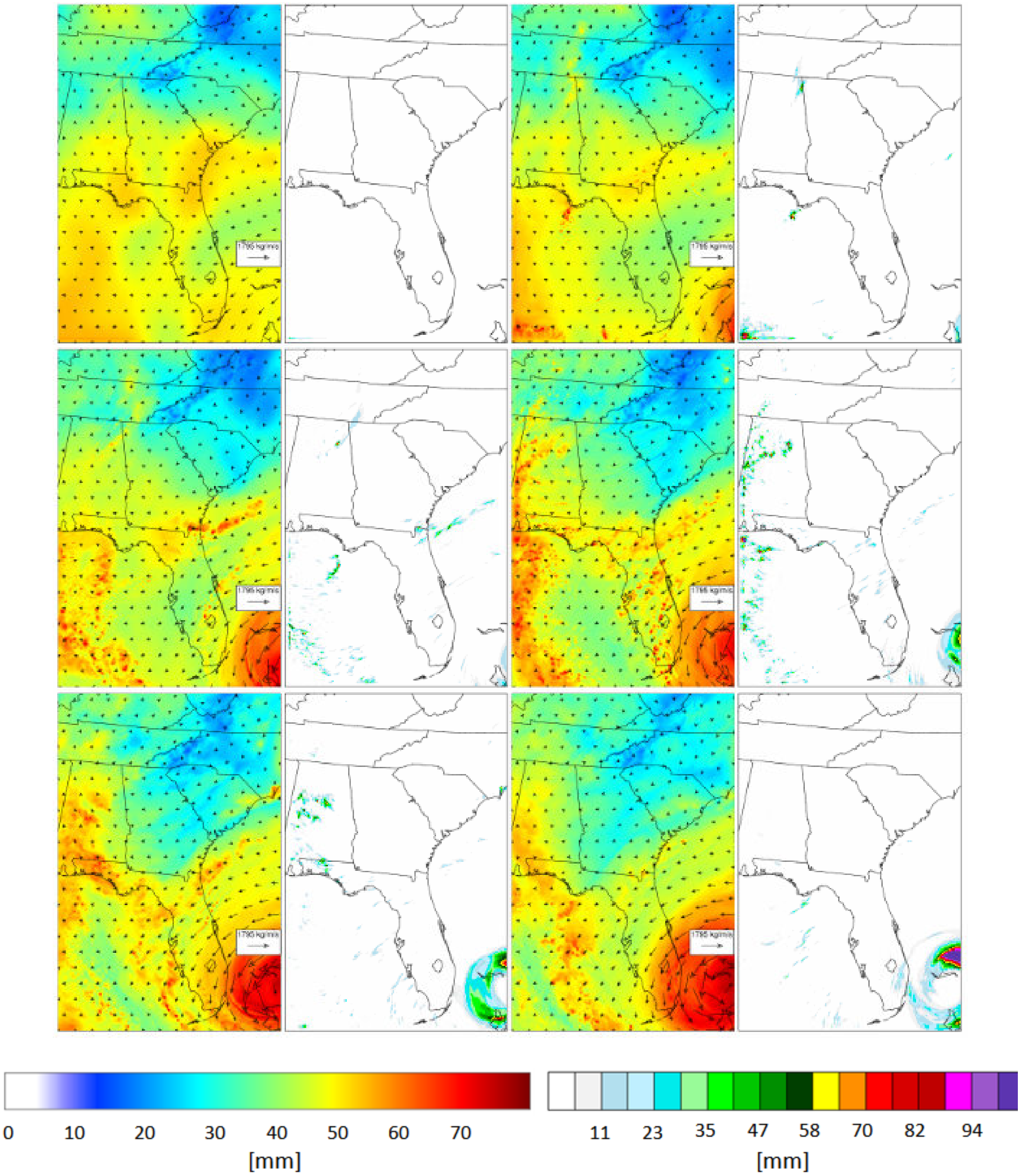

Figure B-17 6-Hourly Simulated Precipitable Water and Integrated Water Vapor Transport (Left) and its Corresponding 6-Hourly Accumulated Simulated Precipitation (Right) for Hurricane Frances

The sequence goes from 09/03 00h until 09/10 00h. The reference arrow in the white box (⟶) shows an IVT vector with a magnitude of 1795 kg m^{-1} s^{-1}.

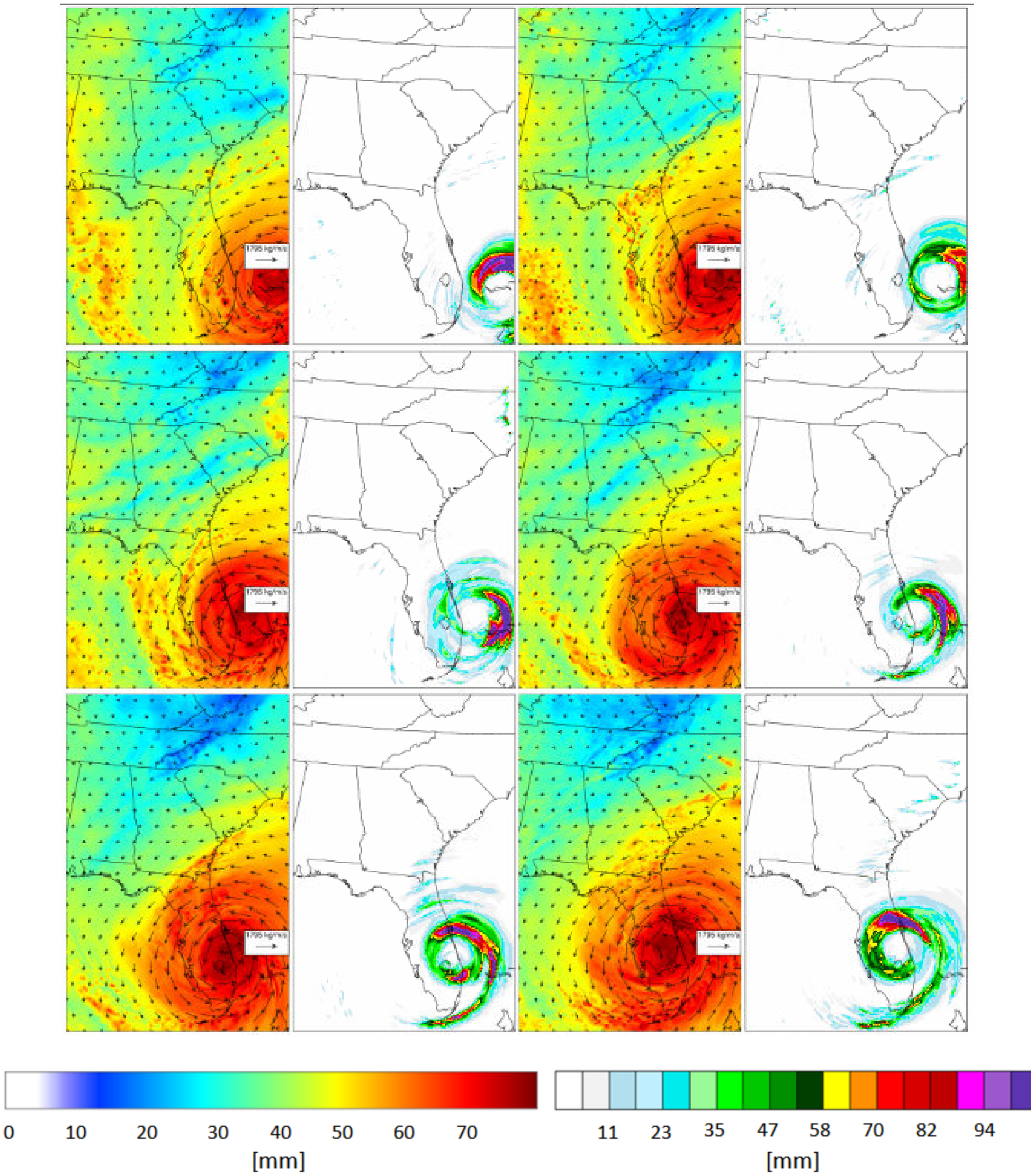

Figure B-17 6-Hourly Simulated Precipitable Water and Integrated Water Vapor Transport (Left) and its Corresponding 6-Hourly Accumulated Simulated Precipitation (Right) for Hurricane Frances

The sequence goes from 09/03 00h until 09/10 00h. The reference arrow in the white box (⟶) shows an IVT vector with a magnitude of 1795 kg m^{-1} s^{-1} (Continued).

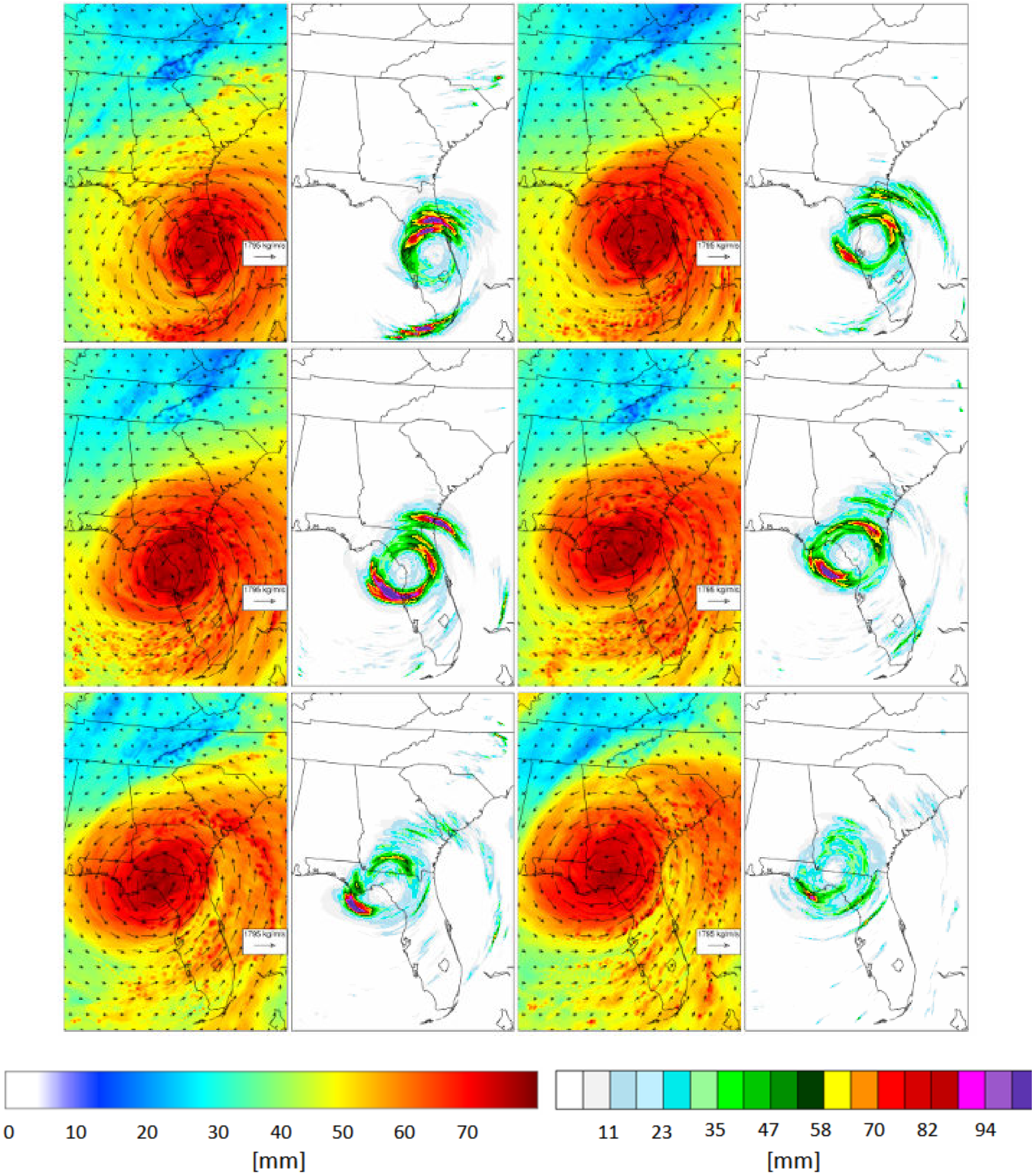

Figure B-17 6-Hourly Simulated Precipitable Water and Integrated Water Vapor Transport (Left) and its Corresponding 6-Hourly Accumulated Simulated Precipitation (Right) for Hurricane Frances

The sequence goes from 09/03 00h until 09/10 00h. The reference arrow in the white box (⟶) shows an IVT vector with a magnitude of 1795 kg m^{-1} s^{-1} (Continued).

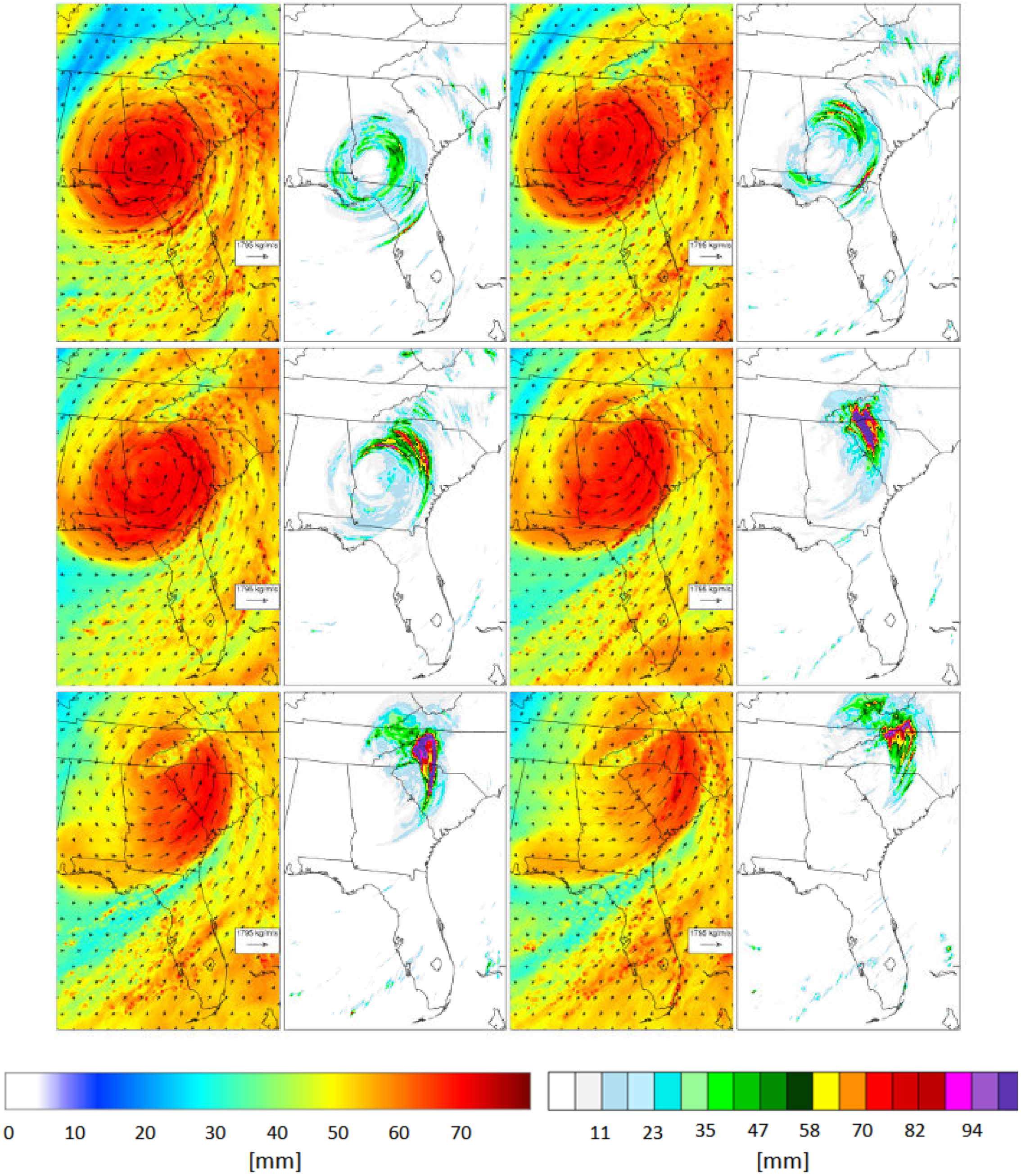

Figure B-17 6-Hourly Simulated Precipitable Water and Integrated Water Vapor Transport (Left) and its Corresponding 6-Hourly Accumulated Simulated Precipitation (Right) for Hurricane Frances

The sequence goes from 09/03 00h until 09/10 00h. The reference arrow in the white box (⟶) shows an IVT vector with a magnitude of 1795 kg m^{-1} s^{-1} (Continued).

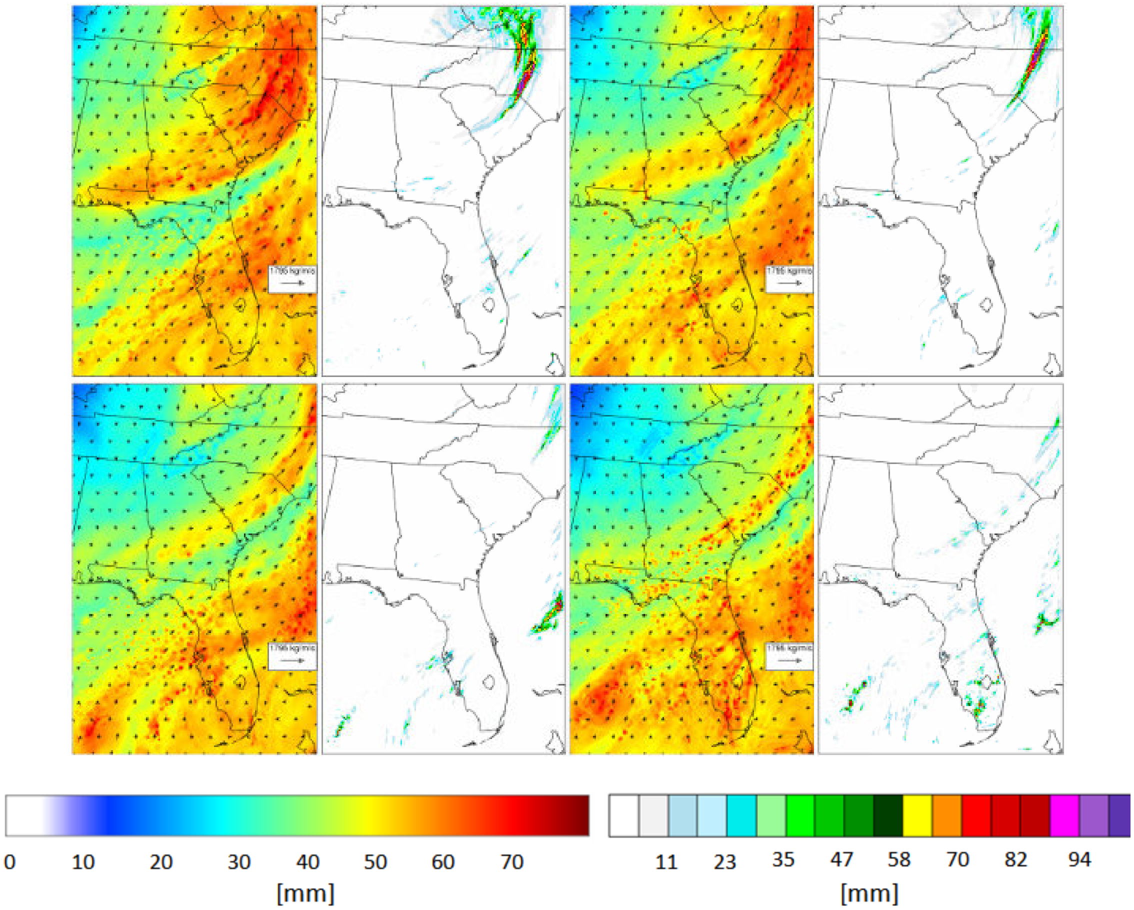

Figure B-17 6-Hourly Simulated Precipitable Water and Integrated Water Vapor Transport (Left) and its Corresponding 6-Hourly Accumulated Simulated Precipitation (Right) for Hurricane Frances

The sequence goes from 09/03 00h until 09/10 00h. The reference arrow in the white box (⟶) shows an IVT vector with a magnitude of 1795 kg m^{-1} s^{-1} (Continued).

B.2.4 Hurricane Ivan (2004)

Figure B-18 shows the 6-hourly evolution of the reconstructed PW field and IVT field in Hurricane Ivan. It also shows the 6-hourly accumulated precipitation field associated with the PW and IVT.

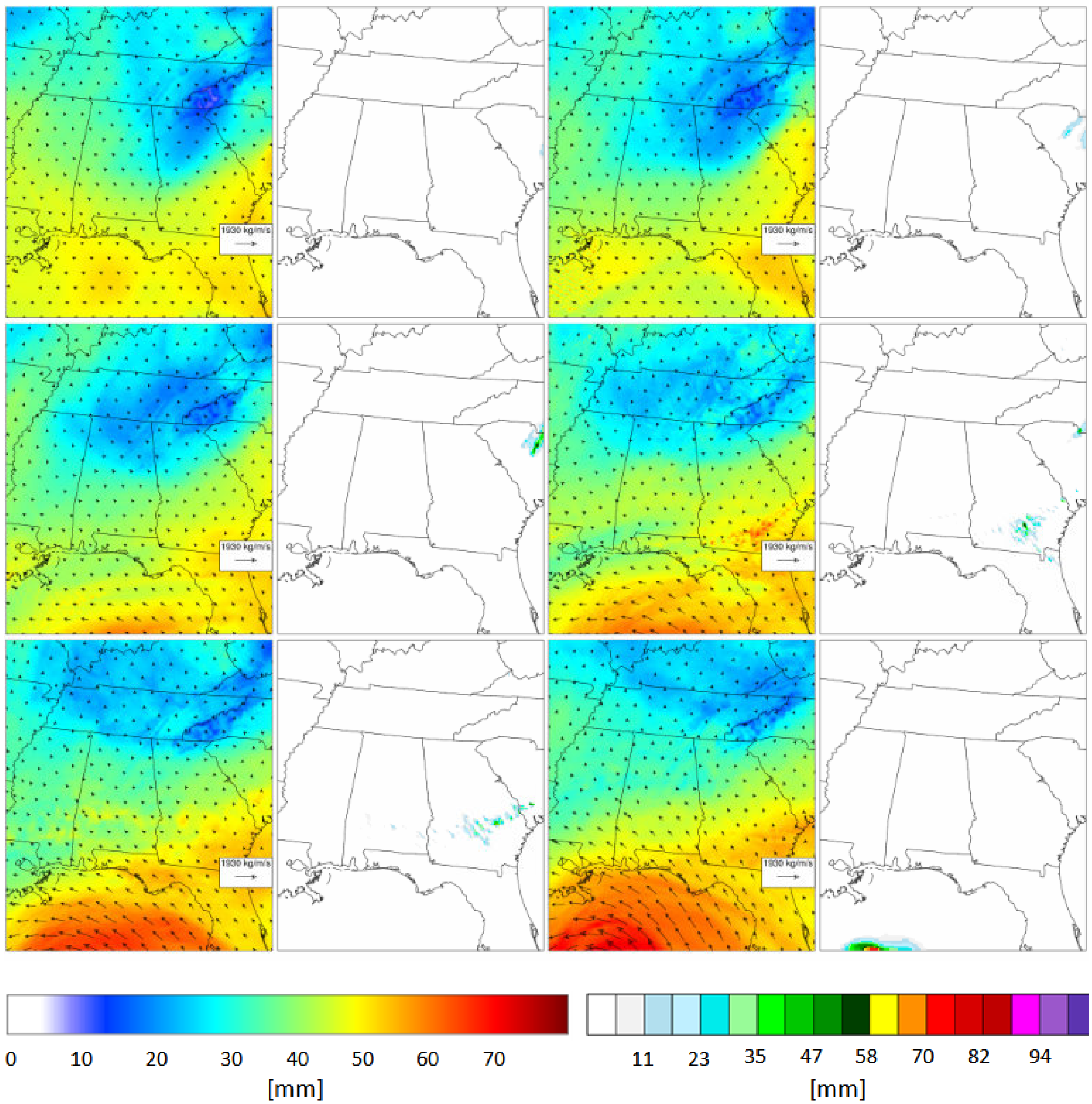

Figure B-18 6-Hourly Simulated Precipitable Water and Integrated Water Vapor Transport (Left) and its Corresponding 6-Hourly Accumulated Simulated Precipitation (Right) for Hurricane Ivan

The sequence goes from 09/14 00h until 09/19 00h. The reference arrow in the white box (⟶) shows an IVT vector with a magnitude of 1930 kg m^{-1} s^{-1}.

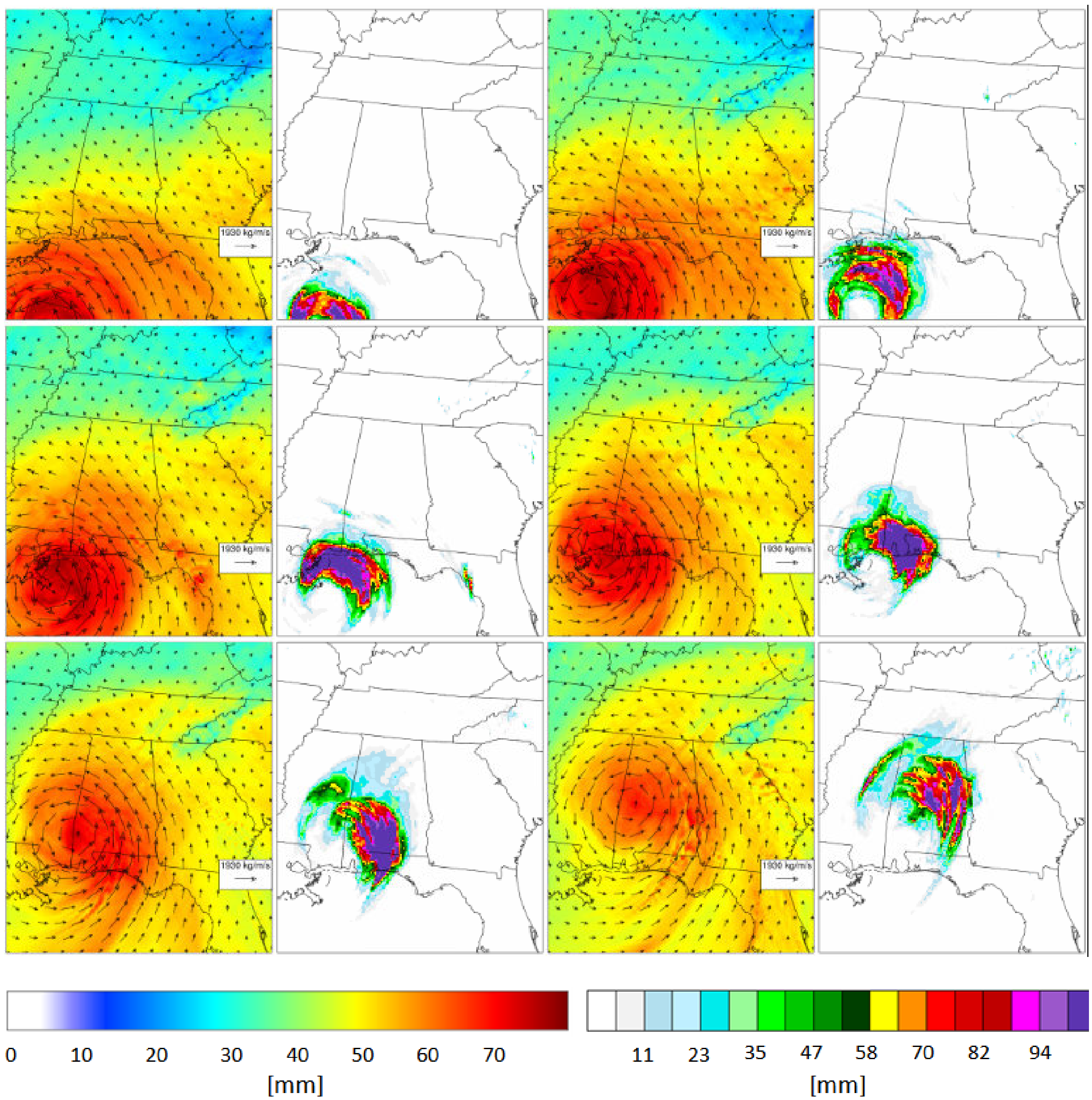

Figure B-18 6-Hourly Simulated Precipitable Water and Integrated Water Vapor Transport (Left) and its Corresponding 6-Hourly Accumulated Simulated Precipitation (Right) for Hurricane Ivan

The sequence goes from 09/14 00h until 09/19 00h. The reference arrow in the white box (⟶) shows an IVT vector with a magnitude of 1930 kg m^{-1} s^{-1} (Continued).

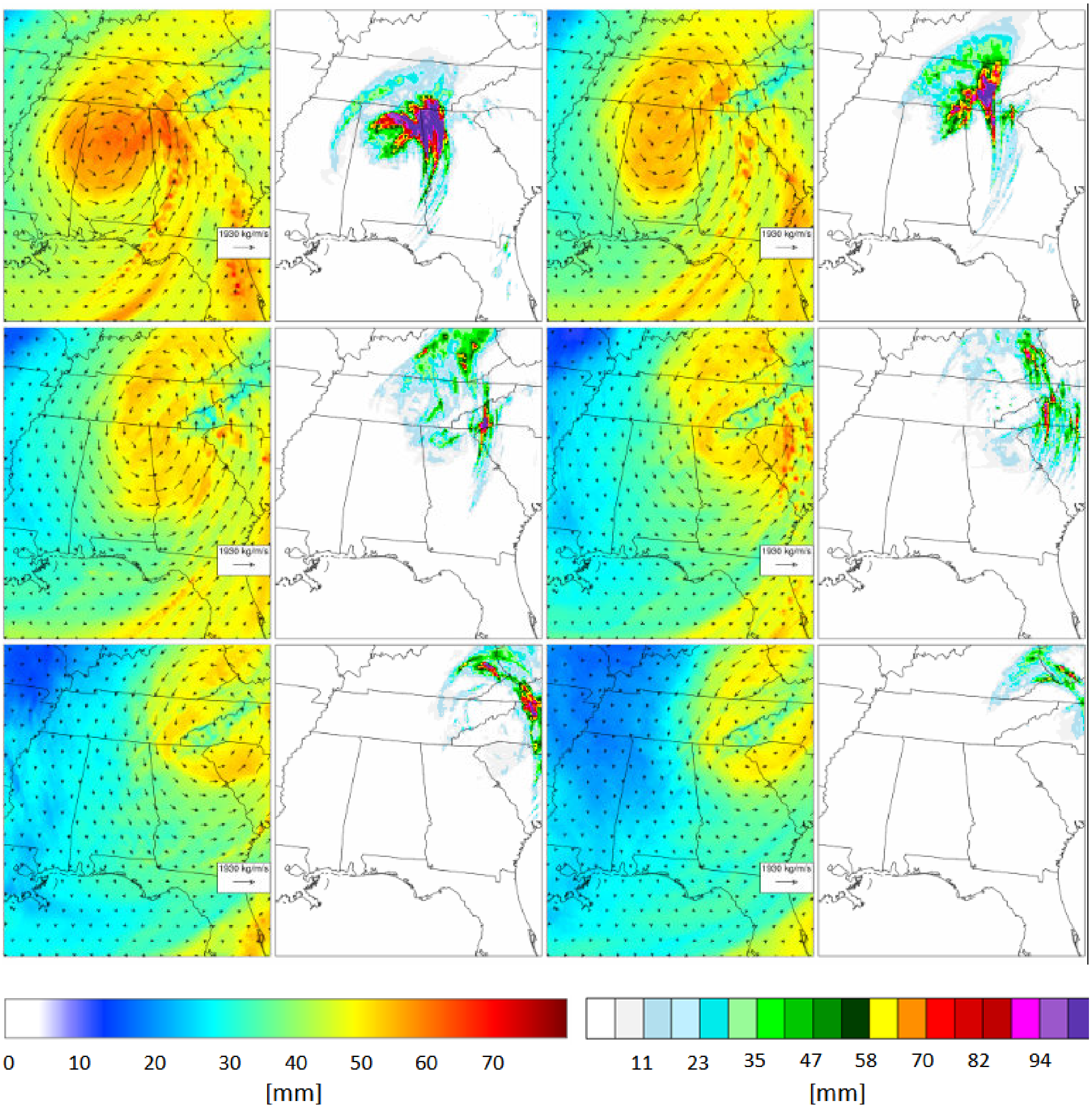

Figure B-18 6-Hourly Simulated Precipitable Water and Integrated Water Vapor Transport (Left) and its Corresponding 6-Hourly Accumulated Simulated Precipitation (Right) for Hurricane Ivan

The sequence goes from 09/14 00h until 09/19 00h. The reference arrow in the white box (⟶) shows an IVT vector with a magnitude of 1930 kg m^{-1} s^{-1} (Continued).

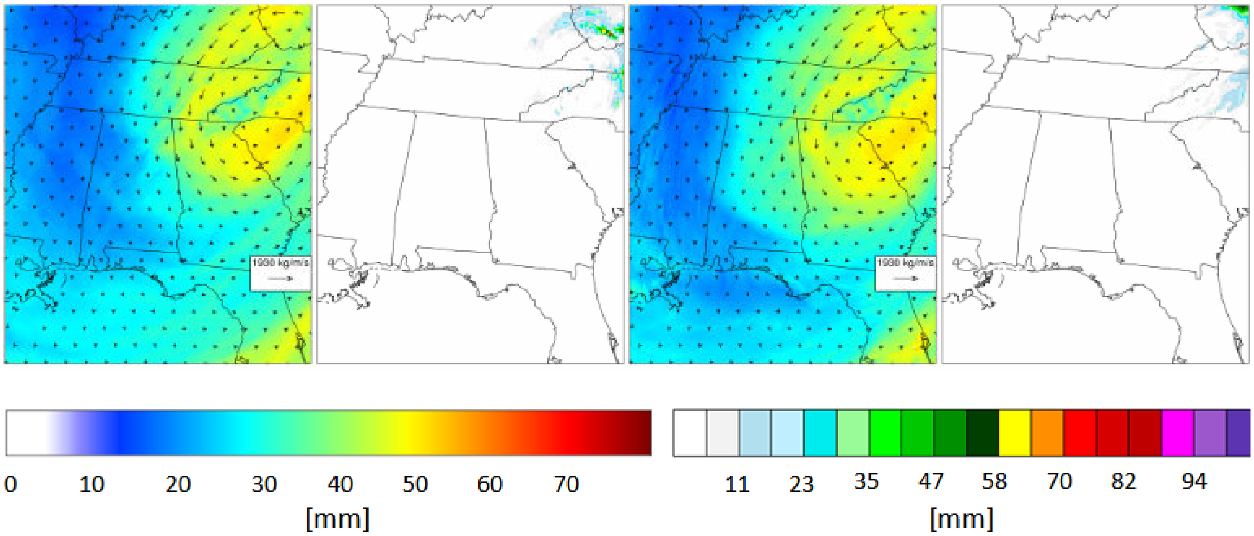

Figure B-18 6-Hourly Simulated Precipitable Water and Integrated Water Vapor Transport (Left) and its Corresponding 6-Hourly Accumulated Simulated Precipitation (Right) for Hurricane Ivan

The sequence goes from 09/14 00h until 09/19 00h. The reference arrow in the white box (⟶) shows an IVT vector with a magnitude of 1930 kg m^{-1} s^{-1} (Continued).

B.2.5 Hurricane Jeanne (2004)

Figure B-19 shows the 6-hourly evolution of the reconstructed PW field and IVT field in Hurricane Jeanne. It also shows the 6-hourly accumulated precipitation field associated with the PW and IVT.

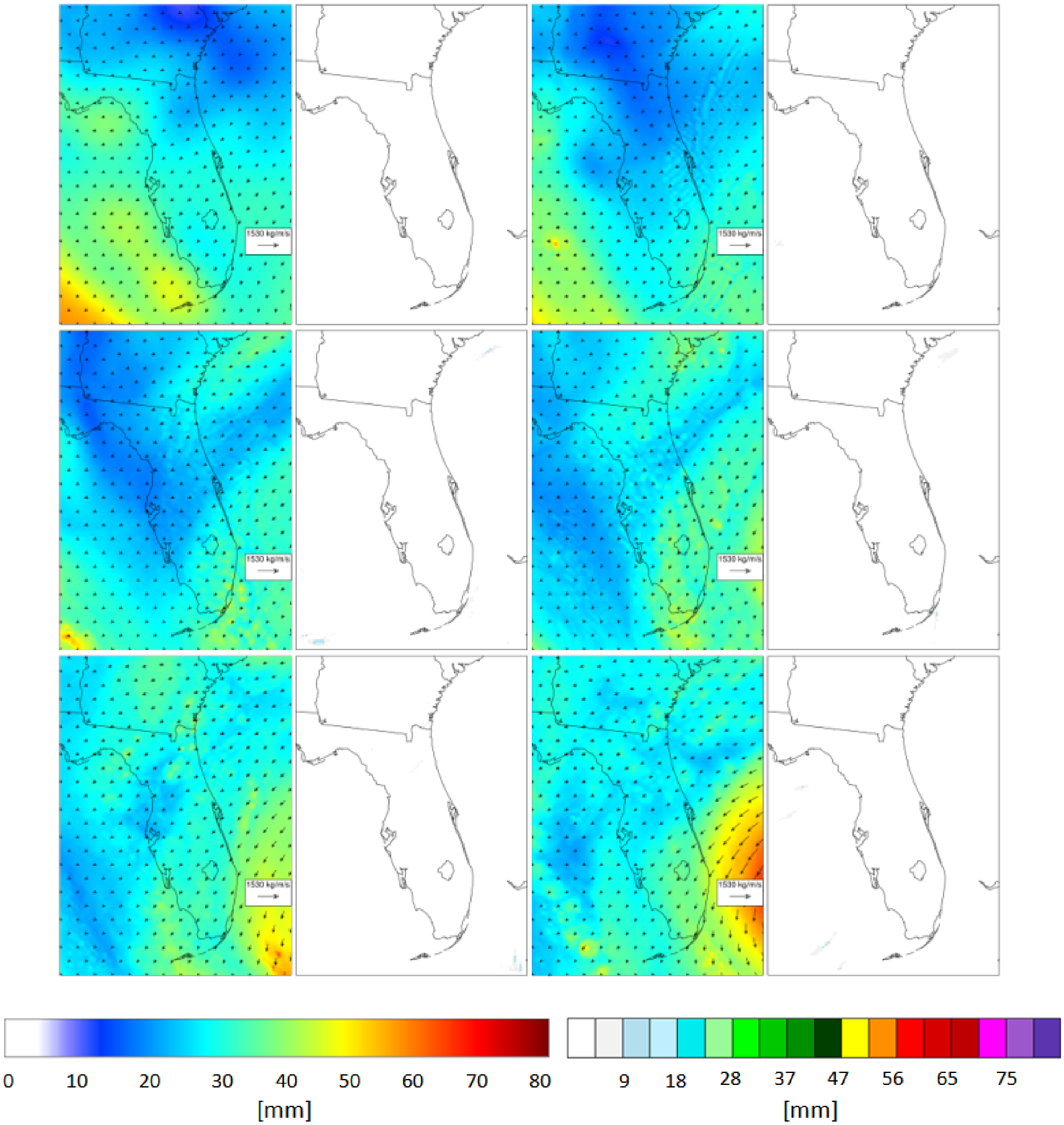

Figure B-19 6-Hourly Simulated Precipitable Water and Integrated Water Vapor Transport (Left) and its Corresponding 6-Hourly Accumulated Simulated Precipitation (Right) for Hurricane Jeanne

The sequence goes from 09/24 00h until 09/30 18h. The reference arrow in the white box (⟶) shows an IVT vector with a magnitude of 1530 kg m^{-1} s^{-1}.

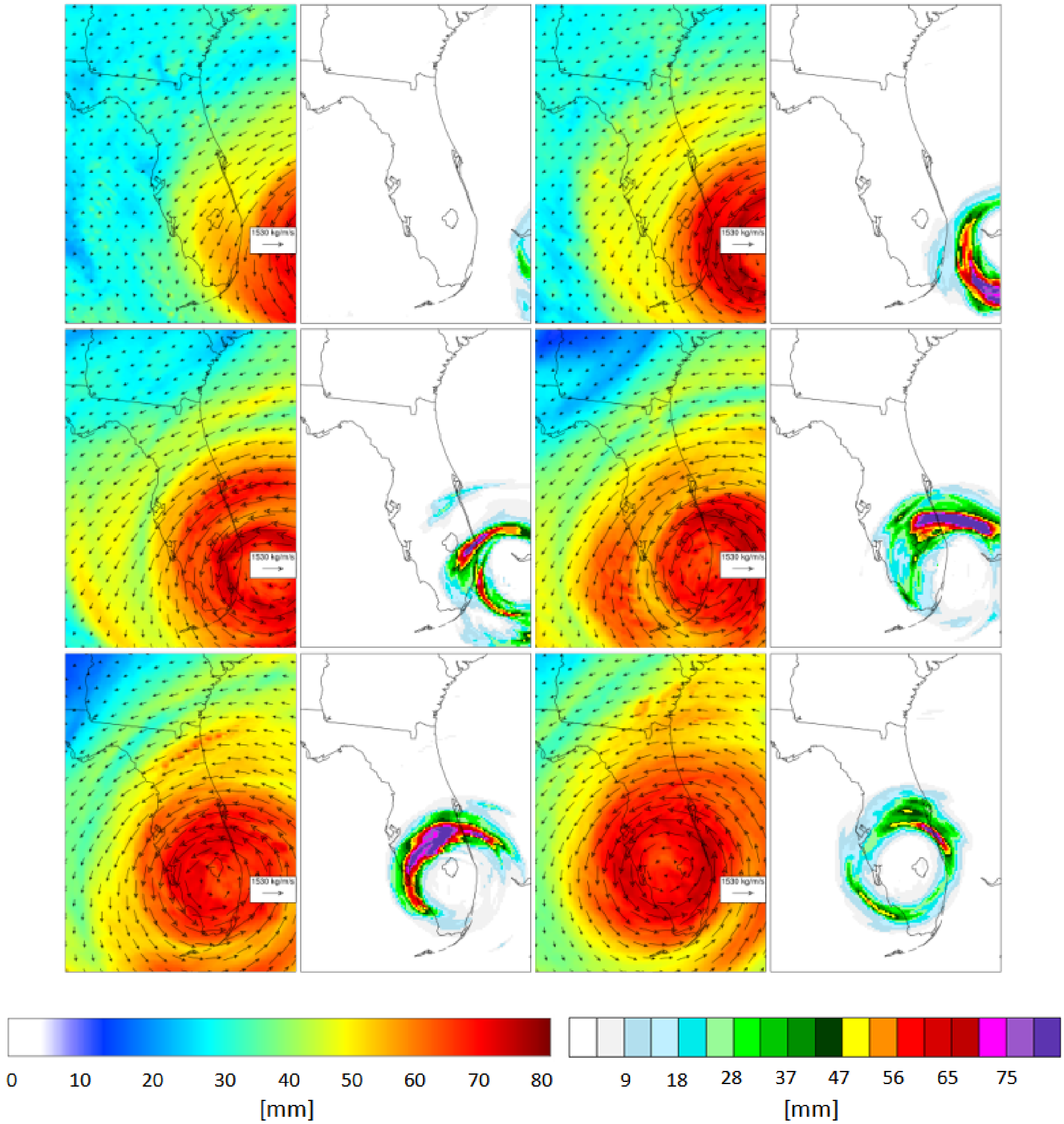

Figure B-19 6-Hourly Simulated Precipitable Water and Integrated Water Vapor Transport (Left) and its Corresponding 6-Hourly Accumulated Simulated Precipitation (Right) for Hurricane Jeanne

The sequence goes from 09/24 00h until 09/30 18h. The reference arrow in the white box (⟶) shows an IVT vector with a magnitude of 1530 kg m^{-1} s^{-1} (Continued).

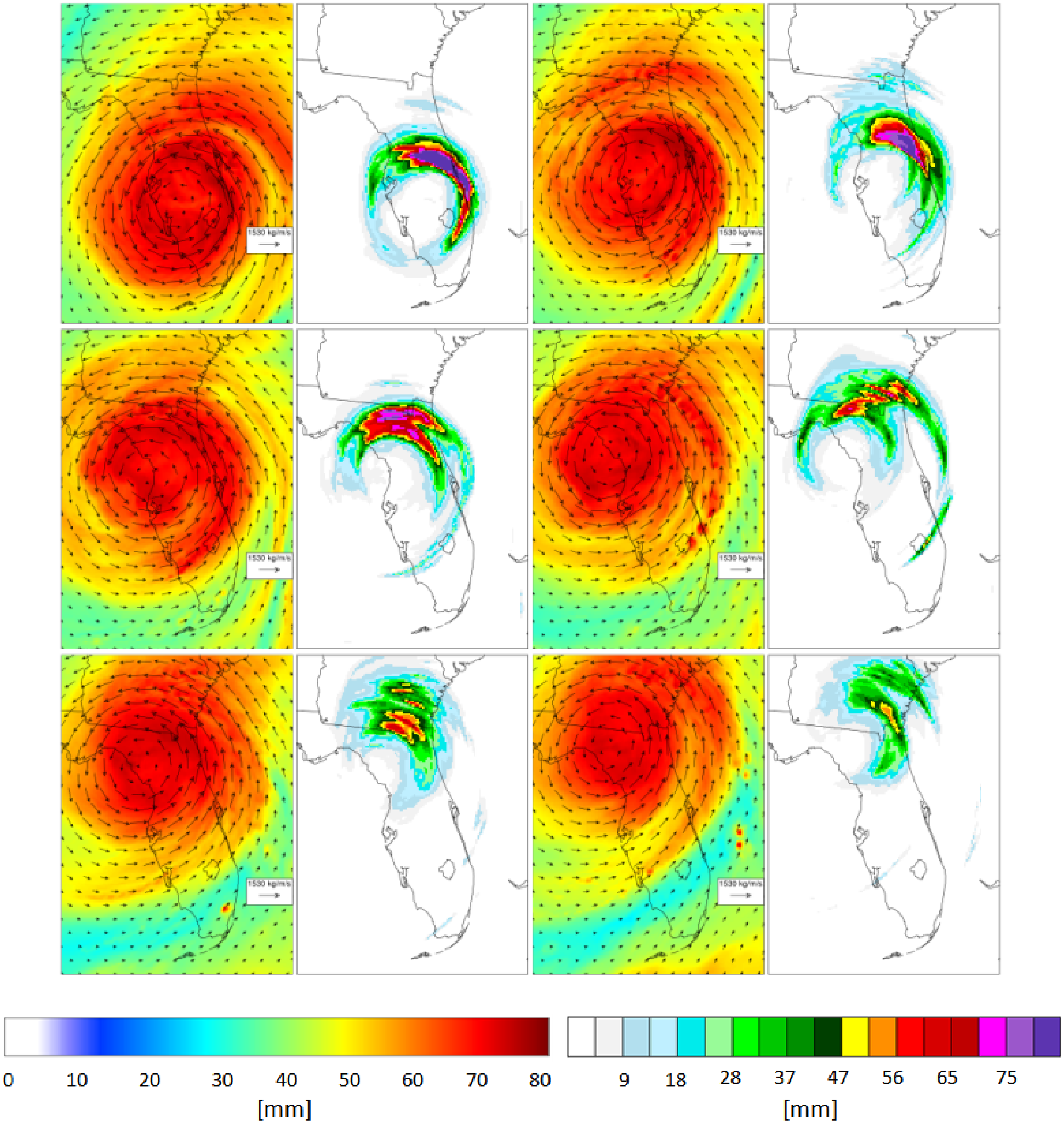

Figure B-19 6-Hourly Simulated Precipitable Water and Integrated Water Vapor Transport (Left) and its Corresponding 6-Hourly Accumulated Simulated Precipitation (Right) for Hurricane Jeanne

The sequence goes from 09/24 00h until 09/30 18h. The reference arrow in the white box (⟶) shows an IVT vector with a magnitude of 1530 kg m^{-1} s^{-1} (Continued).

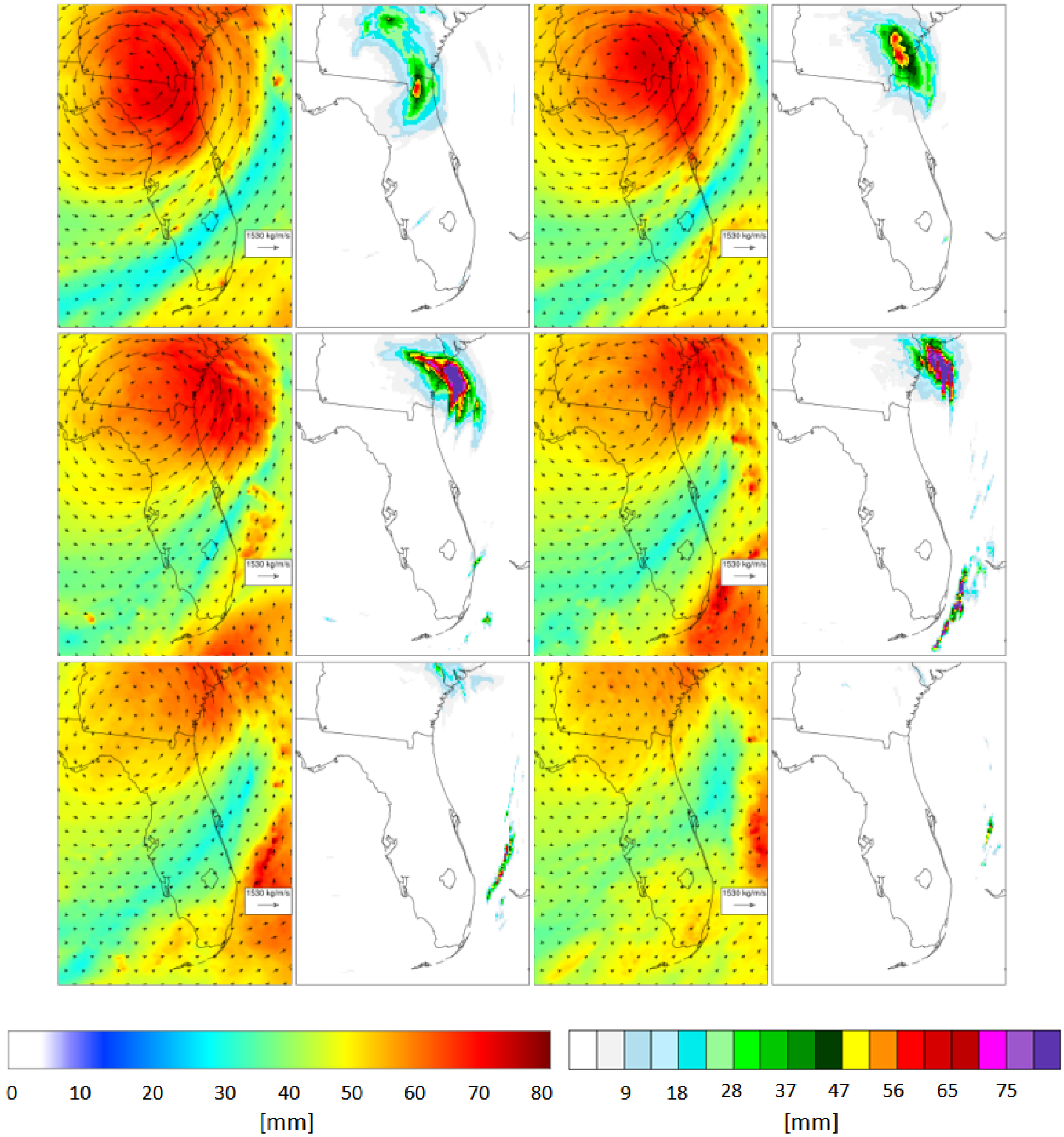

Figure B-19 6-Hourly Simulated Precipitable Water and Integrated Water Vapor Transport (Left) and its Corresponding 6-Hourly Accumulated Simulated Precipitation (Right) for Hurricane Jeanne

The sequence goes from 09/24 00h until 09/30 18h. The reference arrow in the white box (⟶) shows an IVT vector with a magnitude of 1530 kg m^{-1} s^{-1} (Continued).

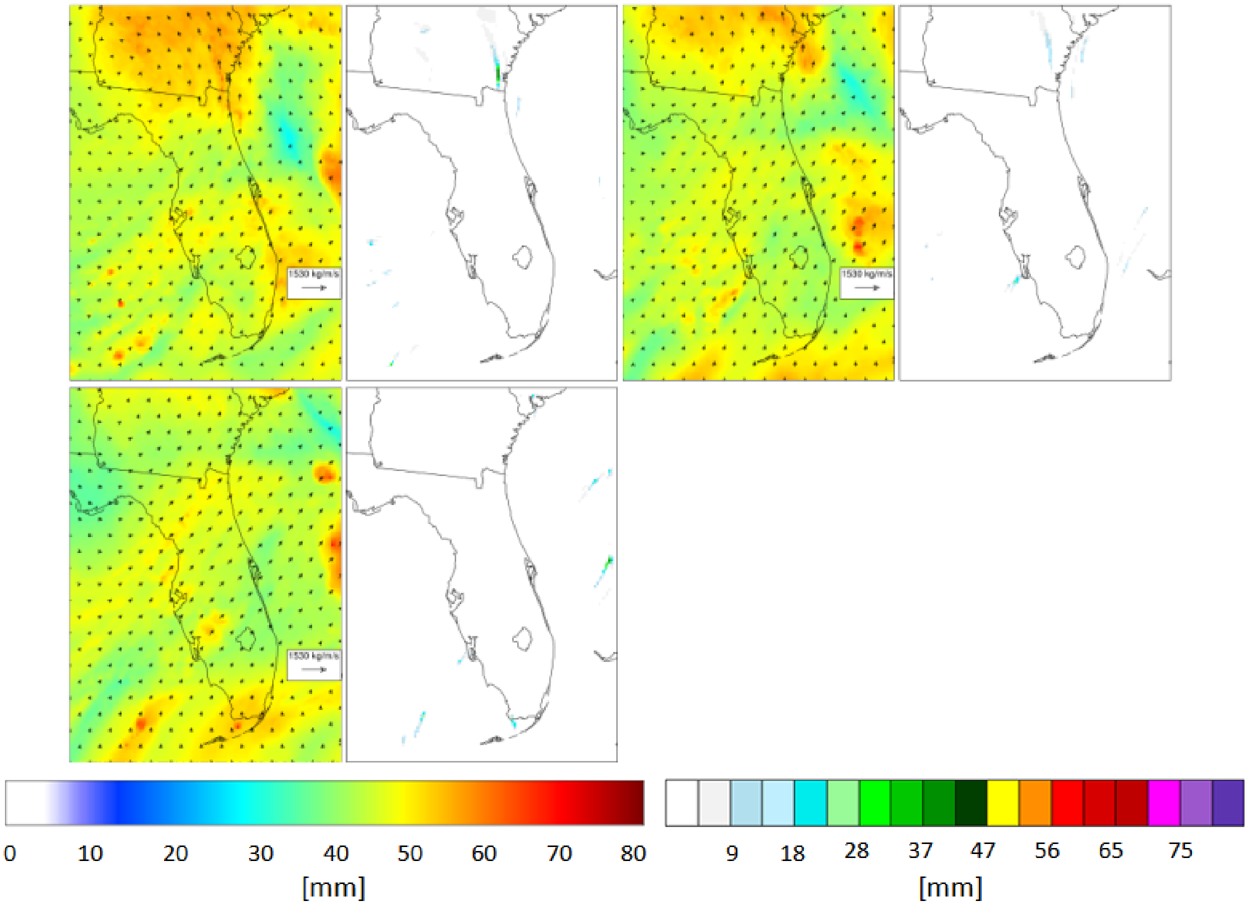

Figure B-19 6-Hourly Simulated Precipitable Water and Integrated Water Vapor Transport (Left) and its Corresponding 6-Hourly Accumulated Simulated Precipitation (Right) for Hurricane Jeanne

The sequence goes from 09/24 00h until 09/30 18h. The reference arrow in the white box (⟶) shows an IVT vector with a magnitude of 1530 kg m^{-1} s^{-1} (Continued).

B.2.6 Hurricane Ernesto (2006)

Figure B-20 shows the 6-hourly evolution of the reconstructed PW field and IVT field in Hurricane Ernesto. It also shows the 6-hourly accumulated precipitation field associated with the PW and IVT.

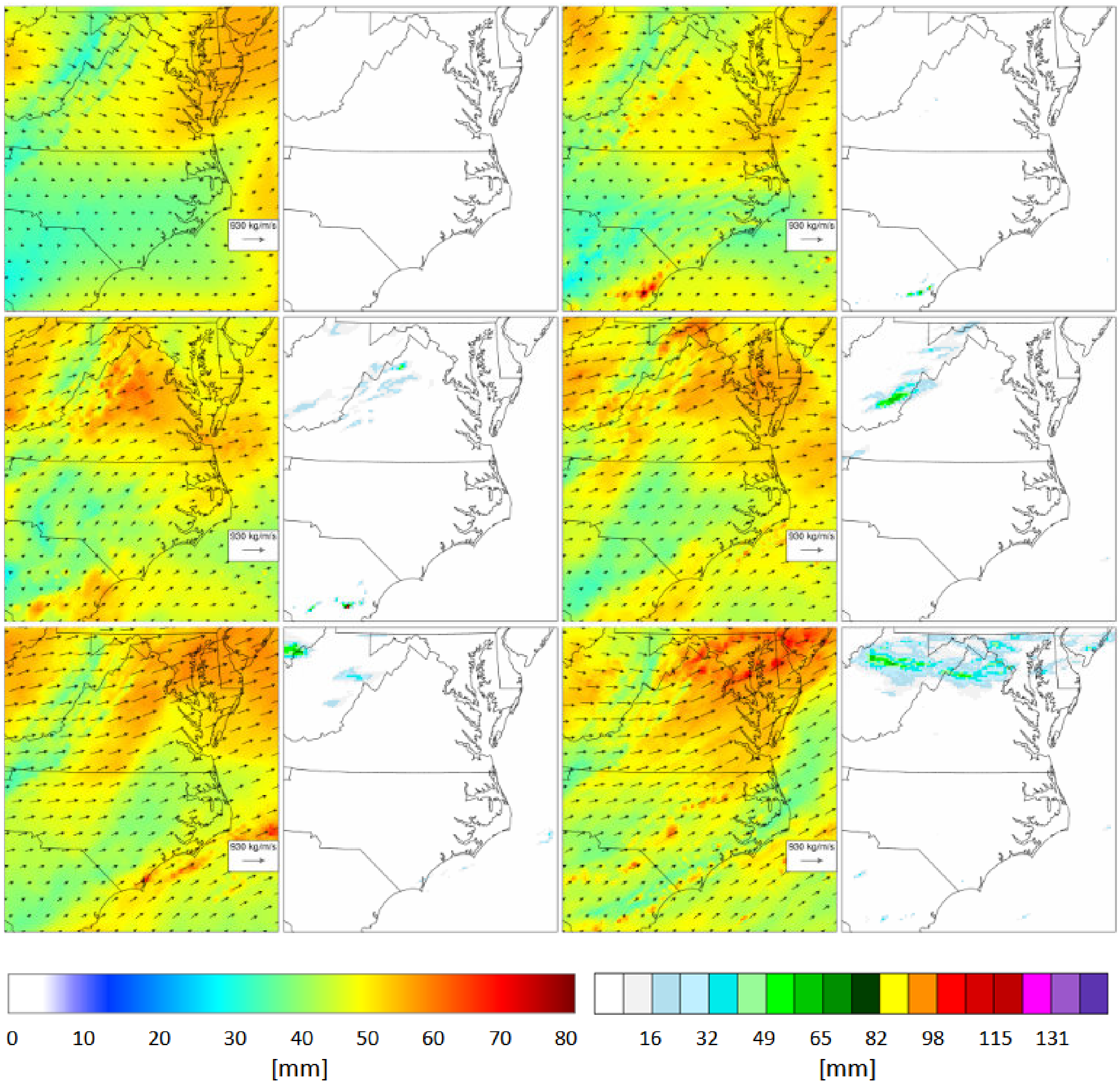

Figure B-20 6-Hourly Simulated Precipitable Water and Integrated Water Vapor Transport (Left) and its Corresponding 6-Hourly Accumulated Simulated Precipitation (Right) for Hurricane Ernesto

The sequence goes from 08/28 12h until 09/05 00h. The reference arrow in the white box (⟶) shows an IVT vector with a magnitude of 930 kg m^{-1} s^{-1}.

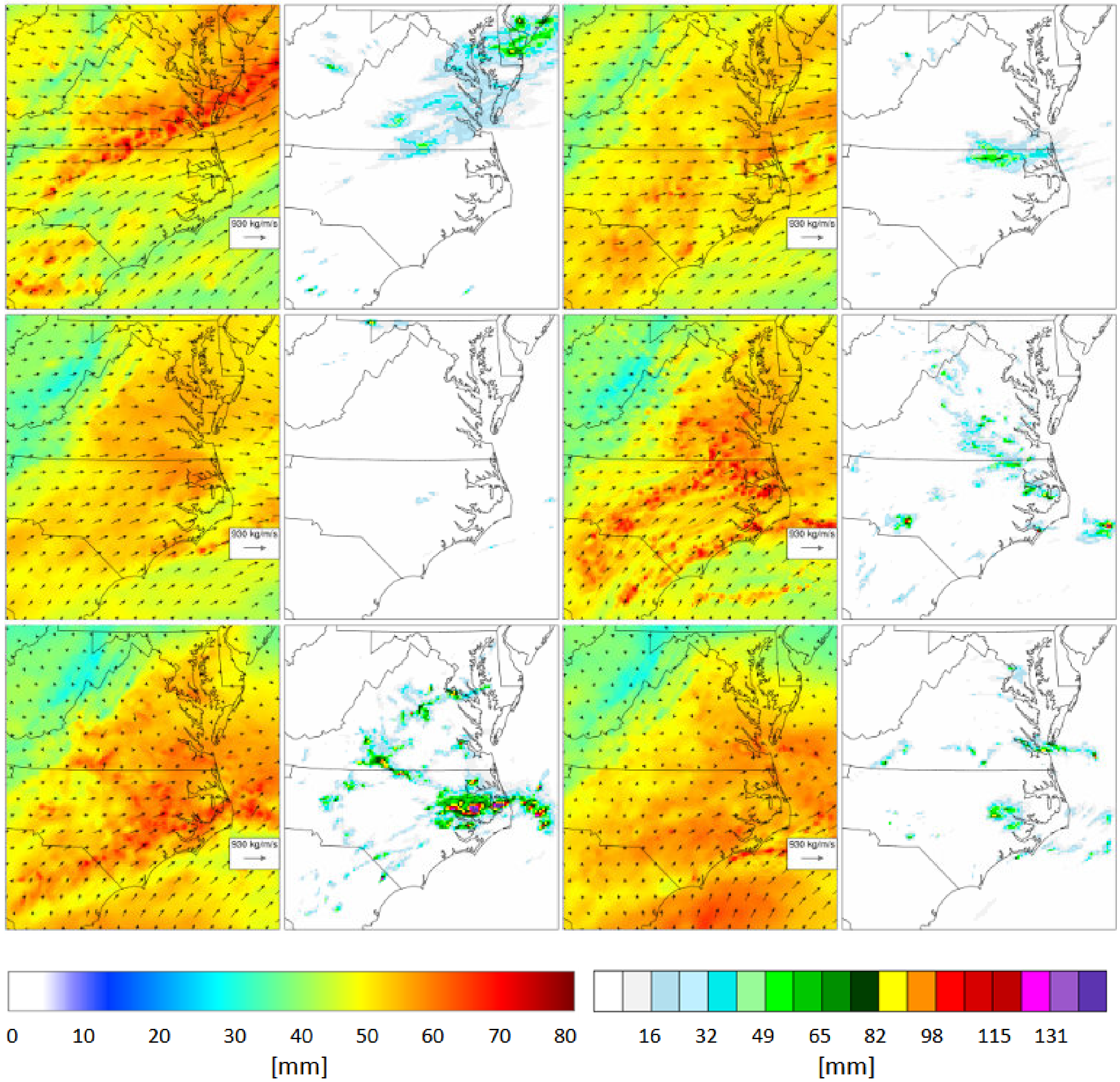

Figure B-20 6-Hourly Simulated Precipitable Water and Integrated Water Vapor Transport (Left) and its Corresponding 6-Hourly Accumulated Simulated Precipitation (Right) for Hurricane Ernesto

The sequence goes from 08/28 12h until 09/05 00h. The reference arrow in the white box (⟶) shows an IVT vector with a magnitude of 930 kg m^{-1} s^{-1} (Continued).

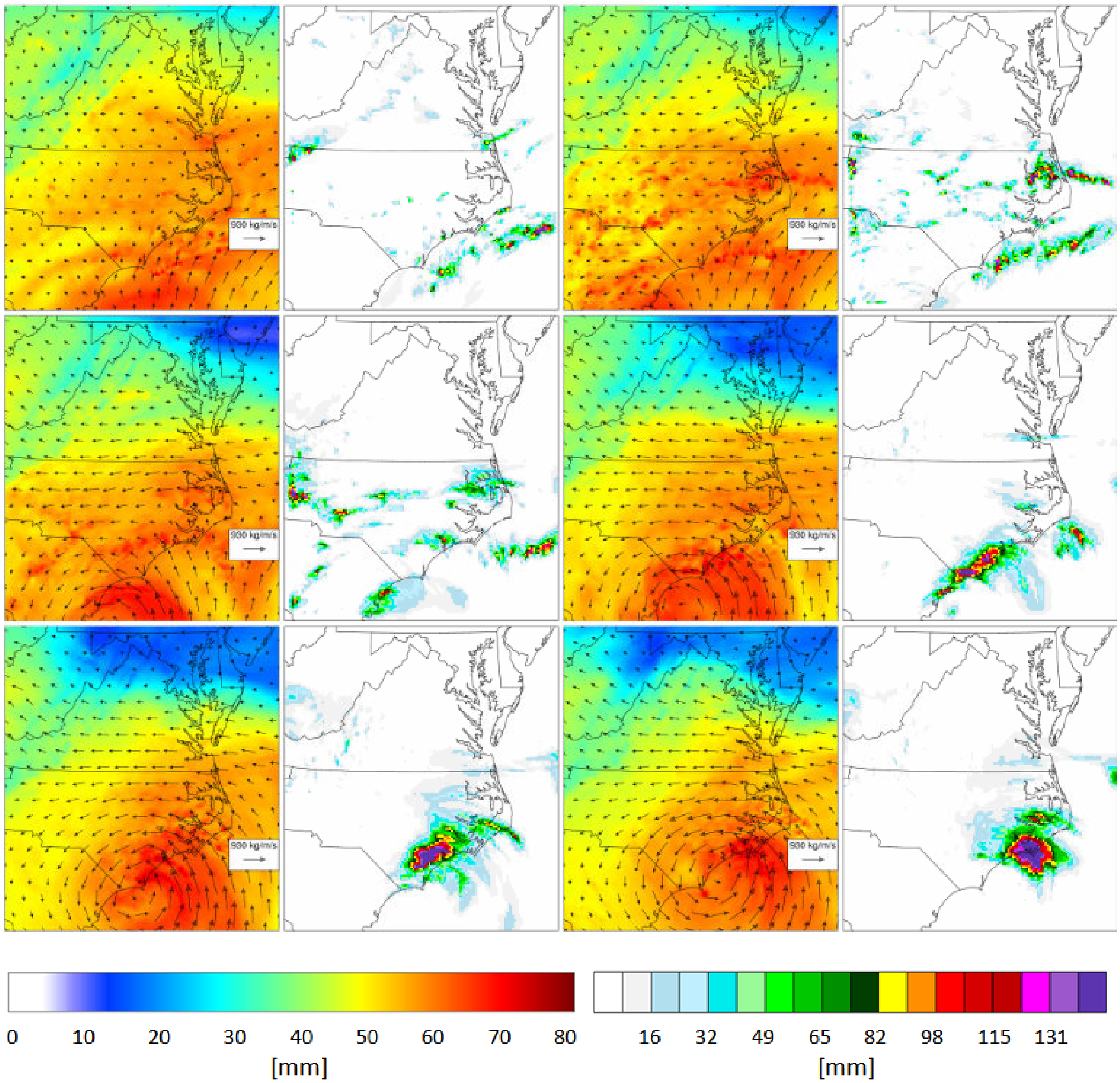

Figure B-20 6-Hourly Simulated Precipitable Water and Integrated Water Vapor Transport (Left) and its Corresponding 6-Hourly Accumulated Simulated Precipitation (Right) for Hurricane Ernesto

The sequence goes from 08/28 12h until 09/05 00h. The reference arrow in the white box (⟶) shows an IVT vector with a magnitude of 930 kg m^{-1} s^{-1} (Continued).

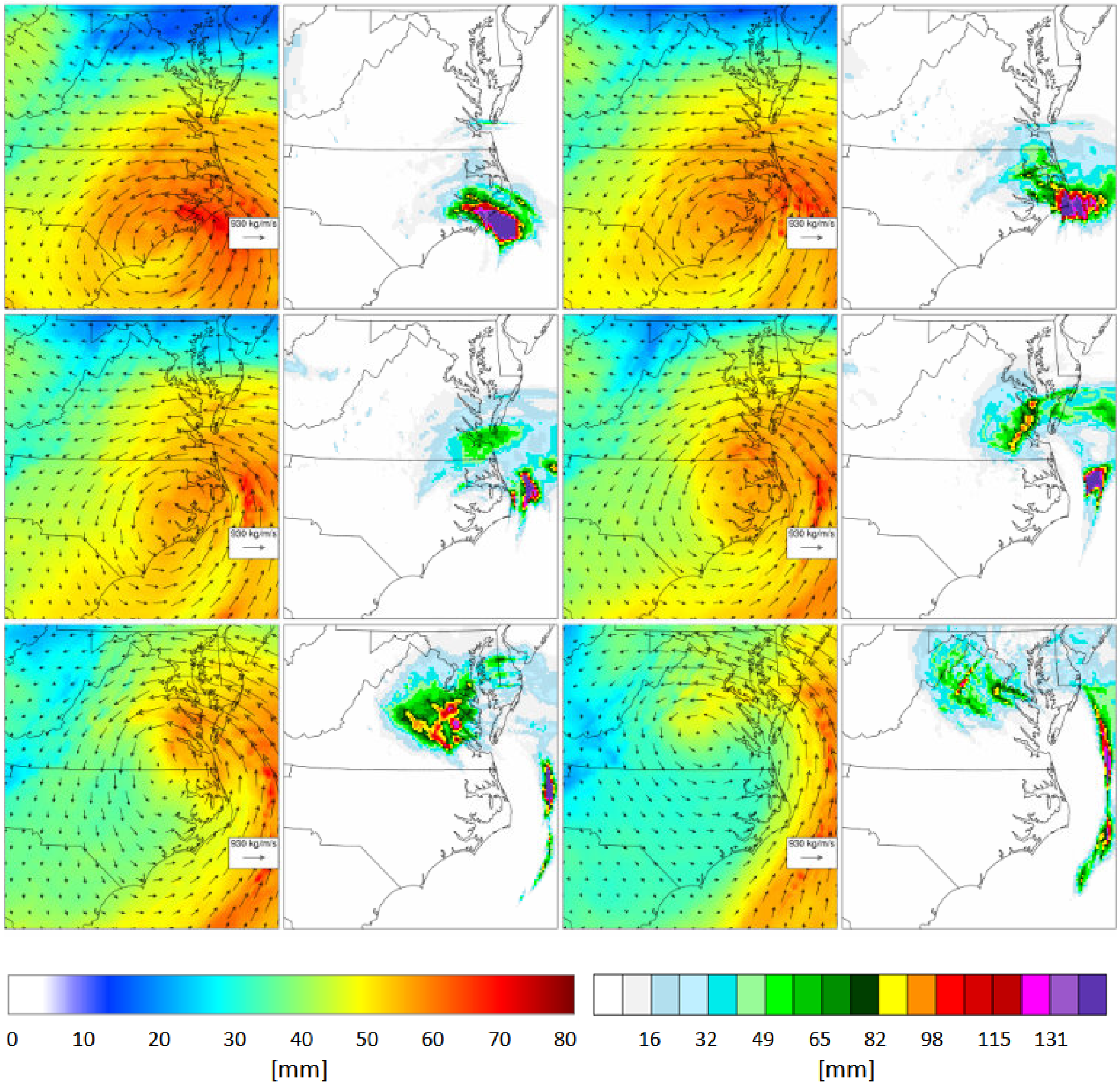

Figure B-20 6-Hourly Simulated Precipitable Water and Integrated Water Vapor Transport (Left) and its Corresponding 6-Hourly Accumulated Simulated Precipitation (Right) for Hurricane Ernesto

The sequence goes from 08/28 12h until 09/05 00h. The reference arrow in the white box (⟶) shows an IVT vector with a magnitude of 930 kg m^{-1} s^{-1} (Continued).

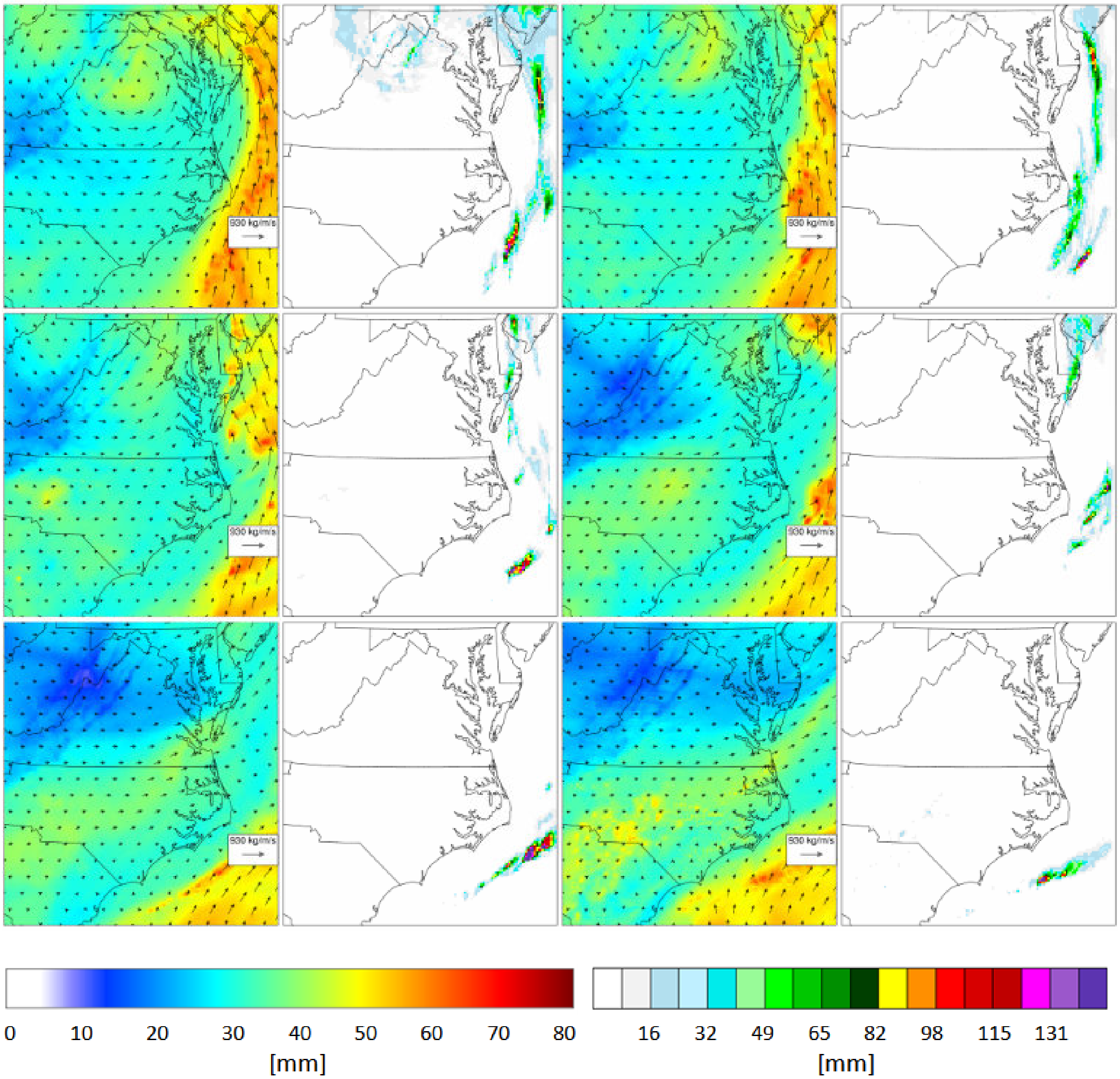

Figure B-20 6-Hourly Simulated Precipitable Water and Integrated Water Vapor Transport (Left) and its Corresponding 6-Hourly Accumulated Simulated Precipitation (Right) for Hurricane Ernesto

The sequence goes from 08/28 12h until 09/05 00h. The reference arrow in the white box (⟶) shows an IVT vector with a magnitude of 930 kg m^{-1} s^{-1} (Continued).

B.2.7 Tropical Storm Fay (2008)

Figure B-21 shows the 6-hourly evolution of the reconstructed PW field and IVT field in TS Fay. It also shows the 6-hourly accumulated precipitation field associated with the PW and IVT.

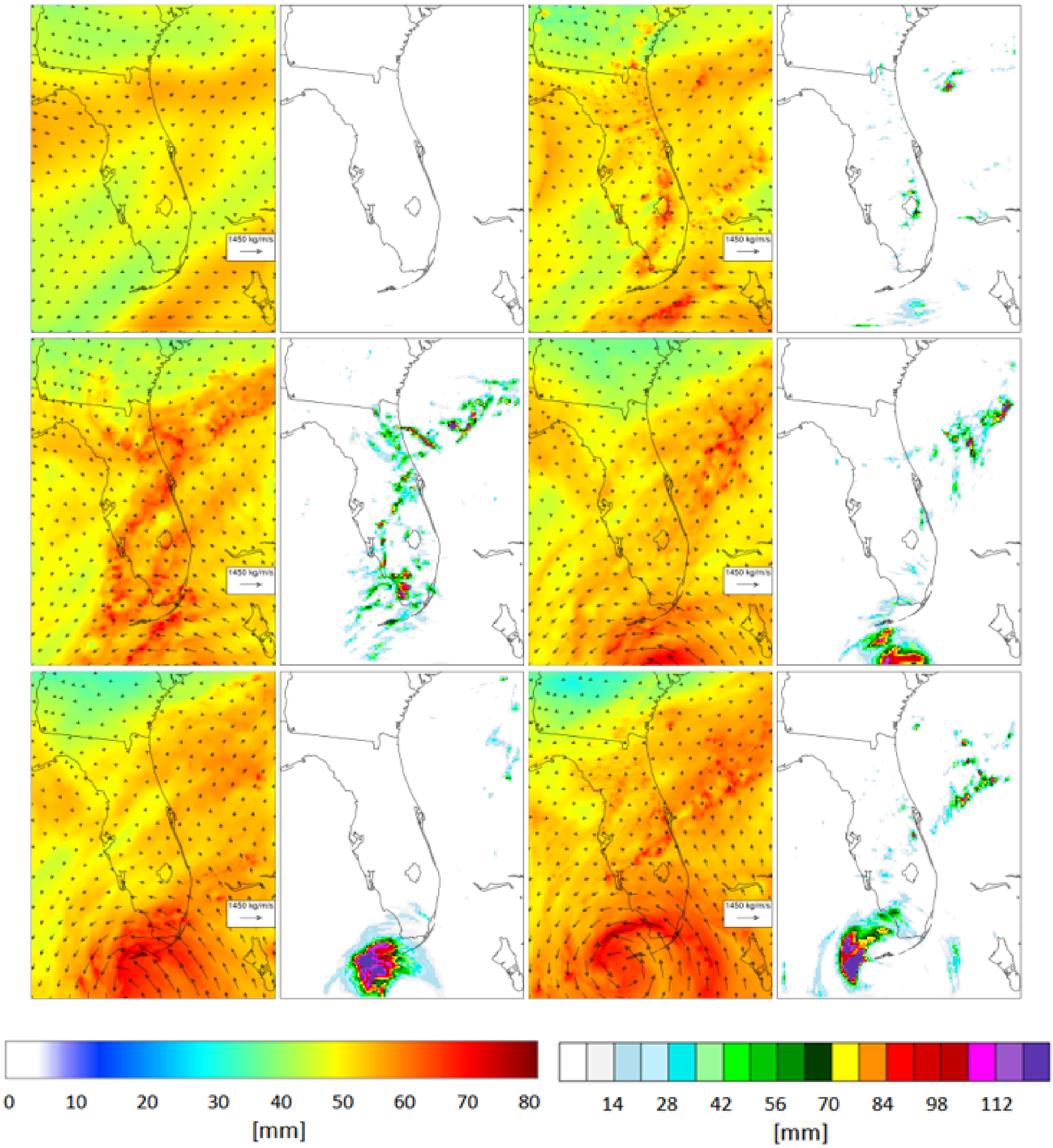

Figure B-21 6-Hourly Simulated Precipitable Water and Integrated Water Vapor Transport (Left) and its Corresponding 6-Hourly Accumulated Simulated Precipitation (Right) for TS Fay

The sequence goes from 08/17 18h until 08/26 00h. The reference arrow in the white box (⟶) shows an IVT vector with a magnitude of 1450 kg m^{-1} s^{-1}.

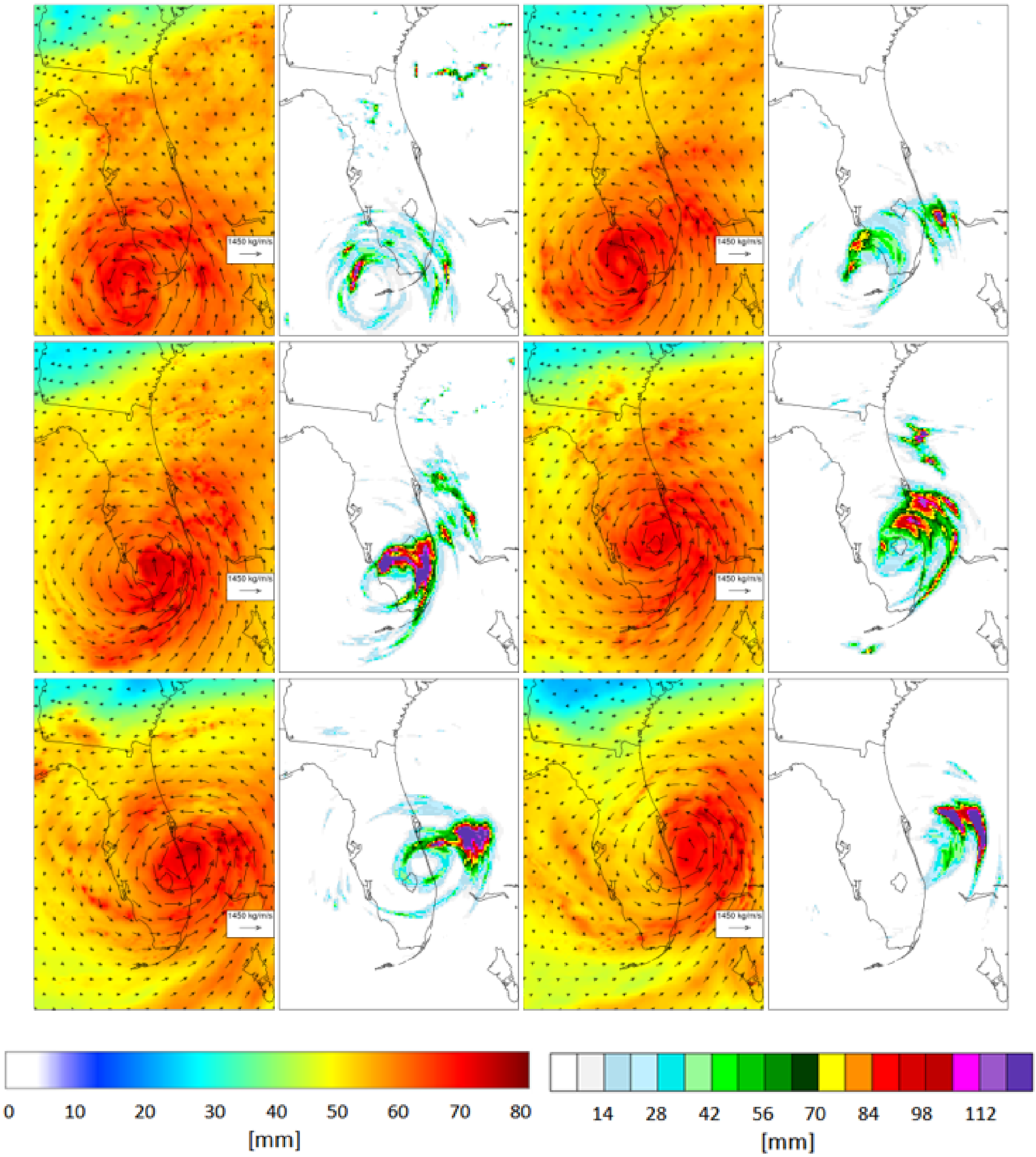

Figure B-21 6-Hourly Simulated Precipitable Water and Integrated Water Vapor Transport (Left) and its Corresponding 6-Hourly Accumulated Simulated Precipitation (Right) for TS Fay

The sequence goes from 08/17 18h until 08/26 00h. The reference arrow in the white box (⟶) shows an IVT vector with a magnitude of 1450 kg m^{-1} s^{-1} (Continued).

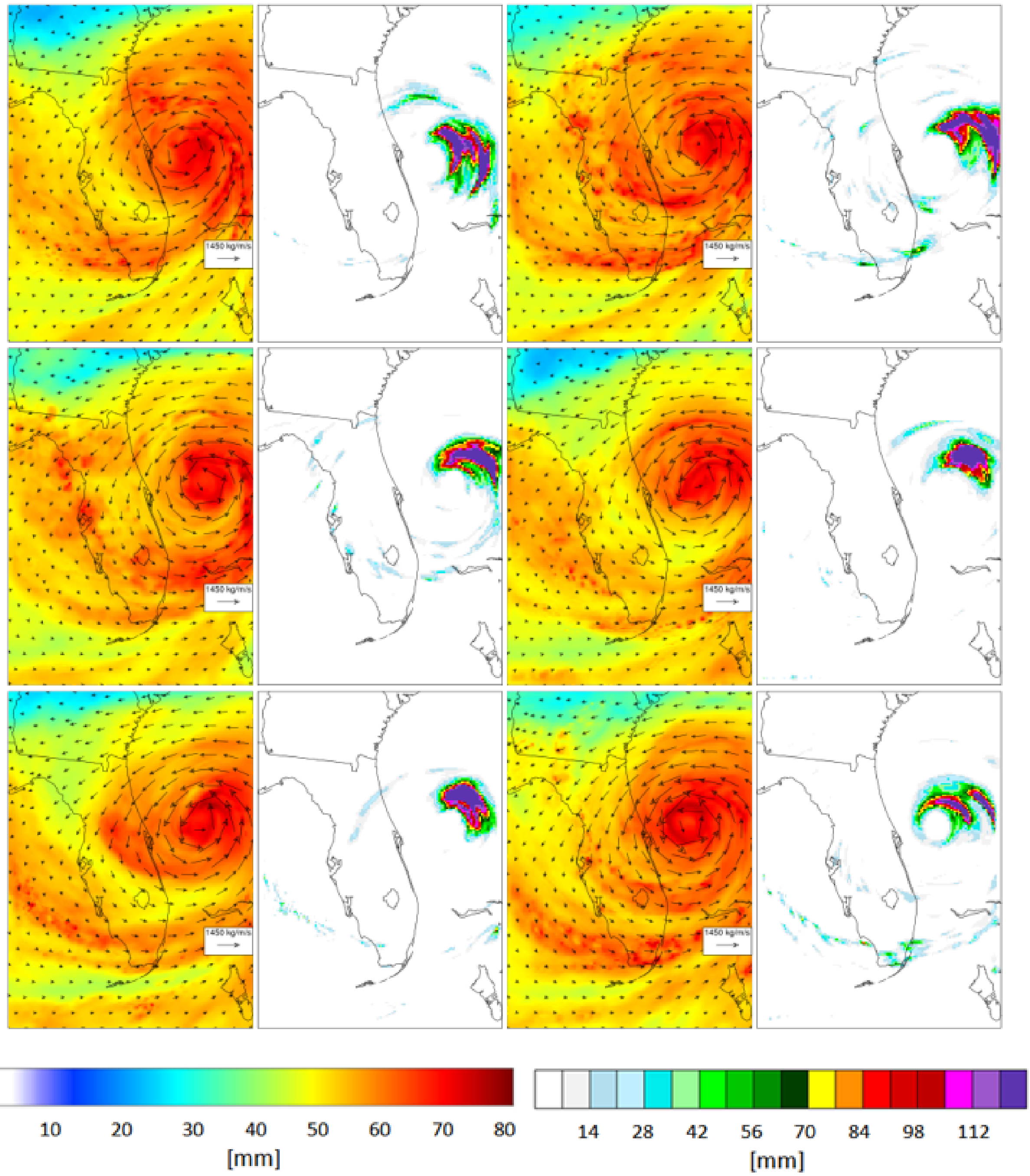

Figure B-21 6-Hourly Simulated Precipitable Water and Integrated Water Vapor Transport (Left) and its Corresponding 6-Hourly Accumulated Simulated Precipitation (Right) for TS Fay

The sequence goes from 08/17 18h until 08/26 00h. The reference arrow in the white box (⟶) shows an IVT vector with a magnitude of 1450 kg m^{-1} s^{-1} (Continued).

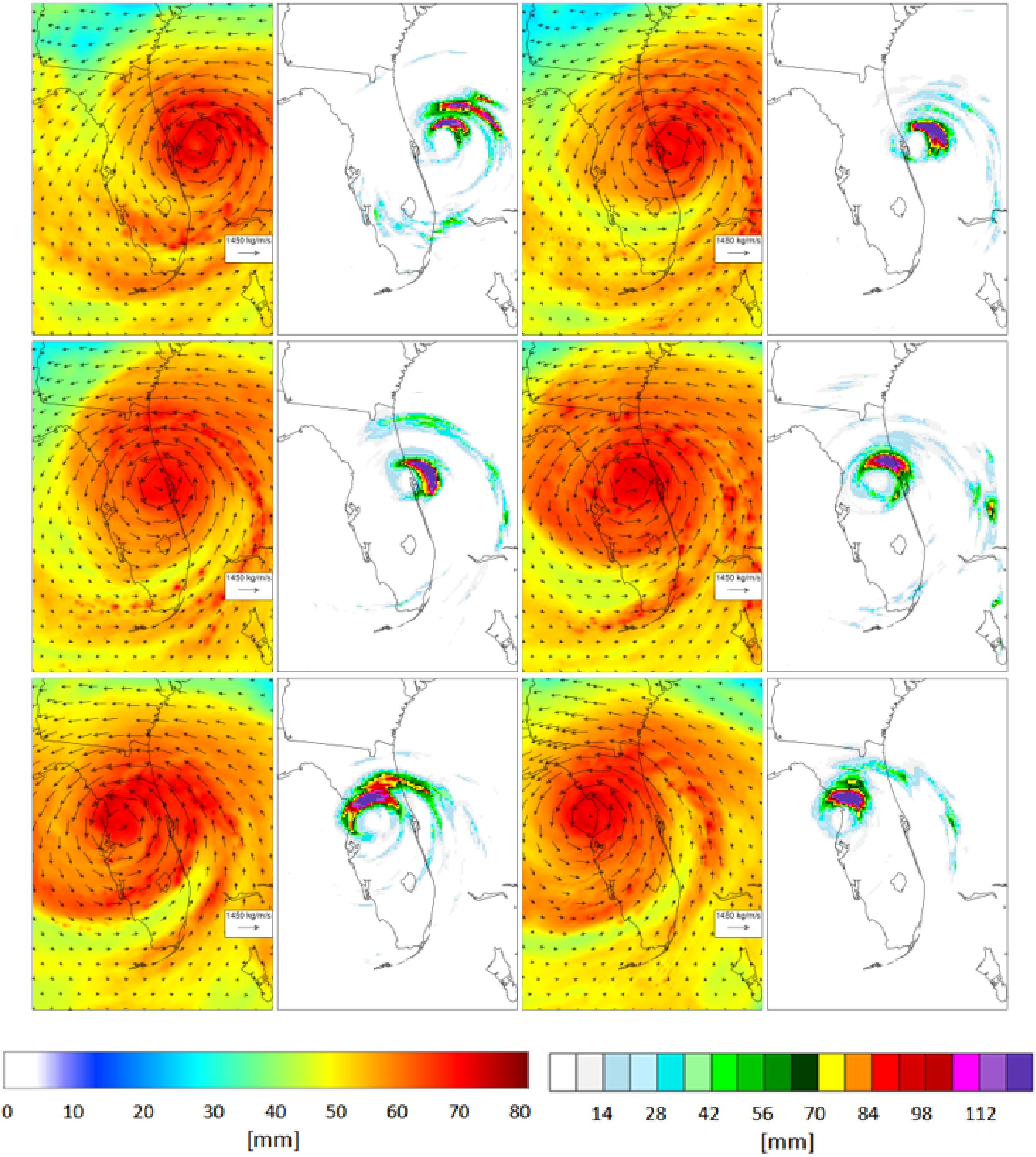

Figure B-21 6-Hourly Simulated Precipitable Water and Integrated Water Vapor Transport (Left) and its Corresponding 6-Hourly Accumulated Simulated Precipitation (Right) for TS Fay

The sequence goes from 08/17 18h until 08/26 00h. The reference arrow in the white box (⟶) shows an IVT vector with a magnitude of 1450 kg m^{-1} s^{-1} (Continued).

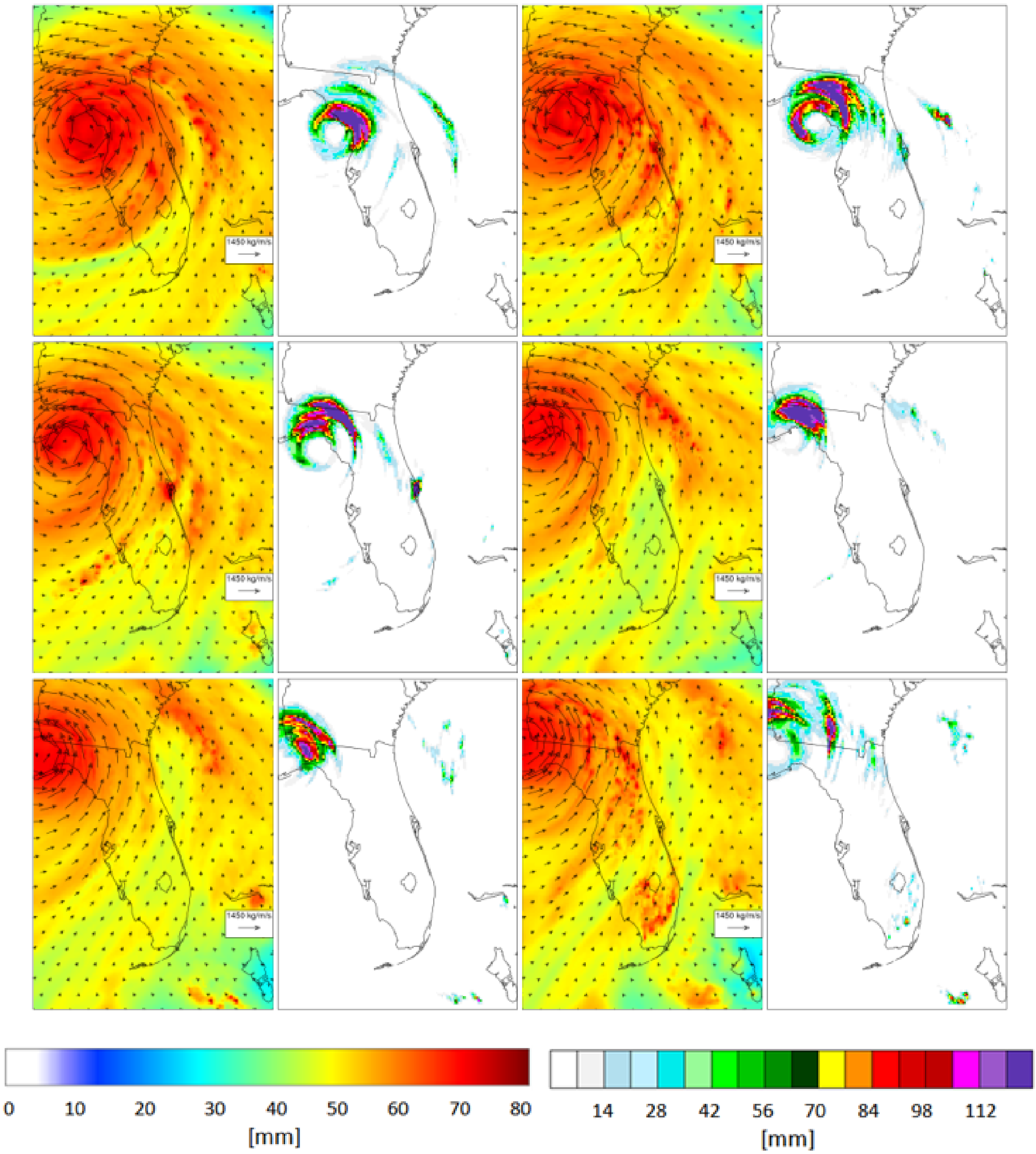

Figure B-21 6-Hourly Simulated Precipitable Water and Integrated Water Vapor Transport (Left) and its Corresponding 6-Hourly Accumulated Simulated Precipitation (Right) for TS Fay

The sequence goes from 08/17 18h until 08/26 00h. The reference arrow in the white box (⟶) shows an IVT vector with a magnitude of 1450 kg m^{-1} s^{-1} (Continued).

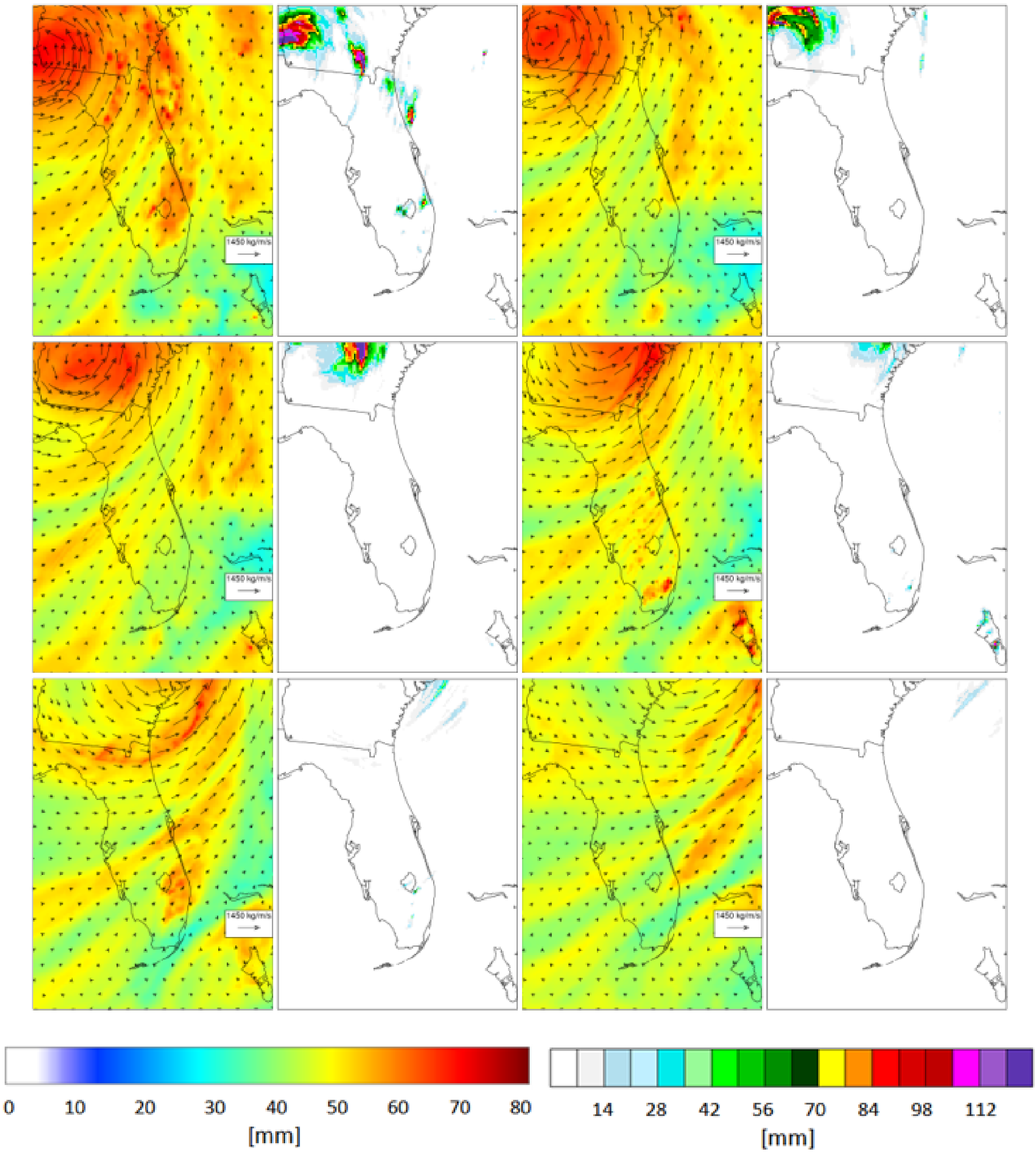

Figure B-21 6-Hourly Simulated Precipitable Water and Integrated Water Vapor Transport (Left) and its Corresponding 6-Hourly Accumulated Simulated Precipitation (Right) for TS Fay

The sequence goes from 08/17 18h until 08/26 00h. The reference arrow in the white box (⟶) shows an IVT vector with a magnitude of 1450 kg m^{-1} s^{-1} (Continued).

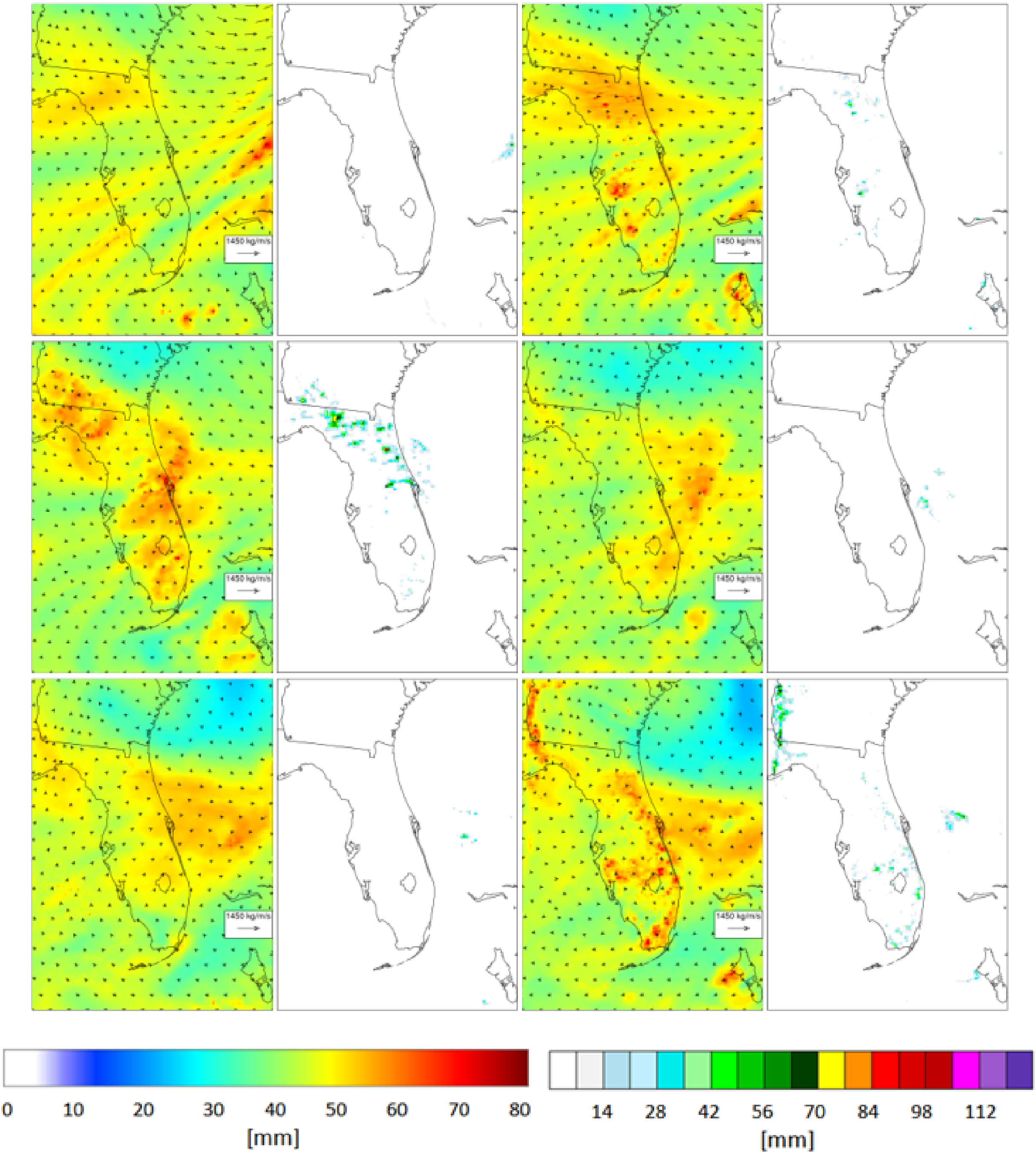

Figure B-21 6-Hourly Simulated Precipitable Water and Integrated Water Vapor Transport (Left) and its Corresponding 6-Hourly Accumulated Simulated Precipitation (Right) for TS Fay

The sequence goes from 08/17 18h until 08/26 00h. The reference arrow in the white box (⟶) shows an IVT vector with a magnitude of 1450 kg m^{-1} s^{-1} (Continued).

B.2.8 Hurricane Gustav (2008)

Figure B-22 shows the 6-hourly evolution of the reconstructed PW field and IVT field in Hurricane Gustav. It also shows the 6-hourly accumulated precipitation field associated with the PW and IVT.

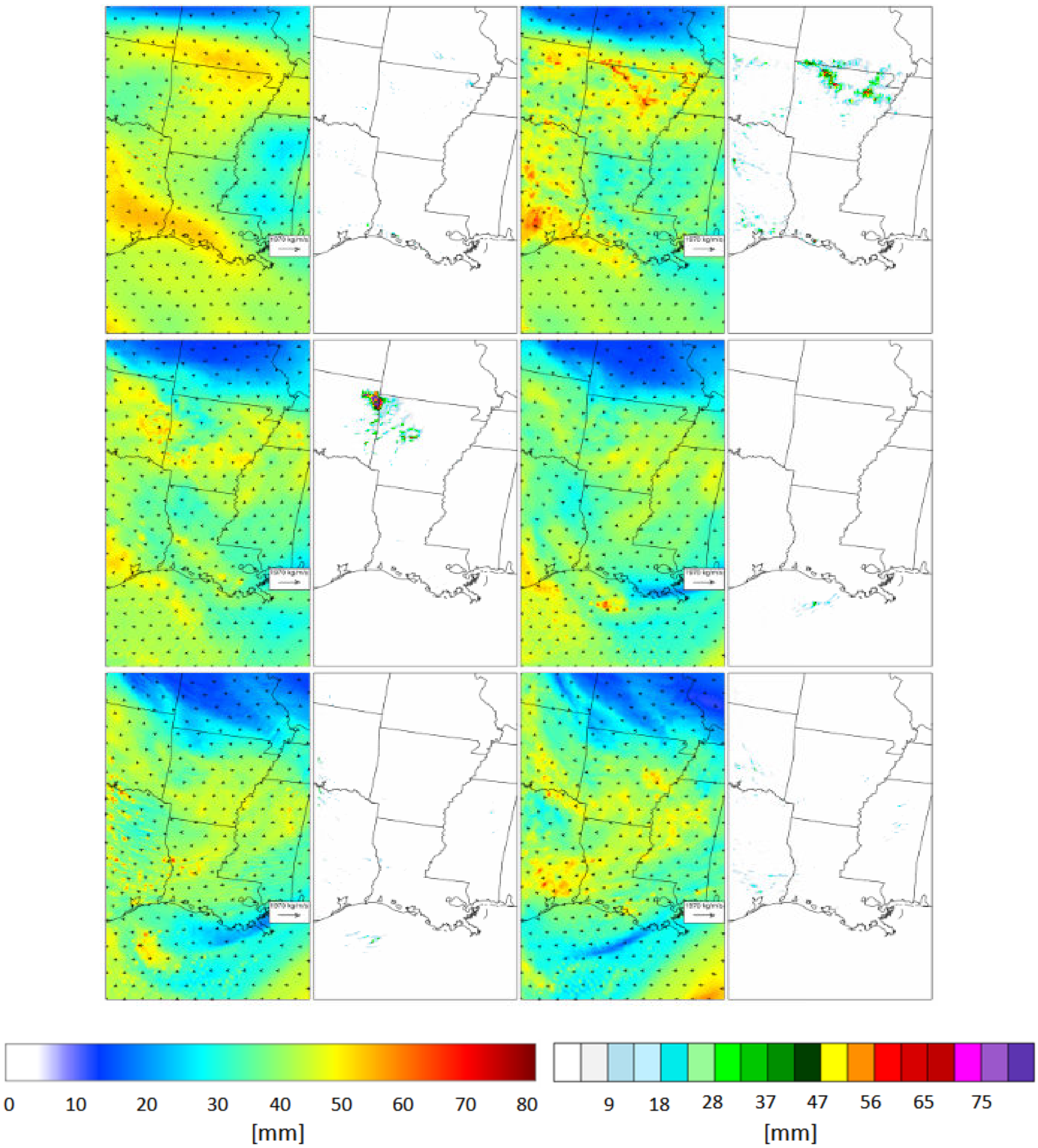

Figure B-22 6-Hourly Simulated Precipitable Water and Integrated Water Vapor Transport (Left) and its Corresponding 6-Hourly Accumulated Simulated Precipitation (Right) for Hurricane Gustav

The sequence goes from 08/29 18h until 09/05 12h. The reference arrow in the white box (⟶) shows an IVT vector with a magnitude of 1970 kg m^{-1} s^{-1}.

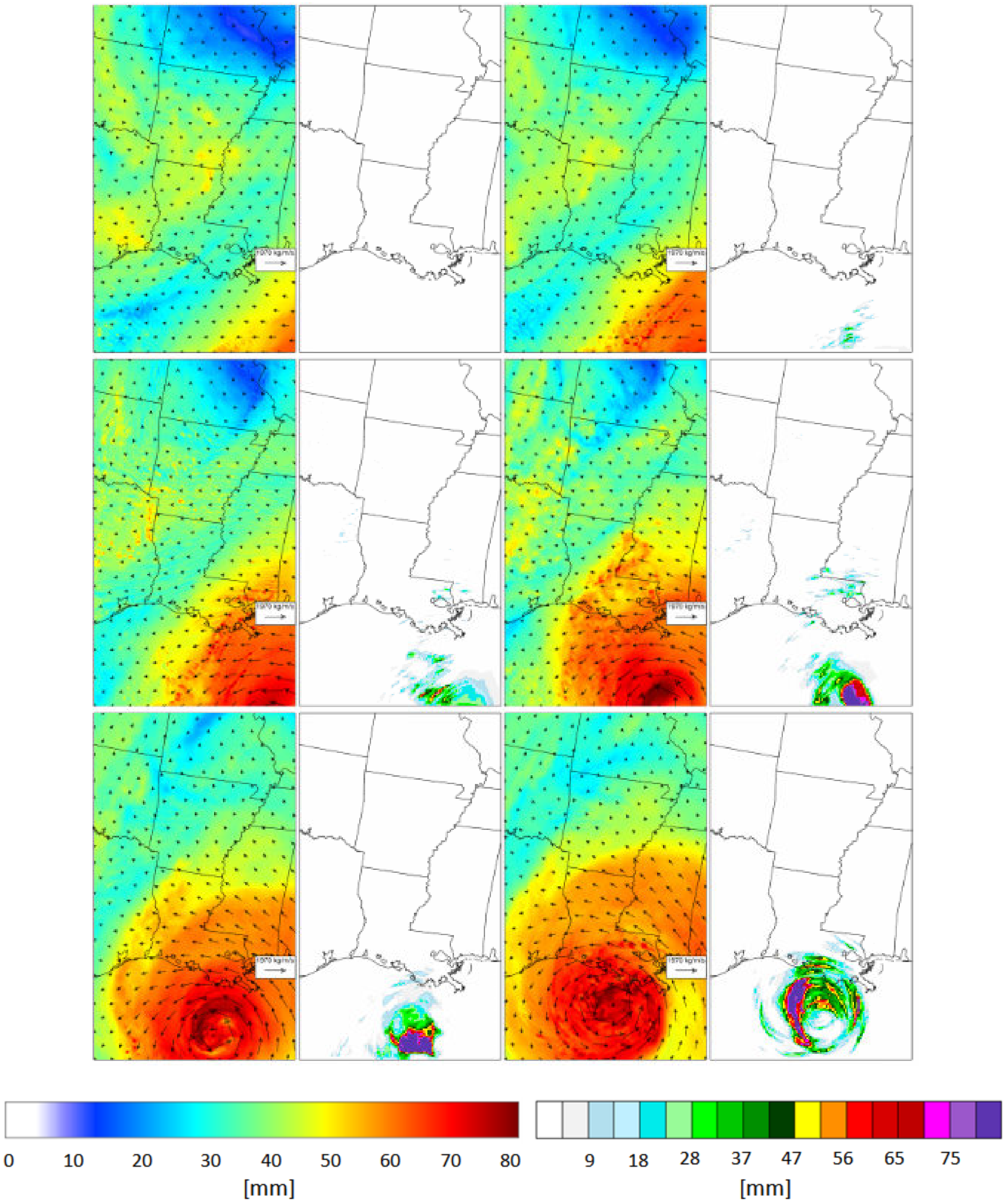

Figure B-22 6-Hourly Simulated Precipitable Water and Integrated Water Vapor Transport (Left) and its Corresponding 6-Hourly Accumulated Simulated Precipitation (Right) for Hurricane Gustav

The sequence goes from 08/29 18h until 09/05 12h. The reference arrow in the white box (⟶) shows an IVT vector with a magnitude of 1970 kg m^{-1} s^{-1} (Continued).

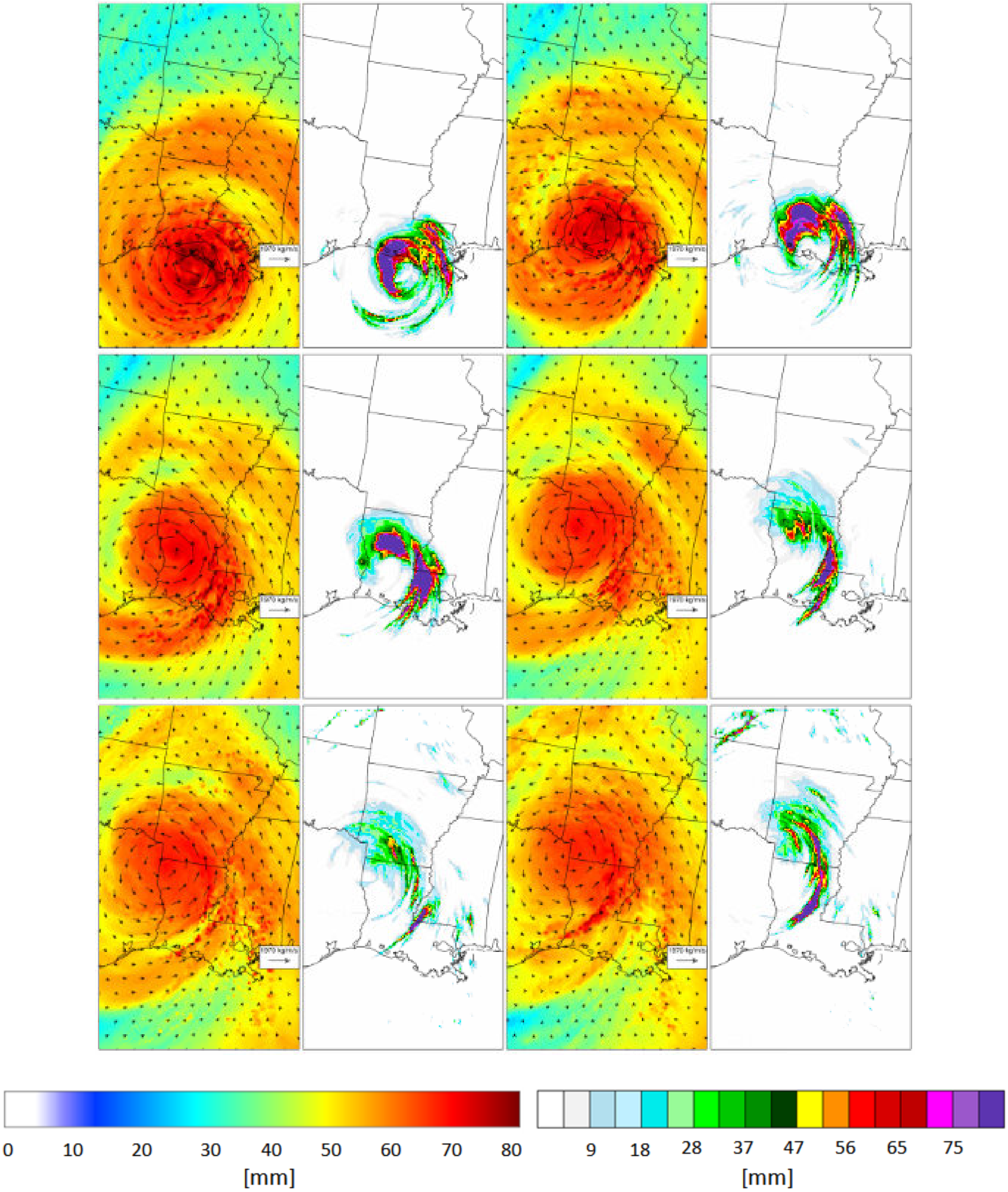

Figure B-22 6-Hourly Simulated Precipitable Water and Integrated Water Vapor Transport (Left) and its Corresponding 6-Hourly Accumulated Simulated Precipitation (Right) for Hurricane Gustav

The sequence goes from 08/29 18h until 09/05 12h. The reference arrow in the white box (⟶) shows an IVT vector with a magnitude of 1970 kg m^{-1} s^{-1} (Continued).

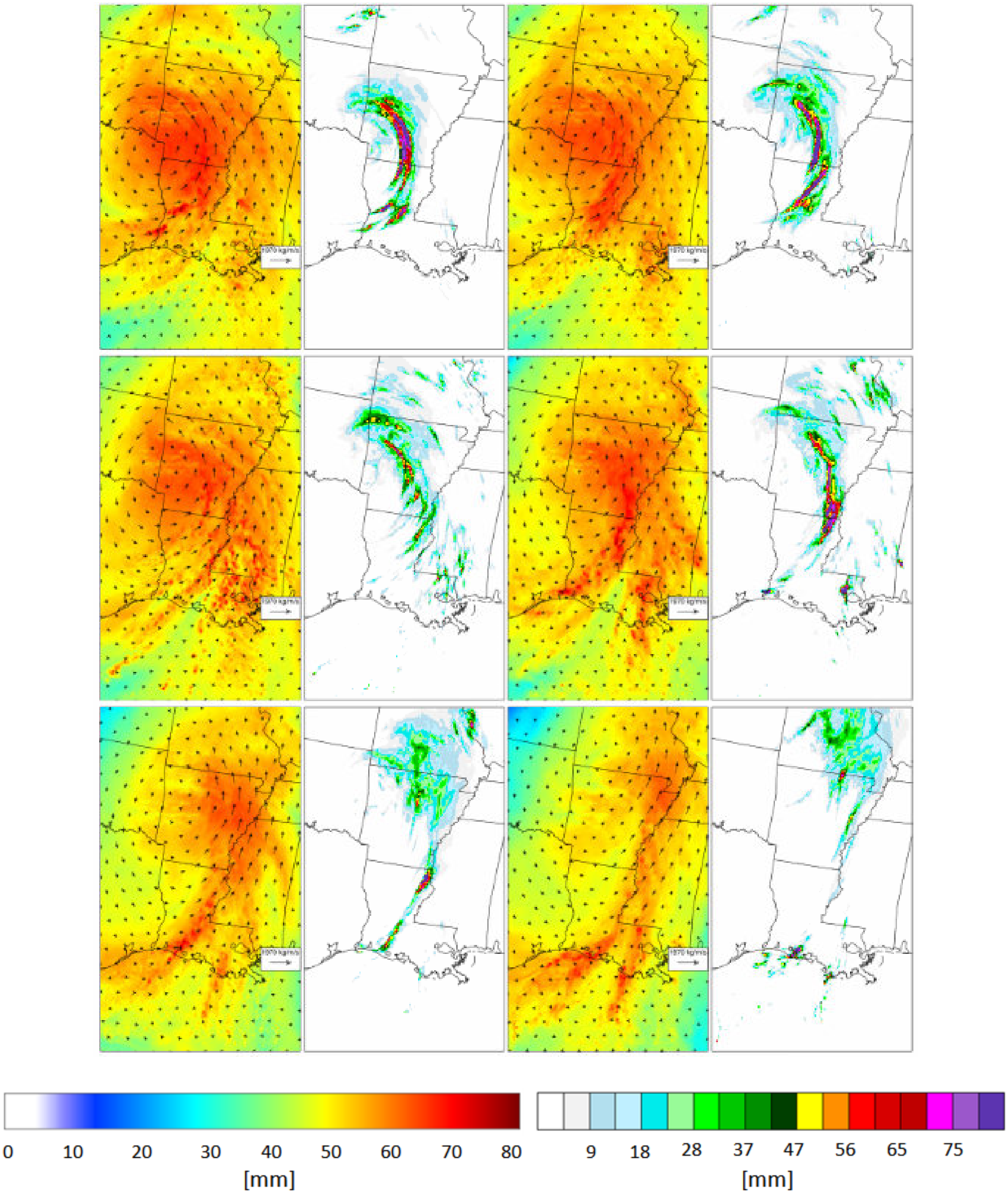

Figure B-22 6-Hourly Simulated Precipitable Water and Integrated Water Vapor Transport (Left) and its Corresponding 6-Hourly Accumulated Simulated Precipitation (Right) for Hurricane Gustav

The sequence goes from 08/29 18h until 09/05 12h. The reference arrow in the white box (⟶) shows an IVT vector with a magnitude of 1970 kg m^{-1} s^{-1} (Continued).

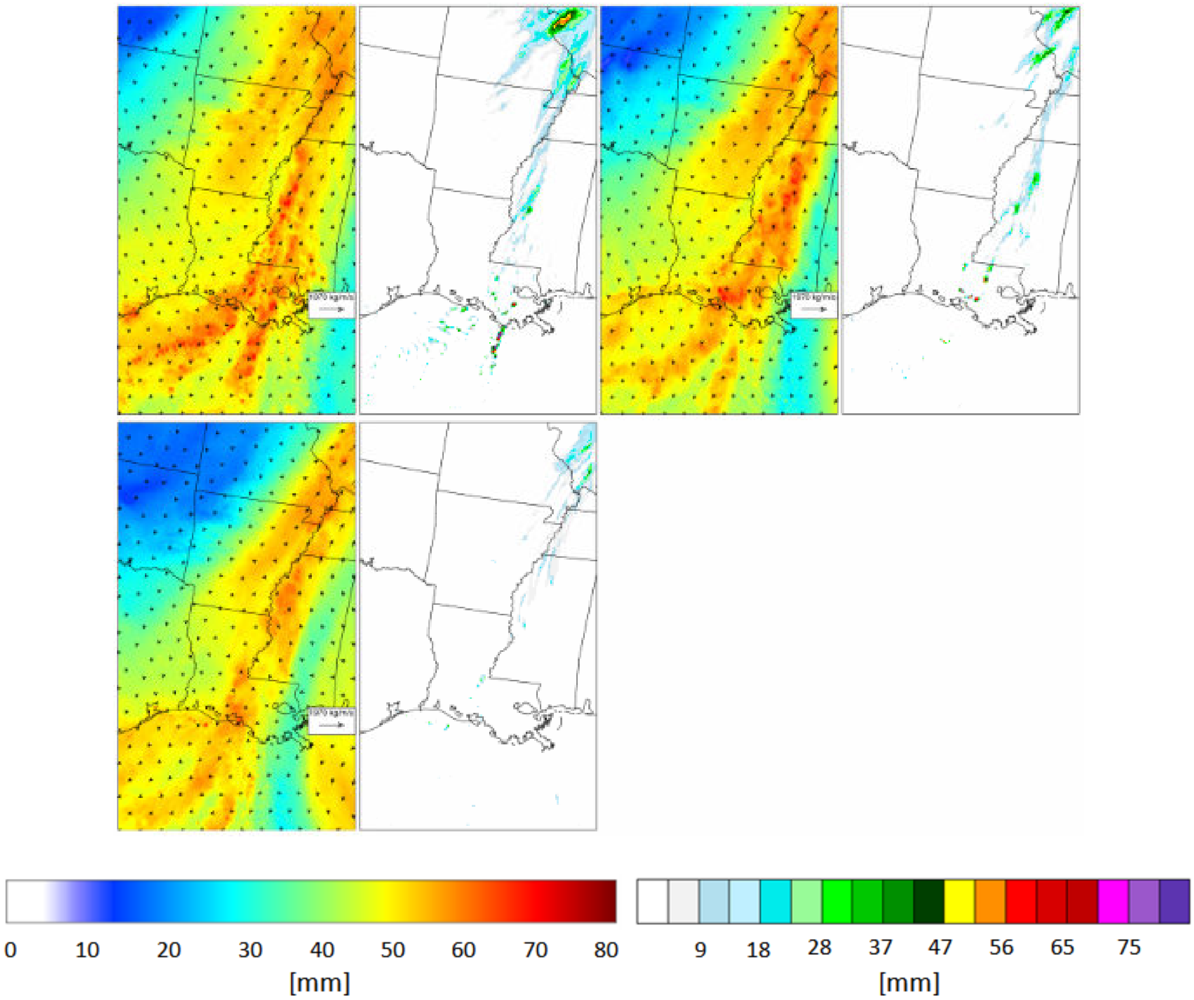

Figure B-22 6-Hourly Simulated Precipitable Water and Integrated Water Vapor Transport (Left) and its Corresponding 6-Hourly Accumulated Simulated Precipitation (Right) for Hurricane Gustav

The sequence goes from 08/29 18h until 09/05 12h. The reference arrow in the white box (⟶) shows an IVT vector with a magnitude of 1970 kg m^{-1} s^{-1} (Continued).

B.2.9 Hurricane Irene (2011)

Figure B-23 shows the 6-hourly evolution of the reconstructed PW field and IVT field in Hurricane Irene. It also shows the 6-hourly accumulated precipitation field associated with the PW and IVT.

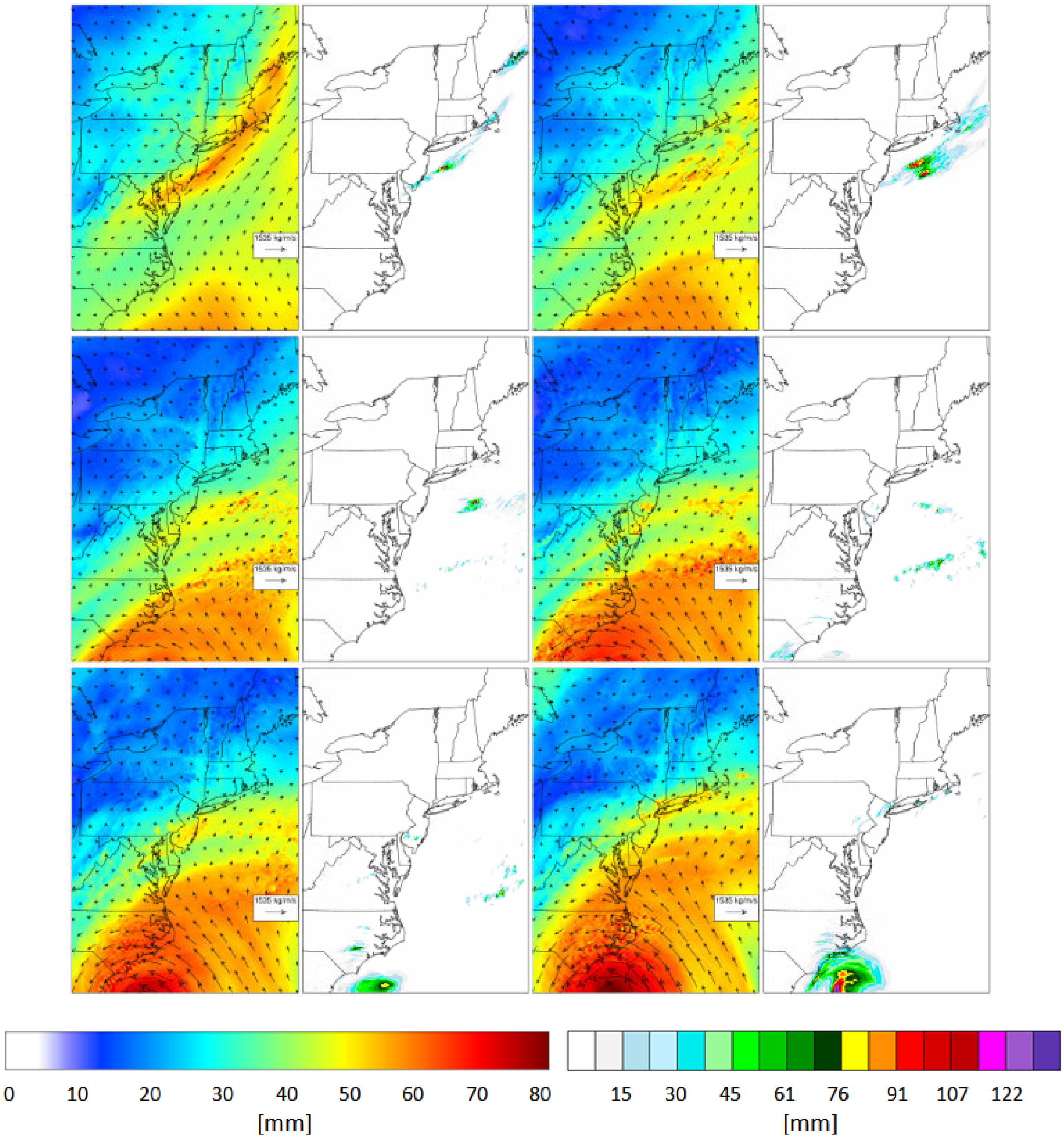

Figure B-23 6-Hourly Simulated Precipitable Water and Integrated Water Vapor Transport (Left) and its Corresponding 6-Hourly Accumulated Simulated Precipitation (Right) for Hurricane Irene

The sequence goes from 08/26 00h until 08/30 12h. The reference arrow in the white box (⟶) shows an IVT vector with a magnitude of 1535 kg m^{-1} s^{-1}.

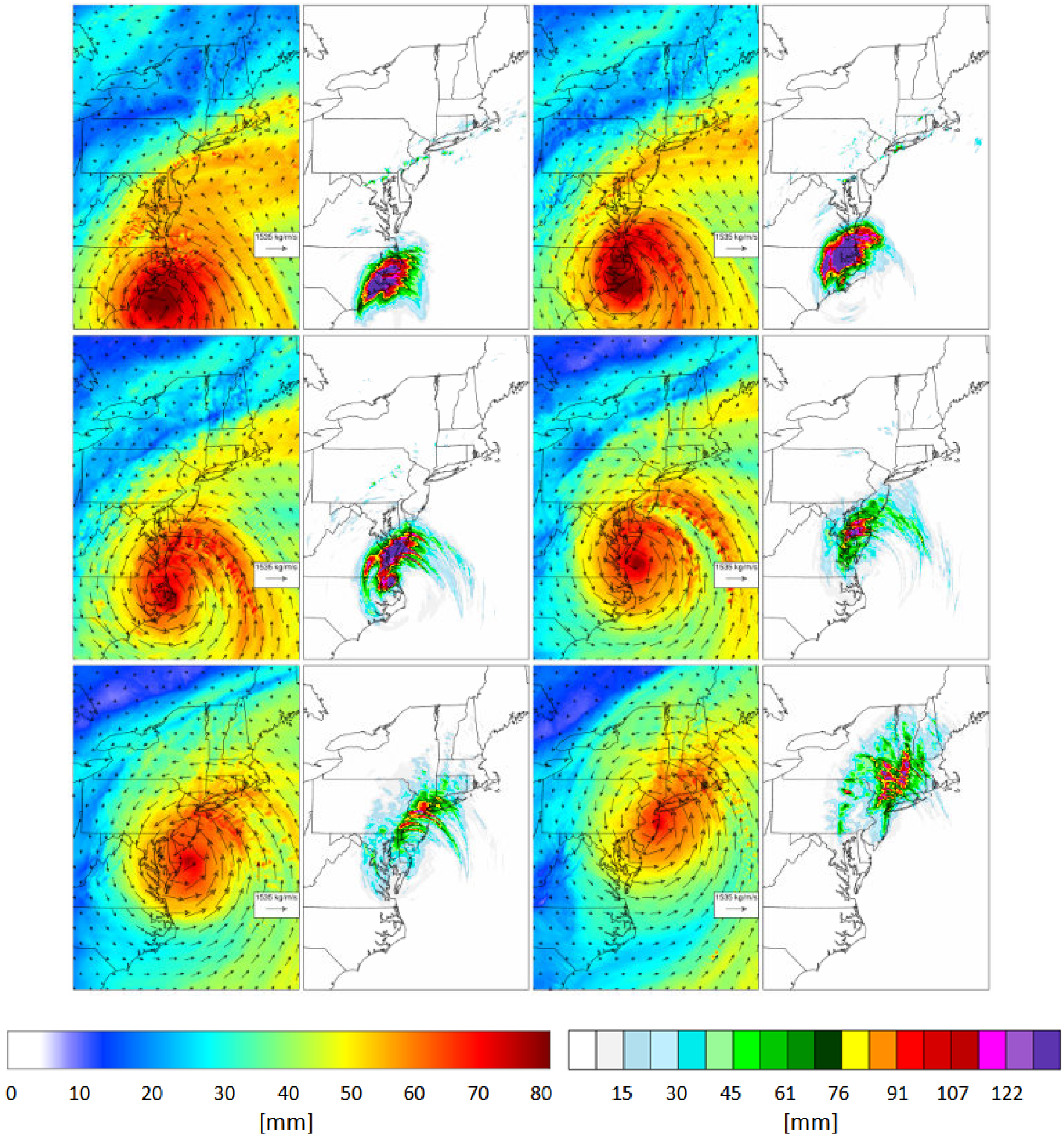

Figure B-23 6-Hourly Simulated Precipitable Water and Integrated Water Vapor Transport (Left) and its Corresponding 6-Hourly Accumulated Simulated Precipitation (Right) for Hurricane Irene

The sequence goes from 08/26 00h until 08/30 12h. The reference arrow in the white box (⟶) shows an IVT vector with a magnitude of 1535 kg m^{-1} s^{-1} (Continued).

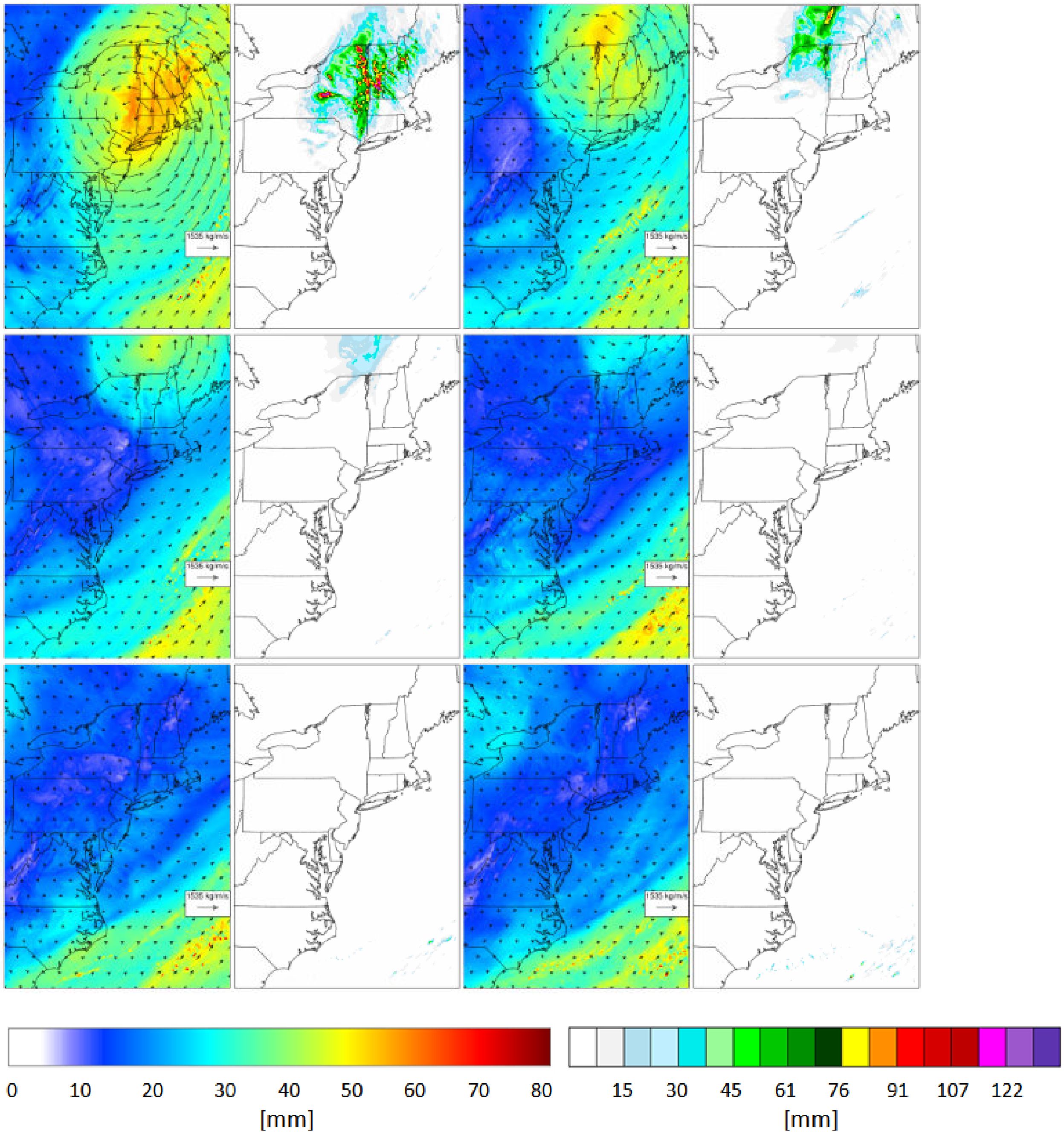

Figure B-23 6-Hourly Simulated Precipitable Water and Integrated Water Vapor Transport (Left) and its Corresponding 6-Hourly Accumulated Simulated Precipitation (Right) for Hurricane Irene

The sequence goes from 08/26 00h until 08/30 12h. The reference arrow in the white box (⟶) shows an IVT vector with a magnitude of 1535 kg m^{-1} s^{-1} (Continued).

B.2.10 Tropical Storm Lee (2011)

Figure B-24 shows the 6-hourly evolution of the reconstructed PW field and IVT field in TS Lee. It also shows the 6-hourly accumulated precipitation field associated with the PW and IVT.

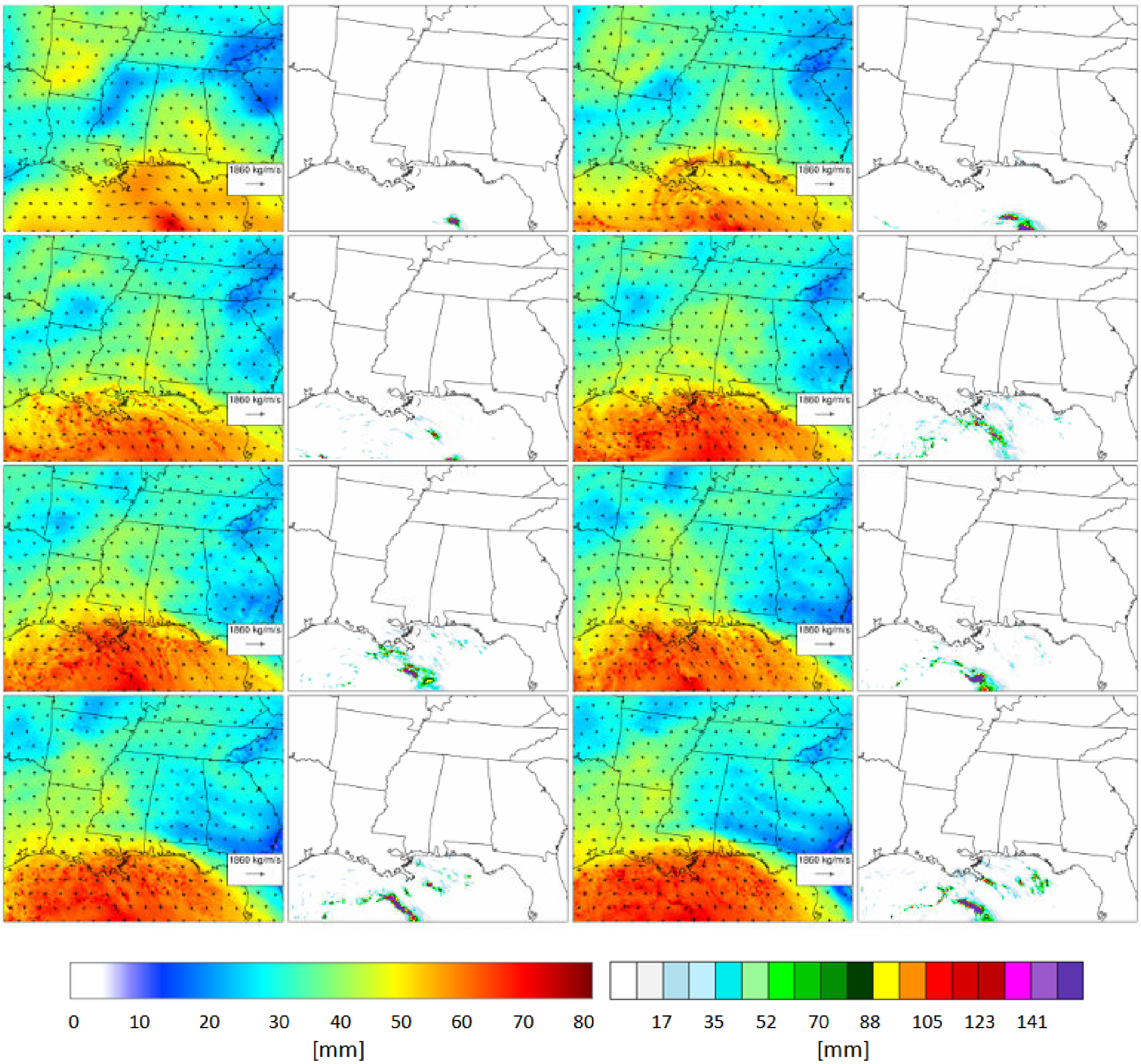

Figure B-24 6-Hourly Simulated Precipitable Water and Integrated Water Vapor Transport (Left) and its Corresponding 6-Hourly Accumulated Simulated Precipitation (Right) for TS Lee

The sequence goes from 09/01 00h until 09/07 00h. The reference arrow in the white box (⟶) shows an IVT vector with a magnitude of 1860 kg m^{-1} s^{-1}.

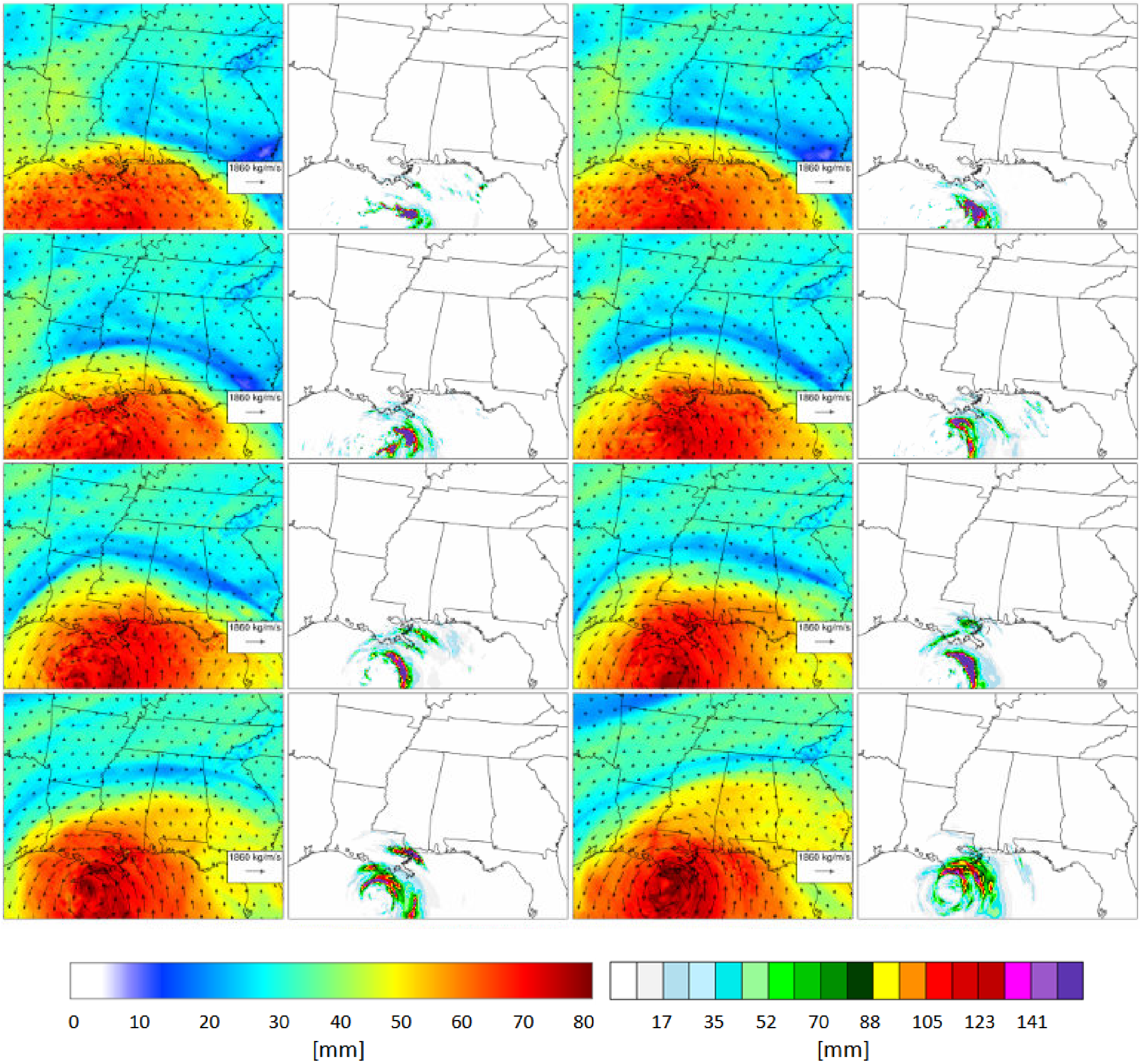

Figure B-24 6-Hourly Simulated Precipitable Water and Integrated Water Vapor Transport (Left) and its Corresponding 6-Hourly Accumulated Simulated Precipitation (Right) for TS Lee

The sequence goes from 09/01 00h until 09/07 00h. The reference arrow in the white box (⟶) shows an IVT vector with a magnitude of 1860 kg m^{-1} s^{-1} (Continued).

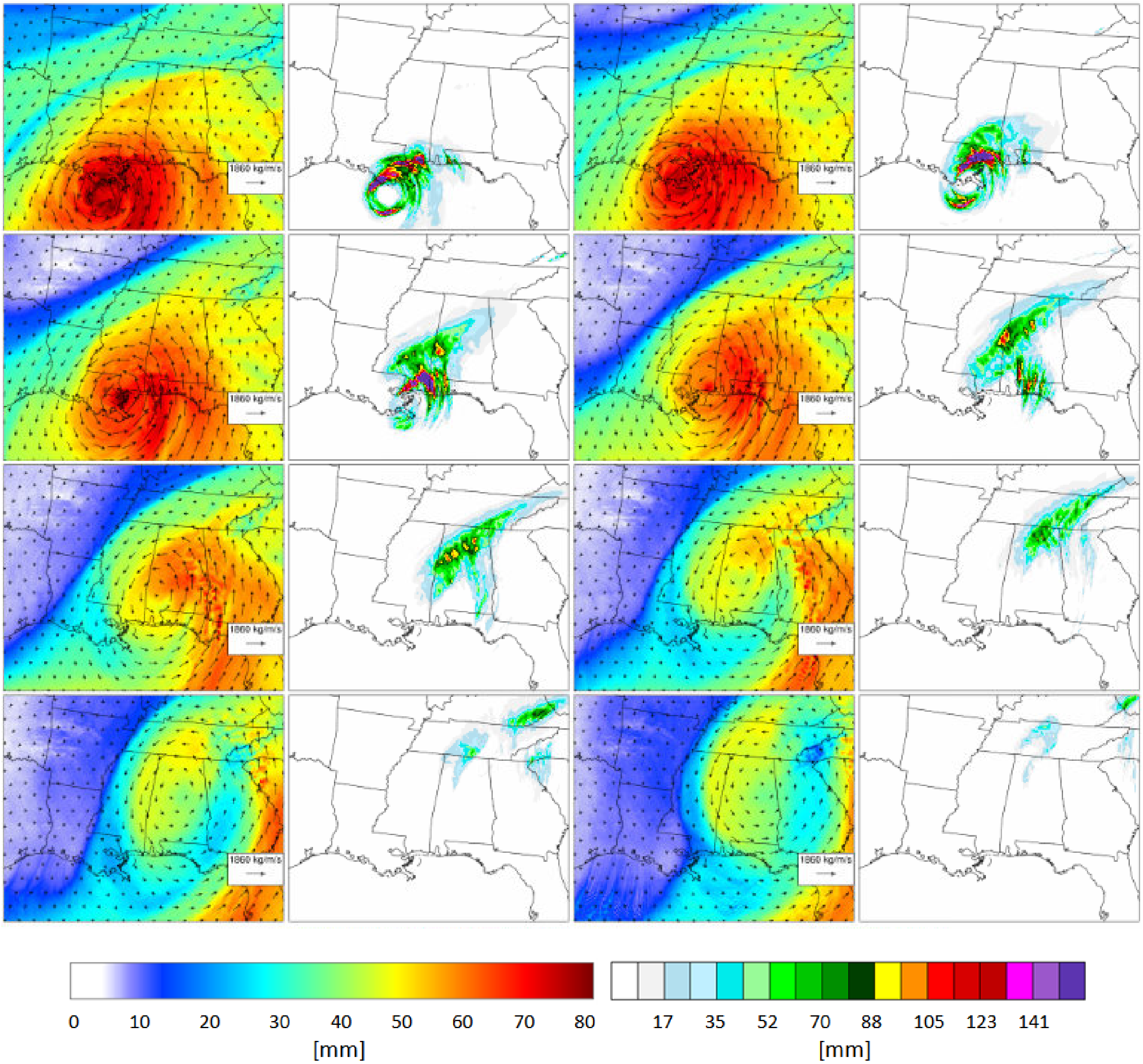

Figure B-24 6-Hourly Simulated Precipitable Water and Integrated Water Vapor Transport (Left) and its Corresponding 6-Hourly Accumulated Simulated Precipitation (Right) for TS Lee

The sequence goes from 09/01 00h until 09/07 00h. The reference arrow in the white box (⟶) shows an IVT vector with a magnitude of 1860 kg m^{-1} s^{-1} (Continued).

B.2.11 Hurricane Isaac (2012)

Figure B-25 shows the 6-hourly evolution of the reconstructed PW field and IVT field in Hurricane Isaac. It also shows the 6-hourly accumulated precipitation field associated with the PW and IVT.

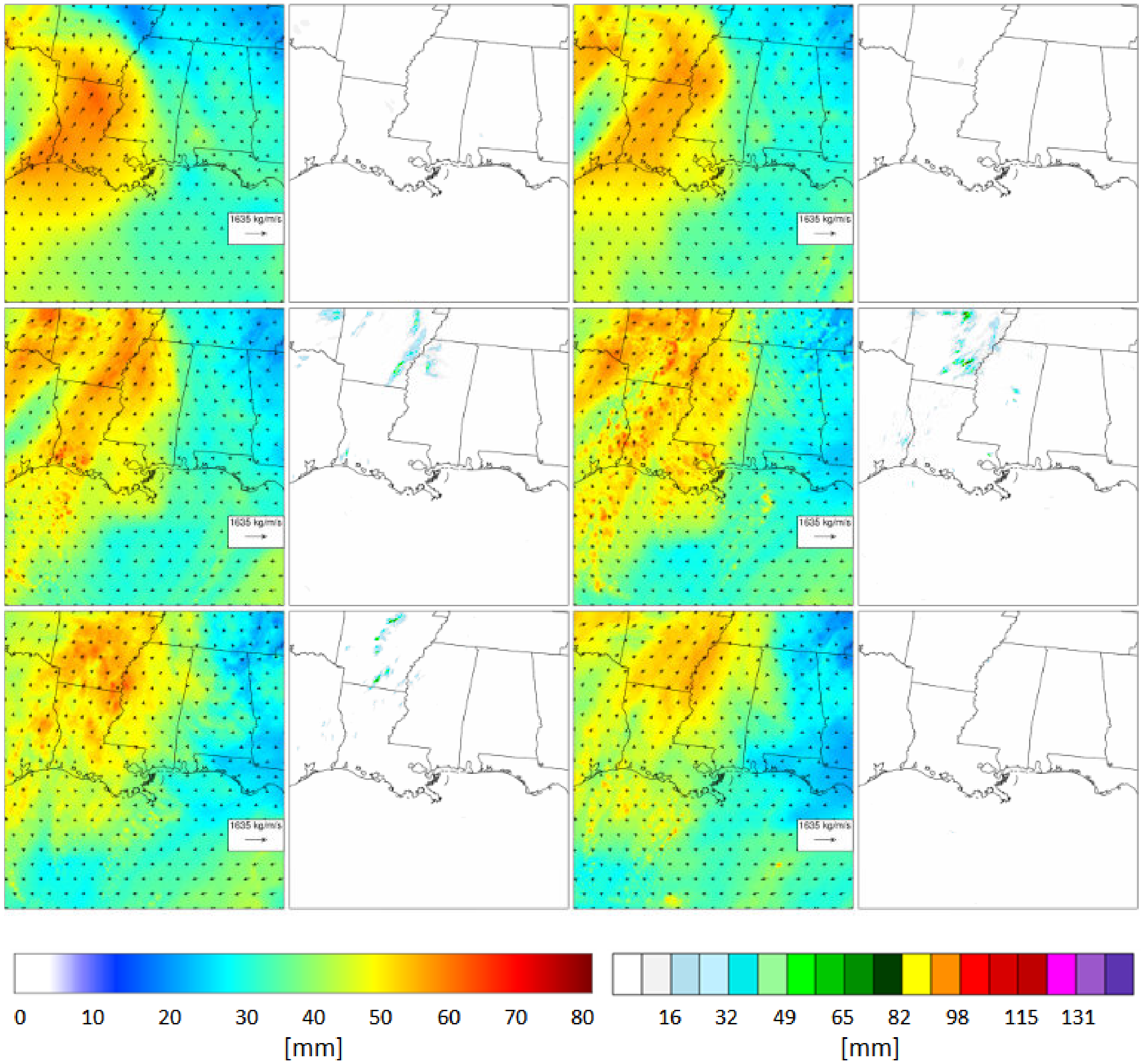

Figure B-25 6-Hourly Simulated Precipitable Water and Integrated Water Vapor Transport (Left) and its Corresponding 6-Hourly Accumulated Simulated Precipitation (Right) for Hurricane Isaac

The sequence goes from 08/25 00h until 09/04 12h. The reference arrow in the white box ( ) shows an IVT vector with a magnitude of 1635 kg m^{-1} s^{-1}.

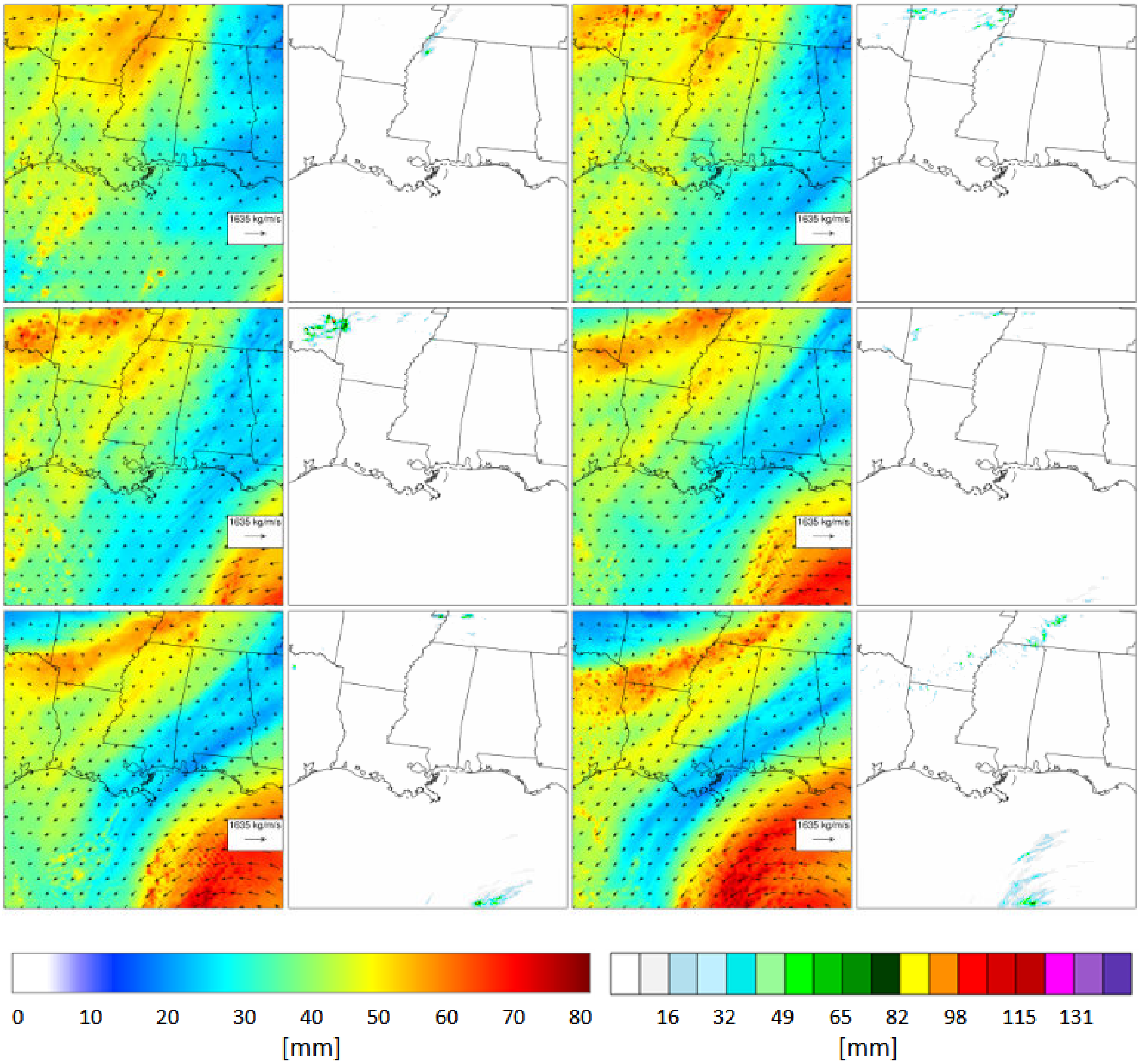

Figure B-25 6-Hourly Simulated Precipitable Water and Integrated Water Vapor Transport (Left) and its Corresponding 6-Hourly Accumulated Simulated Precipitation (Right) for Hurricane Isaac

The sequence goes from 08/25 00h until 09/04 12h. The reference arrow in the white box ( ) shows an IVT vector with a magnitude of 1635 kg m^{-1} s^{-1} (Continued).

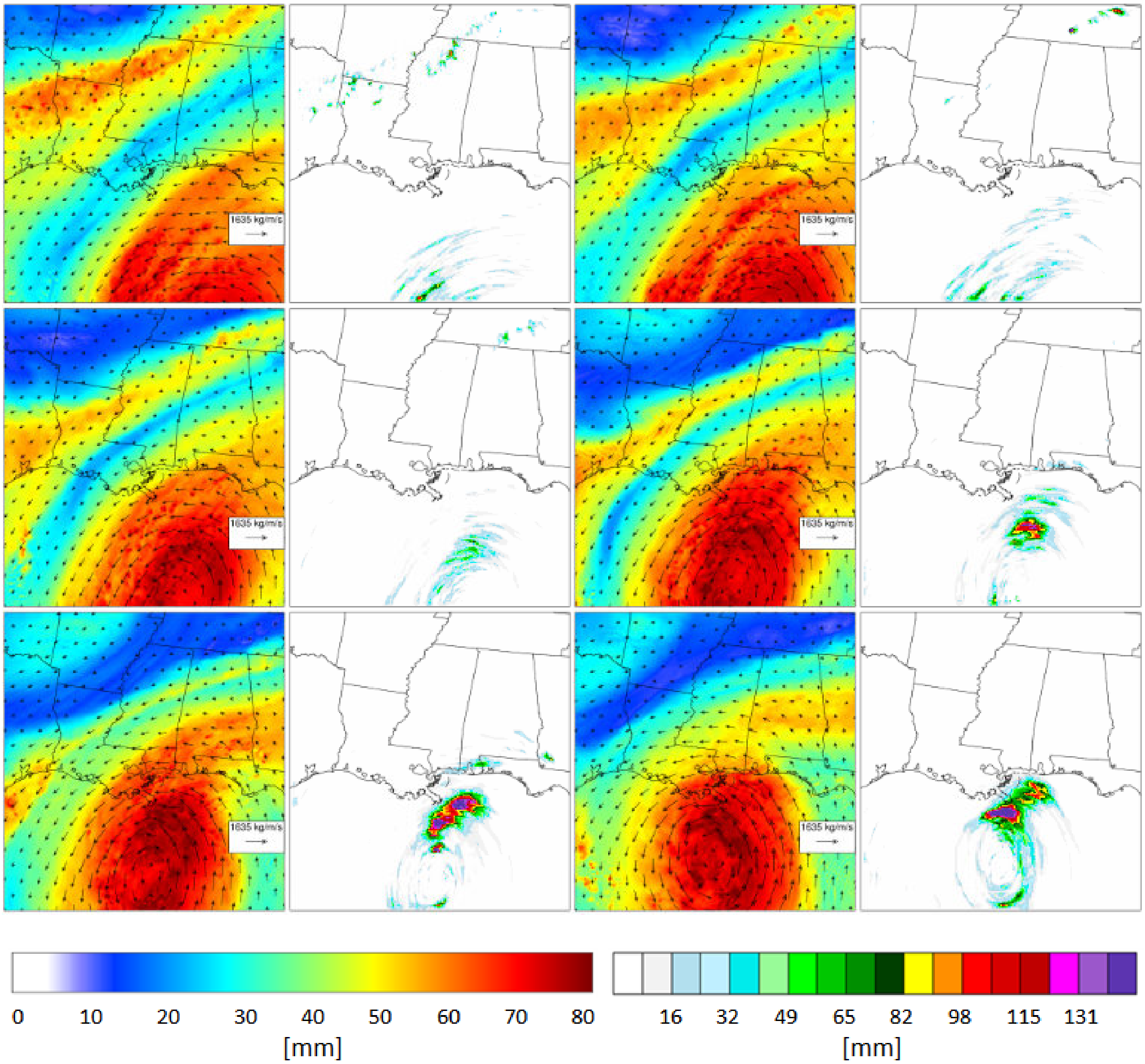

Figure B-25 6-Hourly Simulated Precipitable Water and Integrated Water Vapor Transport (Left) and its Corresponding 6-Hourly Accumulated Simulated Precipitation (Right) for Hurricane Isaac

The sequence goes from 08/25 00h until 09/04 12h. The reference arrow in the white box ( ) shows an IVT vector with a magnitude of 1635 kg m^{-1} s^{-1} (Continued).

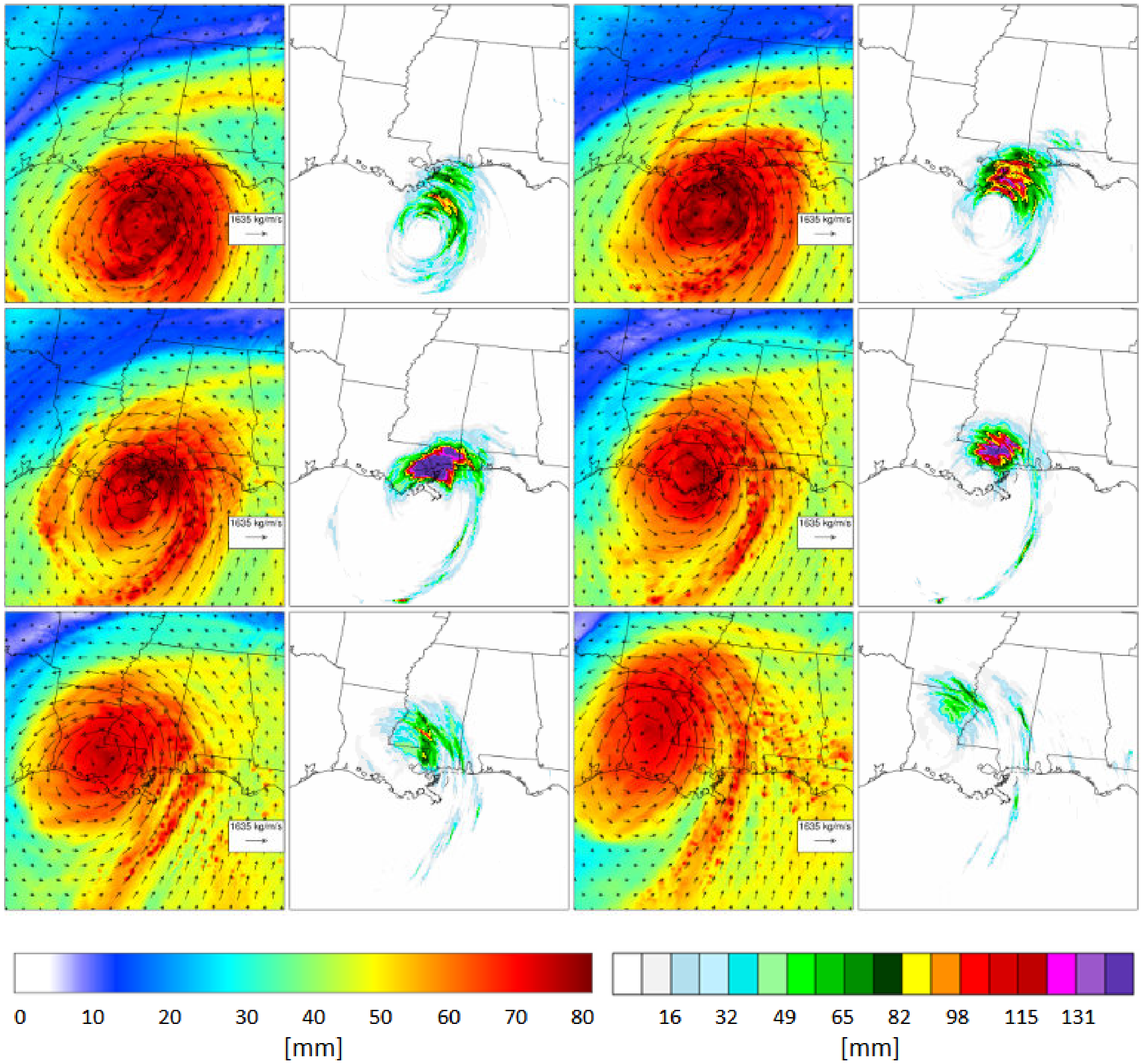

Figure B-25 6-Hourly Simulated Precipitable Water and Integrated Water Vapor Transport (Left) and its Corresponding 6-Hourly Accumulated Simulated Precipitation (Right) for Hurricane Isaac

The sequence goes from 08/25 00h until 09/04 12h. The reference arrow in the white box ( ) shows an IVT vector with a magnitude of 1635 kg m^{-1} s^{-1} (Continued).

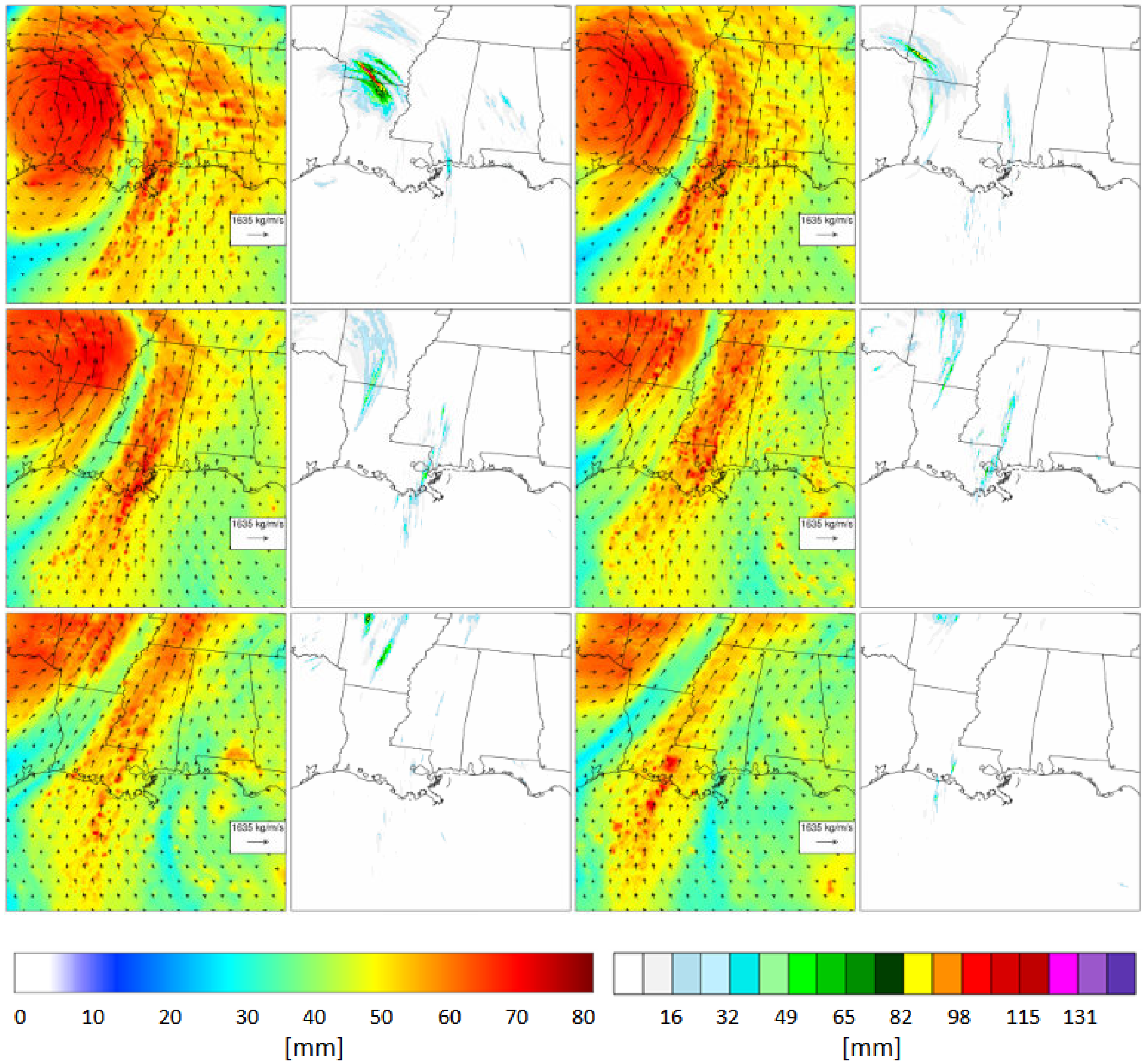

Figure B-25 6-Hourly Simulated Precipitable Water and Integrated Water Vapor Transport (Left) and its Corresponding 6-Hourly Accumulated Simulated Precipitation (Right) for Hurricane Isaac

The sequence goes from 08/25 00h until 09/04 12h. The reference arrow in the white box ( ) shows an IVT vector with a magnitude of 1635 kg m^{-1} s^{-1} (Continued).

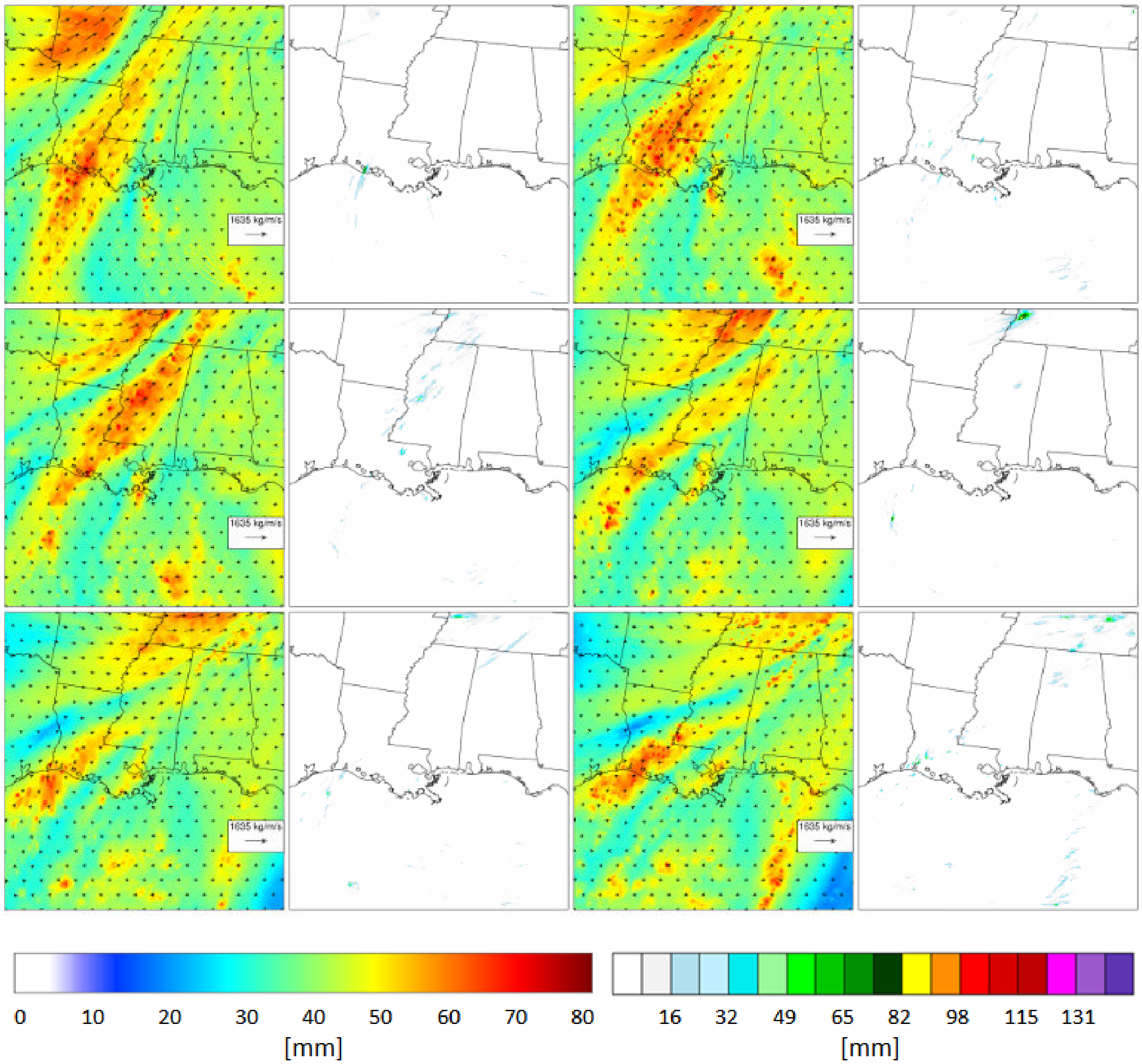

Figure B-25 6-Hourly Simulated Precipitable Water and Integrated Water Vapor Transport (Left) and its Corresponding 6-Hourly Accumulated Simulated Precipitation (Right) for Hurricane Isaac

The sequence goes from 08/25 00h until 09/04 12h. The reference arrow in the white box ( ) shows an IVT vector with a magnitude of 1635 kg m^{-1} s^{-1} (Continued).

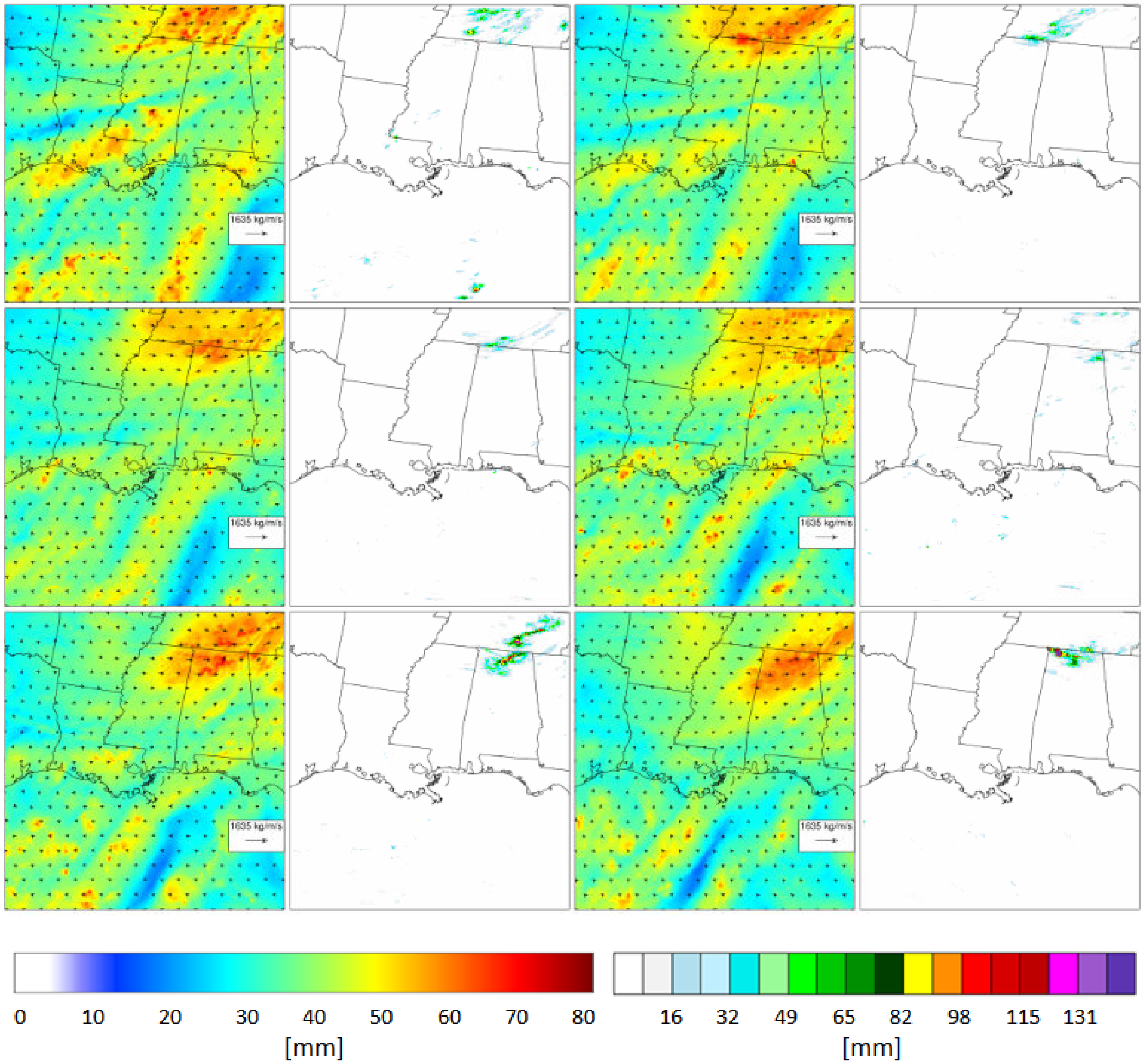

Figure B-25 6-Hourly Simulated Precipitable Water and Integrated Water Vapor Transport (Left) and its Corresponding 6-Hourly Accumulated Simulated Precipitation (Right) for Hurricane Isaac

The sequence goes from 08/25 00h until 09/04 12h. The reference arrow in the white box ( ) shows an IVT vector with a magnitude of 1635 kg m^{-1} s^{-1} (Continued).

B.2.12 Hurricane Sandy (2012)

Figure B-26 shows the 6-hourly evolution of the reconstructed PW field and IVT field in Hurricane Sandy. It also shows the 6-hourly accumulated precipitation field associated with the PW and IVT.

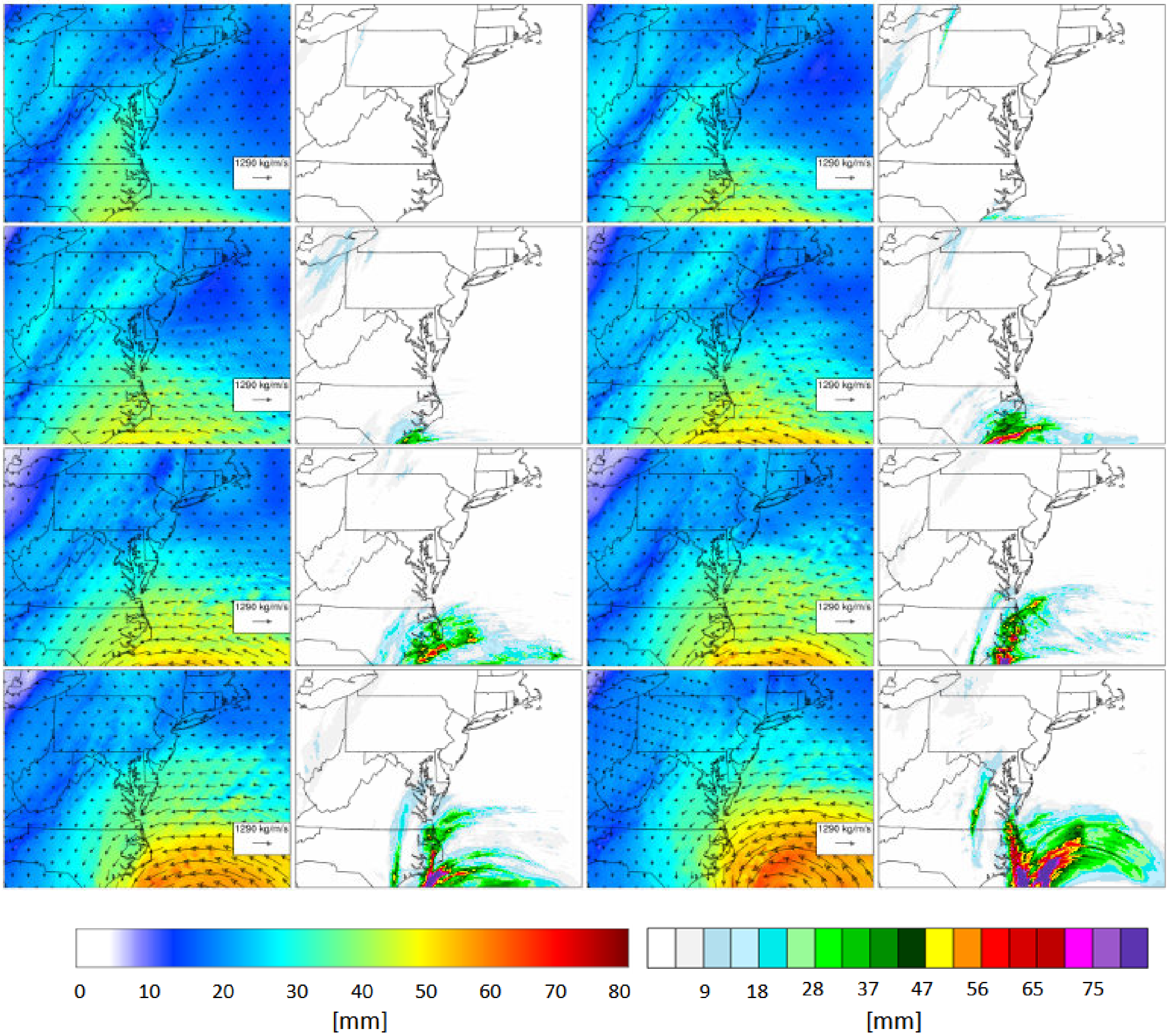

Figure B-26 6-Hourly Simulated Precipitable Water and Integrated Water Vapor Transport (Left) and its Corresponding 6-Hourly Accumulated Simulated Precipitation (Right) for Hurricane Sandy

The sequence goes from 10/27 00h until 10/31 12h. The reference arrow in the white box (⟶) shows an IVT vector with a magnitude of 1290 kg m^{-1} s^{-1}.

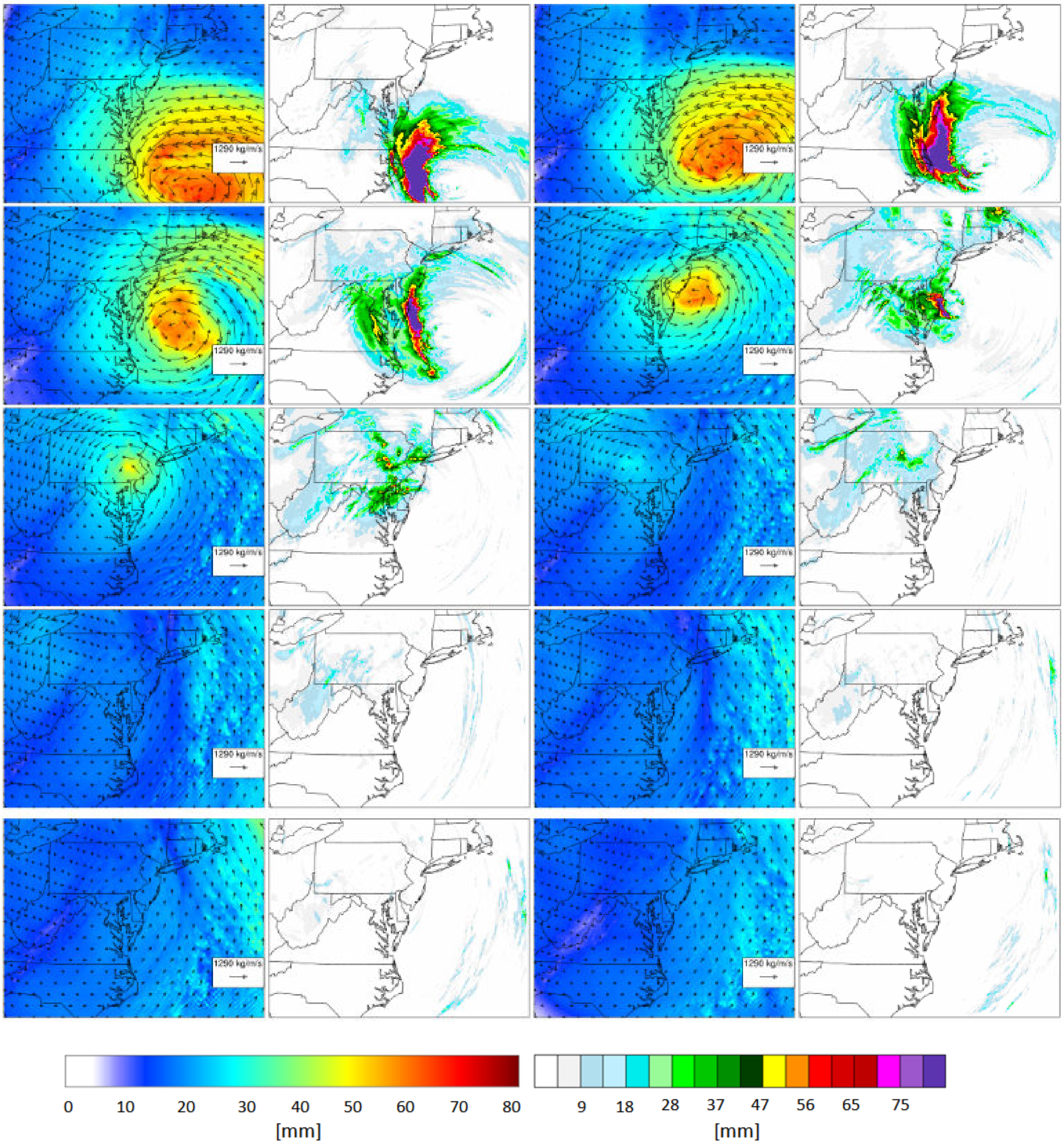

Figure B-26 6-Hourly Simulated Precipitable Water and Integrated Water Vapor Transport (Left) and its Corresponding 6-Hourly Accumulated Simulated Precipitation (Right) for Hurricane Sandy

The sequence goes from 10/27 00h until 10/31 12h. The reference arrow in the white box (⟶) shows an IVT vector with a magnitude of 1290 kg m^{-1} s^{-1} (Continued).

B.2.13 Hurricane Matthew (2016)

Figure B-27 shows the 6-hourly evolution of the reconstructed PW field and IVT field in Hurricane Matthew. It also shows the 6-hourly accumulated precipitation field associated with the PW and IVT.

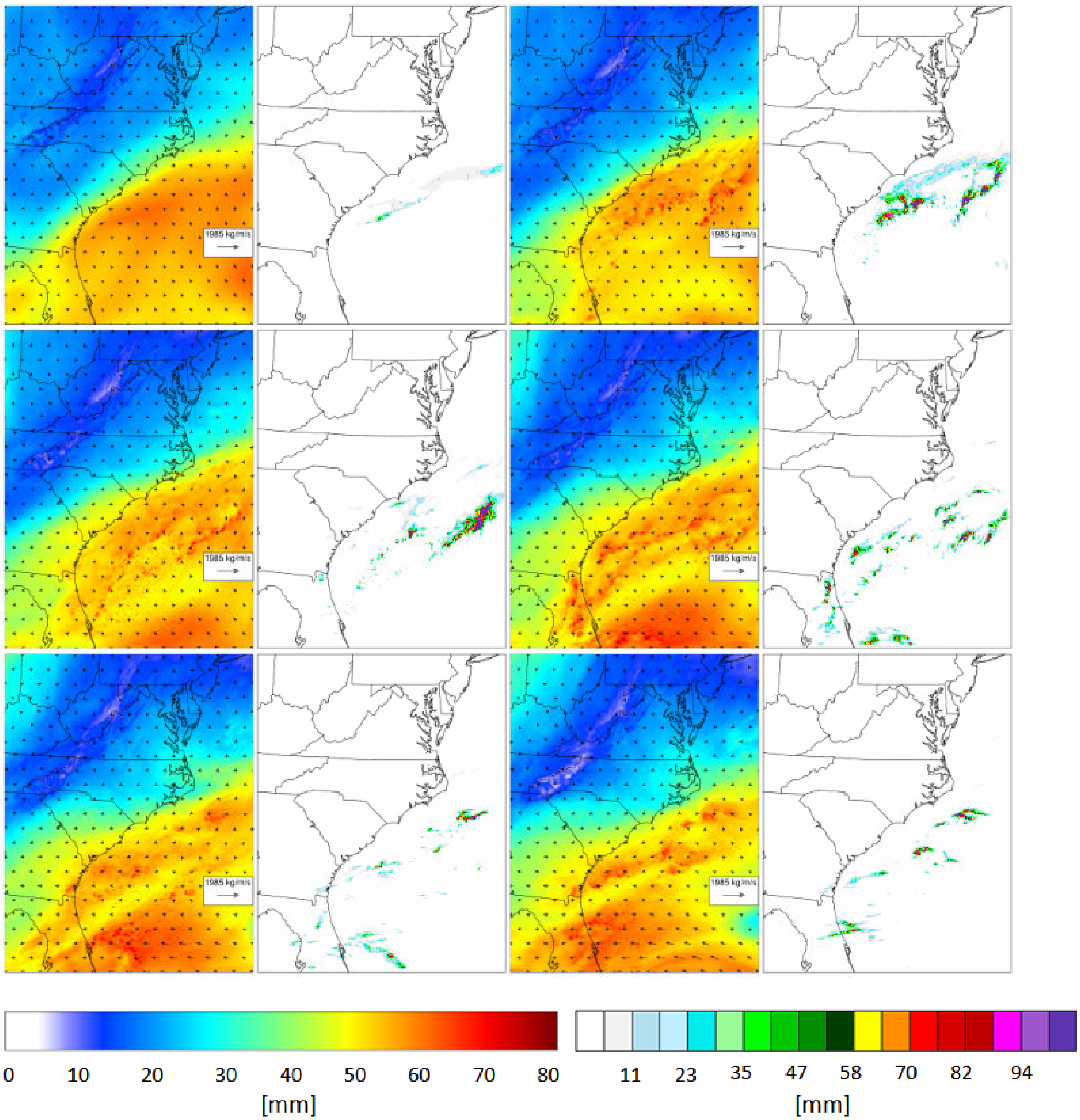

Figure B-27 6-Hourly Simulated Precipitable Water and Integrated Water Vapor Transport (Left) and its Corresponding 6-Hourly Accumulated Simulated Precipitation (Right) for Hurricane Matthew

The sequence goes from 10/05 00h until 10/10 00h. The reference arrow in the white box (⟶) shows an IVT vector with a magnitude of 1985 kg m^{-1} s^{-1}.

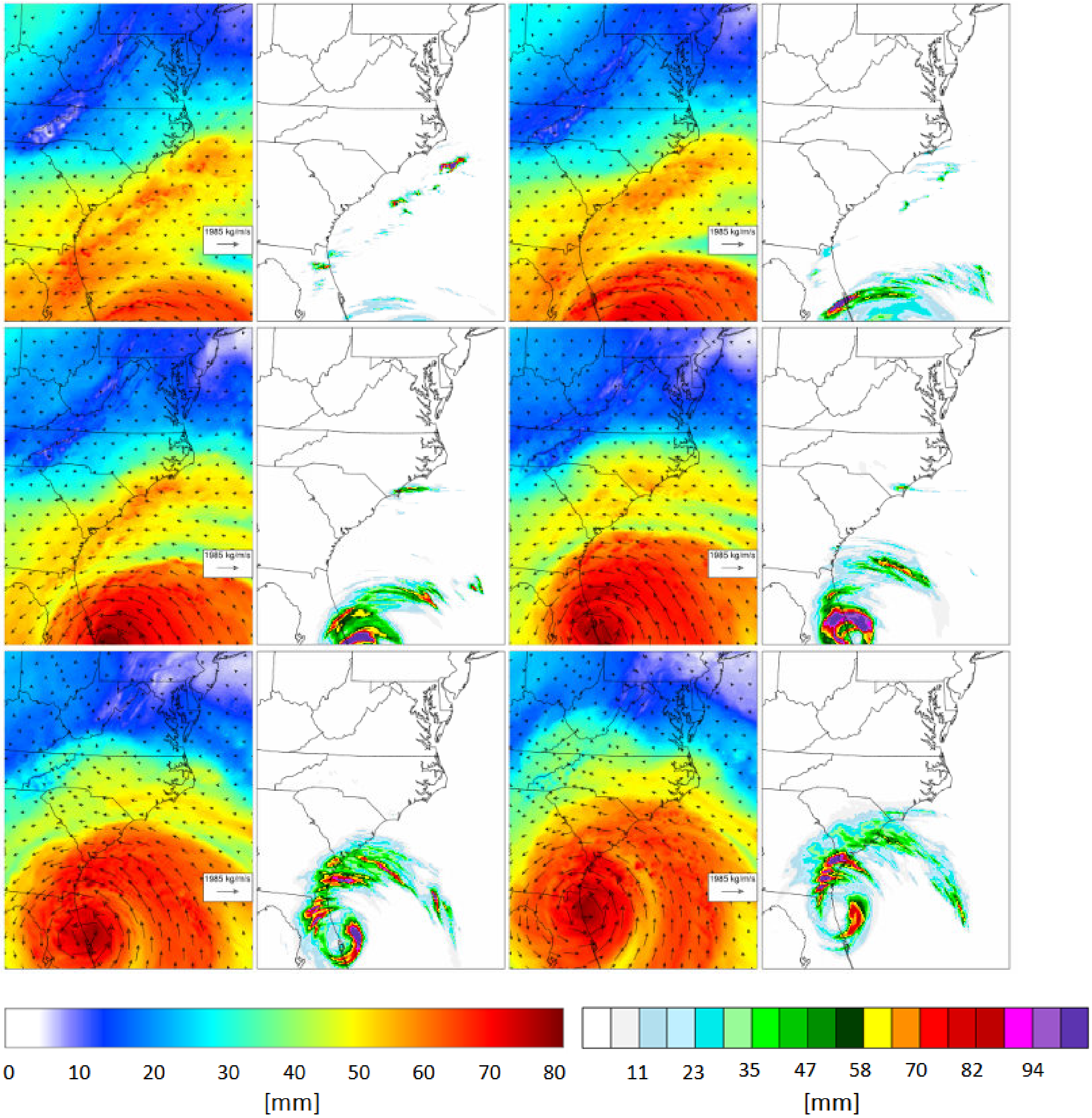

Figure B-27 6-Hourly Simulated Precipitable Water and Integrated Water Vapor Transport (Left) and its Corresponding 6-Hourly Accumulated Simulated Precipitation (Right) for Hurricane Matthew

The sequence goes from 10/05 00h until 10/10 00h. The reference arrow in the white box (⟶) shows an IVT vector with a magnitude of 1985 kg m^{-1} s^{-1} (Continued).

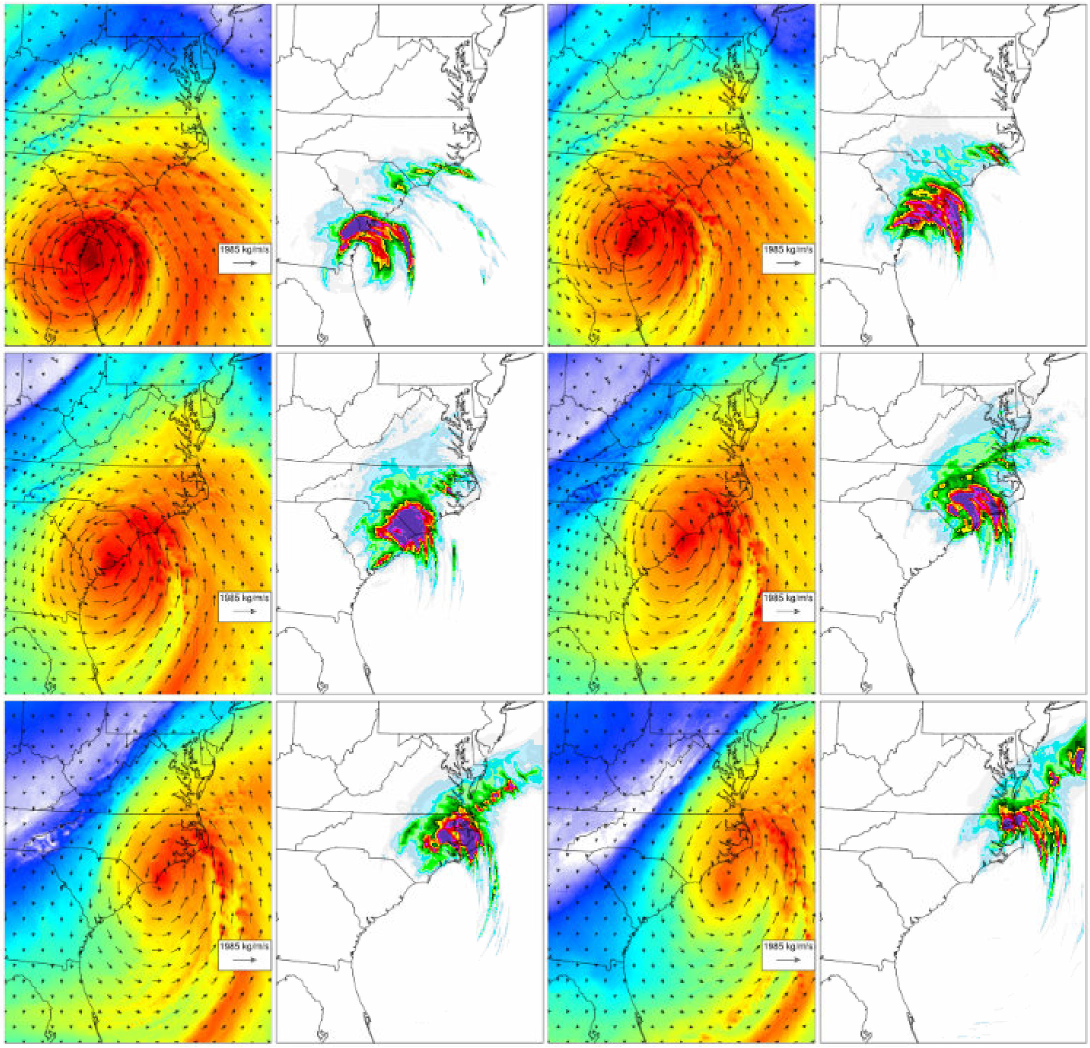

Figure B-27 6-Hourly Simulated Precipitable Water and Integrated Water Vapor Transport (Left) and its Corresponding 6-Hourly Accumulated Simulated Precipitation (Right) for Hurricane Matthew

The sequence goes from 10/05 00h until 10/10 00h. The reference arrow in the white box (→) shows an IVT vector with a magnitude of 1985 kg m^{-1} s^{-1} (Continued).

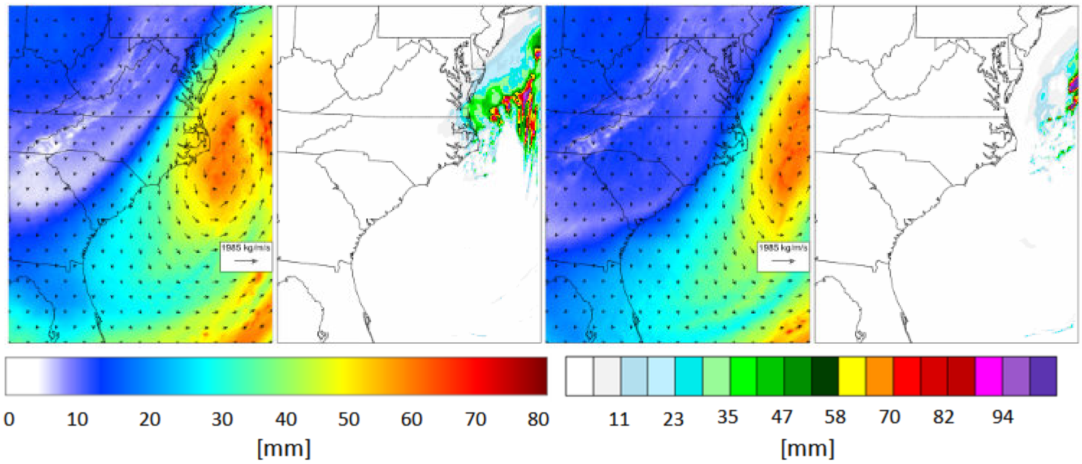

Figure B-27 6-Hourly Simulated Precipitable Water and Integrated Water Vapor Transport (Left) and its Corresponding 6-Hourly Accumulated Simulated Precipitation (Right) for Hurricane Matthew

The sequence goes from 10/05 00h until 10/10 00h. The reference arrow in the white box (⟶) shows an IVT vector with a magnitude of 1985 kg m^{-1} s^{-1} (Continued).

NRC FORM 335 (12-2010) NRCMD 3.7 — U.S. NUCLEAR REGULATORY COMMISSION	1. REPORT NUMBER (Assigned by NRC, Add Vol., Supp., Rev., and Addendum Numbers, if any.)
BIBLIOGRAPHIC DATA SHEET *(See instructions on the reverse)*	NUREG/CR-7287

2. TITLE AND SUBTITLE	3. DATE REPORT PUBLISHED	
Numerical Modeling of Local Intense Precipitation Processes	MONTH: July	YEAR: 2023
	4. FIN OR GRANT NUMBER	

5. AUTHOR(S)	6. TYPE OF REPORT
M. Levent Kavvas, Mathieu Mure-ravaud, Alain Dib, Kei Ishida	Technical
	7. PERIOD COVERED (Inclusive Dates)

8. PERFORMING ORGANIZATION - NAME AND ADDRESS (If NRC, provide Division, Office or Region, U. S. Nuclear Regulatory Commission, and mailing address; if contractor, provide name and mailing address.)

Hydrologic Research Laboratory
Department of Civil & Environmental Engineering, University of California, Davis
1 Shields Ave, Davis, CA 95616

9. SPONSORING ORGANIZATION - NAME AND ADDRESS (If NRC, type "Same as above", if contractor, provide NRC Division, Office or Region, U. S. Nuclear Regulatory Commission, and mailing address.)

Division of Risk Assessment
Office of Nuclear Regulatory Research
U.S. Nuclear Regulatory Commission
Washington, D.C. 20555-0001

10. SUPPLEMENTARY NOTES

E. Yegorova

11. ABSTRACT (200 words or less)

Tropical Cyclones (TCs) and Mesoscale Convective Systems (MCSs) are recognized for their ability to generate intense precipitation that may in turn create disastrous floods. In this study, the suitability of the Weather Research and Forecasting (WRF) model to simulate local intense precipitation processes within severe MCSs and TCs was first assessed. Simulation results were compared with observations from the Stage IV precipitation dataset. Under an appropriate choice of the model's options, the model could reproduce the location, intensity, and structure of the intense precipitation fields. Second, physically-based storm transposition methods for the storm transpositions of MCSs and TCs were developed and applied to one MCS and four TCs. In each case, the objective was to find the amount of shift which maximizes the precipitation depth over a target area. Finally, future conditions from a General Circulation Model were downscaled over two regions (one for MCSs and one for TCs). The most intense future MCS and TC were then transposed to maximize the precipitation depth over the target area.

12. KEY WORDS/DESCRIPTORS (List words or phrases that will assist researchers in locating the report.)	13. AVAILABILITY STATEMENT
Numerical modeling	unlimited
Intense precipitation	14. SECURITY CLASSIFICATION
Mesoscale Convective System	*(This Page)* unclassified
Tropical Cyclone	*(This Report)* unclassified
WRF model	
Dynamical downscaling	15. NUMBER OF PAGES
Storm transposition	
CFSR	16. PRICE
CCSM4	

UNITED STATES
NUCLEAR REGULATORY COMMISSION
WASHINGTON, DC 20555-0001

OFFICIAL BUSINESS

@NRCgov

NUREG/CR-7287 Numerical Modeling of Local Intense Precipitation Processes July 2023